RUSSIAN ACADEMY OF SCIENCES

INSTITUTE FOR PROBLEMS IN MECHANICAL ENGINEERING

Proceedings of the XXXVIII Summer School – Conference

ADVANCED PROBLEMS IN MECHANICS

A P M 2 0 1 0

St. Petersburg (Repino)

July 1 – 5, 2010



http://apm-conf.spb.ru

St. Petersburg, 2010

GENERAL INFORMATION SCIENTIFIC COMMITTEE AND EDITORIAL BOARD

- **H. Altenbach** (Martin-Luter University Halle Wittenberg, Germany)
- **V. V. Beletsky** (Keldysh Institute of Applied Mathematics RAS, Moscow, Russia)
- **A. K. Belyaev** (IPME RAS, St. Petersburg, Russia)
- **E. K. Bezoyan** (Yerevan State University, Armenia)
- **I. I. Blekhman** (IPME RAS, Mekhanobr-tekhnika Corp., St. Petersburg, Russia)
- **M. Cartmell** (University of Glasgow, UK)
- **A. Castellanos** (University of Seville, Spain)
- **E. P. Chen** (Sandia National Laboratories, Livermore, USA)
- **V. A. Eremeyev** (Southern Scientific Center of RAS, Rostov State University, Rostov-on-Don, Russia)
- **A. B. Freidin** (IPME RAS, St. Petersburg, Russia)
- **S. N. Gavrilov** (IPME RAS, St. Petersburg, Russia)
- **J. Goddard** (University of California at San Diego, USA)
- **I. G. Goryacheva** (Institute for Problems in Mechanics RAS, Moscow, Russia)
- **E. F. Grekova** (IPME RAS, St. Petersburg, Russia)
- **D. Harris** (University of Manchester, UK)
- **D. A. Indeitsev** (IPME RAS, St. Petersburg, Russia) — *Co-Chairman*
- **H. Irschik** (Johannes Kepler University of Linz, Austria)
- **B. L. Karihaloo** (Institute of Theoretical, Applied and Computational Mechanics, UK)
- **A. M. Krivtsov** (St. Petersburg State Polytechnical University, IPME RAS, Russia) — *Co-Chairman*
- **O. S. Loboda** (St. Petersburg State Polytechnical University, IPME RAS, Russia) — *Scientific Secretary*
- **E. V. Lomakin** (Moscow State University, Russia)
- **A. Metrikine** (TU Delft, The Netherlands)
- **N. F. Morozov** (St. Petersburg State University, IPME RAS, Russia)
- **V. A. Palmov** (St. Petersburg State Polytechnical University, Russia)
- **E. Pavlovskaia** (University of Aberdeen, UK)
- **S. H. Sargsyan** (National Academy of Sciences, Armenia)
- **E. N. Vilchevskaya** (St. Petersburg State Polytechnical University, IPME RAS, Russia)
- **V. A. Vladimirov** (University of Hull, UK)
- **M. Wiercigroch** (University of Aberdeen, UK)
- **M. V. Zakrzhevsky** (Institute of Mechanics Riga Technical University, Latvia)

© IPME RAS, 2010

PREFACE

Dear Reader,

in this book you will find the Proceedings of the Summer School Conference "Advanced Problems in Mechanics (APM) 2010". The conference had been started in 1971. The first Summer School was organized by Prof. Ya.G. Panovko and his colleagues. In the early years the main focus of the School was on nonlinear oscillations of mechanical systems with a finite number of degrees of freedom. Since 1994 the Institute for Problems in Mechanical Engineering of the Russian Academy of Sciences organizes the Summer School. The traditional name of "Summer School" has been kept, but the topics covered by the School have been much widened, and the School has been transformed into an international conference. Now it is held under the patronage of the Russian Academy of Sciences. The topics of the conference cover now almost all fields of mechanics, being concentrated around the following main scientific directions:

— aerospace mechanics;
— computational mechanics;
— dynamics of rigid bodies and multibody dynamics;
— fluid and gas;
— mechanical and civil engineering applications;
— mechanics of media with microstructure;
— mechanics of granular media;
— nanomechanics;
— nonlinear dynamics, chaos and vibration;
— molecular and particle dynamics;
— phase transitions;
— solids and structures;
— wave motion.

The Summer School – Conference has two main purposes: to gather specialists from different branches of mechanics to provide a platform for cross-fertilization of ideas, and to give the young scientists a possibility to learn from their colleagues and to present their work. Thus the Scientific Committee encouraged the participation of young researchers, and did its best to gather at the conference leading scientists belonging to various scientific schools of the world.

We believe that the significance of Mechanics as of fundamental and applied science should much increase in the eyes of the world scientific community, and we hope that APM conference makes its contribution into this process.

We are happy to express our sincere gratitude for a partial financial support to Russian Foundation for Basic Research, Russian Academy of Sciences, and St. Petersburg Scientific Center. This support has helped substantially to organize the conference and to increase the participation of young researchers.

We hope that you will find the materials of the conference interesting, and we cordially invite you to participate in the coming APM conferences. A part of the papers published in this Volume is planed to be published in Materials Physics and Mechanics Journal by agreement between APM 2010 organizers and Editors of Materials Physics and Mechanics. You may find the information on the future "Advanced Problems in Mechanics" Schools Conferences at our websites:

http://apm-conf.spb.ru

With kind regards,

Co-Chairmens of APM 2010

Dmitri A. Indeitsev, Anton M. Krivtsov

Contents

A. V. Abdrashitov, K. P. Zolnikov, S. G. Psakhie. Simulation of dusty plasma shape and structure in ground state at different configuration of confinement 12

E. L. Aero, A. N. Bulygin, Yu. V. Pavlov. Functionally invariant solutions of sine-Gordon equation with variable amplitude 17

M. A. Antimonov, A. V. Cherkaev, A. B. Freidin. On transformation surfaces construction for phase transitions in deformable solids 23

O. V. Antonova, A. I. Borovkov, A. A. Michailov, I. B. Voynov. The method of determination of thrust bearing pad angle in a fluid flow 30

R. A. Arutyunyan, K. S. Yakimova. Fatigue fracture of aging elastic viscous materials subjected to cyclic compression 35

I. Asonov, I. Berinskiy, J. Ing, A. Krivtsov, S. Le-Zakharov, E. Pavlovskaia, M. Wiercigroch. Brittle fracture of rocks under oblique impact loading 41

J. T. Assis, V. I. Monin, S. M. Iglesias. Application of X-ray tensometry for study of superficial stresses with strong gradient 48

S. V. Astafurov, E. V. Shilko, V. V. Sergeev, S. G. Psakhie. Investigation of influence of nonequiaxial compression on general features of mechanical response of shearing fault zones .. 55

N. V. Banichuk, S. Yu. Ivanova, E. V. Makeev. Contact Optimization Problems with Uncertainties 61

A. Belyaev, D. Indeitsev, V. Polyanskiy, Yu. Yakovlev. Two-continuum models of the dissolved hydrogen influence on strength of materials 67

R. Birikh, A. Mizev, M. Denisova. Development and stability of a convective mass transfer induced by local heterogeneity of surface-active substance distribution near a free liquid surface 72

V. A. Bogoyavlenskaya, Ig. N. Shardakov. Estimation of surface deformation sensitivity to changes in the characteristic parameters of the volcanic system 79

V. Bratov. Numerical implementation of the incubation time fracture criterion 87

C. A. Bushueva, K. G. Kostarev. Dynamics of a ferrofluid layer with a stable rupture of the surface 98

C. A. Bushueva, M. O. Denisova, K. G. Kostarev, A. V. Shmyrov. Terrestrial modeling of surfactant diffusion through the drop-surrounding fluid interface 105

N. Y. Bykov, D. V. Leshchev. Kinetic model of water clusters formation and growth in rarefied gas flows 113

M. V. Cherkay. Relay control in noisy vibration systems 118

N. V. Chertova, Yu. V. Grinyaev. Waves process in media with defects 122

S. A. Chivilikhin. Evolution of free surface of high viscous liquid due to capillary forces 130

Yu. A. Chumakov, A. G. Knyazeva. The stressedly-deformed state of porous burner apparatus under different gas filtration combustion regimes 134

S. Cresseri, F. Genna. Numerical analysis of thrust on structures for active defense against avalanches 140

M. O. Denisova, K. G. Kostarev. The onset of solutocapillary convection in water-alcohol systems 147

A. I. Dmitriev, W. Oesterle, H. Kloss. The influence of copper on tribological characteristics of automotive pad-disc interface. Results of nano-scale modeling 155

A. A. Dobroskok, A. M. Linkov. Two-stage BEM for efficient solving transient thermo-(poro-) elastic problems 161

P. Dyatlova, A. Majorov, V. Lutov. On the problem of interaction between the soft shell and the solid covered by it 165

P. Dyatlova, V. Lutov, E. Polyakova. The strain-stressed state of the band winded up on the ridged body 169

M. J. Espín, M. A. S. Quintanilla, J. M. Valverde, A. Castellanos. Jamming transition and tensile strength of magnetic stabilized fluidized beds 175

S. E. Evlampieva, V. V. Moshev. Role of relaxation in formation of cyclic resistance of elastomeric nanocomposites 185

N. K. Evstigneev, A. G. Knyazeva. Simulation of intermetallic compound synthesis during solid-phase extrusion through a tapered die 189

N. N. Fedorova, I. A. Fedorchenko, M. A. Goldfeld, Yu. V. Zakharova. Supersonic flows in channel of variable cross-section with mass supply 195

A. N. Fedorova, M. G. Zeitlin. Quantum mechanics at different scales. Part 1: Resolution of a (quantum) point 202

A. N. Fedorova, M. G. Zeitlin. Quantum mechanics at different scales. Part 2: Localization, multiscales and complex quantum patterns 211

M. Yu. Filimonov, A. G. Kravets, N. A. Vaganova. Simulation of thermal interaction in a zone of extractive well in permafrost 220

A. B. Freidin, D. O. Kucheyeva. The influence of external strains and material parameters on the kinetics of stationary moving interfaces 225

O. K. Garishin. Polymer/silicate nanocomposites. Nonlinear elastoplastic model with damage accumulation under deformation 231

S. O. Gladkov, S. B. Bogdanova. To the theory of longitudinal magnetic susceptibility in fractal magnets 236

A. L. Glazov, K. L. Muratikov. Comparison of thermoelastic stress analysis and photoacoustic microscopy approaches to the problem of residual stress detection 238

L. A. Golotina, Ig. N. Shardakov. Investigation of the influence of relaxation transition in the amorphous component of amorphous-crystalline polymer on deformation processes 247

V. N. Hakobyan. Contact problem for elastic wedge strengthened by rigid inclusion 253

Wm. G. Hoover, C. G. Hoover, F. Uribe. Flexible macroscopic models for dense-fluid shock-waves: partitioning heat and work; delaying stress and heat flux; two-temperature thermal relaxation 261

J. S. Hoving, A. V. Metrikine. On the coupling of nonlinear discrete element models with continua in the time domain 274

J. Ing, E. Pavlovskaia, M. Wiercigroch, I. Asonov, I. Berinskiy. Particle dynamics to model brittle rocks 282

K. S. Ivanov. Vibrational translation due to transversal strain in a Chelomei pendulum-like system 289

I. P. Kikot, E. A. Zubova, M. A. Mazo, N. A. Kovaleva, L. I. Manevitch. About constructing the new coarse-grained DNA model 299

A. A. Kireenkov. Coulomb law in the generalized differential form in problem about torsion oscillations of the cylindrical rod on the infinite belt 307

A. A. Kireenkov, S. V. Semendyaev. The experimental determination of the coefficients of the coupled two-dimensional model of the combined dry friction 313

G. Kitavtsev, B. Wagner. Critical slippage for droplet migration in nanometric liquid films ... 319

A. G. Knyazeva, S. N. Sorokova. Self-similar regimes of solid phase conversions in media of various rheology 325

L. A. Komar, S. N. Lebedev. Formation of polymer nanofiber in the gap between filler particles in deformed elastomeric nanocomposites 335

Ig. S. Konovalenko, A. I. Dmitriev, A. Yu. Smolin, S. G. Psakhie. Numerical study of the influence of parameters of defects on the strength properties of brittle coating 339

Iv. S. Konovalenko, D. S. Kryzhevich, K. P. Zolnikov, S. G. Psakhie. Investigation of structure-phase changing in titanium crystallite under different rate mechanical loading 346

M. A. Kovaleva, L. I. Manevitch. Localized and periodic solutions of the Oregonator model of BZ reaction 352

N. V. Kozlov, S. V. Subbotin. Vibrational dynamics of a spherical body in a rotating cylinder with liquid 357

A. M. Krivtsov. Molecular dynamics study of chemically induced phase transformation 363

A. M. Kudarova, A. V. Metrikine. On the use of gradient continua for minimizing the wave reflection at a discrete-continuum interface 375

A. M. Kudarova, A. M. Krivtsov. Description of equivalent elastic continuum for graphene lattice 383

V. A. Kuzkin. Comment on the calculation of forces for multi-body interatomic potentials 391

C. Kröner, H. Altenbach, K. Naumenko, A. Kutschke. Generalised Fractional Elements in Rheological Modelling of Polymer Creep 398

T. B. Lavrova. The extent of softening that can be achieved under stable deformation with the Tresca elastic-plastic material 405

A. I. Lutsik, A. I. Mizev. Dynamics of a surface subphase formation in a multicomponent surfactant solution 408

E. V. Lubimov, A. A. Dyda. Symbolic synthesis of control laws for underwater vehicle and robot manipulator 414

O. N. Lyubimova, K. N. Pestov, E. A. Gridasova. Numerical solution of problem fusion penetration metal, when glass welds with metal by diffusion welding 419

A. E. Mamontov. On existence and uniqueness of solutions in several boundary-value problems for the Euler equations 426

L. I. Manevitch. Limiting phase trajectories and "wave – particle" duality in Classical Physics 432

A. V. Manzhirov, S. A. Lychev. Finite deformations of accreted solids 444

A. B. Melentyev, Eu. L. Tarunin. Modulation of gravity in problem of free convection 453

B. E. Melnikov, A. S. Semenov. Multimodel analysis of elasto-plastic problem under complex loading programs 457

M. A. Mikolaychuk, A. G. Knyazeva. Influence mechanisms of strains and stresses to diffusion in loaded plate 464

I. A. Morozov, A. L. Svistkov, O. K. Garishin, O. S. Gileva, E. S. Erofeeva. Investigation of the influence of bleaching on human teeth enamel microstructure 471

N. F. Morozov, P. E. Tovstik. Volume and surface stability of a transversely isotropic material 476

A. Yu. Nikonov, A. I. Dmitriev. Study of the influence of the structure of grain boundaries on their behavior under shear loading 491

S. Palis, F. Palis. Mechanical system simulation via automatic differentiation 498

D. A. Parshin. The stress-strain state of a cylindrical vault built by using a centering 506

M. Perelmuter. Bridged cracks growth criterion 512

S. V. Petinov, I. M. Afanasyeva. Fatigue assessment of structures in high-cycle segment: technique and problems 519

A. Platonov, V. Vitkov, L. Inieva-Mitusova, N. Serbenyuk, O. Trifonov, V. Yaroshevskiy. A high sensitivity device for measuring bio-electrical impedance of human skin 526

M. Podolsky. Direct tensor calculus in the problem of mechanical energy dissipation in fluids . 536

E. Polyakova, V. Lutov, V. Chaikin. On the problem of soft toroidal shells designing 540

A. Polyanskiy, V. Polyanskiy, E. Chernyaeva, Yu. Yakovlev. "SMART Hydrogen" and its determination in micro and nanostructures in materials 545

S. Polyanskiy. The Fourier series expansion in the thermal stress problem on rotating work rolls during hot rolling 551

I. Yu. Popov, O. A. Rodygina, S. A. Chivilikhin, V. V. Gusarov. Solitons and flow in nanotube . 558

M. A. Potapenko. Improvement of the dynamic behaviours of the plant with self synchronizing vibroexciters by means of additional degrees of freedom 561

E. V. Prozorova. Influence the dispersion in nonequilibrium models for continuous mechanics . 568

N. V. Roman, A. Yu. Smolin, I. S. Konovalenko, S. G. Psakhie. Influence of porosity percolation on strength and elastic properties of ceramic materials. 3D simulation using movable cellular automata method 575

E. I. Ryzhak. Ever-topical questions regarding the "ever-Hookean" material 581

S. A. Sazhenkov. Kinetic formulation for the Darcy-Stefan problem on phase transitions in a saturated porous ground 584

V. D. Schipitsyn, A. A. Ivanova. Vibrational lift force acting the cylinder in viscous liquid 591

E. V. Semenko. The force on aerofoil in steady irrotational flow with immobile point vortex . . 597

V. V. Sergeev, A. Yu. Smolin, S. Yu. Korostelev, S. A. Dobrinin. Modeling tribospectroscopy using movable cellular automata 603

V. V. Shadrin, L. A. Komar, G. P. Bashin. Effect of temperature and filler concentration on the dynamic characteristics of polyethylene-based nanocomposites 607

M. V. Shamolin. Dynamical systems with various dissipation: background, methods, applications 612

D. S. Shepelev, V. V. Smirnov, L. I. Manevich. Energy exchange and transition to localization in asymmetric Fermi-Pasta-Ulam oscilliatory chain 622

E. V. Shilko, S. V. Astafurov, A. S. Grigoriev, S. G. Psakhie. Study of features of deformation response of interfacial zones in block-structured medium to low-amplitude dynamic mechanical actions 631

N. N. Smirnov, V. F. Nikitin, V. A. Nerchenko, P. Andreini, G. Manzini. Water droplet non-equilibrium interaction with flame zone 638

M. N. Smirnova, K. A. Kondrat'ev, A. V. Zvyaguin. Wave formation on free surface on interaction with a body moving under free surface 651

A. Yu. Smolin, A. I. Dmitriev, S. A. Dobrynin, E. A. Kolubaev. Time-frequencies analysis of acoustic vibration in friction: comparison of experiment and simulation 659

V. S. Sorokin, I. I. Blekhman, V. B. Vasilkov. Motion of an elastic body in fluid under vibration665

S. N. Sorokova, A. G. Knyazeva. The mathematical modeling of conversion regimes in the gasless systems with regard to mechanical process 675

K. E. Starkov. Bounds for compact invariant sets of nonlinear systems possessing first integrals with applications to two hamiltonian systems 682

V. D. Sulimov, P. M. Shkapov. Hybrid algorithms in computational model updating procedures for hydromechanical systems 688

A. L. Svistkov, A. G. Pelevin, A. A. Adamov, B. Lauke, K. W. Stöckelhuber, G. Heinrich. Structural-phenomenological model of the mechanical behavior of elastomeric nanocomposites based on styrene butadiene rubber 696

A. V. Sylyvonyuk, N. P. Yaroshevich. Experimental research of a run-up process of a vibrating machine with an unbalance excitation 702

B. G. Tarasov. Sear rupture mechanism of super-brittleness of hard rocks 712

A. A. Tikhonov, K. A. Antipov. Tensor approach for mathematical modeling of geomagnetic field 724

P. E. Tovstik, T. P. Tovstik. Two-dimensional models of plates made of an anisotropic material733

E. N. Vilchevskaya, A. B. Freidin. Modeling mechanochemistry of the diffusion controlled chemical reaction front propagation in elastic solids 741

A. A. Vjatkin, V. G. Kozlov, R. R. Sabirov. Heat transfer and overcritical convection in rotating horizontal annulus 750

Yu. Yakovlev, V. Polyanskiy. The hydrogen material interaction during cyclic mechanical loading 756

S. Zavsek, A. V. Dimaki, E. V. Shilko, A. I. Dmitriev, J. Pezdic, S. G. Psakhie. Symbiotic cellular automata method and its application to simulation of the mechanical response of lignite 764

E. Zdanchuk, V. Lalin. The theory of continuous medium with free rotation without coupled stresses. 771

Simulation of dusty plasma shape and structure in ground state at different configuration of confinement

A. V. Abdrashitov K. P. Zolnikov S. G. Psakhie
kost@ispms.tsc.ru

Abstract

Molecular dynamics investigation of dusty plasma structure in the ground state for different confinement configurations was carried out. Interactions between dusty particles of spherical shape which composed simulated clusters are described by pair Yukawa potential. Conditions under which three-dimensional structure of dusty plasma cluster in the ground state (case of isotropic confinement) transforms into two-dimensional one are determined for different anisotropy magnitude (difference of confinement forces along vertical and horizontal directions). Shape, geometric sizes and structure of dusty plasma clusters versus number of dusty particles and anisotropy magnitude are investigated.

1 Introduction

Micro and nanosize particle behavior in complex plasma is actively investigated in many papers [1, 2, 3]. Dusty particles in plasma obtain sufficient negative charges which repulse them and besides gravity action. In order to confine dusty particles in research installation it is necessary to form potential trap which holds them in some plasma region. Usually, dusty particles are held near electrode region where strong electric field acts. Different not only by the physical nature but also their magnitude forces can effect along vertical and horizontal directions. It leads to field structure anisotropy of potential trap holding dusty particles from recession. Anisotropy of confinement influences not only on shape but also on structure of dusty plasma system and therefore on its reply under electric, magnetic, laser or other loadings. In this connection it represents interest to investigate a dependence of dusty plasma structure in the ground state on magnitude of confinement anisotropy. At that, the arranged system of finite number of charged particles (as a rule not more than several thousand) is meant by a dusty plasma cluster [1].

2 Results and discussions

The solution of above set task was fulfilled on the base of the molecular dynamics approach applied to dusty particles of spherical shape having melamine formaldehyde density. This kind of particles is widely used in many experimental works for investigation complex plasma properties and its behavior. In order to compare our results of simulation with available experimental data [4] the diameter of dusty particle is chosen to be equal to $7.10\mu m$ and their charge is equal to 2660e. As well as in the previous works [5, 6] the interparticle interactions are described by Debye potential

$$\phi = \frac{Q}{4\pi\varepsilon_0 r} e^{\left(-\frac{r}{\lambda_d}\right)} \tag{1}$$

where λ_d- Debye screening radius, Q – particle charge.

Confinement is defined as $F = \alpha_z Q z + \alpha_\rho Q \rho$, where $\rho = (x^2 + y^2)^{1/2}$, α_z and α_ρ – coefficients of confinement acting along vertical and horizontal directions, consequently. Dimensionless parameter of confinement anisotropy is introduced for number characterization of anisotropy magnitude $\xi = \frac{\alpha_z}{\alpha_\rho}$. Number of dusty particles in simulated clusters varies from 14 to 2880.

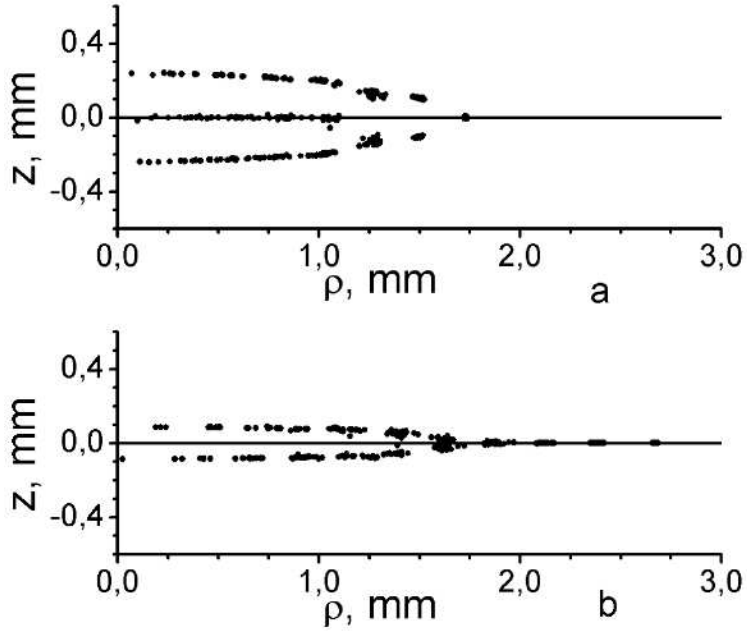


Figure 1: Structure of dusty plasma cluster consisting 360 particles at different magnitudes of anisotropy parameter $\xi = 8$ (a), $\xi = 32$ (b)

Used approach allowed describing with high accuracy a structure of as three-dimension cluster [7] so two dimension one [8]. In particular, it reproduces shell population of Coulomb balls, structure configuration and interparticle distances of plasma clusters.

Structure projection of 360 particle plasma cluster in axes of cylindrical coordinates for different values of dimensionless parameter ξ is presented in Fig. 1. It should be noted that simulated system in isotropic confinement represents itself Coulomb ball with typical shell structure. Increasing of anisotropy magnitude of confinement leads to increase of horizontal size and decrease of vertical one of simulated system (Fig. 1).

The structure of simulated cluster becomes plane at reaching some threshold value of anisotropy parameter. This threshold value depends on number of dusty particles. At that increasing of dusty particle number leads to increasing of threshold value of transformation three-dimension structure of dusty plasma cluster into two-dimension one. It should be noted that simulated dusty particles have tendency to arrange into chain along vertical axis at decrease of dimensionless parameter ξ till value sufficient less than 1.

Results showed that number of dusty particles influences sufficiently on plasma structure cluster as in isotropic so in anisotropic case of confinement. At sufficiently small particle number a simulated cluster in anisotropic confinement forms plane structure. At increase of particle number the structure of simulated cluster becomes more complicated and forms internal shells. Threshold value of dusty particle number at which cluster structure transforms from two- into three-dimension one depends on value of dimensionless parameter ξ. Simulation results of plasma cluster structure with different particle number for $\xi = 32$ are shown in Fig. 2. It is clear seen that additional shells start to form with increasing number of dusty particle number. This behavior of simulated system may be connected with the fact that increase of dusty particle number leads to increase their density in central region of cluster [7] and consequently interparticle Coulomb interaction becomes stronger what may be main reason of plane structure transition into three-dimension one.

Increase of dusty particle number leads to increase of plasma cluster size. Results showed that a "splitting" of dusty plasma cluster along vertical direction (formation three-dimension structure from two-dimension one) depends on as number of dusty particles so on anisotropy value of confinement (Fig. 3). The edge on the curve corresponding to $\xi = 22$ is connected with spasmodic formation a new shell in plasma cluster which leads to spasmodic increase of the cluster size along

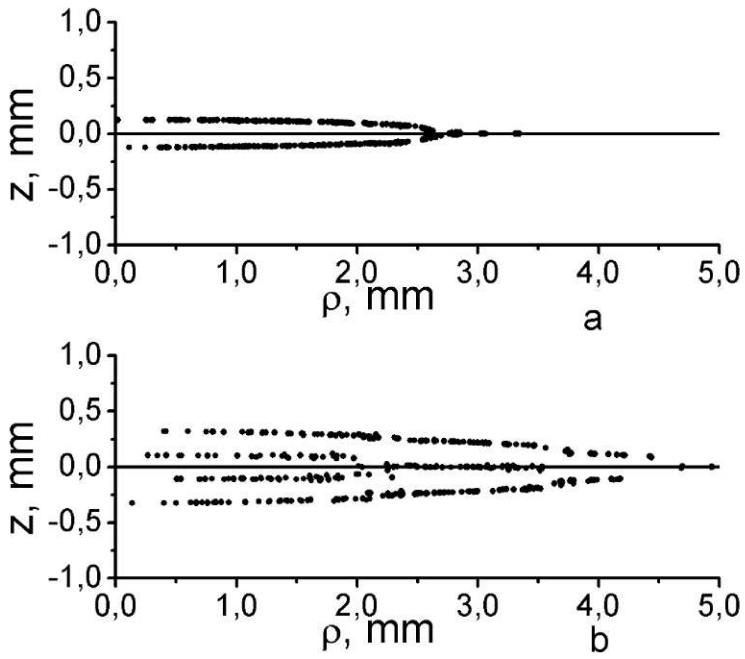


Figure 2: Structure of dusty plasma cluster in anisotropy confinement ($\xi = 32$) for different particle number 720 (a), 2880 (b)

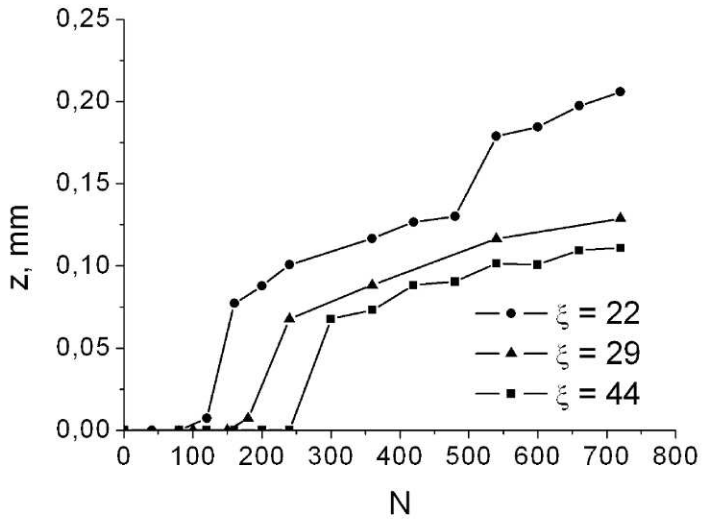


Figure 3: Dependence of dusty plasma size in the ground state along vertical direction on particle number (N) for different anisotropy magnitude of confinement

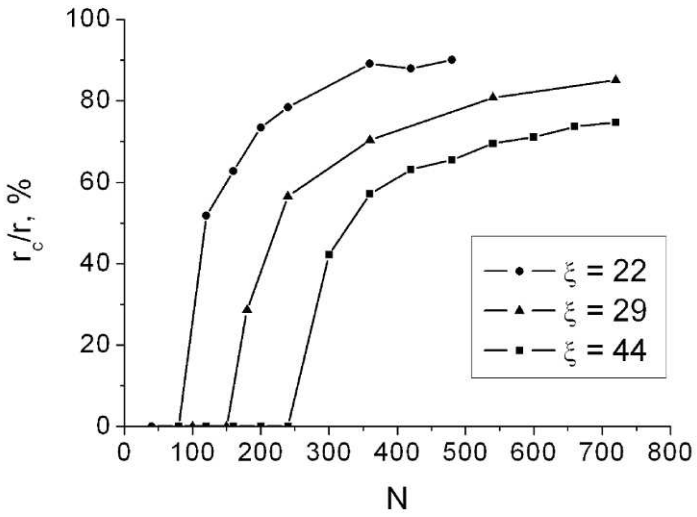


Figure 4: Position of splitting point of cluster structure versus particle number (N) (r_c – distance from splitting point till axes z, r – distance from axes z till cluster edge)

the vertical direction. Splitting plane plasma cluster structure at decrease of anisotropy parameter or increase of dusty particle number starts from central region of the simulated cluster. Boundaries of this region increase in size and move away cluster center with increase of particle number in the simulated system (Fig. 4).

3 Conclusions

In that way obtained results showed that a structure of a dusty plasma cluster in ground state sufficiently depends on anisotropy magnitude of confinement and particle number of the simulated system. At high enough a anisotropy magnitude and low number of particles the simulated system represents a plane cluster. The simulated plane cluster can transform into three-dimension state at decrease of an anisotropy magnitude or increase of particle number. At that a cluster splitting starts from the central region and leads to formation of a shell structure in the ground state.

References

[1] V.E. Fortov, A.G. Khrapak, S.A. Khrapak, V.I. Molotkov, O.F. Petrv Phys. Usp. 174, 495 (2004)

[2] H. Baumgartner, D. Block, M. Bonitz Contrib. Plasma Phys. 49, 281 (2009)

[3] O. Arp, D. Block, A. Piel, A. Melzer Phys. Rev. Lett. 95, 165 004 (2004)

[4] L.M. Vasilyak, S.P. Vetchinin, D.N. Polyakov et al. Physics of Extreme states of Matter -2009. Institute of Problemsof Chemical Physics RAS. Edited by Fortov V.E. et al. Chernogolovka. ISBN 978-5-901675-89-2. P.220-223. (2009)

[5] S.G. Psakhie, K.P. Zolnikov, L.F. Skorentsev, D.S. Kryzhevich and A.V. Abdrashitov PJTP 34, 6 (2008) In Russian

[6] S.G. Psakhie, K.P. Zolnikov, A.V.Abdrashitov PJTP 35, 46 (2009) In Russian

[7] C. Henning, H. Baumgartner, A. Piel Phys. Rev. E. 76, 056403 (2006)

[8] Y.H. Liu, Z.Y. Chen, M.Y. Yu, A. Bogaerts Phys. Rev. E. 74, 056401 (2006)

Andrey V. Abdrashitov, pr. Academicheskii 2/1, Tomsk, 634021 Rissia
Konstantin P. Zolnikov, pr. Academicheskii 2/1, Tomsk, 634021 Rissia
Sergey G. Psakhie, pr. Academicheskii 2/1, Tomsk, 634021 Rissia

Functionally invariant solutions of sine-Gordon equation with variable amplitude

E. L. Aero A. N. Bulygin Yu. V. Pavlov
bulygin_an@mail.ru

Abstract

Solutions $U(x, y, t)$ of (2+1) sine-Gordon equation with variable amplitude are obtained. They are found out for a particular amplitudes, are functionally invariant and contain one or several of arbitrary functions depending on ansatz $\alpha(x, y, t)$. Ansatz $\alpha(x, y, t)$ is defined as a root of the algebraic equation with coefficients in the form of arbitrary functions depending on α. $U(x, y, t)$ forms a sufficiently wide class of functions due to the liberty in the choice of ansatz and arbitrary functions. We hope that obtained solutions will useful in the construction of mathematical models of physical phenomena and processes described by the sine-Gordon equation with a variable amplitude, and the liberty of choice will be sufficient to satisfy the corresponding initial and boundary conditions.

1 Introduction

Sine-Gordon (SG) equation

$$\frac{\partial^2 U}{\partial x^2} + \frac{\partial^2 U}{\partial y^2} - \frac{1}{v^2}\frac{\partial^2 U}{\partial t^2} = p(x, y, t)\sin U \tag{1}$$

appears in many fields of the contemporary natural sciences. It models the deformation of nonlinear crystal lattice [1], [2], orientational structure of liquid crystals [3], orientation of spines in ferromagnets [4], surface metrics [5] etc. Also it describes some processes in the earth shell [6, 7], molecular biology [8], models of the field theory [9] and the elementary particles physics [10].

Up to date effective methods of SG equation have been developed. But most of methods have been developed for the case $p(x, y, t) = \text{const}$. It essentially limits the area SG equation application. For example in the mechanics of the nonlinear crystal lattice case of constant amplitude describes the deformation of the ideal lattice by the field of homogeneous stresses. Deformation of the real lattice with structure defects (dislocations, disclinations, embryos of pores, fractures etc.) by the field of non-homogeneous stresses is described by the SG equation with the variable amplitude. In the mechanics of liquid crystals case $p = \text{const}$ models the deformation of long axes provided that orientational continuum does not contain defects and electromagnetic filed is homogeneous. Alternatively $p(x, y, t) \neq \text{const}$ [11]. In the differential geometry SG equation with $p(x, y, t) = \text{const}$ describes metrics of Chebyshev nets on the surface with constant curvature. If curvature is variable then $p(x, y, t) \neq \text{const}$.

From given examples it is clear that the application area of SG equation is essentially expanding with receiving of solutions with variable amplitude. While modeling of real media structural defects are usually modeled by functions with corresponding singularities (point, line, surface etc.) Singularities could be stationary and propagate with some speed. They may differentiate by the growth measure (logarithmic, power etc.) Widely known media for which non-homogeneities are modeled by regular functions having no singularities and frequently non-homogeneities have regular geometrical arrangement in the space. Form above mentioned it is clear that the adequate model of physical processes described by the SG equation shall consider the specific features of real media by variable amplitude $p(x, y, t)$.

Below using methods of the construction of functionally invariant solutions of differential equations [12, 13] new solutions of SG equation with a variable amplitude are obtained.

Solution of the equation (1) we search in the form

$$U = 4 \operatorname{arctg} e^{\varphi(x,y,t)}. \tag{2}$$

After substitution of (2) into (1) we find that Eq. (1) will be satisfied if function $\varphi(x, y, t)$ simultaneously satisfies to two equations — homogeneous wave equation

$$\frac{\partial^2 \varphi}{\partial x^2} + \frac{\partial^2 \varphi}{\partial y^2} - \frac{1}{v^2} \frac{\partial^2 \varphi}{\partial t^2} = 0 \tag{3}$$

and eikonal equation

$$\left(\frac{\partial \varphi}{\partial x}\right)^2 + \left(\frac{\partial \varphi}{\partial y}\right)^2 - \frac{1}{v^2}\left(\frac{\partial \varphi}{\partial t}\right)^2 = p(x, y, t). \tag{4}$$

Classic eikonal equation, v is speed of the light, $p(x, y, t) = 0$ is basic in the geometrical optics [14]. It describes the propagation of the wave surface (surface of the equal phase) in the medium with non-homogeneous index of refraction. A lot of works [15, 16] have been devoted to the analysis of the equation (4).

Solution of the equation (1) also will be

$$U = 2 \operatorname{arctg} e^{\varphi(x,y,t)}, \tag{5}$$

if $\varphi(x, y, t)$ simultaneously satisfies to two equations

$$\frac{\partial^2 \varphi}{\partial x^2} + \frac{\partial^2 \varphi}{\partial y^2} - \frac{1}{v^2} \frac{\partial^2 \varphi}{\partial t^2} = p(x, y, t), \tag{6}$$

$$\left(\frac{\partial \varphi}{\partial x}\right)^2 + \left(\frac{\partial \varphi}{\partial y}\right)^2 - \frac{1}{v^2}\left(\frac{\partial \varphi}{\partial t}\right)^2 = 0. \tag{7}$$

Therefore integration of the SG-equation with a variable amplitude is reduced to the finding of function $\varphi(x, y, t)$, which is a simultaneous solution of equations (3), (4) or (6), (7). Solutions of (2), (5) assume that $p(x, y, t) > 0$. If $p(x, y, t) < 0$ then solutions will be correspondingly

$$U = \pi + 4 \operatorname{arctg} e^{\varphi(x,y,t)}, \qquad U = \pi + 2 \operatorname{arctg} e^{\varphi(x,y,t)}. \tag{8}$$

The most advanced approach to the finding out the function $\varphi(x, y, t)$ is the method of construction of functionally invariant solutions of differential equations.

2 Functionally invariant solutions of SG equation with variable amplitude

First method. Solution of Eq. (3) is represented in the form

$$\varphi = F(\alpha). \tag{9}$$

Here $F(\alpha)$ is an arbitrary function and argument $\alpha(x, y, t)$ is the root of the equation linear by variables (x, y, t):

$$x\, l(\alpha) + y\, m(\alpha) - v^2 t\, q(\alpha) + g(\alpha) = 0, \tag{10}$$

and coefficients $(l(\alpha), m(\alpha), p(\alpha), g(\alpha))$ are arbitrary functions linked by one relationship

$$l^2(\alpha) + m^2(\alpha) = v^2 q^2(\alpha). \tag{11}$$

Taking into consideration (11) solution of the wave equation (3) takes the form

$$\varphi = F(\alpha), \quad \alpha = t - \theta x \pm y\sqrt{\frac{1}{v^2} - \theta^2}, \quad \theta = \text{const}. \tag{12}$$

If $\theta^2 < 1/v^2$ ansatz $\alpha(x, y, t)$ is real and solution of (12) is a plane wave. With plus sign wave propagates to the boundary of half-space $y = 0$, and with minus sign — from the boundary $y = 0$.

Real ansatz allows to construct [17, 18] functionally invariant solution of the SG equation with a constant amplitude ($p(x, y, t) = 1$).

If $\theta^2 > 1/v^2$ then real ansatzes transforms to a complex-conjugated ones

$$\zeta = t - \theta x + iy\sqrt{\theta^2 - \frac{1}{v^2}}, \quad \tilde{\zeta} = t - \theta x - iy\sqrt{\theta^2 - \frac{1}{v^2}}. \tag{13}$$

As the solution of SG equation is supposed be real, then function

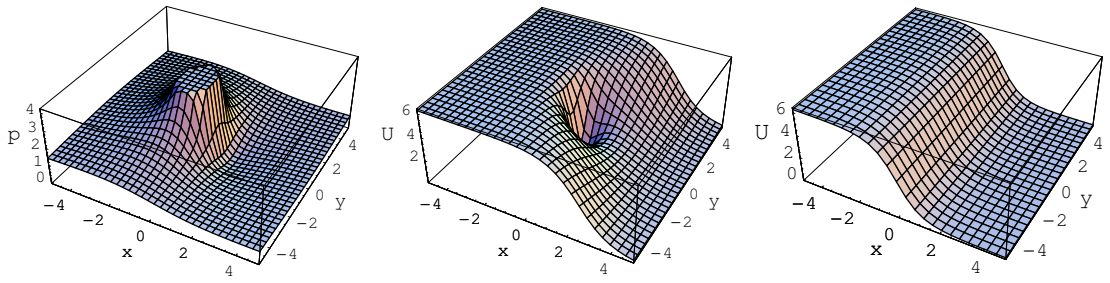
$$U = 4\,\mathrm{arctg}\, e^{\varphi(x,y,t)}, \quad \varphi(x, y, t) = \frac{1}{2}\left[F(\zeta) + F(\tilde{\zeta})\right] \tag{14}$$

will be the solution of (1) with amplitude

$$p(x, y, t) = \left(\theta^2 - \frac{1}{v^2}\right) F'(\zeta) \cdot F'(\tilde{\zeta}). \tag{15}$$

Here and further the prime denotes a derivative with respect to argument. As $F(\zeta)$ is any function then (15) represents a wide class of amplitudes $p(x, y, t)$, for which (14) is a solution of SG equation.

On Fig. 1 spatial images of amplitude (15) with $F(\zeta) = \zeta + 2\ln\zeta$, $v = 1$, $\theta = \sqrt{2}$ (Fig. 1a) and solution $U(x, y, t)$ (Fig. 1b) are shown for $t = 0$. It can see that $U(x, y, t)$ is a perturbed kink.



a) b) c)

Figure 1: Spatial image of amplitude and solution for the case (15).

If amplitude is constant ($p(x, y, t) = 1$), perturbations disappear and solutions take the form of common kink (Fig. 1c).

Ansatz α could be selected by another way. For simplicity assume that

$$v\, q(\alpha) = 1, \quad g(\alpha) = 0. \tag{16}$$

Then condition (11) will be satisfied if

$$l = \cos\alpha, \quad m = \sin\alpha\,. \tag{17}$$

Substituting (17) into (10) we obtain

$$x\cos\alpha + y\sin\alpha = vt, \tag{18}$$

$$\alpha = \varphi \pm \arccos\frac{vt}{\rho} + 2n\pi, \quad \mathrm{tg}\,\varphi = \frac{y}{x}\,, \quad n = 1, 2\ldots, \quad \rho = \sqrt{x^2 + y^2}. \tag{19}$$

By the direct calculation we find out that

$$\varphi = A(\alpha) + \frac{B(\alpha)}{s}, \qquad s^2 = x^2 + y^2 - v^2 t^2 \tag{20}$$

satisfies to the wave equation (3). Here $A(\alpha), B(\alpha)$ are arbitrary functions.

Eq. (4) will be satisfied if

$$p(x, y, t) = \frac{B^2(\alpha)}{s^4}. \tag{21}$$

Therefore (20) will be a solution of SG-equation with amplitude (21). Note that in this case solution of (20) and amplitude (21) are singular. At the initial moment of time ($t = 0$) singular is the point ($x = 0, y = 0$), and in the following moments of time point transforms into the circumference with radius vt.

Second method. Let define ansatz $\alpha(x, y, t)$ from the equation

$$[x - \xi(\alpha)]^2 + [y - \eta(\alpha)]^2 = v^2(t - \alpha) \tag{22}$$

and construct function

$$\varphi(x, y, t) = \frac{f(\alpha)}{\sqrt{\tau}}. \tag{23}$$

Here

$$\tau = l(\alpha)\,(x - \xi) + m(\alpha)\,(y - \eta) - v^2 q(\alpha)\,(t - \alpha). \tag{24}$$

and $(l(\alpha), m(\alpha), q(\alpha), \xi(\alpha), \eta(\alpha))$ — arbitrary functions related by two conditions

$$l(\alpha)\xi'(\alpha) + m(\alpha)\eta'(\alpha) = v^2 q(\alpha), \tag{25}$$

$$l^2(\alpha) + m^2(\alpha) = v^2 q^2(\alpha). \tag{26}$$

Function φ satisfies to the wave equation (3) and eikonal equation (4) with amplitude

$$p(x, y, t) = \frac{f^2(\alpha)}{2\tau^2}\frac{w}{\sigma} - \frac{ff'}{\tau\sigma}, \tag{27}$$

$$w = l'(\alpha)\,(x - \xi(\alpha)) + m'(\alpha)\,(y - \eta(\alpha)) - v^2 q(\alpha)\,(t - \alpha), \tag{28}$$

$$\sigma = \xi'(\alpha)\,(x - \xi(\alpha)) + \eta'(\alpha)\,(y - \eta(\alpha)) - v^2(t - \alpha). \tag{29}$$

Therefore

$$U = 4 \operatorname{arctg} e^{\varphi(x,y,t)}$$

is the solution of SG-equation with amplitude $p(x, y, t)$ defined by the relationship (27).

Note the simple particular cases of the obtained solution. Let

$$vq(\alpha) = 1, \qquad l = \cos\theta, \qquad m = \sin\theta, \qquad \xi = v\alpha l, \qquad \eta = v\alpha m, \qquad \theta = \text{const}. \tag{30}$$

Then

$$\tau = x\cos\theta + y\sin\theta - vt, \qquad \sigma = v\tau, \qquad w = 0, \tag{31}$$

$$\alpha = \frac{s^2}{2\sigma}, \qquad p(x, y, t) = -\frac{f(\alpha)f'(\alpha)}{\sigma}. \tag{32}$$

From (31), (32) it is clear that in this case amplitude $p(x, y, t)$ has a singularity in the form of line propagating parallel to itself with speed v. If $\theta = 0$ line degrades into singular point moving with speed v along axis x. If $\theta = \pi/2$ singular point moves along y axis.

Second particular case is realized if

$$\xi(\alpha) = 0, \quad \eta(\alpha) = 0, \quad l(\alpha) = 1, \quad m(\alpha) = i, \quad q(\alpha) = 0. \tag{33}$$

Then

$$\tau = x + iy, \quad \alpha = t - \frac{\rho}{v}, \quad w = 0, \quad \sigma = -v\rho, \tag{34}$$

and φ is Poisson wave function [12]

$$\varphi = \frac{f(\alpha)}{\sqrt{x + iy}}. \tag{35}$$

Real wave functions will be

$$\varphi_+(x, y, t) = \frac{f(\alpha)}{\rho}\sqrt{\rho + x}, \quad \varphi_-(x, y, t) = \frac{f(\alpha)}{\rho}\sqrt{\rho - x}. \tag{36}$$

Functions (φ_+, φ_-) will be solutions of Eq. (4) if

$$p_+(x, y, t) = \frac{f^2}{2\rho^3} + \frac{ff'(\rho + x)}{\tau\rho^3}, \quad p_-(x, y, t) = \frac{f^2}{2\rho^3} + \frac{ff'(\rho - x)}{\tau\rho^3}. \tag{37}$$

On the Fig. 2 are represented spatial images of amplitude $p_+(x, y, t)$ for the case $f(\alpha) = \sin\alpha$ $(t = 0)$ and corresponding solution $U(x, y, t)$. It is clear that cylindrical wave corresponds to the localized perturbation.

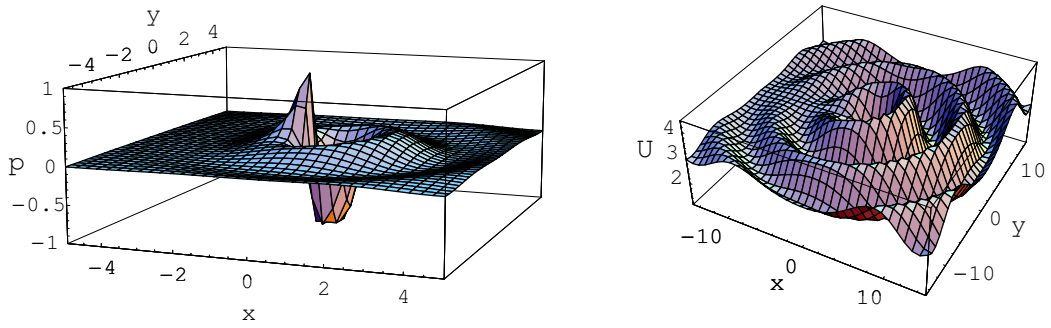


Figure 2: Spatial image of the amplitude and solution for the case (37).

Obtained solutions of SG-equation with a variable amplitude are constructed on the basis of function $\varphi(x, y, t)$ satisfying to Eqs. (3), (4). Similarly Eq. (1) could be solved on the basis of function $\varphi(x, y, t)$ satisfying Eqs. (6), (7). Below is given the example of such approach.

Let again select ansatz $\alpha(x, y, t)$ as a root of Eq. (22). It is easy to show that arbitrary function $f(\alpha)$ of ansatz $\alpha(x, y, t)$ will satisfy to the Eq. (7). Eq. (6) will be solved if

$$p(x, y, t) = \frac{f'(\alpha)}{\sigma}, \tag{38}$$

σ is defined by Eq. (29). Therefore

$$U = 2\,\mathrm{arctg}\, e^{f(\alpha)} \tag{39}$$

will be a solution of Eq. (1) if $\alpha(x, y, t)$ is a root of Eq. (22) and amplitude $p(x, y, t)$ is equal to (38).

3 Conclusion

Obtained solutions are without any doubt particular. However they represent sufficiently wide class of solutions. It follows from the method of their construction. Ansatz α is selected as the

root of the algebraic equation with coefficients as arbitrary functions of α. Though coefficients shall satisfy to some conditions liberty in the choice of α remain. Solution is obtained in the form of an arbitrary function of α. We hope that obtained solutions will be useful for construction of mathematical models of physical phenomena and processes described by SG-equation with variable amplitude and remaining liberty of choice will be sufficient for matching to the corresponding initial and boundary conditions.

Functionally invariant solutions of SG-equation are constructed for two-dimensional space. However proposed method could be easily generalized for the space with any dimensionality. Moreover in [19] it was shown that with the increasing of the dimensionality of space number of ansatz α choices is also increasing and number of obtained solutions of multidimensional SG-equation grows accordingly.

Acknowledgements

This work was supported by RFBR, grants 09-08-00634-a and 10-01-00243-a.

References

[1] E. L. Aero, A. N. Bulygin. Izv. Ross. Akad. Nauk. Ser. Mekh. Tverd. Tela No. 5, (2007) 170–187.

[2] E. L. Aero. J. Engineering Math. **55**, (2006) 81–95.

[3] P. G. de Gennes. The Physics of Liquid Crystals. Clarendon Press, Oxford, 1974.

[4] P. Guéret. IEEE Trans. Magnetics **11**, (1975) 751–754.

[5] P. L. Chebyshev. Uspekhi Matem. Nauk **1**, N 2, (1946) 38–42.

[6] V. G. Bykov. Nonlinear Wave Processes in Geological Media. Dalnauka, Vladivostok, 2000.

[7] I. A. Garagash, V. N. Nikolaevskiy. Vychislit. Mekhanika Sploshnikh Sred **2**, (2009) 44–66.

[8] A. S. Davydov. Solitons in Bioenergetics. Naukova Dumka, Kiev, 1986.

[9] L. A.Takhtadzhyan, L. D. Faddeev. Hamiltonian Approach in the Theory of Solitons. Nauka, Moscow, 1986.

[10] L. A. Takhtadzhyan., L. D. Faddeev. Theor. Math. Phys. **21**, (1974) 1046–1057.

[11] E. L. Aero Vysokomolekulyarnye Soedineniya **37**, N 8, (1995) 1286–1299.

[12] H. Bateman The Mathematical Analysis of Electrical and Optical Wave–Motion: On the Basis of Maxwell's Equations. Dover, New York, 1955.

[13] S. L. Sobolev. Trudy Fiz.-Mat. Inst. V.A. Steklova **5**, (1934) 259–264.

[14] L. D. Landau, E. M. Lifshitz. The Classical Theory of Fields. Oxford: Pergamon Press, 1983.

[15] M. Born, E. Wolf. Principles of Optics. Pergamon Press, New York, 1968.

[16] A. V. Borovskikh. Siberian Math. J. **47**, (2006) 813–834.

[17] E. L. Aero, A. N. Bulygin, Yu. V. Pavlov. Teor. Matem. Fiz. **158**, No. 3, (2009) 370–377 [English transl.: Theor. Math. Phys. **158**(3), (2009) 313–319].

[18] E. L. Aero, A. N. Bulygin, Yu. V. Pavlov. Nelineinii Mir **7**, N 7, (2009) 513–517.

[19] N. P. Erugin 1948, Uch. Zap. Leningrad Univ. N **15**, (1948) 101–134.

E. L. Aero, A. N. Bulygin, Yu. V. Pavlov,
Institute of Problems in Mechanical Engineering, RAS,
61 Bol'shoy, V.O., Saint Petersburg, 199178, Russia

On transformation surfaces construction for phase transitions in deformable solids

Mikhail A. Antimonov Andrej V. Cherkaev Alexander B. Freidin
mike.antimonov@gmail.com, cherkaev@gmail.com, alexander.freidin@gmail.com

Abstract

We consider stress-induced phase transitions of martencite type and develop a procedure for transformation surfaces construction in a strain space. We discuss and use together two approaches. The first one is based on a local thermodynamic equilibrium condition. The second one is based on finding an energy lower bound and showing two phase structures at which the lower bound is reached.

1 Introduction

We consider stress-induced phase transitions in deformable solids. Crystal latices of materials change due to such transitions but adjacent atoms remain adjacent. This leads to appearance of sharp interface and jumps of elastic moduli (see, e.g., [17]) and motivates considering the problem of two-phase structures as a problem of a composite material with unknown interfaces. We focus on a transformation surface construction in a strain space. The phase transformation cannot begin until the external (average) strain reaches the transformation surface that acts as a yield surface in a plasticity theory.

We use together two approaches. The first approach is based on a local thermodynamic equilibrium considerations and uses a semi-inverse method. The new phase nucleus shape is prescribed and external strains at which such a nucleus can satisfy the local thermodynamic condition is found (see, e.g., [19, 8] and reference therein). Then some kind of transformation surface can be constructed as an envelope of the surfaces which correspond to external strains at which the appearance of different types of new phase nuclei becomes possible.

This approach, supplemented by a local stability analysis (see, e.g., [14, 12, 9, 5]), on one hand allows us to describe specific shapes of new phase nuclei (layers, ellipsoids, elliptical cylinders [14, 16, 15, 6, 2, 10, 8]), to study local strains in relation with external stains, to find the nucleus geometry in dependence on a strain state and estimate stress concentrations due to new phase appearance. On the other hand, the local equilibrium condition is only a necessary condition for the energy to be minimal. Even if this condition is satisfied, we cannot be sure that we found a local minimizer without additional stability analysis, and only necessary stability conditions can be examined if we do not know in advance that we found a global minimizer. Therefore we are led to inquire whether other two-phase structures can appear before the above mentioned envelope of the appearance surfaces is reached. Another question is whether there are other two phase structures which, given average strain, have less free energy then the prescribed structures.

The second approach is based on the construction of the free energy lower bounds [4, 18] (see also [3]). If at given average strains and new phase volume concentration we construct such a bound, then the transformation surface can be constructed as a result of further energy minimization with respect to the new phase volume concentration and finding average strains at which the optimal concentration tends to zero. This will give a transformation surface such that equilibrium new phase domains cannot exist until this surface is reached whatever the domain shape is. Other types of new phase domains (simple laminates, second and third order laminates) than it was found by the semi-inverse method can be found in this way, and after all we can compare the energy values obtained by two approaches.

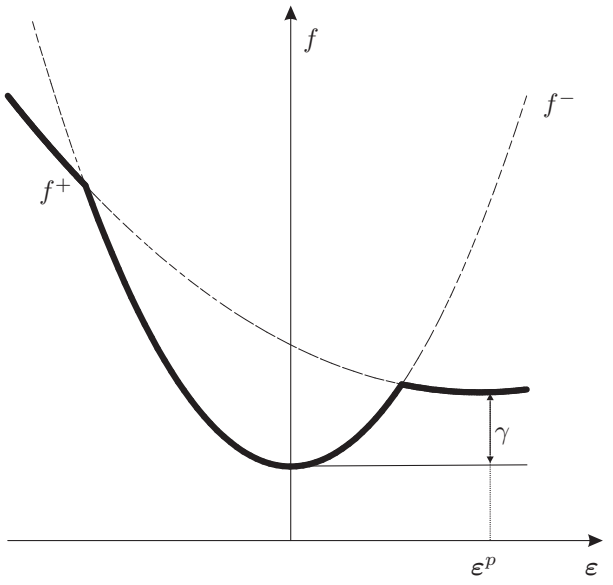


Figure 1: Free energy

The present paper represents an implementation of such a strategy. First, we give shortly a review of solutions for different types of new phase equilibrium domains basing on [16, 10, 8, 11, 2]. Then we construct the envelope of the surfaces of different types nuclei appearance. Then basing on the translation method [13, 4] we consider exact lower energy bounds construction following [1]. This in turn allows us to construct the transformation surface. Finally, we compare this surface with the envelope surface.

2 Domains of new phase inclusions appearance

Equilibrium two-phase configuration of an elastic solid have to satisfy the following conditions:

$$\mathbf{x} \notin \Gamma: \quad \nabla \cdot \boldsymbol{\sigma} = 0, \quad \theta = \text{const}, \tag{1}$$

$$\mathbf{x} \in \Gamma: \quad [\mathbf{u}] = 0, \quad [\boldsymbol{\sigma}] \cdot \mathbf{n} = 0 \tag{2}$$

$$[f] - \boldsymbol{\sigma} : [\boldsymbol{\varepsilon}] = 0 \tag{3}$$

where $\mathbf{x}$ is a radius-vector of a material point, Γ denotes interfaces, $\mathbf{u}$ is the displacement, $\boldsymbol{\varepsilon} = (\nabla \mathbf{u})^s$ is the strain tensor, $\boldsymbol{\sigma}$ is the stress tensor, θ is the temperature, $f = f(\boldsymbol{\varepsilon}, \theta)$ is the Helmholz free energy density, square brackets denote a jump across the interface: $[\cdot] = (\cdot)^+ - (\cdot)^-$, indices "+" and "−" denote different phase states, further we relate "+" with a new phase and "−" with a parent phase.

We consider a two-well energy

$$\begin{aligned} &f(\boldsymbol{\varepsilon}, \theta) = \min_{-,+} \{f_-(\boldsymbol{\varepsilon}, \theta), f_+(\boldsymbol{\varepsilon}, \theta)\}, \\ &f_\pm(\boldsymbol{\varepsilon}, \theta) = f^0_\pm(\theta) + \frac{1}{2}(\boldsymbol{\varepsilon} - \boldsymbol{\varepsilon}^p_\pm) : \mathbf{C}_\pm : (\boldsymbol{\varepsilon} - \boldsymbol{\varepsilon}^p_\pm). \end{aligned} \tag{4}$$

where $f^0_\pm$ are free energies of phases in stress free states, $\mathbf{C}_\pm$ are the elasticity tensors, $\boldsymbol{\varepsilon}^p_\pm$ are strains in stress free states, if $\boldsymbol{\varepsilon}^p_- = 0$ then $\boldsymbol{\varepsilon}^p_+ \equiv \boldsymbol{\varepsilon}^p$ is a transformation strain tensor. One-dimensional analogue of such energy density is shown in Fig. 1 where $\gamma = [f_0]$ is a difference between free energies of stress free phases.

By (4), stresses and strains in areas occupied by the phases "+" and "−" are related as

$$\boldsymbol{\sigma}_\pm = \mathbf{C}_\pm : (\boldsymbol{\varepsilon} - \boldsymbol{\varepsilon}^p_\pm) \tag{5}$$

The thermodynamic equilibrium condition (3) imposes the restrictions on the possibility of the existence of new phase areas and their geometry.

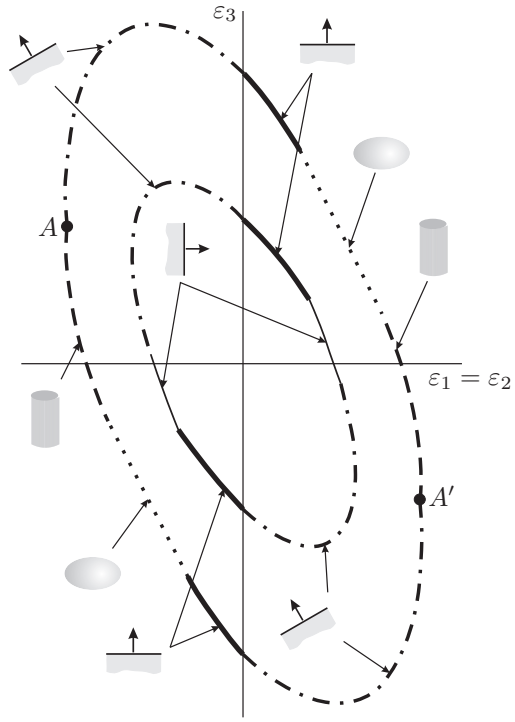


Figure 2: Axisymmetric cross-section of the envelope surface for new phase layers, ellipsoids and cylinders nucleation, ε_1=ε_2

Summarizing the results obtained for ellipsoidal [16], cylindrical [2] and plane [7, 10] new phase inclusion one can construct the envelope of the existence domains in the space of external strains. An example of the envelope of such domains is shown in Fig. 2 for the case of isotropic phases and the negative determined tensor $\mathbf{C}_1 = \mathbf{C}_+ - \mathbf{C}_-$. The internal line corresponds to the direct transformation (the phase "+" nucleates inside the phase "−"). The external line corresponds to the reverse transformation when the phase "−" areas nucleate inside the phase "+". The lines of different types correspond to different geometries of inclusions. Dashed lines correspond to cylindrical new phase inclusions nucleation, dotted lines correspond to ellipsoidal inclusions, solid thin and thick lines correspond to simple laminates with normals co-directed with eigenvectors corresponding to the maximal absolute eigenvalue of the external strain tensor, dash-dotted lines correspond to simple laminates with normals situated in eigen plane corresponding to maximal and minimal eigenvalues of the external strain tensor. One can see how a strain state affects the geometry of the new phase nuclei.

As we mentioned in the Introduction this procedure cannot guarantee that other two phase structures cannot appear before the constructed surface is reached. We also note that this surface is not convex everywhere (see at points A and A'). That is why in the next section we study two-phase structures which provide the global minimum of the free energy.

3 Free energy exact lower bound and transformation surface construction

In this section, using the translation method [13, 4] we construct an exact lower bound of free energy, following [1]. We first find free energy lower bound estimation regardless of microstructure considerations. Then we consider energy of different rank laminates and minimize it with respect to structure parameters. If the laminates energy reaches the lower bound estimation then the energy exact lower bound is constructed.

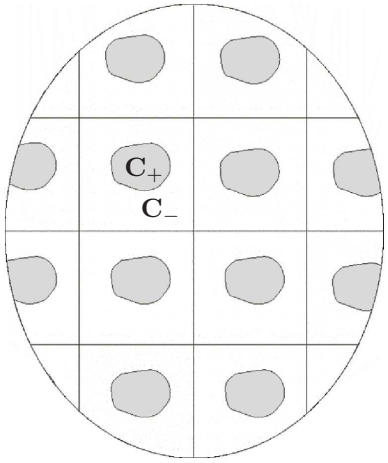


Figure 3: Periodical two phase structure

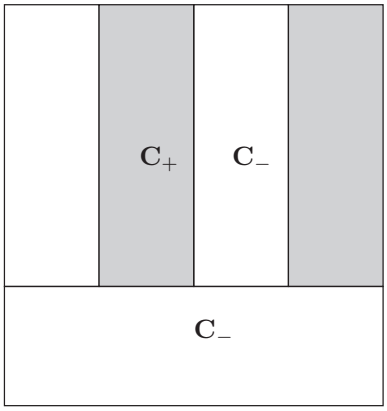


Figure 4: Second rank laminate

We consider periodical two phase structure with a given new phase volume fraction m_+ and a parent phase volume fraction m_-, $m_- + m_+ = 1$ (Fig. 3). For simplicity sake we assume here that $\boldsymbol{\varepsilon}^p_\pm = 0$.

The mean strain and stress are given by the integrals within the periodicity cell $V = V_- \cup V_+$ of a unit volume:

$$\boldsymbol{\varepsilon}_0 = \int\limits_V \boldsymbol{\varepsilon} dV, \quad \boldsymbol{\sigma}_0 = \int\limits_V \boldsymbol{\sigma} dV.$$

Then the effective elasticity tensor $\mathbf{C}_0$ of the composite satisfies the relationship

$$\boldsymbol{\sigma}_0 = \mathbf{C}_0 : \boldsymbol{\varepsilon}_0$$

Tensor $\mathbf{C}_0$ depends on the elasticity tensors of the phases and the shape and distribution of new phase areas inside the periodicity cell.

Free energy of the cell is

$$F = \int\limits_V (f^0 + \frac{1}{2}\boldsymbol{\varepsilon} : \mathbf{C} : \boldsymbol{\varepsilon}) dV \tag{6}$$

where

$$\mathbf{C} = \chi_-(\mathbf{x})\mathbf{C}_- + \chi_+(\mathbf{x})\mathbf{C}_+, \quad f^0 = \chi_-(\mathbf{x}) f^0_- + \chi_+(\mathbf{x}) f^0_+(\mathbf{x})$$
$$\chi_\pm(\mathbf{x}) = \begin{cases} 1, & \mathbf{x} \in V_\pm \\ 0, & \mathbf{x} \notin V_\pm \end{cases},$$

are characteristic functions of the domains occupied by the phases "±", $\int\limits_V \chi_\pm(\mathbf{x}) dV = m_\pm$.

To construct the lower bound we build polyconvex envelope. We add to and subtract from the integrand a polyconvex function $\phi(\boldsymbol{\varepsilon}, \Upsilon)$ named translator

$$F = \int\limits_V (f^0 + \frac{1}{2}\boldsymbol{\varepsilon} : \mathbf{C} : \boldsymbol{\varepsilon} - \frac{1}{2}\phi(\boldsymbol{\varepsilon}, \Upsilon)) dV + \int\limits_V \frac{1}{2}\phi(\boldsymbol{\varepsilon}, \Upsilon) dV$$

where Υ is a vector in 3D space of parameters of translator. Translator has the following property

$$\int\limits_V \phi(\boldsymbol{\varepsilon}, \Upsilon) dV = \phi(\boldsymbol{\varepsilon}_0, \Upsilon)$$

Let Θ be a set of admissible translator parameters at which functions ϕ and $(\boldsymbol{\varepsilon} : \mathbf{C} : \boldsymbol{\varepsilon} - \phi)$ remain polyconvex in the set $\boldsymbol{\varepsilon} \in \Xi$. Then the lower bound is defined as

$$\mathcal{PF} = \max_{\Upsilon \in \Theta} \inf_{\int\limits_{V_\pm} \chi_\pm(\mathbf{x}) dV = m_\pm} \min_{\boldsymbol{\varepsilon} \in \Xi} \left\{ \int\limits_V (f + \frac{1}{2}\boldsymbol{\varepsilon} : \mathbf{C} : \boldsymbol{\varepsilon} - \frac{1}{2}\phi(\boldsymbol{\varepsilon}, \Upsilon)) dV + \frac{1}{2}\phi(\boldsymbol{\varepsilon}_0, \Upsilon) \right\} \tag{7}$$

On the next steps we find energy of different rank laminates and minimize it by the choice of the structural parameters. Finally we demonstrate that on this way we reach the lower bound (7).

Laminate microstructure construction is a multistep process. At the fist step we take a simple laminate consisting of layers of the phases "+" and "−". At the second step we have a mix of parent phase layers and layers which have more complicate structure. Each such a layer is itself a simple laminate (Fig. 4), it is called a second-rank layer. On the third step we transform the new phase layers introduced at the second step into the laminate and obtain third-rank layers. We show that these three steps give an opportunity to construct the exact lower bound for all strains. We emphasize that the volume fractions of the phases "+" and "−" remain equal to m_- and m_+ at every step. The microstructure obtained at the $k-th$ step is characterized by the set of normals $\mathbf{n}_i$ to the sub-layers and structural parameters ρ_i $(i = 1, ..., k)$ which characterize volume fractions of phases inside layers on each step of the laminate structure construction, $\sum\limits_{i=1}^{d} \rho_i = 1$. For brevity sake we do not write down here the expressions for ρ_i.

The energy of the laminates is calculated as

$$F = m_+\gamma + \frac{1}{2}\boldsymbol{\varepsilon}_0 : \mathbf{C}_0 : \boldsymbol{\varepsilon}_0, \tag{8}$$

where the elasticity tensor $\mathbf{C}_0$ in a case of $d-$rank laminate can be written as

$$\mathbf{C}_0 = \mathbf{C}_- + m_+ \left((\mathbf{C}_+ - \mathbf{C}_-)^{-1} + m_- \sum_{i=1}^{d} \rho_i \mathbf{K}_-(\mathbf{n}_i) \right)^{-1}, \tag{9}$$

where $\mathbf{K}_-(\mathbf{n}) = \{\mathbf{n} \otimes (\mathbf{n} \cdot \mathbf{C}_- \cdot \mathbf{n})^{-1} \otimes \mathbf{n}\}^s$.

Substituting (9) into (8) for the case of isotropic phases we get the expression for the free energy dependence on the structural parameters ρ_i and the normals $\mathbf{n}_i$ $(i = 1, ..., d)$. Then we minimize the energy by a proper choice of the parameters ρ_i and the normals $\mathbf{n}_i$ $(i = 1, ..., d)$ and compare the energy value with the bound value (7). It can be shown that the lower bound (7) can be reached on this way and it is enough to consider laminates of ranks $d = 1, 2, 3$ (see also [1]). As a result we obtain the expression for the exact lower bound as a function of the external strain $\boldsymbol{\varepsilon}_0$ and the volume fraction m_+ $(m_- = 1 - m_+)$, and different rank laminates correspond to the bound in different domains of the strain space.

The results are presented in Fig. 5 for the case $\gamma > 0$, negative definite tensor $\mathbf{C}_1 = \mathbf{C}_+ - \mathbf{C}_-$ and zero Poison's ratio. The strain space is projected to the δ_1, δ_2-plain where $\delta_1 = \dfrac{\varepsilon_1}{\varepsilon_3}$, $\delta_2 = \dfrac{\varepsilon_2}{\varepsilon_3}$, ε_1, ε_2, ε_3 are the eigenvalues of the mean strain tensor $\boldsymbol{\varepsilon}_0$ and $|\varepsilon_3| \geq \max\{|\varepsilon_1|, |\varepsilon_2|\}$. Note that $\delta_1, \delta_2 \in [-1, 1]$. The bound corresponds to the energy of simple (rank-one) laminates in the domains 1, 5, 5′, 6, 6′, the second rank laminates in the domains 2, 2′, 4, 4′, 7, and the third rank laminates in the domain 3. Note that there are two types of second rank laminates. The normals $\mathbf{n}_1$ and $\mathbf{n}_2$ for the second rank laminates are orthogonal and coincide with eigenvectors of external strain tensor in the domains 2 and 2′. The second rank laminates in the domains 4, 4′ and 7 are inclined and the normals $\mathbf{n}_1$ and $\mathbf{n}_2$ are not orthogonal and don't lie in eigen plains of the external strains tensor.

To construct the transformation surface we further minimize the energy with respect to new phase fraction and find $\boldsymbol{\varepsilon}_0$ at which

$$\left. \frac{\partial \mathcal{PF}(\boldsymbol{\varepsilon}_0, m_+)}{\partial m_+} \right|_{m_+=0} = 0 \tag{10}$$

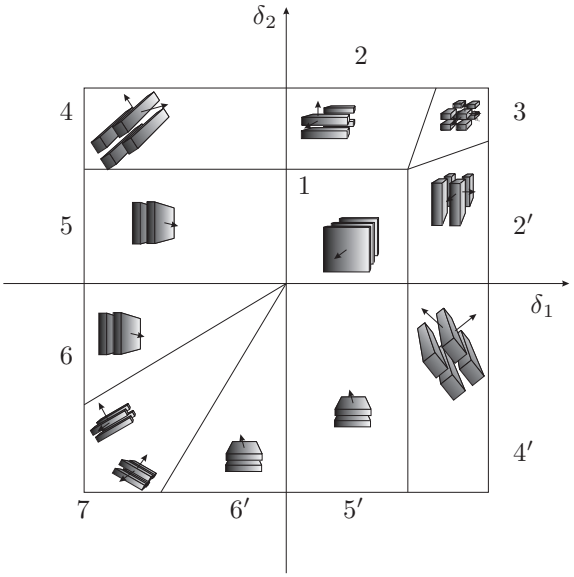


Figure 5: Optimal two-phase structures on δ_1, δ_2-plane

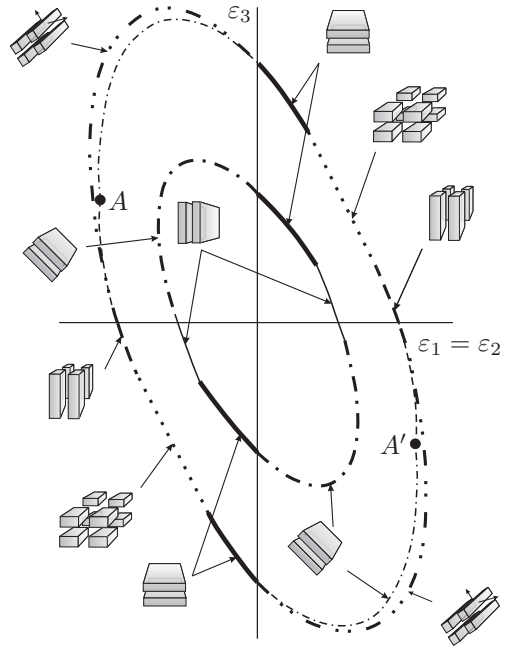


Figure 6: Axisymmetric cross-section of the transformation surface, ε_1=ε_2

The reverse transformation surface can be found from the condition

$$\left.\frac{\partial \mathcal{PF}(\boldsymbol{\varepsilon}_0, m_-)}{\partial m_-}\right|_{m_-=0} = 0 \tag{11}$$

(recall that $m_- + m_- = 1$).

The cross-section of the transformation surface by the plane $\varepsilon_1 = \varepsilon_2$ is shown in Fig. 6. One can see that the transformation surface has common domains with envelope surface shown in Fig. 2. Domains corresponding to the third rank laminates coincide with domains of ellipsoidal new phase inclusions. Domains of second rank laminates with orthogonal normals $\mathbf{n}_1$, $\mathbf{n}_2$ partially coincide with domains of cylindrical new phase inclusions. Of course, domains of simple laminates coincide with domains of new phase layers.

The difference is that the transformation surface is convex. The convexisation is resulted from an opportunity to minimize the energy due to formation of the inclined second rank laminates at strains that correspond to domains 4, $4'$ and 7 in Fig. 6 (dash-two-dotted lines).

Acknowledgements

This work was supported by RFBR (grant No 10-01-00670-a) and National Science Foundation, DMS-0707974. ABF also greatly appreciates the support of DFG (Grant No. AL 341/35-1)

References

[1] M. A. Antimonov, A. V. Cherkaev. On optimal 3D structures with minimal stiffness. Proceedings of international school-conference of young scientists “Mechanic 2009”, Aghavnadzor, Armenia, 2009. pp 145–151.

[2] M. Antimonov, A. Freidin. Equilibrium cylindrical new phase inclusion. Proceedings of the XXXVII Summer School – Conference APM 2009. pp. 57–64.

[3] I. V. Chenchiah, K. Bhattacharya. The relaxation of two-well energies with possibility unequal moduli. (2008) Archive for Rational Mechanics and Analysis. vol. 187. Issue 3, pp. 409-479.

[4] A. V. Cherkaev. 2000. Variational Methods for Structural Optimization. Berlin / Heidelberg / London / etc.: Springer-Verlag.

[5] V. A. Eremeyev, A. B. Freidin, L. L. Sharipova. The stability of the equilibrium of two-phase elastic solids. Journal of Applied Mathematics and Mechanics (PMM) 71 (2007) 61–84.

[6] A. B. Freidin. Crazes and shear bands in glassy polymer as layers of a new phase, Mechanics of Composite Materials (1989) (1) 1-7.

[7] A.B. Freidin, Small strains approach to the theory on solid-solid phase transformations under the process of deformation, Studies on Elasticity and Plasticity, St. Petersburg State University, 18 (1999) 266-290 (in Russian).

[8] A. B. Freidin. On new phase inclusions in elastic solids, Z. Angew. Math. Mech. (ZAMM) 87(2) (2007) 102–116.

[9] A. B. Freidin, Y. B. Fu, L. L. Sharipova, E. N. Vilchevskaya. Spherically symmetric two-phase deformations and phase transition zones, Int. J. Solids and Struct, 43 (2006) 4484–4508.

[10] A. B. Freidin, L. L. Sharipova. On a model of heterogenous deformation of elastic bodies by the mechanism of multiple appearance of new phase layers. Meccanica (2006) 41: 321–339.

[11] A. B. Freidin, E. N. Vilchevskaya. Multiple development of new phase inclusions in elastic solid, Int. J. Engineering Sciences. 2009. V. 47. P. 240–260.

[12] Y. B. Fu, A. B. Freidin. Characterization and stability of two-phase piecewise-homogeneous deformations// Proc. Roy. Soc. London. Ser. A. 2004. V. 460. P. 3065–3094.

[13] L. V. Gibiansky, A. V. Cherkaev. (1997) Design of composite plates of extremal rigidity. In Cherkaev A. V. and Kohn R. V., editors "Topics in the Mathematical Modelling of Composite Materials" volume 31 of Progress in nonlinear differential equations and their applications, pages 95-137. Birkhäuser Boston, Boston, MA. Translation.

[14] M. A. Grinfeld. Thermodynamic methods in the theory of heterogeneous systems, Longman, New York, 1991.

[15] I. M. Kaganova, A. L. Roitburd, Equilibrium of elastically interacting phases, Sov. Physics JETP, 67 (1988) 1174-1186.

[16] L. B. Kublanov, A. B. Freidin. J. Appl. Math. Mech. (PMM USSR) 52, 382–389 (1988) (translation of Prikl. Matem. Mekhan., 52, 493–501).

[17] V. A. Loboduk, E. I. Estrin. Martensite transitions. Moskow, Fizmatlit, 2009. pp. 352.

[18] G. W. Milton. The theory of composites. Cambgidge university press. 2004. pp. 719.

[19] N. F. Morozov, A. B. Freidin. Phase transition zones and phase transformations of elastic solids under different stress states, Proc. Steklov Math. Inst. 223 (1998) pp.220-232.

Mikhail A. Antimonov, Alexander B. Freidin, Institute for problems in mechanical engineering, Bolshoy pr., 61, V. O., St. Petersburg, 199178, Russia
Andrej V. Cherkaev, Department of Mathematics, 155 S 1400 E, University of Utah, Salt Lake City, Utah 84112 U.S.A.

The method of determination of thrust bearing pad angle in a fluid flow

O. V. Antonova A. I. Borovkov A. A. Michailov I. B. Voynov
antonova@compmechlab.com

Abstract

The non-reversing thrust bearing of hydrogenerator is investigated. Cycle symmetry of construction is considered. The angle of the thrust bearing position in fluid flow is determined.

1 Introduction

One of the most critical hydrogenerator nodes is a thrust bearing. In the large vertical aggregates the bearing undergoes huge axial loads caused by weight of rotating parts and reaction of water to the turbine wheels. The thrust bearing undergoes only axial loads. Despite performing a series of tests and implementing new design solutions, a problem of ensuring the reliable operation of the bearings is still extremely actual [1]. The main goal of the presented research is a method for determination of the pad angle in a fluid flow, satisfying the condition of equality of the forces acting on the thrust bearing. This will allow to determine numerically the working capacity of the thrust bearing during design process.

2 CAD-model

In this paper the thrust bearing configuration with eight segments is considered. Cyclic symmetry of the construction is taken into account. The main results are shown for only one trust bearing segment. At Fig. 1 The CAD (Computer Aided Designed)-models of the main thrust bearing parts are shown: bearing segment, support and teflon lining.

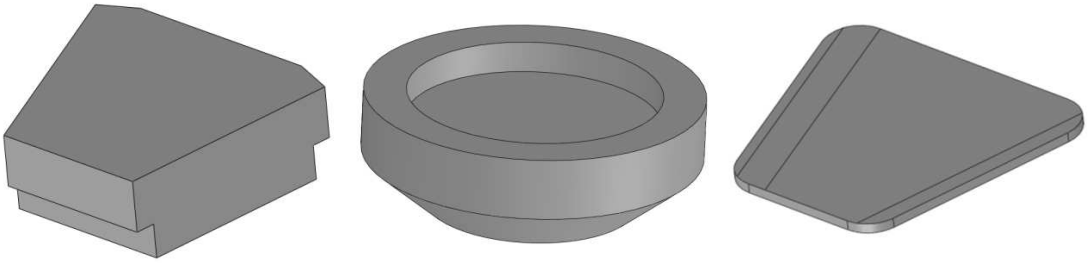


Figure 1: CAD-models of the main segment parts (segment, support, teflon lining)

It should be noticed, that the teflon lining model includes the detailed geometry of the input and output edges. This is necessary for a correct simulation of the oil-film wedge formation due to the oil flow, so the geometric characteristics of the emerging oil-film wedge between the bearings and the runner plate determine the bearing carrying capacity as a whole. At Fig. 2 one can see the developed assembly, including all basic elements of the simulated thrust bearing.

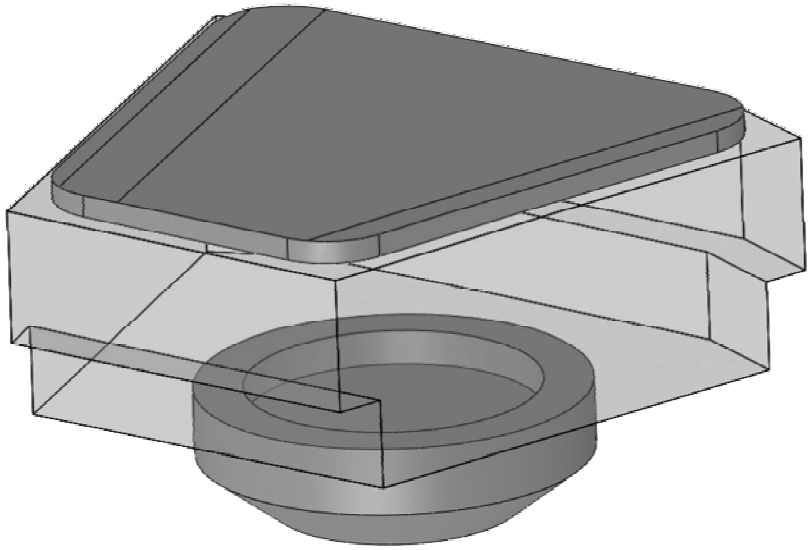


Figure 2: Thrust bearing assembly

For normal operation of the non-reversing thrust bearing the support point is to be shifted relative to the center of gravity of the pad working surface (see Fig 3, [2]). The offset OO_1 is called the tangential eccentricity.

3 Computation of the pad angle under fluid flow

In the process of a fluid flow, the segment rotates relative to the runner plate forming an oil-film wedge. A fluid flow through the oil wedge induces pressure on the segment surface, preventing a contact interaction with the bearing during its normal operation. The minimum gap which occurs between the runner plate and the teflon lining output edge is typically measured in hundredths or thousandths of millimeter. Thus, the oil wedge can be considered as a thin film. However, the usage of the hydrodynamic lubrication theory is not applicable for the determination of the gap and therefore the problem should be solved from the standpoint of the general hydrodynamics. There are several manuals [2, 3], that describe various procedures to determine the angle of the thrust bearing position and the distance between thrust bearing output edge and heel. These procedures are based on semi-empirical dependencies and contain a number of factors that are to be determined by the way of complex and expensive experiments. In this paper it is suggested to fulfill the determination of the thrust bearing position angle by solving a series of hydrodynamics problems. The problems were solved in isothermal formulation. For flow description the Navier-Stokes equations were used [4]:

$$\frac{\partial V}{\partial t} + (V \cdot \bigtriangledown)V = -\frac{1}{\rho} grad P + \nu \bigtriangledown^2 V \tag{1}$$

To obtain the closed system of equations it's necessary to add the equation of continuity:

$$\frac{\partial \rho}{\partial t} + div\,(\rho V) = 0 \tag{2}$$

Where $\nu = \mu/\rho$ – kinematic viscosity coefficient, μ – kinematic viscosity, ρ – fluid density, V – velocity vector, P – pressure.

Hydrodynamic models of thrust bearing workspace filled by liquid lubricant were developed using advanced software system for computational fluid dynamics (CFD) - ANSYS/CFX. There

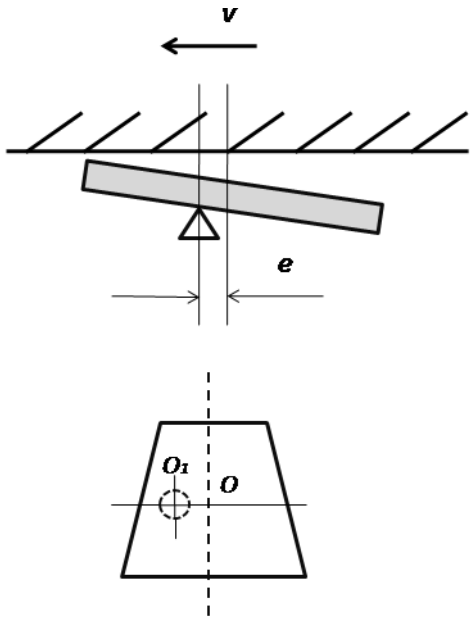


Figure 3: Scheme of non-reversing pad bearings support

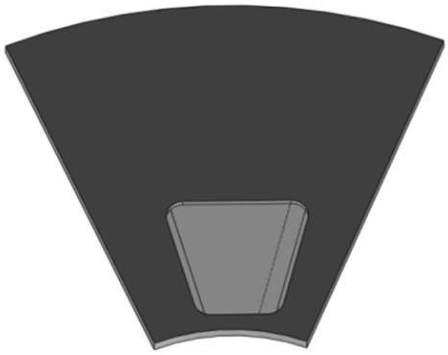


Figure 4: 3-D CAD-model of thrust bearing workspace

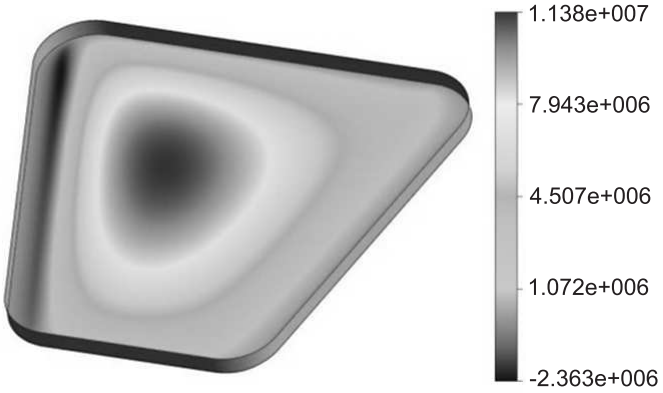


Figure 5: Typical pressure distribution on segment surface is shown, Pa

are 996 006 calculational cells in CFD-model. Numerical hydrodynamic model, which includes an oil-film wedge and the surrounding region between the work area of pad and the runner plate (except non-working surface of the pad and segment) is shown at Fig. 4. On the periodical faces equalities of pressure and components of velocity vector were set. On the runner plate and shaft faces the constant angular velocity corresponding to the frequency of shaft rotation was assigned.

At fig. 5 typical pressure distribution on segment surface is shown.

Assuming that the stiffness of the thrust bearing and steel parts is such that in the process of work a significant deformation in bearing does not appear, it is suggested to neglect the most parts forming the structure and consider the operation of the bearing segment only. In the operation process the following loads are acting on the trust bearing located in the holder:

- gravity (P), arising due to presence of eccentricity, and tending to increase the angle of the thrust bearing (see Fig 6.1);

- hydrodynamic pressure (p = p (x, y, z)) that is generally unevenly distributed over the working surface of the thrust bearing and tends to reduce the angle of the thrust bearing (see Fig 6.2).

The balance of these forces determines the bearing position angle, and as a result it allows to calculate the carrying capacity of the bearing at the given distance between the thrust bearing output edge and surface of heel.

Tipping moment due to the own weight relative to the contact point is:

$$M_o^{weight} = P \cdot e \cdot \cos(\alpha) \tag{3}$$

Tipping moment relative to the contact point due to the action of hydrodynamic pressure is calculated by the following formulae:

$$dF = p(x, y, z) \cdot dS \tag{4}$$

$$m = dF \cdot l \tag{5}$$

$$m_1 = dF_1 \cdot l_1 \tag{6}$$

$$M_0^{pressure} = \int\limits_S m \cdot dF - \int\limits_{S_1} m_1 \cdot dF_1 \tag{7}$$

where dF_i – the force arising from the pressure acting on the area dS, m_i – the moment of the force acting on the area S_i, $i = 1, 2$.

Moments around the point of support, acting to the shoe in the gravitational field:

$$M_y^0 = (m_{1y} \cdot l_{1y} - m_{2y} \cdot l_{2y}) \cdot g \tag{8}$$

$$M_z^0 = (m_{2z} \cdot l_{2z} - m_{1z} \cdot l_{1z}) \cdot g \tag{9}$$

where $m_{1y}, m_{2y}, m_{1z}, m_{2z}$ – masses of relevant parts of the segment and $l_{1y}, l_{2y}, l_{1z}, l_{2z}$ – the distances from the axis to the gravity center of the segment relevant part (see Fig. 7.1 and 7.2); g – acceleration of gravity, assumed to be 9.81 m/s^2.

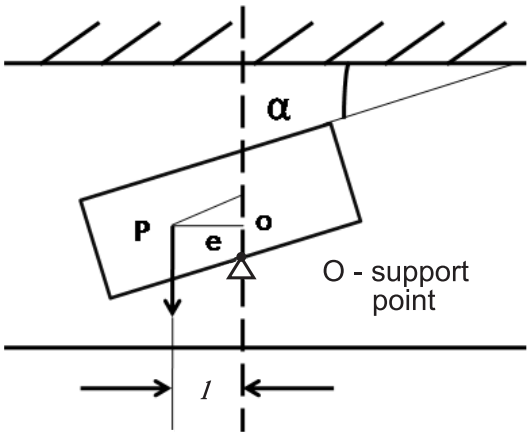


Figure 6.1: The scheme for determination of tipping moment due to gravity

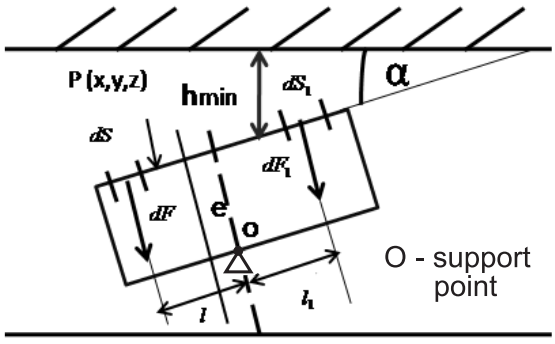


Figure 6.2: The scheme for determination of tipping moment due to the action of hydrodynamic pressure

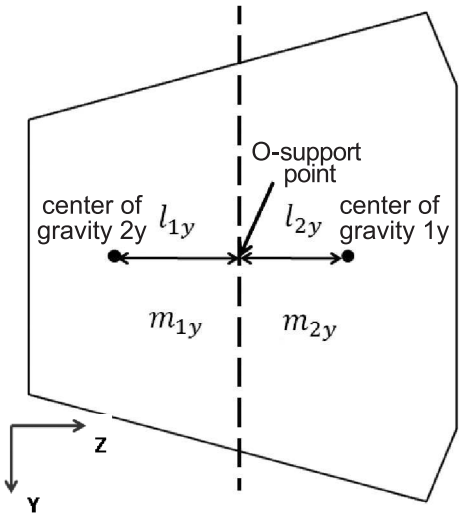


Figure 7.1: Definition of the moment acting on the pad in the gravitational field about Y axis

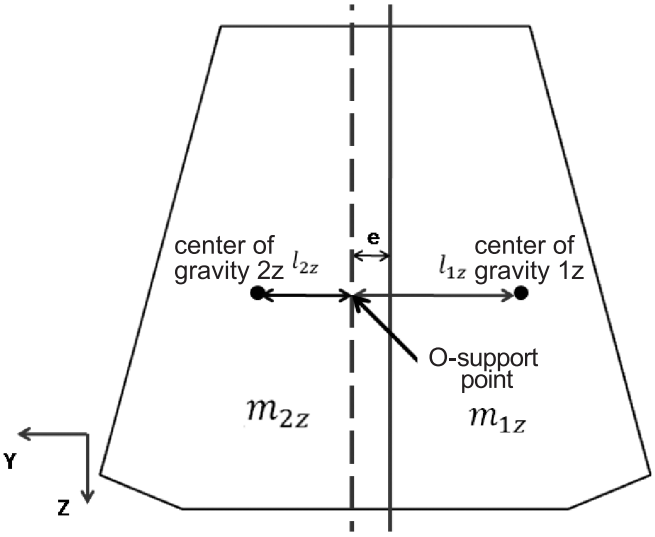


Figure 7.2: Definition of the moment acting on the pad in the gravitational field about Z axis

The equation of moments equilibrium gives the following condition to define the position angle:

$$M_0^{weight} + M_0^{pressure} = 0 \tag{10}$$

Distribution of hydrodynamic pressure is a function of thrust bearing location, thus we have a closed system of equations, depending on the parameters of the thrust bearing position. Fixing the parameters of the thrust bearing location, we can determine the forces acting on the thrust bearing. Using these forces in the equation of equilibrium mentioned above, one can check whether the system is self-balanced. If the system is self-balanced, the bearing capacity of the thrust bearing can be calculated. After performing the comparison of results obtained with the rated capacity, one can make conclusions about compliance of the thrust bearing location parameters to the real data. This algorithm does not require multidisciplinary analysis with conjugation to the solid and fluid conditions for consideration of the current problem. As a result it allows to iteratively determine the parameters of the thrust bearing location in the fluid flow.

4 Conclusions

In this work the algorithm for determination of the thrust bearing pad angle in a fluid flow is proposed. Numerical parametric model for CFD calculations is developed. Usage of the developed algorithm allows to obtain more accurate values of oil-film wedge thickness compared to estimates obtained by semi-empirical method, because current algorithm takes into account moments from gravity acting on the thrust bearing.

References

[1] A.E. Aleksandrov. Hydrogenerator thrust bearings: Energy press, 1975. (In Russian).

[2] V.A. Voskresensky, V.I. Diakonov. Design and analysis of the sliding bearings (thin-film lubrication): Handbook. Mashinostroenie, Moscow, 1980. 224 p. (In Russian).

[3] Machinery handbook, 26th edition. Industrial press Inc, New York, 2000. 2640 p.

[4] L.G. Loytsyanskiy. Fluid mechanics, M., 1987. (In Russian).

Olga.V. Antonova, SPbSTU, 29 Politekhnicheskaya str., 195251 St. Petersburg, Russia

Fatigue fracture of aging elastic viscous materials subjected to cyclic compression

Robert A. Arutyunyan Kira S. Yakimova
Robert.Arutyunyan@paloma.spbu.ru

Abstract

The problem of fatigue fracture of aging elastic-viscous materials subjected to cyclic compression is considered. Investigations of the mechanical properties of polyurethane in the experiments on pressure were carried out. In the experiments the specimens without aging and with the climate and deformation aging (about twelve years) were used. The problem of thin layer made of incompressible viscous material subjected to compression by two long parallel plates is considered. The stress diagrams for the unaged and aged material are constructed. It is shown, that on the surface and inside of the pressed layer the state of hydrostatic pressure is occurred. The value of this state is increased with the increasing of aging effect and the loading rate. Superposition of these effects is the main cause of degradation and fracture of material in the process of cyclic pressure. The received results can be applied to estimate the fatigue life of different elastic viscous materials (natural and artificial rubbers, polyurethane, asphaltic concrete) and the items where these materials are used as working elements, for example, tires, roads, the pressing shafts with the rubber or polyurethane cover and others.

Financial support of the Russian Foundation for Basic Research (Grant N08-08-00201) is gratefully acknowledged.

As an example of aging behavior of polymers the investigations of the mechanical properties of polyurethane in the experiments on pressure were carried out. In the climate aging experiments three specimens of the dimensions: 20x20x30 *mm.* were used. To draw the original stress-strain curve one specimen was tested. This curve is noted in Figure 1 by number 1. In this figure the $\sigma - \varepsilon$ curve (the curve is noted by number 2) received in pressure experiments for the specimens aged during about twelve years. The same type $\sigma - \varepsilon$ curve was found in the experiments with the second aged specimen. Compare the $\sigma - \varepsilon$ curves for aged and unaged material we can see the significant (10-15 times) increase of strength value in the middle region of the $\sigma - \varepsilon$ curves.

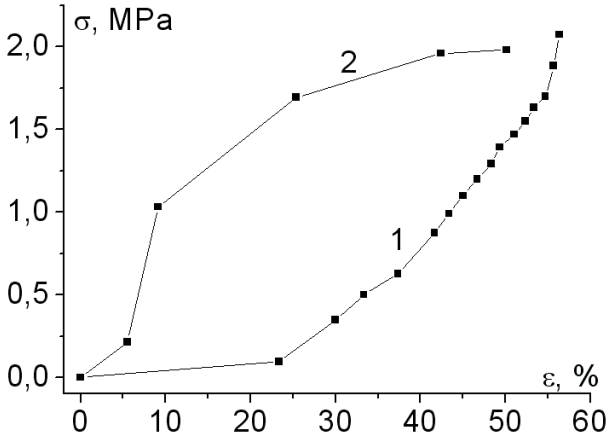


Figure 1: The $\sigma - \varepsilon$ diagrams: 1 - for unaged, 2 - for aged during about twelve years specimens.

In deformation aging experiments one specimen of the dimensions: 150x15x20 mm were used. The specimen was aged during about twelve years after testing by deep pressure. The $\sigma - \varepsilon$ curve received in this experiment is shown in Figure 2. The curve is noted by number 2. In this figure the curve $\sigma - \varepsilon$ for the unaged specimen, noted by number 1, is also presented. The increase of strength in aging process is very high (about 40 times according the middle region of the $\sigma - \varepsilon$ curves).

To draw the curves $\sigma - \varepsilon$, shown in Figures 1, 2, during the experiments the current value of specimen length were measured. The current value of the cross section area was calculated using the incompressibility condition: $l_0 F_0 = lF$ (l_0, F_0 are the initial and l, F are the current length and cross section area of the specimen).

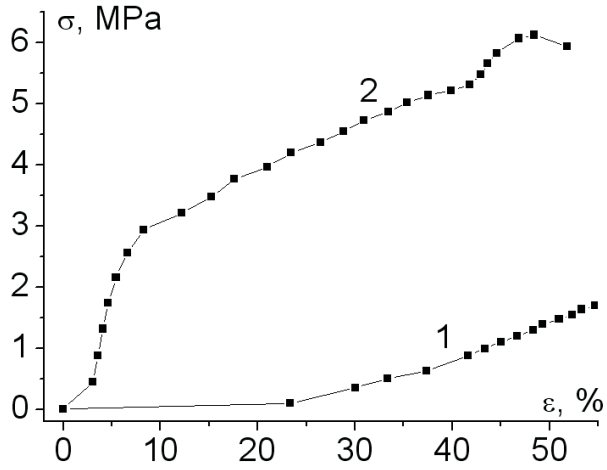


Figure 2: The $\sigma - \varepsilon$ diagrams: 1 - for unaged, 2 - for deformation aged during about twelve years specimens.

To describe the aging processes in elastic-viscous materials the Maxwell model expressed in scale of effective time ω is considered. The parameter ω is defined by the following relation [1]

$$d\omega = f_1(\omega, \varepsilon, t)dt + f_2(\omega, \varepsilon, t)d\varepsilon. \tag{1}$$

The case of plane strain is considered and the Maxwell equations for this problem are expressed as

$$\begin{aligned} &\dot{\varepsilon}_x^e = \frac{\partial}{\partial \omega}\left[\frac{3}{2E(\omega)}(\sigma_x - \sigma)\right] \qquad \dot{\varepsilon}_y^e = \frac{\partial}{\partial \omega}\left[\frac{3}{2E(\omega)}(\sigma_y - \sigma)\right] \\ &\dot{\gamma}_{xy}^e = \frac{\partial}{\partial \omega}\left[\frac{3\tau_{xy}}{E(\omega)}\right] \qquad \sigma = \frac{1}{2}(\sigma_x + \sigma_y) = \sigma_z \end{aligned} . \tag{2}$$

$$\begin{aligned} &\dot{\varepsilon}_x^v = \frac{\partial \varepsilon_x^v}{\partial \omega} = \frac{1}{2\eta(\omega)}(\sigma_x - \sigma) \qquad \dot{\varepsilon}_y^v = \frac{\partial \varepsilon_y^v}{\partial \omega} = \frac{1}{2\eta(\omega)}(\sigma_y - \sigma) \\ &\dot{\gamma}_{xy}^v = \frac{\partial \gamma_{xy}^v}{\partial \omega} = \frac{\tau_{xy}}{\eta(\omega)} \end{aligned} . \tag{3}$$

In (2)-(3) the indexes "e", "v" are used for the elastic and creep deformations. The rate of full deformation is equal to $\dot{\varepsilon} = \dot{\varepsilon}^e + \dot{\varepsilon}^v$.

For the case of pure linear viscous material in the scale of real time the equations (2)-(3) will be reduced as

$$\begin{aligned} &\sigma_x - \sigma = 2\,\eta\,\dot{\varepsilon}_x, \;\; \tau_{x\,y} = \eta\,\dot{\gamma}_{x\,y}, \\ &\sigma_y - \sigma = 2\,\eta\,\dot{\varepsilon}_y. \end{aligned} \tag{4}$$

$$\sigma = 1/2(\sigma_x + \sigma_y) = \sigma_z. \tag{5}$$

The system of equations (4)-(5) in application to the plane strain problem of thin layer of $2a$ width, $2b$ length and $2h$ thickness, made of high elastic material subjected by two long parallel plates, were solved [2].

According to the received solutions the stress components are expressed in the form

$$\sigma_x = -P + 2\eta\dot{\varepsilon}_x = \frac{P_0}{a^2}\left(x^2 - 3y^2 - a^2 + 2h^2\right),$$

$$\sigma_y = -P + 2\eta\dot{\varepsilon}_y = \frac{P_0}{a^2}\left(x^2 + y^2 - a^2 - 2h^2\right), \tag{6}$$

$$\tau_{xy} = -\eta\dot{\gamma}_{xy} = -\frac{3\eta\, v_0 xy}{h^3}.$$

As it follows from these relations, in arbitrary cross section plane $x = const$ the normal stresses are distributed by parabolic law. Along the length and in the cross section plane the shear stresses are distributed by linear law.

The diagrams of the stresses were built using the formulae (6) where the following values of parameters $v_0 = 1\ mm/min.$, $2h = 25\ mm$, $2a = 10,8\ mm$, $\eta = 2,265\ MPa \cdot min.$ are introduced. As follows from the formulae (6) the functions σ_x and σ_y have maximums at the point (0, 0).

The diagrams of the stresses σ_x are shown in Figure 3 for the two cross sections $x = 0$ and $x = a$. The maximum stresses are positive and at $x = a$ they are $\sigma_x = 0,54\ MPa$. With approaching to the planes $y = \pm h$ the stress σ_x changes the sign into the negative and at $y = \pm h$ $\sigma_x = -0,27\ MPa$. As it follows, the negative values of σ_x are observed in the thin stratum about $3\ mm$ in thickness near the contact planes.

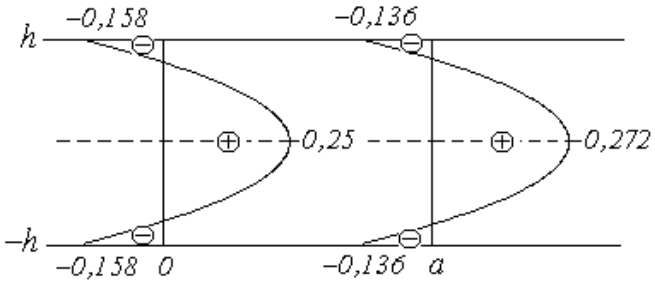


Figure 3: The diagrams of stresses σ_x.

The values of the stress σ_y are negative with the maximum at the point (0, 0) equal to $\sigma_y = -0,294\ MPa$. With the moving off from the plates $x = 0$ the stresses σ_y are decreased and for the big values of a they will tend to zero. The diagrams of the stresses σ_y for the two cross sections $x = 0$ and $x = a$ are shown in Figure 4.

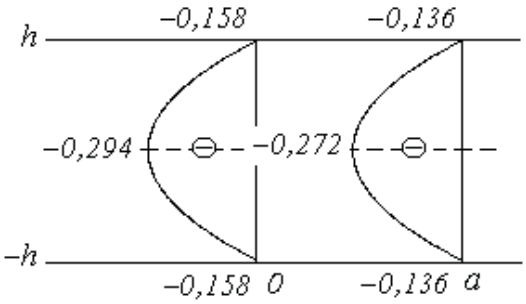


Figure 4: The diagrams of stresses σ_y.

As follows from the plane strain problem, $\sigma_z = 1/2(\sigma_x + \sigma_y)$, so comparing the values of three normal stresses, one can come to the following conclusion. On the surface of pressed plane and in

the inside points of the thin stratum about 3 mm in thickness near the contact planes the stress condition approaches to the state of hydrostatic pressure. So in these regions the brittle fracture will be appeared. These effects, strengthened by the aging processes, can be considered as the main cause of the degradation and fracture of material. To support these conclusions we will consider the stress diagrams σ_x and σ_y for the thin layer material undergoing the different regimes of aging, in accordance with the changes of viscosity coefficient η. These diagrams are shown in Figures 5 and 6. The calculations were carried out for two values of viscosity coefficient $\eta = 0,5\ MPa \cdot min.$ and $\eta = 4\ MPa \cdot min.$

As it is seen from these diagrams, the stresses σ_x and σ_y are increasing when the viscosity coefficient η is increasing. The hydrostatic component of stress is also changing. For example the value of the hydrostatic stress is equal to $-0,035\ MPa$, when $\eta = 0,5\ MPa \cdot min.$ If the viscosity coefficient is increased to the value of $\eta = 4\ MPa \cdot min.$, then the hydrostatic component of stress is increased to the value of $-0,278\ MPa$.

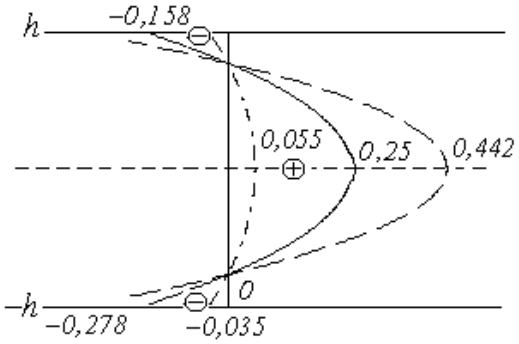


Figure 5: The σ_x diagrams for different values of viscosity coefficient η.

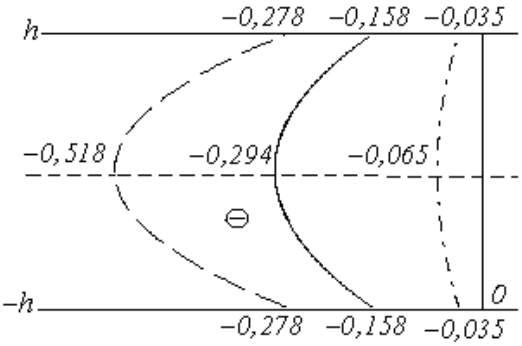


Figure 6: The σ_y diagrams for different values of viscosity coefficient η.

So the aging of material provide the increasing of hydrostatic component of stresses, the embrittlement processes [3, 4] and accelerating the fracture of surface layer.

The receive results we will use to estimate the cyclic strength of layer made of high elastic materials, for example, polyurethane in high elastic state. This polymer is used as a cover of pressure cylinders employed, for example, in paper industry. The very thin paper layer is rolled between the two pressed to each other rotating steel cylinders. One of cylinders is covered by thin polyurethane layer. In engineering practice three are many observations of cyclic failure of polyurethane layer so the estimation of the cyclic strength of this layer will be very useful for the practical applications.

From our pressure experiments, carried out on the specimens made of polyurethane, follows that several minutes are needed for the full recovery of deformation after unloading. So for the fixed surface layer element the deformation accumulated during active loading by pressure can't be

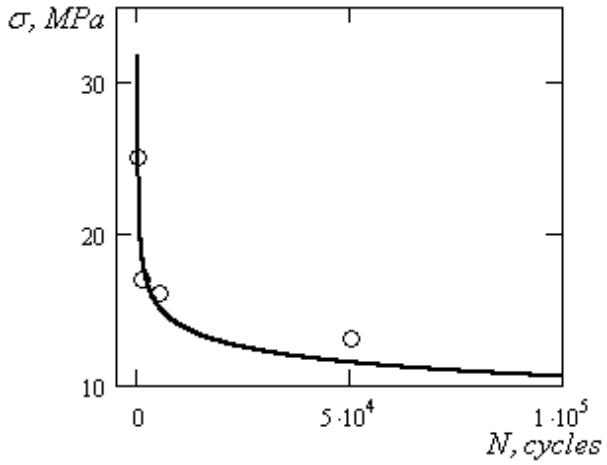


Figure 7: Fatigue fracture curve according to the criterion (9), points - experimental results.

fully recovered in the unloading process. As a result, under the action of cyclic loading the polymer layer will be in the deformed state when the pressure cylinder is rotating uninterruptedly. And what is more, the so called cyclic creep deformation will accumulate from cycle to cycle. However, in the thin layer near the contact planes where the stress condition approaches to the state of hydrostatic pressure the deformations are met with difficulties, so on the contact planes and in the inner points inside the stratum the material failure will be appeared. As a result of the structure damage of material the permanent deformation will be accumulated. Within one cycle this value is rather small, but in the process of high cycling the accumulated damage will reach the limiting failure value. Taking into account these results we will formulate the fatigue fracture criterion.

Let's consider the small element of polymer layer. For this element we will apply the mass conservation law. The material density ρ is changed in accordance with the mass conservation law $\rho_0 V_0 = \rho V$, where ρ_0, V_0 are initial and ρ, V current values of density and volume of the element. Using this law and introducing the notation $\varepsilon_V = V/V_0 - 1$, we will have the following relation $\rho/\rho_0 = 1 + \varepsilon_V$. Taking logarithm from the last relation we will receive the following approximate relation

$$\ln(\rho_0/\rho) = \varepsilon_V = \varepsilon_x + \varepsilon_y + \varepsilon_z = (1 - 2\nu)\varepsilon_x, \tag{7}$$

where ν is the current value of the coefficient of lateral deformation.

If $\varepsilon_x = \varepsilon_x^e + \varepsilon_x^v$, where ε_x^e is elastic, ε_x^v is viscous components of full deformation. Taking into account the Hook's law $\varepsilon_x^e = \sigma/E$, and considering the fracture moment when $\varepsilon_x = \varepsilon_*$, $\rho = \rho_*$, $\nu = \nu_*$, $E = E_*$, the relation (7) can be expressed in the form [4]

$$\frac{\sigma}{E_*} + \varepsilon_* = \frac{\ln(\rho_0/\rho_*)}{1 - 2\nu_*}. \tag{8}$$

In experiments [5, 6] direct correlation between the function $\ln(\rho_0/\rho)$ and the modulus of elasticity E are observed. According to our investigations and the investigations of other authors [5] the value of elasticity modulus for polyurethane specimen is essentially reduced with fatigue cycles. So when formulating the fatigue fracture criterion, based on the relation (8), we will consider the following approximation for the current value of elastic modulus $E = E_0(1 - \alpha \ln(\rho_0/\rho))$, where α is constant, E_0 is the initial value of modulus of elasticity. Introducing this relation into (8) and considering the nonlinear law for the viscous component of deformation we will receive the following fatigue fracture criterion

$$\frac{\sigma}{E_*} + B\sigma^n N^m = \frac{1}{1 - 2\nu_*} \frac{1}{\alpha} \left(\frac{E_0 - E_*}{E_0} \right), \tag{9}$$

where N is the number of cycles to fracture, B, m, n are constants.

The theoretical fatigue criterion (9) is shown in Figure 7 by solid line. The points in this figure are corresponding to the experimental results for cyclic pressure experiments, carried out on the specimens made of polyurethane. To construct the theoretical curve the following parameters in criterion (9) are introduced: $E_0 = 180\ MPa$, $E = 40\ MPa$, $B = 6 \cdot 10^{-2}\ [MPa]^{-0,5}\ [cycl.]^{-0.06}$, $n = 0,5$, $m = 0,06$, $\alpha = 10$, $\nu_* = 0,4$.

References

[1] R.A. Arutyunyan, K.S. Yakimova. Damage accumulation and fracture of high elastic thin layer subjected to cyclic compression // Assessments of reliability of materials and structures: problems and solutions. International conference, St. Petersburg, Russia, 17-20 June, 2008. SPb: SPb State Polytechnic University. 2008. P. 29-30.

[2] Arutyunyan R.A. The problem of deformation aging and prolonged fracture in material sciences. Sankt-Petersburg: S.-Petersburg university press. 2004. 252p. (in Russian).

[3] Bruijn de J.C.M. The failure behavior of high density polyethylene with an embrittled surface layer due to weathering. Delft: Delft University press. 1992. 118p.

[4] Struik L.C.E. Physical aging in amorphous polymers and other materials. Amsterdam, Oxford, New York: Elsevier Sci. Publ. Comp. 1978. 229p.

[5] J. Mead, S. Singh, D. Roylance, J. Patt. Nonlinear response and thermomechanochemical degradation of a urethane elastomer // Polymer engineering and science. 1987. vol. 27. N 2. P. 131-140.

[6] Cheremskoi P.G., Slezov V.V., Betechtin V.I. Pores in solids. M.:Energoatomizdat. 1990. 376p. (in Russian).

Robert A. Arutyunyan, St.-Petersburg State University, Faculty of Mathematics and Mechanics, Sankt-Petersburg, Petrodvoretz, Universytetskii prospect, 28, 198504, Russia

Brittle fracture of rocks under oblique impact loading

I. Asonov I. Berinskiy J. Ing A. Krivtsov S. Le-Zakharov E. Pavlovskaia
M. Wiercigroch
iberinsk@gmail.com

Abstract

In this paper the effects of oblique impact loading of brittle rocks are investigated. The drilling process in hard rocks is simulated using particles dynamics (PD). The rock sample and impactor are described by particles with different bond strength. Impact is generated by applying a dynamical force to the impactor. The results are compared with the predictions obtained according to a simple analytical model of a drifting oscillator [1]. It is shown that the models correspond to each other reasonably well but there are a number of differences in their predictions. The results of the computer simulations aim to provide a valuable insight into the brittle fracture of rocks subjected to impact loading and eventually improve analytical model of this process.

1 Introduction

This paper is devoted to the modelling of brittle fracture in rocks subjected to oblique impact loading. For this purpose a numerical model using particle dynamics (PD) technique was developed, which is based on the earlier model by Krivtsov *et al.* [2]. In new numerical model the type of loading was changed for better simulation of real drilling process. To validate the obtained results, the PD simulations are compared with predictions using the analytical model which was proposed in [1]. This simplest theoretical model includes a massive rigid body (the drilling tool) subjected to static and dynamic excitation forces and interacting with the drilled formation, which was model by the constitutive equations of the material resistance based on dry friction. In the case of a one dimensional representation this can be reduced to a system with one degree of freedom, but due to essential nonlinearity even this elementary description leads the equations which can be solved analytically only in some certain cases. Despite quite radical simplifying assumptions, the model was able do describe the fall of material removal rate for a higher static loading with a good agreement to experimental investigations. In [1] the material removal rate was investigated as a function of the static force and the amplitude of the harmonic force. Later in [3]–[4] a more complex model was proposed where the visco-elastic properties of the drilled formation have been taken into account. As a result the system moves forward in stick-slip phases, and its behavior may vary from periodic to chaotic motion. In the current work numerical PD simulations are used to consider a number of new features such as rotation torque of the tool, explicit debris removal, and geometry of the contacting bodies.

2 Particle Dynamics model

In particle dynamics method the objects (tools, targets etc.) are made of particles arranged in crystal lattices. Every particle represent some part of the object material such as a grain or a domain. Usually 10^3—10^4 particles are used for the standard tests and 10^5—10^6 particles are used to obtain more accurate results. In this work two massive bodies are considered, namely the tool (drill bit) and the specimen (rock material). A 2D model with a close-packed hexagonal lattice is constructed and the motion of the particles is obtained through integration of the Newtonian

equations of motion with the prescribed interaction forces:

$$F_1(r) = \begin{cases} F(r) & \text{for } 0 < r \le b; \\ k(r)F(r) & \text{for } b < r \le a_{cut}, \end{cases} \tag{1}$$

where $F(r)$ is the force corresponding to the Lennard-Jones potential with the equilibrium distance a and bond energy D; quantity b is the brake distance for the Lennard-Jones interaction:

$$F(r) = f_0 \left[\left(\frac{a}{r}\right)^{13} - \left(\frac{a}{r}\right)^{7} \right], \qquad f_0 = \frac{12D}{a}, \qquad b = \sqrt[6]{\frac{13}{7}} \approx 1.1a; \tag{2}$$

$k(r)$ is a shape function:

$$k(r) = (1+\alpha)\left(1 - \left(1 + \sqrt{\frac{\alpha}{1+\alpha}}\right)\left(\frac{r^2 - b^2}{{a_{cut}}^2 - b^2}\right)^2\right)^2 - \alpha\,, \tag{3}$$

where α is a positive parameter, defining brittleness of the material, $a_{cut} > b$ is the cut-off distance for the interaction. Increasing α results in the repulsion appearing in the vicinity of the cut-off distance. This produces a potential barrier for joining two particles, which were separated due to the impact fracture. The parameter α changes from 0 to 2, and the value $\alpha = 2$ corresponds to a brittle material. The geometry and loading of the drilling tool is shown at Fig. 1.

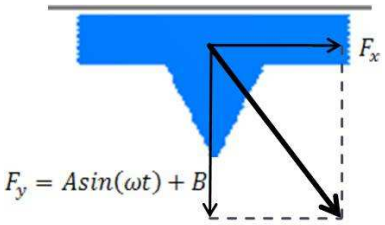


Figure 1: Geometry and loading applied to the drilling tool

Periodic kinematic boundary conditions are applied on the left side and on the right side of the tool and the specimen, and the specimen is rigidly fixed at the bottom. The material of the drill bit is considered to be 10 times harder than material of the specimen. It is simulated with different bond energies for the particles of the specimen and the drill bit.

The applied loading in the new model is closer to reality than in the previous one [2], where the initial velocities of the particles were applied before every strike of the drill bit. Instead, now the dynamical conditions are applied to every particle at every time step. Thus the external axial force $F_y = A\sin\omega t + B$ directly corresponds to the force used in the analytical model [1]. The shear loading force F_x is introduced to model a rotation torque. As a result the external loading is described by three independent parameters namely by the amplitude of dynamic axial force A, magnitude of static force B, and the shear force F_x (Fig. 1).

Parameter	*Value*
Particles number	$(5\text{–}30)\cdot 10^3$
Avg. thermal velocity	$0.01v_d$
Number of strikes	5–10
Time of modeling	$(147\text{–}295)T_0$
Period of strikes	$(4.69\text{–}100)T_0$
Integration step	$0.02T_0$
Cut-off radius (a_{cut})	$1.4a$
Brittleness (α)	2
Strength: Tool/Specimen (D_1/D_2)	10

Table 1: Parameters of the model.

Numerical parameters of the model are presented in table 1. Here v_d is a dissociation velocity of the particle; T_0 is a period corresponding to the natural frequency of the particle as

$$T_0 = 2\pi\sqrt{\frac{C}{m}}, \qquad v_d = \sqrt{\frac{2D}{m}}, \tag{4}$$

where m is the particle mass and $C = -F'(r) = 72D/a^2$ is the stiffness of particle interaction.

It should be noted here that the proposed numerical model also allows to simulate wear and tear of drill bit as well as the rock fracture.

3 Results of the particle dynamics simulation

A numerical study was conducted to identify the optimal parameters of loading. Static tests for model with about 10000 particles indicate that a value of $0.01f_0$ may be chosen as a maximum value of static loading force B. The value of $B = 0.002f_0$ was chosen as a minimum value. The simulations were carried out for a number of B values taken with the step of $0.002f_0$. It was obtained in [1] that the optimal ratio between the static force and the amplitude of the dynamic force is $B/A = 0.387$ and therefore this value was used in computer simulations. For the chosen values of axial loading the dependence between the shear force F_x and material removal rate (MRR) was constructed and the results are shown in Fig. 2. MRR is defined here as the quantity of material removed during one strike of the tool, and the average MRR for different distributions of the initial velocities of the particles (different heat distribution) is presented. It is assumed that the material is removed if it has been divided into separate particles. To make comparison of the obtained results easier, a scaled value of MRR has been introduced as

$$\widehat{MRR} = \frac{MRR - MRR_{min}}{MRR_{max} - MRR_{min}}, \tag{5}$$

where MRR_{min} and MRR_{max} are the minimum and maximum value of MRR for given B.

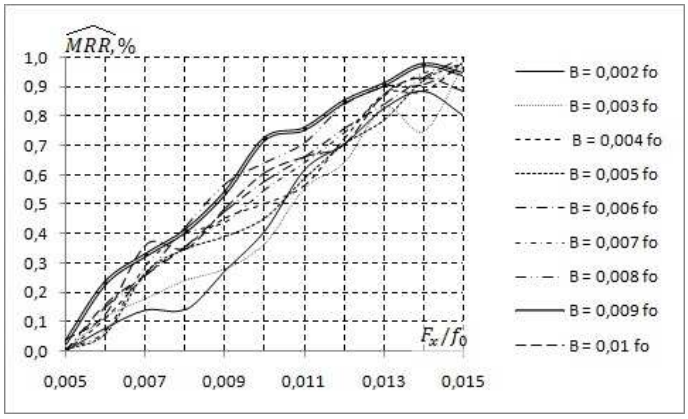


Figure 2: $\widehat{MRR}$ as a function of the shear force F_x computed for different values of the static force B.

An average $\widehat{MRR}$ as a function of the shear force F_x is shown for different static force values B in Fig. 2. As can be seen from these graphs, for all values of the static force the modified material removal rate shows the same trend. It grows with the increase of the shear force. In order to obtain the results independent of the static force value, averaging of $\widehat{MRR}$ over static force B for each value of the shear force has been done, and the result is shown in Fig. 3. As one can see the obtained dependence is near the linear. Therefore the difference of $\widehat{MRR}$ and a linear fit (LF) versus the shear force F_x has been calculated and is presented in Fig. 4. From the results in Fig. 4 the optimal value of F_x where the removal rate is maximal is obtained as $0.007f_0$. It should be noted that as simulations have shown values of F_x bigger than $0.01f_0$ could lead to fast wear and destruction of the tool.

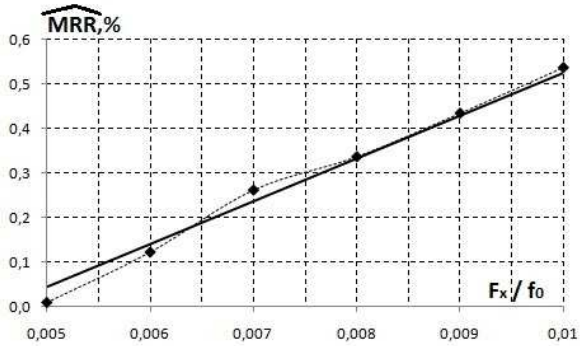


Figure 3: $\widehat{MRR}$ averaged with respect to B as a function of the shear force F_x.

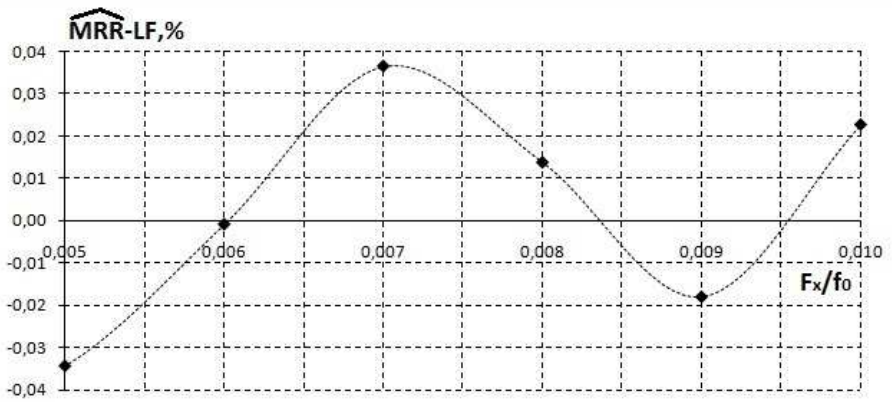


Figure 4: $\widehat{MRR}$ - LF as a function of the shear force F_x.

Further a value of $F_x = 0.007 f_0$ is chosen to plot the diagrams for $\widehat{MRR}$ dependencies on B/A and A/B (Fig. 5 – Fig. 6). Here R_{max} is a maximum value of $\widehat{MRR}$ for the minimal of considered A.

4 Analytical dry friction model

Let us compare results of computer simulations obtained above with the results of analytical modeling proposed in[1]. Below for convenience of reader the equations of motion and some results are included. In this model mass m is used to represent the tool, $F(t)$ is the overall drilling force, $P(\dot{y})$ is the resistive force, x is the displacement of the tool's tip, and y is the displacement of the dry friction element, which represents the progression of the drilling surface. The equation of motion of the mass takes the following form

$$x < y \Rightarrow m\ddot{x} = F(t)\,, \qquad x > y \Rightarrow m\ddot{x} = F(t) - P(\dot{y}). \tag{6}$$

which depends on the relative displacement between x and y. In turn, the equation of motion for the slider can be expressed as

$$\dot{x} \geq 0 \Rightarrow y = x\,, \qquad \dot{x} < 0 \Rightarrow y = 0. \tag{7}$$

For simplicity is assumed that the overall drilling force $F(t)$ has the form

$$F(t) = A \sin \Omega(t - t_0) + B\,, \tag{8}$$

where A and Ω are the amplitude and frequency of the harmonic force, B is the static force, t the time, and t_0 is the time constant. The resistive force $P(\dot{y})$ is modelled usig Coulomb dry friction

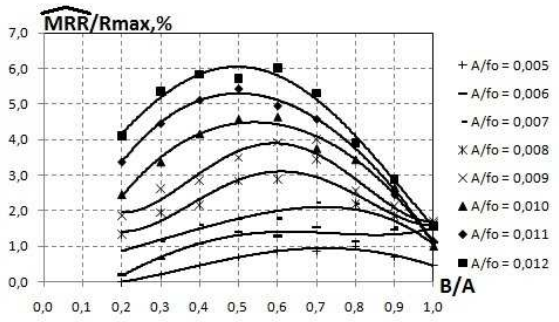


Figure 5: MRR as a function of the relative force B/A (A = constant) for different A/f_0

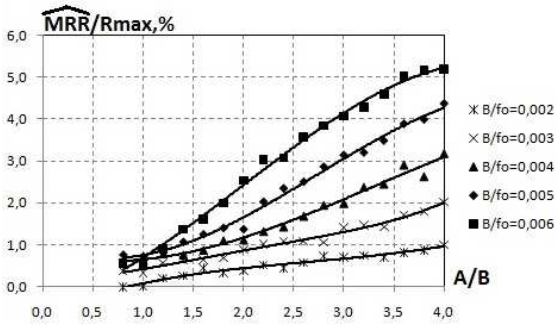


Figure 6: MRR as functions of the relative amplitude of the harmonic force A/B (B = constant) for different B/f_0

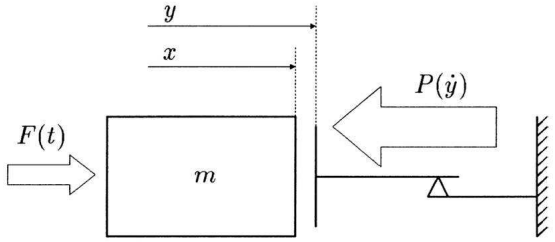


Figure 7: Dry friction model. Adopted from [1].

fulfilling the following conditions

$$\dot{y} > 0 \Rightarrow P(\dot{y}) = Q\,, \qquad \dot{y} = 0 \Rightarrow P(\dot{y}) \leq Q\,, \tag{9}$$

where Q stands for the modulus of the dry friction force. It is worth noting that the resistive coefficient, Q has a distinct value for any drilled material. On the contrary, the amplitude of the harmonic force and the static force can vary, and can be used as control parameters for the drilling process.

MRR as a function of the relative force, B/A (A = constant) and the relative amplitude of the harmonic force, A/B (B = constant) from [1] is shown in Fig. 8 – 9. Different graphs correspond to varying values of the relative excitation amplitude, $a = A/Q$ for Fig. 8, and to different values of the relative force, $b = B/Q$ as depicted in Fig. 9. The lowest (thick) curve in both figures corresponds to the small excitation case $a \to 0$ or $b \to 0$. In Fig. 8 higher curves are calculated for $a = 0.1;\ 0.2;\ \ldots;\ 0.5$. In Fig. 9 higher curves correspond to $b = 0.05;\ 0.10;\ \ldots;\ 0.25$. Both figures are related to the maximum values of the MRR for the small excitation (R_{max}) that depend on friction force Q [1].

The following comparison of the functions of MRR obtained from different models can be made. From Fig. 8 it follows that the MRR function of the static force, B (while A is kept constant) has a well-pronounced maximum, which is taken at $B = 0.39A$ for a small excitation and shifts to the right for greater excitation. Looking at Fig. 5 it can be noticed that the MRR functions has maxima near $B = 0.7A$ but there is no exact dependence of the maximum displacement on different B. From Fig. 9 it follows that the MRR is monotonically increasing function of the amplitude of the harmonic force, A. In the case of small excitation this function becomes constant. Looking at Fig. 5 one can notice the monotonic dependence but there is no asymptotic limit. The difference between the results may be connected with the different behavior of the material in the considered models. For example, the drill bit penetrates into the specimen for any dynamical load in analytical model. Instead, the numerical model has a lower limit of loading so that if the loading is smaller than this there is purely elastic deformation of the rock. On the other hand the R_{max} values for

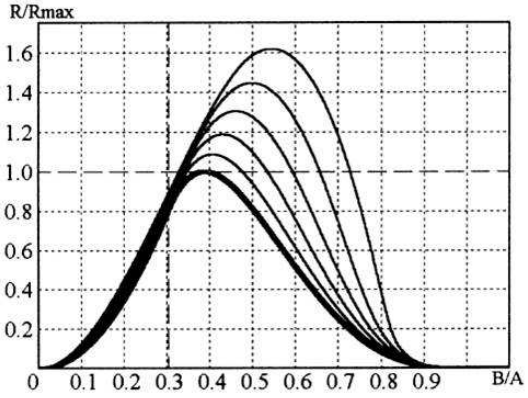


Figure 8: MRR as functions of the relative force B/A (A = constant) for vatying A/Q. Adopted from [1].

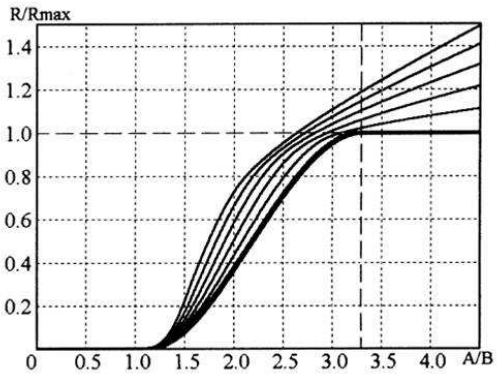


Figure 9: MRR as functions of the relative amplitude of the harmonic force A/B (B = constant) for varying B/Q. Adopted from [1].

the analytical model differ from that values for the numerical model because it is hard to determine the explicit analog of the dry friction force Q in the PD model. In further work the comparison of the numerical model with more complex analytical model considered in [3]–[4] will be undertaken.

5 Concluding Remarks

In this work drilling process of hard rocks was simulated using particle dynamics method. As a result new numerical model based on particle dynamics method was developed. The main difference of the presented model with the previous one is dynamical loading. This type of loading is more realistic and it is better for comparison with the analytical model. The comparison shows that the numerical model could give similar results to the results obtained with the analytical model. A value of the optimal relation between the static and dynamical amplitudes of the axial force was found. It differs from the previous result obtained with the analytical model. The optimal value of the shear force F_x was found as well. In further work the numerical model must be validated with an experimental data to obtain the qualitative results.

Acknowledgements

The support from RFBR (grant 09-01-92603-KO_a) and the Royal Society of London is gratefully acknowledged.

References

[1] A. M. Krivtsov, M. Wiercigroch. Penetration rate prediction for percussive drilling via dry friction model. Chaos, Solitons and Fractals 11 (2000) 2479–2485

[2] A. M. Krivtsov, E. E. Pavlovskaia, M. Wiercigroch. Impact fracture of rock materials due to percussive drilling action. XXI ICTAM, 15–21 August 2004, Warsaw, Poland

[3] E. Pavlovskaia, M. Wiercigroch. Modeling of an impact system with a drift. Physical Review E 64 (2001) 056224

[4] E. Pavlovskaia, M. Wiercigroch. Periodic solution finder for an impact oscillator with a drift. Journal of Sound and Vibration 267 (2003) 893–911

Igor Asonov, St. Petersburg State Polytechnical University, Russia

Igor Berinskiy, Institute for Problems in Mechanical Engineering of Russian Academy of Sciences, Russia
James Ing, University of Aberdeeen, United Kingom
Anton Krivtsov, Institute for Problems in Mechanical Engineering of Russian Academy of Sciences, Russia
Sergey Le-zakharov, St. Petersburg State Polytechnical University, Russia
Ekaterina Pavlovskaia, University of Aberdeeen, United Kingom
Marian Wiercigroch, University of Aberdeeen, United Kingom

Application of X-ray tensometry for study of superficial stresses with strong gradient

Joaquim T. Assis Vladimir I. Monin Susana M. Iglesias
monin@iprj.uerj.br

Abstract

Study of superficial stress gradients arising after different modern treatments of materials like material modifications by ion beam technologies or surface treatments by laser is very important problem both for theoretical and experimental mechanics and physics. X-ray diffraction method is widely used method for stress measurements because of its accuracy, facility and non-destructivity. But there are some difficulties with using of X-ray tensometry for study of stresses with strong gradient related with incompleteness of theoretical and experimental analysis of this problem. Computer simulation of diffraction profile formed by superficial layers subjected with stress gradient gives possibility to resolve the problem of determination of stresses characterized with strong gradient and allows restoring stress distribution in superficial layers of material. The objective of the presented paper is to develop the methodology of determination X-ray of stress gradient parameters and application of this methodology for measurements of mechanical stresses with strong gradient.

1 Introduction

Modern technologies create on the treated surfaces of materials significant residual stresses characterized by high level and strong gradient. Presence of this stress gradient complicates both analytical analysis and experimental study of superficial stress state. In this case stress measurements by traditional mechanical methods like "strain-gage" method have difficulties associated with insignificant thickness of superficial stress state when removing of small volume of material does not produce relaxation deformation. Deformation measurements by X-ray diffraction technique are localized in units or dozens of micrometers of superficial thickness that permits to conclude that the X-ray method is suitable for this kind of stress measurements. But when penetration of X-rays into materials, including metals and alloys, becomes comparable with layer thickness where inhomogeneous stress distribution exists then this distribution causes some problems with interpretation of stress measurements by X-ray diffraction technique. Actually, the stress value measured by X-ray diffraction method is averaged over layer of X-ray penetration. Obviously, that in the case of strong gradient the difference between the true stress value on the surface and stress value measured by X-ray diffraction method can be significant. Experimental or analytical solution of these problems is complicated because of both difficulty to prepare the samples with significant stress gradient and faults of sufficient parameters to describe superficial stress state with strong gradient. Computer simulation allows either to find the criterion of existence of stress gradient in analyzed material or to develop the methodology of correction of stress values determined by X-ray diffraction technique. The objective of this paper is to develop the methodology of correction of stress measurements made by X-ray diffraction technique to obtain the true stress value on the surface of material and to evaluate distribution of superficial residual stresses. Developed methodology was tested by stress measurements with using steel blades samples where stress gradient was created by.

2 Methodology of computer simulation of diffraction profile

Methodology of computer simulation is based on separation of material surface on sequence of individual layers and account of contribution of these layers for forming intensity and position of total diffraction line [1]. Taking into account an attenuation of X-rays into material and path for incident and diffracted beams it is possible to obtain the intensity reflected by any subsurface layer. There are two equations describing the process of formation of total diffraction profile. The first is related with attenuation of intensity of profiles reflected by individual surface layers and other gives angle position of individual diffraction lines depending of distribution or gradient of analyzed stress state. The equation for diffraction intensity of superficial layers can be expressed in the following form:

$$I_{dif} = a * I_0 e^{-\mu t * (1/\cos(\psi+90-\theta)+1/\cos(\psi-90+\theta))} \tag{1}$$

Here I_0 is the initial intensity of incident beam, t is the depth of the individual surface layer penetrated by X-ray beam, ψ is the polar angle characterizing inclination of incident beam to the surface of material, θ is the value of diffraction angle, μ is the X-ray absorption coefficient of the analyzed material and a is a coefficient of proportionality for intensity of diffracted beam I_{dif} depending of material crystal structure and geometry of diffraction experiment. Equation can be interpreted as contribution of each subsurface layer for the total intensity of diffraction line.

Angular position of diffraction profiles depends of the crystal interplanar distance that is the function of stress distribution $\sigma(t)$. For linear distribution the stress dependence from depth t can be written as:

$$\sigma(t) = \sigma_0 + kt \tag{2}$$

where σ_0 is the stress value on the surface of material and k is the stress gradient. Equation (2) allows to obtain the magnitude of strain for any layer t and for any direction ψ. From the theory of elasticity the strain $\epsilon_{\varphi\psi}$ in arbitrary direction for plane stress state can be expressed as [2]:

$$\epsilon_{\varphi\psi} = (1+\nu)\sigma(t)\sin^2\psi/E - \nu(\sigma_1+\sigma_2)/E \tag{3}$$

where ν and E are the material elastic constants, σ_1 and σ_2 are the principal stresses. In the case of uniaxial stress state $\sigma_1 = \sigma(t)$ and $\sigma_2 = 0$ equation (3) is transformed as:

$$\epsilon_\psi = (1+\nu)\sigma(t) * \sin^2\psi - \nu/E \tag{4}$$

Equation (4) can be expressed in diffraction terms too. Using Bragg's law it can be written as:

$$\epsilon_\psi = (d_\psi - d_0)d_0 = -\cot\theta * (\theta_\psi - \theta_0) \tag{5}$$

where $d_0, d_\psi, \theta_0, \theta_\psi$, are the interplanar distances and diffraction angles for unstressed and analyzed material, respectively. Equalizing and then simplifying the equations (4) and (5) we can obtain the formula for diffraction angle as a function of depth t and polar angle ψ:

$$\theta_\psi = \theta_0 - \sigma(t) * (\sin^2\psi - \nu\cos^2\psi)/E * \cot\theta_0 \tag{6}$$

Equation (6) characterizes the angle position of individual diffraction lines reflected by any subsurface layer into depth t. Therefore, computer simulation of diffraction profile formed by superficial layer is based on the using of equations (1) and (6) which determine the intensity and angle position of individual diffraction profiles from each subsurface layer with stress distribution $\sigma(t)$ into depth t. The sum of these individual profiles forms the total diffraction line.

The thickness of each individual layer for our simulation was 0,1mkm and simulation process was finished when the intensity of X-ray reflection of layer into depth t becomes less then the 1% of initial intensity of incident beam.

Approximated function used for individual profiles was the Cauchy function. The width and doublet distance $K\alpha_1 - \alpha 2$ of standard profile corresponds to experimental diffraction lines of steel sample with using of $Cr - K_\alpha$ radiation and (211) reflection. Fig.2,3 show simulation process

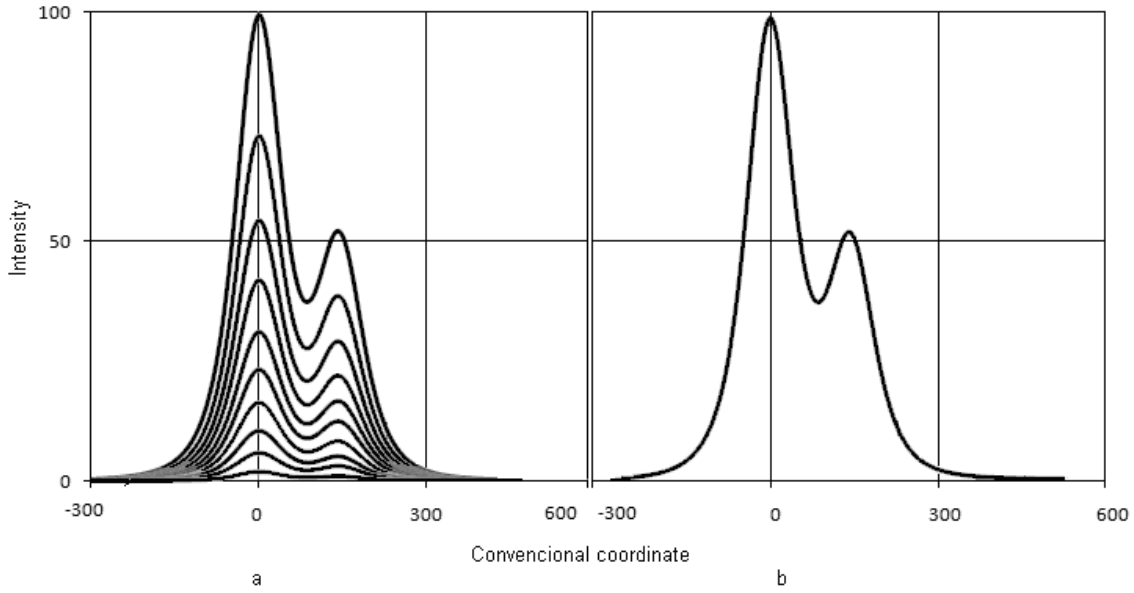


Figure 1: Simulation of diffraction profile for homogeneous constant stress distribution: a - profiles formed by individual layers; b - total profile formed as the sum of all layers.

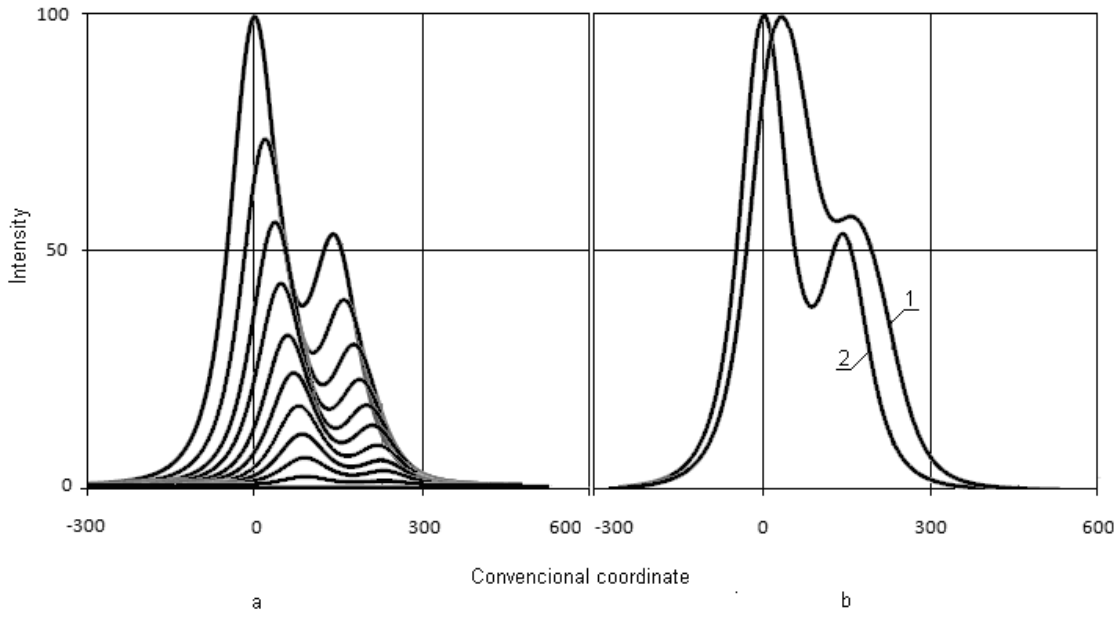


Figure 2: Simulation of diffraction profile for linear stress distribution $\sigma(t) = 500 - 100t$;a- profiles formed by individual layers; b- total profile (1) formed by sum of all profiles and standard profile (2) corresponding to constant stress.

associated with determination of individual and total diffraction profiles for constant stress and inhomogeneous distribution with stress gradients k = 100Mpa/mkm.

The result presented in Fig.2 shows that stress gradient causes both displacement and broadening of diffraction line which are proportional to the value of stress gradient.

With using of developed computer simulation and X-ray diffraction profiles it is possible to obtain the calibration graph representing relationships between broadening of diffraction line and the magnitude of stress gradient. This graph is shown in Fig. 3.

Broadening of diffraction line is expressed as relative increment of integral width $B_{grad.} - B_0/B_0$,

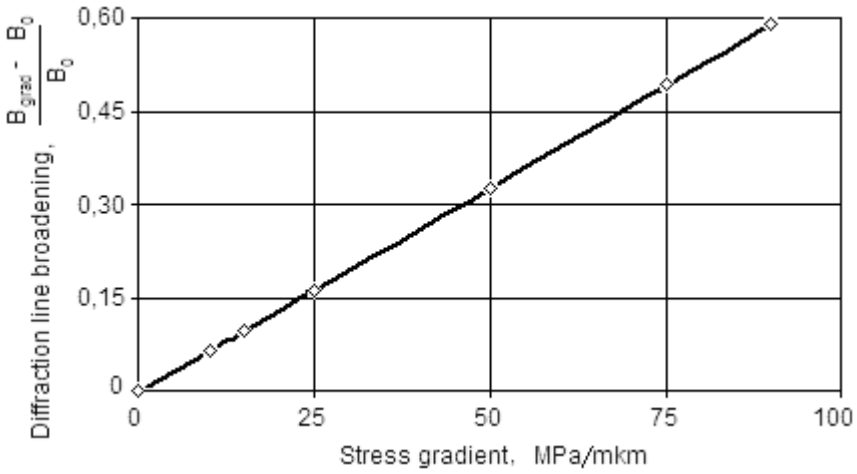


Figure 3: Relationships between broadening of diffraction line and stress gradient.

where B_0 and B_{grad}, are defined as division of diffraction profile area to his maximum intensity. Therefore, this calibration graph permits experimentally to determine the parameter of stress gradient from broadening of diffraction line for steel samples.

3 Methodology of stress measurements by X-ray diffraction technique

3.1 $Sin^2\psi$- method for homogeneous stress distribution.

Principal method of stress measurements by X-ray diffraction technique is the $sin^2\psi$- method [3][4] which is based on the measuring of diffraction angle characterizing the angular position of the diffraction line. Fundamental equation of this method is mentioned above equation of theory of elasticity (1) for strain in arbitrary direction:

$$\epsilon_{\varphi,\psi} = \frac{1+\nu}{E}\sigma_\varphi \sin^2\psi - \frac{\nu}{E}(\sigma_1 + \sigma 2) \tag{7}$$

where E, ν are elastic constants, φ and ψ are azimuthal and polar angles in spherical coordinate system, σ_φ is measured stress component in φ-direction , σ_1 and σ_2 are principal stresses.

This strain related to the diffraction experiment can be expressed as:

$$\epsilon_{\phi,\psi} = \frac{\Delta d}{d} = \cot\theta * \delta\theta \tag{8}$$

where $d_{\varphi,\psi}$, d_0, $\theta_{\varphi,\psi}$, θ_0 are interplanar distances and diffraction angles for analyzed and free of stress material, respectively. From these equations the diffraction angle $\theta_{\varphi,\psi}$ corresponding to strain in arbitrary direction, can be written as:

$$\theta_\psi = \theta_0 + \sigma_\varphi \frac{(1+\nu}{E}\frac{\sin^2\psi}{\cot\theta} - \frac{\nu}{E * \cot\theta}(\sigma_1 + \sigma_2) \tag{9}$$

The slope of linear function $\theta_{\varphi,\psi} = f(\sin^2\psi)$ allows to determine the stress value as:

$$\sigma_\varphi = \frac{E}{1+\nu}\cot\theta(\theta_{\phi=90} - \theta_{\phi=0}) \tag{10}$$

where $(\theta_{\phi=90} - \theta_{\phi=0})$ is the values of diffraction angles obtained by extrapolation to ϕ-angles equal to 0 and 90 degrees, respectively. Therefore, the principal parameters of X-ray tensometry are experimental diffraction angles measured as angular positions of diffraction lines.

3.2 $\sin^2\psi$- method in the case of stress gradient.

Influence of the stress gradient on the $\sin^2\psi$-method can be analyzed by computer simulation of diffraction line based on using of equations (1) and (6). Polar angle ψ in equations (1) and (6) participates at formation of diffraction profile when the surface layers are subjected by stress with gradient. Influence of ψ-angle is associated with dependence of X-ray penetration from the inclination of X-ray incident beam to the surface of analyzed material. Really, increasing of incidence angle reduces the thickness of surface layer penetrated by X-rays and diminishes contribution of internal layers of material at formation of diffraction profile. Methodology of computer simulation allows to analyze the position or/and width of diffraction line depending of stress distribution $\sigma(t)$ and polar angle ψ. Therefore, this methodology permits to simulate the "$\sin^2\psi$- method" of stress measurements both for homogeneous and heterogeneous stress distributions. Fig.4 presents the results of this simulation for residual stress measurements in steel samples with using of $Cr - K_\alpha$ radiation for constant stress equal to $\sigma_0 = 500MPa$ and stress distribution $\sigma(t) = 0 + kt$, where stress on the surface of steel sample is the same and equal to $\sigma_0 = 500MPa$ and gradient is equal to k = 100 MPa/ mkm.

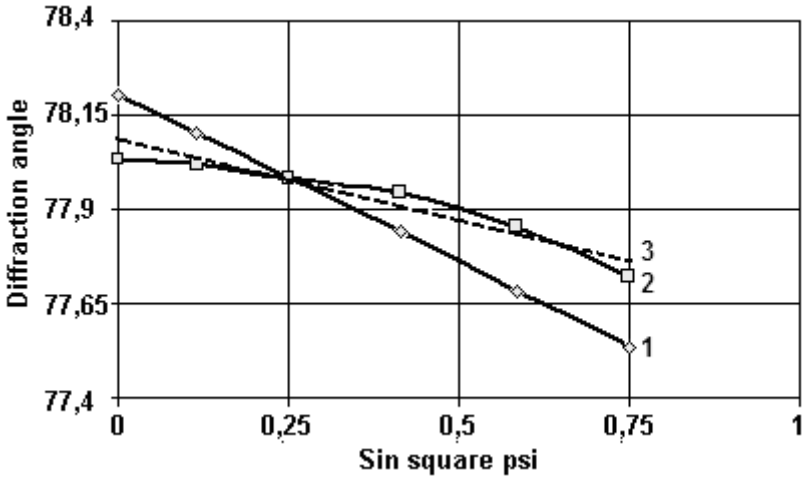


Figure 4: Diffraction angle θ_ψ versus $\sin^2\psi$ (equation (6)) : 1-constant stress $\sigma_0 = 500MPa$; 2-linear stress distribution $\sigma(t) = 500 - 100t$; 3- straight line is calculated by linear regression using experimental points of the curve 2.

Calculation of stress value by formula (10) with using of inclination of straight line 3 in Fig.3 gives the value of calculated stress equal to 270 MPa. This result shows that measurements by X-ray diffraction technique of stresses with strong gradient brings to great difference between the real stress on the surface of steel that is equal to $\sigma_0 = 500MPa$ and measured stress value corresponding to $\sigma_{x-ray} = 270MPa$. Therefore, in this case the difference $\Delta\sigma$ between truth stress value on the surface of steel and experimental stress value is equal to 230 MPa. With this conclusion the problem of stress measurements by X-ray diffraction technique is how to make correction of experimental results when analyzed stress state is characterized by strong gradient.

The procedure of developed computer simulation of diffraction stress measurements shown in Fig.4 can be used to calculate $\Delta\sigma$ for various stress gradients and obtain calibration graph for this correction. This calibration graph for steel samples is shown in Fig.5.

Developed methodology of correction stress measurements made by X-ray diffraction method was tested for razor blade samples loaded by bending. It is known [2] that stress distribution in bended plate is linear. If the radius of bending is R then stress on the surface of plate can be calculated as:

$$\sigma = tE/2R \tag{11}$$

where t is the plate thickness, E is elasticity modulus and R is the radius. In this case stress distribution can be written as $\sigma(t) = \sigma_0 - kt$, where k is stress gradient. Razor blade with

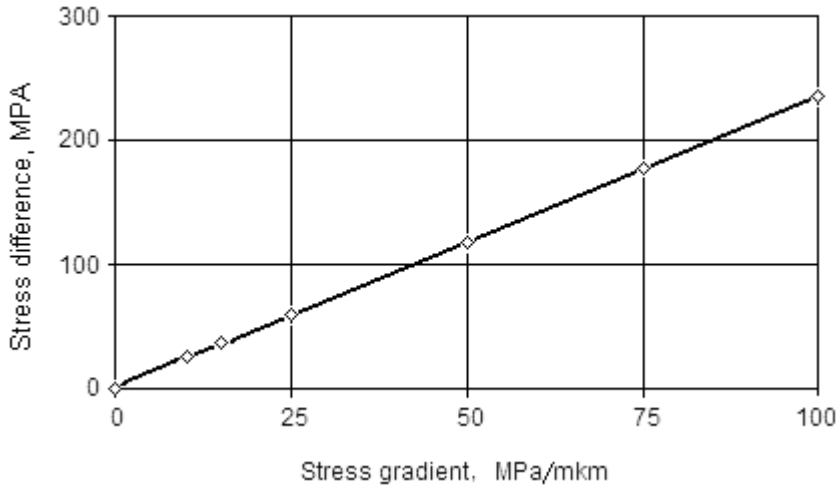


Figure 5: Difference between stresses measured by X-ray diffraction technique and stress gradient parameter.

thickness t=0,1mm subjected to thermal treatment at $700 \circ C$ during half hour had yield stress equal approximately 500MPa, then following stress distribution can be used for stress measurements by X-ray diffraction technique:

$$\sigma(t) = 500 - 10t \tag{12}$$

Here stress gradient k is equal to 10 MPa/mkm. X-ray diffraction stress measurements have been shown both broadening of diffraction line and difference between applied stress and measured stress.

There were obtained the following experimental parameters:

$$B_{grad.} - B_0/B_0 = 0,06;$$
$$k = 10MPa/mkm;$$
$$\sigma_{load} = 500MPa;$$
$$\sigma_{x-ray} = 460MPa;$$
$$\Delta\sigma = 40MPa;$$

These experimental data have good agreement with parameters of calibration graphs determined by computer simulation which are presented in Fig.3,5.

Conclusions

It has been presented methodology of computer simulation of diffraction experiment that has been applied for stress measurements by X-ray diffraction technique when analyzed stress state characterized by strong gradient. The calibration graphs determined by developed methodology permits evaluate the stress gradient parameter and to make correction of stresses measured by X-ray diffraction method. Developed methodology has been tested on thin razor blade samples where stress gradient was obtained by bending.

References

[1] V.I.Monin, J. T.Assis, S.Philippov. Study of Stress Gradients using Computer Simulation of Diffraction Data, Spie, Bellingham, USA, v. 5400, p. 196-199, 2004.

[2] S.P.Timoshenko, N.J.Goodier, Theory of Elasticity, McGraw-Hill, New York, 1980.

[3] I.S. Noyan, J.B. Cohen, Residual Stress. Measurement by diffraction and interpretation, Springer Verlag, New York, Berlin, 1987.

[4] V. Hauk, Structural and Residual Stress Analysis by Nondestructive Methods, Elsevier, Amsterdam, 1997.

Instituto Politecnico do Estado do Rio de Janeiro, Brasil
Rua Alberto Rangel, s/n. Vila Nova. 28630-050. Nova Friburgo/RJ.

Investigation of influence of nonequiaxial compression on general features of mechanical response of shearing fault zones

Sergey V. Astafurov, Evgenii V. Shilko, Valerii V. Sergeev, Sergey G. Psakhie
astaf@ispms.tsc.ru

Abstract

On the base of computer-aided simulation using movable cellular automaton method regularities of mechanical response of model block-structured medium under constrained shear loading were investigated. Results of investigations showed that increasing of value of inner stress in block-structured medium led to step-by-step involvement of deformation mechanisms of more and more higher scale level up to generation of discontinuities and cracks at interblock interfaces. It was shown that under constrained loading conditions generation of discontinuities took place at early stages of shear loading. Rate of accumulation of damages increases with increasing of degree of constraint and role of that deformation mechanism becomes dominate. This leads to changing of main characteristics of mechanical response of block-structured medium such as decreasing of shear strength and ultimate shear strain of the medium.

1 Introduction

It is well known that stress state of geological media is nonuniform and complex and one of its main features are constrained conditions. Degree of constraint, determined through a value of applied stresses, greatly determines deformation mechanisms and fracture regime of the medium [1, 2]. Significant parts of massifs, in particular, zones of active faults, are in very complex conditions, including, as compressive and significant shear components. These loading conditions can be characterized by the scheme "shear+compression". So, deformation of shearing fault zones takes place under nonequiaxial compression conditions. In this current study is the influence of relationship of normal and lateral pressures on the character of deformation and fracture of the geological medium under shear loading [3]. An important feature of the structure of geological media is a multiscale hierarchical organization of the block structure [1]. The structural blocks separated by a "surface relaxations", characterized by lower effective strength in comparison with the material blocks itself [4]. This helps to alleviate the slipping on interblock interfaces and thus leads to leads to occurrence of large number of additional degrees of freedom (mobility) fragments of the medium [1, 5]. Therefore it is important to analyze the role of the block structure of the medium, in particular, the processes of formation of discontinuities and cracks growth at the interfaces of structural elements. This paper is devoted to the theoretical investigation of the effect of this factor on the deformation parameters, shear strength and other characteristics of the response of block-structured medium under constrained shear loading conditions. The study was carried out on the base of computer-aided simulation using movable cellular automaton method [6, 7].

2 Statement of problem of computer-aided simulation

In this paper, regularities of response of block-structured media under shear deformation were studied on the example of system with blocks of the same size, separated by interfaces (fig. 1 a). Analogue interblock interfaces constituted zones with reduced strength and deformation characteristics. It promotes the localization and accumulation of irreversible strains on them. Note that in the case of a real geological medium these features are determined by highest content in the interface zones (in comparison with the blocks) of damages, porosity, etc. This model of

block-structured medium was realized in the framework of two-dimensional version of the movable cellular automaton method [8]. For the mathematical description of the elastic-plastic response of the blocks and the interfaces applied the model described in [6, 7], in approximation, a similar to plain-stress state approximation. For automata that simulate the blocks linear response function was used, which correspondes to high-strength elastic materials (curve 1 in fig. 1 b). Response functions of automata that simulate the interfaces were characterized by a long section, corresponding to the accumulation of irreversible deformation (curves 2 and 3 in fig. 1 b). This section simulates the integral influence of defects and damages of the lower scale levels, existing originally and formed during deformation, and also the reduction of local resistance to the interface shear. In accordance with the above section of the accumulation of irreversible deformation corresponds to the so-called process of "destructive degradation" of the material interface. It is well known that in the central parts of the shearing zones degree of degradation of the structure and mechanical properties of the material is higher [9]. This feature was simulated by specifying low strength characteristics of interblock interfaces in the central zone (curve 2 in fig. 1 b) in compare with interfaces in layers near the top and bottom surfaces of the specimen (curve 3 in fig. 1 b). In fig. 1 a central zone is schematic bounded by thin solid horizontal lines.

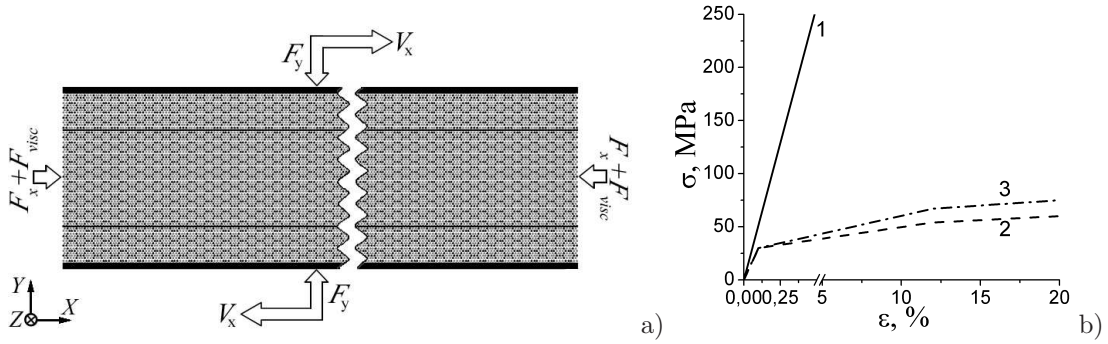


Figure 1: Structure of the simulated specimen and the scheme of loading (a) and response function of the automata (b) of blocks (1), interblock interfaces in the inner region of the specimen (2) and in the "surface" layers (3).

Value of linear dimensions of the modeled area was $L/H = 5$, where L is length (the size along the axis X), H is width of the sample (the size along the axis Y). Initial stress state of the sample set by nonequiaxial compression by forces F_x and F_y (fig. 1 a). The value of F_y in all calculations was the same, and its specific value (σ_y) was 40% of the value of the elastic limit (σ_{yield}) of response function of the material of interblock interfaces (curve 2 in fig. 1b). Constrained specimen was subjected to a shear deformation with a small constant velocity V_x (Fig. 1 a). To account for the inertial and dissipative properties of the surrounding medium of the simulated fragment of block-structured medium to the lateral sides of the specimen surface in addition to compressive force F_x acting viscous forces $F_{visc} = \alpha v_x$, where v_x is X component of the velocity of the automata at side surface. Degree of nonequiaxiality of compression of the specimen was characterized by the dimensionless parameter C_σ, which is defined as the ratio of the relative values of compresses in the horizontal direction force F_x (denote it as σ_x) to a specific value of the vertical compressive force F_y (denote it as σ_y): $C_\sigma = \sigma_x/\sigma_y$. Parameter C_σ characterizes the relative magnitude of compression of the system in the direction of shear. In the paper the value of C_σ varied in the range from 0 to 2.4, which corresponds to the achievement of stress magnitude of the elastic limit yield of material of interblock interfaces.

3 Results of computer-aided simulation

The simulation results showed that the increase in the degree of nonequiaxiality of compression of shearing zone leads to a directed change of its integral strength and deformation characteristics, which can be characterized by dependencies of shear strength of the specimen τ_c and the corresponding "ultimate" shear angle γ_c on the parameter C_σ (fig. 2). Both curves shown in fig. 2, have

a pronounced threshold character. The values of the parameters τ_c and γ_c increase to a certain "threshold" value of the degree of nonequiaxiality of compression ($C_\sigma \approx 0.3$). Then ($C_\sigma > 0.3$) τ_c begins to decrease monotonically. The relevant section of the curve $\tau_c(C_\sigma)$ can be approximated by a linear dependence (fig. 2 a). At the same time, a similar dependence of the $\gamma_c(C_\sigma)$ for large values of C_σ has pronounced non-linear view with the attainment of saturation at $C_\sigma > 1.4$ (fig. 2 b). All this indicates a change of the character of deformation and fracture of block-structured medium with increasing degree of nonequiaxiality of compression.

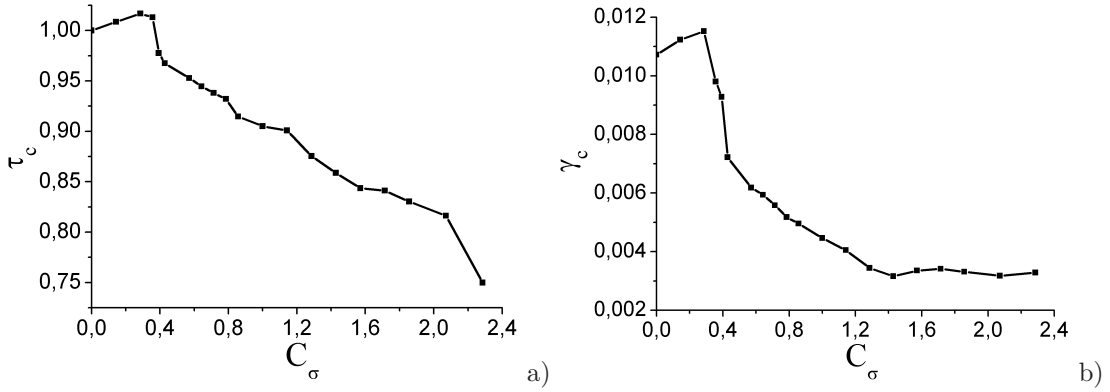


Figure 2: Dependences of the relative shear strength of the simulated specimen τ_c (a) and "ultimate" value of shear angle γ_c (b) on parameter C_σ.

Indeed, during shear deformation of the medium, the loading diagrams are characterized by three main sections: quasi-elastic, quasi-plastic and section of softening and residual strength. Quasi-plastic sections of loading diagrams are related mainly with the localization process of irreversible deformation at interblock interfaces. With the exhaustion of their ability to be activated relaxation mechanisms of deformation of a higher scale level. In the considered block-structured medium it is manifested through the generation of "meso scale injuries" whose dimensions are comparable to the width of interblock interfaces. Fig. 3 a shows the number of arising injuries N vs. shear angle γ for various degrees of constraint. Analysis of the loading diagrams and curves in fig. 3 a shows that in the region of quasi-elastic response of the block-structured medium the main role play deformation mechanisms with a relatively low threshold of activation (effectively taken into account through the irreversible deformation of interface automata). With the transition to the section of quasi-plastic response begins the process of rapid accumulation of "meso scale injuries". It should also be noted that the achievement of shear strength and the transition to a section of softening associated with the involvement of the deformation mechanism of the "macro scale level" (germination of interblock cracks).

Reducing of deformability of the simulated block-structured medium and the value of its shear strength with increasing of degree of nonequiaxiality of compression is due to the fact that increasing of σ_x leads to increasing of volume fraction of interfaces is largely degraded to the beginning of the application of shear stress. Subsequent shear deformation of the specimens leads to the rapid achievement of the ultimate strength at degraded areas of interblock interfaces and the emergence of "meso scale injuries". As can be seen in fig. 3 a, the increase in C_σ leads to the activation of process of accumulation of damages at a lower magnitude of the shear strain, as well as the average rate of accumulation of damage at the interfaces of structural elements (V_c) (fig. 3 b). In this case the value of $V_c = N_c/\gamma_c$ is defined as the ratio of amount of damage N_c, accumulated in the sample at the time of achieving the "ultimate" condition, to the value of the "ultimate" shear angle γ_c. Dependence $V_c(C_\sigma)$ has a pronounced three-stage character. In the first stage, with $C_\sigma < 0,4$, the value of V_c is changed slightly. Increasing of the degree of nonequiaxiality of compression accompanied by a significant (almost three-fold) increase in the rate of damage accumulation (second stage) with the attainment of saturation at $C_\sigma > 1,6$ (third stage). Thus, in the process of shear deformation of constrained samples is rapid exhaustion of the resources of the deformation mechanisms of low levels (whose influence is taken into account by irreversible forming of cellular automata) and the involvement of the mechanism of "meso scale level" connected with continuity

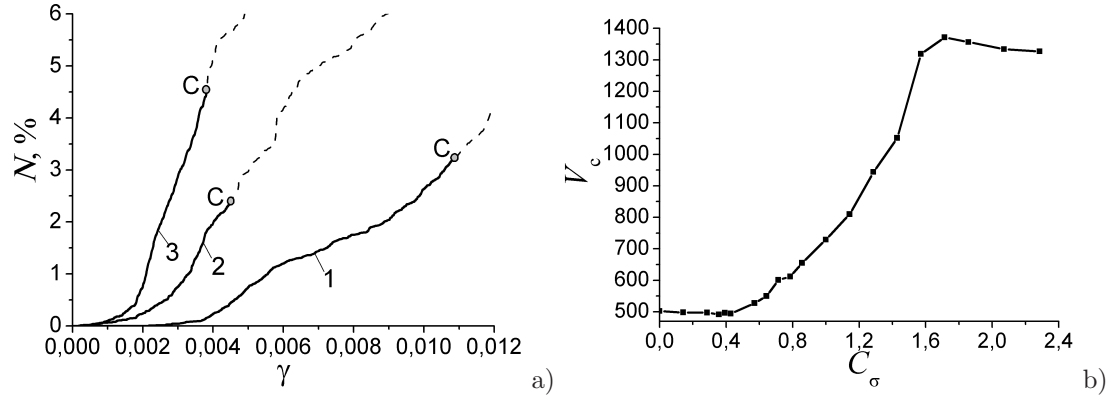


Figure 3: (a) Dependence of the amount of accumulated in the process of shear deformation "meso scale injuries" N from the shear angle γ at different values of C_σ: 1 - $C_\sigma = 0$, 2 - $C_\sigma = 1$, 3 - $C_\sigma = 1,6$ (point "C" represents moments of maximum resistance shear force achievement); b) the dependence of the average rate of accumulation of "meso scale injuries" V_c to the time of achieving of "ultimate" state on parameter C_σ.

violation of interface zones. In fact, with increasing lateral pressure acting in the direction of shear deformation, takes place a "washout" of "microscopic" deformation mechanisms, which in many respects determined the strength and deformation characteristics of block-structured medium. Such "depletion" of the spectrum of mechanisms provides a reduction of integral characteristics of the mechanical response of block-structured medium in straitened conditions (fig. 2).

An important characteristic of the response of fragments of geological media is a change of their geometric dimensions in the process of loading. When the shear deformation of block-structured media usually takes place dilatancy, determined by the change in volume of the material. Dilatancy of medium depends on several factors: the stress state, physical and mechanical characteristics of structural elements, the regime of deformation, etc. One of the characteristics of the medium associated with its dilatancy is the relative change in the width of the shear zone ε_H, which in this case defined as the ratio of the absolute change in the height of the specimen ΔH (ie, change its size along the axis Y) to the original value (H). An important integral characteristic of the structure and mechanical properties of the medium is changing of the width of the shear zone (ε_H^c) at the time of achieving of the "ultimate state", ie, the transition point to the stage of softening (γ_c). Figure 4 a shows the dependence of ε_H^c on the degree of nonequiaxiality of compression (C_σ). It is clear that with increasing of C_σ value of ε_H^c increases monotonically. At the same time at small values of C_σ there is integral narrowing of shear zone ($\varepsilon_H^c < 0$). And starting with a certain characteristic value of C_σ (in this case, $C_\sigma \approx 0.4$), takes place its integral extension in the process of shear deformation.

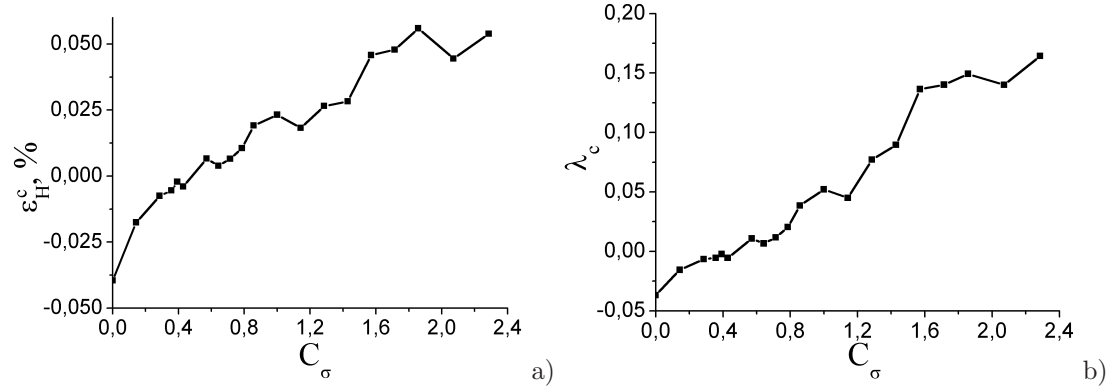


Figure 4: Dependences of the variation of the width of the shear zone ε_H^c (a) and coefficient of variation of the width of the shear zone λ_c (b) to the time of achieving of "ultimate" state on C_σ.

Change of sign of ε_H^c with increasing of C_σ significantly associated with the above mentioned changing of the dominant mechanism of irreversible deformation of block-structured medium. Thus, for small values of C_σ decisive contribution to the changing of the width of the shear zone has made "plastic" deformation of interblock interfaces (a mechanism that effectively takes into account the contribution of deformation processes at lower structural levels). However, until then, while compressing of interfaces, accompanied by the "extrusion" of the material in a direction perpendicular to the plane (in the direction of the axis Z), is the dominant factor (range of values of $C_\sigma < 0.4$), there is a narrowing of the integral shear zone (fig. 4 a). When $C_\sigma > 0.4$ the role of mechanisms of deformation of "low" scale levels starts to decline, because already at the initial stage of deformation a large number of "meso scale injuries" are formed. Formation of "meso scale injuries" leads to fragmentation of the specimen and leads to activation of the "mesoscopic" dilatation mechanisms associated with the local sliding along surfaces of "mesoscopic" flaws and partial repacking of formed fragments [10]. The intensive involvement of the mechanisms of a higher rank provides a change of sign of the parameter.

In mathematical models of geomedia dilatancy characterized by a number of parameters, the most common of which is the coefficient of dilatancy. It is determined by the ratio of the rate of irreversible changes of volume of the medium to the intensity of plastic strain rates [11, 12]. By analogy with this parameter in the paper was suggested coefficient of changing of the width of shearing zone $\lambda = \varepsilon_H/\gamma$. This parameter can be interpreted as some effective rate of expansion/contraction of the shearing zone in the conditions of deformation at a constant speed. Figure 4 b shows the dependence of λ to the time of achieving of "ultimate" state of the sample (λ_c) on the ratio of lateral and normal pressure (C_σ). One can see that the value of λ_c increases throughout the considered range of values of C_σ, and the character of this dependence is close to linear. In the framework of the considered model obtained values of λ_c characterize the contribution to changing of the width of the shearing zone of damages, the scale of which does not exceed the thickness of the interblock interface zones. As seen from fig. 4 b, their role in changing of the geometrical parameters of the simulated fragment of the medium increases with the degree of nonequiaxiality of compression. This reflects a marked depletion of the spectrum of deformation mechanisms.

4 Conclusions

The results of the theoretical investigation of the general regularities of behavior of block-structured, including geology, media in conditions of shear deformation have shown that an important factor in determining the relative contribution of different deformation mechanisms in the integrated mechanical response of the block system is the degree of nonequiaxiality of compression of the specimen. Thus, the increase in compressive stress in the direction of application of shear loading leads to reducing of contribution of deformation mechanisms of low scale levels, leading to the accumulation of irreversible deformation in the interblock interface areas. The reason for this is increasing of the degree of degradation of medium in the initial stress-strain state, which leads to rapid formation of discontinuities in the most weak interfaces in the process of shear deformation. At high degrees of constraint formation of these "mesoscopic" flaws and their association into interblock cracks become the dominant deformation mechanism in the block-structured medium. Changing of the dominant mechanism of deformation is manifested as a change of the trend and in some cases of the sign of the integral characteristics of the deformation response of the medium, such as shear strength, the ultimate value of shear strain and changing of the width of shearing zone. In general, results suggest the possibility of introducing of some dimensionless parameter characterizing regime of the mechanical response of the medium during shear deformation. This parameter should be a function which links the applied stresses and rheological characteristics of the medium (in particular, the elastic limit of the material of interblock interfaces).

Acknowledgements

This work was supported by grant of the President of Russian Federation (MK-130.2010.5), RFBR grant No.09-05-00968-a and project of program of the Presidium of RAS 11.2.

References

[1] Nikolaevskiy V.N. Fractured structure of the crust as its genetic feature. Russ Geol Geophys, 2006;47(5):642-654.

[2] Psakhie S.G., Ruzhich V.V., Smekalin O.P., Shilko E.V. Response of the geological media to dynamic loading. Phys Mesomech, 2001;4(1):63–66.

[3] Grigoryev A.S., Volovich I.M., Mikhailova A.V., Rebetsky Yu.L., Shakhmuradova Z.E. Relationships between the kineamatics of the top of a layer and the state of stress within it due to block motion at its bottom (in connection with the interpretation of recent movements). J. of Geodyn, 1988;10(2-4):127–138.

[4] DKostyuchenko V.N., Kocharyan G.G. Pavlov D.V. Deformation characteristics of inter-block gaps of different scales. Phys Mesomech, 2002;5(5):23–42.

[5] Psakhie S.G., Ruzhich V.V., Shilko E.V., Popov V.L., Astafurov S.V. A new way to manage displacements in zones of active faults. Tribol Int, 2007;40(6):995–1003.

[6] Shilko E.V., Smolin A.Yu., Astafurov S.V., Psakhie S.G. Development of movable cellular automaton method for simulation of deformation and fracture of heterogeneous elastoplastic materials and media. In: Proc. Of the International conference on particle-based methods. Fundamentals and applications (Particles-2009). 2009. pp. 349–352.

[7] Psakhie S.G., Horie Y., Ostermeyer G.P. et al. Movable cellular automata method for simulating materials with mesostructure. Theor Appl Frac Mech, 2001;37(1-3):311–334.

[8] Psakhie SG, Shilko EV, Astafurov SV. Peculiarities of the mechanical response of heterogeneous materials with highly deformable interfaces. Tech Phys Lett, 2004;30:237–239.

[9] Marone C. Laboratory-derived friction laws and their application to seismic faulting. Annu. Rev. Earth Planet. Sci., 1998; 26:643–96.

[10] Nur A. A note on the constitutive law for dilatancy. Pure Appl Geophys, 1975;113:197–206.

[11] Stefanov Yu.P. Deformation localization and fracture in geomaterials. Numerical modeling. Phys Mesomech, 2002;5(5):107–119.

[12] Garagash I.A. Conditions of the formation of regular systems of shear and compaction bands. Russ Geol Geophys, 2006;47(5):655–666.

Sergey V. Astafurov, ISPMS SB RAS, Akademicheskii pr., 2/4, Tomsk, Russia, 634021
Evgenii V. Shilko, ISPMS SB RAS, Akademicheskii pr., 2/4, Tomsk, Russia, 634021
Valerii V. Sergeev, ISPMS SB RAS, Akademicheskii pr., 2/4, Tomsk, Russia, 634021
Sergey G. Psakhie, ISPMS SB RAS, Akademicheskii pr., 2/4, Tomsk, Russia, 634021

Contact Optimization Problems with Uncertainties

Nickolay V. Banichuk Svetlana Yu. Ivanova Evgeniy V. Makeev
banichuk@ipmnet.ru

Abstract

In this study we investigate problems of optimal shape design of punch interacted with elastic medium under conditions incomplete information regarding the external actions. In formulating and solving problems with incomplete data we apply the probabilistic approach. As a result the optimal designs of the punch with circular base are obtained and presented.

The problem of contact interaction of rigid punch and elastic medium occupied the half-space $z \geq 0$ in rectangular coordinate system xyz is considered. The boundary of elastic half-space Ω $(z = 0)$ contains the domain of contact Ω_f representing the base of the punch, the region Ω_0, which is free of loading, and the regions Ω_q^i $(i = 1, 2, ..., N)$ of application of external forces, i.e.

$$\Omega = \Omega_f + \Omega_0 + \Omega_q,\ \Omega_q = \bigcup_{i=1}^{i=N} \Omega_q^i \tag{1}$$

$$\Omega_f \bigcap \Omega_0 = 0,\ \Omega_f \bigcap \Omega_q^i = 0,\ \Omega_q^i \bigcap \Omega_0 = 0 \tag{2}$$

The surface of the punch penetrated into elastic medium without friction is given by the equation $z = f(x, y)$, $(x, y) \in \Omega_f$ and $z = 0$, $(x, y) \in \partial\Omega_f$, where $f(x, y)$ is positive continuous and smooth. In what follows this function will be considered as unknown design variable. External forces $q^i = q_x^i, q_y^i, q_z^i$ applied to the domain Ω_q^i are considered as functions depending on two random variables ξ, η, i.e.

$$\begin{array}{l} q_j^i = q_j^i(x, y, \xi, \eta),\ (x, y) \in \Omega_q^i \\ j = x, y, z;\ i = 1, 2, ..., N \end{array} \tag{3}$$

Random variables ξ, η have the following joint probability densities $g^i(\xi, \eta)$ and the corresponding joint probability distribution functions $F^i(\xi, \eta)$, where

$$g^i(\xi, \eta) = \frac{\partial^2 F^i}{\partial\xi\partial\eta} \tag{4}$$

Boundary conditions at the Ω have the form

$$\sigma_{xz} = \sigma_{yz} = 0,\ w = f(x, y),\ (x, y) \in \Omega_f \tag{5}$$

$$\sigma_{xz} = \sigma_{yz} = \sigma_{zz} = 0,\ (x, y) \in \Omega_0 \tag{6}$$

$$\sigma_{xz} = q_x^i(x, y, \xi, \eta),\ \sigma_{yz} = q_y^i(x, y, \xi, \eta),\ \sigma_{zz} = q_z^i(x, y, \xi, \eta),\ (x, y) \in \Omega_q^i \tag{7}$$

Here σ_{xz}, σ_{yz}, σ_{zz} - components of the stress tensor and w - projection of the displacement vector on the z-axis. The contact pressure distribution $p(x, y, \xi, \eta) = -\sigma_{zz}(x, y, \xi, \eta)$ defined at the bottom of the punch $((x, y) \in \Omega_f)$ can be used for determination of the resulting force P applied to the punch and the total applied moments M_x, M_y (with respect to the axes x and y) by means of the following expressions

$$\begin{array}{l} P(\xi, \eta) = \int_{\Omega_f} p(x, y, \xi, \eta) d\Omega_f, \\ M_x(\xi, \eta) = \int_{\Omega_f} yp(x, y, \xi, \eta) d\Omega_f,\ M_y(\xi, \eta) = \int_{\Omega_f} xp(x, y, \xi, \eta) d\Omega_f \end{array} \tag{8}$$

Evaluation of the reaction of elastic medium is performed with the help of the Betti's reciprocity theorem [1]. We consider two punches with the same contact region Ω_f. The first is standard rigid punch with the plane bottom having the shape described by a linear function

$$z = f^0(x,y) = \alpha + \beta x + \gamma y,\ (x,y) \in \Omega_f \tag{9}$$

with given coefficients $\alpha,\ \beta,\ \gamma$. This standard punch is penetrated into elastic half-space in the case, when

$$q_x^i(x,y,\xi,\eta) = q_y^i(x,y,\xi,\eta) = q_z^i(x,y,\xi,\eta) = 0,\ (x,y) \in \Omega_q^i \tag{10}$$

for $i = 1,2,...,N$. Contact pressure p^0 $((x,y) \in \Omega_f)$ and displacements $u^0,\ v^0,\ w^0$ $((x,y) \in \Omega_f,$ $i = 1,2,...,N)$ along the axes $x,\ y,\ z$ corresponding to the first standard punch penetration without friction are supposed to be known. These values can be represented in the form [2]

$$p^0 = \alpha p_\alpha^0(x,y) + \beta p_\beta^0(x,y) + \gamma p_\gamma^0(x,y),\ (x,y) \in \Omega_f \tag{11}$$

$$\begin{array}{l} u^0 = \alpha u_\alpha^0(x,y) + \beta u_\beta^0(x,y) + \gamma u_\gamma^0(x,y), \\ v^0 = \alpha v_\alpha^0(x,y) + \beta v_\beta^0(x,y) + \gamma v_\gamma^0(x,y), \\ w^0 = \alpha w_\alpha^0(x,y) + \beta w_\beta^0(x,y) + \gamma w_\gamma^0(x,y), \end{array} \tag{12}$$

where $(x,y) \in \Omega_q^i,\ i = 1,2,...,N$. The functions $p_\alpha^0(x,y),\ p_\beta^0(x,y),\ p_\gamma^0(x,y)$ $((x,y) \in \Omega_f)$ and $u_\alpha^0(x,y),\ u_\beta^0(x,y),...,\ w_\gamma^0(x,y)$ $((x,y) \in \Omega_q^i)$ do not depend on the constants $\alpha,\ \beta,\ \gamma$.

The second considered punch has unknown (optimized) shape described by the shape function $f = f(x,y)$. The second punch with desired shape is penetrated to elastic half-space in accordance with the boundary conditions (5)-(7) in general case, when $q_j^i \neq 0$ $(j = x,\ y,\ z)$. To write out the reciprocity relation consider two different systems of values. The first system $w^0 = f^0,\ p^0,$ $((x,y) \in \Omega_f),\ u^0,\ v^0,\ w^0$ $((x,y) \in \Omega_q^i,\ i = 1,2,...,N)$ corresponds to the contact problem with a standard punch, and the second system $w = f,\ p,$ $((x,y) \in \Omega_f)$ and $q_x^i,\ q_y^i,\ q_z^i$ $((x,y) \in \Omega_q^i,$ $i = 1,2,...,N)$ is realized in the contact problem with optimized punch. In accordance with the Betti's reciprocity theorem [1] we have

$$\int_{\Omega_f} p^0 f d\Omega_f = \int_{\Omega_f} f^0 p d\Omega_f + \sum_{i=1}^N \int_{\Omega_q^i} \left(u^0 q_x^i + v^0 q_y^i + w^0 q_z^i\right) d\Omega_q^i \tag{13}$$

If we substitute the expressions (9), (11), (12) for $f^0,\ p^0,\ u^0,\ v^0,\ w^0$ into the relation (13) and perform elementary transformations, we obtain

$$\begin{array}{l} \alpha\left(\int_{\Omega_f} p d\Omega_f - \int_{\Omega_f} p_\alpha^0 f d\Omega_f + \sum_{i=1}^N \int_{\Omega_q^i} \left[u_\alpha^0 q_x^i + v_\alpha^0 q_y^i + w_\alpha^0 q_z^i\right] d\Omega_q^i\right) + \\ +\beta\left(\int_{\Omega_f} x p d\Omega_f - \int_{\Omega_f} p_\beta^0 f d\Omega_f + \sum_{i=1}^N \int_{\Omega_q^i} \left[u_\beta^0 q_x^i + v_\beta^0 q_y^i + w_\beta^0 q_z^i\right] d\Omega_q^i\right) + \\ +\gamma\left(\int_{\Omega_f} y p d\Omega_f - \int_{\Omega_f} p_\gamma^0 f d\Omega_f + \sum_{i=1}^N \int_{\Omega_q^i} \left[u_\gamma^0 q_x^i + v_\gamma^0 q_y^i + w_\gamma^0 q_z^i\right] d\Omega_q^i\right) = 0 \end{array} \tag{14}$$

Then consider the values $\alpha,\ \beta,\ \gamma$ as an arbitrary constants. To satisfy the equation (14) for any $\alpha,\ \beta,\ \gamma$ it is necessary to equate the expressions in the round brackets to zero. As a result we obtain the following presentations for the total force P and the moments M_j applied to the optimized punch

$$P = P_f(f) - P_q(q) \tag{15}$$

$$M_j = M_j^f(f) - M_j^q(q),\ j = x,y \tag{16}$$

where $P_f(f),\ M_j^f(f)$ are the linear functionals given by the expressions

$$\begin{array}{l} P_f(f) = \int_{\Omega_f} p_\alpha^0 f d\Omega_f, \\ M_x^f(f) = \int_{\Omega_f} p_\gamma^0 f d\Omega_f,\ M_y^f(f) = \int_{\Omega_f} p_\beta^0 f d\Omega_f \end{array} \tag{17}$$

and the linear functionals $P_q(q),\ M_j^q(q)$ depending on random forces $q_x^i(x,y,\xi,\eta),\ q_y^i(x,y,\xi,\eta),$ $q_z^i(x,y,\xi,\eta)$ are expressed with the help of the following formulas

$$\begin{array}{l} P_q(q) = \sum_{i=1}^N \int_{\Omega_q^i} \left[u_\alpha^0 q_x^i + v_\alpha^0 q_y^i + w_\alpha^0 q_z^i\right] d\Omega_q^i, \\ M_x^q(q) = \sum_{i=1}^N \int_{\Omega_q^i} \left[u_\gamma^0 q_x^i + v_\gamma^o q_y^i + w_\gamma^o q_z^i\right] d\Omega_q^i, \\ M_y^q(q) = \sum_{i=1}^N \int_{\Omega_q^i} \left[u_\beta^0 q_x^i + v_\beta^o q_y^i + w_\beta^o q_z^i\right] d\Omega_q^i \end{array} \tag{18}$$

Consider the case when the random external pointed load $q_j = q(x,y,\xi,\eta),\ j = x,y,z$ are applied to the only domain $\Omega_q = \{x_1 \le x \le x_2,\ y_1 \le y \le y_2\}$ and these loads are statistically independent and uniformly distributed, i.e.

$$g = g(\xi,\eta) = g_\xi(\xi) g_\eta(\eta),$$

$$g_\xi(\xi) = \begin{cases} 0,\ \xi < x_1 \\ \dfrac{1}{x_2 - x_1},\ x_1 < \xi < x_2 \\ 0,\ \xi > x_2 \end{cases}, \quad g_\eta(\eta) = \begin{cases} 0,\ \eta < y_1 \\ \dfrac{1}{y_2 - y_1},\ y_1 < \eta < y_2 \\ 0,\ \eta > y_2 \end{cases}, \tag{19}$$

$$F_\xi(\xi) = \begin{cases} 0,\ \xi < x_1 \\ \dfrac{\xi - x_1}{x_2 - x_1},\ x_1 < \xi < x_2 \\ 1,\ \xi > x_2 \end{cases}, \quad F_\eta(\eta) = \begin{cases} 0,\ \eta < y_1 \\ \dfrac{\eta - y_1}{y_2 - y_1},\ y_1 < \eta < y_2 \\ 1,\ \eta > y_2 \end{cases}$$

where $x_1,\ x_2,\ y_1,\ y_2$ - given values $(x_1 < x_2,\ y_1 < y_2)$.

Mathematical expectations of the total reaction force $\hat{P}$ and moments $\hat{M}_x,\ \hat{M}_y$ evaluated with the help of the formulas

$$\begin{array}{l} \hat{P} = \mathcal{E}(P) = P_f(f) - \mathcal{E}(P_q(q)), \\ \hat{M}_j = \mathcal{E}(M_j) = M_j^f(f) - \mathcal{E}(M_j^q(q)),\ j = x,y \end{array} \tag{20}$$

Consider shape optimization problem for rigid punch-shell that consists of minimization of mass functional

$$J = \rho \int_{\Omega_f} \sqrt{1 + (\nabla f)^2} d\Omega_f \approx \rho S_f + \frac{\rho}{2} \int_{\Omega_f} (\nabla f)^2 d\Omega_f \to \min_f \tag{21}$$

under the following constraints

$$\hat{P} = P^*,\ \hat{M}_x = M_x^*,\ \hat{M}_y = M_y^* \tag{22}$$

imposed on mathematical expectations of the total reaction force and moments. Here $S_f = \text{meas}\Omega_f,\ \rho = h\rho_0$ (h - thickness of the considered rigid shell, ρ_0 - density of the material of the shell-punch) and $h,\ \rho,\ P^*,\ M_x^*,\ M_y^*$ - given problem parameters. In what follows we suppose that the domain Ω_f is a circular with given radius a ($\Omega_f :\ x^2 + y^2 \le a^2$). Let us now construct the Lagrange augmented functional corresponding to optimization problem (21), (22)

$$J^L = \int_{\Omega_f} \left[\frac{\rho}{2}(\nabla f)^2 - \lambda_\alpha p_\alpha^0 f - \lambda_\beta p_\beta^0 f - \lambda_\gamma p_\gamma^0 f\right] d\Omega_f \tag{23}$$

where $p_\alpha^0(r),\ p_\beta^0(r,\theta),\ p_\gamma^0(r,\theta)$ are represented as

$$\begin{array}{l} p_\alpha^0(r) = E / \left[\pi(1-\nu^2)\sqrt{a^2 - r^2}\right],\ r = \sqrt{x^2 + y^2} \\ p_\beta^0(r,\theta) = \dfrac{2Er\cos\theta}{\pi(1-\nu^2)\sqrt{a^2 - r^2}},\ p_\gamma^0(r,\theta) = \dfrac{2Er\sin\theta}{\pi(1-\nu^2)\sqrt{a^2 - r^2}} \end{array} \tag{24}$$

and Lagrange multipliers $\lambda_\alpha,\ \lambda_\beta,\ \lambda_\gamma$ are determined with the help of conditions (22). The radius r and the angle θ belong to the domain $\Omega_f = \{0 \le r \le a,\ 0 \le \theta \le 2\pi\}$. Necessary optimality condition and boundary condition for desired function f constitute the following boundary-value problem

$$\triangle f \equiv \frac{\partial^2 f}{\partial r^2} + \frac{1}{r}\frac{\partial f}{\partial r} + \frac{1}{r^2}\frac{\partial^2 f}{\partial \theta^2} = -\frac{\lambda_\alpha}{\rho} p_\alpha^0(r) - \frac{\lambda_\beta}{\rho} p_\beta^0(r,\theta) - \frac{\lambda_\gamma}{\rho} p_\gamma^0(r,\theta) \tag{25}$$

$$(f(r,\theta))_{r=a} = 0,\ 0 \le \theta \le 2\pi \tag{26}$$

It is convenient to represent the desired bounded solution of the Poisson equation (25) with the Dirichlet condition (26) in the following form

$$\begin{aligned} &f(r,\theta) = f_\alpha(r) + f_\beta(r,\theta) + f_\gamma(r,\theta) \\ &f_\alpha(r) = \lambda_\alpha \chi_\alpha(r),\ f_\beta(r,\theta) = \lambda_\beta \chi_\beta(r,\theta),\ f_\gamma(r,\theta) = \lambda_\gamma \chi_\gamma(r,\theta) \end{aligned} \tag{27}$$

Shape functions χ_i $(i = \alpha, \beta, \gamma)$ must satisfy the following boundary-value problems

$$\begin{aligned} &\triangle \chi_i = -\frac{1}{\rho} p_i^0,\ i = \alpha, \beta, \gamma \\ &(\chi_i)_{r=a} = 0,\ (\chi_i)_{r\to 0} < \infty \end{aligned} \tag{28}$$

and Lagrange multipliers λ_i $(i = \alpha, \beta, \gamma)$ are determined with the help of the isoperimetric conditions (22). Taking into account that in the case $i = \alpha$ the function $p_\alpha^0 = p_\alpha(r)$ is axisymmetric with respect to z-axis we solve the boundary-value problem (28) and find corresponding symmetric shape function

$$\chi_\alpha(r) = E\left[\sqrt{a^2 - r^2} - a \ln\left(\frac{a + \sqrt{a^2 - r^2}}{a}\right)\right] / \left(\rho\pi(1 - \nu^2)\right) \tag{29}$$

Optimal axisymmetric shape function (29) corresponds to the case where only constraint on the

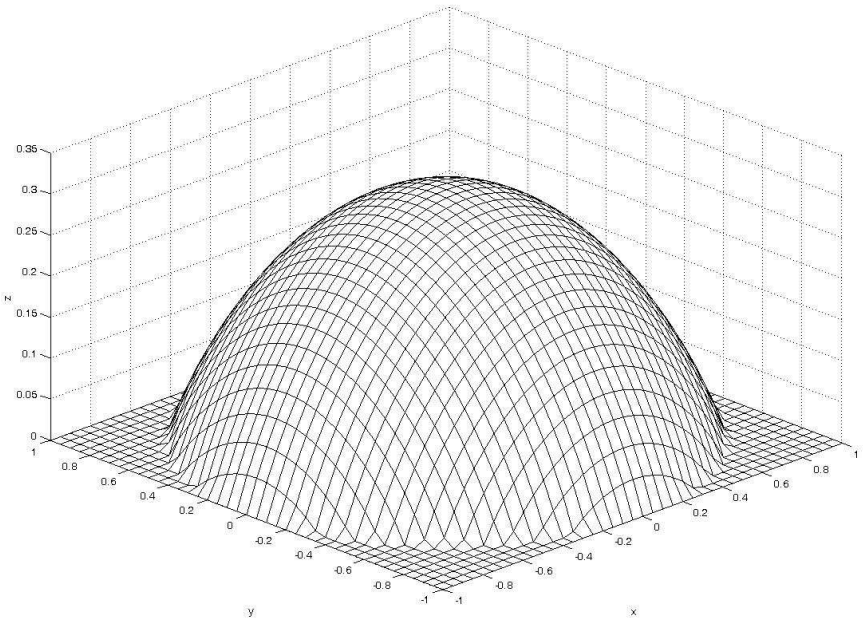


Figure 1: Axisymmetric shape function $z = \chi_\alpha \rho\pi(1 - \nu^2)/E$

external load is taken into account. This case is illustrated in Fig. 1 where the value $a = 1$ and the value $\chi_\alpha \pi\rho(1 - \nu^2)/E$ is shown along the axis oz.

In the case when $i = \beta, \gamma$ the corresponding solutions of the boundary-value problem (28) can be also found in analytical form. To find shape function we rewrite the equation (28) as

$$\frac{\partial^2 \chi_\beta}{\partial r^2} + \frac{1}{r}\frac{\partial \chi_\beta}{\partial r} + \frac{1}{r^2}\frac{\partial^2 \chi_\beta}{\partial \theta^2} = -\frac{2}{\rho} r p_\alpha^0(r) \cos\theta \tag{30}$$

and represent the solution of the equation (30) as

$$\chi_\beta(r,\theta) = (\cos\theta)\chi^0(r) \tag{31}$$

Substituting (31) into (30) and performing elementary transformations we will have

$$\frac{d^2\chi^0}{dr^2} + \frac{1}{r}\frac{d\chi^0}{dr} - \frac{1}{r^2}\chi^0 = \frac{2K}{\rho}\frac{d}{dr}\left(\sqrt{a^2 - r^2}\right) \tag{32}$$

where $K = E/\pi(1-\nu^2)$. Performing two times integration of the equation (32) we obtain

$$r\chi^0(r) = -\frac{2K}{3\rho}(a^2 - r^2)^{3/2} + \frac{C}{2}r^2 + D \tag{33}$$

Here C and D are the arbitrary constants of integration. To find these constants we use the boundary condition boundedness condition (28). We have $C = -4Ka/3\rho$, $D = 2Ka^3/3\rho$. As a result we find $\chi_\beta(r,\theta)$ and by a similar manner $\chi_\gamma(r,\theta)$ as

$$\begin{array}{l} \chi_\beta(r,\theta) = \chi^0(r)\cos\theta = 2E\cos\theta\left\{a(a^2-r^2) - (a^2-r^2)^{3/2}\right\}(3\pi(1-\nu^2)\rho r) \\ \chi_\gamma(r,\theta) = \chi^0(r)\sin\theta = 2E\sin\theta\left\{a(a^2-r^2) - (a^2-r^2)^{3/2}\right\}(3\pi(1-\nu^2)\rho r) \end{array} \tag{34}$$

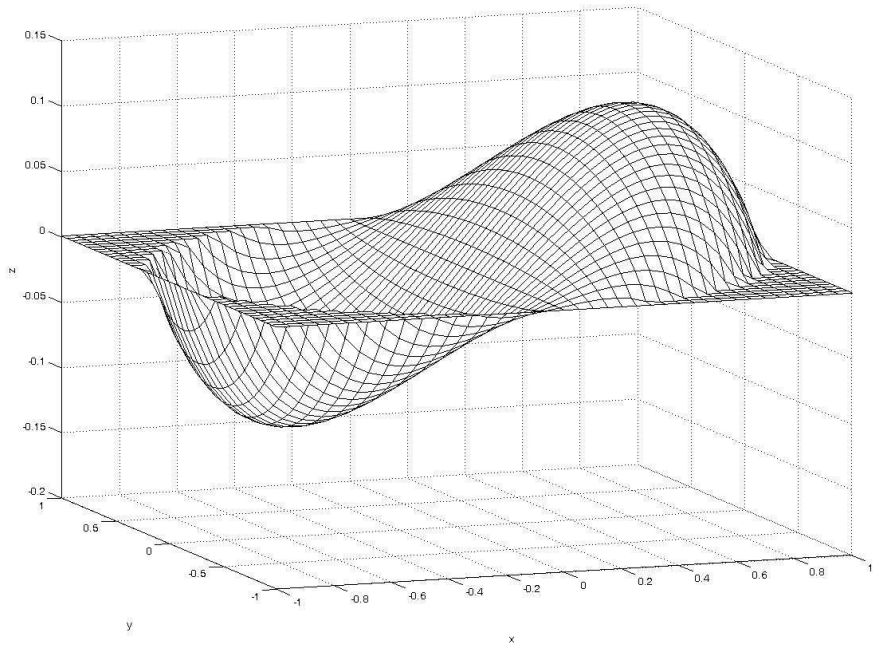


Figure 2: Shape function $z = \chi_\beta 3\pi\rho(1-\nu^2)/(2E)$

Fig. 2 corresponds to the case when we take into account the constraint on the moment M_y. Here the value $\chi_\beta 3\pi\rho(1-\nu^2)/(2E)$ is shown along the axis oz. The value $\chi_\gamma 3\pi\rho(1-\nu^2)/(2E)$ represented in Fig. 3 describes the shape function under the constraint on M_x. It is seen, in particularly, that the functions shown in Fig. 2 and Fig. 3 are not symmetrical. Both in Fig. 2 and Fig. 3 the value $a = 1$.

Note that the application of the reciprocity theorem gave us the possibility to represent the original constraints on $\mathcal{E}(P)$ and $\mathcal{E}(M_j)$ in the form (21), (22). As it is seen from (20), (22) each of the expressions for $\hat{P}$, $\hat{M}_x$, $\hat{M}_y$ can be divided to two parts. The first part is a linear functional of the unknown optimized shape f and the second part represents an integral depending on the joint probability density $g()\chi, \eta$ and the solution of the contact problem for standard punch with plane bottom. If this solution is known then the second part of the constraint can be independently estimated. Thus, with the application of Betti's theorem the original probabilistic optimization problem is reduced to estimation of probabilistic parts of the constraints and solution of deterministic optimization problem. More general discussion and methods can be find in [3].

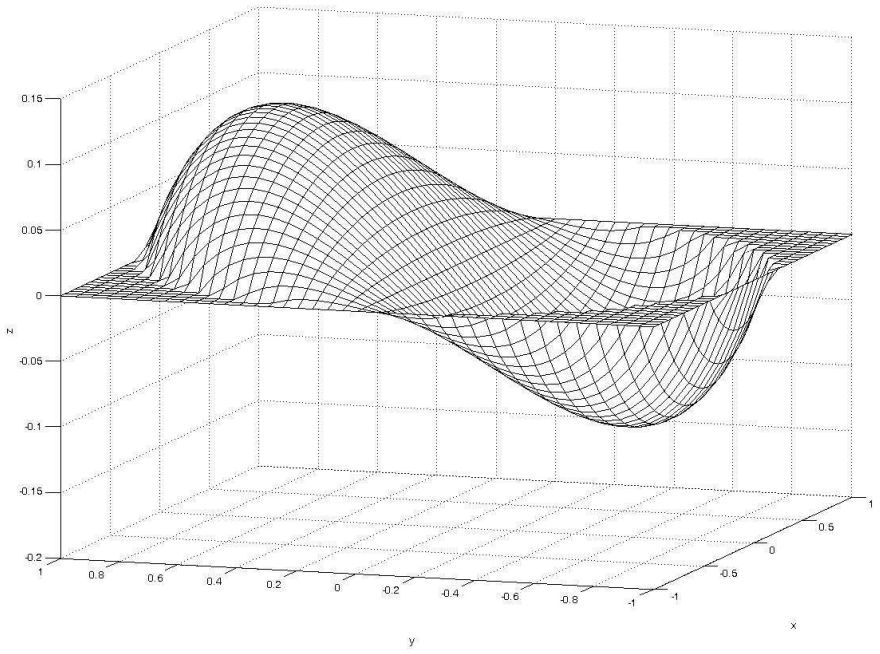


Figure 3: Shape function $z = \chi_\gamma 3\pi\rho(1-\nu^2)/(2E)$

Acknowledgements

The work is performed under support of RFBR (grant No 08-08-00025-a), RAS Program No 13, Program of Support of Leading Scientific Schools (grant No 169.2008.1).

References

[1] A.E.H. Love. A Treatise on the Mathematical Theory of Elasticity. Dover Publications. Inc., New York, 1944.

[2] V.I. Mossakovskii. Application of the reciprocity theorem for total forces and moments determination in space contact problems. PMM, XVII (4), 477-482, 1953 (in Russian).

[3] N.V. Banichuk, P.J. Neittaanmaki. Structural Optimization with Uncertainties. Springer, Dordrecht Heidelberg London New York, 2010.

Nickolay V. Banichuk, Prospekt Vernadskogo, 101, bld.1, Moscow, Russia
Svetlana Yu. Ivanova, Prospekt Vernadskogo, 101, bld.1, Moscow, Russia
Evgeniy V. Makeev, Prospekt Vernadskogo, 101, bld.1, Moscow, Russia

Two-continuum models of the dissolved hydrogen influence on strength of materials

Alexander Belyaev Dmitry Indeitsev Vladimir Polyanskiy
Yury Yakovlev
vice.ipme@gmail.com

Abstract

The main hydrogen influence mechanism in that case is diffusive redistribution of the hydrogen in tensile stresses zones (Gorsky's effect). The hydrogen material interaction increases the hydrogen bonding energy in those zones and decreases local mechanical properties of the material.

These effects can be described by a two-continuum model. The presentation is concerned with the model itself and its most important properties. The presence of the second continuum allows one to describe simultaneously the hydrogen embrittlement and superplastic transformations in the stress-strain diagram in the form of certain structural instability.

1 Introduction

The influence of small natural concentrations of hydrogen on material properties is very considerable. It becomes observable at the level of about a single atom per 50000 atoms of matrix of the matter.

On one hand, this influence of hydrogen can not be ignored since, in many cases, it is the only explanation of changes in material properties in time and under external loading. On the other hand, this influence is difficult to describe due to smallness of this factor and variety of consequences. For example, under change in the hydrogen concentrations by three-four times at the level of one atom per 10000 matrix atoms the mechanical properties of the material can change from brittleness to superplasticity.

An important role is played by the bonding energy of hydrogen in material. It is known that, inside the materials, hydrogen is found in traps with different bonding energies. In steels the total hydrogen content is 0.1-6 n.cm^3/100g, while it is only hydrogen with a low binding energy that affects the strength, i.e. diffusively mobile hydrogen. In aluminum alloys the entire hydrogen diluted in the metal has a low binding energy - about 0.2-0.8 eV. The concentrations that are critical for the mechanical strength of weakly bound hydrogen in steels and aluminum alloys are similar - they are decimal ppm fractions. In aluminum alloys it includes the entire diluted hydrogen, while in steels it amounts to 5-10% of the total amount of diluted hydrogen.

Quite the contrary, the hydrogen with low bonding energy tends to zones of tensile stresses (Gorsky's effect [1]).

Accumulation of hydrogen in the destruction zone occurs both by the input from outside and by redistribution of natural hydrogen inside the material.

The well-known models of hydrogen influence for the materials properties are based on the experimental dependences [2]. These models describe only degradation of the material properties during hydrogen saturation.

There exists no approach which models the SMART-influence on properties of these structures. In contrast to the homogeneous materials, the nanocrystal materials in the presence of hydrogen demonstrate stabilization of their properties as hydrogen decreases the surface energy of crystals in material and prevent their increasing up to the micro size.

2 Two continuum model

The hydrogen with low bound energy is diffuse however its interaction with material is very weak. The high bound hydrogen interacts with material very intensively. This interaction is the main mechanism of the hydrogen stabilization and accumulation. The mechanical material properties degrade owing to this hard interaction.

This is the reason why suggested model must describe both the hydrogen diffusion and its interaction with material.

The mass equation for diffusely hydrogen inside the volume V:

$$m_H^- = \int\limits_V \rho_H^- dV$$

Here m_H^- and ρ_H^-- are mass and volume density of the diffuse hydrogen respectively.

The differential form of this equation can be presented as follows

$$\frac{\partial \rho_H^-}{\partial t} + \nabla \cdot (\underline{v}_H^- \rho_H^-) = j_H^-$$

Hear j_H^- - denotes the mass flux density and $\underline{v}_H^-$ - is the velocity of hydrogen particles.

In terms of the concentration $N_H^- = \rho_H^-/m_H$ this mass balance equation has the form

$$\frac{\partial N_H^-}{\partial t} + \nabla \cdot (\underline{v}_H^- N_H^-) = \frac{j_H^-}{m_H}$$

The bond hydrogen obeys the same equation of the mass balance:

$$\frac{\partial N_H^+}{\partial t} + \nabla \cdot (\underline{v}_H^+ N_H^+) = \frac{j_H^+}{m_H}$$

Here N_H^+ , $\underline{v}_H^+$ are the concentration and particle velocity for bound hydrogen (and bounded with them material particles). $-j_H^- = j_H^+ = j$ is the redistribution flux inside the material. Since the concentrations are low we can assume a linear dependence for this flux.

$$j = \alpha N_H^- - \beta N_H^+$$

This equation describes the hydrogen redistribution over the different bound energy levels.

The equation of dynamics for the material (first continuum) is

$$\nabla \cdot \underline{\underline{\tau}} = (\rho_0 + \rho_H^+)\dot{\underline{v}}_H^+ + j\underline{v}_H^+ + \underline{R}$$

Here $\underline{\underline{\tau}}$ the strain tensor and $\underline{R}$ is the force of interaction between the continua.

Only the spherical part of strain tensor is important for the second continuum (the diffuse hydrogen). This spherical part is characterised by pressure p. Then we can set the dynamic equation as

$$-\nabla p = \rho_H^- \dot{\underline{v}}_H^- - j\underline{v}_H^- - \underline{R}$$

The hydrogen particles velocities are very low because the hydrogen diffusion has time constant of the order from few hour to years. Hence we can put the dynamic equation in the form

$$\nabla \cdot \underline{\underline{\tau}} = (\rho_0 + \rho_H^+)\frac{\partial \underline{v}_H^+}{\partial t} + j\underline{v}_H^+ + \underline{R}$$

$$-\nabla p = \rho_H^- \frac{\partial \underline{v}_H^-}{\partial t} - j\underline{v}_H^- - \underline{R}$$

The interaction force is proportional to the difference in the continuum particles velocities

$$\underline{R} = \underline{\underline{A}} \cdot (\underline{v}_H^+ - \underline{v}_H^-)$$

The tensor $\underline{\underline{A}}$ is determined in terms of such material properties as crystal grain surface area and crystal boundary volume.

The strain energy is known to have two parts, namely those of the volumetric deformation and shear energy. The Gorsky effect means that the volume deformation energy determines the hydrogen diffusion and its interaction with material. So we can define the spherical part of the strain tensor $\underline{\underline{\tau}}$.

$$\underline{\underline{\tau}} = \sigma \underline{\underline{E}} + \underline{\underline{S}}$$

The dynamic equations have now the form:

$$\nabla\sigma = (\rho_0 + \rho_H^+)\frac{\partial \underline{v}_H^+}{\partial t} + j\underline{v}_H^+ + \underline{R} - \nabla \cdot \underline{\underline{S}}$$

$$-\nabla p = \rho_H^- \frac{\partial \underline{v}_H^-}{\partial t} - j\underline{v}_H^- - \underline{R}$$

We can determine $\underline{\underline{S}}$ as linear elastic part of the strain tensor. The constitutive equation for spherical part should be

$$\sigma = E_\Sigma \varepsilon$$

$$E_\Sigma = \frac{E_H E_0}{n_0 E_H + n_H^+ E_0}$$

$$n_0 = \frac{N_0}{N_\Sigma},\ n_H^+ = \frac{N_H^+}{N_\Sigma},\ n_0 + n_H^+ = 1.$$

Here N_Σ is the full number of particles in elementary volume, N_0 - the number of the particles connected by unspoiled bonds, N_H^+ is the number of hydrogen particles attached to a lattice with the bonds by rigidity C_H. Further, n_0 , n_H^+ are the concentrations of the above mentioned particles, respectively.

The equivalent elastic modulus for the lattice E_Σ can decrease essentially, since $E_H \ll E_0$ ($C_H \ll C_0$), and has a strong dependence on the concentration of the attached (bound hydrogen) particles n_H^+.

The number of the lattice settled hydrogen particles depends on the stress state of the lattice in every point and, generally, on time. The unknown functional dependence of E_Σ on $n_H^+(\varepsilon, x, t)$ should be determined from model of the two-component continuum.

Substantiation of the theory of two-component continuum can be found in Ref. [3]; Here we present only the final results with some necessary explanations.

The state equation $\sigma = \sigma(\varepsilon, n_H^+(\varepsilon, x, t))$, can be presented in form

$$\sigma = E_0 \varepsilon \left[1 - \frac{n_H^+}{n_H^+ + n_0 E_H E_0}\right],$$

and the essential dependence of the stress state on concentration of the bonded hydrogen becomes evident.

The hydrogen concentration is described by equation for n_H^+.

$$\frac{\partial^2 n_H^+}{\partial t^2} + (\alpha + \beta)\frac{\partial n_H^+}{\partial t} + A \cdot D(\varepsilon_{st}) \left[\beta \frac{\partial^2 n_H^+}{\partial x^2} + \frac{\partial^3 n_H^+}{\partial t \partial x^2}\right] = 0$$

Here $A = C_H^2 kj$, α, β are constants and $D(\varepsilon_{st})$ denotes the hydrogen diffusion constant.

This two equation are used for modeling the hydrogen influence on the $\sigma(\varepsilon)$ dependence of the material.

The dependence (Fig.1) describes the material properties modification during the hydrogen redistribution within the material.

The part of the $\sigma(\varepsilon)$ dependence with $\frac{d\sigma}{d\varepsilon} < 0$ can not be realized. The growth of the $\varepsilon > \varepsilon_{cr}$ causes to hydrogen embrittlement and destruction.

However the hydrogen saturation leads to decreasing of the breaking point σ_{cr}.

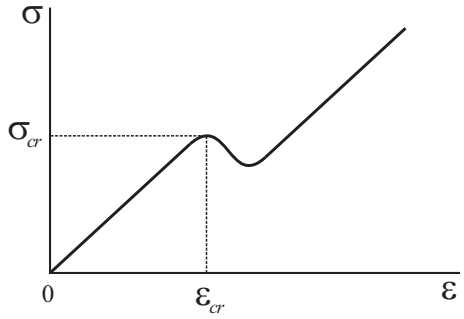


Figure 1: $\sigma(\varepsilon)$ dependence of the material with hydrogen redistribution

The two continuum model describes the hydrogen redistribution in zones of tensile stresses. We can develop a finite element model for real structures if we take into account the outside hydrogen saturation.

The form of $\sigma(\varepsilon)$ curve depend on $\alpha - \beta$ ratio. For the case $\alpha \ll \beta$ the form of $\sigma(\varepsilon)$ is shown in Fig.2

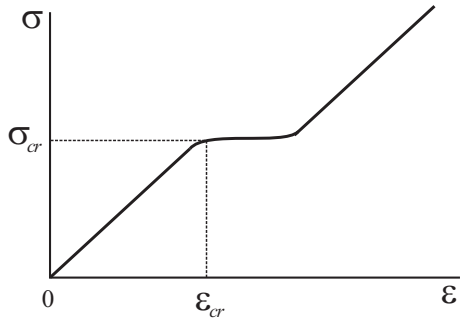


Figure 2: $\sigma(\varepsilon)$ dependence of the material in case $\alpha \ll \beta$

The plane of quasi plasticity changes the unstable part of the $\sigma(\varepsilon)$ curve.

3 Discussion

Similar $\sigma(\varepsilon)$ curves were observed in the experiments with titanium alloys with large hydrogen concentration. This effect was referred to as the superplasticity of the titanium alloys.The experimental $\sigma(\varepsilon)$ curve for alloy VT20 is shown on the Fig.3.

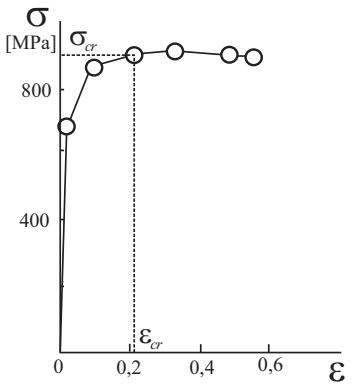


Figure 3: $\sigma(\varepsilon)$ for VT 20 + 0.5% H_2 [4]

Our model describes only two hydrogen bound energy levels. In that case the loading process is reversible which is in contradiction with experimental data.

We can suppose that the hydrogen has three or more bound energy levels in the titanium alloys. The third energy level is the chemical bound (1.4 eV).

The experimental data confirms this hypothesis. The titanium alloys with hydrogen gives hydride nanoparticles under mechanical loading [5]. The average diameter of the hydrides is 50 nm.

4 Conclusions

A model is constructed which allows one to describe the kinetics of hydrogen in metals, and in particular to estimate the hydrogen transition from mobile into bonded state depending on the stress state and to describe the localization of the connected hydrogen resulting in the destruction of a material such localization places.

We suggest a novel approach to modeling the solids with account for the influence of hydrogen on the properties of free surface on monocrystals of various scales.

Application of two-continuum models to describing multiscale materials allows obtaining adequate results which describe SMART-influence on properties of these structures. In contrast to the homogeneous materials, the nanocrystal materials in the presence of hydrogen demonstrate stabilization of their properties as hydrogen decreases the surface energy of crystals in material and prevent their increasing up to the microsize.

Acknowledgements

The financial support of the Sandia Corporation, contract 891092, and the Russian Foundation for Basic Research, grants 08-08-00737 and 08-01-12017, is acknowledged.

References

[1] W.S. Gorsky “Theorie des elastichen Nachwirkung in ungeordneten Mischkristallen (elastische Narchwirkung zweiter Art)”, Physikalische Zeitschrift der Sowjetunion, 8, pp. 457-471, (1935)

[2] D.C. Ahn, P. Sofronis, R. Dodds Jr. “Modeling of hydrogen-assisted ductile crack propagation in metals and alloys” Int. J. Fract. pp.145:135-157 (2007)

[3] D.A. Indeitsev, B.N. Semenov “About a model of structural-phase transformations under hydrogen influence” Acta Mechanica Vol.195, pp.295-304 (2008)

[4] M. Galdeshn, L.Anisimova, E.Boitcova, ISAEE 9(17), p.p. 26-29 (2004)

[5] G.A. Salishchev, M.A. Murzinova, S.V. Zherebtsov, D.D. Afonichev, S.P. Malysheva “Influence of Reversible Hydrogen Alloying on Formation of SMC Structure and Superplasticity of Titanium Alloys”, ICSAM 2000, Orlando, Florida, USA August 1-4, 2000, p.p. 315-320.

Alexander Belyaev, Institute of Problems in Mechanical Engineering, Russian Academy of Sciences, 199178 V.O., Bolshoj pr., 61, St.-Petersburg, Russia
Dmitry Indeitsev, Institute of Problems in Mechanical Engineering, Russian Academy of Sciences, 199178 V.O., Bolshoj pr., 61, St.-Petersburg, Russia
Vladimir Polyanskiy, State Polytechnic University of St. Petersburg, 195251 Politekhnicheskaya, 29 St.-Petersburg, Russia
Yury Yakovlev, State Polytechnic University of St. Petersburg, 195251 Politekhnicheskaya, 29 St.-Petersburg, Russia

Development and stability of a convective mass transfer induced by local heterogeneity of surface-active substance distribution near a free liquid surface

R. Birikh A. Mizev M. Denisova
alex_mizev@icmm.ru

Abstract

Abstract. The onset and stability of a solutal (buoyancy and Marangoni) convection induced by a localized source of surface-active substance placed under an interface were studied both experimentally and theoretically. It was shown that the competition between the buoyancy and solutocapillary convection can lead to the onset of oscillatory convection. The period of observed oscillations appreciably depends on both the Grasshoff and Marangoni numbers and on the size of the source. It was found out that an increase of buoyancy contribution leads to the onset of stationary convection instead of oscillatory one. It was pointed out that the solutal dynamic Bond number can be used by the analogy with thermal one to characterize the studied problem.

1 Introduction

This paper presents the results of experimental and theoretical investigations on the onset and stability of the solutal (gravitational and Marangoni) convective flows in the presence of a source of weakly soluble surfactant located in the vicinity of the interface. Unfortunately, in the literature there have been only a few studies on this topic in contrast to the related papers dealing with the case of a heat source. The majority of papers on this subject can be found in the physical-chemical literature and they are devoted to exploring the phenomenon of autooscillations of surface tension. For the first time this phenomenon was reported in [1]. The authors of this study found out that the surface tension coefficient of the interface experiences periodic changes in the presence of the soluble surfactant source in the form of a drop located near the surface. Later in [2]-[4] this phenomenon was investigated for the liquid-gas and liquid-liquid systems for a variety of surfactants. It was shown that when the depth of source immersion exceeded a certain critical value, the variations of the surface tension occurred in the mode of oscillations. At smaller depth the first oscillation of the surface tension was followed by its monotonic variation in time. Many of the authors reported the existence of the convective motion at the surface involving the changes in the surface properties. In [3] the authors proposed a theoretical model by recognizing that the observed phenomenon of self-oscillations resulted form the competition between the adsorption-desorption processes and the Marangoni convection. The experimentally observed transition from the oscillatory to quasi-stationary mode under changes of the position of the surfactant source with respect to the interface was supported by numerical simulation. However, until recent times the problem dropped out of direct hydrodynamic studies which could verify the validity of the proposed model.

The paper presents the results of experimental and theoretical investigations of surfactant distribution and convection flow velocity in the case of the immersed surfactant source. It has been shown that part of the experimental data reported in the previous papers comes out from incorrect experiment leading to misinterpretation of the observed phenomenon. Based on correctly made experiments described in the paper we propose a new theoretical model, which is based on the competition between two convection mechanisms: gravitational and solutocapillary.

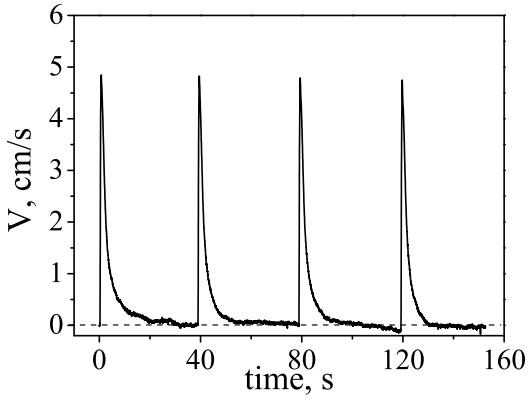


Figure 1: Flow velocity *vs* time for the n-hexanol drop of d=1.5 mm. Depth of drop immersion H=2.1 mm.

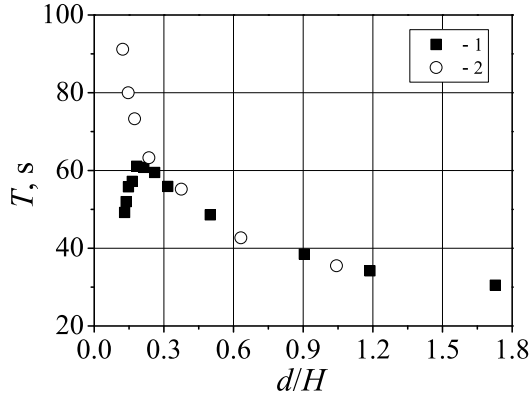


Figure 2: Period of oscillations *vs* nondimensionalized depth of source immersion. Size of n-hexanol drop: 1 - 1.9 mm, 2 - 1.2 mm.

2 Experiment

The experiments were carried out in the Hele-Shaw cell, the dimensions of which were 9 × 4.5 × 0.38 cm. The parallel walls of the cell form the working cell of the Fiseau interferometer, which was used for visualization of the dissolved surfactant distribution. The use of the standard trace particle method allowed us to visualize the velocity field in the cell. Apart from general visualization of the velocity field there has been the possibility to measure the velocity of the convective flow at some selected point by means of the home-made anemometer of small (0.3 mm) size.

Triply deionized water was used as a surrounding liquid. The drops were prepared from weakly soluble alcohols of the same homologous series (from butanol to hexanol) having ultimate solubility in water which allowed us to obtain a distinct interface between alcohol and water. The drop was formed at the end of a thin needle with the external diameter of 0.9 mm, which was introduced into the cell through an orifice at the cell bottom. The vertical position of the needle section with respect to the air-water interface could be varied within the accuracy of 0.1 mm. During the experiments we varied the size of the drop and the depth of its immersion to gain a more complete picture of the distributions of surfactant concentration and convective flow velocity.

The observations shows that some time (of order of diffusion time) after the formation of the drop a cloud of dissolved surfactant forms around and begin to buoy under the action of the Archimedean force in the form of a convective jet. Upon approaching the interface the jet gives rise to intensive solutocapillary convection. In a short time the arising convective vortex destroys the jet and equalizes the surfactant concentration along the surface. As a result the Marangoni convection ceases rather quickly. After this the diffusion and gravitational convection restore the initial distribution of the surfactant in the fluid which leads to another onset of the solutocapillary convective motion. Such a non-harmonic autooscillation mode can proceed over a very long period of time (of the order of several hours for weakly soluble alcohols) up to a complete dissolution of the drop.

Fig.1 shows the time dependence of the flow velocity measured by the anemometer, which was placed at a distance of 1 mm away from the symmetry axis of the jet and at a depth of 1 mm under the water surface. One can see that at the time when the surfactant rises to the surface the velocity increases form practically a zero value to its maximum over a very short period of time, which is followed by the period of a rather slow decrease up to the zero value.

The period of the observed autooscillations depends on the depth of immersion of the surfactant source and the size of the drop. The dependence of the oscillations period on the reverse depth H, non-dimensionalized with respect to the drop diameter d, is given in Fig.2 for two hexanol drops differing in diameter. In the case of a relatively large source the curve goes through a maximum. When the source immersion depth is higher than the penetration depth of the Marangoni convection the fluid motion destroys only a small near-surface part of the jet. In this case, the oscillation period is rather short because the time it takes for the system to restore the original surfactant

distribution is short, too. The maximum period is observed in the case when the flow destroys not only the jet but also the diffusion boundary layer near the drop surface. A further decrease in the immersion depth of the surfactant source leads to a decrease of time, during which the newly formed jet reaches the surface. In the case of small drops the solutocapillary convection arises at smaller depths compared to the case of large drops. In such a close proximity to the surface the source and the resulting torch immediately find themselves in the zone of an active Marangoni convection which accounts for the absence of a maximum on the curve.

As it follows from Fig.2 the oscillatory mode of convection occurs even at very small depths and proceeds up to the point when the drop surface touches the water-air inter-face. On the other hand, during experimental investigation [2]-[4] made for similar fluids the authors observed a transition to a monotonic decrease of the surface tension with time as the source was approaching the surface. To gain a clear understanding of the reason for such essential contradictions a series of additional experiments, where the needle was inserted into the fluid through the water-air interface like in experiments [2]-[4], were carried out. In this case the drop of the surfactant, which is lighter than the surrounding liquid, is held at the end of the needle only by the capillary forces, acting on the line of contact of three phases at the sharp end of the needle. In the case of a small depth of the source immersion both a rather intensive convective flow existing around the drop and Archimedean force lead to a detachment of the contact line of the drop from the sharp edge of the needle. As a result, part of the drop spreads in the form of a thin film along the lateral side of the needle toward the surface forming there a permanent source of the surfactant. This rise of the surfactant to the surface is the very factor that provided a slow stationary decrease of the surface tension observed in [2]-[4]. Therefore the inconsistent interpretation of the experimental data in [2]-[4] is the result of incorrect realization of the experiment. It is clear that the theoretical model based on these results has nothing to do with the real situation and should be revised. Such a refined model will be proposed below.

The results discussed above disclose an essential difference in the modes of convective flows initiated by the immersed surfactant source and the heat source. An oscillatory mode of convection is commonly observed in the case of a surfactant source [5] whereas in the case of a heat source located near a thick fluid layer the Marangoni convection is always stationary [5]-[9]. As it has been mentioned above, the oscillatory mode of convection is the result of competition between the gravitational and capillary mechanisms. Due to a relatively weak gravitational mechanism and a slow diffusion the amount of the surfactant supplied to the water-air interface from the drop is not sufficient for sustaining an intensive surface convection initiated by the capillary mechanism. In the thermal problems the relative contributions of the gravitational and thermocapillary forces are determined in terms of the dimensionless parameter, the dynamic Bond number, $Bo^T_{dyn} = \rho g \beta_T h^2/\sigma_T$, which represents the relation between these forces and is equal to the ratio of the Rayleigh to the Marangoni number. For the characteristic dimension of 1 mm the value of this parameter for most of the investigated fluids is of the order of 10^{-2}. By analogy with the thermal case one can introduce a solutal dynamic Bond number $Bo^c_{dyn} = \rho g \beta_c h^2/\sigma_c$. Estimations give the values of this parameter for alcohols used in our tests for a depth of 1 mm from 10^{-4} for n-hexanol to 10^{-2} for n-butanol. It is seen that for alcohols with shorter molecules the value of the Bond number rapidly grows approaching the value typical for the thermal case. As the estimates show the Marangoni number remains nearly constant in the range of the values of order 10^7. It follows then that the growth of the Bond number is caused by an increase in the contribution of the gravitational forces (the Grashof number) by two orders of magnitude.

Fig.3 illustrates the time variation of the flow velocity measured by the anemometer for a drop of n-butanol. During the experiment the distance from the drop to the surface gradually decreases from 2 mm to 1 mm. (only the most interesting portion of the curve is shown). One can see that the oscillation period is one order of magnitude less than the one for a hexanol drop with the same dimension and immersed at the same depth. The increased contribution of the gravitational convection and a higher diffusion coefficient results in a more intensive supply of the surfactant from the drop to the interface and, hence, to a more rapid creation of the necessary conditions for initiation of new oscillations. What is most interesting is that at a certain depth of the drop immersion the oscillatory mode of convection changes into a stationary mode. The amount of the surfactant carried from the drop surface to the jet proves to be quite sufficient for sustaining a uniform distribution of surfactant concentration near the water surface and, consequently, a

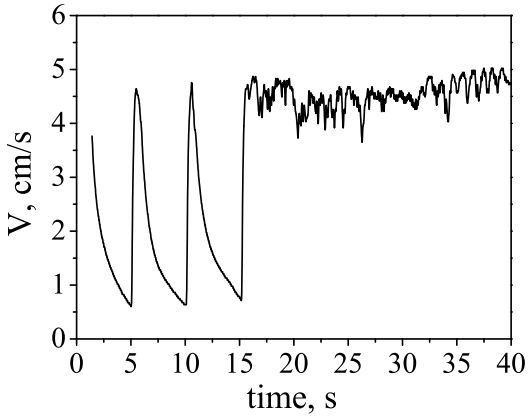


Figure 3: Flow velocity *vs* time for the n-butanol drop of d=1.2 mm.

constant value of the convective motion intensity.

Thus, the experimental results show that in the case of the immersed surfactant source we can observe both the oscillatory and stationary convection modes depending on the ratio of the Grashof to the Marangini numbers (the dynamic solutal Bond number).

3 Theory

In the simple mathematical model given below we will show that the competition between the gravitational solutal convection and the Marangoni convection (at large values of the Schmidt number) can lead to an oscillatory convection. Let us consider a two-dimensional problem on a solutal convection in a plane horizontal layer with a free upper boundary, which contains a localized source of the soluble surfactant placed at the layer bottom. The surface tension at the free surface σ is related to surfactant concentration c as $\sigma = \sigma_0 - \sigma_1 c$ Compared to the surrounding fluid the surfactant has lower density which is given as $\rho = \rho_0(1 - \beta c)$. In the gravitational field inhomogeneity of the solution density leads to the onset of gravitational convection.

The fluid motion is described in terms of the stream function ψ, vortex φ and surfactant concentration c, using the Boussinesq approximation:

$$\begin{aligned} &\frac{\partial \varphi}{\partial t} + \frac{\partial \psi}{\partial y}\frac{\partial \varphi}{\partial x} - \frac{\partial \psi}{\partial x}\frac{\partial \varphi}{\partial y} = \Delta\varphi - Gr\frac{\partial c}{\partial x},\ \Delta\psi = -\varphi \\ &\frac{\partial c}{\partial t} + \frac{\partial \psi}{\partial y}\frac{\partial c}{\partial x} - \frac{\partial \psi}{\partial x}\frac{\partial c}{\partial y} = Sc^{-1}\Delta c \end{aligned} \tag{1}$$

Here the dimensionless parameters $Gr = g\beta C_0 h^3/(\nu)^2$ and $Sc = \nu/D$ - the Geashof and Schmidt numbers - are defined through the layer thickness h, surfactant concentration C_0 near the source and the fluid characteristics: ν - kinematic viscosity, D - coefficient of diffusion.

All boundaries of the cavity are impermeable to the surfactant. At the lower boundary, which is the place of source location, the surfactant concentration is assumed constant. There is the no-slip condition in the lower and lateral solid boundaries, and the free upper surface is assumed to be plane and meet the requirement of a balance of tangential stresses.

$$\begin{aligned} &y = 0 : \psi = 0, \frac{\partial \psi}{\partial y} = 0,\ \ |x| > d : \frac{\partial c}{\partial y} = 0,\ \ |x| \le d :\ \mathrm{c} = 1 \\ &x = \pm L : \psi = 0, \frac{\partial \psi}{\partial x} = 0, \frac{\partial c}{\partial x} = 0 \\ &y = 1 :\ \psi = 0,\ \varphi = MaSc^{-1}\frac{\partial c}{\partial x},\ \ \frac{\partial c}{\partial y} = 0 \end{aligned} \tag{2}$$

Here $Ma = \sigma_1 C_0 h/\rho\nu D$ is the Marangoni number, which defines the intensity of soluto-capillary convection. Initially the surfactant in the fluid is absent and the fluid is as-sumed to be in a quiescent state ($c = 0$, $\psi = 0$, $\varphi = 0$).

The non-stationary boundary value problem is solved by the finite difference method on the 200×40 - 800×160 square meshes using the implicit Crank- Nicolson scheme. The solution of the Poisson equation is found by the subsequent upper relaxation method.

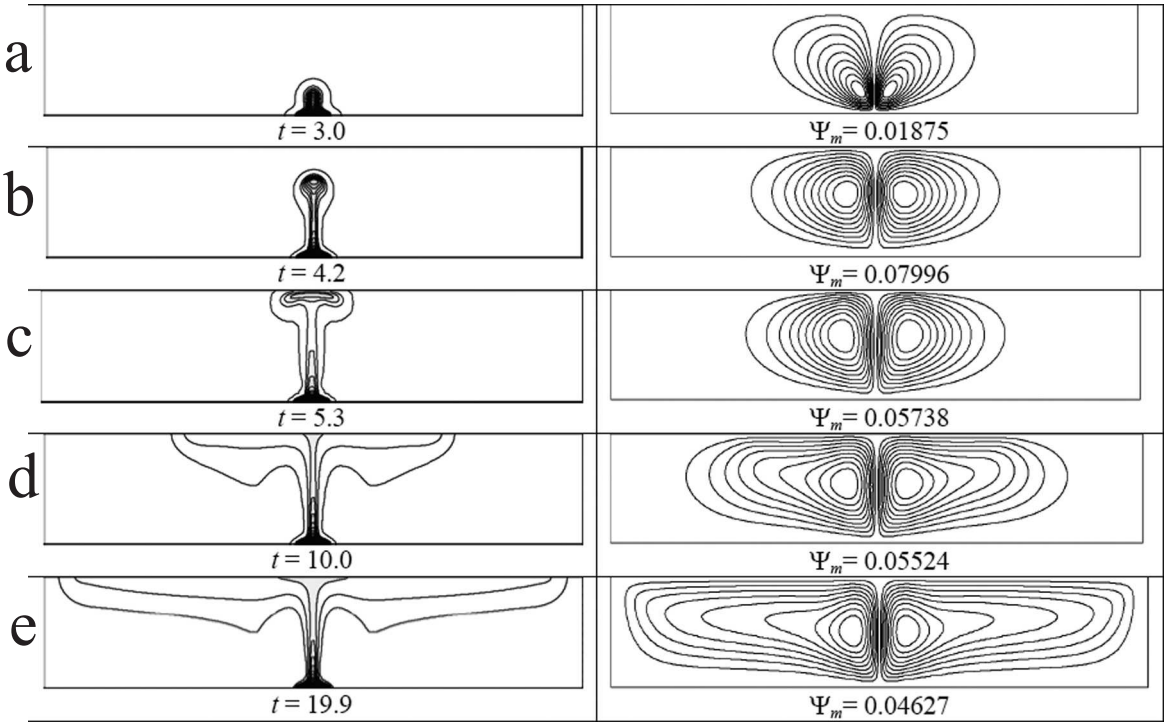


Figure 4: Concentration isolines and stream functions for $d = 1/8$ and $Gr = 500$, $Ma = 0$

It was found out that the oscillatory convection mode is observed in a wide range of the Grashof and Marangoni numbers. Due to gravitational convection the surfactant in the form of the concentration jet raises to the free surface (Fig.5) which cause an out-burst of the intensive Marangoni convection. The jet is destroyed by this motion, and the surfactant concentration is equalized all over the surface. After a time a new convective jet carries the next portion of the surfactant to the surface and the situation repeats itself. For the Grashof number of 500 and the Marangoni number of $7 \cdot 10^5$ at $d = 1/8$ the oscillation period is equal to 3 units of the viscous time, inside of which the Marangoni convection lasts less than one unit. At the outburst of the Marangoni convection the flow rate of the fluid in the convective vortex is an order of magnitude higher than the flow rate in the case of the background gravitational convection.

Variation of the convective flow intensity ($\psi_m(t)$ -the maximal value of the stream function in the cavity determining the flow rate in the convective vortex) at $Gr = 500$ and half-width of the source $d = 1/8$ for different values of the Marangoni number is shown in Fig.5. The evolution of purely gravitational convection ($Ma = 0$) is denoted by dash-dot line in Fig. 5a. At small values of the Marangoni number (Fig.5a, solid line) an outburst of the solutocapillary convection occurs as soon as the jet reaches the surface. However, it is not followed by the onset of the oscillatory mode. For these parameters the oscillatory mode occurs at $Ma > 2 \cdot 10^5$. Alternation of the gravitational and Marangoni convection is illustrated in Fig 5b and 5c.

The distributions of the surfactant concentration obtained by numerical calculations at different phases of oscillations agree with the experimental results. Evidently, the observed autooscillations are caused by a competition between the gravitational convection supplying the surfactant to the free surface and the Marangoni convection equalizing the surfactant concentration near the boundary. The oscillation period strongly depends on the Grashof number - it decreases with the

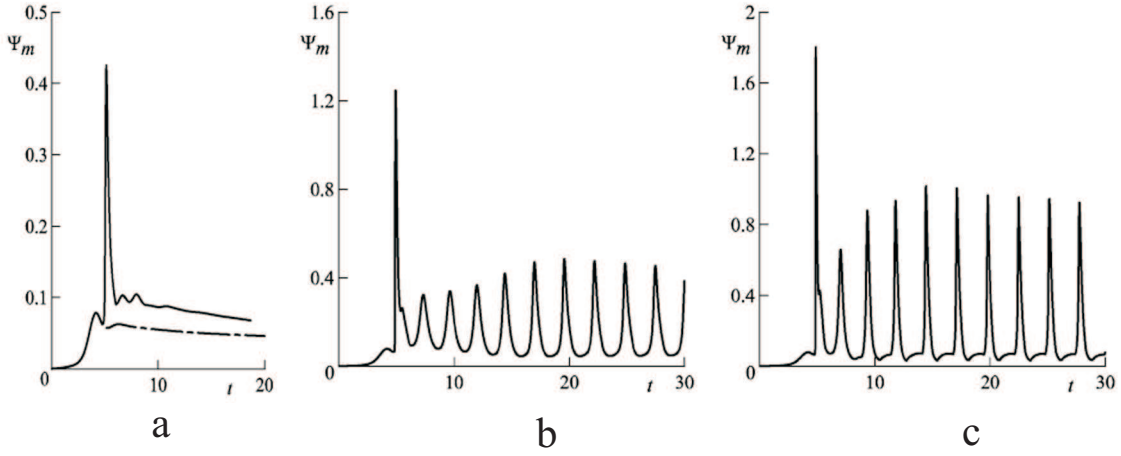


Figure 5: Variation of the convection intensity with time for different Marangoni number: a - $Ma = 0$ (dash-dot line) and $Ma = 10^5$ (solid line), b - $Ma = 4 \cdot 10^5$, c - $Ma = 7 \cdot 10^5$

growth of the Grashof number.

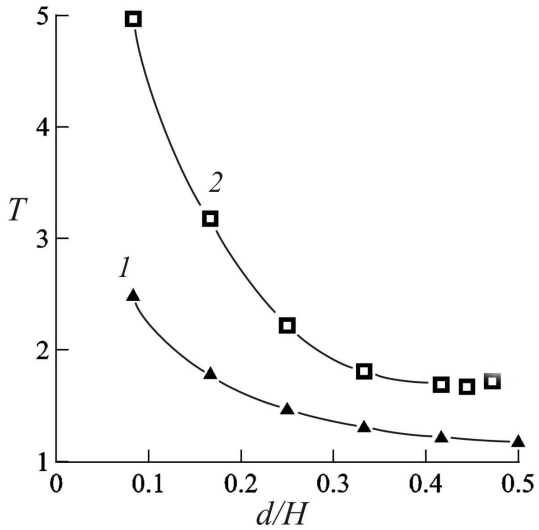


Figure 6: Dependence of non-dimensionalized period of oscillations on the relative depth of source immersion. $Ma = 5 \cdot 10^7$, $Gr = 500(1)$, $Gr = 1000(2)$

The oscillation period also depends on the depth of the source immersion. Since in our numerical simulations the distance from the source to the free surface is taken as the unit of length, the depth of immersion is simulated with respect to the source width. In Fig.6 the period of the developed oscillations is plotted as a function of the source width. As might be expected, the oscillation period decreases with the growth of the Grashof number and the increase in the source width (with decrease in the distance from the source to the surface).

4 Conclusion

The results of experimental and numerical investigations clearly demonstrate that the reason for the periodic changes in the surface tension or in the surface electrical potential, observed in [2]-[4] is the time dependent mass transfer of the surfactant from the source to the interface caused by the oscillatory nature of the convective flow. It has been found that a transition from the oscillatory mode of convection to the stationary mode at small depth of the source immersion observed for all

examined substances in [2]-[4] is the result of incorrect realization of experiments. The design of the experimental setup used in our experiments allowed us to investigate the problem more correctly. The results of the laboratory and numerical experiments are in good qualitative agreement. The oscillation period and the mode of convection (the oscillatory or stationary mode) strongly depend on the Grashof and Marangoni numbers, i.e., on the relative contribution of the gravitational and solutocapillary forces. It has been suggested to use the solutal analog of the dynamic Bond number as a measure of the contribution ratio. Experimentally it has been shown that when the values of this parameter are close to the values typical for the thermal case the oscillatory mode of convection changes to a stationary mode which is characteristic of the immersed heat source.

The work was supported by the RFBR grant No 08-01-00503 and the Program No 09-T-1-1005 of Ural Branch of RAS.

References

[1] Dupeyrat M. and Nakache E. Direct conversion of chemical energy into me-chanical energy at an oil water interface // Bioelectrochem. Bioenerget. 1978. 5. p. 134-141.

[2] Kovalchuk N. M. and Vollhardt D. Autooscillations of surface tension in water-alcohol systems // J. Phys. Chem. B. 2000. 104. p. 7987 7992.

[3] Kovalchuk N. M. and Vollhardt D. Marangoni instability and spontaneous non-linear oscillations produced at liquid interfaces by surfactant transfer // Adv. in Col-loid and Interface Sci. 2006. 120. p. 1-31.

[4] Kovalchuk N. M. and Vollhardt D. Effect of substance properties on the appear-ance and characteristics of repeated surface tension auto-oscillation driven by Ma-rangoni force // Phys. Rev. E. 2004. 69. 016307.

[5] Zuev A.L., Kostarev K.G. Specific features of solutocapillary convection // Physics Uspekhi (Advances in Physical Sciences). 2008. V. 178. 10. P. 1065-1085.

[6] Mizev A. Experimental investigation of thermocapillary convection induced by a local temperature inho-mogeneity near the liquid surface. 1. Solid source of heat // Journal of Applied Mechanics and Technical Physics, Vol. 45, No. 4, pp. 486-497, 2004.

[7] Mizev A. Experimental investigation of thermocapillary convection induced by a local temperature inho-mogeneity near the liquid surface. 2. Radiation-induced source of heat// Journal of Applied Mechanics and Technical Physics, Vol. 45, No. 5, pp. 699-704, 2004

[8] Zuev A.L., Kostarev K.G. Thermal and solutal Marangoni convection around the air bubble in a fluid // Hydrodynamics. V. 14. Perm: PSU. 2004. P. 88 99.

[9] 9. Bezugluy B. A., Fliagin V. M. Thermocapillary convection in a fluid layer with a quasipoint heat source in the substrate // Bulletin of RAS. Fluid mechanics. 2007. 6. P. 124 134.

Institute of Continuous Media Mechanics, Ural Branch of Russian Academy of Sciences, Acad. Korolev Str. 1, 614013 Perm, Russia.

Estimation of surface deformation sensitivity to changes in the characteristic parameters of the volcanic system

Varvara A. Bogoyavlenskaya, Igor N. Shardakov
varvara@icmm.ru

Abstract

This paper suggests that fiber-optic sensors (2.3 m base) may be used for monitoring of surface deformation in the vicinity of the volcanic edifice, which allows making measurements with an accuracy up to 10^{-8}. To prove the efficiency of these devices for surface deformation monitoring, a number of problems are solved. An axisymmetric model of a volcanic system consisting of a volcanic edifice, a magma chamber, a volcanic channel and surrounding rocks is considered. The space heterogeneity of rocks is not taken into account. Numerical experiments are conducted to study the influence of the size, shape and depth of the volcanic chamber on surface deformations. The proposed approach is used to estimate the size of regions near the volcanic edifice where the surface deformation can be measured with the given accuracy, to investigate the possibility of registration of changes in the location of the plug inside the channel and to analyze the behavior of the volcanic system in the presence of several chambers.

1 Introduction

At present, there are many methods of monitoring volcanic activity. The most widespread approach to this problem is based on the methods of registration and analysis of seismic waves caused by volcanic activity. However, seismic events can be recorded only at the stage of high eruptive activity. From the point of view of prediction possibility, the quasi-static deformation processes that precede the dynamic processes are of primary interest.

One of the key factors determining the quasi-static state of the volcanic system is the hydrostatic pressure in the volcanic chamber. However, the direct measurement of this pressure in the volcanic chamber is impossible. Therefore, it is necessary to develop indirect methods for registration of chamber pressure evolution. As an indicator of changes in the pressure inside the volcanic chamber, the earth's surface deformation observed in the vicinity of the volcanic edifice has been taken.

Registration of earth's surface deformations near the volcanic edifice is performed using geodesic or satellite data. The necessity of refining the monitoring grid for volcanic regions has been justified in works [1, 2]. Besides, the monitoring results have indicated that the registration of deformation precursors of eruptions requires continuous measurements [1]. In this study, we suggest that fiber-optic sensors (2.3 m base) can be used for monitoring of surface deformations. The proposed approach allows us to make accurate measurements (up to 10^{-8}) and to construct the monitoring system based on these sensors. The principal scheme of the monitoring system is shown in figure 1.

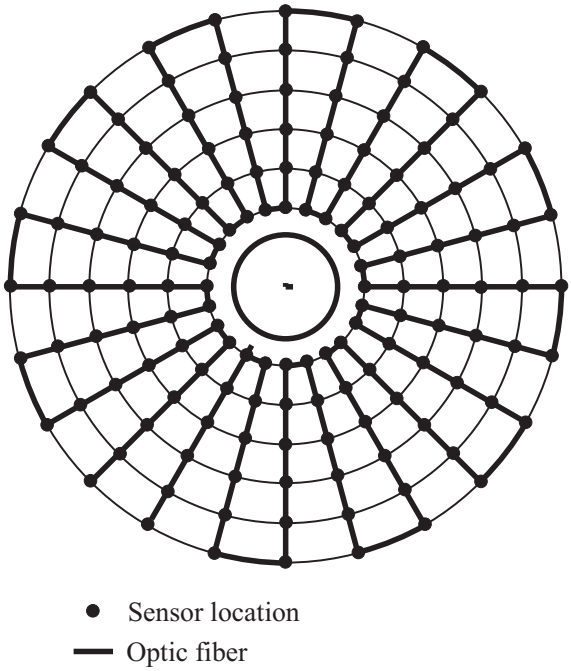


Figure 1: Principal scheme of the monitoring system

A number of numerical experiments have been carried out to prove the potential of fiber-optic sensors for measuring surface deformations in the vicinity of volcanic edifice.

2 Problem formulation

The purpose of our investigation is to determine the possibility for tracing the pressure evolution in the volcanic chamber by measuring the deformation characteristics on the surface and to find parameters being most sensitive to changes in the state of the volcanic system. This analysis is based on the accuracy of measurements of the following parameters: the accuracy of deformation measurements up to 10^{-6}; and the accuracy of registration of excess pressure up to 10 atm. The reason to choose the latter parameter is as follows. Eruption takes place when the pressure in the chamber reaches its critical value of about 200 atm. Therefore, an increase of pressure by 10 atm is considered acceptable for tracing the changes in the state of the system.

The system under consideration consists of a volcanic edifice, a magma chamber, a volcanic channel and surrounding rocks (fig. 2). The height of the edifice is 1000 m. The sizes of the structure are chosen so that the boundaries have no effect on the behavior of the system. In a first approximation, the rock material is assumed to be homogeneous, isotropic and elastic with the elastic modulus of 5000 MPa [4] and Poisson's ratio equal to 0.2. The problem is solved in an axisymmetric formulation.

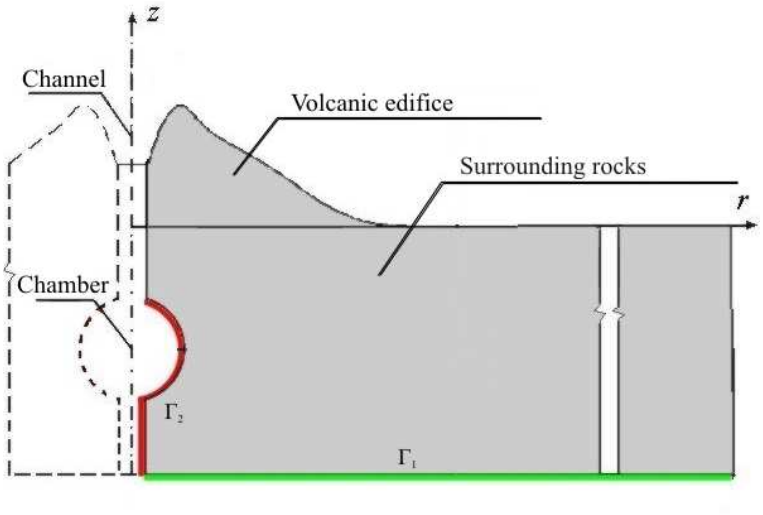


Figure 2: Loading diagram

The volcanic system is in a quasi-static state and is subjected to the applied pressure equal to 10 atm and distributed over the chamber surface and part of the channel. The bottom boundary of the system is fixed in a vertical direction. Other boundaries are free.

Thus, in the framework of the theory of linear elasticity, the behavior of the volcanic system can be described using the following system of equations

$$\begin{aligned}
&\nabla \cdot \sigma = 0, \\
&\sigma = \lambda I_1(\varepsilon)\,\mathbf{g} + 2\mu\varepsilon, \\
&\varepsilon = \tfrac{1}{2}\left(\nabla \mathbf{u} + (\nabla \mathbf{u})^T\right).
\end{aligned}$$

This system is supplemented by the following boundary conditions:

$$\begin{aligned}
&u_z|_{\Gamma_1} = 0, \\
&\sigma_{rz}|_{\Gamma_1} = 0, \\
&\sigma_n|_{\Gamma_2} = -p\mathbf{n}, \\
&\sigma_r|_{\Gamma_2} = 0, \\
&\sigma \cdot \mathbf{n}|_{\Gamma \setminus (\Gamma_1 \cup \Gamma_2)} = 0.
\end{aligned}$$

The problem has been solved by the finite element method using the software complex ANSYS Mechanical (license No. 392853).

3 Results

The influence of the chamber size on surface deformations has been examined subject to the condition that the distance between the chamber surface and the earth's surface is constant. In this case, the chamber is assumed to be spherical with the radius of 500, 1000, 1500, 2000 and 2500 m. Figure 3 shows the distribution of surface deformations along the natural coordinate that first follows the slope of the volcanic edifice and then the line z = 0.

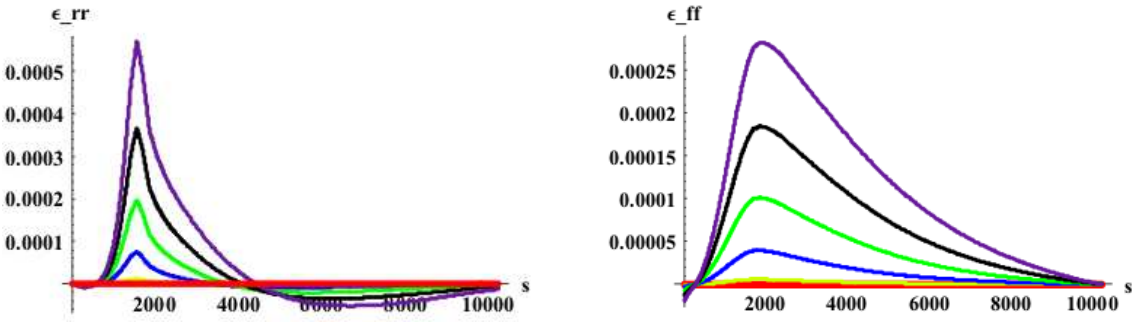


Figure 3: Distribution of surface deformations at different values of the chamber radius (R=500m; R=1000m; R=1500m; R=2000m; R=2500m)

Figure 4 presents the curves showing the dependence of the size of the zone around the volcanic edifice, where the surface deformation can be measured with an accuracy up to 10^{-6}, on the chamber radius. It is seen that with the increase in the chamber radius the deformation can be measured at a large distance from the edifice.

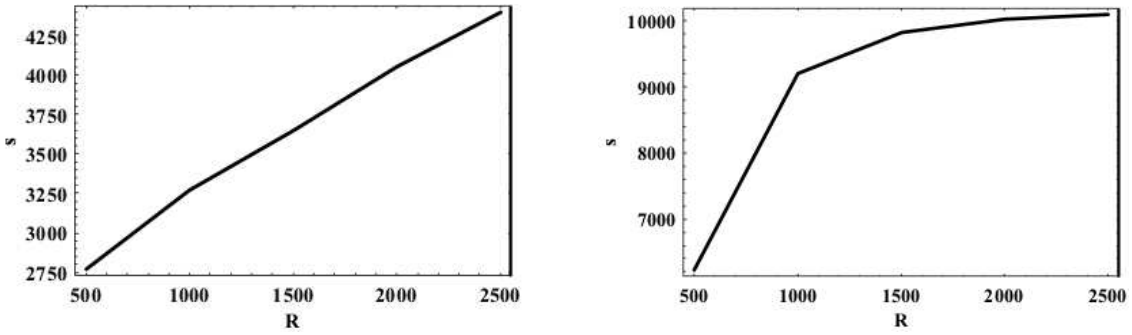


Figure 4: Dependence of the size of the zone around the volcanic edifice, where the surface deformation can be measured with an accuracy up to 10^{-6}, on the chamber radius for ε_{rr} (left) and for $\varepsilon_{\varphi\varphi}$ (right)

The influence of the chamber location depth on surface deformations has been studied assuming that the chamber radius (R = 1000 m) is fixed. Figure 5 shows the surface deformation distribution for different chamber location depth (4000, 4500, 5000, 5500, 6000, 6500 and 7000 m).

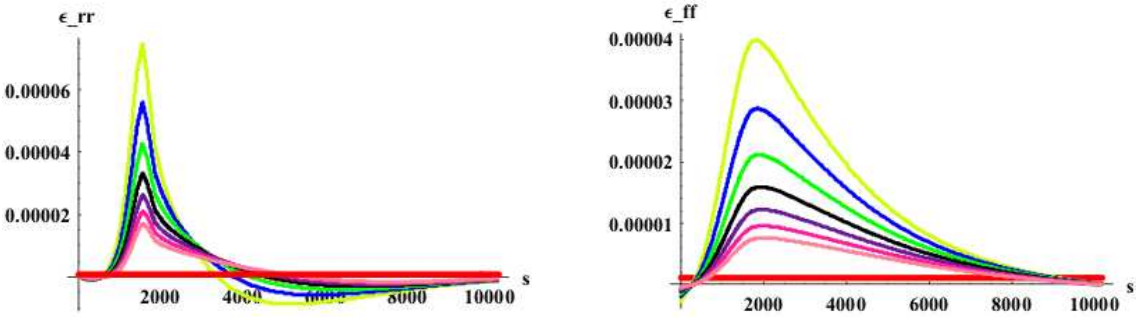


Figure 5: Distribution of surface deformations at different depth of chamber location (h=4000m; h=4500m; h=5000m; h=5500m; h=6000m; h=6500m; h=7000m)

When plotting the dependence of the zone size on the chamber location depth, we have found that, as the depth of chamber location increases, the distance from the volcanic edifice, where deformations exceed 10^{-6}, increases for ε_{rr} and decreases for $\varepsilon_{\varphi\varphi}$ (fig. 6).

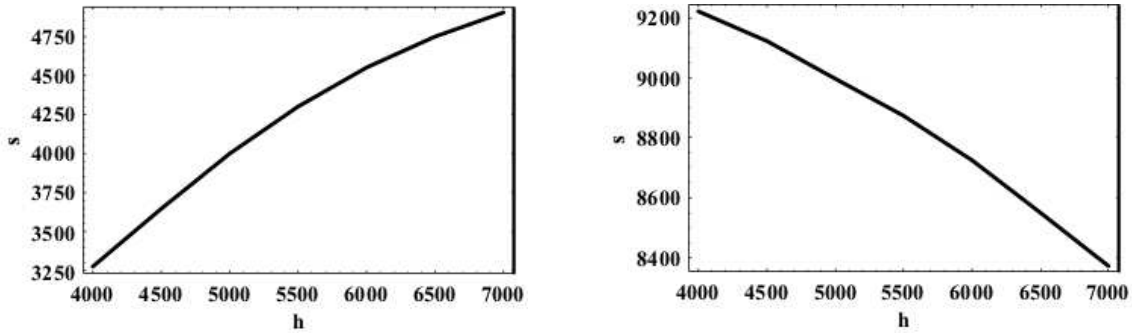


Figure 6: Dependence of the size of the zone around the volcanic edifice, where surface deformations can be measured with an accuracy to 10^{-6}, on the depth of chamber location for ε_{rr} (left) and for $\varepsilon_{\varphi\varphi}$ (right)

When investigating the influence of the chamber shape on surface deformations, we have also considered the axisymmetric structure, in which the chamber is an ellipsoid of rotation flattened in a vertical direction. The sizes of the ellipsoid are chosen subject to the condition that the volume of the ellipsoid is equal to that of the sphere with the radius of 1000 m: $\frac{4}{3}\pi ab^2 = \frac{4}{3}\pi R^3$, which yields expressions for the semi-axes of the ellipsoid: $a = \frac{R}{\sqrt[6]{1-\varepsilon^2}}$ – semi-major axis, $b = R\sqrt[3]{1-\varepsilon^2}$ – semi-minor axis, $0 \leq \varepsilon < 1$ – eccentricity ($\varepsilon = 0$ referred to the sphere). The distance between the earth's surface and the chamber surface is constant. The sizes and shapes of magma chambers at different eccentricities are shown in figure 7.

Figure 8 shows the distribution of surface deformations ε_{rr} and $\varepsilon_{\varphi\varphi}$ for different shapes of the chamber.

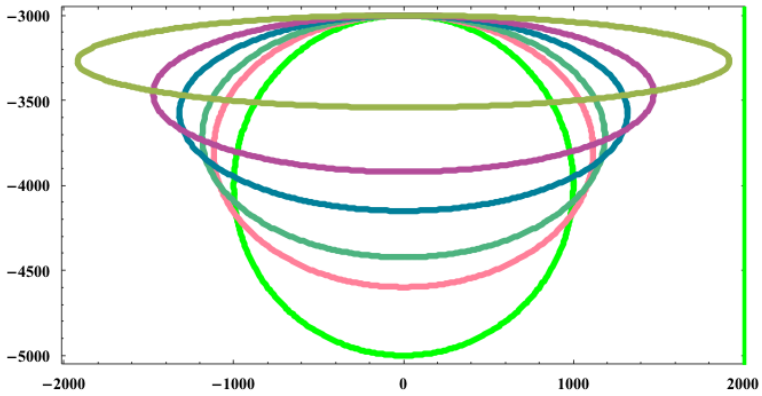


Figure 7: Sizes and shapes of chambers ($\varepsilon =$ 0, 0.7, 0.8, 0.9, 0.95, 0.99)

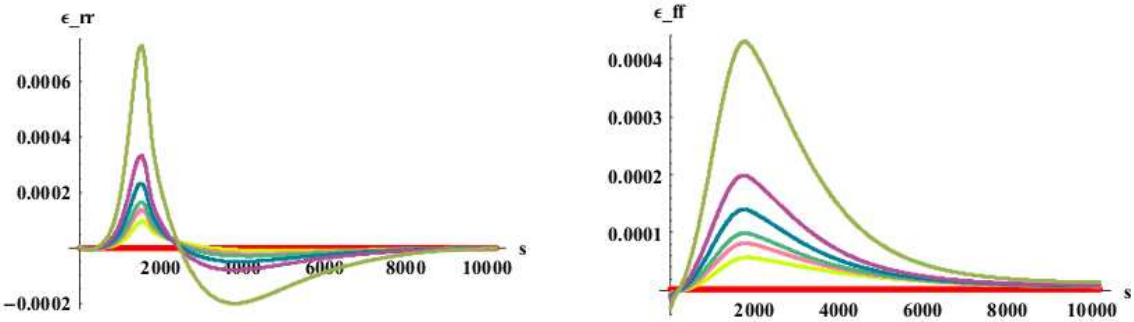


Figure 8: Distribution of surface deformations for different shapes of the chamber ($\varepsilon =$ 0, 0.7, 0.8, 0.9, 0.95, 0.99)

It is seen that with the increase of eccentricity the peak value of deformations increases both for radial deformations ε_{rr} and for deformations $\varepsilon_{\varphi\varphi}$ (fig. 9.).

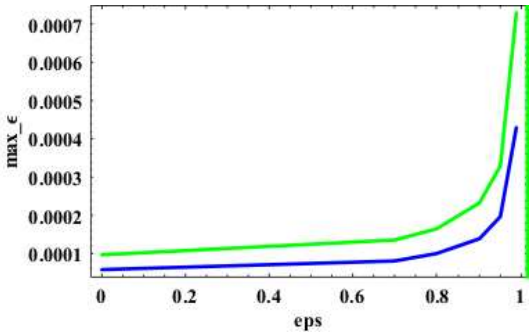


Figure 9: Dependence of the peak value of deformations on eccentricity (ε_{rr} and $\varepsilon_{\varphi\varphi}$)

To analyze the possibility for registration of the motion of a plug in the volcanic channel, we consider a system of axisymmetric shape with a spherical magma chamber. The center of the chamber is assumed to be at a fixed depth of 4000 m, and its radius is a constant value and equals 1000 m. The system is subjected to an applied pressure distributed over the chamber surface and part of the channel bounded above by the plug being at depth H from the crater (fig. 10). The bottom boundary of the system is fixed in a vertical direction. Other boundaries are free as before.

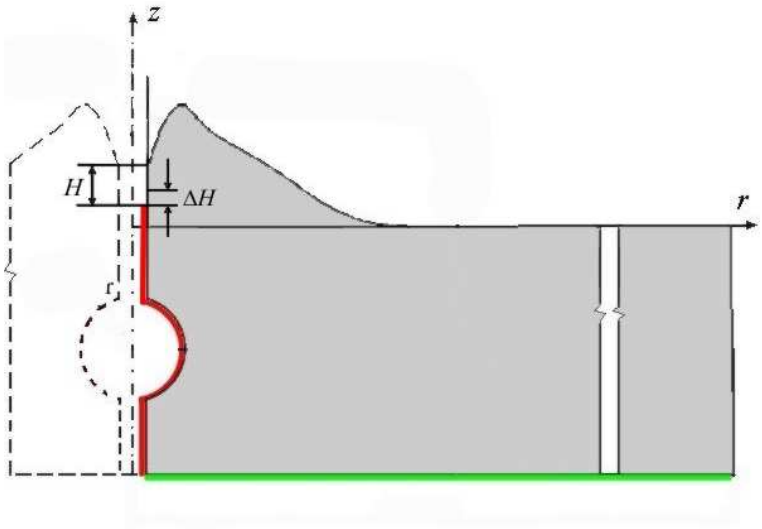


Figure 10: Loading diagram showing the influence of the plug motion in the volcano channel on surface deformations

In this case, we consider the deformation difference of surface deformations for two values of the plug depth H and $H-\Delta H$, which corresponds to the initial and changed locations of the plug. At the same time, the pressure is distributed according the law illustrated in figure 11.

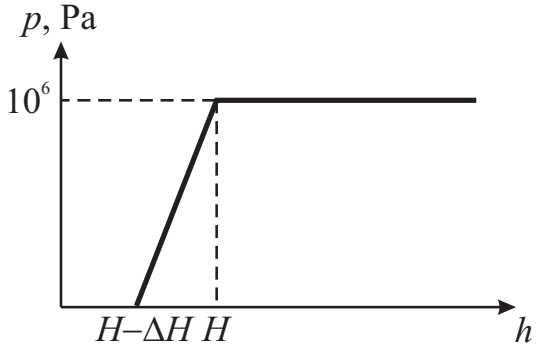


Figure 11: Pressure versus depth

The distributions of deformation increments are obtained for different initial locations of the plug in the volcanic channel (fig. 12).

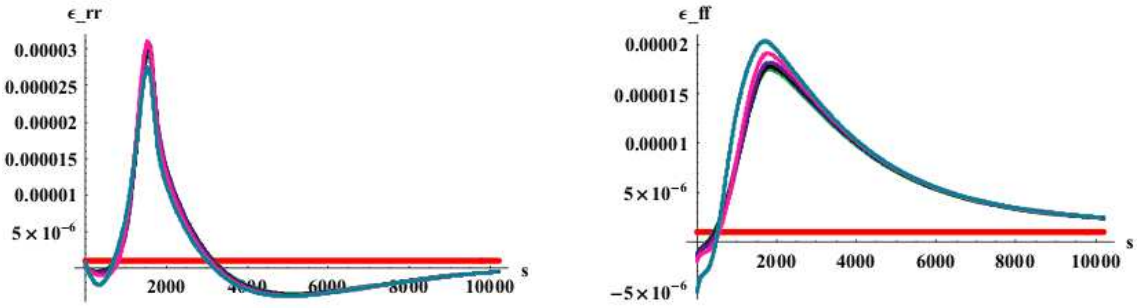


Figure 12: Distribution of deformation increments for different initial locations of the plug (H=3600m; H=3100m; H=2600m; H=2100m; H=1600m; H=1100m; H=600m; H=100m)

The plots show that, as the plug rises, the increments of surface deformations change only slightly, and therefore we cannot judge the change in the magma level in the volcanic channel.

To study the influence of a number of magma chambers and their geometry on surface deformations, an ellipsoidal area at a given depth has been considered. This area consists of several magma chambers divided by the layers of rocks (fig. 13). We have studied the cases of a single ellipsoidal chamber, three ellipsoidal chambers and five ellipsoidal chambers having the same semi-minor axes. The distances between the chambers are also identical and equal to the semi-minor axis.

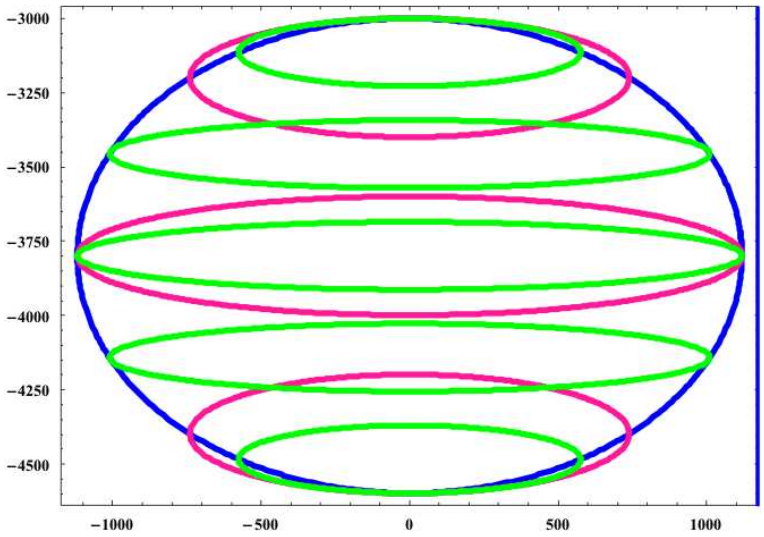


Figure 13: Sizes and shapes of the chambers

Figure 13 illustrates the case of $\varepsilon = 0.7$; calculations are also performed for the values of the eccentricity of 0 and 0.8.

Figure 14 gives the results of calculations of the surface deformation fields for $\varepsilon = 0.7$. Similar qualitative results have also been obtained for the remaining values of eccentricity.

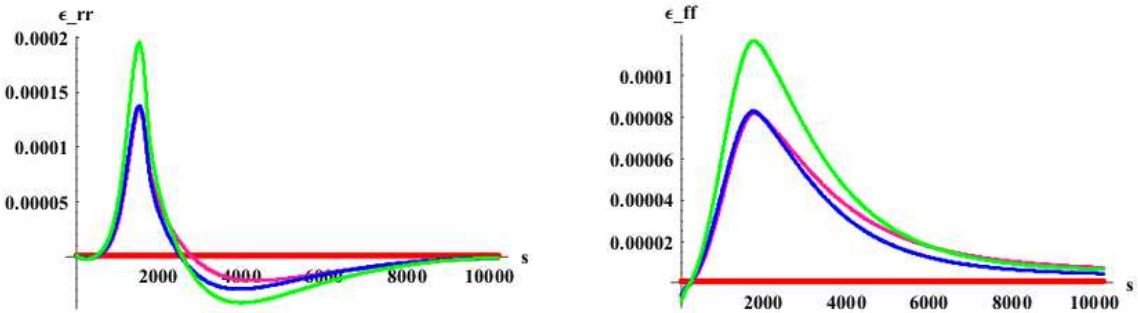


Figure 14: Distribution of surface deformations for different number of chambers

As one can see, the most significant impact on surface deformations is observed in the case of five magma chambers.

4 Conclusions

We have investigated the influence of the sizes, shapes and location depth of the chamber on the earth's surface deformation. We have performed numerical calculations of the sizes of the zone in the vicinity of the volcanic edifice, where the surface deformations can be measured with the given accuracy. We have analyzed the possibility of registration of the plug location in the channel and examined the behavior of the volcanic system in the presence of several chambers.

The obtained results indicate that the deformations ε_{rr} are less sensitive to changes in the parameters of the volcanic system, and the deformations $\varepsilon_{\varphi\varphi}$ can be preferably used for recording changes in the state of the volcanic system.

In the framework of the approach developed, the problems have been solved in an axisymmetric formulation taking into account the homogeneity and isotropy of rocks. We plan to extend the capability of our model by examining the space heterogeneity of rocks until the abandonment of the axial symmetry.

Acknowledgements

This study was supported by the RAS Presidium Program (project No 09-П-1-1010).

References

[1] Levin V.E., Maguskin M.A., Barhtiarov V.F. et al. Multisystm geodetic monitoring of recent crustal movements in Kamchtka and the Commander islands. // Volcanology and seismology. 2006. No. 3. P. 54-67.

[2] Maguskin M.A., Fedotov S.A., Levin V.E. et al. Deformations related to a large (M=6.9) earthquake, the magma discharge, and eruptions in the Karymskii volcanic center in 1996-2005. // Volcanology and seismology. 2008. No. 5. P. 22-40.

[3] Slezin Yu.B. Mechanism of volcanic eruptions (stationary model). 1998.

[4] Efimov A.B., Ershova T.Ya. Maguskin M.A. Numerical modelling of the Earth's surface displacement in the region of Karymsky volcano. // Volcanology and seismology. 1993. No. 6. P. 72-98.

[5] Kotyuk A.F. Sensors in modern measurements. 2006.

Institute of Continuous Media Mechanics, Ural Branch of Russian Academy of Sciences,
Acad. Korolev Str. 1, 614013, Perm, Russia

Numerical implementation of the incubation time fracture criterion

Vladimir Bratov
Vladimir@bratov.com

Abstract

The paper is discussing problems connected with embedment of the incubation time criterion for brittle fracture into finite element computational schemes. Incubation time fracture criterion is reviewed, practical questions of its numerical implementation are extensively discussed. Several examples of how the incubation time fracture criterion can be used as fracture condition in finite element computations are given. The examples include simulations of dynamic crack propagation and arrest, impact crater formation (i.e. fracture in initially intact media), spall fracture in plates, propagation of cracks in pipelines. Applicability of the approach to model initiation, development and arrest of dynamic fracture is claimed.

1 Introduction

Numerical methods are of a vital importance while solving problems of dynamic fracture mechanics. First of all this is connected to the fact that an overwhelming majority of problems of dynamic fracture are impossible to solve analytically. Framework of dynamic problems allowing analytical solution is limited to few classical solutions (e.g. see the book of Freund [1] for exhaustive collection of these solutions). Turning to problems of dynamic fracture evolution (fracture development and arrest) a possibility to construct analytical solution is completely vanishing (not accounting for couple of solutions for steady-state dynamic crack propagation).

Central issue while solving problems of dynamic fracture (no matter, numerically or analytically) is rupture criterion to be used in order to assess if fracture should happen at a given state of a system. For several decades it is known that classical fracture criteria (criteria based on the idea of the ultimate stress for intact media and on the idea of the critical stress intensity factor for cracked bodies) are not able to provide satisfactory coincidence with known experiments (see, e.g. [2]). Moreover, it is easy to show that these criteria contradict the common sense being applied to transient problems (as discussed in [3]).

In [4],[2],[3] a new criterion based on the introduced concept of the incubation time of a fracture process was proposed in order to predict conditions of initiation of brittle fracture in solids undergoing dynamic impact loading. Later in this paper the incubation time fracture criterion (ITFC) will be discussed in detail. Here some distinguishing properties of the ITFC that make it especially attractive to be embedded into numerical computational schemes are outlined.

In this connection the important feature of the incubation time fracture criterion is that it is able to predict fracture initiation conditions with reliability and correctness in *"static"* case of *"slow"* changing loads and *"slow"* changing geometry as well as in *"dynamic"* case of high-rate loads and *"fast"* changing geometry (see, e.g., [2], [3]). Moreover, the criterion is supplying a smooth transition between these two cases [5]. The result is that using this approach one does not need to care about time scale of the problem – the criterion is giving correct predictions in a wide range of loading rates from static problems to the extreme dynamic ones. Even distinguishing between *"static"* and *"dynamic"* situation is not obligatory needed anymore, though the ITFC itself is providing a perfect possibility to do this.

It is easy to show (see e.g. [6]) that for *"static"* problems with *"slow"* changing loads and *"slow"* changing geometry the ITFC is coinciding with well-known Neuber-Novozhilov fracture

criterion [7] ,[8]. It can be proven [3], [6], [9] that with the right choice of spatial parameter d, used in criterion formulation, Neuber-Novozhilov criterion is giving predictions coinciding with critical tensile stress (ultimate stress) criterion in the case of rapture of initially intact media and the critical stress intensity factor (Griffith - Irwine, K_{IC}) criterion in the case of rupture in a tip of a macroscopic crack. The important outcome is that the criterion is governing two cases that are normally treated separately in a single (and rather simple) rupture condition – it can be applied to predict brittle fracture of materials with arbitrary size of defect, from intact undamaged media to media with macroscopic cracks. The Neuber-Novozhilov criterion is also providing smooth transition between these two cases. As a result the criterion is perfectly applicable to fracture problems with fracture surface geometry that is not known *a priori*. In such problems fracture in initially intact material can be initiated somewhere in a body and, as it evolves, transform into a macroscopic crack. The whole fracture evolution can be predicted with a single fracture criterion.

In a big number of works (see, e.g., [3], [5], [10]) authors, applying the introduced ITFC to predict critical fracture conditions in different dynamic fracture experiments (e.g., [11]) proved that the ITFC can be successfully used to predict initiation of brittle fracture appearing as a result of high-rate deformation applied somewhere in a body. In the same works a material parameter τ - the incubation time of brittle fracture, constituting the essence of the ITFC and characterizing the temporal dependence of media strength was computed for many of widely used materials.

Lately an approach making it possible to embed the ITFC into numerical computational schemes based on finite element method (FEM) was developed [12], [13]. Utilizing this approach simulation of several different experiments on dynamic impact fracture caused by high-rate loads was performed [12], [14]. These works testify that the ITFC used as a rupture criterion in FEM numerical simulations is able to predict correctly and precisely experimentally observed phenomena of dynamic fracture initiation, evolution and arrest.

As a matter of fact, not including the ITFC and approaches based on classical fracture criteria that are obviously inapplicable to predict high-rate fracture, nowadays only one approach exists that is pretending to correct prediction of dynamic fracture. This approach is originating from the works of Freund [15],[16],[17] and was later developed by Rosakes. It is based on an assumption that fracture criterion in a tip of a crack can be received as a function of stress intensity factor rate: $K^d(t) \leq K^d_C(\dot{K}(t))$, with K^d being the dynamic stress intensity factor, changing in time, K^d_C being its critical value and dot denoting time derivative. As discussed by Bratov and Petrov [12], this approach in many cases is contradicting the common sense and is applicable to predict dynamic fracture initiation (not even mentioning high-rate fracture evolution) in a very limited set of problems with strict requirements on material, loading history, fractured sample geometry etc.

The main idea of this paper is to convince the reader that the ITFC is the most promising, precise and convenient among available criteria suitable for embedding into numerical codes in order to predict dynamic fracture. The paper is also giving exhaustive information about the ITFC in connection with possibilities of its numerical implementation into FEM. The main problems of this implementation are discussed and the algorithm in order to embed the ITFC into FEM is explicitly given.

2 Numerical Implementation of the Incubation Time Fracture Criterion

Incubation time criterion for brittle fracture at a point x at time t reads as [4],[2],[3]:

$$\frac{1}{\tau}\int_{t-\tau}^{t}\frac{1}{d}\int_{x-d}^{x}\sigma(x',t')dx'dt' \geq \sigma_c, \tag{1}$$

where τ is the microstructural time of a fracture process (or fracture incubation time) – a parameter characterizing the response of the studied material to applied dynamic loads (i.e. τ is constant for a given material and does not depend on problem geometry, the way a load is applied, the shape of a load pulse and its amplitude). d is the characteristic size of a fracture process zone and is constant for the given material and the chosen scale level. σ is normal stress at a point, changing with time and σ_c is its critical value (ultimate stress or critical tensile stress found in quasistatic conditions). x' and t' are the local coordinate and time.

Assuming

$$d = \frac{2}{\pi}\frac{K_{IC}^2}{\sigma_c^2}, \tag{2}$$

where K_{IC} is a critical stress intensity factor for mode I loading (mode I fracture toughness), measured in quasistatic experimental conditions. It can be shown that within the framework of linear elastic fracture mechanics for the case of fracture initiation in the tip of an existing crack, (1) is equivalent to

$$\frac{1}{\tau}\int_{t-\tau}^{t} K_I(t')dt' \geq K_{IC}. \tag{3}$$

Condition (2) arises from the requirement that (1) is equivalent to Irwin's criterion ($K_I \geq K_{IC}$), in the case of $t \to \infty$.

Once again it should be noticed that for slow loading rates and, hence, times to fracture that are much bigger than τ, condition (3) for crack initiation gives the same predictions as Irwin's criterion of a critical stress intensity factor. In the case when the stress field is not singular in the vicinity of point x (locally intact material) and under condition of quasistatic load applied to the media, condition (1) is reduced to critical tensile stress fracture criterion. It should be outlined that (1) in the quasistatic case is equivalent to critical stress intensity factor criterion under assumption that square root asymptotic solution is valid in the vicinity of a singular point x. In the case of a singular field that is not controlled by a square root singularity (for example asymptotic field appearing in the tip of an angular notch), when Griffith-Irwin critical stress intensity factor criterion is not applicable, condition (1) can be successfully used to predict fracture in such a singular point [18].

Thereby, (1) automatically ensures correct fracture prediction in a very wide range of quasistatic problems with materials fracturing following brittle scenario. It has been proven in multiple works (see, e.g., [4], [2], [3], [5], [10], [19]) that for dynamic problems (1) (under condition that incubation time τ is correctly identified for the studied material) is correctly predicting stressed state at the moment of initiation of brittle rupture (in the case of fracture of initially intact media, as well as in the case of initiation of macroscopic crack). First of all this concerns problems with loads applied at high and ultra-high rates.

In this work it will be demonstrated that condition (1) can be also used to predict evolution of quasi-brittle fracture (fracture and fragmentation of initially intact media, growth and arrest of macroscopic cracks etc.).

3 Numerical implementation

Several questions are to be discussed in connection to FEM implementation of the ITFC:

- *FE mesh.* Additional requirement to FE mesh to be used in simulation with the ITFC utilized as fracture criterion consists in limitation on the size of finite elements in a vicinity of points where rupture is possible. Obviously, size of an element in this region should not exceed d (see formula (2)). Otherwise it will not be possible to perform sufficiently precise spatial integration in fracture condition (1). Also, meshing the sample, one should keep in mind that material should be separated once fracture criterion is executed somewhere in the sample. This applies both to the choice of mesh in problems without adaptive meshing (mesh is not changing throughout the simulation) and the choice of adaptive mesh that can depend on current geometry of fracture zone and other factors.

- *Time step.* In order to have a possibility to perform sufficiently precise time integration in (1) one should require that the time integration step is small as comparing to incubation time τ of the material modeled.

- *Control of fracture criterion (1) execution.* Implementation of control of fracture condition execution does strongly depend on a problem to be modeled. In some problems (for example, in the majority of problems on propagation of a macroscopic crack in unbounded media)

fracture is possible only in a tip of an existing crack. In this case it is sufficient to keep track of execution condition (1) only in a single point (the tip of the crack). In other problems (for example, in the majority of problems on fracture of initially intact media) it is necessary to trace execution of (1) in rather extent zone or even in the whole modeled body. Under condition that the zone where implementation of (1) should be traced is defined and also that time step and mesh are correctly chosen, calculation of the left side in (1) does not make a big difficulty. In the examples presented later in this paper execution of (1) is controlled by an external program after every computational time step. However, with the lapse of time it is planned to create special elements for commercial FEM packages ([20], [21], etc.) with criterion (1) being explicitly embedded into their formulation. Creation of such elements will considerably simplify the problem and will give a possibility to completely automate numerical simulations of brittle fracture.

- *Spatial size of defect increment (2d problems).* Incubation time theory for brittle fracture [4], [19] is introducing linear size corresponding to an elementary cell of fracture on a chosen scale level. This size can also be interpreted as a typical size for the defect that one can call fracture on the chosen scale level. This size d depends on modeled material and the scale level and can be computed using (2). It makes sense to consider that once (1) is implemented in some point of the modeled body, fracture surface should be increased by the size of the elementary fracture cell d. In this connection having zones where fracture is possible meshed by elements sized d seems to be a reasonable choice.

- *Creation of a new surface.* In finite element formulation there exist several possibilities to create a new surface appearing as a result of material fracture. In the case of a crack extending along symmetry axis (in problems with symmetry) node release technique can be utilized (see, e.g., [12]). In problems without remeshing when fracture geometry is changed, node splitting technique or technique implying removal of restrictions on nodal dimensions of freedom (dof's) [14] can be used. In other situations one can use schemes assuming remeshing of the modeled body when fracture zone is changed (incremented). This approach is the most universal but at the same time the most difficult in implementation (apart from remeshing one should care about remapping of nodal values (displacements, velocities, accelerations) to new mesh). Remeshing and remapping also normally require substantial computational expense. The conclusion is that for every new problem technique to create a new surface should be specially chosen having in mind expense connected with model development and time needed for computations.

4 Examples

4.1 Dynamic crack propagation

To check the applicability of the criterion (1) to predict dynamic crack propagation, an attempt was made to simulate the classical fracture dynamics experiments reported by Ravi-Chandar and Knauss [11]. Detailed description of the model used in simulations and results of simulation of these experiments using FEM with the ITFC as a condition for crack extension can be found in [12]. Here some basic principles and main results are presented.

In these experiments [11] a rectangular sample with a cut simulating a crack is loaded by applying an intense load pulse to the crack faces. The sample behavior is described by equations of linear elasticity everywhere but the path of the crack, where fracture condition is given by (1). ANSYS [21] finite element package is used in order to solve linear elastic equations while implementation of (1) is controlled by an external program after each substep. The problem is symmetrical and the path of the crack is following the line of symmetry. This gives a possibility to model only half of the sample.

Nodes along the crack path are subjected to symmetrical boundary conditions up to the moment when the condition (1) is satisfied at a particular node (node movements in the vertical direction are restricted). At this moment the restriction on movement of the particular node is removed and a new surface is created. The technique used is similar to the node release technique.

The size of elements along the crack path was taken to be exactly d (see (2)). Small elements with sizes equal to d are placed adjacent to the crack path to provide the needed accuracy of computation. Distant elements are larger in order to minimize the computational time and expense.

Material parameters typical for Homalite-100, used in the experiments of Ravi-Chandar and Knauss, were used in the calculations. These parameters are presented in Table 1. The microstructural time of the fracture process, τ, for Homalite-100 was found by Petrov et al. [5] from analysis of experiments by Ravi-Chandar and Knauss [11]. The values of the critical stress intensity factor and the ultimate tensile stress gives a value for d. It appears to be 0.1 mm for Homalite-100 on a laboratory size scale.

Density, ρ, $\frac{kg}{m^3}$	1230
Young's modulus, E, MPa	3900
Poisson's ratio, ν,	0.35
Critical stress intensity factor, $K_{IC}, MPa\sqrt{m}$	0.48
Ultimate tensile stress, σ_c, MPa	48
Incubation time of fracture, $\tau, \mu s$	9

Table 2: Properties of Homalite-100 used in numerical simulations

Time profile of the load applied on the cut faces can be approximated by two consequently following trapezoids. Unfortunately in the paper by Ravi-Chandar and Knauss there was no information about amplitude of this load. Performing multiple ANSYS computations for different amplitudes it was found that amplitudes around 5 MPa result in crack extension histories very close to those observed by Ravi-Chandar and Knauss [11]. In figure 1 the computational result for $A = 5.1\ MPa$ is compared to the experiments reported by Ravi-Chandar and Knauss [11].

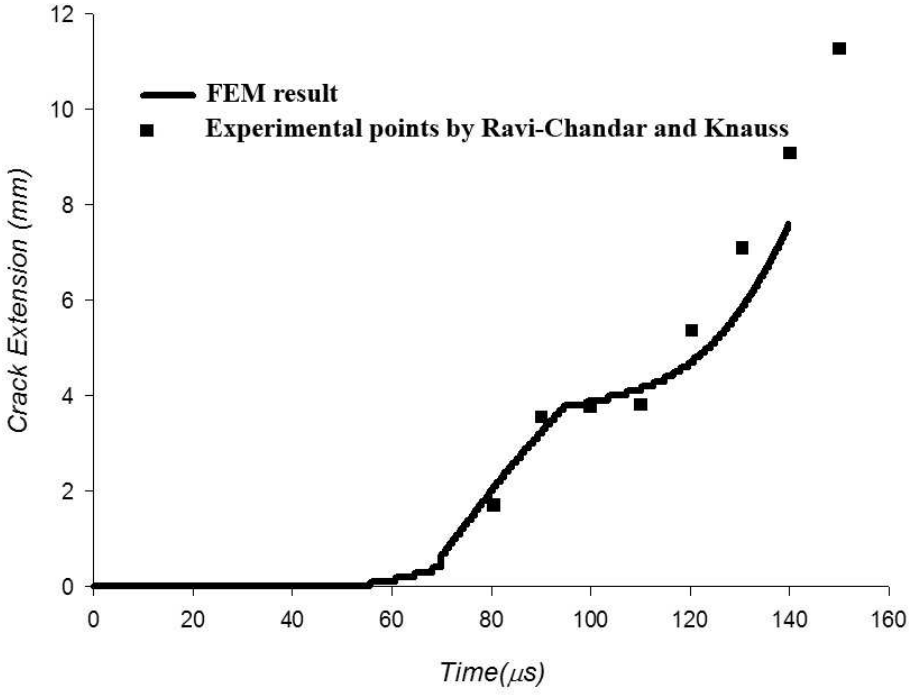


Figure 1: Crack extension history. Comparison of simulation results to experimental points received in [11]

It is demonstrated that utilizing the FE code solving the problem of linear elasticity joint with the ITFC (1) used to predict critical condition for crack extension it is possible to correctly predict evolution of dynamically loaded cracks. Apparently the ITFC with d chosen from the condition that (1) coincides with Griffith-Irwine fracture criterion in quasistatic conditions, can be utilized

in order to predict initiation, growth and arrest of dynamic cracks. This approach can be also used to predict growth of cracks with paths that are not known a priori (i.e. cracks that can change growth direction and branch). In this case one should check for (1) implementation on all the planes passing through the crack tip (all the possible orientations).

4.2 Impact crater formation (fracture of initially intact media)

In this section an attempt to incorporate incubation time approach into finite element (FE) code and to simulate conditions of satellite SMART1 lunar impact conducted by ESA year 2006 [22],[23] is presented. Aim of the simulation is to compare dimensions of crater created due to SMART1 contact to the moon surface to results received using FE method utilizing the ITFC as the critical rupture condition.

The traditional way to create new surface in FE formulation is associated with splitting of existing nodes. Using this approach is reasonable in most cases, though this normally requires remeshing and remapping, that are rather time consuming procedures. For the studied problem the situation is different. To guarantee correct integration in (1) one should use small (as comparing to τ) time steps. Thus the solution is resulting in long series of tiny substeps. Solution (convergence) on every substep is achieved comparably fast - FE solver is almost not iterating. It was found, that in this case it is more effective to use multiple nodes in the same location from the beginning, rather than split the node in question. Each element the full model is constructed of, is not sharing nodes with other elements.

2-D problem with rotational symmetry is solved. Quadratic 4-node elements are used. Dimensions of every element is exactly d times d (where d is given by (2)). Obviously, 4 nodes have the same location for inner points of a body and 2 nodes have the same location for the points belonging to the boundary. These nodes originally have their DOF's coupled. This results in exactly the same FE solution before the fracture condition is implemented in a respective point as if elements had shared nodes. When the fracture condition is fulfilled, restriction on nodes DOF's is removed – a new surface is created. This is done automatically by FE code after every substep.

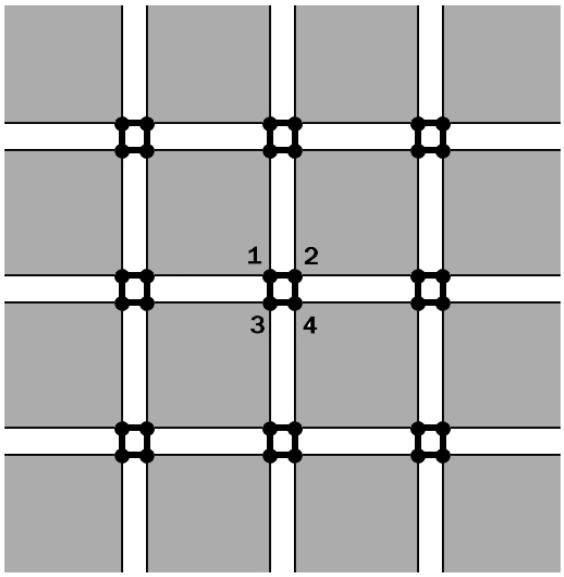


Figure 2: Model consisting of elements without shared nodes

Figure 2 gives a schematic representation of internal points of a body. Originally all 4 nodes sharing the same location have all of their DOF's coupled. Condition (1) for this point can be written:

$$\frac{1}{\tau}\int_{t-\tau}^{t}\sigma_{ii}(t')dt' \geq \sigma_c, \tag{4}$$

where i assumes values 1 and 2. Repeating indices do not dictate summation in this case. Spatial integration is removed, because the stress in the respective direction calculated by FE program is already a mean value over size d (since d is the element size being used). If (4) is fulfilled for σ_{11} and σ_{22} then displacements of nodes 1,2,3 and 4 on figure 2 get uncoupled. If (4) is fulfilled for σ_{11}, two new couple sets consisting of nodes 1, 2 and 3,4 are created. If (4) is fulfilled for σ_{22}, new couple sets are created for nodes 1, 3 and 2,4. For later times condition (4) in applicable direction is traced for newly created couple sets separately. Contact between separated fragments is not modeled.

The problem is solved for half-space. Half-space representing the moon had following material properties: σ_c=10.5MPa, $K_{IC} = 2.94MPa\sqrt{m}, \tau = 80\mu s, E = 60GPa, \rho = 2850kg/m^3, \nu = 0.25$ typical for earth basalt. This results in $d = 5cm$. Half-space is impacted by a cylinder with diameter of 1 meter and height of 1 meter. Density for the cylinder is chosen so that its mass is the same as the one of SMART1 satellite. We suppose material of cylinder is linear elastic and has no possibility to fracture. Elastic properties are: $E = 200GPa, \nu = 0.32$, typical for steel. SMART1 satellite had a form close to cubic with side of 1meter and had a mass of $366kg$. SMART1 impacted the moon surface at a speed of approximately $2000m/s$. In FE formulation the cylinder was given an initial speed of $2000m/s$ prior its contact to the half-space boundary. Size of the sample, representing the half-space is chosen from the condition that the waves reflected from the sample boundaries are not returning to the region where the crater is formed in the process of the simulation. The total of 17328 nodes and 17252 elements were used in FE model. Time step was chosen to be equal to time needed for the fastest wave to pass the distance equal to d.

ANSYS finite element package (ANSYS User's Guide [21]) was used to solve the stated problem. Control of the fracture condition (4) fulfillment in all of the sample points and new surface creation when rupture criterion is implemented was carried out by a separate ANSYS ADPL subroutine.

In figure 3 locations of nodes where the fracture occurred are marked. This gives a possibility to assess dimensions of crater that is formed after the SMART1 impact. Damaged zone is found to be about 10 meters in diameter and about 3 meters deep. Zone where the material is fully fragmented (crater formed) can be assessed having 7-10 meters in diameter and 3 meters deep. This result is coinciding with ESA estimations of dimensions of crater formed due to SMART1 impact [22],[23].

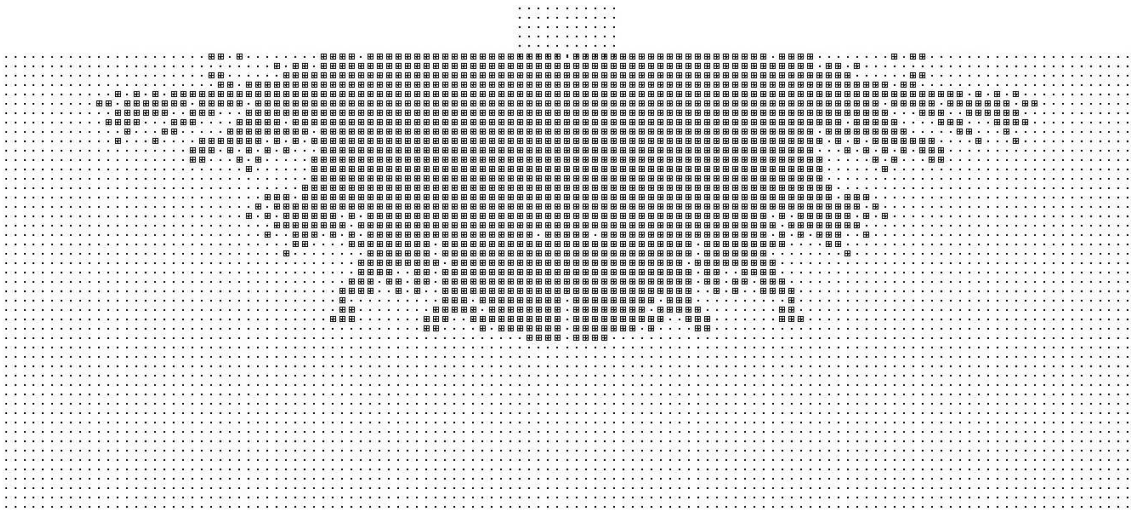


Figure 3: Locations of ruptured nodes

4.3 Spall fracture in plates

Utilizing method used while modeling SMART1 lunar impact it is possible to perform simulations in rather extent class of problems including brittle fracture of different materials. In this example spall fracture in a circular plate was studied. One of the plate's surfaces is loaded by dynamic

pressure pulse having rectangular time-shape. Duration of the load is supposed to be small as comparing to the time needed for the fastest wave to travel the distance equal to the plate's thickness. Compressive stresses are changing their sign being reflected from the free surface of the plate and tension stresses are appearing at some distance from the free surface of the plate (for loads with rectangular time-shape this distance is equal to half-distance the longitudinal wave can travel within load duration). For pressure pulses with sufficient amplitude fracture takes place as a result of emerging tensile stresses. This scheme is typical for many, if not the majority of dynamic fracture experiments. In figure 4 results of one of the experiments modeled are presented graphically.

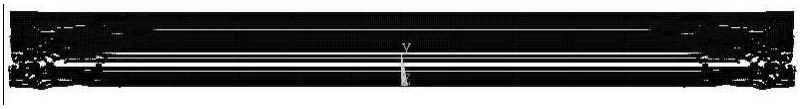


Figure 4a: Plate with spall fracture

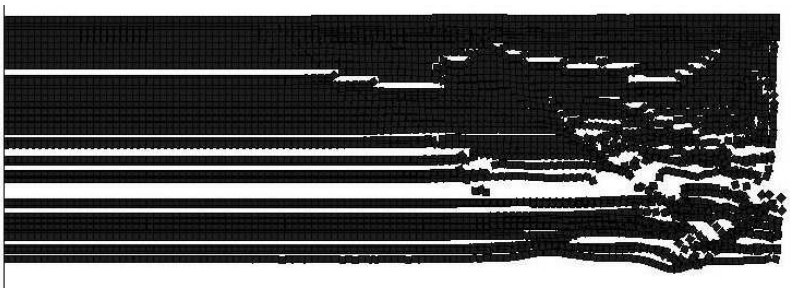


Figure 4b: Plate with spall fracture (magnification)

4.4 Growth of crack in gas pipeline

In the last of the presented examples the developed approach is applied to simulate growth of a dynamic crack in a gas pipeline. Finite element model giving a possibility to predict fracture of gas pipeline subjected to quasistatic and dynamic loads is developed. It is assumed that the crack can grow along the line parallel to the pipe axis. Computations were performed for $\frac{1}{4}$ of the presented model (symmetry across planes ZX and XY is used).

Simulation is performed for pipeline with length of 18 m. Pipeline diameter is 1.22 m. 36600 nodes and 17940 elements are used in the FE model. Pipeline is loaded by internal pressure close to operational pressures in gas pipelines. Drop of pressure in the pipeline as a result of crack extension was modeled as movement of two wavefronts: the front of the front wave of pressure drop (velocity of this front is equal to velocity of the acoustic wave in gas – about 400 m/s for natural gas) and the back front of pressure drop travelling at a lower speed. After passage of the back front the pressure inside the pipeline is equal to the external atmospheric pressure. Between the two fronts pressure is supposed to be linearly dependent on coordinate.

The pipeline was quasistatically loaded by internal pressure. Fracture was initiated by a small defect (crack) that was artificially introduced. This is imitating appearance of a crack in a pipeline (for example, fatigue crack). When the defect is introduced it starts to grow if the internal pressure is big enough to advance defect of the introduced size. In figure 5 view of the pipeline is presented for different times. It was found that in the modeled situation the speed of the crack is close to the speed of the acoustic wave in gas that determines the speed of the front of the pressure drop. This leads to a conclusion about instability of crack propagation regimes in the modeled situation – a small change in properties of the pipeline material can result in qualitative change it crack propagation regime: should the speed of the crack be higher than the speed of acoustic signal in gas, the crack will never arrest.

Received instability of crack propagation regimes is in a good coincidence with experiments on dynamic cracking in gas pipelines. In these experiments a section of gas pipe was loaded by internal pressure close to operational pressure inside the gas pipeline. A furrow was made in the part of



Figure 5: Pipeline with a macroscopic crack

the pipe parallel to its central axis. The furrow was filled with an explosive substance. When the explosive is blasted the crack starts to propagate from the furrow. Pipelines made of several different pipe steels were tested. It was found that length of the resulting crack does strongly depend on material of the pipeline and the length of the resulting crack does vary significantly (from 3 to 300 meters) though all steels had similar properties.

5 Conclusions

It was demonstrated that the area where the incubation time criterion for brittle fracture can be successfully used in order to simulate fracture is rather extent. An overwhelming majority of practical problems in dynamic fracture cannot be solved analytically and require numerical methods to be used in order to receive the solution. In this connection the incubation time approach had

significant advantages – it is applicable to predict both in static and dynamic fracture. Thus, there is no necessity in having different fracture criteria for different load rates. It was demonstrated that the ITFC embedded into finite element code is giving a possibility to predict initiation, development and arrest of dynamic fracture.

All this gives a reason to recommend the ITFC to be included into commercial and research FE codes as standard fracture criterion to be utilized while modeling structures that can undergo loads of the dynamic range.

Acknowledgements

The research and publication preparation was financially supported by research grant MK-1610.2009.1 (President of the Russian Federation council), state contracts 02.740.11.0619 and 02.740.11.5171, RFBR research grants 10-01-00810-a, 08-01-00646-a, and academic programs of the Russian Academy of Sciences.

References

[1] Freund, L.B., 1990. Dynamic fracture mechanics, Cambridge University Press, Cambridge.

[2] Petrov, Y.V., Morozov, N.F., 1994. On the modeling of fracture of brittle solids. J. Appl. Mech. 61,710–712.

[3] Morozov, N., Petrov, Y., 2000. Dynamics of fracture, Springer-Verlag, Berlin.

[4] Petrov, Y.V., 1991. On 'Quantum' Nature of Dynamic Fracture of Brittle Solids. Dokl. Akad. Nauk USSR 321,66–68.

[5] Petrov, Y.V., Morozov, N.F., Smirnov, V.I., 2003. Structural micromechanics approach in dynamics of fracture. Fatig. Fract. Eng. Mater. Struct. 26,363–372.

[6] Bratov, V., 2004. Energy behavior in dynamic fracture of materials. Dissertation, St.-Petersburg State University

[7] Neuber, H., 1937. Kerbspannunglehre: Grundlagen fur Genaue Spannungsrechnung, Springer-Verlag, Berlin.

[8] Novozhilov, V.V., 1969. About the necessary and sufficient brittle strength criterion. Prikl. Mat. Mekh. 33(2),212-222.

[9] Kornev, V.M., Kurguzov, V.D., 2004. Interrelation between toughness and both strength and structural parameters of material. Int. J. Frac. 128,195–203.

[10] Petrov, Y.V., Sitnikova, E.V., 2007. Dynamic Cracking Resistance of Structural Materials Predicted from Impact Fracture of an Aircraft Alloy. Tech. Phys. 49(1),57-60.

[11] Ravi-Chandar, K., Knauss, W.G., 1984. An experimental investigation into dynamic fracture: I. Crack initiation and arrest. Int. J. Fract. 25,247–262.

[12] Bratov, V., Petrov, Y., 2007. Application of incubation time approach to simulate dynamic crack propagation. Int. J. Fract. 146,53-60.

[13] Bratov, V., Petrov, Y., 2007. Optimizing energy input for fracture by analysis of the energy required to initiate dynamic mode I crack growth. Int. J. Solid. Struct. 44,2371–2380.

[14] Bratov, V.A., Morozov, N.F., Petrov, Y.V., 2008. Simulation of SMART1 Satellite Impacting the Moon Surface. Dokl. Phys. 419(1),54-58.

[15] Freund, L.B., 1972. Crack propagation in an elastic solid subjected to general loading. I: Constant rate of extension. J. Mech. Phys. Solid. 20,129–140.

[16] Freund, L.B., 1972. Crack propagation in an elastic solid subjected to general loading. II: Nonuniform rate of extension. J. Mech. Phys. Solid. 20,141–152.

[17] Freund, L.B., 1972. Energy flux into the tip of an extending crack in an elastic solid. J. Elast. 2,341–349.

[18] Kashtanov, A., Petrov, Y. , 2004. Fractal models in fracture mechanics. Int. J. Fract. 128,271-276.

[19] Bratov, V., Morozov, N., Petrov, Y., 2009. Dynamic Fracture of Continuum. St.-Petersburg University press, St.-Petersburg

[20] ABAQUS, 2002. ABAQUS/Standard User's Manual, HKS Inc., USA.

[21] ANSYS, 2006. User's Guide, Release 11.0. ANSYS Inc., Pennsylvania, USA.

[22] ESA, 2006. Impact landing ends SMART-1 mission to the Moon. Available online. `http://www.esa.int/esaCP/SEM7A76LARE_index_0.html` Accessed 10 Feb 2010.

[23] ESA, 2006. Intense final hours for SMART-1, Available online. `http://www.esa.int/esaCP/SEMV386LARE_index_0.html` Accessed 10 Feb 2010.

Vladimir Bratov, IPME RAS, Bolshoy pr. V.O., 61, 199178, St.-Petersburg, Russia

Dynamics of a ferrofluid layer with a stable rupture of the surface

C. A. Bushueva K. G. Kostarev
Christina.Bushueva@icmm.ru

Abstract

The paper deals with the results of experimental studies made to examine the behavior of a thin horizontal layer of a ferrofluid, lying on a liquid substrate and subjected to the action of differently oriented magnetic fields. The use of the magnetic field applied parallel to the layer surface caused redistribution of the ferrofluid along the field direction. This led to a displacement of the rupture with respect to the cuvette center which was accompanied by the change of its shape of a circle to that of an ellipse. With a further increase in the field intensity the rupture rapidly approached the cuvette wall and took the form of a trapezoid provided that the initial diameter of the rupture was larger than the cuvette radius. In the opposite case, with increase of the field intensity the rupture took the form of a "drop" and then closed.

The non-uniform magnetic field perpendicular to the layer surface could have a twofold effect: it could deform the stable rupture by increasing its diameter or provoke rupture formation in the case of layer integrity. In this situation, application of the magnetic field caused first a redistribution of the ferrofluid in the upper layer. Then, as the field intensity increased to the critical value, the layer deformation spread deep into the layer until it reached the surface of the liquid substrate. At this point there occurred a threshold rupture of the layer in the form of a circle, the diameter of which is determined by the initial layer thickness, the ferrofluid density and the difference in the surface tension of the fluids. It should be noted that application of the uniform magnetic field directed perpendicular to the continuous layer surface leads to a transformation of the layer into an ordered system of drops, which then changes into a system of cones submersed into the fluid of the substrate. During our investigation we determined the dependence of different characteristics of ruptures and drops on the field intensity and the value of ferrofluid magnetization.

1 Introduction

We investigate the behavior of a two-layer liquid system with a stable rupture of the upper layer caused by the action of ponderomotive forces. Such a system has only recently been explored [1]. A distinguishing feature of the system is that the layer rupture exists in the absence of any external force and has the shape of a circle, inside which the fluid of the lower layer comes into contact with gas. Due to the absence of contact with solid surfaces the rupture is highly sensitive to the external effects and therefore can deform and move even under the action of arbitrarily small forces. Thus, in the case when the upper layer is formed by a ferrofluid, the application of the external magnetic fields to the system can cause a displacement of the rupture and a change in its shape. In this case the degree of changes is proportional to the field intensity.

In the experiment a layer of the ferrofluid was applied on a substrate made of perfluorooctane H_8F_{18}, which had higher density and smaller surface tension compared to the basic fluid [2]. The fluid system was placed in a cuvette in the form of Petri dish. The initial thickness of the ferrofluid layer was defined as $h = m/(\rho_2 S)$, where m is the fluid mass, $S = D_1^2/4$ is the area of the initial (continuous) layer, which is taken to be flat, D_1 is the inner diameter of the cuvette. During experiments the estimated thickness of the ferrofluid layer was varied from 1 mm to 3.5 mm. The thickness of the liquid substrate was varied, accordingly, from 10 to 20 mm. During tests, to initiate rupture of the layer of ferrofluid its free surface was subject for a short-time to an air jet of small diameter.

The preliminary experiments revealed the dependence of the diameter of rupture on the thickness of the breaking layer and the dependence of their critical values on the cuvette size in the absence of the magnetic field. Thus, the diameter of the forming rupture monotonically decreased with the growth of the layer thickness until the rupture closed in a threshold manner at the maximal layer thickness $h = h_{max}$ (and at corresponding minimal diameter $d = d_{min}$. Fig. 1 shows the dependence of h_{max} (curves *2* and *3* in Fig. 1*a*) and d_{min} (curves *2* and *3* in Fig. 1*b*) on cuvette diameters.

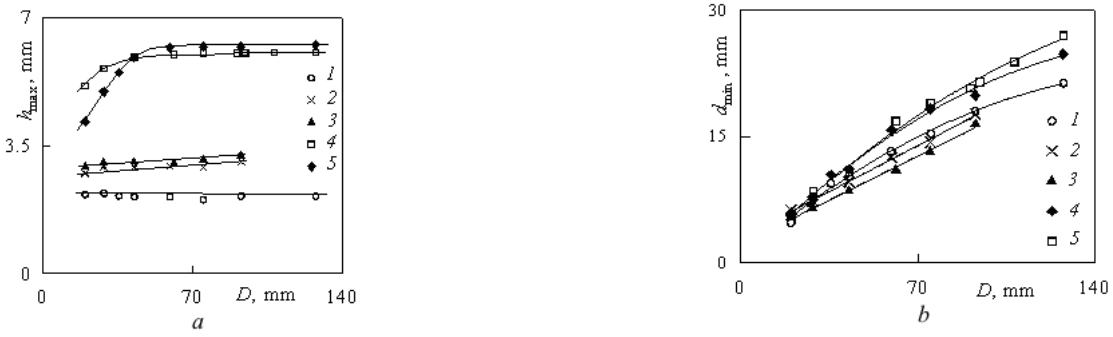


Figure 1: Maximal layer thickness (a) and minimal diameter of the layer rupture (b) versus cuvette diameter for kerosene (*1*), ferrofluids No 2 and No 1 (*2* and *3*), water on the C_8F_{18} substrate (*4*), and water on the CCl_4 substrate (*5*)

For comparison we present similar dependencies for kerosene - the base of the ferrofluid - and water including the case of using carbon tetrachloride as a substrate [12]. The physicochemical properties of the fluids are given in Table 1.

Fluid	Density, g/cm^3	Surface tension, dyne/cm
kerosene	0.82	26
ferrofluid No1	1.37	28.0
ferrofluid No2	1.37	25.8
water	1.00	71.2
C_8F_{18}	1.76	15.8
CCl_4	1.59	26.8 [11]

From a comparison of curves it follows that h_{max} is defined mainly by the surface tension difference and density of the upper fluid, and d_{min} - by the magnitude of the contact angle, which is formed by the meniscus of the fluid of the upper layer and the sidewall of the cuvette. In particular, the maximal thickness h_{max} of the stable rupture can be defined to the first approximation by

$$h_{max} = 2 * \sqrt{\frac{2(\sigma_2 - \sigma_1)}{\rho_2 g}} \tag{1}$$

2 Stable rupture behavior under the action of the homogeneous magnetic field applied parallel to the surface of the ferrofluid layer

In this experiment the cuvette was placed on a horizontal platform located inside the Helmholtz rings along their axis of symmetry. Then the two-layer liquid system contained in the cuvette was deformed to initiate rupture of the upper layer. The applied magnetic field caused a redistribution of the ferrofluid along the field direction and, consequently, a displacement of the rupture relative to the cuvette center which occurred simultaneously with a change of the rupture shape from a

regular circle (Fig. 2*a*) to that of an ellipse (Fig. 2*b*). In turn, with an increase of the field intensity the ellipsoidal rupture took the form of a drop (Fig. 3*c*) or a trapezoid (Fig. 3*f*) while being pressed against the wall (the trapezoidal ruptures occurred only if the initial rupture diameter was larger than the cuvette radius).

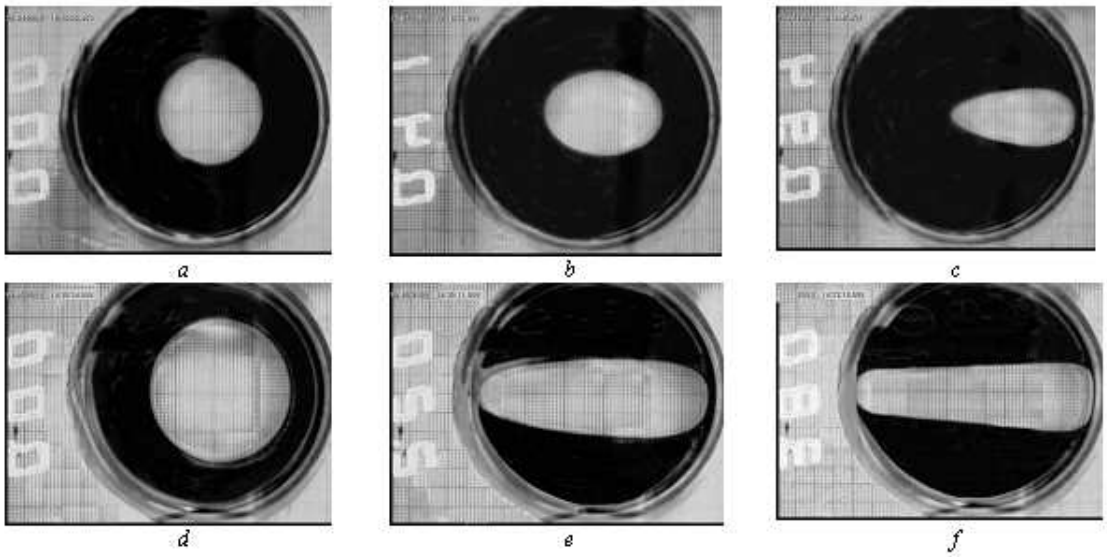


Figure 2: Variation of the rupture configuration in the longitudinal magnetic field. Field intensity H, kA/m: 0 (*a*); 0.9 (*b*); 2.0 (*c*); 0 (*d*); 5.0 (*e*); 8.0 (*f*). Cuvette diameter $D_1 = 59.4$ mm

Fig. 3 shows the variation of the large and small axes of the rupture with the field intensity. The vertical lines A and B mark the boundaries of the regions where the circle is changed, respectively, into an ellipse and a drop/trapezoid. The character of the rupture distortion strongly depends on the value of the initial rupture diameter compared to the cuvette radius.

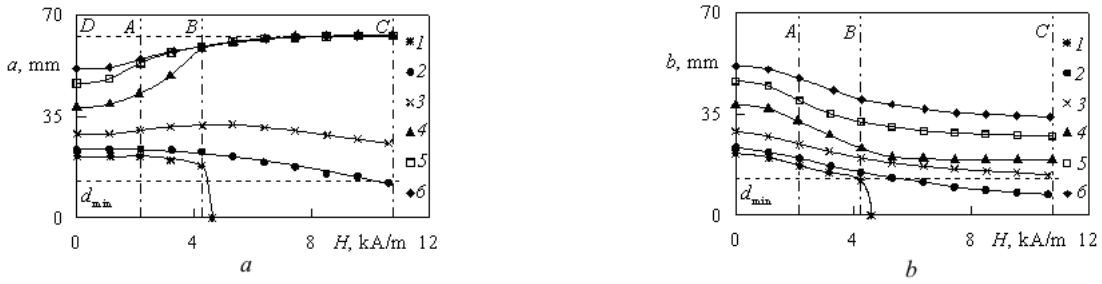


Figure 3: The lengths a and b of the large and small axes of the ferrofluid layer rupture versus magnetic field intensity. The initial diameter of the layer rupture d, mm: 21.2 (*1*); 23.3 (*2*); 28.8 (*3*); 38.0 (*4*); 46.3 (*5*); 51.3 (*6*). Cuvette diameter $D_1 = 59.4$ mm

If the diameter of the rupture is smaller than the cuvette radius, an increase in the field intensity eventually promotes its closure (Fig. 3*a*, curves *1-3*). Note that by this time the transverse dimension of the rupture is essentially smaller than the minimal diameter of the stable rupture in the absence of the field (Fig. 3*b*, curves *1-2*). If the initial diameter of the stable rupture is comparable with the cuvette radius or larger the deformation behavior changes markedly. Although the transverse dimension of the rupture monotonically decreases with the growth of the magnetic field, its longitudinal dimension extends rapidly as far as the cuvette walls displacing the near-wall meniscus (Fig. 3*a*, curves *4-6*). In the stress intensity range used in our experiments such ruptures remained unclosed.

Fig. 4 shows the dependence of the rupture area s ($s = d^2/4$), normalized to the area of the cuvette bottom, on the layer thickness under the action of the magnetic field. It is readily seen that in the absence of the field (Fig. 4, curve *1*) the dependence $s/S = f(h)$ is linear over the whole interval of h, at which the layer rupture exists, except for the region in the vicinity of h_{max}. Note however, that at a fixed value of the layer thickness the relative area of the rupture in the ferrofluid decreases monotonically with the growth of the magnetic field intensity (Fig. 5).

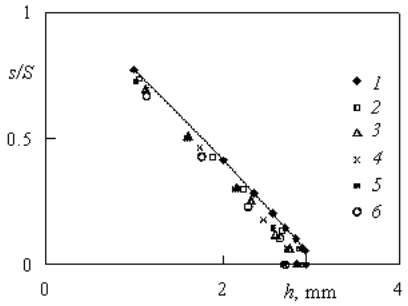


Figure 4: Relative area of the rupture versus thickness of the layer of ferrofluid No 2 for cuvette with $D_1 = 59.4$ mm. The intensity of the magnetic field H, kA/m: 0 (*1*); 3.2 (*2*); 5.3 (*3*); 6.4 (*4*); 8.5 (*5*); 10.6 (*6*)

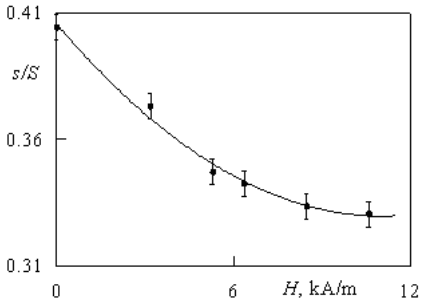


Figure 5: Relative area of the rupture versus magnetic field intensity at the layer thickness $h = 2$ mm for the cuvette with $D_1 = 59.4$ mm)

The use of ferrofluids having different values of magnetic susceptibility (Fig. 6) revealed an essential dependence of the rupture deformation on the value of the ferrofluid magnetization. Fig. 7 illustrates the variation in the area of the ferrofluid rupture under the action of the magnetic field at different initial values of the layer thickness. It is seen that with increasing magnetization of the ferrofluid the response of the layer rupture to the action of the magnetic field increases. Thus, the ruptures of the ferrofluid No 1 having a higher value of magnetization than that of the ferrofluid No 2, deform more severely and close at much lower values of the magnetic field intensity, all other factors being equal.

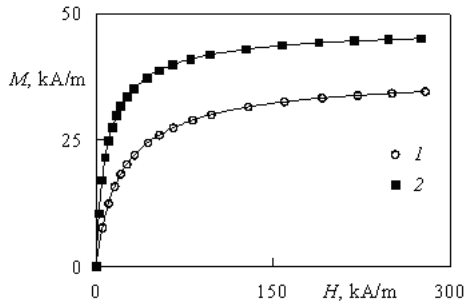


Figure 6: Magnetization curves for ferrofluids No 2 (*1*) and No 1 (*2*)

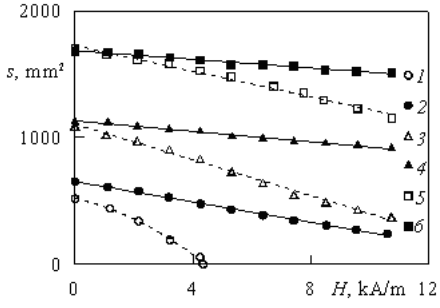


Figure 7: Layer rupture area versus magnetic field intensity. $D_1 = 59.4$ mm. The initial layer thickness h, mm: 1.41 (*1*), 1.93 (*3*), 2.42 (*5*) (ferrofluid No 2); 1.07 (*2*), 1.89 (*4*), 2.31 (*6*) (ferrofluid No 1)

3 The evolution of strong deformation of a ferrofluid layer under the action of nonhomogeneous magnetic field applied normal to the surface

The subsequent experiments showed, that the magnetic field had a twofold effect: it could close a stable rupture of the ferrofluid layer and could generate a rupture by deforming the integrity of

the layer. To demonstrate this effect we placed the cuvette inside the horizontally located coil. The height of the coil was 8 mm and the inner diameter coincided with the external diameter of the cuvette ($D_2 = 99$ mm). Then we generated in the cuvette a two-layer system.

The application of the magnetic field normal to the layer surface caused a redistribution of the ferrofluid along the cuvette radius. Since the upper and lower boundaries of the layer were free it could readily deform. In such a case, its thickness decreased near the center of the cuvette and increased at the walls. When the magnetic field intensity reached a critical value the layer deformation approached the surface of the substrate. This led to a layer rupture, which had the form of a regular circle. An increase in the field intensity led to a growth of the rupture diameter whereas a decrease in the field intensity - to a closure of the rupture. However, it was found that the rupture did not disappear even after the removal of the magnetic field, provided that the initial thickness of the ferrofluid layer was equal or less than h_{max}.

The measurements indicated that the value of the critical field intensity determined in the cuvette at the axis of symmetry (on the level of the layer) was linear dependent on the initial thickness of the ferrofluid layer h (Fig. 8).

When the field intensity is below the critical value the field plays the role of the additional factor, supporting the main mechanism of rupture creation (mechanical deformation of layer by an air jet). In Fig. 9, curve *1* describes the dependence of the stable rupture diameter on the thickness of the ferrofluid layer in the absence of the magnetic field, and curve *2* describes the analogous dependence in the case of the fixed field intensity. Moreover, the magnetic field plays the role of an additional force, which prevents a closure of the layer rupture (curves *1* and *2* can also be obtained by way of introducing an additional amount of a ferrofluid into the layer which has been already ruptured).

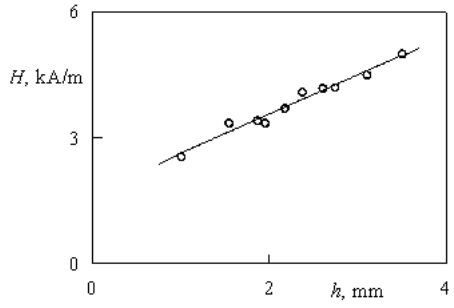


Figure 8: Critical intensity of the magnetic field versus initial thickness of the ferrofluid layer during rupture for cuvette with $D_1 = 59.4$ mm

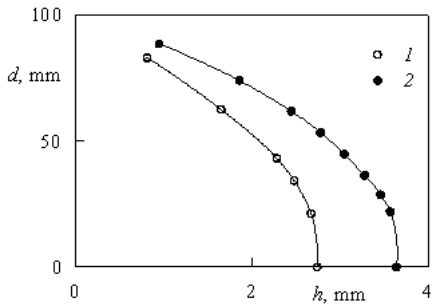


Figure 9: Rupture diameter versus initial thickness of the ferrofluid layer in the cuvette of diameter $D_1 = 59.4$ mm subjected to the magnetic field of different intensity $H = 0$ kA/m (*1*); $H = 1.5$ kA/m (*2*)

4 The formation of ordered system of drops in a continuous ferrofluid layer under the action of uniform magnetic field

The use of the uniform magnetic field directed perpendicular to the layer surface leads to instability of the ferrofluid layer and its transformation into different spatially ordered systems. As it is seen in Fig. 10, in the case of a solid layer the application of the vertical magnetic field leads to appearance of the relief in the form of hexagonal cells, which, as soon as the magnetic field reaches the critical intensity, form separate drops (Fig. 10, *a* - *c*). A further increase of the field intensity transforms the drops into the cones submersed into the fluid of the substrate. The wave number of the arising drop system decreases monotonically with the growth of the initial layer thickness.

Application of the magnetic field to the layer with already existing stable rupture also leads to the formation of periodic structures. However, in this case the evolution of the layer deformation depends on the dimensions of the rupture. For ruptures with the initial diameter approaching d_{min}, a transition to the drop structures begins with the formation of a "star" (Fig. 10, *d* - *f*). On

the other hand, after application of the field the ruptures with dimensions as large as half of the cuvette diameter first grow in size displacing the ferrofluid in the zone of the near-wall meniscus. A further increase of the field intensity leads to meniscus instability, which manifests itself as the appearance of "a sprout" growing toward the cuvette center. After a while, the sprout is detached from the meniscus and turns into a horseshoe structure, which is then decomposed into separate drops (Fig. 10, g - i).

Note, that along with the initial size of the rupture the value of ferrofluid magnetization is also of considerable significance for evolution of the layer deformation. Thus, the formation of drop structures in a ferrofluid with lower magnetic susceptibility is observed at much higher values of the field intensity (Fig. 10f and Fig. 10i).

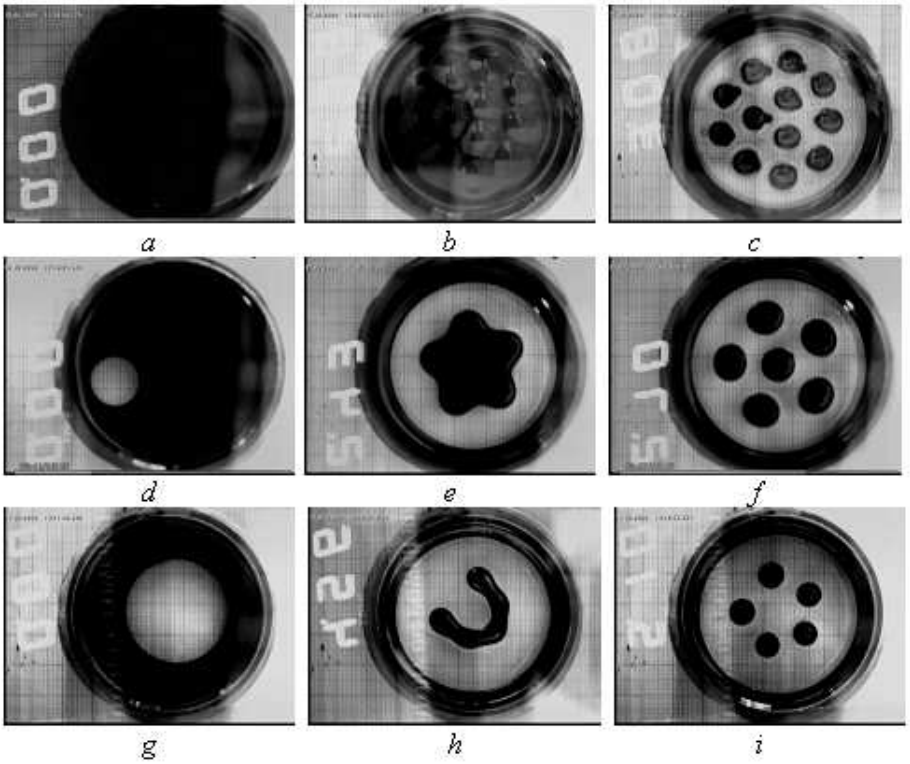


Figure 10: Formation of spatially ordered structures in a ferrofluid layer in uniform magnetic field. Ferrofluid No 1, initial thickness of layer $h = 2.8$ mm; Field intensity H, kA/m: 0 (a); 6.4 (b); 6.5 (c); Ferrofluid No 1, $h = 2.7$ mm; H, kA/m: 0 (d); 5.2 (e); 5.7 (f); Ferrofluid No 2, $h = 2.2$ mm; H, kA/m: 0 (g); 9.7 (h); 10.8 (i)

5 Conclusion

The results of our studies support the view that the examined two-layers system opens a new chapter in studying the problems on statics and dynamics of fluids and can have considerable promise for technological applications. The existence of a stable rupture drastically increases the susceptibility of the system to the action of the external forces including that of the magnetic field. The magnetic field depending on its orientation with respect to the surface of the ferrofluid layer can cause both a layer rupture and its closure.

Acknowledgements

The work was supported by the grants of the research program of the RAS No 09-T-1-1005, grant of UB RAS for young researchers, the RFBR projects No 10-01-00337 and 10-02-96022.

References

[1] Stoylov Yu.YU. Oscillation of evaporating liquids and ispalator paradoxes // Phys.-Usp. 2000. V. 170, No 1. P. 41-56.

[2] Rosensweig, R.E.: Ferrohydrodynamics. Cambridge University Press, Cambridge (1985).

[3] Shmyrov A.V., Kostarev K.G. Stable ruptures in two-layer fluid systems: an influence of edge effects // Hydrodynamics. 2007. V. 16. Pp.142-148. (In Russian)

[4] Bratukhin Yu.K., Zuev A.L., Kostarev K.G., Shmyrov A.V. Stability of stationary rupture of the liquid layer on an immiscible fluid surface // Fluid Dynamics. 2009. V.41, No 3. P. 514-520

[5] Richter, R., Lange, A.: Surface Instabilities of Ferrofluids. Lect. Notes Phys. 763, 157-247 (2009) DOI 10.1007/978-3-540-85387-9 3

[6] Lebedev A.V., Engel A., Morozov K.I., Bauke H. Ferrofluid drops in rotating magnetic fields // New Journal of Physics. 2003. V. 5. Pp. 57.1-57.20.

[7] M.Sh. Shliomis. Magnetic fluids // Physics-Uspekhi, 1974, V. 112, No 3. P 3.

[8] Ching-Yao Chena, C.-S. Li. Ordered microdroplet formations of thin ferrofluid layer breakups. PHYSICS OF FLUIDS 22, 014105 (2010).

Institute of Continuous Media Mechanics, UB Russian Academy of Sciences Acad. Korolev Str. 1, 614061 Perm, Russia.

Terrestrial modeling of surfactant diffusion through the drop-surrounding fluid interface

C. A. Bushueva M. O. Denisova K. G. Kostarev A. V. Shmyrov
kostarev@icmm.ru

Abstract

Considerable progress in the development of the space materials science is impossible without understanding the specific behavior of many of the known physical-chemical mechanisms in microgravity conditions. However the possibilities of conducting purely scientific experiments on board the space vehicle are strongly restricted due to high cost of delivery of the goods to the space station, low power of the solar batteries, etc. This problem can be partially solved by attempting a terrestrial modeling of the examined processes under conditions of maximum suppression of the effects caused by the gravitational force. Regarding hydrodynamics and heat/mass transfer phenomenon one can refer to such effects the gravitational convection, the intensity of which is determined by the characteristic vertical dimension of the cavity.

In this paper we discuss the results of terrestrial modeling of mass transfer caused by diffusion of a surfactant through the fluid-fluid interface. Visualization of the concentration fields showed that surfactant diffusion is accompanied by further development of both the capillary effects and the gravitational convection. The main reason for the onset of the gravitational convection is large characteristic times of surfactant diffusion, which are responsible for generation of density gradients at both sides of the interface.

Nevertheless, the comparison of results obtained in terrestrial and space conditions permits to conclude that the laboratory study of surfactant transfer, despite the existence of the gravitational flow, can give proper estimations of the characteristic times of capillary motion and predict the structure of concentration fields. We also give interpretation of some other results of comparison and discuss the results of terrestrial modeling of surfactant diffusion.

1 Introduction

Interest in the behavior of three-component liquid systems with an interface is related to their wide application in technological processes. The simplest example is the system composed of two immiscible fluids containing a solution of the third non-uniformly distributed fluid. Even in such an ordinary system the existence of the interface and the difference in the values of density, viscosity and diffusion coefficients of the constitutive fluids turns the mass transfer study into a time-consuming multi-parametric problem, the solution of which presents considerable difficulties from the theoretical and experimental viewpoint. The problem becomes more intricate when a diffusing fluid is surface-active with respect to other fluids of the system.

In this case any local change in the mixture concentration at the interface leads to a change of the surface tension which causes an intensive motion of the interface and adjacent fluid layers in the direction of its increase. Since formation of the surface tension inhomogeneities is not related to the level of gravitation, this process can pretend to the role of the main mechanism responsible for the development of the fluid flow in microgravity conditions.

Indeed, numerous space experiments provide enough evidence in support of the leading role of the capillary convection in the non-isothermal liquid systems [1]. However, the analogy between the thermal and solutocapillary convection mechanisms of the fluid motion should be used with great caution because of considerable difference between the characteristic times of thermal and impurity diffusion. In the thermal case, the times of thermal diffusion and viscous dissipation of impulse are comparable which provides conditions for sustaining a constant capillary motion (the

heat transported by the capillary motion together with the entrapped fluid volume has enough time to diffuse into the environment before the motion ceases). By contrast, in the solutal case due to the large diffusion times the content of the surfactant in the volume of the fluid carried out by the flow is still high at the moment of flow cessation, which explains the appearance of high surfactant concentration zone near the interface.

Under normal gravity the free convection motion provides further motion of this zone creating thereby the favorable conditions for recovering the percentage composition of the liquid mixtures near the interface. With reduction in the gravity level the outflow of both the diffusing component and depleted mixture decreases. Lowering of the concentration difference normal to the interface reduces the probability of formation of the concentration inhomogeneities along this boundary. Therefore the possibility for the occurrence of solutocapillary motion during mass transfer processes under microgravity conditions is still an open question.

In the framework of terrestrial modeling of a space experiment aimed at studying the evolution of the capillary convection during surfactant diffusion we carried out laboratory experiments to provide insight into the nature of surfactant transfer between the drop and the surrounding liquid in a horizontal layer.

2 Mass transfer between a drop and initially homogeneous surfactant solution

The use of the layer of small thickness gave us twofold benefits. First, it allowed a maximum reduction of intensity of the gravitational flow and second it allowed us to use a particular experimental technique - generation of a drop in the form of a short and wide vertical cylinder. The drop is bounded at the top and the bottom by solid surfaces and has a free lateral surface which offers new possibilities for visualization of the surfactant distribution inside and outside the drop by means of optical methods. During this experiment we investigated diffusion of isopropyl alcohol (used as a surfactant) from its aqueous solution to the drop of chlorobenzene. The initial mass concentration C_0 of the alcohol in the solution ranged from 1% to 50%. All fluids and their solutions used in tests were transparent. Visualization of the surfactant distribution was made with the help of the Fiseau interferometer [2]. Its working cell 1.2 mm thick was used to create a thin fluid layer. The surfactant distribution in fluid layer inside the cell was visualized on its wide side.

In the isothermal case, the results of visualization of the concentration inhomogeneities in the fluid solutions were obtained as a system of interference bands representing isolines of equal optical path length. Reasoning from the fact that the mixture composition varies only across the transmitted light beam we could identify the interference bands with certain values of the surfactant concentration. Thus, for the layer 1.2 mm thick a transition from one band to another corresponded to a variation in the alcohol content in water from 0.27% at $C_0 = 5\%$ to 0.81% at $C_0 = 45\%$. In the case of chlorobenzene, a similar transition in the drop occurred due to a change in the alcohol concentration by 0.10%. The initial diameter D_0 of the cylindrical drops injected into the layer of aqueous solution with a medical syringe varied from 3.5 to 9.5 mm. The ambient temperature of experiments was $(23 \pm 1)^0 C$.

The diffusion of surfactant in the system of two fluids leads to generation of the solutal Marangoni convection at their interface even though the fluids are initially homogeneous. The reason for initiation of the capillary effects is large characteristic times of mixture diffusion, due to which in the process of mass transfer a concentration gradient is formed near the interface. It gives rise to local density difference and, as a result, to gravitational convection, which generates the vertical concentration gradient (along the free boundary of drop) - the driving mechanism of the capillary convection.

It was found that saturation of the drop with alcohol turned into a three-dimensional process when concentration of the solution was as high as $C_0 = 10\%$: after penetration into the drop of chlorobenzene the alcohol buoyed to its upper surface forming a thin layer. Due to the fact that the cell was horizontal the layer of alcohol in the drop was of uniform thickness and, accordingly, this region on the interferogram was of the same color (Fig. 1*a*). A growth of the layer thickness or an increase in the alcohol content by a certain value resulting in the additional optical difference of light beam path in the half of the wave length led to a change in the image color (Fig. 1*b* and

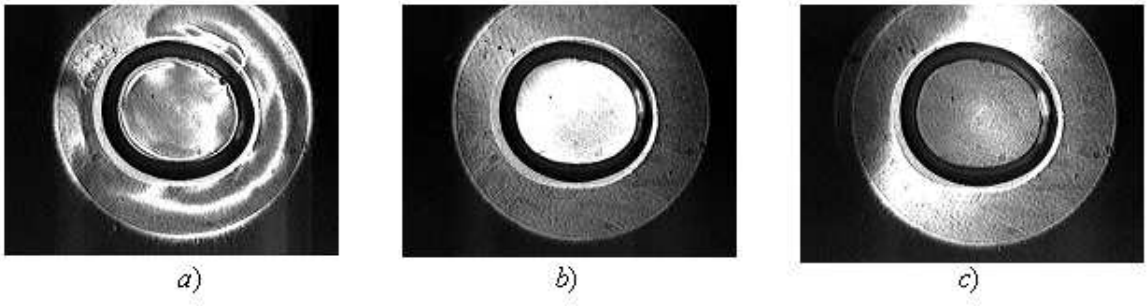


Figure 1: Saturation of a chlorobenzene drop with isopropyl alcohol from its solution filling the horizontal Hele-Shaw cell. $C_0 = 10\%$, $D_0 = 5.2$ mm. t, minutes 0.5 (a), 10 (b), 30 (c)

Fig. 1c). In such a way, by tracing the variation of the drop color with time one can get a clear vision of how intensively the drop absorbs the alcohol and how long does this process last (Fig. 2).

Absorption of the alcohol from its solution should cause a growth of drop volume which in the case of the cylindrical drop with the fixed thickness is manifested as an increase of its area. Indeed, saturation of the drop with alcohol was accompanied by a change of its area. However, this variation was of a complicated nature, which was specified by the initial concentration of the surfactant in the solution (Fig. 3). The reason for such a behavior of the absorbing drop was an increase in the reciprocal solubility of water and chlorobenzene with a growth of concentration of their common solvent, viz., the alcohol in their solutions. The maximum increase ($\sim 20\%$) in the drop area was observed at the initial stage of its saturation at $C_0 = 40\%$ (curve *3* in Fig. 3). Then the drop began to dissolve due to increasing diffusion of chlorobenzene in the surrounding solution. A delay in the dissolution was caused by insufficient content of the surfactant inside the drop. The desired concentration was achieved only some time after injection of the drop into the solution. In the solution containing 45% of alcohol (curve *4* in Fig. 3) concentration of the absorbed surfactant at the drop boundary immediately grew to the value at which chlorobenzene began to dissolve in the surrounding solution. The process of the surfactant extraction turned into the reverse - dissolution of the extragent.

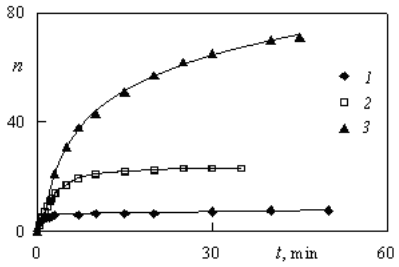


Figure 2: The number of isolines inside the drop as a function time for different concentrations of solution C_0, %: 10 (*1*), 20 (*2*), 30 (*3*)

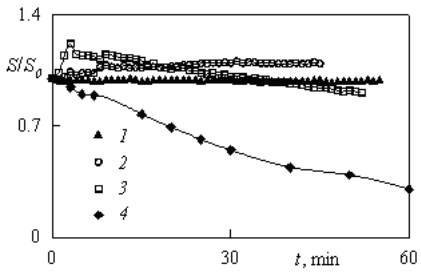


Figure 3: The relative area of the chlorobenzene drop as a function of time for isopropyl solutions of various concentrations. The initial drop area is $S_0 \sim 35$ mm^2. C_0, %: 10 (*1*), 30 (*2*), 40 (*3*), 45 (*4*)

Dissolution of chlorobenzene gave rise to an intensive gravitational flow in the surrounding solution. This process every so often was accompanied by generation of both the vertical and longitudinal (lying the layer plane) difference of the surfactant concentration at the drop surface provoking the development of a large-scale capillary flow.

In our case such a flow occurred in the form of two quasi-stationary vortices lying in the horizontal plane (Fig. 4). Note that the flow was sustained by a small difference ($\sim 3\%$) in the surfactant concentration between the "western" and "eastern" poles of the drop. The initial solution entrained by the flow reached the drop surface in the form of the concentration "tongue", which then split into streams flowing round the drop. As they spread along the drop surface they



Figure 4: Distribution of concentration of isopropyl alcohol during its absorption by the drop of chlorobenzene from the solution with initial concentration $C_0 = 45\%$. t, min: 0 (a); 70 (b); 190 (c)

lost part of the alcohol due to diffusion. After that they again merged into a single flux, which drifted away from the drop carrying part of the alcohol-chlorobenzene mixture.

In turn, the alcohol penetrated into the drop and formed two fluxes, which first traveled along the interface and then after collision at the western pole of the drop spread deep into the drop generating an internal two-vortex flow.

3 Dissolution of binary mixture drops in thin horizontal layer of homogeneous liquid

The flow initiated by diffusion of isopropyl alcohol from the drop of its mixture with chlorobenzene in a shallow layer of water looks quite different. Although the driving mechanism of a convective flow is identical to that for a drop in the homogeneous surfactant solution, it is necessary to take into account the following circumstance. The coefficient of the equilibrium distribution of isopropyl alcohol in the chlorobenzene-water system is of order of 0.1 at small alcohol concentrations. In practice this means that as soon as the concentration of alcohol in chlorobenzene reaches 1% it ceases to diffuse from its 10% solution in water. Hence the reason for the development of the capillary motion vanishes. At the inverse ratio of alcohol concentrations in water and chlorobenzene there occurs an intensive diffusion of alcohol into water which initiates a gravitational flow which in its turn provokes the onset of the Marangoni convection. As a result, the development of the capillary flow under conditions of alcohol diffusion from the drop of chlorobenzene can be observed as soon as the initial alcohol concentration reaches 2-3%.

A typical series of interferograms of the concentration field generated around a dissolving drop of the mixture containing surfactant is shown in Fig. 5. The capillary convection occurred practically immediately after formation of the drop. It developed in the form of three-dimensional nonstationary cells symmetrically arising at both sides of the interface. A complicated structure of the cells should be attributed to the solutal stratification of the surfactant solutions under the action of the buoyancy force. In a short time the size of the cells became comparable with the drop radius, which provided conditions for a rapid decrease of the surfactant concentration due to a continuing transfer of the mixture from the central region of the drop to the interface. Note that the capillary flow had a rather weak effect on the gravitational flow responsible for the propagation of the concentration front in a direction away from the drop boundary (such level of the interaction manifests itself in a dramatic distinction between two types of the convective motion shown in Fig. 5a). At the same time, the boundary of the concentration front had still the traces of the originating cell flow.

A decrease of the surfactant content in the drop smoothed down the concentration differences at the interface and the capillary flow decayed. After this the evolution of the concentration field was governed solely by the buoyancy force, which essentially simplified its structure (Fig. 5b). As long as the amount of surfactant in the drop remained rather high, regeneration of the vertical solutal stratification at the interface led again to the development of the intensive capillary convection

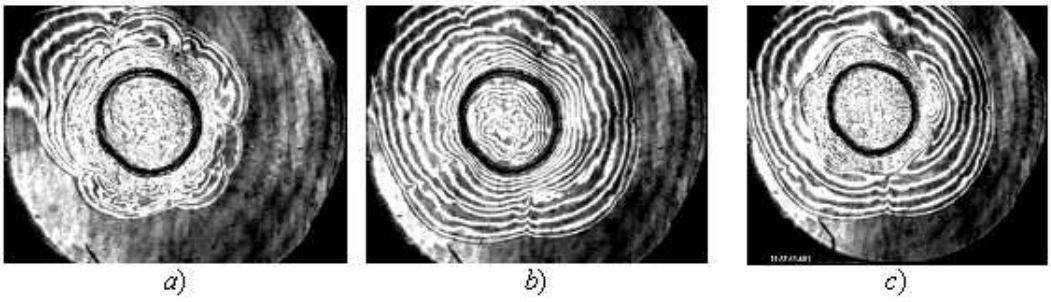


Figure 5: Evolution of alcohol distribution during its diffusion from the drop of $d = 4.7$ mm with $C_0 = 15\%$ in a horizontal layer 1.2 mm thick. The elapsed time from the beginning of the test t, sec: 7 (a); 13 (b); 15 (c)

(Fig. 5c). However, the arising cell motion continued for no more than a few seconds and was followed by the gravitational flow with essentially lower characteristic velocities. Depending on the initial surfactant concentration the number of such "outbursts" of the capillary convection could vary in the range from one or two at $C_0 = 5\%$ to eight at $C_0 = 20\%$ (it is to be noted that the number of outbursts markedly varied from test to test at the same value of C_0). The period of the alternation of different convective flow patterns was rather short (≤ 2 min). Completion of the surfactant dissolution from the drop proceeded under conditions of quasi-diffusion. Depending on the values of C_0 and D_0 the time of full dissolution varied from 7 to 10 minutes, which was tens times shorter than the characteristic times of diffusion.

As viewed from the top the transmitted light beam travels through the optical medium whose properties change along the line of beam propagation. In this situation, the intensity of the dissolution process (Fig. 6) and the velocity of propagation of the alcohol concentration front from the dissolving drop (Fig. 7) can be judged from the variation in the number and position of the interference bands.

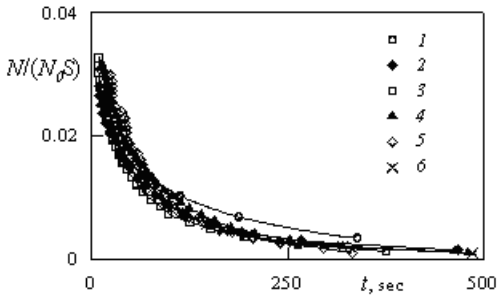


Figure 6: Variation of the normalized number of the interference bands with time for drops with different initial surfactant concentration C_0, %: 1 (*1*); 3 (*2*); 5 (*3*); 10 (*4*); 15 (*5*); 20 (*6*)

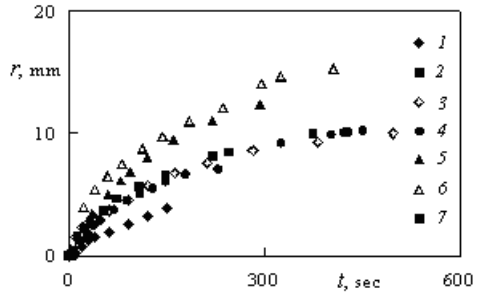


Figure 7: Variation of the concentration front position with time for drops with different initial surfactant concentration C_0, %: 1 (*1*), 3 (*2*), 5 (*3*), 10 (*4*), 15 (*5*), 20 (*6*), 30 (*7*)

On the interferograms the process of alcohol dissolution is seen as a group of concentric bands which draw closer and closer together toward the drop center until they coalesce. Therefore it makes sense to characterize the dynamics of mass transfer according to variation of the number of bands in this region. As might be expected the total number of the coalesced interference bands depends on the area of the drop and initial alcohol concentration. Fig. 6 shows variation of the normalized number of the interference bands at the center of the drop during dissolution of alcohol. For normalization we used the drop area and the total number of the bands at the initial instant of time obtained by approximating the experimental relation $N = f\,(t)$. As it is seen from the Figure the process of dissolution of drops with various initial concentrations of the surfactant proceeds

in nearly the same manner except for the drops with the minimal initial concentrations (curve *1*), the dissolution of which does not initiate a capillary motion. Such a behavior of mass transfer can be observed only in the case when its intensity at all stages of dissolution is proportional to the initial surfactant concentration.

The experiments made have revealed some specific features of the dissolution process for drops with a low content of the surfactant. Among these is the non-linear dependence of the diffusion front velocity on the surfactant concentration (curves *2* and *3* in Fig. 7). The intensification of dissolution was found to be caused by the oscillations of the free surface of the quiescent drop which occurred due to a periodic onset of the local capillary convection at small alcohol concentrations ($C_0 \sim$ 3-5%). Further increase in the initial surfactant concentration resulted in cessation of the surface oscillations (by this time the Marangoni convection spread over the whole surface of the drop), which reduced the rate of dissolution (at C_0 from 7 to 11%, curve *4*). It should be noted that similar periodic ejections of the surfactant from the interface at small values of C_0 were observed in the case of free (spherical) drops of a binary mixture dissolving in hydroweightlessness conditions. They occurred as weak vertical oscillations of the drop or as periodic up-and-down motion of the emulsion over the drop surface (at $C_0 \sim 1\%$) [3].

4 Dissolution of binary mixture drops in thin layer of homogeneous liquid in microgravity conditions

The results of investigations described in the previous sections clearly demonstrate that in many cases the gravitational motion provides conditions for development of intensive capillary flows by way of recovering the percentage composition of the liquid mixtures at both sides of the interface. On the other hand, due to analogy with the thermocapillary many of the authors often appeal to the supposition that reduction of the gravity level brings to the forefront of mass transfer process the solutocapillary convection. This, however, leads to a decrease in the outflow of both the diffusing components and depleted mixture from the boundary region. Lowering of the concentration difference normal to the interface reduces the probability of formation of concentration inhomogeneities along this boundary. Therefore the possibility for generation of solutocapillary motion in the mass transfer processes under microgravity conditions is not clear.

The object of investigation in microgravity conditions was the process of dissolution of a binary drop in the initially homogeneous fluid. To obtain the drop we prepared a mixture containing 85% (by mass) of chlorobenzene and 15% of isopropyl alcohol. The distilled water was used as a fluid surrounding the drop. It filled the cuvette in form of hollow disk which was 1.2 mm in thickness and 35 mm in diameter. The ends of the disk were formed by two plane-parallel glass plates with semitransparent mirror coating. Such design of experimental cuvette allowed us to use the interferometer for visualization of the alcohol concentration distribution in the cylindrical drop and the surrounding fluid. The composition of the mixture changed only across the transmitted light beam, so each interference band was identified with a certain value of the surfactant concentration. In our case, when heat generation due to dissolution of alcohol was negligibly small a transition from one self-colored interference band to another corresponded to a change in the concentration of the isopropyl alcohol by 0.27% in water and by 0.10% in chlorobenzene. The experiment was performed during the flight of the space satellite "Foton M-3" (Sept.2007) [4].

Fig. 8 shows a short series of interferograms depicting the process of drop formation and the beginning of its dissolution in microgravity conditions. The first interferogram reproduces the moment when a growing drop, hanging at the end of needle comes into contact with pure water. It leads to initiation of intensive solutocapillary motion of the drop surface due to generation of the surface tension difference. As a result, the drop executes several oscillatory motions with large amplitude (Fig. 8*a*) like a drop in the known Lewis and Pratt experiment [5]. The oscillations of the drop extend the boundaries of the region containing liquid enriched with the alcohol. This leads to a decrease of the concentration gradient at the interface and the growing drop again quiets down.

The second interferogram illustrates the moment when an abrupt increase in the velocity of drop forming breaks down the established concentration field in drop. The vortex flow spreads over the whole drop while pure water reaches the surface of the drop in the zone of its contact with

needle. This leads to a repeated outburst of capillary convection (Fig. 8*b*) Development of the Marangoni convection is accompanied by deformation of the drop itself and the surrounding front of surfactant concentration, which gains a quasi-periodic structure. Then, as in the first case, a flow of the diffused surfactant into the zone, where pure water comes into contact with the solution of the drop, causes retardation of the capillary motion. At this point the drop reaches maximal diameter $d_0 = 6.2$ mm.

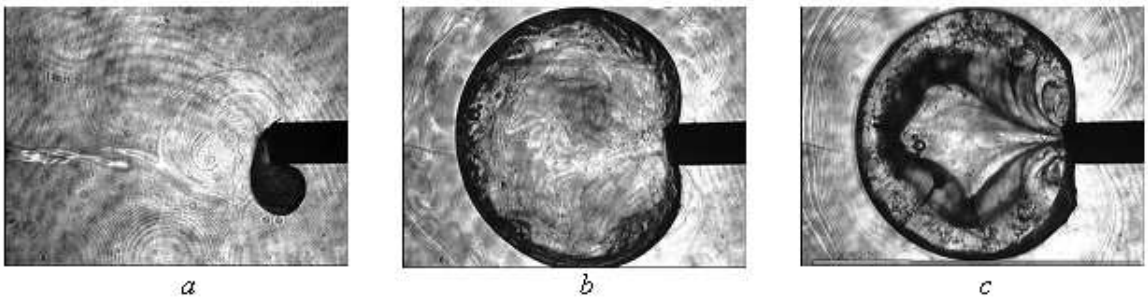


Figure 8: Evolution of the concentration field and flow structure during drop formation. External diameter of needle is 1.0 mm. Time from the test outset t, s: 5 (*a*); 10 (*b*); 88 (*c*)

The last interferogram represents the dissolving drop inside which the capillary convection occurs for the third time in the form of two symmetric vortices at both sides of the needle. The reason of the capillary effects is the alcohol, which diffuses from the needle after cessation of mixture supply. It creates a surfactant concentration difference at the free surfaces of the gas bubbles, which appear due to reduction of the ultimate dissolution of air as a result of decreasing the content of alcohol in the solution.

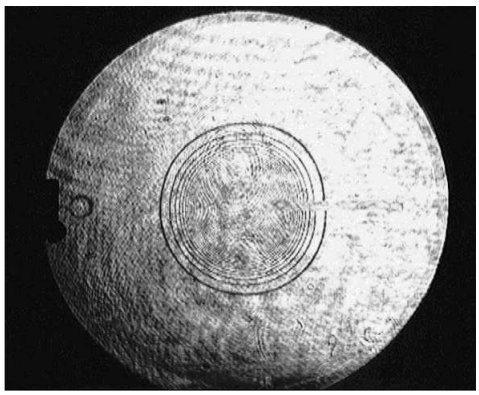


Figure 9: Interferogram of the concentration field during alcohol diffusion from the drop. The elapsed time from the moment of drop formation, $t = 28.5$ minutes

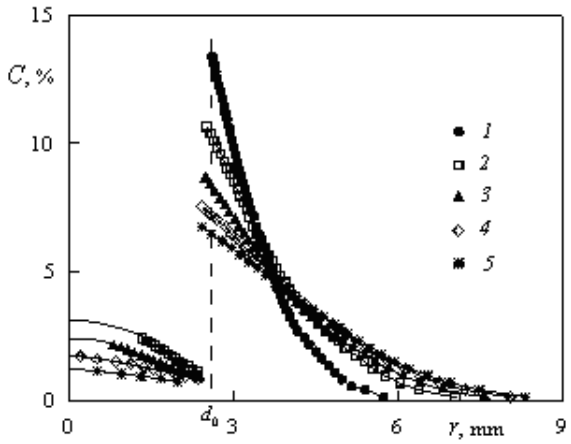


Figure 10: Variation of radial distribution of surfactant concentration in the vicinity and inside the drop with time t, min: 4.9 (*1*); 21.3 (*2*); 31.0 (*3*); 42.5 (*4*); 50.7 (*5*)

5 Conclusion

As is evidenced by the experiments, an attempt of using a thin horizontal layer for modeling surfactant diffusion in microgravity conditions can hardly be considered successful. A small coefficient of surfactant diffusion facilitated generation of differential density in the originally homogeneous surrounding fluid. This difference was large enough for development of gravitational motion inside and outside the drop. Nevertheless a relative contribution of the Marangoni convection to the process considerably increased - it was just the capillary mechanism that governed the rate of mass transfer at the beginning of surfactant distribution.

Because of a three-dimensional structure of the flow the interference method has proved to be rather difficult to apply in the laboratory conditions. We can use only qualitative characteristics for description of evolution of the concentration field. However, this allows us to refine upon our methods for investigation of the concentration distribution in microgravity conditions. It has been shown that the most valuable information can be gained by tracking variations of the maximum surfactant concentration in the drop and the structure of concentration field around drop.

Acknowledgements

The work was supported by the RFBR project No 10-01-96028 and the program of the Department of Power Engineering, Mechanical Engineering, Mechanics and Control Processes of RAS No 09-T-1-1005.

References

[1] Myshkis A.D., Babskii V.G., Kopachevskii N.D., Slobozhanin L.A. and. Tyuptsov A.D., Low-Gravity Fluid Mechanics, 1987, Springer, the Netherlands.

[2] Kostarev K.G., Pshenichnikov A.F. Gravitational convection of a liquid mixture in a horizontal cylindrical gap at moderate grashof numbers //Cosmic research. 2004, Vol.42, N2, pp.115-122.

[3] Kostarev, K. G., Briskman, V. A., 2001, "Dissolution of a Drop with a High Content of a Surface-Active Substance", J. Physics Doklady 46(5), pp. 349-351.

[4] Kostarev K.G., Levtov V.L., Romanov V.V., Shmyrov A.V., Viviani A. Experimental study of surfactant transfer in fluid systems in microgravity conditions // Acta Astronautica, 2010, Vol. 66, Is. 3-4, pp. 427-433.

[5] Lewis, J. B., Pratt, H. R. C., 1953, "Instabilities induced by mass transfer and deformable fluid interfaces", Nature, 171, p. 1155-1161.

Institute of Continuous Media Mechanics, Ural Branch of Russian Academy of Sciences, Acad. Korolev Str. 1, 614013 Perm, Russia.

Kinetic model of water clusters formation and growth in rarefied gas flows

Nikolay Y. Bykov Dmitry V. Leshchev
nbykov2006@yandex.ru

Abstract

The kinetic model of water clusters formation has been developed for the direct simulation Monte Carlo method. The model describes hierarchy of reactions which lead to growth and decay of water clusters, including water dimer formation process. It was considered two mechanisms of water dimer formation: under binary collisions and as a result of three-body recombination. The different approaches were applied for estimation of sticking probabilities of such processes. The model was employed for the direct simulation of expanding spherical rarefied flow of water molecules. The influence of the dimerization rates predicted by different approaches on condensation process was analyzed.

1 Introduction

The kinetics of molecular clusters formation in rarefied flows is of great interest for large number of applications in science and technology. In particular, the formation of clusters in rarefied flows of water molecules is a very important process for planetary science. Understanding of origin and behavior of space bodies like comets requires observation and analysis of the near-nucleus atmosphere formed by jets of water molecules evaporated from dusty-ice comet surface. Near-nucleus comet atmosphere parameters are affected strongly by water clusters formation processes [1] and correct interpretation of observations results requires taking into account condensation process.

The aims of present research are to develop the model water clusters growth in rarefied flows and to analyzed the influence of model parameters on results of direct simulation Monte-Carlo (DSMC) of 1D rarefied expansion of water molecules from spherical surface. Our previous studies [2] consider the hierarchy of reactions in flow volume including water dimer formation under three-body collisions. Here we add reaction of water molecules association under binary collisions. The key moment of the model application is in description of sticking probability for this reaction which influence strongly on the nucleation rate. Different approaches are considering with the purpose of such probability estimation.

2 Kinetic model of water clusters formation

The model of clusters formation has been elaborated recently for the DSMC method [2, 3]. The clusters are characterized by number of monomers k, mass, radii (determined by modified drop spherical mode [2]), translation velocity, rotation and vibration degrees of freedom and corresponding rotation and vibration internal energies.

In general case [2] the model takes into account such kinetic processes as (i) dimer formation under triple collision of monomers, (ii) reaction of the monomer-cluster association under binary collisions of these particles, (iii) reaction of the cluster-cluster association under mutual collisions of clusters, (iv) cluster decay by one monomer evaporation. For the conditions of low temperature flow of water molecules the probabilities of association during particles collisions for reactions (i)-(iii) were supposed to equal unity [2]. The new feature of the developed model for water clusters formation is in consideration of additional reaction (v) which allow to form dimer directly under binary collision of water molecules $H_2O + H_2O \xrightarrow{p} (H_2O)_2$, where p — probability of association.

Opposite the case of atomic dimer formation, for our problem this reaction may take place due to enough large capacity of vibration modes of water dimer. The rate of this reaction in rarefied flows may be essentially larger than the rate of dimer formation under triple collisions. The correct estimation of p is necessary for adequate description of whole nucleation process. We present three possible approaches for such probability determination: (i) by the approach of orbiting complex (OC approach), (ii) by the data on the reaction rate constants (RC approach), (iii) by the molecular dynamic (MD) simulations [4] (MD approach).

(i) In the OC approach it is supposed that two colliding particles interact with U(R) potential:

$$U(R) = \frac{C_6}{R^6} \tag{1}$$

where R — the particles distance, C_6 — constant, for water equals $84.9 \cdot 10^{-79} J \cdot m^6$ [5]. Then the cross-section of reactions without activation is [6]

$$\sigma_r(\varepsilon_t) = 2\pi \int_0^\infty P_r \cdot bdb = \pi b_c^2 = \frac{3\pi}{2^{\frac{2}{3}}} \left(\frac{C_6}{\varepsilon_t}\right)^{\frac{1}{3}} \tag{2}$$

$$P_r(b, \varepsilon_t) = \begin{cases} 1, & b_c \geq b \\ 0, & b_c < b \end{cases} \tag{3}$$

where P_r — reaction probability, b — impact parameter, b_c — critical impact parameter, ε_t — kinetic energy of collision. It was suggested to determine the association probability p as relation of the reaction cross-section to full collision cross-section σ_T (for hard-sphere model).

$$p = \frac{\sigma(\varepsilon_t)}{\sigma_T} \tag{4}$$

(ii) The RC approach provides knowledge of data on reaction rates constants [7]. The variation of number density of water molecules for the considering reaction may be defined as

$$\frac{dn_w}{dt} = k_r(T) n_w^2, \tag{5}$$

where n_w — the number density of water molecules, $k_r(T)$ — the rate constant, T — temperature. At the same time for equilibrium conditions

$$\frac{dn_w}{dt} = N_{bin} \int_0^\infty p(E_c) f\left(\frac{E_C}{k_b T}\right) d\left(\frac{E_c}{k_b T}\right) \tag{6}$$

where N_{bin} — the number of binary collisions per unit time and unit volume, E_C — the total energy of collision, k_b — Boltzmann constant, f — energy distribution function, which under assumption of equilibrium conditions and continuum spectrum of energy may be presented as

$$f\left(\frac{E_C}{k_b T}\right) = \frac{1}{\Gamma\left(\frac{\zeta_C}{2}\right)} \left(\frac{E_C}{k_b T}\right)^{\frac{\zeta_C}{2}-1} e^{-\left(\frac{E_C}{k_b T}\right)} \tag{7}$$

ζ_C — the total number of degrees of freedom of colliding pair, Γ — the gamma function. For the reactions without activating barrier the rate constant depends on T as [8]

$$k_{ass} = aT^b, \tag{8}$$

where a,b — constants. On the base of equations (5) and (7) the probability of association under binary collision without activating barrier for the case of hard-sphere model dynamics may be obtained as

$$p = CE_C^x, x = b - 0.5, C = \frac{a\sqrt{\pi m_r}}{k_b^b \sigma_T \sqrt{2}} \frac{\Gamma\left(\frac{\zeta_C}{2}\right)}{\Gamma\left(b - 0.5 + \frac{\zeta_C}{2}\right)} \tag{9}$$

where σ_T — collision cross-section (for hard spheres model), m_r — the reduced mass of colliding pair.

The key question for application of this equation is existence of data on a and b. Here we consider different assumptions on values of a and b:the estimations [8] give a in the range $10^{-10} - 10^{-14} cm^3/mole \cdot s$, b = 0. In the presented below simulations we use three values of a = $10^{10} cm^3/mole \cdot s$ (RC1 case), $10^{12} cm^3/mole \cdot s$ (RC2 case), $10^{14} cm^3/mole \cdot s$ (RC3 case).

(iii) The data on sticking probability of water molecules under binary collision was obtained by MD methods in [4].

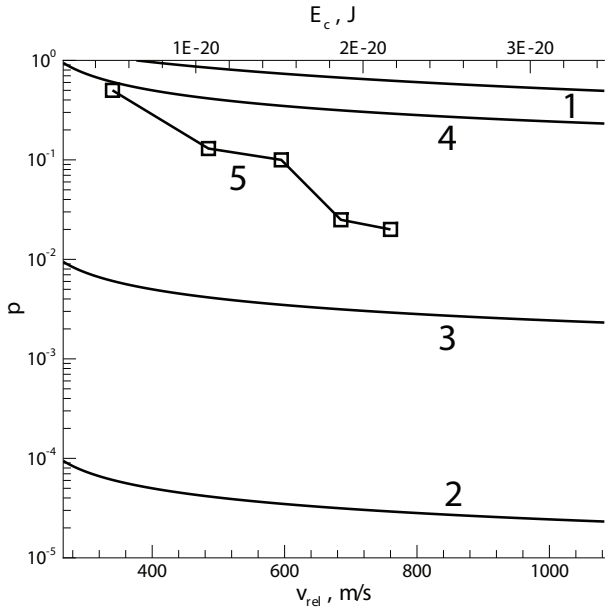


Figure 1: The sticking possibility under binary collisions of water molecules. 1 — OC approach, 2 — RC1 case, 3 — RC2 case, 4 — RC3 case, 5 — MD case

3 Results and discussion

For water vapor flow we consider all discussed cases of sticking possibility definition: the approach of orbiting complexes (OC), the approaches based on data about rate constants (RC) and molecular dynamic (MD) approach. The generalized information about probability dependences on relative velocity or total energy of colliding molecules are presented in Fig.1. The OC approach (line 1) predicts large values of reaction cross-section and possibility of sticking under binary collisions near unity. This probability depends slightly on relative velocity of water molecules. The values of p in the OC approach depend strongly on parameter a in equation (4). For a=$10^{10} cm^3/mole \cdot s$ (RC1 case, line 2) the probability decreases slightly from values $9.5 \cdot 10^{-5}$ for total energy of collision $2.07 \cdot 10^{-21} J$ (for equilibrium conditions it corresponds to relative velocity 265 m/s) toward $2.3 \cdot 10^{-5}$ for 1080 m/s. Sufficiently large values of p observed for the cases a = $10^{12} cm^3/mole \cdot s$ (case RC2, line 3) and a =$10^{14} cm^3/mole \cdot s$ (case RC3, line 4). For RC3 case the values of probability are again closely to unity for small values of total collision energy. MD approach (MD case, squares) predicts more dramatic decreasing of sticking probability from 0.5 corresponded relative velocity 340 m/s to 0.02 for 760 m/s.

According the data on Fig.1 there is high uncertainty in determination of sticking probabilities of water molecules under binary collisions. Therefore it is very important to analyze influence of model parameters on results of simulation. For this purpose we consider rarefied flow of water molecules from spherical surface in vacuum.

The water molecules are evaporating according semi-Maxwellian function [2] into vacuum from

spherical surface with the radius R=900 m. The temperature of the surface is supposed to be 200 K and equilibrium number density was set $1,32 \cdot 10^{17} m^{-3}$. For considering set of initial parameters characteristic the Knudsen number was $Kn = \lambda_w / R_{eff} = 5 \cdot 10^{-3}$ (λ_w — free path near the surface). This value corresponds to enough rarefied flow regime. Other parameters of modeling were the same as in [2]. The direct simulation Monte Carlo technique with taking into account cluster formation, growth and decay processes was applied for flow modeling.

The degree of condensation may be defined as

$$\alpha_S = \frac{\sum\limits_{k=2} kN_k}{\sum\limits_{k=1} kN_k} \tag{10}$$

where N_k — the total number of clusters with size k in the considering flowfield. For OC approach we obtain maximal condensation degree 0.45, for MD approach $\alpha_S \cong 0.3$, $\alpha_S \cong 0.001$ for RC1 case, $\alpha_S \cong 0.1$ for RC2 case and $\alpha_S \cong 0.4$ for RC3 case. For RC3, OR and MD cases we obtain enough close results for condensation degree ($0.3 < \alpha_S < 0.45$). It should be underlined that efficiency of dimer formation by three-body recombination of water molecules is negligible for this rarefied regime.

The behavior of gasdynamic parameters in expanding spherical flows were considered in [2] for the cases with and without condensation processes. Here we demonstrate the distribution of average water cluster size along flow axies (Fig.2a) for cases , RC approach (RC2 case — line 1, RC3 case — line 2) and MD approach (line 3). The OC approach gives approximately the same results as RC3 case and not presented in figure. The behavior of an average cluster size along flow axis seems approximately the same for cases OC, RC2, RC3, MD in the vicinity of surface ($R < r < 3R$). The case RC1 in frames of our accuracy of simulation predicts very small condensation degree and maximal cluster size k=2. Fig.2b shows the cluster size distribution in the whole volume of considering flow field for the case of MD approach.

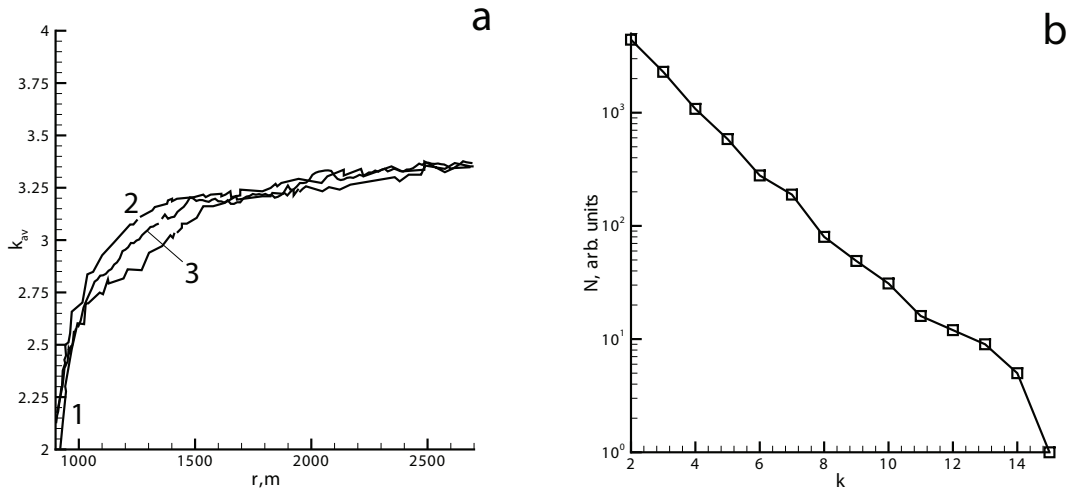


Figure 2: a: the spatial distribution of average cluster size (1 — RC2 case, 2 — RC3 case, 3 — MD case). b: the size distribution of clusters for MD case

4 Summary

The model of water cluster formation for the DSMC method was developed. The process of water molecules association under binary collision was taken into account. Some approaches for sticking probabilities determination for this process were discussed. The predicted by considering approaches dependences of probability on collision energy or relative velocity differ significantly

from each other. As an example of model application 1D expansion of water molecules from spherical source was simulated by DSMC technique in the range parameters corresponding to rarefied flow (Knudsen number is of order 10^{-2}). In spite of the fact of uncertainty of sticking probability determination the estimated values of condensation degree and spatial distributions of an average cluster size demonstrate close behavior for majority of the approaches for considering rarefied conditions. Only one case with asymptotically small values of sticking probability ($p < 10^{-4}$) predicts different results with practically absence of condensation process.

References

[1] J.F. Crifo. *Water clusters in the coma of comet Halley and their effect on the gas density, temperature, and velocity,* Icarus, 1990, V.84, pp. 414-446.

[2] N. Yu. Bykov. *Modeling of condensation process under spherical expansion of water vapor in vacuum,* Teplofiz. Aeromekh., 2009, No 2, V. 16, pp. 189-199.

[3] N. Yu. Bykov and G. A. Lukyanov. *Direct simulation Monte Carlo of pulsed laser ablation of metals with clusterization processes in vapor,* Teplofiz. Aeromekh., 2006, No 4, V. 13., pp. 523-535.

[4] Z. Li, J. Zhong, D.A. Levin, B. J. Garrison, *Kinetic nucleation model for free expanding water condensation plume simulations,* In proceedings of 26th int. symposium on RGD, AIP conference proceedings, Melville, New York, 2009, Vol. 1084, pp. 613-618.

[5] Zatsepina G.N. Properties and structure of water. M: Izd.Moskoskogo Universiteta, 1971, 168 p.

[6] Umanskiy, S.Y. *Theory of elementary chemical act in gas. Physicochemical kinetic in gasdynamic.* V.4, 2006, http://www.chemphys.edu.ru/volume/11/.

[7] Boyd, I.D., *Analysis of Vibration-Dissociation-Recombination Processes Behind Strong Shock Waves of Nitrogen,* Physics of Fluids A, Vol. 4 (1), 1992, pp. 178-185.

[8] Physic-chemical processes in gasdynamics. Handbook, Vol. I, Editors G.G. Chernyi, S.A. Losev, Moscow: Moscow state university press, 1995, 350 p.

Nikolay Y. Bykov, Saint-Petersburg State Polytechnical University, Polytechnicheskaya 29, 195251 St.-Petersburg, Russia
Dmitry V. Leshchev, Saint-Petersburg State Polytechnical University, Polytechnicheskaya 29, 195251 St.-Petersburg, Russia

Relay control in noisy vibration systems

Mikhail V. Cherkay
chmv2007@rambler.ru

Abstract

D. A. Tomchin and A. L. Fradkov proposed and investigated new control methods for some systems modeling rotor electromotor on a platform[1]. This sophisticated relay feedback allows to avoid resonance effects in system functioning, the important advantage of this method is the energy minimization. The need energy is defined by a feedback coefficient M_d. We have studied rotor systems where the platform is under a noise. The noise is simulated by a time dicsrete Ornstein-Uhlenbeck process. This process is defined by two parameters, memory parameter and noise amplitude. To study problem, we have used numerical simulations by MATLAB 2009. We applied a slightly modified relay feedback control. The results are as follows. The feedback coefficient is an increasing function of the noise amplitude and decreasing function of the memory parameter. The noise influence is negative: to stabilize the system functioning under the noise, we must use a larger feedback coefficient.

1 Mechanical vibration model

Last decades, many researchers consider different mechanical models in a noise environment [1, 2, 6]. We consider mechanical model, which consists of a debalance rotor electromotor on a platform, which making hard oscillations along axe y using two springs. This vibration model has two degree of freedom - connected with electromotor rotation and hard platform oscillations. It is known the main parameters of this model: forcing control moment of electromotor(momentum) - M_d, the mass of debalance rotor and platform - m and M correspondingly, momentum of debalance rotor - J, eccentricity center of mass rotor - ρ, angle of rotor rotation - ϕ, axes hard of the spring - c, total axes dempher of the spring - k_d and value of viscous friction - k_c, this scheme of this model in (Figure 1). This model has been studied in [1], there a new control method is proposed. The

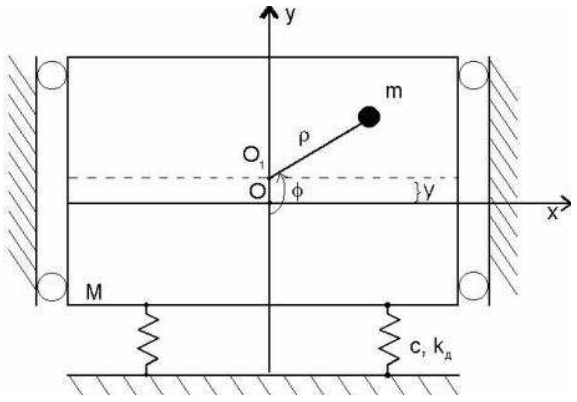


Figure 1: One rotor electromotor vibration system

goal of this control is to obtain a prescribed angular rate of the rotor. If M_d is small, that system exhibits a Sommerfeld effect [3]. Namely, this effect arises when the rotor frequency approaches to resonance frequency of the carrier body. On this condition we should be increase M_d for subsequent rotor angular rate. The relay control proposed by [1] allows to avoid this resonance effect. In this

paper we study this system under noise. We investigate a modified relay feedback control in order to eliminate to noise effects.

2 Dynamic equations and relay feedback control vibration system under noise

To simulate the noise we use a discrete Ornstein-Uhlenbeck [4] process:

$$x(t+1) = \beta x(t) + \varepsilon\xi(t), \tag{1}$$

where: $t = 1, 2, ...$, $\beta \in (0, 1)$ - memory parameter, $\varepsilon > 0$ - the noise level, $\xi(t)$ - white noise. We consider the following equations describe vibration system [1] and (1):

$$\left\{ \begin{array}{lcl} (M+m)\ddot{y} - m\rho\ddot{\phi}\sin\phi - m\rho\phi^2\cos\phi + (M+m)g + k_d\dot{y} + 2cy & = & x(t) \\ J\ddot{\phi} + k_c\dot{\phi} - m\rho\ddot{y}\sin\phi - m\rho g\sin\phi & = & u(t) \end{array} \right. \tag{2}$$

Here $u(t)$ is a control. The simplest control choise is $u(t) \equiv M_d$. However, in this case the Sommerfeld effect occurs, and the electromotor consumes a lot of energy. To decrease energy level we use the following sophisticated relay control (similar to [1]):

$$u(t) = \left\{ \begin{array}{l} M_d, \quad \gamma(t) = 1 \quad \wedge \quad (H < H^*) \quad \wedge \quad t \in [t_{min}, t_{max}] \\ M_d, \quad \gamma(t) = 0 \quad \wedge \quad (\psi(t) - \dot{\phi}(t)) < 0 \quad \wedge \quad t \in [t_{min}, t_{max}] \\ 0, \quad else \\ -M_d sign(H - H^*), \quad t \in [0, t_{min}[\cup]t_{max}, +\infty] \\ T_\psi\dot{\psi} = -\psi + \dot{\phi} \end{array} \right. \tag{3}$$

Here $\gamma(t) = \underset{0\le\tau\le t}{max} \quad H_v(H_t - H^*)$, H, H_* is the energy of the rotation subsystem and the maximum of possible energy of the rotation subsystem correspondingly, ψ - the filter of low frequencies, T_ψ - time variable of low frequency filter, H_v - Heaviside function. This control can be explained by the following general ideas. Let $q = q(t)$ be a vector of coordinates, $p = p(t)$ be a vector of impulses, $u = u(t)$ be a vector of control and $H = H(p, q)$ be a Hamiltonian. Let us consider a Hamiltonian system with a control:

$$\dot{p} = -\left(\frac{\partial H}{\partial q}\right)^T + Bu, \quad \dot{q} = \left(\frac{\partial H}{\partial p}\right)^T. \tag{4}$$

We assume that this system consists of two subsystems - a rotation subsistem with the energy $H_1(p(t), q(t))$ and a subsystem with the energy $H_2(p(t), q(t))$. Let $H_{12}(p(t), g(t))$ be an energy of interaction. This the full system energy is defined by:

$$H(p(t), q(t)) = H_1(p(t), q(t)) + H_2(p(t), q(t)) + H_{12}(p(t), q(t)). \tag{5}$$

To overcome the resonance effects, we apply a control, where the control target is defined by:

$$(H_1(p(t), q(t)) - H^*)^2 \to 0, \quad t \to \infty, \tag{6}$$

where H^* is a fixied value. The relay control (3) is based on ideas of by A.L. Fradkov [5].

3 Numerical simulations

In all numerical simulations, we use the following parameter choice: m=1.5[kg], M=9[kg], J=0.014[kgm^2], ρ=0.04[m], c=5300[N/m], k_d=5 [kg/s], k_c=0.01[Dgs]. In the paper [1] it is shown that to avoid resonance effects, it is better to apply the relay control instead of the constant control, $u \equiv M_d$. If the noise is removed for the relay control the electromotor momentum is $M_d = 0.7$ and for the constant control is $M_d = 1.6$. We use the relation $\xi(t) = \varepsilon(2k(t) - 1)$. The number $k(t)$

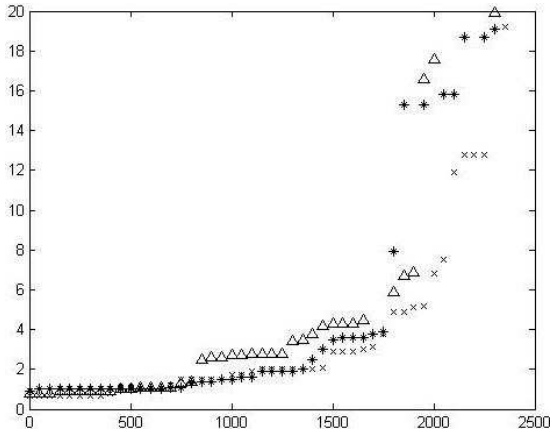


Figure 2: Dependence $M_d(\varepsilon)$ for the relay control, where triangle markers correspond to $\beta = 0.1$, star markers - $\beta = 0.5$ and cross markers - $\beta = 0.9$.

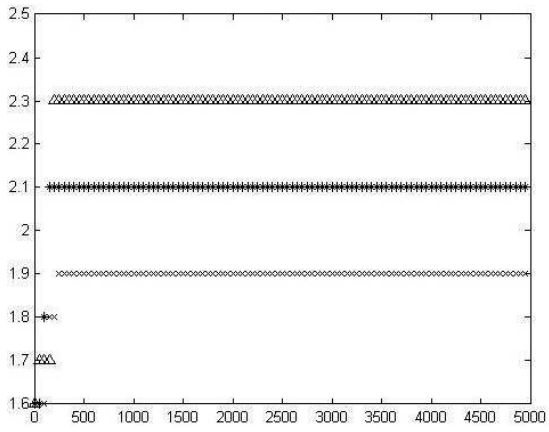


Figure 3: Dependence $M_d(\varepsilon)$ for the constant control, where triangle markers correspond to $\beta = 0.1$, star markers - $\beta = 0.5$ and cross markers - $\beta = 0.9$.

is distributed uniformly on $[0, 1]$. We change the level of fluctuation ε. For $\varepsilon = 1$ we obtain that electromotor momentum should be a $M_d = 1.2$. The first result of this work is that a relay control efficacy decreases as the fluctuation level ε increases. We simulate fluctuation by (1). We consider a values M_d depending on memory parameter (β) and noise amplitude (ε). As the result of our simulations we obtain the following dependance (Figure 2). Namely, the electromotor momentum (M_d) is an increasing function of the noise amplitude (ε) and a decreasing function of the memory parameter(β). It is important that this vibration system with relay control (3) under higher level of noise ($\varepsilon > 1500$) demands a higher electromotor momentum ($M_d > 5$) for eliminating resonance effects.

This momentum level is not sufficient to support relay control for this system in the noise environment. On the contrary, the constant control $u(t) \equiv M_d$ under higher noise level ($\varepsilon < 5000$) demands smaller momentum $M_d < 2.3$ (Figure 3). Thus, under higher level fluctuations, the most effective control is the constant control.

4 Conclusion

We have considered a model of simple vibration system under noise. In our simulations we have compared two kinds of the control: a constant control and relay feedback control. We have obtained a dependence of electromotor momentum on the level noise and on noise parameters. It is shown that the relay control is more effective for lower noise levels. If the noise is high enough, then the constant control is more powerful.

Acknowledgements

The author is greatful to Prof. A.L. Fradkov for usefull remarks.

References

[1] Tomchin D., Fradkov A. Modeling and speed-gradient control of passage through resonance for the two-rotor vibrational unit//20th European Confernce on Modelling and Simulation, May 28th - 31st, 2006, Bonn, Germany.

[2] Tomchina, O.P., Nechaev K.V. Controlling passage through resonances in vibratory actuators// Proc. 5th European Contr. Conf.,Karlsruhe, Sept.1999.

[3] Sommerfeld A. Beitrage zum dynamischen Ausbau der Festigkeitslehre //Zeitsch. VDI. 1902. Bd.XXXXVI, No 11.

[4] D.T.Gillespie. Exact numerical simulation of the Ornstein–Uhlenbeck process and its integral, Phys.Rev.E 54:2084–91, 1996.

[5] Fradkov, A.L. Speed-gradient laws of control and evolution // Prepr. 1st European Control Conf., Grenoble. 1991. P. 1865–1870.

[6] Tomchina, O.P. Passing through resonances in vibratory actuators by speedgradient control and averaging // Proc. Int. Conf. Control of Oscillations and Chaos, IEEE, St.Petersburg, 1997, v.1, pp.138-141.

Mikhail V. Cherkay, St. Petersburg, Russia

Waves process in media with defects

Nadezhda V. Chertova Yurii V. Grinyaev
chertova@ispms.tsc.ru

Abstract

Based on equation of the field theory of defects including the kinematical identities of continual theory of defects and the dynamic equations of gauge theory have been considered the features of propagation of the harmonic waves in the homogeneous viscoelastic and elastic-viscoplastic media and in the presence of the interface boundary. Reflection and refraction coefficients of waves of the elastic displacements and the field defects determining the plastic deformation have been defined. Dependencies of obtained quantities on the parameters of contacting media have been considered.

Keys words: continual description, dislocation, gauge theory, dynamic equation, waves, interface boundary.

1 Introduction

For many years the studying of inelastic behavior of deformed bodies is the topical problem of mechanics and physics deformed solids. It can be explained by the fact that the region of elastic deformation is quite limited and many processes important with respect to creation and usage of new materials and their products take place beyond the elastic limit. At present time it is known that many inelastic properties of materials are due to defects in the crystal lattice; among various types of defects an especially important role is played by dislocations. Theoretical research of defects can be divided into two different types of approaches: microscopic and macroscopic or continual ones [1, 2]. In the case of macroscopic description a medium with the continual distribution of defects is considered characterized by defect density tensor and defect flux density tensor. These parameters are governed by the plastic distortion tensor φ for the dislocation continuum

$$I = -\partial\varphi/\partial t, \alpha = -\nabla \times \varphi,$$

where α is the dislocation density tensor, I is the dislocation flux density tensor. Traditional equation system of the continual theory of defects including the equation of dynamic equilibrium, Hooke's law and the definitions of parameters of the dislocation continuum allows to investigate the problem of stress-strain state of the system if the parameters of defect field are known. This theory doesn't contain the relationships describing the dynamics of dislocation ensemble. The missing equations had been obtained within the framework of gauge formalism, which is a universal approach of theoretical physics [3]. In this work, we study features of inelastic deformation due to dynamics of translational defects on the basis of wave solutions of defects field theory in the homogeneous media and in the presence of the interface boundary.

2 Mathematical formulation of the problem

The equation system of the field theory of dislocations includes the kinematical identities of continual theory of defects

$$\nabla \cdot \alpha = 0, \nabla \times I = \partial\alpha/\partial t \tag{1}$$

and the dynamic equations of gauge theory taking into account dissipation of energy [4]

$$B\nabla \cdot I = -\vec{P}, S\nabla \times \alpha = -\partial I/\partial t - \sigma \tag{2}$$

Here P is the effective momentum, σ is the effective stress tensor, B and S are the theory constants characterizing continuum of defects. The considered equation system describing the dynamics of dislocation ensemble contains the effective impulse and the effective stress tensor acting as source terms for the defect field. By certain assumptions the effective stress tensor can define viscoelastic, viscoplastic and elastic-viscoplastic media. For description of viscoelastic media the well known the constitutive relationship has been used

$$\sigma = C : \nabla\vec{U} + G : \vec{V}, \vec{V} = \partial\vec{U}/\partial t \tag{3}$$

in which the elastic and viscous components of stress tensor are expressed as gradients of the displacement vector U and velocity V, C is the elastic modules tensor, G is the viscosity coefficients tensor. Elasto-viscoplastic media are defined by the relationship

$$\sigma = C : \nabla\vec{U} + \eta : I, \tag{4}$$

where η is the viscosity coefficients tensor. The considered definitions describe media exhibiting viscous behavior in the process of the elastic or plastic deformation. A more general case is the medium, exhibiting viscous behavior both in elastic and plastic deformation, which can be expressed by

$$\sigma = C : \nabla\vec{U} + G : \vec{V} + \eta : I, \tag{5}$$

The mechanisms of energy dissipation are different in elastic and plastic deformations. As a result, the viscosity for elastic and plastic deformation differs by 5-7 orders of magnitude. The stresses and momentum determined by $\vec{P} = \rho\partial\vec{V}/\partial t$ satisfy the equation of dynamic equilibrium $\partial\vec{P} = \nabla \cdot \sigma$ which is the compatibility condition for (1)-(2).

3 Waves solutions

Let us consider the solutions of equations (1)-(2) with constitutive relations (3), (4) in the form

$$\alpha_{ij}(r,t), I_{ij}(r,t), U_i(r,t) = [\alpha_{ij}(\xi), I_{ij}(\xi), U_i(\xi)]exp(-i\omega t) \tag{6}$$

assuming that unknown quantities depend on one coordinate $\xi = m \cdot r$, where m is the unit vector in the direction of the wave propagation. In elastic-viscoplastic and viscoelastic media waves of the elastic displacements

$$U_n = a_n \exp(ik_n\xi) + b_n \exp(-ik_n\xi) \tag{7}$$

propagating in elastic-viscoplastic and viscoelastic media determine the dynamics of components of the dislocation flux density tensor given on the wave front

$$I_{\xi n} = (\rho\omega/Bk_n)[a_n \exp(ik_n\xi) + b_n \exp(-ik_n\xi)] \tag{8}$$

Here ω is the frequency, k_n is the wave vector, a_n, b_n are constants, n=1, 2, 3. Wave propagation velocities for the elastic displacements (7) and the components of the dislocation flux density tensor (8) are determined by velocities of elastic waves and the corresponding loss factors which are connected with the refraction and absorption coefficients. In viscoelastic medium these values are

$$V_1 = \omega/k_1 = C_1\sqrt{1 - itgd_1}, V_2 = \omega/k_2 = C_2\sqrt{1 - itgd_2}, where \tag{9}$$

$$tgd_1 = \omega(\gamma + 2\nu)/(\lambda + 2\mu), tgd_2 = \omega\nu/\mu \tag{10}$$

are the loss factors $C_1 = \sqrt{(2\mu + \lambda)/\rho}$, $C_2 = \sqrt{\mu/\rho}$ are the velocities of elastic waves λ, μ are Lame coefficient γ, ν are the bulk and shear viscosities of the elastic solid. If the viscosity coefficients tensor of the elastic-viscoplastic medium (4) is determined by one constant, the wave propagation velocities are defined as

$$V_1 = C_1\sqrt{1 - itgd}, V_2 = C_2\sqrt{1 - itgd}, \tag{11}$$

where

$$tgd = \eta/(B\omega).$$

The dynamics of components of dislocation flux density tensor given on the plane parallel with the direction of the wave propagation $I_{\varphi i}$ ($\varphi \neq \xi$) is determined by the sum of two waves, excluding the one component.

$$I_{\varphi\xi} = g_1(q_1)exp(\pm ik\xi) + \frac{\omega^3\rho}{Sk_2(k^2-k_2^2)}a_2(-b_2)exp(\pm ik_2\xi)$$

$$I_{\varphi\varphi} = g_2(q_2)exp(\pm ik\xi) + \frac{\omega^3\rho k_1}{Sk_4^2(k^2-k_1^2)}a_1(-b_1)exp(\pm ik_1\xi) \tag{12}$$

$$I_{\varphi\zeta} = g_3(q_3)exp(\pm ik\xi)$$

where g_n, q_n are constants, n=1, 2, 3. New notations introduced in expressions (12) for viscoelastic medium are defined by

$$k_4 = \frac{\omega}{V_4} = \frac{\omega}{C_4\sqrt{1-itgd_4}}, C_4 = \sqrt{\frac{\lambda}{\rho}}, tgd_4 = \frac{\omega\gamma}{\lambda}, k = \frac{\omega}{C} = \frac{\omega B}{S} \tag{13}$$

Similar expressions have been found in the case of elastic-viscoplastic medium

$$I_{\varphi\xi} = g_1(q_1)exp(\pm ik\xi) + \frac{1}{(1-C^2/C_2^2)}a_2(-b_2)exp(\pm ik_2\xi)$$

$$I_{\varphi\varphi} = g_2(q_2)exp(\pm ik\xi) + \frac{C_4^2}{(C_1^2-C^2)}a_1(-b_1)exp(\pm ik_1\xi) \tag{14}$$

$$I_{\varphi\zeta} = g_3(q_3)exp(\pm ik\xi),$$

here

$$k = \omega/V = \omega/(C\sqrt{1-itgd}). \tag{15}$$

With regard to the components of the dislocation density tensor, from the first kinematical identity in (1) it follows that $\alpha_{\xi i} \equiv 0$. The remaining components of the dislocation density tensor can be obtained on the basis of the second identity from (1) and the components of the dislocation flux density tensor derived in (12), (14).

4 Interface boundaries

The derived wave solutions allow us to investigate the wave structure and features of the relationship between elastic waves and the defects field waves, which determine plastic deformation. The study of wave structure and relationship between various types of waves is important for a number of reasons. One of them is that results of this investigation are necessary for the analysis of propagation of defect field waves through the interface boundary between two media. The importance of this problem is governed by the fact that various media in nature often contain interfaces and many known results evidence of the special role of boundaries in deformation processes.

Let us consider the particular case of normal incidence of the wave on the interface. Using the system of boundary conditions for the components of displacement vector ($|m\cdot\vec{U}| = 0, |m\cdot\sigma| = 0$)we can obtain the expressions for reflection and refraction coefficients

$$R_n = \frac{a_n^-}{a_n^0} = \frac{\rho^-V_n^- - \rho^+V_n^+}{\rho^-V_n^- + \rho^+V_n^+}, Y_n = \frac{a_n^+}{a_n^0} = \frac{2\rho^-V_n^-}{\rho^-V_n^- + \rho^+V_n^+} \tag{16}$$

which connect the amplitude of incident wave with the amplitudes of reflected and refracted waves. Here and on the superscripts "$-, +, 0$" denote the reflected, refracted and incident wave and n=1,

2, 3. Corresponding Fresnel coefficients of the components of dislocation flux density tensor (8) are written as

$$R_{\xi n} = \frac{a_n^-}{a_n^0} = R_n, Y_{\xi n} = \frac{B^- V_n^+ \rho^+}{B^+ V_n^- \rho^-} Y_n \tag{17}$$

As regards to the components in the plane of wave propagation (12), (14), it is straightforward to derive Fresnel coefficients of components $I_{\varphi\zeta}$ on the basis of boundary conditions $|m \times I| = 0, |S(m \times \alpha| = 0$

$$R_{\varphi\zeta} = \frac{g_3^-}{g_3^0} = \frac{S^- k^- - S^+ k^+}{S^- k^- + S^+ k^+}, Y_{\varphi\zeta} = \frac{g_3^+}{g_3^0} = \frac{2S^- k^-}{S^- k^- + S^+ k^+} \tag{18}$$

For components $I_{\varphi\xi}, I_{\varphi\varphi}$ representing the sum of two harmonics, the analytical expressions for reflection and refraction coefficients can be found only approximately, for instance, in the framework of slowly varying amplitude approach [5]. Consider for example the component $I_{\varphi\xi}$ determined by wave vectors k and k_2. By introduction of the average wave vector $< k_2 >= (k + k_2)/2$ and the residual $\delta k_2 = k - k_2$, vectors k and k_2 take the form

$$k =< k_2 > +\delta k_2/2, k_2 =< k_2 > -\delta k_2/2. \tag{19}$$

Applying (19), the expression of the component $I_{\varphi\xi}$ can be written as

$$I_{\varphi\xi}(\xi, t) = \psi_{\varphi\xi}(\xi) exp(-i\omega t + i < k_2 > \xi), \tag{20}$$

where

$$\psi_{\varphi\xi}(\xi) = q_1 e^{-i\delta < k_2 > \xi/2} + \frac{\omega^3 \rho}{S(2 < k_2 > -\delta k_2) < k_2 > \delta k_2} a_2 e^{i\delta < k_2 > \xi/2}$$

is the coordinate-dependent amplitude. The approach of slowly varying amplitude assumes that the amplitude (20) is almost constant and its derivative is almost zero $\partial\psi_{\varphi\xi}(\xi) = 0$. It holds when $\delta k_2 \to 0$. The corresponding component of the dislocation density tensor takes the form

$$\alpha_{\zeta\xi}(\xi, t) =< k_2 > I_{\varphi\xi}(\xi, t)/\omega \tag{21}$$

Boundary conditions described for components (20), (21)

$$\psi_{\varphi\xi}^0 - \psi_{\varphi\xi}^- = \psi_{\varphi\xi}^+, \psi_{\varphi\xi}^0 + \psi_{\varphi\xi}^- = \frac{S^+ < k_2 >^+}{S^- < k_2 >^-} \psi_{\varphi\xi}^+,$$

allow us to obtain Fresnel coefficients as functions of the average wave vector

$$R_{\varphi\xi} = \frac{S^- < k_2 >^- - S^+ < k_2 >^+}{S^- < k_2 >^- + S^+ < k_2 >^+}, Y_{\varphi\xi} = \frac{2S^- < k_2 >^-}{S^- < k_2 >^- + S^+ < k_2 >^+} \tag{22}$$

Expressions (22), which are resembling (18), will also hold for components $I_{\varphi\varphi}$, $\alpha_{\zeta\varphi}$, when substituted with the average wave vector $< k_1 >= (k + k_1)/2$.

5 Results and discussion

On the basis of expressions (16), (17) and (22) we have determined the real and imaginary parts of the considered quantities, their modules and arguments. Dependencies of reflection and refraction coefficients of displacement vectors on the ratio of elastic impedances of the contacting media $p_n = \rho^+ C_n^+ / \rho^- C_n^-$ and the loss factors tgd_n^-, tgd_n^+ have been analyzed. It is established that in case of an equal values of loss factors

$$Re(R_n) = \frac{1 - p_n}{1 + p_n}, Re(Y_n) = \frac{2}{1 + p_n}, Im(R_n) = Im(Y_n) = 0. \tag{23}$$

Relations (23) are also correct at zero values of loss factors corresponding to interface boundary between two elastic media. It is known that in the medium characterized by small loss factors $tgd_n \ll 1$ weakly damping waves can propagate [6]. In the case of $tgd_n \gg 1$ the wave process does not occur since the waves are completely damped at very small distances compared to the wave length. The limit values of R_n, Y_n have been determined: $Re(R_n) = 1, Re(Y_n) = 2, Im(R_n) = Im(Y_n) = 0$ at $p_n \to 0$ and $Re(R_n) = 1, Re(Y_n) = 0, Im(R_n) = Im(Y_n) = 0$ at $p_n \to \infty$. Results of numerical calculations of (16) at $p_n = 0.5, 0.9, 1.1, 0.5$ and tgd_n^-, tgd_n^+ varying from 0 to 2 have shown that at $p_n < 1$ the loss factor of the first medium has a larger influence on the value of modulus R_n, which is at its maximum value when tgd_n^- is maximum and $tgd_n^+ = 0$ Fig.1(a). At $p_n > 1$ the influence of loss factors on $|R_n|$ is inverse: maximum $|R_n|$ is reached when tgd_n^+ is maximum and $tgd_n^- = 0$ Fig.1(b). At $p_n \approx 1$ the functional dependence of modulus of reflection coefficient R_n on the loss factors is nearly symmetrical.

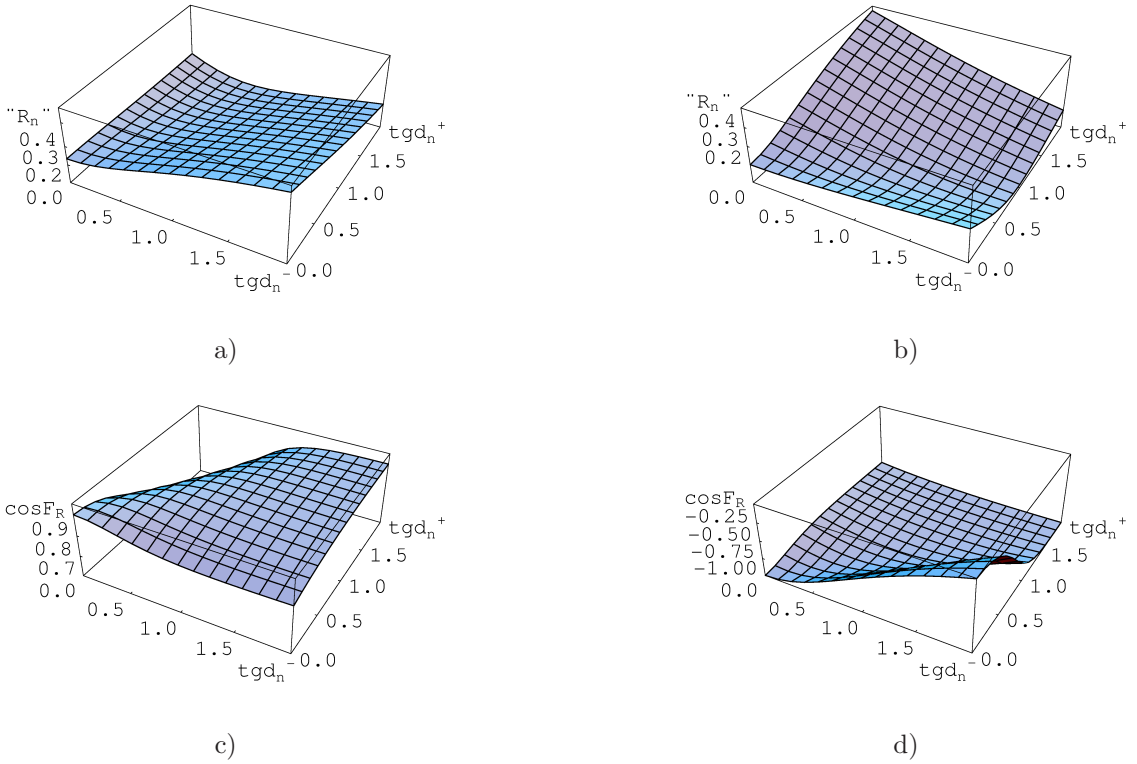


Figure 1: Reflection coefficients of displacement vectors at $p_n < 1$ (a, c) and $p_n > 1$ (b, d)

The ratio of elastic impedances of contacting media p_n does not have an influence on the qualitative dependence of modulus of the refraction coefficient of displacement components Y_n on the values of tgd_n^-, tgd_n^+. At any value p_n absolute magnitude Y_n increases with the increasing tgd_n^- and decreases with the increasing tgd_n^+ Fig.2(a, b). Maximum $|Y_n|$ reached at the largest tgd_n^- and $tgd_n^+ = 0$ decreases with the increase of p_n.

Dependencies of the cosine of R_n argument ($\cos F_R$) on the loss factors have different sign at $p_n < 1$ and $p_n > 1$ Fig.1(c, d). Variation interval of $\cos F_R$ increases with the increasing p_n at $p_n < 1$ and decreases at $p_n > 1$. The character of distribution of the cosine of Y_n argument ($\cos W_Y$) practically does not depend on p_n Fig.2(c, d). In the case of equal loss factors $tgd_n^- = tgd_n^+$ $\cos W_Y = 1$, and $W_Y = 0$, the maximum deviation from zero of argument W_Y occurs at $tgd_n^- = 2, tgd_n^+ = 0$ and at $tgd_n^- = 0, tgd_n^+ = 2$.

Results for components $I_{\xi n}$ can be analyzed on the basis of expressions

$$R_{\xi n} = R_n, Y_{\xi n} = Y_n(p_n/b)T_n, \tag{24}$$

where $T_n = \sqrt{(1 - itgd_n^+)/(1 - itgd_n^-)} = |T_n|exp(i\Phi_T)$. As it follows from (24) the refraction

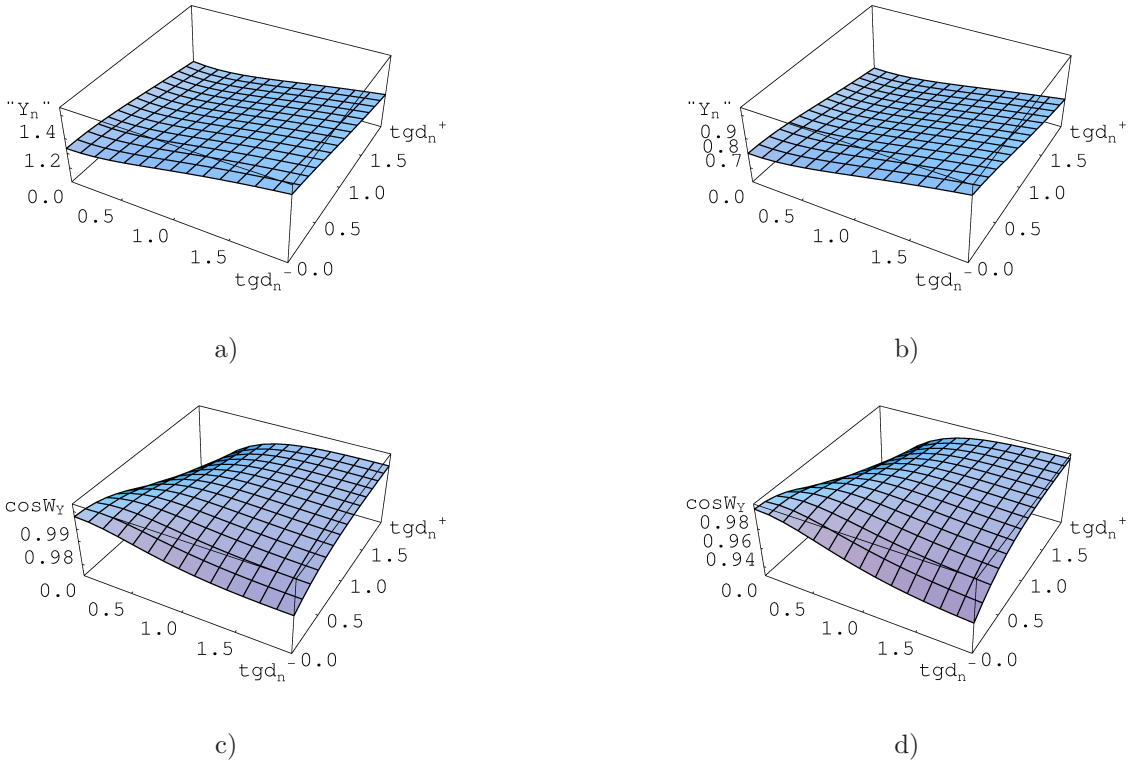


Figure 2: Refraction coefficients of displacement vectors at $p_n < 1$ (a, c) and $p_n > 1$ (b, d)

coefficients of the components of dislocation flux density tensor on the wave front $Y_{\xi n}$ coincide with the same components of displacement vector with accuracy to a certain coefficient, which is determined by the ratio of elastic impedance and constants characterizing the inertia of dislocation ensemble ($b = B^+/B^-$) and the function T_n. Maximum value of $|T_n|$ is reached at maximum tgd_n^+, $tgd_n^- = 0$, minimum $|T_n|$ is at maximum tgd_n^-, $tg_n^+ = 0$. Same values loss factors correspond to the largest deviation of T_n argument from zero. Dependencies of the modulus of $Y_{\xi n}$ and cosine of arguments $W_{\xi n}$ are similar to $|T_n|$ and $\cos\Phi_T$ at different values of contacting media parameters.

Fresnel coefficients of the components $I_{\varphi\xi}, I_{\varphi\varphi}$ in viscoelastic medium can be written in the form

$$R_{\varphi n} = \frac{1 - s/c + D_i^-/c_i^- - sD_i^+/c_i^+ + i(G_i^-/c_i^- - sG_i^+/c_i^+)}{1 + s/c + D_i^-/c_i^- + sD_i^+/c_i^+ + i(G_i^-/c_i^- + sG_i^+/c_i^+)}$$

$$Y_{\varphi n} = \frac{2(1/c_i^- + D_i^-/c_i^- + iG_i^-/c_i^-)}{1 + s/c + D_i^-/c_i^- + sD_i^+/c_i^+ + i(G_i^-/c_i^- + sG_i^+/c_i^+)}, \tag{25}$$

where

$$D_i^{\pm} = \sqrt{\frac{\sqrt{1 + (tgd_i^{\pm})^2} + 1}{2(1 + (tgd_i^{\pm})^2)}}, G_i^{\pm} = \sqrt{\frac{\sqrt{1 + (tgd_i^{\pm})^2} - 1}{2(1 + (tgd_i^{\pm})^2)}},$$

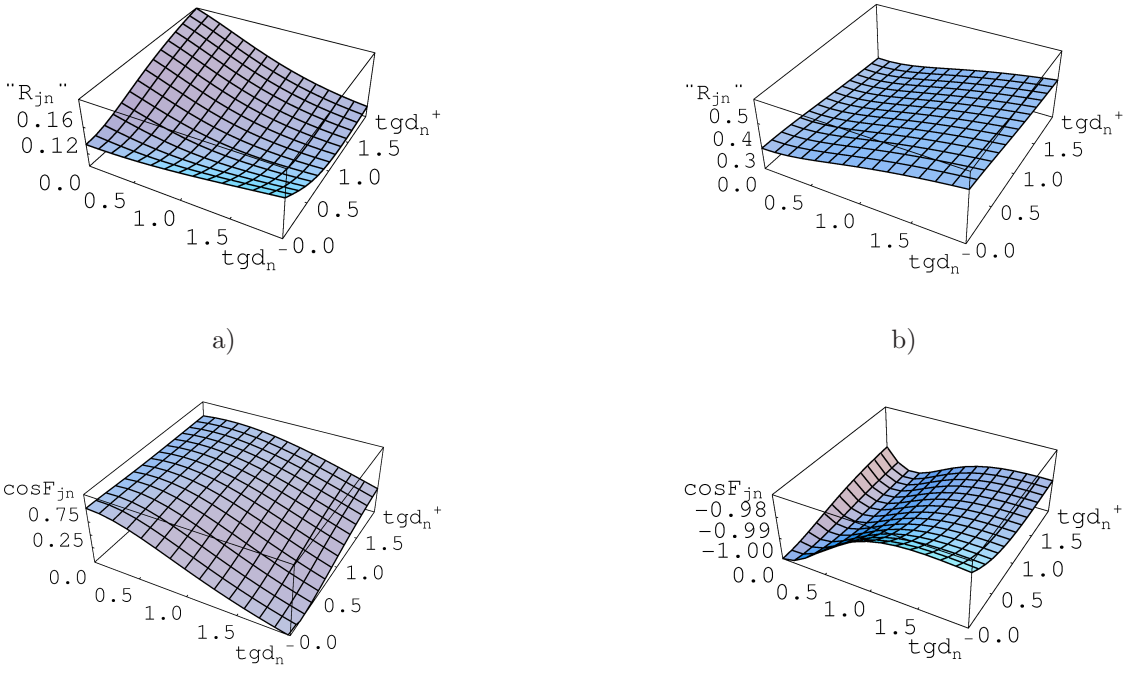
$s = S^+/S^-, c = C^+/C^-, c_i^+ = C_i^+/C^-, c_i^- = C_i^-/C^-$ at n=1 i=2, at n=2 i=1. These expressions can be simplified in the case of small loss factors $tgd_i^{\pm} << 1$, $D_i^{\pm} = 1$, $G_i^{\pm} = 0$ and in the case of equal ones $tgd_i^- = tgd_i^+$, and $D_i^{\pm} = D_i$, $G_i^{\pm} = G_i$. As opposed to Fresnel coefficients for the displacement components, these variables do depend on the loss factor values in case of equal ones. Reflection and refraction coefficients (25) have been investigated at $s < 1$ and $s > 1$. In both cases it is assumed that velocities of elastic waves are higher than velocities of the defect field waves, which determine plastic deformation, $c_i^+ > c, c_i^- > c$. Ratio between elastic waves velocities in the contacting media can be different, both cases $c_i^+ > c_i^-$ and $c_i^+ < c_i^-$ were considered.

It has been established that the qualitative character of dependencies of modulus $Y_{\varphi n}$ and cosine $W_{\varphi n}$ on the loss factors represented in Fig.3(a, b) does not depend on the variation of the media parameters.



a) b)

Figure 3: Refraction coefficients of the components of dislocation flux density tensor in the plane of wave propagation



a) b)

c) d)

Figure 4: Reflection coefficients of the components of dislocation flux density tensor in the plane of wave propagation at $s < 1$ (a, c) and at $s > 1$ (b, d)

At any ratio of elastic velocities, modulus of $R_{\varphi n}$ increases with the increasing tgd_i^- at $s > 1$ and gets its maximum at the maximum value of tgd_i^- and $tgd_i^+ = 0$; it stays constant at $s < 1$, $c_i^- > c_i^+$ and rapidly changes behavior at $s < 1$, $c_i^- < c_i^+$ Fig.4(a, b). Maximum value of $|R_{\varphi n}|$ at $s < 1$ and $c_i^- < c_i^+$ is reached at the highest tgd_i^+ and $tgd_i^- = 0$. Qualitatively and quantitatively similar character of the dependencies of $\cos F_{\varphi n}$ changes a little in the domain of small values of tgd_i^- at $s < 1$ and $c_i^- > c_i^+$ and changes cardinally at $s < 1$, $c_i^- < c_i^+$ Fig.4(c, d). If velocity of dislocation continuum in both media or only in the second one is decreased by an order of

magnitude for the same values of elastic wave velocities, then in the first case calculated reflection and refraction coefficients are similar to ones at $s > 1$ and in the second case these coefficients do not depend on tgd_i^+.

These are the first results of investigation of the plastic deformation propagation across the boundary between viscoelastic and elastic-viscoplastic media, which will be necessary for the future analyses of the waves of defect field passing through a layer and can be applied for non-destructive testing of materials and in seismic interpretation, where the dynamic effects of inelastic deformation determined by the defect structure of materials are important.

Acknowledgements

The study is supported by the Russian Foundation for Basic Research project No 09-01-00264a

References

[1] J. Friedel. Dislocation. Pergamon Press, Oxford,1964.

[2] R.D. Wit. Continual theory of dislocations and stresses. Mir, Moscow, 1977.

[3] A. Kadic, D. Edelen. A gauge theory of dislocation and disclinations. Springer-Verlag, Berlin, 1983.

[4] N.V. Chertova. Int. J. Engng.Sci.1995, V.33, No 9, P.1315-1319.

[5] N.N. Bogolyubov, Yu.A. Mitropolskii. Asymptotically methods in the theory of nonlinear oscillation. Nauka, Moscow, 1974.

[6] M.V. Vinogradova, O.V. Rudenko, A.P.Sukhorukov. Wave theory. Nauka, Moscow,1990.

Nadezhda V. Chertova , Akademicheskii pr. 2/4, Tomsk, 634021, Russia
Yurii V. Grinyaev, Akademicheskii pr. 2/4, Tomsk, 634021, Russia

Evolution of free surface of high viscous liquid due to capillary forces

S. A. Chivilikhin
sergey.chivilikhin@gmail.com

Abstract

We consider some exact results for Stokes flows of viscous liquid in the region $g \subset R^2$ with free multiply connected boundary of arbitrary shape. Taking in account the capillary forces and pressure inside of the bubbles, the strict limitations for the motion of the free boundary are obtained. In particular, the lifetime of the configurations with given number of the bubbles may be predicted.

1 Introduction

Two-dimensional Stokes flow with free boundary attracted the attention of many researches [1] - [4]. Full analytical description of this system is possible for special configurations of boundary only. But some limitations for free boundary dynamics can be obtained for arbitrary geometry of region. In [5] was investigated the dynamics of free boundary due to capillary forces. In this work we obtain some results for capillary force and inner pressure in bubbles. The equations of motion in the quasi-stationary Stokes approximation, the continuity equation and boundary conditions have the form:

$$\partial_\beta P_{\alpha\beta} = 0, \quad \partial_\beta V_\beta = 0, \quad \mathbf{x} \in \mathbf{g}, \tag{1}$$

$$P_{\alpha\beta} n_\beta = f_\alpha, \quad \mathbf{x} \in \boldsymbol{\gamma}, \tag{2}$$

where $P_{\alpha\beta} = -P\delta_{\alpha\beta} + \mu(\partial_\alpha V_\beta + \partial_\beta V_\alpha)$ is the Newtonian stress tensor; V_α, n_α and f_α are the components of the velocity, the vector of the outer normal to the boundary and surface force; P is the poressure, μ is the coefficient of the dynamic viscosity, with assumed constant. Summation over repeated indices is understood. Let γ_0 is the outer boundary of the region, $\gamma_k, k = 1, ..., m$ are the inner boundaries (boundaries of bubbles), $\gamma = \bigcup_{k=0}^{m} \gamma_k$.

The law of the free boundary evolution is determined from the condition of equality of normal velocity U of boundary and the normal component of the velocity of the liquid at the boundary:

$$U = V_\beta n_\beta, \quad \mathbf{x} \in \boldsymbol{\gamma}, \tag{3}$$

In the quasi-stationary case the liquid velocity at the given time depends on the form of the boundary at the same moment of time. In this work we get some apriority estimations of equation (3) solution with the initial condition

$$\gamma|_{t=0} = \gamma^0. \tag{4}$$

The equations of motion and continuity (1) and the boundary conditions (2) can be obtained from the variational principle

$$\delta \left[\frac{1}{4\mu} \int (P_{\alpha\beta} P_{\alpha\beta} - 2P^2) dg - \int f_\alpha V_\alpha d\gamma \right]. \tag{5}$$

2 Calculation of the pressure and velocity

Since (5) is valid for arbitrary variations of the pressure δP and velocity δV_α we choose there so that leave $P_{\alpha\beta}$ unchanged:

$$\delta P_{\alpha\beta} = -\delta P \delta_{\alpha\beta} + \mu(\partial_\alpha \delta V_\beta + \partial_\beta \delta V_\alpha) = 0. \tag{6}$$

In this case (5) give us

$$\frac{1}{\mu}\int P\delta P dg + \int f_\alpha \delta V_\alpha d\gamma = 0. \tag{7}$$

We introduce the one-parameter family of variations $\delta V_\alpha = \frac{1}{2\mu}\chi_\alpha \delta\epsilon$, $\delta P = \psi\delta\epsilon$. Then (6), (7) take the form

$$0.5(\partial_\alpha \chi_\beta + \partial_\beta \chi_\alpha) = \psi\delta_{\alpha\beta}, \tag{8}$$

$$\int P\psi dg = -0.5\int f_\alpha \chi_\alpha d\gamma. \tag{9}$$

These expressions are basic in our theory. Let's get (9) another way. We set in the region g the smooth fields χ_α and ψ where satisfy (8). Multiplying the equation of motion (1) by χ_α, integrating over region g and using (2), (8) we obtain (9).

According with (8), χ_α is a harmonic function and

$$d(\chi_1 + i\chi_2) = (\psi + i\omega)dz. \tag{10}$$

where ω is the harmonic function conjugate to ψ. Let ψ_k is complete set of harmonic functions in the region g. Using (10) we are obtaining the correspondent functions $\chi_{\alpha k}$.

Suppose $\mathbf{x} \in \mathbf{R^N}$. Then it follow from (8) that

$$(N-2)\partial_{\alpha\beta}\psi = 0. \tag{11}$$

Thus, only in two-dimensional case (8) is solvable for any harmonic function ψ. In terms of (6), it is only in two dimensional space that there exist the non-trivial system of pressure and velocity variations with goes to zero the stress tensor variation.

According with (1) the pressure P is a harmonic function. We present it in the form

$$P = \sum_k p_k \psi_k. \tag{12}$$

Using the expression (9) we obtain the algebraic system for coefficients p_k:

$$\sum_k \left(\int \psi_k \psi_n dg\right) p_k = -0.5\int f_\alpha \chi_{\alpha n}, \quad n = 0, 1, ... \tag{13}$$

The method, closed [6], gives us the expression for velocity in the boundary of region:

$$v_\alpha = \frac{1}{2\mu}\left(\int e_{\alpha\beta} f_\beta d\gamma_k - \Phi_\alpha\right), \quad \mathbf{x} \in \boldsymbol{\gamma}_\mathbf{k}, \tag{14}$$

where $e_{\alpha\beta}$ is the unit antisymmetric tensor,

$$0.5(\partial_\alpha \Phi_\beta + \partial_\beta \Phi_\alpha) = P\delta_{\alpha\beta}, \tag{15}$$

3 Limitations for the motion of the boundary

Let's take in account the capillary forces on the boundary, external pressure P_0 and pressure inside of bubbles $P_k = P_b$, $k = 1, 2, ...$ equal in every bubble. Then the boundary force has the form

$$f_\alpha = -\sigma n_\alpha \partial_\beta n_\beta - n_\alpha P_k, \tag{16}$$

where σ is the coefficient of surface tension. The rate of boundary perimeter L changing may be calculated as [6]:

$$\frac{dL}{dt} = -\int \frac{P + f_\beta n_\beta}{2\mu} d\gamma. \tag{17}$$

Using (16), (17) we get

$$\frac{dL}{dt} = -\frac{1}{2\mu}\left[\int P d\gamma - (P_0 L_0 + P_b L_b) + 2\pi\sigma(m-1)\right], \tag{18}$$

where L_0 and L_b are the perimeter of external boundary and summary perimeter of the bubbles correspondingly.

Let's use (9) for $\psi = 1$, $\chi_\alpha = x_\alpha$:

$$\int P dg = P_0 S + (P_0 - P_b) S_b + \frac{\sigma}{2} L, \tag{19}$$

where S and S_b are the area of region and the summary area of the bubbles.

For $\psi = P$, $\chi_\alpha = \Phi_\alpha$:

$$\int P^2 dg = P_0^2 S + (P_0^2 - P_b^2) S_b - \mu(P_0 - P_b)\frac{dS_b}{dt} + \frac{\sigma}{2}\left(P_0 L_0 + P_b L_b + \int P d\gamma\right). \tag{20}$$

Using (18) - (20) and inequality $\int P^2 dg \geq \frac{1}{S}(\int P dg)^2$ we obtain the differential inequality

$$\begin{aligned} &\mu\left[\sigma\frac{dL}{dt} + (P_0 - P_b)\frac{dS_b}{dt}\right] \leq -(P_0 - P_b)[\sigma L_b + (P_0 - P_b) S_b] - \\ &- \frac{1}{S}\left[(P_0 - P_b) S_b + \frac{\sigma}{2} L\right]^2 - \pi\sigma^2(m-1). \end{aligned} \tag{21}$$

This expression gives us to possibility to obtain the strict limitations for the motion of the free boundary in some special cases.

a. The influence of capillary forces only $P_0 = P_b$. In this case the last inequality may be simplified:

$$\frac{dL}{dt} \leq -\frac{\sigma}{2\mu}\left[\frac{L^2}{2S} + 2\pi(m-1)\right]. \tag{22}$$

Let $L_\infty = 2\sqrt{\pi S}$ is the asymptotic value of the perimeter; $\lambda = L/L_\infty$ and $\tau = \dfrac{\sigma t}{2\mu}\sqrt{\dfrac{\pi}{S}}$ are the dimensionless perimeter of region and dimensionless time. Then, according to (22)

$$\begin{cases} (\lambda_0 + th(\tau))/(1 + \lambda_0 th(\tau)), & m = 0 \\ \lambda_0/(1 + \lambda_0\tau), & m = 0 \\ \dfrac{\sqrt{m-1}(\lambda_0 - \sqrt{m-1}tg(\sqrt{m-1}\tau))}{\sqrt{m-1} + \lambda_0 tg(\sqrt{m-1}\tau)}, & m \geq 2. \end{cases} \tag{23}$$

Therefore, if we have no bubbles in the region, the characteristic dimensionless time of relaxation of the boundary to the circle $\tau_0 \leq 1$. In case of one bubble ($m = 1$), the bubble must be closed or break on the two bubbles in time $\tau_* \leq 1 - 1/\lambda_0$. In case of $m > 2$ bubbles, such configuration will exist during the time

$$\tau_* \leq \frac{1}{\sqrt{m-1}} arctg\left(\frac{\sqrt{m-1}(\lambda_0 - 1))}{\lambda_0 + m - 1}\right). \tag{24}$$

b. The infinite region. The outer boundary of the region is the circle with large radius R. The bubbles localized around of center of circle. Using the expressions $\S = \pi R^2 - S_b$, $L = 2\pi R + L_b$, we can see the inequality (21) in the limit $R \to \infty$ takes the form

$$\mu \frac{dW}{dt} \leq -(P_0 - P_b)W - \pi\sigma^2 m, \tag{25}$$

where $W = -\sigma L_b + (P_0 - P_b)S_b$. Therefore, at $P_0 - P_b > 0$

$$W + \frac{\pi\sigma^2 m}{P_0 - P_b} \leq \left(W(0) + \frac{\pi\sigma^2 m}{P_0 - P_b}\right) exp\left(-\frac{P_0 - P_b}{\mu}t\right). \tag{26}$$

This configuration exist without changing of bubbles number during the time

$$t_* \leq \frac{\mu}{P_0 - P_b} \ln\left[1 + \frac{P_0 - P_b}{\pi\sigma^2 m}(\sigma L_b(0) + (P_0 - P_b)S_b(0))\right]. \tag{27}$$

Acknowledgements

The work is supported by grant 2.1.1/4215 of the program "Development of the potential of high school of Russia 2009-2010".

References

[1] Ionesku D.G. Theory of analytic functions and hydrodynamics. In: Applications of the theory of functions in the mechanics of continuous media. V.2. Mechanics of liquids and gases [in Russian]. Nauka. Noscov. 1965.

[2] Voinov O.V. Asymptotic behavior of the free surface of a viscous fliod in creeping motion and dependence of the boundary wetting angle on the velocity. Dokl. Acad. Nauk SSSR. 243. 1422. 1978.

[3] Antonovskii L.K. Dynamics of an interface under the effect of capillary forces. Quasi-stationary plane-parallel flow. Prikl. Mekh. Tekh. Fiz. 3. 1988.

[4] Hopper R.W. Plane Stokes flow driven by capillarity on free surface. J. Fluid Mech. 213. P.349. 1990.

[5] Chivilikhin S.A. Dynamics of multiply connected free surface of a fiscous liquid. Dokl. Acad. Nauk SSSR. 315. 3. 1990

[6] . N. I. Muskhelishvilli. Basic problems in the mathematical theory of elasticity [in Russian]. Nauka. Moscov. 1966

S.A.Chivilikhin, St.-Petersburg State University of Information Technologies, Mechanics and Optics, Kronverkskiy, 49, St.-Petersburg, 197101, Russia

The stressedly-deformed state of porous burner apparatus under different gas filtration combustion regimes

Yurii A. Chumakov Anna G. Knyazeva
yura014@rambler.ru

Recently, the porous radiation burner began the widespread use .This technology differs from conventional combustion processes that natural fuel combustion takes place in the special heat generators made of metal meshes, porous and metal ceramic. The improvement properties of same heat-generators are not exhaust now. Partially, the heat-generator properties may be improved to operate the gas combustion regimes by changing of physicochemical, structural and composition properties used porous body.

To optimize operation of existing burners and develop new options, it is necessary to study possible regimes of gas combustion with variations of technological parameters (including geometric parameters).It is rather difficult to vary the parameters within wide limits in experimental research. Therefore, mathematical modeling is often used to study various combustion regimes. Mathematical modeling is also necessary to determine the range of allowable parameters to optimize and design of radiation burner.

The material burner strength properties have not been clearly studied now. Therefore, the production of heat-generators based on diffusion combustion device need to additional theoretical and experimental investigation.

In this work the nonstationary gas combustion model in cylindrical hollow burner is studied.

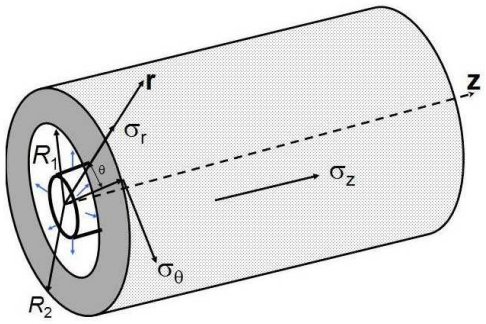


Figure 1: Burner scheme

In experimental conditions [1], a combustible gas enters the inner volume of the cylinder to internal of cylinder (The inner (R_1) and outer (R_2) radii and porosity m of the porous body of the burner are set in advance fig.1)) and is then redistributed by special devices so that the velocity of the gas V_g entering the porous body over the entire burner length (along the cylinder) is approximately identical. A heat propagates through the porous layer by gas and solid heat conductivity, and also by gas flow heat convective transport. Due to higher solid carcass heat conductivity the internal gas temperature differs from that of fresh gas [2]. This fact may be considered as the assumption that heat-exchange between fresh gas and internal solid wall take place under Newton's heat-exchange conditions. We consider chemical conversations in gas are described by the overall reaction scheme "reagent-product"

Under the assumptions made, the mathematical formulation of the problem in a cylindrical coordinate system includes the equations of heat conduction for the gas and the solid:

Under the assumptions made, the mathematical formulation of the problem in a cylindrical coordinate system includes the equations of heat conduction for the gas and the solid:

$$c_g\rho_g\left(\frac{\partial T_g}{\partial t}+V_g\frac{\partial T_g}{\partial r}\right)=\frac{1}{r}\frac{\partial}{\partial r}\left(\lambda_g r\frac{\partial T_g}{\partial r}\right)-\frac{\alpha}{m}\left(T_g-T_S\right)+\rho_g Q\phi\left(\eta,T_g\right), \tag{1}$$

$$c_s\rho_s\frac{\partial T_s}{\partial t}=\frac{1}{r}\frac{\partial}{\partial r}\left(\lambda_s r\frac{\partial T_s}{\partial r}\right)+\frac{\alpha}{1-m}\left(T_g-T_S\right), \tag{2}$$

equation of diffusion in the gas phase with convective terms and heat and mass sources owing to the chemical reaction

$$\rho_g\left(\frac{\partial \eta}{\partial t}+V_g\frac{\partial \eta}{\partial r}\right)=\frac{1}{r}\frac{\partial}{\partial r}\left(D\rho_g r\frac{\partial \eta}{\partial r}\right)-\rho_g\phi\left(\eta,T_g\right), \tag{3}$$

equation of continuity:

$$\frac{\partial \rho_g}{\partial t}+V_g\frac{\partial \rho_g}{\partial r}+\frac{\rho_g}{r}\frac{\partial}{\partial r}\left(rV_g\right)=0. \tag{4}$$

In the case of incompressible gas we use

$$\frac{\partial \rho_g}{\partial t}+V_g\frac{\partial \rho_g}{o}r\partial r=0 \quad \nabla\cdot\vec{V}_g=0$$

instead of (4).

The creeping flow motion equation may be used for low velocity V_g

$$\rho_g\frac{\partial V_g}{\partial t}=-\frac{\partial p}{\partial r}-\frac{\mu s}{k}V_g. \tag{5}$$

The gas pressure in the pores and its temperature are assumed to be uniquely related by the equation of state. The equation of state of an ideal gas is often assumed to be valid for such models in publications. We write the equation in the form

$$p=\frac{\rho_g R T_g}{m_r\eta+(1-\eta)m_p} \tag{6}$$

In (1)-(6) T_g is the temperature of the gas mixture, T_s is the temperature of the porous skeleton, m_r and m_p are the mole weights of the reagent and reaction product, η is the fraction of the reagent, t is the time, r is the spatial coordinate, λ_g and λ_s are the effective thermal conductivities of the gas and solid, respectively, α is the coefficient of interphase (internal) heat transfer, c_g and c_s are the specific heat of the gas at constant volume and the specific heat of the solid body, ρ_g and ρ_s are the densities of the gas and the solid skeleton, Q is the thermal effect of the overall reaction in the gas phase, $k$is the rate constant, $n$is the order of the reaction, E_a is the activation energy, $R$is the universal gas constant, and D is the diffusion coefficient, k is the penetrability of material, μ is the gas viscosity, s is the sponginess, $\phi\left(\eta,T\right)=k_0\cdot\eta^n\exp(E_a/(RT))$

The model is closed by initial and boundary conditions.

We consider gas and temperature are given, reactant concentration equal 1, gas pressure equal excess pressure of injection gas, density follow from equation of state (6) in initial time.

$$t=0: T_g(r,0)=T_s(r,0)=T_0, \eta=1,\ V_g(r,0)=0,\ \mathrm{P}=\mathrm{P}_0, \rho=(P_0 m_p)/(RT_0). \tag{7}$$

The ignition process of methane-air mixture is considered to initiate by action of hot solid wall with temperature T_i during time t_i. In a real burner [1], the outer surface of the skeleton is heated to high temperatures and starts radiation , which ensures heat transfer with the heat exchanger. Heating of the outer surface ($r=R_2$) can be caused both by intense heat exchange inside the porous burner and by heat exchange between the outer surface of the porous body and the gas

(combustion products), which is turbulized at the exit from the working body and ensures a high value of the external heat-transfer coefficient. With allowance for that, the boundary conditions for system (1-5) acquire the form $r = R_2 : \eta = 0, p = p_e$.

$$\begin{aligned}
&t \le t_i : T_g\left(R_2, t\right) = T_s\left(R_2, t\right) = T_i \\
&t > t_i : \quad -\lambda_g \frac{dT_g}{dr} = \alpha_{e,g}\left(T_g - T_b\right),\ -\lambda_s \frac{dT_s}{dr} = \alpha_{e,s}\left(T_s - T_b\right) + \varepsilon_0 \sigma\left(T_s^4 - T_h^4\right). \\
&r = R_1 : -\lambda_g \frac{\partial T_g}{\partial r} = c_g \rho_g V_g (T_g - T_0),\ -\lambda_s \frac{\partial T_s}{\partial r} = \alpha_{e,s}(T_s - T_0),\ \eta = 1,\ p = p_0, \\
&\rho_g = \frac{p_0(m_r \eta + (1-\eta) m_p))}{R T_g}, V_g = \frac{A}{R_1 \rho_g}
\end{aligned} \tag{8}$$

Here T_0 is the initial temperature, p_0 is the initial pressure, T_b is the gas temperature at the exit from the porous body (burning temperature of the gas), $\alpha_{e,g}$and $\alpha_{e,s}$ are the coefficients of heat transfer between the gas in the burner and combustion products and between the solid and combustion products, respectively ($\alpha_{e,s} >> \alpha$), η_b is the remaining fraction of the reagent, ε_0 is the emissivity, σ is the Stefan-Boltzmann constant, T_h is the heat-exchanger temperature.

In dimensionless variables

$$\theta = \frac{T - T_*}{R T_*^2} E_a;\ \xi = \frac{r}{R_2};\ \tau = \frac{t}{t_*};\ \pi = \frac{p}{p_*};\ u = \frac{V_g}{V_{g*}}, \omega = \frac{\rho_g}{\rho_*}, \theta_g = \frac{T_g - T_*}{R T_*^2} E_a,$$

$$\theta_s = \frac{T_s - T_*}{R T_*^2} E_a, s_r = \frac{\sigma_r}{\sigma_*}; s_\theta = \frac{\sigma_\theta}{\sigma_*};\ s_z = \frac{\sigma_z}{\sigma_*};\ e_r = \frac{\varepsilon_r}{\varepsilon_*};\ e_\theta = \frac{\varepsilon_\theta}{\varepsilon_*}$$

the system (1)-(9) has a form

$$\frac{\partial \theta_g}{\partial \tau} + m \cdot \omega \cdot u \frac{\partial \theta_g}{\partial \xi} = \delta^{-1} \frac{1}{\xi} \frac{\partial}{\partial \xi}\left(\xi \frac{\partial \theta_g}{\partial \xi}\right) - \frac{Bi}{m}\left(\theta_g - \theta_s\right) + m\omega \cdot \phi\left(\theta_g, \eta\right), \tag{9}$$

$$K_c \frac{\partial \theta_s}{\partial \tau} = \frac{K_\lambda}{\delta} \frac{1}{\xi} \frac{\partial}{\partial \xi}\left(\xi \frac{\partial \theta_s}{\partial \xi}\right) + \frac{Bi}{1-m}\left(\theta_g - \theta_s\right), \tag{10}$$

$$\frac{\partial \eta}{\partial \tau} + u \frac{\partial \eta}{\partial \xi} = \delta^{-1} Le \frac{1}{\xi} \frac{\partial}{\partial \xi}\left(\xi \frac{\partial \eta}{\partial \xi}\right) - \gamma \cdot \phi\left(\theta_g, \eta\right) \tag{11}$$

$$\frac{\partial \omega}{\partial \tau} + u \frac{\partial \omega}{\partial \xi} + \frac{\omega}{\xi} \frac{\partial}{\partial \xi}(\xi u) = 0 \tag{12}$$

or in the case of incompressible gas

$$\frac{\partial \omega}{\partial \tau} + u \frac{\partial \omega}{\partial \xi} = 0, (\nabla \cdot u = 0)$$

$$\pi = \frac{\pi_1 \omega\left(\beta\theta + 1\right)}{\left(\eta + (1-\eta)\mu_{pr}\right)}, \tag{13}$$

$$\omega \frac{\partial u}{\partial \tau} = -\frac{\partial \pi}{\partial \xi} - K_f u \tag{14}$$

$$\tau = 0 : \theta_g = \theta_s = -\theta_0, \eta = 0, u = 0, \omega = \frac{\pi_0 \mu_{pr}}{\pi_1\left(1 - \beta\theta_0\right)}, \tag{15}$$

$$\xi = \xi_1 : \quad \frac{\partial \theta_g}{\partial \xi} = \delta u \omega(\theta_g + \theta_0), \frac{\partial \theta_s}{\partial \xi} = \frac{Nu K_\alpha}{K_\lambda}(\theta_s + \theta_0),\ \eta = 1, \tag{16}$$

$$\pi = \pi_0, \omega = \frac{\pi\left(\eta + (1-\eta)\,\mu_{pr}\right)}{\pi_1 \theta}, \quad u = \frac{Pe}{\omega}$$

$$\xi = 1 : \ , \eta = \eta_e, \pi = \pi_e$$

$$\tau \le \tau_i \quad \theta_g\left(1, \tau\right) = \theta_s\left(1, \tau\right) = \theta_i \tag{17}$$

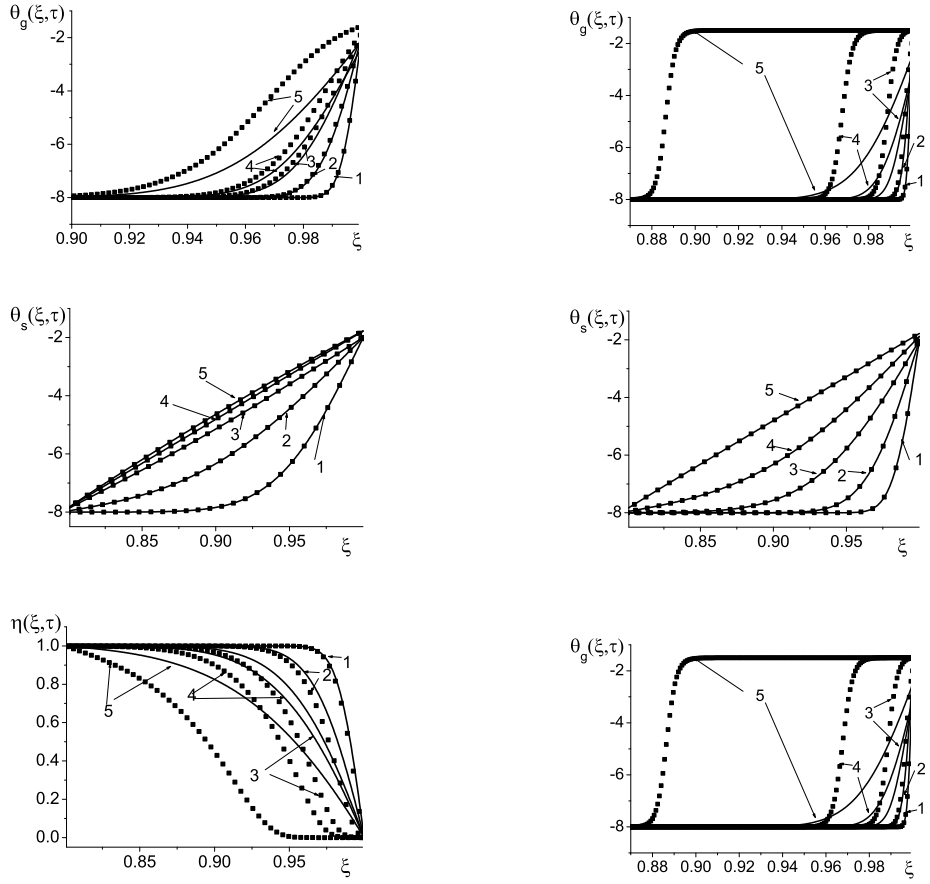


Figure 2: Distribution of gas (a) and solid (b) temperature, reactant concentration (c) along the burner radius τ_i= 0.1, θ_i=-2, θ_0=8, θ_b=1.5, θ_h=0.2, K_α=10;K_c=100;K_λ=100; K_f=8; Nu=220.5, Bi=0.01; ξ_1=0.8; β=0.12; π_0=2.54, π_e=2.44, π_1=1,μ_{pr}=0.99; Le=0.015 ;Pe=0.1. Left graphs: δ=10; τ = 1. 0.01; 2. 0.04; 3. 0.1; 4. 0.15; 5. 0.4. Right graphs: δ=100 τ = 1. 0.01; 2. 0.04; 3. 0.1; 4. 0.15; 5. 1.4

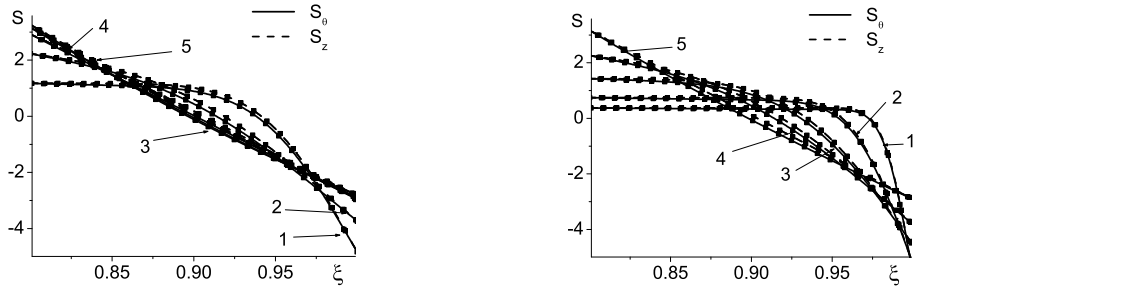
$$\tau > \tau_i \quad \frac{\partial \theta_g}{\partial \xi} = Nu(\theta_g + \theta_0) \qquad -\frac{\partial \theta_s}{\partial \xi} = \frac{NuK_\alpha}{K_\lambda}(\theta_s + \theta_b) + \frac{Sk}{\beta} \cdot \left[(\beta\theta + 1)^4 - \theta_h^4\right]$$

where $\phi(\theta_g, \eta) = \eta^n \exp\left(\frac{\theta}{1+\beta\theta}\right)$

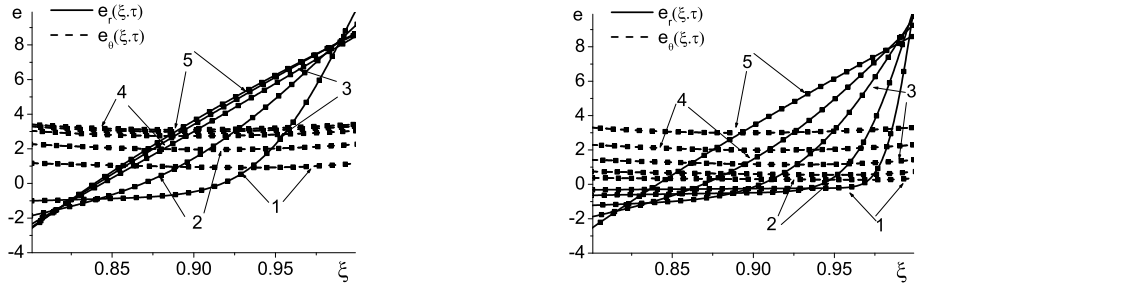
$$\xi_1 = \frac{R_1}{R_2}, \quad \delta = \frac{c_g R_2^2 \rho_*}{\lambda_g t_*}, \quad \gamma = \frac{RT_*^2 c_g}{E_a Q}, \quad \beta = \frac{RT_*}{E_a}, \quad K_c = \frac{c_s \rho_s}{c_g \rho_*}, \quad Le = \frac{Dc_g\rho_*}{\lambda_g},$$
$$K_a = \frac{\alpha_s}{\alpha_g}, \quad K_f = \frac{t_* \mu s}{\rho_* k}, \quad \mu_{pr} = \frac{m_p}{m_r}, \quad Nu = \frac{\alpha_g R_2}{\lambda_g}, \quad Sk = \frac{\varepsilon_0 \sigma R_2 T^3}{\lambda_g},$$
$$T_* = T_0 + \frac{Q}{c_g \rho_g}, \quad t_* = \frac{c_g R T_*^2}{E_a Q k_0} \exp\left(\frac{E_a}{RT_*}\right), \quad V_{g*} = \frac{R_2}{t_*}, \quad \theta_0 = \frac{T_* - T_0}{RT_*^2} E_a,$$
$$\theta_i = \frac{T_* - T_i}{RT_*^2} E_a, \theta_b = \frac{T_* - T_b}{RT_*^2} E_a, \quad \theta_h = \frac{T_h}{T_*}.$$

We used well-known solution of the problem on equilibrium of hollow cylinder (free on influence of external forces in which the distribution of temperature is given) for estimation thermal stress [4].

In accordance with the model of gas combustion described above, the skeleton temperature is independent of the axial coordinate and of the angle θ. The cylinder has a concentric (circular)



d



e

Figure 3: Stress (d) and strains (e) tensor components along the burner radius τ_i= 0.1, θ_i=-2, θ_0=8, θ_b=1.5, θ_h=0.2, K_α=10;K_c=100;K_λ=100; K_f=8; Nu=220.5, Bi=0.01; ξ_1=0.8; β=0.12; π_0=2.54, π_e=2.44, π_1=1,μ_{pr}=0.99; Le=0.015 ;Pe=0.1. Left graphs: δ=10; τ = 1. 0.01; 2. 0.04; 3. 0.1; 4. 0.15; 5. 0.4. Right graphs: δ=100 τ = 1. 0.01; 2. 0.04; 3. 0.1; 4. 0.15; 5. 1.4

hole. Then, the components of the stress tensor σ_r, σ_θ, and σ_z (see Fig. 1) differ from zero in a cylindrical coordinate system. All three shear strains and shear stresses are equal to zero by virtue of symmetry with respect to the axis and constant conditions in the axial direction. Then, in accordance with theory [3], in dimensionless variables we get

$$s_r = \frac{1}{\xi^2}\left[\frac{\xi^2-\xi_1^2}{1-\xi_1^2}\int\limits_{\xi_1}^{1}(\theta_s+\theta_0)\,xdx - \int\limits_{\xi_1}^{\xi}(\theta_s+\theta_0)\,xdx\right], \tag{18}$$

$$s_\theta = \frac{1}{\xi^2}\left[\frac{\xi^2+\xi_1^2}{1-\xi_1^2}\int\limits_{\xi_1}^{1}(\theta_s+\theta_0)\,xdx + \int\limits_{\xi_1}^{\xi}(\theta_s+\theta_0)\,xdx - (\theta_s+\theta_0)\,\xi^2\right] \tag{19}$$

$$s_z = \frac{2}{1-\xi_1^2}\int\limits_{\xi_1}^{1}(\theta_s+\theta_0)\,xdx - (\theta_s+\theta_0)\,. \tag{20}$$

$$e_r = (\theta_s+\theta_0) - \pi_{_T}(\pi-\pi_0) + \frac{s_r-\nu(s_\theta+s_z)}{1-\nu}, \tag{21}$$

$$e_\theta = (\theta_s+\theta_0) - \pi_{_T}(\pi-\pi_0) + \frac{s_\theta-\nu(s_r+s_z)}{1-\nu}, \tag{22}$$

where

$$\sigma_* = \frac{3\alpha_T E R T_*^2}{(1-\nu)E_a}, \varepsilon_* = \frac{\sigma_*(1-\nu)}{E} = 3\alpha_T(T_*-T_0), \pi_{_T} = \frac{\gamma_p p_* E_a}{\alpha_T R T_*^2}.$$

The problem was solved numerically. The differential equations included into system (9)-(17) were approximated by difference equations; the resultant system of linear algebraic equations was

solved by a sweep method. The integrals in the system (18)-20) were calculated by trapezium method.

As an example, Fig. 2–3 shows the spatial distributions of the dimensionless gas and solid temperature, reagent concentration, stress and strains tensor components along the burner radius in the case of compressible and incompressible gas for different values of parameter δ. The gas compressibility influences on gas temperature and reactant concentration and that of doesn't influence on carcass temperature profiles and distribution of stress and strains tensor components at the given parameters values. The increasing of value δ, for example, dealing with external radius extension, leads to displacement of reaction and heating zone to external surface.

As model analysis shown, the maximal thermal stresses and strains arise at the beginning operation stage of burner (when the ignition of methane-air mixture and heating of porous carcass take place), then that of values decrease at the stationary regime of gas burner operation.

References

[1] Kirdyashkin A.I., Maksimov Yu.M. Porous ceramic infrared burner// 8th International exhibition-congress on Energy saving and Energy effectivity, Tomsk, 16-17 November, 2005, pp. 24-25.

[2] Polyaev V.M., Mayorov V.A, Vasileva L.L. Hydrodynamics and heat-echange in porous constructional element of flying vehicle / M.: Mashinostroenie, 1988, 168 P.

[3] Timoshenko S.P., Goodier J.N. Theory of elasticity / M.:Nauka 1975, 576 P.

[4] Chumakov Yu.A, Knyazeva A.G. Regimes of gas combustion in a porous body of a cylindrical heat generator / Combustion, Explosion, and Shock Waves, 2008, V.45, N. 1 P. 14-24

Yurij A. Chumakov, Anna G. Knyazeva, Akademicheskij str. 2/4, Tomsk, Russia

Numerical analysis of thrust on structures for active defense against avalanches

Silene Cresseri Francesco Genna
francesco.genna@ing.unibs.it

Abstract

A new elastic-viscoplastic constitutive model for the description of the mechanical behavior of dry metamorphosed snow is adopted for the analysis of the thrust exerted by snowpacks on mountain slopes against avalanche defense structures. First we validate the model by comparison with published results; next, we study some practical application case, comparing the results with those provided by the design specifications of the Swiss Technical Guideline. It is found that, in some cases, the thrust values computed according to the Guideline are smaller than those predicted by the numerical analyses, which raises some questions about the safety margin involved by the currently holding design rules.

1 Introduction

Snow mechanics has received increasing interest in recent years, both in scientific and in technological terms. Nevertheless, both theoretical and engineering progress has been relatively slow, owing on one side to the difficulties in acquiring reliable experimental data and, on the other, to several sources of uncertainty, that make it difficult to correctly prescribe design rules.

A mechanical model for the description of the stress–strain behavior of dry metamorphosed snow as a viscoplastic material has been recently developed [1], with the aim of allowing the Finite Element simulation of real engineering situations, such as the stability of a full mountain slope over a time period of several months. Here, we apply and test this model with reference to the analysis of the thrust exerted by snowpacks, on mountain slopes, against avalanche protection structures, a specially important topic that appears to be still in an early stage of understanding.

We first reproduce, using the constitutive model of [1], a literature result concerning the measurement of the thrust against a protection work, protracted over a significantly long period of time [3], with the aim of understanding the ability of the model to correctly follow the evolution with time of the thrust.

Thereafter, we study the influence of several parameters (geometry of the snowpack; extension of the back-pressure zone; influence of the distance of the structure from either the ridge of the slope or another structure positioned uphill; snow density; height of the structure; slope inclination; friction coefficient) on the snow pressure against the protection work. Finally, we test the predictions of the model against the instructions furnished by the Swiss Technical Guideline [4] for the design of defense structures in avalanche starting zones. Some contradictions emerge, that may be due either to the inadequacy of the constitutive model, or to that of the Guideline, or both. In any case, we feel that this is a subject that requires a good deal of further investigation.

2 Constitutive equations

A detailed description of the constitutive model developed for dry metamorphosed snow is given in [1]. Here we report only the system of the governing incremental equations, that reads as follows:

$$\frac{1}{Z_1} \cdot \left(\dot{\boldsymbol{\sigma}} - \boldsymbol{D}^e \, \dot{\boldsymbol{\varepsilon}} + \boldsymbol{D}^e \, \beta \, \frac{\partial g}{\partial \boldsymbol{\sigma}}_{|norm} \right) = \mathbf{0} \tag{1}$$

$$\frac{g\left(\boldsymbol{\sigma}, P_{gc}\right)}{Z_2} = 0 \tag{2}$$

$$\frac{1}{Z_1} \cdot \left(\dot{P}_0 + \frac{v\, P_0}{\lambda - \kappa}\, \dot{\varepsilon}_v^{irr} \right) = 0 \tag{3}$$

$$\dot{P}_m - \pi_m\, b_{max}\, \dot{S} = 0 \tag{4}$$

$$S - \tanh\left(0.05\, \frac{t_s}{t_b}\right) \left[1 - \tanh\left(C \int_0^t \sqrt{\left(\dot{\varepsilon}_v^{irr}\right)^2 + \left(\dot{\varepsilon}_d^{irr}\right)^2}\, dt\right)\right] = 0 \tag{5}$$

where $\boldsymbol{\sigma}$ is stress, $\boldsymbol{\varepsilon}$ is strain, a superimposed dot indicates a derivative with respect to time, $\boldsymbol{D}^e$ is the elasticity matrix, that contains terms depending on the hydrostatic pressure p and the specific volume v, beside elastic constants; β is the equivalent of a viscous nucleus, defined as

$$\beta = \theta \frac{\sqrt{q^2 + p^2}}{\sqrt{3} P_0} \exp[\alpha f] \tag{6}$$

where q is the von Mises equivalent stress, f is a yield function quite similar to the Cam-Clay one, θ and α are material parameters, and P_0 is an internal variable that appears in the definition of the yield function f.

In eqs. (1–5), g denotes an irreversible flow potential function, similar to the yield function f but governed by a set of independently chosen material parameters, thus able to define a non-associated flow law; P_{gc} and P_m are internal variables that appear in the yield and the potential functions, and govern hardening; λ and κ are constitutive parameters related to the slope of the compressibility curves in the virgin and in the unloading-reloading stages; S represents the degree of internal bonding among snow grains, governed by the variable b that is the ratio between the mean intergranular neck radius and the mean grain radius; b_{max} is a function, appearing in the expression for b, of temperature and grain size, constructed empirically by matching some available experimental data; t is time, and t_s and t_b are characteristic times associated to the evolution of sintering; C and π_m are constitutive parameters governing the evolution of sintering, and Z_1 and Z_2 are normalizing factors.

So, eq. (1) represents elasticity, in which the inelastic part is of a viscoplastic type; eq. (2) enforces the irreversible strain potential surface to pass always through the stress state image point; eq. (3) is the evolution law for P_0; eq. (4) is the evolution law for P_m, and eq. (5) is the evolution law for the current amount of bonding S. The system of non linear differential equations (1–5) is integrated numerically adopting a Backward Euler technique with automatic subincrementation to guarantee a stable behavior for the volumetric stress–strain components. A detailed explanation of all the equations and symbols, with the rationale for their adoption, as well as of the numerical integration details, is given in [1].

3 Validation of the model for a case of snow pressure against rigid defense works

Reference [3] is the only work we could find that reports measurements of the snow pressure against a steel structure, positioned on a mountain slope as an active defense against avalanches. We refer to [3] for all the details of the experimental in-situ setup, that we have simulated by means of the Finite Element code ABAQUS [2], exploiting the constitutive model summarized in the previous section, implemented into a "UMAT" user subroutine.

The following points have created some difficulties in the numerical analysis of the experimental setup discussed in [3]:

- the real geometry of the structure is not fully reported, and one must obtain it from a figure, assuming everything is in scale;
- nothing is said about the snowfall history previous to the beginning of the measurements. Therefore, we assumed, as a loading condition, a sequence of 5 days of snowfall, 2 months before the beginning of the measurements, each day filling a layer of 0.83 m, in such a way that, at the start of measurements, and accounting for snow settlement during the 2 months prior to the measurements, the height of the snowpack was 3.1 m, as reported in [3];

- no information is given in [3] about the distance of the structure from the ridge of the mountain, essential in defining the thrust (see also the next section). We defined such a distance in such a way that the last total thrust obtained in situ, after 4 months of measurements and a total simulated time period of more than 6 months, matched the numerically computed one, which implied a distance of 7.7 m from the ridge. All the other pressure diagrams obtained numerically made reference to this situation;
- we employed a plane strain model of a slope with an inclination of 25°, which forced the description of a continuous supporting structure. In reality, the structure is made of 5 vertical cantilevers that support 6 horizontal beams, with empty spaces between them. This causes two difficulties: (i) the necessity of defining an equivalent plane strain vertical supporting structure, and (ii) the necessity of obtaining smooth pressure curves, as reported in [3], from discontinuous values, jumping from zero (in correspondence to the empty spaces between the horizontal beams) to some peaks in correspondence to the horizontal beams;
- nothing is said, in [3], about the friction condition between snow and ground surface;
- finally, the pressure curves reported in [3] are obtained indirectly, from the strains furnished by strain gauges placed on the vertical cantilevers.

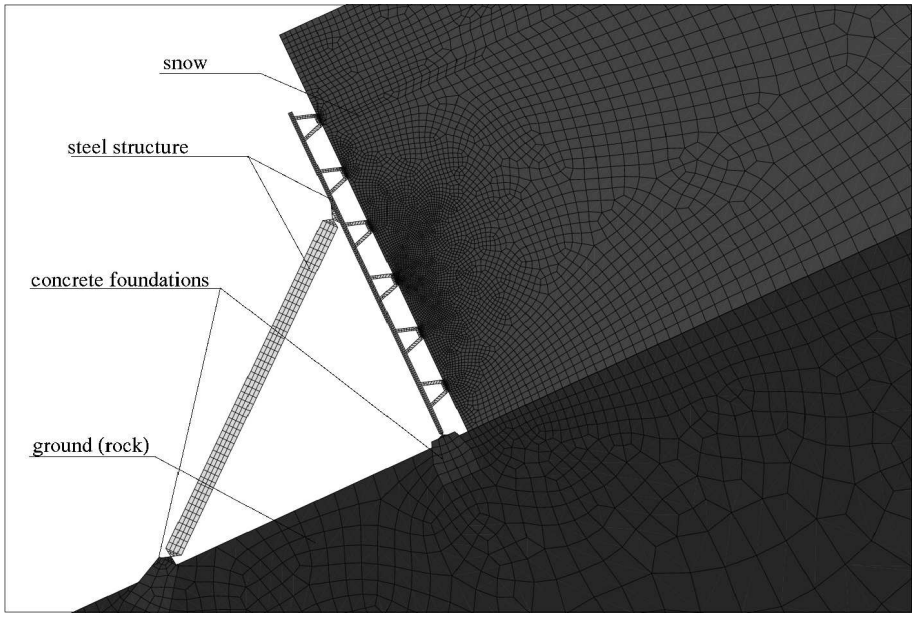


Figure 1: Detail of the adopted FEM mesh.

All this causes uncertainties both in the data definition and in the interpretation of the obtained results. Figure 1 shows a detail of the numerical model, and Figure 2 reports the experimental and the numerical pressure curves at several temporal intervals, spanning about 4 months. The obtained agreement seems quite satisfactory, in view of the mentioned difficulties. One must consider that

- the indirect technique adopted in [3] to obtain the snow pressure apparently provides underestimates of the actual values, as was proved numerically by comparing actual pressure results with pressure values obtained from the numerical data using exactly the indirect technique of [3]. Moreover, this technique can not account for snowpacks higher than the supporting structure, which was the case with the situation studied in [3]. As said in the next section, this factor can profoundly alter the pressure curves due to snow;
- the presence of a discontinuous obstacle to the snowpack (i.e., in this case, the steel frame) causes a slightly smaller thrust than that of an equivalent, continuous one, as was proved numerically;

- other errors may be due to the lack of information about all the boundary conditions, as well as about friction.

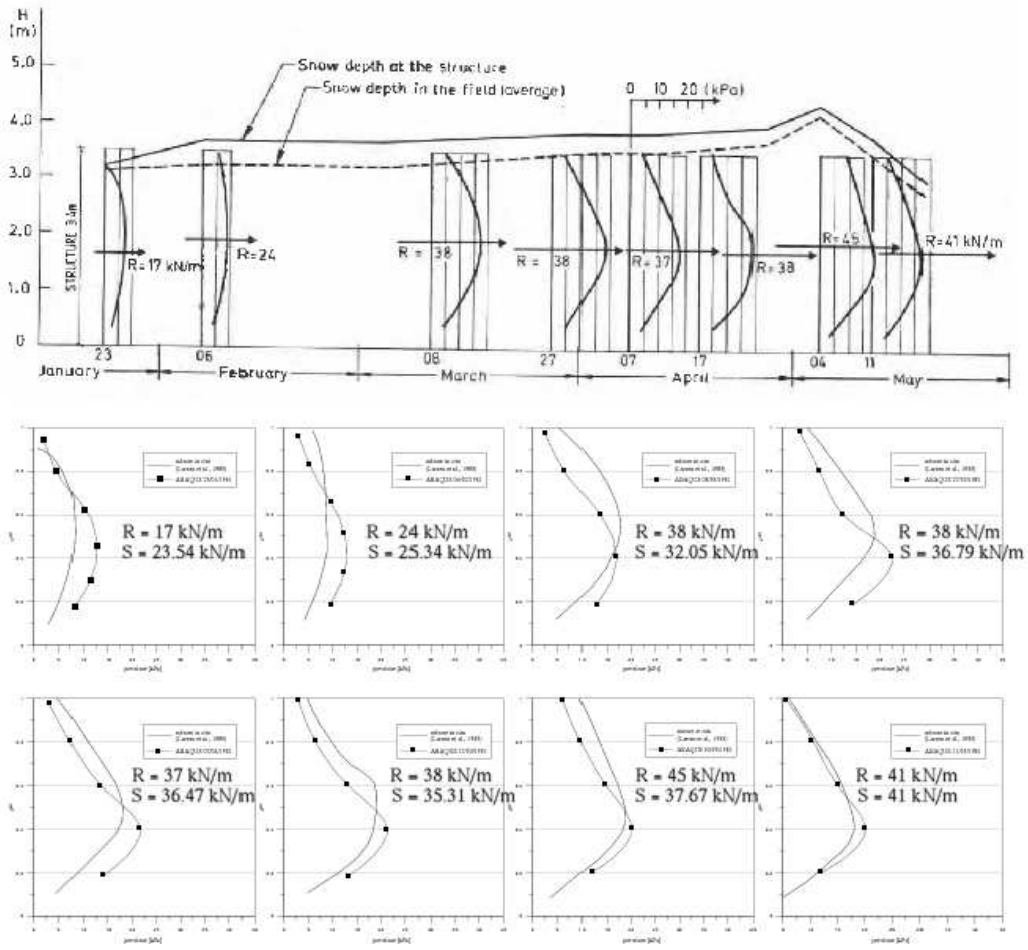


Figure 2: Snow pressure at several subsequent dates: comparison between experimental [3] (top, and solid lines) and numerical (curves with square symbols) results. R values are experimental thrusts; S values are numerical ones.

Considering all these factors, one may conclude that the numerical predictions are quite satisfactory, and that the constitutive model summarized in Section 2 is a good engineering tool to model snowpacks of the type considered in [3].

4 Analysis of the thrust against defense works

Here we briefly report the results provided by several groups of analyses, performed adopting the constitutive model of Section 2, with the aim of understanding how several factors might influence the thrust exerted by a snowpack on avalanche protection works. The adopted numerical model has always been a simplified one, in which a plane strain mesh of a mountain slope has been considered, varying several parameters in order to highlight their effect. There is no space, here, to go into all the details, so we will limit ourselves to summarizing the main findings, so far:

1. defense works seem to be necessary for slopes steeper than about 30°, as is recommended also by the technical guideline [4]. For smaller values of this inclination, in fact, the numerical simulations of a snowpack with no defense structure indicate a slow, stable downward motion

of the snowpack, solely due to homogeneous viscous effects; for larger values, the snow behavior becomes dominated by a localized viscoplastic flow, that indicates a possible detachment of a snow layer. It must be remarked, however, that this result was obtained keeping fixed the friction coefficient, and equal to $\mu = 0.6$; this appears to be a reasonable value for the friction coefficient between the snowpack and the ground, but it is by no means easy to be precisely assessed. In the presence of a defense structure, the calculated thrust is roughly constant for slope inclinations lower than 30°, and increases linearly with the inclination for larger angles;

2. the back-pressure zone, where the compressive stress in the snowpack is significantly affected by the presence of a supporting structure, comprises a distance equal to about $2 - 3$ times the height of the structure, as suggested in [4];

3. the thrust depends linearly with the snow density, at least in the range we have explored (up to values of 4.5 kN/m^3);

4. the thrust decreases linearly with increasing values of the friction coefficient, until a critical value of μ is reached, after which the thrust remains constant;

5. the thrust depends in a roughly quadratic way on the height of the supporting structure;

6. it is essential to account for the possible occurrence of a snow cover height exceeding that of the supporting structure, as shown in Figure 3, that displays the snow pressure in the case of a snowpack that is in one case as high as the structure (3.4 m), and in the other 10 cm higher than the structure;

7. finally, the snow thrust depends linearly on the distance, in the uphill direction, between the structure and either the next defense work or the slope ridge.

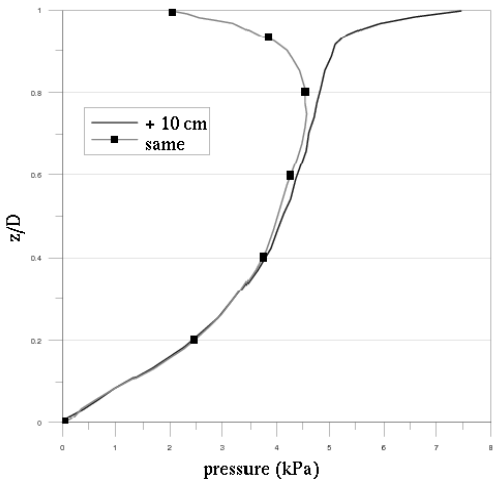


Figure 3: Snow pressure profiles in the case of a snowpack as high as the structure (curve with square symbols) and of a snowpack 10 cm higher than the structure (solid curve). D indicates the height of the defense structure.

5 Comparison with the prescriptions of the Swiss Technical Guideline [4]

The Swiss Technical Guideline [4] furnishes several expressions to approximately compute the thrust of a snowpack against an avalanche defense work. The most commonly adopted is the

following one:

$$S'_N = \frac{1}{2}\gamma H^2 K N \tag{7}$$

where S'_N is the total thrust in the direction parallel to the slope, that is then assumed to cause a uniform pressure distribution; γ is the specific weight of the snow; H is the height of the snowpack measured vertically; K is a so-called creep factor, depending on both the slope inclination ψ and the snow density according to values given in a Table, with $0.7 \leq K/\sin(2\psi) \leq 1.05$; N is a so-called glide factor, that depends on both the ground roughness and the slope exposure (solar exposure), again according to values given in a Table, with $1.2 \leq N \leq 3.2$. Moreover, instructions are given to compute further components of the thrust deriving from other design variables; here, however, we concentrate exclusively on eq. (7), trying to evaluate its appropriateness according to the results of the numerical simulations.

Several ingredients appear correctly captured by eq. (7) and associated instructions: the apparent linear dependence on the snow density and the quadratic dependence on the structure height in the first place; but also, as said previously, the definition of the back-pressure zone, and the prescription of using defense works for slopes steeper than 30°.

Other results appear to contradict the prescriptions of [4]. In the first place, eq. (7) does not account for the ratio between the height of the snowpack and that of the structure. As shown in Figure 3, if this ratio is larger than 1 the pressure curve has a quite significant peak at the top of the structure, that appears important enough to be considered in the design. Secondly, the assumption of uniform pressure, used to design the structure, is obviously not respected (see Figures 2 and 3) in any case.

Then one may consider the effect of the creep factor K, that, for a given value of the snow density, provides a thrust increasing with $\sin(2\psi)$, instead of linearly as is obtained from the numerical simulations, at least for values of ψ larger than a critical value (below which no support structure is indeed required); for increasing snow density values, and a constant slope ψ, the definition of K provides a thrust increasing in a moderately non linear way. These features disagree with the results reported in Section 3, but it is quite difficult, at the current stage of the knowledge, both theoretical and experimental, to fully assess the causes of these discrepancies.

A more critical factor proves to be the glide coefficient N in eq. (7), that, according to [4], is loosely correlated both to the ground roughness, divided into 4 categories, and to the slope exposure, divided into 2 categories (WNW-N-ENE and ENE-S-WNW). Such a factor is obviously and strictly related to the friction existing between the snowpack and the ground, or that existing between different layers in the snowpack, separated by a possibly weak interface. No apparent direct way to consider such a relation is given in [4], specially when the distance between the structures along the line of slope is prescribed. Here, actually, several contradictions seem to emerge: first of all, no rationale is given as to the definition of such a distance, that must be provided in such a way as to account for the dependence of the thrust on the length of the snowpack in the uphill direction, dependence that, according to our calculations, is linear. Moreover, the calculation of this maximum distance must be made according to Figure 13, at page 35 of [4], where it appears that for larger N values, i.e., for situations leading to larger thrusts, the structures can be placed farther apart from each other than in the case of small N values (i.e., when the friction/exposition conditions are more favorable). One would think that the exact opposite should occur, unless there is either a misunderstanding of the meaning of Figure 13 in [4], and relevant associated Tables, or some plain mistake.

In any event, we have run several analyses on test cases obtained designing the supporting structures according to the prescriptions given in [4], and in several cases we have found that the thrust computed by eq. (7) is smaller than the thrust computed numerically, sometimes of about 30%. This gives a warning about a possible drawback in the prescriptions of [4], since they may underestimate the real thrusts on these structures and thus lead to an unsafe design.

6 Conclusions

We can not say with certainty that the contradictions emerged during the calculations summarized in the previous section are due to mistakes or other imprecisions in the guideline [4], because the

discrepancies with our numerical results might well be due to a possible poorness of the adopted numerical model. Nevertheless, at least 3 modifications emerge as necessary, in [4], from these results:

1. the inclusion, into any formula for the snow thrust, of the ratio between the height of the snowpack and that of the structure;
2. a clear correlation should be provided between the glide factor N and the friction coefficient governing the interaction among the snow layers and between snow and ground. This could be obtained, at least in principle, exploiting the same numerical model that we have adopted here;
3. a clarification of Figure 13 in [4], and associated Tables, leading to (i) understanding why, under "bad" friction conditions (large N values), one is allowed to place a smaller number of structures (larger distance in the slope direction) than in the case of "good" friction conditions (small N values), and (ii) to understanding the condition that leads to the definition of the distance factor in the same Figure.

Apart from these observations, strictly relevant to the guideline [4], here we may conclude that the numerical tool based on the constitutive model developed in [1] appears to be potentially very useful to explore several situations in which the knowledge of the stress and strain fields in snow is of practical importance.

Acknowledgements

Research partially supported by the Italian Ministry of University and Research (MIUR). The first author was supported by a research grant ("Assegno di Ricerca") provided by the University of Brescia. The Finite Element code ABAQUS has been run under an academic license. Finally, the authors wish to thank Miss Elisabetta Gaioni for her help with the numerical analyses.

References

[1] Cresseri S., Genna F., Jommi C. Numerical integration of an elastic-viscoplastic constitutive model for dry metamorphosed snow. *Int. J. Anal. Num. Meth. Geomech.*, in press, 2010.

[2] Hibbitt, Karlsson, & Sorensen. ABAQUS Users' Manuals, Release 6.9, Dassault Systèmes, Providence, RI, USA, 2009.

[3] Larsen J. O., McClung D., Hansen S. B. The temporal and spatial variation of snow pressure on structures. *Canad. Geotechn. J.*, **22**(2), 166–171, 1985.

[4] Margreth S. *Defense structures in avalanche starting zones.* Technical guideline as an aid to enforcement. Environment in Practice no. 0704. Federal Office for the Environment, Bern; WSL Swiss Federal Institute for Snow and Avalanche Research SLF, Davos, 134 pp., 2007.

Silene Cresseri, Francesco Genna, Department of Civil Engineering, University of Brescia, via Branze 43, 25123 Brescia, Italy

The onset of solutocapillary convection in water-alcohol systems

M. O. Denisova K. G. Kostarev
maria.denisova@icmm.ru

Abstract

A threshold nature of the evolution of capillary flows was explained quite recently owing to application of the advanced visualization techniques. This effect frequently observed in experiments contradicts a traditional view on the initiation of motion in Newtonian fluids. It was found that formation of the surface tension gradient capable of initiating the Marangoni convection was closely related to the layer of uncontrolled impurities adsorbed on the free surface of the fluid [1]. The structure of this layer can fail only at sufficiently high shear stresses, which, in the solutal case, are obtained by creating the surfactant concentration difference of several weight percents.

In this paper we discuss the results of experimental investigation of the solutal Marangoni convection developed on the free surface of water due to a local injection of aqueous solutions of a surfactant. For surfactants we used monatomic alcohols forming homologous series. Such a choice allowed us to determine the dependence of the concentration threshold on the physical-chemical properties of the alcohols including their surface activity. It was found that the value of the threshold decreases with an increase in the length of the surfactant molecule and characteristic dimensions of the free surface. The dependence of the flow structure on the degree of alcohol solubility was analyzed. The obtained relationships allowed us to obtain estimates of the threshold temperature gradients in the case of thermocapillary convection.

1 Introduction

It is well known that the Marangoni convection is a fluid motion driven by the capillary forces at the interface. These forces carry the fluid toward the regions with higher surface tension. In general, these are the regions with lower temperature and/or the regions with lower concentration of a surface-active substance (surfactant).

Since Newtonian fluids have zero force of rest friction, it is generally assumed that their free surface begins to move even at an arbitrary small difference in surface tension. On the other hand, in some cases, for example, in the case of surfactant diffusion from a drop of binary mixture into the surrounding homogeneous fluid the development of the Marangoni effects begins only at a certain proportion of liquid components in a drop [1]. A delay in the development of capillary motion is also observed in experiments investigating inhomogeneous surfactant solutions with gas and liquid inclusions [2,3] and buoyancy of higher concentration jets from the submerged surfactant sources [3,4]. The use of interferometry in these experiments provides visual evidence that the interface motion begins only after formation of a marked (up to several percents) difference in the surfactant concentration. Moreover, in the case of a drop, initiation of the capillary motion is observed just after penetration of a surfactant through the interface and formation of its initial distribution in the drop. The analysis of the obtained results shows that the appearance of the surfactant concentration threshold in the observed phenomena should be related to the existence of the original adsorption layer at the surface of a Newtonian fluid, owing to which the fluid acquires rheological properties. The source of the layer is a group of surfactants, which cannot be removed by standard purification methods. During tests these impurities escape from the fluid and accumulate at the free surface. Hereafter they will be referred to as uncontrollable surfactants examined fluids.

2 Experimental procedure

The simplest object for studying the rheological properties of the interface is a free horizontal surface of water, which, owing to its high surface tension ($\sim$ 72 dyne/cm), creates favorable conditions for maximum adsorption of uncontrollable surfactants dissolved in this fluid. A certain dose of controllable surfactant locally placed on such a surface should provoke the development of the Marangoni convection provided that the arising shear stress exceeds a threshold value. An important point is that local insertion of the surfactant eliminates the problem of Pearson's equilibrium stability of a fluid and the use of the horizontal surface -the problem of possible confrontation between the gravitational and capillary mechanisms of motion observed at curvilinear surfaces. Moreover, addition of a small amount of controllable surfactant to water prior to injection of a drop would be expected to ensure a certain control over the properties of the adsorbed film. To change the degree of its relative deformation one can use cuvettes, in which the area of the free surface of the fluid can vary (the drop in this case should have a fixed volume).

Consideration was given to the process of initiation of a capillary motion caused by a local injection of a droplet of water with controllable surfactant concentration C_d onto the free surface of a distillate or an aqueous solution of this surfactant with lower concentration C_s. In the experiment, the roles of the controllable surfactant were played by liquid monatomic alcohols forming homologous series $C_nH_{2n+1}OH$. These alcohols differ in density ρ, and surface tension σ, which change in the range 0.78 - 0.80 g/cm^3 and 22 - 25 dyne/cm, respectively, but their surface activity $g = -\delta\sigma/\delta C$ increases by 3.2 times with every new hydrocarbon group OH_2.(Traube's rule)

To generate a droplet of such a solution with a volume of 5 μL we used a mechanical pipette with accuracy of 0.1 μL. manufactured by BIOHIT company. Then the formed drop smoothly came into contact with a free surface of a base fluid or was injected into the fluid near its free surface. During tests the ambient temperature and the fluid temperature was $(23\pm1)^o$C.

The cuvette filled with a base fluid had the form of a vertical rectangular cavity with dimensions of 90×40 mm and thickness b ranging from 1.2 to 20 mm. The walls of the cuvette were formed by parallel glass plates covered with a semi-transparent mirror film which with appropriate adjustment allowed us to create a working cell of the Fiseau interferometer for making observation of the concentration fields on the side of a wide face.

In view of the supposition that a certain amount of uncontrollable surfactant always exists on the fluid surface one can infer that the amount of such surfactants is specified both by the degree of purification of the fluid and by quality of cuvette preparation. In our experiments, for the zero level of preparation we adopted the threshold for initiation of the solutal Marangoni convection in distillate or in a water solution of isopropyl alcohol in the cuvette, which was washed three times by isopropyl alcohol, then, during 15 minutes, by running water and finally by distillate. The improvements in preparation of the cuvette led to development of a new technique according to which a cuvette after each series of tests was washed several times with concentrated detergent "Fairy" followed by mechanical cleaning of the cuvette walls, after which it was washed for an hour with running water and a liter of distillate. The next step toward improvement of the process of water purification was the use of deionizer "Vodoley" manufactured by Khimelectronika company (Moscow, Russia). Deionized water (with electrical conductivity of 0.1μS) was used in the experiments as a basic fluid and for final washing of the cuvette (repeated several times).

3 Structure of convective motion initiated by a local injection of a surfactant

At first, the development of convective motion was investigated in the situation, in which a drop of the surfactant solution was placed on the free surface on the side of a gas phase. In this case, a drop hanging at the end of the needle was placed slowly at the surface of the fluid. As soon as the drop touched the surface it was sucked into the bulk of water under the action of capillary forces minimizing the arising total surface (Figure 1*a*). As a result, the surfactant lying on the drop surface immediately landed on the surface of the fluid. The higher was the surfactant concentration in the drop, the smaller was the depth, to which the drop sinks, and the large was the fraction of the drop that contributes to the formation of the convective flow.

When a drop of the surfactant solution was introduced on the side of the liquid phase it didn't deform the free surface of the fluid, although the time it took for the drop to reach the interface as a buoyant jet (Figure 1c) was rather long. Despite the fact that the whole bulk of the surfactant solution rose to the surface as a single portion it did not have its own surface. Therefore the processes of mixing and dissolution began well before the surfactant reached the fluid surface and caused a decrease in concentration of the solution coming into contact with the fluid surface. The experiments showed that the initiation of a capillary motion on a horizontal free surface of the working fluid occurred in a threshold manner like in the case of curved interfaces [2.3]. An example is given in Figure 1, which shows a series of interferograms of the concentration field in the case when surfactant concentration in the drop is higher than the threshold value for a given thickness of the cuvette. Therefore, as soon as the drop reaches the fluid surface, there appears an intensive but rapidly damping capillary motion in the form of two cells (Figure 1a - 1b) or two convective cell chains (Figure 1c - 1d) [4] whose occurrence is related to simultaneous diffusion of the alcohol to the free surface at several places (within the boundaries of the jet spreading under the surface)

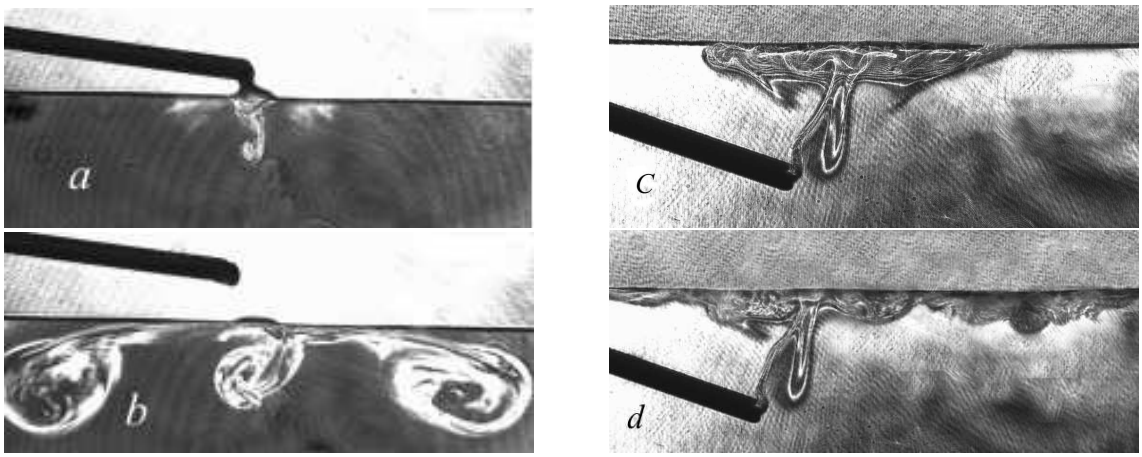


Figure 1: Injection of a drop of the isopropyl alcohol solution onto the free surface of water in cuvette b = 1.2 mm on the side of gas phase(the elapsed time t,s: a - 0.2; b - 0.9),C_d = 6%; on the side of liquid phase (the elapsed time t, s: c- 2.1; d- 2.6), C_d=12%.

As it might be expected, the value of the surfactant concentration threshold decreases with increasing the degree of preliminary water purification and cleaning of the cuvette walls. Figure 2 shows the dependence of the threshold difference ΔC in the initial isopropyl alcohol concentration between the droplet and the basic fluid on its content in the fluid and the degree of purification. It is seen that the use of a new procedure for preparation of the cuvette and deionization of water reduces the value of the threshold by 50%, yet a non-threshold development of solutal-capillary convection has not been achieved. Note that a similar behavior of the water surface is observed after injection of a microdrop of the isopropyl alcohol solution on the side of the gas phase: a threshold value of the concentration difference is 7.0% for distillate, 5.0%- for distillate in the cuvette prepared in accordance with the new purification procedure and 3.0% - for deionized water and cleaned cuvette (cuvette thickness b = 3.8 mm).

4 Conditions for development of the capillary convection at the free surface of water and aqueous solution of isopropyl alcohol

As it is evident from Figure 2, the value of the threshold essentially depends on the content of an alcohol in water reaching a maximal value at minimal concentration of the surfactant in the solution. The obtained results confirm the supposition as to a complicated composition of the group of surfactants forming the initial adsorption layer at the free surface of the fluid. Most of

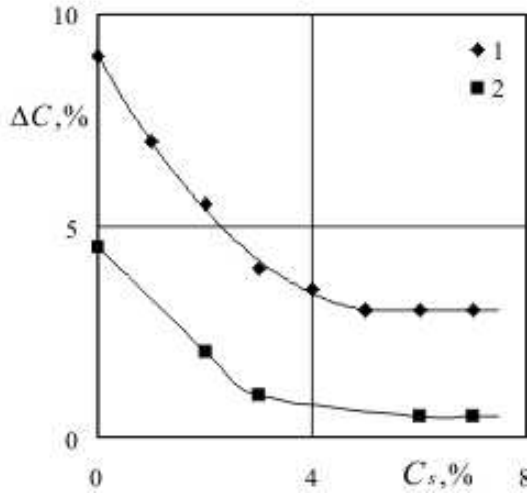


Figure 2: Threshold difference of alcohol concentration in drop and in basic liquid versus alcohol concentration in base fluid for a drop injected on the side of the liquid phase in cuvette b =3.8 mm for different degrees of water purification: 1-distillate, 2 -deionized water

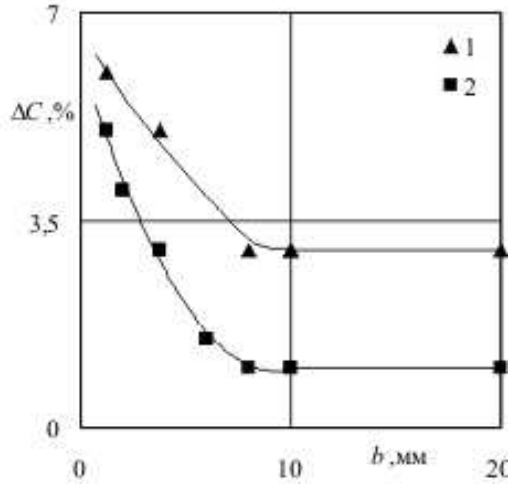


Figure 3: Threshold alcohol concentration versus cuvette thickness for a drop injected on the side of the gas phase for different degrees of water purification:
1- distillate, 2 -deionized water

them have the boiling point above 100^0C and therefore survive during water distillation. Half of the surfactants (group A) can be removed by means of ion-exchange filter and cleaning of cuvette walls. The second half (group B) do not have electrical charges and therefore stay in the solution. Co-linearity of curves 1 and 2 in Figure 2 means that the surfactants of the group A are not sensitive to changes in the concentration of the alcohol in water and are held on the fluid surface as separate molecules. By contrast, the surfactants of the group B form the so-called hard film [5]. An increase of the alcohol concentration in a base fluid gradually destroys the film but does not remove molecules of the surfactants from the surface which preserves conditions for delay of motion.

The assumption concerning the properties of the film formed by surfactants of the group B is supported by its poor deformability in thin cuvettes which is the reason for adding a greater amount of the alcohol for sustaining capillary convection (Figure 3).

Of no less importance for overcoming the threshold and development of the capillary motion is the direction in which the drop of the alcohol solution is injected onto the surface of the basic fluid. Figure 4 shows that for deionized water the value of the threshold decreases by 1.5 times in the case when the isopropyl alcohol is introduced on the side of the gas phase (then, initial rupture of the film of non-controllable surfactants is realized mechanically). With the growth of alcohol concentration in the base solution the threshold concentration difference rapidly decreases, and curves for different directions of surfactant injection converge until they coincide at $C_s \sim 4 - 6\%$ and then tend to an asymptotic value, which in the examined interval C_s remains non-zero ($\Delta C \sim 0.5\%$). It should be noted that an increase in the surfactant concentration reduces the surface tension of the base solution which provides explanation for the fact that the observed tendency to reducing the concentration threshold with increase of C_s agrees well with the results of investigations concerning development of capillary convection on the free surface of gas bubbles in vertically stratified solutions of some surfactants [2].

In cuvettes of different thickness and, accordingly, with different characteristic dimensions of the free surface, the direction of surfactant injection has a much greater effect on the development of capillary motion (Figure 5). Thus after injection of a droplet on the side of the gas phase the resulting local rupture of the adsorption layer accompanied by formation of longitudinal gradient of alcohol concentration at the surface of deionized water reduces the concentration threshold for initiation of the solutal Marangoni convection approximately by 3 times for all cuvettes used in

the tests.

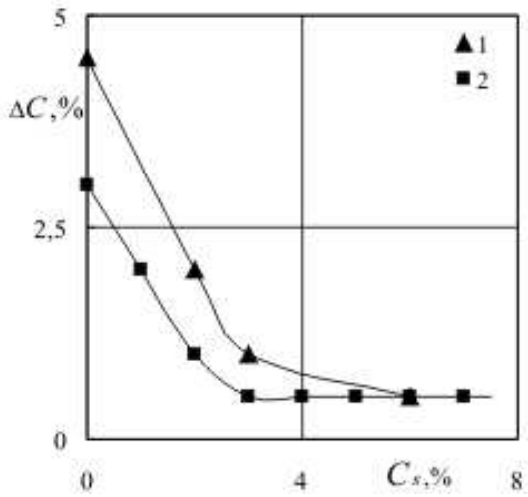


Figure 4: Threshold difference of alcohol concentration versus alcohol content in the basic fluid in the case of drop injection on the side of liquid(*1*) and gas (*2*) phase (b =3.8 mm)

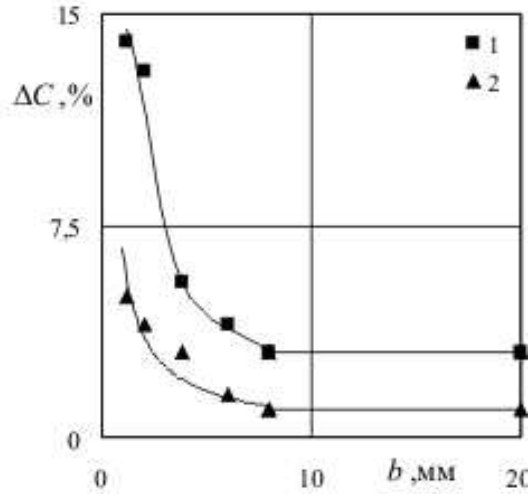


Figure 5: Threshold alcohol concentration versus cuvette thickness in the case of drop injection on the side of liquid (*1*) and gas (*2*) phase

An abrupt decrease of the concentration threshold in cuvettes of thickness more than 10 mm accounts for the fact that retardation of the Marangoni motion is not discussed in most of the problems considering stability of shallow layers and films.

It is also of interest to analyze the results of tests, in which the boundary of the free surface of the basic fluid (water) coincides with the edge of the cuvette, which allows us to change the curvature of the free surface and, respectively, the length of the arc connecting the walls of the cuvette, while keeping the characteristic dimensions of the cavity unchanged. The tests showed that in the absence of meniscus (the length of the arc is minimal) the concentration threshold increases markedly (C = 7%), whereas in the presence of the meniscus (no matter whether it is convex or concave) the concentration threshold decreases (ΔC= 5% at the meniscus deflection of 1.1-1.3 mm beneath or above the horizontal plane for cuvette with b =3.8 mm).

5 The influence of the adsorbed film on the evolution of solutocapillary convection

We can suggest one more characteristic of the convective phenomena associated with the existence of the adsorbed film - "the delay time", which is the interval between the moment of the visual contact of the free fluid surface with the buoying jet of the surfactant and the beginning of the Marangoni convection. The proposed parameter reflects the time of diffusion of the controllable surfactant onto the fluid surface and the formation of its gradient, which is essential for initiation and sustenance of the capillary flow. Fig.6 shows the delay time Δt as a function of the alcohol concentration difference ΔC between the drop of the solution and the base fluid. It is seen that an increase in the concentration difference leads to an abrupt decrease in the delay time which is agrees well with the first Fick law (variation of concentration with time in a given cross section normal to the diffusion direction and coinciding, in this particular case, with the free surface occurs is proportional to the gradient of the volume percent concentration).

Evidently, the reason of the discrepancy between the relations $\Delta t = f(\Delta C)$ for such base fluids as water (curve1) and aqueous solutions (curve 2) is that in the first case it takes additional time for the film of uncontrollable surfactants to partially deform, whereas in the second case the mechanical properties of the film are reduced initially.

Fig.7 provides supporting evidence for the assumption that relative deformation of the adsorbed

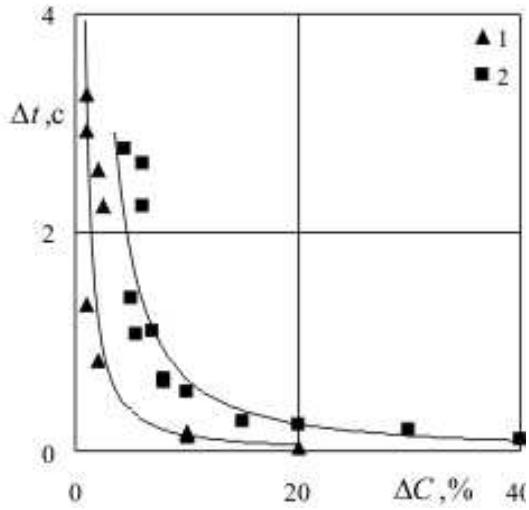


Figure 6: Delay time versus concentration difference: *1*- between the drop and aqueous solution of alcohol ($\Delta C = C_d - C_s$) *2*- between the drop and water ($\Delta C = C_d$) (b =3.8 mm)

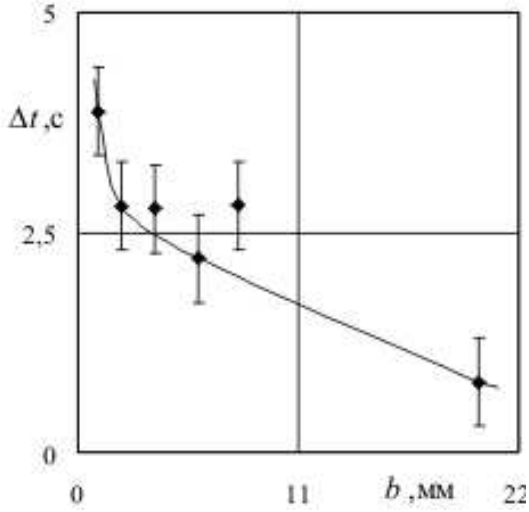


Figure 7: Delay time versus cuvette thickness for the case of drop injection into pure water under critical concentration

film of uncontrollable surfactants is rather low. In this case, an increase in the area of the free surface suggests that the capillary motion is initiated at a lower shear stress and, accordingly, at lower surface concentration, which is attained for a shorter time.

6 Specific features of evolution of solutocapillary convection in monatomic alcohols

As it follows from the above results the value of the concentration threshold should be defined by the value of the surface tension difference between the drop and the base fluid and also by the ability of the injected surfactant to dissolve the adsorbed film of uncontrolled surfactants. To verify the validity of this statement we carried out a series of tests, in which for the surfactants we used methyl, ethyl, butyl, amyl, hexyl alcohols forming a homologous series. One of the distinguishing features of these alcohols is a rather rapid decrease of their ultimate solubility in water and, respectively, an increase of their surface activity with increasing number of the hydrocarbon groups in the molecule.

In Fig.9 the value of the concentration threshold of amyl alcohol is plotted as a function of cuvette thickness in the case when the drop is placed on the surface of water on the side of the fluid (*1*) and on the side of the gas phase (*2*). From a comparison of Figures 9 and 4 follows the conclusion that an increase in the molecular mass of alcohol reduces its threshold concentration value as well as the ability to dissolve surfactants from the group B, because in the cuvette thickness range under consideration the threshold value is not asymptotic. The Fig.9 shows the dependence of the concentration threshold on the number of the hydrocarbon groups in the molecule of alcohol. It is seen that an increase of the surface activity together with a decrease of its solubility in water lead to an abrupt reduction of the concentration threshold.

7 Conclusion

The performed experiments support the view that the reason for the observed delay in the development of the capillary motion at the surface of water and water solutions is the adsorption layer which is formed on the basis of uncontrolled surfactants showing different properties. Some of such surfactants can be removed by preliminary purification of water with the aid of ion -exchange filters. However even the remaining part of uncontrolled surfactants will suffice for generation of a

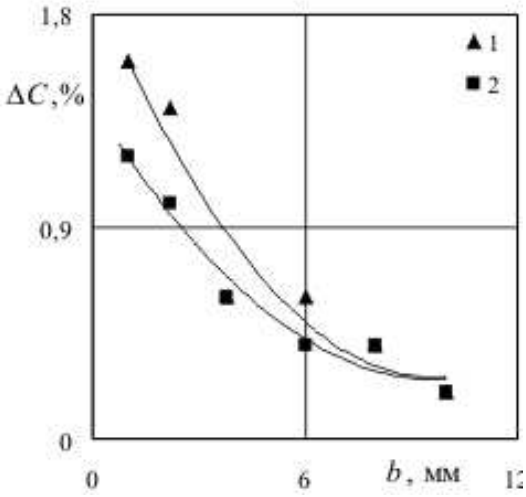


Figure 8: Threshold concentration of amyl alcohol versus cuvette thickness in the case when the drop is placed on the surface of water on the side of the liquid (*1*) and gas (*2*) phase

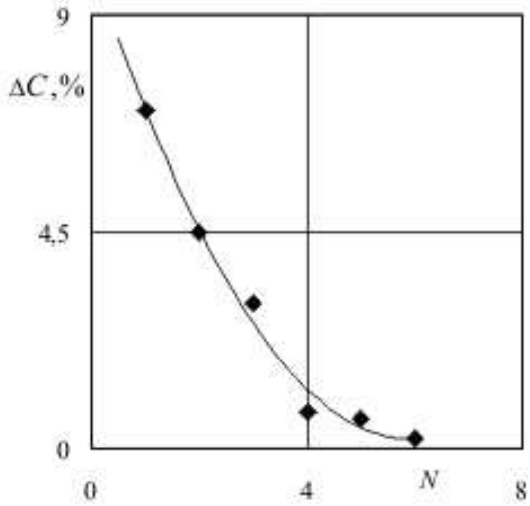


Figure 9: Threshold difference of alcohol concentration versus the number of hydrocarbon groups in an alcohol molecule

rather high concentration threshold especially in the case of a free surface or interface with small characteristic dimensions. The existence of the adsorption layer on the interface can lead not only to the appearance of the threshold concentration responsible for the onset of Marangoni convection but they can also exert an essential influence on the stability and structure of the already developed surface flow. The revealed effects are supposed to make the most critical contribution to the development of capillary phenomena in liquid systems of small volumes (emulsions, bubble suspensions, etc.). For such systems the use of visual methods of observation of flows and concentration fields meets serious difficulties and the existence of nonuniform temperatures and concentrations suggests the need to introduce in calculations the correction for possible development of the Marangoni convection.

Acknowledgements

The work was supported by the project of RFBR No 09-01-00484; the joint project of SB, UB and F-E B of RAS No 116/ 09-C-1-1005 and grant of UB RAS for young researchers The work was supported by Russian Foundation for Basic Research (RFBR-Ural Grant No. 07-01-96053).

References

[1] Bushueva K.A., Denisova M.O., Zuev A.L., Kostarev K.G. Flow development at the surfaces of bubbles and droplets in gradient solutions of liquid surfactants // Colloid J. 2008. V. 70. No 4. P. 416-422.

[2] Lewis J.B., Pratt H.R.C. Instabilities induced by mass transfer and defomable fluid interfaces // Nature. 1953. V. 171. P. 1155 - 1161.

[3] Kostarev K.G. The Study of the Extraction of Surface-Active Component of a Binary Liquid from Model ("Cylindrical") Droplets// Colloid Journal, 2005, Vol.67, No 3,pp.357-362.

[4] Kovalchuk V.I., Kamusewitz H., Vollhardt D., Kovalchuk N. M. Auto-oscillation of surface tension // Phys. Rev. E. 1999. V. 60, No 3. P. 2029 - 2036.

[5] Kovalchuk V.I., Kamusewitz H., Vollhardt D., Kovalchuk N. M. Auto-oscillation of surface tension // Phys. Rev. E. 1999. V. 60, No 3. P. 2029 - 2036. 3. Kostarev K.G. The Study of the Extraction of Surface-Active Component of a Binary Liquid from Model ("Cylindrical") Droplets// Colloid Journal, 2005, Vol.67, No3,pp.357-362.

[6] Kovalchuk N.M. and Vollhardt D. Effect of substance properties on the appearance and characteristics of repeated surface tension auto-oscillation driven by Marangoni force // Phys. Rev. E. 2004. V. 69, 016307. P. 1 - 13.

[7] Birikh R.V., Zuev A.L., Kostarev K.G., Rudakov R.N. Convective self-oscillations near air-bubble surface in horizontal rectangular channel// Fluid Dynamics, Vol.41, No 4, 2006, pp.514-520.

M. O. Denisova, Institute of Continuous Media Mechanics, Ural Branch of Russian Academy of Sciences, Acad. Korolev Str. 1, 614013 Perm, Russia.

The influence of copper on tribological characteristics of automotive pad-disc interface. Results of nano-scale modeling

Andrey I. Dmitriev Werner Oesterle Heinz Kloss
dmitr@ispms.tsc.ru

Abstract

In spite of many fundamental studies have been conducted to understand the processes taking place in brake system this still remains a challenging area of research. Modern pad materials are polymer matrix composites which usually contain more than 10 ingredients, such as steel fibres, brass and copper chips, as well as various fillers, abrasives and solid lubricants. The main aim of the paper is to show by modelling how nanocrystalline copper at the surfaces of brake pads behave during tribologiocal stressing in comparison to primary contact sites provided by steel fibers. The boundary conditions of the model were adjusted to experimental observations obtained by Transmission Electron Microscopy (TEM). Theoretical investigation of copper or brass as a pad ingredient was carried out on the basis of modeling by the method of movable cellular automata (MCA).

1 Introduction

An important prerequisite in respect to new material designs is to obtain a better understanding how the system works. In spite of many fundamental studies have been conducted to understand the processes taking place in brake system this still remains a challenging area of research.

Automotive brake pads usually consist of a large number of macro- and micro- constituents bound together by cured phenolic resin. Although the variety of pad formulations is huge, almost all of them contain macro-particles of copper or brass or a combination of both. On the other hand, concerns about the usage of copper in brake pads have evolved because of environmental impacts and demands for reduction have been partly accepted by the automotive industries. For developing new pad formulations with reduced copper content, it is very important to know why and how the experienced system works, i.e. we should know, what exactly is the role of copper in respect to good brake performance.

Obviously, one reason for using copper or brass as pad ingredient is their excellent thermal conductivity. Additional impacts of copper on brake performance are not thus clear. Macro-particles of copper and brass - preferably in the form of chips - may serve as reinforcements, similar as the steel fibers described by Eriksson et al. [1] and Ostermeyer et al. [2].

Pad manufacturers appreciate copper not only for its high thermal conductivity and its capability to provide primary contact sites, but also as a soft metal which is capable to provide smooth sliding conditions and reduce the propensity for noise generation at elevated temperatures. This function may be understood best if we assume that soft copper nanoparticles are incorporated in the surface films which form during braking. Nanoscopic modelling assuming soft graphite inclusions in brittle oxide films has revealed how velocity accommodation between a rotating brake disc and fixed pad is achieved, how friction force fluctuations are minimized and how the desired friction level depends on the composition of the surface films [3, 4, 5, 6]. We expect a similar behaviour after substitution of graphite with copper nanoparticles and want to prove this by corresponding modelling.

The objective of the present paper is to show by modelling the influence of copper on tribological characteristics of automotive brake pad-disc interface The results of simulation are given in comparison with results of our previous study [3, 4, 5, 6] where primary contact was provided by steel fiber and friction layer was contained the graphite inclusions as particles of solid lubricant.

2 The modelled setup

Theoretical investigation of copper or brass as a pad ingredient was carried out on the basis of modeling by the method of movable cellular automata (MCA). This choice was determined by the features of the MCA method to simulate such complicated processes as: mass mixing, damage generation and accumulation and so on. The formalism of the MCA method has already been described in [5, 7].

The type of modeled setup to investigate the impact of copper, either as substrate material or as an ingredient of the friction layer was a modification of the setup used in our previous studies [3, 4, 5, 6]. The scheme of chosen two-dimensional setup is depicted in Fig. 1. It simulates a primary contact site according to Eriksson et al. [1], which is realized on the scale of the order of 1 micron. Instead of a steel fibre serving as supporting substrate for bearing the friction layer we now assumed a copper macro-particle (copper chip) as supporting substrate material. Since the severely deformed superficial layers of copper macro-particles show a nanocrystalline structure, mechanical properties of nanocrystalline copper at room temperature [8] were assumed for MCA-modelling of the supporting material at the pad side (Table 3). The supporting material on the disc side is pearlitic steel which is the matrix of cast iron. Like in our previous studies the free surfaces of both contacting bodies (first bodies) were covered with an oxide film consisting of nanoparticles of iron oxide and inclusions of solid lubricant. All previous simulations were based on the assumption that the solid lubricant had properties similar to graphite. In section 3.2 we intended to simulate the friction behaviour of a typical contact at elevated temperature ($500C$), and therefore we assumed that graphite will be substituded by copper. Increasing the temperature from $24C$ to $500C$ causes a reduction of strength properties of copper by at least 50%, according to engineering textbooks like e.g. [8]. The mechanical properties of the different bulk materials in terms of the numerical model are summarized in Table 3. Furthermore, the following boundary conditions for modelling were used. A constant sliding velocity (V) equal to 10 m/s was applied on all particles of the bottom layer of the disc. At the same time their position in vertical direction was fixed. A constant normal force corresponding to the contact pressures in the range between P = 15 MPa and P = 50 MPa for different calculations was acted upon all the elements of the upper layer of pad. For both types of loading a linear procedure of value increasing was used with the following scheme. Initially the surfaces of pad and disc were separated. Then the loading with increasing velocity was applied on the particles of the bottom layer of the disc. Normal pressure was applied on the pad after all particles of the disc (not only layer under loading) reach the maximum value of sliding velocity. Periodic boundary conditions were applied along the sliding direction. So, the number of particles was constant in the simulation, only redistribution of particles in the contact zone was studied.

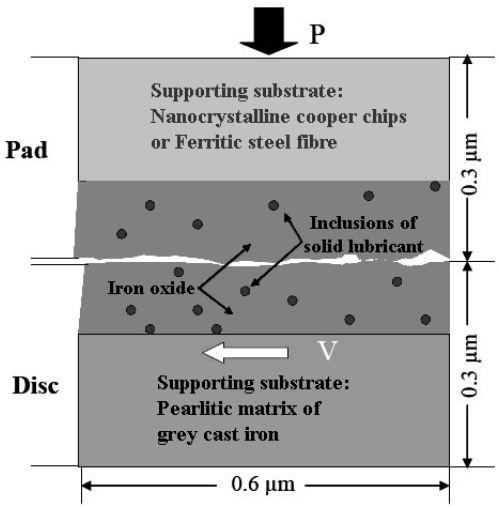


Figure 1: Schematic presentation of the modelled pad-disc interface.

The size of automata was adjusted to 10 nm, according to experimental observations of nanocrystalline friction layers [3]. The time step for simulation was defined by characteristic

Table 3: Parameters of model materials

	Young modulus E, GPa	Poisson ratio ν	Elastic limit σ_{y1}, MPa	Yield strength σ_{y2}, MPa	Ultimate tensile strength σ_s, MPa	Strain at σ_{y2} ϵ_{y2}	Breaking strain ϵ_s
Ferritic steel	206	0.28	450	500	550	0.04	0.106
Pearlitic steel	206	0.28	520	800	920	0.04	0.106
Iron oxide	380	0.3	290	305	340	0.008	0.009
Graphite	20	0.3	15	35	45	0.05	0.15
Copper	125	0.35	350	390	430	0.03	0.11
Soft copper	120	0.35	175	185	215	0.03	0.11

size of particles and elastic properties of the modelled materials. It was of the order of 10^{-13} s. Since the time step was such small, temperature changes during the simulation were neglected.

A surface profile with roughness on the nanometer scale was set deliberately prior to simulation. As shown previously, this setting exerts no major impact on the results of simulation [3]. The model calculates position and binding state of each automaton (particle) as well as resulting tangential forces or Coefficients of Friction (CoF) at the micro-contact for each time step.

3 Results of modelling on the nanometre scale

Two questions should be solved by modelling: 1) Are copper macro-particles suitable for providing primary contact sites just like steel fibers, and 2) what effects will occur if graphite nanoparticles in friction layers are substituded by copper nanoparticles.

3.1 Effect of copper macro particles as primary contact sites

Since copper macroparticles always developed nanocrystalline superficial layers at the rubbed surface the mechanical properties of nanocrystalline copper at room temperature were regarded as relevant for modelling the behaviour of "normal" friction layers (iron oxide with graphite nanoinclusions) supported by these copper macroparticles. A literature survey revealed several papers describing the stress-strain behaviour of nanocrystalline copper [9, 10]. The data of Shpeizman et al. and the SMAT-30 Cu sample of the study of Guo et al. seemed to be most appropriate. Since the deformation mode in our case was shearing under pressure, higher strains before fracture are plausible.

Fig.2,a shows the simulation results for the contact situation described above. For comparison corresponding results obtained in [5, 6, 7] for the same setup with ferritic steel as a substrate material are shown. The volumetric concentration of particles of solid lubricant in the friction layer was 27.5% in both cases. The applied loading was equivalent to the pressure of 17.5 MPa. Obviously, the substitution of the steel substrate by nanocrystalline copper does not change the features of material behaviour in the mechanically mixed layer (MML) (Fig.2,a). The thickness of the MML at the stage of steady state motion was not essentially different for both cases and was of the order of 130 nm. Fig.2,b shows the structure of inter-automata bonds during steady state motion. Steady state here means that a constant thickness of the MML does not change any more during further sliding. Pairs of particles in a linked state are marked by a line connecting their centers. Obviously, the structure of the MML is a mixture of loose particles of solid lubricant with particles of iron oxide, either in the form of single particles or as small agglomerates with diameters up to 50 nm.

Fig.3 shows the calculated time dependency of the friction coefficient (CoF) in case of the nanocrystalline copper substrate. The CoF was calculated as the quotient of overall tangential and normal forces acting on the upper layer of the pad during the simulation. Mean values of CoF for both considered cases (steel and copper substrate) are depicted as bold curves. It is quite clear that there is no essential difference of mean values for the two contact situations. Furthermore, the fluctuations in the instantaneous values of CoF are also in good agreement with the simulation results obtained in [4, 5] for the contact with steel substrate.

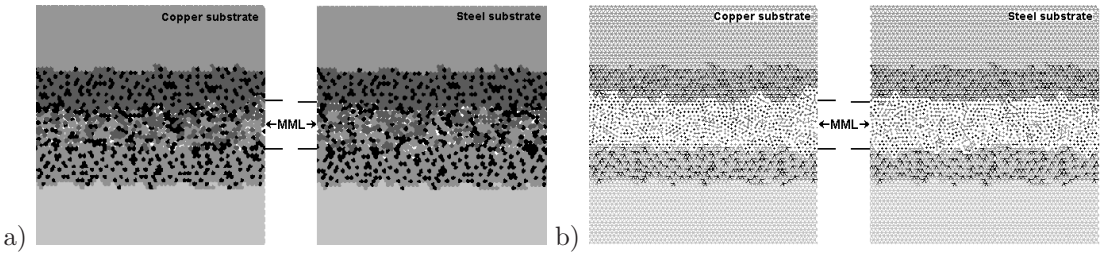


Figure 2: Comparison of (a) automata positions and (b) inter-automata relationships (bonding states) after simulation until having achieved steady state conditions (0.48 ms) assuming graphite-bearing friction layers on either copper or steel substrates

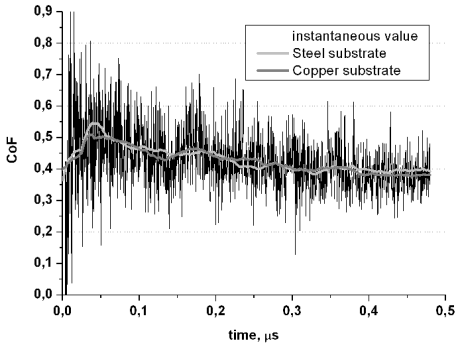


Figure 3: Evolution of instantaneous CoF for the friction layer shown in Fig.2 on copper substrate and comparison of mean CoF-values for the two substrate materials

3.2 Substitution of graphite nanoparticles by copper nanoparticles

The modelling setup was the same as in our previous studies [3, 4, 5, 6] except that graphite was substituted by soft copper. The material properties which were attributed to the automata of the model are summarized in Table 3. Based on the observation of recrystallized copper nanoparticles in the friction layers it was assumed that flow and tensile stresses are reduced at least by 50% compared to the properties of the bulk nanocrystalline material (hard copper) at the surface of the primary contact sites.

With this assumption the following simulation results were obtained. Fig. 4,a shows the structure of inter-automata bonds of the central fragment of the simulated setup after 0.48 μs. The concentration of automata with soft copper properties in the third body was 27.5 vol% and the value of external pressure was fixed at 35.1 MPa. According to the simulation the steady state motion is accompanied by MML formation with thickness of 100 nm. For comparison Fig. 4,b shows the results of modeling after 0.48 μs for the simulated setup with the same initial structure where the initial positions of soft copper particles were substituted with graphite inclusions. It is seen that the thickness of MML depicted in Fig. 4,b is higher, namely about 200 nm.

Thus, the substitution of automata with graphite properties by those of soft copper properties leads to an increase of the calculated mean value of CoF as shown in Fig. 4,c, viz., for the setup with graphite inclusions the mean value of CoF after 0.2 μs stabilized close to 0.30, in contrast to the setup with soft copper particles when it stabilized at 0.37. The time dependence of instantaneous values of friction coefficient provided by inclusions of copper in the third body are also characterized by larger amplitude oscillations, which is consistent with the observed reduced MML thickness.

Despite of these differences the principal sliding mechanism i.e. granular flow within the MML has not changed. The formation of a MML provides the stabilization of CoF near the value 0.37.

A completely different behaviour was obtained with a setup with relatively low volumetric concentration of particles of solid lubricant in the third body. The formation of a MML was not observed, rather damaging of surface layers by the formation of cracks is taking place. Also

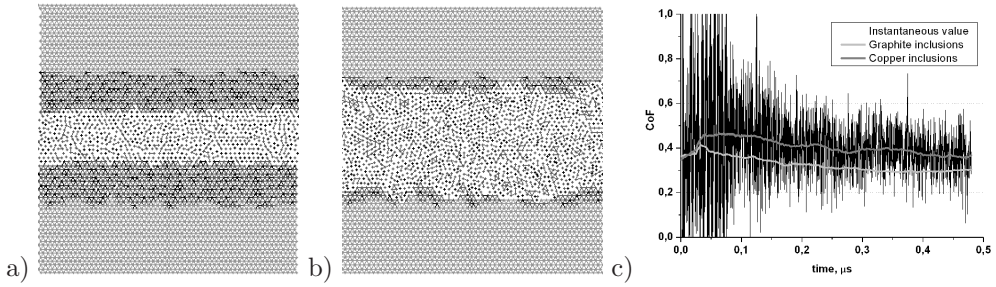


Figure 4: MML formed from friction layers with 27.5% of a) copper and b) graphite inclusions at P=35.1 MPa after 0.48 *m*s c) Evolution of instantaneous CoF for the friction layer shown in Fig.4a and comparison of mean CoF-values for the two solid lubricant inclusions i.e. soft copper and graphite

CoF fluctuations are extremely high in this case. A steady state of structure formation is not achieved. Therefore we suspect that cracking will gradually spread into the substrate materials and finally will cause the production of much larger wear particles compared to the situation with MML formation. Evidence for this suggested mechanism was obtained recently during a study of steel sliding against cast iron which showed friction induced delamination at the graphite- pearlite interface of the cast iron microstructure [5]. The mean values of CoF are close to 0.5. The sliding mechanism is completely different compared to the situation discussed before. It corresponds to a "stick-slip" mode of friction, and can be explained by competing processes of "gearing points" formation and their destruction.

Based on previous results of modeling described in [4, 5, 6], it is expected that there should exist some critical concentration of copper inclusions in the third body, which leads to a transition from a "stick-slip" mode of friction to a mode with a MML formation. For graphite inclusions the critical concentration for this transition was observed at 10%. The modelling data available for copper suggest a similar value, albeit it might be at a somewhat higher concentration. Further modeling is needed to clear this point.

4 Conclusion

The results of simulation have shown that copper as a constituent of brake pad materials has a number of positive qualities. Apart from providing good thermal conductivity, copper macro-particles have the capability to act as primary contact sites in a similar way as steel fibers do. Although bulk copper is much softer than steel the surfaces and superficial layers of the copper macro-particles are strengthened by severe plastic deformation leading to a nanocrystalline microstructure. At elevated temperatures nanocrystals at the surface recrystallize and thus form soft inclusions in the friction layer. Although harder than graphite, the presence of particles of soft copper or copper oxide in a friction layer obviously provide a similar effect as graphite inclusions, namely to act as a solid lubricant. According to the results of modeling the presence of copper particles in a certain volumetric concentration leads to the stabilization of smooth sliding mode by forming a granular layer of mechanically mixed materials from the friction layers which are screening primary contact sites of pad and disc. Like in previous results the layer formation is accompanied by lowering the mean value of CoF, and reducing the amplitude of fluctuations of the instantaneous CoF-values.

Despite of many simplifications which had been necessary to establish the model, the most important features for braking, namely friction force stabilization and smooth sliding conditions can be simulated quite well provided that the friction layers show the favorable microstructure and composition which has been identified experimentally.

Acknowledgements

Financial support from the German Research Foundation (DFG OS77/9-1 and DFG OS77/14-1) and program of the specialized branches of RAS, project No. 13.13.3, program No. 127 of SB RAS with exterior organization is gratefully acknowledged.

References

[1] Eriksson M, Bergmann F, Jacobson S.: On the nature of tribological contact in automotive brakes // Wear 2002, V.252.- pp.26-36

[2] Ostermeyer G P, Muller M.: New insights into the tribology of brake systems. / Proc. IMechE Vol. 222 Part D: J. Automobile Engineering (2008) special issue paper.- pp.1167-1200

[3] Oesterle W., Kloss H., Urban I., Dmitriev A.I.: Towards a better understanding of brake friction materials // Wear 2007, V.263.- pp.1189-1201

[4] Oesterle W., Kloss H., Dmitriev A.I.: Friction control during automotive braking: experimental observations and simulation at nanometre scale // Tribology-Materials, Surfaces & Interfaces 2009, N.3.- pp.196-202

[5] Dmitriev A.I., Oesterle W.: Modeling of brake pad-disc interface with emphasis to dynamics and deformation of structures // Trib. Int. 2010, V.43.- No4.- pp.719-727

[6] Dmitriev, A.I., Oesterle W., Kloss H. Numerical simulation of typical contact situations of brake friction materials, Tribology Int., 41.- 2008, pp. 1-8

[7] Psakhie S.G., Horie Y., Ostermeyer G.-P., et al Movable Cellular Automata method for simulating materials with mesostructure // Theor. Appl. Fracture Mech.- V.37.- 2001. P.311-334

[8] Eschelbach R. in Taschenbuch der metallischen Werkstoffe. Franck'sche Verlagsbuchandlung, Stuttgart, 1969, p.258

[9] Shpeizman V.V., Nikolaev V.I., Smirnov B.I., et al Deformation characteristics of nanocrystalline copper and nickel at low temperatures // Physics of the Solid State 1998.- V.40.- pp.1151-1154

[10] Guo J.Y., Wang K., Lu L.: Tensile properties of Cu with deformation twins induced by SMAT. // J.Mater.Sci.Technol. 2006, V.22.- pp.789-792

Andrey I. Dmitriev, pr. Academicheskii 2/4, Tomsk, 634021 Russia
Werner Oesterle, Unter den Eichen 87, Berlin, D-12200 Germany
Heinz Kloss, Unter den Eichen 87, Berlin, D-12200 Germany

Two-stage BEM for efficient solving transient thermo-(poro-) elastic problems

Anastasia A. Dobroskok Alexander M. Linkov
anastasiadobroskok@hotmail.com

Abstract

The paper presents a two-stage method to efficiently solve uncoupled thermo-(poro-) elastic problems for blocky systems with pores, inclusions and open surfaces of dicontinuity (cracks, thin inclusions). On the first stage, a transient problem for the diffusion equation is solved by using dual reciprocity method. The solution is represented by the sum of the quasi-steady part and the part, which is a linear combination of standard functions resulting from chosen radial basis functions (RBF). On the second stage, these two parts are used to find the solution of thermo-(poro-) elastic problem as the sum of a well-known solution for a quisi-steady part and a linear combination of particular solutions, corresponding to RBF. The needed particular solutions are given in explicit form for Gaussian RBF both for three and two dimensional problems. An example illustrates a practical application of the method developed to evaluate tilts caused by pressure shock applied to the surface of a hydraulic fracture.

1 Introduction

A two-stage method to solve uncoupled thermo- (poro-) elastic problems for blocky systems with pores, inclusions and open surfaces of discontinuity (cracks, thin inclusions) is suggested. It employs the fact that the equations for displacements and stresses do not contain time explicitly, they contain only the potential (temperature or pressure) and its gradient at a considered time instant. On the other hand, the potential and its gradient do not depend on elastic quantities, and they may be found in advance at the first stage of calculations by solving the diffusion equation. Having the potential and its gradient, one may solve an elasticity problem with potential depending terms considered as specific body forces. The solution of this problem is found on the second stage of calculations. The question is: how to do it efficiently with minimal changes in the common BEM?

The method suggested solves this problem both in 2-D and 3-D cases by using an important feature of the dual reciprocity method, DRM (e.g. [2], [4]), when the latter is applied on the first stage to find transient heat (liquid) flow. The feature is: a solution of a diffusion problem obtained by the DRM is represented as the sum $T = \widetilde{T} + T^*$ of (i) a quasi-steady part $\widetilde{T}$, satisfying the Laplace equation, and (ii) a pseudo-temperature T^*, which is a linear combination of standard pseudo-temperatures corresponding to standard radial basis functions (RBF):

$$T^*(\mathbf{x}, t) = \sum_{s=1}^{N} c_s(t) T_s^*(r_s),$$

where $c_s(t)$ are time-dependent coefficients found on the first stage; $\mathbf{x}$ is a point of a region under consideration; r_s is the distance from $\mathbf{x}$ to a fixed point $\mathbf{x}_{s\mathbf{0}}$, the center of the s-th RBF; N is the number of the RBF used.

Therefore, on the second stage, it is sufficient to combine solutions for (i) quasi-steady part and (ii) pseudo-temperature. A solution for a quasi-steady part is found by the common BEM (e.g. [1]) for a steady thermo-(poro-) elastic problem; it accounts for singular points such as crack tips, edges of thin inclusions, corner points and common apexes of grains. A particular solution (displacements $u_i^P(\mathbf{x}, t)$ and stresses $\sigma_{ij}^P(\mathbf{x}, t)$) for the pseudo-temperature T^* is available as a linear combination of standard displacements $u_{si}^*(r_s)$ and stresses $\sigma_{sij}^*(r_s)$, generated by the standard pseudo-temperatures $T_s^*(r_s)$:

$u_i^P(\mathbf{x},t) = \sum_{s=1}^N c_s(t) u_{si}^*(r_s)$, $\sigma_{ij}^P(\mathbf{x},t) = \sum_{s=1}^N c_s(t)\sigma_{sij}^*(r_s)$.

By superposing this solution with additional fields of displacements and stresses, which satisfy homogeneous elasticity equations, one may use a common BEM of elasticity problems. Finally, a common BEM for an elastic problem becomes applicable to the considered problems with two additional easily evaluated terms on the r. h. s. One of them corresponds to the known quasi-steady part $\widetilde{T}$; the other is generated by the written linear combination of standard displacements $u_{si}^*(r_s)$ and stresses $\sigma_{sij}^*(r_s)$ with known coefficients $c_s(t)$. Remind that the quasi-steady potential $\widetilde{T}$, its gradient and coefficients $c_s(t)$ are found on the first stage.

2 Particular solution for 3D problems

For 3-D thermo-(poro-) elastic problems, the explicit formulae for standard functions $T_s^*(r_s)$, dT_s^*/dr_s, $u_{si}^*(r_s)$ and $\sigma_{sij}^*(r_s)$, corresponding to the Gaussian RBF $f_B(r_s) = exp(-p^2)$, are:

$T_s^*(r_s) = a_s^2 T_B(p)$, $dT_s^*/dr_s = a_s dT_B/dp$, $u_{si}^*(r_s) = a_s^3 u_{Bi}$, $\sigma_{sij}^*(r_s) = a_s^2\sigma_{Bij}$.

Herein, $p = r_s/a_s$, a_s is the scaling parameter, $T_B(p)$, dT_B/dp are standard functions of the normalized distance p:

$T_B(p) = -\frac{1}{2p}\frac{\sqrt{\pi}}{2} erf(p)$, $\frac{dT_B}{dp} = -\frac{1}{2p}[2T_B(p) + \exp(-p^2)]$.

The standard functions u_{Bi} and σ_{Bij} are given by equations:

$u_{Bi} = \frac{1-2\nu}{1-\nu}\frac{\gamma}{\mu} u_B \frac{p_i}{p}$,

$\sigma_{Bij} = \frac{1-2\nu}{1-\nu}\gamma\left[\frac{du_B}{dp}\frac{p_i}{p}\frac{p_j}{p} + \frac{1}{p}u_B\left(\delta_{ij} - \frac{p_i}{p}\frac{p_j}{p}\right) + \frac{\nu}{1-2\nu}\delta_{ij}\left(\frac{du_B}{dp} + \frac{2}{p}u_B\right)\right] - \gamma\delta_{ij}T_B(p)$, where $u_B = \frac{1}{4}\left[\frac{dT_B}{dp} + 2pT_B(p)\right]$, $\frac{du_B}{dp} = -\frac{1}{2p}\frac{dT_B}{dp}$, $\gamma = 2\mu\alpha\frac{1+\nu}{1-2\nu}$ for 3-D thermoelastic problems, $\gamma = 1$ for poroelastic problems; μ, ν, α are the shear modulus, Poisson's ratio and the coefficient of thermal expansion, respectively, at the point $\mathbf{x}(x_1, x_2, x_3)$; $p_i/p = (x_i - x_{s0i})/r_s$ is the cosine of the angle between the vector $\mathbf{x} - \mathbf{x}_{s0}$ and the i-th coordinate axis; x_{s0i} are the coordinates of the center $\mathbf{x}_{s0}$ of the s-th RBF; δ_{ij} is the Kroneker's delta; i, $j = 1, 2, 3$.

3 Particular solution for 2D problems

Analogous formulae for 2-D problems in the complex variable (CV) form immediately follow from a particular solution given in [6]. Denote $z = x_1 + ix_2$ the complex coordinate of a point in the plane with the Cartesian coordinates x_1, x_2; $u(z) = u_1 + iu_2$ is the CV displacement vector with the components $u_1$and u_2 on the axes x_1, x_2, respectively; $\sigma_n(z) = \sigma_{n1} + i\sigma_{n2}$ is the CV traction vector on an area with the normal n and with the components σ_{n1} and σ_{n2} on the axes x_1, x_2, respectively. Then by using the equations of [6] we obtain the following CV particular solutions $u_s^*(z)$ and $\sigma_{sn}^*(z)$, corresponding to the Gaussian RBF $f_B(r_s) = exp(-p^2)$:

$u_s^*(z) = \frac{1}{2}\frac{1}{\mu}\frac{\kappa-1}{\kappa+1}\gamma a_s^3\frac{z-z_s}{a_s}[\Phi_s(p^2) - \varphi_s(p^2)]$,

$\sigma_{sn}^*(z) = -\frac{\kappa-1}{\kappa+1}\gamma a_s^2\left[\Phi_s(p^2) + \exp(-2i\alpha_z)\frac{z-z_s}{\overline{z}-\overline{z_s}}\varphi_s(p^2)\right]$,

where $p^2 = (z - z_s)(\overline{z} - \overline{z_s})/a_s^2$ is the squared normalized distance from a field point z to the center of an RBF; $\Phi_s(p^2) = \frac{1}{4}[\ln p^2 + Ei(p^2)] + C$, $Ei(x)$ is the integral exponent, we have $\Phi_s(0) = 1$ for the value $C = 1.827216$; $\varphi_s(p^2) = \frac{1}{4}\{1 + [\exp(-p^2) - 1]/p^2\}$; as above, a_s is the scaling parameter, μ is the shear modulus; the overbar denotes complex conjugation. For *plane strain* problems $\kappa = 3 - 4\nu$; for *plane stress* problems $\kappa = \frac{3-\nu}{1+\nu}$. In *poroelastic* problems $\gamma = 1$; in *thermoelastic* plane strain problems $\gamma = 2\mu\alpha\frac{1+\nu}{1-2\nu}$; in *thermoelastic* plane stress problems $\gamma = 2\mu\alpha\frac{1+\nu}{1-\nu}$; as above, μ is the shear modulus, ν is the Poisson's ratio, α is the coefficient of thermal expansion.

4 Example: pressure shock on surfaces of hydraulic fracture

The application of the method is illustrated by considering pressure shock on surfaces of hydraulic fracture created in rock to increase oil production from a borehole. A vertical fracture with the height $2l_c$ has its middle at the depth H from the earth surface; the length of the fracture is

large enough to assume conditions of plane strain in the vertical cross-section orthogonal to the fracture at its middle part. In situ vertical stress is σ_{11}^0, in situ horizontal stress orthogonal to the fracture is σ_{22}^0, in situ porous pressure is p^0. A borehole is closed sufficiently long, so that the pore pressure in the fracture is close to p^0 before the initial moment $t = 0$. At this moment, the pressure sharply drops to a value, which is small as compared with p^0. We assume that it happens instantly; therefore a pressure shock $-p^0$ is applied to the fracture surfaces at $t = 0$. We are interested in calculation of displacements and tilts induced by the shock on the earth surface by the pressure shock. Being compared with data of direct observations, they may serve to evaluate important characteristics of the site, such as the geometry of a hydraulic fracture and the diffusivity of rock.

The results are obtained by using the CV DRM [4] on the first stage of calculations and the CV hypersingular BEM (e.g. [7], [5]) on the second stage. We consider a square box with the side a large as compared with the fracture length $2l_c$. For certainty, we take $2l_c/a = 0.1$. The center of the fracture is located in the center of the box; the upper horizontal side of the box coincides with the earth surface. The contour of the box serves as a boundary of fluid supply to the fracture.

At both stages of calculations, the BEM mesh is taken the same: each side of the box is represented with 14 boundary elements; the hydraulic crack is represented with 140 ordinary and 2 tip elements accounting for the square-root singularity of the flux (on the first stage) and stresses (on the second stage). All the elements, both ordinary and tip, are three-node elements. Thus the total number of unknown boundary values is $(14{\cdot}4{+}140{+}2){\cdot}3 = 594$ on the first stage and two-fold greater (1188) on the second stage. As shown in [3], [5], such a mesh and approximations provide at least three correct digits in flux intensity factors and stress intensity factors for a steady flow. To account for the transient process, 400 Gaussian RBF with equidistantly located centers are used. According to the estimations of [4], this number and location of the RBF provides accurate evaluation of changes in fields induced by a shock for time instances as small as $t_n = 0.002$, at least (t_n is the time normalizes as explained below).

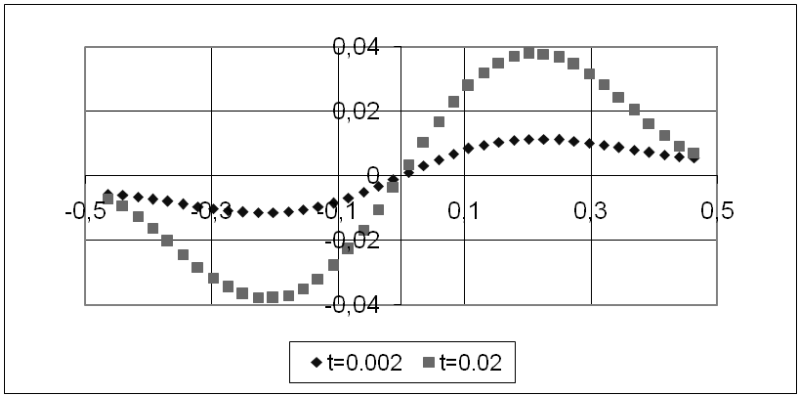


Figure 1: Normalized tilts on the surface at two time instances

For certainty, we set $\sigma_{11}^0/p^0 = -2.5$, $\sigma_{22}^0/p^0 = -1.67$. The calculated tilts on the earth surface are given in Fig. 1 for two time instances ($t_n = 0.002$ and $t_n = 0.02$), which although differ ten-fold, are still quite close to the moment of pressure shock what may serve for characterization of the diffusion parameter. The tilts are normalized by the ratio p^0/E of the in situ pore pressure p^0 to the rock elasticity modulus E. The origin of the abscissa is located exactly above the fracture, the abscissa goes along the earth surface and normalized by the box side length a. The time t_n is dimensionless: $t_n = \frac{\beta}{a^2}t$, where β is the diffusion coefficient. When analyzing the results, one may assume the following reference values: the depth $H = 300$ m, the fracture height $2lc = 60$ m, the box side length $a = 600$ m, $p^0 = 3$ MPa, $E = 2 \cdot 10^4$ MPa. Then from the graphs it follows that in the considered case, the actual tilts are of order $10^{-2}p^0/E = 1.5{\cdot}10^{-6}$. Such tilts may be measured by modern tiltmeters, which provide reliable measurements of tilts as small as 10^{-8}. As could be expected, the tilts are antisymmetric with the zero point above the hydraulic fracture. This may serve for locating the latter by using tilt measurements. At last, the maximal tilts at $t_n = 0.002$ and $t_n = 0.02$ differ some three times. Having actual tilts measured in real time, these data may serve to evaluate the average diffusivity β and to conclude on the accuracy of its estimation.

Acknowledgements

The authors appreciate the support of the Russian Fund for Fundamental Researches (Grant 09-05-00104).

References

[1] Benerjee P. K., Butterfield R. Boundary Element Methods in Engineering Science. London, McGrow-Hill, 1981.

[2] Blobner J. , Bialecki R., Kuhn G. Transient non-linear heat conduction-radiation problems – A boundary element method formulation. Int. J. Numer. Meth. Engng. 46: 1865–1882, 1999.

[3] Dobroskok A. A., Linkov A. M. Complex variable equations and numerical solution of harmonic problems for piece-wise homogeneous media. Appl. Math. Mech. 73: 313-325, 2009.

[4] Dobroskok A. A., Linkov A. M. CV dual reciprocity BEM for transient flow in blocky systems with singular points and lines of discontinuities. Engng. Anal. Bound. Elem. 34: 238-247, 2010.

[5] Dobroskok A. A., Linkov A. M. CV BEM for transient thermo-(poro-) elastic problems concerning with blocky systems with singular points and lines of discontinuities. Int. J. of Engineering Science, doi: 10.1016/j.ijengsci.2010.02.008, 2010.

[6] Linkov A. M. The complex variable hypersingular BIE of thermoelasticity for plane inhomogeneous bodies with cracks and cavities. Proc. Int. Conf. Mathematical Problems of Mechanics of Non-Homogenous Structures, G. S. Kit editor, L'vov, National Academy of Sciences of Ukraine: 250–252, 2003.

[7] Linkov A. Boundary Integral Equations in Elasticity Theory. Dordrecht, the Netherlands: Kluwer Academic Publishers, 2002.

Alexander M. Linkov, IPME, Saint-Petersburg, Russia
Anastasia A. Dobroskok, University of New Mexico, Las Cruses, USA

On the problem of interaction between the soft shell and the solid covered by it

Polina Dyatlova Alexandr Majorov Vitaly Lutov
polinadyatlova@mail.ru

Abstract

The variational method for investigation of interaction between elastic soft shell and surface of rigid body covered by the shell is developed. The method is based on principle of minimization of strain energy functional of the shell in its equilibrium state. Extremals of the functional are sought in form of linear combinations of coordinate functions which are chosen in accordance with boundary conditions that are prescribed for the shell's edges. The nonlinear equations set for determination of coefficients of these linear combinations are investigated by numerical methods for various cases of solid's and shell's shapes.

1 Introduction

Simplicity of manufacturing, using and transportation of soft, i.e. not resist the bending forces shells, leads to a rapid expansion of the sphere of their applications. It is also in much measure stimulated by emergence of new knitting materials, which using for the manufacturing of shells can improve their quality characteristics, such as strength, heat resistance, chemical inertness and other. Evaluating the development prospects of production and consumption of soft knitted shells, one could argue that their research and, in particular, the study of their mechanical properties, will become increasingly urgent question.

Soft shell significantly deforms and changes its shape, with changes of applied to it external forces. Soft shell immediately after being made and the same shell in exploiting conditions usually have little in common in the characteristics of its geometry and mechanical properties. It is why research of such shells gives us wide variety of very difficult and interesting mathematical problems.

2 Mathematical model of the problem

We consider the linear-elastic soft shell stretched on the solid surface, which shape is given by the equation

$$\rho = \rho(\psi, z). \tag{1}$$

Here ρ, ψ and z are cylindrical coordinates. (See Fig. 1)

It is assumed that the shell has a structure of the orthogonal net and in the undeformed state is a cylindrical pipe with radius r. It is also assumed that the warp set of filaments is located on the generating curves of the pipe, and the weft set of filaments on its directing curves. Lagrangian coordinates φ and ζ of some particle M of the shell are counted in its undeformed state along the filaments from the lower edge of the shell and, respectively, from arbitrary fixed generating curve.

The density of the potential energy of deformation corresponding to unit area of parametric plane $\varphi\zeta$ is given by formula [1], [2]

$$u(\varphi, \zeta) = \frac{1}{2}k_1\varepsilon_1^2 + \frac{1}{2}k_2\varepsilon_2^2 \tag{2}$$

where ε_1 and ε_2 are relative elongation of the coordinate lines, k_1 and k_2 are characteristics of elasticity. It should be remarked that $u(\varphi, \zeta)$ as well as k_1 and k_2 has the dimention of force.

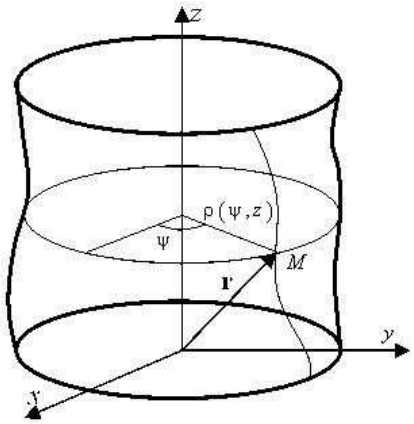


Figure 1: The form of the shell fitted on the solid's surface.

Metric coefficients of undeformed tube are given by the formulas

$$g_{11}^0 = r^2, g_{22}^0 = 1, g_{12}^0 = g_{21}^0 = 0. \tag{3}$$

Lets suppose that the distribution of the shell on the surface of the covered by its solid is characterized by functions $\theta(\varphi, \zeta)$ and $w(\varphi, \zeta)$ which are introduced by the equalities

$$\psi = \varphi + \alpha\theta(\varphi, \zeta), z = \zeta + \alpha w(\varphi, \zeta), \tag{4}$$

where α is parameter, which will be considered as a small quantity of first order.

$$\rho(\psi, z) = r + \alpha f(\psi, z), \tag{5}$$

where f is the function, which is considered as known, determines the deviation of the solid's surface from the cylindrical one.

Metric coefficients of the deformed shell are calculated by the formulas

$$g_{11} = r^2 + 2\alpha r^2 \left(\frac{f(\varphi, \zeta)}{r} + \frac{\partial\theta(\varphi, \zeta)}{\partial\varphi} \right), \tag{6}$$

$$g_{22} = 1 + 2\alpha \frac{w(\varphi, \zeta)}{\partial\zeta},$$

$$g_{12} = \alpha \left(r^2 \frac{\partial\theta(\varphi, \zeta)}{\partial\zeta} + \frac{\partial w(\varphi, \zeta)}{\partial\varphi} \right).$$

Relative elongations of coordinate lines are defined by

$$\varepsilon_1 = \sqrt{\frac{g_{11}}{g_{11}^0}} - 1, \varepsilon_2 = \sqrt{\frac{g_{22}}{g_{22}^0}} - 1. \tag{7}$$

The full stress-strain energy of the shell can be represented as follows [2], [3]

$$U = \frac{1}{2} \iint\limits_S \left(k_1\varepsilon_1^2 + k_2\varepsilon_2^2 \right) \sqrt{g_{11}^0 g_{22}^0 - g_{12}^{02}} d\varphi d\zeta. \tag{8}$$

To linearize the expressions for the deformations ε_1 and ε_2 the magnitudes of the higher order than α will be neglected. This yields

$$\varepsilon_1 = \alpha \left(\frac{\partial\theta}{\partial\varphi} + \frac{f}{r} \right), \varepsilon_2 = \alpha \frac{\partial w}{\partial\zeta}. \tag{9}$$

Now the energy of the shell is given by formula:

$$U = \alpha^2 \int\int_S \left[k_1 \left(\frac{\partial\theta}{\partial\varphi} + \frac{f}{r} \right)^2 + k_2 r \left(\frac{\partial w}{\partial\zeta} \right)^2 \right] d\varphi d\zeta, \tag{10}$$

We seek the function θ and w by the Galerkin method so as to minimize the functional (10).

For example, the problem corresponding to the following boundary conditions imposed on the displacement w has been considered:

$$at\zeta = 0w = P_1(\varphi); at\zeta = Hw = P_2(\varphi). \tag{11}$$

At the angular displacement θ of the shell, as well as at the displacement w, we impose periodicity conditions with respect to the angle φ

$$w(\varphi,\zeta) = w(\varphi + 2\pi,\zeta); \theta(\varphi,\zeta) = \theta(\varphi + 2\pi,\zeta). \tag{12}$$

We use the following representation of the functions $w(\varphi,\zeta)$ and $\theta(\varphi,\zeta)$:

$$w = \frac{\zeta}{H}P_2(\varphi) + \frac{H-\zeta}{H}P_1(\varphi) + \sum_{k=1}^{\infty} A_k w_k(\varphi,\zeta), \tag{13}$$

$$\theta = \sum_{k=0}^{\infty} B_k \theta_k(\varphi,\zeta). \tag{14}$$

where the coordinate functions $w_k(\varphi,\zeta)$ and $\theta_k(\varphi,\zeta)$ must satisfy the following conditions for all k:

$$\begin{aligned} &w_k(\varphi,0) = w_k(\varphi,H) = 0, \\ &w_k(\varphi,\zeta) = w_k(\varphi + 2\pi,\zeta), \\ &\theta_k(\varphi,\zeta) = \theta_k(\varphi + 2\pi,\zeta). \end{aligned} \tag{15}$$

Substituting $w(\varphi,\zeta)$ and $\theta(\varphi,\zeta)$ from (13) and (14) in (10) we obtain the expression for the energy of the shell as a function of the coefficients A_k and B_k:

$$U = U(A_k, B_k). \tag{16}$$

Now, to determine the values A_k and B_k corresponding to minimum of magnitude U, we obtain a set of linear algebraic equations

$$\frac{\partial U}{\partial A_k} = 0, \frac{\partial U}{\partial B_k} = 0, \forall k. \tag{17}$$

Let's restrict consideration by the case when the deviation from the cylindrical shape of the solid is given by the function

$$f = \left(1 + \cos\frac{\pi\zeta}{H}\right)(1 + \sin\varphi). \tag{18}$$

The partial sums of series (13) and (14) will be presented in form

$$w = \frac{\zeta}{H}P_2(\varphi) + \frac{H-\zeta}{H}P_1(\varphi) + A_1\left(1 - \cos\frac{2\pi\zeta}{H}\right) \tag{19}$$

$$\theta = B_0 + B_1\left(1 + \cos\frac{\pi\zeta}{H}\right)(1 - \cos\varphi). \tag{20}$$

Substituting these expressions in (10), we obtain

$$\begin{aligned} U = \alpha^2 \int\int_S \left[k_1\left(1 + \cos\frac{\pi\zeta}{H}\right)^2\left(B_1\sin\varphi + \frac{1}{r}(1 + \sin\varphi)\right)^2\right] d\varphi d\zeta + \\ + \alpha^2 \int\int_S \left[k_2 r\left(\frac{P_2(\varphi)}{H} - \frac{P_1(\varphi)}{H} + A_1\frac{2\pi}{H}\sin\frac{2\pi\zeta}{H}\right)^2\right] d\varphi d\zeta. \end{aligned} \tag{21}$$

It is easy to see that the value U can be represented as

$$U = K_1 B_1^2 + K_2 B_1 + K_3 A_1^2 + K_4 A_1 + K_5, \tag{22}$$

where

$$K_1 = \alpha^2 \int\int_S \left[k_1 \left(1 + \cos\frac{\pi\zeta}{H}\right)^2 \sin^2\varphi \right] d\varphi d\zeta, \tag{23}$$

$$K_2 = \alpha^2 \int\int_S \left[k_1 \frac{2}{r} \left(1 + \cos\frac{\pi\zeta}{H}\right)^2 \sin\varphi(1 + \sin\varphi) \right] d\varphi d\zeta = \frac{2}{r} K_1,$$

$$K_3 = \alpha^2 \int\int_S \left[k_2 r \left(\frac{2\pi}{H}\right)^2 \sin^2\frac{2\pi\zeta}{H} \right] d\varphi d\zeta,$$

$$K_4 = \alpha^2 \int\int_S \left[k_2 r \frac{4\pi}{H} \left(\frac{P_2(\varphi)}{H} - \frac{P_1(\varphi)}{H}\right) \sin\frac{2\pi\zeta}{H} \right] d\varphi d\zeta = 0.$$

Now equation (17) lead to the following equalities

$$2K_1 B_1 + K_2 = 0, \tag{24}$$
$$2K_3 A_1 + K_4 = 0.$$

Hence, in view of (23) we obtain

$$B_1 = -\frac{1}{r}, \qquad A_1 = 0. \tag{25}$$

3 Conclusion

In this paper we propose the method for calculating the stresses and strains arising in the shell fitted on the solids surface, as well as for determination of the shell's pressure on the solid. The method is asymptotic and is good for those cases when the shape of the shell differs but little from the shape of the solid covered by it. The study is detailed in the assumption that the undeformed shell is a cylindrical tube with a linear elastic properties, and solids shape differs little from the cylinder. The energy method based on calculation of the extremals of the shell's potential energy is used.

The results show that the calculations carried out fully coincide with results obtained by the small parameter method.

Acknowledgements

The authors gratefully acknowledge the support for this work provided by Ministry of Education and Science of Russia.

References

[1] Dyatlova P., Polyakova E., Chaikin V.: Constitutive equations for soft shells with network microstructures. Proceedings of XXXIV Summer school "Advanced problems in mechanics", Saint-Petersburg, 2006, P. 146 - 153

[2] Polyakova E., Chaikin V.: Applied problems of a mechanics of soft shells and fabrics. Saint-Petersburg, SPSUTD, 2006, 193 pp. (Russian)

[3] Dyatlova P., Polyakova E., Chaikin V.: On the finite elements method for investigations of the interaction of soft shells with solids' surfaces. Proceedings of XXXV Summer school "Advanced problems in mechanics", Saint-Petersburg, 2007, P. 85 - 92.

Polina Dyatlova, St-Petersburg State University of Technology and Design, Bolshaya Morskaya St. 18, St.-Petersburg, 191186, Russia

The strain-stressed state of the band winded up on the ridged body

Polina Dyatlova Vitaly Lutov Ekaterina Polyakova
polinadyatlova@mail.ru

Abstract

The combined equations in partial derivatives for analysis of interaction between a tube and an elastic tape that is reinforcing the tube are obtained. The exact solution is obtained under supposition that the tube is circular cylinder with smooth surface and the strain-stress state of the tape has the helical symmetry.

1 Introduction

Problems of reinforcing of composite shells and, in particular, pipes by winding tapes and yarns made of polymeric materials, are gaining increasing attention. The successes of polymer chemistry allow to achieve high quality of reinforcement on various consumer wants with insignificant economic cost of used industrial equipment and consumables. Constant expansion of the range and volumes of reinforced shells determines the practical value of researches aimed at developing methods of calculation and optimization of composite structures [1], [2].

Methods for reinforcing composite articles by winding yarns and tapes are widely used in the creation of different products, providing it with high strength indices by the rational selection of geometric parameters of winding paths [1]. The transition from the use of threads to the tapes using can often without reducing the quality of reinforcement significantly reduce the complexity and time of manufacturing, by lessening the number of reinforcing material coils. Significant advances in the study of the use of reinforcing tapes made in [1], [3], [4]. In [5] considered the problem of taking into account the relaxation properties of the tapes, in the process of winding on a cylindrical tube. In the present work within the general theory of soft shells is developing a method of mathematical modeling of stress-strain state of tape wound on the tube's surface.

2 The equilibrium equations

We consider the tape, reinforcing the pipe, as continual orthotropic surface consisting of weft and warp threads. The particles tape are identified with the Lagrangian coordinates h and s introduced on the undeformed tape, in such way that coordinates h of the particles M will be regarded as the distance measured along the weft thread from the bottom edge of the tape (see Figure) to the particle, while the coordinates s we will consider as the length of the warp threads between the points M and arbitrarily fixed weft thread. Using the cylindrical coordinates $\rho\varphi z$ and Cartesian coordinate $Oxyz$, we represent the radius vector $\vec{r}$ of the particle M (see Figure) by formula

$$\begin{aligned}\vec{r} = \vec{r}(s,h) = \vec{i}R\left(\varphi(s,h), z(s,h)\right)\cos\varphi(s,h) + \\ + \vec{j}R\left(\varphi(s,h), z(s,h)\right)\sin\varphi(s,h) + \vec{k}z(s,h),\end{aligned} \tag{1}$$

where $\vec{i}$, $\vec{j}$ and $\vec{k}$ are orts of system $Oxyz$, $\rho = R(\varphi, z)$ is some assumed as known function, which determines the tube's shape. When the tube is a smooth circular cylinder, R is considered as a constant. The required functions $\varphi(s,h)$ and $z(s,h)$ determine the distribution of tape's material on the tube's surface.

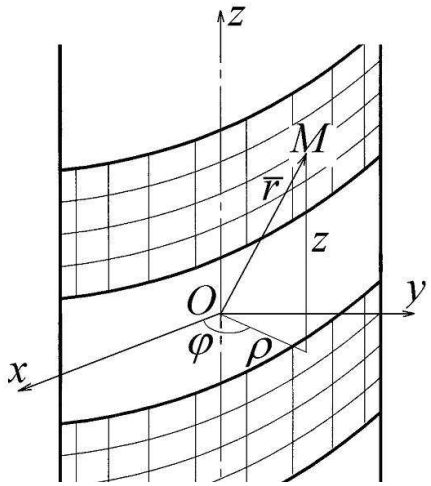


Figure 1: The tape helically wound on the circular cylindrical surface.

We introduce the following notation:

$$\vec{r_1}(s,h) = \frac{\partial \vec{r}(s,h)}{\partial s}, \vec{r_2}(s,h) = \frac{\partial \vec{r}(s,h)}{\partial h}. \tag{2}$$

Elongation factors λ_1 and λ_2 [6, 7] of warp and weft threads in force of (1) and (4) are defined by

$$\lambda_1 = |\vec{r_1}|, \lambda_2 = |\vec{r_2}|. \tag{3}$$

Borrowing from [7] equilibrium equations, we have

$$\frac{\partial}{\partial s}(\vec{\sigma}_1|\vec{r}_2|) + \frac{\partial}{\partial h}(\vec{\sigma}_2|\vec{r}_1|) + \vec{q}\sqrt{(\vec{r}_1)^2(\vec{r}_2)^2 - (\vec{r}_1 \cdot \vec{r}_2)^2} = \bar{0}. \tag{4}$$

Here $\vec{\sigma}_1$ and $\vec{\sigma}_2$ are actual stresses on the coordinate lines and , respectively. The stresses are presented in the form

$$\vec{\sigma}_1 = \vec{e}_1\sigma_{11} + \vec{e}_2\sigma_{12}, \vec{\sigma}_2 = \vec{e}_1\sigma_{21} + \vec{e}_2\sigma_{22}; \tag{5}$$

where $\vec{e}_1$ and $\vec{e}_2$ are orts tangent to the coordinate lines, respectively, $h = const$ and $s = const$ are defined by

$$\vec{e_1} = \frac{\vec{r}_1}{|\vec{r}_1|} = \frac{\vec{r}_1}{\lambda_1}, \vec{e_2} = \frac{\vec{r}_2}{|\vec{r}_2|} = \frac{\vec{r}_2}{\lambda_2}; \tag{6}$$

q is intensity of the external forces acting on the surface of the tape provided in the form of

$$\vec{q} = \vec{e}_1 q_1 + \vec{e}_2 q_2 + \vec{n} q_n; \tag{7}$$

$\vec{n}$ is unit vector of outward normal to the surface of the tube.

Assumptions made about the structure of the textile tape and the linear elasticity of its constituent filaments, allow obtaining the following expressions for the stress components

$$\sigma_{11} = k_1\frac{\lambda_1 - 1}{\lambda_2}, \sigma_{22} = k_2\frac{\lambda_2 - 1}{\lambda_1}, \sigma_{12} = \sigma_{21} = 0, \tag{8}$$

where k_1 and k_2 are the coefficients of tape elasticity in direction of warp and, accordingly, weft threads.

Taken into account (5) - (8), we can rewrite (4) in the form

$$k_1\frac{\partial \vec{e}_1}{\partial s}(\lambda_1 - 1) + k_1\vec{e}_1\frac{\partial \lambda_1}{\partial s} + k_2\frac{\partial \vec{e}_2}{\partial h}(\lambda_2 - 1) + k_2\vec{e}_2\frac{\partial \lambda_2}{\partial h} + \tag{9}$$

$$+\vec{q}\sqrt{(\vec{r}_1)^2(\vec{r}_2)^2-(\vec{r}_1\cdot\vec{r}_2)^2}=\bar{0}.$$

Successively multiplying the vector equation (9) by unit vectors $\vec{e}_1$, $\vec{e}_2$ and $\vec{n}$, we obtain the following equivalent to (9) the set of three scalar equations

$$k_1\frac{\partial\lambda_1}{\partial s}+k_2\vec{e}_1\cdot\frac{\partial\vec{e}_2}{\partial h}(\lambda_2-1)+k_2\vec{e}_1\cdot\vec{e}_2\frac{\partial\lambda_2}{\partial h}+q_1\sqrt{(\vec{r}_1)^2(\vec{r}_2)^2-(\vec{r}_1\cdot\vec{r}_2)^2}=0, \tag{10}$$

$$k_1\vec{e}_2\cdot\frac{\partial\vec{e}_1}{\partial s}(\lambda_1-1)+k_1\vec{e}_2\cdot\vec{e}_1\frac{\partial\lambda_1}{\partial s}+k_2\frac{\partial\lambda_2}{\partial h}+q_2\sqrt{(\vec{r}_1)^2(\vec{r}_2)^2-(\vec{r}_1\cdot\vec{r}_2)^2}=0, \tag{11}$$

$$k_1\vec{n}\cdot\frac{\partial\vec{e}_1}{\partial s}(\lambda_1-1)+k_2\vec{n}\cdot\frac{\partial\vec{e}_2}{\partial h}(\lambda_2-1)+q_n\sqrt{(\vec{r}_1)^2(\vec{r}_2)^2-(\vec{r}_1\cdot\vec{r}_2)^2}=0. \tag{12}$$

Equations (10) and (11) are used to determine the functions $\varphi(s,h)$ and $z(s,h)$, while equation (12) - to determine the tape pressure on the pipe's surface.

3 Case of the helical symmetry of the winding tape

Let the tube is a circular cylinder of radius . In this case the following equality is valid

$$\lambda_1=\sqrt{R^2\left(\frac{\partial\varphi}{\partial s}\right)^2+\left(\frac{\partial z}{\partial s}\right)^2}, \tag{13}$$

$$\lambda_2=\sqrt{R^2\left(\frac{\partial\varphi}{\partial h}\right)^2+\left(\frac{\partial z}{\partial h}\right)^2}.$$

and

$$\vec{n}=\vec{i}\cos\varphi+\vec{j}\sin\varphi, \tag{14}$$

Let's confine ourselves to the most typical case, when the state of the tape has helical symmetry, which is expressed mathematically in the fact that the derivatives of the characteristics of the state, i.e. of magnitudes λ_1, λ_2, σ_{11} and σ_{22} with respect to the coordinate s is equal zero.

The following conditions

$$\frac{\partial\lambda_1}{\partial s}=\frac{\partial\lambda_2}{\partial s}=0, \tag{15}$$

by (13) yields

$$R^2\frac{\partial\varphi}{\partial s}\frac{\partial^2\varphi}{\partial s^2}+\frac{\partial z}{\partial s}\frac{\partial^2 z}{\partial s^2}=0, \tag{16}$$

$$R^2\frac{\partial\varphi}{\partial h}\frac{\partial^2\varphi}{\partial s\partial h}+\frac{\partial z}{\partial h}\frac{\partial^2 z}{\partial s\partial h}=0.$$

.

By screw location of any warp thread, individualized by Lagrangian coordinate h, the linear dependence of the coordinate z of this thread's particle on the Lagrangian coordinates s of the particle is caused. Therefore, considering the first of equalities (16), we conclude that the following equalities hold on

$$\frac{\partial^2\varphi}{\partial s^2}=\frac{\partial^2 z}{\partial s^2}=0. \tag{17}$$

Considering further that for every warp thread the ratio between the coordinates z and s of its points should not depend on the choice of this thread, we conclude that

$$z=ps+\zeta(h), \tag{18}$$

where p is constant, and ζ is a function of h.

Now, on the basis of equality (18) and the second of equalities (16) we conclude that

$$\varphi = qs + f(h), \tag{19}$$

where q is constant, and f is a function of h.

Further, according to (13), (18) and (19), we obtain

$$\lambda_1 = \sqrt{R^2q^2 + p^2}, \tag{20}$$
$$\lambda_2 = \sqrt{R^2f'^2 + \zeta'^2}.$$

According to (1) and (2) with (18) and (19), we have

$$\vec{r}_1 = -\vec{i}Rq\sin\varphi + \vec{j}Rq\cos\varphi + \vec{k}p, \tag{21}$$
$$\vec{r}_2 = -\vec{i}Rf'\sin\varphi + \vec{j}Rf'\cos\varphi + \vec{k}\zeta',$$
$$\vec{e}_1 = \frac{-\vec{i}Rq\sin\varphi + \vec{j}Rq\cos\varphi + \vec{k}p}{\lambda_1},$$
$$\vec{e}_2 = \frac{-\vec{i}Rf'\sin\varphi + \vec{j}Rf'\cos\varphi + \vec{k}\zeta'}{\lambda_2}.$$

From (21) follows

$$\frac{\partial\vec{e}_1}{\partial s} = \frac{-\vec{i}Rq^2\cos\varphi - \vec{j}Rq^2\sin\varphi}{\lambda_1}, \tag{22}$$
$$\frac{\partial\vec{e}_2}{\partial h} = \frac{-\vec{i}Rf''\sin\varphi + \vec{j}Rf''\cos\varphi + \vec{k}\zeta''}{\lambda_2} + \frac{-\vec{i}Rf'^2\cos\varphi - \vec{j}Rf'^2\sin\varphi}{\lambda_2} -$$
$$- \frac{-\vec{i}Rf'\sin\varphi + \vec{j}Rf'\cos\varphi + \vec{k}\zeta'}{\lambda_2^2}\frac{\partial\lambda_2}{\partial h}.$$

Taken into account (21), (22) and (14), we obtain

$$\vec{e}_2\cdot\frac{\partial\vec{e}_1}{\partial s} = 0, \vec{e}_2\cdot\vec{e}_1 = \frac{R^2f'q + p\zeta'}{\lambda_1\lambda_2}, \vec{n}\cdot\frac{\partial\vec{e}_1}{\partial s} = -\frac{Rq^2}{\lambda_1}, \tag{23}$$
$$\vec{n}\cdot\frac{\partial\vec{e}_2}{\partial h} = -\frac{Rf'^2}{\lambda_2}, \vec{e}_1\cdot\frac{\partial\vec{e}_2}{\partial h} = \frac{R^2qf'' + p\zeta''}{\lambda_1\lambda_2} + \frac{R^2qf' + p\zeta'}{\lambda_1\lambda_2^2}\frac{\partial\lambda_2}{\partial h},$$
$$\sqrt{(\vec{r}_1)^2(\vec{r}_2)^2 - (\vec{r}_1\cdot\vec{r}_2)^2} = R(pf' + q\zeta').$$

Now, using (23) and (15), we rewrite the equation (10) - (12) as follows:

$$k_2\left(\frac{R^2qf'' + p\zeta''}{\lambda_1\lambda_2} + \frac{R^2qf' + p\zeta'}{\lambda_1\lambda_2^2}\frac{\partial\lambda_2}{\partial h}\right)(\lambda_2 - 1) + \tag{24}$$
$$+ k_2\frac{R^2f'q + p\zeta'}{\lambda_1\lambda_2}\frac{\partial\lambda_2}{\partial h} + q_1R(pf' + q\zeta') = 0,$$

$$k_2\frac{\partial\lambda_2}{\partial h} + q_2R(pf' + q\zeta') = 0, \tag{25}$$

$$-k_1\frac{Rq^2}{\lambda_1}(\lambda_1 - 1) - k_2\frac{Rf'^2}{\lambda_2}(\lambda_2 - 1) + q_nR(pf' + q\zeta') = 0. \tag{26}$$

4 On the problem of stress-strain state of the tapes at various conditions of its winding on the tube's surface

To be logically self-contained problem of calculating the mechanical characteristics of the mechanical system "tape-pipe" above obtained equations (20) and (24) - (26), containing unknown magnitudes q, p, f, ζ, q_1, q_2 and q_n must be supplemented with information that allows write up four more equations. This information is determined by the choice of technology winding tape on the pipe and its subsequent fastening.

It is natural to assume that the lead angle of the tape in the process of winding is given directly, and therefore, we can put

$$p = \tan\alpha. \tag{27}$$

Let us consider the case when during winding the tape and after its fixation on the surface of the pipe forces moving the particles of the tape in respect of the surface are not existing, i.e. the following equalities hold on

$$q_1 = q_2 = 0. \tag{28}$$

In this case from (24) and (25) we obtain

$$\lambda_2 = const, (R^2 q f'' + p\zeta'')(\lambda_2 - 1) = 0. \tag{29}$$

Equalities (29) give reason to expect that there may be two kinds of the tape's states. The first kind of the states is characterized by the condition

$$\lambda_2 = 1. \tag{30}$$

The second kind of the states corresponds to the equalities

$$\lambda_2 = const, R^2 q f'' + p\zeta'' = 0. \tag{31}$$

Condition (30) means that the weft threads of the tape are not stretched and $\sigma_{22} = 0$. It is clear that in this case may be realized various forms of location of the weft threads that do not depend on the Lagrangian coordinates s of these threads. The differences of these forms will affect the angles between the warp and weft threads, as well as the bandwidth occupied by the tape on the pipe's surface. If for technological reasons, a form of weft threads and the multiplicity of elongation warp threads are given, then equations (18) - (20) are defining magnitudes f' and ζ' , and the pressure of the tape on the pipe is calculated by formula

$$q_n = \lambda_1 \frac{pf' + q\zeta'}{k_1 q^2(\lambda_1 - 1)}. \tag{32}$$

Considering the second kind of possible states of the tape, taking into account (20), we rewrite equality (31) in the form

$$R^2 f'^2 + \zeta'^2 = C_1, R^2 q f' + p\zeta' = C_2, \tag{33}$$

where C_1 and C_2 are constants.

From (33), (18) and (19) we conclude that with exactness up to additive constants following equalities are true

$$z = ps + p_1 h, \varphi = qs + q_1 h, \tag{34}$$

where p_1 and q_1 are constants whose values, as well as the value q, determined by the parameters of technological process of winding tape. Pressure tape on the pipe in this case is calculated by formula (32) with appropriate values of f' and ζ'.

It is clear that in this case, the weft threads are located on the geodesic lines of the tube, which generally speaking, are not orthogonal to the warp filaments.

5 Conclusion

In conclusion, it should be noted that the practical relevance of calculations based on (27) - (29) will be determined by how exactly the geometry of weft threads location will be known from the information about winding tape technology on the pipe. Further generalization of the results of this work can be obtained by the perturbation methods, which for example, allows take into account the relaxation properties of tapes, as well as inaccuracies in satisfying the conditions (27) - (29), and also to study the tapes with other textile structures.

Acknowledgements

The authors gratefully acknowledge the support for this work provided by Ministry of Education and Science of Russia.

References

[1] Obraztsov, I.F., Vasil'ev V.V., Bunakov V.A. Optimal reinforcement of shells of revolution made of composite materials // Machinery, 1977. – 144 pp.

[2] Steigmann D. J., Ogden R. W. Elastic surface-substrate interaction. //Proceedings of Royal Society. London. A. 1999. Vol. 455. P. 437–474.

[3] Krikanov A.A. Calculation of stresses in the composite shell of revolution, formed by winding tapes of finite width // IPRIM Sciences Mechanics of composite materials and structures, 2002, Volume 8, No 2. – P. 151 - 160.

[4] Komkov M.A., Bulanov I.M., Shyshatskiy V.A. Choice of the width unidirectional tapes with a dense winding of toroidal shells // Coll. Proceedings MVTU them. N. E. Bauman, 1986, No 21. - P. 55–63.

[5] P. Dyatlova, M. Rudaya, A. Majorov. Analysis of the stress-strained state of the tape during it's winding around the cylindrical solid.
Proceedings of XXXVII Summer School - Conference "Advanced problems in Mechanics". St. Petersburg, 2009. pp. 204 - 210.

[6] Polyakova E.V., Chaikin V.A. Applied problems of mechanics of soft shells and fabrics. Monograph. Saint-Petersburg.: SPGUTD, 2006. – 193 pp.

[7] Chaikin V.A., Polyakova E.V., Dyatlova P.A. Applied problems of the theory of soft shells. Monograph. Saint-Petersburg.: SPGUTD, 2009. – 166 pp.

Polina Dyatlova, St-Petersburg State University of Technology and Design, Bolshaya Morskaya St. 18, St.-Petersburg, 191186, Russia

Jamming transition and tensile strength of magnetic stabilized fluidized beds

M. J. Espín M. A. S. Quintanilla J. M. Valverde A. Castellanos
quintani@us.es

Abstract

A magnetic stabilized fluidized bed consists on a bed of magnetizable particles agitated by a gas flow in the presence on a magnetic field. In the absence of magnetic field, there is a given gas velocity at which the particles can form a permanent network capable of sustaining small stresses. This gas velocity marks the jamming transition of the bed. For gas velocities above the jamming transition, the bed resembles a liquid. Below the jamming transition, the bed behaves as a weak solid and, in the case of the particles we have used in our studies, it shows a tensile strength when the gas flow is increased. The tensile strength has its origin in non-magnetic attractive forces acting between particles. In the presence of a magnetic field, the gas velocity corresponding to the jamming transition and the tensile strength of the bed depend on the field strength. Both facts are a consequence of the magnetic attraction between particles arising from their magnetization. However, the tensile strength and the jamming transition of particles with similar magnetic susceptibility but different strength of the non-magnetic forces show a different response to the magnetic field. The differences can be explained if the non-magnetic forces influence the network of contacts, which in turn act as a magnetic circuit for the field lines. This view is in contrast with the customary approach of considering that magnetized particles behave as point dipoles that arrange themselves in chain-like structures along field lines.

1 Non-magnetic fluidized beds of fine particles

A simple version of a fluidized bed consists on an open vessel fitted with a horizontal porous plate (the distributor) and filled with a granular material. A fluid is forced to pass through the distributor and the granular material. The fluid exerts drag forces on the particles that depend on the relative velocity between the particles and the fluid and on the solid fraction of the volume occupied by the granular material. Those drag forces result in a fluid pressure drop Δp across the granular material. As neither the velocity of the particles, nor the velocity of the gas in the spaces between particles is easy to measure, the custom is to use the superficial fluid velocity U, which is defined as the fluid flow divided by the cross section of the vessel, that is, the velocity of the fluid if the vessel were empty. If the superficial fluid velocity U is increased from zero, the fluid pressure drop Δp increases linearly with U and the particles remain stationary until Δp equals the material weight per unit area W. We will refer to the value of the superficial gas velocity when this condition is met as the minimum fluidization velocity U_m. From this point onwards, the behaviour of the bed depends on factors such as whether the fluid is a liquid or a gas, the size of the particles and the density difference between particles and fluid.

Granular beds of relatively large particles (particle diameter $d_p \sim 100$ μm or more) fluidized by gas are usually unstable: when the superficial gas velocity is increased beyond U_m, the particles are agitated by the gas but most of the gas passes through the bed in the form of bubbles. As the bubbles serve as channels for the additional flow of gas, the gas pressure drop across the material remains equal to W. Any additional gas flow for superficial gas velocities beyond U_m is used to increase the bubble size and frequency of appearance. When the superficial gas velocity is decreased, the gas pressure drop remains equal to W until the superficial gas velocity takes

the value U_m, in which the agitation of the particles stop. This type of behavior is the so-called Geldart B behavior according to the Geldart's diagram [1].

When fluidizing smaller particles (typically sized between $d_p >\sim 20\ \mu$m and $d_p < 50\ \mu$m) in gas, the particles remain stationary until the gas pressure drop across the bed Δp exceeds by a certain amount the weight per unit area of the particles W. The stress $\Delta p - W$ is required to overcome the adhesion between particles in contact before the particles begin to move relative to each other and the bed becomes fluidized. The difference $\Delta p - W$ is taken as the tensile strength of the bed σ_t. For this type of materials, we define the minimum fluidization velocity U_m as the superficial gas velocity at which the bed reaches its tensile strength. If the superficial gas velocity is increased beyond U_m, the bed does not show bubbling although the particles are agitated by the gas until a value U_b of the superficial gas velocity in which bubbles appear. U_b is called the minimum bubbling velocity. The interval $U_m \to U_b$ is called the interval of homogenous fluidization. In the interval of homogeneous fluidization, particles are not truly homogeneously dispersed in the gas because that solution of the multiphase flow equations that describe fluidization is not stable. In fact, instabilities in the form of regions of lower than average solid fraction do appear although they do not grow to form bubbles as they propagate towards the free surface of the bed.

For gas velocities $U > U_m$, the pressure drop across the powder bed is equal to the particle weight per unit area W as long as the superficial gas velocity is increased monotonically. The increased gas to particle drag due to the additional gas flow for superficial gas velocities beyond U_m is compensated by expansion of the bed as a lower solid fraction yields a lower gas-particle drag for the same superficial gas velocity. As a result, for $U > U_m$ the solid fraction ϕ of the bed is a function of the superficial gas velocity: $\phi_+(U)$. If the superficial gas velocity is decreased from a value larger than U_b, the gas pressure drop remains equal to W and the relationship between the solid fraction ϕ and the superficial gas velocity U is given by $\phi_+(U)$ down to a superficial gas velocity U_J between U_m and U_b. For $U < U_J$ the gas pressure drop Δp falls below the particle weight per unit area W and the dependence of the solid fraction with the superficial gas velocity deviates from the value given by the relationship $\phi_+(U)$. The value of the superficial gas velocity U_J marks the jamming transition of the bed. This fluidization behaviour is called Geldart A [1].

At the jamming transition ($U = U_J$), the relative position of the particles in the bed become frozen in a permanent network of contacts capable of sustaining small stresses: ideally just at the jamming transition the stress limit capacity of the bed is infinitesimally small. If the superficial gas velocity is slightly decreased from U_J the yield stress limit of the contact network is surpassed (remember a lower superficial gas velocity causes less gas-particle drag) and the contact network rearranges itself in a slightly denser state with larger yield stress limit. This process determines the relationship $\phi_-(U)$ between the solid fraction ϕ and the superficial gas velocity U for monotonically decreasing values of U. The stress σ carried by the network of contacts for $U < U_J$ is given by the difference $W - \Delta p$.

When, after having increased and then decreased the superficial gas velocity, it is increased from a value $U_o < U_J$, the pressure drop Δp increases again linearly with U until it equals the particle weight per unit area W plus a value of the tensile strength σ_t which is smaller than the measured value when the superficial gas velocity was increased from zero. In consequence, the tensile strength σ_t is a function of the consolidation stress σ that acted on the granular material at the superficial gas velocity U_o and the same happens for the minimum fluidization velocity U_m. In general U_m increases with decreasing consolidation stress $\sigma(U_o)$ because the solid fraction ϕ of the powder bed decreases with σ, which implies less gas-particles drag force for the same superficial gas velocity and this effect predominates over the decrease in the tensile strength.

The adhesive forces acting between particles are the cause of this hysteretic behaviour. For fine dry powders, van der Waals forces make the largest contribution to the adhesion. The strength of the van der Waals forces depends on the contact area between particles, which assuming some degree of plastic deformation of the particles' surface asperities, increases with the previous consolidation stresses that have acted on the powder. The hysteresis in the solid fraction ϕ and the pressure drop Δp for $U < U_J$ can be explained by a different evolution of the contact network due to different values of the interparticle adhesion in both branches of the hysteresis loop, because the force needed to break a contact under either compressive and tensile stresses depends on the contact adhesion.

In the branch corresponding to increasing values of the superficial gas velocity U, at $U = U_m$ a

continuum medium analysis of the stresses predicts that the tensile strength of the bed is reached on a plane close to the bottom of the bed, where the contacts have larger adhesion because they have been more consolidated than contacts in the upper layers. If we wait enough time at each increment of U, the contact network will reform itself from the bottom to the topmost layers to adopt a configuration that offers less resistance to the passage of gas. However, the contacts on each layer of the powder bed would have a distribution in the values of the adhesion, so at each increment of U the gas would break only the weakest contacts between particles in each layer. As the restructuring of the contact network occurs to equilibrate the gas-particle drag with the particles' weight per unit area, $\Delta p = W$ in this branch of the hysteresis loop. Additionally, since some of the contacts do not experience restructuring, the local solid fraction in their surroundings remains unaltered and the average solid fraction of the bed is larger than that in the branch corresponding to decreasing values of the superficial gas velocity. Only up to certain superficial gas velocity are all the contacts broken and the powder becomes truly fluidized.

In the branch corresponding to decreasing values of the superficial gas velocity U, contacts are first formed at $U = U_J$ at a negligibly small consolidation: then, only weak contacts are formed in all layers of the powder bed. When U is slightly decreased, the contacts in each layer fail due to the weight of the upper layers and the bed compacts. As some consolidation stress is needed to cause this compaction, in this branch of the friction loop $\Delta p < W$. At each decrement of the superficial gas velocity contacts would be formed with the minimum strength needed to support the contact network at the given value of U, which implies minimizing the gas-particle drag, hence the solid fraction would take the smallest possible value compatible with the mechanical rigidity of the contact network .

Finally, the superficial solid fraction at the jamming transition U_J depends on the strength of the interparticle adhesive forces when the consolidation is infinitesimally small.

2 Magnetic fluidized beds

In a magnetic fluidized bed the particles of the granular material are magnetizable and the fluidized bed is immersed in an external magnetic field. The external magnetic field strength is kept in the range where the magnetization of the particles is reversible. The magnetic forces between the particles are added to the non-magnetic adhesion. Between a pair of particles, these magnetic forces can be either attractive or repulsive depending on the relative orientation of the line joining the particles' centers and the vectors of their total magnetization. However, several experimental works have shown that attraction between particles predominate in the overall effect of the magnetic forces in a fluidized bed. As a result, for a non-zero magnetic field the tensile strength of the bed increases with respect to the situation for zero external field and the same consolidation stress. This effect has been reported by Lee [2], who investigated the discharge rate of fluidized beds of coarse magnetite grains in the presence of magnetic fields. In his experiments he observed that a measurable yield stress appeared in the bed that increased monotonically with the increase of the applied field strength.

The behaviour of the bed is more complicated for fine particles, because the effect of the magnetic field on the tensile strength of the bed does not become noticeable until the magnetic forces are comparable to the natural adhesion between particles. In a previous research using magnetite powder [3], we have found that if, in the absence of magnetic field, the bed describes an hysteresis loop of the type described in Section 1 and the field is turned on when the superficial gas velocity is increased again from a value $U_o < U_J$, the tensile strength of the bed does not change significantly from that measured in the absence of magnetic field for the same U_o. On the contrary, the tensile strength of the bed increases significantly if the magnetic field is maintained during the whole length of the hysteresis loop. Since particles are free to rearrange their relative positions only when $U > U_J$, this implies the existence of a mechanism by which structure of the bed at the particle level can influence the tensile strength of the whole bed. In the present work we focus on the behavior of the bed when the magnetic field is maintained during the whole length of the fluidization hysteresis loops.

Apart from this, the increased attractive forces due to the action of the magnetic field cause a shift in the superficial gas velocity at the jamming transition U_J to larger values when the

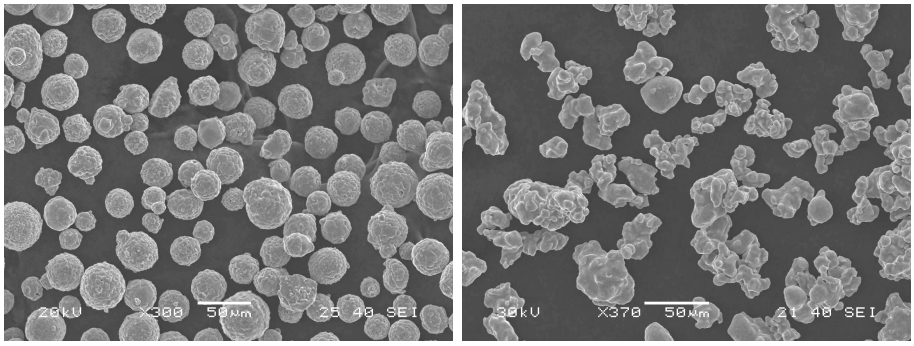


Figure 1: Scanning electron images of the magnetite (left) and steel (right) particles used in the experiments.

magnetic field is applied. Alternatively, f the external magnetic field is applied when the superficial gas velocity is in the range $U > U_J$, at a given value of the external field H_J the fluidized bed experiences a jamming transition at constant superficial gas velocity [4].

3 Experimental set-up and materials

The experimental setup used in this work is based on the Seville Powder Tester (SPT), whose functioning has been reported in detail elsewhere [5]. The powder sample is held in a vertically oriented cylindrical vessel (2.54cm internal diameter in the experiments reported in this paper) and rests on a porous plate that acts as gas distributor (5 μm pore size). By means of a series of computer controlled valves and mass flow controllers, a controlled flow of filtered and dried air is pumped through the powder bed while the gas pressure drop Δp across it is read from a differential pressure transducer. The height of the bed, used to calculate its solid fraction ϕ, is measured with an ultrasonic sensor placed on top of the vessel. In all the experimental runs, enough material was used to give a packed bed height of approximately 2 cm after the sample is initialized.

The fluidized bed was immersed in an horizontal uniform magnetic field created by a pair of square Helmholtz coils (50×50 cm). The magnetic field strength is measured by a Hirst Magnetics Gaussmeter using an axial probe with an accuracy less than 0.1 mT. Experimental measurements show that, within this experimental accuracy, the external field strength is homogeneous in the volume of the cell occupied by the material (approx. 10 cm^3). The orientation of the magnetic field is horizontal, that is, perpendicular to the gas flow.

The powders used in the experiments are unmagnetized synthetic magnetite and steel powders made by Xerox Co. Their respective particle densities ρ_p, measured with a AccuPyc 1330 pycnometer, are 5060 kg/m^3 and 7920 kg/m^3. Scanning Electron Microscope photographs of both powders 1 show a relevant difference of particle morphology. Steel particles are irregularly shaped while magnetite particles are roundly shaped with a rough surface. Circular equivalent diameters particle size distributions are shown in Fig. 2 obtained by means of a Morphologi G3S analyzer. Number average size are 26.2 μm for the magnetite powder and 27.0 μm for the steel powder.

The magnetic powders employed in our experiments were not permanently magnetized (note that ferromagnetic particles of this size are multidomain and can have zero total magnetization). Thus, for the small field strengths applied in our work ($H_0 < 5$ kA/m), the magnetic response of the powders should be linear and reversible [6]. For an isolated particle,the magnetization M_p would be therefore linearly related to the external field H_0 by means of the linear relationship $M_p = \chi_p H_0$, where χ_p is the initial particle susceptibility. However, the particle susceptibility does not coincide with the bulk susceptibility of the powder due to the effect on each individual particle's magnetization of its neighboring particles. The bulk susceptibility χ has been measured in a magnetometer (Squid Quantum Design MPMS XL), as shown in Fig. 3. The inset in Fig. 3 depicts the dependence of the particle magnetization on the magnetic field up to the saturation magnetization of a fresh sample of each powder. In the main Figure, data is shown only for fresh

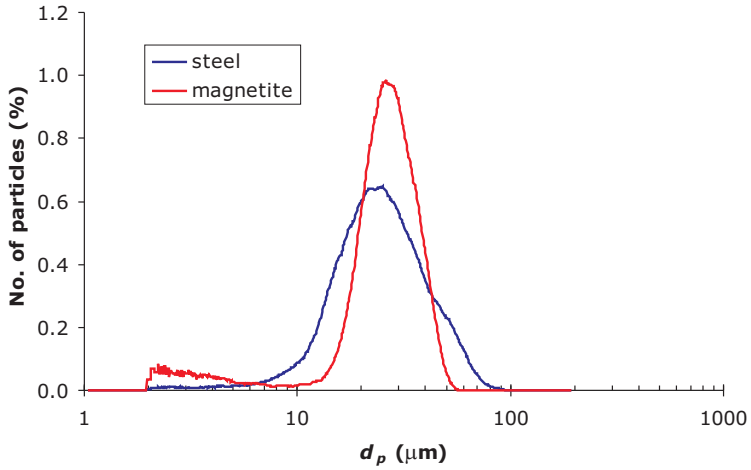


Figure 2: Circular equivalent diameter particle size distributions of the powders used in this work. The cut in the distributions below 2 μm corresponds to the lower limit of resolution of the instrument (Morphologi G3S).

samples in the range of fields applied in the fuidization experiments. From the data in the main Figure 3, $\chi = 2.976$ for the magnetite powder and $\chi = 4.075$ for the steel powder.

4 Results

The superficial gas velocity at the jamming transition U_J is plotted in Fig. 4 for both materials as a function of the total magnetic field strength H. The effect of the magnetic field on U_J only becomes noticeable when $H > 2$ kA/m for both powders. For $H > 2$ kA/m, U_J increases steadily as the magnetic field strength is increased and the solid fraction ϕ_J at the jamming transition decreases. The decrease in the solid fraction at the jamming transition is a consequence of the increase in the strength of the attractive forces between particles [7], in this case, due to the interaction between their magnetic moments. The increase of the superficial gas velocity at the jamming transition U_J should be explained as a consequence of the decrease in the solid fraction at the jamming transition: the gas-particle drag increases with the solid fraction of the bed and the superficial gas velocity. Hence, a smaller value of ϕ_J means that a larger superficial gas velocity is needed to support the particles' weight at the jamming transition.

When the gas-particle drag equilibrates the particles' weight, the superficial gas velocity U and the solid fraction ϕ are related by [8]:

$$U = v_t \left(1 - \phi\right)^n \ . \tag{1}$$

The exponent n depends on the Reynolds number $d_p v_t/\mu$ [8], where d_p is the diameter of the particles, v_t its terminal velocity in the interstitial gas and μ the cinematic viscosity of the gas. For our magnetite particles in air at 20^o, $n = 4.56$, while for the steel particles $n = 4.51$. According to Eq. 1, a change in the solid fraction at the jamming transition ϕ_J should correspond with a change in the superficial gas velocity ΔU_J given by:

$$\frac{\Delta U_J}{U_J^o} = -n\frac{\Delta\phi_J}{1-\phi_J^o} \ , \tag{2}$$

where ϕ_J^o and U_J^o are respectively the solid fraction and the superficial gas velocity at the jamming transition in the absence of magnetic field. In Fig. 5 we present both ΔU_J and $-n\Delta\phi_J/(1-\phi_J^o)$ as a function of the total field H. In Eq. 2 we have calculated the values of $\Delta\phi_J$ using a linear fit to the data in Fig. 4. It is seen that the expansion of the bed can not explain the increase of the

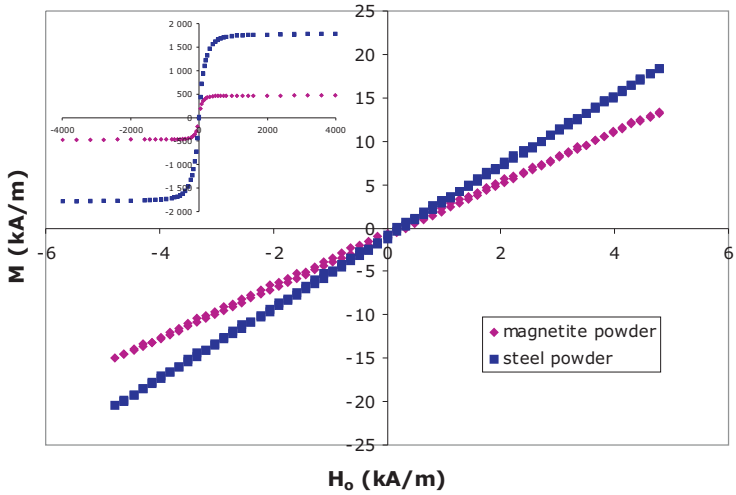


Figure 3: Bulk magnetization of the powders used in the experiments as a function of the strength of the external applied field.

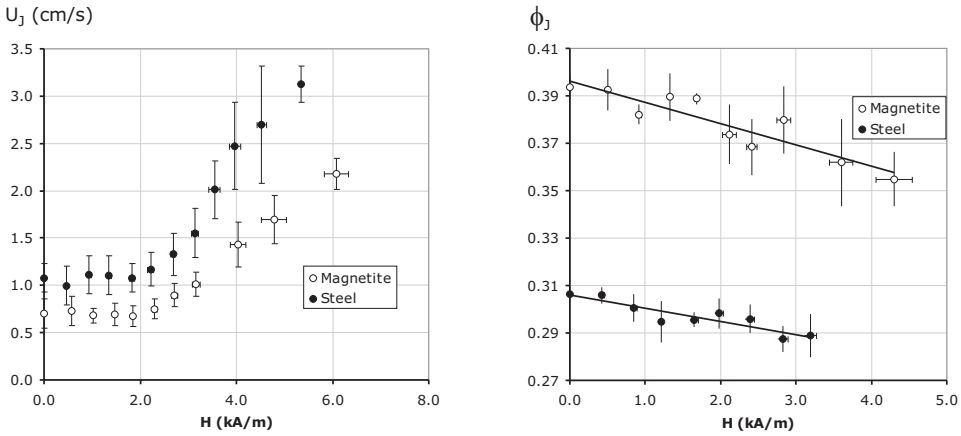


Figure 4: Superficial gas velocity U_J and solid fraction ϕ_J at the jamming transition as a function of the total field H for the magnetite and steel powders. The lines in the plot of ϕ_J are linear fits to the data used in the discussion in the text.

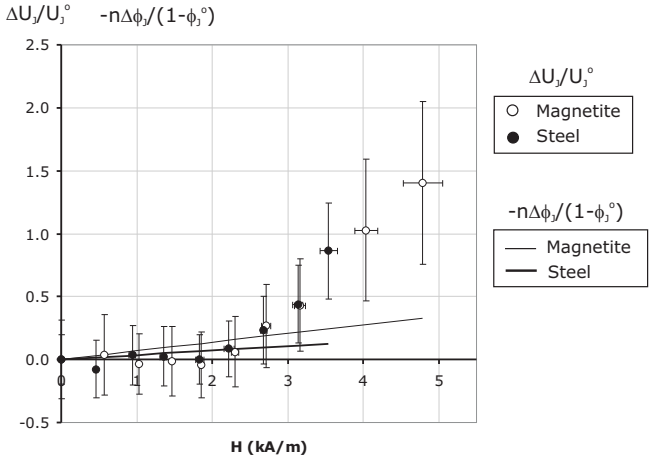


Figure 5: Circles: Relative increase in the superficial gas velocity at the jamming transition U_J with respect to its value at zero magnetic field U_J^0 as a function of the magnetic field. Solid lines: Relative increase in U_J attributable to the decrease in the solid fraction ϕ_J at the jamming transition according to Eq. 2.

superficial gas velocity at the jamming transition for total fields larger than about 3 kA/m, that is, the region where the increase of U_J with the magnetic field becomes marked. As Eq. 1 was derived for beds of individual particles distributed at random, the difference between the change in U_J predicted by Eq. 2 and that measured experimentally may be due to the fact that for fields over 3 kA/m particles in contact have preferential orientations due to the action of the field. This effect may decrease the tortuosity of the flow lines of the gas among the particles resulting in smaller gas to particle drag. Hence, larger superficial gas velocities are needed to support the particles' weight per unit area that those required in a bed of the same solid fraction in which the contacts have random orientations.

The strengthening of the interparticle attractive forces due to the action of the magnetic field also causes an increment of the tensile strength σ_t of the powder bed for $U < U_J$, as shown in Fig. 6. To show the effect of the magnetic field on σ_t it is necessary to fix the initial superficial gas velocity U_o in the lower branch of the fluidization loop because σ_t is a function of U_o in the absence of magnetic field. For the data in Fig. 6, $U_0 = 0.51$ cm/s.

If we distinguish between magnetic and non-magnetic contributions to the tensile strength of the bed, then:

$$\sigma_t = \sigma_t^{nat}(\sigma_c) + \sigma_t^{mag}(H)\,. \tag{3}$$

The term σ_t^{mag} represents the contribution to the tensile strength from magnetic forces, while σ_t^{nat} is the non-magnetic tensile strength of the bed which arises from the interparticle adhesion. σ_t^{nat} depends on the consolidation stress σ_c that has acted on the bed at the initial superficial gas velocity U_o. The reason is that σ_c is related to the consolidation forces acting on particle contacts. Larger consolidation forces cause larger contact areas between particles, which in turn cause an increase in the adhesion and therefore in σ_t^{nat}. If we want to calculate the magnetic contribution to the tensile strength form the data in Fig. 6, we have to take into account the fact that, even for the same initial superficial gas velocity U_o, the consolidation stress depends on the magnetic field. In consequence, the term $\sigma_t^{nat}(\sigma_c)$ is not the same for all the data points in Fig. 6. The term $\sigma_t^{nat}(\sigma_c)$ can be evaluated from measurements of the tensile strength of the bed as a function of the consolidation stress in the absence of magnetic field such as those presented in Fig. 7.

Theoretically, σ_t^{nat} should be larger than zero for any consolidation stress σ_c up to 0 Pa (which happens at $U = U_J$), as the interparticle adhesion does not vanish when the consolidation contact forces become zero. However, both the data for magnetite and steel have a positive intercept with the $\sigma_t^{nat} = 0$ axis. The reason is that the value of the tensile stress falls below the accuracy of our

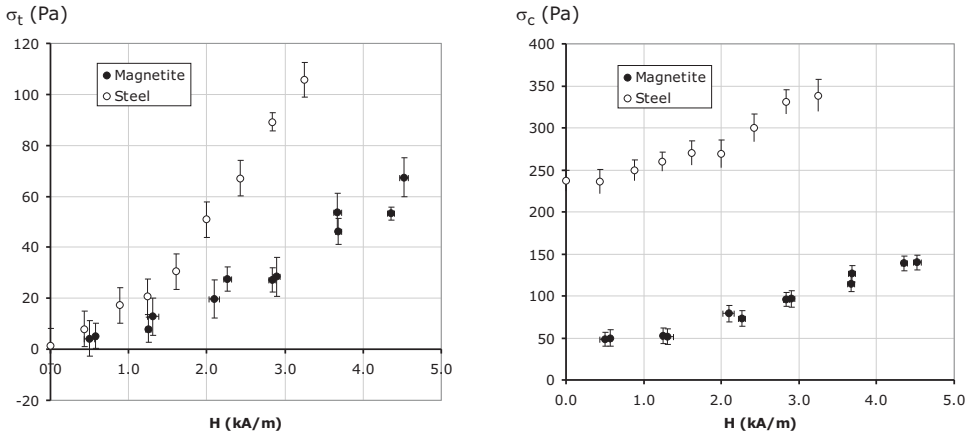


Figure 6: Left: Tensile strength σ_t of the steel and magnetite powder beds as a function of the total magnetic field H for an initial superficial gas velocity $U_0 = 0.51$ cm/s. Right: Consolidation stress σ acting on the powder bed at the initial superficial gas velocity U_o as a function of H.

pressure drop measurements (about 10 Pa) before the superficial gas velocity U_0 reaches the value U_J.

To calculate the contribution of magnetic forces to the tensile strength, we need to substract the curve $\sigma_t^{nat}(\sigma_c)$ to the tensile strength data as a function of the initial gas velocity $U < U_J$ for a constant field H in Fig. 6. To this aim we have fitted the data of σ_t^{nat} in Fig. 7 with a straight line. The resulting data are shown in Fig. 7 as a function of the square of the total magnetic field. It is seen that, within experimental error, σ_t^{mag} is proportional to H^2. If fact, as σ_t^{mag} should depend on the particle magnetization $M_p = \chi_p H_o$ and the solid volume fraction ϕ, a simple dimensional analysis leads to the equation [9]:

$$\sigma_t^{mag} = \mu_0 f(\phi) \chi_p^2 H_o^2 \,. \tag{4}$$

χ_p is the particle's susceptibility, H_0 is the magnetic field inside the sample and the function $f(\phi)$ takes into account any dependence of σ_t^{mag} on the solid fraction ϕ. The bulk susceptibility χ is related to the particle susceptibility χ_p and the solid fraction ϕ. According to Bruggeman's rule:

$$(1-\phi)\frac{\chi_0 - \chi}{3 + \chi_0 + 2\chi} + \phi \frac{\chi_p - \chi}{3 + \chi_p + 2\chi} = 0 \,. \tag{5}$$

Eq. 5 gives implicitly $\chi(\chi_p, \phi)$, because χ_0 is the susceptibility of the interstitial medium and for the case of aire we can make $\chi_0 = 0$. If the dependence with the solid fraction ϕ is included with the function $f(\phi)$ in Eq. 4, we get:

$$\sigma_t^{mag} = \mu_0 g(\phi) \chi^2 H^2 \,. \tag{6}$$

Where the field inside the sample H_o has been related to the total field H by means of a demagnetization factor k that has also been included in the function $g(\phi)$ as it only depends on the sample's geometry and therefore, since the sample mass and cross section are fixed, it can be expressed in terms of the sample solid fraction ϕ.

Using 6, we obtain for the magnetite particles: $\mu_0 g(\phi)\chi^2 = 2.51 \pm 0.12$ N/kA^2, while for the steel particles $\mu_0 g(\phi)\chi^2 = 9.61 \pm 0.46$ N/kA^2. This gives $g(\phi) = 0.226 \pm 0.011$ for magnetite, with $\phi \simeq 0.44$, while for steel $g(\phi) = 0.471 \pm 0.022$, with $\phi \simeq 0.35$.

If the magnetic stresses inside the bed were calculated assuming that each particle in the bed is a magnetic dipole and the magnetic stresses are the result of the interaction between all dipoles, we would have found that the magnetic stresses in a plane parallel to the the magnetic field are negative [9]. The discrepancy with the experimental results arises from having neglected the higher order terms in the multipole expansion of the fields inside each particle. A FEM calculation of

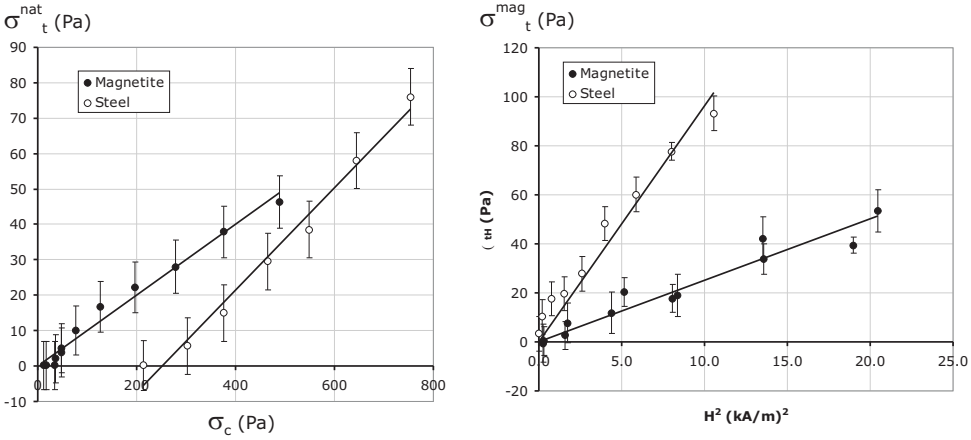


Figure 7: Left: Non-magnetic tensile strength of the bed σ_t^{nat} as a function of the consolidation stress σ. The lines corresponds to linear fits to the data used in the discussion in the text Right: Magnetic contribution to the tensile strength σ_t^{mag} obtained from the data in Fig. 3 as explained in the text.

the magnetic field in an array of particles, such as the one presented in Fig 8, shows that particles act as magnetic circuits for the magnetic flux density field lines, with the magnetic flux passing from one particle to its neighbors through the contacts. In consequence, at each contact a north pole at the surface of one particle confronts a south pole on the surface of its neighbor, resulting on attractive interaction irrespectively of the contact orientation relative to the external magnetic field.

Apart from this, when particles are represented by dipoles one would expect $g(\phi)$ to decrease with the solid fraction ϕ, on the contrary with what we have found here, as a smaller solid fraction implies an increase in the average distance between particles. A possible explanation may be that, given the fact that the magnetic forces at contact are attractive whatever the contact orientation, in the structure formed by the steel particles a larger fraction of contacts is oriented in the vertical direction, although the magnitude of the attractive magnetic force may be smaller than if the contacts were aligned with the external field, its vertical component is larger, resulting in a larger contribution to the tensile strength of the bed.

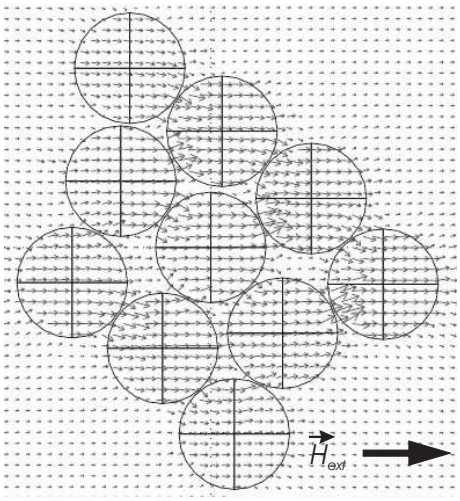


Figure 8: Magnetic flux density lines obtained by FEM for packed bed of spherical beads ($\chi_p = 7.19$). The externally applied field H_{ext} is horizontal.

Acknowledgements

We acknowledge Spanish Government Agency Ministerio de Ciencia y Tecnología (contract FIS2006-03645) and Junta de Andalucía (contract FQM 421). We want to express our gratitude to IESMAST. S.A. for measuring the particle size distributions of the materials used in this work.

References

[1] Geldart D. Powder Technol. 7, 285-293 (1973).

[2] Lee W. K. Powder Technol. 64, 69-80 (1991).

[3] Valverde J. M., Espin M. J., Quintanilla M. A. S. and A. Castellanos. Phys. Rev. E 79, 031306 (2009).

[4] Siegell J. H. Powder Technology 55, 127-132 (1988).

[5] Valverde J. M., Castellanos A., Ramos A., Perez A. T., Morgan M. A. and P. K. Watson. Rev. Sci. Instrum. 71, 2791-2795 (2000).

[6] Mills A. A., Annals of Science. 61, 273319 (2004).

[7] J.M. Valverde, M. A. S. Quintanilla, and A. Castellanos, Phys. Rev. Lett. 92, 258303 (2004).

[8] Jackson R. The dynamics of fluidized particles, Cambridge University Press, Cambridge, 2000.

[9] Rosensweig R. E. Ferrohydrodynamics, Dover publications, New York, (1997).

M.J. Espín. University of Seville, Dept. of Applied Physics II. Avenida Reina Mercedes s/n, 41012, Sevilla, Spain.
M.A.S. Quintanilla, J.M. Valverde, A. Castellanos. University of Seville, Dept. of Electronics and Electromagnetism. Avenida Reina Mercedes s/n, 41012, Sevilla, Spain.

Role of relaxation in formation of cyclic resistance of elastomeric nanocomposites

Svetlana E. Evlampieva Valery V. Moshev
evl@icmm.ru moshev@icmm.ru

Abstract

A structural approach modeling the cyclic behavior of elastomeric nanocomposites is offered. It takes into account a relaxation mechanism peculiar to the model under consideration. The calculated hysteretic loops are close to the experimental ones.

1 Introduction

The mechanical behavior of elastomeric nanocomposites is complicated. Their cyclic behavior until now has not found a clean-cut structural explanation [1].

Analyzing the available literature data, one may suppose that the complicated mechanical behavior of these materials may be regarded as the result of joint action of several structural mechanisms. Early-on, an attempt was made to formulate a structural model where the variability of the mechanical behavior came to some constant interface friction [2, 3]. This approach explained some important peculiarities of inter-alias residual strains. However, this version of the model did not take into account the time dependence of elastomeric nanocomposites.

The structural mechanism modeling the time dependence of elastomeric nanocomposites was offered later [4], and it demonstrated both the creep and relaxation processes.

In cycling tests, the time dependence of the mechanical behavior manifests itself in a rather quaint form and deserves a separate consideration.

2 Description of a structural cell

The geometry of the model (fig. 1) represents a spring of length L_0, simulating a rubber molecule, two substrates, U_m, and a space, L_g, between the substrates simulating filler volume concentration.

To simulate, as close as possible, the elastic resistance of macromolecular chains under extension, we use the expression for macromolecules with freely joint segments

$$\lambda = \lambda_m(Cth\ f - 1/f) + 1.0,$$

where λ is the elongation ratio of the spring under the tensile force f (in a dimensionless form) with λ_m being the breaking value of λ

This expression is transformed into

$$\Delta L = L_0\sqrt{L_0}(Cth\ f - 1/f),$$

where ΔL is the stretch of the spring, L_0 is the segmental length of the spring.

It is assumed that the spring is retained on the surface of substrates by the force simulating mobile adhesive bonding. This force is regarded as a kind of specific interphase friction. Numerous experimental data [5] let representing the friction force T as a function of the rate of sliding V in the form

$$f = kV^m,$$

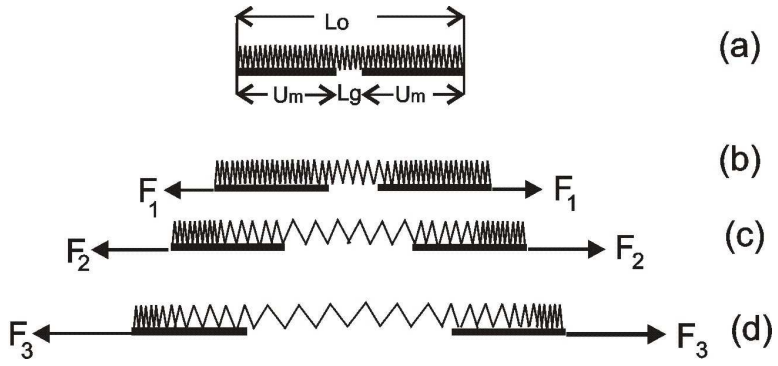


Figure 1: Geometry of the structural cell of the proposed model.

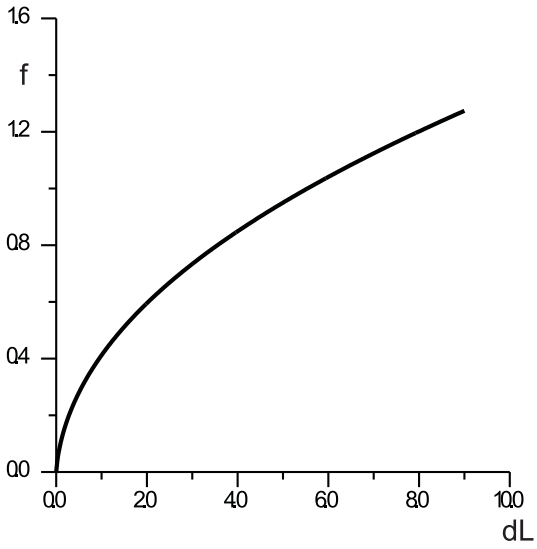


Figure 2: Tensile curve for rate $W = 2.0$.

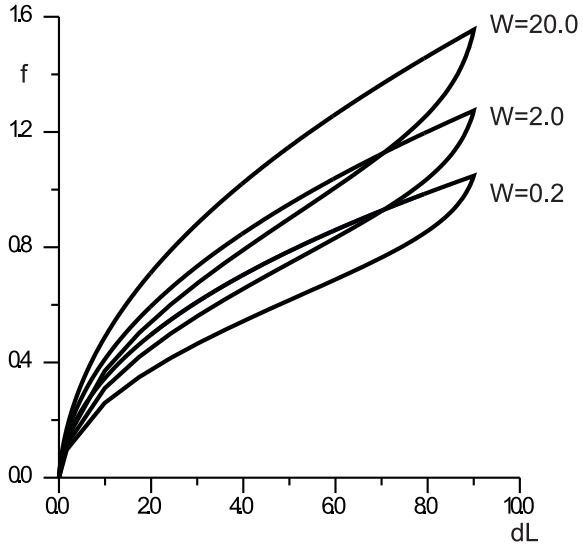


Figure 3: Tensile and contraction curves for various rates of deformation W.

where k and m are empirical constants.

Figure 2 demonstrates the typical relationship between the force and deformation of the model, which is realized as an increase of the spring disposed between the substrates.

3 Structural rearrangement in hysteretic cycles

Hysteretic testing discloses the relationships between forces and deformations observed during cyclic extensions and contractions of the model. In this case, the internal structural rearrangement concomitant with hysteretic testing may be represented in the following way.

During the extension of the model, the spring between the substrates at each time interval becomes more and more stressed. This provokes slipping the spring from the substrates into the gap between them.

Contrariwise, during the contraction of the model, the stress in the gap between the substrates at each time interval goes down, provoking thus the coming back of the spring from the gap onto the substrates.

Thus, the relaxation specificity is determined by the interaction of two time dependent processes: the specified rate of extension and contraction (W) and the friction between the substrate and the moving spring ($k = 0.15$, $m = 0.15$). Such data display satisfactorily the shapes of relaxation hysteretic loops observed experimentally.

4 Correlation between the structure of the model and its hysteretic behavior

Varying the individual structural parameters makes it possible to establish their individual influence on the behavior of the model on the whole.

Figure 3 demonstrates the loops calculated for various rates of deformation. Increasing W makes hysteretic loops wider. The variability of the cycles in the case, where the rates of extension and contraction differ from each other, is shown in figure 4.

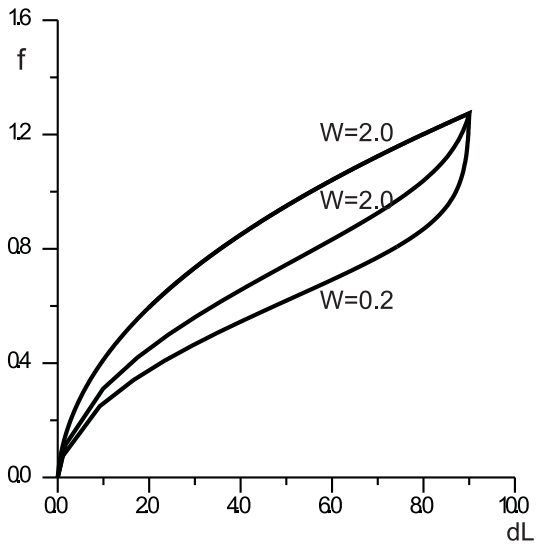


Figure 4: Tensile and contraction curves at different rate of contraction.

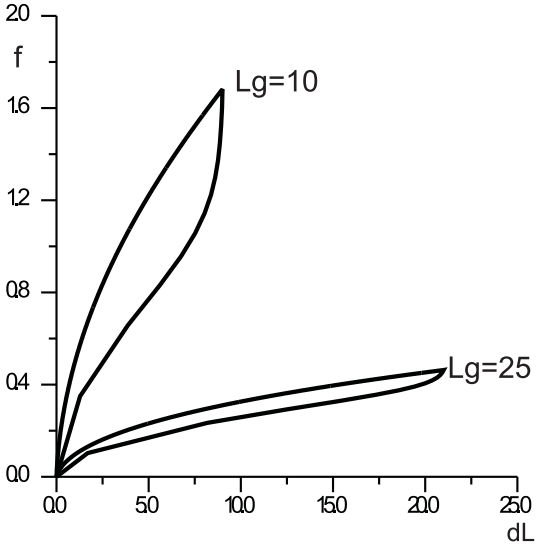


Figure 5: Tensile and contraction curves for various gaps between the substrates Lg.

Increasing the gap between the substrates changes considerably the shape of loops (fig. 5), which has been confirmed experimentally.

5 Discussion of results

The model of relaxation cycles explains the microstructural backgrounds of the phenomenon under study. From this standpoint, it may be useful for scientists who develop new time-dependent nanocomposites.

At the same time, the material presented can be regarded as a constituent part of the future structural model capable of taking into account some other important specificities, for instance, static friction.

6 Conclusions

The model is recommended for using in the development of new elastomeric nanocomposites.

Acknowledgements

The research was supported by the Fundamental research program of the Department of Power engineering, Mechanical Engineering, Mechanics and Control Processes of RAS "Tribological and strength properties of structured materials and surface layers" N 09-T-1-1006.

References

[1] Leonard Mullins.Engineering with rubber. Chemtech December, 1987, V. 17, N. 12, pp. 720 - 727.

[2] Moshev V.V., Evlampieva S.E. Filler-reinforcement of elastomers viewed as a triboelastic phenomenon. International Journal of Solids and Structures, 2003, N.40, pp. 4549-4562.

[3] V.V. Moshev, S.E. Evlampieva. Potentiality of the triboelastic approach for clarifying the filler reinforcement mechanism in elastomers. International Journal of Solids and Structures, 2005, N.42, pp. 5129-5139.

[4] V.V. Moshev, S.E. Evlampieva. Modeling of Time Dependence of Nano-Structural Rubber Composites. Proceeding of the EUROMECH Colloquium 502, Dresden, Germany, 08 -10 September, 2008, pp. 129-132.

[5] Kovrov V.N., Moshev V.V. Mechanical hysteresis in rubbers and its relation with strength. Structural-mechanical investigation of composite materials and structures, Sverdlovsk: USC AS USSR, 1984, pp. 19-22.

Svetlana E. Evlampieva, Institute of Continuous Media Mechanics, Korolev Str., 1, 614013, Perm, Russia
Valery V. Moshev, Institute of Continuous Media Mechanics, Korolev Str., 1, 614013, Perm, Russia

Simulation of intermetallic compound synthesis during solid-phase extrusion through a tapered die

N. K. Evstigneev A. G. Knyazeva
evstigneev.nk@rambler.ru, anna@ispms.tsc.ru

Abstract

Mathematical model of SHS-synthesis of intermetallic compound is suggested. Various rheological models of extruding mixture such as: viscoelastic, viscous, hypoelastic are considered, the qualitative difference between them is shown. The problem takes into account coupling between the fields of temperature, deformation and conversion degree. Parametric investigation of the full problem (in viscoelastic statement) is carried out. Deflected mode of the mixture is analyzed. The influence of process variables is shown.

1 Introduction

At present time composite materials based on nickel aluminides find application in diverse fields of industry. First of all, they are used as a protective coating of the surfaces of machine components which are exposed to various kinds of destructive influences [1]. In particular, Ni_3Al compound is used as a thermostable and heatproof coating of aircraft engines' turbine blades. Production of this compound using traditional methods of powder metallurgy requires much time and high power inputs. SHS synthesis in a thermal explosion mode is used to solve the task.

The experiments show that using a tapered die may help to produce submicrocrystalline structure in a synthesized alloy [2]. But there is a necessity of optimization of technological processes. Methods of mathematical simulation are very effective in such cases because they let both deeper understanding of the processes and substantial reducing the number of experiments.

As a rule, when simulating rheology of similar systems the model of a viscous compressible liquid is used. In the present paper the influence of various rheological correlations corresponding to materials with different rheological properties on the distributions of temperature, conversion degree, stress and strain tensor components and velocities at various geometry, heating and loading conditions is analyzed. In the hypoelastic model increments of stress tensor components are connected with increments of strain tensor components, temperature and conversion degree in a linear way. In the model of viscous media well-known analogy of correlations between stress and strain tensor components is extended to internal stresses which are caused by nonuniform heating and changing the matter properties during the conversion. Viscoelastic model takes into account all the named effects. All models are considered both with and without the coupling effect.

2 Physical problem definition

A cylindrical chamber with tapered outlet is considered. The material is extruded into a cylindrical nozzle. 3Ni+Al powder was chosen as a reaction mixture. Exothermic chemical reaction is initiated in the chamber by heating chamber walls for a certain period of time and the reaction product forms. Then the extrusion of chamber matter composition by press starts. After completion of chemical reaction the system starts to cool, which is described by Newton law. The model takes into account that internal stresses, which influence the reaction together with external loading, appear in the system during the process of heating and chemical conversion. The problem is axially

symmetric and it is formulated in 2D in a cylindrical coordinate system. The aim of the work is to investigate the fields of temperature, conversion degree and mechanical stresses and strains which appear during the reaction, explore the influence of coupling between chemical and physical phenomena on the process, estimate the influence of geometry on product structure formation.

3 Choosing of rheological correlations and movement equations definition

Let's divide stress tensor into two constituents: elastic part and viscous one, $\hat{\sigma}_{ij} = \sigma^e_{ij} + \sigma^v_{ij}$. We have the generalized Duhamel-Newmann relations [3] for elastic stresses:

$$\sigma^e_{ij} = 2\mu \cdot \varepsilon_{ij} + \delta_{ij}\left[\lambda\varepsilon_{kk} - K\omega\right].$$

Using full analogy we may write the next for the viscous stresses:

$$\sigma^v_{ij} = 2\mu_v \cdot \dot{\varepsilon}_{ij} + \delta_{ij}\left[\left(\zeta - \frac{2}{3}\mu_v\right)\dot{\varepsilon}_{kk} - \zeta\dot{\omega}\right].$$

As a result we have:

$$\hat{\sigma}_{ij} = 2\mu \cdot \varepsilon_{ij} + 2\mu_v \cdot \dot{\varepsilon}_{ij} + \delta_{ij}\left[\lambda\varepsilon_{kk} + \left(\zeta - \frac{2}{3}\mu_v\right)\dot{\varepsilon}_{kk} - K\omega - \zeta\dot{\omega}\right],$$

where σ_{ij} and ε_{ij} are stress and strain tensor components respectively, λ, and μ are Lame coefficients, μ_v is the coefficient of dynamic viscosity, ζ is the second coefficient of viscosity, K is the compression modulus, $\omega = 3\left[\alpha_T\left(T - T_0\right) + \left(\alpha_p - \alpha_r\right)\eta\right]$ is the function of volumetric expansion, α_T is the coefficient of thermal expansion, α_p and α_r are the coefficients of structural expansion of reaction product and reagent respectively, T is the temperature, "0" index is related to initial conditions. Point above the values denotes the time derivative.

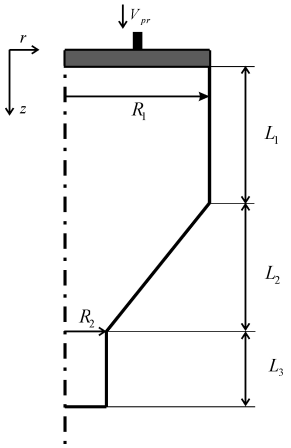


Figure 1: Illustration to problem definition

Substituting the mentioned expression for the stresses into the motion equations and taking into account Cauchy relations, we get the equations for the velocities:

$$\begin{aligned}
&\overline{\rho}\rho_s\frac{dv_r}{dt} = \left(\zeta + \frac{4}{3}\mu_v\right)\frac{\partial^2 v_r}{\partial r^2} + \mu_v\frac{\partial^2 v_r}{\partial z^2} + \left(\zeta + \frac{\mu_v}{3}\right)\frac{\partial^2 v_z}{\partial r\partial z} + \\
&+\frac{1}{r}\cdot\left[\left(\zeta + \frac{4}{3}\mu_v\right)\frac{\partial v_r}{\partial r} + \left(\zeta - \frac{2}{3}\mu_v\right)\frac{\partial v_z}{\partial z}\right] + \left(\lambda + 2\mu\right)\frac{\partial\varepsilon_{rr}}{\partial r} + \lambda\frac{\partial\varepsilon_{zz}}{\partial r} + \\
&+2\mu\frac{\partial\varepsilon_{rz}}{\partial z} - K\frac{\partial\omega}{\partial r} - \zeta\frac{\partial\dot{\omega}}{\partial r} + \frac{1}{r}\left[\left(\lambda + 2\mu\right)\varepsilon_{rr} + \lambda\varepsilon_{zz}K\omega - \zeta\dot{\omega}\right],
\end{aligned} \tag{1}$$

$$\begin{aligned}
&\overline{\rho}\rho_s\frac{dv_z}{dt} = \left(\zeta + \frac{4}{3}\mu_v\right)\frac{\partial^2 v_z}{\partial z^2} + \mu_v\frac{\partial^2 v_z}{\partial r^2} + \left(\zeta + \frac{\mu_v}{3}\right)\frac{\partial^2 v_r}{\partial r\partial z} + \frac{\mu_v}{r}\cdot\left[\frac{\partial v_r}{\partial z} + \frac{\partial v_z}{\partial r}\right] + \\
&+2\mu\frac{\partial\varepsilon_{rz}}{\partial r} + 2\mu\frac{\varepsilon_{rz}}{r} + \left(\lambda + 2\mu\right)\frac{\partial\varepsilon_{zz}}{\partial z} + \lambda\frac{\partial\varepsilon_{rr}}{\partial z} - K\frac{\partial\omega}{\partial z} - \zeta\frac{\partial\dot{\omega}}{\partial z}.
\end{aligned} \tag{2}$$

Here ρ_s is the density of incompressible basis, and $\overline{\rho}$ is the relative density which is equal to $1 - \pi$, where π is the porosity.

Using the dimensionless variables

$\overline{v}_r = \frac{v_r}{v_*}, \overline{v}_z = \frac{v_z}{v_*}, \overline{r} = \frac{r}{r_*}, \overline{z} = \frac{z}{z_*}, \overline{\omega} = \frac{\omega}{\omega_*}$,

where

$$v_* = \frac{x_*}{t_*}, x_* = \sqrt{\frac{\lambda_T t_*}{c\rho_s}}, t_* = \frac{c\rho RT_*^2}{EQk_0}\exp\left(\frac{E}{RT_*}\right), T_* = T_0 + \frac{Q}{c\rho}, \omega_* = 3\alpha_T(T_* - T_0),$$

we can formulate the problem (1)-(2) as:

$$\overline{\rho}N\frac{d\overline{v}_r}{d\tau} = \left(H_1+\frac{4}{3}\right)\frac{\partial^2\overline{v}_r}{\partial\overline{r}^2} + \frac{\partial^2\overline{v}_r}{\partial\overline{z}^2} + \left(H_1+\frac{1}{3}\right)\frac{\partial^2\overline{v}_z}{\partial\overline{r}\partial\overline{z}} + \\ + \frac{1}{\overline{r}}\cdot\left[\left(H_1+\frac{4}{3}\right)\frac{\partial\overline{v}_r}{\partial\overline{r}} + \left(H_1-\frac{2}{3}\right)\frac{\partial\overline{v}_z}{\partial\overline{z}}\right] + \\ + \frac{\phi}{1-h_1}\cdot\left[\frac{\partial e_{rr}}{\partial\overline{r}} + (1-h_1)\frac{\partial e_{zz}}{\partial\overline{r}} + h_1\frac{\partial e_{rz}}{\partial\overline{z}} - \frac{3-2h_1}{3}\frac{\partial\overline{\omega}}{\partial\overline{r}}\right] + \\ + \frac{\phi}{1-h_1}\cdot\left[\frac{1}{\overline{r}}\left(e_{rr}+(1-h_1)e_{zz} - \frac{3-2h_1}{3}\cdot\overline{\omega}\right)\right] - \omega_* H_1\left(\frac{\partial\dot{\overline{\omega}}}{\partial\overline{r}} + \frac{\dot{\overline{\omega}}}{\overline{r}}\right), \tag{3}$$

$$\overline{\rho}N\frac{d\overline{v}_z}{d\tau} = \left(H_1+\frac{4}{3}\right)\frac{\partial^2\overline{v}_z}{\partial\overline{z}^2} + \frac{\partial^2\overline{v}_z}{\partial\overline{r}^2} + \left(H_1+\frac{1}{3}\right)\frac{\partial^2\overline{v}_r}{\partial\overline{r}\partial\overline{z}} + \frac{1}{\overline{r}}\cdot\left[\frac{\partial\overline{v}_r}{\partial\overline{z}} + \frac{\partial\overline{v}_z}{\partial\overline{r}}\right] + \\ + \frac{\phi}{1-h_1}\cdot\left[h_1\left(\frac{\partial e_{rz}}{\partial\overline{r}} + \frac{e_{rz}}{\overline{r}} + \frac{1}{h_1}\frac{\partial e_{zz}}{\partial\overline{z}}\right) + (1-h_1)\frac{\partial e_{rr}}{\partial\overline{z}} - \frac{3-2h_1}{3}\frac{\partial\overline{\omega}}{\partial\overline{z}}\right] - \\ - \omega_* H_1\frac{\partial\dot{\overline{\omega}}}{\partial\overline{z}}, \tag{4}$$

4 Change of variables

For the numerical analysis it is suitable to have not a triangular but a rectangular region, so within the tapered die, $\overline{z}\in\left[\overline{L}_1,\overline{L}_1+\overline{L}_2\right]$, the change of variables was made: $\overline{x}_2 = \overline{r}\cdot\overline{R}_1/(B\overline{z}+C)$, where $B=-(\overline{R}_1-\overline{R}_2)/\overline{L}_2$, $C=\overline{R}_1+\overline{L}_1/\overline{L}_2\cdot(\overline{R}_1-\overline{R}_2)$. In the area of the nozzle we also made the change of variables $\overline{x}_3 = \overline{r}\cdot\overline{R}_1/\overline{R}_2$, which let us examine a rectangular area $\overline{x}\in\left[0,\overline{R}_1\right]$ for any values of $\overline{z}$ variable.

We'll use the variable $\overline{x}$ further suggesting that $\overline{x}=\overline{r}$ within the cylindrical chamber, $\overline{x}=\overline{r}\cdot\overline{R}_1/(B\overline{z}+C)$ within the tapered die and $\overline{x}=\overline{r}\cdot\overline{R}_1/\overline{R}_2$ within the nozzle. So, in every area the governing equations will be different, because the derivative $\partial/\partial\overline{r}$ will have different relations with the $\overline{x}$ variable. Namely, $\partial/\partial\overline{r}=\overline{R}_1/(B\overline{z}+C)\cdot\partial/\partial\overline{x}$ within the tapered die and $\partial/\partial\overline{r}=\overline{R}_1/\overline{R}_2\cdot\partial/\partial\overline{x}$ within the nozzle.

Then the boundary conditions for the equations (3)–(4) we'll write as:

$$\overline{x}=0:\frac{\partial\overline{v}_r}{\partial\overline{x}}=0,\frac{\partial\overline{v}_z}{\partial\overline{x}}=0;\ \overline{x}=\overline{R}_1:\overline{v}_r=0,\overline{v}_z=0,$$
$$\overline{z}=0:\overline{v}_r=0,\overline{v}_z=\overline{v}_{pr};\ \overline{z}=\overline{L}:\overline{v}_r=0,\overline{v}_z=\overline{v}_{ex}\left(\overline{R}_1^2-\overline{x}^2\right),$$

where $\overline{v}_{pr}=v_{pr}/v_*,\overline{L}=L/x_*$.

5 Heat propagation problem in the dimensionless variables

In the dimensionless variables

$$\theta=\frac{T-T_0}{T_*-T_0},\tau=\frac{t}{t_*},e_{ij}=\frac{\varepsilon_{ij}}{\varepsilon_*},s_{ij}=\frac{\sigma_{ij}}{\sigma_*},$$

where $\varepsilon_*=3\alpha_T(T_*-T_0),\sigma_*=3K\alpha_T(T_*-T_0)$,
the problem (3)-(4) takes the form:

$$\frac{\partial\theta}{\partial\tau} = \frac{\partial^2\theta}{\partial\overline{x}^2} + \left(\frac{1}{\overline{x}}-\overline{v}_r\right)\frac{\partial\theta}{\partial\overline{x}} + \frac{\partial^2\theta}{\partial\overline{z}^2} - \overline{v}_z\frac{\partial\theta}{\partial\overline{z}} + \frac{\partial\eta}{\partial\tau} - \delta(\theta+\sigma_T)\frac{\partial e_{kk}}{\partial\tau} + \delta s_{ij}^v\frac{\partial e_{ij}}{\partial\tau}$$

$$\frac{\partial\eta}{\partial\tau} = \frac{1-\eta}{\theta_0}\exp\left(\frac{\theta-1-\delta A(\sigma_T+1)\sum\limits_{i,j}s_{ij}e_{ij}}{\beta(\theta+\sigma_T)}\right),$$

$$\overline{\omega} = \theta + g \cdot \eta.$$

Initial and boundary conditions are:

$$\tau = 0 : \theta = 0, \eta = 0,$$
$$\overline{x} = 0 : \frac{\partial \theta}{\partial \overline{x}} = 0,$$
$$\overline{x} = \overline{R}_1 : \begin{cases} \theta = \theta_e, \tau \leq \tau_{comb}, \\ \dfrac{\overline{R}_1 cos(\gamma)}{B\overline{z} + C} \cdot \dfrac{\partial \theta}{\partial \overline{x}} + sin(\gamma) \cdot \dfrac{\partial \theta}{\partial \overline{z}} = Nu \cdot \theta, \tau > \tau_{comb}, \end{cases}$$

where Nu is the Nusselt number, γ is the half of the cone angle.

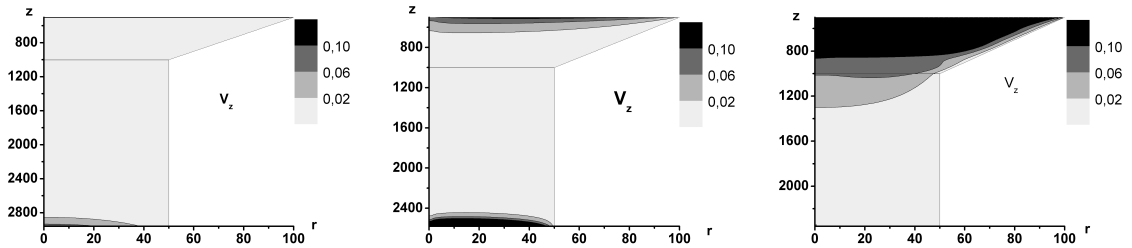
The problem deals with the next dimensionless parameters: $\delta = \dfrac{K\alpha_T\omega_*}{c\rho}$, $\sigma_T = \dfrac{T_0}{T_* - T_0}$, $\theta_0 = \dfrac{1}{\beta(\theta + \sigma_T)}$, $A = \dfrac{k_\sigma Q}{E}$, $\beta = \dfrac{RT_*}{E}$, $g = \dfrac{\alpha_p - \alpha_r}{\alpha_T(T_* - T_0)}$, $P = \dfrac{\sigma_{st} x_* (T_* - T_0)^3}{\lambda_T}$.

Physical interpretation of these values is as follows: δ is the coefficient of coupling between heat transfer and deformation processes, σ_T is the ratio of initial temperature to heat warming up, θ_0 is Zel'dovich number, A is the coefficient of reaction rate sensitivity to the work of stresses, β is the small parameter, characterizing reaction rate sensitivity to temperature, g is the relative volume change in the process of chemical conversion (ratio of concentration deformation to the thermal one), P is the intensity of radiative heat exchange.

6 Computational results

The problem was solved numerically using the alternating direction method [4].

It seemed interesting to compare the rheological models in order to determine the one which best describes the process under study.

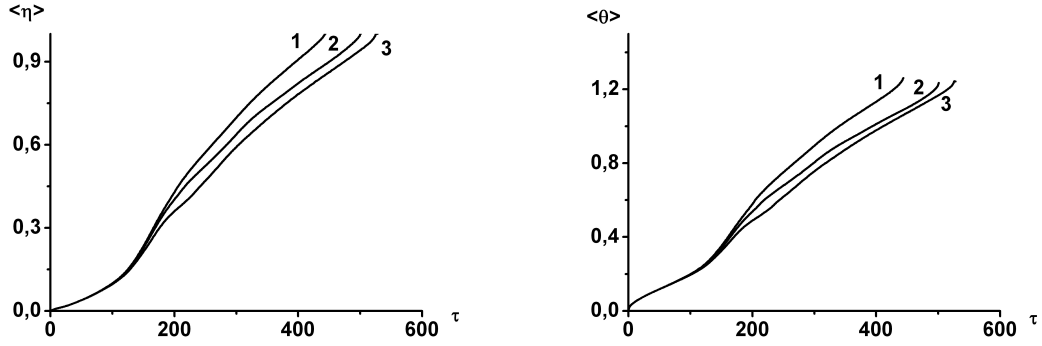


a b c

Figure 2: Distributions of velocity component v_z. a-viscous model, b-elastic model, c-viscoelastic model.

The difference between the models can be illustrated in the best way by v_z velocity component. Fig. 2 shows the velocity distribution at the moment of time when the press has passed the chamber.

As it can be seen, the viscous model (fig. 2, a) is the worse to describe the transmission of disturbance caused by the press. In case of the hypoelastic model (fig. 2, b) despite the absence of disturbance in the bulk of the mixture volume, the values of velocity in the end of the nozzle are relatively high. It can be explained by the fact that at every time step the Poiseuille profile was set as the boundary condition at the upper moving boundary. It appears that additional considerations are necessary in order to write a correct boundary condition at the moving boundary. The best results were shown by the full, viscoelastic model (fig. 2, c). The next calculations were made using this model. On order to choose the time of heating of chamber walls we should know the minimum heating time necessary for the steady ignition and combustion of the mixture, τ_{comb}. Therefore, the problem of ignition of the chosen mixture was considered. Parametric investigation



a – average conversion degree

b – average temperature

Figure 3: Influence of coupling effect on average conversion degree and temperature. 1 - $\delta = 0, A = 0, 2 - \delta = 0.03, A = 10, 3 - \delta = 0.06, A = 20. \beta = 0.1, \rho_0 = 0.5, v_{pr} = 0.16, \phi = 1.8, H_1 = 0.8, N = 31, P = 0.003, Nu = 6.5 \cdot 10^{-4}, \overline{R}_1 = 100$.

showed that τ_{comb} does not depend on δ and A parameters and there is a non-linear dependency on the σ_T parameter.

Analyzing the fields of temperature and conversion degree one may find out that the chemical reaction ends by the time $\tau = 444$ if there is no coupling effect.

Taking into account the coupling effect results in deceleration of the conversion. As a result, the time of chemical conversion grows up to $\tau = 528$ (at $\delta = 0.06, A = 20$) when taking into account the coupling between the fields of temperature and stresses. Fig. 3 illustrates that fact. Average conversion degree and temperature were calculated as $\langle \eta \rangle = \dfrac{1}{R_1 L} \int\limits_0^L \int\limits_0^{R_1} \eta\,(x,z)\,dxdz$, $\langle \theta \rangle = \dfrac{1}{R_1 L} \int\limits_0^L \int\limits_0^{R_1} \theta\,(x,z)\,dxdz$.

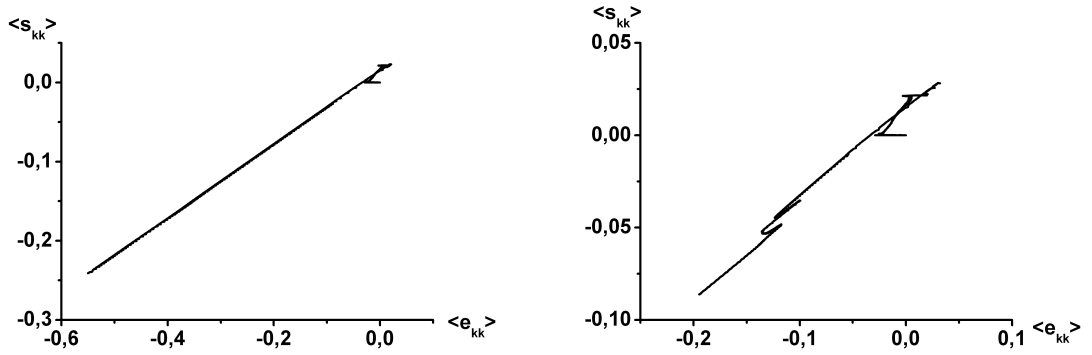
In order to investigate the mode of deformation of the mixture the average "sigma-epsilon" diagrams were made. The mean values of stress and strain tensors' first invariants were calculated as

$$\langle s_{kk} \rangle = \frac{1}{R_1 L} \int\limits_0^L \int\limits_0^{R_1} s_{kk}\,(x,z)\,dxdz,\ \langle e_{kk} \rangle = \frac{1}{R_1 L} \int\limits_0^L \int\limits_0^{R_1} e_{kk}\,(x,z)\,dxdz.$$

It was found out that if the press velocity is relatively high, the $\langle s_{kk} \rangle\,(\langle e_{kk} \rangle)$ dependency is linear. When the press moves slower, the picture becomes more complicated as it is shown on fig. 4. The curve deviations from the linear dependency are caused by the thermal stresses (fig. 4, b indicates that in the beginning of the process the deformations are positive). Comparing fig. 4, a and fig. 4, b, one can conclude that if the press velocities are high, the material deforms to a greater extent but it happens in "elastic mode". For the lower velocities we may obtain a more complicated behavior of the material. It seems that there should be a separate examination of the revealed problem. In general, we should note that there's no good in too slow motion of the press, as it leads to cooling-down of the material. And when the temperature of the extrudate falls below the so-called vitality temperature the material loses its ability to be deformed. For the mixture under study such value of the press velocity is $v_{pr} = 0.16$.

Parameter g plays an important role in the process of chemical reaction. If $g > 0$, then the conversion progresses with volume expansion, if $g < 0$ - with volume contraction. In case of volume expansion the greatest compression strains are achieved in the process of conversion.

Choosing the press geometry is of interest for the real technological applications. The calculations indicate that the more is R_1/R_2 ratio, the greater are the deformations of the material. On the one hand, it may lead to decreasing of the grain size in the product and to obtaining the ultra-fine-grained material. On the other hand, besides the growth of deformation we observe the



a – v_{pr}=0.4 b – v_{pr}=0.2

Figure 4: Influence of v_{pr} on "sigma-epsilon" diagram. $\beta = 0.1, \rho_0 = 0.5, \delta = 0.03, A = 10, \phi = 1.8, H_1 = 0.8, N = 31, P = 0.003, Nu = 6.5 \cdot 10^{-4}, \overline{R}_1 = 100$.

growth of inner stresses which may result in inner defects of the product. Extension of the chamber length causes increasing of the time necessary for the extrusion, so that, the material suffers mechanical pressure for a longer period of time and the deformations are greater. To sum it up, we should say that the greater the γ angle is the more is the deformation extent of the mixture.

References

[1] A.S. Verin. Thin-walled part casting from alloy based on Ni_3Al intermetallid // Liteinoe proizvodstvo, 1998. No. 9. P. 10-12.

[2] V.E. Ovcharenko. Effect of plastic deformation on microstructure and phase composition of Ni_3Al intermetallic synthesized under pressure // Rare metals, 2009. V. 28. Spec. issue. P. 250-253.

[3] B. Boley, J. Weiner. Theory of Thermal Stresses. Wiley, NY, 1960.

[4] A.A. Samarskii. The Theory of Difference Schemes. Marcel Dekker, NY, 2001.

N.K. Evstigneev, 36 Lenina pr., Tomsk, Russia
A.G. Knyazeva, 2/1 Akademicheskii pr., Tomsk, Russia

Supersonic flows in channel of variable cross-section with mass supply

Natalya N. Fedorova Irina A. Fedorchenko Marat A. Goldfeld
Yulia V. Zakharova
nfed@itam.nsc.ru

Abstract

In the paper, turbulent supersonic flows in a plane channel with a cavity presenting a model combustion chamber are studied. The flows are investigated experimentally and numerically with / without taking into account the mass supply into the supersonic turbulent boundary layer before the cavity.

The experiments were performed at $M = 2.8$ in the IT–302M hotshot wind tunnel (ITAM SD RAS). As an instrument for the numerical study, RANS model complemented with several two–equation turbulence models has been chosen. The parametric study with changing of the flow Mach number, the cavity length to depth ratio, the aft angle and length of the channel before the cavity was conducted numerically.

1 Introduction

It is known [1], that an open cavity is considered to be a promising candidate for a scramjet flame–holder. The cavity "traps" vortexes containing hot low–speed gas and, under certain conditions, may serve origin of ignition. "Trapped Vortex" (TV) ignition concept are based on the estimation of particle residence time that depends to a great extent on the cavity geometry, number and sizes of the vortexes and the mass exchange with the main flow.

The work focuses on the fundamental investigations of channel flowfield over an open cavity with aft ramp wall. It is known from the previous research [2], that such a cavity is the good candidates for flame–holding in supersonic flow since it provides stable combustion with low pressure drag.

2 Experimental Model description

The experiments were conducted at ITAM SD RAS in the IT–302M hotshot wind tunnel with arc heating. The experimental channel has a rectangular cross-section. The model of total length 800 mm consists of the injector and expanding sections. Cavity of 16 mm depth is installed on the top wall of the first section. The channel width in the first section is 50 mm.

Installation of injectors, pressure taps, thermocouples, and gas sampling for measurements were available at the top and bottom walls of the channel. In the tests, pressure distributions in the cavity and along the channel and flow visualization were obtained. The experimental model has the special insertion for gaseous fuel injection into the channel before the cavity forward wall.

The typical experimental conditions for the IT–302M facility and incoming gas dynamical parameters are shown in Table 4. Here P_0 is the stagnation pressure, T_0 is the stagnation temperature; M_e is the incoming Mach number, P_e is the static pressure, T_e is the static temperature, ρ_e is the density and U_e is the velocity above the boundary layer developed on the channel walls. It should be mentioned that main flow parameters (P_0, T_0 and Re) are changing during the experimental run in the short–duration facility while Mach number M_e remains constant. Case N 5 of Table 4 presents the conditions of the real experimental run for some intermidiate time moment.

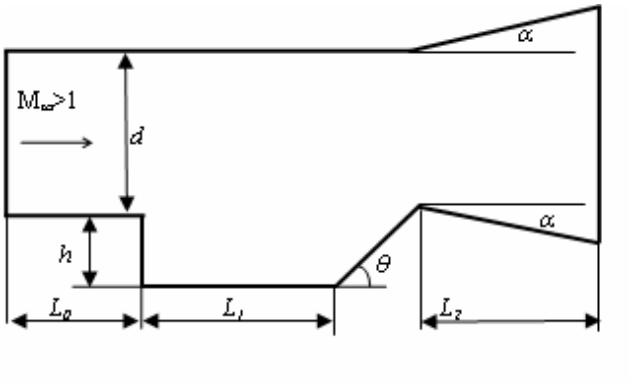


Figure 1: Scheme of the computational domain.

N	M_e	P_0, bar	T_0, K	Re_1 $10^6/m$	P_e, bar	ρ, kg/m^3	T_e, K	U_e, m/s
1	2	20	1500	33	2.556	1.069	833.3	1157
2	2	30	1500	50	3.834	1.66	833	1157
3	2.5	30	1800	30	1.755	0.765	800	1417
4	3	30	2000	19	0.817	0.398	714	1600
5	2.8	32	2270	23	1.1	0.46	821	1640

Table 4: Gas dynamical parameters of flows under investigation.

The computations in the channel with a cavity were conducted with the help of ANSYS CFD 12.0 instrumentation. The simulation of 2D flow has been carried out on density–based Navier–Stokes coupled solution. The standard $k-\omega$ turbulence model and SST modification has been used.

The computations have been performed under the conditions presented in Table 4 for simplified 2D channel geometry shown in Figure 1. Here $h = 16$ mm is the cavity depth, $d = 50$ mm is the channel width, L_0 is the plate length before the cavity, L_1 stands for the cavity length, L_2 is a length of expansion part, θ is aft angle and α is an angle of channel expansion. For the computational convenience, the cavity was placed on the bottom of the channel. The geometrical parameters of the configurations considered in the computations are shown in Table 5.

N	L_0, mm	L_1/h	θ, °	α, °
1	800	4.5	22.5	0
2	800	4.5	45	0
3	800	8	45	0
4	800	4.5	90	0
5	800	3.5	22.5	3
6	500	3.5	22.5	3
7	1000	3.5	22.5	3

Table 5: Geometrical parameters of a channel with cavity.

Typically, the entrance section of the computational domain was chosen at distance of about 100 mm upstream of the cavity front wall. To adjust the experimental conditions, the computations with long plate have been carried out with the incoming parameters from the Table 4. Boundary layers are developing along the channel walls. As the experimental measurements at $M = 2.8$ have shown, the boundary layer thickness at the entrance of test section for this case was about 10 mm. The same thickness was achieved in the computations at $x = 800$ mm. The profiles of all the turbulent and gas–dynamics parameters taken from this section were set at the entrance of the short computational domain of the cavity computations near the top and bottom channel walls.

The regular grid was used with quadrilateral cells. The grid was condensed towards the channel and cavity walls. As a rule, grids consist of 650 cells in x direction and 200 cells in y direction. About 50 cells lay in the boundary layers on the top and bottom channel walls.

3 Numerical results on cavity flow without mass supply

3.1 Computational results at various Mach numbers

The simulation results for cavity geometry N 1 were performed at various incoming Mach numbers. In Fig. 2 the computed static pressure distributions along the channel bottom wall are presented for cases N 1, N 3 and N 4 of Table 4. Increasing the Mach number results in pressure rise at the reattachment region and decreasing the base pressure. Pressure local maxima at $x = 0.072$ m corresponds the beginning of ramp aft wall. In Fig. 3, the computed Mach number fields are shown for the flow case N 3. The picture exhibits a flow pattern typical for an open cavity. Before the cavity region, the turbulent boundary layer (1) is developing on the top and bottom walls of the channel. On the cavity forward face, the boundary layer separates forming the mixing layer (2) that falls on the cavity aft wall. In the reattachment region, the compression wave arise that further form the shock (3). After the reattachment, the expansion waves are observed (4). Inside the cavity the flow is subsonic. Depending on geometry and flow conditions, the expansion wave or shock may origin from the external corner at the cavity forward face. For the cases presented in Fig. 3, it is slight expansion wave that is confirmed by pressure distributions (Fig. 2).

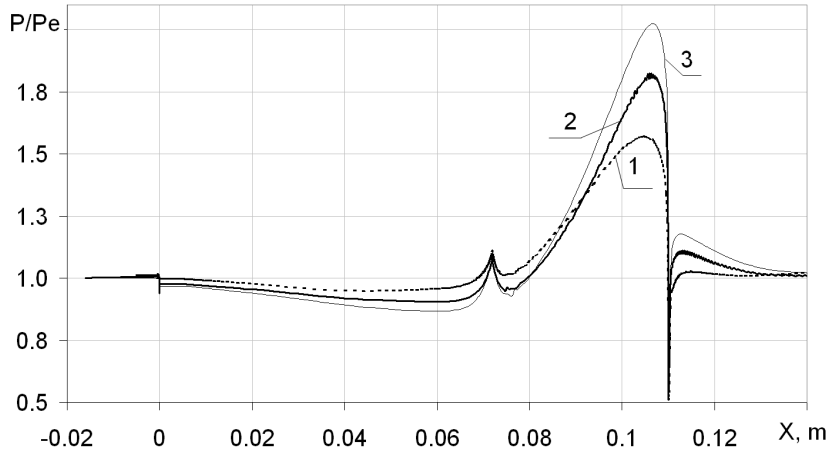


Figure 2: Computed static pressure distributions along the bottom wall for $M_e = 2$ (1), $M_e = 2.5$ (2) and $M_e = 3$ (3).

3.2 Simulation results for various cavity lengths and aft angles

For flow conditions N 1, the computations have been carried out for various cavity lengths (geometry N 2 and N 3). Static pressure distributions along the cavity wall (Fig. 4) shows that after the cavity front wall the pressure increases in a case of cavity with shorter length, while for a longer cavity it decreases. The effect may be explained by different circumstances of mixing layer development. Analysis of Mach number fields shows that for a longer cavity the mixing layer goes down in the centre of cavity that leads to flow expansion. For a shorter cavity, on the contrary, the boundary layer thickness increases in vicinity of cavity front wall and, consequently, static pressure is increasing. The whole wave structure in the channel changes because instead of expansion wave, shock comes to the upper channel wall that under certain conditions may cause the boundary layer separation and significant pressure rise and even a channel unstart.

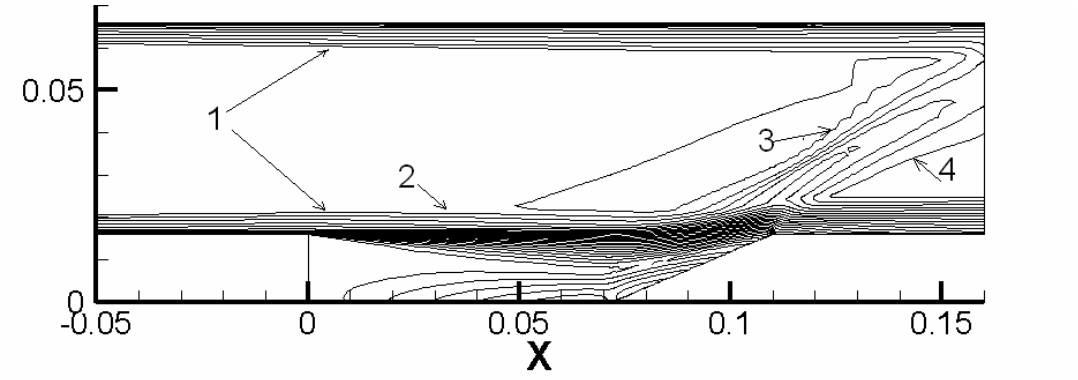


Figure 3: Computed Mach number contours for $M_e = 2.5$.

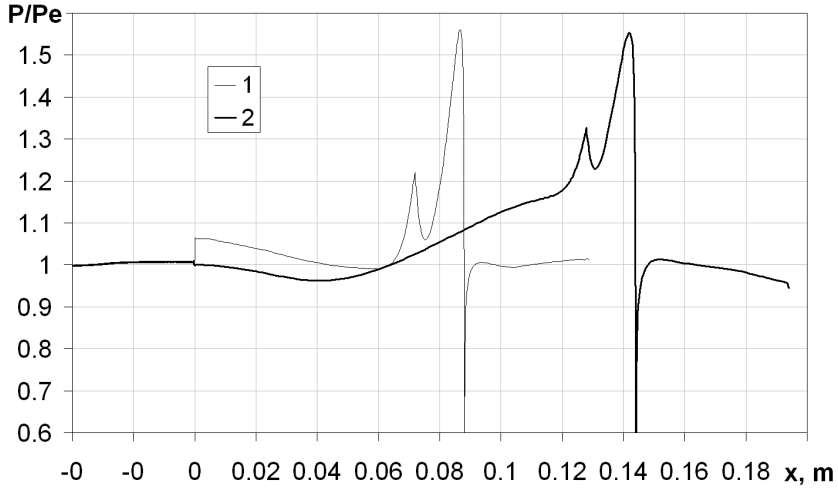


Figure 4: Computed static pressure distributions along the bottom wall at $M_e = 2$ for $L/h = 4.5$ (1) and $L/h = 8$ (2).

For flow conditions N 1, the study of the aft angle influence was performed. The results are presented in Fig. 5. Static pressure distributions along the bottom wall show that increasing the aft angle results in changing the wave picture in the channel. At small aft angle ($\Theta = 22.5°$), the expansion wave is observed in vicinity of the cavity forward wall. At larger aft angles ($\Theta = 45°, 90°$), the mixing layer forms a virtual ramp here, and slight shock is arising in this region with further pressure decreasing down to incoming pressure level. The sharp spike in pressure distribution can be seen for the case of $\Theta = 90°$ in the reattachment region followed by fast expansion in the vicinity of the external corner at the back wall.

3.3 Investigation of the boundary layer thickness influence

For the flow condition N 5 of Table 4 the computations were performed for the channel configuration N $5 \div N$ 7 of of Table 5. The results are shown in Fig. 6. Pressure distributions along the bottom wall show that for a thinner boundary layer the pressure maximum at the reattachment point is higher then that for a thicker boundary layer because Mach number in the external flow is lower in the second case. This computations were performed under cold wall temperature conditions $T_w = 300K$ that corresponded to the real condition in the short–duration facilities. The computed static temperature fields are presented in Fig. 6, a, b. Flow streamlines shown in the Fig. 6 demonstrates the cavity vortex structures. Two–vortex structure is observed with the main vortex occupying the most of the cavity region and small one in the inner corner near the forward cavity

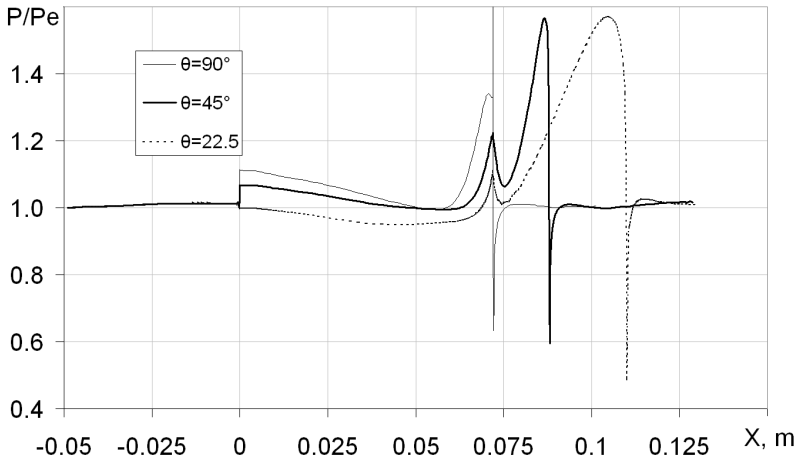


Figure 5: Computed pressure distributions at $M_e = 2$ for various aft wall angles.

wall. In a case of thicker boundary layer, the center of the small vortex shifts up and the region of very low temperature exists in the inner corner.

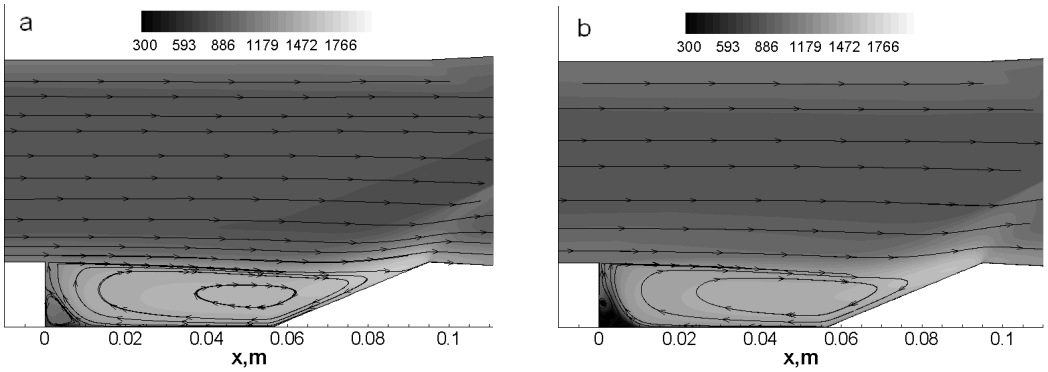


Figure 6: Computed static temperature fields and flow streamline at $M_e = 2.8$ for $L_0 = 500$ mm (a) and 1000 mm (b).

4 Numerical results on flows with mass supply

In experiments, the mixing process in a channel with cavity was examined for different injected gases. Primary, non–reacting helium was injected through round orifices of 2 mm diameter disposed at 25 mm distance upstream of the cavity front edge. Three holes were equally distributed in span direction of about 100 mm. As a first approximation to the experimental conditions, the 2D slot injection was modeled in the computations for two different injected gases: air and helium.

4.1 Flow with air jet

Numerical simulation of the cavity flow with mass supply has been provided in 2D approach. In the first place, an air injection into the channel flow has been realized at $x = -25$ mm. The freestream Mach number is equal to 2.8, density 0.676 kg/m^3, jet flow static pressure is $5 \cdot 10^5$ Pa, jet static temperature is $250K$. In order to keep the experimental mass flow rate, the Mach number of the jet is taken to be 3.33.

Mach number field obtained in the calculations is presented in Fig. 7. The separation shock (*1*) is arisen ahead of the separation bubble organized by the jet issue. It reflects later from the upper wall and forms the reflecting shock (*4*). Behind the jet the flow reattachment takes place and the rarefaction fan (*2*) emerges which interacts with the reflecting wave (*4*) and meets the upper wall of the channel afterwards. Subsonic areas of the flow are located in the cavity where the big re–circulating zone is organized and in front of the jet where a strong stagnation of the flow is appeared. At the aft wall of the cavity where the mixing layer (*6*) falls onto the wall the compression wave (*3*) is formed. It interacts with the reflected shock (*4*) and goes further downstream along with the reflected shock wave (*5*).

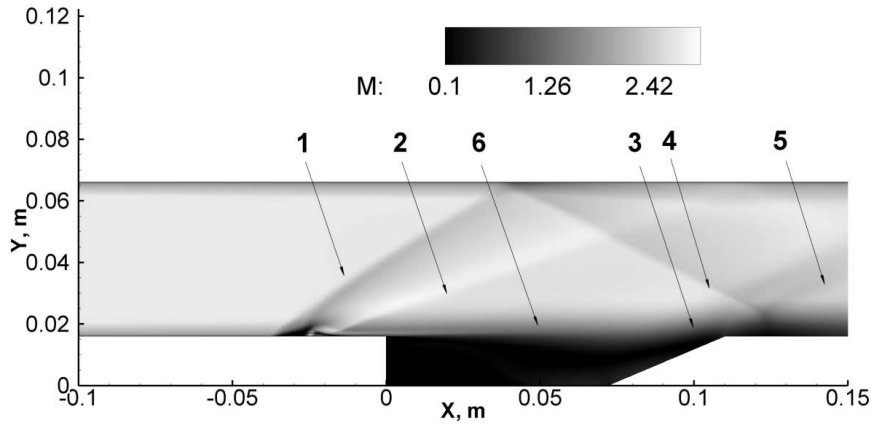


Figure 7: Computated Mach field (b) for the cavity case with air jet.

4.2 Flow with helium jet

The helium injection has been modeled at the same freestream parameters. The static pressure of the jet is $5 \cdot 10^5$ Pa, the static temperature is $220K$ and the jet exit Mach number is about 1. The main flow structure remains similar to the air jet flowfield described above. Distribution of mass fraction of helium in Fig. 8, b shows good mixing level inside the cavity, and the location of the reflected shock wave is indicated by the layer increase. Nevertheless further downstream of the cavity the volume occupied with the mixture has no tend to increase and is located at the bottom part of the channel.

5 Conclusions

High-speed high–enthalpy flows in a channel with cavity of open type have been investigated experimentally and numerically in a wide range of incoming flow conditions. Series of computations have been performed in a frame of Reynolds averaged Navier-Stokes equations using ANSYS Fluent instrumentation. Cavity flows was modeled taking into account air and helium injection into the supersonic flow. Typical flow patterns were studied numerically under conditions of experimental facility for 2D simplified channel geometry. It was shown that different flowfield structure may occur in the channel depending on the situation in vicinity of the cavity front edge.

Acknowledgments

The work has been supported by Ministry of Education and Sciences of Russian Federation, AVC Program "Development of Scientific Potential of Higher School", grant No 2.1.1/4674 and by RFBR in a frame of grant No 09-08-01001-a.

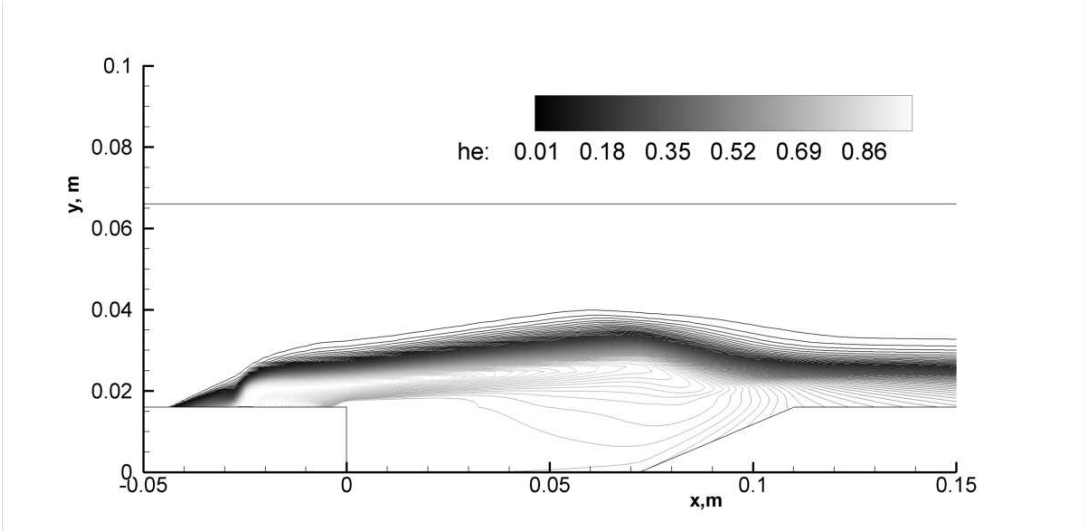


Figure 8: Computational helium mass fraction field.

References

[1] Ben–Yakar, A., Hansin, R.K. Cavity flame–holders for ignition and flame stabilization in scramjets: an overview. Journal of Propuls. Power. Vol. 17, No. 4, pp. 869–878, 2001.

[2] M. R. Gruber, R. A. Baurle, T. Mathur, K.–Y. Hsu, Fundamental Studies of Cavity–Based Flameholder Concepts for Supersonic Combustors, Journal of Propulsion and Power, 17, pp. 146–153, 2001

Natalya N. Fedorova, Institutskaya, 4/1, Novosibirsk, 630090, Russia

Quantum mechanics at different scales. Part 1: Resolution of a (quantum) point

Antonina N. Fedorova Michael G. Zeitlin
anton@math.ipme.ru, zeitlin@math.ipme.ru

Abstract

We consider some generalization of the theory of quantum states, which is based on the analysis of long standing problems and unsatisfactory situation with the possible interpretations of quantum mechanics. We demonstrate that the consideration of quantum states as sheaves can provide, in principle, more deep understanding of some phenomena. The key ingredients of the proposed construction are the families of sections of sheaves with values in the category of the functional realizations of infinite-dimensional Hilbert spaces with special (multiscale) filtration.

1 Quantum states: functions vs. patterns/sheaves

During a relative long period, it is well-known that there is a great difference between (at least) the mathematical levels of the investigation of quantum phenomena in different regions. Really, in the area of the so-called Strings (Math)Physics, one needs all existing machinery [1], like deformation quantization, non-commutative geometry, etc while more applicable in real life Quantum Mechanics/Physics uses old routines mainly. Of course, Physics at planckian scales demands a new vision regarding Physics of (realizable) Quantum Devices (like future CPU) but, at the same time, we deal with the same phenomenon (at least on qualitative level). It is impossible to imagine that some hypothetical object can be more quantum or less quantum. It seems that it can be only quantum or not quantum, i.e. classical (surely, we ignore, at the moment, quasi-classics). At the same time, even advanced modern Mathematics cannot help us in the final (at least practically accepted) analysis of the long standing quantum phenomena and the final classification of a zoo of interpretations. The well-known incomplete list is as follows:

(L)

entanglement, measurement, wave function collapse, decoherence, Copenhagen interpretation, consistent histories, many-worlds interpretation/ multiverse (MWI), Bohm interpretation, ensemble interpretation, (Dirac) self-interference, "instantaneous" quantum interaction, hidden variables, etc. [2]

As a result, beyond a lot of fundamental advanced problems at planckian scales we are still even unready to create the proper theoretical background for the reliable modeling and constructing of quantum devices far away from planckian scales.

So, let us expose one more approach in an attempt to understand, in unified framework, some set of well-known phenomena.

Mathematical side

Let us presume that Quantum Dynamics can be properly described via Wigner-Weyl approach which covers other ones. It means that:

i) we use the language, machinery and ideology of the theory of pseudo-differential operators;

ii) we work with the symbols of operators instead of the operators;

iii) Quantum Evolution is described by (pseudo-differential) Wigner-like equations (Wigner-von Neumann-Moyal-Lindblad);

iv) the adequate analysis of the full set of possible phenomena described by **iii)** demands the using of Microlocal Analysis [3] (although there are some phenomena which can be described more traditionally);

v) we need to consider Quantum State not as a function but as a sheaf [3].

It is actually more proper (at least from formal, mathematical, point of view) if we actually want to take into account a lot of internal arguments from points **i)-iv)** above.

Physical side

It is very hard to believe that trivial simple solutions, like gaussians, can exhaust all variety of possible quantum states needed for the resolution of all contradictions, hidden inside the list **(L)** mentioned above. So, let us propose the following (physical) hypothesis:

(H1)

the physically reasonable really existing Quantum States cannot be described by means of functions. Quantum state is a complex pattern which demands a set/class of functions/patches instead of one function for proper description and understanding.

There is nothing unusual in **(H1)** for physicists since Dirac's description of monopole. All the more, there is nothing unusual for mathematicians who successfully used sheaves, germs, etc in different areas. Definitely, the introducing of **(H1)** causes a number of standard topics, the most important of them are motivations, formal (exact) definition and (at least) particular realizations. Actually, why need we to change our ideology after a century (since Planck) of success? The answer is trivial and related to the list **(L)** which is overcompleted with contradictions and misunderstanding after many decades of discussions.

2 On the route to right description: (quantum) patterns as sheaves

2.1 Motivations

In the following description, it is possible to find some features or reminiscences of previous models and interpretations from the list **L**, where the most important points for allusions are the hidden variables, localization, ensemble/statistical interpretation, MWI, Dirac's "self-interference". Let us sketch the main ingredients.

1). Arena for Quantum Evolution

First of all, we need to divide the kinematical and dynamical features of a set of Quantum States (QS). From the formal point of view it means that one needs to consider some bundle (X, H, H_x) whose sections are the so-called $|\psi>$ functions or QS. Here X is (kinematical) space-time base space with the proper kinematical symmetry group (like Galilei or Poincare ones), H is a total formal Hilbert space and $H(x) = H_x$ are fibers with their own internal structures and hidden symmetries. In addition, such a bundle has the corresponding structure group which connects different fibers. Of course, in a very particular case we have the constant bundle with the trivial structure group but non-trivial fiber symmetry. Anyway, as we shall demonstrate later, it is very reasonable to provide the one-to-one correspondence between Quantum States and the proper sections

$$|QS>: \quad X \longrightarrow H, \qquad QS: \quad x \longmapsto H_x = H(x).$$

As a result, we have, at least, three different symmetries inside this construction: kinematical one on space-time, hidden one inside each fiber and the gauge-like structure group of the bundle as a whole. It is obvious that the kinematical laws (like relativity principles) depend on the proper

type of symmetry and are absolutely different in the base space and in the fibers. It should be noted that the functional realizations of fibers and the total space are very important for our aims. Roughly speaking, it can be supposed that physical effects depend on the type of the particular functional realization of formal (infinite dimensional) Hilbert space. E.g., it is impossible to use infinite smooth approximations, like gaussians, for the reliable modeling of chaotic/fractal phenomena. So, the part of Physics at quantum scales is encoded in the details of the proper functional realization.

2). Localization and a Tower of Scales

It is well-known that nobody can prove that gaussians (or even standard coherent states, etc) are an adequate and proper image for Quantum States really existing in the Nature. We can suggest that at quantum scales other classes of functions or, more generally, other functional spaces (not C^∞, e.g.) with the proper bases describe the underlying physical processes. There are two key features we are interested in. First of all, we need the best possible localization properties for our trial base functions. Second, we need to take into account, in appropriate form, all contributions from all internal hidden scales, from coarse-grained to finest ones. Of course, it is a hypothesis but it looks very reasonable:

(H2)

there is a (infinite) tower of internal scales in quantum region that contributes to the really existing Quantum States and their evolution.

So, we may suppose that the fundamental generating physical "eigen-modes" correspond to a selected functional realization and are localized in the best possible way. Let us note the role of the proper hidden symmetries which are responsible for the quantum self-organization and resulting complexity.

3). An Ensemble of Scales: Self-interaction

As a result of the description above, we may have non-trivial "interaction" inside an infinite hierarchy of modes or scales. It resembles, in some sense, a sort of turbulence or intermittency. Of course, here the generating avatar is a representation theory of hidden symmetries which create the non-trivial dynamics of this ensemble of hierarchies.

4). Hidden Parameters and Hidden Symmetry

It is well-known that symmetries generate all things (at least) in fundamental physics. Here, we have a particular case where the generic symmetry corresponds to the internal hidden symmetry of the underlying functional realization. Moreover, as it is proposed above, we have even the more complicated structure because we believe that QS is not a function but a sheaf. As a result, we have interaction between two different symmetries, namely hidden symmetry in the fiber, that corresponds to the internal symmetry of the functional realization, and the structure "gauge" group of a sheaf, which provides multifibers transition/dynamics. Both these algebraic structures can be parametrized by the proper group parameters which can play the role of famous "hidden variables" introduced many decades ago.

5). MWI

Of course, MWI or Multiverse interpretation can be covered by the structure sketched above. Quantum States are the sections of our fundamental sheaf, so we can consider them as a collection of maps between the patches of base space and fibers. All such maps simultaneously exist and, as an equivalence class, represent the same Quantum State. We postpone the detailed description to the next Section but here let us mention that each member of the full family can be considered as an object belonged to some fixed World. Obviously, before measurement we cannot distinguish samples but after measurement we shall have the only copy at our hands.

2.2 On the way to definition

The main reason to introduce sheaves as a useful instrument for the analysis of Quantum States is related to their main property which allows to assign to every region U in space-time X some family $F(U)$ of algebraic or geometric objects such as functions or differential operators. The family can be restricted to smaller regions, and the compatible collections of families can be glued to give a family over larger regions, so it provides connection between small and large scales, local and global data[3].

Informal construction is as follows.

Let X be the space-time base space (some topological space) with a system of open subsets $U \subset X$, then for every U and map F the image $F(U)$ is some object with internal structure (more generally, $F(U)$ takes values in some category $\mathbf{H}$) such that for every two open subsets, U and V, $V \subset U$ there is the so-called restriction map (more generally, morphism in the category $\mathbf{H}$), $r_{V,U} : F(U) \to F(V)$ (restriction morphism). A map F will be a **presheaf** if restriction morphism satisfies the following properties:

(a) for every open subset $U \subset X$, the restriction morphism $r_{U,U} : F(U) \to F(U)$ is the identity morphism,

(b) if there are three open subsets $W \subset V \subset U$, then $r_{W,V} r_{V,U} = r_{W,U}$. This property provides the connection or ordering of the underlying scales. In other words, let $O(X)$ be the category of open sets on X, whose objects are the open sets of X and whose morphisms are inclusions. Then a presheaf $\mathbf{F}$ on X with values in category $\mathbf{H}$ is the contravariant functor from $O(X)$ to $\mathbf{H}$. $F(U)$ is called the section of $\mathbf{F}$ over U and we consider it as some pre-image for adequate Quantum State $|QS>$. But our goal, in this direction, is a **sheaf**, so we need to add two additional properties.

Let $\{U_i\}_{i \in I}$ be some family of open subsets of X, $U = \cup_{i \in I} U_i$.

(c) If Ψ_1 and Ψ_2 are two elements of $F(U)$ and $r_{U_i,U}(\Psi_1) = r_{U_i,U}(\Psi_2)$ for every U_i, then $\Psi_1 = \Psi_2$.

(d) for every i let a section $\Psi_i \in F(U_i)$. $\{\Psi_i\}_{i \in I}$ are compatible if, for all i and j, $r_{U_i \cap U_j, U_i}(\Psi_i) = r_{U_i \cap U_j, U_j}(\Psi_j)$. For every set $\{\Psi_i\}_{i \in I}$ of compatible sections on $\{U_i\}_{i \in I}$, there exists the unique section $\Psi \in F(U)$ such that $r_{U_i,U}(\Psi) = \Psi_i$ for every $i \in I$.

The section $\mathbf{\Psi}$ is called the gluing of the sections Ψ_i. Definitely, we can consider this property as allusion to the hypothesis of wave function collapse. Really, $\mathbf{\Psi}$ looks as Multiverse Quantum State Ensemble $\{\Psi_i\}$ while Ψ_i is the result of measurement in the patch U_i. And it is unique!

The next step is to specify the Quantum Category $\mathbf{H}$. According to our Hypothesis **H2**, we consider the category of the functional realization of (infinite-dimensional) Hilbert spaces provided with proper filtration, which allows to take into account multiscale decomposition for all dynamical quantities needed for the description of Quantum Evolution. The well-known type of such filtration is the so-called multiresolution decomposition [4]. It should be noted that the whole description is much more complicated because it demands the consideration of both structures together, namely, the fiber structure generated by internal hidden symmetry of the chosen functional realization and the family of gluing sections $\mathbf{\Psi}$ in the unified framework.

2.3 Realization via multiresolution: dynamics, measurement, decoherence, etc.

In the companion paper[5], we shall consider in details one important realization of this construction based on the local nonlinear harmonic analysis which has, as the key ingredient, the so-called Multiresolution Analysis (MRA)[4]. It allows us to describe internal hidden dynamics on a tower of scales. Introducing the Fock-like space structure on the whole space of internal hidden scales [6], we have the following MRA decomposition:

$$H = \bigoplus_i \bigotimes_n H_i^n$$

for the set of n-partial Wigner functions (states):

$$W^i = \{W_0^i, W_1^i(x_1;t), \dots, \qquad W_N^i(x_1,\dots,x_N;t), \dots\},$$

where $W_p(x_1,\dots,x_p;t) \in H^p$, $H^0 = C$, $\quad H^p = L^2(R^{6p})$ (or any different proper functional space), with the natural Fock space like norm:

$$(W,W) = W_0^2 + \sum_i \int W_i^2(x_1,\dots,x_i;t) \prod_{\ell=1}^{i} \mu_\ell.$$

Now we consider some phenomenological description which presents some attempt of the qualitative description of quantum dynamics as a whole and in comparison with its classical counterpart. It is possible to take, for reminiscence, the famous Dirac's phrase that "an electron can interact only itself via the process of quantum interference". Let G be a hidden/internal symmetry group on the spaces of Quantum States, which generates, via MRA, the multiscale/multiresolution representation for all dynamical quantities, unified in object $O(t)$, such as states, observables, partitions (e.g., Wigner quasi-distributions):

$$O^i(t) = \{\psi^i(t), Op^i(t), W_n^i(t)\},$$

where i is the proper scale index.

Then, the following commutative diagram represents the details of quantum life from the point of view of the representations of G on the chosen functional realization which leads to the decomposition of the whole quantum evolution into the orbits or scales corresponding to the proper level of resolution. Morphisms $W(t)$ describe Wigner-Weyl evolution in the algebra of symbols, while the processes of interactions with open World, such as the measurement or decoherence, correspond to morphisms (or even functors) $m(t)$ which transform the infinite set of scales, characterizing the quantum object, into finite ones, sometimes consisting of one element (demolition/destructive measurement)

$$\begin{array}{ccc} & W(t) & \\ \{O^i(t_1)\} & \longrightarrow & \{O^j(t_2)\} \\ \downarrow m(t_1) & \widetilde{W(t)} & \downarrow m(t_2) \\ \{O^{i_c}(t_1)\} & \longrightarrow & \{O^{j_c}(t_2)\}, \end{array}$$

where the reduced morphisms $\widetilde{W(t)}$ correspond to (semi)classical or quasiclassical evolution. So, qualitatively, **Quantum Objects** can be represented by an infinite or sufficiently large set of coexisting and interacting subsets while **(Quasi)Classical Objects** can be described by one or a few only levels of resolution with (almost) suppressed interscale self-interaction. It is possible to consider Wigner functions as some measure of the quantum character of the system: as soon as it becomes positive, we arrive to classical regime and so there is no need to consider the full hierarchy decomposition in the MRA representation. So, Dirac's self-interference is nothing else than the multiscale mixture/intermittency. Certainly, the degree of this self-interaction leads to different qualitative types of behaviour, such as localized quasiclassical states, separable, entangled, chaotic etc. At the same time, the instantaneous quantum interaction or transmission of (quantum) information from Alice to Bob takes place not in the physical kinematical space-time but in Hilbert spaces of Quantum States in their proper functional realization where there is a different kinematic life. To describe a set of Quantum Objects, we need to realize our Space of States (Hilbert space) not as one functional space but as the so-called and well known in mathematics, scale of spaces, e.g. $B^s_{p,q}$, $F^s_{p,q}$ [5]. The proper multiscale decomposition for the scale of spaces provides us by the method of the description of a set of quantum objects in case if the "size" of one Hilbert space of states is not enough to describe the complicated internal World. We will consider it elsewhere, while here we consider the one-scale case (to avoid possible misunderstanding, we need to mention that one-scale case is also described by an infinite scale of spaces, but it is the internal decomposition of the unique, attached to the problem, Hilbert space). Definitely, the full family of sections of non-trivial sheaf, as a model of QS, demands to take into account the double-hierarchy of the underlying internal scales generated by means of the corresponding hidden symmetries. As a result, on the proper orbits, we have nontrivial entangled dynamics, especially in contrast with its classical counterpart.

3 Conclusions

It seems very reasonable that there are no chances for the solution of long standing problems and novel ones if we constraint ourselves by old routines and the old zoo of simple solutions like gaussians, coherent states and all that. Evidently, that even the mathematical background of regular Quantum Physics demands new interpretations and approaches. Let us mention only the procedures of quantization as a generic example. In this respect, we can hope that our sheaf extension of representation for QS, which is natural from the formal point of view, may be very productive for the more deep understanding of the underlying (Quantum) Physics, especially, if we consider it together with the category of multiscale filtered functional realizations decomposed into the entangled orbits generated by actions of internal hidden symmetries. In such a way, we open a possibility for the exact description of a lot of phenomena like entanglement and measurement, wave function collapse, self-interference, instantaneous quantum interaction, Multiverse, hidden variables, etc. In the companion paper [6] we consider the machinery needed for the generation of a zoo of the complex quantum patterns during Wigner-Weyl evolution.

4 Summary and perspectives

We considered some generalization of the theory of quantum states, which is based on the analysis of long standing problems and unsatisfactory situation with possible interpretations of quantum mechanics. We demonstrate that the consideration of quantum states as sheaves can provide, in principle, more deep understanding of some phenomena. The key ingredients of the proposed construction are the families of sections of sheaves with values in the category of the functional realizations of infinite-dimensional Hilbert spaces with special (multiscale) filtration.

The questions we hope to answer are:

i) How may we enlarge the amount of (physical) information stored in one (quantum) physical point?

ii) Relation between structureless geometrical points and physical points (or point objects like (point) particles) with rich (possible hidden) structure.

iii) How we may "resolve" (physical) point/quantum state to provide such a structure.

iv) A new look in new framework for localization, entanglement, measurement, and all that.

v) How we may to explain/re-interpret a standard zoo of standard interpretations/phenomena (multiverse, wave functions collapse, hidden parameters, Dirac self-interference, ensemble interpretation, etc, etc. [2]) of Quantum Mechanics in the new framework.

The goal of the first part (of two) is to compare the following key objects which are basic for any type of the exposition of Quantum Mechanics (and other related areas):

Geometrical points vs. Physical Points (or Point Objects, or One-Point-Patterns);

Point functions vs. Sheaves;

Partial Differential Equations (and proper orthodox approaches)

vs.

Pseudodifferential Equations (via Microlocal analysis and all that).

We will continue heuristic Part 1 by more technical Part 2 where we compare:

Fourier/Gaussian modes vs. (pretty much) Localized (but non-gaussian) Physical Modes;

Fourier Analysis vs. Local Nonlinear Harmonic Multiscale Analysis (including wave- and other -lets and multiresolution);

Standard Quantum Images vs. Quantum Patterns generated by Multiresolution;

and as a final point,

Categorification Procedure(s) for Quantum Mechanics (QM).

It is more or less obvious that we don't have any unified framework covering a zoo of (mostly) discrepant interpretations [2] of QM, as well as satisfactory explanation/understanding of main ingredients of a phenomena like entanglement, etc.

The starting point is an idea to describe (to resolve) the key object of the area, namely point objects (physical points). Usually, for the modeling of real physical point objects, one can consider equivalence between them and standard geometrical points (at the moment, the concrete description of the set to which such points belong as one-element subsets, does not matter).

As direct consequence, our dynamical variables (like wave function or density matrix or the Wigner function) are described by means of point functions or what mathematicians mean by standard functions. But, as we can understand, a geometrical point is structureless and it seems that we need much more to enlarge the amount of data/information corresponding to this generic object. To advocate this Hypothesis in the present context it is worth noting Dirac's famous sentence "an electron can interact only itself via the process of quantum inteference". Roughly speaking, from this perspective it means that a "point particle" needs and must have a non-trivial complicated structure. It seems reasonable to have the rich structure for a model of the (quantum) physical point (usually named as "particle") in comparison with the structureless geometrical point. All above looks like Physical Hypothesis and it may be not so clear but at the same time it is more or less well known from the mathematical point of view if we accept the right (Wigner-Moyal) picture for description of Quantum World. In that framework, more exactly Strict Deformation Quantization approach, all equations are pseudodifferential and as immediate consequence we need to change point functions by sheaves what provides the clear resolution of the (Physical) Point: as a result it is no more structureless but acquires the rich (possible hidden at first glance) structure.

To summarize, our first three Hypotheses are as follows:

(Physical) Hypothesis 1

Physical Point Object (physical point, point particle) is not a structureless object and cannot be described by means of the geometrical point (in the standard math sense). Instead of, Physical Points have a rich infinite hidden structure.

(Physical version) Hypothesis 2

Quantum Dynamical Variables (wave functions, density matrix, Wigner functions) are not point functions but sheaves defined on the properly chosen space-time manifold (or topological space, or variety, or even scheme).

(Math version) Hypothesis 2

To provide the structureness of the Physical Point, allowing to enlarge a number of useful properties and increase the amount of corresponding data inside, we consider it together with a proper generalization of wave function as a section/fiber of proper sheaf (in a proper category of objects) defined on a proper model (category) of space-time.

(Physical) Hypothesis 3

Deformation Quantization Picture (roughly speaking, Wigner-Weyl-Moyal) is not in contradiction with Hypotheses 1 and 2 and allow us to consider the proper description.

(Math) Hypothesis 3

Microlocal Analysis of proper Pseudodifferential Dynamical Equations (like the Wigner one) allows to create a model of infinite hierarchy for the correct representation of Physical Point.

In such an approach **Quantum States** are (roughly speaking) sections of the so-called **coherent sheaves** or **contravariant functors** from the proper category describing space-time to other one properly describing the complex dynamics of Quantum States/Patterns. As we will explain in Part 2 [6], the objects of this category are some filtrations on the Hilbert space of States. In this picture, a result of **measurement** corresponds to **direct (inductive) limit**.

Definitely, we need a proper analytical/numerical machinery to realise such approach. It is exactly the subject of Part 2. It is not worth mentioning that all above is well known in Mathematics long ago. But we hope to convert this knowledge to a physical acceptable and computational form.

Papers/(arXiv)preprints [7]–[21] of authors can be found on web pages below.

Acknowledgements

We are very grateful to to Alexey G. Sergeyev for his constant encouragement.

References

[1] A. Connes, M. Marcolli, *Noncommutative Geometry, Quantum Fields and Motives*, 2009

[2] http://en.wikipedia.org/wiki/Interpretation of quantum mechanics and references therein.

[3] M. Kashiwara, P. Schapira, Sheaves on Manifolds (Springer, 1994).

[4] Y. Meyer, *Wavelets and Operators* (Cambridge Univ. Press, 1990);

[5] H. Triebel, *Theory of Functional Spaces* (Birkhauser, 1983).

[6] A.N. Fedorova and M.G. Zeitlin, Quantum mechanics at different scales. Part 2: Localization, multiscales and complex quantum patterns, this Volume.

[7] A.N. Fedorova and M.G. Zeitlin, Quasiclassical Calculations for Wigner Functions via Multiresolution, Localized Coherent Structures and Patterns Formation in Collective Models of Beam Motion, in *Quantum Aspects of Beam Physics*, Ed. P. Chen (World Scientific, Singapore, 2002) pp. 527–538, 539–550; arXiv: physics/0101006; physics/0101007.

[8] A.N. Fedorova and M.G. Zeitlin, BBGKY Dynamics: from Localization to Pattern Formation, in *Progress in Nonequilibrium Green's Functions II*, Ed. M. Bonitz, (World Scientific, 2003) pp. 481–492; arXiv: physics/0212066.

[9] A.N. Fedorova and M.G. Zeitlin, Pattern Formation in Wigner-like Equations via Multiresolution, in *Quantum Aspects of Beam Physics*, Eds. Pisin Chen, K. Reil (World Scientific, 2004) pp. 22-35; Preprint SLAC-R-630; arXiv: quant-phys/0306197.

[10] A.N. Fedorova and M.G. Zeitlin, Localization and pattern formation in Wigner representation via multiresolution, *Nuclear Inst. and Methods in Physics Research, A*, **502A/2-3**, pp. 657 - 659, 2003; arXiv: quant-ph/0212166.

[11] A.N. Fedorova and M.G. Zeitlin, Fast Calculations in Nonlinear Collective Models of Beam/Plasma Physics, *Nuclear Inst. and Methods in Physics Research, A*, **502/2-3**, pp. 660 - 662, 2003; arXiv: physics/0212115.

[12] A.N. Fedorova and M.G. Zeitlin, Classical and quantum ensembles via multiresolution: I-BBGKY hierarchy; Classical and quantum ensembles via multiresolution. II. Wigner ensembles; *Nucl. Instr. Methods Physics Res.*, **534A** (2004)309-313; 314-318; arXiv: quant-ph/0406009; quant-ph/0406010.

[13] A.N. Fedorova and M.G. Zeitlin, Localization and Pattern Formation in Quantum Physics. I. Phenomena of Localization, in *The Nature of Light: What is a Photon? SPIE*, vol.**5866**, pp. 245-256, 2005; arXiv: quant-ph/0505114;

[14] A.N. Fedorova and M.G. Zeitlin, Localization and Pattern Formation in Quantum Physics. II. Waveletons in Quantum Ensembles, in *The Nature of Light: What is a Photon?SPIE*, vol. **5866**, pp. 257-268, 2005; arXiv: quant-ph/0505115.

[15] A.N. Fedorova and M.G. Zeitlin, Pattern Formation in Quantum Ensembles, *Intl. J. Mod. Physics* **B20**(2006)1570-1592; arXiv: 0711.0724.

[16] A.N. Fedorova and M.G. Zeitlin, Patterns in Wigner-Weyl approach, Fusion modeling in plasma physics: Vlasov-like systems, *Proceedings in Applied Mathematics and Mechanics (PAMM)*, Volume **6**, Issue 1, p. 625, p. 627, Wiley InterScience, 2006.

[17] A.N. Fedorova and M.G. Zeitlin, Localization and Fusion Modeling in Plasma Physics. Part I: Math Framework for Non-Equilibrium Hierarchies, pp.61-86, in *Current Trends in International Fusion Research*, Ed. E. Panarella, R. Raman, National Research Council (NRC) Research Press, Ottawa, Ontario, Canada, 2009; arXiv: physics/0603167.

[18] A.N. Fedorova and M.G. Zeitlin, Localization and Fusion Modeling in Plasma Physics. Part II: Vlasov-like Systems. Important Reductions, pp.87-100, in *Current Trends in International Fusion Research*, Ed. E. Panarella, R. Raman, National Research Council (NRC) Research Press, Ottawa, Ontario, Canada, 2009; arXiv: physics/0603169.

[19] A.N. Fedorova and M.G. Zeitlin, Fusion State in Plasma as a Waveleton (Localized (Meta)-Stable Pattern), p. 272, in *AIP Conference Proceedings*, Volume **1154**, Issue 1, *Current Trends in International Fusion Research*, Ed. E. Panarella, R. Raman, AIP, 2009.

[20] A.N. Fedorova and M.G. Zeitlin, Exact Multiscale Representations for (Non)-Equilibrium Dynamics of Plasma, p.291, in *AIP Conference Proceedings*, Volume **1154**, Issue 1, *Current Trends in International Fusion Research*, Ed. E. Panarella, R. Raman, AIP, 2009.

[21] A.N. Fedorova and M.G. Zeitlin, Fusion Modeling in Vlasov-Like Models, *J.Plasma Fusion Res. Series*, Vol. **8**, pp. 126-131, 2009.

Antonina N. Fedorova, Michael G. Zeitlin,
IPME RAS, St. Petersburg, V.O. Bolshoj pr., 61, 199178, Russia,
http://www.ipme.ru/zeitlin.html, http://mp.ipme.ru/zeitlin.html

Quantum mechanics at different scales. Part 2: Localization, multiscales and complex quantum patterns

Antonina N. Fedorova Michael G. Zeitlin
anton@math.ipme.ru, zeitlin@math.ipme.ru

Abstract

We present a family of methods which can describe complex behaviour in quantum ensembles. We demonstrate the creation of nontrivial (meta) stable states (patterns), localized, chaotic, entangled or decoherent, from the basic localized modes in various collective models arising from the quantum hierarchy described by Wigner-like equations.

1 New localized modes and patterns: why need we them?

It is widely known that the currently available experimental techniques in the area of quantum physics as well as the present level of the understanding of phenomenological models, outstrips the actual level of mathematical description [1]. Considering the problem of describing the really existing and/or realizable states, one should not expect that (gaussian) coherent states would be enough to characterize complex quantum phenomena. The complexity of a set of relevant states, including entangled (chaotic) ones is still far from being clearly understood and moreover from being realizable [2], [3]. Our motivations arise from the following general questions: how can we represent a well localized and reasonable state in mathematically correct form? is it possible to create entangled and other relevant states by means of these new localized building blocks? The general idea is rather simple: it is well known that the generating symmetry is the key ingredient of any modern reasonable physical theory. Roughly speaking, the representation theory of the underlying (internal/hidden) symmetry (classical or quantum, finite or infinite dimensional, continuous or discrete) is the useful instrument for the description of (orbital) dynamics. The proper representation theory is well known as "local nonlinear harmonic analysis", in particular case of the simple underlying symmetry, affine group, aka wavelet analysis [4]–[6]. From our point of view the advantages of such approach are as follows:

i) the natural realization of localized states in any proper functional realization of (Hilbert) space of states,

ii) the hidden symmetry of a chosen realization of the functional model describes the (whole) spectrum of possible states via the so-called multiresolution decomposition.

Effects we are interested in are as follows:

1). a hierarchy of internal/hidden scales (time, space, phase space);

2). non-perturbative multiscales: from slow to fast contributions, from the coarser to the finer level of resolution/decomposition;

3). the coexistence of the levels of hierarchy of multiscale dynamics with transitions between scales;

4). the realization of the key features of the complex quantum world such as the existence of chaotic and/or entangled states with possible destruction in "open/dissipative" regimes due to interactions with quantum/classical environment and transition to decoherent states.

At this level, we may interpret the effect of mysterious entanglement or "quantum interaction" as a result of the simple interscale interaction or intermittency (with allusion to hydrodynamics), i.e. the mixing of orbits generated by multiresolution representation of the hidden underlying symmetry. Surely, the existence of such a symmetry is a natural physical property of the model as well as the space of representation and its proper functional realization. So, instantaneous quantum interaction materializes not in the physical space-time variety but in the space of the representation of hidden symmetry along the orbits/scales constructed by proper representations. Such an approach provides the explicit analytical construction for solutions of c- and q-hierarchies and their important reductions starting from the quantization of c-BBGKY hierarchy [7]–[21]. It is based on tensor algebra extensions of multiresolution representation [4] for states and observables and variational formulation [7]–[21]. We give explicit representation for the hierarchy of n-particle reduced distribution functions in the base of the high-localized generalized coherent (regarding underlying generic symmetry (affine group in the simplest case)) states given by the polynomial tensor algebra of our basis functions (wavelet families, wavelet packets [5]–[6]), which takes into account contributions from all underlying hidden multiscales from the coarsest scale of resolution to the finest one to provide full information about (quantum) dynamical process. The difference between classical and quantum case is concentrated in the structure of the set of operators included in the set-up and, surely, depends on the method of quantization. But, in the naive Wigner-Weyl approach for the quantum case, the symbols of operators play the same role as usual functions in the classical case. In some sense, our approach for ensembles (hierarchies) resembles Bogolyubov's one and related approaches but we don't use any perturbation technique (like virial expansion) or linearization procedures. Most important, that numerical modeling in all cases shows the creation of various internal (coherent) structures from localized modes, which are related to the (meta)stable (equilibrium) or unstable type of behaviour and corresponding patterns (waveletons) formation [7]–[21].

We start from the second quantized representation for an algebra of observables $A = (A_0, A_1, \dots, A_s, ...)$ in the standard form

$$A = A_0 + \int dx_1 \Psi^+(x_1) A_1 \Psi(x_1) + \dots$$
$$+(s!)^{-1} \int dx_1 \dots dx_s \Psi^+(x_1) \dots \Psi^+(x_s) A_s \Psi(x_s) \dots \Psi(x_1) + \dots .$$

N-particle Wigner functions allow to consider them as some quasiprobabilities. The full description for quantum ensemble can be done by the hierarchy of functions (symbols):

$$W = \{W_s(x_1, \dots, x_s), s = 0, 1, 2 \dots\},$$

which are solutions of Wigner equations:

$$\frac{\partial W_n}{\partial t} = -\frac{p}{m}\frac{\partial W_n}{\partial q} + \sum_{\ell=0}^{\infty} \frac{(-1)^\ell (\hbar/2)^{2\ell}}{(2\ell+1)!} \frac{\partial^{2\ell+1} U_n(q)}{\partial q^{2\ell+1}} \frac{\partial^{2\ell+1} W_n}{\partial p^{2\ell+1}}. \tag{1}$$

The similar equations describe the important decoherence processes [2].

2 Variational multiresolution representation

We obtain our multiscale/multiresolution representations for solutions of Wigner-like equations (1) via the variational-wavelet approach. We represent the solutions as decomposition into localized eigenmodes related to the hidden underlying set of scales:

$$W_n(t, q, p) = \bigoplus_{i=i_c}^{\infty} W_n^i(t, q, p),$$

where value i_c corresponds to the coarsest level of resolution c in the full multiresolution decomposition (MRA) of the underlying functional space [4]:

$$V_c \subset V_{c+1} \subset V_{c+2} \subset \dots$$

and $p = (p_1, p_2, \dots)$, $q = (q_1, q_2, \dots)$, $x_i = (p_1, q_1, \dots, p_i, q_i)$ are coordinates in phase space. We introduce the Fock-like space structure on the whole space of internal hidden scales

$$H = \bigoplus_i \bigotimes_n H_i^n$$

for the set of n-partial Wigner functions (states):

$$W^i = \{W_0^i, W_1^i(x_1; t), \dots, W_N^i(x_1, \dots, x_N; t), \dots\},$$

where $W_p(x_1, \dots, x_p; t) \in H^p$, $H^0 = C$, $H^p = L^2(R^{6p})$ (or any different proper functional space), with the natural Fock space like norm:

$$(W, W) = W_0^2 + \sum_i \int W_i^2(x_1, \dots, x_i; t) \prod_{\ell=1}^{i} \mu_\ell.$$

First of all, we consider $W = W(t)$ as a function of time only, $W \in L^2(R)$, via multiresolution decomposition which naturally and efficiently introduces an infinite sequence of the underlying hidden scales [4]. We have the contribution to the final result from each scale of resolution from the whole infinite scale of spaces. The closed subspace $V_j (j \in \mathbf{Z})$ corresponds to the level j of resolution and satisfies the following properties: let D_j be the orthonormal complement of V_j with respect to V_{j+1}: $V_{j+1} = V_j \bigoplus D_j$. Then we have the following decomposition:

$$\{W(t)\} = \bigoplus_{-\infty<j<\infty} D_j = \overline{V_c \bigoplus_{j=0}^{\infty} D_j},$$

in case when V_c is the coarsest scale of resolution. The subgroup of translations generates a basis for the fixed scale number: $\mathrm{span}_{k \in Z}\{2^{j/2}\Psi(2^j t - k)\} = D_j$. The whole basis is generated by the action of the full affine group:

$$\mathrm{span}_{k \in Z, j \in Z}\{2^{j/2}\Psi(2^j t - k)\} = \mathrm{span}_{k,j \in Z}\{\Psi_{j,k}\} = \{W(t)\}.$$

After the construction of the multidimensional tensor product bases [4], the next key point is the so-called Fast Wavelet Transform (FWT) [4]–[6], demonstrating that for a large class of operators the wavelet functions are a good approximation for true eigenvectors and the corresponding matrices are almost diagonal. We have the simple linear parametrization of the matrix representation of our operators in the localized wavelet bases and of the action of these operators on arbitrary vectors/states in the proper functional space. FWT provides the maximum sparse and useful form for the wide classes of operators [4], [6]. After that, we can obtain our multiscale/multiresolution representations for observables (symbols), states, partitions via the variational approaches.

Let L be an arbitrary (non)linear differential/integral operator with matrix dimension d (finite or infinite), which acts on some set of functions from $L^2(\Omega^{\otimes^n})$: $\Psi \equiv \Psi(t, x_1, x_2, \dots) = \Big(\Psi^1(t, x_1, x_2, \dots), \dots, \Psi^d(t, x_1, x_2, \dots)\Big)$, $x_i \in \Omega \subset \mathbf{R}^6$, n is a number of particles:

$$\begin{aligned} L\Psi &\equiv L(Q, t, x_i)\Psi(t, x_i) = 0, \\ Q &\equiv Q_{d_0,d_1,d_2,\dots}(t, x_1, x_2, \dots, \partial/\partial t, \partial/\partial x_1, \partial/\partial x_2, \dots, \int \mu_k) \\ &= \sum_{i_0,i_1,i_2,\dots=1}^{d_0,d_1,d_2,\dots} q_{i_0 i_1 i_2 \dots}(t, x_1, x_2, \dots)\Big(\frac{\partial}{\partial t}\Big)^{i_0}\Big(\frac{\partial}{\partial x_1}\Big)^{i_1}\Big(\frac{\partial}{\partial x_2}\Big)^{i_2} \dots \int \mu_k. \end{aligned}$$

Let us consider the N mode approximation:

$$\Psi^N(t,x_1,x_2,\dots)=\sum_{i_0,i_1,i_2,\cdots=1}^{N} a_{i_0 i_1 i_2 \dots} A_{i_0}\otimes B_{i_1}\otimes C_{i_2}\dots(t,x_1,x_2,\dots).$$

We will determine the expansion coefficients from the following conditions (related to the proper choosing of variational approach):

$$\ell^N_{k_0,k_1,k_2,\dots}\equiv\int (L\Psi^N)A_{k_0}(t)B_{k_1}(x_1)C_{k_2}(x_2)\mathrm{d}t\mathrm{d}x_1\mathrm{d}x_2\cdots=0. \tag{2}$$

Thus, we have exactly dN^n algebraical equations for dN^n unknowns $a_{i_0,i_1,\dots}$. This variational approach reduces the initial problem to the problem of solution of functional equations at the first stage and some algebraical problems at the second one. It allows to unify the multiresolution expansion with variational construction [7]–[21]. As a result, the solution is parametrized by the solutions of two sets of reduced algebraical problems, one is linear or nonlinear (depending on the structure of the generic operator L) and the rest are linear problems related to the computation of the coefficients of reduced algebraic equations. It is also related to the choice of exact measure of localization (including the class of smoothness), which is proper for our set-up. These coefficients can be found via functional/algebraic methods by using the compactly supported wavelet basis or any other wavelet families [5], [6]. As a result, the solution of the hierarchies as in c- as in q-region, has the following multiscale or multiresolution decomposition via nonlinear localized eigenmodes

$$\begin{aligned} W(t,x_1,x_2,\dots)&=\sum_{(i,j)\in Z^2} a_{ij}U^i\otimes V^j(t,x_1,\dots),\\ V^j(t)&=V_N^{j,slow}(t)+\sum_{l\geq N} V_l^j(\omega_l t),\ \omega_l\sim 2^l,\\ U^i(x_s)&=U_M^{i,slow}(x_s)+\sum_{m\geq M} U_m^i(k_m^s x_s),\ k_m^s\sim 2^m, \end{aligned} \tag{3}$$

which corresponds to the full multiresolution expansion in all underlying time/space scales. The formulae (3) give the expansion into a slow part and fast oscillating parts for arbitrary N, M. So, we may move from the coarse scales of resolution to the finest ones for obtaining more detailed information about the dynamical process. In this way, one obtains contributions to the full solution from each scale of resolution or each time/space scale or from each nonlinear eigenmode. It should be noted that such representations give the best possible localization properties in the corresponding (phase)space/time coordinates. Formulae (3) do not use perturbation techniques or linearization procedures. Numerical calculations are based on compactly supported wavelets and wavelet packets and on the evaluation of accuracy on the level N of the corresponding cut-off of the full system regarding Fock-like norm:

$$\|W^{N+1}-W^N\|\leq\varepsilon.$$

3 Conclusions

By using high localized nonlinear eigenmodes with their best phase space localization properties, we can describe the full zoo of possible complex patterns generated from localized (coherent) structures/orbits in quantum systems with complicated behaviour due to process of quantum self-organization (Figs. 1–7). The numerical simulation demonstrates the formation of various (meta) stable patterns or orbits generated by internal hidden symmetry from generic high-localized fundamental modes. These (nonlinear) eigenmodes, definitely, are more realistic for the modeling of classical/quantum dynamical process than the smooth linear gaussian-like coherent states. Here we mention only the best convergence properties of the expansions based on wavelet packets, which realize the minimal Shannon entropy property and the exponential control of the convergence of expansions like (3). Fig. 1 demonstrates direct modeling for the non-trivial Wigner function for three best localized wavelet packets [6]. Fig. 4 (waveleton state generated by a finite number

of fundamental modes) corresponds to the (possible) result of einselection [3] after decoherence process started from chaotic/entangled state (Fig. 5). Figs. 2, 3 and 6, 7 demonstrate the steps of multiscale resolution (or the degrees of interference) during the quantum interaction/evolution of entangled states or quantum self-organization leading to the growth of the degree of entanglement.

It should be noted that we can control the type of behaviour on the level of the reduced algebraic system (generalized dispersion relation) (2). We hope that it will be important in practical applications.

Papers/(arXiv)preprints [7]–[21] of the authors can be found on web pages below.

Acknowledgements

We are very grateful to to Alexey G. Sergeyev for his constant encouragement.

References

[1] D. Sternheimer, Deformation Quantization: Twenty Years After, arXiv: math/9809056;

[2] W. P. Schleich, *Quantum Optics in Phase Space* (Wiley, 2000);

[3] W. Zurek, Decoherence, einselection, and the quantum origins of the classical, *Rev. Mod. Phys.* **75**, 715 (2003), arXiv quant-ph/0105127.

[4] Y. Meyer, *Wavelets and Operators* (Cambridge Univ. Press, 1990);

[5] F. Auger e.a., *Time-Frequency Toolbox* (CNRS, 1996);

[6] D. Donoho, *WaveLab* (Stanford, 2000).

[7] A.N. Fedorova and M.G. Zeitlin, Quasiclassical Calculations for Wigner Functions via Multiresolution, Localized Coherent Structures and Patterns Formation in Collective Models of Beam Motion, in *Quantum Aspects of Beam Physics*, Ed. P. Chen (World Scientific, Singapore, 2002) pp. 527–538, 539–550; arXiv: physics/0101006; physics/0101007.

[8] A.N. Fedorova and M.G. Zeitlin, BBGKY Dynamics: from Localization to Pattern Formation, in *Progress in Nonequilibrium Green's Functions II*, Ed. M. Bonitz, (World Scientific, 2003) pp. 481–492; arXiv: physics/0212066.

[9] A.N. Fedorova and M.G. Zeitlin, Pattern Formation in Wigner-like Equations via Multiresolution, in *Quantum Aspects of Beam Physics*, Eds. Pisin Chen, K. Reil (World Scientific, 2004) pp. 22-35; Preprint SLAC-R-630; arXiv: quant-phys/0306197.

[10] A.N. Fedorova and M.G. Zeitlin, Localization and pattern formation in Wigner representation via multiresolution, *Nuclear Inst. and Methods in Physics Research, A*, **502A/2-3**, pp. 657 - 659, 2003; arXiv: quant-ph/0212166.

[11] A.N. Fedorova and M.G. Zeitlin, Fast Calculations in Nonlinear Collective Models of Beam/Plasma Physics, *Nuclear Inst. and Methods in Physics Research, A*, **502/2-3**, pp. 660 - 662, 2003; arXiv: physics/0212115.

[12] A.N. Fedorova and M.G. Zeitlin, Classical and quantum ensembles via multiresolution: I-BBGKY hierarchy; Classical and quantum ensembles via multiresolution. II. Wigner ensembles; *Nucl. Instr. Methods Physics Res.*, **534A** (2004)309-313; 314-318; arXiv: quant-ph/0406009; quant-ph/0406010.

[13] A.N. Fedorova and M.G. Zeitlin, Localization and Pattern Formation in Quantum Physics. I. Phenomena of Localization, in *The Nature of Light: What is a Photon? SPIE*, vol.**5866**, pp. 245-256, 2005; arXiv: quant-ph/0505114;

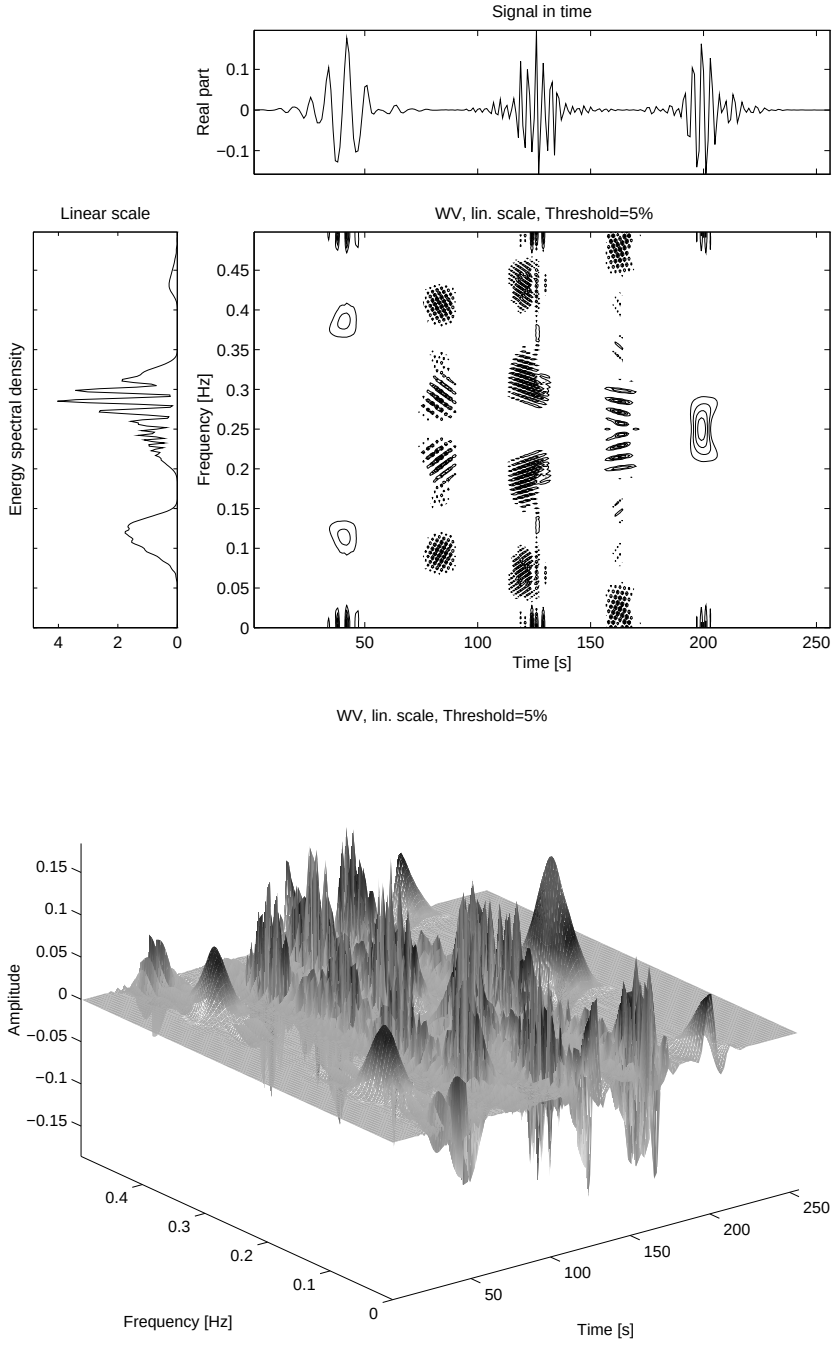


Figure 1: Wigner function modeling for three wavelet packets.

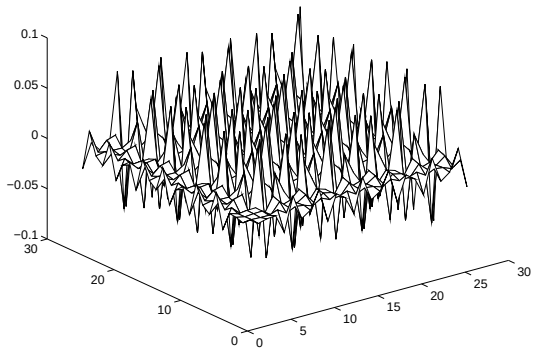


Figure 2: Level 4 MRA approximation for Wigner function.

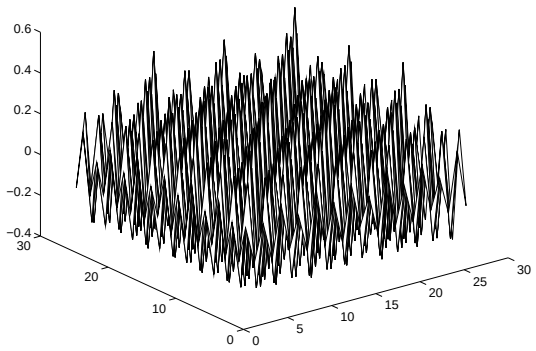


Figure 3: Level 6 MRA approximation for Wigner function.

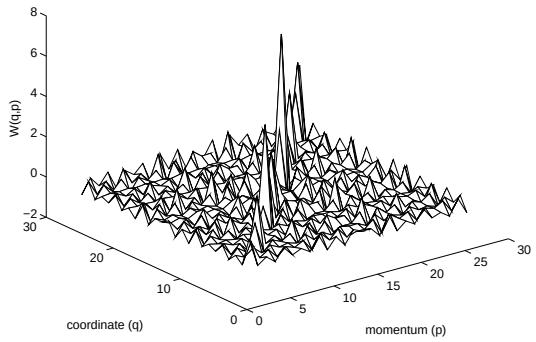


Figure 4: Localized pattern, (waveleton) Wigner function.

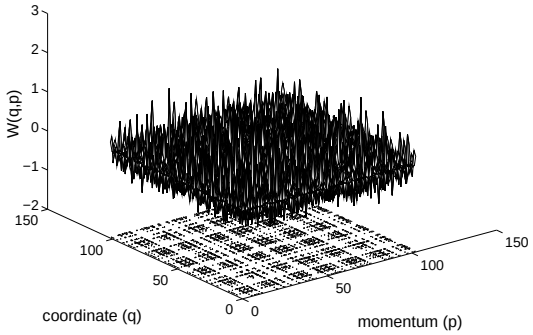


Figure 5: Entangled-like Wigner function.

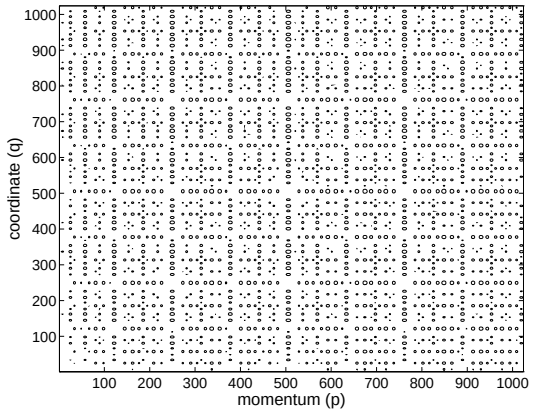


Figure 6: Interference picture on the level 4 approximation for Wigner function.

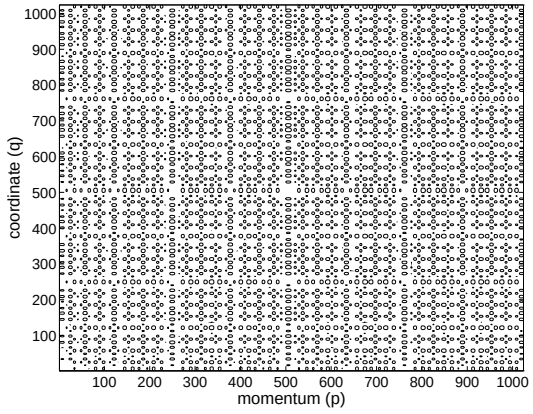


Figure 7: Interference picture on the level 6 approximation for Wigner function.

[14] A.N. Fedorova and M.G. Zeitlin, Localization and Pattern Formation in Quantum Physics. II. Waveletons in Quantum Ensembles, in *The Nature of Light: What is a Photon?SPIE*, vol. **5866**, pp. 257-268, 2005; arXiv: quant-ph/0505115.

[15] A.N. Fedorova and M.G. Zeitlin, Pattern Formation in Quantum Ensembles, *Intl. J. Mod. Physics* **B20**(2006)1570-1592; arXiv: 0711.0724.

[16] A.N. Fedorova and M.G. Zeitlin, Patterns in Wigner-Weyl approach, Fusion modeling in plasma physics: Vlasov-like systems, *Proceedings in Applied Mathematics and Mechanics (PAMM)*, Volume **6**, Issue 1, p. 625, p. 627, Wiley InterScience, 2006.

[17] A.N. Fedorova and M.G. Zeitlin, Localization and Fusion Modeling in Plasma Physics. Part I: Math Framework for Non-Equilibrium Hierarchies, pp.61-86, in *Current Trends in International Fusion Research*, Ed. E. Panarella, R. Raman, National Research Council (NRC) Research Press, Ottawa, Ontario, Canada, 2009; arXiv: physics/0603167.

[18] A.N. Fedorova and M.G. Zeitlin, Localization and Fusion Modeling in Plasma Physics. Part II: Vlasov-like Systems. Important Reductions, pp.87-100, in *Current Trends in International Fusion Research*, Ed. E. Panarella, R. Raman, National Research Council (NRC) Research Press, Ottawa, Ontario, Canada, 2009; arXiv: physics/0603169.

[19] A.N. Fedorova and M.G. Zeitlin, Fusion State in Plasma as a Waveleton (Localized (Meta)-Stable Pattern), p. 272, in *AIP Conference Proceedings*, Volume **1154**, Issue 1, *Current Trends in International Fusion Research*, Ed. E. Panarella, R. Raman, AIP, 2009.

[20] A.N. Fedorova and M.G. Zeitlin, Exact Multiscale Representations for (Non)-Equilibrium Dynamics of Plasma, p.291, in *AIP Conference Proceedings*, Volume **1154**, Issue 1, *Current Trends in International Fusion Research*, Ed. E. Panarella, R. Raman, AIP, 2009.

[21] A.N. Fedorova and M.G. Zeitlin, Fusion Modeling in Vlasov-Like Models, *J.Plasma Fusion Res. Series*, Vol. **8**, pp. 126-131, 2009.

Antonina N. Fedorova, Michael G. Zeitlin,
IPME RAS, St. Petersburg, V.O. Bolshoj pr., 61, 199178, Russia,
http://www.ipme.ru/zeitlin.html, http://mp.ipme.ru/zeitlin.html

Simulation of thermal interaction in a zone of extractive well in permafrost

Mikhail Yu. Filimonov Alexandr G. Kravets Natalia A. Vaganova
fmy@imm.uran.ru

Abstract

A new 3D mathematical model of thermal interaction in a zone of extractive well in permafrost is constructed. An algorithm of numerical solution of 3D Stephan's problem and numerical results of permafrost defrosting in a ground surface with and without of thermal insulation are presented. Using the elaborated program complex a number of computations of permafrost defrosting in a zone of influence of extractive well is carried out with taking into account of real soils characteristics. In contrast to another, not only different engineering construction of wells but also seasons, solar activity and temperature changing are included into this computations.

1 Introduction

Construction and operation of oil wells in areas of permafrost leads to a number of essential features. Permafrost holds 65 % of Russian land. These territories are extremely important for our economy because here it is extracted about 93 % of Russian natural gas and 75 % of oil, which estimations of cost provides 70 % of export of the country. Average thickness of permafrost in these zones varies within from 10 m up to 800 m. When planning of one, or several wells, it is necessary to consider distribution of heat from a well, leading to permafrost defrosting. For the given statement of the problem a new mathematical model of distribution of heat in well–permafrost system in which there are included not only geometrical and insulating characteristics of engineering constructions around of the well and various variants of isolation on the ground surface, but also seasonal changing of temperatures in view to solar radiation during the year. For this model numerical algorithm for computing of solution of the Stefan problem are realized on the base of ideas [1] in which smoothing factors in the equation of heat conductivity for temperature in the area closed to the phase transition.

2 Mathematical model of heat distribution in a well-permafrost system

Let $T = T(t, x, y, z)$ — distribution of temperature for the time moment t, (x, y, z) — a point of a considered domain. The considered domain is a three-dimensional parallelepiped from which a vertical cylindrical well is removed. Axes x and y are parallel to the ground surface, and an axis z is inside of the parallelepiped. The materials and soils inside of the parallelepiped may be different in dependence of engineering constructions around the well. Process of heat distribution taking into account phase transition is described by the following heat equation:

$$\rho\big(c_\nu(T) + k\delta(T - T^*)\big)\frac{\partial T}{\partial t} = \operatorname{div}(\lambda(T)\operatorname{grad} T), \tag{1}$$

where ρ is density $[kg/m^3]$, T^* is temperature of phase transition $[K]$,

$$c_\nu(T) = \begin{cases} c_1, & T < T^*, \\ c_2, & T > T^*, \end{cases} \text{ is specific heat [J/kg K]},$$

$\lambda(T) = \begin{cases} \lambda_1, & T < T^*, \\ \lambda_2, & T > T^*, \end{cases}$ is thermal conductivity coefficient [Wt/m K],

k is a heat of phase transition, δ is the Dirac delta function. Possibility of using this equation to describe the permafrost defrosting in a soil without the explicit separation of the phase boundary is given in [2].

Let in the initial time moment the temperature in the soil is

$$T(0, x, y, z) = T_0(x, y, z). \tag{2}$$

We assume that the coefficients in equation (1) may vary at different points in the computational domain (heterogeneity of soil by layers and possible thermal insulation of the well).

Boundary conditions. The basic heat flows are taken into the model are shown in Fig. 1.

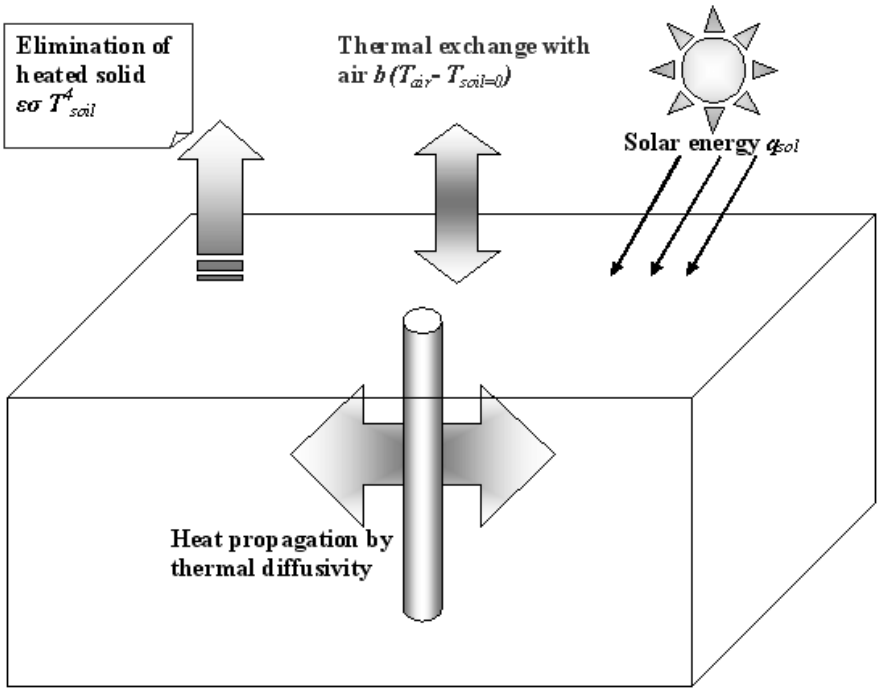


Figure 1: Model of heat distribution.

On the surface of the well the constant temperature (the temperature of wells or oil) is defined. On the bottom and lateral faces of the computational domain the conditions of the zero heat flow are given, moreover, the conditions of constant temperature may be given. The size of the computational domain is chosen such as the influence of lateral boundaries has no significant effect on the temperature distribution. At the top (daily) surface the condition of heat flow balance is given with taking into account the main climate factors: average air temperature and the power of solar radiation (as a rule "in summer"). Note that the solar radiation, as shown in [3], has significant influence on the temperature of the ground surface. The balance of thermal flows on the earth's surface rises the condition

$$q_1 + q_2 = q_3 + q_4,$$

where $q_1 = \alpha q$ is solar radiation, depending on the state of the atmosphere, angle of incidence of sunlight, i.e. latitude and time, α is fraction of energy spent on heating the soil.

q_2 denotes the heat exchange with air. If the temperature of the air is equal to T_{air}, and the temperature of the surface is equal to $T_{z=0}$, then $q_2 = b(T_{air} - T_{z=0})$, where b is a coefficient of heat transfer, depending on the nature and type of the surface.

q_3 denotes an emission of "black body". Then $q_3 = \varepsilon\sigma T^4_{z=0}$, where σ is Stefan–Boltzmann constant, ε is a coefficient related with properities of the ground.

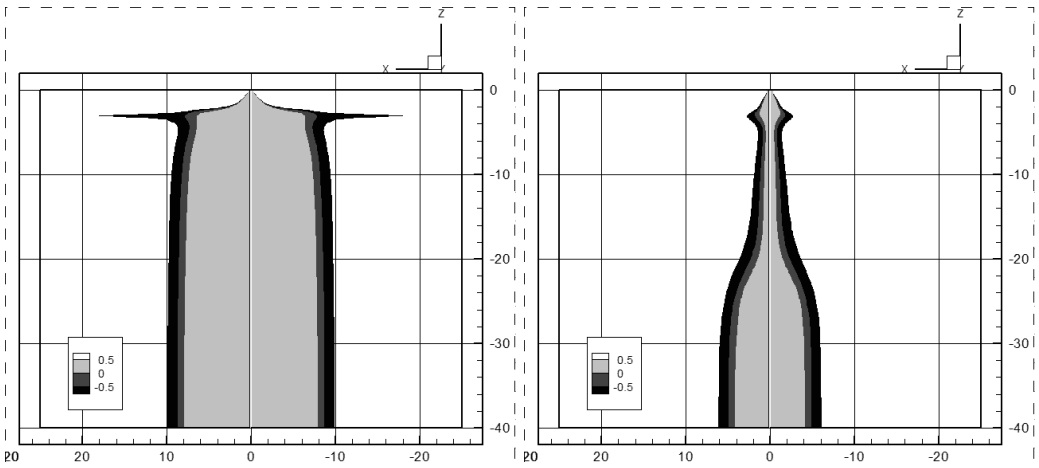
q_4 denotes a heat transfer caused by the internal heat flow, which is equal to $q_4 = \lambda\dfrac{\partial T}{\partial z}$, where λ is the thermal conductivity of soil, forming the upper surface.

Thus, on the surface $z = 0$ is given the following condition:

$$\alpha q + b(T_{air} - T_{z=0}) = \varepsilon\sigma T^4 + \lambda\frac{\partial T}{\partial z}. \tag{3}$$

Thus, the simulation of heat transfer in three-dimensional domain with the phase transition is reduced to solving the initial-boundary value problem (1)–(3). In contrast to the known results on the calculations of permafrost defrosting, in this mathematical model includes not only geometric and thermal insulation characteristics of engineering structures around the well but also various options for thermal insulating the outer surface of the well.

3 Numerical results



(a) (b)

Figure 2: Temperature (°C) arount the wells.

To compute heat distribution by equations (1)–(3) in a three-dimensional domain a finite-difference method with splitting by spatial variables is used. Computations are carried out on orthogonal grid, uniform or adapted by layers and to the well. The basic heat equation is approximated by an economical implicit finite-difference pattern in each of spatial dimensions. System of linear difference equations has a three-diagonal form and may be solved by a sweep method.

In numerical experiments we used the following area.

	X	**Y**	**Z**
Size of area, m	50	50	40
Number of points	101	101	101
Spatial steps	variable	variable	variable
Radius of the well, m	0.084		

For thermal insulation of the well the following materials are used:

Parameter	**Units**	**Value**
Cement 1		
Density	kg/m^3	2500
Heat conductivity	Wt/(m K)	1.69
Specific heat	J/(kg K)	$0.84 * 10^3$
Cement 2		
density	kg/m^3	960
Heat conductivity	Wt/(m K)	0.21
Specific heat	J/(kg K)	$0.84 * 10^3$
Penoplex		
Density	kg/m^3	80
Heat conductivity	Wt/(m K)	0.031
Specific heat	J/(kg K)	$1.53 * 10^3$

For thermal insulation of the ground surface the following materials are used:

Parameter	**Units**	**Value**
Concrete (slab thickness of 0.3 m)		
Density	kg/m^3	2500
Heat conductivity	Wt/(m K)	1.69
Specific heat	J/(kg K)	$0.84 * 10^3$
sand (layer thickness 1.7 m)		
Density	kg/m^3	1600
Heat conductivity	Wt/(m K)	0.47
Specific heat	J/(kg K)	$0.84 * 10^3$

In the numerical calculations it was assumed that the initial temperature of the soil has a temperature of $-3°C$ and the soil has the following parameters:

soil (top layer to 10 m.)			
Humidity 20 %		frozen	melted
Heat conductivity	Wt/m K	2.4	2.2
Volumetric heat	$J/(m^3K)$	$2.2 * 10^6$	$2.7 * 10^6$
Volumetric heat of phase transition	J/m^3	$10.0 * 10^7$	
soil (bottom layer after 10 m)			
Humidity 20 %		frozen	melted
Heat conductivity	Wt/m K	2.5	2.3
Volumetric heat	$J/(m^3K)$	$2.25 * 10^6$	$2.6 * 10^6$
Volumetric heat of phase transition	J/m^3	$10.4 * 10^7$	

Figure 2 shows the temperature distribution in the plane (z, x) from two different constructions of wells for 10 years after the start of their operation. The left well is assumed to be without of thermal insulation (Figure 2a), the right well is used with thermal insulation (Figure 2b). The temperature of oil in the wells is $40°C$. The simulation results indicate that the insulation of wells significantly slows the permafrost defrosting.

Thus, the developed program complex allows to carry out a series of computational experiments which allow to make the long-term forecasts of permafrost defrosting in the presence of thermal insulated heat source (well and engineering constructions) taking into account the annual cycle of thawing/freezing upper layers of soil under the influence of seasonal changes in air temperature and intensity of sunlight. The results of numerical simulation allow experts to examine and make recommendations for thermal insulation and placement of wells on working platform.

Acknowledgements

This work is partially supported by Russian Foundation for Basic Research – URAL 10–08–96014, by the Program of the Presidium of the Russian Academy of Sciences and the Program of Integrative

Projects between Ural Branch, Siberian Branch, and Far Eastern Branch of Russian Academy of Sciences.

References

[1] A. A. Samarsky, B .D. Moiseenko. ZhVMiMF, **5**, 5 1965.

[2] A. A. Samarsky, P .N. Vabishchevich. Computational Heat Transfer. M.: Editorial URSS, 2003.

[3] E. I. Kiryakov, V. V. Sipikin. Vestnik TGASU, **4**, 2007.

Mikhail Yu. Filimonov
Institute of Mathematics and Mechanics UrB RAS, S. Kovalevskaya str. 16, Ekaterinburg, 620990, Russia

The influence of external strains and material parameters on the kinetics of stationary moving interfaces

Alexander B. Freidin Daria O. Kucheyeva
alexander.freidin@gmail.com, dasha-kucheyeva@yandex.ru

Abstract

We study plane stationary moving interfaces in elastic isotropic solids. We construct modified phase transition zones (PTZ) formed by all strains which can exist on the interfaces moving with a given interface velocity. We focus on the PTZ boundaries. Every point of the PTZ boundary corresponds to some interface spreading with a given velocity, and the orientation of the interface depends on the relationship between eigenstrains. We give examples of the PTZ boundaries construction for various interface velocities and various material parameters. This in turn allows us to study how material parameters and external strain affect the interface velocity and orientation.

1 Conditions on a quasistatic moving interface

Two-phase configuration of an elastic solid with a quasistatic moving interface have to satisfy the following conditions:

$$\mathbf{x} \notin \Gamma \quad : \qquad \nabla \cdot \boldsymbol{\sigma} = 0, \quad \theta = \text{const}, \tag{1}$$

$$\mathbf{x} \in \Gamma \quad : \qquad [\mathbf{u}] = 0, \quad [\boldsymbol{\sigma}] \cdot \mathbf{n} = 0, \tag{2}$$

$$D = -\int_\Gamma ([f] - \langle \boldsymbol{\sigma} \rangle : [\boldsymbol{\varepsilon}]) v_n^\Gamma d\Gamma \geq 0, \quad \langle \boldsymbol{\sigma} \rangle = \frac{1}{2}(\boldsymbol{\sigma}_+ + \boldsymbol{\sigma}_-) \tag{3}$$

where $\mathbf{x}$ is a radius-vector of a material point, Γ denotes interfaces, $\mathbf{u}$ is the displacement, $\boldsymbol{\varepsilon}$ and $\boldsymbol{\sigma}$ are the strain and stress tensors, θ is the temperature, $f = f(\boldsymbol{\varepsilon}, \theta)$ is the Helmholtz free energy density, the brackets $[\cdot] = (\cdot)_+ - (\cdot)_-$ denote the jump across Γ, super- or subscripts "$-$" and "$+$" identify the values being taken for a material in the "$-$" and "$+$" phase states, respectively, $\mathbf{n}$ is the unit normal to the interface Γ directed from " $+$" to "$-$", $v_n^\Gamma = \mathbf{v}^\Gamma \cdot \mathbf{n}$ is a normal component of the interface velocity $\mathbf{v}^\Gamma$. Body forces, thermoelastic effects and surface energy are not taken into account.

The conditions (2) are common contact conditions and can be satisfied at any contact surface in a body, as it is in composite materials. The additional thermodynamic condition (3) is related to an additional degree of freedom caused by an unknown phase boundary and follows from the dissipative inequality [15] written for the quasistatic moving interface. Note that due to the displacement and traction continuity at the interface $\langle \boldsymbol{\sigma} \rangle : [\boldsymbol{\varepsilon}] = \boldsymbol{\sigma}_+ : [\boldsymbol{\varepsilon}] = \boldsymbol{\sigma}_- : [\boldsymbol{\varepsilon}]$.

Now it is well known that in a case of the thermodynamically equilibrium interface

$$[f] - \langle \boldsymbol{\sigma} \rangle : [\boldsymbol{\varepsilon}] = 0 \tag{4}$$

In a case of moving interface

$$\chi = [f] - \langle \boldsymbol{\sigma} \rangle : [\boldsymbol{\varepsilon}] \tag{5}$$

acts as the thermodynamical force (Eshelby's driving force [3, 4, 15, 1], configuration or material force [18, 12, 14]). Then one can add to the conditions (1), (2) a kinetic equation in a form

$$v_n^\Gamma = \Phi(\chi) \quad \text{or} \quad \chi = \Phi(v_n^\Gamma) \tag{6}$$

In a linear thermodynamic approach one can accept the simplest linear kinetic relation

$$v_n^\Gamma = -L^{-1}\,\chi, \quad L = const > 0 \tag{7}$$

For the phase transformation to be possible the free energy density f is to be modelled by a number of quadratic functions of $\boldsymbol{\varepsilon}$. The number of functions depends on the symmetry groups of the phases. Further we consider a two-well strain-energy function:

$$f(\boldsymbol{\varepsilon},\theta) = \min_{-,+}\left\{f^-(\boldsymbol{\varepsilon},\theta), f^+(\boldsymbol{\varepsilon},\theta)\right\}, \tag{8}$$

$$f^\pm(\boldsymbol{\varepsilon},\theta) = f_0^\pm(\theta) + \frac{1}{2}(\boldsymbol{\varepsilon}-\boldsymbol{\varepsilon}_\pm^p) : \mathbf{C}_\pm : (\boldsymbol{\varepsilon}-\boldsymbol{\varepsilon}_\pm^p).$$

Here and further upper and lower scripts "+" and "−" in relationships correspond to each other.

The constitutive relations take the form:

$$\boldsymbol{\sigma}_\pm(\boldsymbol{\varepsilon}) = \mathbf{C}_\pm : (\boldsymbol{\varepsilon}-\boldsymbol{\varepsilon}_\pm^p), \quad \boldsymbol{\varepsilon} \in \mathcal{E}_\pm \tag{9}$$

where $\mathcal{E}_\mp$

$$\mathcal{E}_- = \{\boldsymbol{\varepsilon} :\ \varphi(\boldsymbol{\varepsilon}) > 0\}, \quad \mathcal{E}_+ = \{\boldsymbol{\varepsilon} :\ \varphi(\boldsymbol{\varepsilon}) < 0\}, \quad \varphi(\boldsymbol{\varepsilon}) = f^+(\boldsymbol{\varepsilon}) - f^-(\boldsymbol{\varepsilon})$$

are the domains of definition of the phases "−" and "+" in strain space.

The parameters $\mathbf{C}_\pm$, $f_0^\pm$ and $\boldsymbol{\varepsilon}_\pm^p$ are the elasticity tensors, free energy densities and strain tensors in unstressed phases "±", respectively. If $\boldsymbol{\varepsilon}_+^p = 0$ or $\boldsymbol{\varepsilon}_-^p = 0$, then $[\boldsymbol{\varepsilon}^p] \equiv \boldsymbol{\varepsilon}^p$ is the transformation eigenstrain. If $\mathbf{C}_\pm$ and $\boldsymbol{\varepsilon}_\pm^p$ do not depend on the temperature, then the energy parameter $\gamma(\theta) = [f_0]$ acts as the temperature.

From (2) it follows that the traction continuity condition $(2)_2$ can be rewritten as a relationship which expresses the jumps in strain or in stress across the interface through the strain (or stress) on one side of the interface ("+" or "−") [17, 16, 7]:

$$[\boldsymbol{\varepsilon}] = \mathbf{K}_\mp(\mathbf{n}) : \mathbf{q}_\pm, \quad \mathbf{K}_\mp(\mathbf{n}) = \{\mathbf{n}\otimes\mathbf{G}_\mp(\mathbf{n})\otimes\mathbf{n}\}^s, \quad \mathbf{G}_\mp(\mathbf{n}) = (\mathbf{n}\cdot\mathbf{C}_\mp\cdot\mathbf{n})^{-1}, \tag{10}$$

where $\mathbf{q}_\pm = -\mathbf{C}_1 : \boldsymbol{\varepsilon}_\pm + [\mathbf{C} : \boldsymbol{\varepsilon}^p]$, $\mathbf{C}_1 = \mathbf{C}_+ - \mathbf{C}_-$.

Making use of (8)-$(10)_1$ results in representation of the thermodynamic force in a reduced forms that contains only the strain (or stress) on one side of the interface and the normal to the interface (see [16, 5] or rather recent paper [11] and reference therein):

$$\chi = \gamma + \frac{1}{2}\,[\boldsymbol{\varepsilon}^p : \mathbf{C} : \boldsymbol{\varepsilon}^p] + \frac{1}{2}\,\boldsymbol{\varepsilon}_\pm : \mathbf{C}_1 : \boldsymbol{\varepsilon}_\pm - \boldsymbol{\varepsilon}_\pm : [\mathbf{C} : \boldsymbol{\varepsilon}^p] \pm \frac{1}{2}\,\mathbf{q}_\pm : \mathbf{K}_\mp(\mathbf{n}) : \mathbf{q}_\pm \tag{11}$$

If $\mathbf{C}_1^{-1}$ is nonsingular then (11) can be rewritten in terms of $\mathbf{q}$ taken on one side of the interface [19]:

$$\chi = \gamma_* + \frac{1}{2}\,\mathbf{q}_\pm : \left(\mathbf{C}_1^{-1} \pm \mathbf{K}_\mp(\mathbf{n})\right) : \mathbf{q}_\pm, \tag{12}$$

$$\gamma_* = \gamma + \frac{1}{2}\,[\boldsymbol{\varepsilon}^p] : \mathbf{B}_1^{-1} : [\boldsymbol{\varepsilon}^p], \quad \mathbf{B}_1 = \mathbf{B}_+ - \mathbf{B}_-, \quad \mathbf{B}_\pm = \mathbf{C}_\pm^{-1}$$

From (7), (11) and (12) it follows that kinetic relation can be written in forms

$$\widehat{\gamma} + \frac{1}{2}\,[\boldsymbol{\varepsilon}^p : \mathbf{C} : \boldsymbol{\varepsilon}^p] + \frac{1}{2}\,\boldsymbol{\varepsilon}_\pm : \mathbf{C}_1 : \boldsymbol{\varepsilon}_\pm - \boldsymbol{\varepsilon}_\pm : [\mathbf{C} : \boldsymbol{\varepsilon}^p] \pm \frac{1}{2}\,\mathbf{q}_\pm : \mathbf{K}_\mp(\mathbf{n}) : \mathbf{q}_\pm = 0 \tag{13}$$

$$\widehat{\gamma}_* + \frac{1}{2}\,\mathbf{q}_\pm : \left(\mathbf{C}_1^{-1} \pm \mathbf{K}_\mp(\mathbf{n})\right) : \mathbf{q}_\pm = 0 \tag{14}$$

where

$$\widehat{\gamma} = \gamma + Lv_n^\Gamma, \quad \widehat{\gamma}_* = \gamma_* + Lv_n^\Gamma \tag{15}$$

Recall that γ and $\gamma_\star$ are material parameter if the temperature is given. Then, given γ, the relationships (13), (14) can be considered as the equations relating the strains on one side of the interface, the direction of the normal and the normal component of the interface velocity. We emphasize that the interface velocity enters the equation only through the parameter $\widehat{\gamma}$. That is why the further analysis can be reduced to the considerations of equilibrium interfaces made earlier (see, e.g., [7, 8, 9]) if we simply replace γ by $\widehat{\gamma}$.

2 Phase transition zones for moving plane interfaces

Further we focus on a new phase plane layer thickening or thinning under the action of uniform external strain $\boldsymbol{\varepsilon}_0$. In this case $\boldsymbol{\varepsilon}_- = \boldsymbol{\varepsilon}_0$ [5, 13].

Given $\widehat{\gamma}$ and $\boldsymbol{\varepsilon}_-$ the equation (13) may be satisfied by a proper choice of a unit normal $\mathbf{n}$ or may not be satisfied whatever the normal is. Those $\boldsymbol{\varepsilon}_-$ at which the the condition can be satisfied form the phase transition subzone "$-$". In other words, given $\widehat{\gamma}$, the subzone "$-$" consists of all strains which can exist at the "$-$" – side of interfaces satisfying the condition (13). The subzone "$+$" is determined analogously and together with the subzone "$-$" forms the phase transition zone (PTZ).

The PTZ construction for the equilibrium interfaces has been considered for finite strains and small strains (see, e.g., [6, 7, 8, 10, 9]) and reference therein). In the present paper we show how the PTZ concept works in the case of moving interface.

For brevity sake consider only the case of nonsingular $\mathbf{C}_1$. The equation (14) takes the form of two equations which are equivalent if (10) is taken into account:

$$\varphi(\widehat{\gamma}_*, \mathbf{q}_-) = K_+(\mathbf{q}_-, \mathbf{n}), \quad \varphi(\widehat{\gamma}_*, \mathbf{q}_+) = -K_-(\mathbf{q}_+, \mathbf{n}) \tag{16}$$

where

$$\varphi(\widehat{\gamma}_*, \mathbf{q}) = 2\widehat{\gamma}_* + \mathbf{q} : \mathbf{C}_1^{-1} : \mathbf{q}, \quad K_\pm(\mathbf{q}_\mp, \mathbf{n}) = \mathbf{q}_\mp : \mathbf{K}_\pm(\mathbf{n}) : \mathbf{q}_\mp \tag{17}$$

The PTZ subzones "$-$" and "$+$" in $q-$space are formed by all tensors $\mathbf{q}$ which satisfy the inequalities

$$\mathrm{PTZ}^-: \ K^+_{\min}(\mathbf{q}) \le \varphi(\mathbf{q}) \le K^+_{\max}(\mathbf{q}), \quad \mathrm{PTZ}^+: \ K^+_{\min}(\mathbf{q}) \le -\varphi(\mathbf{q}) \le K^+_{\max}(\mathbf{q}), \tag{18}$$

where

$$K^+_{\max}(\mathbf{q}) = \max_n K_+(\mathbf{q}, \mathbf{n}), \quad K^+_{\min}(\mathbf{q}) = \min_n K_+(\mathbf{q}, \mathbf{n}).$$

It can be shown that the PTZ-boundaries are given by the equations

$$\mathrm{PTZ}^-: \quad \varphi(\mathbf{q}) = K^+_{\max}(\mathbf{q}) \text{ (external bound)} \quad \varphi(\mathbf{q}) = K^+_{\min}(\mathbf{q}) \text{ (internal bound)} \tag{19}$$

$$\mathrm{PTZ}^+: \ -\varphi(\mathbf{q}) = K^-_{\max}(\mathbf{q}) \text{ (external bound)} \ -\varphi(\mathbf{q}) = K^-_{\min}(\mathbf{q}) \text{ (internal bound)} \tag{20}$$

If the phases "$\mp$" are isotropic then

$$\mathbf{C}_\mp = \lambda_\mp \mathbf{E} \otimes \mathbf{E} + 2\mu_\mp \mathbf{I}, \quad \boldsymbol{\varepsilon}^p = \frac{\vartheta^p}{3}\mathbf{E} \quad (\boldsymbol{\varepsilon}^p_- = 0) \tag{21}$$

$$\mathbf{K}_\pm(\mathbf{n}) = \frac{1}{\mu_\pm}(\mathbf{n} \otimes \mathbf{E} \otimes \mathbf{n})^s - \frac{1}{2\mu_\pm(1-\nu_\pm)}\mathbf{n} \otimes \mathbf{n} \otimes \mathbf{n} \otimes \mathbf{n} \tag{22}$$

where $\mathbf{E}$ is the second rank unit tensor, $(\mathbf{E} \otimes \mathbf{E})_{ijkl} = \delta_{ij}\delta_{kl}$, $\mathbf{I}$ is the symmetric fourth rank unit (isotropic) tensor, $I_{ijkl} = 1/2(\delta_{ik}\delta_{jl} + \delta_{jk}\delta_{il})$, δ_{ik} is Kronecker's delta, λ and μ are Lame constants, ν is Poisson's ratio.

All terms in the inequalities (18) have been derived for the isotropic phases earlier (see, e.g., [5, 7, 8]). Let $q_{\min}$, $q_{\max}$ and $|q|_{\min}$, $|q|_{\max}$ are maximal and minimal eigenvalues of the tensor $\mathbf{q}$, and maximal and minimal absolute values of the eigenvalues. Let $n_{\max}$ and n_{mid} are the projections of the normal onto the eigenaxes of $\mathbf{q}$ which correspond to the maximal and intermediate eigenvalues $q_{\max}$ and q_{mid}. The normals $\mathbf{n}_{ex}$ and $\mathbf{n}_{in}$ to the interfaces which correspond to the external and internal PTZ boundaries and corresponding values of $K^-_{\max}$ $K^-_{\min}$ are given by the following relationships.

If

$$q_{\min}q_{\max} < 0 \text{ or } \begin{cases} q_{\min}q_{\max} > 0 \\ (1-\nu_-)|q|_{\min} < \nu_-|q|_{\max} \end{cases}, \tag{23}$$

then

$$n^2_{\max} = \frac{(1-\nu_-)q_{max} - \nu_- q_{min}}{q_{max} - q_{min}}, \ n_{\mathrm{mid}} = 0, \tag{24}$$

$$K^-_{\max}(\mathbf{q}_+) = \frac{1-\nu_-}{2\mu_-}(q^2_{\max} - q^2_{\min}) - \frac{\nu_-}{\mu_-}q_{\max}q_{\min}. \tag{25}$$

The normal lies in the eigen plane or the tensor $\mathbf{q}$ corresponding to the maximal and minimal eigenvalues.

If (23) are not satisfied then

$$\mathbf{n}_{ex} = \mathbf{e}_{|q|_{max}}, \tag{26}$$

$$K^{-}_{\max}(\mathbf{q}) = \frac{1-2\nu_-}{2\mu_-(1-\nu_-)}|q|^2_{\max} \tag{27}$$

The minimal value of K is reached at the normal

$$\mathbf{n}_{in} = \mathbf{e}_{|q|_{\min}} \tag{28}$$

and

$$K^{-}_{\min}(\mathbf{q}) = \frac{1-2\nu_-}{2\mu_-(1-\nu_-)}|q|^2_{\min} \tag{29}$$

Note that only an eigenvalue corresponding to $\mathbf{e}_{|q|_{max}}$ suffers a jump across the interface corresponding to the PTZ boundary with $K^{-}_{\max}$ given by (27). Jumps in the eigen plane with a shear mode take place across the interfaces corresponding to the PTZ boundary with $K^{-}_{\max}$ given by (25).

The PTZ boundaries are formed by the second-order surfaces. Examples of the PTZ cross-sections by the plane $\varepsilon_2 = \varepsilon_3 = \varepsilon$ are shown in Fig 1,2 for various sets of parameters where $k_\pm$ are the bulk moduli. We recall that the interface velocity is hidden in the parameter $\widehat{\gamma}$. We emphasize that the zones are closed if the tensor $\mathbf{C}_1$ is sign-definite and the zones are unclosed if $\mathbf{C}_1$ is not sign-definite.

The lines 1 represent the external PTZ boundaries, ant the orientations of the corresponding interfaces are also shown. The lines 3 are the internal PTZ boundaries. The line 2 corresponds to the equation $\varphi(\widehat{\gamma}_*, \mathbf{q}) = 0$. We emphasize that, given $\widehat{\gamma}$, the direction of the normal corresponding to the PTZ external boundaries depends on the strain state.

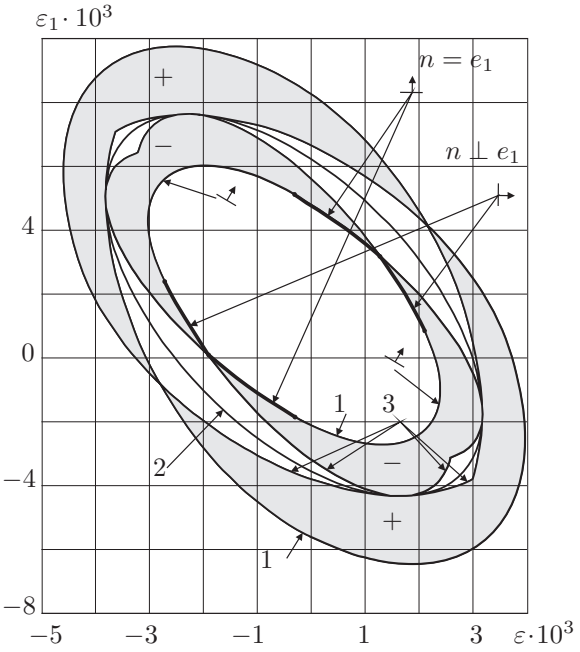


Figure 1: PTZ cross-section for $\vartheta^p = 0.001$, $k_- = 78$, $\mu_- = 30$, $k_+ = 39$, $\mu_+ = 15$, $\widehat{\gamma} = 0.0006755$

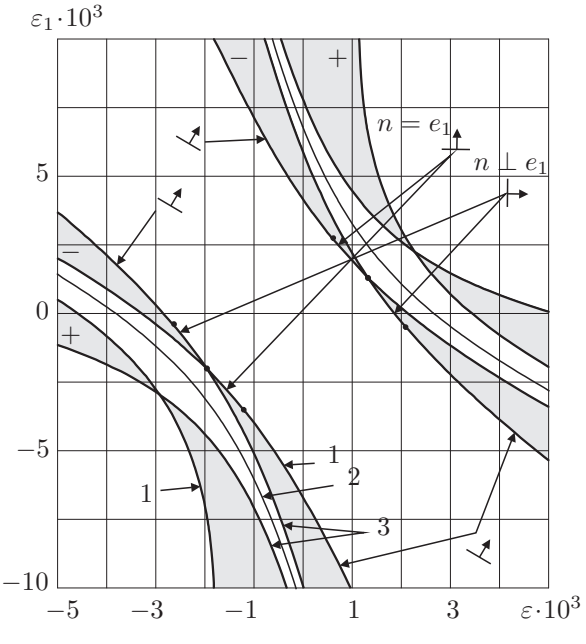


Figure 2: PTZ cross-section for $\vartheta^p = 0.001$, $k_- = 78$, $\mu_- = 15$, $k_+ = 39$, $\mu_+ = 30$, $\widehat{\gamma} = 0.0006755$

Fig. 3 and 4 show how transformation strain ϑ^p and the interface velocity affect the external "−" PTZ boundary for the case $k_1 = k_+ - k_- < 0$, $\mu_1 = \mu_+ - \mu_- < 0$. We are interested namely

in this PTZ boundary at such sings of k_1, μ_1 because of stability reasons. In a case of a new phase layer these figures show how external strains affect the interface orientation and velocity and how this dependence is related with the transformation strain. The dots denote the points of the interface orientation changing. The thin lines correspond to the shear interface orientation.

These figures can be reconstruct as a dependencies of the interface velocity on external strains on different loading paths. In the context of biomechanical applications to the biological growth plate in long bones announced in [20, 2] the results presented mean that the growth plate orientation may strictly depend on the strain state, and the role of the volume growth parameter ϑ^p may be significant.

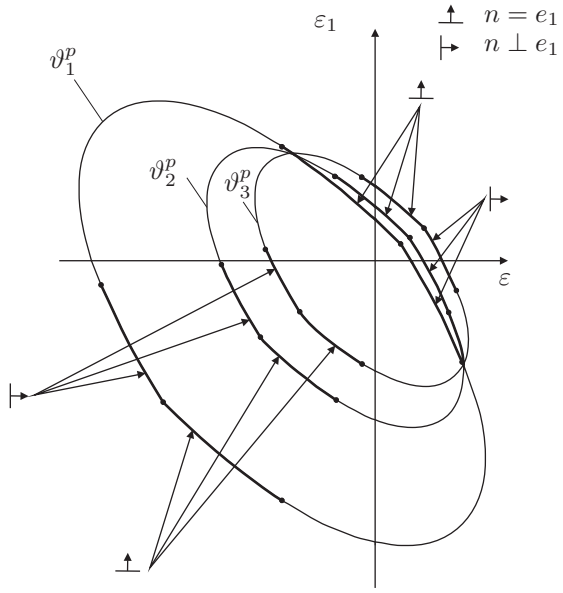


Figure 3: External PTZ boundaries for the subzone "−" and the interface orientation at various transformation strains ϑ^p: $0 < \vartheta_3^p < \vartheta_2^p < \vartheta_1^p$, $\mu_1 < 0, k_1 < 0, \widehat{\gamma} > 0$.

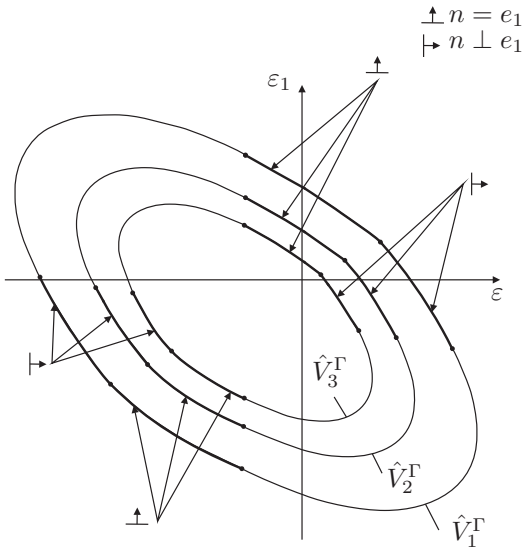


Figure 4: External "−"PTZ boundaries and the interface orientation at various interface velocities $\hat{V}^\Gamma = v_n^\Gamma / L$: $0 = \hat{V}_3^\Gamma < \hat{V}_2^\Gamma < \hat{V}_1^\Gamma$, $\vartheta^p > 0, \mu_1 < 0, k_1 < 0, \gamma > 0$.

Acknowledgements

This work was supported by RFBR (Grants 09-01-00849, 10-01-00670) and Scientific Programs of RAS. ABF also gratefully acknowledge the support of DFG (Grant AL 341/35-1)

References

[1] Abeyaratne R., Knowles J.K. Elovution of phase transformation. A continuum theory. Cambridge University Press, 2006. 241 p.

[2] Modeling the mechanical loading influence on the kinetics of the growth plate. In: Mathematical modeling and biomechanics in the modern universitet. Proc. of V Russian School-Seminar. Rostov-on-Don. 1-5 June 2009. P.38-39.

[3] J.D. Eshelby, The force on an elastic singularity. Phil. Trans. Roy. Soc. Lond. A **244**, 87-112 (1951).

[4] J.D. Eshelby, in: Inelastic Behavior of Solids, edited by M. Kanninen, W. Adler, A. Rosenfield, and R. Jaffee (McGraw-Hill, New York, 1970), 77-115.

[5] A.B. Freidin. Crazes and shear bands in glassy polymer as layers of a new phase, Mechanics of Composite Materials (1989) (1) 1-7.

[6] A.B. Freidin and A.M. Chiskis, Phase transition zones in nonlinear elastic isotropic materials. Part 1: Basic relations. Izv. RAN, Mekhanika Tverdogo Tela (Mechanics of Solids) **29** (1994) Part 1: Basic relations. No.4, 91-109. Part 2: Incompressible materials with a potential depending on one of deformation invariants. No.5, 46-58.

[7] A.B. Freidin, Small strains approach to the theory on solid-solid phase transformations under the process of deformation, Studies on Elasticity and Plasticity, St. Petersburg State University, 18 (1999) 266-290 (in Russian).

[8] A.B. Freidin, E.N Vilchevskaya and L.L. Sharipova, Two-phase deformations within the framework of phase transition zones, Theoretical and Apllied Mechanics, **28-29**, 149-172 (2002).

[9] A.B. Freidin, L.L. Sharipova. On a model of heterogenous deformation of elastic bodies by the mechanism of multiple appearance of new phase layers. Meccanica (2006) 41: 321–339.

[10] Freidin A.B., Fu Y.B., Sharipova L.L., Vilchevskaya E.N. Spherically symmetric two-phase deformations ans phase transition zones, Int. J. Solids and Struct. 2006. Vol. 43. P. 4484-4508.

[11] A. B. Freidin. On new phase inclusions in elastic solids, Z. Angew. Math. Mech. (ZAMM) 87(2) (2007) 102-116.

[12] M.E. Gurtin, Configurational Forces as Basic Concepts of Continuum Phisics (Springer, Berlin, 2000).

[13] Kanaun S.K., Levin V.M. Self-consistent methods for composites. Vol. 1: Static Problems, Springer, 2007.

[14] R. Kienzler and G. Herrmann, Mechanics in Material Space with Application to Defect and Fracture Mechanics (Springer, Berlin, 2000).

[15] J.K. Knowles, On the dissipation associated with equilibrium shocks in finite elasticity, J. Elasticity, **9**, 131-158 (1979).

[16] L. B. Kublanov, A. B. Freidin. J. Appl. Math. Mech. (PMM USSR) 52, 382-389 (1988).

[17] I.A. Kunin, Elastic Media with Microstructure II (Springer-Verlag, Berlin, New York, etc., 1983).

[18] G. Maugin, Material Inhomogeneities in Elasticity (Chapman & Hall, London, 1993).

[19] N.F. Morozov, I.R. Nazyrov and A.B. Freidin, One-dimensional problem of phase transformation of an elastic ball', Dokl. Akad. Nauk (Proc. Russian Academy of Sciences), **346** (2), 188-191 (1996).

[20] L.L. Sharipova, G.A. Maugin, A.B. Freidin. Modelling the influence of mechanical factors on the growth plate. 2nd International Conference on Recent Advances in Nonlinear Mechanics, RANM2009, 24-27 August 2009, Kuala-Lumpur, Malaysia. Book of abstracts. Eds. Jee-Hou Ho, M.Wiercigroch, Ko-Choong Woo.P.102-103.

Alexander B. Freidin, Daria O. Kucheyeva, Institute of Problems in Mechanical Engineering, Russian Academy of Science, Bolshoy pr., 61, V. O., St. Petersburg, 199178, Russia

Polymer/silicate nanocomposites. Nonlinear elastoplastic model with damage accumulation under deformation

Oleg K. Garishin
gar@icmm.ru

Abstract

Computer simulation of process of a nonlinear elastic-plastic straining polymer/silicate nanocomposite with allowance for its volume modification caused by internal damage accumulation is accomplished. The main subject of research is nano-composites on a basis of polyolefin binder and lamellar silicate minerals as filler.

It is experimentally established that these nanocomposite systems can change essentially their volume under deformation due to accumulation of internal defects (pores, cracks, interphase debondings). This phenomenon has been described by means of a structurally-phenomenological model of the heterogeneous solid continuum, capable to carry significant nonlinear elastic and plastic deformations accompanied with appreciable volume change. To obtain the constitutive equations, the differential approach based on interpretation of the mechanical behavior of material with the help of symbolical circuits and the additive decomposition of the rate of deformation tensor in elastic and plastic parts is used.

Numerical dependences between stresses, relative volume change and deformation of pure polyethylene and polyethylene/clay nanocomposite material were constructed with the help of this approach. The assaying of the gained outcomes testifies to availability, at least, two structural factors generating mechanical properties formation: 1) On the one hand filler promotes interior structural damage accumulation, i.e. the material in the course of a straining becomes softer and is easier gives in to plastic flow. 2) On the other hand the same corpuscles hinder reorientation of polymeric molecules and permolecular structural objects (like spherulites and so on) in a polyethylene matrix, which, on the contrary, should hinder development of plastic flowages.

Outcomes of complex experimental and theoretical studies of elastoplastic properties of polyolefin polymers and composites on its basis filled by laminose clayey mineral nanoparticles are presented. Now they start all to be applied more widely in the most various fields of the industry, successfully competing with traditional materials [1, 2].

These systems consist of mixture of a polymeric matrix (continuous phase) and the filler in the form of assemblage of ultrathin silicate plates width in some nanometers and the transversal size from 30 nm to several micrometers (dispersed phase). Particles can form separate packs from several parallel located lamellae with several molecules of matrix polymer in the gaps or to be distributed on material volume chaotically (exfoliated filler).

It is experimentally established that these nanocomposite systems can change essentially their volume under deformation due to accumulation of internal defects (pores, cracks, interphase debondings). A relative volume change in such systems can reach 20–25%, and ultimate deformations — 700-800%. This phenomenon has been described by means of a structural-phenomenological model of the heterogeneous solid continuum, capable to carry significant nonlinear elastic and plastic deformations accompanied with appreciable volume change [3]. The choice of an elastoplastic statement of problem was justified by that experiences were made at very small strain rates (a share of inverse minutes), i.e. there was an equilibrium loading of a material (so slow, that it is possible to neglect relaxation processes linked to a viscous flow).

To obtain the constitutive equations, the differential approach based on interpretation of the mechanical behavior of material with the help of symbolical circuits and the additive decomposition of the rate of deformation tensor of continuum $\mathbf{D}$ in elastic ($\mathbf{D}_1$) and plastic ($\mathbf{D}_2$) parts is used [4].

The computational scheme of the model consists of two elements connected in tandem: elastic (1) and plastic (2). In this case stress tensors in elements should be identical and equal to total medium stress tensor T. Rate of deformation tensor of the whole system $\mathbf{D} = \mathbf{D}_1 + \mathbf{D}_2$ and only this one can be expressed through a deformation gradient $\mathbf{F}$ of continuum.

Mechanical properties of elastic element are described by conventional equations of the theory of elasticity for compressible media. It is assumed that only the elastic element answers for the volume change, which completely corresponds to the standard hypotheses of the plasticity theory. The elastic potential for the "compressible" medium is written down as the sum of two summands w^* and w^+. If the volume of a body does not vary ($V = V_0 = const$) that $w^+ = 0$, at all-round hydrostatic expansion $w^* = 0$. For maintenance of this condition a new "normalized on volume" variable is entered

$$\alpha_i = \frac{\lambda_i}{J^{1/3}} = \frac{\lambda_i}{(\lambda_1\lambda_2\lambda_3)^{1/3}}, \quad w = w^*(\alpha_1, \alpha_2, \alpha_3) + w^+(J), \tag{1}$$

where $J = \lambda_1\lambda_2\lambda_3$ — relative change of volume, λ_i — stretch ratios. The idea of normalization of independent variables is frequently applied to the description of elastic behavior of compressible media [5].

Function w^* for the "compressible" elastic medium is set in the form of square-law degree potential

$$w^* = C_2\left(\alpha_1^2 + \alpha_2^2 + \alpha_3^2 - 3\right) = C_2\left(J^{-2/3}\mathrm{tr}\left(\mathbf{V}_1^2\right) - 3\right), \tag{2}$$

where $\mathbf{V}_1$ — elastic element stretch tensor.

Assuming, that the dependence between average stress and volumetric deformation is linear, volumetric function w^+ is taken in the following kind (K is elastic bulk modulus of the medium)

$$w^+ = \frac{K}{2}(J-1)^2. \tag{3}$$

The plastic element behavior is defined as the basic Prandtl-Reuss equations [6, 7] of the classical plastic flow theory. The proportional association between the deviator of a rate of deformation tensor of the whole system $\mathbf{D}$ and the deviator strain rate tensor of the plastic element $\mathbf{D}_2$ is used for closure of constitutive equations system ($\mathbf{D}_2 = \mathrm{dev}\mathbf{D}_2$).

$$\sqrt{\mathbf{D}_2 \cdot \mathbf{D}_2} = \kappa\sqrt{\mathrm{dev}\mathbf{D} \cdot \mathrm{dev}\mathbf{D}}, \tag{4}$$

where κ is the nonnegative parameter indicating the what share are made by a plastic strain rate in common strain rate of the media. If $\kappa = 0$ the material behaves as only elastic, at $0 < \kappa < 1$ — as elastoplastic with hardening, a case when $\kappa = 1$ corresponds to ideal plasticity and, at last, at $\kappa > 1$ true stress-strain curve becomes descending, i.e. a material softening is observed.

In model plastic parameter κ is set through yield function Φ: $\kappa = 0$ if $\Phi(\mathbf{V}) < q$, else $\kappa = \zeta(q)$ if $\Phi(\mathbf{V}) = q$. Function q is an analogue of Odkvist parameter of hardening from the classical theory of plasticity [7], $\mathbf{V}$ — left stretch tensor from polar decomposition of deformation gradient $\mathbf{F}$=$\mathbf{VR}$. In this model the yield function is taken as

$$\Phi = \sqrt{\mathrm{dev}\,\mathbf{V} \cdot \mathrm{dev}\,\mathbf{V}}. \tag{5}$$

Thus, it is necessary to know the dependence $\zeta(q)$ for the description of plastic behavior of a material. This information was received from the analysis of experimental data.

By means of the yielded approach the experimental curves of uniaxial elongation for pure polyethylene and two polymer/silicate nanocomposites on its basis with filler concentration 2%-mas. and 8%-mas. Works on synthesis and an experimental research of mechanical properties of such composite materials have been executed in the Institute of Petrochemical Synthesis RAS (Moscow) [8, 9]. These experiments also have shown that rather significant dilatation is observed

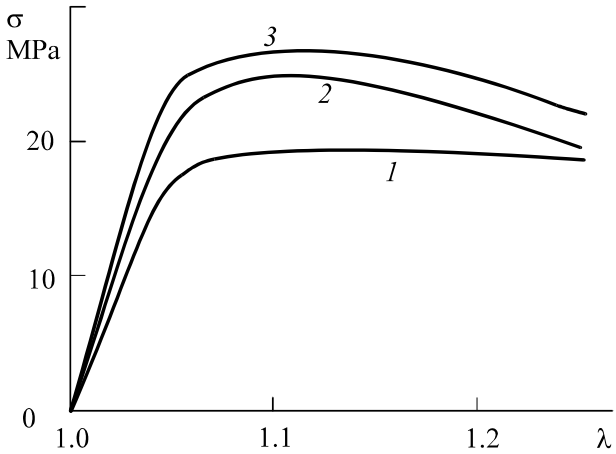


Figure 1: Modeling dependences of true stresses on specimen stretch ratio λ at the initial stage of loading. 1 — $\varphi_m = 0\% - mas.$, 2 — $\varphi_m = 2\% - mas.$, 3 — $\varphi_m = 8\% - mas.$

under deformation. Most likely, it is connected with development of internal damage accumulation. Polyethylene of high density (PE) was used as a matrix. Intercalated sodium montmorillonite (MMT), modified by surface-active substances was taken as a filler. The examined composite contained 2% in mass of the filler in intercalated state. The average size of particles was about 80 nm in diameter and few 10 nm thin (for tactoids).

The experimental data represented dependences of true (σ) and nominal (σ^0) tensile stresses on stretch ratio λ. So, it is possible to receive the information on change of a specimen volume using standard association $\sigma = \sigma^0\lambda/J$.

Model stress–strain dependences and also appropriate associations $J(\lambda)$, $\kappa(\lambda)$ and $K(\lambda)$ for λ values from 1 till 1.25 have been as a result built. At major elongation the origination and development of plastic "neck" was observed. At this stage the material loses the macroscopic homogeneity, and application of the above described model becomes unauthorized.

Modeling dependences of true stress (σ) on "specimen" main stretch ratio λ are shown in fig. 1. Modeling curves practically coincide with experimental ones (distinction is no more than one percent). Fig. 2 depicts appropriate dependences between relative volume change J and λ. It is visible on graphics, that nanofiller adding to matrix causes a rise of a material hardness but, thus, promotes interior structural damage accumulation. Parameter J in this case can be observed as a measure of material interior damage degree, as pure unimpaired polyethylene is practically incompressible. It is possible to guess availability of two structural mechanisms. On the one hand feeding into polymer considerably harder particles should raise increase the hardness of a material, and with other these inclusions provoke appearance of the local microfaults relaxing system.

Deformation dependences of parameter $\kappa(\lambda)$ describing a ratio between plastic and total medium deviators of rate of deformations tensors $\mathbf{D}_2$ and $\mathbf{D}$ are shown in fig. 3. Fig. 4 shows how the bulk module of material K changes at sample stretching.

Accounts have displayed, that purely elastic straining of a material was observed only on the most initial section of a loading (at a strain not above 1–2%). Then there was a fast development of plastic flow that corresponded to sharp growth of parameter κ, which has exceeded unity at $\lambda > 1.1$. It means that practically all strain rate of the medium at this stage was set by the plastic flow accompanied by a loss of strength. The κ values calculated for pure polyethylene and for nanocomposites have appeared to be close, i.e. at this stage plastic flow development(evolution) feebly depends on filler concentration (naturally, it is valid only for observed densities).

Also it has been established, that there was a sharp falling of a bulk modulus of material K on an initial section of a loading, and, the above there was a filler concentration, the curve was bent downwards. Possibly, it is linked to appearance and disclosure of the micropores which origination is promoted by dispersible inclusions.

The carried out investigations have displayed adequacy and perspectivity of the offered model

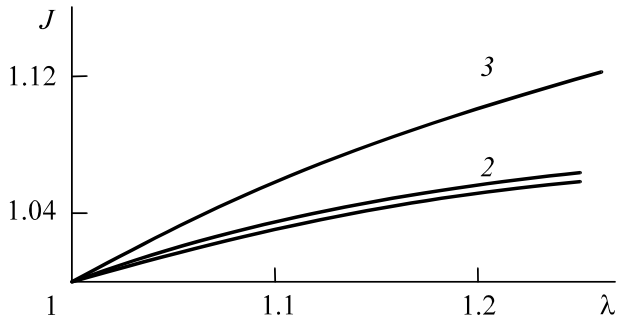


Figure 2: Modeling dependences of relative volume change J on λ. 1 — $\varphi_m = 0\% - mas.$, 2 — $\varphi_m = 2\% - mas.$, 3 — $\varphi_m = 8\% - mas.$

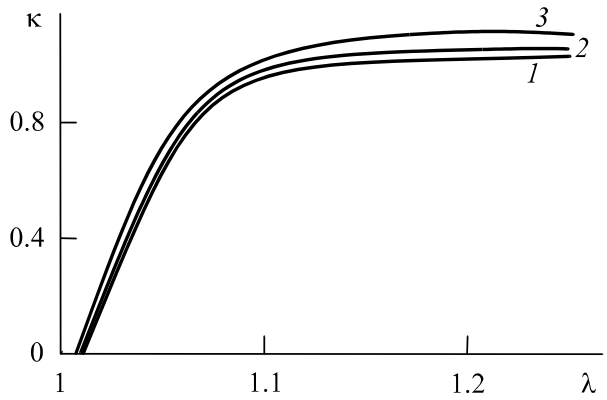


Figure 3: Modeling dependences of plastic parameter κ on λ. 1 — $\varphi_m = 0\% - mas.$, 2 — $\varphi_m = 2\% - mas.$, 3 — $\varphi_m = 8\% - mas.$

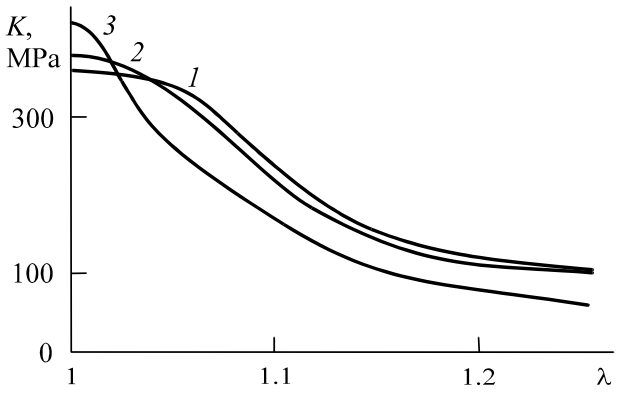


Figure 4: Modeling dependences of bulk modulus K on λ. 1 — $\varphi_m = 0\% - mas.$, 2 — $\varphi_m = 2\% - mas.$, 3 — $\varphi_m = 8\% - mas.$

for exploration of mechanical behavior nanocomposites on the basis of polyolefins and laminose clayey minerals. It is represented, that the combination of new experimental outcomes to further perfecting of the yielded theoretical approach will allow to make a number of new useful outputs and inferences about those interior processes that happen in structure of similar materials at their straining.

Acknowledgements

Work is executed at financial support of Russian Foundation for Basic Research (Grants 09-08-00339,09-06-00402) and Program of Presidium of RAS 09-C-1-1008.

References

[1] Chvalun S. N. Polymer nanocomposites // Priroda, (2000), N 7, P. 22–30.

[2] Fengge G. Clay/polymer composites: the story // Materials Today, (2004), N 11, P. 50–55.

[3] Garishin O. K. Nonlinear highly elastic-plastic model of the continuum with volume changing under deformation // XXXVI Summer school "Advanced problems in mechanics": Proceedings. St.-Petersburg (Repino), (2008), P. 237–242.

[4] Palmov V. A. Large strains in viscoelastoplasticity // Acta Mechanica., (1997), V. 125, P. 129–139.

[5] Peng S. T. J., Landel R.F. Stored energy function and compressibility of compressible rubberlike materials under large strain // J. Appl. Phys., (1975), V. 46, N 6, P. 2599–2604.

[6] Reuss E. Account of elastic deformation in the theory of plasticity // In book The theory of plasticity. Moscow: Inostrannaya literatura, (1948), P. 202–222 (in Russian).

[7] Odkvist F. K. G. Mathematical theory of creep and creep rupture. Stockholm: Darendon Press, (1966), 170 p.

[8] Guseva M. A. The structural and physic-mechanical properties of nano-composites on the basis of not polar polymer and layer silicate. Diss. cand. phys.-math. sci., (2005), Moscow, 162 p. (in Russian).

[9] Gerasin V. A., Guseva M. A., Merekalova N. D., Garishin O. K., Svistkov A. L., Antipov E. M. Formation of polymer-silicate nanocomposites. The structure and deformation properties // IV International Scientific-practical Conference "New polymeric composite materials": Proceedings, (2008), Nalchik, P. 97–100. (in Russian).

Oleg K. Garishin, Institute of Continuous Media Mechanics, Perm, Russia

To the theory of longitudinal magnetic susceptibility in fractal magnets

S. O. Gladkov S. B. Bogdanova
Sglad@newmail.ru, Sonjaf@list.ru

Abstract

The dependence of longitudinal magnetic susceptibility of fractal ferrite dielectrics on frequency field ε, temperature T, exponent ε and other characteristics of structure were calculated. The unconventional behavior of longitudinal susceptibility as function of temperature was proved. It was demonstrated, that anisotropy of magnon spectrum has a very strong effect on all physical dissipative coefficient such as magnetic structure due to exponent ε. The calculations are based on using of quasiclassical kinetic equation for distribution function of magnons.

In this work the tensor of magnetic susceptibility $\chi_{ik} = \dfrac{\partial \mathrm{M}_i}{\partial h_k}$ [1] is calculated in fractal magnet. Fractal object has Hausdorf's dimension greater-than topological dimension d [2]. Mathematical examples of such types are Koch's curve and Serpinsky's triangular napkin. They have Hausdorf's and topological dimension accordingly equal $d_F = \dfrac{ln4}{ln3} = 1,26$, $d_F = \dfrac{ln3}{ln2} = 1,58$ and $d = 1$.

We direct the external magnetic field along axis z and so there is $h(t) = (0, 0, h_z(t))$, where $h_z(t) = h_0 e^{-i\omega t}$, h_0 – amplitude of field, ω – frequency. From definition of susceptibility [3,4], where the distribution function of magnons is $f_k = f_0 + \delta f$, where $f_0 = \frac{1}{e^{\frac{\varepsilon(k)}{\mathrm{T}}} - 1}$ is their equilibrium distribution function, $f_0 = \frac{\partial f_0}{\partial T_0}\delta \mathrm{T}$ and

$$\delta \mathrm{T} = \frac{i\omega\mu_e h_z \tau_k}{1 - i\omega\tau_k} \tag{1}$$

$$\chi_{zz} = -\frac{\mu_e}{a^3} V \frac{\partial}{\partial h_z} \int \delta f \frac{d^3k}{(2\pi)^3} = -\frac{\mu_e^2 V}{(2\pi a)^3} \frac{i\omega\bar{\tau_\varepsilon}}{1 - i\omega\bar{\tau_\varepsilon}} \frac{\partial}{\partial \mathrm{T}} \int \frac{1}{e^{\frac{\varepsilon(k)}{\mathrm{T}}} - 1} d^3k \tag{2}$$

where μ_e is electronic magnetic moment, a is interatomic distance.

The relaxation τ_k of magnon with wave vector $\vec{k}$ has been replaced by relaxation's average time $\vec{\tau}_k$ due to the mean-value theorem. Note that the average relaxation time depends on ε. Spectrum of magnon ε_k for fractal magnetic structure was founded in [5].

To calculate the dispersion of ε_k we use the following formula for magnetic Hamiltonian [3,6]:

$$H_0 = \int_V (\frac{\alpha}{2}(\frac{\mathfrak{d} M_i}{\mathfrak{d} x_k})^2 - \vec{M}\vec{H} - \frac{\beta}{2}\vec{M}^2) dV \tag{3}$$

where α is an exchange integral, β is a magnetic anisotropy constant.

For fractal structure ordinare operation of differentiation on space coordinates is not usable and we shall use the fractal differential operator [7,8]:

$$A_x f(\vec{r}) = \int_V i k_x^{1-\varepsilon} f_k e^{i\vec{x}\vec{k}} d^3k \tag{4}$$

The action of(4) on projection of magnetic moment $\vec{M} = (M_x, M_y, M_z)$, where $M_x = \frac{M^+ + M^-}{2}$ and $M_y = \frac{M^+ - M^-}{2i}$, gives us the following relation:

$$(A_i\vec{M})^2 = \frac{AM^+AM^-}{2} + \frac{AM^-AM^-}{2} + (AM_z)^2 \tag{5}$$

Due to the method of secondly quantization [9] in accordance of Goldstein-Primakoff's transformations we introduce the creation operator $a^+ = a^+(\vec{r})$ and annigilation operator $a = a(\vec{r})$ of magnons.

After Fourier-expansions

$$a^+(\vec{r}) = \frac{1}{\sqrt{N}} \sum_k a_k^+(\vec{r}) e^{-i\vec{k}\vec{r}}, a(\vec{r}) = \frac{1}{\sqrt{N}} \sum_k a_k(\vec{r}) e^{-i\vec{k}\vec{r}} \tag{6}$$

where N is a number of lattices site. From (3)-(6) we find the following magnon spectrum in fractal ferromagnetic dielectric

$$\varepsilon_k = \alpha M_0^2 (k_x^{2-2\varepsilon} + k_y^{2-2\varepsilon} + k_z^{2-2\varepsilon}) + \mu_e (H_0 + \beta M_0) \tag{7}$$

After transition in the expression (2) due to the apherical coordinates in accordance (7) the magnetic susceptibility of fractal ferrodielectric will be the following

$$\chi_{zz} = \frac{3\mu_e^2 V}{2(2\pi a)^3} \frac{i\omega\bar{\tau}}{1 - i\omega\bar{\tau}} \frac{\Gamma(\frac{3\varepsilon}{2\varepsilon-2})}{(1-\varepsilon)^2} exp(-\frac{\mu_e(H_0 + \beta M_0}{T_0}) \times \\ \times (\frac{T_0}{\alpha M_0^2})^{\frac{3}{2-2\varepsilon}} \zeta(\frac{3}{2-2\varepsilon}) \int d\varphi \int g^{\frac{3}{2-2\varepsilon}}(\varphi, \vartheta) d\vartheta \tag{8}$$

where function $g(\varphi, \vartheta) = sin^{2-2\varepsilon}\vartheta \cdot cos^{2-2\varepsilon}\varphi + sin^{2-2\varepsilon}\vartheta \cdot sin^{2-2\varepsilon}\varphi + cos^{2-2\varepsilon}\vartheta$.

In conclusion we are to note:

1. The theory of longitudinal susceptibility of fractal ferromagnetic dielectric has been constructed.
2. Depedence of χ_{zz} on different parameters (temperature, frequency of external oscillating field and dimension ε) has been found.

References

[1] L.D.Landau and E.M.Lifshitz. Electrodinamics of continuos media. V.8. Moscow, 1986.

[2] B.Mandelbrot. The fractal geometry of nature. New York. 1983.

[3] A.I.Ahiezer, V.G.Bar'yahtar, S.V.Peletminsky. Spin waves. Moscow. 1969.

[4] S.O.Gladkov. The kinetics of nuclear magnetically ordered systems. Phys.Rep. 1989. V.182. N4,5. PP.211-364.

[5] S.B.Bogdanova,S.O.Gladkov. To the question of magnon's spectrum in the structures of not whole dimension. Work 10 conference "Actual Problems of Modern Science". Samara. 2009. PP. 56-60.

[6] S.O.Gladkov.Physics of composite: thermodynamic and dissipative properties. Moscow. 1999.

[7] S.O.Gladkov. To the theory of one-dimensional and quasi-n-dimensional objects. Journal of Technical Physics. 1997. V.67. PP. 8-12.

[8] S.B.Bogdanova,S.O.Gladkov.The heat-transfer theory for quasi-n-dimensional systems. Journal of Physics: Condenced Matter. 2010. V.405. PP.1973-1975.

[9] L.D.Landau and E.M.Lifshitz.Quantum mechanics. V.3. Moscow. 1986.

S.B.Bogdanova,S.O.Gladkov. Moscow State Regional University. Moscow, Radio str, 10a, 105005, Russia.

Comparison of thermoelastic stress analysis and photoacoustic microscopy approaches to the problem of residual stress detection

Alexei L. Glazov Kyrill L. Muratikov
klm.holo@mail.ioffe.ru

Abstract

Scientific foundations of the thermoelastic stress analysis and photoacoustic method of the stress detection are compared. Experimental results obtained by the photoacoustic method for Vickers indentation zones in ceramics. It is demonstrated the influence of the given external and residual stresses on the photoacoustic images of Vickers indentations. The experimental results obtained by photoacoustic method are compared with the available theoretical models of the photoacoustic effect in stressed materials is made.

1 Introduction

The performance of a component is strongly determined by residual stresses. Residual stresses result from virtually all manufacturing processes and they are often a cause of premature failure of critical components. Therefore the problem of residual stress detection and measurement is urgent in modern engineering, mechanics and materials science. A good deal of effort has been undertaken in developing various methods to detect residual stresses [1]. Optical, ultrasonic, Raman spectroscopy, magnetic, X-ray and neutron diffraction methods are effectively applied for the residual stress detection in many cases. Today there are also two methods based on thermoelastic properties. These are thermoelastic stress analysis (TSA) and photoacoustic (PA) microscopy. The TSA now becomes a well-known experimental technique providing information on surface stress fields in structures [2]. The PA microscopy is an acknowledged method for non-destructive evaluation but makes initial steps in residual stress investigation.

In the TSA a material is subjected to a cyclic load. The strain induced produces a cyclic temperature variation that can be detected by an appropriate infrared detector. Two systems of this type are commercially available at present. These are a scanning system with a single infrared detector and system DeltaTherm by Stress Photonics using planar array infrared detectors. These techniques have been already implemented effectively for mechanical stress detection in various components. There was also proposed a technique using a pulsed laser as a thermal strain source [3].

The PA microscopy uses usually piezoelectric element to detect acoustic waves generated in a sample by modulated laser radiation. The PA images result from scanning a focused laser beam with relation to the sample surface. The PA methods have the micrometer resolution, are non-destructive and very attractive for modern diagnostics and imaging of near-surface defects. Essentially less attention has been paid to developing the PA technique for the stress detection. The first PA detection of residual stress took place about twenty years ago [4]. Since then, there were a number of works in this direction [5, 6, 7, 8]. Nevertheless, applications of the PA method for residual stress detection are not widely accepted yet. The problem is due to obscure a relation between residual stresses and the PA signal. Our previous systematical experimental and theoretical investigations of the PA effect in stressed solids [8, 9, 10, 11] were aimed to reveal this relation.

The main purpose of this work is to compare theoretical foundations of the TSA and the PA stress analysis and demonstrate some experimental results on residual stress evaluating by the PA microscopy.

2 Theoretical model of photoacoustic thermoelastic effect in stressed solids

The theoretical comparison of the PA and TSA approaches to the problem of residual stress detection can be performed using modern thermoelastic theory for elastic solids. Introducing the explicit form of the thermoelastic parameter in the system of thermoelasticity equations in instead of the coefficient of linear expansion it may be represented as [12]

$$\nabla^2 T - \frac{1}{\kappa}\dot{T} - T_0 \frac{3\lambda + 2\mu}{\lambda_T} \rho C_\epsilon K_\epsilon \nabla \cdot \dot{\vec{u}} = -\frac{Q}{\lambda_T}, \tag{1a}$$

$$\rho \ddot{\vec{u}} = \mu \nabla^2 \vec{u} + (\lambda + \mu) \nabla \nabla \cdot \vec{u} - (3\lambda + 2\mu) \rho C_\epsilon K_\epsilon \nabla T + f, \tag{1b}$$

where T is the temperature of the body, T_0 is the environmental temperature, vector $\vec{u}$ denotes deformations of the body, Q is the heat produced in the body by external sources, λ and μ are Lame's elastic constants, λ_T and κ are thermal conductivity and diffusivity, ρ and C_ϵ are the density and specific heat of the body at constant volume respectively; K_ϵ is the thermoelastic parameter of the material; f is the external force.

It is of general importance for both the TSA and PA techniques that the thermoelastic parameter K_ϵ depends on a stress [13]. Under adiabatic conditions the thermoelastic parameter is related to the first stress invariant by

$$K_\epsilon = K_\epsilon^{(0)} + K_\epsilon^{(1)} = \frac{1}{\rho C_\epsilon}\big(\alpha_T - \frac{1}{E^2}\frac{\partial E}{\partial T}\sigma\big), \tag{2}$$

where $K_\epsilon^{(0)} = \alpha_T / \rho C_\epsilon$ is the well-known thermoelastic parameter in the unstressed state of a body; $K_\epsilon^{(1)}$ denotes the linear stress dependent part of the thermoelastic parameter. α_T is the coefficient of linear thermal expansion; E is Young's modulus; $\sigma = \sigma_{ii}$ is the first stress invariant. σ is usually considered in the TSA as the mean stress value or the residual stress.

According to the TSA approach a sample is subjected to a cyclic external load ($f \neq 0$) resulted in the cyclic strain due to Eq.(1b), while the external heat sources Q=0. In accordance with Eq.(1a) this strain generates a cyclic temperature variation.

Thermal diffusivity processes are usually neglected in the TSA. Then Eq.(1a) gives the basic TSA relationship

$$\Delta T = -T_0 K_\sigma \Delta\sigma, \tag{3}$$

where ΔT is the sample temperature modulation due to the applied cyclic external stress $\Delta\sigma$, K_σ is the thermoelastic parameter of the material at constant pressure.

Eqs.(2) and (3) show the relation between the residual stress σ and the temperature variations. This provides an opportunity for stress measurements by detecting infra-red radiation. It should be noted, however, that practical applications of the TSA needs special calibration procedures for stress measurements [14].

Let us consider the basis of the PA technique. In contrast to the TSA the initial source of the PA signal is intensity modulated laser spot on the top sample surface ($Q \neq 0, f = 0$). This heat source generates strongly damped thermal waves in the sample. The distance of their propagation is limited by the length $l_T = \sqrt{2\kappa/\omega}$, where ω is the cyclic frequency of the laser beam modulation. Therefore the thermal waves are localized in the light spot vicinity. The cyclic temperature gradient produces cyclic local deformations in the body according to Eq.(1b). In the PA microscopy these deformations are detected by a piezoelectric transducer attached to a body. The details of our PA microscopy setup for investigation of stressed materials are described, for example, in [11]. It is important that the term with the temperature gradient in Eq.(1b) includes the same thermoelastic

parameter which is presented in Eq.(1a). It means that cyclic deformations of a body are influenced by stresses existing near the pump beam position.

To calculate the PA signal one needs to get the strain of a sample at the piezoelectric transducer, that is to solve Eq.(1b). A solution of this equation is a complicated mathematical problem in a general case. We analyzed this problem within the framework of the perturbation theory in quasi-static approximation assuming that elastic and thermoelastic inhomogeneties of the object are small. Quasi-static approximation assumes additionally that the length of acoustic waves exceeds essentially the length of thermal waves in the material. This assumption is valid for the most PA microscopy experiments up to the light modulation frequencies of hundreds mega Hertz. Under these conditions we showed that the PA images display mainly the near surface thermoelastic properties of a sample [15, 16]. In this case the PA signal determined by thermoelastic inhomogeneties of a sample can be represented in the form

$$V(\vec{r_0},\omega) = C \int K_\epsilon^{(1)}(\vec{R}) T^{(0)}(\vec{R} - \vec{r_0},\omega) d^3R, \tag{4}$$

where C is the coefficient dependent on the piezoelectric sensor characteristics, $T^{(0)}$ is the non-stationary distribution of the temperature generated by a pump laser radiation in the homogeneous sample, $\vec{R} = (x, y, z)$, vector $\vec{r_0} = (x_0, y_0, 0)$ denotes a position of the laser beam center at the sample surface $z = 0$.

Plugging $K_\epsilon^{(1)}$ from Eq.(2) into Eq.(4) gives

$$V(\vec{r_0},\omega) = C' \int R(\sigma_{xx}(\vec{R}) + \sigma_{yy}(\vec{R})) T^{(0)}(\vec{R} - \vec{r_0},\omega) d^3R, \tag{5}$$

where $C' = -\dfrac{1}{\rho C_\epsilon} \dfrac{1}{E^2} \dfrac{\partial E}{\partial T} C$, σ_{xx} and σ_{yy} are the components of the stress tensor. It is assumed here that $\sigma_{zz} \approx 0$ near the sample surface. Eq.(5) represents the PA signal detection on the near surface mechanical stresses.

The presented simplified outline demonstrates that the TSA and PA techniques have a common scientific origin. The PA signal is proportional to $\sigma_{xx} + \sigma_{yy}$ as well as the TSA signal [17]. The difference between the TSA and PA approaches is only the difference in physical parameters that are measured. In the TSA the temperature cycle is used for the detection of stresses, whereas in the PA the deformation cycle is used for this purpose.

3 Application of proposed theoretical model to analysis of photoacoustic signal behavior near vertical crack tips

Eq.(5) was obtained under rather general conditions. It demonstrates the dependence of the PA signal on stresses. Thermal waves decay strongly with the increase of the distance from the point of excitation. It means that in accordance with Eq.(5) the PA signal is determined mainly by the stress tensor distribution near the focal point of the laser beam at the sample surface. The depth of thermal wave penetration in a material is also limited by their wavelength. Hence, Eq.(5) shows that only the near surface layer compared with the thermal wave length contribute to the PA signal. Eq.(5) can be applied for analysis of the PA signal behavior in different situations. In particular, it can be used for the study of the PA signal behavior near defects of different types where mechanical stresses are usually concentrated.

We apply Eq.(5), for example, for analysis of the PA signal behavior near the radial crack tips in Vickers indented ceramics [18]. By taking into account that only thin near surface layer is responsible for the formation of the PA signal these cracks were considered as plane ones. It is known that the components of the stress tensor near a plane crack tip in a thick sample are determined by equations [19]

$$\sigma_{xx} = \frac{K_I}{\sqrt{2\pi r}} \cos\theta(1 - \sin\theta \sin 3\theta) - \frac{K_{II}}{\sqrt{2\pi r}} \sin\theta(2 + \cos\theta \cos 3\theta), \tag{6a}$$

$$\sigma_{yy} = \frac{K_I}{\sqrt{2\pi r}} \cos\theta(1 + \sin\theta \sin 3\theta) + \frac{K_{II}}{\sqrt{2\pi r}} \sin\theta \cos\theta \cos 3\theta, \tag{6b}$$

where K_I and K_{II} are the stress intensity factors defining the normal and shear components of the total stress produced both by residual and external stresses; r is the distance between the crack tip and a variable point at the sample surface, θ is the half angle between the crack direction and the direction from the crack tip to a variable point.

The stress intensity factors of a crack in general case are determined by the total action of residual stresses and stresses produced by external loading. In linear crack mechanics the total stress intensity factors of a crack can be represented in the form

$$K_I = K_I^{(0)} + K_I^{(1)}, K_{II} = K_{II}^{(0)} + K_{II}^{(1)}, \tag{7}$$

where $K_I^{(0)}$ and $K_{II}^{(0)}$ are the stress intensity factors related to residual stresses, $K_I^{(1)}$ and $K_{II}^{(1)}$ are the stress intensity factors characterizing the crack behavior under external loading.

From Eqs.(6) and (7) we can obtain near the radial crack tip for Eq.(5)

$$\sigma_{xx} + \sigma_{yy} = \frac{2}{\sqrt{\pi r}}\big[\big(K_I^{(0)} + K_I^{(1)}\big)\cos\theta(x,y,0) - \big(K_{II}^{(0)} + K_{II}^{(1)}\big)\sin\theta(x,y,0)\big].$$

Then, Eq.(5) can be simplified under the condition that stresses do not undergo an essential change at distances compared with the thermal wave length l_T:

$$V(\vec{r_0},\omega) = C' g(\vec{r_0},\omega)\sqrt{\frac{2}{\pi}}\big[\big(K_I^{(0)} + K_I^{(1)}\big)\cos\theta_0 - \big(K_{II}^{(0)} + K_{II}^{(1)}\big)\sin\theta_0\big], \tag{8}$$

where

$$g(\vec{r_0},\omega) = \int \frac{T^{(0)}(\vec{R} - \vec{r_0},\omega)}{\sqrt{r}} d^3R,$$

and θ_0 is the half angle between the crack direction and the direction from the crack tip to the laser beam center at the sample surface.

In the case $r_0 \gg l_T$ we get $g(\vec{r_0},\omega) \approx \int T^{(0)}(\vec{R} - \vec{r_0},\omega) d^3R$.

Let us consider in more details the PA signal behavior near the radial crack tips of Vickers indentation under external loading using the obtained results. The stress intensity factors of the radial cracks for residual stresses produced by Vickers indentation are given by expressions [20]

$$K_I^{(0)} = \chi P / L^{2/3}, \qquad K_{II}^{(0)} = 0, \tag{9}$$

where P is the indentation loading, χ is the dimensionless coefficient determined by the shape of a crack, and L is the length of a crack.

The stress intensity factors of a crack accounting the external loading depend both on the value of this loading and on the angle between the crack and external stress direction (see Fig.1). For the case of the vertical crack these stress intensity factors are determined by equations [19]

$$K_I^{(1)} = \psi_I \sigma_{app}\sqrt{L}\sin^2\phi, \qquad K_{II}^{(1)} = \psi_{II}\sigma_{app}\sqrt{L}\sin\phi\cos\phi, \tag{10}$$

where ϕ is the angle between the crack and direction of the external loading, ψ_I and ψ_{II} are the dimensionless coefficients determined by the crack shape, σ_{app} is the stress produced by external loading.

Using Eqs.(5-10) the PA signal near the radial crack tips can be expressed as

$$\begin{aligned} V(\vec{r_0},\omega) \;=\; & C' g(\vec{r_0},\omega)\sqrt{\tfrac{2}{\pi}}\big[\big(\chi P/L^{2/3} + \psi_I\sigma_{app}\sqrt{L}\sin^2\phi\big)\cos\theta_0 - \\ & - \psi_{II}\sigma_{app}\sqrt{L}\sin\phi\cos\phi\sin\theta_0\big], \end{aligned} \tag{11}$$

Eqs.(7), (8) and (11) can be used for analysis of the PA signal behavior near the radial crack tips. In accordance with these results both residual and external stresses influence on the PA signal. The results show that the PA measurements can be principally used for estimation of the stress intensity factors of cracks. Eq.(11) demonstrates also that external normal and shear stresses

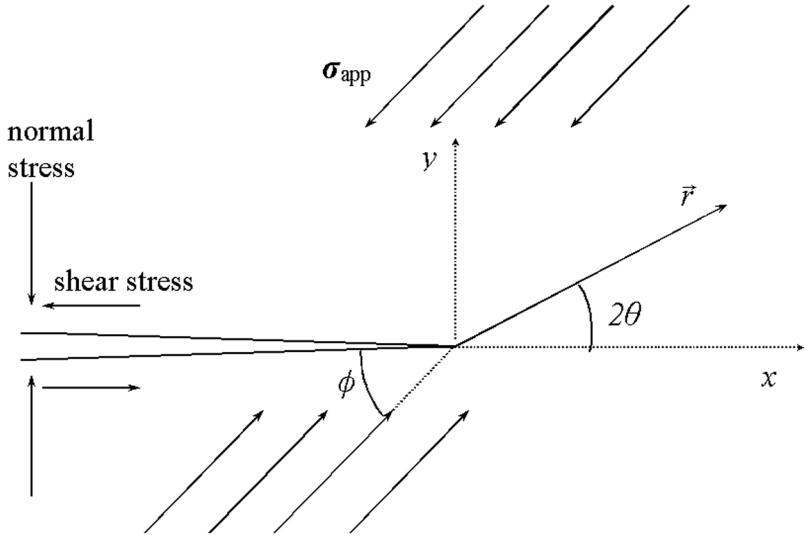


Figure 1: The configuration of a crack and external loading.

contribute to the PA signal near the radial crack tips in different ways. The contribution of normal stresses is proportional to $\cos\theta_0$, while the contribution of shear stresses is proportional to $\sin\theta_0$. This difference can be used for a separate measurement of normal and shear stresses from the PA measurements near the radial crack tips. It should be noted that in accordance with Eq.(11) the function $g(\vec{r_0},\omega)$ depends on the distribution of thermal waves $T^{(0)}(\vec{R},\omega)$ inside the homogeneous sample. Therefore, function g is known as soon as the thermal problem for a homogeneous sample is solved.

When the condition $r_0 \gg l_T$ is hold, Eqs.(8) and (11) are similar to expressions describing the behavior of the TSA thermoelastic signals near the vertical crack tips [17]. Therefore, the PA approach can use for estimating the stress intensity factors in this case the methods similar to those developed for the TSA techniques [21, 22]. In particular, in pure loading modes I and II the stress intensity factors can be obtained from the PA signal measurements along horizontal lines parallel to the x-axis. For more general case of mixed-mode loading the representation of the TSA signal near the crack tips in the form of the "apple-shaped" curve (a cardioid) centered on the crack tip can be used [23]. In accordance with the presented results similar measurements can be done by the PA microscopy methods. In these PA measurements the factor C' should be determined by separate calibration.

At present the TSA techniques are effectively applied for imaging at a millimeter scale [23]. This limitation arises due to relatively low modulation frequencies usually used in the TSA systems for external dynamic load of components. Much higher modulation frequencies of the pump laser radiation can be easily used in PA microscopy. Therefore the PA microscopy can be used for imaging at a micrometer scale. Several examples of the PA microscopy applications to the stress fields imaging in Vickers indented materials with a micrometer resolution are presented in the next section.

4 Experimental results of photoacoustic study of ceramics with residual stresses

Experimental investigations presented in this work were performed by the PA microscopy method on Al_2O_3-SiC-TiC. The PA signal was detected by a piezoelectric transducer with a resonance frequency of about 140 kHz which was attached to the rear side of a sample. The pump laser radiation was focused on the front sample surface in a spot with the diameter of about 1μm. The depth of thermal wave penetration in silicon nitride ceramic was about 10μm at modulation frequency 140 kHz according to our estimation. The PA experiments were performed on ceramic

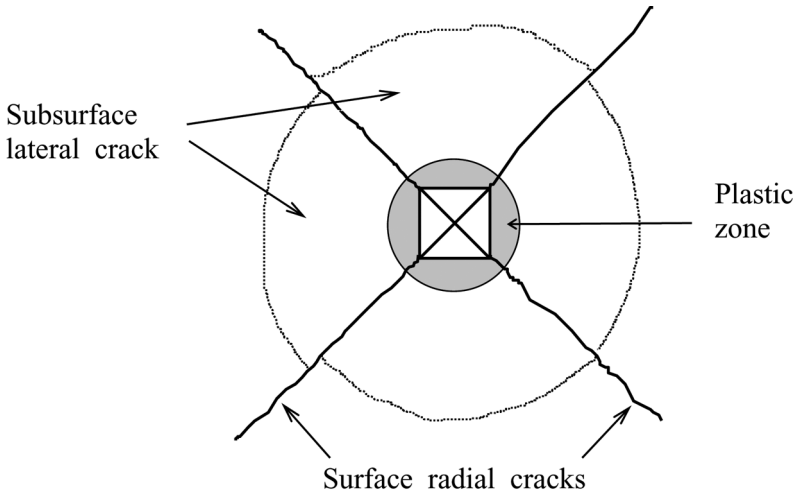


Figure 2: Plan view sketch of the Vickers indentation crack system for brittle solid.

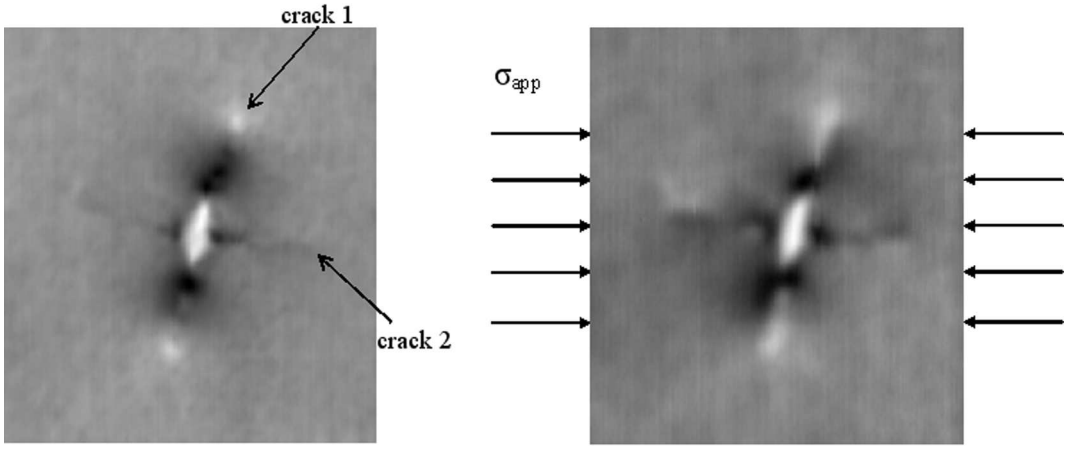
samples with dimensions 2.5×3×5.9 mm^3. The PA images were formed using the computerized setup that moves a sample along two coordinate axes with 2.5μm step.

In this work the main attention was paid to investigation of external stresses influence on the PA images of this ceramic. Residual stresses were introduced in ceramic samples by Vickers indentation. Vickers indentation has a rather complicated structure. The typical structure of Vickers indentation in a brittle solid includes core, plastic and elastic zones, radial or median cracks (Fig.2). However, in this work the main attention was paid only to investigation of the PA signal behavior near the radial crack tips where strong residual stresses are normally concentrated.

The influence of external loading on the PA response was investigated in *in situ* experiments with Al_2O_3-SiC-TiC ceramic composite. A known compressive external loading was applied parallel to the sample surface. The PA images of the Vickers indented area presented in Fig.3 in initial and loaded states are typical for brittle materials. First of all, one can see in Fig.3a a well detectable increase of the PA signal near the tips of two radial cracks. Similar PA signal behavior is absent for the other pair of cracks. An assumption was made in [6] that some cracks are invisible for certain the piezoelement modes. We performed PA imaging of ceramic samples before indentation and an approximately uniform level of the PA signal was observed for the piezoelement used. The images are also do not differ by varying mutual position of samples and the piezodetector. Our previous PA experiments with ceramics annealing [24, 25] showed that this increase corresponds to residual stress fields near the tips of radial cracks. It gradually disappears with annealing time. Basing on these results we can assume that the second pair of cracks are initially in the unstressed state. It should be noted that other samples demonstrated various behavior of the PA signal near cracks and indentation prints. The main reason for this phenomenon is residual stress fields presenting in the samples befor the indenting.

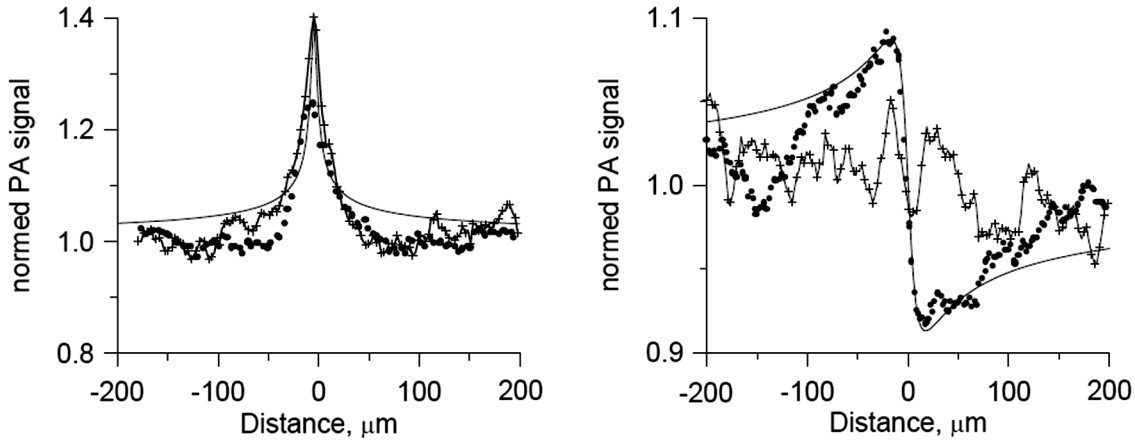
In Fig.3b one can see modifications of the PA signal near cracks under external loading. For crack 1 the angle $\psi \approx 75^\circ$, therefore the external loading produces almost normal compressive stress near the tip. This compressive stress partially compensates initial tensile stresses near the crack tip reducing the PA signal. For crack 2 the angle $\psi \approx 17^\circ$ and external loading produces nearly pure shear stress. Fig.4 represents the behavior of the PA signal near the radial crack tips as an image crosssection along lines perpendicular to the corresponding cracks near the crack tips. The signal is presented for both initial and loaded states. For a comparison the results of theoretical calculations based on Eq.(11) are presented in the figure. The calculationa were made for the PA signal related to the initial normal stress distribution in crack 1 and to residual stress distribution under the external loading in crack 2. The fitted distances between the crack tip and the crosssection line were 5 mm and 20 mm for crack 1 and 2 respertively.

Results presented in Fig. 4 demonstrate a good agreement between experimental data and the behavior of the photoacoustic signal near crack tips predicted by our theoretical model for the both presented cases. Some quantitative disagreement between experimental and theoretical results at



a) b)

Figure 3: The PA image of Vickers indentation area in Al_2O_3-SiC-TiC ceramic sample. a) without external load, b) under external compressive stress 175 MPa. Image area is 480×500 m^2



a) b)

Figure 4: The behavior of the PA signal across the tips of radial cracks. a) for crack 1, b) for crack 2. Crosses denote experimental data for the sample without external loading, circles denote experimental data for the sample under the pressure 175 MPa, a solid line denotes a theoretical curve.

distances away from the crack tips is due to an asymptotic character of the expressions used for stress tensor components in Eq.(5) which are valid only for short distances. It is seen from Fig.4 that the external compressive stress compensates partially tensile residual stress acting near the tip of crack 1. We have estimated the external loading as 340 MPa that needed to decrease the PA signal down to the average level for the sample and by this way to get unstressed crack tip. It is also clearly seen that the shear stress produces residual stresses of opposite sign along different sides of crack 2.

Thus, PA results presented here for Al_2O_3-SiC-TiC composite ceramic and our previous results for silicon nitride ceramic demonstrate the usefulness of the PA microscopy for imaging of stress fields in ceramics.

5 Conclusion

Comparison of theoretical foundations of the TSA and PA techniques demonstrates that the both techniques are based on the thermoelastic parameter dependence on stress. The principle difference

consists only in using different physical approaches for measuring signal. The PA piezoelectric technique uses deformation cycle for detection instead of the temperature cycle used by the TSA. The results presented in this work demonstrate the feasibility of the PA piezoelectric imaging for residual stresses detection near the crack tips in ceramics. The influence of external mechanical stresses on the PA images of the radial crack tips is shown by experiments. The results of PA experiments with the given external loading provide an opportunity for the quantitative estimation of residual stresses. It is demonstrated that our theoretical model of the PA effect in solids gives a good fit to experimentally found stress field variations near the radial crack tips in ceramics. It is essential that the PA technique is able to provide imaging of mechanical stress fields in different materials with the high spatial resolution.

Acknowledgements

This research was supported by the RFBR under award Nos.04-02-17622 and 06-02-17148

References

[1] P.M. Withers and H.K. Bhadeshia. Mater. Sci. Technology, vol.17, pp.355-375, 2001.

[2] G. Pitarresi and E.A. Patterson. J. Strain Analysis, vol.38, pp.405-417, 2003.

[3] D.S. Mountain and G.P. Cooper. Proc. SPIE, vol.1084, pp.103-110, 1989.

[4] J.H. Cantrell, M. Qian, M.V, Ravichandran and K.M Knowles. Appl. Phys. Lett., vol.57, pp.1870-1872, 1990.

[5] R.M. Burbelo, A.L. Gulyaev, L.I. Robur, M.K. Zhabitenko, B.A. Atamanenko and Ya.A Kryl. J. de Phys. 4, vol.C7, pp.311-314, 1994.

[6] H. Zhang, S. Gissinger, G. Weides and U. Netzelman. J. de Phys. 4, vol.C7, pp.603-606, 1994.

[7] R.M. Burbelo and M.K. Zhabitenko. In: Progress in Natural Science, edited by Shu-yi Zhang, Taylor & Francis, London and Washington, Suppl., 6 , pp.720-723, 1996.

[8] K.L. Muratikov, A.L. Glazov, D.N. Rose, J.E. Dumar and G.H. Quay. Tech. Phys. Lett., vol.23, pp.188-190, 1997.

[9] K.L. Muratikov, A.L. Glazov, D.N. Rose and J.E. Dumar.J. Appl. Phys., vol.88, pp.2948-2955, 2000.

[10] K.L. Muratikov, A.L. Glazov, D.N. Rose and J.E. Dumar. High Temperatures-High Pressures, vol.33, pp.285-292, 2001.

[11] K.L. Muratikov, A.L. Glazov, D.N. Rose and J.E. Dumar. Rev. Sci. Instrum., vol.74, pp.3531-3535, 2003.

[12] L.D. Landau and E.M. Lifshitz. Theory of Elasticity, 187 p., Pergamon, New York (1986).

[13] A.K. Wong, R. Jones and J.G. Sparrow. J. Phys. Chem. Solids, vol.48, pp.749-753, 1987.

[14] J.M.Dulieu-Barton, P.Stanley. J. of Strain Analysis, vol.33, No.2, pp.93-104, 1998.

[15] K.L. Muratikov. Tech. Phys. Lett., vol.30, pp.956-958, 2004.

[16] K.L. Muratikov. Tech. Phys. Lett., vol.31, pp.839-842, 2005.

[17] P. Stenley and J.M. Dulieu-Smith. Experimental Techniques, vol.20, pp.21-23, 1996.

[18] K.L. Muratikov. Rev. Sci. Instrum., vol.74, pp.722-724, 2003.

[19] L.I. Sedov. Mechanics of Continuous Medium. Vol.2, p.568, Nauka, Moscow, Russia, 1970 (in Russian).

[20] S.M. Smith and R.O. Scattergood. J. Am. Ceram. Soc., vol.75, pp.305-315, 1992.

[21] K.L. Muratikov, A.L. Glazov, D.N. Rose and J.E. Dumar. Tech. Phys. Lett., 2002, vol.28, pp.377-381,2002.

[22] K.L. Muratikov, A.L. Glazov, V.I. Nikolaev, D.N. Rose and J.E. Dumar. High Temperatures-High Pressures, vol.34, pp.585-590, 2002.

[23] J.M. Dulieu-Barton and K. Worden. Meas. Sci. Technol., vol.14, pp.176-183, 2003.

[24] K.L. Muratikov, A.L. Glazov, V.I. Nikolaev, D.N. Rose and J.E. Dumar. Tech. Phys. Lett., vol.27, pp.500-503, 2001.

[25] K.L. Muratikov and A.L. Glazov. Proc. SPIE, vol.5066, pp.78-83, 2003.

Alexei L. Glazov, Ioffe Physical-Technical Institute, Polytekhnicheskaya 26, 124021 St.Peterburg, Russia
Kyrill L. Muratikov, Ioffe Physical-Technical Institute, Polytekhnicheskaya 26, 124021 St.Peterburg, Russia

Investigation of the influence of relaxation transition in the amorphous component of amorphous-crystalline polymer on deformation processes

Lyudmila A. Golotina Igor N. Shardakov
golotina@icmm.ru

Abstract

This paper is concerned with amorphous-crystalline polymers in which amorphous and crystalline phases may coexist in stable equilibrium. For modeling the thermo-mechanical behavior of these materials, the system of constitutive equations describing the relationship between the stress-strain state and the processes of crystallization and glass transition is constructed using the approaches proposed in earlier research. The distinctive feature of the developed constitutive equations is that they take into account the influence of relaxation transitions (glass-transition type) in the amorphous component of a two-component system on the stress-strain state of crystallizing polymer. Additional kinetic equations are derived to characterize the energy evolution of the segmental mobility of a polymer network caused by the bonds of intermolecular interactions. The proposed system of constitutive equations can be used to describe the peculiarities of the thermo-mechanical behavior of the amorphous component of polymers and to study the influence of these specific features on the behavior of the two-component system during the process of crystallization and after its completion.

The present paper deals with consideration of a wide class of amorphous-crystalline polymers in which amorphous and crystalline phases may coexist. Under specific thermomechanical conditions, the amorphous phase may change into the crystalline phase, and the glass transition may take place. Using previous approaches, we have constructed a new variant of constitutive equations for describing the relationship between the stress-strain state and the crystallization and glass transition processes. It is to be noted that the polymer crystallization is distributed along the time and space coordinates in contrast to, for instance, metals having the pronounced crystallization front.

To describe the space-time distribution of temeparature T and the crystallization degree β characterizing the specific volume content of crystallized structures , we offer to use the system involving the following differential equations:
nonstationary thermal conductivity equation

$$\frac{\partial T}{\partial t} = \frac{1}{c\rho} div(\lambda grad T) + \frac{1}{cp} Q_\beta \frac{d\beta}{dt}, \tag{1}$$

and kinetic equation of crystallization

$$\frac{d\beta}{dt} = C_\beta^0 \exp\left(-\frac{E_1}{T - T_c} - \frac{E_2}{T_a - T}\right)(\beta_p(T) - \beta)(1 + C_\beta^1 \beta), \tag{2}$$

where $c\rho$, λ - are thermal physical constants, Q_β – denote the intensity of heat sources caused by crystallization, $C_\beta^0, C_\beta^1, E_1, E_2, T_a, T_c$ – are the kinetic constants measured in calorimeter tests, and β_p – is the equilibrium degree of crystallization. The functional form of expressions in equations (2) can be changed depending on the polymerization and crystallization type. In particular, these processes may be autocatalytic or realized according to the autoretardation scheme [1].The system of equations (1,2) must be complemented with the corresponding boundary-value and initial conditions.

The constitutive equations capable of describing the evolution of the stress-strain state of the polymer material during phase transition are constructed in the framework of a phenomenological theory of continuum mechanics. The developed approach to the construction of constitutive equations for polymerized polymer utilizes the results provided in [2 - 5].

Within this approach, the crystallizing polymer materials are considered as a two-component mixture of amorphous and crystalline structures, whose specific fractions are defined by the degree of crystallization β. We assume that at the moment of transition to the crystalline state each part of the polymer amorphous structure that is proportional to the increment in the degree of polymerization $\Delta\beta$ is in the state of zero stress and matches the earlier structure with respect to the strain state.

This approach corresponds to the variant described in [6], wherein the specific free energy of the two-component system is expressed as

$$F[\varepsilon(t)] = \int_0^{\beta(t)} F_c[\varepsilon(t) - \varepsilon(\tau)]\, d\beta(\tau) + F_a[\varepsilon(t)](1 - \beta(t)), \tag{3}$$

where F_c – is the specific free energy of the crystalline structure, and F_a – is the specific free energy of the amorphous structure.

Using the following expression F_c , F_a , and taking into account (3), the following constitutive relations can be conventionally obtained as

$$\sigma_{ij}(t) = \partial F / \partial \varepsilon_{ij}. \tag{4}$$

The proposed variant differs from the previously described [6] in that it takes into account the influence of relaxation transitions (of glass-transition type) on the stress-strain state. It is clear that this approach can take place only in the amorphous part of the two-component system. Hence, the specific free energy of the amorphous component F_a can be written in the form

$$\begin{aligned} F_a = {} & \frac{\mu_1}{2} e_{ij} e_{ij} + \frac{\mu_2}{2}(e_{ij} - e^*_{ij})(e_{ij} - e^*_{ij}) + \frac{k_1}{2}\varepsilon^2_{kk} + \\ & + \frac{k_2}{2}(\varepsilon_{kk} - \varepsilon^*_{kk})^2 - (k_1 + k_2)\alpha_T(T - T_0)\varepsilon_{kk}, \end{aligned} \tag{5}$$

where $\mu_1, k1$ – are the shear and volume moduli characterizing the elastic properties of the polymer in the viscoelastic state, $\mu_2, k2$ – are the shear and volume moduli characterizing the elastic properties of the polymer caused by intermolecular interactions in the polymer network, e_{ij} – are the deviator strain tensor components, ε_{kk}– is the relative volume deformation, and $e^*_{ij}, \varepsilon^*_{kk}$– are the tensor variables characterizing the evolution of intermolecular interactions on the phenomenological level.

From relations (4,5), we obtain the following physical equations:

$$S_{ij} = \frac{\partial F}{\partial e_{ij}} = \int_0^{\beta(t)} 2G_c[e_{ij}(t) - e_{ij}(\tau)]d\beta(\tau) + [\mu_1 e_{ij} + \mu_2(e_{ij} - e^*_{ij})](1 - \beta(t))$$

$$\begin{aligned} \sigma_{kk} = 3\frac{\partial F}{\partial \varepsilon_{kk}} = {} & \int_0^{\beta(t)} \{B_c[\varepsilon_{kk}(t) - \varepsilon_{kk}(\tau)] - 3B_c\alpha_c(T)[T(t) - T(\tau)]\}d\beta(\tau) + \\ & + [3k_1\varepsilon_{kk} + 3k_1(\varepsilon_{kk} - \varepsilon^*_{kk}) - 3(k_1 + k_2)\alpha_T(T - T_0)](1 - \beta(t)). \end{aligned} \tag{6}$$

where S_{ij} – are the stress tensor deviator components,σ_{kk} – is the first invariant of the sress tensor, $\alpha_c(T)$ – is the coefficients of thermal expansion.

To define the tensor variables e^*_{ij} , ε^*_{kk} we construct the kinetic equations

$$\begin{aligned}\dot{e}^*_{ij} &= A_a \exp\left[-\frac{U_a - \frac{\mu_2}{2}(e_{ij}-e^*_{ij})(e_{ij}-e^*_{ij})}{T_k}\right](e_{ij}-e^*_{ij})\\ \dot{\varepsilon}^*_{kk} &= A_b \exp\left[-\frac{U_b - \frac{k_2}{2}(\varepsilon_{kk}-\varepsilon^*_{kk})}{T_k}\right](\varepsilon_{kk}-\varepsilon^*_{kk}),\end{aligned} \tag{7}$$

Where U_a, U_b– are the variables characterizing the activation energy of the polymer network segment mobility by the physical bonds of intermolecular interactions, T_k – is the energetic temperature, and A_a , A_b – are the exponential factors characterizing the quantity that is inversely proportional to the characteristic time of transition of the intermolecular bonds into the equilibrium state.

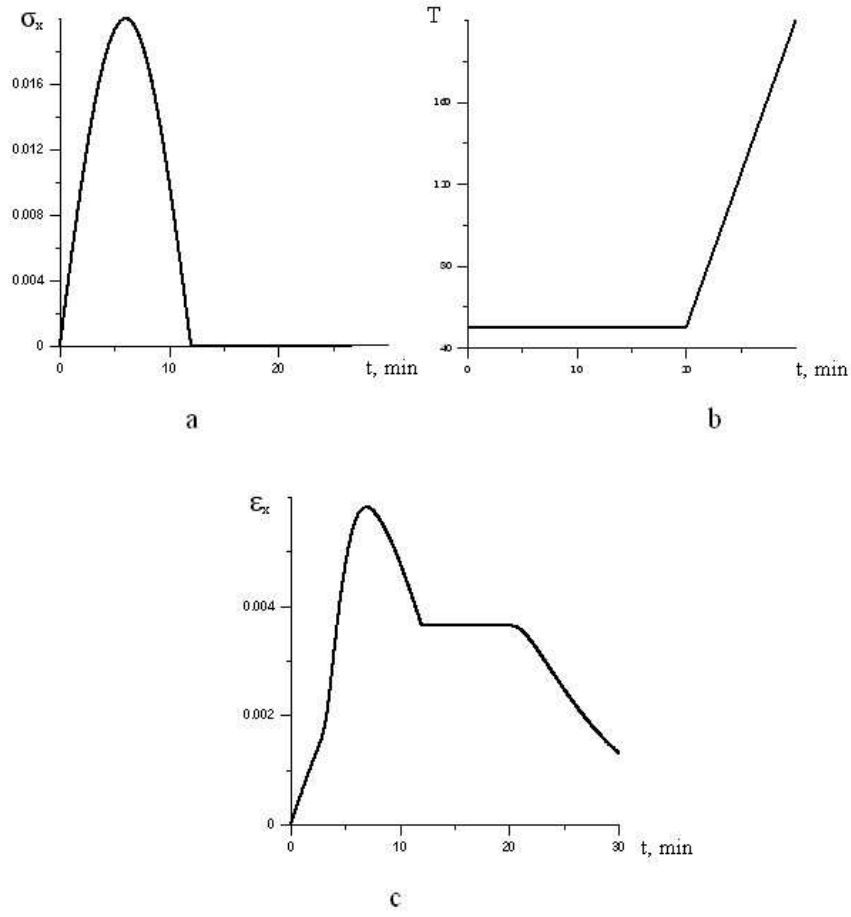


Figure 1: Results of modeling the thermo-mechanical behavior of the amorphous components of the polymer in the uniaxial stress state.

Using such terms as “activation energy of physical bonds of intermolecular interactions”, “characteristic time of transition of intermolecular bonds into the equilibrium state”, we realize that all these parameters are phenomenological and responsible for the corresponding macrolevel processes of the behavior of the amorphous component of the polymer material.

The proposed system of constitutive equations can be used to describe the peculiarities of the thermo-mechanical behavior of the amorphous component of polymers and to study the influence of these specific features on the behavior of the two-component system during the process of crystallization and after its completion. The results of numerical experiments carried out to investigate

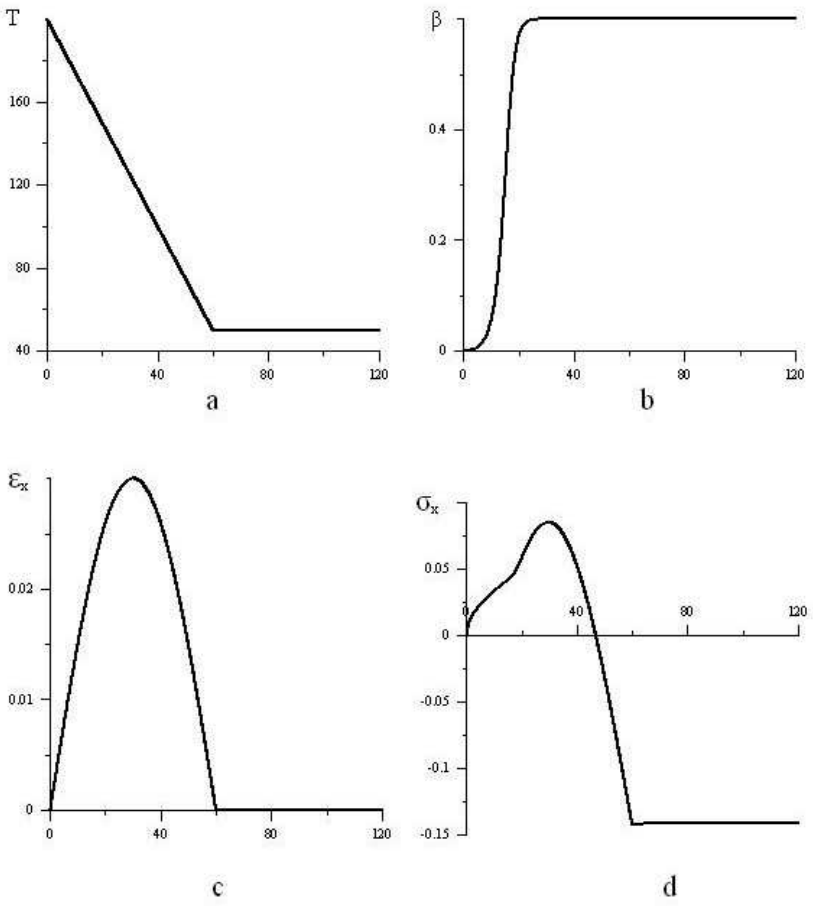


Figure 2: Occurrence of residual stresses in a two-phase medium due to crystallization.

different uniform stress-strain states demonstrate the potential of the developed constitutive equations for description of some thermo-mechanical effects observed in materials under relaxation and phase transitions.

Figure 1 presents the results of modeling the thermo-mechanical behavior of the amorphous components of the polymer in the uniaxial stress state. The character of change in stress $\sigma_x = \sigma_x(t)$ is prescribed, all other components are taken to be equal to zero. Temperature variations are prescribed under conditions of force loading. The analysis of the above physical relations and kinetic equations provides the non-zero components of the strain tensor. Hereafter we use the stress components reduced to the dimensionless form after dividing them by the modulus value μ_1. The energy temperature T_k is prescribed as a linear function of temperature. To perform a calculation, the following values of constant have been used. $\mu_1 = 1; \mu_2 = 5; k_1 = 4,667; k_2 = 93,33; U_a = 1,0 \cdot 10^{-5}; U_b = 1,0 \cdot 10^{-3}$; $A_a = 1,0c^{-1}$; $A_b = 0,1c^{-1}$.

The time dependence of the given stress value is presented in Figure 1a. Figure 1b illustrates the character of temperature variation. Figure 1c presents the diagram showing deformation changes, as the response to the total (force and temperature) action, and illustrates the effects of "freezing" an "defrosting" of residual deformations.

Figure 2 demonstrates the occurrence of residual stresses in a two-phase medium due to crystallization. Unlike the above, the external action in this case is prescribed by time variations in deformation $\varepsilon_x(t)$ and temperature, and the response is a normal stress component $\sigma_x = \sigma_x(t)$. Figure 1a presents a diagram showing temperature variations. Figure 1b gives a relevant diagram illustrating how the degree of crystallization changes during the cooling stage. Figure 1d shows stress variations at a prescribed change of deformation (Fig.1c) in the case of a phase transition. Phase transformations that take place during the deformation process give rise to compressive

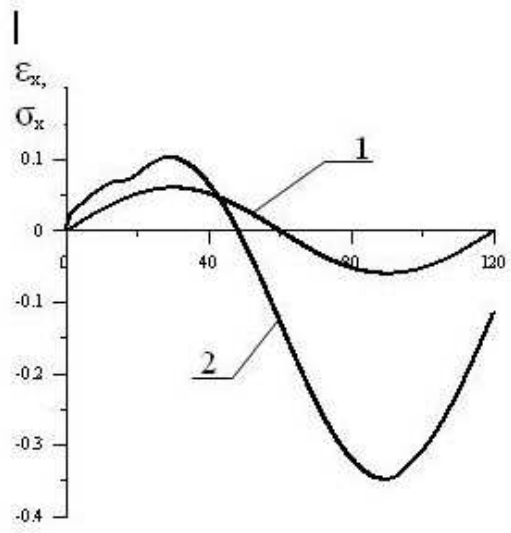


Figure 3: Appearance of the phase shift between the values of stress (curve 2) and strain (curve 1) after the completion of crystallization at a prescribed change in deformation $\varepsilon_x(t)$ under the periodic law.

residual stresses.

Figure 3 shows the appearance of the phase shift between the values of stress (curve 2) and strain (curve 1) after the completion of crystallization at a prescribed change in deformation $\varepsilon_x(t)$ under the periodic law. The character of variations in temperature and crystallization degree is assumed to be similar to that of the previous example.

Additionally, the approach proposed in this study can be used to describe some other distinguishing features of the behavior of amorphous-crystalline polymers within a wide temperature range, including the intervals of high elastic and glass transition states of the amorphous phase.

Acknowledgements

The work has been supported by the Russian Foundation for Basic Research (grant No 10-01-96032).

References

[1] Malkin A.Ya., Begishev V.P..Chemical formation of polymers. M.: Chemistry, 1991. 240 p.

[2] Begishev V.P.,Shadrin O.A., Shardakov I.N On approach to definition of residual stresses in polymer structures: Proceedings of All-Russia symposium in residual stresses and control methods. M.: 1982. P. 87-90.

[3] Malkin A.Ya., Begishev V.P.., Shardakov I.N., Shadrin O.A.,Bolgov S.A. Residual stresses caused by crystallization of molten polymer // High-molecular compounds. 1987. V. XXIX A. N 9. P. 1992-1999.

[4] Begishev V., Matveyenko V., Trufanov N., Shardakov I. Simulation of thermomechanical behavior of polymer and polymer base composites during vitrification and crystallization. Int. symp. “Advances in Structured and Heterogeneous Continua”. Abstracts. Moskow, Russia, 1993, p. 98.

[5] Begishev V.P., Matveyenko V.P., Pistsov N.V., Shardakov I.N. Simulation of thermomechanical behavior of polymer materials in the process of crystallization. Proceedings of the First Int. symp. "Thermal Stresses'95". Shizuoka university, Hamamatsu, Japan. 1995, pp. 537-540.

[6] Begishev V.P., Matveyenko V.P., Pistsov N.V., Shardakov I.N. Simulation of thermomechanical processes in crystallizing polymer. // Solid mechanics N 4 1997. P. 120-132.

Lyudmila A.Golotina, 1., Ak. Korolev str., Perm, Russia

Contact problem for elastic wedge strengthened by rigid inclusion

Vahram N. Hakobyan
vhakobyan@sci.am

Abstract

The contact problem for two similar symmetrically located smooth punches and elastic wedge, which is strengthened by absolutely rigid thin inclusion on some section of its midline, is considered. The interaction of punches with inclusion depending on distance of punches and inclusion from wedge vertex is researched. In general case, this problem mathematically is formulated as the system of two singular integral equations of the first-kind, which is solved by the method of Chebyshev orthogonal polynomials. The special cases of this problem are considered. In two cases the close solutions are obtained.

1 The statement of problem and solution in the general case

The elastic wedge with angle 2α is considered in polar coordinate system, the origin coincides with vertex of wedge and the line $\varphi = 0$ coincides with the midline of wedge. The wedge is strengthened by the absolutely rigid thin inclusion in section $[a_1, b_1]$ and it is deformed by two smooth punches symmetrically situated on wedge sides $\varphi = -\alpha$ and $\varphi = \alpha$. It is required to find the stresses acting under the punches and on the junction line of rigid inclusion with the wedge, as well as stress intensity factor at the end-points of punches and inclusion. Taking into account the symmetry relatively $\varphi = 0$ line only one half of the wedge, occupying the region $D = \{0 \le \varphi \le \alpha\,;\, 0 \le r < \infty\}$, is considered. The following boundary conditions take place in this region:

$$\begin{array}{cc} u_\varphi(r,0) = \tau_{r\varphi}(r,\alpha) = 0 & (0 < r < \infty)\,; \\ \tau_{r\varphi}(r,0) = 0 & (0 < r < a_1; b_1 < r < \infty)\,; \\ \sigma_\varphi(r,\alpha) = 0 & (0 < r < a_2; b_2 < r < \infty)\,; \\ u_r(r,0) = const & (a_1 < r < b_1)\,; \\ u_\varphi(r,\alpha) = f(r) - \delta & (a_2 < r < b_2)\,. \end{array} \tag{1}$$

Here, $u_\varphi(r,\varphi)$and $u_r(r,\varphi)$ are the components of wedge points displacements, satisfying Lame equations and connected with the stress components $\sigma_\varphi(r,\varphi)$and $\tau_{r\varphi}(r,\varphi)$ by well-known Hooke's law, a_2 and b_2 are the end-points of punch, $f(r)$ is the known function, describing the base of punch, and δ is the rigid displacement of punch. In order to construct the solution of the mixed boundary-value problem, first of all radial displacements of points $\varphi = 0$ line and normal displacements of points $\varphi = \alpha$ will be expressed in unknown contact normal stresses $q(r)$, acting under the punch, and in shearing stresses $\tau(r)$, acting in splice line of inclusion with wedge. Solving this auxiliary problem by using Mellin's generalized integral transform and satisfying to the last two conditions (1), previously differentiated by r, the following system of singular integral equations of the first-

kind will be obtained for determination of contact stresses $\tau(r)$ and $q(r)$.

$$\begin{aligned}
&\vartheta_1 \int_{a_1}^{b_1} \left[\frac{1}{\ln\xi - \ln r} + K_{11}\left(\ln(\xi/r)\right)\right] \tau(\xi)\, d\xi - \int_{a_1}^{b_1} K_{12}\left(\ln(\xi/r)\right) q(\xi)\, d\xi = 0 \\
&\qquad\qquad (a_1 < r < b_1) \\
&\vartheta_2 \int_{a_2}^{b_2} \left[\frac{1}{\ln\xi - \ln r} + K_{22}\left(\ln\xi/r\right)\right] q(\xi)\, d\xi + \int_{a_1}^{b_1} K_{21}\left(\ln\xi/r\right) \tau(\xi)\, d\xi = r f'(r) \\
&\qquad\qquad (a_2 < r < b_2)
\end{aligned} \tag{2}$$

Here, $K_{i,j}(z)$ $(i,j=1,2)$ are the regular functions with its first partial derivatives, the values of which are not shown.

$$\vartheta_2 = \frac{\chi_1}{2\pi\mu};\ \ \vartheta_1 = \frac{\chi(\lambda+\mu)}{2\pi\mu(\lambda+2\mu)};\ \ \chi = \frac{\lambda+3\mu}{\lambda+\mu};\ \ \chi_1 = \frac{\lambda+2\mu}{\lambda+\mu};$$

λ and μ - Lame constants.

At the same time the conditions of equilibrium of punches and inclusion, as well as conditions of smooth contact should be satisfied:

$$\int_{a_1}^{b_1} \tau(\xi)\, d\xi = 0\,; \int_{a_2}^{b_2} q(\xi)\, d\xi = P_0\,; \tag{3}$$

$$q(a_2) = q(b_2) = 0\,. \tag{4}$$

After determination of functions $\tau(r)$ and $q(r)$ it is not difficult to find contact stresses, acting under the inclusion, by the formula

$$\sigma_\varphi(r,0) = \int_{a_1}^{b_1} Q_1\left(\ln(r_0/r)\right) \tau(r_0)\, dr_0 + \int_{a_2}^{b_2} Q_2\left(\ln(r_0/r)\right) q(r_0)\, dr_0\,; \tag{5}$$

where

$$Q_1(t) = \frac{2}{\pi r} \int_0^\infty \frac{\mu sh^2(\alpha z) + (\lambda+\mu) z^2 \sin^2\alpha}{(\lambda+2\mu)\Delta(z)} \sin(zt)\, dz + \frac{2}{\pi r} \int_0^\infty \frac{z\sin^2\alpha}{\Delta(z)} \cos(zt)\, dz;$$

$$Q_2(t) = \frac{2}{\pi r} \int_0^\infty \frac{\cos\alpha sh(\alpha z) + z\sin\alpha ch(\alpha z)}{\Delta(z)} \cos(zt)\, dz.$$

In order to build the solution for system of integral equations (2), the new variables should be introduced by formulas $\xi = \exp(d_1 s + c_1)$ and $r = \exp(d_1 x + c_1)$ in first equation, and in second equation of this system by formulas $\xi = \exp(d_2 s + c_2)$, $r = \exp(d_2 x + c_2)$. Then, taking into account the notations

$$\begin{aligned}
&\varphi_1(x) = \frac{\tau\left[\exp(d_1 x + c_1)\right]}{\exp(-d_1 x - c_1) P_0};\ \ \varphi_2(x) = \frac{q\left[\exp(d_2 x + c_2)\right]}{\exp(-d_2 x - c_2) P_0}; \\
&F(x) = \frac{f'\left[\exp(d_2 x + c_2)\right]}{\exp(-d_2 x - c_2)\vartheta_2 P_0};\quad d_j = \ln\sqrt{b_j/a_j}\,;\quad c_j = \ln\sqrt{a_j b_j}\quad (j=1,2)\,.
\end{aligned} \tag{6}$$

The following system of singular integral equations of the first-kind is obtained:

$$\begin{cases} \int\limits_{-1}^{1}\left[\dfrac{1}{s-x}+d_1K_{11}\left(d_1\left(s-x\right)\right)\right]\varphi_1\left(s\right)ds- \\ \qquad\qquad -\dfrac{d_2}{\vartheta_1}\int\limits_{-1}^{1}K_{12}\left(d_2s-d_1x+c\right)\varphi_2\left(s\right)ds\ =0 \\ \int\limits_{-1}^{1}\left[\dfrac{1}{s-x}+d_2K_{22}\left(d_2\left(s-x\right)\right)\right]\varphi_2\left(s\right)ds+ \\ \qquad\qquad +\dfrac{d_1}{\vartheta_2}\int\limits_{-1}^{1}K_{21}\left(d_1s-d_2x-c\right)\varphi_1\left(s\right)ds\ =F\left(x\right)\ . \\ \qquad\qquad\qquad\

From first two conditions (8) and using the orthogonality of Chebyshev polynomials the following is found:

$$X_0^{(1)} = 0; \quad X_0^{(2)} = \frac{1}{\pi} d_2 \,; \tag{11}$$

and the last conditions (8) reduce to relations:

$$\sum_{n=0}^{\infty} X_n^{(2)} = 0; \quad \sum_{n=0}^{\infty} (-1)^n X_n^{(2)} = 0 \,; \tag{12}$$

Thus, the closed system of equations, composed of the system of infinite algebraic equations (10) and equations (12) is obtained for the determination of expansion coefficients of contact stresses ($j = 1, 2 \,; n = 1, 2, ...$) and size a_2, b_2 of contact zone.

2 Some special cases.

In this section some particular cases of the above mentioned problem are considered.

a) At first, the case, when $\alpha = \pi/2$, i.e. the elastic half-plane with thin absolutely rigid inclusion in region (a_1, b_1) of midline is deformed by two same smooth punches symmetrically situated in regard to origin. In this case the equations (2) become to the following:

$$\begin{gathered}
\int\limits_{a_1}^{b_1} \left[\frac{1}{\xi - r} + \frac{1 - 2\chi_1^2/\chi}{\xi + r} + \frac{2\xi\,(\xi - r)}{\chi\,(\xi + r)^3} \right] \tau\,(\xi)\, d\xi + \\
+ \frac{2}{\vartheta_1} \int\limits_{a_2}^{b_2} \left[\frac{\vartheta_2 r}{\xi^2 + r^2} - \frac{r\xi^2}{\mu\pi \left(\xi^2 + r^2\right)^2} \right] q\,(\xi)\, d\xi = 0; \quad (a_1 < r < b_1) \,; \\
\int\limits_{a_2}^{b_2} \left[\frac{1}{\xi - r} - \frac{1}{\xi + r} \right] q\,(\xi)\, d\xi - \\
- \frac{2}{\vartheta_2} \int\limits_{a_1}^{b_1} \left[\frac{\vartheta_2 r}{\xi^2 + r^2} + \frac{r\xi^2}{\mu\pi \left(\xi^2 + r^2\right)^2} \right] \tau\,(\xi)\, d\xi = f'\,(r)\,/\vartheta_2; \quad (a_2 < r < b_2) \,.
\end{gathered} \tag{13}$$

After representation the system of singular integral equations in interval $(-1, 1)$, using the change of variable $\xi = s\,(b_1 - a_1)\,/2 + (b_1 + a_1)\,/2$, in first equation and $\xi = s\,(b_2 - a_2)\,/2 + (b_2 + a_2)\,/2$, $r = x\,(b_2 - a_2)\,/2 + (b_2 + a_2)\,/2$ in second equation, as well as after introduction of notations

$$\frac{\varphi_1\,(x)\, 2P_0}{b_2 - a_2} = \tau\left(\frac{x\,(b_1 - a_1) + (b_1 + a_1)}{2} \right); \; \frac{\varphi_2\,(x)\, 2P_0}{b_2 - a_2} = q\left(\frac{x\,(b_1 - a_1) + (b_1 + a_1)}{2} \right);$$

$$K_{11}\,(x, s) = \frac{1 - 2\chi_1^2/\chi}{x + s + 2\lambda_1} + \frac{2\,(s - x)\,(s + \lambda_1)}{\chi\,(x + s + 2\lambda_1)^3}; K_{22}\,(x, s) = -\frac{1}{x + s + 2\lambda_3};$$

$$K_{12}\,(x, s) = \frac{2\lambda_2\vartheta_2}{\vartheta_1} \left\{ \frac{(x + \lambda_1)}{(s + \lambda_3)^2 + \lambda_2^2\,(x + \lambda_1)^2} - \frac{1}{\pi\mu\vartheta_2} \frac{(x + \lambda_1)\,(s + \lambda_3)^2}{\left[(s + \lambda_3)^2 + \lambda_2^2\,(x + \lambda_1)^2\right]^2} \right\};$$

$$K_{21}\,(x, s) = -\frac{2\,(x + \lambda_3)}{(x + \lambda_3)^2 + \lambda_2^2\,(s + \lambda_1)^2} - \frac{2\lambda_2^2}{\pi\mu\vartheta_2} \frac{(x + \lambda_3)\,(s + \lambda_1)^2}{\left[(x + \lambda_3)^2 + \lambda_2^2\,(s + \lambda_1)^2\right]^2}; F_1\,(x) = 0;$$

$$\frac{2\vartheta_2 P_0 F_2\,(x)}{b_2 - a_2} = f'\left(\frac{x\,(b_2 - a_2) + (b_2 + a_2)}{2} \right); \lambda_1 = \frac{b_1 + a_1}{b_1 - a_1}; \lambda_2 = \frac{b_1 - a_1}{b_2 - a_2}; \lambda_3 = \frac{b_2 + a_2}{b_2 - a_2}$$

the following system of singular integral equations of the fist kind is obtained:

$$\sum_{j=1}^{2}\int_{-1}^{1}\left[\frac{\delta_{i,j}}{s-x}+K_{i,j}(x,s)\right]\varphi_j(s)\,ds=F_i(x)\,(i=1.2\,;\,-1<x<1) \tag{14}$$

At that the conditions (3) and (5) become

$$\int_{-1}^{1}\varphi_1(s)\,ds=0;\qquad \int_{-1}^{1}\varphi_2(s)\,ds=1;\varphi_2(\pm1)=0. \tag{15}$$

Then, after representation of functions $\varphi_j(x)\,(j=1,2)$ in expansion (9), and using the general procedure, the quasi-completely regular system of (10) – type linear algebraic equations is obtained, where

$$A_{m,n}^{(j,i)}=\frac{2}{\pi^2}\int_{-1}^{1}U_{m-1}(x)\sqrt{1-x^2}dx\int_{-1}^{1}K_{j,i}(x,s)\frac{T_n(s)}{\sqrt{1-s^2}}ds;c_m^{(j)}=a_m^{(j)}-\sum_{i=1}^{2}A_{m,0}^{(j,i)}X_0^{(i)};$$

$$a_m^{(1)}=0;\ a_m^{(2)}=-\frac{2}{\pi^2}\int_{-1}^{1}F_2(x)\sqrt{1-x^2}U_{m-1}(x)\,dx;\ (i,j=1,2\,;\,m,n=1,2,...)\ .$$

From first two conditions (15) $X_0^{(1)}=0$; $X_0^{(2)}=1/\pi$ be found. The next two conditions (15), which will bring to equations (12), will be used for determination the values for a_2 and b_2. The numerical calculations are carried out when $f(r)=0$, $\lambda_2=1$, $\nu=0.3$ and $b_2-a_2=b_1-a_1=2$, i.e. punches and inclusion have the same length. The results of calculations are shown in Tables. 1 and 2. It becomes obvious from Table 1 that the absolute value of shearing stress intensity factors at the end-points of inclusion $K_{II}(a_1)$and $K_{II}(b_1)$increase while the inclusion is moving off the bound of half-plane, and then, they decrease, tending to zero. As expected, $K_{II}(a_1)$practically become zero while the inclusion is situated sufficiently near the bound of half-plane. The normal stress intensity factors under the punches $K_I(a_2)$ and $K_I(b_2)$ remain almost unchanged. From Table 2 it becomes clear, while the distance between punches increases the contact stress intensity factors under the punches increase at the near end-points of contact zones, and decrease at farther end-points, tending to the same constant value, describing the distribution of contact stress under the one punch. The shearing stresses on the banks of inclusion tend to zero, while punches move off each other. But there are two defined values of distance between the punches for which the stress intensity factor becomes zero at the one end of inclusion.

Table 6: $\lambda_3=1.5$

λ_1	$K_{II}(a_1)$	$K_{II}(b_1)$	$K_{II}(a_2)$	$K_{II}(b_2)$
1.2	0.00073	-0.05929	0.11547	0.29422
1.5	0.02045	-0.06715	0.11243	0.29587
2	0.05077	-0.07584	0.11409	0.29780
2.5	0.06852	-0.07982	0.11821	0.29827
3	0.07777	-0.08046	0.12169	0.29769
5	0.07689	-0.06979	0.12787	0.29368
8	0.05715	-0.05187	0.12953	0.29136
20	0.02463	-0.02347	0.12994	0.29060
50	0.00987	-0.00968	0.12995	0.29058
150	0.00328	-0.00326	0.12995	0.29058
1000	0.00049	-0.00049	0.12995	0.29058

b) In second case, it is assumed that $\alpha=\pi$, $a_1=0$, and there are no punches, and the force with value $2\tau_0$ is acting at the end-point of inclusion $r=0$.

In other words, the stress state of elastic plane with thin absolutely rigid inclusion, at the one end of which the semi-infinite crack exists, is investigated.

Table 7: $\lambda_1 = 1.5$

λ_3	$K_{II}(a_1)$	$K_{II}(b_1)$	$K_{II}(a_2)$	$K_{II}(b_2)$
1.2	0.04730	-0.08457	0.06522	0.315027
1.5	0.02045	-0.06715	0.112427	0.295867
1.93	-0.00009	-0.04264	0.151029	0.27892
2	-0.00177	-0.03910	0.154998	0.27695
2.5	-0.00753	-0.01884	0.173745	0.266531
3	-0.00836	-0.00654	0.183849	0.259887
3.47	-0.00784	-0.00003	0.190029	0.255419
5	-0.00517	0.00604	0.20135	0.246548
8	-0.00238	0.00448	0.210544	0.238731
20	-0.00041	0.00095	0.21938	0.230637

In this case the only one integral equation of the following type is obtained:

$$\int_0^{b_1} \left[\frac{1}{\xi - r} + \lambda \frac{\sqrt{\xi / r}}{\xi - r} \right] \tau(\xi)\, d\xi = 0 \quad \left(\lambda = \frac{\chi}{\chi_1^2 - 1};\ 0 < r < b_1 \right). \tag{16}$$

This integral equation should be considered under the equilibrium condition for inclusion

$$\int_0^{b_1} \tau(\xi)\, d\xi = \tau_0. \tag{17}$$

In order to construct the closed solution of equation (16), the functions of complex variable $\Omega_j(z)$ $(j = 1, 2)$ should be considered:

$$\Omega_j(z) = \Phi_1(z) + (-1)^j\, i\sqrt{\lambda}\Phi_2(z) \tag{18}$$

$$\Phi_1(z) = \frac{1}{2\pi i} \int_0^{b_1} \frac{\tau(\xi)\, d\xi}{\xi - z};\ \Phi_2(z) = \frac{1}{2\pi i} \int_0^{b_1} \frac{\sqrt{\xi / z}\tau(\xi)\, d\xi}{\xi - z}; \tag{19}$$

Here, the one-valued analytical branch of function $\sqrt{z}$ should be chosen, which is positive on the positive half-axis $0 < x < \infty$.

Taking into account the properties of Cauchy-type integral [2], the functions $\Omega_j(z)$ $(j = 1, 2)$ are analytical in whole complex plane (z), cutting along the axis $0x$ to infinite interval $(-\infty, b_1)$.

It is not difficult to see that the values of these functions satisfy to the following relations on the upper and lower edges of the slit $\Omega_j^{\pm}(x)$ $(j = 1, 2)$ $(-\infty < x < b_1)$:

$$\begin{cases} \Omega_1^+(x) = \nu(x)\, \Omega_2^-(x) \\ \Omega_2^+(x) = \mu(x)\, \Omega_1^-(x) \end{cases} \qquad (-\infty < x < b_1); \tag{20}$$

here

$$\nu(x) = \begin{cases} 1 & x \in (-\infty, 0); \\ -\chi & x \in (0, b_1); \end{cases} \quad \mu(x) = \begin{cases} 1 & x \in (-\infty, 0); \\ -\chi^{-1} & x \in (0, b_1). \end{cases}$$

Then, taking into account the results of paper [3] it is not difficult to build the solution for problem (20):

$$\Omega_j(z) = \frac{C \left[\frac{\sqrt{b_1 - z} - \sqrt{b_1}}{\sqrt{b_1 - z} + \sqrt{b_1}} \right]^{-(-1)^j \beta i}}{\sqrt{z(z - b_1)}} \qquad \left(\beta = \frac{\ln \chi}{2\pi};\ j = 1, 2 \right). \tag{21}$$

Here, the branches of radicals having asymptotic for large values z are chosen:

$$\sqrt{z(z - b_1)} \cong z + o\left(z^{-1}\right);\ \left[\frac{\sqrt{b_1 - z} - \sqrt{b_1}}{\sqrt{b_1 - z} + \sqrt{b_1}} \right]^{(-1)^j \beta i} \cong 1 + o\left(z^{-1}\right); \tag{22}$$

Here, C is an unknown constant. Furthermore, there were the relations

$$\Omega_j^{\pm}(x) = \mp \frac{ci\left[\frac{\sqrt{b_1}-\sqrt{b_1-x}}{\sqrt{b_1}+\sqrt{b_1-x}}\right]^{\mp(-1)^j\beta i}}{\left(\sqrt{\chi}\right)^{(-1)^j}\sqrt{x\,(b_1-x)}} \qquad (0<x<b_1;\ j=1,2)\,. \tag{23}$$

In order to find the contact stresses $\tau(x)$, Plemelj-Sokhocki formulas should be considered

$$\tau(x) = \Phi_1^+(x) - \Phi_1^-(x) \qquad (0<x<b_1)\,. \tag{24}$$

After representation of function $\Phi_1(z)$ from (18) by functions $\Omega_j(z)$ $(j=1,2)$ and substitution into (24), as well as after some elementary transformations the following is obtained:

$$\tau(x) = \frac{C(\chi+1)\cos\left[\beta\ln\left(\frac{\sqrt{b_1}-\sqrt{b_1-x}}{\sqrt{b_1}+\sqrt{b_1-x}}\right)\right]}{i\sqrt{\chi}\sqrt{x\,(b_1-x)}} \qquad (0<x<b_1)\,. \tag{25}$$

Based on Cauchy-type integral behavior at infinity, from condition (17) the following can be written:

$$\Phi_1(z) \cong -\frac{\tau_0}{2\pi i z} + o\left(z^{-2}\right) \qquad z\to\infty\,. \tag{26}$$

On the other hand, using $\Phi_1(z)$ functions representation by the functions $\Omega_j(z)$ $(j=1,2)$ and (21)

$$\Phi_1(z) \cong \frac{c}{z} + o\left(z^{-2}\right) \qquad z\to\infty\,. \tag{27}$$

Comparing the expressions (26) and (27) $C=-\tau_0/2\pi i$ is found. Finally, after substitution the constant C into (25), the expression for $\tau(x)$ is obtained:

$$\tau(x) = \frac{\tau_0(\chi+1)\cos\left[\beta\ln\left(\frac{\sqrt{b_1}-\sqrt{b_1-x}}{\sqrt{b_1}+\sqrt{b_1-x}}\right)\right]}{2\pi\sqrt{\chi}\sqrt{x\,(b_1-x)}} \qquad (0<x<b_1)\,. \tag{28}$$

For the determination of normal contact stresses, acting under the inclusion, from (5) the following expression is got:

$$\sigma_\varphi(r,0) = -\frac{\tau_0(\chi+1)\sin\left[\beta\ln\left(\frac{\sqrt{b_1}-\sqrt{b_1-r}}{\sqrt{b_1}+\sqrt{b_1-r}}\right)\right]}{2\pi\sqrt{\chi}\sqrt{r\,(b_1-r)}} \qquad (0<r<b_1)\,. \tag{29}$$

The obtained results are showing that the normal and shearing stresses have the root oscillating singularity in point $r=0$. The shearing stresses have common root singularity and normal stresses are finite and have the value:

$$\sigma_\varphi(b_1,0) = -\frac{\tau_0\beta(\chi+1)}{\pi\sqrt{\chi}\,b_1} \quad . \tag{30}$$

This fact is explained by the symmetry of the considered problem relatively to $0x$ axis. .

c) Finally, one more private case with close solution is considered. In this case it is assumed that there is no inclusion, $\alpha=\pi$ and $f(r)=0$, i.e. the stress state of plane with half-infinite slit is considered. The plane is deformed under the action of two punches with flat foundations symmetrically situated on the banks of slit.

$$\int_{a_2}^{b_2}\frac{\sqrt{\xi}q(\xi)}{\xi-r}d\xi = 0 \qquad (a_2<r<b_2)\,; \tag{31}$$

The solution of equation should be satisfied to second condition from (3). This solution is following:

$$q(r) = \frac{P_0\sqrt{b_2}}{2K(k)\sqrt{r\,(r-a_2)\,(b_2-r)}} \qquad (a_2<r<b_2)\,. \tag{32}$$

For the failure stresses $\sigma_\varphi(r,0)$ and stress intensity coefficient K_I at the end-point of slit $r=0$ from (5) the following expressions are obtained:

$$\sigma_\varphi(r,0) = -\frac{P_0\sqrt{b_2}}{2K(k)\sqrt{r(r+a_2)(b_2+r)}} \;;\; K_I = \frac{P_0}{2\sqrt{a_2}K(k)};\; \left(k=\sqrt{1-a_2/b_2}\right); \tag{33}$$

Here, $K(k)$ is the complete elliptic integral of first kind with module k. It becomes obvious from (33) that the intensity coefficient K_I is increased, when $a_2 \to 0$, i.e. the punches are near to end-point of slit.

References

[1] Arutyunyan N., Mkhitaryan S. Some contact problems for half-planes with partially bound elastic strip. Proceedings, Academy of Armenia, Mechanics, 1972, vol. 25, N2, pp.15-35.

[2] Muskhelishvili N. Some fundamental problems for mathematical theory of elasticity. Moscow, "Nauka", 1966, 708 p.

[3] Cherepanov G. Solution of one Riemann linear boundary-value problem for two functions and its application to some mixed problems of plane theory of elasticity. Applied Mathematics and Mechanics (PMM), 1962, vol.26, issue 5, pp.907-912.

Vahram N.Hakobyan, Institute of Mechanics, National Academy of Sciences, Armenia, Yerevan 0019, Baghramyan 24B ave.

Flexible macroscopic models for dense-fluid shockwaves: partitioning heat and work; delaying stress and heat flux; two-temperature thermal relaxation

Wm. G. Hoover Carol G. Hoover Francisco Uribe
hooverwilliam@yahoo.com hoover1carol@yahoo.com paco@xanum.uam.mx

Abstract

Macroscopic models which distinguish the longitudinal and transverse temperatures can provide improved descriptions of the microscopic shock structures as revealed by molecular dynamics simulations. Additionally, we can include three relaxation times in the models, two based on Maxwell's viscoelasticity and its Cattaneo-equation analog for heat flow, and a third thermal, based on the Krook-Boltzmann equation. This approach can replicate the observed lags of stress (which lags behind the strain rate) and heat flux (which lags behind the temperature gradient), as well as the eventual equilibration of the two temperatures. For profile stability the time lags cannot be too large. By partitioning the longitudinal and transverse contributions of work and heat and including a tensor heat conductivity and bulk viscosity, all the qualitative microscopic features of strong simple-fluid shockwave structures can be reproduced.

1 Properties of Dense–Fluid Shockwaves

Stationary shockwaves provide the simplest possible opportunity for the study of highly nonlinear transport in dense fluids. In the shock-centered steady-state coordinate frame, the nonequilibrium shock process converts an incoming steady stream of "cold" material into an outgoing stream of "hot" fluid. See Figure 1. Shockwave gradients can be huge, with strainrates in the terahertz range and correspondingly large pressure and temperature gradients, 10^{15} atmospheres/centimeter and 10^{12} kelvins/centimeter[1]. Despite the wildly irreversible nature of such a nonequilibrium conversion, so long as the shock is stationary the overall internal energy change, $E_H - E_C$, can be expressed in terms of the equilibrium pressures and volumes of the incoming and outgoing streams of fluid:

$$\Delta E = E_H - E_C = (P_H + P_C)(V_C - V_H)/2 \ .$$

In the steady-state coordinate frame centered on the shockwave (Figure 1), the incoming cold material, moving at the shock velocity u_s, is decelerated to $u_s - u_p$ by the shockfront, where u_p is the "particle", or "piston", velocity.

The Hugoniot relation for the energy change ΔE, just given, can be derived by eliminating the two velocities u_s and u_p from the three conservation equations for mass, momentum, and energy[2]. An alternative shock-creation mechanism, quite practical for computer simulation, uses the symmetric collision of two blocks of cold fluid. For problems with a nonzero initial pressure confining pistons are required. In either case the two blocks approach each other with velocities $\pm u_p$, and generate two mirror-image shockwaves identical in structure to those obtained with steady-state boundary conditions. See again Figure 1, as well as Figure 2, for the geometries of these two methods for generating shockwaves.

Over the last forty years a wide variety of atomistic shockwave simulations, based on molecular dynamics, have been carried out[3, 4, 5, 6, 7, 8, 9, 10]. These particle-based simulations established three interesting facts which simplify numerical treatments of shockwaves. First fact: the *boundary*

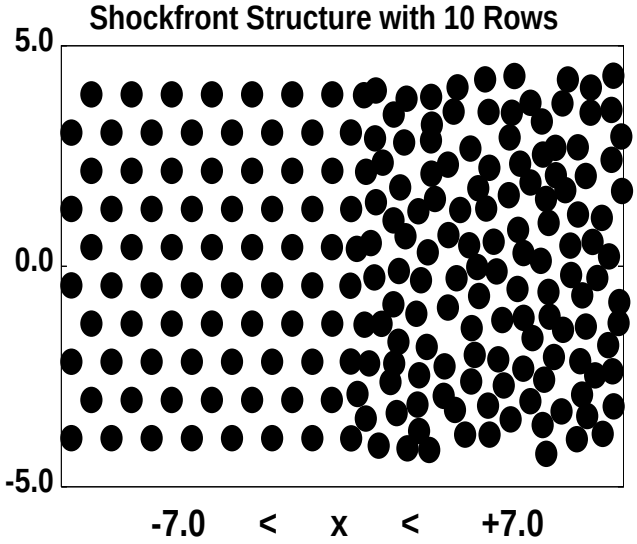


Figure 1: The steady flow shown here pictures cold material, moving to the right at speed u_s and decelerated by slower hot fluid, moving to the right at speed $u_s - u_p$, with u_s and u_p chosen to fix the shockwave location in space, $u_{wave} = 0$. An alternative way to generate such shockwaves is shown in Figure 2.

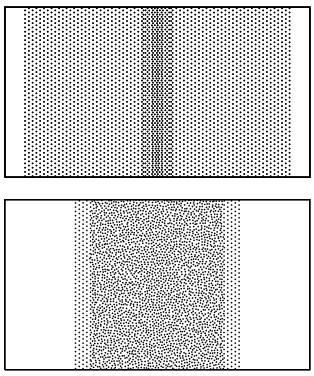


Figure 2: Here two identical blocks of zero-pressure material at $\pm u_p$ have collided with sufficient velocity to compress the fluid to twice the initial density. The two shockwaves at the interface between the moving cold material and the stationary hot fluid are separating at velocities $\pm(u_s - u_p)$. The forces between particles, here and in Figures 1, 3, and 4, are short-ranged repulsive forces derived from the pair potential $\phi = (10/\pi)(1 - r)^3$.

conditions enclosing the shockwave can be implemented easily because they are simply equilibrium states when viewed in a moving coordinate system. See again Figures 1 and 2. Second fact: shockwave thicknesses are indeed only a few mean free paths[4, 5, 11], as predicted for gases by numerical solutions of the Boltzmann equation[12, 13, 14, 15, 16, 17]. The small scale of shockwaves makes molecular dynamics simulations relatively simple to carry out. Third fact: one-dimensional shockwaves are stable[7], as shown in Figure 3. Stability means that it is sensible to measure and compute shockwave profiles in which density, velocity, and energy are all expressed as functions of a single longitudinal coordinate, here chosen to define the x axis.

In addition to these simplifying facts there are three more facts which complicate rather than simplify numerical treatments. They deserve more discussion and form the heart of the present work: fourth fact: temperature within the shockwave is a *tensor*, with different longitudinal and transverse values. Mott-Smith predicted the details of this complication for gases[13], by using an approximate bimodal velocity distribution (a spatially-varying linear combination of the cold and hot Maxwellian distributions). We discuss the meaning of "temperature" in the following Section II[7, 8, 9, 12, 13, 14, 18].

A fifth fact, discovered in the course of comparisons of atomistic simulations with continuum predictions, is that the nonlocality of atomistic interactions introduces an essential dependence of spatial averages on the averaging algorithm itself. Any continuum treatment which aims to describe two- or three-dimensional phenomena must come to grips with an appropriate choice of averaging algorithm. Lucy's one-, two-, and three-dimensional weighting functions used in smooth particle applied mechanics[19, 20, 21] provide a particularly appealing solution to the problem. Averaging is addressed in Section III.

Last, a sixth fact, discovered more recently, is that relaxation and lag are characteristic of shockwaves. Strong shockwaves display cause-and-effect relaxation, with the shear stress, $\sigma = (P_{yy} - P_{xx})/2$, responding to the strain rate $\dot{\epsilon} = (du/dx)$ and the heat flux Q_x responding to the temperature gradient ∇T only after noticeable delays. These observed delay times are of the order of the particle-particle collision time[9]. Lag, relaxation, and delay are addressed in Section IV.

Existing models for shockwave structure, such as the linear-transport Navier-Stokes equations[11, 22] or the nonlinear-transport Burnett equations[10, 15, 16, 17, 23], need to be improved to take these recent shock-structure observations into account. Delay has to be included in the models and temperature needs to have its longitudinal and transverse components treated separately. The present work is devoted to developing and exploring a comprehensive description of shock dynamics and developing the numerical techniques necessary to implement the new findings into continuum simulations.

Following these discussions of thermal anisotropy, spatial nonlocality, and relaxation, we introduce a well-posed continuum model incorporating all these ideas and illustrate a numerical method for solving particular special cases in Section V. Section VI contains a summary of our results and an assessment of the prospects for future progress.

2 Kinetic Temperature and its Measurement

Gibbs and Boltzmann related microscopic mechanics to macroscopic thermodynamics by showing that an ideal-gas thermometer[18] satisfied the Zeroth law of thermodynamics[24]. Two systems at thermal equilibrium with a Maxwell-Boltzmann ideal gas at the kinetic temperature

$$T_{gas} = T_{eq} \equiv \langle p_x^2/mk \rangle = \langle p_y^2/mk \rangle = \langle p_z^2/mk \rangle \ ,$$

are necessarily in thermal equilibrium with each other. Thus the ideal gas is a reliable thermometer and can be used to measure temperature in other gases, or in liquids, or in solids. Consider applying the ideal-gas definition of temperature to a steady, but nonequilibrium, shockwave. Then there are substantial coordinate-dependent disparities between the longitudinal and transverse kinetic temperatures,

$$\langle p_x^2/mk \rangle = T_{xx} \ ; \ \langle p_y^2/mk \rangle = T_{yy} \ .$$

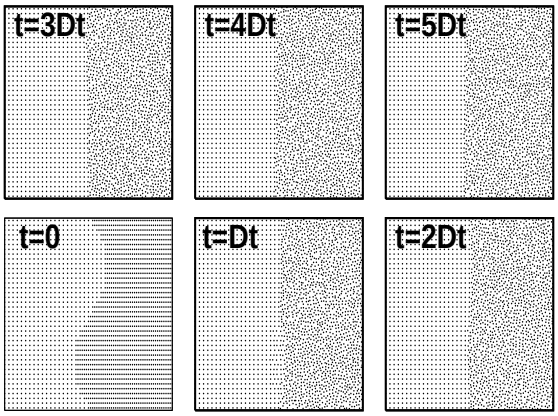


Figure 3: Six snapshots, equally spaced in time, showing the underdamped oscillation of a sinusoidal shockwave. The hot shocked fluid is at twice the density of the cold unshocked material.

These kinetic temperatures are velocity fluctuations about the local mean velocity so that in the comoving measurement frame the mean values of the momenta vanish:

$$u(x) = \langle \dot{x} \rangle \ ; \ p_x \equiv m(\dot{x} - \langle \dot{x} \rangle) = m(\dot{x} - u(x)) \ ; \ \langle p_x \rangle = \langle p_y \rangle = 0 \ .$$

The kinetic definitions for the nonequilibrium longitudinal and transverse temperatures arise naturally if one imagines "measuring" them, for particular degrees of freedom, by putting the nonequilibrium fluid into diagnostic contact with a comoving ideal-gas thermometer[18]. Such a thermometer is best thought of as a tiny sample of equilibrated gas, with the gas made up of very many very small hard particles. These thermometric particles undergo impulsive collisions with selected system degrees of freedom. If the ideal-gas particles are very small the temperature measurement doesn't change the dynamical state of the nonequilibrium fluid[18]. The ideal-gas nature of the thermometer makes it possible to analyze the collisions from the two-body standpoint of the Boltzmann equation. Hard-disk or hard-sphere interactions between the thermometer and the system change, on average, the total kinetic energy of a system particle if it deviates from the thermometer's temperature. If the thermometer particles are instead pictured as parallel hard cubes (parallel squares in two dimensions) with their orientations constrained, then the temperatures T_{xx} and T_{yy} can be independently distinguished.

The equilibrium velocity distributions, in the thermometer, are Maxwell-Boltzmann distributions. Kinetic theory shows[18] that such an ideal-gas thermometer transfers energy to/from a degree of freedom if the kinetic energy of that degree of freedom is less/greater than kT_{gas}. When this simple mechanical definition of temperature is used to analyze shockwave structure cause-and-effect relaxation and thermal anisotropy are revealed. Both these novel features need to be tackled and described by any realistic and comprehensive shockwave model.

3 Local Averages and Their Measurement

The temperature measurements just discussed require choosing a velocity for the thermometer. It must be *comoving* with the material in order to measure fluctuations. But exactly what is the velocity about which the fluctuations are measured? A useful answer can be found based on the weight functions used in smooth particle applied mechanics, "SPAM"[19, 20]. Lucy suggested that averages, at a fixed point in space, be computed using a weight function $w(r < h)$ centered there, with an arbitrary width h, and normalized, so that the integral of $w(r)$ over all space is unity. The simplest weight function is a polynomial chosen so that it has a smooth maximum at the origin, $r = 0$, and two continuous derivatives everywhere. These requirements guarantee that averages

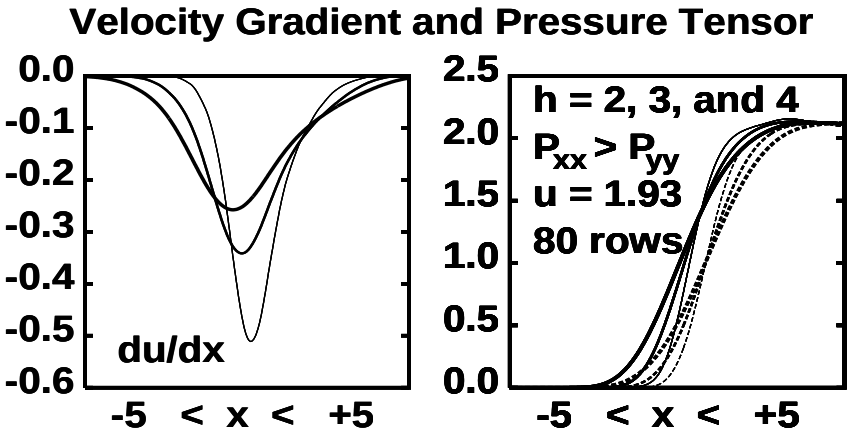


Figure 4: Dependence of the strainrate and the pressure tensor components P_{xx} and P_{yy} on the range of Lucy's weighting function $w(r < h)$ for the stationary shockwave shown in Figure 1 (but with a system width eight times larger than that of Figure 1). The widths of the curves in the Figure increase with increasing h.

computed with the weight function,

$$\langle F(r)\rangle \equiv \sum_j w_{rj}F_j / \sum_j w_{rj} \ ; \ w_{rj} \equiv w(|r - r_j|) \ ,$$

where $F(r)$ is a "field variable" like density, velocity, temperature, or stress, have also two continuous spatial derivatives. In the sums over nearby particles $\{j\}$ it is usual to choose the range h so that several dozen particles are included.

These conditions on the weight function are sufficient to determine its functional form:

$$w_{Lucy}(r < h) \propto [1 - 6(r/h)^2 + 8(r/h)^3 - 3(r/h)^4] \ .$$

Hardy's approach[21] to defining averages in shockwaves uses the same idea as Lucy's. Evidently h must be large enough to avoid wiggles in the resulting averages, while remaining sufficiently small for averages to be local and inexpensive to compute. In shockwaves a value for h of about three times the interparticle spacing is a good choice. Figure 4 shows explicitly the dependence of the pressure tensor and the velocity gradient averages on the range of the weight function.

When constructing continuum models designed to reproduce atomistic simulations it is essential to specify the spatial averaging technique. The fact that the resulting constitutive equation depends on h is simply a reminder that atomistic mechanics and continuum mechanics, though similar, are not the same.

4 Relaxation Models for Stress and Heat Flux

4.1 Maxwell's Model and its Extension to Heat Flux

Maxwell modeled the stress relaxation characteristic of viscoelastic fluids by introducing a stress relaxation time τ_σ:

$$\sigma + \tau_\sigma \dot{\sigma} = \eta\dot{\epsilon} \ .$$

In the shockwave problem η is the shear viscosity and $\dot{\epsilon}$ is the strainrate, (du/dx). Both time derivatives, indicated by the superior dots, are comoving with the fluid. In the absence of relaxation, $\tau_\sigma = 0$, Maxwell's fluid model reduces to the usual Newtonian viscous incompressible

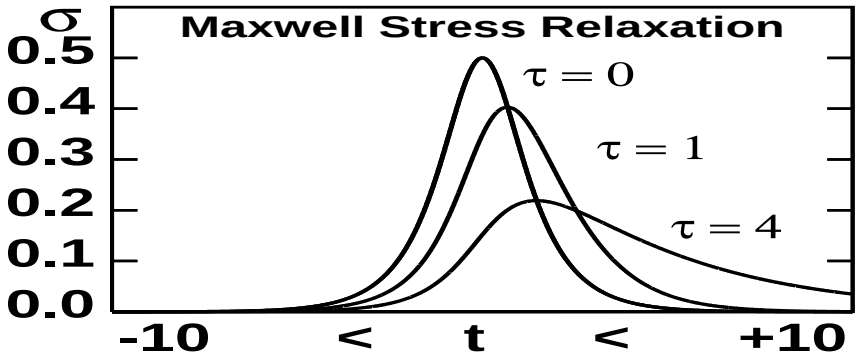


Figure 5: Delayed stress σ in response to the strain rate $1/[e^{-t} + e^{+t}]$ with unit viscosity, $\eta = 1$. Maxwell's relaxation time τ controls the stress response: $\sigma + \tau\dot{\sigma} = \eta\dot{\epsilon}$.

fluid, with shear stress σ proportional to the instantaneous value of $\dot{\epsilon}$. In the absence of any imposed strainrate ($\dot{\epsilon} = 0$) the initial stress decays with a characteristic relaxation time τ_σ. For a delta-function strain rate, at $t = 0$, the stress decays exponentially from its initial value:

$$\dot{\epsilon} = \delta(t = 0) \longrightarrow \sigma = (\eta/\tau)e^{-t/\tau} \ .$$

For a relatively-simple case, with $\eta = \tau = 1$, and a localized strain rate, like that in the Landau-Lifshitz description of a weak shock[2]:

$$\dot{\epsilon} = \frac{1}{e^{-t} + e^{+t}} \ ,$$

Maxwell's model has an analytic solution:

$$\sigma(t) = e^{-t} \ln \sqrt{1 + e^{+2t}} \ .$$

Figure 5 illustrates the stress response for the Newtonian case $\tau = 0$, and for two Maxwellian relaxation times, $\tau_\sigma = 1$ and $\tau_\sigma = 4$. Recent molecular dynamics shockwave simulations have shown that both stress and heat flux exhibit delayed responses[9].

Exactly the same ideas can be, and have been[25], applied to heat flux. If we introduce the relaxation time τ_Q into Fourier's law for heat flow, the result is the Cattaneo equation:

$$Q + \tau_Q \dot{Q} = -\kappa \nabla T \ ,$$

and the heat flux lags behind the temperature gradient by a time of the order of τ.

On physical grounds the time derivative here is again comoving with the fluid. The Cattaneo equation describes heat flux and predicts its decay, just as did Maxwell's formulation of stress decay:

$$\nabla T \propto \frac{1}{e^{-t} + e^{+t}} \longrightarrow Q(t) \propto -e^{-t} \ln \sqrt{1 + e^{+2t}} \ .$$

In the following Section we illustrate how to incorporate these relaxation effects for stress and heat flux into a simple dense-fluid shockwave model.

4.2 Krook-Boltzmann Thermal Relaxation

The Boltzmann equation[12] models the dynamics of a dilute gas in which the gas particles undergo occasional two-body collisions. The evolution of the velocity distribution function, $f(p, r, t)$ for the

phase-space density of particles with momentum p at location r at time t, can be approximated by an exponential relaxation toward equilibrium:

$$(df/dt) \equiv [f_{eq} - f]/\tau \longleftrightarrow f + \tau(df/dt) = f_{eq} \ .$$

This approximate "Krook-Boltzmann" equation has exactly the same form as do the Maxwell and Cattaneo relaxation equations. Here the relaxation time τ defined by this approximate equation is of the order of the mean collision time. Because two-body "conservative" collisions conserve mass, momentum, and energy, the equilibrium distribution, toward which f relaxes, necessarily has the same density, stream velocity, and energy, as does the nonequilibrium distribution f.

Shockwaves convert macroscopic longitudinal kinetic energy into microscopic "thermal" internal energy,

$$\Delta u^2/2 \longrightarrow \Delta e \ ,$$

through collisions, so that it is reasonable to expect shockwave stresses and temperatures to relax and equilibrate in a time of order the collision time τ. We include these delay and relaxation effects in the macroscopic model formulated in the next Section.

5 Formulation of a Macroscopic Model

Any solution of the continuum evolution equations,

$$\dot{\rho} = -\rho \nabla \cdot u \ ; \ \rho \dot{u} = -\nabla \cdot P \ ; \ \rho \dot{e} = -\nabla u : P - \nabla \cdot Q \ ,$$

requires constitutive models giving the pressure tensor P and heat flux Q in terms of the underlying variables $\{ \ \rho, u, e \ \}$, the density, velocity, and energy per unit mass. For completeness, in view of the relaxational results from molecular dynamics simulations, we must include separate tensor temperature components, T_{xx} and T_{yy}, in the list of state variables. In a gas the difference is simply related to the pressure tensor:

$$(T_{xx} - T_{yy}) = (P_{xx} - P_{yy})/(\rho k) \ ,$$

where k is Boltzmann's constant per unit mass.

In a dense fluid, the potential contribution to anisotropicity is comparable to the kinetic contribution[26]. A semiquantitative description of the potential part of the shear stress results if the equilibrium fluid structure is sheared, at the strainrate $\dot{\epsilon}$, for the Maxwell relaxation time τ_σ. The shear distortion of the pair distribution function in dense fluids has been studied experimentally[27] and modeled with molecular dynamics[26]. In both cases Maxwell's relaxation provides a good description of the potential contribution to the shear stress. Thus the gas-phase description of shear anisotropy must be modified in order to describe dense fluids.

To solve this problem we choose to separate the work and heat contributing to energy change into separate longitudinal and transverse parts. The simplest choice is a time-independent division of work and heat into longitudinal and transverse parts:

$$-\alpha \nabla u : P \longrightarrow \Delta T_{xx} \ ; \ -(1-\alpha) \nabla u : P \longrightarrow \Delta T_{yy} \ ;$$

$$-\beta \nabla \cdot Q \longrightarrow \Delta T_{xx} \ ; \ -(1-\beta) \nabla \cdot Q \longrightarrow \Delta T_{yy} \ .$$

The Navier-Stokes equations correspond to the choice $\alpha = \beta = 1/2$. In a shockwave, where the kinetic energy is initially longitudinal, we would expect instead $\alpha \simeq \beta \simeq 1$.

To explore the consequences of this division we consider in what follows a simple van der Waals model, with the energy and equilibrium pressure expressed as sums of density-dependent and temperature-dependent contributions. A slightly more flexible model[8] can be based on Grüneisen's separation of the energy and pressure into corresponding "cold" and "thermal" parts.

Away from equilibrium we include Maxwell's delayed viscous response in the pressure tensor. For a two-dimensional fluid undergoing uniaxial compression and with shear viscosity η and vanishing bulk viscosity, we have:

$$P_{xx} = P_{\rm eq} - \sigma \ ; \ P_{yy} = P_{\rm eq} + \sigma \ ; \ \sigma + \tau_\sigma \dot{\sigma} = \eta (du/dx) \ .$$

The stress relaxation time τ_σ describes the delay in the response of the shear stress σ to the strainrate $\dot{\epsilon} = (du/dx)$.

If the longitudinal and transverse temperatures are constrained to differ, we would expect the stationary nonequilibrium heat flux vector to obey a tensor form of Fourier's law:

$$Q_x = -\kappa_{xx}(dT_{xx}/dx) - \kappa_{yy}(dT_{yy}/dx) \ .$$

In the shockwave problem the effects of delay and eventual equilibration both need to be included. For simplicity we add on corresponding delays and thermal relaxation to the continuum evolution equations for the heat flux and the temperatures:

$$\dot{Q}_x \supset -Q_x/\tau_Q \ ; \ \dot{T}_{xx} \supset (T_{yy} - T_{xx})/\tau_T \ ; \ \dot{T}_{yy} \supset (T_{xx} - T_{yy})/\tau_T \ .$$

To model a dense N-particle van der Waals fluid, as opposed to a dilute gas, we approximate the potential part of the thermal energy by setting it equal to the kinetic part:

$$E_\Phi - E_{\rm Cold} \simeq E_K = Nk(T_{xx} + T_{yy})/2 \ \longrightarrow E_{\rm Thermal} = Nk(T_{xx} + T_{yy}) \ .$$

The motivation for studying such simple continuum models derives from the results of molecular dynamics simulations of stationary shockwaves[8, 9, 10]. Just as in the continuum case, these microscopic molecular dynamics simulations conserve mass, momentum, and energy, so that the stationary fluxes of these quantities,

$$\rho u \ , \ P_{xx} + \rho u^2 \ ; \ \rho u[e + (P_{xx}/\rho) + (u^2/2)] + Q_x \ ,$$

are constant throughout the flow. These simulations show further that both the stress and heat flux lag behind the strainrate and temperature gradient. The lags are physically reasonable from the collisional cause-and-effect standpoint.

Newton's viscosity and Fourier's heat conduction both describe *instantaneous* relationships. Taken literally, these two linear laws imply that the stress σ and heat flux Q respond instantaneously, and supersonically, to the strainrate $\dot{\epsilon}$ and temperature gradient ∇T.

Certainly such an instantaneous response is impossible. If we imagine reversing a time-reversible Newtonian motion of the shock process, another apparent shortcoming of the Navier-Stokes formulation is revealed. Newton's and Fourier's laws,

$$\sigma \propto \dot{\epsilon} \ ; \ Q_x \propto -(dT/dx) \ ,$$

if applied to a time-reversible flow, imply that the stress changes sign (as $\dot{\epsilon}$ changes sign when the motion is reversed) while the heat flux does not (as the temperature gradient has no time-dependence). Both conclusions are inconsistent with time-reversible Newtonian dynamics.

A detailed atomistic analysis of the pressure tensor and the heat flux vector[24] shows that these functions are respectively even and odd functions of time, so that Newton's and Fourier's ideas are necessarily inexact as they lack the proper delay time inherent in interparticle collisions. Lacking a more fundamental approach to time-reversible irreversibility, we seek to learn more by exploring explicitly the irreversible nature of continuum models.

6 Solutions: van der Waals' Shockwave Model

A one-dimensional "staggered grid", with density evaluated within N_c cells of length dx, bounded by $N_n = N_c + 1$ nodes, and with the remaining long list of time-dependent variables $\{u, e, T_{xx}, T_{yy}, \sigma, Q\}$ given at the nodes, provides a basis for an iterative solution of the continuum equations[10, 28]. Our assumption relating the energy change to the changes in the two temperatures gives the set of nodal variables $\{u, T_{xx}, T_{yy}, \sigma, Q\}$ with the internal energy density given by

$$e \equiv (\rho/2) + kT_{xx} + kT_{yy} \ .$$

We have found that such an approach can be applied to wave-structure relaxation with longitudinal and transverse work and heat separation, as well. The Landau-Lifshitz weak-shock solution[2] –

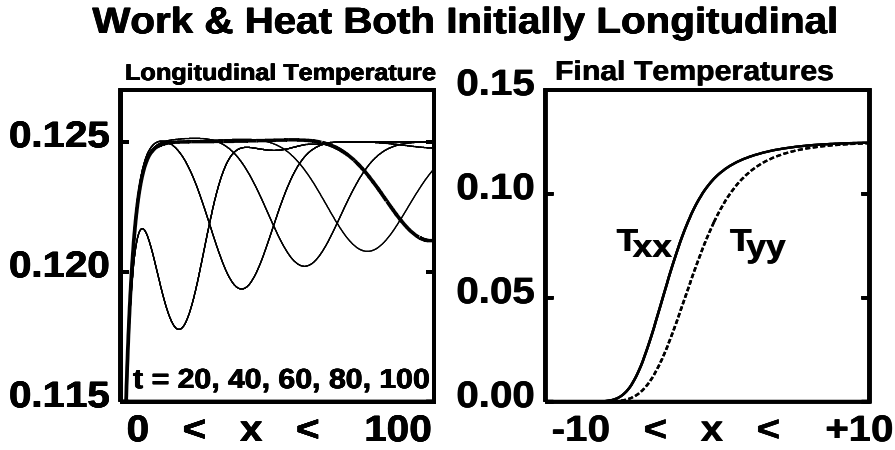


Figure 6: Development of the stationary temperature profiles in a shockwave with shear viscosity ($\eta = 4$), heat conductivities $\{\kappa_{xx} = \kappa_{yy} = 2\}$ and relaxation times $\{\tau_\sigma = \tau_Q = \tau_r = 1\}$. The converged temperatures are shown at the right. Here the work done and the heat transfer initially affect only the longitudinal temperature.

for constant shear viscosity and thermal conductivity, and without any relaxation – makes a useful initial condition. In the stationary-shockwave coordinate system errors in the initial condition move to the right, away from the shockwave, at approximately the speed of sound. See Figures 6 and 7 for transient results from typical solutions of the continuum equations.

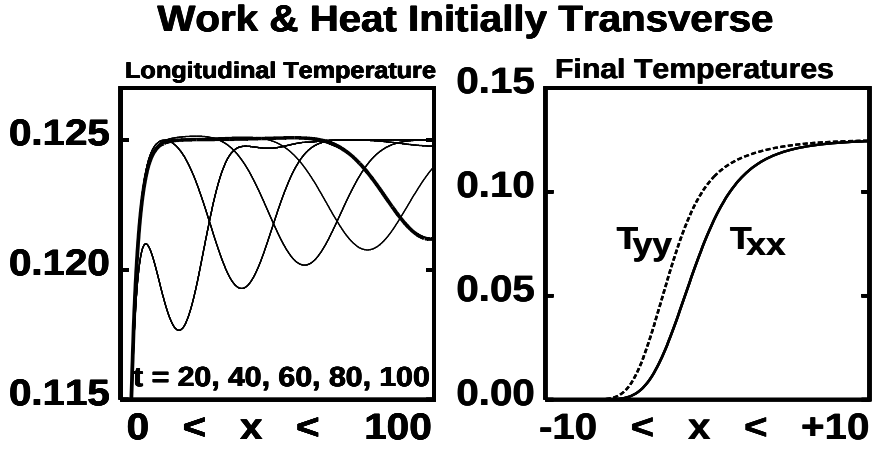


Figure 7: Development of the stationary temperature profiles in a shockwave with shear viscosity ($\eta = 4$), heat conductivities $\{\kappa_{xx} = \kappa_{yy} = 2\}$ and relaxation times $\{\tau_\sigma = \tau_Q = \tau_r = 1\}$. The converged temperatures are shown at the right. Here the work done and the heat transfer initially affect only the transverse temperature.

A successful numerical evolution algorithm proceeds from an initial guess by iterating a series of four steps: (i) specify the six dependent variables $\{\rho_c, v_n, T_{xxn}, T_{yyn}, \sigma_n, Q_n\}$ at all the interior cells and nodes; (ii) compute all the remaining variables and all the gradients with centered sums and differences:

$$u_c(x) = [u_n(x - dx/2) + u_n(x + dx/2)]/2 \; ; \; \rho_n(x) = [\rho_c(x - dx/2) + \rho_c(x + dx/2)]/2 \; ;$$

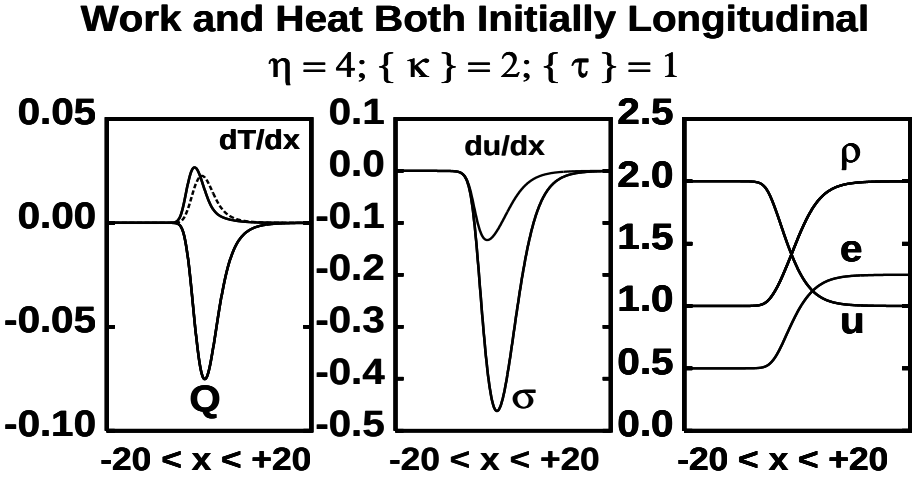


Figure 8: Stationary profiles showing the longitudinal and transverse temperature gradients [(dT_{xx}/dx) is solid; (dT_{yy}/dx) is dashed] as well as the velocity gradients. Notice that the heat flux and shear stress lag behind the gradients which "cause" them.

$$dT_{ii}/dx = [T_{ii}(x + dx/2) - T_{ii}(x - dx/2)]/dx \ ;$$

(iii) compute the righthandsides of the six sets of differential equations.

For instance, the change in energy at a particular node could be evaluated as follows:

$$(\partial e/\partial t)_n = -u_n(de/dx)_n - [(P_{xx}du/dx)_n + (dQ_x/dx)_n]/\rho_n \ ;$$

(iv) use the fourth-order Runge-Kutta method to integrate the $N_c + 5N_n$ ordinary differential equations for one timestep dt, providing the information necessary for a return to step (i) for the execution of the next timestep. The numerical values of the mass, momentum, and energy, as well as their fluxes can be used to help estimate the initial conditions. For the twofold compression shockwave we use to illustrate these ideas, the fluxes and boundary values are the following:

$$P_{eq} = \rho e \ ; \ e = (\rho/2) + T_{xx} + T_{yy} \ ; \ e_{eq} = (\rho/2) + 2T \ ;$$

$$\rho u = 2 \ ; \ P_{xx} + \rho u^2 = 9/2 \ ; \ (\rho u)[e + (P_{xx}/\rho) + (u^2/2)] + Q_x = 6 \ ;$$

$$\rho : (2 \to 1) \ ; \ u : (1 \to 2) \ ; \ P : (1/2 \to 5/2) \ ; \ T : (0 \to 1/8) \ ; \ e : (1/2 \to 5/4) \ .$$

Here the cold and hot boundary values are linked by arrows: $(cold \to hot)$. Both Q_x and σ necessarily vanish at the boundaries, $Q_x : (0 \to 0) \ ; \ \sigma : (0 \to 0)$.

Figures 6, 7, and 8 illustrate typical solutions. In order to circumvent numerical instabilities in the numerical work one can (i) increase the number of cells, (ii) reduce the timestep and/or cell size, (iii) introduce an explicit artificial time-dependence in the parameters $\{\eta, \kappa, \tau\}$ in order to enhance convergence. In this way we have obtained solutions of the continuum shockwave model for a wide range of parameters. The same ideas can be used to study special cases in which stress or heat flux are not delayed or in which temperature is scalar rather than tensor. The sample solutions shown in Figures 6-8 show how the partition of heat and work can affect the stationary shockwave.

7 Conclusions and Prospects

The simulation of nonequilibrium stationary states with molecular dynamics, particularly in the two-block geometry of Figure 2, emphasizes Loschmidt's reversibility paradox[12, 24, 29, 30]. Evidently a movie of exactly the same dynamical states, played backward in time, satisfies all the microscopic motion equations. Such reversed motions contradict macroscopic physics and are never

observed in practice. They would be inherently Lyapunov unstable, with any small perturbation (such as roundoff in the last place) growing exponentially in time and so destroying the reversed trajectory.

Because time-reversed solutions of the Newtonian equations of motion are not observable it is legitimate to use time-irreversible models in interpreting the solutions. The noticeable time-delays, for both stress and heat flux, observed in these solutions legitimates also the use of Maxwell-Cattaneo-Krook relaxation. These innovations are useful to the goal of finding macroscopic descriptions conforming to microscopic observations.

Although we have been able to find stable solutions for the most general description considered here (three relaxation times, partition of heat and work, tensor temperature) there are stringent limits on the parameter ranges for which such solutions exist. On physical grounds stress and heat flux relaxation must be relatively rapid. A fluid's memory cannot be too long. A systematic study of stability is complicated by the large number of parameters involved. Nevertheless, carefully chosen example cases should shed additional light on the physics of relaxation and of strong shockwaves. At the moment the step of generalizing the physical ideas further, for instance by considering the state dependence of the relaxation times, is premature. But we can confidently expect progress there in the future.

Acknowledgements

We specially thank Brad Holian for his comments, suggestions, and prepublication copies of Reference 10. Vitaly Kuzkin provided the motivation for this work, through his invitation and support for WGH and CGH's contributions to the International Summer School–Conference "Advanced Problems in Mechanics–2010" organized by the Institute for Problems in Mechanical Engineering of the Russian Academy of Sciences in Mechanics and Engineering under the patronage of the Russian Academy of Sciences.

References

[1] C. E. Ragan, III, " Shockwave Experiments at Threefold Compression", Physical Review A **29**, 1391-1402 (1984).

[2] L. D. Landau and E. M. Lifshitz, *Fluid Mechanics* (Pergamon, Oxford, 1959). Chapter IX is devoted to shockwaves.

[3] R. E. Duff, W. H. Gust, E. B. Royce, M. Ross, A. C. Mitchell, R. N Keeler, and W. G. Hoover, "Shockwave Studies in Condensed Media", in *Behavior of Dense Media under High Dynamic Pressures*, Proceedings of the 1967 Paris Conference, pages 397-406 (Gordon and Breach, New York, 1968)

[4] V. Y. Klimenko and A. N. Dremin, "Structure of Shockwave Front in a Liquid", pages 79-83 in *Detonatsiya, Chernogolovka* (Akademia Nauk, Moscow, 1978).

[5] B. L. Holian, W. G. Hoover, B. Moran, and G. K. Straub, "Shockwave Structure *via* Nonequilibrium Molecular Dynamics and Navier-Stokes Continuum Mechanics", Physical Review A **22**, 2798-2808 (1980).

[6] B. L. Holian, "Modeling Shockwave Deformation *via* Molecular Dynamics", Physical Review A **37**, 2562-2568 (1988).

[7] Wm. G. Hoover and C. G. Hoover, "Tensor Temperature and Shockwave Stability in a Strong Two-dimensional Shockwave", Physical Review E **80**, 011128 (2009).

[8] Wm. G. Hoover and C. G. Hoover, "Well-Posed Two-Temperature Constitutive Equations for Stable Dense Fluid Shockwaves using Molecular Dynamics and Generalized Navier-Stokes-Fourier Continuum Mechanics, Physical Review E **81**, 046302 (2010).

[9] Wm. G. Hoover and C. G. Hoover, "Shockwaves and Local Hydrodynamics; Failure of the Navier-Stokes Equations", in *New Trends in Statistical Physics, Festschrift in Honor of Leopoldo García-Colín's 80th Birthday*, edited by Alfredo Macias and Leonardo Dagdug (World Scientific, Singapore, 2010).

[10] B. L. Holian and M. Mareschal, "A New Heat-Flow Equation Motivated by the Ideal-Gas Shockwave", (unpublished, 2009); B. L. Holian, M. Mareschal, and R. Ravelo, "Test of a New Heat-Flow Equation for Dense-Fluid Shockwaves", Journal of Chemical Physics (submitted, 2010).

[11] W. G. Hoover, "Structure of a Shockwave Front in a Liquid", Physical Review Letters **42**, 1531-1534 (1979).

[12] L. Boltzmann, *Lectures on Gas Theory* , translated by S. G. Brush (University of California Press, Berkeley, 1964).

[13] H. M. Mott-Smith, "The Solution of the Boltzmann Equation for a Shockwave", Physical Review **82**, 885-892 (1951) .

[14] K. Xu and E. Josyula, "Multiple Translational Temperature Model and its Shock Structure Solution", Physical Review E **71**, 056308 (2005).

[15] E. Salomons and M. Mareschal, "Usefulness of the Burnett Description of Strong Shock Waves", Physical Review Letters **69**, 269-272 (1992).

[16] F. J. Uribe, R. M. Velasco, and L. S. García-Colín, "Burnett Description of Strong Shock Waves", Physical Review Letters **81**, 2044-2047 (1998).

[17] F. J. Uribe, R. M. Velasco, L. S. García-Colín, and E. Díaz-Herrera, "Shockwave Profiles in the Burnett Approximation", Physical Review E **62**, 6648-6666 (2000).

[18] W. G. Hoover, B. L. Holian, and H. A. Posch, "Comment I on 'Possible Experiment to Check the Reality of a Nonequilibrium Temperature"', Physical Review E **48**, 3196-3198 (1993).

[19] L. B. Lucy, "A Numerical Approach to the Testing of the Fission Hypothesis", The Astronomical Journal **82**, 1013-1024 (1977).

[20] Wm. G. Hoover, *Smooth Particle Applied Mechanics; the State of the Art* (World Scientific, Singapore, 2006).

[21] R. J. Hardy, "Formulas for Determining Local Properties in Molecular-Dynamics Simulations: Shockwaves", Journal of Chemical Physics **76**, 622-628 (1982).

[22] D. Gilbarg and D. Paolucci, "The Structure of Shockwaves in the Continuum Theory of Fluids", Journal of Rational Mechanics Analysis **2**, 617-642 (1953).

[23] B. L. Holian, C. W. Patterson, M. Mareschal, and E. Salomons, "Modeling Shockwaves in an Ideal Gas: Going Beyond the Navier-Stokes Level", Physical Review E **47**, R24-R27 (1993).

[24] Wm. G. Hoover, *Computational Statistical Mechanics* (Elsevier, Amsterdam, 1991, available without charge at the author's website, http://williamhoover.info/book.pdf).

[25] D. D. Joseph and L. Preziosi, "Heat Waves", Reviews of Modern Physics **61**, 41-73 (1989) with an Addendum in Reviews of Modern Physics **62**, 375-391 (1990).

[26] W. T. Ashurst and W. G. Hoover, "Dense-Fluid Shear Viscosity *via* Nonequilibrium Molecular Dynamics", Physical Review A **11**, 658-678 (1975). See Figure 6.

[27] N. A. Clark and B. J. Ackerson, "Observation of the Coupling of Concentration Fluctuations to Steady-State Shear Flow", Physical Review Letters **44**, 1005-1008 (1980).

[28] A. Puhl, M. M. Mansour, and M. Mareschal, "Quantitative Comparison of Molecular Dyanmics with Hydrodynamics in Rayleigh-Bénard Convection", Physical Review A **40**, 1999-2012 (1989).

[29] B. L. Holian, W. G. Hoover, and H. A. Posch, "Resolution of Loschmidt's Paradox: The Origin of Irreversible Behavior in Reversible Atomistic Dynamics", Physical Review Letters **59**, 10-13 (1987).

[30] Wm. G. Hoover, *Time Reversibility, Computer Simulation, and Chaos* (World Scientific, Singapore, 2001).

Wm. G. Hoover(hooverwilliam@yahoo.com) and Carol G. Hoover(hoover1carol@yahoo.com), Ruby Valley Research Institute, Highway Contract 60, Box 598, Ruby Valley, Nevada 89833;
Francisco J. Uribe(paco@xanum.uam.mx), Department of Physics, Universidad Autónoma Metropolitana, Mexico City, Mexico 09340.

On the coupling of nonlinear discrete element models with continua in the time domain

Jeroen S. Hoving Andrei V. Metrikine
J.S.Hoving@tudelft.nl

Abstract

When the behaviour of a material is governed by nonlinear phenomena, such as dry friction, discrete elements are often used to model that material. From a numerical point of view, it is desirable to minimize the number of degrees of freedom considered in the discrete element models. To minimize the number of degrees of freedom, the discrete model is coupled to a continuum of the same dimension, allowing for the description of nonlinear phenomena near a load source using discrete elements, while the linear behaviour far from the source is described by a continuum. To execute the coupling between the discrete and continuum segments of the model, their interaction is described such that the wave reflection is minimized at the discrete-continuum interface. This interaction is described by a force-displacement relation known as the dynamic stiffness that follows from the Green's function of the continuum.

Sometimes the Green's function can be obtained in the time domain analytically by applying the inverse Laplace transform to the frequency-domain Green's function. Often it is the case however that the time-domain Green's function has to be calculated numerically by truncating the originally infinite limits of the inverse Laplace transform. This may lead to instability of the numerical scheme, should the truncation be chosen improperly. This contribution shows how to deal with this problem.

The featured solution method is explained by evaluating the coupling of the nonlinear discrete and linear continuous segments of a one-dimensional model. The kinematic behaviour of the discrete elements in this material is described using springs, dashpots and dry friction elements, to account for wave propagation, energy dissipation and stick-slip behaviour respectively. The result of the coupling in the time domain is illustrated by showing the response of the discrete-continuous model due to a pulse load at several moments in time.

1 Introduction

The dynamic behaviour of materials is often modelled describing these materials as discrete particle systems. For example, to predict dynamic soil settlements, a non-linear lattice capable of describing large deformations at high excitation frequencies is used, since the deformations due to the dry friction between soil particles can hardly be captured by continuum models [1]. The presence of such nonlinear phenomena in discrete particle modelling implies that it is a necessity to model these processes in the time domain, rather then in the frequency domain.

One of the main disadvantages of considering a discrete particle system is that it is impossible to consider an infinite number of particles or nodes. From a numerical point of view, it is even desirable to minimize the number of nodes considered. This becomes especially important if we consider multi-dimensional models. To minimize the number of nodes and thus the number of degrees of freedom, we couple the discrete particle system, be it one-, two- or three-dimensional, to a continuum of the same dimension. This coupling then allows us to describe nonlinear behaviour of a material near a load source by a meticulous system, while the linear behaviour of that material at a certain distance from the load source is described by a continuum. In this case, our main interest is the behaviour of the material at the nonlinear discrete domain, the behaviour of the continuum part of the model may also be of interest however, for example, to study vibrations at a substantial distance from the load. Before considering the discrete-continuous coupling in

a two- or three-dimensional model, it is vitally important to understand this coupling for the one-dimensional case.

To execute the coupling between a discrete system and a continuum properly, the interaction between the discrete system and the continuum must be described such that the wave reflection at the discrete-continuum interface is minimized. In the time domain, this is achieved by introducing an integral force-displacement relation at the discrete-continuum interface. The frequency domain counterpart of this relation is the well-known dynamic stiffness. While the dynamic stiffness can usually be computed with a desirable accuracy, its inversion into the time domain almost always has to be done numerically. This approximate numerical inversion may lead to the instability of the numerical scheme. This contribution shows how to deal with this problem.

2 Dynamic stiffness

To couple the discrete system and the continuum such that the wave reflection is minimized at the discrete-continuum interface, the discrete system and the continuum must describe the same material. Additionally, the interaction of the discrete system and the continuum is always described through a relation known as the dynamic stiffness, describing the ratio between a dynamic load and the response to its action. The dynamic stiffness is described by the force-displacement relation in the frequency domain as:

$$F(s) = -\chi(s)U(s) \tag{1}$$

In equation (1), $\chi(s)$ is the dynamic stiffness in the frequency domain and the frequency is described in terms of the complex Laplace parameter s as $s = i\omega + \sigma$, where ω is the frequency and σ is a real constant describing the offset from the imaginary axis in the complex plane. The force $F(t)$ in the time domain then follows from applying the inverse Laplace integral transform to equation (1) and is found as the convolution of $\chi(t)$ and $U(t)$ as:

$$F(t) = -\chi(t) * U(t) = -\int_0^t \chi(t-\tau)U(\tau)d\tau \tag{2}$$

3 The semi-infinite nonlinear BKV material

Let us consider the one-dimensional nonlinear semi-infinite model depicted in figure 1. The discrete segment of this model consists of N nodes in series, where each node n has a mass M^n. Here, the mass at node $n = 0$ is loaded by a dynamic force $F(t)$. The interaction between any two nodes is described by a nonlinear visco-elastic kinematic relation that consists of a Kelvin-Voigt and a Bingham element in series and is therefore referred to as the Bingham-Kelvin-Voigt element or, in short, the BKV element. The springs and dashpots in the Kelvin-Voigt sub-element respectively have a stiffness K_e and a damping C_e. Additionally, the dashpot and the dry friction element in the Bingham sub-element respectively have a damping C_f and a critical friction force F_{cr}.

To describe the behaviour of the BKV elements in the time domain, we apply Lagrange's formalism [2, 3, 8]. Lagrange's formalism states that the equation of motion for a node in a discrete material is found applying the Euler-Lagrange differential equation for the displacement of that node [8]. Next to the degree of freedom of the nodes, given by the displacement U^n of a node n, we also have to take into account the degree of freedom introduced by the kinematic duality of the BKV element. For an element between nodes n and $n+1$, this additional degree of freedom is given by the displacement $U^{n,n+1}$ of the intermediate node between the Kelvin-Voigt and Bingham sub-elements. The system of equations of motion for nodes $n = 1..N-1$ follow from the Euler-Lagrange differential equations for displacement $U^{n,n+1}$ of node n and the displacement $U^{n,n+1}$ of the node intermediate nodes n and $n+1$ as:

$$\frac{\partial \mathcal{L}}{\partial U^n} - \frac{d}{dt}\frac{\partial \mathcal{L}}{\partial \dot{U}^n} = 0 \tag{3}$$

$$\frac{\partial \mathcal{L}}{\partial U^{n,n+1}} - \frac{d}{dt}\frac{\partial \mathcal{L}}{\partial \dot{U}^{n,n+1}} = 0 \tag{4}$$

Here, the upper dot denotes a time derivative and $\mathcal{L}$ is the Lagrangian that is found as the difference between the kinetic and potential energies associated with node n, i.e. $\mathcal{L}^n = E^n_{kin} - E^n_{pot}$. To enable the use of the Euler-Lagrange differential equations, we consider the Kelvin-Voigt and Bingham sub-elements as springs with respective stiffnesses $\widehat{K}_e$ and $\widehat{K}_f$. The Lagrangian L^n for a node n in the BKV material is found as:

$$\mathcal{L} = \frac{M^n}{2}(\dot{U}^n)^2 - \frac{\widehat{K}_e}{2}(e^{n-1,n}_{KV})^2 - \frac{\widehat{K}_f}{2}(e^{n-1,n}_{B})^2 - \frac{\widehat{K}_e}{2}(e^{n,n+1}_{KV})^2 - \frac{\widehat{K}_f}{2}(e^{n,n+1}_{B})^2 \tag{5}$$

Here, $e^{n-1,n}_{KV}$ and $e^{n,n+1}_{KV}$ are the elongations of the Kelvin-Voigt sub-elements between respectively nodes $n-1$ and n and nodes n and $n+1$. Furthermore, $e^{n-1,n}_{B}$ and $e^{n,n+1}_{B}$ are the elongations of the Bingham sub-elements between respectively nodes $n-1$ and n and nodes n and $n+1$.

Substituting the Lagrangian $\mathcal{L}$ into the Euler-Lagrange differential equations yields the equation of motion for an isolated system, i.e. a system that satisfies the law of conservation of energy [2]. Consequently, Lagrange's formalism only considers conservative forces. However, since any equation of motion obtained through the Euler-Lagrange differential equations, is in fact an equilibrium of forces, we are allowed to introduce non-conservative forces as long as this equilibrium is maintained [2].

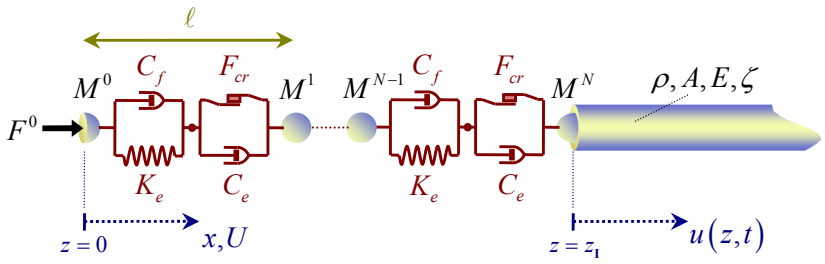


Figure 1: The semi-infinite nonlinear BKV material

Due to the dry-friction element, BKV elements behave according to so-called stick- and slip-modes, each of these modes yields its own equations of motion. Consequently, the governing equations for the BKV material are derived separately for each of these modes.

A BKV element is in stick-mode when the forces on the Bingham sub-element do not overcome the critical friction force F_{cr} of the dry friction element, so that the Bingham sub-element is not activated. Ergo, during stick-mode, the elongation of the Bingham sub-element is obstructed and the Bingham sub-element can be considered a rigid beam. Therefore, the elongation $e^{n,n+1}_B$ of the Bingham sub-element between nodes n and $n+1$ is constant during stick-mode and equal to its elongation previous to the transition into stick-mode, this elongation-constant is denoted as $\varepsilon^{n,n+1}_B$. Assuming that all elements in the BKV material are in stick-mode and additionally substituting $\widehat{K}_e = K_e + C_e\partial/\partial t$ and $\widehat{K}_f = C_f\partial/\partial t$, the equations of motion for the node $n = 0$ and nodes $n = 1..N-1$ are respectively found from Euler-Lagrange differential equation (3) as:

$$M^0\ddot{U} - C_e\dot{e}^{0,1} - K_e(e^{0,1} - \varepsilon^{0,1}) = F(t) \tag{6}$$

$$M^n\ddot{U}^n + C_e(\dot{e}^{n-1,n} - \dot{e}^{n,n+1}) + K_e(e^{n-1,n} - \varepsilon^{n-1,n}_B - e^{n,n+1} + \varepsilon^{n,n+1}_B) = 0 \tag{7}$$

The displacements of the massless nodes intermediate nodes n and $n+1$ during stick-mode are found through the time-independent relation $U^{n,n+1} = U^{n+1} - \varepsilon^{n,n+1}_B$.

For a BKV element between nodes n and $n+1$, the transition from stick- to slip-mode occurs when the friction force $F^{n,n+1}_{fr}$ acting on the Bingham sub-element, exceeds the critical friction force $F^{n,n+1}_{cr}$ of the dry friction element, i.e. slip occurs when $F^{n,n+1}_{fr} > F^{n,n+1}_{cr}$. Here, the critical friction force $F^{n,n+1}_{cr}$ is a constant valued property of the dry friction element and the friction force $F^{n,n+1}_{fr}$ is equal to the force in the Kelvin-Voigt sub-element between nodes n and $n+1$ during stick-mode and is therefore found as:

$$F_{fr} = C_e\dot{e}^{n,n+1} + K_e(e^{n,n+1} - \varepsilon^{n,n+1}_B) \tag{8}$$

The system of equations of motion for the BKV material with its elements in slip-mode follows from substituting the Lagrangian $\mathcal{L}$ into Euler-Lagrange differential equations (3) and (4). Including the non-conservative external force $F(t)$ and the critical friction force F_{cr}, without jeopardizing the equilibrium of forces, as well as substituting $\widehat{K}_e = K_e + C_e\partial/\partial t$ and $\widehat{K}_f = C_f\partial/\partial t$, the equations of motion for the BKV material with all its elements in slip-mode for respectively node $n = 0$, nodes $n = 1..N-1$ and the massless nodes intermediate nodes n and $n+1$ are found as:

$$M^0\ddot{U} - C_e\dot{e}_{KV}^{0,1} - K_e e_K^{0,1} V = F(t) \tag{9}$$

$$M^n\ddot{U}^n + C_f\dot{e}_B^{n-1,n} + F_{cr}^{n-1,n}\mathbf{sgn}\dot{e}_B^{n-1,n} - C_e\dot{e}_{KV}^{n,n+1} - K_e e_{KV}^{n,n+1} = 0 \tag{10}$$

$$C_e\dot{e}_{KV}^{n,n+1} + K_e e_{KV}^{n,n+1} - C_f\dot{e}_B^{n,n+1} - F_{cr}^{n,n+1}\mathbf{sgn}\dot{e}_B^{n,n+1} = 0 \tag{11}$$

Here **sgn** is an abbreviation of signum, so that $\mathbf{sgn}\dot{e}_B^{n,n+1} = 1$ if the elongation rate of the Bingham sub-element is positive and $\mathbf{sgn}\dot{e}_B^{n,n+1} = -1$ when the elongation rate of the Bingham sub-element is negative.

The transition from slip- to stick-mode is governed by the elongation rate of the dry friction element [4, 5, 6]. Because slip may occur in a dry-friction element both under pressure and under tension, the transition from stick- into slip-mode occurs when the elongation rate of the dry friction element becomes equal to zero or changes sign. Since the elongation rate of the dry friction element is equal to the elongation rate of the Bingham sub-element, slip-to-stick transition occurs when $\mathbf{sgn}\dot{e}_B^{n,n+1}(t) \neq \mathbf{sgn}\dot{e}_B^{n,n+1}(t - dt)$.

4 Discrete-continuous coupling

As stated in the introduction, it is our aim to describe the nonlinear behaviour of a material near a load using nonlinear discrete elements, while the linear behaviour of that material at a distance from the load source is described by the continuum. This implies that the continuum in a coupled discrete-continuous model is always located at such a distance from the load that nonlinear phenomena only occur in the discrete domain. Consequently, the discrete segment of the BKV material is coupled to a visco-elastic semi-infinite rod at node N, where node N is chosen such that the BKV element between nodes N and $N-1$ behaves exclusively in stick-mode. The visco-elastic semi-infinite rod has a density ρ, cross section area A, Young's modulus E and damping ζ. The equation of motion for the visco-elastic semi-infinite rod is found as:

$$\ddot{u}(x,t) - \zeta\ddot{u}''(x,t) - c^2u''(x,t) = 0 \tag{12}$$

Here, $u(x,t)$ is the axial displacement in the semi-infinite visco-elastic rod and the prime denotes a space derivative. Furthermore, c is the wave speed found as $c^2 = E/\rho$. To assure correspondence in the material properties of the coupled discrete-continuous system and thus to find the relation between its discrete and continuous properties, we apply the Taylor expansion to the equation of motion for a node n in stick-mode, previously given by equation (7). Comparing the result of the Taylor expansion with equation (12), we find the following relations between the discrete and continuum properties of the BKV material:

$$M^n = \rho A\ell, \qquad C_e = \frac{\rho A\zeta}{\ell}, \qquad K_e = \frac{EA}{\ell} \tag{13}$$

Here, ℓ is the initial distance between two nodes in the BKV material. Note here that the masses M^0 and M^N represent only half the distance ℓ and thus for a correct distribution of the mass over the length of the discrete model, we find that $M^0 = M^N = M^n/2$.

At the interface $x = x_I$, there are two interface conditions that relate the motion of the discrete and continuous parts of the coupled system at node N. The first interface condition follows from the equality of the displacement U^N of interface node N and the displacement $u(x,t)$ of the semi-infinite rod at $x = x_I$. The second interface condition is found from the equilibrium of forces at $x = x_I$. We introduce the following dimensionless parameters for time, spatial coordinate and damping:

$$T = t\omega_0, \qquad X = x\frac{\omega_0}{c}, \qquad \zeta = \zeta^{dim}\frac{\omega_0}{c^2} \tag{14}$$

Here, ω_0 is the natural frequency of the discrete system found as $\omega_0 = \sqrt{K_e/M^n} = c/\ell$. The dimensionless problem statement that includes the discrete-continuum interface conditions and the equation of motion of the continuum is then found as:

$$\ddot{u}(X_I,T) - \zeta\dot{u}''(X_I,T) - u''(X_I,T) = 0 \tag{15}$$

$$u(X_I,T) = U^N \tag{16}$$

$$u'(X_I,T) + \zeta\dot{u}'(X_I,T) = M^N\ddot{U}^N + C_e\dot{e}^{N-1,N} + K_e e^{N-1,N} \tag{17}$$

Here, the dimensionless variables M^N, C_e and K_e are respectively found as:

$$M^N = \frac{M^{N,dim}\omega_0}{\rho Ac}, \qquad C_e = \frac{C_e^{dim}}{\rho Ac}, \qquad K_e = \frac{K_e^{dim}}{\rho Ac\omega_0} \tag{18}$$

Applying the Laplace integral transform to equations (15) to (17) yields:

$$s^2\tilde{u}(X_I,s) - (\zeta s+1)\tilde{u}''(X_I,s) = 0 \tag{19}$$

$$\tilde{u}(X_I,s) = \tilde{U}^N \tag{20}$$

$$(\zeta s+1)\tilde{u}'(X_I,s) = M^N s^2\tilde{U}^N + (C_e s + K_e)\tilde{e}^{N-1,N} \tag{21}$$

Here, the tilde placed over a variable denotes that variable as its Laplace transform and s is the complex Laplace parameter. Assuming that $\Re\sqrt{s^2/(\zeta s+1)} > 0$ and accounting for the appropriate behaviour of the visco-elastic rod at $X \to \infty$, the equation of motion at the interface node N follows from equations (19) to (21) as:

$$M^N s^2\tilde{U}^N + (C_e s + K_e)\tilde{e}^{N-1,N} + \chi(s)\tilde{U}^N = 0 \tag{22}$$

Here, the dynamic stiffness $\chi(s)$ of the visco-elastic rod is found as:

$$\chi(s) = (\zeta s+1)\sqrt{\frac{s^2}{\zeta s+1}} \tag{23}$$

Note here that the dynamic stiffness may only be simplified as $\chi(s) = s\sqrt{\zeta s+1}$, by choosing the branch such that $Res\sqrt{\zeta s+1} > 0$. Applying the inverse Laplace transform to (22) allows us to write the equation of motion for the interface node N in the time domain as:

$$M^N\ddot{U}^N + C_e\dot{e}^{N-1,N} + K_e e^{N-1,N} + \int_0^T \chi(T-\tau)U^N(\tau)d\tau = 0 \tag{24}$$

The inverse Laplace transform of the dynamic stiffness $\chi(s)$ of the visco-elastic rod in the frequency domain, given in equation (23), cannot be obtained analytically. Instead, we have to apply the inverse Laplace transform numerically. The numerical procedure is addressed in the following section.

5 Numerical implementation of the interface equations

Application of the inverse Laplace transform to an arbitrary function $f(s)$, yields integration over a semi-infinite domain of the complex Laplace parameter s. Thus, to obtain the inverse Laplace transform numerically, we need to truncate the infinite domain of integration over s. Taking into account that the real and imaginary parts of a Laplace integrand are respectively symmetric and anti-symmetric and assuming that the arbitrary function $f(s)$ converges to zero within the truncated dimensionless frequency domain $\Omega\epsilon 0..\Omega_{tr}$, the inverse Laplace transform $f(T)$ can be written as:

$$f(T) = \frac{1}{\pi}\int_0^{\Omega_{tr}} \Re\left(f(s)\exp(sT)\right)_{s=i\Omega+\sigma}\, d\Omega \tag{25}$$

Here, Ω is the dimensionless frequency that is expressed in terms of the dimensional angular frequency as $\Omega = \omega/\omega_0$. Important to note here is that truncating the domain of integration of any integral is only allowed if the integrand is properly convergent. Ergo, we are only allowed to apply the numerical inverse Laplace transform to the dynamic stiffness $\chi(s)$, if the dynamic stiffness converges sufficiently fast. The dynamic stiffness of the visco-elastic rod given in equation (23) however, is not convergent. We overcome this problem by dividing the equation of motion at the discrete-continuous interface by the dynamic stiffness. This yields the interface equation in the frequency domain, previously given by equation (22), as:

$$\chi^{-1}(s)\left\{M^N s^2 \tilde{U}^N + (C_e s + K_e)\tilde{e}^{N-1,N}\right\} + \tilde{U}^N = 0 \tag{26}$$

Due to the division of the interface equation by the dynamic stiffness, the interface equation in the time domain given by equation (24) no longer holds. Instead, applying the inverse Laplace transform to equation (26) now yields the interface equation in the time domain as:

$$U^N + \int_0^T \chi^{-1}(T-\tau)\left\{M^N \ddot{U}^N(\tau) + C_e \dot{e}^{N-1,N}(\tau) + K_e e^{N-1,N}(\tau)\right\} d\tau = 0 \tag{27}$$

Here, $\chi^{-1}(T)$ is the numerically obtained inverse Laplace transform of the inverse dynamic stiffness, which is found as:

$$\chi^{-1}(T) = \frac{1}{\pi}\int_0^{\Omega_{tr}} \Re\left(\frac{\exp(sT)}{\chi(s)}\right)_{s=i\Omega+\sigma} d\Omega \tag{28}$$

Although the integrand in equation (28) is convergent, this convergence is slow ($1/(s\sqrt{\zeta s})$). Moreover, solving the inverse Laplace transform according to equation (28) numerically still poses problems when substituting $T = 0$ due to the deletion of the exponent. To avoid this problem and to improve the convergence of the integrand, thereby improving the performance of the numerical inverse Laplace transform, we extract the approximation of the dynamic stiffness for large values of s, denoted as $\chi_\uparrow(s)$, from the original inverse dynamic stiffness in the frequency domain. Thus, the inverse dynamic stiffness in the time domain finally becomes:

$$\chi^{-1}(T) = \chi_\uparrow^{-1}(T) + \frac{1}{\pi}\int_0^{\Omega_{tr}} \Re\left(\frac{\exp(sT)}{\chi(s)} - \frac{\exp(sT)}{\chi_\uparrow(s)}\right)_{s=i\Omega+\sigma} d\Omega \tag{29}$$

The approximate dynamic stiffness $\chi_\uparrow(s)$ for large values of s is found as $\chi_\uparrow(s) = s\sqrt{\zeta s}$. The approximate inverse dynamic stiffness $\chi_\uparrow^{-1}(T)$ for the visco-elastic rod is found analytically in the time domain as $\chi_\uparrow^{-1}(T) = 2\sqrt{T/\pi\zeta}$. Additionally, the integrand of the numerical integration in equation (29) has a much better convergence then the integrand in equation (28).

To isolate the major contribution of the convolution integral in equation (27) to the current integration step, the interface equation is differentiated. Using Leibniz' integral rule for derivatives of integrals, applying the first order Newton-Cotes formula, also known as the trapezium rule, to the convolution integral and assuming initial conditions $\ddot{U}^N = \dot{U}^N = U^N = 0$, allows us to write the interface equation in the time domain as:

$$\begin{aligned} &U^N + \left(\chi^{-1}(0) + \tfrac{\Delta T}{2}\dot{\chi}^{-1}(0)\right)\left\{M^N \ddot{U}^N + C_e \dot{e}^{N-1,N} + K_e e^{N-1,N}\right\} \\ &+ \sum_{h=1}^{jj} \Delta T\, \dot{\chi}^{-1}(T_{jj-h})\left\{M^N \ddot{U}^N(T_h) + C_e \dot{e}^{N-1,N}(T_h) + K_e e^{N-1,N}(T_h)\right\} d\tau = 0 \end{aligned} \tag{30}$$

Here, the domain of integration over time is divided in jj equal time steps ΔT, so that the time step ΔT is related to the current dimensionless time T as $\Delta T = T/jj$. Consequently, T_h refers to the dimensionless time after h time steps.

6 Results

Equations (6) and (7) together with equation (30) describe the complete system of equations of motion for the semi-infinite BKV material when all elements are in stick-mode. In this situation, the BKV material can be considered as a purely visco-elastic material. Figure 2 shows the response of this purely visco-elastic one-dimensional material due to the applied pulse load $F(T) = \widehat{F}sin(\Omega T)$ at several moments in time.

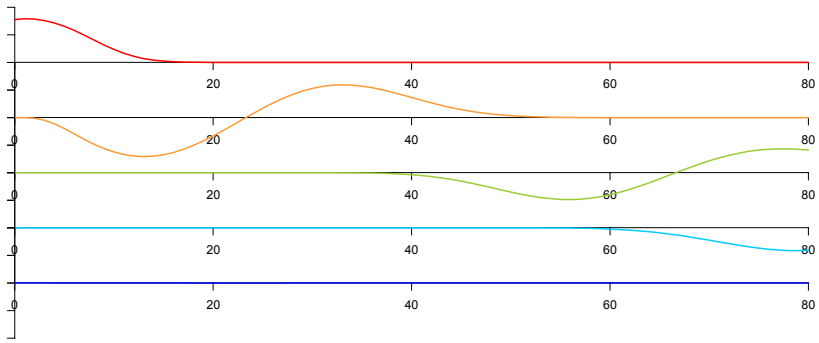


Figure 2: The response of the purely visco-elastic material

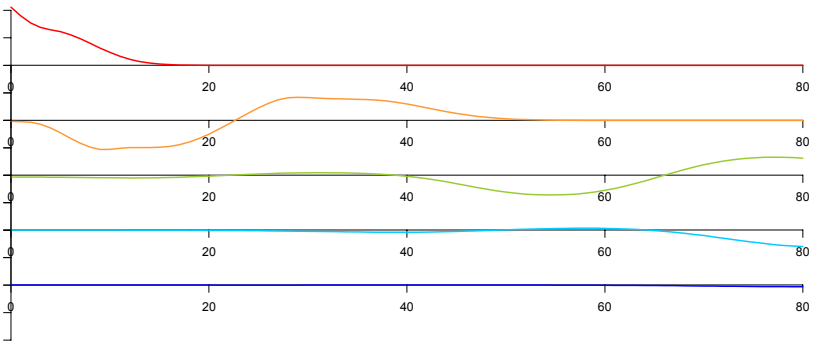


Figure 3: The response of the semi-infinite nonlinear BKV material

In any material that allows for multiple modes, it will rarely occur that all elements are in the same mode; therefore, the modes in each element are monitored at any given moment in time according to the mode transitions discussed in section 3. Figure 3 shows the response of the semi-infinite BKV material due to the applied pulse load $F(T) = \widehat{F}sin(\Omega T)$ at several moments in time allowing for both stick- and slip-modes.

7 Conclusions

This contribution has addressed the coupling of a nonlinear discrete element model with a corresponding continuum in the time domain. It has been shown how to deal with several problems that may occur when coupling discrete systems and continua. Because the inverse Laplace transform of the dynamic stiffness cannot always be obtained analytically, we are forced to obtain it numerically. In order to obtain convergence and thereby enabling truncation of the numerical scheme, the Laplace inversion has been applied to the inverse dynamic stiffness. Additionally, the asymptotic values of the inverse dynamic stiffness were extracted from the numerical scheme in order to reach the necessary accuracy. The results show that the wave reflection at the discrete-continuum interface is minimized. Further research will be done to employ the proposed method in two- and three-dimensional systems.

References

[1] J.S. Hoving, F. Molenkamp, A.V. Metrikine, "The dynamic response of a discrete lattice containing dry-friction elements to a surface load", Proceedings of the XXXIII Summer School, Advanced Problems in Mechanics, p.224-232, St. Peterburg, Russia, 2005.

[2] C. Lanczos, "The Variational Principles of Mechanics", 3rd edition, University of Toronto Press, Toronto, 1966.

[3] H. Goldstein, C. Poole and J. Safko, "Classical Mechanics", 3rd edition, Addison-Wesley Publishing Company Inc., San Fransisco, 2002.

[4] K. Popp, N. Hinrichs and M. Oestreich, Series on Stability, Vibration and Control of Systems Series B: Vol.7, p.1-35, "Analysis of a self-excited friction oscillator with external excitation", World scientific publishing Co. Pte. Ltd., Singapore, 1996.

[5] U. Andreaus and P. Casini, Journal of Sound and Vibration 245, p.685-699, "Dynamics of friction oscillators excited by a moving base and/or driving force", Academic Press, Elsevier Ltd, 2001.

[6] G. Cheng and J.W. Zu, Journal of Sound and Vibration 275, p.591-603, "Dynamics of a dry friction oscillator under two-frequency excitations", Academic Press, Elsevier Ltd, 2004.

[7] F.P. Bowden and D. Tabor, "The Friction and Lubrication of Solids", Oxford Classic Series, Oxford University Press, New York, 2001, first published in 1954.

[8] L.D. Landau and E.M. Lifshitz, "Mechanics", Pargamon, Oxford, 1976.

Jeroen S. Hoving, Delft University of Technology, Faculty of Civil Engineering and GeoSciences, P.O. Box 5048, 2600 GA, The Netherlands
Andrei V. Metrikine, Delft University of Technology, Faculty of Civil Engineering and GeoSciences, P.O. Box 5048, 2600 GA, The Netherlands

Particle dynamics to model brittle rocks

James Ing Ekaterina Pavlovskaia Marian Wiercigroch Igor Asonov
Igor Berinskiy
j.ing@abdn.ac.uk

Abstract

Particle dynamics can be used to model materials on the macroscale. This method is selected to tackle the problem, since FE and analytical methods do not describe material damage accumulation well. For modelling rocks, a polycrystaline material of specified grain size is simulated by controlling the cooling rate of a fluid of Lennard-Jones particles. Modification of the standard 6-12 potential is made in order to tune the ultimate strain of the material, which is also shown to be dependent upon grain size. Simulations using such a material show that micro crack formation occurs along grain boundaries. These cracks eventually join together and result in failure of the material.

1 Introduction

Particle dynamics can be used to model many materials, but the material properties must be matched in order to be able to make quantitative predictions from PD simulations. Often a lattice of particles is used, which means that the macroscopic material properties such as elastic modulus can be matched to the bond strength, by making use of the regularity of the close packed lattice and analysing a representative volume element [1]. For brittle materials such as rock which are nonhomogenous, have high elastic modulus, and relatively low strength due to brittleness, capturing these features can be problematic. For this reason simulations of impact fracture of rocks using particle dynamics have been mostly qualitative [2], although in this realm the method is successful. Modification of the traditional Lennard-Jones potential needs to be made in order to capture the material properties of rock. Then simulations are to be conducted in order to obtain a polycrystaline material for which the microscopic parameters can be set to match the correct macroscopic behaviour by simulating the same kinds of test which might be made for a real material in a laboratory. The randomness which results from the obtained polycrystaline material compares well to results taken from real samples, in that averaging of behaviour is required to obtain useful results. This is due to residual strains in the grain boundaries, which account for the lowering of the elastic modulus and ultimate strain of the polycrystaline material.

This paper first introduces a generalised Lennard-Jones potential, and associated properties, in section 2. The simulation of grains and the control of the grain size for further systematic studies are detailed in section 3. Determination of the ultimate stress and strain, and the modification of the Lennard-Jones potential required to model very brittle materials are given in section 4. Finally conclusions are given in section 5.

2 Definition of potentials

The standard Lennard-Jones 6-12 potential has two parameters: σ, which determines particle size. This is related to the size of the physical system being modelled and the computational time for the problems. The other parameter, ϵ, which determines the size of the potential well is related to the elastic stiffness of the material being simulated. Further parameters are needed to control the ultimate strain that the material can support. Therefore a generalised LJ potential, V, is used for this study given by,

$$V = 4\epsilon\{-(\sigma/r)^p + (\sigma/r)^q\}. \tag{1}$$

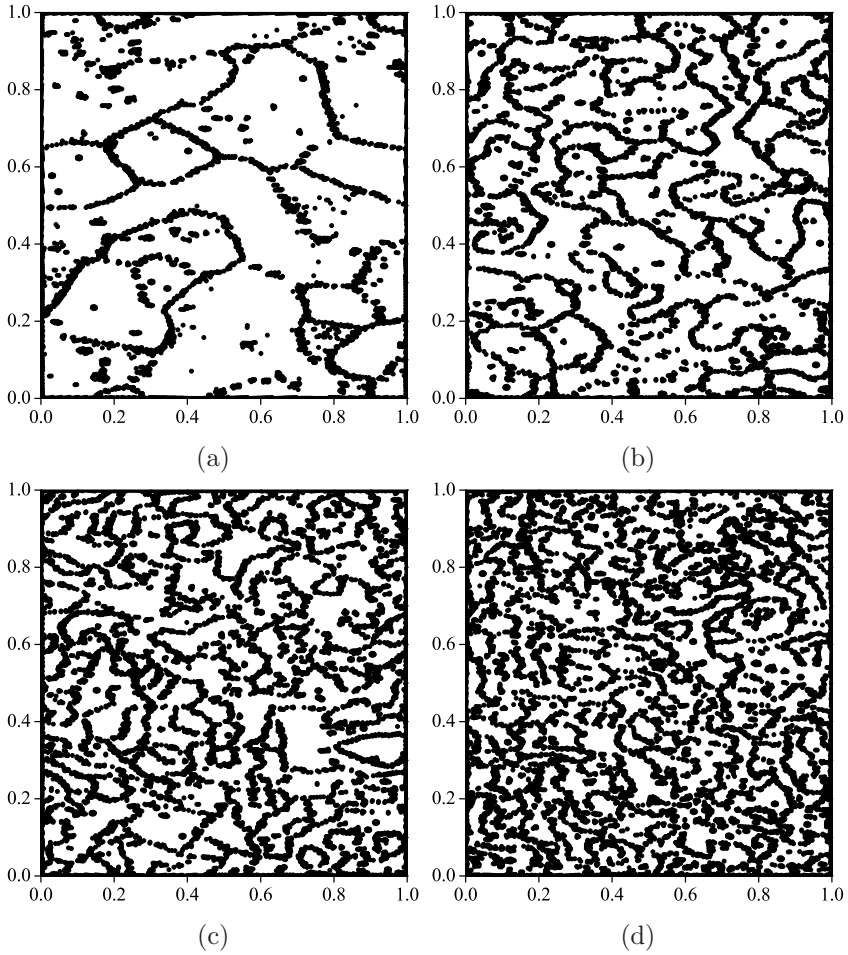


Figure 1: Structure of 0.05% permeability sample under different cooling rates (cooling rate is increasing with each sample). The crystal size dependence on damping ratio is clearly seen. This allows the scale of simulation to be defined by the grain size of the real sample under consideration. Damping ratios are as follows: (a) $\xi = 0.01$ (b) $\xi = 0.1$ (c) $\xi = 0.5$ (d) $\xi = 10$

The minimum, r_{min}, occurs at $r_{min} = 2^{\frac{1}{q-p}}\sigma$ and particle size for a potential of given degree is dependent only on σ. The lattice spacing can be scaled to accommodate different p,q. Increasing p and q means decreasing the width of the potential well and therefore the dissociation length at which bonds are broken. In practice the potential is truncated at 3.5σ for computational efficiency.

3 Simulations of grains

Rocks are heterogenous materials and it is well known that when they begin to fail the structure of the cracks depends very much on the structure of the material. For example granite has many crystaline grains consisting of quartz, mica and feldspar. The relative orientation and stress state of these grains determines the ultimate strength of the sample, and the propagation of cracks occurs along grain boundaries and existing faults and/or voids. The initial configuration of the LJ particles therefore is very important. The following procedure (similar to that suggested in [3]) is used to generate a polycrystaline material. A close packed triangular lattice is placed into a simulation domain with periodic boundary conditions equal in size to the lattice size divided by the required porosity. A sufficiently high temperature is set for the particles to behave as a fluid. Linear viscous damping is added to the equation of motion and the simulation is run until the

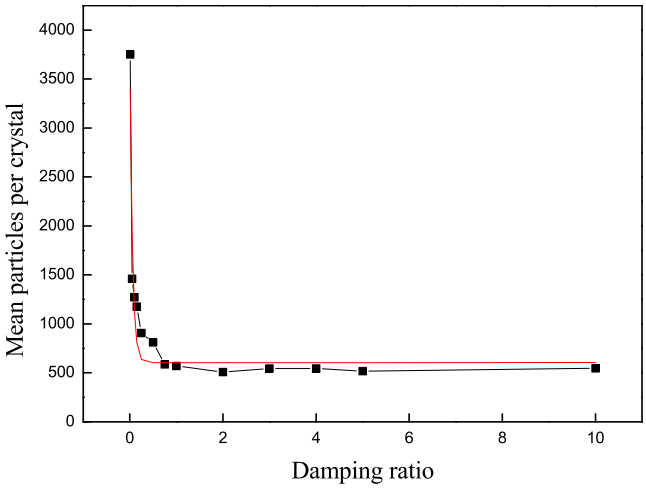


Figure 2: Plot of grain size against damping ratio for a linear viscous damped LJ fluid. The grains were determined by marking high strain bonds. These occur on the boundary between grains with different lattice orientations and form a surface demarking the grain boundaries. A linear/expontential curve is fitted to the results using nonlinear optimisation. With this relationship it is possible to specify the grain size for future simulations.

temperature is sufficiently below the melting point of the particles. As the fluid begins to cool, there is local solidification, and particles begin to pack into a lattice. This occurs simultaneously in in different regions of the simulation domain, and the resulting crystals are obviously randomly aligned with respect to each other. The rate of cooling (i.e. the damping ratio) determines the rate of formation of these crystals and therefore their ultimate size. This relationship, and the effect of crystal size on the material properties needs to be determined from simulation. Figure 1 shows a simulation domain for various polycrystal materials obtained for different damping ratios. The grain boundaries can be seen from the stretched bonds which result from the interface of differently aligned lattices of particles. As can be seen from figure 1, there is a strong dependence of the crystal size on the rate of cooling (i.e. linear viscous damping ratio). This dependence needs to be determined from numerous simulations in order to be able to control the physical size of the simulation domain, which is determined by the characteristic grain size of the rock in question. From figure 2 it is clear that there is a monotonic relationship between the damping parameter and the obtained grain size. This allows the grain size to be controlled in simulations, from the empirical equation,

$$A = b + c\xi + de^{t\xi} \tag{2}$$

which defines the grain size A (number of particles) in terms of damping parameter ξ, and the fit parameters b, c, d and t. From the nonlinear optimisation the following values were determined: $b = 0$, $c = 520$, $d = 300$ and $t = -0.14$. It can be seen that there is a sensitive dependence for some values of damping, but for small damping ratios, but there is a saturation approaching the value of around 500 particles per grain after which increased damping is not effective. This can be understood since very small grains are likely to be able to align with each other when joining, but larger grains are not. The required number of particles per grain for a particular simulation depends on the number of particles in the whole domain, and the physical size of the problem. For each case the elastic modulus of the resulting material needs to be determined, in order to calibrate the simulation. Figure 3 shows different samples of failed material resulting from tensile loading. In simulation the loading was achieved by increasing the size of the simulation domain in one dimension by a constant factor, while holding the others constant. The simulations were made scale free by the use of periodic boundary conditions in both directions. Care was taken to ensure that the stretching was done quasistatically, to avoid rate dependence. Clearly the fracture patterns are dependent on the microstructure, since cracks propagate along the grain boundaries

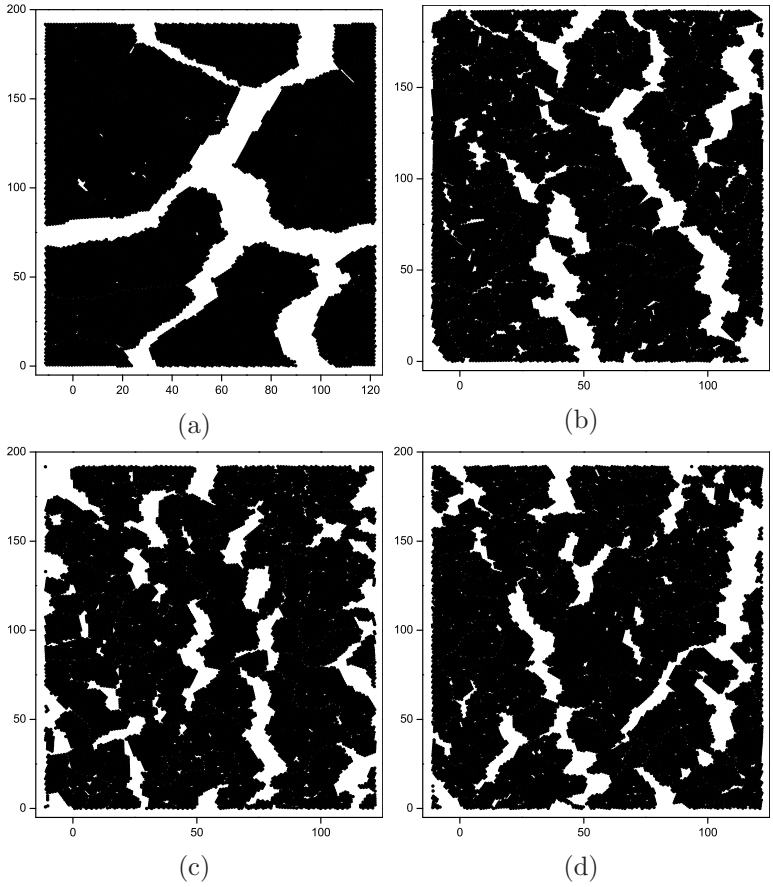


Figure 3: Crack propagation and failure for LJ samples with different grain sizes under tensile loading. Cracks form along the grain boundaries, so it is clear that modelling damage accumulation using PD requires capturing the small scale structure of the physical system under consideration. Damping ratios are as follows: (a)$\xi = 0.01$ (b) $\xi = 0.1$ (c) $\xi = 5$ (d) $\xi = 10$

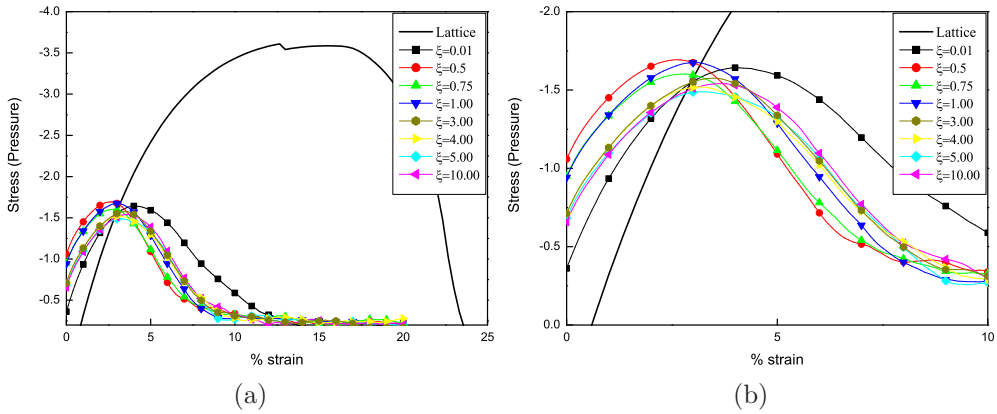
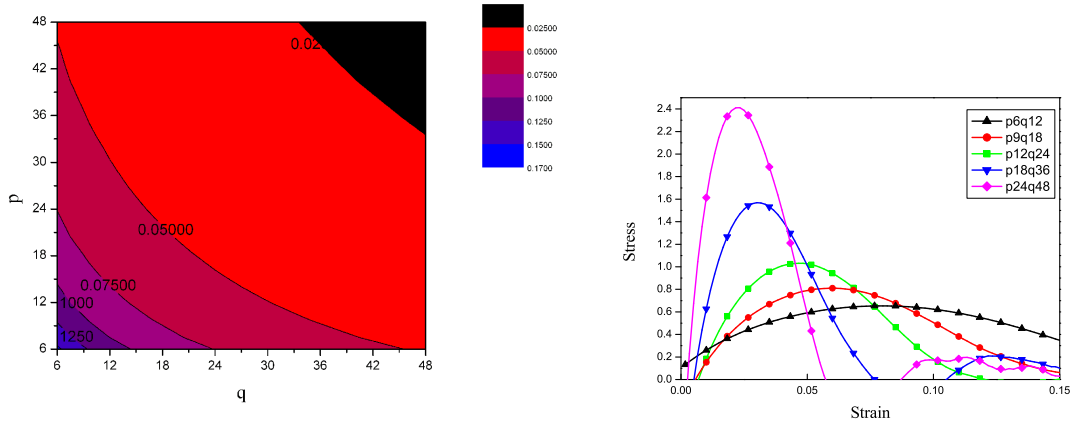


Figure 4: (a) The effect of damping ratio on ultimate stress and strain, and (b) a zoom of the polycrystaline plots. While it is clear that the presence of grains significantly weakens the sample in comparison to a perfect crystal, the effect of grain size is small.

of the sample. Therefore as grain size decreases in each case shown, the complexity of the cracks increase. This relationship also needs to be determined for the purpose of calibrating the samples. The effect of grain size may play an important role in the strength of the obtained materials. It

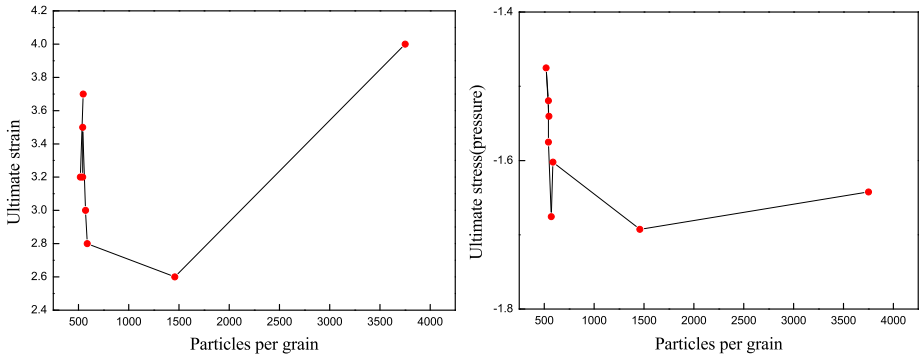


(a) (b)

Figure 5: (a) The effect on a perfect lattice of increasing p and q on the dissociation point of the bonds, which corresponds to the maximum of the stress-strain curves for a lattice. (b) The simulated stress-strain curves of a polycrystal material with 1000 particles per grain, for various p and q.

has been shown that in rocks, grain size can effect the ultimate strength [4]. While the effect may be small, it needs to be accounted for in the calibration of the potential, and therefore the stress/strain vs grain size dependence should be investigated. Figure 4 shows this relationship by plotting the stress-strain curves for materials obtained using a number of different damping parameters. During simulations the pressure tensor was calculated from the virial components and the P_{xx} component was used to give the overall stress in the sample. This was plotted as a function of the strain for various values of the damping parameter. While it is clear that the presence of a grain structure significantly weakens the sample with respect to a perfect lattice, the effect of grain size is less apparent. Figure 6 shows the relationship between grain size and the ultimate stress and strain. A small correlation is seen, which can explain the behaviour seen in real rocks, but does not provide strong enough correlation to allow damping to provide an extra parameter in modelling rocks.

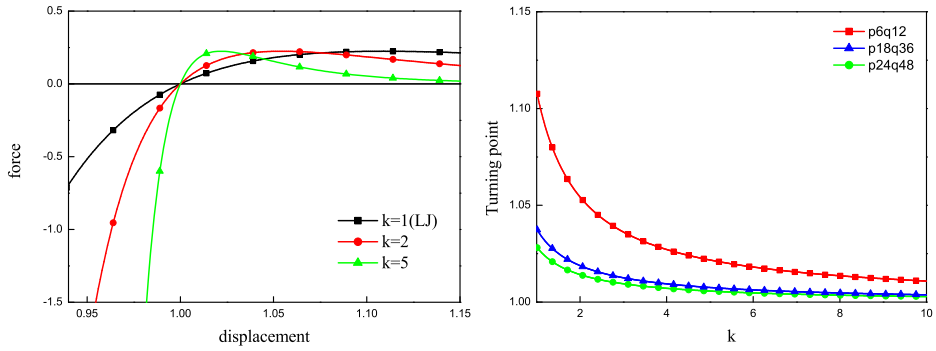
4 Ultimate stress and strain



(a) (b)

Figure 6: Plots of ultimate stress (a) and ultimate strain (b) (found by stretching the simulation domain and finding the maxima of the stresses in the bonds). There is a slight dependence on the grain size, although variation from specific instances of each grain size are significant.

The ultimate strength of the material is determined mainly by the elastic modulus and the ultimate strain that the material can support. For rocks such as granite and sandstone the ultimate strain is $10^{-2} - 10^{-3}$, [5]. For a Lennard-Jones material the elastic modulus determines the bond energy, ϵ, and the crystal size has been shown only to have a weak correlation with the ultimate strain, therefore further parameters are needed in order to model very brittle materials. The generalised Lennard-Jones potential introduces a further two parameters, which have the effect of increasing the brittleness, but from figure 5(a) it is clear that the effect on the bond dissociation distance of increasing p and q decreases with increasing p and q. This diminished return does not allow the very highly brittle behaviour of many rocks to be captured, e.g. 0.2% strain. Figure 5(b) shows simulations of the stress-strain curves for different p,q combinations, calculated for a granular material (∼1000 particles per grain). The combined effect of both the granular structure and the generalised LJ potential allows materials with ∼2% ultimate strain to be simulated. Still this falls short of the very highly brittle fracture of granitic and sandstone type rocks. Therefore a further modification of the potential is needed.



(a) (b)

Figure 7: (a) The modification to the LJ potential for various values of the scale factor k. The effect on the maximum of the force is shown in (b) for different values of k and different combinations of p,q. The y-axis has been scaled so that $r_{min} = 1$ and therefore the strain can be read directly. It is clear that in combination these parameters allow a full range of brittle behaviour that encompasses rocks such as granite.

It is proposed to introduce the following scaling to the separation distance to obtain the required reduction of the ultimate strain,

$$\hat{r} = k(r - r_0) + r_0. \tag{3}$$

Figure 7 shows the effect of varying values of k on the turning point of the force. This corresponds closely to the strain required for breaking of bonds and hence the ultimate strength. Simulations are required to obtain the appropriate relationship for k, p and q, and grain size, in order to obtain the required material.

5 Conclusions

Simulation of rock fracture using PD requires a careful description of the rock, including not just the elastic modulus, but also grains and the ultimate stress/strain. The traditional LJ potential is not sufficient for this, nor is a generalised LJ potential. Although grains can be constructed by controlled cooling of a LJ fluid, for the highly brittle behaviour of rock to be adequately described in simulations, the introduction of a scaled particle displacement, along with a grain structure and a generalised LJ description are all needed to capture all the required properties. Using this description, a sample of granite was simulated, and fracture of the sample was observed to be caused by microcracks which accumulate in the grain structure, exactly as cracks are observed to form in real experiments.

Further work in this field will be to fully calibrate the model against experimental data, and to use the calibrated model to predict such features as the onset of plastic deformation in rocks, the crack propagation patterns for different loading parameters, and the stiffness and energy dissipation characteristics as a function of the loading parameters.

Acknowledgements

This work is supported by EPSRC (EP/EO11535), RFBR (09-01-92603-KO_a), and the Royal Society of London

References

[1] Martin Ostoja-Starzewski. Lattice models in micromechanics. Appl Mech Rev 55, 1, (2002)

[2] Anton M. Krivtsov, Ekaterina E. Pavlovskaia, Marian Wiercigroch. Impact fracture of rock materials due to percussive drilling action. XXI ICTAM, 1521 August (2004), Warsaw, Poland

[3] Anton M. Krivtsov and Marian Wiercigroch. Molecular dynamics simulation of mechanical properties for polycrystal materials. Mater. Phys. Mech. 3 (2001) 45–51

[4] Kiyoo Mogi. Influence of the dimensions of speicmens on the fracture strength of rocks. Bulletin of the Earthquake Research Institute, 40, (1962) 175-185

[5] Shixin Liu, A.H.M. Faisal Anwar, Byung Cheol Kim and Yasuaki Ichikawa. Observation of microcracks in granite using a confocal laser scanning microscope. International Journal of Rock Mechanics & Mining Sciences 43 (2006) 1293–1305

James Ing, Centre for Applied Dynamics Research, School of Engineering, University of Aberdeen
Ekaterina Pavlovskaia, Centre for Applied Dynamics Research, School of Engineering, University of Aberdeen
Marian Wiercigroch, Centre for Applied Dynamics Research, School of Engineering, University of Aberdeen
Igor Asonov, St. Petersburg State Polytechnical University, Russia
Igor Berinskiy, Institute for Problems in Mechanical Engineering of Russian Academy of Sciences, Russia

Vibrational translation due to transversal strain in a Chelomei pendulum-like system

K. S. Ivanov
ivanoff.k.s@gmail.com

Abstract

The vibrational translation phenomenon in a Chelomei pendulum-like system was studied with putting forward hypothesis of alternative mechanism of its possible origin. The new case of the translation which doesn't require transversal deformation of a rod was physically described and mathematically explained. The complete mathematical explanation led to numerical algorithm developing, which allows to predict some average characteristics in the translation. Using the algorithm it was obtained some possible conditions under which the translation would occur.

1 Introduction

V.N. Chelomey made a number of experiments with a washer, fitted with a gap at the hinged bar, the base of which is exposed to vibration. In these experiments the occurrence of sustained "high" vertical position of the bar, similar to "overturned" position of the Stephenson-Kapitza pendulum, was observed. At the same time, the washer also moved towards its free top end. The first theoretical models were built on the assumption of a perfectly rigid bar material and the presence of a gap between it and the washer (Fig. 1 a). In his article, devoted to the description of a series of experiments, including an experiment with a pendulum, Chelomey [1] states the problem exactly this way. The system of equations stated in this paper, however, was drawn up for the washer fitted without a gap, and its numerical investigation, which agrees with the experiment, allowed Chelomey to assume that for the described behavior of the system to occur pure longitudinal oscillations of the bar were sufficient. Later the problem was dealt with in several works, and the analytical studies [2,4] led the authors to conclude that the necessary condition for stabilization of the washer on the bar was the presence of its transverse oscillations.

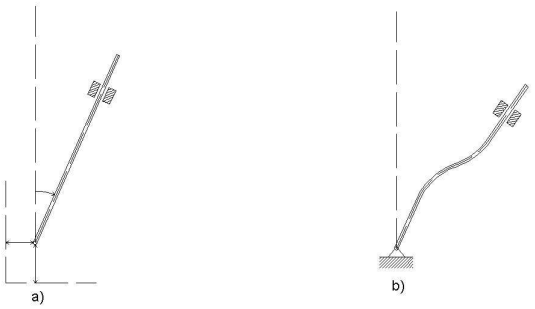


Figure 1: Options for problem setting

In [3] a further numerical study of differential equations system, proposed by Chelomey, was carried out. The confirmation of the hypothesis that pure longitudinal oscillations of the bar are sufficient to cause the described effect in the behavior of the washer in this work was the result

of calculation errors. In the future, the problem was viewed in wider settings, involving lateral bending of the bar, as well as taking into account the effect the weight of the washer makes on the shape of its bending oscillations (Fig. 1 b) [5,6,8]. Most of these papers argued that the presence of lateral deformation or displacement in the system is the necessary condition for the occurrence of force, capable to move the washer along the bar.

2 Examination of the Problem in the Case of Quasi-Static Deformation of the Bar

In our previous article the we have put forward a hypothesis concerning the possible mechanism of moving the washer with purely longitudinal harmonic oscillations of the fixed end of the bar. The hypothesis meant that the motion of the washer during such oscillations can be affected by the change in the thickness of the bar due to tension or compression. This, for example, in case of the absence of the gap, leads to a corresponding change in contact force, and thus in the force of dry friction between the washer and the bar (Figure 2). In setting this task, it is expedient to take into account some correlations of parameters. Namely, when the excitation frequency is sufficiently small, compared with the first natural oscillation frequency of the bar, we can assume its deformation as quasi-static. If the excitation frequency is not small compared with the first natural oscillation frequency, we should consider the longitudinal oscillations of the bar in the standing-wave mode. In this paper, a theoretical consideration of the quasi-static setting is made, the expressions for the main parameters that characterize the patterns of washer translations are found, the algorithm for numerical modeling of the process and for retrieval of steady-state modes is developed.

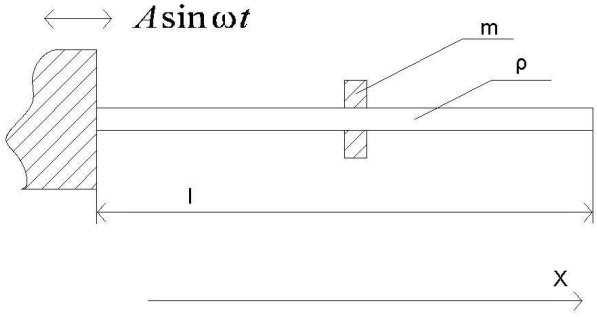


Figure 2: Model configuration

We can write the equations for the washer in the model shown in Figure 2:

$$\begin{aligned} & m\ddot{x} = F_i(t) + F_f(t, x, \dot{x}) \\ & F_f = \begin{cases} -fN(t,x), & \dot{x} > 0 \\ -mA\omega^2 \sin\omega t, & \dot{x} \equiv 0 \\ fN(t,x), & \dot{x} < 0 \end{cases}, \\ & F_i(t) = mA\omega^2 \sin\omega t \end{aligned} \tag{1}$$

where x is coordinate of the bar cross-section in the moving frame of reference associated with the oscillating base and at the same time coordinate of the washer near this section, $F_i(t)$ - the inertia force in relative motion, $F_f(t)$ - the friction force that occurs between the washer and the bar, m – the mass of the washer, A – the amplitude of the bar base oscillations, ω - their frequency, f - the friction coefficient, $N(t)$ - the elastic interaction force between the washer and the bar, the change of which is determined by its vibrational excitation. The frictional force is determined by Coulomb's law, not exceeding $|fN(t)|$ in absolute value, and balancing other effects at rest (in this case, the inertia force). In essence, the motion of the washer is determined by the character of change in the forces of elastic interaction between the washer and the bar during the oscillation period. To derive the expressions for the elastic force, it should be clarified that the system consists

of a bar with a rectangular cross-section of an elastic incompressible material and a hard washer fitted onto it, touching the bar with two faces, with the distance between them slightly smaller than the corresponding size of the bar. Now we will consider the elastic force emerging in the area where contact the bar and the washer contact (Figure 3).

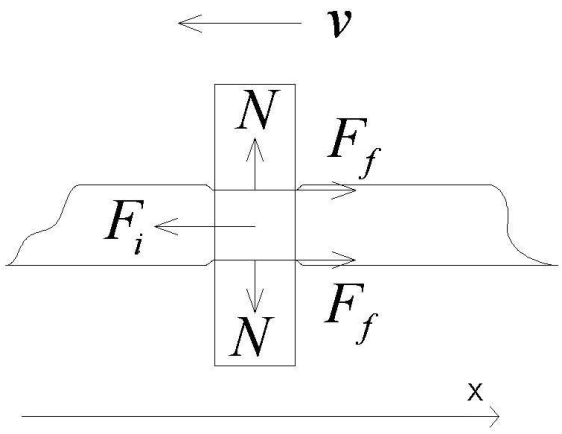


Figure 3: The contact area forces diagram

Under our assumptions, the normal force N_x in a certain section of the bar should satisfy the relation:

$$N_x = \rho w S(l - x), \tag{2}$$

where *rho* is the density of the bar material, S - the area of its cross-section, l - its length in the undeformed state, x - the coordinate of the cross-section, w - the acceleration of the base. Basing on the Saint-Venant principle, we can neglect the influence of restraint on the character of the bar expansion in the cross-sections sufficiently remote from it, then

$$\begin{array}{c} \sigma_x = \frac{N_x}{S} = \rho w(l - x) \\ \varepsilon_x = \frac{\sigma_x}{E} \end{array}, \tag{3}$$

where E is the Young's modulus. Assuming that the bar material is incompressible, we can find the corresponding lateral deformation, which would have occurred if the bar was free from the washer:

$$\varepsilon_n = -\frac{\varepsilon_x}{2} = -\frac{\rho w(l - x)}{2E} = -\frac{\rho A\omega^2(l - x)\sin\omega t}{2E}, \tag{4}$$

We tentatively assume that the elastic force that occurs between the washer and the stressed bar, corresponds to the force of interaction of the same washer with the unstressed bar, the width corresponding to the width of the initial bar in the stressed state. In addition, to avoid the occurrence of a gap between the bar and the washer, we assume that the washer is fitted onto the bar with a certain initial stress, sufficient to prevent it. Full lateral deformation of the bar can be written as

$$\varepsilon_n^* = \varepsilon_n + \varepsilon^0, \tag{5}$$

Where ε^0 is the initial deformation, which should provide the continuous intact washer motion. To meet this requirement over the entire length of the bar it is sufficient to assume

$$\varepsilon^0 \geq \frac{\rho A\omega^2 l}{2E}, \tag{6}$$

From this we can calculate the stress of the bar in a direction perpendicular to its axis, in the area where it contacts with the washer:

$$\sigma_n^* = E\varepsilon_n^* = -\frac{1}{2}\rho A\omega^2(l - x)\sin\omega t + E\varepsilon^0, \tag{7}$$

and obtain the elastic forces value in the area of the bar-washer contact:

$$N = \eta\sigma_n^* S_c, \tag{8}$$

Here $\eta > 1$ is the correction factor for the influence of the parts of the bar near the washer contact area, S_c - the area of the contact. Given this expression for the force of elasticity we can rewrite equation (1) as

$$\begin{array}{l} m\ddot{x} = mA\omega^2 \sin\omega t + F_f \\ F_f = \left\{ \begin{array}{ll} -\eta f S_c E \left(\varepsilon_n^0 - \frac{\rho A\omega^2 (l-x)}{2E} \sin\omega t\right), & \dot{x} > 0 \\ -mA\omega^2 \sin\omega t, & \dot{x} \equiv 0 \\ \eta f S_c E \left(\varepsilon_n^0 - \frac{\rho A\omega^2 (l-x)}{2E} \sin\omega t\right), & \dot{x} < 0 \end{array} \right. , \end{array} \tag{9}$$

When considering the oscillations in the standing-wave mode, or under its quasi-static compression, the force of elastic interaction between the washer and the bar is a function of the coordinate and time, and can be represented as

$$N(x,t) = N_s(x)\sin\omega t$$

In our previous article, we have examined the case of deformation of the bar uniform on the entire length, excluding the impact of the washer ($N_s(x) = const$). In that case the motion of the washer has taken on the character of vibrational translation with constant velocity. We consider the problem under the assumption that at a distance corresponding to the translation of the washer during one oscillation period the amplitude of the bar cross-section vibration and its deformations change only slightly and may be regarded as locally constant. The solution of the problem in this formulation has formed the basis for the algorithm of process numerical modeling and is performed at each iteration. A theoretical analysis of the system allows to explore locally in space and time all options for the impact on the washer (movement forward or backward along the broadened or narrowed bar under different initial conditions), and accordingly, all variations of basic movements in the form of which all arbitrary behavior of the washer in such a system can be represented. At the time the motion of the washer can be characterized by assigning it to one of three types - the relative trest or sliding in a positive or negative direction. Each type can be related with a phase of motion, in which the washer will always behave in accordance with this type. When considering a particular problem not all of them will necessarily take place, depending on the model parameters. From equation (9), we can consider every possible phase of the washer motion. It is convenient to begin by breaking the time axis into intervals of three types, determined character of the washer motion, which turned up in their course on the bar with zero relative initial velocity. Such an approach is similar to that used in [7] when considering the problem of motion of a body on a rough inclined (at α angle) vibrating plane (with β angle of vibration against the plane). It is even possible to compare the equation (1) (or to be more precise(9)) with the corresponding equation of motion of a particle on an inclined vibrating plane:

$$m^*\ddot{x} = m^* A^* \omega^* 2\cos\beta \sin\omega^* t - m^* g\sin\alpha + F^*,$$

Here m^* is the particle mass, A^* and ω^* - the amplitude and cyclic plane oscillation frequency, g - the acceleration of gravity, α and β - the angles mentioned above. At the same time, friction is

$$F^* = \left\{ \begin{array}{ll} -f^* N^*, & \dot{x} > 0 \\ f^* N^*, & \dot{x} < 0 \end{array} \right.$$

$N^* = m^*\cos\alpha - m^* A^* \omega^* 2\sin\beta\sin\omega^* t$ is support reaction force influencing the particle on the part of vibrating plane, and f^* is the coefficient of sliding friction. Comparing equation (1) and (1 *), we can obtain the following relations:

$$\left\{ \begin{array}{l} m^* = m \\ A^*\cos\beta = A \\ g\sin\alpha = 0 \\ f^* m^* \cos\alpha = \eta f S_c E \varepsilon_n^0 \\ m^* A^* \omega^* 2\sin\beta = \frac{\rho A\omega^2 l}{4E} \end{array} \right. , \tag{10}$$

These relationships allow us to use the findings from [7] for the accurate solution of the problem on the steady-state motion or velocity of vibrational translation locally, at a fixed variable x. However, the final formula [7] are oriented at the use of tables and graphical methods for finding roots of transcendental equations that emerge in the process of solving the problem, while the availability of simple and effective computer methods makes an alternative formulation of the findings more convenient. We will describe the dynamics of the washer motion for all three types of intervals. Interval of "motion in positive direction"

$$I_+ : F_i(t) > fN(t), \tag{11}$$

The positive inertia force exceeds the maximum possible friction force opposing it. The washer which found itself on the bar at the time, belonging to this interval in the state of relative rest, immediately starts to move in positive direction. Interval of "motion in negative direction"

$$I_- : F_i(t) < -fN(t), \tag{12}$$

Similarly, the negative inertia in the absolute magnitude exceeds the possible friction force. Within this interval, the washer which has originally found itself in the state of relative rest starts to move in negative direction. Interval of "relative rest"

$$I_0 : |F_i(t)| \; < \; |fN(t)|, \tag{13}$$

The friction force fully compensates for the inertia force and the washer will stay in relative rest for some time. Now we will find the boundaries of these intervals. To do so, we disclose expressions (11-13). From the condition (11) we obtain:

$$mA\omega^2 \sin\omega t \; > \; \eta f S_c E \left(\varepsilon_n^0 - \tfrac{\rho A\omega^2 (l-x)}{2E} \sin\omega t\right)$$

$$A\omega^2 \left(m + \tfrac{1}{2}\eta f S_c \rho (l-x)\right) \sin\omega t \; > \; \eta f S_c E \varepsilon_n^0$$

And for the first interval:

$$\sin\omega t \; > \; z_+, \qquad z_+ = \frac{2\eta f S_c E \varepsilon_n^0}{A\omega^2 \left(2m + \eta f \rho S_c (l-x)\right)}, \tag{14}$$

Similarly, disclosing the condition (12), we obtain:

$$mA\omega^2 \sin\omega t \; < \; -\eta f S_c E \left(\varepsilon_n^0 - \tfrac{\rho A\omega^2 (l-x)}{2E} \sin\omega t\right)$$

$$A\omega^2 \left(m - \tfrac{1}{2}\eta f S_c \rho (l-x)\right) \sin\omega t \; < \; -\eta f S_c E \varepsilon_n^0$$

As $\varepsilon_n^0 - \frac{\rho A\omega^2 (l-x)}{2E} \sin\omega t > 0$ - is a positive value, I_- takes place only in the intervals where the inertial force is negative, and taking into account the positive value $\eta f S_c E \varepsilon_n^0$, we can conclude that for the I_- interval to occur the expression $m - \frac{1}{2}\eta f S_c \rho (l-x)$ must be positive. Otherwise z_- would have been positive and exceeded z_+, which would mean that the interval I_- is included into the interval I_+ (see Fig. 4). Thus, for this interval it can write the following:

$$\sin\omega t \; < \; z_-, \qquad z_- = -\frac{2\eta f S_c E \varepsilon_n^0}{A\omega^2 \left(2m - \eta f \rho S_c (l-x)\right)}, \tag{15}$$

Obviously, the interval will contain the points not belonging to I_+ and I_-. The condition of belonging to this point in time interval can be written as:

$$\begin{cases} \sin\omega t - z_+ < 0 \\ \sin\omega t - z_- > 0 \end{cases}, \tag{16}$$

Now from (14) and (15) we find the boundaries of the intervals:

$$\sin\omega t_+^{(k)} = \sin\delta_+^{(k)} = z_+, \quad \sin\omega t_-^{(k)} = \sin\delta_-^{(k)} = z_-, \tag{17}$$

where $\delta_+^{(k)} = \omega t_+^{(k)}, \quad \delta_-^{(k)} = \omega t_-^{(k)}$. For further calculations, it is convenient to determine "major" roots (17):

$$\delta_+ = \arcsin z_+ \;\; \delta_- = \pi - \arcsin z_-, \tag{18}$$

All the other roots can be easily expressed through values δ_+ and δ_- . It is worth noting that some intervals may not exist for the given specific parameters of the system. In the case shown in Figure 3 a) all three types of intervals take place, but, for example, when $z_+ > 1$ the inequality that determines I_+ cannot be satisfied in principle, and similarly when $z_- < -1$ the interval I_- cannot exist (see Fig. 3 b), c)). If, however, we have both $z_+ > 1$ and $z_- < -1$, the washer cannot break away from the bar and will oscillate in conjunction with it, and such case is presented in Figure 3 d). On the other hand, when the friction coefficient is zero, or when the gap between the washer and the bar is large (here this case is not considered), the washer will move along the bar without resistance, regardless of directions (Fig. 3 e).

As noted above, the motion of the washer can be represented as a set of sliding phases and phases of relative rest. For each of these phases, the motion is described by simple linear differential equations, and the major difficulty in direct approach to solving the problem is finding the points of phase change. We will obtain the equations for these points from the motion equations integrals. Let in the initial time $t = t^*$ be known that $\dot{x}(t^*) = \dot{x}^*$, and $x(t^*) = 0$ (without loss of generality, we can always choose the origin of coordinates this way). Then integrating (9) and taking into account the initial conditions, we obtain:

$$\dot{x}(t) = \mp\frac{fS_cE\varepsilon_n^0}{m}\left(t - t^*\right) - A\omega\left(1 \pm \frac{fS_c\rho(l-x)}{2m}\right)\left(\cos\omega t - \cos\omega t^*\right) + \dot{x}^*, \tag{19}$$

$$\begin{array}{l} x(t) = \mp\dfrac{fS_cE\varepsilon_n^0}{2m}\left(t - t^*\right)^2 + A\omega\left(1 \pm \dfrac{fS_c\rho(l-x)}{2m}\right)\cos\omega t^*\left(t - t^*\right) - \\ -A\left(1 \pm \dfrac{fS_c\rho(l-x)}{2m}\right)\left(\sin\omega t - \sin\omega t^*\right) + \dot{x}^*(t - t^*) \end{array}, \tag{20}$$

Top marks are for the positive, and bottom marks are for a negative initial velocities, respectively. Equations (19) and (20) make sense until the point of sign change or velocity vanishing. At this point either the direction of the washer motion changes, or the phase of relative rest is set. The transition point $t^(**)$ is determined in the transcendental equation:

$$\dot{x}(t^{**}) = \mp\frac{fS_cE\varepsilon_n^0}{m}\left(t^{**} - t^*\right) - A\omega\left(1 \pm \frac{fS_c\rho(l-x)}{2m}\right)\left(\cos\omega t^{**} - \cos\omega t^*\right) + \dot{x}^* = 0, \tag{21}$$

which can be modified as:

$$\mp\frac{fS_cE\varepsilon_n^0}{A\omega^2(2m \pm fS_c\rho(l-x))}\left(\omega t^{**} - \omega t^*\right) - \cos\omega t^{**} + \cos\omega t^* + \frac{\dot{x}^* m}{A\omega(2m \pm fS_c\rho(l-x))} = 0$$

Featuring the characteristic values $z_\pm$ introduced previously, introducing the phase angles for stopping points $\varphi_\pm = \omega t^{**}$, $\delta_\pm = \omega t^*$ - the phase angles for the points of the beginning of motion in positive or negative direction, and as well denoting $a_\pm = \frac{\dot{x}^* m}{A\omega(2m \pm fS_c\rho(l-x))}$, the resulting equation can be written in a more compact form:

$$-z_\pm\left(\phi_\pm - \delta_\pm\right) + \cos\delta_\pm + a_\pm = \cos\phi_\pm, \tag{22}$$

Equation (22) is known as Kepler's equation. The data obtained allow to examine the process as a whole. Using formula (20) and the points of the beginning and end of all the washer motion phases, we can derive a formula for the translations at each stage of sliding:

$$\begin{array}{l} S_\pm = \mp\dfrac{fS_cE\varepsilon_n^0}{2m\omega^2}\left(\varphi_\pm - \delta_\pm\right)^2 + A\left(1 \pm \dfrac{fS_c\rho(l-x)}{2m}\right)\cos\omega t^*\left(\varphi_\pm - \delta_\pm\right) - \\ -A\left(1 \pm \dfrac{fS_c\rho l}{2m}(l-x)\right)\left(\sin\varphi_\pm - \sin\delta_\pm\right) + \dfrac{\dot{x}^*}{\omega}\left(\varphi_\pm - \delta_\pm\right) \end{array}, \tag{23}$$

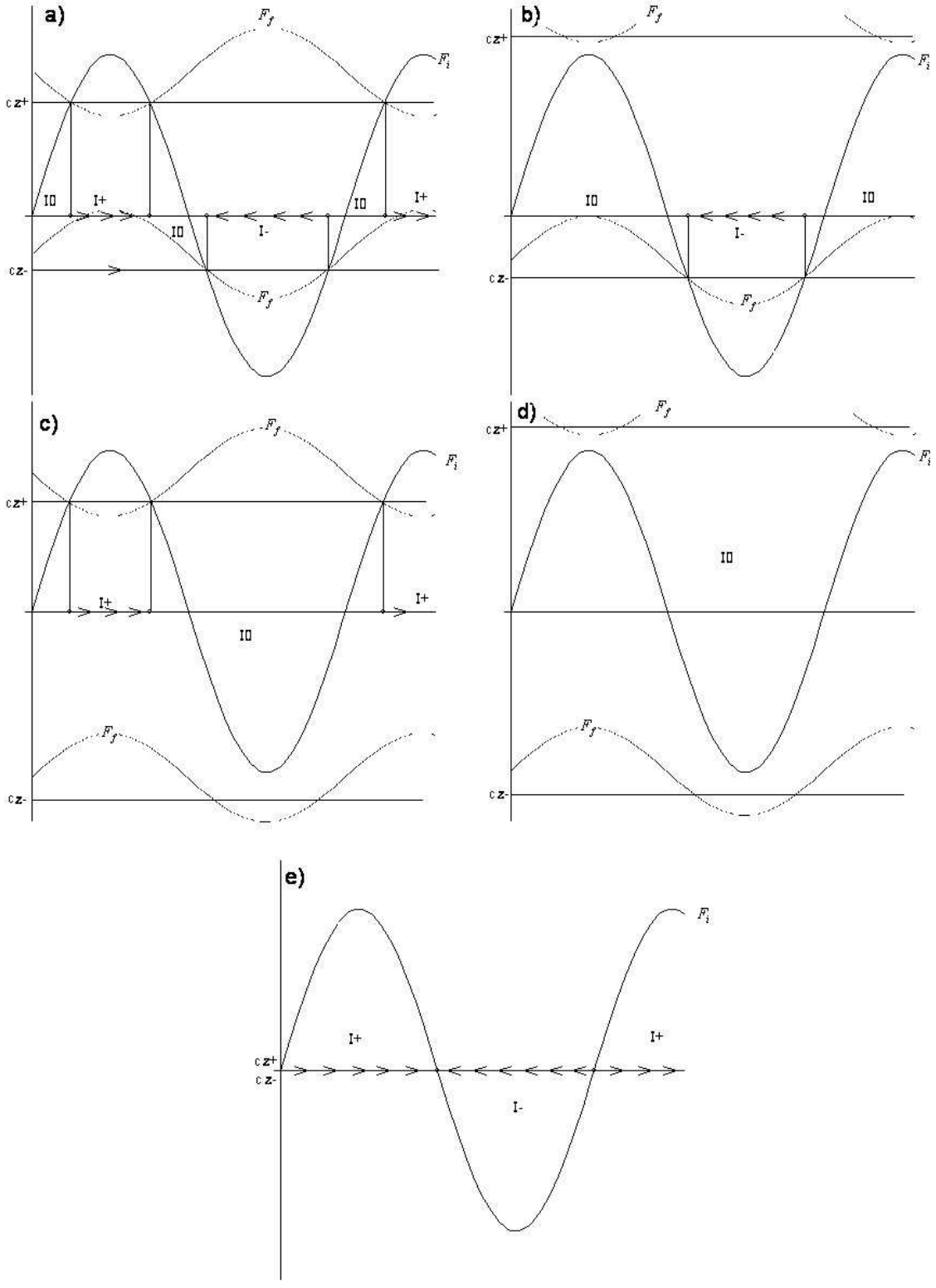


Figure 4: Inertial and possible friction forces variation in time

Using this expression can get the average velocity developed by the washer at a given phase. In the framework of this approach to the problem, we can explore the regular established modes

of the washer motion with the switching period equal to the period of the bar base oscillations. In total there are four classes of such modes. The scheme of possible motions would be quite similar to presented in [7]. Mode 1 - has a slide in both directions, while the motion phases involve non-zero duration "stops" between them. Mode 2 - differs from the Mode 1 in that that the stops are instantaneous. Mode 3 - rotational sliding in two directions with one long and one instantaneous stops. Mode 4 - sliding in one direction with a long stop.

Basing on the described approach to solving the problem a program has been works out which allows to model the process of washer moving along the bar. The algorithm of this program for the case study of a steady-state process can be represented by the following scheme:

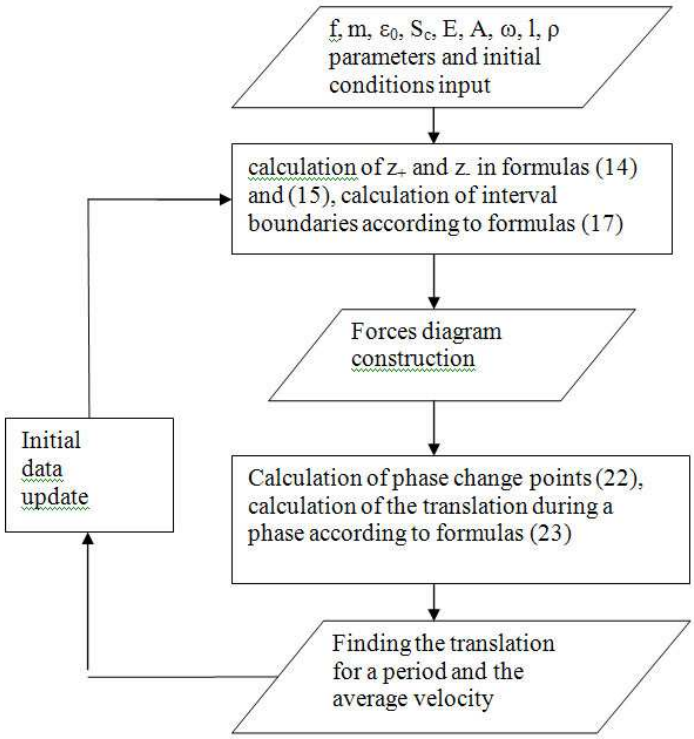


Figure 5: algorithm of numerical modelling

For example, when the friction coefficient f is 0.15, the mass of the washer m is 50 g, the area of contact S_c is 0.5 cm^2, the amplitude of vibration A is 5 mm, the cyclic frequency ω is 150 c^-1, the initial deformation ε_0 is 0.000003, Young's modulus E is 2210^11 Pa, the length of the bar l is 0.4 m, the density ρ is 7850 kg/m^3, at the beginning of the motion from the middle of the bar, the use of an algorithm and the corresponding program for one period has shown the average velocity of the translations is 0.0474 m/c. Graphs of velocity, translations and force during the period are displayed in Fig. 6.

3 Conclusions

In this article we present a new possible mechanism of vibrational translation in a system similar to the Chelomey pendulum. The analytical study of the system has been carried out using the vibrational mechanics approach. The basic relations characterizing the described effect have been obtained, as well as an algorithm and the corresponding program worked out. We have shown some examples of the implementation of the algorithm which demonstrate the potential experimental verifiability of the theory.

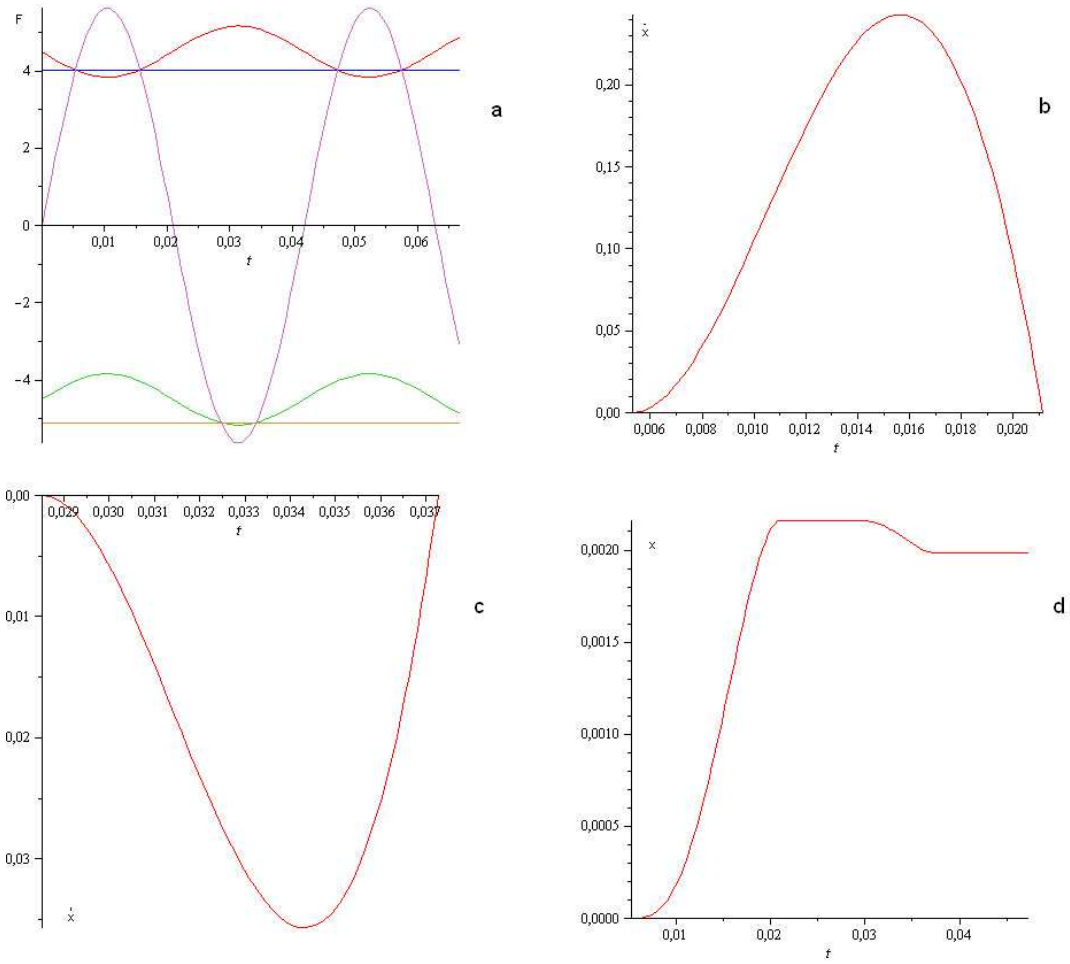


Figure 6: A period. a) Forces, b) velocity during the "positive" phase, c) velocity during the "negative" phase, d) Position change during the period

Acknowledgements

The work is executed within the Wave and vibrational processes in machinery OEM RAS fundamental researches program

References

[1] Chelomey V.N. Paradoxes in mechanics due to vibrations. Doklady Academii nauk SSSR. Mechanics - 1983. v. 270, No 1. - pp. 62-67.

[2] Blekhman I.I. Vibrational Mechanics. World Scientific Publishing Co. Pte. Ltd. Singapore, New Jersey, Hong Kong, 2000. - 509 p.

[3] Kurbatov A.M., Chelomey S.V., Khromushkin A.V. On a Chelomey pendulum issue. Izvestiya Academii nauk SSSR, 1986, No 6, pp. 63-65.

[4] Menyaylov A.I., Movchan A.V. On a rod-washer systems stabilization with vibration influenced hinge. Izvestiya Academii nauk SSSR, 1984, No 6, pp. 35-40.

[5] Blekhman I.I., Malachova O.Z. On a quasi-equilibrium Chelomey pendulum states. - Doklady Academii nauk, 1988, v. 287, No 2, pp. 290-294.

[6] Myalo E.V. Dynamics of a flexible rod with an easy fitted ring in parametric excitation. Master of Sciences dissertation. Russian Academy of Sciences. 2008.

[7] Blekhman I.I. and Dzhanelidze G. Yu. Vibrational Displacement. - Moscow, Nauka, 1964. 410 p. (in Russian).

[8] Thomsen, J.J Vibrations and Stability: Advanced Theory, Analysis, and Tools, (2nd ed., revised). Springer-Verlag, Berlin Heidelberg, 2003

Ivanov K.S., V.O., Bolshoy av., 61, Saint-Petersburg, 199178, Russia

About constructing the new coarse-grained DNA model

I. P. Kikot E. A. Zubova M. A. Mazo N. A. Kovaleva L. I. Manevitch
irakikotx@gmail.com

Abstract

Current coarse-grained (CG) models of DNA are useful due to their computational efficiency, but are generally not as versatile as the computationally much more expensive all-atom models. Here we propose an alternative CG model based on preserving the main (ribose) mobility of the DNA backbone by appropriately choosing the coarse grains. Construction of the model and the choice of the corresponding CG potential function are discussed.

1 Introduction

Mechanical properties of DNA molecules are interesting not only because of their biological importance but also because of wide-spread using of DNA in current nanotechnologies. These properties depend on temperature, base sequence, type of solution and other conditions.

One of the most powerfool tools for investigating of nucleic acids is molecular modeling. Nowadays the most wide atomic force fields are CHARMM27 [1] and AMBER [2]. The validity of these force fields has been checked by many simulation. These atomic-level models provide very thorough and detailed description of the molecule and the solution. But such models are restricted in sequence length and in time scale - the longest published simulation was $1.2\mu s$[3]. Implicit solvent approach decreases the amount of calculation but not crucially. At once DNA molecules considered in experiments often have much larger length that one available in all-atomic modelling, and many phenomena have much larger time scale than microsecond, so they cannot be observed in unrestrained all-atomic simulations. Hence constructing the reliable, adequate coarse-grained models is one of the most important tasks in the domain.

There exist several coarse-grained models. Most of them are aimed at modeling of only one phenomenon. For example, model, described in [4], is created for modeling of melting and reproduce correctly melting sequence and temperature dependence. The model in [5] describes low-temperature fluctuations near equilibrium point (B-form of DNA). The model [6] represents each nucleotid as orthonormal reper and investigates Brownian dynamics. The model [7] is rather complex and is aimed at simulating of B-form DNA.

DNA molecule has two different structural part: sugar-phosphate backbone and nucleic base pairs [8]. Base pairs are organized in twisted pile, and their main biological destination is to code information. The second structural part is sugar-phospate backbone. It consists of two threads which are also twisted into helix and forms a layer between base pairs and solvent. It should be noted that sugar-phosphate backbone is rather flexible [3, 9] and often exhibits locally distorted conformations[3] what can influence the mechanical properties. These facts are usually not taken into account in coarse-grained models. So in present paper mobility of the backbone is analyzed very thoroughly from different sources - all-atomic molecular dynamics simulation and crystallogaphic structures - for constructing the coarse-grained model which is able to reproduce physical mechanisms of the backbone flexibility.

Sure, DNA structure is influenced by sequence of base pairs and environment: type of the solvent, salt concentration, water number [10]. But this paper is dedicated to investigation of the backbone mobility only.

Main challenge of constructing of coarse-grained model is to find structural elements which are essential for describing of physiologically important dynamics of the molecule. The main backbone mobility is one related with sugar puckering. The aim of the paper is to investigate how local

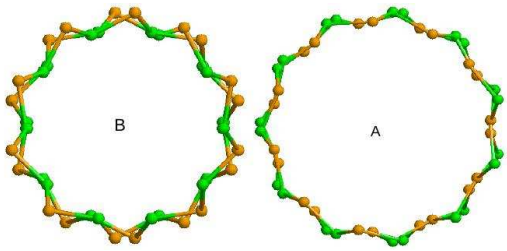


Figure 1: P and C4' atoms in A and B forms. P atoms are light and C4' atoms are dark.

helix geometric parameters are connected with sugar conformation and what is the minimal set of elements and corresponding potentials able to describe the influence of the ribose mobility on helix local geometry.

2 Choosing of the grains

We should choose grains so that all types of mobility which are considered below would be implemented in our model. We suppose that grains are localised on some atoms. Such approach enable us to compare our coarse-grained model dynamics with all-atomic dynamics. So what atoms our grains should be localised on? Firstly, one grain for backbone should be localised on the phosphor atom because the phosphate group has rather rigid structure and is heavy and charged. Another point we are interested in is the atom $C1'$ which is the point of connection between sugar-phosphate backbone and nitrogen bases. This atom is one of the ends of the glycosid bond which is an axis for base rotation, and line $C1' - C1'$, connecting $C1'$ atoms from complementary nucleotide is an axis for rotation of base pair[11]. One would suppose that these two points are sufficient for describing the sugar-phosphate backbone but it isn't the case. These two points don't describe 3-dimensional structure of backbone fragment. Particularly one has to have a stationar value for direction to the $C1'$ atom and base for describing base opening. But if there isn't the third point there isn't origin for this value. Besides there is another reason. DNA molecule has helical structure, which is related with torsions. But time dependence of torsions in $P - C1' - P - C1'$ chain doesn't show oscillating near equilibrium point, so they cannot govern twisting of the helix and potentials of angles and torsions which implement a backbone motion during A-B transition and base opening would be very sophisticated. So minimal structure which describe local geometry of the backbone should consist of 3 grains per nucleotide. There are two possible variants of choosing the third point: it is atoms $C3'$ and $C4'$. But there are some reasons for $C3'$ be more preferable than $C4'$. Firstly, atom $C4'$ changes its position according phosphates during A-B transition (see Fig. 1) while $C3'$ doesn't. Secondly, atoms $C3'$ keeps the distances to P and $C1'$ atoms (it's shown below). So, the third point for backbone was chosen to be $C3'$.That is backbone fragment of 1 nucleotide is described by 3 grains, localized on $P, C3', C1'$ atoms (see Fig. 2). The chain $.. - P - C3' - P - ...$ remains almost immobile during conformational transitions (such as A-B transition and base openings), and rotation of the $C3' - C1'$ bond around adjacent phosphor lines stand for motion of ribose during base openings.

The next section proves following: if we consider pyramid with points $P_1, C1', C3', P_2$ (with $C1'$ and $C3'$ atoms belonging to the ribose which is between two adjacent phosphorous atoms P_1 - from $5'$ side and P_2 - from $3'$ side), we'll see that this geometric structure has two equilibrium point - A-like and B-like ones. More concretly, the distances between atoms P_1, P_2 and $C1'$ have two different equilibrium points(A-like and B-like values), while distances between atom $C3'$ and three other atoms have only one equilibrium point. This tendency can be seen from a stable trajectory of both B-form in water and A-form in ethanol-water solution and from "ideal" crystallographic structure. In section 4 one can find how this fact is implemented by potentials of our model.

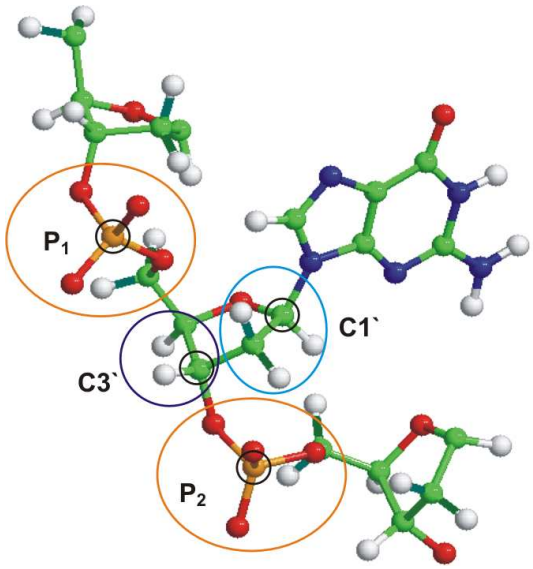


Figure 2: Choosing of the grains on the backbone

3 Sugar repuckering and concerted switches of local backbone geometry

Sugar puckering is described by pseudorotational angle, which is calculated from torsions of sugar ring. The two main sugar conformations are $C3'$-*endo* and $C2'$-*exo*, but intermediate conformations are also possible and have been seen in crystallographic structures [9] as well as in MD simulations [3].

The sugar switching goes along with A-B transition, and sugar conformations is one of the feature distinguishing A- and B-form [9].

The analysis, decribed below, shows that sugar switching strongly correlates with deformations of the local backbone structure. We have investigated pairwise distances in the neighbouring backbone fragment in order to understand which ones of them change during the sugar switching and which ones remain. Our analysis is based upon several sources. Firstly, we have found several local sugar *switches* in stable trajectories and investigated concerted distance switches. We have found that sugar repuckering corelate with sugar-phosphate backbone switches to the A-like structure. It enables us to use second source of information about this type of mobility: differences and similarities in stable structures of A- and B-form (both average MD structures and crystallographic structures were considered) became the basis for the grain choosing.

3.1 Analysis of MD trajectories

20-ns MD trajectory of B-form in aquaeuos solution was considered. B-form is rather flexible structure and pseudotorsional angle spend about 5-10 % of the time in non-canonical regions [3]. We were interested in local switches of pseudorotational angles and their correlations with structure transformations. We prove that sugar switches are not independent, they accompany changing of the local structure toward A-like conformation. One can see from the time dependence (see Fig. 3) that sugar switches are simultaneous with $P - P$ distance switch to a smaller ("non-canonical") value. The similar effects can be found for distances between atoms $C1'$ and P.

A-form stable trajectory in water-ethanol solution, which was cordially presented by Dr. Noy and Prof. Orozco, has also been considered. In this trajectory one can also notice sugar switches concerted with local backbone transformations when some distances exhibit "non-canonical values", which differ from mean ones significantly.

Canonical and non-canonical values observed in trajectories are summarized in the Table 8. It should be noticed that non-canonical values for B-form are close to canonical ones in A-form

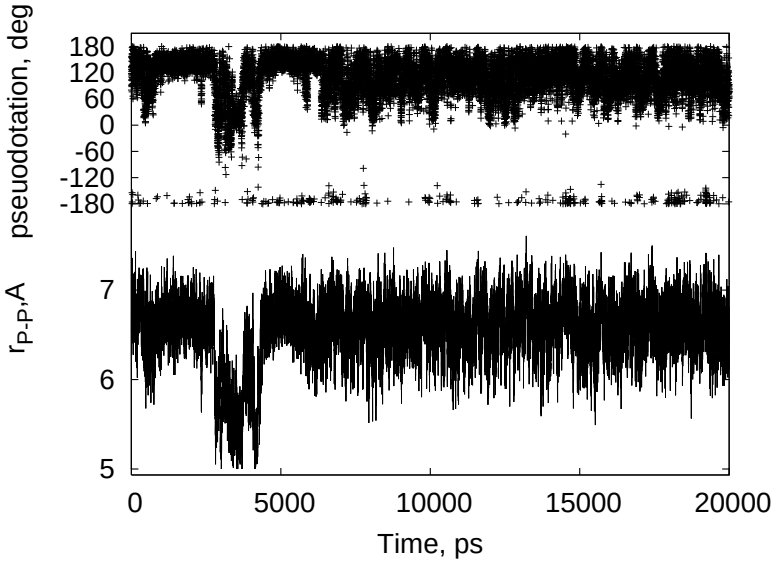


Figure 3: Correlation between sugar and distance switches

distance between atoms	A-form in ethanol/water, non-canonical values	B-form in water, canonical values	B-form in water, non-canonical values	A-form in ethanol/water, canonical values
$C1' - P_2$	4.32 ± 0.29A(36%)	4.38 ± 0.36A	4.7 ± 0.19A	4.78 ± 0.2A(64%)
$P_1 - C1'$	5.03 ± 0.29A(15%)	5.27 ± 0.39A	4.8 ± 0.25A	5.39 ± 0.34A(85%)
$P_1 - P_2$	6.94 ± 0.36A(25%)	6.76 ± 0.59A	6.1 ± 0.4A	6.14 ± 0.67A(75%)
$C3' - C1'$	no n/c values	2.4 ± 0.15A	no n/c values	2.38 ± 0.17A
$C3' - P1$	no n/c values	4.53 ± 0.37A	no n/c values	4.52 ± 0.25A
$C3' - P2$	no n/c values	2.66 ± 0.1A	no n/c values	2.65 ± 0.11A

Table 8: Canonical and non-canonical values and their deviations obtained from MD trajectory of A- and B-forms. Per cents in brackets is per cent of time spent in close to the value domain.

and vice versa. So we can conclude that there are two different stable conformations for sugar-phosphate backbone: A-like and B-like, and sugar repuckering is one of the effects of such mobility. It's important that sugar repuckering is the "softest" mobility of the backbone, that is the energy barrier is the smallest (as compared with ther types of mobility). One can suggest that sugar switches play the role of bampers which enable to react on stress outside influence.

3.2 Analysis of crystallographic structures

As revealed in previous section, the analysis of A-DNA can provide us by realiable data about mobility of sugar-phosphate backbone even in stable B-DNA. Let us consider "ideal" crystallographic structures of A- and B-form. Consideration of the distances from previous section yields the values which slightly differ from mean values in trajectory(see Table 9). But we can also notice that the pairwise distances between atoms $C3'$ and $C1'$, $C3'$ and P_1, $C3'$ and P_2 are rather similar in both forms while distances between $C1'$ and P_2, between P_1 and P_2 differ significantly.

4 Obtaining the potentials

General approach for obtaining the potentials was to mimic all-atomic interactions as much as possible. One of the potential estimating method is based on statistical mechanics: every value (for example, distance between two atoms l) has some distribution $\rho(l)$. We suppose that this

distance	B-form	A-form
$P_1 - P_2$	6.54A	5.63A
$P_2 - C1'$	3.7A	4.6A
$C1' - P1$	4.9A	5.4A
$C3' - C1'$	2.36A	2.37A
$C3' - P1$	4.07A	4.16A
$C3' - P2$	2.37A	2.36A

Table 9: Values from "ideal" cristallographic structures

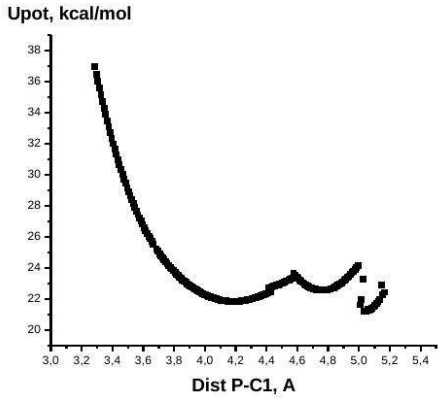


Figure 4: Model potential for distance between $C1'$ and P_2 obtained by considering of isolated fragment

value has Boltzman distribution, that is $\rho(l) \sim e^{-\frac{U(l)}{kT}}$ with $U(l)$ being the potential of this value. So, knowing distribution $\rho(l)$ from stable MD trajectory we can obtain potential $U(l)$. Of cource such method can yield only rough upper estimates for potentials which are to be tuned by further analysis of coarse-grained dynamics.

Another method for obtaining the potentials is the detailed consideration of all-atomic potentials in small fragment. It will be described on example of bond between atoms $C1'$ and P_2. Let's consider a fragment consisting of sugar ring and phosphate (from the $C3'$ - side). For energy being dependent only from this distance one should avoid other degrees of freedom. It can be done by minimisation procedure: the all-atomic system is relaxing with fixed distance between these atoms. So, energy in relaxed state is taken as the value of model potential of this distance.

The result of such procedure is shown on Fig 4. It worth noting that obtained potential is two-well one. Moreover, the positions of the minimums correspond to equilibrium values of this distance in A- and B-DNA, and values of pseudorotational angle in relaxed position also correspond to A-and B-DNA (see Fig. 5). This is an additional confirmation of the existence of two stable backbone conformations. Also we can conclude that it is a particular property of backbone but not consequence of different conditions.

So we have obtained all potentials for our model combining different methods. We can now list them all: it is harmonic bonds for distances $C3' - P_1, C3' - P_2, C3' - C1', C1' - C1'$. Bond $C1' - P_2$ is two-well. Distances $P_1 - P_2, P_1 - C1'$ correlates very well with the sugar switches, hence with distance $C1 - P_2$, so instead of two-well potential for them we introduce the harmonic restraint for such linear combination $l_{P-P} + tl_{C1'-P_2}$ which has similar values in A and B-forms. Also we introduce torsions around bonds $P_2 - C3'$ and $C3' - P_2$ to maintain helical structure and to govern base openings. Potential of interactions between bases and backbone will be discussed elsewhere.

So all-atomic helical backbone in our model is replaced by sequence of "pyramides" having two stable conformations which are connected by torsions. This description is rather simple, but it enables to take into account the geometric structure of the backbone and implement the ribose

mobility.

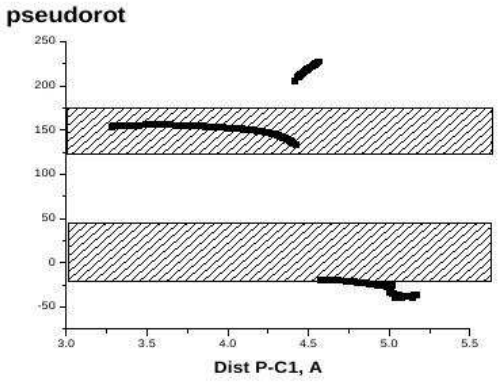


Figure 5: Dependence of pseudorotational angle in relaxed state from distance $C1' - P_2$. Dashed are regions typical for B-(upper one) and A-(lower one) forms of DNA.

5 Other types of backbone mobility

There are three types of backbone mobility, which dominate the conformational freedom of the DNA molecule [3]. It is: (i) sugar puckering, (ii)rotations around ζ, ϵ torsions, (iii) rotations about α, γ torsions. These types of mobility govern the backbone flexibility, so it was necessary to consider them all to reproduce the mechanical properties of the molecule within the framework of our model. We have yet considered the sugar repuckering, so let's consider other two ones.

The concerted rotation around $\zeta - \epsilon$ torsions generates two major confomers: BI and BII [12]. In long MD simulation [3] a dinucleotide spends around 85% of the time in the canonical BI conformer and 15% in the BII form, in agreement with experimental data[13].

It's still unclear how it can be implemented in our model. This mobility is considered to provide base opening [14] and can be taken into account by changing the torsion ppotentials which describe base opening.

Although conformational changes around α, γ torsions are less prevalent, the population of noncanonical α, γ torsions is not negligible, since a dinucleotide spends around 1.5% of the time in these regions [3] in agreement with experimental evidence [15].

We have found that the transitions of α, γ torsions are almost always simultaneous and are concerted with changing of the distance between atoms $C3'$ and P_1. It is the foundation of how this type of mobility can be complemented in our model. The forementioned procedure of obtaining the potential from investigating the separate fragment applied to distance between atoms $C3'$ and P_1 also gives two-well potential. It is a consequence of existing two different conformation with different α, γ torsions. That is α, γ mobility can be implemented in our model by introducing two-well potential for this bond.

It should be noted that the population of noncanonical α, γ torsions depends strongly on the force field. For example, in *parm95* they were much more common, but it was considered as an artifact and then force field was impoved to decrease noncanonical α, γ population [16].

6 Methods

B-form trajectory in water: As is common in the field, Dickerson's dodecamer ($d(CGCGAATTGCGC)_2$) was chosen as model system. This sequence is a very stable B-duplex containing a full helical turn. The crystal structure was added by 6004 water molecules and neutralized by 24 Na+ ions. The AMBER *parmbsc0* force field [16] for DNA and TIP3P model for water molecules have been used. The simulation consisted of 4 steps. Firstly 100 steps of minization were done with DNA fixed to X-ray cooridnates with harmonic restraints of $5kcal/mol/A^2$.

Then system was equilibrated for 5 ns in NPT ensemble with restraints of $1.0 kcal/mol/A^2$, with temperature increasing from 0 to 300K. After that the second stage of equilibration was done also for 5 ns, when restraints decreased to $0.1 kcal/mol/A^2$ and temperature was 300K throughout. The production run was done with no restraints at all for 20 ns, temperature was 300K. Only this last step was involved into analysis.

A-form trajectory in ethanol/water mixture: The same sequence was considered. The DNA was neutralized by 22 counterions and solvated into 1301 molecules of ethanol and 694 water molecules. *parm99* [17] force field was used to represent DNA interactions while TIP3P and OPLS parameters were used for solvents. Length of the trajectory is 10 ns.

Analysis: For the considered values in A-form hystogram were obtained and then approximated by two-peaks gaussian distribution. Parameters of gaussian distributions are mean values and mean-squared deviations in the Table 8. Per cents were obtained from relation of areas under two gaussians. For B-form non-canonical values are less common, so hystograms usually don't have the second peak. So mean values and mean-squared deviations were obtained as averaged over all observed sugar switches.

7 Conclusions

Main types of backbone mobility, that is ribose and $\alpha - \gamma$ ones, were analyzed thoroughly from different sources - MD simulation and crystallographic structures. It is shown that the minimal set of knots which can describe all types of backbone mobility is three points per nucleotide for the backbone. The sugar-phosphate backbone is replaced by sequence of pyramides whose mutual disposition is described by torsions. The potentials for the grains which implement analyzed mobility are obtained.

We speculate that such an approach enables to reproduce the physical mechanisms which are responsible for local transitions so the model can correctly reproduce all-atomic dynamics and yield reliable data about mechanical and physical properties in DNA molecule. The conjecture will be tested in a forthcoming publication. Our model is supposed to be used for investigating such properties of DNA molecule as bending and torsion stiffness, heat conductivity. Simplicity of the model gives an opportunity for analytical description.

Acknowledgements

The research was supported by Division of Chemistry and Materials Technologies of RAS (grant program N3), RFBR (grant 08-04-91118-a) and CRDF (grant RUB2-2920-MO-07). The authors are also deeply grateful to Dr. A. Noy and Prof M. Orozco for the trajectory of the A-DNA in ethanol/water solution and thank Prof. A. Onufriev for helpful discussions and for obtaining the MD trajectory of B-DNA in water.

References

[1] N. Foloppe, A.D. MacKerell. All-atom empirical force field for nucleic acids. I. Parameter optimization based on small molecule and condensed phase macromolecular target data. *J Comput Chem* **2000**, V.21, pp. 86–104

[2] D. A. Case, T. E. Darden, T. E. Cheatham, J. Wang, R. E. Duke, R. Luo. AMBER8. University of California, San Francisco

[3] A. Perez, F.J. Luque, M. Orozco. Dynamics of B-DNA on the microsecond time scale. *Journal of American Chemical Society* **2007**, V. 129, pp. 14739–14735

[4] T. A. Knotts et al. A coarse grain model for DNA. *J. Chem. Physics* **2007**, V. 126, 084901

[5] N. A. Kovaleva, L. I. Manevitch, A. I. Musienko et al. Low-frequency localized oscillation of DNA double helix. *Polymer Science* **2009** Vol. 51, N. 7 (in Russian)

[6] Alexey K. Mazur. Kinetic and Thermodynamic DNA Elasticity at Micro- and Mesoscopic Scales *J. Phys. Chem. B* **2009**, V. 113, pp. 2077–2089

[7] A. Morriss-Andrews, J. Rottler, and Steven S. Plotkin. A systematically coarse-grained model for DNA and its predictions for persistence length, stacking, twist, and chirality. *J. Chem. Phys.* **2010** V. 132, 035105

[8] J. D. Watson, F. H. Crick. A structure of deoxyribose nucleic acid. *Nature* **1953**, V. 171, pp. 737-738

[9] W. Saenger. Principles of Nucleic Acids Structure. **1984**, Springer, New York

[10] M. Y. Tolstorukov, V. I. Ivanov, G. G. Malenkov, R. J. Jernigan, V. B. Zhurkin. Sequence-dependent B-A transition in DNA Evaluated with dimeric and trimeric scales. *Biophys J* **2001**, V. 81, pp. 3409–3421

[11] S.Niedle. Principles of Nucleic Acid Structure. **2008**, Elsevier, USA

[12] B. Hartmann, D. Piazzola, R. Lavery. BI - BII transitions in B-DNA. *Nucleic Acids Research* **1993**, Vol. 21, No.3, pp. 561–568

[13] H. O. Bertrand, T. Ha-Duong, S. Fermandjian, B. Hartmann. *Nucleic Acids Research* **1998**, Vol. 26, No.5, pp. 1261–1267

[14] U. D. Priyakumar, A. MacKerell. Computational Approaches for Investigating Base Flipping in Oligonucleotides. *Chemical Reviews* **2006** V. 106, No. 2. pp. 489–505

[15] P. Varnai, D. Djuranovic, R. Lavery and B. Hartmann. α/γ Transitions in the B-DNA backbone *Nucleic Acids Research* **2002**, Vol. 30, No. 24, pp. 5398–5406

[16] A. Perez, I. Marchan, D. Svozil, J. Sponer, T.E. Cheatham III, C.A. Laughton, M. Orozco. Refinement of the AMBER force field for nucleic acids: improving the description of alpha/gamma conformers. *Biophys J* **2007**, V. 92, pp. 3817–3829

[17] T. E. Cheatham, P. Cieplak,P. A. Kollman. A modified version of the Cornell et al. force field with improved sugar pucker phases and helical repeat. *J. Biomol. Struct. Dynam* **1999**, V. 16, pp. 845–862

Irina P. Kikot, 119991, Kosygina 4, Moscow, Russia

Coulomb law in the generalized differential form in problem about torsion oscillations of the cylindrical rod on the infinite belt

Alexey A. Kireenkov
kireenk@ipmnet.ru

Abstract

It is proposed the coupled exact integral model of the sliding and spinning friction built on the supposing of the validity of the generalized Coulomb law in differential form for elementary area inside of contact spot. It is shown that as in case of using classical Coulomb law in differential form, the normal component of friction force is zero. The friction force is direct opposite the relative velocities of sliding, but additional polynomials terms appear in expressions for friction force and torque. To escape using of the integral expressions in the equation of motion, the model based on Pade expansions of the first and second order are constructed. Additional polynomials terms which are appeared in expressions for friction force and torque lead to arising self-exited torsion oscillations in the systems consist of the spring-supported cylindrical rod one end of that is bearing to the infinite belt moved with the constant velocity.

1 Introduction

It is known that the classical Coulomb law for friction is violated in the case of the combined kinematics when rubbing elastic solids participate simultaneously in sliding and spinning motions. One of the first models describing the relation between the sliding and spinning friction in the case of nonpoint contact between rubbing bodies was proposed by P. Contensou[1]. However, the model restricted itself only to the calculation of the friction force without considering the friction force moment. A principally new development of the Conten-sou theory was given by V.F.Zhuravlev [2]. With use of the transport of the coordinate system origin to the instant velocity center, exact analytical expressions were obtained for the friction force and moment in elementary functions. For convenience of using these functions in the problems of dynamics, V.F. Zhuravlev constructed the corresponding Pade approximations. This approach made it possible to develop a principally new two dimensional model of sliding and spinning friction and, further, resulted in the development of a number of models of the combined dry friction based on the Pade approximations [3]. The distinguishing feature for all these models was the fact that all of them were constructed under the assumption of validity of the Coulomb law in differential form for a small area element inside the contact spot (Fig.1).

However, it is known [4] that the real law of friction is nonlinear and can be described by the function

$$F = f(\operatorname{sgn} v + \mu_1 v^3 - \mu_2 v)$$

where v is the velocity of the relative slip of rubbing bodies, f is the friction coefficient, while μ_1 and μ_2 are the coefficients, which can be determined experimen-tally.

The use of the Coulomb law in the generalized form in the case of the combined kinematics, when the rubbing bodies participate simultaneously in sliding and spinning mo-tions, gives the differentials $d\mathbf{F}$ and $\mathbf{dM_C}$ of the friction force and moment, respec-tively, with respect to the

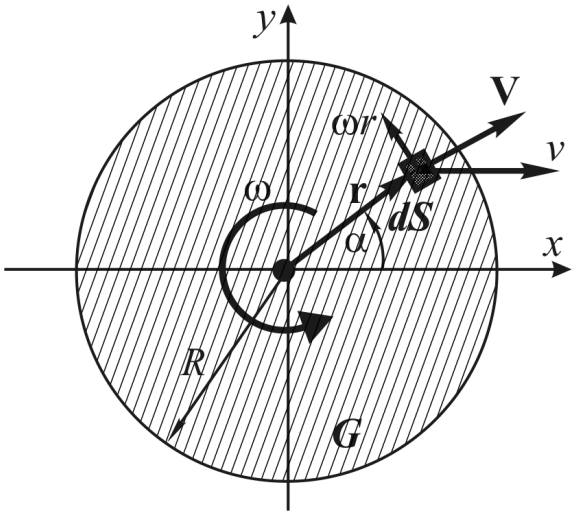


Figure 1: Scheme of contact spot

contact circle center (Fig.1):

$$
\begin{aligned}
&d\mathbf{F} = -f\sigma\frac{\mathbf{V}}{|\mathbf{V}|}\left(1+\mu_1|\mathbf{V}|^3-\mu_2\,|\mathbf{V}|\right)dS,\\
&d\mathbf{M_C} = -f\sigma\frac{\mathbf{r}\times\mathbf{V}}{|\mathbf{V}|}\left(1+\mu_1|\mathbf{V}|^3-\mu_2\,|\mathbf{V}|\right)dS,\\
&\mathbf{V} = (v-\omega y,\omega x),\ \mathbf{r} = (x,y)
\end{aligned}
\tag{1}
$$

where ω is the angular velocity of spinning and σ is the distribution of normal contact stresses.

As example of the systems with combined dry friction in which proposed above model can be applicable consider the system consist of the spring-supported cylindrical rod one end of that is bearing to the infinite belt moved with the constant velocity v (Fig.2).

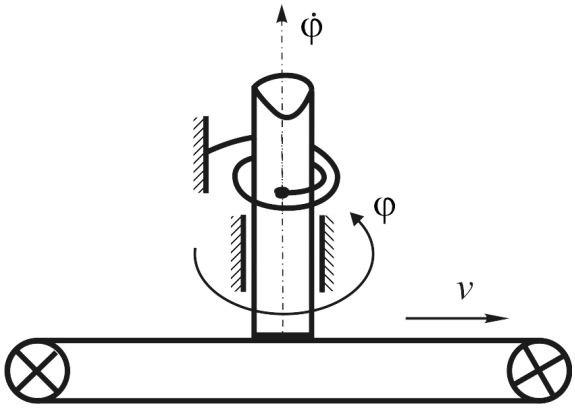


Figure 2: Typical system with torsional oscillations

The dynamics of this system was investigated in details in [5] at the supposition that the bar end has hemispherical form, and, consequently, the distribution of normal contact stresses is obeyed to Hertz low. Because the distinguish of the using of the Coulomb low in the generalized differential form from the classical form is especially considerable the more the large the contact area then below it is supposed that the bar end has form of the flat circle. In this case the distribution on normal contact stresses inside of contact circle is described by the Galin law.

2 Coupled models of the sliding and spinning friction

The integration of equation (1) over the contact spot gives the force $\mathbf{F}$ and the moment $\mathbf{M_C}$. In the assumption that the distribution of normal contact stresses for circular contact platforms has the central symmetry property, it is conven-ient to write corresponded integrals in the polar coordinate system $\{r, \varphi\}$ with the pole at the contact spot center (Fig.1) [6]:

$$\begin{aligned} F &= fN \int_0^{2\pi}\int_0^1 \frac{r\sigma(r)(v - ur\sin\varphi)drd\varphi}{\sqrt{v^2 - 2vur\sin\varphi + u^2r^2}} + \\ &+ 2\pi fN\left((\mu_1 v^3 - \mu_2 v)\int_0^1 r\sigma(r)dr + 2\mu_1 vu^2\int_0^1 r^3\sigma(r)dr\right) \\ M_C &= fNR\int_0^{2\pi}\int_0^1 \frac{r^2\sigma(r)(ur - v\sin\varphi)drd\varphi}{\sqrt{v^2 - 2vur\sin\varphi + u^2r^2}} + \\ &+ 2\pi fNR\left((2\mu_1 v^2 - \mu_2)u\int_0^1 r^3\sigma(r)dr + \mu_1 u^3\int_0^1 r^5\sigma(r)dr\right) \end{aligned} \tag{2}$$

where N is the normal compressing force and R radius of contact spot.

Thus, as in the case of the use of the classical Coulomb law in differential form, the friction force normal component vanishes. The friction force is directed oppositely to the relative slip velocity.

However, in comparison with the results of [3], additional polynomial terms appear in the expressions for the friction force and moment. At the same time, the first terms in the right hand sides of equation (2) are exactly the same as those investigated in [3] under the assumption of validity of the classical Coulomb law in differential form.

The coefficients of the polynomial terms in (2) represent the first moments of distribution of normal contact stresses: $I_1 = \int_0^1 r\sigma(r)dr$ is the first order moment, $I_3 = \int_0^1 r^3\sigma(r)dr$ is the third order moment, and $I_5 = \int_0^1 r^5\sigma(r)dr]$ is the fifth order moment.

If the distribution of normal contact stresses follows the Galin law [7]: $\sigma(r) = \left(2\pi\sqrt{1-r^2}\right)^{-1}$ they are $I_1 = 1/(2\pi),\ I_3 = 1/(3\pi),\ I_5 = 4/(15\pi)$.

The first integrals in (2) also can be calculated in elementary functions for the transport of the coordinate system origin to the instant velocity center if the distribution of normal contact stresses is described by the Hertz [2] or Galin [3] laws. As a result [6], the exact analytical expressions for the friction force are smooth and convex functions of two variables u and v.

Exact integral models (2) give a good description of the effects of combined dry friction but are inconvenient for solving the problems of dynamics because it requires the calcula-tion of multiple integrals in the right hand sides of the differential equations of motion. It is possible to avoid this laborious procedure by replacing the exact integral expressions with the corresponding Pade expansions. The simplest of them is the linearfractional approximation (the generalized two dimensional first order model) [6]:

$$\begin{aligned} M_C &= M_0\left(\frac{u}{u+mv} + 2\pi\left((2\mu_1 v^2 - \mu_2)uI_3 + \mu_1 u^3 I_5\right)\right), \\ F &= F_0\left(\frac{v}{v+au} + 2\pi\left((\mu_1 v^3 - \mu_2 v)I_1 + 2\mu_1 vu^2 I_3\right)\right), \\ M_0 &= fNR,\ \ \frac{1}{m} = \frac{v}{M_0}\frac{\partial M_C}{\partial u}\bigg|_{u=0},\ F_0 = fN,\ \ \frac{1}{a} = \frac{u}{F_0}\frac{\partial F}{\partial v}\bigg|_{v=0} \end{aligned} \tag{3}$$

Linear–fractional Pade approximations (3) retain the values of the first integral terms in (2) at zero and correctly describe the behavior and their first derivatives at infinity. However, the first order model gives no possibility to describe correctly the behavior of all first partial derivatives of

these terms at zero. But, as is shown in [3], for the majority of problems of dynamics, it suffices to use first order model. Moreover, model based on Pade expansions can be considered as the generalized rheological two dimensional model of friction of the first order because it coefficients can be determined from experiments for the solution of real problems.

3 Dynamics of the spring-supported cylindrical rod on the infinite belt

The equations of motion of the considered system in the dimensional time have the following form [5]:

$$\ddot{\varphi} + \varphi = -\frac{1}{k} M \tag{4}$$

where φ angle of the rod rotation, J moment of inertia relatively vertical axes, k spring constant and M – moment of combined dry friction which is defined on the base on the generalized two dimensional model of the first order (3). Thus, right side in equa-tion (4) is defined by the follows formulas:

$$\begin{aligned} M &= M_0 \left(\frac{\dot{\varphi}}{|\dot{\varphi}| + \alpha} + \alpha_1 \dot{\varphi} - \alpha_2 \dot{\varphi} + \alpha_3 \dot{\varphi}^3 \right) \\ \alpha &= \frac{3\pi v \sqrt{m_c}}{4\sqrt{2k}},\ \alpha_1 = \frac{4\mu_1 \sqrt{2k} v^2}{3\sqrt{m_c}},\ \alpha_2 = \frac{2\mu_2 \sqrt{2k}}{3\sqrt{m_c}},\ \alpha_3 = \frac{8\mu_1 (\sqrt{2k})^3}{15(\sqrt{m_c})^3} \end{aligned} \tag{5}$$

The equation of motion (5) is analyzed at the supposition of smallness of friction coef-ficient f that allows using of the Krilov-Bogolubov's method of averaging [8]. After introducing of the new variables: $x = \varphi,\ y = \dot{\varphi}$, the Cauchy normal form of the equation (5) is

$$\begin{aligned} \dot{x} &= y \\ \dot{y} &= -x - \tfrac{1}{k} M(y) \end{aligned} \tag{6}$$

The transition to the standard form of method of averaging is realized by the change of variables $(x, y) \to (r, \tau)$:

$$x = r \sin \tau, \quad y = r \cos \tau \tag{7}$$

This changing denotes the transition in phase space of the system (3) from fast Cartesian coordinates: $(\varphi, \dot{\varphi})$ to the slow polar coordinates: (r, τ), so name "amplitude-phase"' variables. In result, system (4) has the following standard form

$$\begin{aligned} \dot{r} &= -\frac{1}{k} M(r \cos \tau) \cos \tau \\ \dot{\tau} &= 1 + \frac{1}{rk} M(r \cos \tau) \sin \tau \\ M(r \cos \tau) &\equiv M_0 \left(\frac{r \cos \tau}{r\,|\cos \tau| + \alpha} + \alpha_1 r \cos \tau - \alpha_2 r \cos \tau + \alpha_3 (r \cos \tau)^3 \right) \end{aligned} \tag{8}$$

The following analysis of the system (8) depends on relationship between values of the coef-ficients α_2 and α_3 in formulas (5). If they have the same order which is equivalent to one then sufficiently to build the first approximation of method of av-eraging, but in the other case the higher approximations are required. Averaging of the system (8) with respect to the explicit en-tering time τ yields $\dot{\tau} = 1$. This implies that the frequency of oscillations does not depend on the ampli-tude and, consequently, the first equation in (8) can be studied undependably.

The procedure of the averaging of the first term in the right side of the first equation of system (8) leads to the need of enumerating the integral

$$J(r) = \frac{1}{2\pi} \int_0^{2\pi} \frac{r \cos^2(\tau)\, d\tau}{r\,|\cos(\tau)| + \alpha} \tag{9}$$

which although can be obtained in the elementary functions, result proves to be too cumber-some and inconvenient for further analysis. Therefore, is convenient to use the same method, as upon transfer from the exact integral model (2) to the model on basis of Pade approxima-tions (3), i.e., to use the procedure of their direct construction, based on the properties of the function $J(r)$:

$$J(0) = 0, \quad \lim_{r\to\infty} J(r) = 2/\pi, \quad J'(0) = (2\alpha)^{-1}, \quad \lim_{r\to\infty} J'(r) = 0 \tag{10}$$

In accordance with properties (10), integral (9) is substituted by the following linear-fractional Pade approximation

$$J(r) = \frac{2r}{\pi r + 4\alpha} \tag{11}$$

Taking into account formula (11) the first averaged equation of system (8) takes the form:

$$\begin{aligned} &\dot{r}_1 = -\frac{2r_1}{\pi r_1 + 4} - k_1 r_1 + k_2 r_1 - k_3 r_1^3, \quad r_1 = \frac{r}{\alpha},\ \tau_1 = \frac{M_0}{k\alpha}\tau\ , \\ &k_1 \equiv \alpha\alpha_1 = \pi\mu_1 v^3/2,\ k_2 \equiv \alpha\alpha_2 = \pi\mu_2 v/2,\ k_3 \equiv \alpha\alpha_3 = 9\pi^3\mu_1 v^3/40 \end{aligned} \tag{12}$$

Different from zero equilibrium positions in equation (12) can be found from the solution of the following algebraic equation

$$2 + (k_1 - k_2 + k_3 r_1^2)(\pi r_1 + 4) = 0 \tag{13}$$

An investigation of equation (13) with the aid of the system of the computer algebra *maple 12* showed that in it there is two complex and one real roots. The presences of real root in equation (13) means that in the considered system is possible the appearance of self-oscillations.

4 Conclusions

It is proposed the coupled exact integral model (2) of the sliding and whirling friction built on the supposing of the validity of the generalized Coulomb law in differential form for elementary area inside of contact spot. It is shown that as in case of using classical Coulomb law in differential form, the normal component of friction force is zero. The friction force is direct opposite the relative velocities of sliding, but in comparing with results of work [3], ad-ditional polynomials terms appear in expressions for friction force and torque. To escape us-ing of the integral expressions in the equation of motion, the model based on Pade expansions of the first order is constructed. This models can be considered as reological models, because there are no required in solving of real problems to calculate the double integrals, defined the coefficients of Pade approximations. These coefficients can be defined from the experiments. The appearance of the polynomials terms in expressions (2)-(3) for friction torque can lead to arising self-exited torsion oscillations in the systems with combined dry friction consist of the spring-supported torsion shaft one end of that is bearing to the infinite belt moved with the constant velocity v (Fig. 2).

References

[1] P.Contensou, Couplage Entre Frottenmentde Glissementet Frottenment de Pivotement Dans la Theorie de la Toupie. in Kreiselprobleme Gyrodynamics: IUTAM Symp. Celerina, 1962 (Springer, Berlin etc., 1963; Mir, Moscow, 1967), 201–216(60–77).

[2] V.Ph. Zhuravlev, The Model of Dry Friction in the Problem of the Rolling of Rigid Bodies. Prikl. Mat. Mekh., 62 (5), 762–767, 1998.

[3] A.A. Kireenkov, On the motion of the homogeneous rotating disk alone the plane in the case of combined friction, Izv. Akad. Nauk .Mekh. Tverd. Tela, 1, 60–67, 2002.

[4] Ya.G. Panovko, Foundations of applied theory of oscillations and strike. Moscow, Nauka, 306, 1976.

[5] A.A. Kireenkov, About Torsional Oscillations in Systems with Combined Dry Friction, Akad. Nauk. Mekh. Tverd. Tela, No. 3, 36 40, 2009.

[6] A.A.Kireenkov, Generalized two dimensional model of sliding and spinning friction. Doklady Akademii Nauk, 2010, Vol. 431, No. 4 (Doklady Physics, 2010, Vol. 55, No. 4), 482–486(186–190).

[7] A.Galin, Contact Problems of Elasticity and Viscoelasticity. Moscow, Nauka, 1980

[8] V.Ph. Zhuravlev, D.M Klimov, Applied methods in oscillation theory. Moscow, Nauka, 1988.

Alexey A. Kireenkov, Institute for Problems in Mechanics RAS, Prospekt Vernadskogo 101, korp.1, 119526 Moscow, Russia

The experimental determination of the coefficients of the coupled two-dimensional model of the combined dry friction

Alexey A. Kireenkov Sergey V. Semendyaev
kireenk@ipmnet.ru

Abstract

For the purpose of the adequacy checking of the offered theoretical models the experimental installation has been developed for experimental definition of the dry friction force at rectilinear sliding of rubbing solids at the presence of spining.

Installation allows the coefficients defining of the dry fiction models based on Padé expansions for the various contact areas of the rubbing solids. Moreover, the unit parameters give the chance to make experiments for a wide range of changing of the kinematics parameters defining a power state at the various values of the normal pressure.

Experimental measurement of the friction was spent for the steel disk consistently displaced from the centre of the rotating steel platform to its edge, at various variants of loading.

Results of the spent experiments brightly demonstrate that at the conditions of the combined kinematics the real friction laws have principle differences from the classical Coulomb law. This difference is especially strong when the instant centre of velocities lies inside of contact spot. The behavior of the friction force in the region of small velocities is similar to the viscous friction. The rest friction is escaping and any infinitesimal force parallel directed to the contact spot cause to sliding.

1 Two dimensional models of combined dry friction

It is known that in the case of combined kinematics, when the rubbed solids participate simultaneously in translational and spinning motions, there are violations in the classical Coulomb law. However, till now, in a majority of publications, the authors use the Coulomb dry friction model, where the force at the point of contact is assumed to be directed opposite to the relative sliding velocity and be independent of its modulus. One of the first models described the relation between the sliding and whirling friction in the case of nonpoint contact between the moving bodies was proposed by P.Contensou [1]. One of the first models describing the relation between the sliding friction and the rolling friction in the case of nonpoint contact between the moving bodies (Fig.1) was proposed by P.Contensou [1], where the theory of Hertz contact stresses was used to obtain the numerical dependence of the dry friction force on the ratio $k = \frac{v}{\rho\omega}$ of the sliding velocity v to the spinning velocity $\rho\omega$ (Fig.1) under the assumption that both contacting surfaces are locally spherical.

In this case, in [1], only the friction force was calculated, the frictional moment was not considered. A principally new development of the Contensou theory was given in [2], where the origin of the coordinate system was transferred to the instantaneous center of velocities, which permits obtaining exact analytic expressions for the resultant vector F and the frictional moment M for circular contact sites under the assumption that the distribution of contact stresses in the contact spot obeys the Hertz law. In [2], to apply the obtained depend-encies to problems of dynamics, the linear-fractional Padé approximations of these dependencies were constructed:

$$F = F_0 \frac{v}{|v| + a\,|u|}, \quad M = M_0 \frac{u}{|u| + m\,|v|}$$
$$F_0 = F(u,v)|_{u=0}, \quad M_0 = M(u,v)|_{v=0}, \quad \frac{1}{a} = \frac{|u|}{F_0}\frac{\partial F}{\partial v}\bigg|_{v=0}, \quad \frac{1}{m} = \frac{|v|}{M_0}\frac{\partial M}{\partial u}\bigg|_{u=0} \tag{1}$$

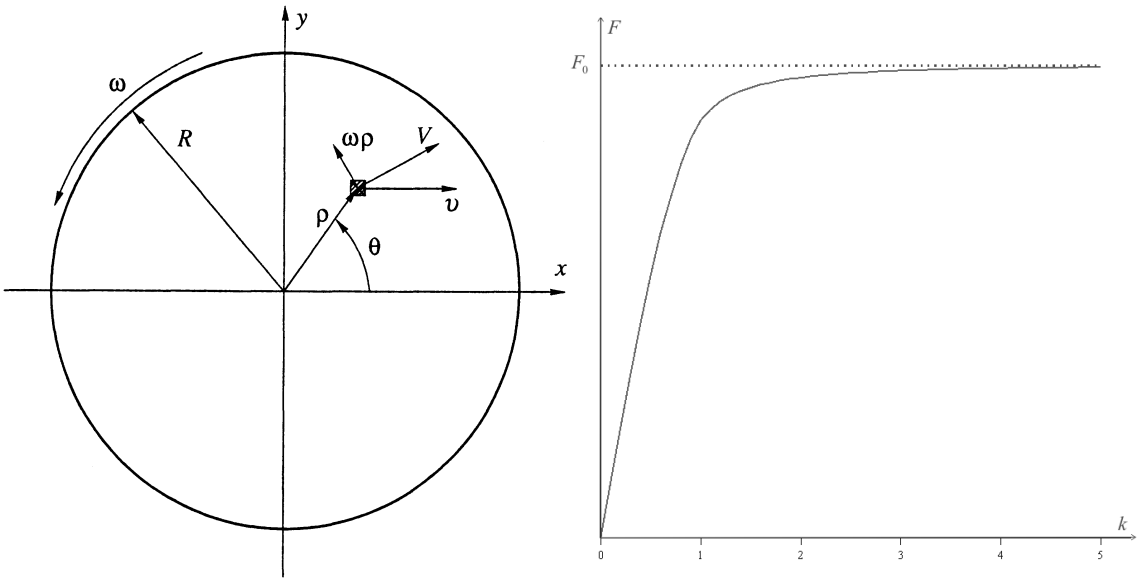


Figure 1: Friction law in the case of combined kinematics(two–dimensional model)

Zhuravlev's theory was used to study the dynamics of a homogeneous circular disk slid-ing with rotation on a plane [3]. Under the assumption that the distribution of contact stresses obeys the Galin law [4], exact analytic expressions for the resultant vector and the frictional moment were obtained and their linear–fractional Padé approximations were constructed. It is appears that Padé expansions has the same kind as (1), with small distinguish in corresponded coefficients. One of the distinctions of the problems studied in [2, 3] is that, first, one constructs exact expressions for the resultant vector and the frictional moment and then, on the basis of them, one constructs the Padé approximations, which are used to study the dynamics. This approach, just as a majority of the earlier approaches, requires calculating multiple integrals over the contact spot, which is possible only for a bounded number of forms of distributions of contact stresses, and the expressions obtained by integration are extremely cumbersome and inconvenient for solving the dynamics problems. Moreover, the laws of distribution of contact stresses are a priori unknown in actual problems, and often can be obtain only empirically. Many authors tries to solve this problem, but all the attempts were restricted to either simplifying assumptions about the friction law or expansions in the Taylor series of the integrands [5], depending on the relations between the sliding and rotation velocities. A method of direct construction of Padé approximation, without calculations of the corresponding integrals, was developed for solving this problem. The convenience in the use of the Padé approximations, which permit describing the effects of combined dry frictions for the entire range of angular and linear velocities, allowed one to construct principally new friction models on the basis of these approximations, and these new models can be treated as rheological models, because there coefficients can be determined experimentally. For formalization of the developed theory, the notion of dimension of the dry friction model is introduced depending on the number of kinematic parameters determining the force state, and the notion of order of the model is introduce depending on the order of the required Padé approximations [6]. For example, for circular contact sites with centrally symmetric distribution of contact stresses, the two force factors, namely, the friction force directed opposite to the sliding velocity and the moment, depend on the two kinematic factors, namely, the angular and linear velocities (the two-dimensional model):

$$F = \frac{F_0 v}{|v| + a\,|u|} \equiv \frac{F_0 k}{|k| + a}, \quad u = \omega R, \;\; k = \frac{v}{u} \tag{2}$$

where R radius of contact spot, v linear speed of relative sliding, and ω angular speed of rotation of the contact circle centre (Fig.1). The dimensionless factor a and force of a friction of rest F_0 can be defined or analytically if distribution of normal contact pressure is defined, for example, by Hertz [2] or Galin [3] law or experimentally. For the purpose of the adequacy checking of the offered

theoretical models the ex-perimental installation has been developed for experimental definition of the dry friction force at rectilinear sliding of rubbing solids at the presence of spinning. Laboratory stand allows to measure force of a friction for various areas of contact of rubbing bodies at the various loading.

2 Scheme and basic components of the laboratory stand

At creation of experimental installation possibility to define coefficients of the dry friction models based on Padé expansions for various areas of contact of rubbing bodies and for a wide range of change of the kinematics parameters defining a force state has been provided, varying the enclosed loading in the field of contact. The modular design has been as a result created (Fig. 2), allowing to spend independent completion.

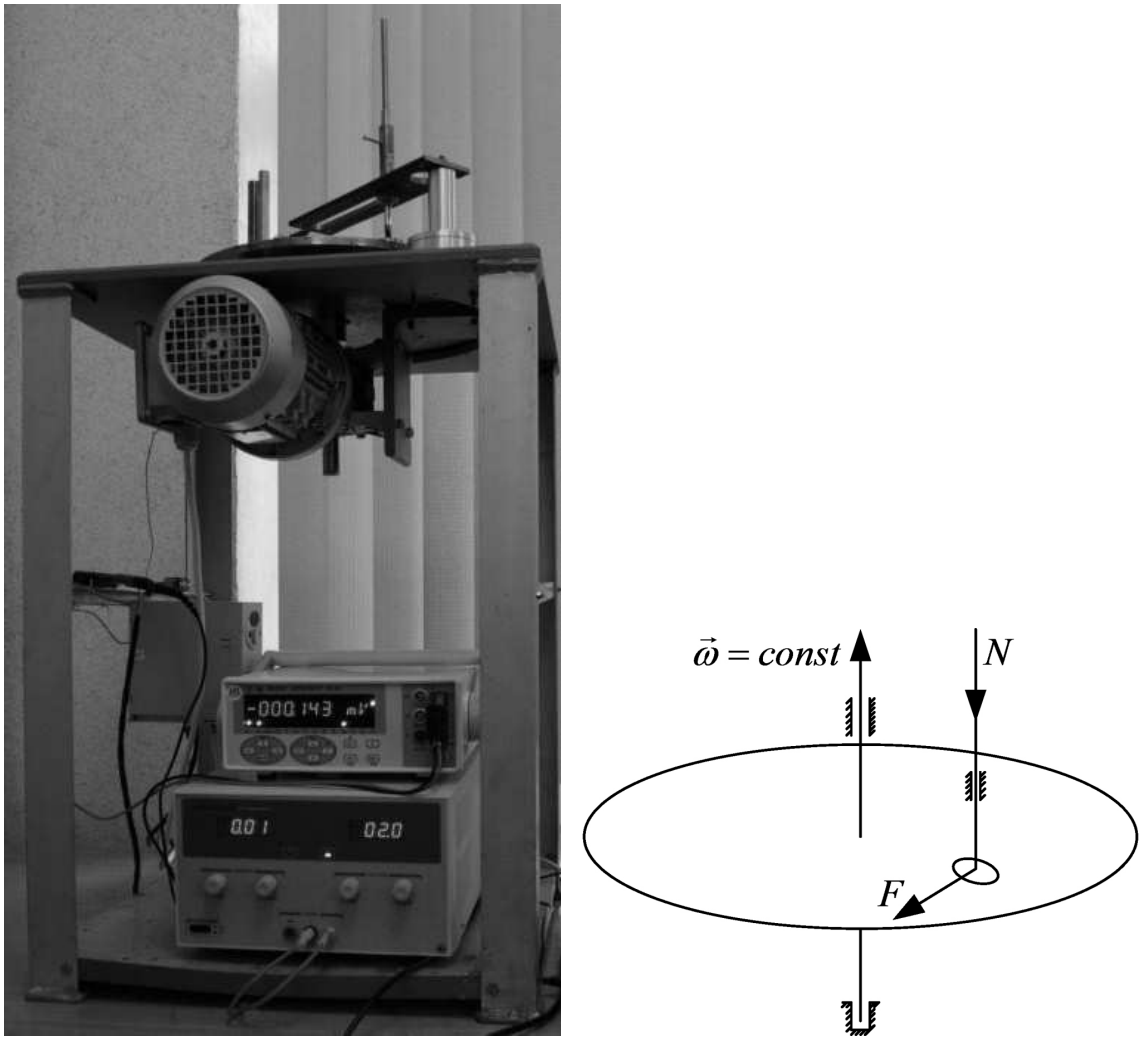


Figure 2: Experimental stand and pricipale scheme

Structurally, installation consists of following basic elements: the power block, the block of creation of movement with sliding in the presence of spinning, the block of mainte-nance of mechanical contact, the block of normal loading, the measuring block and the block of processing of results. The block of maintenance of mechanical contact represents a moving bar in the bear-ing of sliding (steel-brass). Use of effect of selective carrying over allows receiving the minimum friction and wear. On the end of a bar contacting to a platform, it is fixed various contact elements – indentors, allowing to simulate various models of area of contact and distribution of contact pres-

sure: a steel ball – dot contact on Hertz , cylindrical disks of various diameter – Galin distribution of contact pressure, rings – for model of a thin ring. Besides, the design supposes carrying out of experiments for other forms of stains of contact, by installation indentors of other form. The contact bar has two degrees of freedom. It can compulsorily move in a vertical plane and across, under the influence of forces of a friction in contact. Moving to horizon is provided with the console on which the contact bar is fixed. The console can turn concerning the case of the block of creation of movement in two radial ball bearings. The block of normal loading creates the set distribution of normal pressure (loading) in the field of contact and consists of a set of the fixed weights from 0 to 50 H with which the contact bar is loaded. The block of measurements consists of a measuring beam of equal resistance which compensates forces of a dry friction arising in contact and interferes with console moving to a horizontal plane.

3 Results of carried out experiments and they analysis

Experimental measurement of the friction was spent for the steel disk consistently displaced from the centre of the rotating steel platform to its edge, at various variants of loading. At such statement of experiment, the friction force at constants loading and the samples sizes depends only on distance from the centre of the rotating basis to the centre of the sample. One more distinctive feature of this problem is that model (1) coefficients can be calculated analytically [3]: $a = 4/\pi$, $F_0 = fN$, where f friction coefficient, and N compressing force.

Results of the spent experiments at speed of rotation of a platform 177.3 rpm are presented on Fig.3–Fig.5.

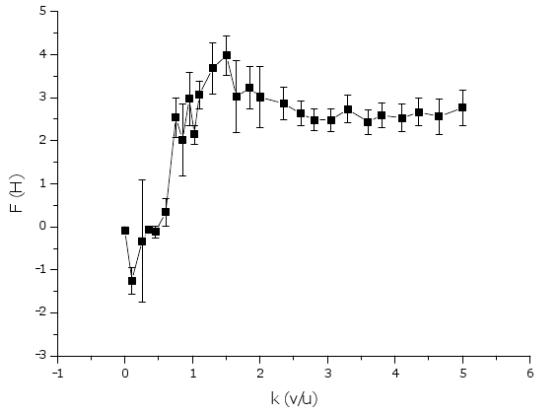


Figure 3: Steel disk: radius R=2 sm, compressing force N=12.88 H

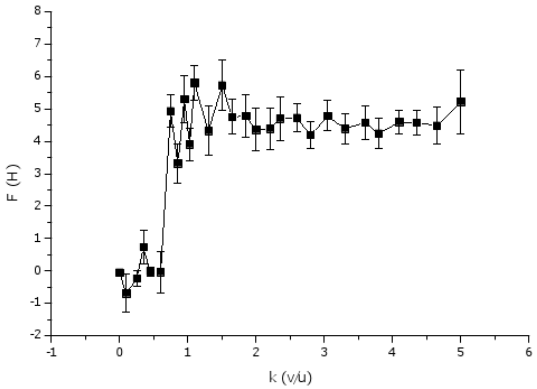


Figure 4: Steel disk: radius R=2 sm, compressing force N=22.04 H

The presented dependences brightly demonstrate that at the conditions of the com-bined kinematics the real friction laws have principle differences from the classical Coulomb law. This difference is especially strong when the instant centre of velocities lies inside of contact spot. The behavior of the friction force in the region of small velocities is similar to the viscous friction. The rest friction is escaping and any infinitesimal force parallel directed to the contact spot cause to sliding. The characteristic curves of the two–dimensional models of friction of the type of those represented in Fig. 1, approximate well experimental dependences. At the same time, on obtained experimental data is clearly evident the appearance of a local maximum with the low values k, with subsequent small failure of characteristic (local minimum) and its withdrawal with the great significances k to infinity. Moreover difference from the dependence with Fig. 1.a is the greater, the greater the radius of the contact area or the coefficient of friction. This effect is connected with the fact that during the construction of the two–dimensional models of friction, described by the formulas of form (1) it was assumed the validity of classical Coulomb law in the differential form for the small element of area inside the contact area. The use of the generalized differential forms of Coulomb law as this was done into [7] leads to the appearance in formulas (1) of additive

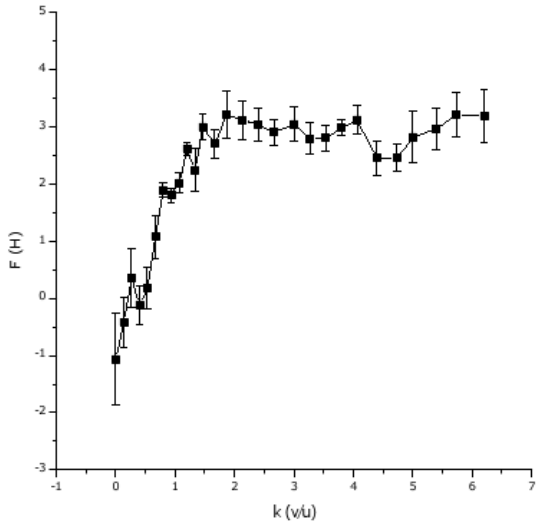


Figure 5: Steel disk: radius R=1.5 sm, compressing force N=12.49 H

polynomial terms:

$$F = F_0 \left(\frac{v}{v + au} + 2\pi \left((\mu_1 v^3 - \mu_2 v) I_1 + 2\mu_1 v u^2 I_3 \right) \right) \tag{3}$$

Additional coefficients μ_1 and μ_2 appeared in model (3) also can be calculated analytically [7], if the distributions of normal contact stresses are described by the Hertz or Galin laws or they are determined from the results of the carried out experiments The dispersions in the friction force values at the fixed loading, angular speed of a platform and the fixed indentor position are caused by the natural physical errors of measurements stipulated by the following major factors: discrepancy of processing of surfaces; wear process of materials in the course of a friction; inclination of an axis of rotation in relation to an axis of symmetry of a platform and infringement of full contact between rubbing surfaces.

References

[1] P.Contensou, Couplage Entre Frottenmentde Glissementet Frottenment de Pivotement Dans la Theorie de la Toupie. in Kreiselprobleme Gyrodynamics: IUTAM Symp. Celerina, 1962 (Springer, Berlin etc., 1963; Mir, Moscow, 1967), 201 – 216(60 – 77).

[2] V.Ph. Zhuravlev, The Model of Dry Friction in the Problem of the Rolling of Rigid Bodies. Prikl. Mat. Mekh., 62 (5), 762–767, 1998.

[3] A.A. Kireenkov, On the motion of the homogeneous rotating disk alone the plane in the case of combined friction, Izv. Akad. Nauk .Mekh. Tverd. Tela, 1, 60–67, 2002.

[4] A.Galin, Contact Problems of Elasticity and Viscoelasticity. Moscow, Nauka, 1980

[5] [4] R.I.Leine and Ch.Glocker, A Set-valued force law for spatial Coulomb-Contensou friction. European J. Mech. 2003. v.22,No.2.,193–216.

[6] V.Ph. Zhuravlev and A.A. Kireenkov, Padé Expansions in the Two-Dimensional Model of Coulomb Friction. Izv. Akad. Nauk .Mekh. Tverd. Tela, 2, 3–14, 2005.

[7] A.A.Kireenkov, Generalized two dimensional model of sliding and spinning friction. Doklady Akademii Nauk, 2010, Vol. 431, No. 4 (Doklady Physics, 2010, Vol. 55, No. 4), 482–486(186–190).

Alexey A. Kireenkov, Institute for Problems in Mechanics RAS, Prospekt Vernadskogo 101, korp.1, 119526 Moscow, Russia
Sergey V. Semendyaev, Moscow Institute of Physics and Technology (State University), 9, Institutskii per. 9, 141700 Dolgoprudny, Moscow Region, Russia

Critical slippage for droplet migration in nanometric liquid films

Georgy Kitavtsev Barbara Wagner
kitavtsg@mathematik.hu-berlin.de

Abstract

In this talk the topic of reduced ODE models corresponding to a family of one-dimensional lubrication equations derived by [2] is addressed. This family describes the dewetting process of nanoscopic thin liquid films on hydrophobized polymer substrates due to the presence of several intermolecular forces and takes account of different ranges of slip-lengths at the polymer substrate interface. Reduced ODE models derived from underlying lubrication equations allow for an efficient analytical and numerical investigation of the latest stage of the dewetting process: coarsening dynamics of the remaining droplets. We give an asymptotical derivation of these models and use them to investigate the influence of slip-length on the coarsening dynamics. In a so called strong-slip case we find a unique critical slip-length at which the direction for migration of droplets changes.

1 Lubrication and Reduced ODE Models

The last several decades showed considerable interest and intensive research among scientists and engineers on topics concerning such physical processes and phenomena as dewetting in micro and nanoscopic liquid films on a solid polymer substrate. In this study we are interested in the last stage of the dewetting process, namely the long-time coarsening process that originates in the breaking up of the evolving in time nanoscopic thin liquid film into small droplets and is characterized by subsequent slow-time coarsening dynamics, which is driven essentially by collapse of the smallest droplets and collision of neighboring ones. In the mathematical modeling of thin films it has been shown to be of great advantage to reduce the governing equations to an equation for the free surface $h(x,t)$ using lubrication theory. Asymptotic arguments, based on the magnitude of the slip length show that within a lubrication scaling there are two *distinguished limits*, see [2].

These are the well-known *weak-slip* model

$$\partial_t h = -\partial_x\Big((h^3 + b\,h^2)\partial_x\left(\partial_{xx}h - \Pi_\epsilon(h)\right)\Big) \tag{1}$$

with b denoting the slip-length parameter, and the *strong-slip* model

$$Re\left(\partial_t u + u\partial_x u\right) = \frac{4}{h}\partial_x(h\partial_x u) + \partial_x\left(\partial_{xx}h - \Pi_\epsilon(h)\right) - \frac{u}{\beta h}, \tag{2a}$$

$$\partial_t h = -\partial_x\left(hu\right), \tag{2b}$$

respectively. Here, $u(x,t)$, $h(x,t)$ denote the average velocity in the lateral direction and height profile for the free surface, respectively. The slip-length parameters b and β are related by orders of magnitude via $b \sim \nu^2\beta$, where the parameter ν with $0 < \nu \ll 1$ refers to the vertical to horizontal scale separation of the thin film. The high order of the lubrication equations (1) and (2a)–(2b) is a result of the contribution from surface tension at the free boundary, reflected by the linearized curvature term $\partial_{xx}h$. A further contribution to the pressure is denoted by $\Pi_\epsilon(h)$ and represents one from the intermolecular forces, namely long-range attractive van der Waals and short-range Born repulsive intermolecular forces. A commonly used expression for it is given by

$$\Pi_\epsilon(h) = \frac{\epsilon^2}{h^3} - \frac{\epsilon^3}{h^4},$$

where small parameter $0 < \epsilon \ll 1$ gives to the leading order thickness of the ultra-thin layer between droplets.

Recently for the weak-slip (1) and strong-slip (2a)–(2b) models the corresponding reduced ODE models describing effective dynamics of an array of $N+1$ droplets were derived in [3] and [1], respectively. They describe evolution in time of pressures P_j and positions ξ_j for $N+1$ droplets and have in both cases a form

$$\frac{dP_j}{dt} = C_{P,j}(J_{j,j+1} - J_{j-1,j}), \quad \frac{d\xi_j}{dt} = -C_{\xi,j}(J_{j,j+1} + J_{j-1,j}),\ j = 0, ...N, \tag{3}$$

where $J_{j-1,j}$ denotes the flux between neighboring j-th and $j+1$-th droplets. A so called *pressure coefficient* is also the same in both cases and is given as

$$C_P := \frac{1}{-\int_{-\tilde{L}}^{\tilde{L}} \partial_P \hat{h}_\epsilon \, dx}, \tag{4}$$

but *mobility coefficient* $C_{\xi,j}$ is different in the weak- and strong-slip cases. In the weak-slip case it has a form

$$C_\xi = \frac{\displaystyle\int_{-\tilde{L}}^{\tilde{L}} \frac{\hat{h}_\epsilon - \hat{h}_\epsilon^-}{\hat{h}_\epsilon^3 + b\,\hat{h}_\epsilon^2}\, dx}{\displaystyle\int_{-\tilde{L}}^{\tilde{L}} \frac{\left(\hat{h}_\epsilon - \hat{h}_\epsilon^-\right)^2}{\hat{h}_\epsilon^3 + b\,\hat{h}_\epsilon^2}\, dx}. \tag{5}$$

In contrast in the strong-slip case it depends on the slip-length β and is given as

$$C_\xi = \frac{\displaystyle\int_{-\tilde{L}}^{\tilde{L}} \left(\frac{\hat{h}_\epsilon - \hat{h}_\epsilon^-}{\hat{h}_\epsilon^2} - \beta\, T(\hat{h}_\epsilon, \partial_x \hat{h}_\epsilon, \partial_{xx} \hat{h}_\epsilon) \right) dx}{2 \displaystyle\int_{-\tilde{L}}^{\tilde{L}} \left(\frac{\left(\hat{h}_\epsilon - \hat{h}_\epsilon^-\right)^2}{\hat{h}_\epsilon^2} - \beta\, T(\hat{h}_\epsilon, \partial_x \hat{h}_\epsilon, \partial_{xx} \hat{h}_\epsilon)(\hat{h}_\epsilon - \hat{h}_\epsilon^-) \right) dx}, \tag{6}$$

where

$$T(\hat{h}_\epsilon, \partial_x \hat{h}_\epsilon, \partial_{xx} \hat{h}_\epsilon) := 4\,\hat{h}_\epsilon^- \left(\frac{\hat{h}_\epsilon \partial_{xx} \hat{h}_\epsilon - (\partial_x \hat{h}_\epsilon)^2}{\hat{h}_\epsilon^3} \right). \tag{7}$$

Above $\hat{h}_\epsilon$ denotes the function describing stationary droplet profile for its given pressure and position and $\hat{h}_\epsilon^-$ denotes its minimum.

2 Critical Value of Slippage

One of the characteristic properties of the weak-slip model (1) is the following fact: the droplet migrates always opposite to the effective applied flux, see in particular the detailed discussion in [4]. In the case of the j-th droplet in the array of $N+1$ droplets the effective flux applied on it is

$$J_{eff} = J_{j,j+1} + J_{j-1,j}.$$

In contrast, in the case of the strong-slip model the analysis of the motion equation in (3) and (6) shows, that a droplet can migrate opposite or in the same direction of the applied effective flux depending on the value of the slip-length β. This fact is explained by the influence of the new term (7) in the expression for the mobility coefficient (6), which is connected with the presence of the Trouton viscosity term in the system (2a)–(2b). Namely, in [1] the following proposition was proved.

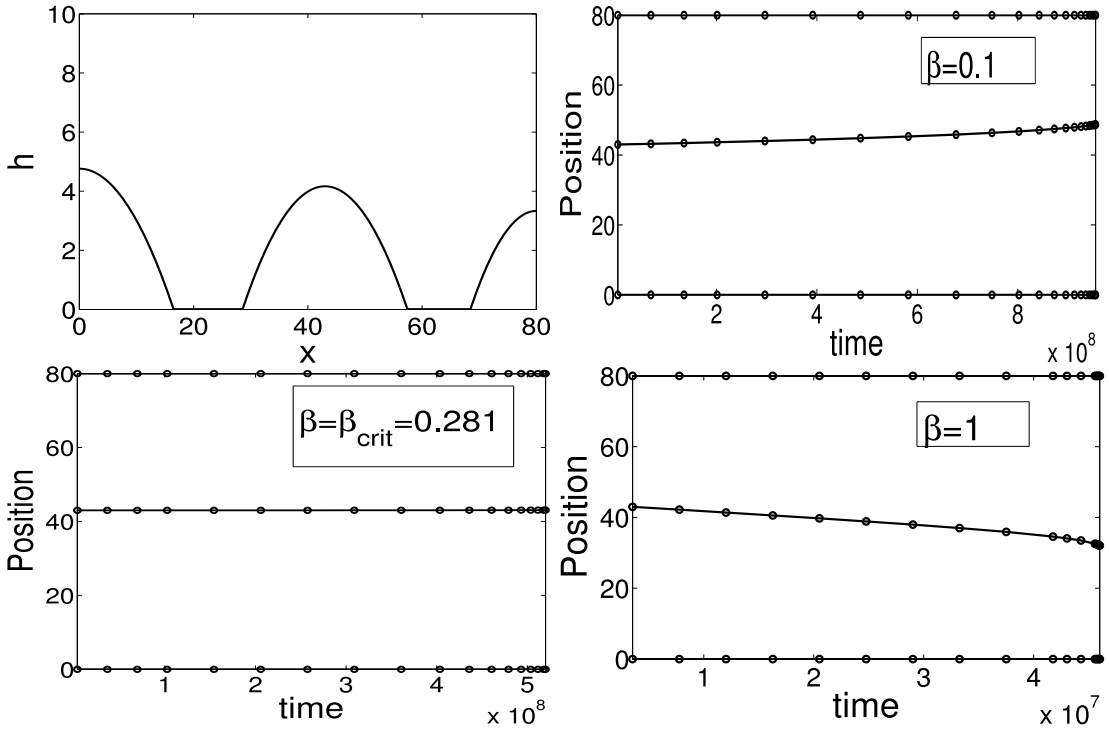


Figure 1: Migration of the middle droplet in the array of three droplets (upper-left) for different β. $L = 80$, $\epsilon = 0.01$, $Re = 0$, $P_2 = 0.4$.

Proposition *For fixed positive ϵ and P there exist a unique zero $\beta = \beta_{crit}$ of (6) considered as a function of β. Moreover,*

$$\beta_{crit} = K\epsilon \ln\left(\frac{2}{3\epsilon P}\right) + o(\epsilon) \tag{8}$$

and $C_\xi > 0$ ($C_\xi < 0$), i.e direction of droplet migration is opposite to (in the direction of) the flux when $\beta < \beta_{crit}(P, \epsilon)$ ($\beta > \beta_{crit}(P, \epsilon)$).

This migration effect is illustrated numerically in Figure 1. For a given initial array of three droplets β_{crit} for the middle one was calculated and then solutions of the reduced ODEs (3) with coefficients (4) and (6) for three different values for the slip parameter $\beta_1 < \beta_2 = \beta_{crit} < \beta_3$ were obtained. Note that in the case $\beta = \beta_{crit}$ the middle droplet almost does not move. Using given parameters of the droplet array one can calculate that the effective flux applied on the middle droplet in all three cases is negative. So in the case $\beta < \beta_{crit}$ it moves opposite to the flux and in the case $\beta > \beta_{crit}$ in the direction of the flux.

Additionally, we recall that for the weak-slip model it was shown in [3] that collisions are typically observed for a system of at least three droplets, when two bigger droplets are attracted by a smaller droplet in between. For the strong-slip model (2a)–(2b) two-droplet collisions are typically admitted when $\beta > \beta_{crit}$. An example of a two-droplet collision is shown in Figure 2 with $\beta = 1$. It is a consequence of the fact that a droplet can migrate in the direction of the applied flux. We remark that in the case $\beta < \beta_{crit}$ (see Figure 2 with $\beta = 0.1$) a two-droplet collision is not possible and the strong-slip model behaves just as the weak-slip one (1).

3 Coarsening Patterns for Increasing Slippage

In this section we try to analyze how the presence of critical slip-length β_{crit} given by (8) influences on the coarsening dynamics on a macro-level, that is on the coarsening of large arrays of droplets.

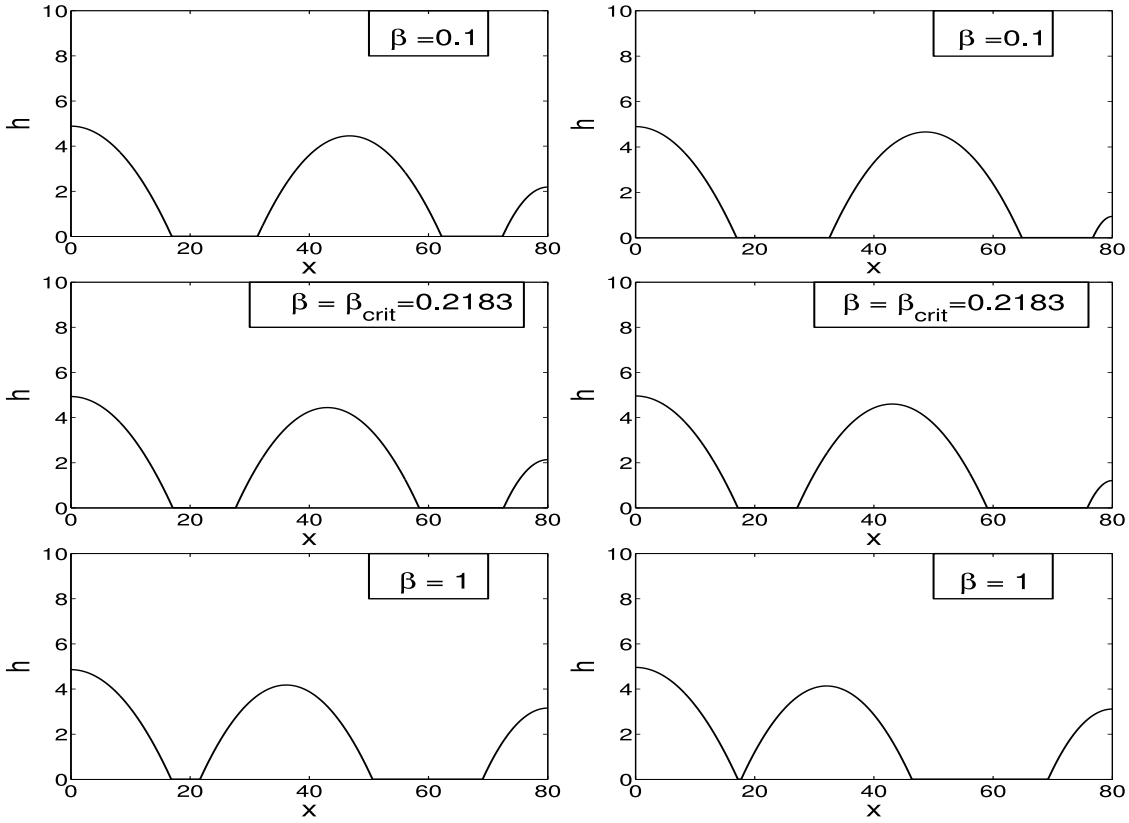


Figure 2: The evolution of three droplets for three different β with initial profile and parameters as in Figure. 1. The first and second column correspond to middle and the end of the evolution of the droplets, respectively.

We consider a modeling example of coarsening process of initially ten droplets and look how the coarsening scenario changes with slippage in comparison to the intermediate-slip case. Starting from an initial array of ten droplets as shown in Figure 3 we follow the paths of the first eight droplets in time in Figure 4, where we vary slippage while keeping $\epsilon = 0.1$ fixed. First simulating intermediate-slip regime and then increasing slippage in the strong-slip regime we observe several changes in coarsening behavior, first due to the existence of different β_{crit} for each droplet in the array, and second (also as a consequence of the first fact) because migration and hence collision rates change with slippage in comparison with collapse ones.

For every droplet in the array with initial pressure P_j one can calculate $\beta_{crit,j} = \beta_{crit}(P_j)$. In the example we chose, the values for $\beta_{crit,j}$ do not differ much from each other and are approximately contained in the interval $I = [1.18,\ 1.3]$. When slippage is below 1.18 all droplets move opposite to the flux, but the value of their mobility coefficient in the reduced ODE (3) with coefficients (4), (6) tends to zero as $\beta \to 1.18$, and therefore migration rates also approach zero. This effect can be seen in Figure 4 for $\beta = 0.3$ and $\beta = 0.5$. In the former case the first two coarsening effects are the same as for the intermediate-slip case, namely first collapse of the 6th droplet and then collision of the 2nd and 3rd ones. But in the case $\beta = 0.5$ migration becomes so slow that the 2nd and the 3rd drops can not collide, instead the former one collapses first.

The next qualitative change in the coarsening behavior occurs when passing the critical interval I. We observe that one droplet after another change their migration direction from opposite to the flux to the same direction of the flux. For example in the case $\beta = 1.25$ smaller droplets (like the 2nd, 3rd, 6th and 7th) have already changed their migration direction, but the bigger ones not. Nevertheless, we do not observe any change in coarsening events in comparison with the case $\beta = 0.5$.

To see new events we need to increase slippage further. As a consequence the migration coefficients in the reduced model increase and hence the migration rates as well. This, together with

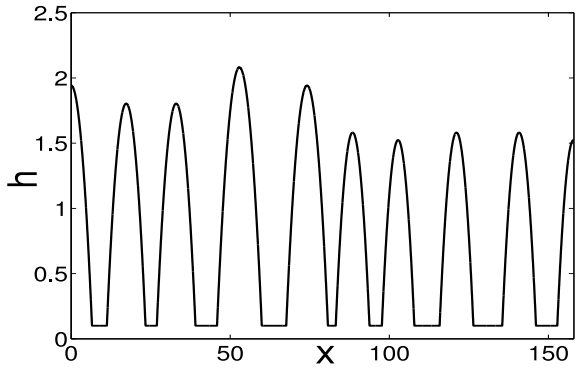


Figure 3: Initial profile used for all the coarsening simulations in figure 4

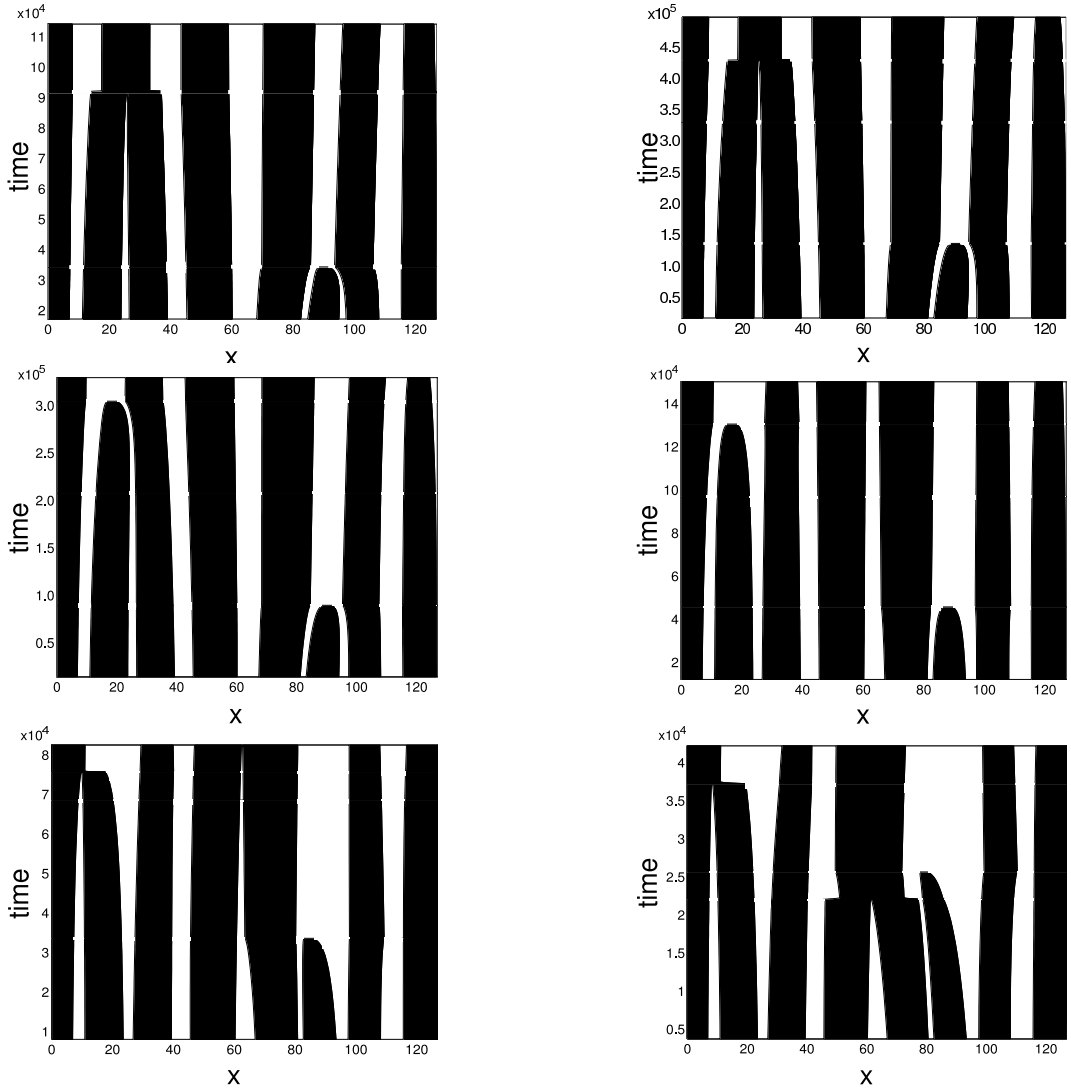


Figure 4: First two coarsening events in the initial array of eight droplets for six different slip values: Intermediate-slip model, strong-slip model with $\beta = 0.3$, $\beta = 0.5$, $\beta = 1.25$, $\beta = 2$, $\beta = 3.5$ (arranged from left to right and from top to bottom). In black evolution of droplet cores is plotted.

the fact that now all droplets migrate in the same direction as the flux, considerably changes the coarsening events in our example. For example, when $\beta = 2$ we see that both the 5th and 6th droplets migrate to the left. In contrast, in the intermediate-slip case they moved to each other together with the 4th droplet, which now migrates to the right. Moreover, the 2nd and 3rd droplets do not attract each other anymore, rather, the former one collides with the first droplet and this becomes the second coarsening event in our system. The first one is collapse of the 6th droplet.

Increasing slippage even higher, here up to $\beta = 3.5$, we see that migration rates increase further, so that now the 4th and 5th droplet collide (first coarsening event) before the 1st and 2nd ones, and the 6th collapses (second coarsening event). In principle, one could increase slippage further, so that one after the other coarsening event should change from collapse to collision.

In summary we demonstrated that increasing slippage, here in the interval [0, 3.5], several different coarsening behaviors for an initial droplet array can be distinguished. They illustrate that the existence of β_{crit} influences the coarsening dynamics by changing the direction of migration and as well as migration rates. They decrease to zero, when β approaches the critical slippage interval I, and collisions become dominant after further increase of the slip-length. The latter effect is new and characteristic only for the strong-slip model, because as it was shown in [4] in all other slip cases the migration of droplets either negligible or at most comparative with collapse component of the coarsening process. In contrast to that, in strong-slip case with sufficiently large slip-lengths migration strongly dominates the process.

Acknowledgements

GK is deeply grateful to the DFG Graduate Training Program 1128 "Analysis, Numerics and Optimization of Multiphase Problems" for the support.

References

[1] G. Kitavtsev and B. Wagner. Coarsening dynamics of slipping droplets. *J. Engr. Math.*, 66: 271–292, 2010.

[2] A. Münch, B. Wagner, and T. P. Witelski. Lubrication models with small to large slip lengths. *J. Engr. Math.*, 53:359–383, 2006.

[3] K. B. Glasner and T. P. Witelski. Coarsening dynamics of dewetting films. *Phys. Rev. E*, 67: 016302, 2003.

[4] K. Glasner, F. Otto, T. Rump, and D. Slepcev. Ostwald ripening of droplets: the role of migration. *European J. Appl. Math.*, 20(1):1–67, 2009.

Georgy Kitavtsev, Mohrenstr. 39, 10117, Weierstrass Institute for Applied Analysis and Stochastics, Berlin, Germany
Barbara Wagner, Mohrenstr. 39, 10117, Weierstrass Institute for Applied Analysis and Stochastics, Berlin, Germany

Self-similar regimes of solid phase conversions in media of various rheology

A. G. Knyazeva S. N. Sorokova
anna@ispms.tsc.ru

Abstract

It was shown by authors that coupling character of various physical and chemical phenomena is principal for detecting of conversion regimes in deformed media. Analytical estimations were received for the rates and product temperature of some regimes and numerical solutions of the problems on the propagation of low temperature radical reactions, heavy metals aside decomposition, metal-thermal reactions etc. It was ascertained that low conversion regimes (solid phase combustion) and quick regime (solid phase detonation) are connected with the prevalence of different energy transfer mechanism and various processes interrelation. In this paper the rheology properties influence are analyzed on the characteristics and existence conditions of low and quick regimes. The joint expansion method is used for problem solutions. The practical employments of found result are discussed.

1 Introduction

Solid-phase conversions (or the conversions with participation of solid substances) are manifold. In contrast to the conversions in gazes or liquids, where the reagents are patent to each other, and the reaction products can relatively without difficulties be extracted from the reaction zone, in the solid phase there are the features which are connected with the presence of feed-backs between the numerous physical phenomena. In terms of the continua mechanics, the fields of various physical nature interrelate with each other, that leads to complex kinetic regularities for the solid phase conversions. The mechanical processes play a special role in the solid-phase conversions: stresses and strains accompanying the conversions of the substances each other or their interaction appear because the substance properties are different, there are the temperature gradient, structure phase transition etc., and when we speak about micro level, the difference in the mobility of the species, the admixture and structure imperfection are observed etc.. By-turn, due to the presence of numerous feed-backs, stresses and strains can effect on the conversion rate in various ways. The role of the mechanical processes and connected with their medium mobility does not be reduced to additional heat sources and losses and to kinetic function form. Investigation of these questions leads to the development necessity of common approach to the coupling models construction for the physical-chemical conversions in the media of different rheology properties.

It was shown in the line of the papers, that coupling models for exothermal conversions assume the various regimes existence [1, 6]. The rate of the low stationary conversion regimes is determined by the energy transfer due to the thermal conduction. The rate of the quick regimes (or solid-phase detonation) is defined by the energy transfer together with mechanical perturbation wave. Taking into consideration the features if the medium where the conversions are possible (structure heterogeneities, stresses and strains of various types, density and other properties change in the reactions etc.) we shall obtain new regularities.

2 Governing equations

We formulate here the particular models of conversion front propagation in term of coupling models of thermo mechanics assuming that the reaction front is plane. Than one-dimensional equations

of discontinuity and motion take the view

$$\frac{d\rho}{dt} + \rho\frac{d\mathrm{v}}{dx} = 0$$
$$\rho\frac{d\mathrm{v}}{dt} = \frac{\partial\sigma_{11}}{\partial x},$$

where t is the time, x is the space coordinate, v and σ_{11} are the components of the rate vector and full stress tensor in the direction of front motion.

The energy equation (in the form of thermal conductivity equation) and chemical kinetic equation for summary reaction "reagent to the product", connecting with strains and stresses, look like these

$$\rho\, c_\varepsilon\frac{dT}{dt} = \lambda_T\frac{\partial^2 T}{\partial x^2} - 3\alpha_T KT\frac{d\varepsilon_{kk}}{dt} + \sigma_{11}^V\frac{\partial\mathrm{v}}{\partial x} + Q_r k_r\varphi_1(y)\,\varphi_2(T,\Pi),$$
$$\frac{dy}{dt} = k_r\varphi_1(y)\,\varphi_2(T,\Pi),$$

where T is the temperature, y is the conversion degree, λ_T is the thermal conductivity equation; ε_{kk} is the fist invariant of the strain tensor, c_ε is the capacity at the strain constancy, α_T is the linear thermal expansion coefficient, K is the bulk module, Q_r is the heat release in the summary reaction, k_r is the rate constant; $\varphi_1(y)$ is the kinetic function; the function φ_2 reflects the dependence of the reaction rate on the temperature and the stresses work Π; σ_{11}^V is the component of viscous stress tensor in the front direction.

In the case of plane front we have $\varepsilon_{kk} \approx \varepsilon$, where ε is the strain tensor component in the direction of their propagation.

It is necessary to complement these equations by the rheology relations and strain definition and find the solutions of moving wave type – self-similar solutions in the form of the wave of constant profile.

In the coordinate system connecting with the reaction front moving to the right with the rate v_n, we have the stationary model

$$-m\frac{d\rho}{dx} = -\rho^2\frac{d\mathrm{v}}{dx} \tag{1}$$
$$-m\frac{d\mathrm{v}}{dx} = \frac{d\sigma_{11}}{dx} \tag{2}$$
$$-m\, c_\varepsilon\frac{dT}{dx} = \lambda_T\frac{d^2T}{dx^2} + 3\alpha_T T\frac{K}{\rho}m\frac{d\varepsilon}{dx} + \sigma_{11}^V\frac{d\mathrm{v}}{dx} - \frac{Q_r}{\rho}m\frac{dy}{dx}, \tag{3}$$
$$-m\frac{dy}{dx} = \rho k_r\varphi_1(y)\,\varphi_2(T,\Pi), \tag{4}$$

where $m = \rho(\mathrm{v_n} - \mathrm{v})$ is mass combustion rate.

The conditions in the reagents ($x \to +\infty$) are given:

$$T = T_0, \quad \rho = \rho_0, \quad \mathbf{v} = 0, \quad \varepsilon = 0, \quad \sigma_{11} = 0, \quad y = 0.$$

In the reaction product ($x \to -\infty$), all perturbations attenuate.

In the approximation of plane front and small strains one can profit the relationship

$$\varepsilon_{kk} \approx \frac{\gamma - \gamma_0}{\gamma_0} = \frac{\rho_0}{\rho} - 1 \approx \varepsilon,$$

where γ is specific volume.

In this case we have

$$\frac{d\varepsilon}{dx} = -\frac{\rho_0}{\rho^2}\frac{d\rho}{dx}. \tag{5}$$

Than, taking into account (1), we shall find

$$\frac{d\varepsilon}{dx} = -\frac{\rho_0}{m}\frac{d\mathrm{v}}{dx}. \tag{6}$$

These relations allow integrating the presented below particular models.

3 Rheology relations

In the particular case of elastic body ($\sigma^V = 0$), small difference in the properties of the reagent and products and exothermal reaction, the basic role belongs to thermal stresses.

Than $\sigma_{11} = \sigma^e_{11}$ and constitutive equation can be presented in the form

$$\frac{d\sigma^e_{11}}{dx} = (\lambda + 2\mu)\frac{d\varepsilon}{dx} - 3K\alpha_T\frac{dT}{dx}, \tag{7}$$

are λ and μ the Lame constants.

If the properties of the summary reagent and summary product differ essentially, it is necessary to modify the relation (7). One of the variant of rheology relation takes the difference between the specific volume of the reagent and the product:

$$\frac{d\sigma^e_{11}}{dx} = (\lambda + 2\mu)\frac{d\varepsilon}{dx} - 3K\left[\alpha_T\frac{dT}{dx} + (\alpha_p - \alpha_r)\frac{dy}{dx}\right], \tag{8}$$

where α_p and α_r are the concentration expansion coefficients fro reagent and product correspondingly. We can present the equation (8) as

$$\frac{d\varepsilon}{dx} = \frac{1}{\lambda + 2\mu}\frac{d\sigma^e_{11}}{dx} + \frac{3K}{\lambda + 2\mu}\left[\alpha_T\frac{dT}{dx} + (\alpha_p - \alpha_r)\frac{dy}{dx}\right]$$

or

$$\frac{d\varepsilon}{dx} = \frac{d\varepsilon^e}{dx} + \left[\frac{d\varepsilon^T}{dx} + \frac{d\varepsilon^C}{dx}\right],$$

where ε^e is reversible elastic strain, $\varepsilon^T$is thermal strain, ε^C is chemical strain (irreversible due to the irreversibility of chemical reaction, corresponding to the equation (4)). One can talk the relation (7) leads to the variant of the plasticity theory [7]. Nonlinear rheology equation could be obtained from (7), when we take into consideration that the mechanical properties of the reagent and product and their thermal expansion coefficients differ. For example, one can take

$$\alpha_T = \alpha_{Tr}(1 - y) + \alpha_{Tp}y$$

in the first approximation.

In term of the thermodynamically based model for the deformable medium with chemical reactions [7] one can construct more complex rheology relations corresponding to media of various properties. So, rheology equations can include viscous stresses of various natures.

Let viscous stress tensor is spherical, then we have $\sigma^V_{ij} = -p^V\delta_{ij}$. If unique reaction runs in the system, then one can write the equation system [7, 8]

$$\begin{aligned} p^V &= -\kappa_V\nabla\cdot\mathbf{v} + \gamma_V A, \\ \varphi &= -\gamma_V\nabla\cdot\mathbf{v} + k_r A, \end{aligned} \tag{9}$$

for scalar processes(chemical reaction rate and viscous pressure). Here κ_V volume viscosity, A is the affinity of the chemical reaction with the rate φ. The coefficient γ_V is the chemical viscosity. The second from the equalities (9) describes the chemical reaction rate change due to the mobility medium variation. There is the information on this occasion in chemical literature, but there is neither attempt to measure corresponding coefficient. In compliance with thermodynamics the equality

$$\kappa_V k_{ch} - \gamma_V^2 \geq 0$$

must be true, that is the result of second thermodynamics law.

The chemical reaction affinity is determined by the equality

$$A = -\sum_{k=1}^{n}\nu_k m_k g_k,$$

in general case, where ν_k are stochiometric coefficients, m_k are molar masses, g_k are chemical potentials of species, n the number of the components participating in the reaction. For summary reaction and plane reaction front we can write

$$p^V = -\kappa_V \frac{d\mathrm{v}}{dx} + \gamma_V \varphi_1 \varphi_2, \qquad (10)$$
$$\varphi = -\gamma_V \frac{d\mathrm{v}}{dx} + k_r \varphi_1 \varphi_2,$$

Therefore, we have

$$\sigma_{11} = \sigma_{11}^e - p^V$$

and

$$\sigma_{11} = (\lambda + 2\mu)\,\varepsilon - 3K\left[\alpha_T\,(T - T_0) + (\alpha_p - \alpha_r)\,y\right] + \kappa_V \frac{d\mathrm{v}}{dx} - \gamma_V \varphi_1 \varphi_2.$$

Subject to (6) we shall find

$$\sigma_{11} = (\lambda + 2\mu)\,\varepsilon - 3K\left[\alpha_T\,(T - T_0) + (\alpha_p - \alpha_r)\,y\right] - \frac{\kappa_V m}{\rho_0}\frac{d\varepsilon}{dx} - \gamma_V \varphi_1 \varphi_2. \qquad (11)$$

This equation is nothing short of "generalization" of the model of elastic viscous Voigt solid:

$$\sigma_{11} = (\lambda + 2\mu)\,\varepsilon - 3K\left[\alpha_T\,(T - T_0) + (\alpha_p - \alpha_r)\,y\right] + \frac{\kappa_V}{\rho_0}\frac{d\varepsilon}{dt} - \gamma_V \varphi_1 \varphi_2.$$

The last relation is relation (11) in the fixed coordinate system.

Note that equation (11) can be considered as "generalization" of the model of Bingham solid, taking into consideration thermo activation character of chemical conversions. The stresses do not appear, the substance current is not observed while the reaction is not activated. Then in the relation

$$\sigma = \sigma_0 + \mu'\dot{\varepsilon},\ \sigma > \sigma_0,$$

the value σ_0 will be connected with the activation energy of the chemical reaction immediately.

Some "generalization" of the simplest variant of the model viscoelastic Maxwell body follows from (11), (2), (6) at the condition that "elastic stresses" of the type (7) do not emerge. Then from (11) we have

$$\sigma_{11} = -\frac{\kappa_V}{m}\frac{d\sigma_{11}}{dx} + \frac{\gamma_V m}{\rho k_r}\frac{dy}{dx}$$

or based on the definition of irreversible strains, presented above, we find

$$\sigma_{11} = -\frac{\kappa_V}{m}\frac{d\sigma_{11}}{dx} + \frac{\gamma_V m}{\rho k_r}\frac{\lambda + 2\mu}{3K\,(\alpha_p - \alpha_r)}\frac{d\varepsilon^C}{dx}$$

or

$$\sigma_{11} + \frac{\kappa_V}{m}\frac{d\sigma_{11}}{dt} = \frac{\gamma_V m}{\rho k_r}\frac{\lambda + 2\mu}{3K\,(\alpha_p - \alpha_r)}\frac{d\varepsilon^C}{dt}. \qquad (12)$$

In this case the parameter of Maxwell model (shear module, dynamic viscosity coefficient) will be connected immediately with the formal kinetic parameters of the chemical reaction. It is interesting to note that the deformation rate can included into the relation (12) with distinct sign (that depends on conversion type)

$$\frac{\sigma_{11}}{\mu''} + \frac{1}{\kappa_V''}\frac{d\sigma_{11}}{dt} = \pm\frac{d\varepsilon^C}{dt}.$$

In general rheology model of viscoelastic body ones use the operating relationship between the deviators of stress and strain tensors [9]

$$As_{ij} = Be_{ij}, \tag{13}$$

where A, B are differential operators linear in time,

$$s_{ij} = \sigma_{ij} - \frac{1}{3}\sigma_{kk}\delta_{ij}, \quad e_{ij} = \varepsilon_{ij} - \frac{1}{3}\varepsilon_{kk}\delta_{ij}.$$

Invariants the full stress and strain tensors σ_{kk} and ε_{kk} are connected by the relation

$$\sigma_{kk} = 3K\left(\varepsilon_{kk} - w\right),$$

where w is the function depending on temperature, concentrations and other state variables. In the case of unique chemical reaction we have

$$w = 3\left[\alpha_T\left(T - T_0\right) + \left(\alpha_p - \alpha_r\right)y\right].$$

Then, assuming

$$A = \frac{1}{2\mu}\frac{\partial}{\partial t} + \frac{1}{2\kappa_V}, \quad B = \frac{\partial}{\partial t},$$

we shall find

$$\frac{\partial\sigma_{ij}}{\partial t} + \frac{\mu}{\kappa}\sigma_{ij} = 2\mu\frac{\partial\varepsilon_{ij}}{\partial t} + \delta_{ij}\left[\frac{\partial}{\partial t}\left(\lambda\varepsilon_{kk} - Kw\right) + \frac{\mu}{\kappa}K\left(\varepsilon_{kk} - w\right)\right]. \tag{14}$$

where κ is the shear viscous coefficient. In the limiting case $\kappa \to \infty$ the generalized Duhamel-Neyman relations follow from (14), in the case $\kappa \to 0$ we have the relations between the components σ_{ij} and ε_{ij} for ideal viscous liquids with spherical stress tensor.

The relations (14) correspond to viscoelastic Maxwell model correct for the description of mechanical behaviour of media possessing the properties liquids and solids simultaneous.

In the case of plane reaction front we shall obtain

$$\frac{\partial\sigma_{11}}{\partial t} + \frac{\mu}{\kappa}\sigma_{11} = \left(2\mu + \lambda\right)\frac{\partial\varepsilon}{\partial t} - K\frac{\partial w}{\partial t} + \frac{\mu}{\kappa}K\left(\varepsilon - w\right). \tag{15}$$

Note, the Maxwell model (14) can be obtained on the base of thermodynamic model [7, 8], when volume and shear viscosities are taken into consideration simultaneous.

4 Examples of self-similar solutions

For first example we use the rheology relation (7). Viscous stresses are equal to zero. The chemical reaction rate does not depend on stress work. Taking (5) and (2), we shall find

$$m\frac{d\mathrm{v}}{dx} = \frac{\rho_0}{\rho^2}\left(\lambda + 2\mu\right)\frac{d\rho}{dx} + 3K\alpha_T\frac{dT}{dx}.$$

Using the continuity equation (1) to find the derivative of the density, we come to the equation

$$\frac{d\mathrm{v}}{dx} = \frac{3mK\alpha_T}{\left[m^2 - \rho_0\left(\lambda + 2\mu\right)\right]}\frac{dT}{dx}. \tag{16}$$

Analogously we have

$$\frac{1}{\rho^2}\frac{d\rho}{dx} = \frac{3K\alpha_T}{\left[m^2 - \rho_0\left(\lambda + 2\mu\right)\right]}\frac{dT}{dx}. \tag{17}$$

Hence, allowing for (5), substitute the thermal conductivity equation (3) by the equation

$$-m\ c_\varepsilon\frac{dT}{dx} = \lambda_T\frac{d^2T}{dx^2} - \frac{\left(3K\alpha_T\right)^2 T\ m\rho_0}{\rho\left(m^2 - \rho_0\left(\lambda + 2\mu\right)\right)}\frac{dT}{dx} - \frac{Q_r}{\rho}m\frac{dy}{dx}. \tag{18}$$

In dimensionless variables

$$\theta = \frac{T - T_0}{T_* - T_0}, \quad \xi = \frac{x}{x_*}, \quad \bar{\rho} = \frac{\rho}{\rho_0}, \quad v = \frac{v}{v_{n*}},$$

where

$$T_* = T_0 + \frac{Q_r}{c_\varepsilon \rho}, \quad v_{n*}^2 = k_r \kappa_T \exp\left(-\frac{1}{\beta}\right), \quad x_* = \frac{\kappa_T}{v_{n*}},$$

from (16) - (18) and (4), we shall derive

$$\frac{d\bar{v}}{d\xi} = \frac{V\varepsilon_*}{(\alpha V)^2 - 1}\frac{d\theta}{d\xi}; \tag{19}$$

$$\frac{1}{\bar{\rho}^2}\frac{d\bar{\rho}}{d\xi} = \frac{\varepsilon_*}{(\alpha V)^2 - 1}\frac{d\theta}{d\xi}; \tag{20}$$

$$-V\left(1 + \frac{\omega\ (\theta + \sigma)}{1 - (\alpha V)^2}\ \bar{\rho}^{-1}\right)\frac{d\theta}{d\xi} = \frac{d^2\theta}{d\xi^2} + \ \varphi_1(y)\,\varphi_2(\theta), \tag{21}$$

$$-V\frac{dy}{d\xi} = \varphi_1(y)\,\varphi_2(\theta), \tag{22}$$

where

$$\varphi_2(\theta) = \exp\left[-\frac{1-\theta}{\beta(\theta+\sigma)}\right] = \exp\left[-\frac{(1-\theta)(1+\sigma)}{\gamma\ (\theta+\sigma)}\right]$$

$$\omega = \frac{(3\alpha_T K)^2}{\lambda + 2\mu}\frac{T_* - T_0}{c_\varepsilon \rho_0}, \quad V = \frac{m}{\rho_0 v_{n*}}, \quad \alpha^2 = \frac{\rho_0}{\lambda + 2\mu}v_{n*}^2, \quad \varepsilon_* = \frac{3K\alpha_T(T_* - T_0)}{\lambda + 2\mu}.$$

$$\sigma = \frac{T_0}{T_* - T_0}, \quad \beta = \frac{RT_*}{E_a}, \quad \gamma = \frac{c_\varepsilon \rho R T_*^2}{E_a Q_r}.$$

The value ε_* presents the factum of thermal strains $\alpha_T(T_* - T_0)$ and the relation of the rates of volume and longitudinal mechanical waves $3K/(\lambda + 2\mu)$; β and γ are small parameters of combustion theory; ω is the coupling coefficient; V is mass combustion rate.

The boundary conditions in the reagents take the form:

$$\xi \to +\infty: \quad \theta = 0, \quad y = 0 \tag{23}$$

In the region of the products, all perturbations attenuate:

$$\xi \to -\infty: \quad y = 1, \quad \frac{d\theta}{d\xi} = 0, \tag{24}$$

so the product temperature $\theta = \theta_b$, $\theta_b = \frac{T_b - T_0}{T_{b0} - T_0}$, must be found

Using the conditions in the reagents, we come to the expressions

$$\bar{\rho} = \frac{1}{1 + \frac{\varepsilon_* \theta}{1 - (\alpha V)^2}}, \quad \bar{v} = -\frac{\varepsilon_* \cdot V}{1 - (\alpha V)^2}\theta, \tag{25}$$

that is the density and the rate are determined by the temperature.

Therefore, instead the equation (21), we have

$$-V\left[1 + \frac{\omega\ (\theta + \sigma)}{1 - (\alpha V)^2}\ \left(1 + \frac{\varepsilon_* \theta}{1 - (\alpha V)^2}\right)\right]\frac{d\theta}{d\xi} = \frac{d^2\theta}{d\xi^2} + \varphi_1(y)\,\varphi_2(\theta). \tag{26}$$

Some properties this equation (which is Lienard's equation in the particular case $\varphi_1(y) = 1$), allowing to judge the qualitative character of their solutions, are described in [5].

To find front rate in the problem (26), (22) with the conditions (23), (24), we use the method of joint asymptotical expansion. The detailed computations are presented in [6]. In zero approximation we had obtain the equations

$$M = \exp\left(-\frac{1-\theta_b}{\gamma}\right) - \exp\left(-\frac{1}{\gamma}\right) \approx \exp\left(-\frac{1-\theta_b}{\gamma}\right),$$
$$\left(1+\frac{\omega\sigma}{1-\alpha_1}\right)\theta_b + \left(1+\frac{\varepsilon_*\sigma}{1-\alpha_1}\right)\frac{\omega}{1-\alpha_1}\frac{\theta_b^2}{2} + \frac{\omega\varepsilon_*}{(1-\alpha_1)^2}\frac{\theta_b^3}{3} - 1 = 0,$$

where $M = V^2\gamma^{-1}$; $\alpha_1 = \alpha^2 V^2$, for combustion rate and temperature product.

Analysis shows that, for real region of parameter change, this equation has one, or to, or three real positive solutions. If $\alpha_1 < 1$, the values $\theta_b < 1$ give the mass combustion rate for subsonic regime, that with the temperature and rate values depend weakly on the parameter ε_* (that is., on the parameter, characterizing the mechanical properties). Another situation is observed in supersonic region. If α_1 exceeds the unity to a little degree, there is unique positive root of the equation for the product temperature θ_b. It can be less or more than unity. This regime is one temperature. If $\theta_b < 1$, we have "low temperature low rate" detonation. When $\theta_b > 1$, we find $M >> 1$. If α_1 exceeds some critical value and ε_* is less than some critical value (depending on other parameters), the equation for the temperature has three positive roots, and we come to "three temperature" combustion regime (with complex structure of reaction zone).

Second example of the model is based on the viscoelastic Maxwell model of the medium (that is the rheology equation (15) is used). It is assumed that strains and rates are small, that allows using the approximation of constant density. In this case, from the Cauchy equation of motion the we go to the motion equation lake this

$$\rho\frac{\partial^2 u}{\partial t^2} = \frac{\partial\sigma_{11}}{\partial x},$$

where u is the displacement vector component in the front direction. Differentiating this equation twice, we shall obtain

$$\rho\frac{\partial^2\varepsilon}{\partial t^2} = \frac{\partial^2\sigma_{11}}{\partial x^2}.$$

Than in the coordinate system connecting with the plane reaction front moving to the right, we shall find instead (2) the equation

$$\rho v_n^2\frac{d^2\varepsilon}{dx^2} = \frac{d^2\sigma_{11}}{dx^2}. \tag{27}$$

The thermal conductivity and kinetic equations will include linear reaction front rate (we neglect the work of viscous stresses and dependence of the reaction rate on the stress work):

$$-\rho v_n\, c_\varepsilon\frac{dT}{dx} = \lambda_T\frac{d^2T}{dx^2} + 3\alpha_T TK\rho v_n\frac{d\varepsilon}{dx} - Q_r \mathrm{v}_n\frac{dy}{dx}, \tag{28}$$

$$-\rho v_n\frac{dy}{dx} = k_r\varphi_1(y)\,\varphi_2(T) \tag{29}$$

At the condition, that the thermal stresses prevail in the reaction zone, the relation (15) takes the form

$$-\mathrm{v}_n\frac{d\sigma_{11}}{dx} + \frac{\mu}{\kappa}\sigma_{11} = -(2\mu+\lambda)\,\mathrm{v}_n\frac{d\varepsilon}{dx} + 3K\alpha_T\mathrm{v}_n\frac{dT}{dx} + \frac{\mu}{\kappa}K(\varepsilon - 3\alpha_T(T-T_0)) \tag{30}$$

in the moving coordinate system.

The boundary conditions are analogous to previous ones.

In dimensionless variables

$$\theta = \frac{T-T_0}{T_*-T_0};\quad \xi = \frac{x}{x_*};\quad y;\quad e = \frac{\varepsilon}{\varepsilon_*};\quad S = \frac{\sigma_{11}}{\sigma_*},$$

where $\sigma_* = 3K\alpha_T (T_* - T_0)$, and other symbols the same, the equation (27) – (30) go to the view

$$-\frac{d\theta}{d\xi} = \frac{d^2\theta}{d\xi^2} + \omega(\theta + \sigma)\frac{de}{d\xi} - \frac{dy}{d\xi}; \tag{31}$$

$$-V\frac{dy}{d\xi} = \varphi_1(y)\varphi_2(\theta); \tag{32}$$

$$(\alpha V)^2 \frac{d^2e}{d\xi^2} = \frac{d^2S}{d\xi^2}; \tag{33}$$

$$-\frac{dS}{d\xi} + \frac{S}{\tau_V} = -\frac{de}{d\xi} + \frac{d\theta}{d\xi} + \frac{h^2e - \theta}{\tau_V}. \tag{34}$$

The new parameters appear in the model:

$$\tau_v = \left(\kappa v_n^2\right)/(\mu\kappa_T) \quad h^2 = K/(\lambda + 2\mu).$$

The first is dimensionless relaxation time of viscous stresses. The second is the square of the relation of volume and longitudinal elastic wave. Because, besides the temperature, concentrations, stresses and strains, the linear front rate is required value (no mass as in previous model), so parameter V changes: $V = v_n/v_{n*}$.

From the equation (33) we find direct the first integral: $S = (\alpha V)^2 \cdot e$, than the equation (34) goes to:

$$\left(1 - (\alpha V)^2\right)\frac{de}{d\xi} + \frac{(\alpha V)^2 - h^2}{\tau_V}e = \frac{d\theta}{d\xi} + \frac{\theta}{\tau_V}.$$

Unfortunately, following exact integration is not possible. To solve this problem, we employ the joint asymptotic expansion method also. The solution is succeeding for two limiting cases – small and large values of the relaxation time of viscous stresses. The result for the front rate and for the product temperature has a view (in the same variables):

$$M \approx \exp\left(\frac{\theta_b - 1}{\gamma}\right);$$

$\tau_V >> 1$:

$$a\theta_b^3 + b\theta_b^2 + c\theta_b + 1 = 0,$$

where

$$a = \frac{\tau_V}{3}\left(\frac{\omega}{\alpha_1 - h^2}\right)^3\left(1 - \frac{1-\alpha_1}{\alpha_1 - h^2}\right),$$

$$b = \tau_V\left(1 - \frac{1-\alpha_1}{\alpha_1 - h^2}\right)\frac{\omega}{\alpha_1 - h^2}\left(\frac{\sigma\omega}{3} + \frac{1}{2}\right) - \frac{1}{2}\frac{\omega}{\alpha_1 - h^2},$$

$$c = \tau_V\left[1 - \frac{1-\alpha_1}{\alpha_1 - h^2}\right]\frac{\sigma\omega}{\alpha_1 - h^2}\left(\frac{\sigma\omega}{\alpha_1 - h^2} + 1\right) - 1 - \frac{\sigma\omega}{\alpha_1 - h^2};$$

$\tau_V << 1$:

$$1 - \theta_b - \omega_1\left(\frac{\theta_b^2}{2} + \sigma\theta_b\right) + \frac{2}{\tau_V}\left(1 - 2\alpha_1 + h^2\right)\left[\theta_b - \left(\sigma + \frac{2}{\omega_1}\right)\ln\left(\frac{2 + \theta_b\omega_1 + 2\sigma\omega_1}{2 + 2\sigma\omega_1}\right)\right] = 0,$$

where $\omega_1 = \dfrac{\omega}{1 - (\alpha V)^2}$.

The analysis shows that solutions of two types exist in this problem: low rate $\alpha < 1$ and high rate $\alpha > 1$, as it was in the case of pure elastic stresses [1]. In contrast to the models for elastic media, here there are the features, which are described partially in [10].

Note, that the distributions of all values in the reaction front and the values of the stresses and strains in the product are found also during investigation. As the front rate, the values of stresses and strains depend essentially on parameters of the models under study. The obtained results speak about, that it is necessary to take into consideration the rheology properties of media not only, when experimental data are discussed or effective properties are evaluated, but when the possible conversion regimes for phase and chemical conversions are investigated. Indeed, the coupling effect, which is considered as negligible small in macro kinetics and continua mechanics, can play a principal role.

5 Conclusion

In conclusion we accentuate the relevancy of the problem. In the chemical technologies, in the food industry, in the technologies of natural fuel and minerals etc. mining and processing one's deal with the substances and materials, their rheology properties are very complex. From another site, all these processes are accompanied by the various physical-chemical conversions. Therefore, it will be expected that taking into account the rheology features of the media, where the chemical and physical conversions are observed, when the media models are constructed, leads to the new regularities exposure and, hence, to new ideas appearance for technologies development. Associated to physical and chemical conversions the mechanical processes, including wave processes would be studied by the same token with taking into consideration of coupling effects. The examples of coupling models application to real technology processes are presented in [11, 12].

References

[1] Timokhin A.M., Knyazeva A.G. The regimes of the reaction front propagation in the coupling thermal mechanical model of solid-phase combustion // Chemical physics (Translated from Russian), 1995. - V.15, No 10. - P.85-100

[2] Knyazeva A.G., Dyukarev E.A. On the regimes of solid-phase decomposition of individual crystals of initiate explosives // Physical mesomechanics, 2000. – V.3, No 3. -V.97-106

[3] Knyazeva A.G., Dyukarev E.A Thermomechanical model of self-sustaining propagation of the low temperature radical reactions accompanying the fracture // Combustion, Explosion, and Shock waves (translated from Russian), 1998. - V.34, No 4. – P.84-93

[4] Knyazeva A.G. To one cause of quick regimes of solid phase conversions – in "Chemical physics of the processes of the combustion and explosion", XII Symposium on combustion and explosion, part III / Chernogolovka (in Russian): 2000 (11-15 September). – P.89-91

[5] Knyazeva A.G. The solution of thermal elasticity theory in the form of moving wave and its application to the analysis of the possible solid-phase conversion regimes // Prikladnaya mechanica i technicheskaya fizika (ranslated from Russian into English), 2003. - V.44, No 2. - P.14-26

[6] Knyazeva A.G. The rate of solid-phase combustion wave. Asymptotical analysis. // Physical mesomechanics, 2004. - V.7, No 3. – P. 63-70

[7] Knyazeva A.G. Diffusion and rheology in local-reversible thermodynamics. - Mathematical modeling of the system and processes, Ed. by P.V.Trusov, Perm.GTU / Perm. – 2005. – P. 45-60

[8] Knyazeva A.G. On the irreversible processes modeling in the material with large square of internal surfaces // Physical mesomechanics, 2003. - V.6, No 5. – P. 11-27

[9] 9. Boli B. and Ueyner Dj., Teorija temperaturnich naprjageniy / Moscow, Mir, 1964, pp. 517–518.

[10] Sorokova S.N., Knyazeva A.G. Stationary conversion regimes in viscoelastic medium // Combustion, Explosion, and Shock waves (translated from Russian). – 2006. - V.42, No 5. – P. 63-73

[11] Sorokova S.N., Knyazeva A.G. Modeling of coating phase structure formation during electron beam treatment using solid-phase synthesis // Teoreticheskie osnovy chemicheskoi technologii (translated from Russian into English), 2008. - V.42. No 4. P. 457– 465

[12] Sorokova S.N., Knyazeva A.G. Numerical investigation of technology parameters influence on the composition and stress-strain state of the coating synthetized during electron-beam heating // Teoreticheskie osnovy chemicheskoi technologii (translated from Russian into English), 2010. - V.44. – No 2. - P. 184-197

Knyazeva A.G., Akademichesky 2/4, Tomsk, Russia
Sorokova S.N., pr. Akademichesky 2/4, Tomsk, Russia

Formation of polymer nanofiber in the gap between filler particles in deformed elastomeric nanocomposites

Lyudmila A. Komar Sergey N. Lebedev
komar@icmm.ru

Abstract

The present paper reports the results obtained in numerical simulation of the formation of interphase layers (a few nanometers thick) with specific properties that occur near filler nanoparticles in elastomeric nanocomposites. A continuum model based on a hypothesis explaining the interphase layer formation is formulated and explored. The hypothesis stems from the fact that the polymer chains near the surface of particles are able to change the orientation of neighboring chains and dictate them the state in which they themselves have to stay. The model proposed is used to describe the interphase layer formation in the vicinity of the filler particle surface and in the gap between the particles in a two-dimensional case.

1 Introduction

The survey of the available literature has revealed the increasing number of arguments that prove the responsibility of interphase layers for a marked difference in the properties of filled and unfilled elastomers formed in the vicinity of the surface of filler particles of a nanometer scale size. Many researchers thought that these layers play an important role in the formation of the mechanical properties of composite materials.

In general, the influence of interphase layers on the mechanical properties of composite materials has been well studied experimentally. However, we believe that the list of publications related to the development of continuum models capable of describing the interphase layer formation contains a limited number of works.

In the present study, an attempt is made to fill in this gap. We have simulated the formation of the interphase layer taking into account its time-dependent character and the geometrical peculiarities of the designed material. It has been suggested that in the material near the surface of filler particles there occur polymer layers where the polymer molecules are in an oriented state. The regions with a high degree of orientation of polymer molecules dictate an increase in the orientation state of polymer molecules in the neighboring regions. On the other hand, being away from the filler particle surface, polymer molecules can demonstrate a chaotic arrangement. The mathematical model proposed in this study is based on the hypothesis concerning the formation of oriented regions in polymer materials [1].

2 Brief description of model

The evolution equation that defines the interphase layer formation on the filler particle surface and the orientation region in the gap between them is based on the following premises. Suppose that there exists a continuous differentiated tensor function $\mathbf{O}(t, \mathbf{x})$ on time t and spatial vector $\mathbf{x}$. The vector $\mathbf{x}$ specifies the location of the point in the space. Tensor function $\mathbf{O}(t, \mathbf{x})$ is used to calculate the energy of interaction between the i-th polymer link and other links in exactly the same way as in the probability and discrete models. Let the tensor function $\mathbf{O}(t, \mathbf{x})$, being subjected to the action of the neighboring regions, tends to take the value which corresponds to the value averaged over the vicinity of the point under study.

Let us further assume that the process of the polymer orientation is hampered by thermofluctuations that tend to bring the polymer into the non-oriented state. In this case, the evolution process of formation of oriented regions is governed by the evolution equation

$$\frac{1}{b}\frac{D\mathbf{O}}{Dt} = a\, C_\Delta \sum_{i=1}^{2} \frac{\partial^2 \mathbf{O}}{\partial x_i^2} + \left(\frac{\mathbf{I}}{3} - \mathbf{O}\right) + f_*,$$

where x_i are the space coordinates; b is the parameter of the layer formation rate (in this case, it is a decaying scalar function); a is the function that depends on the double scalar product $\mathbf{O} \cdot\cdot\, \mathbf{O}$; C_Δ is a constant; $\mathbf{I}$ is a unit vector. Description of the constant C_Δ and the functions a and b are given in work [1].

Function f_* is a complementary summand, which take into account the peculiarity of the orientation process on the boundary between the oriented layer and the rest of the polymer matrix. At the space points of the oriented layer and polymer matrix, where the molecule demonstrate the chaotic arrangement, $f_* = 0$. The function f_* is written as

$$f_* = (f_u + f_b)\left(\mathbf{O} - \frac{\mathbf{I}}{3}\right),$$

where the functions f_u and f_b are the scalar functions describing the oriented layer formation in the parts of the polymer material in the gap between filler particles and in the parts near the filler particle surface (in the interphase layer), respectively. In the rest of the material, their values are equal to zero. In our investigation, these values are given as

$$f_u = g_u\,(I_u^{max} - \mathbf{O}\cdot\cdot\mathbf{O})(\mathbf{O}\cdot\cdot\mathbf{O} - I_u^{min}), \qquad I_u^{min} < \mathbf{O}\cdot\cdot\mathbf{O} < I_u^{max},$$

$$f_b = g_b\,(I_b^{max} - \mathbf{O}\cdot\cdot\mathbf{O})(\mathbf{O}\cdot\cdot\mathbf{O} - I_b^{min}), \qquad I_b^{min} < \mathbf{O}\cdot\cdot\mathbf{O} < I_b^{max},$$

where g_u, g_b, I_u^{min}, I_u^{max}, I_b^{min}, I_b^{max} are the constants ($g_u = g_b = 2{\cdot}10^4$; $I_u^{min} = 0.65$; $I_u^{max} = 0.83$; $I_b^{min} = 0.37$; $I_b^{max} = 0.41$). The values of constant I_u^{min}, I_u^{max}, I_b^{min}, I_b^{max} are assigned for the region where the function a is defined. This function takes a very large value subject to the equality of the value $\mathbf{O}\cdot\cdot\mathbf{O}$ to the values designated here as I_u^{max} and I_b^{max}. The oriented region of the material involves part of the polymer having the points where the conditions $a > I_u^{max}$ and $a > I_b^{max}$ are fulfilled. The constants I_u^{min} and I_b^{min} specify a condition for initiating the process of orientation of molecules near the layer boundary in an equilibrium situation.

3 Numerical modeling

Evolution equation is used for modeling the propagation of the oriented regions in carbon-black-filled elastomeric materials. We consider the material fragment consisting of an elastomeric matrix surrounding a single inclusion – a carbon black particle. The particle is assumed to be of an ideal circle shape. The particle radius R is equal to 20 nm.

The first step of modeling includes the analysis of the interphase layer formation at the moment of manufacture of the material. The interaction of the polymer matrix with the filler particle orients polymer chains near the interface. In this case, the boundary condition for the orientation tensor is prescribed. Further evolution of the oriented region is defined by evolution equation.

The results of calculations are shown in Fig. 1. Particles are represented by white colour. The areas enclosing to particles illustrate the interphase layers. Elastomeric matrix and interphase layers are represented by grey colour. The initial and final moments of the layer formation are accordingly presented in Fig. 1, a and Fig. 1, c. The intermediate moment is presented in Fig. 1, b. The finished layer thickness of 8 nm (Fig. 1, c) is comparable with half the particle radius.

Further it is considered how deformation of the nanolayer in the gap between filler particles leads to the appearance of nanofibers. Formation of the nanofibre is simulated using the finite element method with use of isotropic models known in the literature (Proni series, the neo-Hookean description of the elastic contribution of stress tensor, neo-Hookean binding). It is studied the pair-wise interaction between filler nanoparticles for the case when the distance between the surfaces

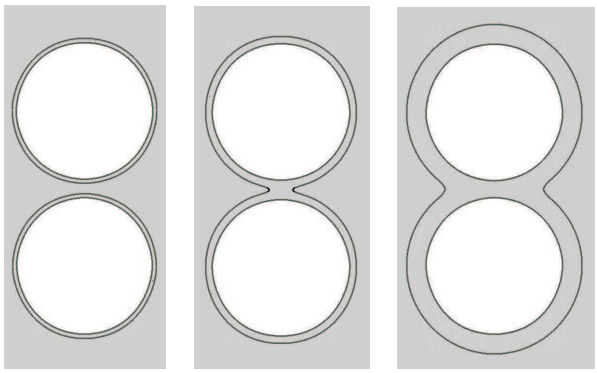


Figure 1: The formation of a layer in time in the vicinity of filler surface. Particles are represented by white colour. The particle radius R=20 nm. The grey areas enclosing to particles illustrate the interphase layers. The time period is measured in arbitrary units: $t = 5$ (a); 10(b); 50(c).

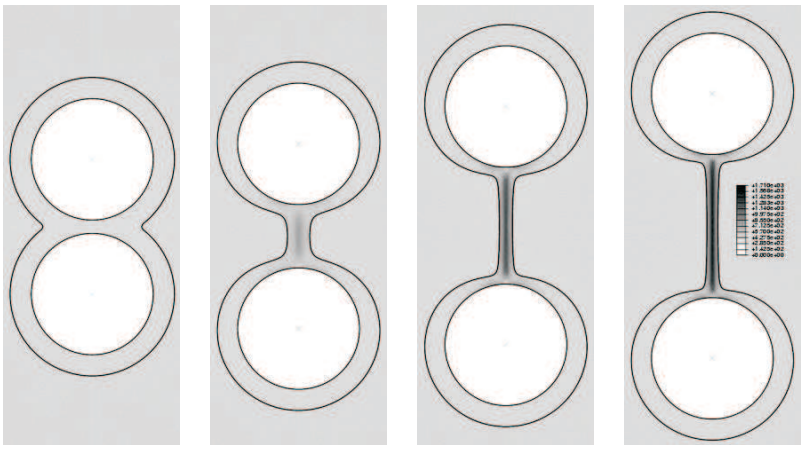


Figure 2: Formation of polymer nanofiber in the gap between two nanoparticles in deformated elastomeric materials. Particles are represented by white colour. The particle radius R=20 nm. The values of the deformations arising in an average point between filler particles, are accordingly equal: 0% (a), 500% (b), 1000% (c) and 1300% (d).

of neighboring particles is so small that the adjacent near-surface layers combine (Fig. 1, c). This layer is able to form nanofiber under large deformation (Fig. 2).

The length of the formed nanofibre can exceed a thickness of a layer in 7 times. The values of the deformations arising in an average point between filler particles, are accordingly equal to 0% (Fig. 2, a), 500% (Fig. 2, b), 1000% (Fig. 2, c) and 1300% (Fig. 2, d). In the figure Fig. 2, d corresponding to the maximal deformations, it is visible, that the interphase layer has changed the form. Its thickness is equal to 3 nanometers in the most thin place.

4 Conclusion

Numerical results obtained in this study have shown that proposed evolution equation can be used to describe the growth of the interphase layers in the filled elastomeric material. Thickness of the interphase layers of 8 nm is comparable with half the particle radius. Under large deformations of the material these nanolayers undergo large loading and somehow change the structure and the form.

Acknowledgements

The research was supported by the RFBR within the limits of the project 09-08-00530-a and Fundamental research program N 09-T-1-1006 of the Department of Power engineering, Mechanical Engineering, Mechanics and Control Processes of RAS "Tribological and strength properties of structured materials and surface layers".

References

[1] Lyudmila A. Komar, Alexander L. Svistkov. Changes in the orientation state of polymer molecules in the space between filler particles // Proceedings of the XXXVII Summer school "Advanced problems in mechanics", St. Petersburg (Repino), 2009, pp. 350-356.

Lyudmila A. Komar, Institute of Continuous Media Mechanics of Russian Academy of Sciences Ural Branch, Str. Acad. Korolev, 1, Perm, Russia
Sergey N. Lebedev, Institute of Continuous Media Mechanics of Russian Academy of Sciences Ural Branch, Str. Acad. Korolev, 1, Perm, Russia

Numerical study of the influence of parameters of defects on the strength properties of brittle coating

Igor S. Konovalenko Andrei I. Dmitriev Alexei Yu. Smolin
Sergeu G. Psakhie
igkon@ispms.tsc.ru

Abstract

A numerical approach to estimate the strength properties of porous ceramics coating was developed in this paper. This approach is based on the preliminary results of indentation tests of coatings with pores of various size and depth. Computer simulations were performed on the basis of movable cellular automaton method. It was shown that strength properties of a coating depend on pore size and depth. The ratio of pore's parameters, pore size and depth of pore corresponding to validity of the revealed tendency was found. The approach developed can be used for investigation of strength properties of material surface layers on the basis of such parameters as depth of pore and pore size, for example, in friction pair analysis.

1 Introduction

The most of the modern machines and devices include various friction units. Their mechanical behavior substantially determines working capacity of these mechanisms as a whole. Life span of a friction unit particularly depends on physico-mechanical characteristics of surface layer of the friction parts. Usually these characteristics increased by using antiwear coating. As a rule, a coating contains some defects, such as micro- and nanopores. Tribotechnical characteristics of a coating substantially determined by the defect parameters. Indentation is the most common experimental test for evaluation of strength and elastic properties of a coating. This test allows getting effective characteristics of a coating for practical use, which values depend on a whole series of factors. At the same time investigation of influence of several factors, such as topological and morphological characteristics, of defects in the coating on its strength properties is very difficult task within the mentioned framework. Using computer simulation can be very effective solution of this task. Computer simulation capabilities allow analyzing influence of various factors (physico-mechanical parameters of the system, loading conditions etc.) on mechanical behavior of a coating. Thus, in this paper the theoretical study on the basis of computer simulation approach was performed to reveal correlation of strength properties of the coating with its pore depth and pore size of a coating.

Calculations were performed within the framework of discrete-continual approach. The detailed description of coupling the discrete and continual approaches, as well as description of the both methods are represented in [1, 2]. The main point of the coupling is assumption of the interface between discrete (described by movable cellular automaton method) and continual (motion equations are solved by finite difference method) zones. This interface belongs to both mentioned zones. A certain network node at the interface corresponds to the certain movable cellular automaton. Movement of interfacial nodes with corresponding movable cellular automata is realized in the grid method. Using of the discrete-continual approach to studying contact problems, where large deformations, fracture and mass mixing are located in narrow region [1] showed its high efficiency.

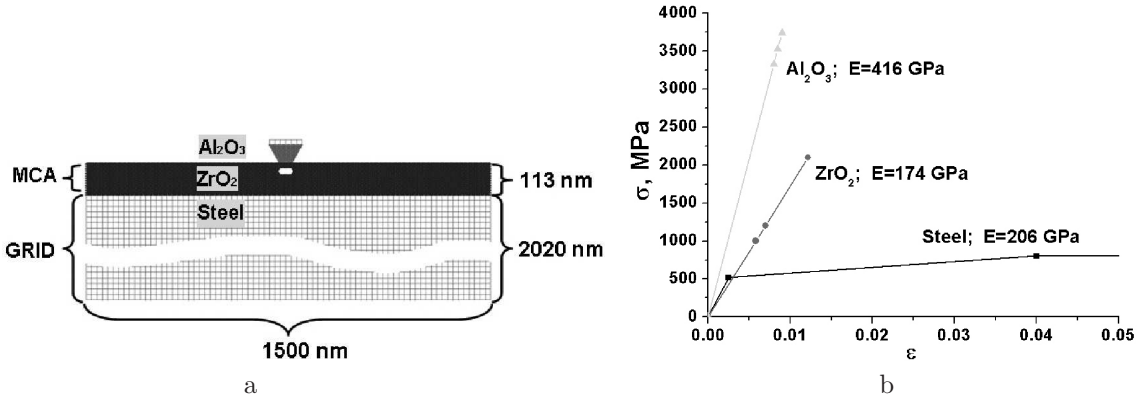


Figure 1: Model assemblage corresponding to ceramic coating on the metal back.The response functions of movable cellular automata and their elastic parameter, corresponding to the model materials

2 Description of modeled object

Indentation test of ceramic coating on the metal substrate was performed according to the scheme proposed in fig. 1,a. It included conical corundum indenter (Young modulus $E = 416$ GPa, Poisson ratio $\nu = 0.3$), nanocrystalline $ZrO_2(Y_2O_3)$ (yttria-stabilized zirconia) coating ($E = 172$ GPa, $\nu = 0.3$) and steel back ($E = 206$ GPa, $\nu = 0.28$). The bottom layer of metal back and top layer of indenter, which undergone elastic loading only, was described by a numerical method of continuum mechanics. Indenter point and coating, the regions undergone maximum deformations, were described on the basis of movable cellular automaton method. The coating thickness was 113 nm. The width of the substrate was 1500 nm, height — 2020 nm. The indenter point was 55 nm in diameter. The pore depth in the coating (the distance from coating outside to top pore wall) was varied from 17.5% to 78.8% of the coating thickness, i.e. from 19.82 to 89.1 nm. The shape of the pore corresponded to rectangular with chamfered corners. The height of the pore was 22.3 nm, and the width vas varied from 55 to 405 nm. It was supposed that pore and indenter is located in the center of model specimen. The loading was simulated by setting the certain constant force (pressure) σ to the top surface of indenter. The value of this force gradually increased from 0 to σ in sinusoidal manner and then remained constant. This regime ensured a quasi-static character of loading and allowed dynamic effects to be avoided until the appearance of the first damage. Response functions of automaton corresponding to different model materials are represented in fig. 1,b. The automaton size according to grain size of ceramics under investigation was 4 nm, step of the grid — 20 nm. The problem was solved under plane stress conditions. The strength properties of coating were characterized by minimal value of pressure to indenter σ_c, that resulted to crack propagation between pore and indenter. This characteristic might be the evaluation of critical stress leading to the change of process regimes in friction pair.

The searching procedure of σ_c was one and the same for all specimens and consisted in the following. At the first stage the draft estimation of σ_c on the basis of indentation test results of particular model assemblage under constant velocity of indenter motion was performed. We denoted this estimate as σ_v. Two value of velocity ($V_1 = 0.5$ and $V_2 = 1.0$ m/s) were considered. The maximal specific resisting force to indenter penetration in the coating (corresponding to crack propagation between indenter and pore) was estimated for each value of velocity. The σ_v was found as arithmetic average of these values. At the second stage the more precise estimation of σ_v was performed. It was done by means of carrying out the series of calculations where the force applied to indenter σ_v was defined as

$$\sigma_i = \sigma_v \pm \Delta \cdot i, \Delta = 0.01 \div 0.1 GPa$$

Required σ_c was defined as $\sigma_c = min(\sigma_i)$, that led to the crack propagation between pore and indenter.

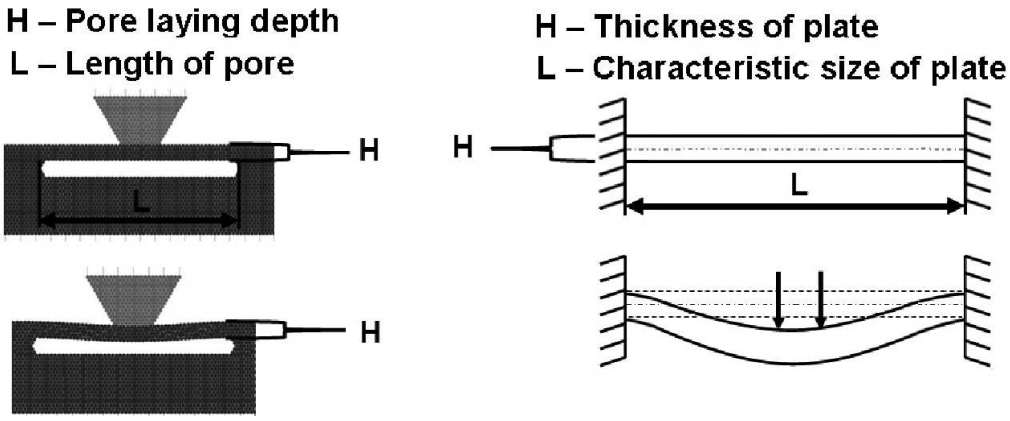


Figure 2: The part of model coating under indentation test, corresponding to bendable plate

3 Analysis of simulation results

3.1 Mechanical behavior features of rectangular plate under bending test

In accordance with definition represented in [3], the part of the model coating, located over the pore and characterizing its strength properties σ_c, in the limit was the rectangular plate with rigid edges (fig. 2). The length of pore L corresponded to characteristic sizes of the plate, and the pore depth H — to the height of the plate. In fact, two characteristic sizes of part of the coating under consideration were appreciably greater then the third one, because the task was solved under plane stress state and the length of pore was appreciably greater then pore depth. Bending deflection of part of the coating under consideration, corresponded to deflection of plate.

In literature the plates are classified according to their geometrical parameters, namely to the ratio L/H. The mechanical behavior of plate, including its ability to resist bending, is substantially depended on the class incorporating this plate [3]. The class of thick ($L/H \leq 8...10$) and thin ($8...10 \leq L/H \leq 80...100$) plates is distinguished. The thick plate is a massive solid, the calculation of mechanical behavior of that is performed with according to all components of stress using the common equations of spatial problem. In the case of thin plates, the membrane forces and deformations in median surface play a vital part in addition to bending force factors [3]. The model coatings under consideration in terms of mentioned classification was a member of thin and thick plates group. Thus, on the basis of mentioned analogy of the coating and plate, we could say before any computer calculations that strength properties of coating with pore σ_c depended on the pore depth (H) and length of pore (L) as well as (L/H). In addition the type of this dependence probably will be different for coatings of different groups in according to mentioned classification.

3.2 Searching correlation of faultiness parameters of coating with peculiarities of its fracture and strength properties

The analysis of simulation results shown that only ratio of values L/H depended on fracture pattern of coating, because it defined what type of forces dominate in region of coating under indenter influence. The separately varying these values (L and H) didn't depend on fracture pattern of coating under condition that L/H lay in the certain range. In this paper the coatings with $0.62 \leq L/H \leq 20.43$ were considered. Simulation results shown that coatings with $0.62 \leq L/H \leq 8.3$ were destroyed as a result of inner macro cracks propagation. These cracks propagated from indenter point to pore in the direction of maximum tangential stress (fig. 3,a,b). Coatings with $8.3 \leq L/H \leq 20.43$, were destroyed as a result of vertical tensile cracks propagation between upper pore wall and free surface as well as symmetrical conjugated fractures propagation in the center of this wall, where the maximal values of compressive-tensile and tangential stress were concentrated (fig. 3,c,d).

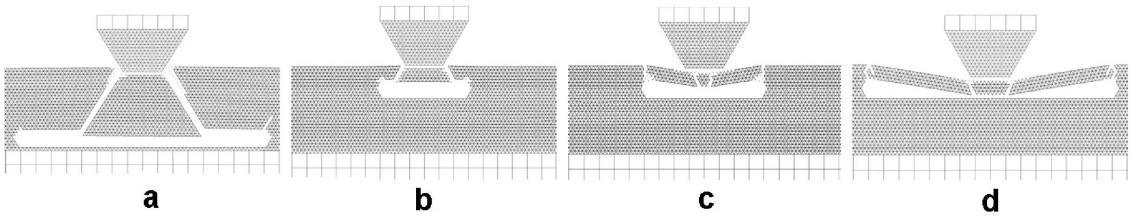


Figure 3: Fracture pattern of model coatings with different values of the ratio L/H: a – 3.76, b – 5.8, c – 8.3, d – 16.9 in the moment of the macro-crack nucleation under indentation test

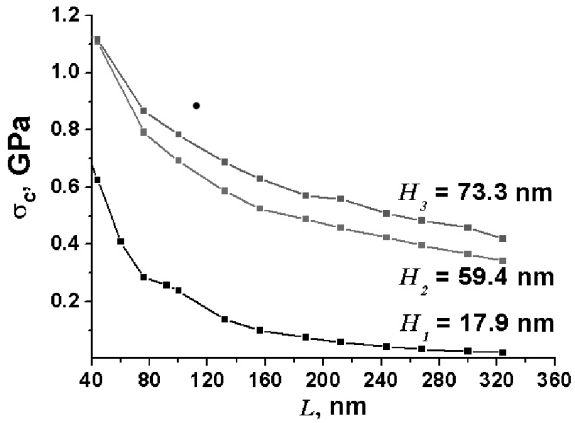


Figure 4: The dependence of strength properties of model coating σ_c on length of pore length L for several pore depths H: $H_1 = 17.9$, $H_2 = 59.4$, $H_3 = 73.3$ nm

Within the framework of mentioned analogy these simulation results was in a good agreement with last one obtained within the bounds of course "strength of materials" [3] for plates. This agreement was observed both for force types, occurring under bending of coating, and for value of $L/H = 8.3$, separating groups of thick and thin coatings.

Simulation results shown that strength properties of (σ_c) is depended on length of pore and pore depth as well as the ratio of these parameters. In particular the increasing pore length (L) as well as the decreasing pore depth (H) resulted in depletion of strength properties of the coating. The dependences, reflecting these tendencies of model coatings are represented at fig. 4. The calculations were performed for coatings with several values of pore depth: maximal, minimal and intermediate one.

The plotting of mentioned dependencies at logarithmical coordinates shown, that they corresponded to power one (fig. 5), with the general form:

$$\sigma_c = A_H \cdot (L)^{-n} \tag{1}$$

where A_H — coefficient possessing the certain value for each pore depth H, n — index of power at the base of power L. Here $n = n(H)$.

Though, the some part of calculated points, corresponding to $H = 17.9$ nm, deviated from this dependence. They were located under approximating curve and evidently could be described by the similar power dependence, but with another value of A and n then for the rest points. The ratio L/H for these points was $8.3 \leq L/H \leq 20.43$ and for the rest points — $0.62 \leq L/H \leq 8.3$. Namely this circumstance shown that strength properties of model coatings depended on L and H as well as ratio (L/H). This consequence confirmed mentioned above one, that had been done under consideration of analogy between bent plate and coating with pore under indentation test. Hereinafter we will consider the model coatings with $0.62 \leq L/H \leq 8.3$ only, because they amount to the majority of performed calculations. It allowed us to exclude the influence of the ratio L/H on the σ_c, consider σ_c only as a $\sigma_c = \sigma_c(L, H)$ function and get the most accurate type of this dependence.

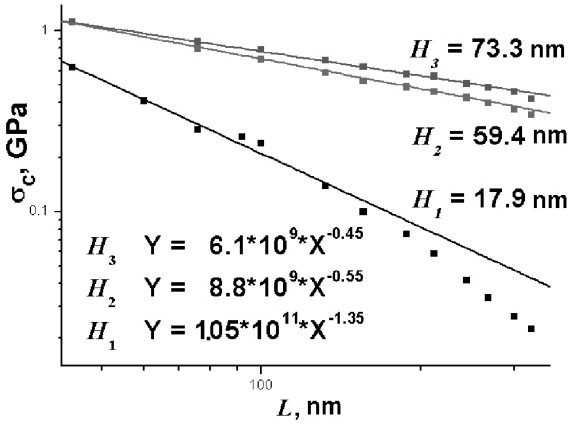


Figure 5: Dependence of strength properties of model coating σ_c on length of pore L in case of some pore depth H and their approximating power functions at logarithmical coordinates. The points corresponds to computer simulation results.

One of the way to get the functional dependence $n = n(H)$ was carrying out the set of calculations to find σ_c of coatings with different values of L and H from mentioned variation interval. This way required considerable computational power though. As a result, the another way to find $n = n(H)$ was proposed. Three points $(H_i,\, n_i) = (17.9, \text{-}1.35)$, $(59.4, \text{-}055)$, $(73.3, \text{-}0.45)$, satisfying the sought dependence and corresponding to mentioned pore depth, were chosen. The assumed type of $n = n(H)$ dependence was chosen according to approximation of this points by different functions. Then the validity of this choice was checked by carrying out two test calculations. The best approximation of chosen points $(H_i,\, n_i)$ was performed using power function (fig. 6)

$$y = 13.5/x^{0.795} \tag{2}$$

In this connection it was supposed that namely function 2 was the sought $n = n(H)$ of coatings under consideration. Thus, it was made a hypothesis, that from the mentioned viewpoint the strength properties of model coatings with varying width of pore (L) and pore depth (H) was described by following dependence

$$\begin{cases} \sigma_c = A_H \cdot (L)^{-n}, \\ n = 13.5/H^{0.795}, \\ 0.62 \le L/H \le 8.3, \\ 55 \le L \le 405\, nm, \\ 19.82 \le H \le 89.1\, nm. \end{cases} \tag{3}$$

3.3 Check obtained correlation for validity

The check of validity of obtained analytical dependence 3 for describing strength properties of coating with pore in according to its parameters was performed in the following way. The certain intermediate value of H_t in mentioned varying interval of pore depth $19.82 \le H \le 89.1$ nm was chosen, namely $H_t = 38.7$ nm. Then, the $n_t = 0.74$, corresponding to this H_t, was found on the basis of (2).

The computer calculations of σ_c of the coating with chosen $H_t = 38.7$ nm and the certain value of L, lieing in the center of range $55 \le L \le 405$ nm, namely $L = 244$ nm, were performed. The required value of σ_c was 0.254 GPa. According to required values of n and σ_c in terms of 1 the value of A_H was calculated, $A_H = 1.5$. Thus, we got the analytic expression for describing strength properties of coating with varying pore length L and pore depth 38.7 nm

$$\sigma_c = 1.5 \cdot (L)^{-0.74} \tag{4}$$

Then computer calculation of the strength properties of the coating σ_c with another length of pore (was chosen $L = 156$ nm) and considered pore depth H_t was performed. Found two calculated

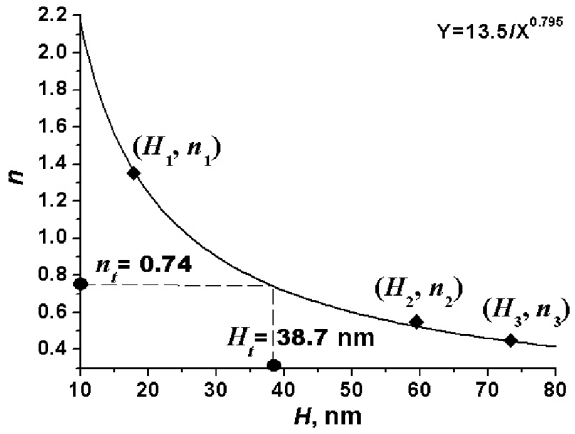


Figure 6: Graphic presentation of power function, approximating three calculated points (H_i, n_i), that satisfy sought dependence $n = n(H)$. (H_i, n_i) = (17.9, 1.35), (59.4, 055), (73.3, 0.45). Determination of the index of power n of dependence 1 corresponding to pore depth $H_t = 38.7$ nm

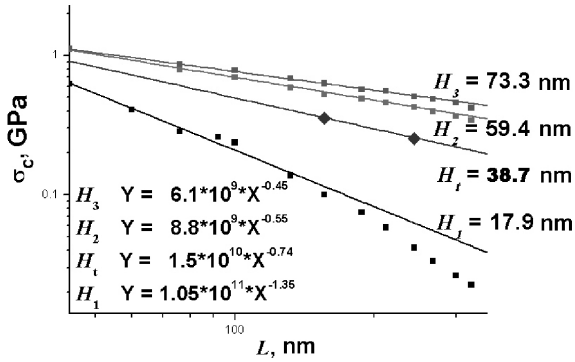


Figure 7: Dependences of the strength properties of model coatings σ_c on the size of pore L for different pore depths H in the logarithmic axes. The points correspond to the computer calculations, the approximate functions — their analytical assessment.

points and the corresponding analytical dependence for H_t, as well as dependencies for other pore depths, shown in Fig. 7. It is seen, that there is good qualitative and quantitative agreement analytical estimates and simulation results. Thus the analytical line, corresponding to H_t, explicitly belonged to the class of lines (corresponding to H_1, H_2, H_3), that were built on the basis of computer calculations results. The deviation of analytical line from the model results (corresponding to $L = 156$ nm) was less than 1%.

This result confirms the put forward a power law dependence $n = n(H)$ and $\sigma_c = \sigma_c(L)$ assumption, therefore the functional dependence 3) can be used to find the strength properties of the coating with turn-down of parameters L, H. Thus, peforming only one model calculation for each value of H and arbitrary value of L allowed getting σ_c of coatings within the entire range of parameters value of the defect with a small time expenses and computation power. It should be noted that considered model was multiparametric one: the width of the indenter, height and length (L) of pore, the pore depth (H).The validity of the proposed assessments wass shown only for the case of two varying parameters L and H, and only in the considered range of values, as they were the most interest for the study. The search of the limits of the full turn-down of parameters, where the proposed dependences are correct, as well as of accounting of dependence of two other parameters on the strength properties of coatings with a pore requires additional investigations.

4 Conclusion

Thus, on the basis of obtained dependencies, we can estimate the strength properties of the coating, knowing the average depth of the nano- or micro-pores and the range of their size. The proposed approach, in fact, represents one of the methods of nondestructive testing and can be used to study the strength properties of the surface layers of materials and, consequently, predicting the critical stress in a friction pair, and to estimate the parameters of meso-defects of coating on the basis of a series of indentation tests. It should be noted that due to the assumption (the indenter is strictly in the center of the pore), the proposed approach estimates the strength properties of the coating and provides only lower assessment that, in some sense, makes it very narrow for practical use. In general, the indenter is asymmetric with respect to the pore and the strength properties of the coating, calculated in accordance with the proposed methodology will be valid with taking into account mentioned correction.

Acknowledgements

This study was supported by the program of the specialized branches of RAS, project No. 13.13.3 "Tribological and strength properties of structured materials and surface layers", program No. 127 of SB RAS with exterior organization, Grant of the President of the Russian Federation for the state supporting young Russian scientists - candidates of sciences (Project MK-5260.2010.8).

References

[1] S.G. Psakhie, A.Yu. Smolin, Yu.P. Stefanov, P.V. Makarov, E.V. Shilko, M.A. Chertov, and E.P. Evtushenko. Simulation of behavior of complex media on the basis of a discrete-continuous approach // Phys. Mesomech. – 2003. – V. 6. – N. 6. – P. 11–21.

[2] A.Yu. Smolin, Yu.P. Stefanov, S.G. Psakhie. Combined discrete-continual method for simulation of deformation and fracture in contact zone. // Phys. Mesomech. – 2004. – V. 7, Part.1. – P. 70–73.

[3] A.V. Aleksandrov, V.D. Potapov, Derzavin B.P. Basis of elasticity and plasticity theory. M. Vyshaya shkola, 1990. – 400 p.

Igor S. Konovalenko pr. Akademicheskii 2/4, Tomsk, 634021 Russia
Andrei I. Dmitriev pr. Akademicheskii 2/4, Tomsk, 634021 Russia
Alexei Yu. Smolin pr. Akademicheskii 2/4, Tomsk, 634021 Russia
Sergei G. Psakhie pr. Akademicheskii 2/4, Tomsk, 634021 Russia

Investigation of structure-phase changing in titanium crystallite under different rate mechanical loading

Iv. S. Konovalenko D. S. Kryzhevich K. P. Zolnikov S. G. Psakhie
ivkon@ispms.tsc.ru

Abstract

Initiation and evolution of plastic deformation in hexagonal close-packed phase of a titanium crystallite with grain boundary under uniaxial tension is carried out on the base of molecular dynamics simulation. Influence of loading rate on structure-phase changing is studied. A correlation between dependences of atom number with slip vector more than 0.06 lattice parameter and potential energy changing on deformation is revealed. It is shown that increasing of loading rate leads to a growth of threshold deformation value under which local atomic displacements are generated in simulated crystallite. Atomic system behavior in regions of local atomic displacement initiation and evolution is investigated.

1 Introduction

Advantages of titanium and its alloys as structural metals are well known [1, 2, 3]. The main impetus to the use of titanium and its alloys in aviation, nuclear power, shipbuilding and engine building is its high specific strength over a wide range of operating temperatures. In addition, titanium alloys have good corrosion resistance in the atmosphere and fairly high strength in the presence of notches. Hcp titanium alloys have relatively low strength, not subjected to heat treatment, but strongly hardening during cold deformation. Alloys are not cold-brittle, easily welded and possess high thermal stability, but their disadvantage is the reduced technological plasticity. Bcc alloys are the most plastic, but with the lowest strength: during heating they do not experience phase transformation, hence they could be used as a corrosion-resistant ones, as well as for short-term operation at high temperatures (up to 1200 C). Alloys consisting of a mixture of hcp and bcc phases are characterized by better technological ductility in the annealed condition, less prone to hydrogen embrittlement in comparison with the hcp alloys and have high strength with the ability to thermal hardening.

Currently, there is an assumption that the mechanical properties of multiphase alloys are determined by not only the structural-phase state, but also by ways of their transformations. In this case, the crucial role the evolution of the stress-strain state of the object plays, in which there is not only the transformation of the defect substructure, but also the formation and decomposition of metastable phases take place. Strength, ductility, crack resistance and other performance properties of the material sufficiently depend on the paths of these phase transformations. It should be noted that opportunities to improve the functional and operational characteristics of these materials is far from exhausted.

An important role in the study of laws and features of deformation processes in polycrystalline materials belongs to the computer simulation methods. In particular, the molecular dynamics method in this context is fundamentally important and widely used for studying of generation, evolution and annihilation of various defects (vacancies and their complexes, dislocations, stacking faults), processes at grain boundaries (including triple junctions), etc. [4, 5].

One of the important tasks in the study of titanium alloys is the establishment of general regularities of hcp-bcc structural-phase transformation obtained by thermomechanical treatment in order to reach high operating qualities. Solution of this problem will determine laws of structural transformations and phase composition of titanium alloys under mechanical and thermal loadings, including ones connected with the martensitic phase transformation.

In connection with above the aim of this work is the molecular dynamics study of the influence of the mechanical loading intensity on the peculiarities of the structural rearrangements generation and development in the crystal phase of titanium at the atomic level.

2 Computer-aided experiment

Posed in this paper, problems are solved on the basis of molecular dynamics method [4, 5] using modern interatomic potentials. This approach is one of the most effective and promising, because it takes into account the discrete structure of the simulated material and gives sufficiently precise description of interatomic interactions. Interatomic interactions are described by many-body potentials obtained by means of the modified embedded-atom method [6, 7]. These interatomic potentials allow describing with high degree of accuracy the elastic, energy and structural properties of the simulated crystallite, adequately taking into account their properties near the grain boundaries and free surfaces. Correct description of the above properties is the key to solving the problems of the study. Verification of used potentials is based on calculations of energy characteristics of point defects in a titanium crystallite (Table 1). It is seen that the results of calculations are in good agreement with data of other authors [8].

Table 1. The results of calculations of energies: the vacancy E_v^f, divacancy E_{2v}^f and divacancy binding E_{2v}^b (in the basal plane – In and out of it – Out). The energies are in eV.

Energetical characteristics of point defects, eV		**Present work**	**Calculation [6]**	**Calculation [7]**	**Experiment [8]**
E_v^f		1.75	1.78	1.79	>1.5
E_{2v}^f	In	3.51	3.69	3.87	
	Out	3.49	3.67	3.90	
E_{2v}^b	In	-0.014	-0.01		
	Out	0.008	-0.11		

The simulated titanium crystallite in hcp phase is a rectangular parallelepiped and includes a symmetrical tilt grain boundary (Fig. 1) formed by the algorithm [9]. The crystallite contains 40 000 atoms. Equilibrium values of the lattice parameters a= 2.95 and c= 4.67 $\AA$ determined from the condition of zero internal pressure in the crystallite. The procedure of artificial velocity damping is used to find the equilibrium state of simulated crystal. The temperature of the studied sample is T= 100 K.

At the two opposite sides of the crystallite, normal to the grain boundary plane, the hard boundary conditions are applied (in the direction of axis X) (Fig. 1). Faces of the sample in the direction of the Y-axis represent the free surfaces, and in the direction of the axis Z periodic boundary conditions are simulated. Crystallite loading (tension) is performed along the direction of hard boundary conditions. For this purpose the constant velocities are assigned to the several atomic planes on the opposite crystallite sides. At these faces (they are analog of specimen grips) atomic velocity modules are equal, but their vectors have opposite directions.

Study of initiation and the evolution of plastic deformation in loaded crystallite is based on analysis of change in the proportion of atoms, characterized by a relative shift of their nearest neighbors. In this paper, the shift is estimated by displacement vector $\vec{P}_i$, which is calculated by the formula:

$$\vec{P}_i = \frac{1}{N_s} \sum_{i \neq j}^{N_s} \frac{(r^{ij} - r_0^{ij})}{|r_0^{ij}|}$$

where j – is the nearest neighbor of the atom i; N_s – is the number nearest neighbors; r^{ij} and r_0^{ij} – the radius vector of the j-th relatively on the i-th atom in the current and original positions,

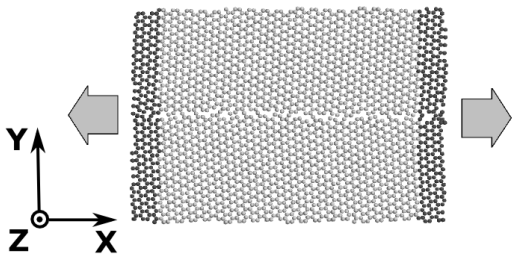


Figure 1: The structure projection and the loading scheme of the simulated crystallite. Black color of the atoms, which are set constant velocity in the direction of the arrows.

respectively. Here and further the value of the displacement vector is given in the lattice parameter a.

3 Results of numerical simulation

While stretching the simulated crystallite speed of each of the specimen grips is 75 m/s. Calculations showed that the potential energy of the crystallite increases monotonically with strain increasing and at the value of $\varepsilon = 9.46$ % it begins to decrease (Fig. 2, curve E_p). The presence of this peak corresponds to the appearance of destruction in the areas of the crystallite where the emergence and development of plastic deformation took place. The dependences of the crystallite atoms proportion (ν) with different values of the displacement vector $\vec{P}_i$ on the deformation are shown in (Fig. 2). One can see that with increasing values of the vector $\vec{P}_i$ proportion of the atoms characterized by such a deflection decreases. In the process of loading the proportion of atoms with different values of local displacement increases (Fig. 2, curve I-IV). Starting with a value of about $\varepsilon = 2.5\%$, curves **II-V** begin to steadily increase, which well correlates with the character of the potential energy behavior on the deformation. Nonmonotonic change of the curve **I** is probably connected with the strong influence of the atoms with small quantities of local displacements caused by thermal vibrations. The more rapid increase in the atoms proportion (ν) (curve IV) near the peak of the curve is due to the nucleation of plastic deformation in the crystal and its subsequent destruction. More later achievement of maximum strain on the curves (IV) in compar with the potential energy curve is due to the fact that the rate of loading exceeds the rate of crystallite characteristic structural relaxation processes.

The dynamics of local atomic displacements in the crystallite loading process is investigated. Studies have shown that such displacements begin in the elastic region and continue in the area of plastic deformation and subsequent destruction of the crystallite. Fig. 3 shows the dependecies of the potential energy (E_p) and the proportion of atoms (ν) with the value of the displacement vector $|\vec{P}_i|$ 0.04 and 0.05 on the deformation. For three values of strain (they are marked by rectangular frames in the graph) the projection of the crystallite structure of the plane XY are shown. The black color indicates atoms characterized by the above values of the displacement vector. One can see that in the initial stages of the crystal deformation the appearance of the local atomic displacements are situated relatively evenly over the entire volume (Fig. 3, structure 1), whereas at high strain the significant proportion of these atoms is localized in the grain boundaries (Fig. 3, structures 2, 3), where the subsequent destruction of the crystallite begins.

To understand the peculiarities of the initiation and evolution of plastic deformation is important to study the behavior of atomic systems in the regions of origin and evolvement of local atomic displacements. For this purpose, in the present paper we study the local atomic rearrangements around the atoms, the displacement vector value $|\vec{P}_i|$ of which is in a certain range of values for some time. For these atoms the behavior of nearest neighbors, located on the first and second coordination spheres, are analyzed. The rate of crystallite deformation is chosen V = 0.5 m/s to

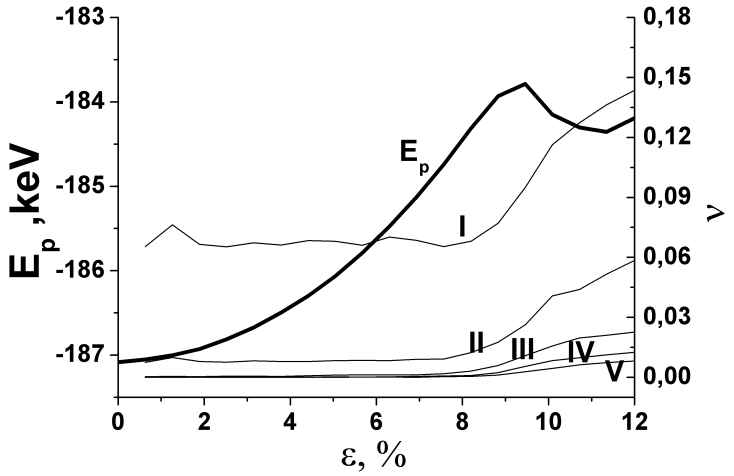


Figure 2: The dependence of potential energy (E_p) and atoms proportion (ν) with displacement vector value $|\vec{P}_i|$: (I) 0.04; (II) 0.05; (III) 0.06; (IV) 0.07; (V) 0.08; on deformation for titanium crystallite. Loading speed V = 75 m/s.

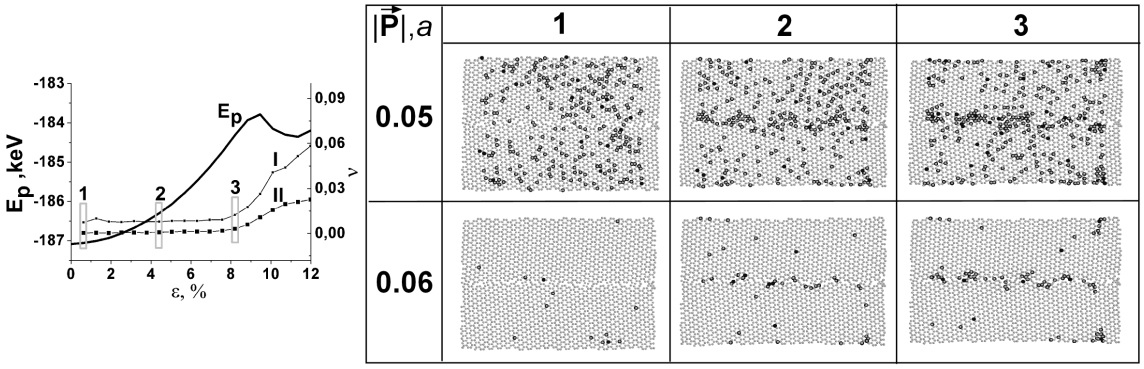


Figure 3: Potential energy (E_p) and proportion of atoms (ν) with displacement vector $|\vec{P}_i|$ values: (I) 0.04; (II) 0.05 vs deformation. Loading speed V = 75 m/s. Projections of the crystallite structure in the XY plane for different values of strain (marked frame): (1) – ε= 0,63%; (2) – ε= 4,41%; (3) – ε= 8,20%; The black color indicates atoms with the above values of the displacement vector.

reduce the influence of dynamic loading on structural changes. The calculations show that the typical behavior of the nearest neighbors of atoms mentioned above is the displacement from the second coordination sphere in the direction of the first coordination sphere (with an increase in the displacement vector $|\vec{P}_i|$) and its subsequent (partial or full) return back to the second coordination sphere (with a decrease in the displacement vector $|\vec{P}_i|$). Fig. 4 shows the neighbors of the atom, the value of the displacement vector $|\vec{P}_i|$ of which is in the range from 0.051 to 0.053 for 15 ps. This atom is marked with black color. Dark gray color denotes the atoms of the first coordination sphere. Light gray color marks the atoms of the second coordination sphere, as well as the atoms distance to which are larger than the radius of the first and smaller than the radius of the second coordination sphere. It is seen that for the value of the displacement vector $|\vec{P}_i|= 0.035$ the atom has 12 neighbors on the first and 6 neighbors on the second coordination sphere (Fig. 4, a). Under increasing the value of the vector ($|\vec{P}_i|= 0.053$), two atoms of the second coordination sphere shift towards the first sphere (Fig 4, b). With a slight decrease in the value of the vector ($|\vec{P}_i|= 0.051$), one of the shifted atoms goes back to the first sphere (Fig. 4, c), while significantly lowering the value of the vector ($|\vec{P}_i|= 0.016$) is accompanied by returning the number of atoms on both spheres to their original values (Fig. 4, d).

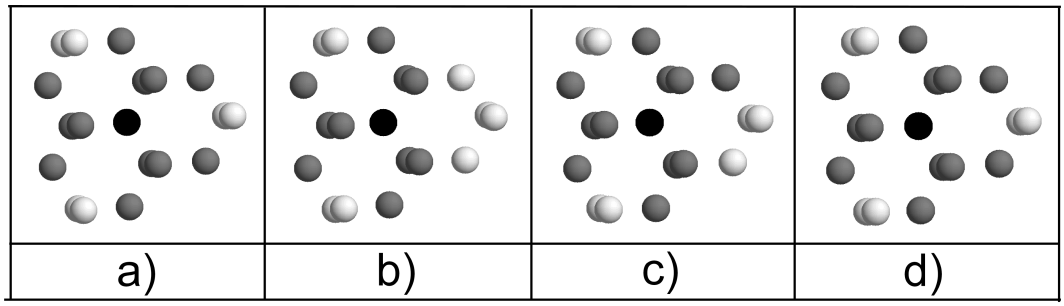


Figure 4: The nearest environment of the atom, in the process of changing the value of its displacement vector $|\vec{P}_i|$: a) t=600 ps, ε=5.04%, $|\vec{P}_i|$=0.035; b) t=610 ps, ε=5.13%, $|\vec{P}_i|$=0.053; c) t=615 ps, ε=5.17%, $|\vec{P}_i|$=0.051; d) t=620 ps, ε=5.22%, $|\vec{P}_i|$=0.016. This atom is marked with black. Atoms of the first coordination sphere are colored by dark gray. Light gray color corespondes to the atoms of the second coordination sphere, as well as the atom distances to which are larger than the radius of the first and smaller than the radius of the second coordination sphere.

The evolution of structural-phase state of the crystallite in the process of deformation is important to study the influence of loading intensity on the peculiarities of structural rearrangements of its atomic system. For this purpose, in the present paper the crystallite tensile with different speeds, ranging from 0.5 to 65 m/s, is carried out. For a given velocity interval the potential energy dependences (E_p) (Fig. 5, a) and the corresponding them dependences of the atom proportion (ν) with the displacement vector $|\vec{P}_i|= 0.06$ (Fig. 5, b) of the strain (ε) are constructed. The figure shows that the increase of the loading rate leads to the growth of the threshold strain value at which the peaks in the curves are observed (Fig. 5, a). The increase in the threshold strain value at increasing of the loading rate is due to the fact that the relaxation processes in the material do not "keep up" with the structural rearrangements imposed to the material. This leads to the fact that with increasing of loading rate the strain threshold values at which there is an avalanche-like growth of atoms with high displacement vector move to the region of higher values (Fig. 5, b).

4 Conclusions

Thus on the base of obtained results it is shown that nucleation of plastic deformation in Ti crystallite is connected with abrupt generation of local structure changing at reaching threshold value of deformation. At that the local structure changing start generation near the grain boundary region.

The results of investigation showed that local structure changes are determined by reconstruction process of first and second atomic coordination spheres. It should be noted that threshold

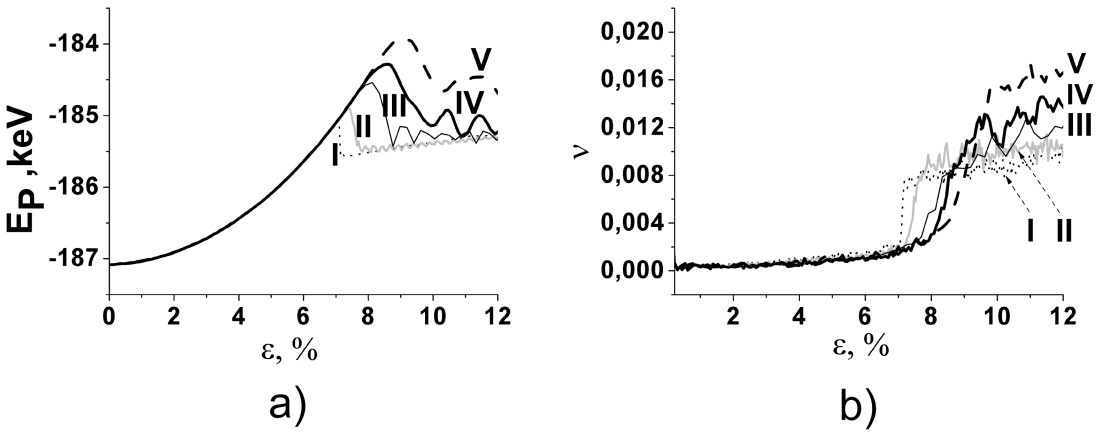


Figure 5: The crystallite potential energy (E_p) (a) and the proportion of its atoms (ν) with the displacement vector $|\vec{P}_i|$= 0.06 (b) vs the strain (ε) for different values of extension rate V: (I) 0.5 m/s; (II) 5 m/s; (III) 25 m/s; (IV) 45 m/s; (V) 65 m/s.

deformation value and number of local structure changes increase at growth of intensity of loading. This behavior of simulated crystallite is connected with sluggishness of relaxation processes under external mechanical loading.

Acknowledgements

The study are supported by the Russian Foundation for Basic Research (project no. 09-08-00498-a).

References

[1] S.G. Glazunov, V.N. Moiseev. Constructional titanium alloys. Metalurgija, Moscow, 1974, 368 P. (in Russian)

[2] B.A. Kolachev, V.A. Livanov, A.A. Bukhanova. Mechanical properties of titanium and its alloys. Metalurgija, Moscow, 1974, 554 P. (in Russian)

[3] E.V. Kollinz. Physical metallurgy of titanium alloys. Transl. from eng. by red. B.A. Verevkin, V.A. Moskalenko. Metalurgija, Moscow, 1988, 224 P. (in Russian)

[4] V.V. Kirsanov, A.N. Orlov. Uspekhi fizicheskikh nauk. 1984. V. 142. Iss. 2. P. 219

[5] D.C. Rapaport. The Art of Molecular Dynamics Simulation. Cambridge University Press, Cambridge, 1995, P. 414.

[6] M.I. Baskes, R.A. Johnson. Modell. Simul. Mater. Sci. Eng. 1994. V. 2. P. 147.

[7] Y-M Kim, B-J Lee, M.I. Baskes. Phys. Rev. 2006. B 74. P. 014101.

[8] F.R. de Boer, W.C.M. Mattens, A.R. Miedema, A.K. Niessen. Cohesion in metals; transition metal alloys. North-Holland, Amsterdam, 1988, 240 P.

[9] A. Suzuki, Y. Mishin. Interf. Sci. 2003. V. 11. P. 131.

Iv.S. Konovalenko, 2/4, pr. Akademicheskii, Tomsk, 634021, Russia
D.S Kryzhevich, 2/4, pr. Akademicheskii, Tomsk, 634021, Russia
K.P. Zolnikov, 2/4, pr. Akademicheskii, Tomsk, 634021, Russia
S.G. Psakhie, 2/4, pr. Akademicheskii, Tomsk, 634021, Russia

Localized and periodic solutions of the Oregonator model of BZ reaction

Margarita A. Kovaleva Leonid I. Manevitch
margarita@shg.ru

Abstract

Belousov-Zhabotinsky Reaction is one of the well known nonlinear phenomena. Different regimes found numerically for this system were seen in experiments, but not properly analytically studied. In this work we present an asymptotic study of the localized and space periodic solutions for the system. We study the classical model of the Belousov-Zhabotinsky Reaction named Oregonator for the unstirred system. Diffusion of the components is taken in account. The stoichiometric factor is used as a controlling parameter. Using the smallness of reaction rates and constants of the system we modify the original system and reduce it to a one representative equation. It describes the evolution of the concentration of one of the reaction species with time in one space dimension. To find the solutions stationary in time we make a time derivative equal to zero and obtain an equation of the nonlinear oscillator with a second derivative in space variable. A phase plane for this equation was studied in a wide range of parameters, quite various behavior of the system was found. For a narrow range of the controlling parameter we found the existence of a localized soliton-type solution corresponding the separatrix trajectory on the phase plane. It separates the region on the phase plane corresponding to periodic in space time-stationary solutions and the region of aperiodic solutions. To prove the stability of the solutions we made a series of numerical simulations of the effective evolution equation and the original system. The stable solutions turn out to be appropriate starting conditions for the realization of the system of stable pulsing solutions in the full model of three equations.

1 Introduction

The Belousov-Zhabotinsky reaction is one of the well studied nonlinear phenomena. Many different regimes found numerically for this system were seen in experiments, but they are not properly analytically studied. In the classical research the planar waves in the Belousov-Zhabotinsky reaction was seen as a composition of two waves: trigger wave, corresponding the leading edge of the wave and a phase wave which describes a relaxation to the unperturbed state (a smooth trailing edge) [1]. Wave front was seen as a line where two different states merge together. Some works were done in the kinematical approach, were the wave speed depends linearly on curvature of the wave front. The spatially nonuniform stationary solutions were described only for simple models, or for the model with the cubic nonlinearity (as a thin boundary between two uniform solutions) [2], some studies were were devoted to the existence of the nonuniform solutions for a class of reaction-diffusion systems [3].

We study at the first time the wave in reaction as one-wave solution that appears due to the cooperation of the nonlinearity of the system and the diffusion of the components. We present a first asymptotic study of the time-stable localized and space periodic solutions for the system.

We study the classical model of the Belousov-Zhabotinsky reaction named Oregonator. It is a system consisting of three reaction-diffusion equations. In the numerical experiments this system demonstrates almost all regimes that appear in the laboratory experiments, and gives a half-quantitative agreement with the experimental data. The model is normally used to prove numerically the experimental regimes. For the unstirred system diffusion of the components is taken in account. In the classical Tyson's [4] version the second equation of the initial three-equation system is considered as a quasi-stable one. This system was normalized by the space

variable to obtain the spatial and temporal derivatives of the same order by small parameter; for generalization all the three equations with the time and space evolution are considered:

$$\varepsilon\frac{\partial u}{\partial t} = u - u^2 + qw - wu + \alpha\varepsilon\Delta u$$
$$\varepsilon^2\frac{\partial w}{\partial t} = fv - qw - wu + \beta\varepsilon^2\Delta w$$
$$\frac{\partial v}{\partial t} = u - v + \gamma\Delta v$$

where u ,w, v are the dimensionless concentrations of the reaction components, α, β, γ – normalized diffusion constants of the components and ε, q are small parameters, which are the combinations of the reaction rates. The stoichiometric factor f is used as a controlling parameter. The Tyson's 'low' parameters are usually used as a typical parameter set for the model.

To prove the asymptotic behavior of the system we choose the small parameter ε equal to zero and consider a one-dimensional system in space. Only the diffusion of one component of the system is significant for this case. Thus we obtain the following system of equations:

$$0 = u - u^2 + qw - wu$$
$$0 = fv - qw - wu$$
$$\frac{\partial v}{\partial t} = u - v + \gamma\frac{\partial^2 v}{\partial \xi^2}$$

Solving the first two equations we reduce the system to a one time-space equation in terms of u variable:

$$v = \frac{1}{f}\frac{u(u-1)(q+u)}{q-u}$$
$$w = \frac{fv}{q+u}$$
$$\left(\frac{1}{f}\frac{-2u^3 + u^2(2q+1) + 2(q-1)qu - q^2}{(q-u)^2}\right)\frac{\partial u}{\partial t} = u - \frac{1}{f}\frac{u(u-1)(q+u)}{q-u}) + \\ + \gamma\frac{\partial}{\partial\xi}\left(\left(\frac{1}{f}\frac{-2u^3 + u^2(2q+1) + 2(q-1)qu - q^2}{(q-u)^2}\right)\frac{\partial u}{\partial \xi}\right)$$

2 Simplified model

To obtain the time-stable solution we suppose the time-derivative equal to zero. Taking q also equal to zero we obtain the equation in a simplified form:

$$\frac{d^2u}{d\xi^2} = \frac{1}{\gamma}\frac{(f-1)u + u^2}{1-2u} - \frac{2}{1-2u}\left(\frac{du}{d\xi}\right)^2$$

From mathematical view point this is a nonlinear oscillator with a second spatial derivative. The first integral of this equation can be easily analytically sought:

$$\left(\frac{du}{d\xi}\right)^2(1-2u)^2 + \frac{1}{\gamma}\left(2(f-1) + \frac{2(3-2f)}{3}u - u^2\right)u^2 = E$$

We have studied a phase plane for the oscillator, stoichiometric factor f using as a controlling parameter. For $f < 3/4$ it turns out that the system has only one stationary point $(u, u') = (0, 0)$, while for $f > 3/4$ it has three stationary points. The phase plane of the nonlinear oscillator for $f > 1$ and $3/4 < f < 1$ is plotted in Fig. 1. The phase plane for $3/4 < f < 1$ demonstrates closed phase trajectories corresponding to the periodic solutions, separatrix trajectory separates the regions of the space-periodic and aperiodic unlocalized solutions. The separatrix solution

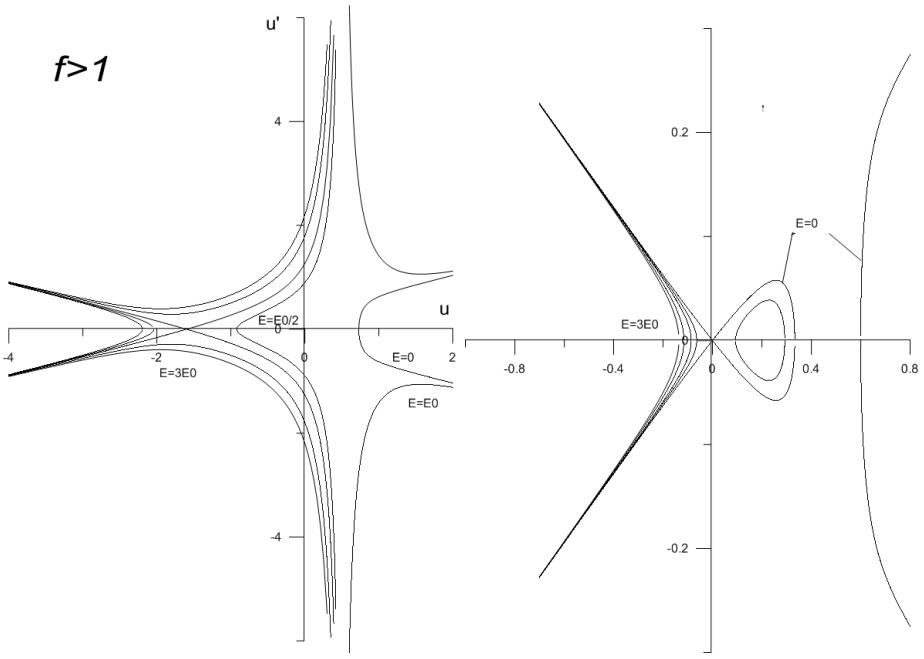


Figure 1: The phase plane of the nonlinear oscillator for $f > 1$ and $3/4 < f < 1$.

corresponding to $E = 0$ can be found in the implicit form:

$$\xi = -\sqrt{\gamma}\ln\left(2\sqrt{u^2+\frac{4f-6}{3}u+1-f}+2u+\frac{4f-6}{3}\right)^2 - \\ -\sqrt{\gamma}\ln\left(\frac{2\sqrt{(1-f)\left(u^2+\frac{4f-6}{3}u+1-f\right)}+\frac{4f-6}{3}u+2(1-f)}{u}\right)^{\frac{1}{\sqrt{1-f}}} + Const$$

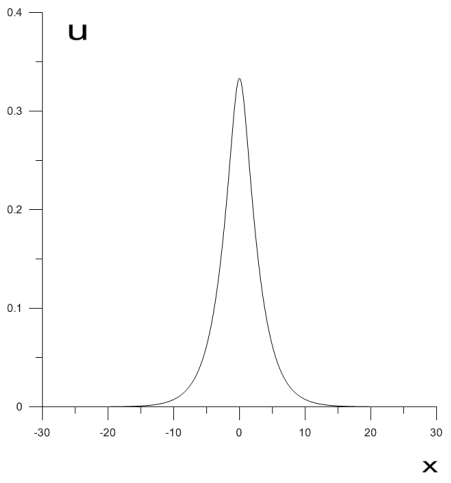


Figure 2: The profile of the separatrix solution.

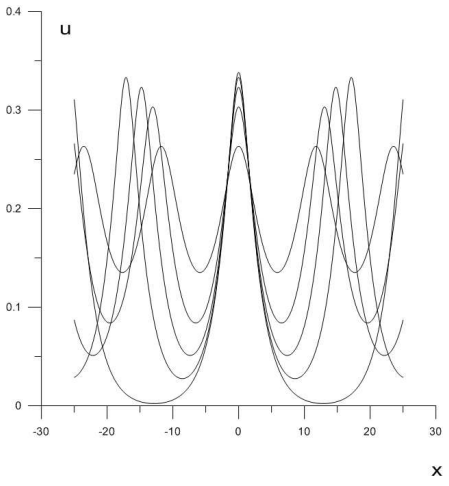


Figure 3: Amplitudes of periodic solutions.

It is a soliton-like localized aperiodic spatial structure. The profile of the separatrix solution is shown in Fig. 2. This solution was also found by the integration of the equation with using the 4th order Runge-Kutta method. All periodic solutions have smaller amplitudes (Fig. 3). The solution

profiles were found for the different first integral constants E using the 4th order Runge-Kutta method.

The stability of these solutions was confirmed in the numerical experiments. For the integration of the equations a sweep method with the step-size control was used. The numerical integration of the time evolution for 1-equation (simplified system) shows the stability of both separatrix and periodical solutions. The numerical experiment shows also an insignificant change of the solution profile because of the numerical errors. For the simulation of the time-evolution for the experimental regimes the two-equations system is usually used. We integrate this system by time; the profiles of stable solutions for the simplified equations are used as the initial conditions. The time evolution of the standard two-equation system shows that the found solutions pulse stationary in time with the same time-period for all the components of the system.

3 Model with q

To obtain the asymptotic solutions for the initial system one should consider the system with small parameter q. The nonlinear oscillator for this case is more complicated:

$$g(u)\frac{d^2u}{d\xi^2} + \frac{dg(u)}{d\xi}\frac{du}{d\xi} + \frac{1}{\gamma}\left(fu - \frac{(u-1)(q+u)u}{q-u}\right) = 0$$
$$g(u) = \frac{1}{f}\frac{-2u^3 + (2q+1)u^2 + 2q(q-1)u - q^2}{(q-u)^2}$$

The first integral of this system can be also analytically sought:

$$\left(\frac{du}{d\xi}\right)^2 \frac{(-2u^3 + (2q+1)u^2 + 2q(q-1)u - q^2)^2}{(q-u)^2} 3\gamma +$$
$$+3q^4(f+1)+6q^3(-1-3f+2fq)u+18fq^2(1-f)u^2+2q(-3(1-f+q)+4fq)u^3+ \quad (1)$$
$$+(-3+3f+12q+2fq-3q^2)u^4+2(3-2f-3q)u^5-3u^6+$$
$$+12fq^2(q-1)(q-u)^2 ln(u-q) = E$$

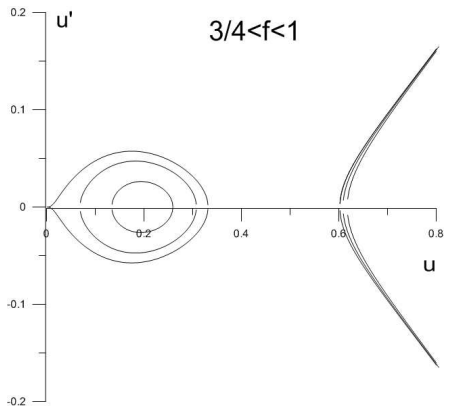


Figure 4: The phase plane for equation (1).

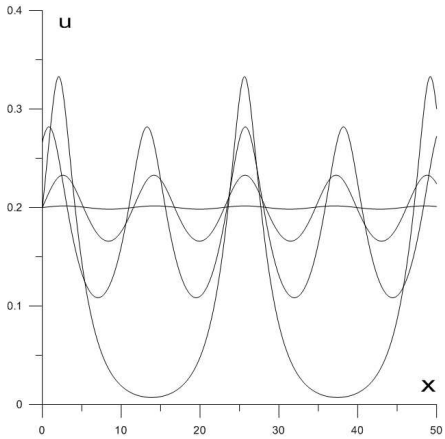


Figure 5: The comparison of the periodic solutions corresponding to different E values for the system with small q.

The phase plane for this equation is shown in the Fig. 4. The equation has a singularity point at $u{=}q$ that separates periodic solutions from a zero point. It makes also impossible to achieve in simulations impractical negative values of concentration. The separatrix trajectory is not closed any more and there is no localized separatrix solution for this case. But the periodic solutions are very similar to those found from the simplified equation. Only close to the singularity point the

solutions differ significantly. The comparison of the periodic solutions corresponding to different E values for the system with small q can be seen in the Fig. 5.

The periodic solutions with amplitudes close to the separatrix one are the combination of the localized solutions. The solutions with smaller amplitudes wich are far from separatrix trajectory have almost harmonic profile.

The simulation of the temporal evolution of the different periodic solutions shows their stability in the case of one effective equation. The small numerical errors lead to an insignificant change of the profiles. The temporal evolution of the whole system with the stationary profiles as initial conditions displays a stationary pulsing for all the concentrations.

4 Conclusions

In this paper we have presented at the first time an analytical study of nonuniform stationary solutions in the Oregonator model of Belousov-Zhabotinsky reaction. The system of equations was firstly reduced to one effective nonlinear oscillator, for which all the regularities can be easily studied. This makes possible to predict the type of the system behaviour for the wide range of parameters.

The stationary structures were found in a narrow range of parameters. For the initial system they correspond to the stationary pulsing patterns. The stability of the structures was confirmed with the numerical simulations.

We presented a new method for the analytical study a Belousov-Zhabotinsky system within different parameter ranges. This method offers the new possibilities for the analytical explanation of different numerical and experimental results that are reported in the last more then 30 years.

References

[1] J.J. Tyson,P.C. Fife. Target Patterns in a Realistic Model of the Belousov-Zhabotinskii reaction. J. Chem. Phys.(1980) 73, p2224-2247.

[2] J.J. Tyson, J. P. Keener. Singular Perturbation Theory of Traveling Waves in Excitable Media. Physica D 21(1988) 32, p327-361.

[3] J.D. Murray, Mathematical Biology 1.An Introduction, Springer, Berlin, 2002.

[4] J. J. Tyson, J. P. Keener.Spiral Waves in Belousov-Zhabotinskii reaction. Physica D 21(1986) p.307-324

[5] Z. Nagy-Ungvarai, J.J. Tyson, B. Hess. J. Phys. Chem. 1989, 93, p707-713

Margarita A. Kovaleva, Quantum Electronics Division, Faculty of Physics Lomonosov Moscow State University, 1, building 2, GSP-2, Leninskiye Gory, Moscow, 119991 Russia
Leonid I. Manevitch, Chemical Physics Institute, Kosygina str. 4, Moscow,119991 Russia

Vibrational dynamics of a spherical body in a rotating cylinder with liquid

N. V. Kozlov S. V. Subbotin
kozlovn@pspu.ru

Abstract

The behaviour of a light spherical body is experimentally investigated in a horizontal cylindrical cavity, filled with low-viscosity liquid and rotating around its axis. The axis of vibrations is normal to the cavity rotation axis; frequency and amplitude of vibrations are varied. In the absence of vibrations at rotation the body lags behind the cavity. Its behaviour is unstable: at constant cavity rotation rate, the body rotation speed changes with time in a complex manner.

The vibrations influence the body behaviour in resonant areas, where the amplitude of its oscillations significantly increases. In the experiment a resonant excitation of the outstripping motion is observed, which is analogous to the one found in the experiments with cylindrical body [1]. Vibrations stabilize the behaviour of the sphere: it displaces in the center of the cavity length, its rotation axis becoming oriented along the cavity one.

The liquid between the body and the cavity end-walls moves as a continuation of the sphere, forming a liquid cylinder, similar to the Taylor – Proudman column [2]. Light-diffusing particles in liquid make it possible to see the column boundary, on which an azimuthal wave propagates, its crests elongated from one of the cavity end-walls to the other. When the sphere rotation axis deflects from the cavity one, the liquid column deflects as well.

1 Introduction

The fluid dynamics in rotating multiphase systems is mainly determined by the role of inertia forces. The action of transversal vibrations on such systems leads to a resonant excitation of a centrifuged interface oscillations [3, 4], which on their turn result in propagation of an azimuthal inertial wave.

In [1] is found the differential rotation of a light solid body in a rotating cavity with liquid – "vibrational hydrodynamic top". It can be caused by an external vibrational action, as well as by the gravity field. This case is particular, because due to the interface non-deformability only one wave mode exists.

In the present work another geometry of the solid body is chosen for investigation. The dynamics of a light sphere in a cylindrical cavity with liquid is considered.

2 Experimental setup and techniques

The experimental setup includes a cylindrical cavity *1*, made of Plexiglas, inside which a light spherical body *2* is placed. The cavity is fixed on a rod in the bearings of a support *3*, installed on the platform of the electro-dynamic vibrator *4*. The cavity is filled with liquid (water or aqueous solutions of glycerin). The rotation is transmitted to the cylinder from a stepper motor *5* via a flexible transmission *6*. The rotation frequency is set up using an electric-signals generator *7*. The motor is powered by a DC power supply *8*. The vibrations are controlled using a generator *9*. The vibration amplitude is measured by an oscillogram, obtained from an accelerometer *10*. The observation is carried out in the light of a stroboscopic lamp *11* with the scintillation frequency set up by an external generator *9* (Fig. 1).

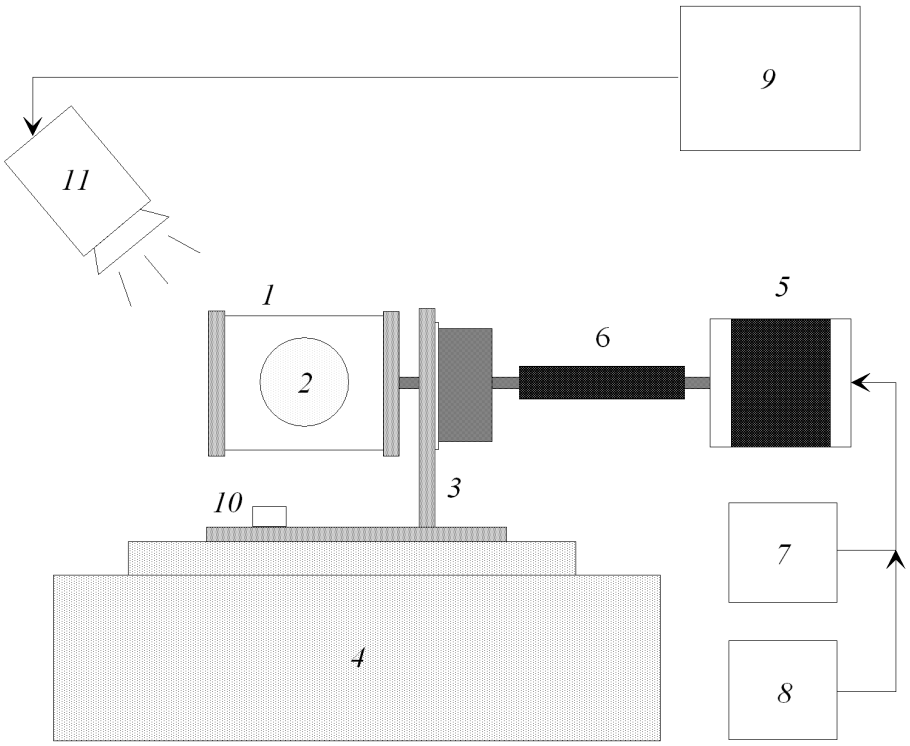


Figure 1: The experimental setup schema

The geometrical parameters of the cavity: diameter of the base $D = 52.0$ mm, length $L = 50.0$ mm. Diameter of the sphere $d = 35.5$ mm, mass $m = 4.0$ g, average density $\rho = 0.17\ g/cm^3$.

The rotation frequency measurement is done by a method of the stroboscopic scintillation frequency synchronization. In the experiment the latter is first adjusted to the cavity rotation frequency f_r, and after a stationary rotation is established – on the body rotation frequency f_s. After the frequencies registration f_r is fluently changed, and the measurements are repeated. Using the obtained data the relative body rotation frequency is taken $\Delta f \equiv f_s - f_r$. Positive values of Δf correspond to the outstripping body motion, negative – to the lagging one.

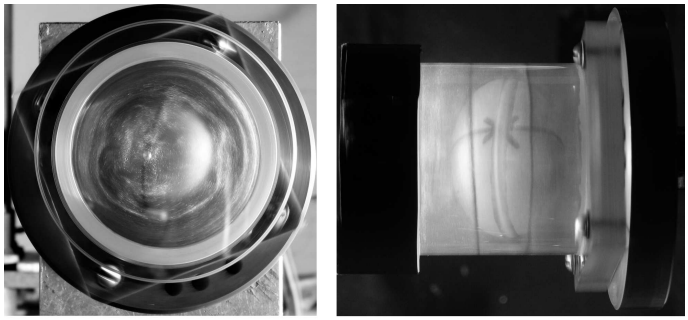
In the centrifuged state the flow pattern is studied using a photo-registration method. Aluminum powder is used as a visualizer. The images are taken from the side of the end-wall, along the cavity axis, and in the direction perpendicular to the axis. At observation from the end-wall a light sheet is used in order to limit a narrow region of the liquid for photo-registration: directly near the end-wall of the cavity and in its central part.

The observations are carried out in the gravity field only, as well as at vibrations, perpendicular to the rotation axis. The vibration parameters are varied: frequency $f_v = 30.0$ Hz and amplitude $b = 0.43$ mm, $f_v = 35.0$ Hz and $b = 0.33$ mm.

3 Experimental results

In the absence of rotation the light body is in the upper part of the cavity. At gradual increase of the cavity speed, the body is trained by the liquid flow and displaces in the direction of rotation, performing chaotic oscillations and hitting against the side-wall.

At certain critical frequency value ($f_r = 16.3$ rps) the body passes in a centrifuged state, i.e. is trained by liquid and occupies a steady equilibrium position in the cavity geometrical center. In the centrifuged state the body moves lagging behind the cylinder walls, so that the relative frequency $\Delta f \equiv f_s - f_r$ is negative. However at constant frequency f_r the sphere rotation speed is inconstant, it varies with time in a certain range of values. The sphere rotation axis inclines relative to the cylinder rotation axis, the body itself at the same time remains in the cavity center.



a *b*

Figure 2: The flows patterns: *a* – seen from the end-wall, *b* – from the side wall

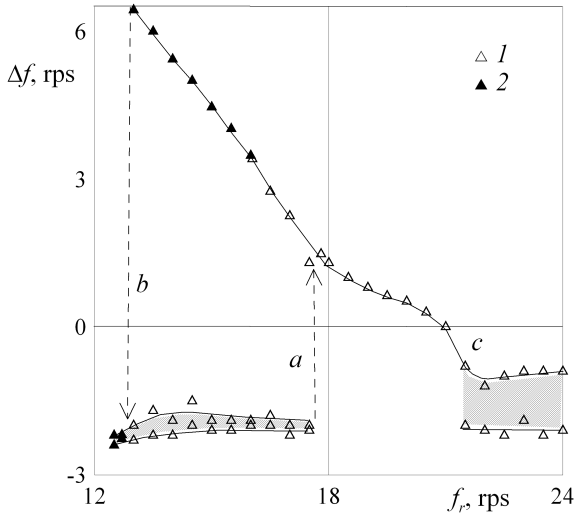


Figure 3: Dependence of the relative body rotation frequency on the cavity rotation frequency at $f_v = 35.0$ Hz and $b = 0.33$ mm; points *1* – increasing f_r, *2* – decreasing

On Fig. 2 are shown the photographs of the flows, arising in the rotating cavity. From the end-wall side one can see the border of a liquid column (Fig. 2, *a*), rotating as a continuation of the sphere, but at a lower rate. The sequence of crests and folds is observed, encircling the body and elongated from one end-wall to the other. It is noticeable that the center of this figure is displaced from the center of the cavity. The liquid column rotation axis coincides with the one of the sphere. The visualizer, which dropped on the cavity walls, traces ring patterns, periodic along the cavity axis (Fig. 2, *b*).

At decrease of the cavity rotation frequency f_r the body rotation speed decreases as well, but at the frequency equal to the centrifugation frequency value the body remains in the steady equilibrium, the character of its motion does not change. The frequency, at which the collapse of the centrifuged state occurs, is $f_r = 12.1$ rps. Thus, a hysteresis is found – inequality of the frequencies of centrifugation and collapse. In the pre-collapse state the sphere performs intensive circular oscillations, its axis moves along a circular trajectory around the cylinder axis.

With the f_r increase the frequency f_s increases in such a way, that the average value of Δf also increases, and the intensity of the lagging in average decreases, however the range of body speed oscillation extends. This is shown on Fig. 3, the hatched area marks the range of the body speed variation and is limited by its maximum and minimum values.

At vibrations, differently from the gravitational case, after centrifugation the body in a resonant way comes to an outstripping motion, occupying the cavity geometrical center and performing circular oscillations with the forcing frequency f_v in the plane perpendicular to the rotation axis. The centrifugation threshold does not change. In this state the body rotation speed remains

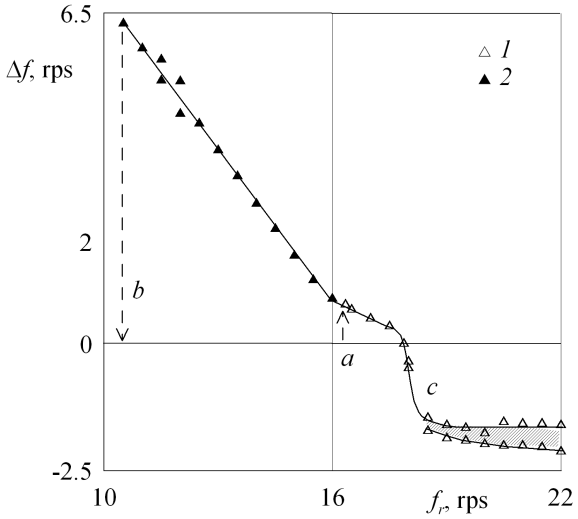


Figure 4: Dependency of the relative body rotation frequency on the cavity rotation frequency at vibrations of the frequency $f_v = 30.0$ Hz and $b = 0.43$ mm; points *1* – increasing f_r, *2* – decreasing

literally constant, and its axis is parallel to the cavity one.

At the consequent increase of the frequency f_r the relative body rotation frequency Δf decreases and at certain point becomes zero, which means the equality of f_s and f_r. After trespassing the soft-excitation threshold (Fig. 3, *c*) the shape of the dependency $\Delta f(f_r)$ changes. At the same time the body behaviour changes qualitatively: the speed oscillations reappear, and the axis of the sphere inclines.

At the cavity rotation frequency decrease in the threshold *c* the resonant excitation of the body oscillations occurs, leading to its intensive outstripping rotation. The further decrease of the frequency f_r results in the intensification of the body differential rotation. At $f_v = 35.0$ Hz in the threshold *b* a breakdown of the outstripping motion is observed, as a result of this the sphere changes its speed and the character of the motion abruptly. The intensity of the body circular oscillations is maximal before the breakdown, as well as the value of the frequency Δf.

At the consequent increase of f_r in the threshold *a* a rough excitation of the resonant body oscillations occurs. The transitions *a* and *b* occur with a hysteresis.

In case of vibrations with the frequency $f_v = 30.0$ Hz the transition *a* coincides with the centrifugation threshold, and the transition *b* – with the threshold of the collapse (Fig. 4). This is figuratively shown by the arrows ending on the axis $\Delta f = 0$. In the pre-collapse area the body frequency f_s periodically takes two values, $f_{s1} = 16.5$ rps and $f_{s2} = 17.2$ rps. This is accompanied by a periodical change of the circular oscillations amplitude – higher the speed, lower the amplitude.

At the fixed value of the relative body radius $R = d/D$ the resonant areas for different parameters of vibrations coincide on the plane $(\Delta f/f_r,\ f_v/f_r)$, similar to the case of the cylindrical body [1]. The system eigenfrequency is determined by the value of the dimensionless vibration frequency f_v/f_r and is the same for both considered cases. On Fig. 5 the dependency of the relative body rotation frequency $\Delta f/f_r$ on the frequency ratio f_v/f_r for $f_v = 30.0$ and 35.0 Hz is shown. Points *1*, *3* correspond to the increase of the cavity rotation frequency, points *2*, *4* – decrease. The thresholds of soft excitation coincide precisely, the thresholds of rough excitation and of breakdown are close, but not equal. Remember that in two cases the vibration amplitude is different, and the resonant area boundaries from the side of the thresholds *a* and *b* strongly depend on the value of the vibration amplitude and the vibration acceleration [3, 4].

Dynamics of the spherical body has some similarities with the one of the cylindrical body. First, the resonant excitation of the outstripping body motion is found at the frequency $f_v/f_r > 1$. The shape of the resonant area is the same for both cases. This allows to suggest the existence of the second resonant frequency $f_v/f_r < 1$, at which the lagging body motion would be intensified. Second, the vibrations stabilize the position of the spherical body in the cavity. Finally, the formation of the ring patterns with the axial periodicity is found, as it was in [1].

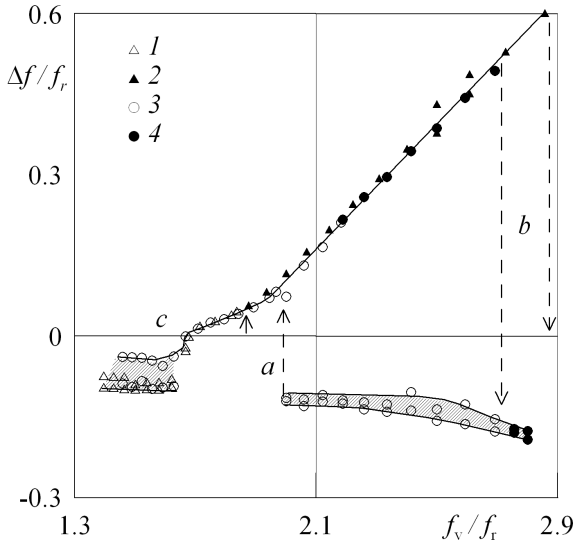


Figure 5: Dependency of the dimensionless frequency of the body rotation $\Delta f/f_r$ on the frequencies ratio f_v/f_r for $f_v = 30.0$ (*1*, *2*) and 35.0 Hz (*3*, *4*)

Some consistent differences exist as well, namely, the fact of incline of the rotation axis of the sphere is still unexplained.

4 Conclusion

The behaviour of a light spherical body is studied experimentally in rotating liquid, limited by the walls of a cylindrical cavity. Vibrations influence the dynamics of the sphere in a resonant area, where its intensive outstripping rotation is excited. The shape of the resonant area and the thresholds on its boundaries are analogous to what was observed in the case of the cylindrical body. The hysteresis exists between the thresholds of rough excitation and breakdown.

At rotation in the absence of vibrations the spherical body undergoes an instability: its rotation axis declines from the cavity rotation axis. Vibrations stabilize the position and the orientation of the sphere in the cavity: the body occupies the position in the middle between the end-walls and rotates coaxially with the cylindrical cavity.

The flow patterns are found, similar to what was observed in the case of the cylindrical body. The continuation of the research is expected.

Acknowledgements

The research was supported by RFBR (grant 09-01-00665) and administration of PSPU (grant 2010).

References

[1] Kozlov V.G., Kozlov N.V. Vibrational Dynamics of a Light Body in a Liquid-Filled Rotating Cylinder // Fluid Dynamics. 2008. V. 43. No. 1. P. 9–19.

[2] Greenspan H.P. The Theory of Rotating Fluids. Cambridge, University Press, 1968.

[3] Ivanova A.A., Kozlov V.G., and Polezhaev D.A. Vibrational Dynamics of a Centrifuged Fluid Layer // Fluid Dynamics. 2005. V. 40. No. 2. P. 297–304.

[4] Salnikova A., Kozlov N., Ivanova A., Stambouli M. Dynamics of rotating two-phase system under transversal vibration // Microgravity sci. technol. Springer. 2009. V. 21. No. 1–2. P. 83–87.

Kozlov N.V., Perm State Pedagogical University, Perm, Russia
Subbotin S.V., Perm State Pedagogical University, Perm, Russia

Molecular dynamics study of chemically induced phase transformation

A. M. Krivtsov
akrivtsov@bk.ru

Abstract

A molecular dynamics model for the phase transformation induced by chemical reaction (oxidation) is presented. The material properties such as density, stiffness and strength are being changed due to the oxidation. In contrast with the previous works [2] the oxidation is considered not only on the material surface, but also inside the material at the phase boundaries. A square specimen with periodic boundaries and central circular hole is considered, which is equivalent to an infinite material with a periodic set of holes. Oxidation starting from the inner surface of the hole and resulting in the hole closure is investigated. Influence of the reaction probability on the velocity of the chemical reaction front, velocity of the hole surface, thermal motion, and defects density are analyzed. In addition oxidation starting from the outer surface of a circular and square specimens is considered.

1 Introduction

The molecular dynamics (MD) models for investigation of mechanical processes in solids become more and more popular in the last decades. However relatively low number of papers are devoted to MD modelling of interaction between chemical and mechanical processes in solids. This paper is making attempt to set up an investigation in this area, considering processes close to the processes taking place in microscopic silicon specimens subjected to mechanical loading and oxidation [1]. The results of such processes can be applied for description of fracture and ware in microelectromechanical systems.

In the previous paper [2] a molecular dynamics model for fracture accompanied by chemical reaction was suggested; crack initiation and development in specimens subjected to an uniaxial loading was considered. The oxidation of the initial and new specimen surfaces during the fracture process were taken into account. It was postulated that the material properties such as density, stiffness and strength were changing due to the oxidation. Influence of the chemical reaction (oxidation) on the fracture scenario was investigated. Fracture process for the specimens of different shape, with and without predefined defects was studied.

In the previous work [2] the chemical reaction was applied only for the boundary particles (the particles having less nearest neighbors then in the perfect crystal). In this case only a surface oxidation takes place. The material is covered by a thin film of oxide, which does not penetrate inside the material. Such situation is realized, for example, for aluminium, for which the oxide coverage preserves the rest of the material from the further oxidation. However, for some other materials, such as silicon, the oxide has porous structure, which allows penetration of oxygen. In such cases the width of the oxide film grows with time. This effect is especially important at micro- and nanoscale, where the relative speed of oxidation is much higher then at the macroscale. In particular, for MEMS made from silicon the oxidation process is essential, since the mechanical properties of the silicon dioxide differs essentially from those of the pure silicon [1]. Investigation of such processes is the main subject of the current paper.

2 Simulation technique

The simulation procedure applied in this work is similar to that used at the previous stage of the project. The basic molecular dynamics technique used below is described in [3, 4], in more details it is described in [5, 6]. The material is represented by a set of particles interacting through a pair potential $\Pi(r)$. The equations of particle motion have the form

$$m\ddot{\underline{r}}_k = \sum_{n=1}^{N} \frac{f(|r_k - r_n|)}{|r_k - r_n|} (\underline{r}_k - \underline{r}_n) - B\dot{\underline{r}}_k, \tag{1}$$

where $\underline{r}_k$ is the radius vector of the k-th particle, m is the particle mass, N is the total number of particles, $f(r) \stackrel{\text{def}}{=} -\Pi'(r)$ is the interparticle interaction force, B is a dissipation coefficient. We use the following notation: a is the equilibrium distance between two particles ($f(a) = 0$), $D \stackrel{\text{def}}{=} |\Pi(a)|$ is the bond energy, C is the stiffness of the interatomic bond in equilibrium, and T_0 is the oscillation period of the mass m under the action of a linear force with stiffness C

$$C \stackrel{\text{def}}{=} \Pi''(a) \equiv -f'(a), \qquad T_0 = 2\pi\sqrt{m/C}. \tag{2}$$

We will use the quantities a and T_0 as microscopic distance and time scales. For a particle of mass m that is in equilibrium in the potential field $\Pi(r)$ its minimum velocity to reach infinity is $v_d = \sqrt{2D/m}$ — so called dissociation velocity. The velocity of long waves of small amplitude in 1D chain is $v_0 = a\sqrt{C/m}$. We will use v_d and v_0 as a velocity scale units. To measure the level of thermal motion in material the velocities deviation Δv (mean-square value of random thermal velocities, further Δv is referred as heat velocity) will be used. When Δv approaches dissociation velocity v_d then the thermal motion break the internal bonds in the material resulting in its melting. The last term in equation (1) is used to describe energy losses of different kind, such as radiation, internal friction, and heat conductivity. The unit for the friction coefficient is

$$B_0 \stackrel{\text{def}}{=} 2\sqrt{mC} \tag{3}$$

that is the critical value of friction for a mass m on a spring C.

Let us consider the classical Lennard–Jones potential:

$$\Pi_{LJ}(r) = D\left[\left(\frac{a}{r}\right)^{12} - 2\left(\frac{a}{r}\right)^{6}\right], \tag{4}$$

where D and a are the bond energy and the equilibrium interatomic distances, introduced earlier. The corresponding interaction force $f(r) = -\Pi'(r)$ has the form

$$f_{LJ}(r) = Q\left[\left(\frac{a}{r}\right)^{13} - \left(\frac{a}{r}\right)^{7}\right], \qquad Q \stackrel{\text{def}}{=} \frac{12D}{a}, \tag{5}$$

where Q is the interparticle force magnitude. In the case of the Lennard–Jones potential, the stiffness C and the bond energy D obey the relation $C = 72D/a^2$; the force (5) reaches its minimum value (the bond strength) at $r = b = \sqrt[6]{13/7}$, where b is the break distance. The corresponding break deformation of the Lennard–Jones bond is $\varepsilon_* = b - a \approx 0.109$. The Lennard–Jones potential is the simplest potential that allows one to take into account the general properties of interatomic interaction: repulsion of particles that approach each other, attraction of particles moving away from each other, and the absence of interaction at large distances between them. For calculations the shortened Lennard–Jones interaction will be used, given by formula

$$f(r) = \begin{cases} f_{LJ}(r), & 0 < r \le b, \\ k(r) f_{LJ}(r), & b < r \le a_{\text{cut}}; \end{cases} \tag{6}$$

where b is break distance for Lennard-Jones potential, a_{cut} is cut-off distance (for $r > a_{\text{cut}}$ the interaction vanishes). The coefficient $k(r)$ is the shape function

$$k(r) = \left[1 - \left(\frac{r^2 - b^2}{a_{\text{cut}}^2 - b^2}\right)^2\right]^2. \tag{7}$$

The cut-off distance will be set as $a_{\text{cut}} = 1.4a$, in this case only the first neighbors are interacting for the close-packed structures. For the general study of the fracture process this simplified potential is sufficient. If necessary the obtained results can be extended to more complex potentials describing the properties of materials more exactly.

For simulation a two-dimensional material will be used, where particles are packed to form an ideal 2D close-packed (triangular) crystal lattice. This is simplified lattice, however its symmetry is same as the symmetry of [111] surfaces of 3D crystal lattices, such as FCC and diamond (the last one is the lattice of silicon crystals). For the computations periodic boundary conditions are applied at all boundaries. The vertical lattice orientation is used for all computations (this means that rhombic elementary cells of the lattice are directed vertically).

The typical values of the mentioned computation parameters are given in Table 11.

3 Chemical reaction modelling

For the oxidation simulation the following model is suggested. The properties of particles adjusting to the surfaces are changed mimicking the difference between the original material and its oxide: size of the particles became slightly bigger, the elastic and strength properties became substantially lower then for the initial particles. This change take place immediately and involves the particles surrounding the original surfaces of the specimen, as well as the particles laying near the new surfaces provided by the fracture and crack development. Since the size of the particles increases, this can provide separation of the pieces of material — the oxidization induced fracture. In this case fracture and chemical reaction can stimulate each other resulting in a self-generating process. Although mainly we will be studying situations when the chemical reaction front propagates due to the oxygen transfer through the oxide.

In the case of oxidation it is postulated that the properties of the particles are being changed. The diameter and force magnitude for the oxidized particles will be denoted as $\tilde{a}$ and $\tilde{Q}$. The vector of the interaction force between two original particles can be represented as following

$$\underline{f} = \Phi(r^2)\underline{r}\,, \qquad \Phi(r^2) \stackrel{\text{def}}{=} f(r)/r. \tag{8}$$

When one or both of the interacting particles are oxidized then the interaction law takes the form

$$\underline{f} = \Phi\left(\lambda(r^2 - \overline{a}^2) + a^2\right)\underline{r}\,, \qquad \lambda \stackrel{\text{def}}{=} a^2/\overline{a}^2, \tag{9}$$

where function Φ is calculated using average values for the particle diameter and force magnitude:

$$\overline{a} \stackrel{\text{def}}{=} (a_1 + a_2)/2\,, \qquad \overline{Q} \stackrel{\text{def}}{=} (Q_1 + Q_2)/2; \tag{10}$$

indexes 1 and 2 correspond to the first and the second interacting particle. This interaction law preserves the width of the potential well independently of the particles sizes.

For the chemical reaction initiation two following mechanisms are used.

Surface oxidation. The particle changes its status from original to the oxidized one if in the distance a_c it has less then n_c neighbors, where n_c is the neighbors count for the perfect crystal (in the case of triangular lattice $n_c = 6$).

Internal oxidation. The particle changes its status from original to the oxidized one if it has at least one oxidized neighbor.

The first mechanism of the oxidation modelling was used in [2]. It gives only the surface oxidation, therefore the chemical reaction can penetrate inside the material only in the case of fracture. The second mechanism is introduced in the current paper and it simulates the oxidation due to the oxygen transfer through the oxidized zone. In paper [2] only the surface oxidation was considered, therefore the oxidation was applied immediately, at every computation step. However if the second mechanism would be used in the same manner it would produce a very fast motion of the chemical reaction front. The corresponding velocity of the reaction front in 1D chain can be calculated as

$$v_c = \frac{a}{\Delta t} \quad \Rightarrow \quad \frac{v_c}{v_0} = \frac{1}{2\pi}\frac{T_0}{\Delta t}. \tag{11}$$

To alternate the front propagation velocity the chemical reaction is applied with probability $0 \leq r_p \leq 1$. This means that at every check a random number $r \in [0, 1]$ is generated and reaction takes place only if $r < r_p$. For 1D chain such algorithm would give for the front velocity v_f

$$v_f = r_p v_c. \tag{12}$$

In 2D crystal with close packed triangular lattice relation (12) holds only for r_p close to 1, in other cases it becomes $2 \div 3$ times grater — see Table 10.

r_p	1	0.1	0.01	0.001	0.0002
$v_f/(r_p v_c)$	0.94	2.49	2.83	2.95	3.02

Table 10: Relation between reaction probability r_p and velocity of the reaction front v_f.

The typical values of the mentioned computation parameters are given in Table 11.

4 Oxidation of material with circular holes

To investigate the oxidation process a square specimen with a central circular hole is considered — see Fig. 1a. The boundary conditions are periodical, so the situation is equivalent to an infinite

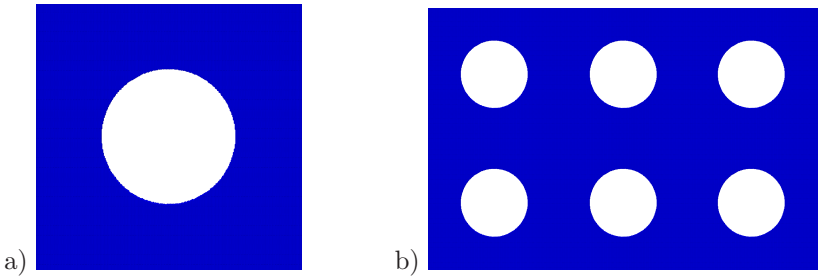


Figure 1: a) The specimen with a circular hole; b) periodic material combined from the specimens.

material with periodically located holes, arranged in a square lattice — Fig. 1b. The hole diameter is taken to be a half of the specimen width, that means that in the periodical material the hole diameter is equal to the width of the material bridge between the holes. In this case the hole volume V_{hole} is slightly less then 20% of the specimen volume V_{spec}:

$$\frac{V_{\text{hole}}}{V_{\text{spec}}} = \frac{\pi R^2}{L^2} = \frac{\pi^2}{16} \approx 0,19635, \tag{13}$$

where R is radius of the hole, L is width of the specimen. The chemical inflation $\tilde{a}/a = 1.2$ will be used in the computer experiments. Therefore if all the material would be oxidized, then enough of additional material volume would be produced to fill the hole. The considered value of the chemical inflation is higher then in the case of silicon oxidation, where $\tilde{a}/a = 1.1$. The higher value is used to have better pronounced results, most of the qualitative conclusions from this investigation can be used for the case of lower value of the chemical inflation.

The computational parameters are listed in Table 11. All the parameters are kept constant except of the last two. The main task would be to study the influence of the reaction probability r_p on the oxidation process. The value of the reaction probability determines the speed of the chemical reaction and consequently, the speed of the chemical front propagation. Therefore, the lower is r_p, the longer calculation time $t_{\max}$ is required (the second parameter being varied in Table 11).

Results of the computer experiment for the value of the reaction probability $r_p = 0.01$ are shown in Fig. 2, and zoom-up of Fig. 2a is presented in Fig. 3. Blue color in the figure represents the original material, cyan color represents the oxide, dark cyan outlines the particles of boundaries and defects (the particles having less then 6 neighbors). The figure shows, that oxidation zone

Parameter	Symbol	Value
Number of particles	N	80 311
Cut-off radius	a_{cut}	$1.4\,a$
Initial velocity deviation	Δv	$0.005\,v_d$
Dissipation coefficient	B	$0.026\,B_0$
Integration step	Δt	$0.02\,T_0$
Chemical inflation	$\tilde{a}/a$	1.2
Chemical strengthening	$\tilde{Q}/Q$	1/3
Neighborhood radius	a_c	$1.2\,a$
Neighbor count	n_c	6
Relative hole diameter	$2R/L$	0.5
Lattice orientation		vertical
Boundary conditions		periodic
Reaction probability	r_p	$0.0002 \div 1$
Calculation time	$t_{\max}$	$400 \div 5000\,T_0$

Table 11: Computation parameters.

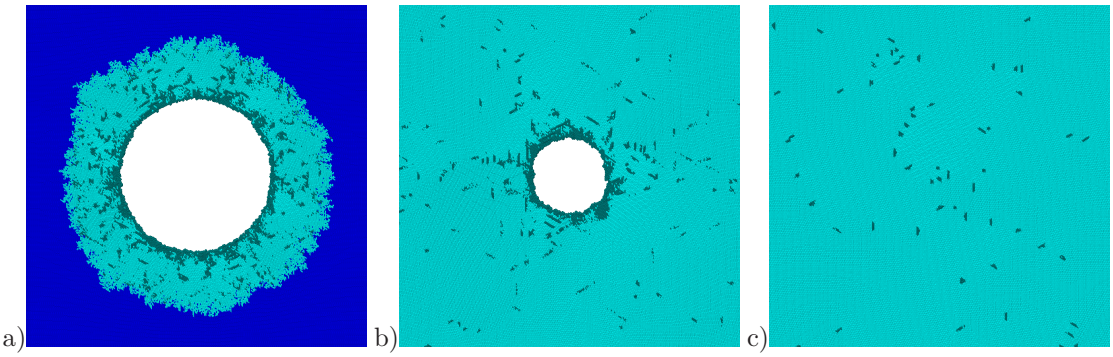


Figure 2: Sequential stages of the oxidation process: a) $t = 30\,T_0$, b) $t = 200\,T_0$, c) $t = 600\,T_0$.

starts from the hole surface, it grows and fills all the specimen, the hole size decreases and finally the hole completely disappears. No sign of the hole is seen in the last frame, only some defects are more or less uniformly distributed across the specimen. The zoom-up of the process of the hole disappearance is shown in Fig. 4. Finally the hole transforms to a group of dislocations, which then move to other parts of the specimen.

Time dependencies of the front radius R_f, and the hole radius R_h for the high and low reaction probability r_p are shown in Fig. 5. The values of the radii are calculated by measuring the volume occupied by the oxide and the volume of the hole, using the assumption that the mentioned areas are circular. For the high reaction probability the chemical front velocity is higher then the hole surface velocity. Therefore in this case all the material is oxidized earlier then the hole disappears. On contrary, for the low reaction probability the hole disappears first, and only after that the remains of the original material are oxidized. This difference can be observed in Fig. 6, where the specimens at the moment when the reaction front reaches the specimen boundaries are shown for different values of the reaction probability. The radii of the oxidized zone for all specimens in Fig. 6 are approximately the same, but the radii of the holes are different: the slower moves the reaction front, the more time the material has to decrease the hole. The oxidized zone is not circular only for $r_p = 1$ — the anisotropy of the lattice takes effect; for the smaller considered values of r_p (0.1 and lower) no anisotropy of the chemical front propagation can be noticed.

The time dependence of the hole surface velocity for the high and low r_p are shown in Fig. 7. Blue curve shows the original plot, black stands for the plot averaged over 5 nearest moments of time. According to the graphs the velocity of the hole surface is not constant, it decreases with time for the high values of r_p and increases with time for the low values. This effect is due to the differences in the front velocity. In the first case for the most of time the whole specimen is

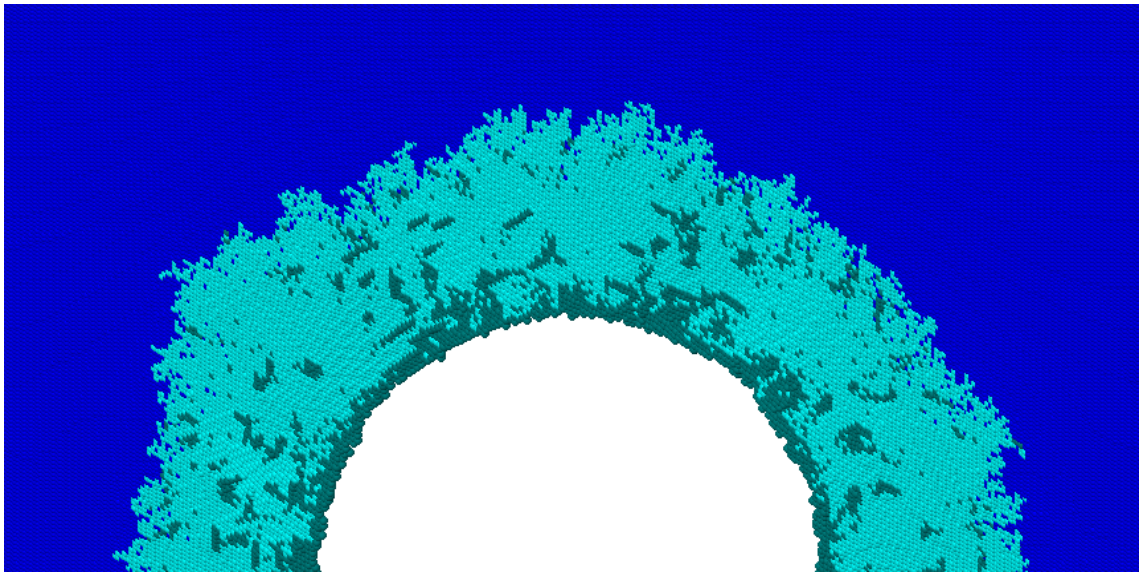


Figure 3: Half of the specimen, $t = 30\,T_0$.

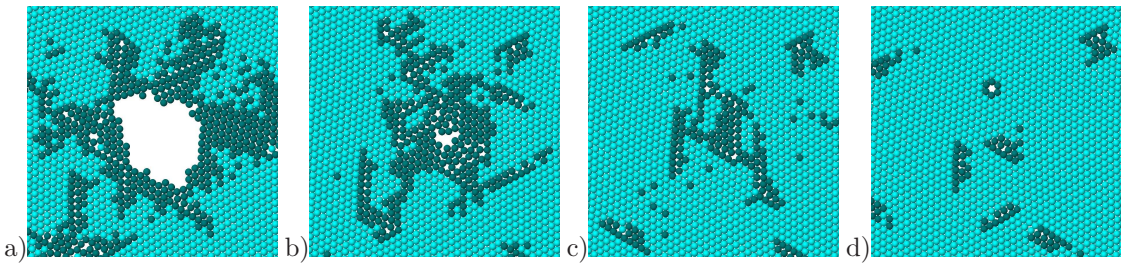


Figure 4: Zoom-up of the hole disappearance: a) $t = 430\,T_0$, b) $t = 480\,T_0$, c) $t = 490\,T_0$, d) $t = 500\,T_0$.

oxidized and the hole closure process is highly dynamical. In the second case the hole closure can be treated as quasistatical process, which follows the slow propagation of the reaction front.

This difference is also illustrated by Fig. 8, where the heat velocity Δv is shown as a function of time for high and low values of r_p. Let us note that the material temperature is proportional $(\Delta v)^2$. The heat velocity is shown in the units of dissociation velocity[1] v_d. In this case Δv approaching unity $(1v_d)$ corresponds to the material melting. From the figures it follows that for the high values of r_p the heating of material is much higher, then for the lower r_p, that is additional proof that the in the first case the process is highly dynamical. In these graphs the defects density is also shown, which is calculated as a ratio of the material volume, occupied by defects to the whole volume of the specimen. The time dependence of the defects density in these two cases is different. For the high r_p the defects density has a sharp maximum at the very beginning, when the oxidation starts, and then it slowly decreases. For the low r_p the defects density demonstrates graph with a well pronounced maximum at intermediate values of time. The explanation of this difference is that the defects are mainly produced by the propagation of the chemical reaction front. If the front propagates slower then the maximum is shifted to the later times. However, according to the graphs, the maximum value in this case is higher — this is an unexpected result requiring some explanation.

The summarizing graphs showing relations of the mentioned above quantities on the reaction probability r_p are presented in Fig. 9. From the graphs in Fig. 9a it follows that the velocities of the reaction front and the hole surface differ a lot for the high values of r_p. As the reaction probability

[1]Here and below for the sake of simplicity the dissociation velocity is calculated as $v_d = \sqrt{2D/m}$, where D is the bond energy for the classical Lennard-Jones potential (4), but not for the shortened Lennard-Jones interaction (6), which is actually used in the computations.

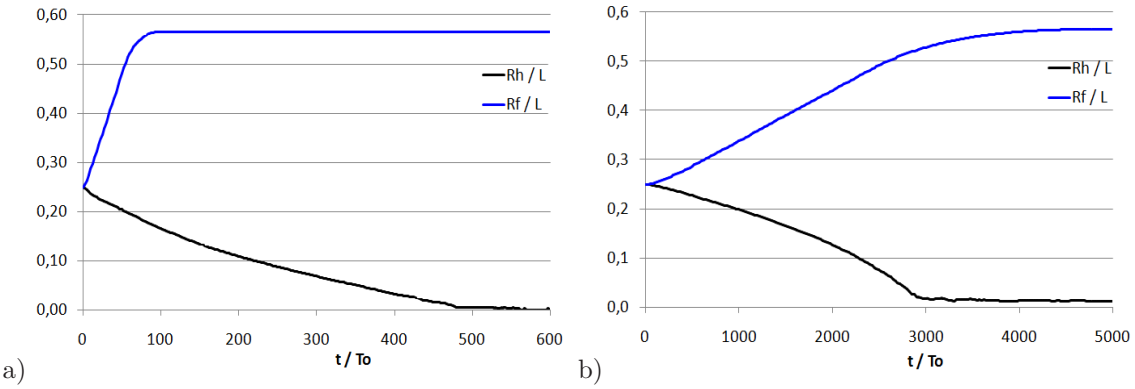


Figure 5: Time dependenceies of the front radius R_f and the hole radius R_h for two values of the reaction probability: a) $r_p = 0.01$, b) $r_p = 0.0002$.

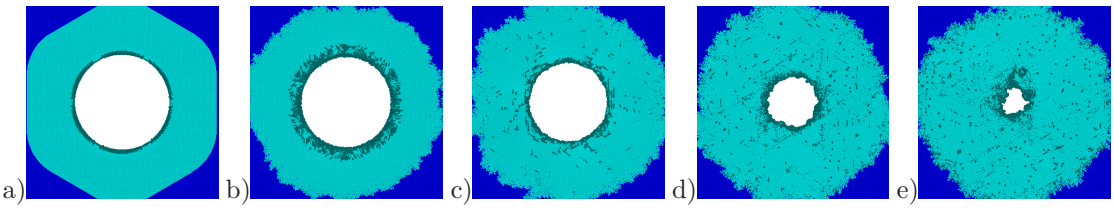


Figure 6: Specimens at the moment when the reaction front reaches their boundaries: a) $r_p = 1$, $t = 1.6\,T_0$; b) $r_p = 0.1$, $t = 6\,T_0$, c) $r_p = 0.001$, $t = 55\,T_0$, d) $r_p = 0.0001$, $t = 540\,T_0$, e) $r_p = 0.00002$, $t = 2600\,T_0$.

decreases then these velocities became closer, demonstrating a quasistatic process. Logarithm scales are used along the both axes. The velocities are shown in the units of v_0 — the sound velocity in the material. For r_p equal to 0.01 or greater the front velocity is even higher then the speed of sound. The hole surface velocity obviously is less then the sound speed, and therefore a great difference between these two velocities is observed for the higher values of r_p. For the lower r_p both velocities became proportional to each other and to the velocity $r_p v_c$ of the reaction front in 1D, which is shown in Fig. 9a by a dashed line.

The heat velocity, according to Fig. 9b is decreasing with decreasing of the reaction probability. This is an expected result, but strange behavior is observed for higher r_p, where the maximum is observed for $r_p = 0.1$. The defects density, also shown in this graph, increases with r_p decrease, and this fact is not explained yet.

Actually the most realistic situation corresponds to the quasistatic processes at the lower values

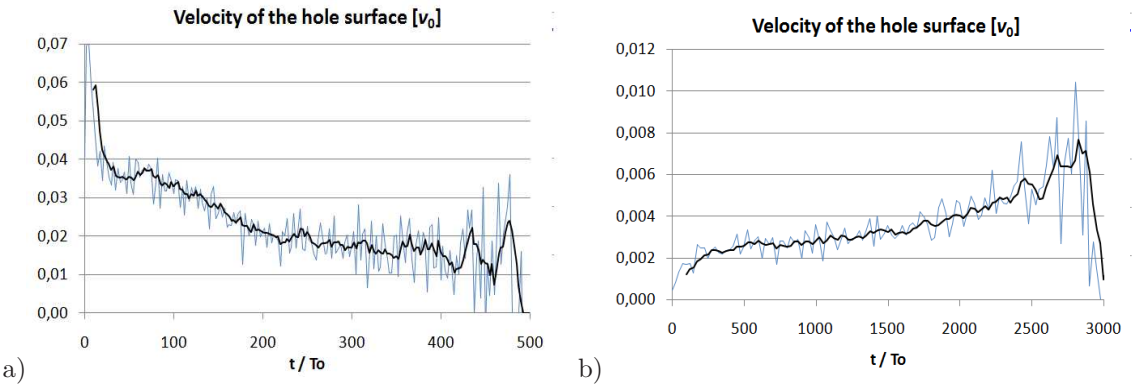


Figure 7: Time dependenceies of the hole surface velocity: a) $r_p = 0.01$, b) $r_p = 0.0002$.

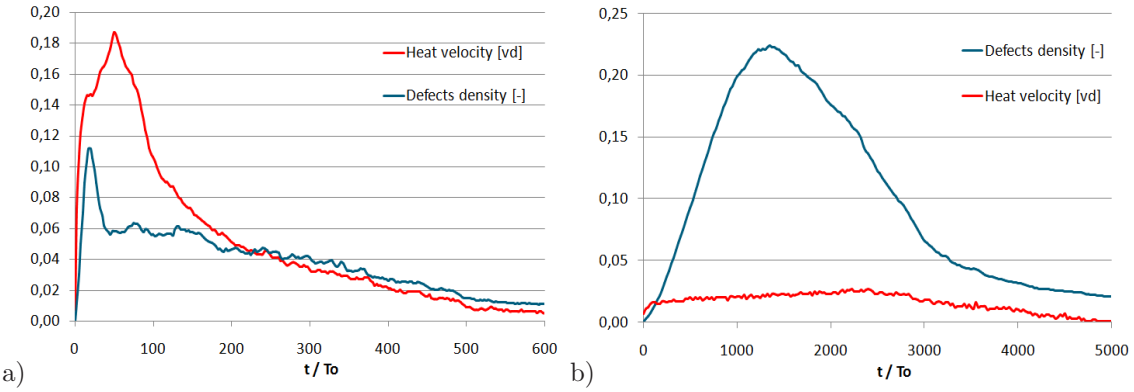


Figure 8: Time dependencies of the heat velocity and relative density of defects: a) $r_p = 0.01$, b) $r_p = 0.0002$.

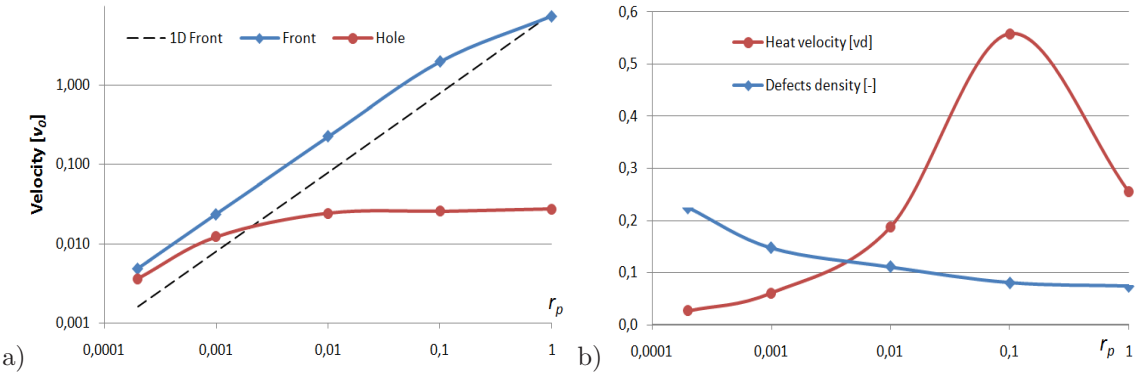


Figure 9: Influence of the reaction probability on: a) chemical front velocity and hole surface velocity; b) heat velocity and relative defects density.

of r_p. However, the lower is r_p, the more time is needed for computation — see Fig. 10. The computation time in the figure is shown as internal time (in units of T_0, left axis) and external time (in minutes, right axis). The external time corresponds to computations on PC with processor Core 2 Duo 2.4 GHz (Sony VAIO VGN-Z21MRN). In the most real situations the front velocity is so low that the corresponding computations would be too long. However the convergence of the results for the lower values of r_p shows that the real situations can be approximated from the realizable computer experiments.

5 Oxidation of circular and square specimens

At the end let us present the computation results where the oxidation starts not from the internal surface, but from the external one. Fig. 11 shows sequential stages of a ball oxidation, Fig. 12 — the same for a square specimen. The ball contains 50 316 particles, the square specimen — 63 920 particles, reaction probability is $r_p = 0.01$, other calculation parameters are same as above. For these experiments the dependencies similar to the above ones can be observed, where instead of the hole surface velocity would act the velocity of the outer surface of the specimen. However the necessary plastic deformations in these cases probably would be lower, then in the case of the internal holes. Indeed, a specimen with an external surface has much better options for relaxation due to export of dislocations and cracks to the surface.

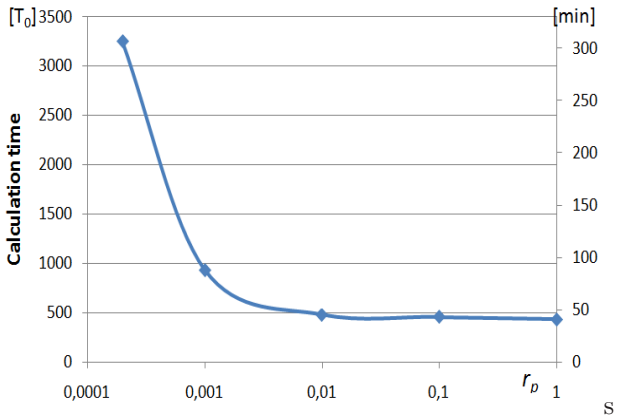


Figure 10: Time of computation as a function of reaction probability r_p.

6 Reaction probability and speed of chemical reaction

In the presented computer experiments it was shown that all parameters of the process depend strongly on the reaction probability r_p and therefore this quantity is very important characteristics for the chemically induced phase transformations and corresponding mechanical processes. The reaction probability has a clear meaning from a computational point of view — it belongs to interval $[0, 1]$ and determines probability of reaction for each particle at each computational step. However, this quantity is not objective from a physical point of view, since the corresponding physical result would depend on the choice of the computational time step Δt. The highest possible value of r_p corresponds to the fastest possible velocity $v_c = a/\Delta t$ of the chemical reaction front propagation. This fastest velocity is pure computational (algorithmic), showing how fast for the current value of time step a computational information can be transferred from one point of the material to another. No physical processes propagating in space faster then v_c can be modelled. However by decrease of Δt this velocity can be set as high as it is needed from the physical point of view. Thus, to characterize the speed of the chemical reaction another physically objective quantity is required. This could be the introduced above velocity v_f of propagation of the chemical reaction front in 1D chain

$$v_f \stackrel{\text{def}}{=} r_p v_c = r_p \frac{a}{\Delta t} = \frac{r_p}{2\pi} \frac{T_0}{\Delta t} v_0. \tag{14}$$

Here v_0 is the sound velocity in 1D chain. To make v_f a physically objective value the ratio $r_p/\Delta t$ should be kept constant with the change of Δt. To do this the required value of r_p can be calculated from formula (14) as

$$r_p = 2\pi \frac{\Delta t}{T_0} \frac{v_f}{v_0}. \tag{15}$$

Another, and, probably, better choice for the quantity characterizing the chemical reaction speed could be

$$\omega_f \stackrel{\text{def}}{=} \frac{r_p}{\Delta t} = \frac{r_p}{2\pi} \frac{T_0}{\Delta t} \omega_0, \tag{16}$$

where $\omega_0 = \sqrt{C/m}$ is an oscillation frequency of a mass m on a string C. Introduce by this way the chemical reaction speed has dimension of frequency, and similarly to (15) the reaction probability should be calculated as

$$r_p = 2\pi \frac{\Delta t}{T_0} \frac{\omega_f}{\omega_0}. \tag{17}$$

In this formula ratio $\Delta t/T_0$ should be set from computational reasons, and ratio ω_f/ω_0 — from physical reasons.

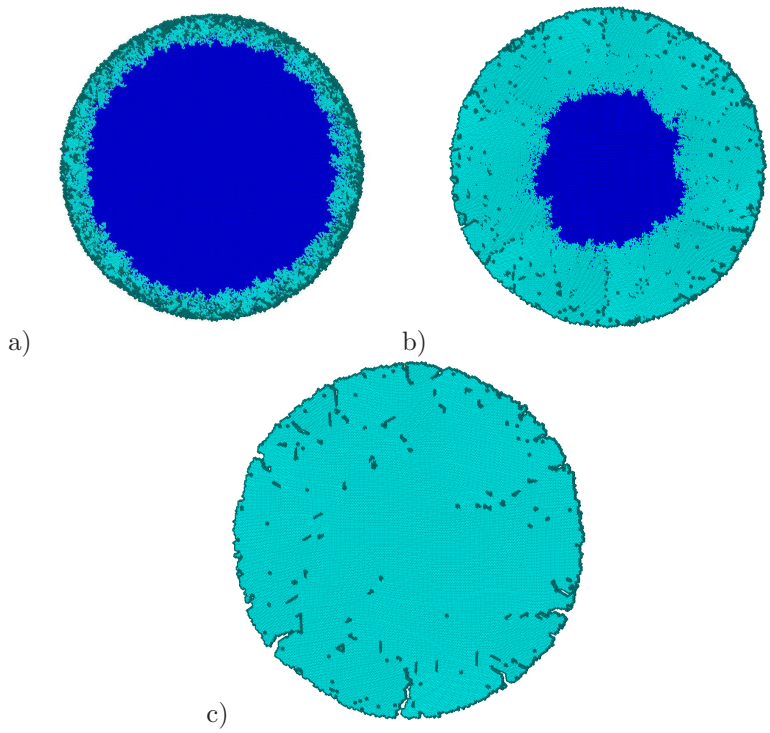


Figure 11: Oxidation of circular specimen: a) $t = 12\,T_0$, b) $t = 40\,T_0$, c) $t = 400\,T_0$.

7 Conclusions

A molecular dynamics model for the phase transformation induced by chemical reaction (oxidation) was presented. It was taken into account that the material properties such as density, stiffness and strength are being changed due to the oxidation. In contrast with the previous stage of the project the oxidation is considered not only on the material surface, but also inside the material at the phase boundaries. To model this phenomenon computational algorithms for the surface and internal oxidation were developed. A reaction probability r_p was introduced to control the speed of the chemical reaction and the velocity of the reaction front. A square specimen with periodic boundaries and central circular hole was considered, which is equivalent to an infinite material with a periodic set of holes. Oxidation starting from the inner surface of the hole and resulting in the hole closure was investigated. Influence of the reaction probability on the velocity of the chemical reaction front, velocity of the hole surface, thermal motion, and defects density were analyzed. In addition oxidation starting from the outer surface of a circular and square specimens was considered.

It was shown that for the high values of the reaction probability the process is dynamical, it is accompanied with a strong thermal effect, the oxidation occurs much faster then mechanical processes such as the hole closure. For the lower values of the reaction probability a quasistatical process with a week thermal effect is realized. In the second case the mechanical processes follow the chemical processes and they have approximately the same speed. This shows that the models for slow chemical processes, which can not be computed directly because of too long time required for such computations, can be extrapolated from the computations with decreasing values of reaction probability. The velocity of the hole surface in the process of the computer experiment is a monotonic function of time, however this function is decreasing for higher reaction probabilities and increasing for lower r_p. As it was mentioned above, the thermal effect of the phase transformation decreases with the decrease of r_p. However this relation has a maximum in the area of the high r_p and it is unexpectedly decreasing when r_p approaches unity. Another unexpected effect is that the density of defects grows with the decrease of the reaction probability. This growth has even accelerative character on the graph with logarithmic r_p-scale — see Fig. 9b. But obviously this

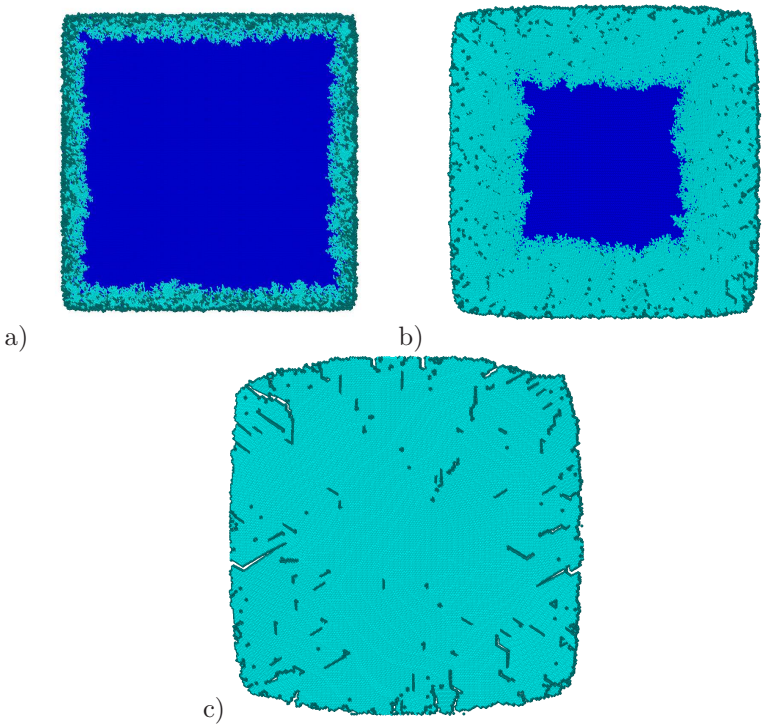


Figure 12: Oxidation of square specimen: a) $t = 12\,T_0$, b) $t = 39\,T_0$, c) $t = 600\,T_0$.

growth can not continue much further since the density of defects can not be too high. Therefore for the lower values of r_p this graph should either tend to a constant value, or should have an extremum (maximum). However these values of r_p were not reached yet due to long computational times, required to perform such calculation.

The listed above questions could be subjects for the further investigations. Besides it would be useful to extend the model of the chemical reaction by modelling the oxygen transfer through the oxide and applying thermodynamic conditions at the reaction front.

Acknowledgements

This work was supported by Sandia National Laboratories and RFBR grants 08-01-00865-a and 09-01-12096-ofi-m. The author is grateful to A. B. Freidin and E. N. Vilchevskaya for the useful discussions.

References

[1] C. L. Muhlstein, S. B. Brown, and R. O. Ritchie. High-cycle Fatigue and Durability of Polycrystalline Silicon Thin Films in Ambient Air. Sensors and Actuators, A 94. Elsevier, pp.177-188 (2001).

[2] A. M. Krivtsov. Influence of defects type and chemical reaction on fracture initiation, molecular dynamics study. Proc. for the Joint U.S. and Russia Conference on Advances in Materials Science. Prague, 2009.

[3] A. M. Krivtsov. MD modeling of low-cycle high-amplitude loading of monocrystal material with defects. Proc. of XXXIII Summer School “Advanced Problems in Mechanics 2005”, St. Petersburg, Russia, 2006, 341-346.

[4] A. M. Krivtsov. Molecular dynamics simulation of plastic effects upon spalling. Phys. Solid State **46**, 6 (2004).

[5] M. P. Allen and A. K. Tildesley. Computer Simulation of Liquids. – Oxford: Clarendon Press. 1987. 385.

[6] A. M. Krivtsov. Deformation and fracture of solids with microstructure. Moscow, Fismatlit. 2007. 304 p. (In Russian).

On the use of gradient continua for minimizing the wave reflection at a discrete-continuum interface

Asiya M. Kudarova Andrei V. Metrikine
asya.kudarova@gmail.com, a.metrikine@tudelft.nl

Abstract

This paper contributes to the studies on the dynamic coupling of discrete systems and continua. The approach based on the use of the Green's function of the continua is employed. The novelty of the presented research is in the use of a gradient model of the continuum instead of the classical one. The enhanced continuum model is chosen for its ability to mimic the wave dispersion properties of discrete systems — a property that can not be granted by the classical model. The wave reflection coefficient is studied in this paper at the interface of a one-dimensional chain of masses and springs and a corresponding continuum. The continuum is modelled using both the classical and a gradient equations of motion. It is shown that the gradient continuum with properly chosen parameters reduces the reflection significantly. This is also confirmed by numerical simulations.

1 Introduction

The coupling of discrete and continuum domains is widely applied in the multiscale and hybrid simulations of mechanical, biological and chemical systems. The hybrid numerical modelling is absolutely essential in order to obtain accurate results within reasonable time. The use of continuum models alone often happens to be insufficient when small spatial and temporal scales are of significance. The discrete models, on the other hand, are very expensive computationally. The hybrid models that include both discrete and continuum domains present an intelligent compromise between the efficiency and accuracy.

In the last decade a number of approaches have been proposed for the coupling of discrete and continuum domains. These approaches can be roughly classified into two main categories. The first category focuses on the coupling between a discrete domain and a continuum domain that is discretized using finite elements. Within this category one can distinguish a bridging domain method and a coarse-grained molecular dynamics method. The bridging domain method is based on the introduction of overlapped subdomains where the Hamiltonian is constructed as a linear combination of the continuum and molecular Hamiltonians [1]. A closely related Hamiltonian for discrete and finite element nodes in a so called handshake domain was proposed by Abraham et. al. [2]. The coarse-grained molecular dynamics method that is based on a statistical prescription of graining allows for a unified finite element formulation of the whole continuum-discrete domain, see Rudd and Broughton [3]. The methods belonging to this category are aimed at description of finite material domains and would become inefficient should a large domain be modelled.

The second category of the hybrid methods is based on the use of the Green's functions of the continuum. The methods belonging to this category are superior if the domain occupied by the continuum part of the model is large or infinite in one or more directions. The idea of these methods is essentially the same as employed in the boundary element methods with the only difference that the boundary elements are introduced at the interface with a discrete model rather than at that with another continuum. It is important to underline that using the indirect boundary element method [5] one can also model interfaces with complex geometry.

As a rule, the Green's functions used to describe the continuum part of a hybrid discrete-continuum model are those of the classical continuum [4]. The advantage of using these functions is

that they are well-known, including their asymptotics. The disadvantage is though that the classical continuum can match the behaviour of the corresponding discrete system at the spatial scales that are large relative to the spatial period of the lattice. At shorter scales (higher frequencies) the perfect matching is impossible as any discrete system is dispersive whereas the classical continuum is not.

In this paper it is proposed to describe the continuum domain with the help of a gradient continuum. The background reason for doing so is obvious: the gradient continua are dispersive and capable of closely resembling the dispersion character of the corresponding discrete systems [6]–[9]. This can facilitate the desired matching of the discrete and continuum domains at the entire frequency band, up to the cut-off frequency of the discrete system. This statement is proven in this paper by studying the wave reflection coefficient at the interface of a one-dimensional chain of masses and springs and a corresponding one-dimensional continuum. Both the classical and a gradient models are used for the continuum. It is shown that the gradient continuum with properly chosen parameters provides a perfect silent boundary at all frequencies which allow the wave propagation in the chain.

2 Model

To analyse the dynamic processes in a hybrid discrete-continuum system, a one-dimensional model is considered depicted in Figure 1. The model consists of a regular chain of N masses and $N-1$ springs that is attached to a one dimensional continuum. The end masses of the chain are chosen to be different from the inner masses to account for the end effects. The end of the chain is subject to a force $F(t)$, whereas the continuity of displacements and forces is assumed at the interface of the chain and the continuum. Two models for the continuum are considered, namely, the classical (the wave equation) and the gradient models, the latter being described in accordance with [6].

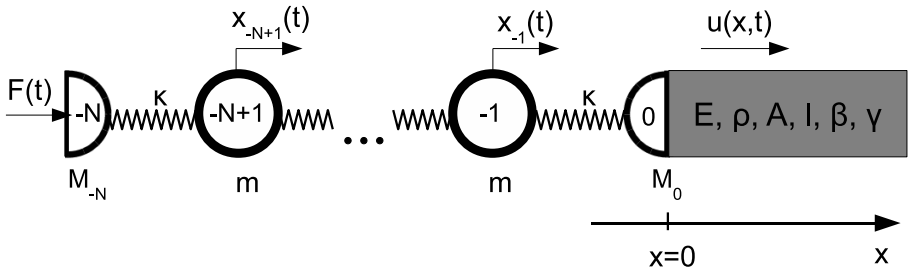


Figure 1: The model

The equations of motion that govern linear vibrations of the chain, including, respectively, those for the end mass, inner masses and interface mass, are given as:

$$M_{-N}\ddot{x}_{-N} + \kappa(x_{-N} - x_{-N+1}) = F(t), \tag{1}$$

$$m\ddot{x}_n + \kappa(2x_n - x_{n+1} - x_{n-1}) = 0, \quad -N < n < 0, \tag{2}$$

$$M_0\ddot{x}_0 + \kappa(x_0 - x_{-1}) = F_{cont}(t). \tag{3}$$

The classical and high-gradient models of the continuum are described, respectively, by the following equations:

$$\rho A\frac{\partial^2 u}{\partial t^2} - c^2\frac{\partial^2 u}{\partial x^2} = 0, \tag{4}$$

$$\rho A\frac{\partial^2 u}{\partial t^2} - EA\frac{\partial^2 u}{\partial x^2} - l^2\beta\frac{\partial^2}{\partial x^2}\left(\rho A\frac{\partial^2 u}{\partial t^2} - EA\gamma\frac{\partial^2 u}{\partial x^2}\right) = 0. \tag{5}$$

At the interface $x = 0$ the continuity of the displacements is required:

$$x_0(t) = u(0,t), \tag{6}$$

and the continuity of the forces, which is enforced by the following expressions for the $F_{cont}(t)$ in (1):

$$F_{cont}(t) = EA\tfrac{\partial u}{\partial x}\big|_{x=0} \quad \text{for the classical continuum and} \tag{7}$$

$$F_{cont}(t) = \left(EA\tfrac{\partial u}{\partial x} + l^2\beta\left(\rho A\tfrac{\partial^3 u}{\partial x \partial t^2} - EA\gamma\tfrac{\partial^3 u}{\partial x^3}\right)\right)\Big|_{x=0} = 0 \quad \text{for the gradient continuum.} \tag{8}$$

Finally, at the interface with the gradient continuum one additional condition is required in the case $\gamma \neq 0$. According to [6], this condition reads

$$\frac{\partial^2 u}{\partial x^2}(0,t) = 0. \tag{9}$$

In (1)–(8) the following notations are used: M_{-N}, m and M_0 are the masses of the end particle, inner particles and interface particle of the chain, respectively, κ is the stiffness of the springs in the chain, $x_n(t)$ is the displacement of the mass n of the chain from its equilibrium, $u(x,t)$ is the axial displacement of the cross-section of the 1D continuum, E, A and ρ are the Young's modulus, cross-sectional area and mass density of the continuum, l is the undisturbed distance between the masses in the chain as well as the lengthscale parameter of the gradient continuum, respectively, β and γ are the dimensionless parameters characterising the dispersive properties of the high-gradient continuum, $F(t)$ and $F_{cont}(t)$ are the external force applied to the end of the chain and the internal force with which the continuum acts on the interface mass.

3 Discrete-continuum correspondence in the long wave limit

The discrete chain and the continuum are supposed to describe one and the same material, just at different lengthscales. These descriptions, however, must coincide in the long wave (low frequency) limit. This can be achieved by imposing a proper relation between the parameters of the chain and those of the continuum. This correspondence can be found by continualizing (2) with the help of the following well-known relations between the discrete and continuum degrees of freedom:

$$x_n(t) = u(x,t), \quad x_{n\pm1}(t) = u(x,t) \pm l\frac{\partial u}{\partial x} + \frac{1}{2}l^2\frac{\partial^2 u}{\partial x^2} + ... \tag{10}$$

With the accuracy to l^2 substitution of (10) into (2) gives

$$m\frac{\partial^2 u}{\partial t^2} - \kappa l^2\frac{\partial^2 u}{\partial x^2} = 0. \tag{11}$$

Comparing the above equation to equation (4), the following correspondence between the parameters can be established:

$$\rho A = \frac{m}{l}, \quad \kappa l = EA. \tag{12}$$

The above relations also set the correspondence between the speed of longitudinal waves in the classical continuum and the natural frequency of the chain:

$$c = \omega_0 l, \quad c = \sqrt{E/\rho}, \quad \omega_0 = \sqrt{\kappa/m}. \tag{13}$$

As will be shown in the next section, the relations between the parameters established in this section assure the non-reflective boundary conditions at the interface in the long wave limit provided that the interface mass is chosen properly.

4 Wave reflection at the interface with the classical continuum

To analyse the wave reflection at the interface, a harmonic incident wave is considered that is given as

$$x_n^{inc}(t) = \tilde{A}e^{i\omega t}e^{-iknl}, \tag{14}$$

where ω is the angular frequency of the wave and k is the wavenumber. The dispersion equation that relates ω and k is well-known and can be obtained by substituting (14) into (2). This yields

$$-m\omega^2 + 4\kappa sin^2\left(\frac{kl}{2}\right) = 0. \tag{15}$$

From the above equation, the following relations can be obtained that will be useful below:

$$cos(kl) = 1 - \frac{1}{2}\Omega^2, \quad sin(kl) = \Omega\sqrt{1 - \frac{1}{4}\Omega^2}, \tag{16}$$

where $\Omega = \omega/\omega_0$ is the dimensionless wave frequency.

At the interface with the continuum the incident wave (14) partly reflects and partly transmits. The displacement fields in the chain and in the continuum that describe this process read:

$$\begin{aligned} x_n &= A^{inc}e^{i\omega t - iknl} + A^{ref}e^{i\omega t + iknl}, \\ u(x,t) &= A^{tr}e^{i\omega t - i\frac{\omega}{c}x}. \end{aligned} \tag{17}$$

The complex amplitudes of the reflected and transmitted waves can be found by substituting the above expressions into equations (3) and (4) and making use of equation (7). The reflection coefficient is found as the absolute value of the ratio of the complex amplitudes of the reflected and incident waves and is given as

$$R = \left|\frac{A^{ref}}{A^{inc}}\right| = \left|\frac{-\frac{M_0}{m} + \frac{1}{2} - i\left(\sqrt{1 - \frac{\Omega^2}{4}} - 1\right)}{\frac{M_0}{m} - \frac{1}{2} - i\left(\sqrt{1 - \frac{\Omega^2}{4}} - 1\right)}\right|. \tag{18}$$

Equation (18) clearly shows that in order to have no wave reflection in the low frequency limit, the mass of the interface particle must be chosen as the half of the inner mass, e.g. $2M_0 = m$ (this relation will be used in the remainder of this paper). With this equation satisfied, the reflection coefficient reduces to

$$R = \left|\frac{\sqrt{1 - \frac{\Omega^2}{4}} - 1}{\sqrt{1 - \frac{\Omega^2}{4}} + 1}\right|. \tag{19}$$

As one can see from the above equation, the reflection coefficient at the interface with the classical continuum is zero only in the limit $\Omega \to 0$. At all other frequencies, the reflection coefficient is not equal to zero. The frequency dependence of this coefficient will be shown in the next section along with the reflection coefficient provided by the gradient continuum. At this point it is just important to underline once again that the classical continuum is capable of providing the silent boundary only at the low frequencies, which correspond to the spatial scales that are much larger that the inter-particle distance in the chain.

5 Wave reflection at the interface with the gradient continuum

When falling on the interface the incident wave introduced in the preceding section by equation (14) generates the following displacement field in the chain and in the gradient continuum (the

latter being described by equation (5)):

$$\begin{aligned} x_n &= A^{inc}e^{i\omega t-iknl} + A^{ref}e^{i\omega t+iknl}, \\ u(x,t) &= A_1^{tr}e^{i\omega t-ik_1 x} + A_2^{tr}e^{i\omega t-ik_2 x}, \end{aligned} \tag{20}$$

where

$$\begin{aligned} k_1 &= \tfrac{1}{2}\sqrt{2\beta\gamma\left(-1+\beta\Omega^2+\sqrt{1-2\beta\Omega^2+\beta^2\Omega^4+4\beta\gamma\Omega^2}\right)}, \\ k_2 &= \tfrac{1}{2}\sqrt{2\beta\gamma\left(-1+\beta\Omega^2-\sqrt{1-2\beta\Omega^2+\beta^2\Omega^4+4\beta\gamma\Omega^2}\right)}. \end{aligned} \tag{21}$$

The unknown complex amplitudes in equations (20) can be found by substituting these equations

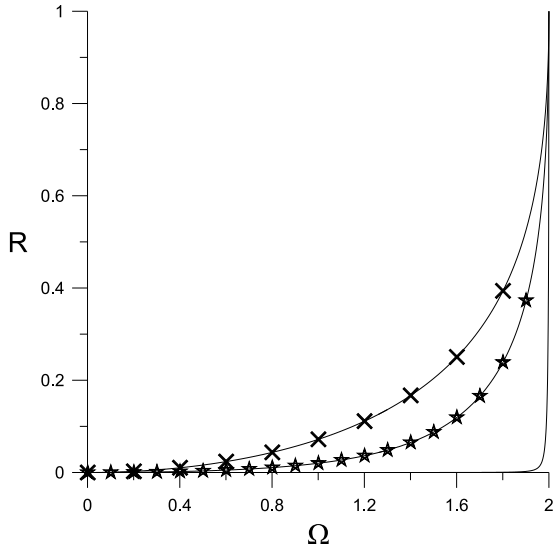


Figure 2: The reflection coefficient

into equations (3), (6) and (8) and making use of equation (7). Dividing the so-obtained complex amplitude of the reflected wave by that of the incident wave, the reflection coefficient can be obtained that characterizes the wave reflection from the gradient continuum. Though easily obtainable the expression for the reflection coefficient is rather long and, therefore, is not given here. Instead, the frequency dependence of the reflection coefficient is shown in Figure 2. This figure contains three graphs: (1) the reflection coefficient given by equation (18) and characterizing the wave reflection from the classical continuum (the line indicated by cross-shaped symbols); (2) the reflection coefficient for the gradient continuum computed with $\beta = 1/7$ and $\gamma = 5/12$ (the line indicated by star-shaped symbols); (3) the reflection coefficient for the gradient continuum computed with $\beta = 0.25$ and $\gamma = 0.0001$ (the symbol-free line). Figure 2 clearly shows that the wave reflection at the interface with the gradient continuum is smaller than at that with the classical continuum. Moreover, it looks like the gradient continuum with $\beta = 0.25$ and $\gamma = 0.0001$ is almost perfectly non-reflective, except for the frequencies very close to the cut-off frequency of the chain $\Omega = 2$. Given the latter, it is interesting to check what happens to the reflection coefficient if $\beta = 0.25$ and $\gamma = 0$. This case is somewhat special as the spatial order of the PDE that describe the gradient continuum is reduced in this case from four to two.

The reflected-transmitted displacement field in the case of $\gamma = 0$ can be found using the following expression:

$$\begin{aligned} x_n &= A^{inc}e^{i\omega t-iknl} + A^{ref}e^{i\omega t+iknl}, \\ u(x,t) &= A^{tr}e^{i\omega t-ik_1 x}, \end{aligned} \tag{22}$$

with $k_1 = \Omega/\sqrt{1-\beta\Omega^2}$, the latter wave number being defined by the dispersion equation of the gradient continuum with $\gamma = 0$. Substituting equations (22) into (3), (6) and(7), the latter taken with $\gamma = 0$, the complex amplitude of the reflected wave can be found, which results into the following reflection coefficient (the interface mass is assumed to be the half of the inner mass):

$$R = \left| \frac{\sqrt{1-\beta\Omega^2} - \sqrt{1-\frac{\Omega^2}{4}}}{\sqrt{1-\beta\Omega^2} + \sqrt{1-\frac{\Omega^2}{4}}} \right|. \tag{23}$$

It is obvious from the above expression that the reflection coefficient turns to zero at *all* frequencies if $\beta = 0.25$. Thus, the high gradient continuum with $\beta = 0.25$ and $\gamma = 0$ presents a perfect silent boundary at the complete frequency band within which the waves can propagate in the chain.

6 Numerical simulation

In this section the wave excitation, propagation and reflection at the interface are visualized for the system depicted in 1. The system of equations of motion, equations (1)-(9), is considered with the external force $F(t)$ given as

$$F(t) = F_0 sin(\theta t) H(2\pi/\theta - t). \tag{24}$$

To solve the problem, the integral Laplace transform is applied assuming the trivial initial conditions. Applying this transform and introducing the dynamic stiffness $K(s)$ that represents the reaction of the continuum, the statement of the problem in the Laplace domain can be written as

$$\begin{aligned} &X_{-N}(\omega_0^2 + s^2\tfrac{M_{-N}}{m}) - \omega_0^2 X_{1-N} = \tilde{F}(s) \\ &X_n(s^2 + 2\omega_0^2) + \omega_0^2(X_{n-1} + X_{n+1}) = 0, \quad N < n < 0 \\ &X_0(\tfrac{s^2}{2} + \omega_0^2 + \tfrac{K(s)}{m}) - \omega_0^2 X_{-1} = 0, \end{aligned} \tag{25}$$

where

$$X_n(s) = \int_0^\infty x_n(t) e^{-st} dt, \quad \tilde{F}(s) = \frac{F_0}{\kappa} \frac{\theta\left(e^{\frac{2\pi s}{\theta}} - 1\right) e^{\frac{-2\pi s}{\theta}}}{s^2 + \theta^2}. \tag{26}$$

The dynamic stiffness for the classical continuum can be found as $K(s) = \kappa\tilde{s}$, where $\tilde{s} = s/\omega_0$, whereas for the gradient continuum this stiffness is given as

$$\begin{aligned} K(s) &= -\tfrac{(1+\beta\tilde{s}^2)(q_1 q_2 - 2\tilde{s}^2) + \beta\gamma\left(q_1^2 q_2^2 + 2\tilde{s}^2(q_1 q_2 + q_1^2 + q_2^2)\right)}{q_1 + q_2}\kappa, \\ q_1 &= -\tfrac{1}{2}\tfrac{\sqrt{2\beta\gamma\left(1+\beta\tilde{s}^2 - \sqrt{1+2\beta\tilde{s}^2+\beta^2\tilde{s}^4-4\beta\gamma\tilde{s}^2}\right)}}{\beta\gamma}, \\ q_2 &= -\tfrac{1}{2}\tfrac{\sqrt{2\beta\gamma\left(1+\beta\tilde{s}^2 + \sqrt{1+2\beta\tilde{s}^2+\beta^2\tilde{s}^4-4\beta\gamma\tilde{s}^2}\right)}}{\beta\gamma}. \end{aligned} \tag{27}$$

The system of linear algebraic equations (25) can be readily solved numerically to give the solution to the problem in the Laplace domain. The numerical application of the inverse Laplace transform to the latter gives the problem solution in the time domain. This procedure has been carried out using the following physical and numerical parameters:

$$\begin{aligned} &\frac{F_0}{\kappa} = 1, \quad \frac{\theta}{\omega_0} = 1, \quad \beta = 0.25, \quad \gamma = 0.0001, \\ &\frac{s}{\omega_0} = 0.02 + i\Omega, \quad \Omega_{maximum} = 50, \quad M_{-N} = 1. \end{aligned} \tag{28}$$

The result is shown in Figure 3 in terms of the successive displacement patterns of the chain. The left figure shows the initiation and propagation of the pulse along the chain, as well as the reflected pulse. The latter is much smaller than the incident one for both the classical and gradient continua. Therefore, the lower line, corresponding to $\omega_0 = 140$, appears as flat in the left figure. The reflected pulse is magnified in the right figure, where two displacement patterns are presented at each time moment: one corresponding to the classical continuum (the solid line) and the other corresponding to the gradient continuum (the dashed bold line). One can see from the right figure that while the classical continuum returns a reflected pulse into the chain, the gradient continuum serves as almost a perfect silent boundary.

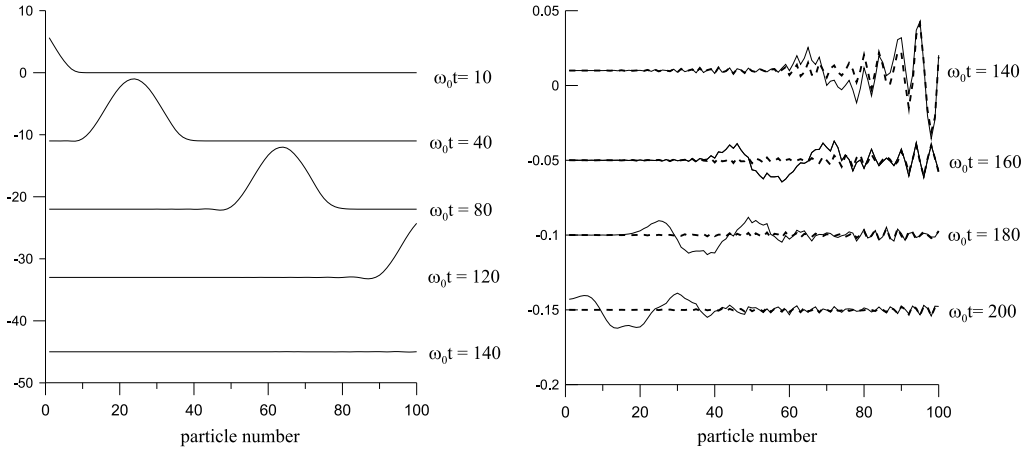


Figure 3: Displacement patterns of the chain

7 Conclusions

A new idea has been presented in this paper that can potentially enable an efficient non-reflective coupling of the discrete and continual computational domains. It has been shown that a properly chosen gradient continuum can serve as a perfect silent boundary for the discrete domain at the entire frequency band. This makes the gradient continua superior to the classical one as the latter is capable of absorbing only the relatively low frequencies. It must be noted though that the final conclusion as to the superiority of the gradient continua over the classical one can not be drawn based on the one-dimensional model considered in this paper. Higher-dimensional formulations should be studied to confirm the conclusions of this paper. The hopes are high, however, as the gradient continua present rich opportunities to reproduce virtually any dispersion dependence that is vital for the good matching and can not be granted by the non-dispersive classical continua.

References

[1] S.P. Xiao, T. Belytschko, A bridging domain method for coupling continua with molecular dynamics, Comput. Methods Appl. Mech. Engrg. 193 (2004) 1645–1669.

[2] F. Abraham, J. Broughton, N. Bernstein, E. Kaxiras, Spanning the continuum to quantum length scales in a dynamic simulation of brittle fracture, Europhys. Lett. 44 (1998) 783–787.

[3] R.E. Rudd, J.Q. Broughton, Coarse-grained molecular dynamics and the atomic limit of finite elements, Physical Review B 58 (1998), pp 5893–5896.

[4] E.G. Karpov, G.J. Wagner, W.K. Liu, Green's function approach to deriving non-reflecting boundary conditions in molecular dynamics simulations, Int. J. Numer. Meth. Engng 2005; 62:1250–1262.

[5] J. Dominguez, Boundary elements in dynamics, Southampton: Computational Mechanics Publications, 1993.

[6] A.V. Metrikine, H. Askes, One-dimensional dynamically consistent gradient elasticity models derived from a discrete microstructure Part 1: Generic formulation, European Journal of Mechanics A/Solids 21(4) (2002) 589-596.

[7] A.V. Metrikine, H. Askes, An isotropic dynamically consistent gradient elasticity model derived from a 2D lattice, Philosophical Magazine 86 (21-22) (2006) 3259-3286.

[8] M.B. Rubin, P. Rosenau, O. Gottlieb, Continuum model of dispersion caused by an inherent material characteristic length, J. of App.Phys. 77 (1995) 4054–4063.

[9] H.B. Muehlhaus, F. Oka, Dispersion and wave propagation in discrete and continuous models for granular materials, Int.J. of Solids and Structures 33 (1996) 2841–2858.

Asiya M. Kudarova, Institute for Problems in Mechanical Engineering RAS, Bolshoy pr. V.O. 61, 199178, Saint Petersburg, Russia
Andrey V. Metrikine, Delft University of Technology, Faculty of Civil Engineering and GeoSciences, P.O. Box 5048, 2600 GA, The Netherlands

Description of equivalent elastic continuum for graphene lattice

Asiya M. Kudarova Anton M. Krivtsov
asya.kudarova@gmail.com

Abstract

The work contributes to the study of equivalent continuum model that is able to describe the elastic moduli of graphene — monolayer of carbon atoms. The moment interaction between the particles that form the lattice is described by four force constants and depends on the position of particles and their orientation in space. An approach is applied to link the macroscopic moduli and the parameters of interaction at microlevel based on the comparison of the energy of the microstructure and the energy of the equivalent continuous plate. The comparison with structural mechanics approach is carried out and the elastic moduli are derived for the parameters of interaction taken from AMBER force field.

1 Introduction

Graphene is the mother structure of most carbon based materials. A single 2-D sheet of graphene is a hexagonal structure with each carbon atom forming three bonds with its nearest neighbours. In the last decade the enhanced attention has been paid to the study of this material due to its unique properties found (e.g. high conductivity, extremely high strength) and the recent possibility to extract a layer of graphene one atom thick. This has induced the development of theoretical models for graphene as well as the experimental study. The combination of atomistic simulations and continuum elasticity focuses on graphene mechanical properties, especially as for the elastic moduli. The experimental studies of graphene membranes suspended on a silicon substrate with holes has been carried out using atomic force microscope [1]–[3]. The Young Modulus of graphene sheet has been found to be around 350 N/m. As for other elastic moduli, there is still a lack of experimental data.

Different approaches are applied to build analytical models for analysis of carbon structures. The empirical force field models are widely used to describe the mechanical behaviour of the systems containing significant number of atoms [4]. In [5]–[6] such models are proposed based on the parametric many-body potentials for carbon structures [7]–[8] and the elastic moduli are evaluated for the equivalent continuum. The mechanical properties of graphene have been derived from the first principles in [9] – [11]. An equivalent continuum model was proposed in [12]–[14]. In [15]–[16] the molecular model based on AMBER force field constants of interaction for covalent bonds has been linked with the space-frame structural mechanics model and FEM simulations have been carried out. However, there is a huge scattering of the results of theoretical studies. The number of parameters of interatomic potentials used in the studies is relatively large and the meaning of these parameters often remains obscure. Such potentials are usually unable to satisfy all elastic constants of the described material. Three-particle interaction, special case of many-body potential, has been considered in [17]. The effective force constants of interaction have been evaluated from the experimental data to provide exact matching in case of in-plane deformation of graphene.

Covalent bond is a directional bond. This can be allowed for by taking into account a so called moment contribution to the interatomic interaction as an alternative to many-body potential models where the potential energy is a function of the positions of N particles regarded as material points. This contribution is usually implicitly considered when torsional and bending properties

of a bond are taken into account (for example, when a bond is modelled as a beam). In [18] it was proposed to represent a particle in the lattice as a set of material points rigidly connected to each other. The interaction between material points from different sets is described by pairwise potential. As the result the moment component of interaction between the particles is present introducing additional transversal stiffness. Another way to account for the moment interaction at microlevel in an explicit form is to consider rotational degrees of freedom of particles forming the lattice. This approach is described in [19] where the relation between constants of interaction and the elastic moduli of in-plane deformation of graphene lattice are obtained. In this paper the latter approach is applied to derive the equivalent continuum able to describe also out-of-plane deformations of graphene. The material is represented as a set of particles (solids) which interact in terms of forces and torques. A method based on the energies equivalence is applied to obtain the relations between the constants of interaction at microlevel and elastic moduli of continuum corresponding to the discrete structure of graphene.

2 Interatomic potential

The discrete structure of a material is presented as a set of particles with three translational and three rotational degrees of freedom. The interaction between nearest neighbours is taken into account. The bonds between the particles are assumed to be transversely-isotropic for the sake of simplicity. Four force constants are proposed to describe the deformation of a bond: A_1 is the bond stretching resistance force constant, A_2 describes the resistance to shear deformations, C_1 — to torsion, C_2 — to bending of the bond. Potential energy of elastic deformation of a crystal structure per unit cell can be presented as a sum of potential energies of deformation of the bonds between some reference particle in the cell and its nearest neighbours:

$$W = \frac{1}{2V_0} \sum_{\alpha} \Pi_\alpha, \tag{1}$$

where Π_α is a potential of interaction between the particle in the cell and its neighbour with index α, V_0 is a volume per particle in the unit cell of the lattice. In general, there can be more than one particle in the unit cell, lattice with one particle in the unit cell is called simple and otherwise complex. The lattice of graphene contains two particles per unit cell and thus is complex. It consists of two triangular sublattices. The potential Π_α can be presented as a quadratic form of strain vectors and stiffness tensors of the bond

$$\Pi_\alpha = \frac{1}{2}\underline{\varepsilon}_\alpha \cdot \underline{\underline{A}}_\alpha \cdot \underline{\varepsilon}_\alpha + \underline{\varepsilon}_\alpha \cdot \underline{\underline{B}}_\alpha \cdot \underline{\kappa}_\alpha + \frac{1}{2}\underline{\kappa}_\alpha \cdot \underline{\underline{C}}_\alpha \cdot \underline{\kappa}_\alpha. \tag{2}$$

Here $\underline{\underline{A}}_\alpha$, $\underline{\underline{B}}_\alpha$, $\underline{\underline{C}}_\alpha$ are stiffness tensors of the bond α and they contain information about the deformation of the bond in different directions:

$$\begin{aligned} &\underline{\underline{A}}_\alpha = A_1 \underline{n}_\alpha \underline{n}_\alpha + A_2 \left(\underline{\underline{E}} - \underline{n}_\alpha \underline{n}_\alpha\right), \\ &\underline{\underline{C}}_\alpha = C_1 \underline{n}_\alpha \underline{n}_\alpha + C_2 \left(\underline{\underline{E}} - \underline{n}_\alpha \underline{n}_\alpha\right), \qquad a\underline{n}_\alpha = \underline{a}_\alpha, \end{aligned} \tag{3}$$

tensor $\underline{\underline{B}}$ is equal to zero if a lattice has two normal to each other planes of symmetry [20]. It holds true in case of graphene lattice. Vector $\underline{a}_\alpha$ connects two neighbour particles, a is a length of a bond in equilibrium configuration, $\underline{\underline{E}}$ is a unit tensor; $\underline{\varepsilon}_\alpha$, $\underline{\kappa}_\alpha$ are strain vectors and are expressed as follows [20]:

$$\underline{\varepsilon}_\alpha = \underline{u}_\alpha - \underline{u} + \frac{1}{2}\underline{a}_\alpha \times (\underline{\varphi}_\alpha + \underline{\varphi}), \qquad \underline{\kappa}_\alpha = \underline{\varphi}_\alpha - \underline{\varphi}. \tag{4}$$

Here $\underline{u}_\alpha$, $\underline{u}$, $\underline{\varphi}_\alpha$, $\underline{\varphi}$ are translations and rotations of the particle with index α and some reference particle relative to their equilibrium position.

Equations (2) – (4) are substitutted into (1) and thus the potential energy of the system of particles is obtained depending on position of particles $\underline{u}$, $\underline{u}_\alpha$, orientation $\underline{\varphi}$, $\underline{\varphi}_\alpha$, geometry of initial configuration $\underline{a}_\alpha$ and constants of interaction A_1, A_2, C_1, C_2.

3 Towards the macroscale

Let us confront the displacements and rotations of the particles with the displacements and rotations of continuum $\underline{u} = \underline{u}(\underline{r}),\ \underline{\varphi} = \underline{\varphi}(\underline{r})$, where $\underline{r}$ is radius-vector in initial configuration. Then displacements and rotations of neighbour particles are $\underline{u}_\alpha = \underline{u}(\underline{r} - \underline{a}_\alpha),\ \underline{\varphi}_\alpha = \underline{\varphi}(\underline{r} - \underline{a}_\alpha)$. Under long-wave approximation[2] these displacement and rotations can be expressed as follows:

$$\underline{u}_\alpha = \underline{u} + \underline{a}_\alpha \cdot \nabla \underline{u} + \eta \underline{\zeta}, \qquad \underline{\varphi}_\alpha = \underline{\varphi} + \underline{a}_\alpha \cdot \nabla \underline{\varphi} + \eta \underline{\psi}, \tag{5}$$

where ∇ is the nabla operator. Parameter η is equal to 1 for lattices that contain two atoms in the unit cell (complex lattice) and to 0 if there is only one atom in the unit cell of the lattice (simple lattice). Vectors $\underline{\zeta},\ \underline{\psi}$ denote relative displacements and rotations of the particles from different sublattices constitutting complex lattice.

Equations (5) can be substitutted in the energy W derived in the previous section. Vectors $\underline{\zeta},\ \underline{\psi}$ correspond to the minimum of potential energy of the lattice and thus can be found from the system of equations

$$\frac{\partial W}{\partial \underline{\zeta}} = 0, \qquad \frac{\partial W}{\partial \underline{\psi}} = 0. \tag{6}$$

Finally, the energy of the corresponding continuum W can be obtained:

$$W = W(\nabla \underline{u}, \nabla \underline{\varphi}, \underline{\varphi}, A_1, A_2, C_1, C_2). \tag{7}$$

It can be also presented as a quadratic form of stiffness tensors of fourth rank and strain tensors:

$$W = \frac{1}{2} \underline{\underline{\varepsilon}} \cdot\cdot {}^4\underline{\underline{A}} \cdot\cdot \underline{\underline{\varepsilon}} + \underline{\underline{\varepsilon}} \cdot\cdot {}^4\underline{\underline{B}} \cdot\cdot \underline{\underline{\kappa}} + \frac{1}{2} \underline{\underline{\kappa}} \cdot\cdot {}^4\underline{\underline{C}} \cdot\cdot \underline{\underline{\kappa}}. \tag{8}$$

Strain tensors are

$$\underline{\underline{\varepsilon}} = \nabla \underline{u} + \underline{\underline{E}} \times \underline{\varphi}, \qquad \underline{\underline{\kappa}} = \nabla \underline{\varphi}. \tag{9}$$

In order to obtain the relations between coefficients of stiffness tensors at macrolevel and force constants of interaction at microlevel the representations (7) and (8) should be compared.

4 The lattice of graphene

The lattice of graphene is 2D lattice where carbon atoms are located in the nodes of hexagons. Let us introduce orthonormal basis $\{\underline{e}_1,\ \underline{e}_2,\ \underline{e}_3\}$, where $\underline{e}_1$ and $\underline{e}_2$ lie in the plane, $\underline{e}_3$ is normal to the plane containing the lattice. Let us name the axes with the unit vectors $\underline{e}_1,\ \underline{e}_2,\ \underline{e}_3$ as x, y and z, respectively. The vectors $\underline{u},\ \underline{\varphi},\ \underline{a}_\alpha$ can be expressed then

$$\begin{aligned} \underline{u} &= u^x(x,y)\underline{e}_1 + u^y(x,y)\underline{e}_2 + u^z(x,y)\underline{e}_3, \\ \underline{\varphi} &= \varphi^x(x,y)\underline{e}_1 + \varphi^y(x,y)\underline{e}_2 + \varphi^z(x,y)\underline{e}_3, \end{aligned} \tag{10}$$

and vectors $\underline{a}_\alpha$ are

$$\underline{a}_1 = \underline{e}_1, \quad \underline{a}_2 = -\tfrac{1}{2}\underline{e}_1 + \tfrac{\sqrt{3}}{2}\underline{e}_2, \quad \underline{a}_3 = -\tfrac{1}{2}\underline{e}_1 - \tfrac{\sqrt{3}}{2}\underline{e}_2. \tag{11}$$

Derivation of the relations between the coefficients of the stiffness tensors of corresponding continuum and parameters of interactions at microlevel is carried out by comparing the multipliers of similar terms of $u^x_{,x}$, $u^x_{,y}$, $u^y_{,x}$, $u^y_{,y}$, $u^z_{,y}$, $u^z_{,x}$, $\varphi^x_{,x}$, $\varphi^x_{,y}$, $\varphi^y_{,x}$, $\varphi^y_{,y}$, $\varphi^z_{,x}$, $\varphi^z_{,y}$, φ_x, φ_y, φ_z in (7) and (8).

[2]The expansion is valid for the waves with lengthes far larger than interatomic distance a_α in initial configuration which is assumed to be a small parameter.

A comma stands for the first derivative with respect to the coordinate that follows. Finally, the coefficients of the stiffness tensors ${}^4\underline{\underline{A}}$, ${}^4\underline{\underline{C}}$ are expressed as:

$$\begin{aligned}
&A_{1111} = A_{2222} = \tfrac{\sqrt{3}}{6}\tfrac{A_1(A_1+3A_2)}{A_1+A_2}, \quad C_{1111} = C_{2222} = \tfrac{\sqrt{3}}{6}\tfrac{C_1(C_1+3C_2)}{C_1+C_2};\\
&A_{1122} = A_{2211} = \tfrac{\sqrt{3}}{6}\tfrac{A_1(A_1-A_2)}{A_1+A_2}, \quad C_{1122} = C_{2211} = \tfrac{\sqrt{3}}{6}\tfrac{C_1(C_1-C_2)}{C_1+C_2};\\
&A_{1212} = A_{2121} = \tfrac{\sqrt{3}}{6}\tfrac{A_2(A_2+3A_1)}{A_1+A_2}, \quad C_{1212} = C_{2121} = \tfrac{\sqrt{3}}{6}\tfrac{C_2(C_2+3C_1)}{C_1+C_2};\\
&A_{1221} = A_{2112} = \tfrac{\sqrt{3}}{6}\tfrac{A_2(A_1-A_2)}{A_1+A_2}, \quad C_{1221} = C_{2112} = \tfrac{\sqrt{3}}{6}\tfrac{C_2(C_1-C_2)}{C_1+C_2};\\
&A_{3131} = A_{3232} = \tfrac{\sqrt{3}}{3}A_2, \qquad\qquad C_{3131} = C_{3232} = \tfrac{\sqrt{3}}{3}C_2.
\end{aligned} \tag{12}$$

The left column shows nonzero components of tensor ${}^4\underline{\underline{A}}$ and the right one — of tensor ${}^4\underline{\underline{C}}$. The obtained equivalent plate is invariant to the rotation around its normal $\underline{e}_3$ and reflection from itself and from two mutually orthogonal planes. This leads to the same symmetry of stiffness tensors due to Curie's Principle and this symmetry is reflected in the results (12) [21]. The relation between some of the components takes place due to the mentioned isotropy:

$$A_{1212} + A_{1221} = A_{1111} - A_{1122}, \qquad C_{1212} + C_{1221} = C_{1111} - C_{1122}. \tag{13}$$

Another relation can be derived from the system of equations (12):

$$A_{3131} = \frac{A_{1111}^2 - A_{1122}^2}{3A_{1122} + A_{1111}}, \qquad C_{1221} = \frac{C_{1122}(C_{1111} - C_{1122})}{3C_{1122} + C_{1111}}. \tag{14}$$

All the components of tensor ${}^4\underline{\underline{B}}$ turned out to be zero — this can also be predicted by applying the theory of symmetry [21]. Tensor ${}^4\underline{\underline{A}}$ provides a relation between stress tensor $\underline{\underline{T}}$ and strain tensor $\underline{\underline{\varepsilon}}$ and tensor ${}^4\underline{\underline{C}}$ — between couple stress tensor $\underline{\underline{\underline{M}}}$ and strains $\underline{\underline{\kappa}}$:

$$\begin{aligned}
&T_{11} = A_{1111}\varepsilon_{11} + A_{1122}\varepsilon_{22}, \quad T_{22} = A_{2211}\varepsilon_{11} + A_{2222}\varepsilon_{22}, \quad T_{21} = A_{1221}\varepsilon_{12} + A_{1212}\varepsilon_{21}\\
&T_{12} = A_{2121}\varepsilon_{12} + A_{2112}\varepsilon_{21}, \quad T_{13} = A_{3131}\varepsilon_{13}, \qquad\qquad T_{23} = A_{3232}\varepsilon_{23}\\
&M_{11} = C_{1111}\kappa_{11} + C_{1122}\kappa_{22}, \quad M_{22} = C_{2211}\kappa_{11} + C_{2222}\kappa_{22}, \quad M_{21} = C_{1221}\kappa_{12} + C_{1212}\kappa_{21}\\
&M_{12} = C_{2121}\kappa_{12} + C_{2112}\kappa_{21}, \quad M_{13} = C_{3131}\kappa_{13}, \qquad\qquad M_{32} = C_{3232}\kappa_{23}.
\end{aligned} \tag{15}$$

The components of strain tensors $\underline{\underline{\varepsilon}}$, $\underline{\underline{\kappa}}$ are:

$$\begin{aligned}
&\varepsilon_{11} = u^x_{,x}, \quad \varepsilon_{12} = u^y_{,x} - \varphi^z, \quad \varepsilon_{13} = u^z_{,x} + \varphi^y, \quad \varepsilon_{21} = u^x_{,y} + \varphi^z,\\
&\varepsilon_{22} = u^y_{,y}, \quad \varepsilon_{23} = u^z_{,y} - \varphi^x, \quad \kappa_{11} = \varphi^x_{,x}, \qquad \kappa_{21} = \varphi^x_{,y},\\
&\kappa_{12} = \varphi^y_{,x}, \quad \kappa_{22} = \varphi^y_{,y}, \qquad \kappa_{13} = \varphi^z_{,x}, \qquad \kappa_{23} = \varphi^z_{,y}.
\end{aligned} \tag{16}$$

The components of the stiffness tensors have the following physical meaning: A_{1111} describes the stretching properties of the material, A_{1122} — the Poisson effect, A_{1212} and A_{1221} relate shear strains and stresses in the plane determined by vectors $\underline{e}_1$, $\underline{e}_2$ and A_{3131} — in orthogonal plane. C_{1111} describes torsion properties of the material, C_{1221} — analogue of Poisson effect in case of torsions. Let us define bending stiffness of the material D as a coefficient between couple stress in a section orthogonal to $\underline{e}_1$ and strain κ_{12} (or $\underline{e}_2$ and κ_{21}). This coefficient is equal to C_{1212} (or C_{2121}):

$$D = \frac{\sqrt{3}}{6}\frac{C_2(C_2 + 3C_1)}{C_1 + C_2}. \tag{17}$$

There is a lack of experiments to determine all of the macroscopic moduli. In order to reduce the number of independent macroscopic moduli a simpler theory can be taken into consideration. Due to the momentless (symmetric) theory the in-plane moduli of tensor ${}^4\underline{\underline{A}}$ should be invariant to transposition of the pairs of indices 12 and 21. For this purpose a new component A^*_{1212} corresponding to the simpler theory should be taken as $(A_{1212} + A_{1221})/2$:

$$A^*_{1212} = A^*_{1221} = A^*_{2121} = A^*_{2112} = \frac{\sqrt{3}}{3}\frac{A_1 A_2}{A_1 + A_2}. \tag{18}$$

The results for coefifcients A_{1111} and A_{1122} that describe in-plane deformation correspond with the results obtained in [19] where experimental data for bulk graphite was applied to find the values of force constants A_1 and A_2. It turned out that $A_2/A_1 = 0.55$: transversal stiffness of covalent bond is the same order as longitudinal one and thus needs to be taken into account. The analysis of relations (18) shows that the Poisson effect is eliminated when $A_1 = A_2$. The same phenomenon takes place in case of equality of torsion and bending stiffnesses C_1 and C_2: there is no twisting in the direction orthogonal to the direction where twisting moment is applied.

5 Comparison with the structural mechanics approach

The method of the linkage of molecular mechanics and structural mechanics was proposed in [16]–[15] to use the AMBER force field [22] for the simulation of covalent bonds. From the viewpoint of molecular mechanics carbon structure can be regarded as a large molecule consisting of carbon atoms. The interactions between the atoms can be described by some force field. The representation of this field as a sum of potential energies that correspond to different interactions is widely used in literature:

$$U = \sum U_r + \sum U_\theta + \sum U_\varphi + \sum U_\omega + \sum U_{vdw}. \tag{19}$$

Here U_r corresponds to a bond stretching, U_θ is for bond angle bending, U_φ — dihedral angle torsion, U_ω — out-of-plane torsion, U_{vdw} — nonbonded van der Waals interaction. For covalent systems the main contribution comes from the first four terms which include four-body potentials. Under assumption of small deformations the simplest harmonic forms of the energies can be considered. The third and the fourth terms are usually merged to a single equivalent term U_τ. After that three harmonic forms are left:

$$U_r = \frac{1}{2}k_r(\Delta r)^2, \qquad U_\theta = \frac{1}{2}k_\theta(\Delta\theta)^2, \qquad U_\tau = \frac{1}{2}k_\tau(\Delta\varphi)^2, \tag{20}$$

where $k_r,\ k_\theta,\ k_\tau$ are force constants and $\Delta r,\ \Delta\theta,\ \Delta\varphi$ are corresponding strains.

In [15] it is assumed that carbon-carbon bond can be simulated by uniform round beam-like element with parameters EI, EA and GJ, where E is the Young modulus of a beam, I is the moment of inertia J is the polar moment of inertia, G is the shear modulus, A is the cross-section area. This parameters are determined by comparing the energies of the deformation of a bond subjected to pure axial force, to pure bending moment and pure torsion:

$$U_A = \frac{1}{2}\frac{EA}{L}(\Delta L)^2, \qquad U_M = \frac{1}{2}\frac{EI}{L}(2\alpha)^2, \qquad U_T = \frac{1}{2}\frac{GJ}{L}(\Delta\beta)^2. \tag{21}$$

It is taken into account that each energy term in (20) represents individual interaction without cross-interactions and that's why strain energies of structural element under individual forces are considered. L is the length of a beam and is assumed to be equal to 0.142 nm — the length of a covalent bond in graphene. By assuming the equivalences

$$\Delta L \iff \Delta r, \qquad 2\alpha \iff \Delta\theta, \qquad \Delta\beta \iff \Delta\varphi \tag{22}$$

and comparing (20) to (21) the following relations are obtained:

$$\frac{EA}{L} = k_r, \qquad \frac{EI}{L} = k_\theta, \qquad \frac{GJ}{L} = k_\tau. \tag{23}$$

The values for k_r, k_θ, k_τ taken from the AMBER force field [22] are:

$$\begin{aligned} &k_r = 6.52 \cdot 10^{-7}\text{N nm}^{-1}, \qquad k_\theta = 8.76 \cdot 10^{-10}\text{N nm rad}^{-2}, \\ &k_\tau = 2.78 \cdot 10^{-10}\text{N nm rad}^{-2}. \end{aligned} \tag{24}$$

The stiffnesses A_1, A_2, C_1, C_2 can be linked with parameters of the beams and thus with force field constants. For Bernoully-Euler beam the relations between the stiffness constants and parameters of a beam are:

$$A_1 = \frac{EA}{L}, \qquad C_2 = \frac{EI}{L}, \qquad C_1 = \frac{GJ}{L}, \qquad A_2 = \frac{12EI}{L^3}. \tag{25}$$

Comparing (23) and (25) and taking into account (24) the following values for the stiffness coefficients are obtained:

$$A_1 = 652\text{N/m}, \quad A_2 = 521\text{N/m}, \quad C_1 = 2.7 \cdot 10^{-10}\text{N nm}, \quad C_2 = 8.7 \cdot 10^{-10}\text{N nm}. \tag{26}$$

Then the following values for stiffness coefficients of macroscopic material can be obtained:

$$\begin{aligned} &A_{1111} = 355 \quad \text{N/m}, \quad C_{1111} = 2 \cdot 10^{-19} \quad \text{N m}; \\ &A_{1122} = 21 \quad \text{N/m}, \quad C_{1122} = -0.4 \cdot 10^{-19} \quad \text{N m}; \\ &A^*_{1212} = 167 \quad \text{N/m}, \quad C_{1212} = 3.7 \cdot 10^{-19} \quad \text{N m}; \\ &A_{3131} = 301 \quad \text{N/m}, \quad C_{1221} = -1.3 \cdot 10^{-19} \quad \text{N m}. \end{aligned} \tag{27}$$

The results for in-plane moduli A_{1111}, A_{1122} give a good correspondence with the results derived from experimental data for bulk graphite [17]. The negative values of C^*_{1122} and C^*_{1221} do not disrupt the positiveness of the potential energy quadratic form that requires the positiveness of the matrixes of the stiffness tensors.

6 Conclusions

The model of the discrete structure of graphene lattice is considered. Four parameters are introduced to model the linear deformation of the covalent bond. Under assumption of long-wave approximation the equivalent continuum is derived. The relations between the elastic moduli of the continuum and the parameters at microlevel are obtained. Thus, if the experiments allow to calculate the macroscopic parameters of interatomic interactions, the elastic moduli can be determined, and vice versa. The available experimental data allow to determine the in-plane components of tensor ${}^4\underline{\underline{A}}$. Component A_{3131} can be determined then for the present model when parameter A_2 is evaluated using the relations with known macroscopic moduli. There is a need to carry out experiments that are able to estimate the moduli of tensor ${}^4\underline{\underline{C}}$. These moduli can be also estimated if parameters of interaction at microlevel are known, for example, from some new experiments or force fields that are already in use. Additional verification is desirable for the results for the components of tensor ${}^4\underline{\underline{C}}$ derived from the parameters of AMBER force field.

References

[1] I.W. Frank, D.M. Tanenbaum, A.M. Van der Zande, P.L. McEuen Mechanical properties of suspended graphene sheets J. Vac. Sci. Technol. B 25 2558–61 (2007)

[2] Changgu Lee et al. Measurement of the Elastic Properties and Intrinsic Strength of Monolayer Graphene Science 321 385–388 (2008)

[3] M. Poot, H.S.J. van der Zant Nanomechanical properties of few-layer graphene membranes Applied Physics Letters 92(6) (2008)

[4] A.R. Leach, Molecular modelling principles and applications, second edition, Pearson Education Limited 2001

[5] M. Arroyo, T. Belytschko Finite crystal elasticity of carbon nanotubes based on the exponential Cauchy-Born rule Physical Review B 69 (11) (2004)

[6] Y. Huang, J. Wu, K.C. Hwang Thickness of graphene and single-wall carbon nanotubes Physical Review B 74 (24) (2006)

[7] J. Tersoff Empirical interatomic potential for carbon, with application to amorphous carbon Phys. Rev. Lett. 61 2879 (1988)

[8] D.W. Brenner Empirical potential for hydrocarbons for use in simulating the chemical vapor deposition of diamond films Phys. Rev. B 42 9458 (1990)

[9] K.N. Kudin, G.E. Scuseria, B.I. Yakobson C2F, BN, and C nanoshell elasticity from ab initio computations Physical Review B 64 (23) (2001)

[10] G. Van Lier, C.V. Alsenoy, V.V. Doren, P. Geerlings Ab initio study of the elastic properties of single-walled carbon nanotubes and graphene Chemical Physics Letters 326(1-2): p. 181–185 (2000)

[11] F. Liu, P.M. Ming, J. Li Ab initio calculation of ideal strength and phonon instability of graphene under tension Physical Review B 76(6) (2007)

[12] C.D. Reddy, S. Rajendran, K.M. Liew Equilibrium configuration and continuum elastic properties of finite sized graphene Nanotechnology 17(3): p. 864–870(2006)

[13] G.M. Odegard , T.S. Gates, L.M. Nicholson, K.E. Wise Equivalent-nontinuum modeling of nano-structured materials Comp. Sci. and Tech. 62 1869–1880(2002)

[14] R.V. Goldstein, A.V. Chentsov, Discrete-continual model of nanotube, Izv. RAS, MTT 2005, No. 4, p. 57-74.(in Russian)

[15] K.I. Tserpes, P. Papanikos, Finite element modeling of single-walled carbon nanotubes, Composites: Part B 36 (2005) 468–477

[16] Chunyu Li, Tsu-Wei Chou, A structural mechanics approach for the analysis of carbon nanotubes, Int. J. of Solids and Structures 40 (2003) 2487–2499

[17] I.E. Berinskiy, A.M. Krivtsov, A.M. Kudarova, Determination of macroscopic characteristics for graphene layer using angle-depending atomic interactions. Proceedings of XXXVI International summer school-conference APM'2008. p. 122-132

[18] I.E. Berinskiy, E.A. Ivanova, A.M. Krivtsov, N.F. Morozov, Application of moment interaction to the construction of a stable model of graphite crystal lattice, Mechanics of Solids, 2007, Vol. 42, No. 5, pp. 663–671

[19] E.A. Ivanova, A.M. Krivtsov, N.F. Morozov, Derivation of macroscopic relations of the elasticity of complex crystal lattices taking into account the moment interactions at the microlevel. J. of App. Math. and Mech., 2007; 71 (4). pp. 543-561

[20] E.A. Ivanova, A.M. Krivtsov, N.F. Morozov, A.D. Firsova, Description of crystal packing of particles takin into account moment interactions, Mechanics of solids, 4, 2003

[21] P.A. Zhilin, The foundations of the theory of shells, St. Petersburg, 2006 (in Russian)

[22] Cornell WD, Cieplak P, Bayly CI, Gould IR, Merz KM, Ferguson DM, et al. A second generation force-field for the simulation of proteins, nucleic acids and organic molecules. J Am Chem Soc 1995;117:5179–97

Asiya M. Kudarova, Institute for Problems in Mechanical Engineering RAS, Bolshoy pr. V.O. 61, 199178, Saint Petersburg, Russia
Anton M. Krivtsov, Institute for Problems in Mechanical Engineering RAS, Bolshoy pr. V.O. 61, 199178, Saint Petersburg, Russia

Comment on the calculation of forces for multi-body interatomic potentials

Vitaly A. Kuzkin
kuzkinva@gmail.com

Abstract

The system of particles (atoms) interacting via multi-body interatomic potential of general form is considered. Possible variants of partition for the total force acting on a single particle into pair contributions are discussed. Two definitions for the force acting between a pair of particles are compared. The forces coincide only if the particles interact via pair or embedded-atom potentials. However in literature both definitions are used in order to determine Cauchy stress tensor. A simplest example of the linear pure shear of perfect square lattice is analyzed. It is shown that, Hardy's definition for the stress tensor gives different results depending on the radius of localization function. The differences strongly depend on the way of the partition for the total force.

1 Introduction

Classical molecular dynamics (MD) [1, 2], based on the numerical solution of the Newtonian equations of motion for many interacting particles, has been widely used for physical modeling and simulation for several decades. Interactions between particles are usually described by so-called empirical interatomic potentials. A variety of potentials has been proposed: starting with simple pair potentials [3], more accurate embedded-atom potential [4] and ending with complex bond-order potentials [5, 6, 7]. The MD simulation technique requires calculation of the total force acting on every particle. If the potential energy is known, then the total force $\mathbf{F}_i$ acting on particle number i is determined by the following formula [8]

$$\mathbf{F}_i = -\frac{\partial U(\{\mathbf{R}_i\}_{i=1}^N)}{\partial \mathbf{R}_i}, \tag{1}$$

where $\{\mathbf{R}_i\}_{i=1}^N$ is the set of particle radius-vectors; N is the total number of particles; U is the total potential energy of the system. Thus formula (1) is sufficient for MD simulation. However interpretation and verification of simulation results are not so straightforward. The usual way is to calculate continuum variables, such as stress tensor and heat flux, during MD simulation and compare the results with predictions of continuum theory. This problem was addressed by many authors starting from the late 19th century [9]. Comprehensive reviews on this topic may be found in papers [10, 11]. In the majority of approaches it is assumed that the total force can be expressed by the summation of pair contributions $\mathbf{F}_{ij}$ satisfying Newton's third law (see, for example, Hardy's formalism [12])

$$\mathbf{F}_i = \sum_{j \neq i} \mathbf{F}_{ij}, \qquad \mathbf{F}_{ij} = -\mathbf{F}_{ji}. \tag{2}$$

Here and below the summation is carried out over all particles in the system. In the paper [11] it was stated that partition (2) can always be carried out. However the physical meaning of $\mathbf{F}_{ij}$ is clear only for pair interactions. Moreover it was stated in [16] that division (2) may be nonunique. Let us explain the reason for the ambiguities. Any system with pair interactions is equivalent to the set of particles connected by longitudinal springs. Therefore $\mathbf{F}_{ij}$ is a force caused by the

deformation of the spring. In contrast the simplest system with multi-body interactions can be imagined as the set of particles connected by longitudinal and angular springs between the bonds. Every angular spring belongs to three particles and causes the forces acting on all of them. Even in this simple case partition (2) is not straightforward. Note that commonly used multi-body potentials, like Tersoff [6], are even more complex. Several definitions for $\mathbf{F}_{ij}$ were proposed in literature. In the paper [13] the quantity $\mathbf{F}_{ij}$, satisfying equation (2), was introduced for systems with three-body forces [5, 6, 7]. The generalization for N-body forces was carried out in [14]. Another definition for $\mathbf{F}_{ij}$ was given in papers [15] and [16]. Both expressions for $\mathbf{F}_{ij}$ mentioned above were used in order to calculate Cauchy stress tensor for a discrete system with multi-body interactions [13], [16][3]. However the comparison of these approaches for calculation of stresses and the analysis of different definitions for $\mathbf{F}_{ij}$ were not carried out.

In the present paper the problem of the partition for the total force into pair contributions is discussed in detail. Two definitions for the force $\mathbf{F}_{ij}$ acting between a pair of particles (material points[4]) are considered. It is shown that the partition is not unique and does depend on the way the potential energy is represented. The influence of the partition on the value of stresses is analyzed for the simplest example — a linear pure shear of a square lattice.

2 Different approaches for partition of the total force

Let us compare possible definitions for the force $\mathbf{F}_{ij}$ acting between two particles. Consider the approach proposed in the paper [13] for the case of three-body interactions. It was shown that both the Stillinger-Weber [5] potential and the Tersoff [6] potential can be expressed in the following form

$$U = \frac{1}{2}\sum_i U_i, \quad U_i = \sum_{j\neq i; k\neq i,j} U_{ijk}(R_{ij}, R_{ik}, R_{kj}). \tag{3}$$

Here and below $\mathbf{R}_{ij} = \mathbf{R}_i - \mathbf{R}_j, R_{ij} = |\mathbf{R}_{ij}|$. Then using definition (1) the total force acting on the i-th particle can be represented in form (2), where the expression for $\mathbf{F}_{ij}$ has form

$$\mathbf{F}_{ij} = -\frac{1}{2}\sum_{k\neq i,j} \frac{\partial(U_{ijk}+U_{kij}+U_{kji}+U_{jik}+U_{ikj}+U_{jki})}{\partial R_{ij}}\mathbf{e}_{ij}. \tag{4}$$

Here and below $\mathbf{e}_{ij} \stackrel{\text{def}}{=} \mathbf{R}_{ij}/R_{ij}$. The definition for the force $\mathbf{F}_{ij}$ acting between particles i and j arises in a natural way while calculating the derivative. On the other hand in the paper [13] it was shown that the same results can be obtained using the following definition

$$\mathbf{F}_{ij} \stackrel{\text{def}}{=} -\frac{\partial U}{\partial R_{ij}}\mathbf{e}_{ij}. \tag{5}$$

One can see that equations (2) are satisfied and furthermore $\mathbf{F}_{ij}$ is central, i.e. parallel to the vector connecting particles i and j. The above mentioned approach was generalized in the paper [14]. Let us assume that the total potential energy depends on all the interatomic distances in the system, i.e.

$$U = U(\{R_{kn}\}_{k,n>k}). \tag{6}$$

Formula (6) is the most general form for potential energy of the atomic system. According to definition (1) the total force $\mathbf{F}_i$ is

$$\mathbf{F}_i = -\sum_{k,j>k} \frac{\partial U}{\partial R_{kj}}\frac{\partial R_{kj}}{\partial \mathbf{R}_i} = -\sum_{j\neq i} \frac{\partial U}{\partial R_{ij}}\mathbf{e}_{ij}. \tag{7}$$

One can see that again definition (5) naturally follows from the derivation. Thus in general case (6) the total force can be expressed in form (2).

[3] Calculations are carried out in the Appendix of the paper [16].

[4] Note that particles with rotational degrees of freedom, internal structure, etc. are not considered.

The partition discussed above requires the potential energy U to be represented as a function of all the interatomic distances in system (6). The requirement is automatically satisfied in the case of pair potentials [3] and the embedded-atom potential [4]. However representation (6) may be inconvenient in the case of bond-order potentials such as Stillinger-Weber [5] and Tersoff [6], which depend on angles between bonds. Let us consider the approach proposed in papers [15] and [16]. Assume that the total potential energy of the system has the form

$$U = \sum_i U_i(\{\mathbf{R}_{ij}\}_{j\neq i}). \tag{8}$$

Obviously all potentials mentioned above can be represented in form (8). In contrast to the previous approach, the geometry of the atomic system should be represented via vectors $\{\mathbf{R}_{ij}\}_{j\neq i}$, but not interatomic distances. At first glance it seems that both approaches are equivalent. Let us show that in general this is not true. Calculating the total force $\mathbf{F}_i$ using definition (1) and expression (8) one obtains

$$\mathbf{F}_i = -\sum_j \sum_{k\neq j} \frac{\partial U_j}{\partial \mathbf{R}_{jk}} \cdot \frac{\partial \mathbf{R}_{jk}}{\partial \mathbf{R}_i} = \sum_{j\neq i} \left(\frac{\partial U_j}{\partial \mathbf{R}_{ji}} - \frac{\partial U_i}{\partial \mathbf{R}_{ij}} \right), \quad \mathbf{F}_{ij} \stackrel{\text{def}}{=} \frac{\partial U_j}{\partial \mathbf{R}_{ji}} - \frac{\partial U_i}{\partial \mathbf{R}_{ij}}. \tag{9}$$

One can see that introduced definition for $\mathbf{F}_{ij}$ satisfies Newton's third law, i.e. $\mathbf{F}_{ij} = -\mathbf{F}_{ji}$. It can be shown that forces $\mathbf{F}_{ij}$ are central in the case of pair potentials and embedded-atom potential. Moreover in these particular cases definitions (5) and (9) exactly coincide. However in general this is not true. Note that the partition of the total energy (8) is not unique. According to formula (9) the partition can, in general, affect the value of the force $\mathbf{F}_{ij}$. However the majority of commonly used potentials are based on partition (8) as well. For example, in the case of the Tersoff potential and the Stillinger-Weber potential the partition is determined by formula (3). The comparison of different partitions will be carried out below for a simple example (see formulas (15), (16)).

Let us compare definitions (5), (9) in the case of three-body potentials. Rewriting the expression for potential energy (3) in the form analogous to (8) one obtains

$$U = \sum_i U_i, \quad U_i = \frac{1}{2} \sum_{k,n\neq k} \widetilde{U}_{ikn}(\mathbf{R}_{ik}, \mathbf{R}_{in}), \quad \widetilde{U}_{ikn}(\mathbf{R}_{ik}, \mathbf{R}_{in}) = U_{ikn}(R_{ik}, R_{in}, R_{kn}). \tag{10}$$

One can show that in this case expression (9) for $\mathbf{F}_{ij}$ takes the form

$$\mathbf{F}_{ij} \stackrel{\text{def}}{=} \frac{1}{2} \sum_{k\neq i,j} \left[\frac{\partial}{\partial \mathbf{R}_{ji}} \left(\widetilde{U}_{jik} + \widetilde{U}_{jki} \right) - \frac{\partial}{\partial \mathbf{R}_{ij}} \left(\widetilde{U}_{ijk} + \widetilde{U}_{ikj} \right) \right]. \tag{11}$$

Let us substitute the last formula from (10) in (11) and calculate the derivatives. Then $\mathbf{F}_{ij}$ can be expressed in the following form

$$\mathbf{F}_{ij} \stackrel{\text{def}}{=} -\frac{1}{2} \sum_{k\neq i,j} \left[\frac{\partial \left(U_{ijk} + U_{ikj} + U_{jik} + U_{jki} \right)}{\partial R_{ij}} \mathbf{e}_{ij} + \right.$$
$$\left. + \frac{\partial \left(U_{jik} + U_{jki} \right)}{\partial R_{ik}} \mathbf{e}_{ik} + \frac{\partial \left(U_{ijk} + U_{ikj} \right)}{\partial R_{kj}} \mathbf{e}_{kj} \right]. \tag{12}$$

One can see that expressions (4) and (12) are different. In particular, from (4) it follows that forces $\mathbf{F}_{ij}$ are parallel to $\mathbf{R}_{ij}$. According to (12) this is not true. Further these statements will be explicitly shown for a simple example (see equations (14), (15), (16)).

3 Calculation of Cauchy stress tensor

Let us consider practical consequences of different ways of partition for the total force. It was mentioned above that results of MD simulation are usually compared with predictions of continuum theory. Equivalent continuum quantities, such as Cauchy stress tensor, are calculated for this purpose. The stress tensor characterizes external forces acting on the material surface surrounding

the volume selected from the continuum media. Therefore the forces should be divided into internal and external in order to calculate stress. The analogous situation occurs if one defines equivalent stress tensor for discrete system. Obviously, it is impossible to express stress tensor in terms of the total forces acting on the particles. Therefore partition (2) is required. It was shown above that the partition is not unique. Thus we obtain the result that stresses in a material can depend on the choice of definition for $\mathbf{F}_{ij}$. Let us consider the simplest example, notably linear pure shear of a perfect zero-temperature square lattice. Let particles interact via angular springs connecting two neighboring bonds. Only nearest neighbors are taken into account. Longitudinal springs may also be added but their contribution to forces $\mathbf{F}_{ij}$ is the same for both expressions (5), (9). Let us consider particle number 0 with radius-vector $\mathbf{R}_0$ and denote its neighbors as in Fig. 1. Note that

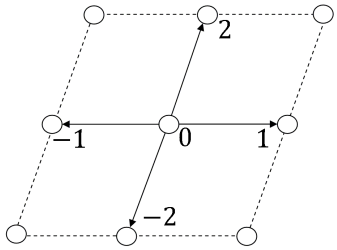


Figure 1: Particle number 0 and its nearest neighbors.

this numbering takes symmetry into account, for example, $\mathbf{R}_{01} = -\mathbf{R}_{0(-1)}$. Assume that potential energy of the spring connecting bonds $\mathbf{R}_{01}$ and $\mathbf{R}_{02}$ is given by the following formula

$$U_{012} = \frac{c}{2}\left(\mathbf{e}_{01}\cdot\mathbf{e}_{02}\right)^2 = \frac{c}{2}\left(\frac{R_{01}^2 + R_{02}^2 - R_{12}^2}{2R_{01}R_{02}}\right)^2. \tag{13}$$

In the case of small deformations formula (13) corresponds to the energy of harmonic angular spring with stiffness c. Let us derive expressions for forces $\mathbf{F}_{01}, \mathbf{F}_{02}, \mathbf{F}_{12}, \mathbf{F}_{1(-2)}$. The remaining forces can be obtained using symmetry or Newton's third law, for example, $\mathbf{F}_{12} = \mathbf{F}_{(-2)(-1)}, \mathbf{F}_{01} = -\mathbf{F}_{10}$. First let us use definition (5). Substituting formula (13) into formula (4) and linearizing the resulting expression in the case of small shear ($\varphi \stackrel{\text{def}}{=} \arcsin(\mathbf{e}_{01}\cdot\mathbf{e}_{02}), \varphi \ll 1$) one obtains

$$\mathbf{F}_{01} \approx 0, \quad \mathbf{F}_{02} \approx 0, \quad \mathbf{F}_{12} \approx \frac{2\sqrt{2}c\varphi}{R}\mathbf{e}_{12}, \quad \mathbf{F}_{1(-2)} \approx -\frac{2\sqrt{2}c\varphi}{R}\mathbf{e}_{1(-2)}, \tag{14}$$

where $R = R_{01} = R_{02}$. Here and below terms of order higher than φ are neglected. It is clear that forces (14) are central.

Let us use definition (9). It was mentioned above that representation (8) of the total energy used in formula (9) is not unique. Let us compare two possible ways of the partition for the total energy. In the case under consideration particle number 0 is surrounded by four nearest neighbors and four corresponding spring. First, let us assume that the energy of the springs contribute to energy U_0 of particle number 0 only. This way of partition is the simplest one and it is similar to the partition used in the definition for the Tersoff potential and the Stillinger-Weber potential (10). Calculating forces $\mathbf{F}_{01}$, $\mathbf{F}_{02}$, $\mathbf{F}_{12}$, $\mathbf{F}_{1(-2)}$ in the framework of the assumptions used during the derivation of formula (14) one obtains

$$\mathbf{F}_{01} \approx -\frac{4c\varphi}{R}\mathbf{e}_{02}, \quad \mathbf{F}_{02} \approx -\frac{4c\varphi}{R}\mathbf{e}_{01}, \quad \mathbf{F}_{12} = \mathbf{F}_{1(-2)} = 0. \tag{15}$$

Obviously forces (15) are non-central and are not equal to the previous result (14). Note that in formula (15) forces $\mathbf{F}_{12}, \mathbf{F}_{1(-2)}$ are exactly equal to zero. The second way of partition for the total energy was proposed in the paper [16]. Energy U_{012} of the spring was divided between particles number 0, 1 and 2 in equal portions. Calculating the forces for this case one obtains

$$\mathbf{F}_{01} \approx -\frac{8c\varphi}{3R}\mathbf{e}_{02}, \quad \mathbf{F}_{02} \approx -\frac{8c\varphi}{3R}\mathbf{e}_{01}, \quad \mathbf{F}_{12} \approx \frac{2\sqrt{2}c\varphi}{3R}\mathbf{e}_{12}, \quad \mathbf{F}_{1(-2)} \approx -\frac{2\sqrt{2}c\varphi}{3R}\mathbf{e}_{1(-2)}. \tag{16}$$

Note that in contrast to formula (15) forces $\mathbf{F}_{12}, \mathbf{F}_{1(-2)}$ determined by formula (16) are not equal to zero.

Let us calculate shear stress acting on crystal's cross-section with normal $\mathbf{e}_{01}$. According to classical continuum mechanics definition, the shear stress acting on the cross-section is equal to the component of the force parallel to vector $\mathbf{e}_{02}$ per unit length. One can prove using formulas (14), (15), (16) that in all the cases the absolute value of shear stress τ can be expressed as

$$\tau = C_{44}^{*}|\varphi|, \quad C_{44}^{*} \stackrel{\text{def}}{=} \frac{4c}{R^2}. \tag{17}$$

The second formula from (17) coincides with the well-known expression for elastic constant C_{44} of the square lattice, obtained, for example, in [17]. Index star is used in order to mark the exact solution. Thus, at least in the case under consideration stresses calculated using different expressions for $\mathbf{F}_{ij}$ are equal.

Application of mentioned above definition for the stress is not very convenient, especially for dynamical problems involving large thermal motion, structural transformations, fracture, etc. Therefore in practice different approaches for calculation of stress are used (see papers [10, 11] for detailed reviews). In particular, Hardy's formalism [12] is frequently applied [11, 13, 16]. In papers [13, 16] it was shown that in the framework of Hardy's formalism the potential part of Cauchy stress tensor at spatial point $\mathbf{R}_0$ has the form

$$\boldsymbol{\sigma}_{pot}(\mathbf{R}_0, t) = -\frac{1}{2}\sum_i \sum_{j \neq i} \mathbf{F}_{ij}\mathbf{R}_{ij} \int_0^1 \psi(\lambda \mathbf{R}_{ij} + \mathbf{R}_j - \mathbf{R}_0) d\lambda, \tag{18}$$

where ψ is so-called localization function (see [16] for details). Formula (18) was used in the paper [13] and in the Appendix of the paper [16]. However the quantity $\mathbf{F}_{ij}$ has different meanings in them. Formula (5) was used as a definition for $\mathbf{F}_{ij}$ in the paper [13]. In contrast in the paper [16] quantity $\mathbf{F}_{ij}$ was calculated using formula (9). It was shown above that, in general, forces calculated with the use of (5) and (9) are different. Thus corresponding stress tensors are also different. The accurate comparison of the stress tensors will be addressed in a separate paper. In the present work only the simplest example is analyzed.

Let us return to the example of linear pure shear of the square lattice. Consider Cauchy stress tensor at the point $\mathbf{R}_0$, where particle number 0 is placed. One can prove substituting formulas (14), (15), (16) into formula (18) that in all these cases stress tensor is symmetric. Note that, in general, this is not obvious as forces (15) and (16) are non-central. Let us calculate elastic constant C_{44} of the system as it completely determines stresses in the case under consideration. The exact solution of this problem is given by the second formula from (17). For simplicity the radial step function was used as a localization function. Function ψ is equal to $1/(\pi r_L^2)$ inside the localization volume and zero in the remaining space. Here and below r_L is radius of the localization volume. The elastic constant calculated with different values of r_L is shown in Fig. 2. One can see from Fig. 2 that for small r_L/R elastic constants calculated using expressions (5) and (9) for $\mathbf{F}_{ij}$ are different. Furthermore in the second case elastic constant C_{44} depend on the partition for the total energy. However the expressions converge to the same value C_{44}^{*} with increasing radius of localization function. Note that the elastic constant that corresponds to definition (5) converges to the exact solution more rapidly. The practical consequence of this fact is that the first approach requires a smaller value of r_L than the second one. Therefore the first approach is more efficient from computational point of view.

4 Results and discussion

Let us summarize the results. The problem of the partition for forces acting in the discrete system with multi-body interactions into pair contributions is analyzed. Two methods for partition, differing in the way of representation for the potential energy U, are discussed. It is shown that in the framework of both methods the total force $\mathbf{F}_i$ is expressed as a sum of pair contributions $\mathbf{F}_{ij}$. In both cases the definition for $\mathbf{F}_{ij}$ is rather natural as the analog of Newton's third law is satisfied, i.e. $\mathbf{F}_{ij} = -\mathbf{F}_{ji}$. However the definitions coincide only in the case of pair potentials and embedded-atom potential. In particular, according to the approach proposed in papers [13, 14] forces $\mathbf{F}_{ij}$ are

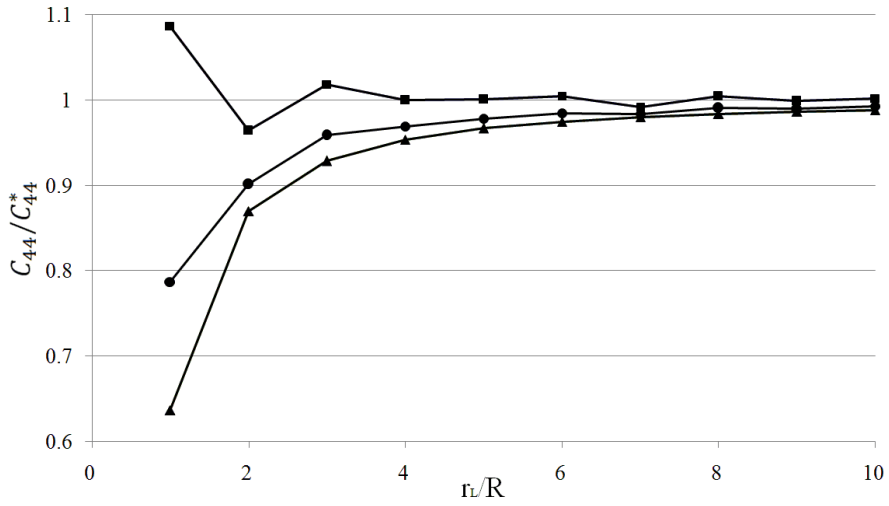


Figure 2: Calculated elastic constant C_{44} divided by the exact solution C^*_{44}. Squares, triangles and circles correspond to elastic constant calculated using expressions (14), (15), (16) respectively.

always central. In the framework of the approach proposed in papers [15, 16] forces $\mathbf{F}_{ij}$ are, in general, non-central. The difference was explicitly shown in the case of three-body potentials. Thus the partition mentioned above is not unique. It depends on the representation of the potential energy. The influence of the partition on the value of stress tensor is analyzed for the simplest example of linear pure shear of perfect zero-temperature square lattice. Two definitions for the stress are considered. If the stress is calculated as a force acting on the cross-section of the crystal per unit length then all expressions for $\mathbf{F}_{ij}$ considered above lead to exactly the same value of stress. In contrast, Hardy's definition (18) gives different values of stress depending on the size of localization volume. The differences depend strongly on the way of force definition. Accurate comparison of different expressions for stress tensor in the case on nonlinear deformation involving thermal motion is addressed in our future work.

Finally let us note that in the case of multi-body interactions a common point of view on the definition for the force acting between two particles does not exist. Summarizing the results of the present paper one can formulate several advantages of definition (5). First, it was mentioned that forces defined by formula (5) are central. In this case equation of angular momentum balance is satisfied for any subsystem of the discrete system [18]. It leads, in particular, to unconditional symmetry of corresponding Cauchy stress tensor. Note that in the framework of classical continuum mechanics the symmetry is required [18]. On the other hand, in the paper [16] it was shown that definition (9) is more appropriate for the formulation of equivalent micromorphic continuum theory for discrete systems. The second appealing feature of definition (5) is that, at least in the considered case, corresponding stress tensor converges to the exact solution more rapidly than in the case of definition (9). In the last case it is shown that the convergence rate depend on the way of partition for the total energy.

Acknowledgements

The author is deeply grateful to Prof. Y. Chen, Prof. W.G. Hoover, Prof. E.A. Ivanova, Prof. A.M. Krivtsov and Prof. J.A. Zimmerman for useful discussions and inspiration.

References

[1] Hoover W.G. Molecular Dynamics. Vol. 258 of Lecture Notes in Physics, Springer–Verlag, Berlin, 1986, 138 p.

[2] Allen M.P., Tildesley D.J. Computer Simulation of Liquids. Clarendon Press, Oxford, 1987, 385 p.

[3] Lennard-Jones J. The determination of molecular fields I. From the variation of the viscosity of a gas with temperature, Proc. R. Soc. Lond. A, Vol. 106, 1924, pp. 441–462.

[4] Daw M.S., Baskes M.I. Embedded-atom-method: derivation and application to impurities, surfaces and other deffects in metals. Phys. Rev. B, Vol. 29, No. 12, 1986, pp. 6443–6453.

[5] Stillinger F.H., Weber T.A. Computer simulation of local order in condensed phases of silicon. Phys. Rev. B, Vol. 31, 1985, pp. 5262–5271.

[6] Tersoff J. New empirical model for structural properties of silicon. Phys. Rev. Lett, Vol. 56, No. 6, 1986, pp. 632–635.

[7] Brenner D.W. Empirical potential for hydrocarbons for use in simulating the chemical vapour deposition in diamond films. Phys. Rev. B, Vol. 42, No. 15, 1990, pp. 9458-9471.

[8] Landau L.D., Lifshitz E.M. Mechanics, Vol. 1, 3ed., Pergamon, 1976, 197 p.

[9] Clausius R.J.E. On a mechanical theorem applicable to heat, Phil. Mag., Vol. 40, 1870, pp. 122–127.

[10] Zhou M. A new look at the atomic level virial stress: on continuum-molecular system equivalence, Proc. R. Soc. Lond. A, 459, 2003, pp. 2347–2392.

[11] Zimmerman J.A., Webb E.B., Hoyt J.J., Jones R.E., Klein P.A., Bammann D.J. Calculation of stress in atomistic simulation. Model. Simul. Mater. Sci. Eng., Vol. 12, 2004, pp. 319–332.

[12] Hardy R.J. Formulas for determining local properties in molecular-dynamics simulations: shock waves. J. Chem. Phys., Vol. 76, No. 1, 1982, pp. 622–628.

[13] Chen Y. Local stress and heat flux in atomistic systems involving three-body forces. J. Chem. Phys, Vol. 124, 2006, 054113.

[14] Delph T.J. Conservation laws for multibody interatomic potentials. Model. Simul. Mater. Sci. Eng., Vol. 13, 2005, pp. 585–594.

[15] Kuzkin V.A., Krivtsov A.M. Thermo-mechanical effects in perfect crystals with arbitrary multibody potential. Proc. of Joint U.S. Russia conference on Advances in Material Science, Prague, 2009, pp. 30-34.

[16] Zimmerman J.A., Jones R.E., Templeton J.A. A material frame approach for evaluating continuum variables in atomistic simulations. J. Comp. Phys., Vol. 229, 2010, pp. 2364–2389.

[17] Krivtsov A.M. Elastic properties of monoatomic and diatomic crystals: tutorial. Polytechnic University press, S.Pb., 2009, 124 p. [in Russian]

[18] Truesdell C. A first course in rational continuum mechanics, Pure and Applied Mathematics, Academic Press, New-York 1977, 295 p.

Vitaly A. Kuzkin, V.O., Bolshoj pr., 61, St. Petersburg, Russia

Generalised Fractional Elements in Rheological Modelling of Polymer Creep

Carsten Kröner Holm Altenbach Konstantin Naumenko Andreas Kutschke
carsten.kroener@iw.uni-halle.de, holm.altenbach@iw.uni-halle.de,
konstantin.naumenko@iw.uni-halle.de, andreas.kutschke@iw.uni-halle.de

Abstract

Viscoelasticity of polymers is often modelled with rheological elements such as Newtonian dashpots and Hookean springs. This way of modelling is reasonable because of the physical background of the basic elements. One major problem especially in creep problems is the large number of these elements needed to cover a wide relaxation spectrum. The introduction of fractional elements leads to significant reduction of parameters to model several time decades. The substitution of dashpots through fractional elements changes the order of the resulting differential equations from integer numbers to fractional ones. This change in the underlying differential equations results in changes of properties which in turn influence techniques to gain a solution. Here the rheological standard model is used as an example to demonstrate the disposal of a fractional element to simulate a one-dimensional tensile creep experiment. The results of the fractional model are compared to experimental data for Ultramid A3K.

1 Introduction

The mechanical response of thermoplastic polymers due to a loading is characterised by two different types of deformation. After the loading an instantaneus, elastic response is observable. Thereby the chains of the polymer coil are stretched to a thermodynamically inappropriate, recoverable status. The degree of this deformation is limited by the free length of entanglements. During time, deformation increases as long as the loading is present. In this process polymer chains are pulled out of their coils along the entanglements with other chains. This mechanism is responsible for the observed viscous flow of thermoplastic polymers. When unloading an elastic retraction and again a time dependent, viscous recovery can be monitored. For the presence of elastic as well as viscous deformations this behaviour is called visoelasticity.

When modelling viscoelasticity rheological equivalent devices are often used to represent the behaviour of the material. Such models possess a clear physical background. Therefore they are well understood and quite popular. Here only creep as one aspect of viscoelasticity is investigated.

These rheological devices consist always of the same basic elements: on the one hand a Hookean spring and on the other hand a Newtonian dashpot. They are described by Eq. (1) and Eq. (2), respectively:

$$\frac{d^0}{dt^0}\varepsilon = \frac{\sigma}{E} \tag{1}$$

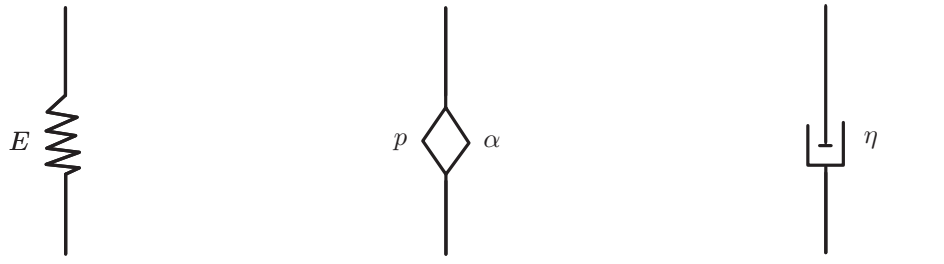
$$\frac{d^1}{dt^1}\varepsilon = \frac{\sigma}{\eta} \tag{2}$$

When comparing the underlying differential equations for these two elements a similarity between them is obvious. They only differ in the parameter which connects stresses and strains and the order of their derivative of ε, namely $\alpha = 0$ for the spring and $\alpha = 1$ for the dashpot. In order to

understand what a fractional element is $\alpha = 0$ and $\alpha = 1$ can be interpreted as limits of the order of the derivative:

$$\frac{d^\alpha}{dt^\alpha}\varepsilon = \frac{\sigma}{p},\ \alpha \in \mathbb{R},\ 0 \leq \alpha \leq 1 \tag{3}$$

Therefore the fractional element is often interpreted as an interpolating element between spring and dashpot. A comparison of this is given in Fig. 1.



Hookean spring | Fractional element | Newtonian dashpot

$$\frac{d^0}{dt^0}\varepsilon = \frac{\sigma}{E} \qquad \frac{d^\alpha}{dt^\alpha}\varepsilon = \frac{\sigma}{p},\quad \alpha \in \mathbb{R},\quad 0 \leq \alpha \leq 1 \qquad \frac{d^1}{dt^1}\varepsilon = \frac{\sigma}{\eta}$$

Figure 1: Comparison of basic rheological elements

2 Definitions, Properties, Solution

2.1 Definition of fractional derivatives

There are several ways to receive a definition of a fractional derivative. The most famous is probably the definition from Grünwald [1]. This approach is very clearly explained in [2] and [3]. The starting point of this approach is the definition of the differential quotient for the first

$$\frac{d^1 f(t)}{dt^1} = \lim_{\Delta t \to 0} \frac{f(t) - f(t - \Delta t)}{\Delta t} \tag{4}$$

and the second

$$\frac{d^2 f(t)}{dt^2} = \lim_{\Delta t \to 0} \frac{f(t) - 2f(t - \Delta t) + f(t - 2\Delta t)}{\Delta t^2} \tag{5}$$

derivative. This definition is generalised with the help of the binomial coefficient

$$\frac{d^n f(t)}{dt^n} = \lim_{\Delta t \to 0} \left[\frac{1}{\Delta t^n} \sum_{j=0}^{n} (-1)^j \binom{n}{j} f(t - j\Delta t) \right]. \tag{6}$$

In Eq. (6) the Gamma function Γ can be introduced to allow real numbers. Additionally the time increment is replaced by t/N, where N is the number of calulated increments. Finally the derivative is definded by:

$$\frac{d^\alpha f(t)}{dt^\alpha} = \lim_{N \to \infty} \left[\left(\frac{t}{N} \right)^{-\alpha} \sum_{j=0}^{N-1} A_{j+1} f\left(t - j\left(\frac{t}{N} \right) \right) \right] \tag{7}$$

with the Grünwald coefficients

$$A_{j+1} = \frac{\Gamma(j - \alpha)}{\Gamma(-\alpha)\Gamma(j + 1)}. \tag{8}$$

Another possible definition starts with the definition of fractional integration [4]. Here the formula of Cauchy for repeated integration builds the basis.

$$I^n \varepsilon(t) = \frac{1}{(n-1)!} \int_0^t (t-\tau)^{n-1} \varepsilon(\tau)\, d\tau \tag{9}$$

Again the factorial function is replaced by the Γ function and n is replaced by the fractional order of integration α:

$$I^\alpha \varepsilon(t) = \frac{1}{\Gamma(\alpha)} \int_0^t (t-\tau)^{\alpha-1} \varepsilon(\tau)\, d\tau \tag{10}$$

Based on this integration operator the fractional differential operator can be derived. Combining the fractional integration operator with the common differential operator results in a fractional differential operator. There are two possible definitions depending on the arrangement of the used operators:

$$D^\alpha = \frac{d^m}{dt^m} I^{m-\alpha}\ , \quad \text{with } m = \lceil \alpha \rceil \tag{11}$$

$$D^\alpha = I^{m-\alpha} \frac{d^m}{dt^m} \tag{12}$$

Applying Eq. (11) on Eq. (10) leads to the definition known from Riemann. Using the inverted arrangement from Eq. (12) the differential operator after Caputo is derived [4].

2.2 Properties

There are two major differences between both definitions. For $f(x) = const$ the derivative after Riemann diverges, while the result of the Caputo derivative is zero [4]. The second difference of great practical importance is related to the type of initial values needed for a solution [5]. Initial values always represent physical quantities, which could be measured by experiments. Therefore they should be interpretable and compareable with the reality. Initial values of a Riemann differential equation are of fractional type in contrast to those for a Caputo differential equation. That means, if to describe a physical process like creep it maybe the better choice to use the differential operator after Caputo.

An important difference between common and fractional differential equations is the nonlocality of the fractional derivative. Hence it is not possible to calculate the derivative just from information of the direct neighbourhood of a point. Instead of this all points in the whole history are needed. Therefore such equations remember their complete loading history. Events in the far past have a lower influence than those in the near past. In literature this fact is associated with the term “fading memory” [6].

2.3 Solution of the initial value problem

There are a few solution methods for these problems described like the Laplace transform, Mellin transform or the power series method [3]. All of these methods lack generality or usability. Problems can be in restrictions to linearity, constant coefficients or in the possibility of formulating them. Another more general approach comes from [7], where a numerical integration scheme is developd, which is similar to those for common differential equations. Differences are caused by the fading memory which is taken into account by a weight function. The fundamental algorithm is of predictor-corrector type [8].

Here a slightly different version of the algorithm after [5] is used. First a fractional differential equation in the sense of Caputo is assumed:

$$D^\alpha \varepsilon(t) = f(t, \varepsilon(t)) \tag{13}$$

Here $D^j\varepsilon\,(t=0) = \varepsilon_0^j$, $(j = 0, 1, 2, ..., m-1)$ are initial values starting from a known function value ε_k. The value for the next step ε_{k+1}^P is estimated by the Euler method

$$\varepsilon_{k+1}^P\,(t) = \sum_{j=0}^{m-1} \frac{t_{k+1}^j}{j!}\varepsilon_0^{(j)} + \frac{1}{\Gamma\,(\alpha)} \sum_{j=0}^{k} b_{j,k+1} f\,(t_j, \varepsilon_j)\,. \tag{14}$$

The superscript P indicates that this quantity is just the value of the predictor as initial guess for the next value. By use of the trapezium formula the final value of the corrector is calculated in one or more iterations

$$\varepsilon_{k+1}^C\,(t) = \sum_{j=0}^{m-1} \frac{t_{k+1}^j}{j!}\varepsilon_0^{(j)} + \frac{1}{\Gamma\,(\alpha)} \left(\sum_{j=0}^{k} a_{j,k+1} f\,(t_j, \varepsilon_j) + a_{k+1,k+1} f\left(t_{k+1}, \varepsilon_{k+1}^P\right) \right). \tag{15}$$

The quantities a and b are the weights for the corrector and the predictor, respectivly. The variable h indicates the size of the time steps. According to [5] they are defined as:

$$b_{j,k+1} = \frac{h^\alpha}{\alpha}\left((k+1-j)^\alpha - (k-j)^\alpha\right)$$

and

$$a_{j,k+1} = \begin{cases} \frac{h^\alpha}{\alpha(\alpha+1)}\left(k\alpha + 1 - (k-\alpha)\,(k+1)^\alpha\right) & , j = 0 \\ \frac{h^\alpha}{\alpha(\alpha+1)}\left((k-j+2)^{\alpha+1} + (k-j)^{\alpha+1} - 2\,(k-j+1)^{\alpha+1}\right) & , 1 \le j \le k \\ \frac{h^\alpha}{\alpha(\alpha+1)} & , j = k+1 \end{cases}$$

3 Results

In the following the application to rheological modelling of a creep experiment is demonstrated. For this reason the dashpot of the Zener model [11] is substituted by a fractional element, see Fig. 2. This model is described by

$$D^\alpha\varepsilon(t) = \frac{\sigma\,(t)}{B} + \frac{A}{B}D^\alpha\sigma\,(t) - \frac{C}{B}\varepsilon(t) \tag{16}$$

with

$$A = \frac{p}{E_1 + E_2}\,, \quad B = \frac{pE_2}{E_1 + E_2}\,, \quad C = \frac{E_1 E_2}{E_1 + E_2}$$

and the initial value

$$\frac{d^0}{dt^0}\varepsilon(t=0) = \frac{\sigma + \sigma A}{B + C}\ .$$

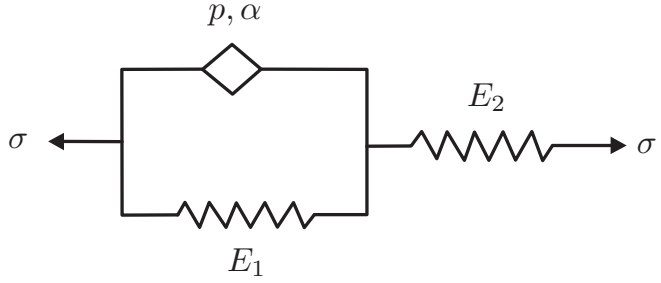


Figure 2: Zener model with a fractional element

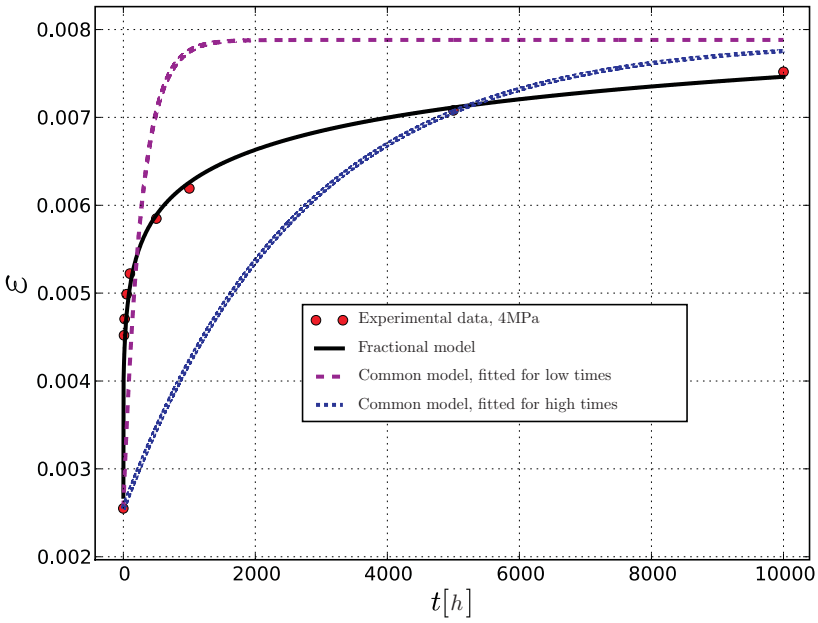


Figure 3: Fractional model vs. common model for Ultramid A3K, data from [9]

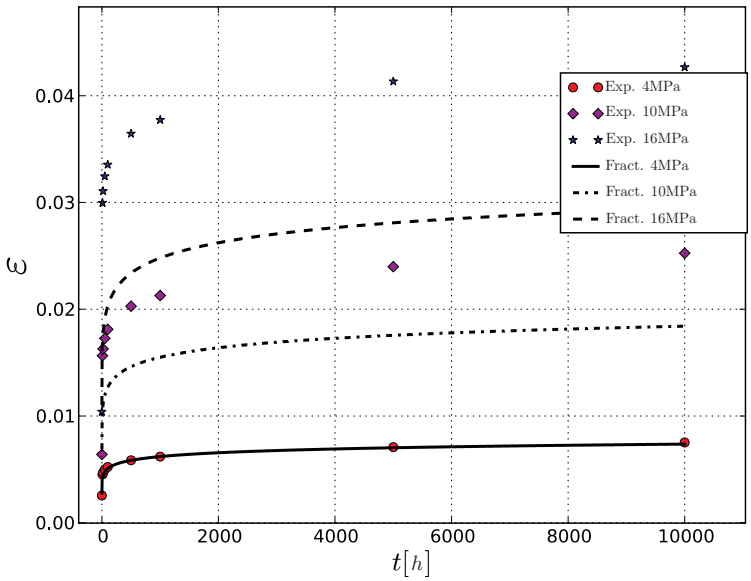


Figure 4: Linear fractional model fitted for Ultramid A3K, data from [9]

In Fig. 3 it is shown that the fractional model fits very well to experimental data. In comparison to the common Zener model it offers much better adaptivity. This is remarkable because the unmodified device with a common dashpot can be used to properly model about one decade. However, the calculated curves for higher stresses show greater deviations from experimental data, see Fig. 4. This comes from the nonlinearity of the material behaviour and is not a problem of the fractional model.

To improve the obtained results over a wider stress range some nonlinearity has to be introduced. The fractional parameter p and the stiffness of the single spring E_2 are formulated as functions of stress. The starting parameters p_0 and $E_{2,0}$ are altered in dependence of the stress, acting on the

corresponding element:

$$p = p_0 \frac{a}{(|\sigma_{frac.}| + c)^b} \tag{17}$$

$$E_2 = E_{2,0} \frac{f}{(|\sigma| + g)^d} \tag{18}$$

With these changes the one-dimensional creep experiment can be simulated. The received results fit much better to the whole stress range, compare Fig. 5.

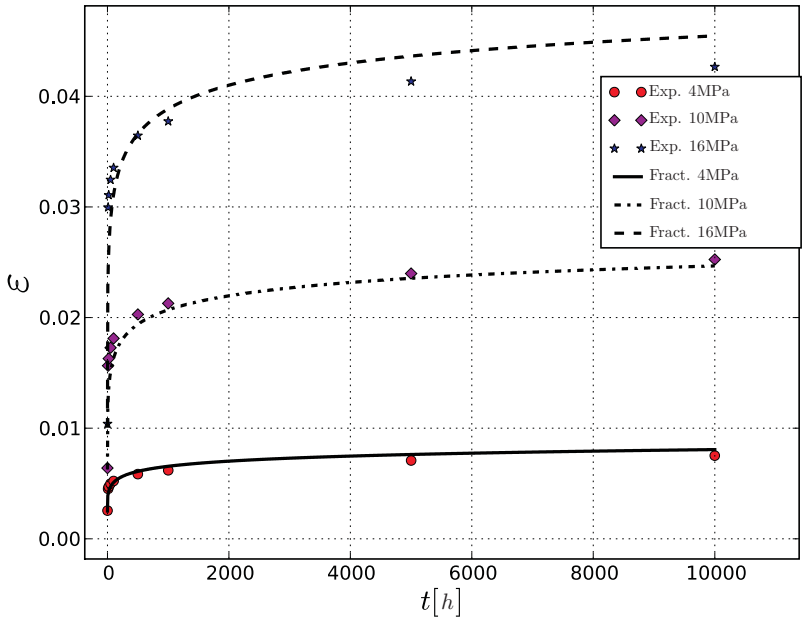


Figure 5: Nonlinear fractional model fitted for Ultramid A3K, data from [9]

All necessary parameters, their values and units are summarised in Table 12.

Parameter	E_1	$E_{2,0}$	α	p_0	a	b	c	d	f	g
Value	360.2	2971	0.3	3077	2.37	0.52	0.59	0.9	4	0.1
Units	MPa	MPa	–	$\frac{Ns^\alpha}{mm^2}$	MPa^b	–	MPa	–	MPa^d	MPa

Table 12: Summarised values and units for all parameters of the nonlinear model

References

[1] A. K. Grünwald. Über 'begrenzte' Deviationen und deren Anwendung. Zeitschrift für angewandte Mathematik und Physik 12: 441-480, 1867.

[2] A. Schmidt and L. Gaul. Bestimmung des komplexen Elastizitätsmoduls eines Polymers zur Identifikation eines viskoelastischen Stoffgesetzes mit fraktionalen Zeitableitungen. ZfP in Anwendung, Entwicklung und Forschung, Berlin, 2001.

[3] I. Podlubny. Fractional Differential Equations. Academic Press, San Diego, 1999.

[4] R. Herrmann. Fraktionale Infinitesimalrechnung. Books on Demand GmbH, Norderstedt, 2008.

[5] D. Blume. Fraktionale Differentialgleichungen mit Maple. Masterthesis, Frankfurt, 2002.

[6] P. Haupt. Continuum Mechanics and Theory of Materials. Springer, Berlin, 2002.

[7] K. Diethelm and N. J. Ford and A. D. Freed. A Predictor-Corrector Approach for the Numerical Solution of Fractional Differential Equations. Nonlinear Dynamics 29: 3-22, 2002.

[8] H. Schwarz. Numerische Mathematik. B. G. Teubner, Stuttgart, 1993.

[9] BASF SE. Campus database, 2008.

[10] A. A. Kilbas and H. M. Srivastava and J. J. Trujillo . Theory and Application of Fractional Differential Equations. Elsevier, Amsterdam, 2006.

[11] M. Reiner. Deformation, strain and flow: an elementary introduction to rheo- logy. Interscience Publishers, New York, 1960.

Carsten Kröner, Holm Altenbach, Konstantin Naumenko, Andreas Kutschke, Kurth-Mothes-Straße 1, 06099 Halle(Saale), Germany

The extent of softening that can be achieved under stable deformation with the Tresca elastic-plastic material

Tatyana B. Lavrova
lavr@ssu.samara.ru

Abstract

The question of realizability of the states of softening for the Tresca elastic-plastic material under deformation testing is studied theoretically. Realizability is identified with stability of the corresponding uniform deformation process. By hardening and softening are meant some possible generalizations of these notions (introduced first by Drucker in the framework of linear solid mechanics, where the initial stresses are considered negligible) for the case of non-zero initial stresses. Specifically, the state for which the quadratic form for the elastic-plastic moduli tensor setting the Jaumann increment of the Cauchy stress, is positive definite (can take negative values), is called that of hardening (softening). Hardening is equivalent to positivity of all the six genuine (according to Rychlewski) moduli of such a fourth-order tensor, whereas softening is equivalent to existence of at least one negative.

It is known that the bounds of stable deformation of a solid are determined by the bounds of validity of the Hadamard inequality for the tensor of elastic-plastic moduli setting the incremental constitutive relation for the Piola stress tensor: there exist the devices in which the uniform deformation within the bounds mentioned is realizable, while beyond the bounds there can be no stability (the Basic Hadamard stability theorem). Thus, the moduli tensors involved in the softening condition and in the Hadamard inequality, are different, but the relation between them is well-known, and the current values of stress enter it. The achievable states of softening are the ones, for which the condition of softening (for corresponding moduli tensor) is compatible with the Hadamard inequality (for another moduli tensor).

When analyzing the achievable extent of softening for the Tresca elastic-plastic materials, one should take into account the existence of edges of the yield surface. Note that the normals to the surface (in the strain space) at the points on the faces are the symmetrized dyads, whereas the edges are characterized by that the normals to adjacent faces are co-axial symmetrized dyads. On the edges of yield surface there are four regimes of the material response: elastic unloading, two regimes of partial plastic loading and that of full plastic loading. It is proved in the work that softening is impossible on the faces of the yield surface, the same being true for the regimes of partial plastic loading on the edges. It is proved also that there is an achievable finite extent of softening that corresponds to the regime of full plastic loading. The achievable extent of softening mentioned is found analytically; it appears to depend on the quantities characterizing the law of full plastic loading on the edge.

1 The achievable extent of softening as that compatible with stability of a solid

Softening of a material is a basic notion of continuum fracture mechanics. The presence of softening is a phenomenological expression of diffuse micro-fracturing of a solid wilhin the bounds when it can be considered as a continuum. Thus, elastic-plastic constitutive relations with softening enable one to describe the initial stages of fracturing using the approach and methods of a solid mechanics. The notions of hardening and softening were introduced by D. C. Drucker [1] in the case of linear solid mechanics as positive definiteness or absence of positive definiteness of the quadratic form

$$(\dot{\boldsymbol{T}})^p : \dot{\boldsymbol{\varepsilon}} = \dot{\boldsymbol{\varepsilon}} : \boldsymbol{L}^p : \dot{\boldsymbol{\varepsilon}}, \tag{1}$$

where the fourth-order tensor $\boldsymbol{L}^p$ is the moduli tensor of elastic-plastic material for incremental plastic response.

A possible correct generalization of (1) for the case of non-linear solid mechanics is based upon the correct incremental constitutive relations for elastic-plastic material with regard for the finite current values of stresses. It reads almost the same, but the difference is that $(\dot{\boldsymbol{T}})^p$ is replaced by $(\overset{\triangledown}{\boldsymbol{T}})^p$, where $\overset{\triangledown}{\boldsymbol{T}}= \dot{\boldsymbol{T}} - \boldsymbol{T}\cdot\dot{\boldsymbol{\omega}} + \dot{\boldsymbol{\omega}}\cdot\boldsymbol{T}$ is the Jaumann rate of the Cauchy stress. The correct incremental constitutive relation (for a smooth yield surface) can be taken in form

$$\overset{\triangledown}{\boldsymbol{T}}= \begin{cases} \boldsymbol{L}^p : \dot{\boldsymbol{\varepsilon}}, & \dot{\boldsymbol{\varepsilon}} : \boldsymbol{S} \geq 0; \\ \boldsymbol{L}^e : \dot{\boldsymbol{\varepsilon}}, & \dot{\boldsymbol{\varepsilon}} : \boldsymbol{S} \leq 0, \end{cases} \tag{2}$$

$$\boldsymbol{L}^p = \boldsymbol{L}^e - \theta \boldsymbol{S}\otimes\boldsymbol{S}, \quad \theta \geq 0. \tag{3}$$

where $\dot{\boldsymbol{\varepsilon}}$ is the strain-rate tensor, the symmetric second order tensor $\boldsymbol{S}$ is the normal to the yield surface in the strain space, the fourth-order tensors $\boldsymbol{L}^p$ and $\boldsymbol{L}^e$ are the moduli tensors for plastic and elastic responses, the scalar quantity θ is related to the function of hardening (or softening), and its positivity means that a material under the elastic response is stiffer than under the plastic one.

In terms of "genuine" moduli in the sense of J. Rychlewski [2] softening is equivalent to negativity of the least genuine modulus for $\boldsymbol{L}^p$ (i. e. the least eigen-value of the corresponding linear operator that maps the space of symmetric second-order tensors into itself).

It is known that the states of softening are achievable in principle as long as softening is compatible with the Hadamard inequality for plastic response [3], whereas any state becomes unstable when the inequality is violated (the Basic Hadamard Stability theorem, generalized for the elastic-plastic case [4]).

The Hadamard inequality

$$\boldsymbol{f}\otimes\boldsymbol{g} : \boldsymbol{C}^p : \boldsymbol{f}\otimes\boldsymbol{g} \geq 0, \quad \forall \boldsymbol{f}, \boldsymbol{g} \tag{4}$$

involves the moduli tensor $\boldsymbol{C}^p$, which is the moduli tensor (under the plastic response) for the Piola stress. The well-known relation between the two moduli tensors using a notation for isomers of tensors, can be expressed as follows:

$$\boldsymbol{C}^p = \boldsymbol{L}^p + \boldsymbol{T}\otimes\boldsymbol{I} + \frac{1}{2}(\boldsymbol{T}\otimes\boldsymbol{I} - \boldsymbol{I}\otimes\boldsymbol{T})^{(1324)} - \frac{1}{2}(\boldsymbol{T}\otimes\boldsymbol{I} + \boldsymbol{I}\otimes\boldsymbol{T})^{(1342)}.$$

The inequality

$$\boldsymbol{f}\otimes\boldsymbol{g} : (\boldsymbol{L}^p - 2\tau_{max}\mathbf{1}^{def}) : \boldsymbol{f}\otimes\boldsymbol{g} > 0, \tag{5}$$

suffices validity of the strict variant of (4); it provides more rough but simple condition for the $\boldsymbol{C}^p$ to be strongly elliptic (here τ_{max} is the maximal shear stress).

2 The Tresca elastic-plastic materials with softening

The Tresca elastic-plastic materials are characterized by the property that their yield surface (in the strain space) is piecewise-smooth with faces and edges on it, and additionally the normals to its faces are symmetrized dyads (of unit norms). Assume that $\boldsymbol{L}^e = 2G\mathbf{1}^{def}$, where G is the modulus and $\mathbf{1}^{def}$ is the orthogonal projector onto the space of symmetric second-order tensors. Then on a face of a Tresca yield surface

$$\boldsymbol{L}^p = 2G\mathbf{1}^{def} - \theta\boldsymbol{S}\otimes\boldsymbol{S} = 2G(\mathbf{1}^{def} - \boldsymbol{S}\otimes\boldsymbol{S}) + (2G-\theta)\boldsymbol{S}\otimes\boldsymbol{S}. \tag{6}$$

The spectral decomposition (6) implies that there are two genuine moduli: $2G$ and $2G-\theta$, the latter being the least, and its negativity $2G-\theta<0$ is the condition of softening. With regard for the properties of $\boldsymbol{L}^p$ and for how it is related to $\boldsymbol{C}^p$ the necessary condition for validity of (4) is the inequality $2G-\theta\geq 0$ which is incompatible with softening; hence, softening cannot be achieved on the faces of yield surface for the Tresca materials.

The normals to the faces adjacent to any edge of a yield surface are co-axial symmetrized dyads. On the edges there are four regimes of incremental material response: elastic unloading, two regimes of partial plastic loading for which the tensor $\boldsymbol{L}$ takes the form (6) with $\boldsymbol{S}_1$ or $\boldsymbol{S}_2$ taken for $\boldsymbol{S}$ ($\boldsymbol{S}_1$ and $\boldsymbol{S}_2$ are the normals to corresponding faces), and ultimately the full plastic loading with

$$\boldsymbol{L}^p = 2G\mathbf{1}^{def} - \theta(\mu'\boldsymbol{S}_1 \otimes \boldsymbol{S}_1 + \mu''\boldsymbol{S}_2 \otimes \boldsymbol{S}_2), \quad \mu' > 0, \mu'' > 0, \mu' + \mu'' = 1 \tag{7}$$

where μ' and μ'' are dimensionless functions of a current state of material.

For the regimes of partial plastic loading the structure of $\boldsymbol{L}$ is the same as on the faces and hence, softening is impossible.

For the full plastic loading the proper tensors of $\boldsymbol{L}^p$ are the same as for the tensor $\mu'\boldsymbol{S}_1 \otimes \boldsymbol{S}_1 + \mu''\boldsymbol{S}_2 \otimes \boldsymbol{S}_2$ and hence, the least genuine modulus of $\boldsymbol{L}^p$ is just the least value of the quadratic form $\dot{\boldsymbol{\varepsilon}} : \boldsymbol{L}^p : \dot{\boldsymbol{\varepsilon}}$ on the normalized above-mentioned proper tensors.

Consider a different quadratic form

$$\boldsymbol{D} : (\boldsymbol{L}^p - 2\tau_{max}\mathbf{1}^{def}) : \boldsymbol{D}, \tag{8}$$

where $\boldsymbol{D}$ is a symmetrized dyad with unit vectors and $\boldsymbol{L}^p$ is specified by (7). Symmetrized dyads as symmetric second-order tensors are completely characterized by the property that one of their eigen-values is zero while two others are opposite in sign. It is proved in the work that the quadratic form (8) attains its minimum on a tensor $\boldsymbol{D}'$ that is co-axial with $\boldsymbol{S}_1$ and $\boldsymbol{S}_2$. Validity of (5) is then equivalent to inequality $\boldsymbol{D}' : (\boldsymbol{L}^p - 2\tau_{max}\mathbf{1}^{def}) : \boldsymbol{D}' > 0$, which can be brought to the form

$$\frac{\theta}{2(G - \tau_{max})} < \frac{\boldsymbol{D}' : \boldsymbol{D}'}{\mu'(\boldsymbol{D}' : \boldsymbol{S}_1)^2 + \mu''(\boldsymbol{D}' : \boldsymbol{S}_2)^2}. \tag{9}$$

Without loss in generality we assume that $\mu'(\boldsymbol{D}' : \boldsymbol{S}_1)^2 + \mu''(\boldsymbol{D}' : \boldsymbol{S}_2)^2 = 1$. The properties of $\boldsymbol{D}'$ enable us to find three possible values of $\boldsymbol{D}'$, and we select among them the one giving the minimal value of the right-hand side of (9), whence we obtain the upper bound for θ, that determines the admissible greatest extent of softening. It is shown that for the full plastic loading on an edge there always exists certain finite achievable extent of softening. The closer μ' and μ'' to each other, the greater is admissible extent of softening, the latter attaining its maximum for $\mu' = \mu''$.

To summarize, unlike the smooth points on the Tresca yield surfaces where softening is impossible due to instability, on the edge there is a finite achievable extent of softening corresponding to the full plastic loading. In principle, it can be realized, identified and measured by means of some real testing machines, namely the so-called triaxial machines.

References

[1] Drucker D.C. A definition of stable inelastic material // J. Appl. Mech. ASME. 1959. V.26. P.101-106.

[2] Rychlewski J. On Hooke's law // Prikl. Mat. Mekh. 1984. V. 48. N3. P. 420-435(in Russian).

[3] Nikitin L. V., Ryzhak E. I. On realizability of the material states corresponding to "falling" portion of a diagram // Mekh. Tv. Tela.1986. N2. P. 155-161(in Russian).

[4] Ryzhak E. I. On necessity of the Hadamard condition for stability of elastic-plastic bodies // Mekh. Tv. Tela.1987. N4. P. 101-104(in Russian).

Tatyana B. Lavrova, Samara State University, Russia.

Dynamics of a surface subphase formation in a multicomponent surfactant solution

A. I. Lutsik A. I. Mizev
nusia-perm@mail.ru

Abstract

Dynamics of the surface subphase formation in an aqueous solution of two surface-active substances, which are strongly different in a surface activity and in a characteristic adsorption time, were studied experimentally. An additive contribution of molecules of both surfactants in the surface layer formation is found out at small total concentration. With a growth of concentration the role of the surfactant with larger surface activity essentially increases. When the concentration of the more active surfactant reaches the critical micelle concentration only the molecules of this surfactant are involved in the formation of the surface subphase whereas the molecules of the less active surfactant remain in the solution volume. On the base of the experimental re-sults the method for definition of a total molar concentration of both surfactants and a partial concentration of each surfactant, by measuring only the surface tension of the mixture solution, is proposed.

Introduction

Multicomponent systems of fluids are one of the less known areas of hydrodynamics. With the advent of each new fluid the system acquires an additional group of physico-chemical properties and a new interphase boundary, which has its own geometry and which can influence on conditions of the momentum, heat or mass transfer. The situation becomes more complicated when a number of the system components are found to be mutually soluble or surface active (surfactant) with respect to other components of the system. In the latter case, the interface properties are specified not only by the concentration of the dis-solved surfactant but also by the history of the interface formation. This is related to the fact that due to the diffusion and adsorption processes accompanied the formation of a new surface of the solution it takes some time for a surfactant to emerge to the interface. In the solutions containing several surfactants the processes of the interface formation may de-pend on the ratio of the surface properties of the surfactants and on the interaction of their molecules both in the bulk and at the surface of the solvent.

In the past few years, interest in investigation of such systems has quickened due to their widespread occurrence both in nature and in industry However, multi-component so-lutions of surfactants are generally studied in the equilibrium states, viz., when the proc-esses of the surface phase formation occurring, for example, after the formation of the fresh interface, have already finished. In this situation researchers are interested mainly in the equilibrium surface concentration of each surfactant, in the processes of micelle formation, interaction between the molecules of different surfactants, etc. Unfortunately with such an approach it is easy to lose information on the processes of the surface layer formation.

In this paper we investigate the processes of surface phase formation and dynamics of the surface activity in multi-component solutions of high-molecular surface-active substances using the methods of tensiometry. We present the results of experimental investigation for a two-component surfactant solution.

In doing research we pursue two main goals. First, we investigate the dynamics of the surface phase formation and the mechanisms governing the variations in the surface properties of the solution due to a change in the absolute (total content of the surfactant in the solution) and the relative (the fraction of each of the components) concentration. Second, we examine the possibility

of measuring the content of each component based solely on the measurements of the surface tension of the solution.

Description of the experimental setup, materials and measuring method

To investigate the surface properties of the solutions we applied the method of maximum pressure in the bubble. This surface tension measuring technique has a number of advantages, owing to which it is best suited to our purposes. Firstly, the method allows us to measure the dynamic surface tension, i.e. to investigate the properties of the interface with allowance for its age. The formation of bubbles at different rates makes it possible to obtain interfaces of different ages at the time when pressure in the bubble reaches its maximum. Secondly, with this method all measurements can be made in a rather small volume of a fluid (of order of one milliliter). One more special convenience of the method is that there is no need to measure the contact angle and to watch the meniscus which allows making measurements in opaque media.

In experiments we used a commercial tensiometer BPA-800P (KSV Ltd., Finland), which is a computer-controlled, completely automated device. The lifetime of the interface ranges from 10 μs to 10 s. Surface tension measurements are in error of 0.1 dyne/cm.

For the objects of investigation we used the solutions of potassium salts of fatty (organic) acids in an aqueous mole (one mole of the substance per a liter of water) solution of potassium alkali. The objective of our study is investigation of a mixture of surfactants of nearly the same nature (namely, the ionic surfactants - the members of the same homologous series) differing only in some parameters. In our case, these are different surface activity caused by the difference in solubility between the members of the series and different time of emergence to the interface determined by the changes in the coefficients of diffusion, adsorption and desorption due to an increase in the length of the molecule in the homologous series. For our study we chose two members of the series-potassium caprylate and potassium laurate, which have nearly a two-fold difference in the molecule length (8 and 14 atoms of carbon in the chain, respectively).

The solutions were prepared on the basis of highly purified water (the first degree of purification in accordance with All-Russia state standard P 52501-2005). To obtain such a degree of purification distilled water was passed three times through the ion exchange filter (deionizer “Vodoley” produced by Khimelectronik company, Moscow) to remove residual impurities.

Since the properties of the examined solutions (surface tension, surfactant solubility, diffusion coefficient, adsorption rate, etc.) depend on temperature, all measurements were made at a constant sample temperature $(23.0 \pm 0.3)^{\circ}C$.

Discussion of results

The dependence of the surface tension on the concentration of potassium laurate in a molar solution KOH for different lifetimes of the interface is shown in Fig.1.

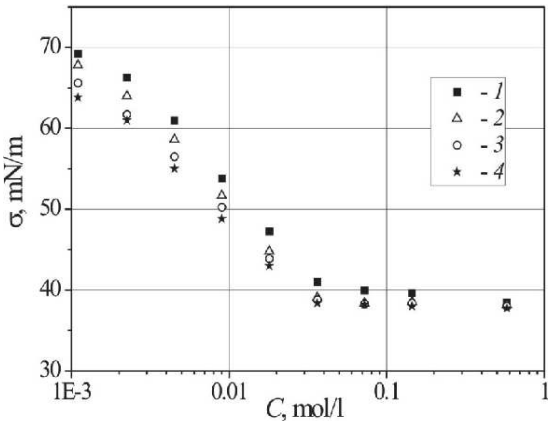


Fig.1. Surface tension versus concentration of potassium laurate for different lifetimes of the interface, s: 1 - 0.01, 2 - 0.1, 3 - 1, 4 - 10

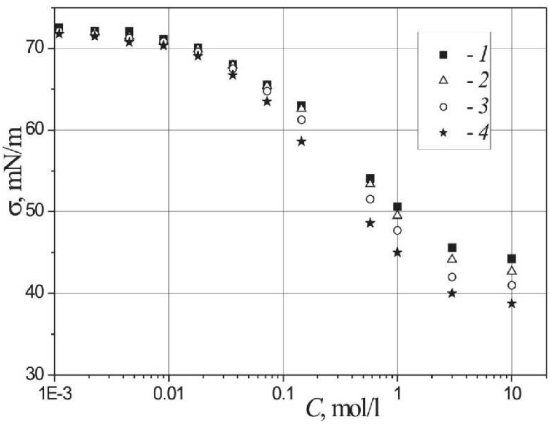


Fig.2. Surface tension versus concentration of potassium caprylate for different lifetimes of the interface, s: 1 - 0.01, 2 - 0.1, 3 - 1, 4 - 10

It is seen that the surface tension surfactant concentration relationships for different life-times of the interface do not coincide. This disagreement is most pronounced at small concentrations of the surfactant. However, starting from a certain value of concentration the curves corresponding to lifetimes longer than ∼1s practically coincide. Moreover, at concentrations higher than ∼0.03 mol/l, the surface tension remains unchanged. It is known that at such concentrations part of the surfactant molecules in the solution of the examined surfactant combine spontaneously into stable formations called micelles. Further addition of surfactant molecules to the solution leads to the formation of a greater number of molecule aggregates and not to the growth of the surface concentration whose variation ceases after reaching the saturation point. For an aqueous solution of potassium laurate the critical micelle concentration (CMC) is approximately equal to 0.026 mol/l which agrees well with the results of our experiment. At concentrations close to or higher than CMC the variation of the surface tension ceases within1 second after the formation of the surface. It means that at concentrations close to CMC the characteristic time of emergence (adsorption) of this particular surfactant to the interface, (it corresponds to the formation of the equilibrium concentration at the interface) is approximately 1 second. At lower concentrations this time is longer. Unfortunately, it cannot be measured more accurately because the maximum life-time limitation of the device we used is 10 seconds.

Fig.2 shows the dependence of the surface tension on the concentration of potassium caprylate in a molar solution of KOH for different lifetimes of the interface.

The figure shows that, unlike the previous case, the surface tension variation with the growth of concentration occurs more slowly which is an indication of a lower surface activity of potassium caprylate. The curves, corresponding to different lifetimes, do not coincide. Moreover, at concentrations exceeding CMC, which for the solution of potassium caprylate is ∼0,4 mol/l, the surface tension continues to decrease even at the maximum tolerated lifetimes of the interface achievable with the device used in our experiment. This suggests that the characteristic time of adsorption (formation of the equilibrium surface phase) of this surfactant is much longer than 10 seconds even at high concentrations.

Hence it was found out that the selected two surfactants differed essentially from one another both in the surface activity and in the characteristic time of adsorption. Therefore it was of interest to investigate the dynamics of the surface phase formation in the solution containing both surfactants. To this end we conducted a series of experiments with solutions of these two surfactants (a mixture of potassium captylate and potassium laurate), in which the molar concentration (the total number of molecules of all surfactants in the unit volume) of the solution was kept constant whereas the relative content of the surfactants was varied. A relative fraction of one of the mixture components was defined by the quantity referred to as a molar fraction of a surfactant in the mixture:

$$X = \frac{\nu_1}{\nu_1 + \nu_2}$$

where ν_1 and ν_2 is the amount of moles of the first and the second surfactant in the mixture, respectively.

Fig.3 shows the behavior of $\sigma(T_{lif})$ at different molar concentrations of the mixture and at different molar fractions of laurate in the mixture of two surfactants.

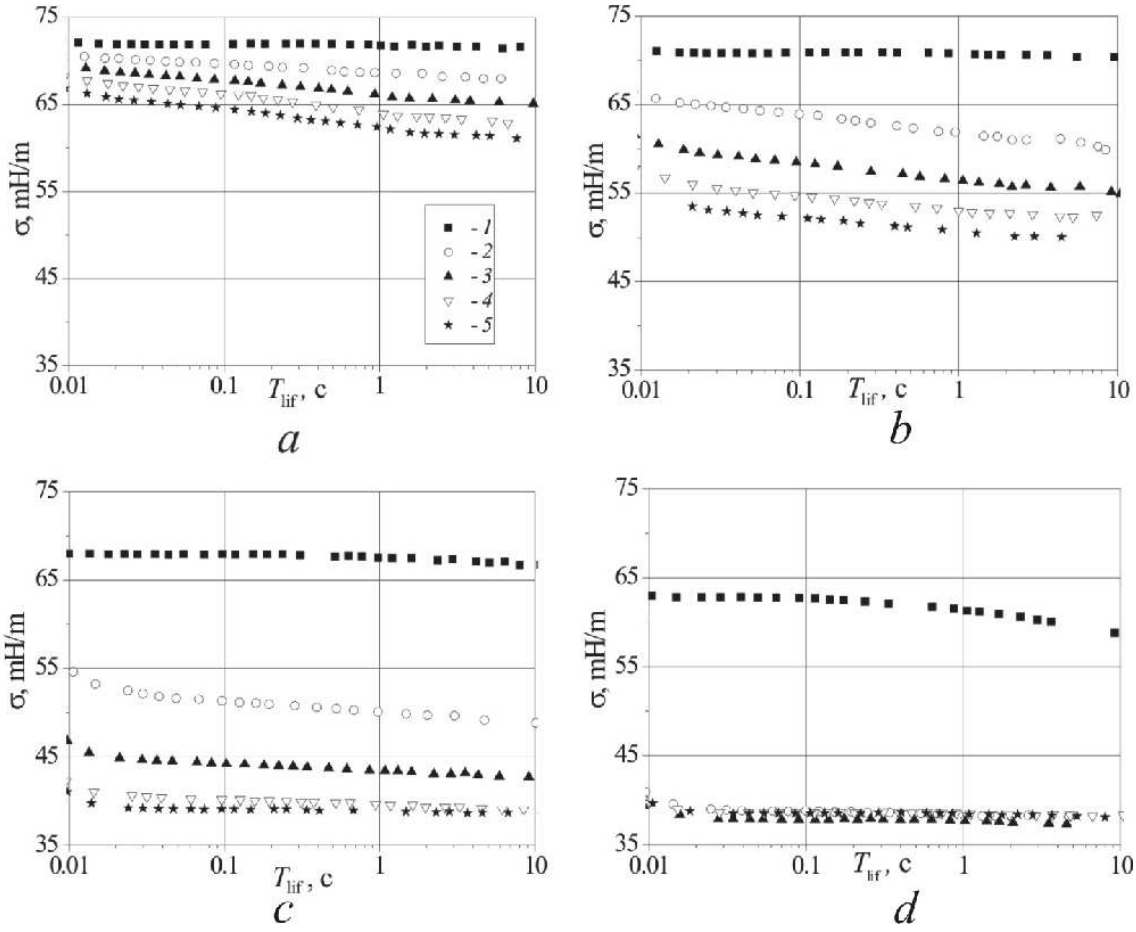


Fig.3. Surface tension as a function of the interface lifetime for solutions with constant molar concentration C, mole/l:
0.0023 (a), 0.0090 (b), 0.0363 (c), 0.1445 (d).
1 - caprylate; 2 - 0.75 of caprylate + 0.25 of laurate; 3 - 0.5 of caprylate + 0.5 of laurate; 4 - 0.25 of caprylate + 0.75 of laurate; 5 - laurate

One can see that there is essential difference between the dependencies plotted in the figure for different concentrations. At low concentrations of the surfactant in the solution the substitution of caprylate molecules for laurate molecules leads to a monotonic growth of the surface tension which is caused by its lower surface activity. The surface phase contains the molecules of both surfactants, which jointly contribute to the formation of a certain surfactant tension of the solution. In this case, we can speak about the additive contribution of two surfactants. At higher total concentrations the situation drastically changes. In the case when caprylate is added to the solution instead of laurate, i.e. as X decreases, the surface tension remains practically unchanged which is an indication of the fact that caprylate molecules are not involved in the formation of the surface phase and remain in the solution. The reasons of such a behavior are the lower surface activity of caprylate and incomparably longer time of its adsorption. The contribution of the surfactants to the formation of the surface tension become non-additive.

Fig.4 illustrates variation of the surface tension of the mixture composed of two surfactants with the total molar concentration at different values of X. All curves shown in the Fig.4 are plotted for

the same value of the interface lifetime T=10 s. It is seen that addition of quite a small amount of laurate (X=0.1) results in a marked decrease of the surface tension and the curve for the mixture comes close to the curve corresponding to pure laurate. Moreover, all curves corresponding to the values of X>0, tend to the same asymptote - to a horizontal line corresponding to the value of the surface tension for a saturated monolayer of laurate. What is interesting, the concentration at which the curve crosses the horizontal line corresponds to the content of potassium laurate in the mixture which is equal to CMC for this substance. This is one further support of the view that at such concentrations only potassium laurate molecules are actively involved in the formation of the surface phase whereas all molecules of potassium caprylate remain in the volume phase of the solution. The above statements are best illustrated by curves describing the dependence of the

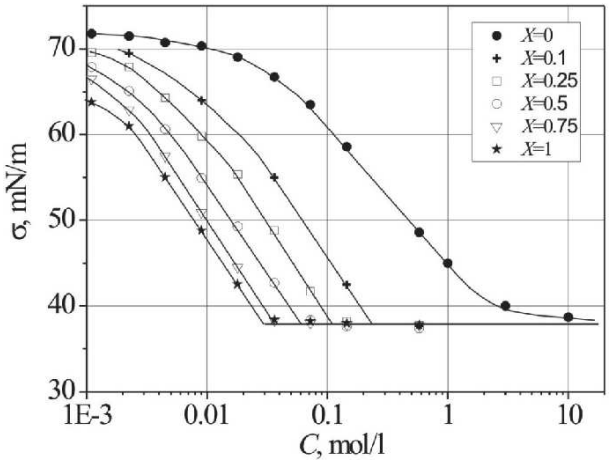


Fig.4. Surface tension versus total concentration of the mixture at different molar fractions of the surfactants

surface tension on the relative fraction of laurate at different values of total molar concentration of both surfactants. Such curves are given in Fig.5 for the case when the lifetime of the interface is 10 seconds. The curves corresponding to other time intervals are qualitatively identical and are not shown in the figure. One can see, that the shape of the curves strongly depends on the

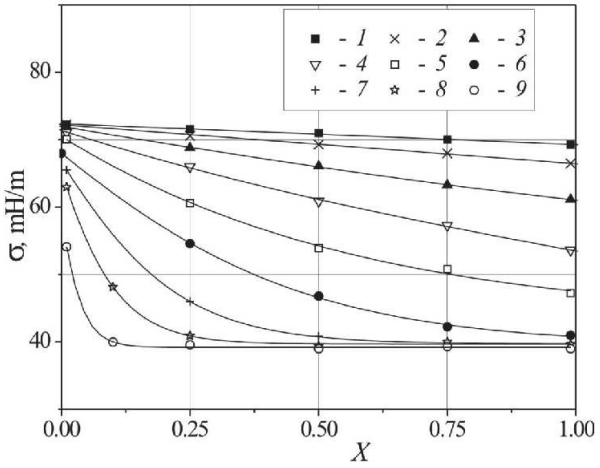


Fig.5. Surface tension versus molar fraction of laurate in the case when the lifetime interface is 10 s at different total molar concentrations C, mole/l:
1 - 0.0011, 2 - 0.0023, 3 - 0.0045, 4 - 0.0090, 5 - 0.0180, 6 - 0.0363, 7 - 0.0723, 8 - 0.1445, 9 - 0.5780

total concentration of both surfactants in the solution. For low concentrations C≤0,005 mol/l

the dependence is linear. This portion of the curve corresponds to an additive contribution of the surfactant, viz., to the case when both surfactants participate in the formation of the surface phase. As the total concentration of the surfactants increases the dependence becomes increasingly non-linear. The part played by the molecules of potassium laurate in the formation of surface properties of the solution becomes more appreciable. At last when laurate in the mixture reaches CMC there appears a horizontal section on the curve, the width of which in-creases with the growth of C. A transition of the curve to a horizontal line is observed at the values of X, at which the relative concentration of laurate in the mixture exceeds CMC. In this case, the contribution becomes essentially non-additive: only laurate molecules participate in the formation of the surface layer.

One of the objectives of our investigation is to ascertain the possibility of determining the content of each component in a composite solution of surfactants based exclusively on the measurements of the surface tension of the solution. In the presence of a linear dependence, at low concentrations such measurements are readily available form the comparison and analysis of the unknown concentration curve $\sigma(X)$ and that showing the analogous dependence corresponding to a mixture with the known concentration and fraction ratio. Indeed, at some fixed lifetime of the interface we can find the function $\sigma(X)$, which unambiguously relates the surface tension of the mixture to the total molar concentration C of both surfactants in the solution and to the relative fraction X of any of the surfactants. To define these two quantities in the unknown solution one should measure the surface tension in the original solution and in the twice-diluted solution for the same life-time of the interface. The value of the relative fraction X will not change whereas the total concentration will be reduced by half. Bearing this in mind and substituting the determined values of the surface tension for the original and dilute solution into the obtained function, we arrive at the system of two equations for two unknowns, which is unambiguously solvable. If the initial solution is highly concentrated, its concentration should be reduced by half-dilution a few times to the point where the obtained solutions will satisfy the initial equation, viz., to the point where the method of subsequent dilution will lead us to the zone of low concentrations corresponding to the linear law.

Conclusion

Dynamics of the surface phase formation in the aqueous solution of two surfactants differing in the degree of surface activity and characteristic time of adsorption has been studied based on the method of maximum pressure in a bubble. It has been shown that contribution of both surfactants to the formation of surface phase is of additive character only in weakly concentrated solutions. At high concentrations the contribution of the surfactants ceases to be additive. In this case, a surfactant with shorter adsorption time and higher surface activity plays a decisive role. On the other hand, the highest possible lifetimes of the interface, which can be realized in our device, prove to be much shorter than the characteristic adsorption time of the more slower surfactant. Probably investigation of the surfaces of multi-component solution of longer lifetime could show other dynamics of the surface phase formation. However this suggestion needs verification by additional experimental studies with application of another device or technique.

The proposed method for determining concentration of each surfactant in a two-component mixture of the unknown concentration based only exclusively on the surface tension measurements, viz., without application of analytical methods of investigation can be used for development of express methods for examination of multi-surfactant systems.

This work was supported by the Program No 09-T-1-1005 of Ural Branch of RAS.

Institute of Continuous Media Mechanics, Ural Branch of Russian Academy of Sciences, Acad. Korolev Str. 1, 614013 Perm, Russia.

Symbolic synthesis of control laws for underwater vehicle and robot manipulator

Evgene V. Lubimov Alexader A. Dyda
berms@mail.ru

Abstract

This paper deals with the problem of the automation of design procedures for nonlinear control systems. As an example the procedure has been realized for the well-known technique consisting of the exact linearization via nonlinear feedback. The developed software achieves the synthesis of control laws in symbolical form that is convenient for further analysis, modeling, and practical implementation of the system. Examples of the software application to underwater vehicle and robot manipulator are given and discussed.

1 Introduction

NONLINEAR control techniques typically involve a certain degree of difficulties due to the calculations which are needed. In fact, when the dimensions of system state, control, and output vectors are large, the control designer faces huge difficulties associated with complicated computations. Indeed, these aspects reduce the possibility of comparing the various control methodologies available for a certain system. A software which automatically generates the various control laws and simulates the controlled system can help the designer to choose the most appropriate control action for a given system.

Motivated by these reasons, this work presents a software which can be used for the automatic generation of a code implementing a certain control strategy. More precisely, we concentrate on the well–known technique of exact nonlinear feedback linearization (NFL). In fact, a number of modern methods used to solve the control synthesis problem for nonlinear systems exploit the idea of linearization. Among them, the exact linearization of the controlled dynamics via nonlinear feedback is one of the most popular techniques. This approach has been applied to various systems and has been extended also in the context of adaptive control, variable structure control, etc. (Isidori, 1995; Nijmeijer and Van der Schaft, 1990; Byrnes, et al., 1997; Kokotovic, et al., 1991). The main advantages of the NFL method consist of the possibility to decouple the controlled subsystems and to provide desired dynamics.

To overcome these aforementioned difficulties to carry out the desired control law, in this work we use the available software to derive procedures for symbolic synthesis and verification, on the basis of the NFL method taken as example.

The paper is organized as follows. In Section II the necessary background on the NFL method is given. Then, we present the main features of the algorithms and the program of symbolic synthesis developed. In Section III the examples of control synthesis for underwater vehicle robot manipulator are presented. The results are derived as symbolical expressions describing the nonlinear control laws. Final comments conclude the paper.

2 The NFL method and its computer symbolical implementation

To begin with, following (Isidori, 1995; Nijmeijer and Van der Schaft, 1990) we briefly review the necessary concepts of feedback linearization. The mathematical model of dynamical control object is supposed to be described by the equations

$$\begin{aligned} \dot{x} &= f(x) + g(x)u, \\ y &= h(x), \end{aligned} \tag{1}$$

where $\dot{x} = (x_1, ...x_n)^T$, $\dot{u} = (u_1, ...u_m)^T$, $\dot{y} = (y_1, ...y_m)^T$ are the state, control, and output vectors, respectively.

The control law

$$u = A^{-1}(x)(w - (x)) \tag{2}$$

ensures the feedback decoupling and linearization.

The decoupling matrix $A(x)$ and the vector (x) are calculated by formulas

$$A(x) = \begin{bmatrix} L_{g_1}L_f^{r_1-1}h_1(x) & .. & .. & L_{g_m}L_f^{r_1-1}h_1(x) \\ L_{g_1}L_f^{r_2-1}h_2(x) & .. & .. & L_{g_m}L_f^{r_2-1}h_2(x) \\ .. & .. & .. & .. \\ L_{g_1}L_f^{r_m-1}h_m(x) & .. & .. & L_{g_m}L_f^{r_m-1}h_m(x) \end{bmatrix}, \tag{3}$$

$$(x) = \begin{bmatrix} L_f^{r_1}h_1(x) \\ L_f^{r_2}h_2(x) \\ ... \\ L_f^{r_m}h_m(x) \end{bmatrix}, \tag{4}$$

where $\dot{r} = (r_1, ...r_m)^T$ is the relative degree vector, and $w = (w_1, ...w_m)^T$ is the new control input, where the Lie derivative of a function $h_j(x)$ along the vector field $f(x)$ is defined as follows

$$L_f h_j(x) = \sum_{i=1}^{n} \frac{\partial h_j(x)}{\partial x_i} f_i(x). \tag{5}$$

The feedback control (2) transforms a nonlinear system (1) into m decoupled chains of r_i cascade–connected integrators and, as consequence, the input–output behavior of the system satisfies the linear equations

$$y_i^{(r_i)} = w_i. \tag{6}$$

Obviously, choosing as new controls

$$w_i = y_{di}^{(r_i)} + k_1 e_i^{(r_i-1)} + ... + k_{r_i} e_i, \tag{7}$$

where $y_d(t)$ is the desirable trajectory vector of the system, with $e(t) = y_d(t) - y(t)$ the error, provides asymptotically stable tracking.

If the output is such that $r_1 + ... + r_m = n$, the system is full–state linearizable. Otherwise, it has an unobservable subsystem, whose dynamics constrained to the zero output is the so–called zero dynamics (for more details see (Isidori, 1995; Nijmeijer and Van der Schaft, 1990)).

For systems of relatively low dimension, the use of the previous formulas is rather simple. But with the increase of the system dimension, of the number of inputs and outputs, the computational complexity soon increases. Hence, symbolic expressions of control laws are convenient for further analysis, modelling, and practical realization.

The complicated work for deriving the symbolic control law based on the NFL method can be essentially facilitated by means of modern software systems such as Maple, MATEMATICA, MATLAB, MATHCAD etc. They have built–in functions for symbolic differentiation, vector and matrix operations, and so on. In particular we used the environment of Maple and MATLAB to derive the NFL–based symbolic synthesis of nonlinear control. The main modules of the software are following:

1. the description of variables (state, control and output vectors);
2. the description of the desirable system trajectory $y_d(t)$;

3. the input of dynamical object model in symbolic form;
4. the derivation of expressions for $f(x)$ and $g(x)$;
5. the determination of the relative degree vector;
6. symbolic calculations of the decoupling matrix $A(x)$ and the vector (x);
7. calculations of the symbolic expressions for the control $\dot{u}$ and the new control w;
8. closed–loop system model and simulation.

3 Example of symbolical control synthesis

To demonstrate the effectiveness of the approach and of the developed software, let us consider the following examples, for whom the symbolic control synthesis and simulation have been performed.

3.1 The Robot Manipulator

The first example of dynamical object to which we will apply the developed software is a robot manipulator UMS–2 (Vucobratovic and Kircansky, 1982). Its dynamics are described by the equation

$$D(q)\ddot{q} + B(\dot{q}, q)\dot{q} + G(q) = U,$$

where $U \in R^3$, $q \in R^6$ are the control and the generalized coordinates vectors. The matrices are determined as follow

$$D(q) = \begin{bmatrix} I_1 + I_2 + I_3 + m_3(q_3 + l_3)^2 & 0 & 0 \\ 0 & m_2 + m_3 & 0 \\ 0 & 0 & m_3 \end{bmatrix},$$

$$B(\dot{q}, q) = \begin{bmatrix} 2m_3(q_3 + l_3)\dot{q}_3 & 0 & m_3(q_3 + l_3)\dot{q}_1 \\ 0 & 0 & 0 \\ -m_3(q_3 + l_3)\dot{q}_1 & 0 & 0 \end{bmatrix},$$

$$G(q) = \begin{bmatrix} 0 & (m_2 + m_3)g & 0 \end{bmatrix}^T.$$

The order of the system is $n = 6$, the number of inputs is $m = 3$. The variables are redefined as $x_1 = q_1, x_2 = \dot{q}_1, x_3 = q_2, x_4 = \dot{q}_2, x_5 = q_3, x_6 = \dot{q}_3$.

The parameters (see (Dyda and Di Gennaro, 1994)) for their definition) are supposed to be constant.

The outputs of the system are the coordinates of the manipulator grasp in the task space

$$h_1 = (x_5 + l_3)\sin(x_1),$$
$$h_2 = (x_5 + l_3)\cos(x_1),$$
$$h_3 = x_3.$$

The desired trajectory $y_d(t)$ is chosen to provide the movement of the grasp along the spatial circle

$$y_{d1} = R\sin(\alpha t),$$
$$y_{d2} = c_1,$$
$$y_{d3} = c_2 - R\cos(\alpha t).$$

The program generates the following symbolic expressions for the control

$$U = \begin{bmatrix} \dfrac{w_1 m_3 x_5^2 \cos x_1 + (2m_3 x_5 l_3 + m_3 l_3^2)(w_1 \cos x_1 - w_2 \sin x_1)}{x_5 + l_3} + \\ + \dfrac{(w_1 \cos x_1 - 2x_2 x_6 - w_2 \sin x_1)I}{x_5 + l_3} \\ (m_2 + m_3)(w_3 + G) \\ \dfrac{m_3(x_2^2 + w_2 x_5 \cos x_1 + w_2 l_3 \cos x_1 + 2x_2^2 x_5 l_3}{x_5 + l_3} + \\ + \dfrac{x_2^2 l_3^2 + x_2^2 x_5^2 + x_5 w_1 \sin x_1 + l_3 w_1 \sin x_1)}{x_5 + l_3} \end{bmatrix},$$

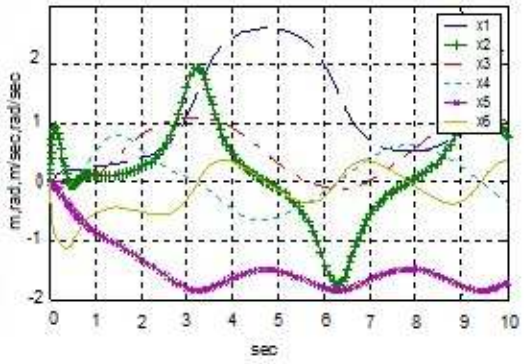


Figure 1: The evolution of the state vector components

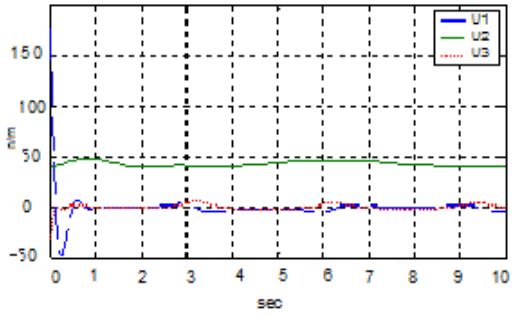


Figure 2: The control vector components

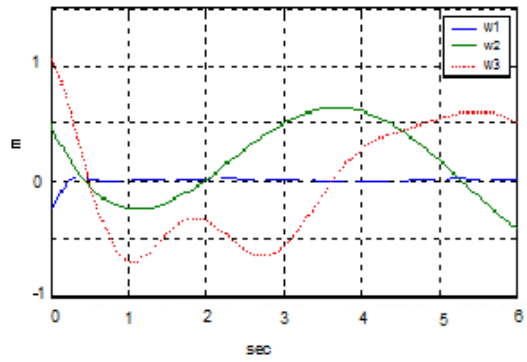


Figure 3: The new control vector components

$$w = \begin{bmatrix} (R\sin\alpha t - (x_5 + l_3)\sin x_1)k_{11} + (R\alpha\cos\alpha t - x_6\sin x_1 - \\ -(x_5 + l_3)x_2\cos x_1)k_{12} - R\alpha^2\sin\alpha t \\ (c_1 - (x_5 + l_3)\cos x_1)k_{21} + ((x_5 + l_3)x_2\sin x_1 - x_6\cos x_1)k_{22} \\ (c_2 - R\cos\alpha t - x_3)k_{31} + (R\alpha\sin\alpha t - x_4)k_{32} + R\alpha^2\cos\alpha t \end{bmatrix}.$$

Figs. 1 – 4 show a simulation of the whole control system.

Due to the space available, only the first output, the reference and the error are given (Fig.4). Clearly, the simulations confirm that the derived control forces the tracking errors to tend asymptotically to zero.

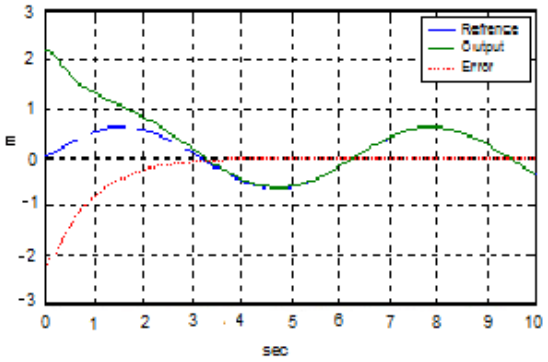


Figure 4: First output, reference, and error

4 Final comments

The software developed in this work can effectively support the procedure of control system design in symbolic form. Clearly, the bigger the dimension of the object mode is, the longer and more complicated symbolic expressions for control will be obtained. For example, one can expect that the program will generate very large expressions describing the control laws for different flexible structures (such as given in (Gennaro and Dyda, 1993)) whose dynamics are approximated by a finite multi–dimensional model. The software helps to designer to solve the problem of the synthesis of nonlinear control systems and to simulate them easily. The NFL has been taken as an example to show the effectiveness of the symbolic computations. Sure, other methodologies can be considered for computer symbolic synthesis, such as adaptive and robust control.

References

[1] Nonlinear Control Systems. Berlin: Springer-Verlag, 1995.

[2] Nonlinear Adaptive Feedback Linearization of Systems. New York: Springer-Verlag, 1990.

[3] Output Regulation of Uncertain Nonlinear Systems. Boston: Birkhauser, 1997.

[4] Adaptive Feedback Linearization of Nonlinear Systems. Foundation of Adaptive Control. Berlin: Springer-Verlag, 1991.

[5] Scietific Fundamentals of Robotics . Vol.1-3 . Berlin: Springer-Verlag, 1982.

[6] Adaptive trajectory control for underwater robot.Proc.OCEANS-94 Osates, Brest, 1994.

[7] Attitude control of a satellite with damping compensation of the flexible beam. Proc. European Control Conf., Groningem, 1993.

Evgene V. Lyubimov, Vladivostok, Russia
Alexander A. Dyda, Vladivostok, Russia

Numerical solution of problem fusion penetration metal, when glass welds with metal by diffusion welding

Olga N. Lyubimova Konstantin N. Pestov Ekaterina A. Gridasova
berms@mail.ru

Abstract

In this paper set a model and method of numerical task solution the process of welding and fusing which relating to the heat conduction in intensive heating glass-metal composite material. The information about thermal field required for prediction deformations and stresses, type of diffusion process, structural changes in heat-affected zone and refining operating practices of welding. This article about mathematical model which take account of conjugate character of heat exchange in system, absorption latent heat of melting by in the time of phase transformation, temperature dependence thermo physical properties base and weld material. Results of calculation by suggested method produce in this paper were compared with quasi-stationary solution of Lejbenzon.

1 Introduction

Technological processes of manufacture of some layered composite materials pass under the influence of heats and the pressure, elements of a composite providing qualitative connection. The technological modes at which the fused component co-operates with a firm component are possible. The speed of course of diffusive processes at connection of layers depends on properties and structure of the co-operating materials, temperature and interaction time [1].

In the given work process of welding of glass and metal in following technological process of manufacturing of a layered composite material of the cylindrical form is investigated. The glass is used as a strengthened material which is placed in the metal glass densely in a firm condition pressing it out executed of two-layer of different metals: fusible and heat resisting ones. Thus the thickness of walls of the internal glass which is directly contacting to a glass core, corresponds to the constructive sizes of a finished product, and it is fixed with a tightness in a cavity of an external glass which plays a role of a rigid bandage.

The technological mode is divided into six stages: I – heating from temperature T_0 to temperature of welding T_w, thus occurs fusion of an internal metal layer and a softening of an external surface of a glass core, temperature of welding is essentially less then the temperature of fusion of a material from which the bandage is produced, II – endurance is executed at welding temperature, at this stage there is a diffusion and a connection of layers, III – cooling to temperature of annealing T_{rel} at which there is a crystallization of the fused internal metal layer, IV – endurance is provided at temperature of annealing, V – responsible cooling to temperature T_1, VI – irresponsible cooling to temperature T_0 (Fig. 1).

Within the limits of the considered technological approach the mathematical model of thermal process in which it is possible not only to describe temperature fields in all layers of assemblage, but also to track structural change of a material, by profusion in the course of heating and then crystallization in the course of cooling of an internal metal layer.

The profusion and metal crystallization is a transition phase of the first sort. The model of process of fusion of pure metal in which phase transition is considered in approach of a mobile interphase surface, is known as a problem of Stefan. Analytical and numerical research of advancement of front of crystallization or fusion is rather uneasy problem to which many works are devoted, including works [2-5]. The decision of any problem of Stefan consists of definition of fields

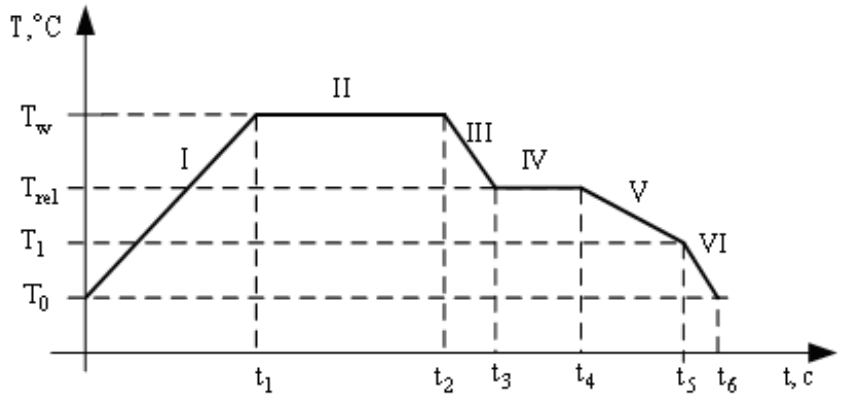


Figure 1: Welding temperature schedule

of melting temperature and a firm phase in areas with mobile border of section, position and which speed of moving should pay off from certain conditions. Thus finite difference analogue of model is under constructed on a grid dynamically adapted for corresponding stage of process, in case of front catching in knot of a grid [2], or includes consideration of biphasic transitive area of final extent, in case of the scheme of through account [3]. Besides, while solving single-phase and biphasic problems of Stefan, the difference schemes based on application of an integrated parity specific heat content are often used which expresses the law of conservation of energy for system as a whole, thus use smoothing of entered function and factors in some narrow interval of temperatures [4].

The model and technique offered in the work allows to track movement of front of profusion in metal without use of a classical condition of Stefan on border of front of transition phase and the function of specific heat content, in the interfaced problem of the heat conductivity considering dependence of thermo-physical factors from temperature and change of a modular condition. The results of numerical experiment received at realization of offered mathematical model and the numerical scheme, do not contradict the results received at the decision of classical problems of Stefan. As a test problem the problem about profusion of the metal cylinder of the big thickness has been considered, the results received in offered model were compared with the first approached decision of Lejbenzon [5].

2 Mathematical statement of a problem and a numerical method of its decision

Let's consider mathematical statement of thermo-diffusive problems for the manufacturing of a two-layer composite core described above technological process on the basis of glass and metal. If r_1, r_2 (borders between glass and metal and between different metals, accordingly) – points of rupture of factors, an interval $(0, r_3)$ in which the problem decision is searched, function of temperature $T(M, t)$ breaks by points of rupture of factors into three parts, in which it satisfies to the heat conductivity equation, and to interface conditions on borders $r = r_1$ and $r = r_2$.

It is known that if to inform the substance for a certain quantity of time a certain quantity of heat which is in a crystalline state then in the beginning its temperature grows, and on reaching temperature of fusion of substance in spite of the fact that warmth is still brought to it, the temperature stops changing and the fusion process begins. After the substance has fused, the temperature starts to change again. The transition of a crystal body in a liquid state demands an expense of a quantity of heat which it is accepted to be called warmth of fusion. For many crystal substances it is known size. We will accept the equation of heat conductivity "switch" $\gamma(T)$ which will allow to pass to a stationary problem and to consider accumulation of the energy spent for phase transition at a given time and in a certain point. Then considering the axial symmetry,

accepting a hypothesis about uniform distribution of temperature on length of the cylinder, the non-stationary equation of heat conductivity can be written down in a kind:

$$\rho(T)c(T)(1-\gamma(T))\frac{\partial T}{\partial t} = \frac{1}{r}\frac{\partial}{\partial r}\left(\lambda(T)r\frac{\partial T}{\partial r}\right) - \gamma(T)W(T), \tag{1}$$

where $\rho(T)$, $c(T)$, $\lambda(T)$ – density, a specific thermal capacity and factor of heat conductivity of a material, accordingly, $W(T)$ – specific capacity of the sources appearing in a body at the phase of transition which is an unknown size and it is defined in the course of the decision, and $\gamma(T)$ it is defined as follows:

$$\gamma(T) = \begin{cases} 1, & \text{if } r \in (r_1, r_2] \text{ and } T = T_l, \\ 0, & \text{if } r \notin [r_1, r_2] \text{ or } r \in [r_1, r_2] \text{ and } T = T_l, \end{cases} \tag{2}$$

where T_l – the temperature of fusion of an intermediate layer.

Glass is a firm amorphous body which is formed at cooling of melt, as a result of increase of its viscosity. As viscosity increases continuously, instead of the exact border separating highly viscosive melt from glass, the transitive area is established, therefore it is possible to watch structural transformations of glass, estimating viscosity. In crystal substances the transitive area aspires to zero and it is considered that there is the exact border dividing phases of a material, therefore thermo-physical characteristics vary in steps. As in the modes considered in work, the intermediate metal layer can be presented simultaneously at two phases: firm and liquid, suppose, that the area separating phases, is defined by a narrow interval of temperatures $[T_l, \hat{T}]$ (here $\hat{T} \to T_l$), and thermo-physical characteristics vary very quickly and can be approximated, for example, by linear function. Considering prospective fusion, and then crystallization thermo-physical characteristics for all composite material of an intermediate layer, are set in a kind:

$$c(T) = \begin{cases} c_g(T), & r \in [0, r_1), \\ c_s, & r \in [r_1, r_2] \text{ and } T_l < T, \\ \dfrac{c_l - c_s}{\hat{T} - T_l}T + \dfrac{c_s\hat{T} - c_l T_l}{\hat{T} - T_l}, & r \in [r_1, r_2] \text{ and } T_l \le T \le \hat{T}, \\ c_l, & r \in [r_1, r_2] \text{ and } T > \hat{T}, \\ c_m(T), & r \in (r_2, r_3], \end{cases}$$

$$\lambda(T) = \begin{cases} \lambda_g(T), & r \in [0, r_1), \\ \lambda_s, & r \in [r_1, r_2] \text{ and } T_l < T, \\ \dfrac{\lambda_l - \lambda_s}{\hat{T} - T_l}T + \dfrac{\lambda_s\hat{T} - \lambda_l T_l}{\hat{T} - T_l}, & r \in [r_1, r_2] \text{ and } T_l \le T \le \hat{T}, \\ \lambda_l, & r \in [r_1, r_2] \text{ and } T > \hat{T}, \\ \lambda_m(T), & r \in (r_2, r_3], \end{cases}$$

$$\rho(T) = \begin{cases} \rho_g(T), & r \in [0, r_1), \\ \rho_s, & r \in [r_1, r_2] \text{ and } T_l < T, \\ \dfrac{\rho_l - \rho_s}{\hat{T} - T_l}T + \dfrac{\rho_s\hat{T} - \rho_l T_l}{\hat{T} - T_l}, & r \in [r_1, r_2] \text{ and } T_l \le T \le \hat{T}, \\ \rho_l, & r \in [r_1, r_2] \text{ and } T > \hat{T}, \\ \rho_m(T), & r \in (r_2, r_3]. \end{cases}$$

Indexes g, s, l, m at thermo-physical factors designate glass, a liquid and firm phase of an intermediate layer, a bandage, accordingly.

The temperature distribution is set at the initial moment of time

$$T|_{t=0} = T_0 = const.$$

Let's consider that there is an ideal thermal contact between boundary surfaces of external and internal metal layers, and also between glass and metal , and the heat exchange between an external surface of metal and the environment is carried out and under the Newton's law

$$\left(\lambda(T)\frac{\partial T}{\partial r}\right)\Big|_{r=r_1-0} = -\left(\lambda(T)\frac{\partial T}{\partial r}\right)\Big|_{r=r_1+0},$$

$$\left(\lambda(T)\frac{\partial T}{\partial r} - \gamma w(T)\right)\Big|_{r=r_2-0} = -\left(\lambda(T)\frac{\partial T}{\partial r}\right)\Big|_{r=r_2+0},$$

$$\frac{\partial T}{\partial r}\Big|_{r=0} = 0,$$

$$\left(\lambda(T)\frac{\partial T}{\partial r}\right)\Big|_{r=r_3} = -\vartheta(T|_{r=r_3} - T_e(t)),$$

where $w(T)$ – the function characterizing a stream of warmth of phase transformation, ϑ – the factor of heat loosing which generally depends on a way of heating (cooling) of an external surface and for certain modes of heating of cooling can accept constant values, function $T_e(t)$ depends on a temperature mode of technological process and is set in the form of burst-continuous function (Fig. 1).

3 The results of numerical experiment

Numerical calculations under the constructed scheme have been spent at following values of parameters: values of thermo-physical material factors:

1 layer – laboratory glass: $c_g = 0.64T + 820\left(\frac{Dg}{kg\,^\circ C}\right)$, $\lambda_g = 0.01T + 8.5\left(\frac{Bt}{m\,^\circ C}\right)$, $\rho_g = 2300\left(\frac{kg}{m^3}\right)$;

2 layer – aluminium: $c_s = 732.8\left(\frac{Dg}{kg\,^\circ C}\right)$, $c_l = 1131.8\left(\frac{Dg}{kg\,^\circ C}\right)$, $\lambda_s = 0.01T + 8.5\left(\frac{Bt}{m\,^\circ C}\right)$, $\lambda_l = 229\left(\frac{Bt}{m\,^o C}\right)$, $\rho_s = 2700\left(\frac{kg}{m^3}\right)$, $\rho_l = 2300\left(\frac{kg}{m^3}\right)$, $\vartheta = 100\left(\frac{Bt}{m^2\,^o C}\right)$, $Q_l = 992.5 \cdot 10^3\left(\frac{kDg}{m^3}\right)$, $T_l = 660\ (^\circ C)$, $\hat{T} = 660.001\ (^\circ C)$;

3 layer – a steel (St3):$c_m = 0.24T + 477\left(\frac{Dg}{kg\,^\circ C}\right)$, $\lambda_m = -0.04T + 63.8\left(\frac{Bt}{m\,^\circ C}\right)$, $\rho_g = -0.29T + 7876\left(\frac{kg}{m^3}\right)$.

The geometrical sizes have been accepted by the following: $r_1 = 8 \cdot 10^{-3}(m), r_2 = 18 \cdot 10^{-3}(m), r_3 = 30 \cdot 10^{-3}(m)$. Temperature mode was defined by following values of temperatures and time: $T_0 = 20(^\circ C), T_w = 900(^\circ C), T_{rel} = 650(^\circ C), T_1 = 250(^\circ C)$.

The particular interest for practice represents a time interval at which the intermediate layer is in a liquid state, and also temperature distribution in time in the points close to border of section of environments in a layered composite as speed of course of diffusive processes depends on it at welding of diverse materials which influences the quality of welding. On fig. 3 schedule 1 corresponds to the schedule of temperature of $T_e(t)$ environment in the temperature mode set in work, schedule 2 reflects distribution of average temperature of a composite material in time, J - figurative schedule 3 characterizes time during which the certain layer of aluminium is in a liquid phase, schedule 3 is detailed on fig. 4.

On schedules 1, 2, 3 and 4, 5 fig. 5 values of a thickness of a liquid phase of an intermediate layer are resulted. Schedules 1, 2 and 3 characterize the process of fusion for the different coordinate grids: 1 - 0,025; 2 - 0,0125; 3 - 0,00625. Schedules 4 and 5 characterize already process of crystallization for coordinate grids: 4 - 0,025; 5 - 0,0125.

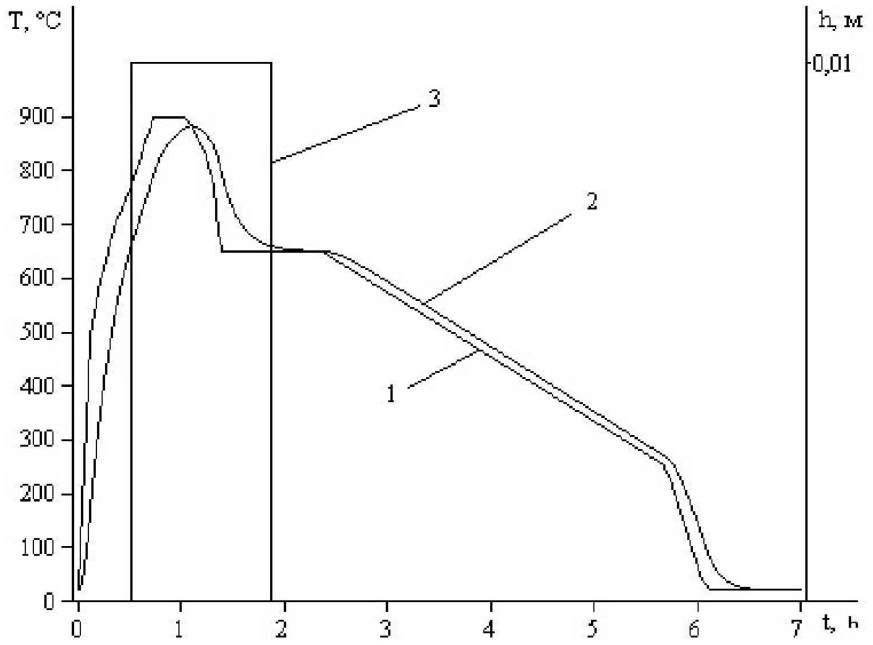


Figure 2: Temperature dependence on time

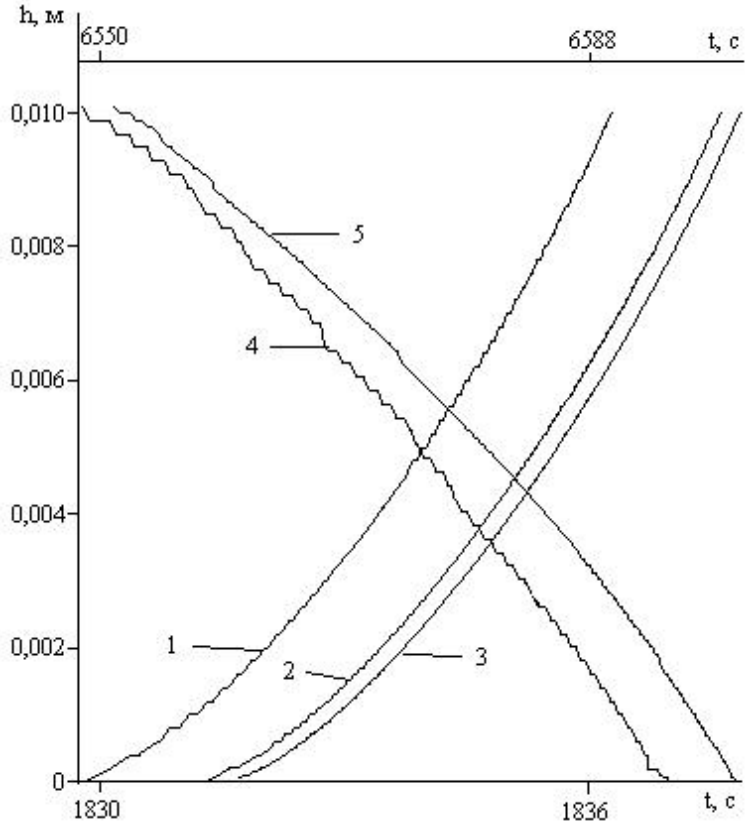


Figure 3: Dependence of a thickness of profusion on time

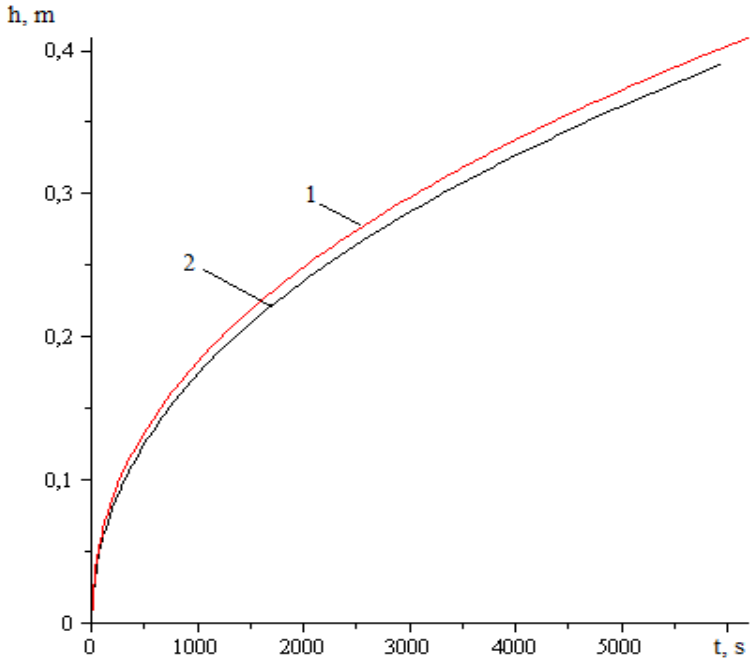


Figure 4: The comparison of the offered technique with the semi-analytical decision of Lejbenzon

On schedules 1, 2 fig. 4 decisions of a problem on profusion of the metal cylinder of big thickness by the method offered in given work and the first approached method of Lejbenzon, accordingly are presented. The problem was dared only for a metal layer with reference temperature $T_0 = T_l$, on which internal surface constant temperature $T_e = 1200\ ^\circ C$, $r_1 = 0.05\ (m)$, $r_2 = 0.35\ (m)$, the step on spatial co-ordinate was constant 0.01.

Thus, the model and the numerical scheme for temperature definition in each point of a composite material and allocation of front of phase transition in a metal layer, moving in the continuous, burst non-uniform cylinder of final radius is constructed. In model on border of interface of materials interface conditions are set at ideal contact to the account of the energy absorbed at the phase transition.

The basic advantage of the offered model and the numerical scheme is the possibility of the decision of interfaced problem with phase transition without application of conditions of Stefan on border of front of phase transition that on the one hand simplifies a problem, and on the other hand allows to complicate problem geometry, boundary and entry conditions and also to consider nonlinearity of process. Moreover, as offered technique allows to track and process of crystallization of metal in the course of cooling, there is a possibility within the limits of one model to track all thermal processes occurring at all stages of technological process, including processes of profusion of an intermediate metal layer in the course of heating and crystallization in the course of the further cooling of all composite material

To consider the possibility of profusion of a bandage because of unsuccessful choice of a material or welding temperatures, in the offered model it is necessary to make changes in conditional transition (2). Besides, in the offered model without essential complication of a problem the quantity of layers and possibility of profusion of the layers executed from different materials can be increased that allows to specify technological modes and parameters of diffusive welding after mathematical modeling process.

References

[1] Bachin V.A. Diffusion welding glass and ceramics with metal. M.: Machine-building, 1984.

[2] Nikitenko N.I. Research of process thermo- and mass transfer of metod net. K.: Nayk. dymka, 1978.

[3] Samarskiy A.A, Moiseenko B.D. Economical scheme of through calculation for multivariate problem of Stefan // Journal. cal. math. and math. phys. 1965. V. 5, No 5 . P. 816-827.

[4] Bydak B.M., Soloviyva E.N., Yspenskiy A.B. Net method with evening-out coefficient for solve problem of Stefan // Journal. cal. math. and math. phys. 1965. V. 5, No 5 . P. 828-840.

[5] Lykov A.V. Theory of thermal conductivity. M.: Higher schol, 1967.

Olga N. Lyubimova, Vladivostok, Russia
Konstantin N. Pestov, Vladivostok, Russia
Ekaterina A. Grigasova, Vladivostok, Russia

On existence and uniqueness of solutions in several boundary-value problems for the Euler equations

Alexander E. Mamontov
mamont@hydro.nsc.ru

Abstract

We consider several boundary-value problems for the Euler equations describing flows of an ideal incompressible fluid in a bounded domain: the problem NP with nonpenetration condition at the boundary as well as so called through flow problems describing flows of the fluid through the domain, with different types of boundary conditions (then three problems appear, we call them TF.I, TF.II and TF.III). We are interested in global (i. e., "in the whole" in time and input data) existence and uniqueness theorems for these problems formulated in the widest possible classes of solutions. Such interest if stimulated by well-known global existence problem for three-dimensional Euler equations, where solutions become nonsmooth even if they are smooth at the initial moment of time, so the named problem seems to meet its solution only in the classes of extremely irregular functions. In the other words, we have to study nonsmooth solutions of the Euler equations and prove their existence and uniqueness. We present two main results. The first result consists in uniqueness of solutions to the problems NP, TF.II and TF.III (for any dimensions of the flow) in the classes with unbounded vorticity. These classes are presented using the Orlicz classes and seem to be easy to verify in applications since they are formulated in a rather clear form as against well-known results. The second result consists in global existence theorem for the two-dimensional problem TF.I in the classes of solutions with unbounded vorticity that belongs to the Lebesgue spaces L_p with $p > 4/3$. Our methods discover curious relations of the named problems with the theory of integral transforms.

1 Introduction

Consider the Euler system which describes nonsteady flows of an ideal incompressible fluid:

$$\frac{\partial \boldsymbol{u}}{\partial t} + (\boldsymbol{u} \cdot \nabla)\boldsymbol{u} + \nabla p = \boldsymbol{f}, \qquad \mathrm{div}\boldsymbol{u} = 0. \tag{1}$$

Here, as usually, $\boldsymbol{u}$ stands for the velocity vector, p is the pressure, and $\boldsymbol{f}$ is the specified vector of external mass forces; all these quantities are functions of the time t and the space variables $\boldsymbol{x} \in \mathbb{R}^n$, $n \in \mathbb{N}$; the operators div and ∇ act in $\boldsymbol{x}$. The model (1) is much simplified in the sense of mechanics, and nevertheless appears to be rather substantial what attracts mathematicians. We can't describe here the large number of existing results, but note that the global solvability of any boundary value problems for (1) in the general three-dimensional case remains an open problem.

The most popular boundary value problems for (1) are the Cauchy one, i. e. the problem in $\mathbb{R}^n \times (0, T)$ with the initial data

$$\boldsymbol{u}|_{t=0} = \boldsymbol{u}_0, \tag{2}$$

and the "nonpenetration problem" in $Q_T = \Omega \times (0, T)$ which describes flows in a bounded domain $\Omega \subset \mathbb{R}^n$, with the initial data (2) and the boundary condition

$$\boldsymbol{u} \cdot \boldsymbol{n}|_{\partial\Omega\times(0,T)} = 0 \tag{3}$$

(which means the impermeable boundary), where $T > 0$ is an arbitrary number, and $\boldsymbol{n}$ is the outward normal to $\partial\Omega$. Most results concerning global solvability and optimal uniqueness classes

for (1) deal namely with these two problems. The latter question (uniqueness in the widest possible classes) is especially actual since the mentioned problem of the global solvability of (1) as $n = 3$ seems to be solved (in the future) only in the classes of rather nonsmooth solutions.

As against the global existence, the dimension of the flow is unessential in the uniqueness problem. The most often way to formulate the uniqueness classes is to express them in terms of the vorticity $\boldsymbol{\omega} = \mathrm{rot}\boldsymbol{u}$. The strongest result in this direction is obtained in [1], where the uniqueness of solutions to the nonpenetration problem

NP={(1),(2),(3)}

is proved in the classes with the vorticity belonging to specially normed scales of the spaces L_p (see also the result [2] in the Besov spaces). Our goal is to give a similar answer in terms of the Orlicz spaces (that leads to more clear and simply verified conditions), and also to extend this result over the through flow problems (describing flows of a fluid through the given domain).

In through flow problems the boundary $\partial\Omega$ of the flow domain Ω splits into three non-intersecting fragments: Γ_1, Γ_2 and Γ_0 (which are the inflow section, outflow section and impermeable section correspondingly), where:

$$\boldsymbol{u} \cdot \boldsymbol{n}|_{\Gamma_0 \times (0,T)} = 0, \tag{4}$$

$$\boldsymbol{u} \cdot \boldsymbol{n}|_{\Gamma_1 \times (0,T)} = g_1 < 0, \tag{5}$$

$$\boldsymbol{u} \cdot \boldsymbol{n}|_{\Gamma_2 \times (0,T)} > 0 \tag{6}$$

(only the sign is specified) or

$$\boldsymbol{u} \cdot \boldsymbol{n}|_{\Gamma_2 \times (0,T)} = g_2 > 0 \tag{7}$$

(the exact value is specified). It is clear that these conditions (as against (3)) are not sufficient now, and the choice of additional boundary conditions leads to several versions of the problem (we follow [3] in the classification of these versions). The most popular version is the through flow problem of the first type, in which the tangent components of the vorticity

$$\boldsymbol{\omega}_\sigma|_{\Gamma_1 \times (0,T)} = \boldsymbol{h} \tag{8}$$

(here $\boldsymbol{h}$ is a tangent vector field, and the index σ stands for tangent component of a vector) are specified at the entrance, that leads to the problem

TF.I={(1),(2),(4),(5),(7),(8)}.

In the two-dimensional case the problem TF.I, as well as NP, is deeply investigated globally. When $n = 2$, the problem may be considered as a three-dimensional one with Ω being the cylinder of infinite height, and the vorticity taking the form $\boldsymbol{\omega} = (0, 0, \omega)$, so that the condition (8) means just that the scalar vorticity ω is specified at the entrance. The problem TF.I is investigated much better than other versions of through flow problem (especially if we seek for global results), but this version has two essential disadvantages: difficult physical interpretation and excessive smoothness in the classes of uniqueness.

In the through flow problem of the second type the full velocity vector is specified at the entrance, i. e. the tangent components of the velocity are specified in addition to (5):

$$\boldsymbol{u}_\sigma|_{\Gamma_1 \times (0,T)} = \boldsymbol{r}, \tag{9}$$

and the pressure (instead of (7)) is specified at the exit:

$$p|_{\Gamma_2 \times (0,T)} = p_*. \tag{10}$$

As a result, we come to the problem

TF.II={(1),(2),(4),(5),(6),(9),(10)}.

Finally, the through flow problem of the third type differs from the preceding one in the condition at the exit which is (7) instead of (10), and the resulting problem is

TF.III={(1),(2),(4),(5),(7),(9)}.

2 Uniqueness in terms of $\nabla \otimes \boldsymbol{u}$

Suppose we are given a number $T > 0$ and a bounded domain $\Omega \subset \mathbb{R}^n$ with the boundary such that the Gauss theorem holds (piecewise C^1 is sufficient). The topological conditions will be mentioned as they will be necessary. Let us consider, following [1], solutions to (1) of the following class:

$$\nabla \otimes \boldsymbol{u},\ \boldsymbol{u}_t \in L_\infty(0, T, L_r(\Omega)), \qquad \forall r < +\infty. \tag{11}$$

This provides the corresponding regularity for p (provided that $\boldsymbol{f}$ is sufficiently regular), so that the equations (1) may be treated almost everywhere, and initial and boundary values in the problems NP, TF.II and TF.III are accepted in the sense of continuity. This way of defining a solution is more convenient in boundary value problems than integral identities. Thus, if $(\boldsymbol{u}_1, p_1)$ and $(\boldsymbol{u}_2, p_2)$ are the solutions to (1) of the mentioned class then their difference $\boldsymbol{u} = \boldsymbol{u}_1 - \boldsymbol{u}_2$ in the problems NP, TF.II and TF.III satisfies the inequality

$$\int\limits_\Omega |\boldsymbol{u}|^2 d\boldsymbol{x} \leqslant 2 \int\limits_0^t d\tau \int\limits_\Omega |\boldsymbol{u}|^2 |\mathbb{D}(\boldsymbol{u}_2)| d\boldsymbol{x} \tag{12}$$

(here $\mathbb{D}(\boldsymbol{v})$ stands for the rate of deformations tensor for the vector field $\boldsymbol{v}$).

In this way, during the proof of uniqueness of solutions in the class (11) we come to the Gronwall-type inequality (Osgood's inequality)

$$\int\limits_\Omega \psi(t, \boldsymbol{x}) d\boldsymbol{x} \leqslant \int\limits_0^t \int\limits_\Omega g(s, \boldsymbol{x}) \psi(s, \boldsymbol{x}) d\boldsymbol{x} ds \tag{13}$$

with nonnegative functions ψ and g, in which it is necessary to prove that $\psi = 0$ (under minimal restrictions for g). This is trivial in the case of bounded g's since it reduces to classical Gronwall's lemma, but the similar result for (13) remains true for some classes of unbounded g's as well. The paper [1] contains a result for (13) in terms of specially normed scales of the spaces L_p, i. e. under the condition of the form

$$\|g\|_{L_\infty(0,T,L_r(\Omega))} \leqslant \theta(r), \qquad r \gg 1 \tag{14}$$

with special (rather bulky) conditions for the growth of the function θ at the infinity, and this result gave the corresponding solution in the uniqueness problem for NP. The idea of our paper is that the result for (13) (and consequently for (1)) may be obtained in more convenient terms of the Orlicz spaces.

Let us remind that any so-called N-function M (convex even function defined in $\mathbb{R}$ and growing at the infinity faster than linear functions) generates the Orlicz class $K_M(\Omega) = \left\{ u \;\middle|\; \int\limits_\Omega M(u(\boldsymbol{x})) d\boldsymbol{x} < \infty \right\}$ and its linear span called the Orlicz space $L_M(\Omega)$. In the case $M(s) = s^p$ this space coincide with L_p, otherwise these classes allow to describe the properties of functions in Ω more precisely. In particular, the paper [4] contains the following exhaust solution of the Gronwall-type problem (13): the required relation $\psi = 0$ follows from (13) provided that $g \in K_\Phi(Q_T)$ with $\Phi \in \mathcal{K}$, where the class $\mathcal{K}$ consists of functions Φ which grow at the infinity rapidly enough, namely,

$$\int^{+\infty} \frac{\ln \Phi(s)}{s^2} ds = +\infty. \tag{15}$$

Otherwise, if $\Phi \notin \mathcal{K}$, a counterexample may be constructed, in which $\psi \neq 0$ and $g \in K_\Phi(Q_T)$ satisfy (13).

This result immediately leads to the uniqueness theorem for the problems NP, TF.II and TF.III in the class

$$\nabla \otimes \boldsymbol{u} \in K_\Phi(Q_T), \qquad \Phi \in \mathcal{K}. \tag{16}$$

3 Uniqueness in terms of vorticity

In order to translate the class (16) into the "vorticity language" we have to study the behavior of the mapping $A : \boldsymbol{\omega} \mapsto \nabla \otimes \boldsymbol{u}$ in the Orlicz spaces. The properties of this mapping are well-known in L_p, at least in the problems NP and TF.III since there A is the operator of the problem

$$\mathrm{rot}\boldsymbol{u} = \boldsymbol{\omega}, \qquad \mathrm{div}\boldsymbol{u} = 0; \qquad \boldsymbol{u} \cdot \boldsymbol{n}|_{\partial\Omega} = g_0, \tag{17}$$

where $g_0 = 0$ in the problem NP, and

$$g_0 = \begin{cases} 0 & \text{at } \Gamma_0, \\ g_1 & \text{at } \Gamma_1, \\ g_2 & \text{at } \Gamma_2 \end{cases} \tag{18}$$

in the problem TF.III. For example, in NP we obtain $\|A\|_{\mathcal{L}(L_r)} \leqslant Cr$ (let us, for the sake of simplicity, consider below only singly connected domains Ω). It is natural now to use the extrapolation results written in [5] in order to obtain the properties of A in the Orlicz spaces as automatic consequences of its properties in L_p (without use of the nature of this operator). As a result, we come to the relation $A \in \mathcal{L}(L_M, L_\Phi)$, where (M, Φ) is a pair of arbitrary rapidly growing N-functions related as $M = \mathbf{S}[\Phi]$, where

$$\mathbf{S}[\Phi](v) = \int\limits_0^{+\infty} e^{-s}\Phi(vs)ds. \tag{19}$$

The condition $\Phi \in \mathcal{K}$ used in (16) corresponds to $M \in \mathcal{K}_1$ under the relation $M = \mathbf{S}[\Phi]$, where the class $\mathcal{K}_1$ consists of functions M that satisfy the condition

$$\int\limits^{+\infty} \frac{\ln\ln M(s)}{s^2} ds = +\infty. \tag{20}$$

The investigation of the problem TF.III is made similarly. As a result, we come to the following

Theorem 1. *The problems NP, TF.II and TF.III cannot have more than one solution in the class (16). In particular, for singly connected domains Ω the problems NP and TF.III (in the latter case the condition $g_0 \in L_\infty(0, T, W^1_\infty(\partial\Omega))$ is sufficient, see (18)) cannot have more than one solution in the class*

$$\mathrm{rot}\boldsymbol{u} \in L_\infty(0, T, L_M(\Omega)), \qquad M \in \mathcal{K}_1 \tag{21}$$

(see (20)). As usual, the uniqueness of the pressure holds to within an additive constant.

It is curious to note that the formulation of the uniqueness in the final terms of the vorticity appeared possible namely in those two problems (NP and TF.III) which admit global (in time) existence results (naturally, only for $n = 2$, moreover, locally with respect to the initial data in the problem TF.III), thus these two problems (after the generalization of well-known existence theorems) admit the global existence and uniqueness of solutions in the class (21) as $n = 2$. In other cases the result of Theorem 1 appears conditional since we cannot guarantee global existence of solutions in the corresponding classes in the framework of known results. In spite of well developed global theory (again, two-dimensional) for the problem TF.I, the smoothness should be one order higher to provide the uniqueness. It is not clear how to avoid this difficulty. However, in the problem TF.I the following result can be obtained:

4 Nonsmooth solvability of the two-dimensional problem TF.I

Consider the through flow problem of the first type for the system (1) as $n = 2$, i. e., the initial and boundary conditions are: (2), (4), (5), (7) and the last condition (8), which takes the form

$$\omega|_{\Gamma_1 \times (0,T)} = \omega_1, \tag{22}$$

where $\omega = \operatorname{rot} \boldsymbol{u}$ stands for the scalar vorticity.

This problem was studied deeply in the papers [7], [6], but only in the case of sufficiently smooth solutions and input data. Here we propose a result in the class $\{\operatorname{rot} \boldsymbol{u} \in L_\alpha\}$ with $\alpha > 4/3$. More exactly, we suppose the following properties of the input data (here $4/3 < \alpha < 2$, the case $\alpha \geqslant 2$ is obviously more simple):

$$\begin{gathered}
\boldsymbol{u}_0 \in L_{\frac{2\alpha}{2-\alpha}}(\Omega), \quad \operatorname{div} \boldsymbol{u}_0 = 0, \quad \omega_0 = \operatorname{rot} \boldsymbol{u}_0 \in L_\alpha(\Omega), \\
g_0 \in L_1(0,\, T, W_\alpha^{1-1/\alpha}(\Gamma)) \cap L_\infty((0,\, T) \times \Gamma_1), \\
\oint\limits_\Gamma g_0 \, ds = 0 \ \text{ for a.e. } t \in (0,\, T), \\
\omega_1 \in L_1(0,\, T;\, L_\alpha(\Gamma_1)), \quad \boldsymbol{f} \in L_1(0,\, T;\, W_\alpha^1(\Omega)), \quad \operatorname{rot} \boldsymbol{f} \in L_1(0,\, T;\, L_\alpha(\Omega))
\end{gathered} \tag{23}$$

(see (18)). Our main goal is to minimize the requirements for ω_1, and this goal is achieved good enough in (23). The requirements for $\boldsymbol{u}_0$, $\boldsymbol{f}$ and g_0 in (23) are minimal in the framework of the class of solutions under consideration (namely, $\operatorname{rot} \boldsymbol{u} \in L_\alpha$ — see the Definition below). The fact typical for the through flow problem of the first type is that the requirements for the vorticity at the vertical surface of the cylinder Q_T (namely, at the entrance) are similar to those at its bottom surface, since the input characteristics present at both surfaces, however this fact disagrees with the idea that the trace of the vorticity on Γ is desirable to be less smooth than the vorticity in the flow domain.

Similar to [7], it is convenient to separate the potential part $\nabla\Phi$ of the velocity as the solution of the Neumann problem

$$\Delta\Phi = 0, \qquad \left.\frac{\partial \Phi}{\partial n}\right|_\Gamma = g_0. \tag{24}$$

Definition. *The vector field $\boldsymbol{u} = \boldsymbol{v} + \nabla\Phi$ is called generalized solution of the problem (1),(2),(4),(5),(7),(22), if $\boldsymbol{v} \in L_1(0,\, T;\, L_{\frac{2\alpha}{2-\alpha}}(\Omega))$, $\boldsymbol{v} \cdot \boldsymbol{n}\,|_\Gamma = 0$, $\operatorname{div} \boldsymbol{v} = 0$ (i. e., $\operatorname{div} \boldsymbol{u} = 0$), $\operatorname{rot} \boldsymbol{v} \in L_\infty(0,\, T;\, L_\alpha(\Omega))$, Φ is the solution of (24), and the integral identity*

$$\begin{gathered}
\int\limits_0^T \int\limits_\Omega \operatorname{rot} \boldsymbol{u} \left[\frac{\partial \varphi}{\partial t} + \boldsymbol{u} \cdot \nabla\varphi\right] d\boldsymbol{x}\, dt + \int\limits_\Omega (\operatorname{rot} \boldsymbol{u}_0)\, \varphi|_{t=0}\, d\boldsymbol{x} + \\
+ \int\limits_0^T \int\limits_\Omega (\operatorname{rot} \boldsymbol{f}) \varphi \, d\boldsymbol{x}\, dt = \int\limits_0^T \int\limits_{\Gamma_1} \omega_1\, g_1\, \varphi \, ds\, dt
\end{gathered}$$

holds for all functions $\varphi \in C^1(\overline{Q})$ vanishing at $(0,\, T) \times \Gamma_2$ and as $t = T$.

Our main result for the two-dimensional problem TF.I is the following

Theorem 2. *Provided (23), the problem (1),(2),(4),(5),(7),(22) has a solution, for which the following estimate is valid:*

$$\begin{gathered}
\|\operatorname{rot} \boldsymbol{u}\|_{L_\infty(0,\, T;\, L_\alpha(\Omega))} \leqslant \left[\|\operatorname{rot} \boldsymbol{u}_0\|^\alpha_{L_\alpha(\Omega)} + \|g_1\|_{L_\infty((0,\, T)\times\Gamma_1)} \|\omega_1\|^\alpha_{L_1(0,\, T;\, L_\alpha(\Gamma_1))}\right]^{\frac{1}{\alpha}} + \\
+ \|\operatorname{rot} \boldsymbol{f}\|_{L_1(0,\, T;\, L_\alpha(\Omega))}.
\end{gathered}$$

The main idea of the proof is to construct the solution of the regularized problem (that is possible due to the results of [6], where smooth solutions, and only them, were considered) and then to pass to the limit with respect to the regularization parameters. A similar idea was used in [7], but there the regularization parameter was a vanishing viscosity, that does not allow to consider solutions with unbounded vorticity (since the estimate for vorticity in L_p, $p < \infty$, uniform in the vanishing viscosity, is hard to obtain).

The results announced here are written completely in our papers [8] and [9].

Acknowledgements

The work is supported by the Russian Foundation for Basic Research (Grant 10-01-00447), by Siberian Branch of the Russian Academy of Sciences (Project 4.3) and by Ministry of Education and Science of the Russian Federation (Project 2.1.1.4918).

References

[1] Yudovich V.I. Uniqueness theorem for the basic nonstationary problem in the dynamics of an ideal incompressible fluid. Mathematical Research Letters, 1995, V. 2, P. 27–38.

[2] Vishik M. Incompressible flows of an ideal fluid with vorticity in borderline spaces of Besov type. Ann. Sci. École Norm. Sup. (4), 1999, V. 32, N 6, P. 769–812.

[3] Kazhikhov A.V. and Ragulin V.V. Nonsteady problems of flow of an ideal fluid through a bounded domain. Doklady of the Russian Academy of Sciences (Doklady Mathematics), 1980, V. 250, N 6, P. 1344–1347.

[4] Kazhikhov A.V. and Mamontov A.E. On a certain class of convex functions and the exact well-posedness classes of the Cauchy problem for the transport equation in Orlicz spaces. Siberian Math. J., 1998, V. 39, N 4, P. 716–734 (previously in Sib. Mat. Zhurn., 1998, V. 39, N 4, P. 831–850 [in Russian]).

[5] Mamontov A.E. Integral representations and transforms of N-functions. II. Siberian Math. J., V. 47, 2006, N 4, P. 669–686 (previously in Sib. Mat. Zhurn, V. 47, 2006, N 4, P. 811–830 [in Russian]).

[6] Yudovich V.I. A two dimensional problem of unsteady flow of an ideal incompressible fluid across a given domain. Amer. Math. Soc. Translations, V. 57, 1966, P. 277–304 (previously in Mat. Sb., 64 (1964), pp. 562–588 [in Russian]).

[7] Alekseev G.V. On solvability of the nonhomogeneous boundary value problem for two-dimensional nonsteady equations of ideal fluid dynamics. Dinamika Sploshnoy Sredy, Novosibirsk, Lavrentyev Institute of Hydrodynamics, Issue 24, 1976, P. 15–35. [in Russian]

[8] Mamontov A.E. On the uniqueness of solutions to boundary value problems for non-stationary Euler equations, in the book: New Directions in Mathematical Fluid Mechanics (The Alexander V. Kazhikhov Memorial Volume); Series: Advances in Mathematical Fluid Mechanics; 2009, Birkhauser Verlag Basel/Switzerland, P. 281–299. Editors: A.V.Fursikov, G.P.Galdi and V.V.Pukhnachev.

[9] Mamontov A.E. and Uvarovskaya M.I. On the global solvability of the two-dimensional through-flow problem for the Euler equations with unbounded vorticity at the entrance. Vestnik of Novosibirsk State University, "Mathematics, Mechanics and Informatics" Series, 2010, to appear. [in Russian]

Alexander E. Mamontov, Lavrentyev Institute of Hydrodynamics, Lavrentyev Prospekt 15, Novosibirsk 630090, Russian Federation

Limiting phase trajectories and "wave – particle" duality in Classical Physics

L. I. Manevitch
lmanev@chph.ras.ru

Abstract

It is well-known that the Classical Mechanics is based on the concept of point-like particles. If interparticle interaction is absent (with the exception of collisions) such a model allows not only to derive the equations of motion but also to solve them efficiently with use of the conservation laws. If the interparticle interaction is strong (e.g., in crystalline lattice) the particle presentation is not adequate in *the linear theory* when analyzing the equations of motion. The reason is that in this case not the particles but collective (wave-like) motions – *normal modes* can be considered as non-interacting ones. It was recognized during the last half of the century that *nonlinear integrable systems* can manifest both types of behavior dependent on the initial conditions: wave-like (*cnoidal waves*) or particle-like (*solitons and breathers*). However, it was not recognized that there exists one more origin of *"wave – particle"* duality outside Quantum Mechanics, becoming apparent even in the framework of linear theory if to single out the important class of *weakly coupled systems*. While in the wave description the key notion is *nonlinear normal mode(NNM),* the particle like behavior can be adequately circumscribed in the framework of new concept with key notion *limiting phase trajectory (LPT)*. We consider the most clear manifestation of the "wave – particle" duality in the framework of this concept.

1 Introduction

The development of nonlinear dynamics during last half century has shown that one of the most important manifestations of nonlinearity is existence of particle-like waves-solitons. In the integrable infinite systems the existence of solitons and their quantity depends on the initial conditions [1], [2]. In general case one deals with both periodic waves and solitons. Moreover, in such systems as Sine-Gordon (SG) or nonlinear Schrodinger (NSE) the localized oscillating excitations (breathers) can also exist [1], [2] while the periodic waves are unstable.

However, it was not recognized that there exists one more origin of *"wave – particle"* duality outside Quantum Mechanics, becoming apparent even in the framework of linear theory if to single out the important class of *weakly coupled systems*.

We have shown recently that the problem of energy localization in finite nonlinear systems [3] is strongly connected with a new concept of LPT, introduced in [8]. This concept allows describing efficiently the intensive energy exchange and the transition to energy localization. In this connection the existence of breathers in infinite chain turns out to be a particular case of much more general situation [4]. At that, the concept of LPT becomes an appropriate foundation for discussion concerning the "wave-particle" duality in Classical Mechanics.

The most clear manifestation of "wave-particle" duality is realized in the system of two weakly interacting nonlinear oscillators when the wave description remains valid for initial conditions corresponding to nonlinear normal modes but ceases to be satisfactory if only one of the oscillators is initially excited. Necessity of particle-like description of intensive energy exchange which can be identified with nonlinear beats becomes evident here due elaboration of specific and efficient mathematical tool for its study.

The extensions in several directions are possible. Firstly, we discuss briefly the transient resonant oscillations in forced nonlinear oscillator supposing that the frequency of excitation can be

variable. In this case the "particle" language turns out to be adequate again for treatment of *intensive energy exchange and transfer* while the "wave" description remains valid for study of *steady state* oscillations.

Following extension relates to fundamental problem of the nature of energy localization in periodic nonlinear chains. It is shown that the way to localization (when the nonlinearity grows) begins from a strong (resonant) interaction of the normal modes in the range of their frequencies densification that makes suitable a transition to particle-like description on the basis of the LPT-concept, the "particle" being the part of the oscillatory chain. So, we can first extend the notion of beats to the systems with many degrees of freedom. The following stage is instability of the boundary mode with appearance of two new NNMs and the separatrix which separates them. Finally, coincidence of LPT and separatrix leads to prohibition of complete energy exchange and inevitable energy localization on the excited part of the chain.

2 The system of two weakly coupled nonlinear oscillators

We begin from the simplest and most clear system: two coupled identical nonlinear oscillators (Fig.1).

If the coupling is absent, the oscillators can be considered as the particles interacting only by collision. In the case of strong coupling, the normal modes (in-phase and out-of-phase) do not interact or interact weakly because their frequencies are strongly different. Weakening of the coupling leads to frequencies coming together. For linear systems it seems unimportant because of the superposition principle that allows predicting the system's motion with arbitrary coupling and initial conditions on the basis normal modes. Therefore, the class of weakly-interacting particles was not really singled out although the superposition principle is absent for nonlinear systems. In fact, the duality "wave – particle" can be revealed just in this case. Really, the wave language is valid as before if the initial conditions correspond to any of modes. However, the modes strongly interact now because their frequencies are close and the resonance relations appear between them that leads to intensification of the intermodal interaction. As a consequence, both modes have to be taken into account if the initial conditions are far from the normal modes and wave description becomes to be non-adequate one. Therefore the particle description becomes more efficient even in the case of linear system, all the more for weakly coupled nonlinear oscillators.

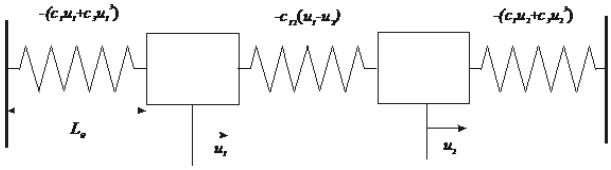


Fig. 1. System under consideration.

Weakness of interaction allows to introduce an additional time scale $\tau_2 = \varepsilon\tau_1$ (alongside with the fast time $\tau_1 = \sqrt{\frac{c_1}{m}}t$) and to use two scale procedure. Then the equations of main asymptotic approximation can be written as follows [5]

$$\begin{array}{l} \frac{df_1}{d\tau_2} + i\beta f_2 - 3i\alpha|f_1|^2 f_1 = 0, \\ \frac{df_2}{d\tau_2} + i\beta f_1 - 3i\alpha|f_2|^2 f_2 = 0, \end{array} \tag{1}$$

which describe, as well as the mechanical system discussed, others including optic couplers, bose-einstein condensates etc [14]. This system in contrast to starting equations is completely integrable and has two integrals:

$$H = \beta(f_2 f_1^* + f_1 f_2^*) - \frac{3}{2}\alpha(|f_1|^4 + |f_2|^4), \tag{2}$$

$$N = |f_1|^2 + |f_2|^2, \tag{3}$$

Here

$$f_j = e^{i\beta\tau_2}\varphi_{j,n}, \quad j = 1, 2, \tag{4}$$

$$\varphi_j = e^{-i\tau_1}(\frac{dU_j}{d\tau_1} + iU_j) \quad \varphi_j^* = e^{i\tau_1}(\frac{dU_j}{d\tau_1} - iU_j), \; 8\alpha\varepsilon = \frac{c_3 L_0^3}{c_1}; \; 2\beta\varepsilon = \frac{c_{12}}{c_1}, \; U_j = \frac{u_j}{L_0}. \tag{5}$$

where u_j $(j = 1, 2)$ – displacements of the oscillators;

$$\varphi_j(\tau_1, \tau_2) = \sum_n \varepsilon^n \varphi_{j,n}(\tau_1, \tau_2), \quad j = 1, 2. \tag{6}$$

The integral (3) allows introducing two real variables θ and Δ characterizing relationship between the oscillators' amplitudes and relative phase shift.

$$f_1 = \sqrt{N}\cos\theta\, e^{i\delta_1}, \quad f_2 = \sqrt{N}\sin\theta\, e^{i\delta_2}, \quad \Delta = \delta_1 - \delta_2 \tag{7}$$

Then the equations of motion are written as follows

$$\frac{d\theta}{d\tau_2} = \beta\sin\Delta, \quad \sin 2\theta\frac{d\Delta}{d\tau_2} = 2\beta\cos 2\theta\cos\Delta + \frac{3}{2}\alpha N\sin 4\theta, \tag{8}$$

The integral (2) has the form following from

$$H = (\cos\Delta + k\sin 2\theta)\sin 2\theta, \; k = \frac{3\alpha N}{4\beta}, \; \alpha > 0 \tag{9}$$

The system (8) is strongly nonlinear even in the case of initially linear problem.

The stationary points at the phase plane (Fig. 2) correspond to Nonlinear Normal Modes (NNMs) [6], [7] which can be realized under appropriate initial conditions when the wave description is valid (only two lower quadrants can be considered because of phase plane periodicity).

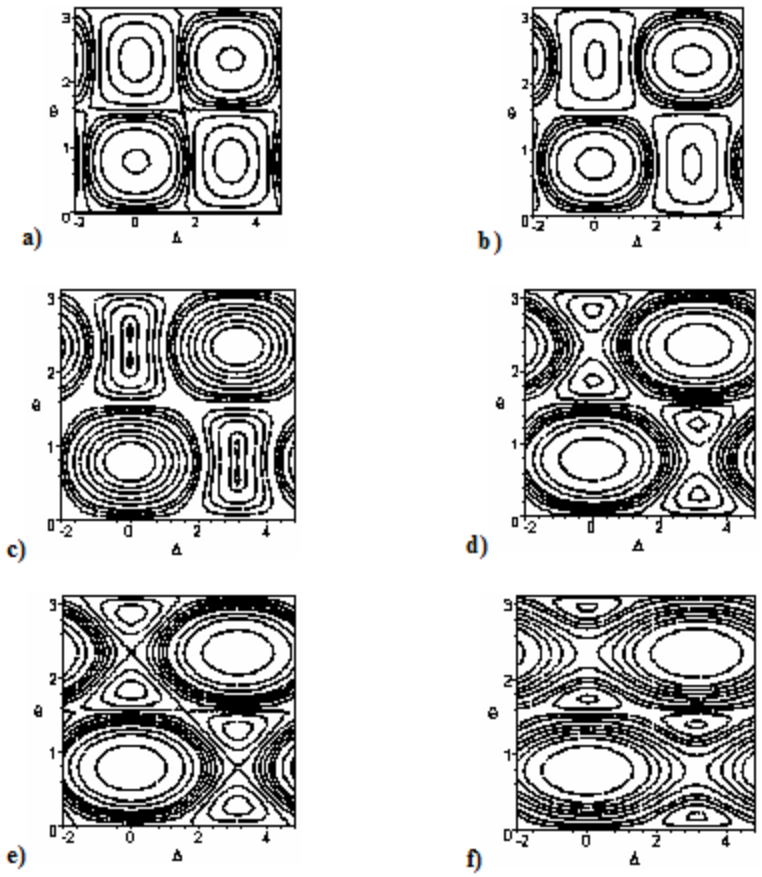


Fig. 2 Phase trajectories in the plane for: (a) $k = 0.2$, (b) $k = 0.4$, (c) $k = 0.55$, (d) $k = 0.9$, (e) $k = 1$, (f) $k = 1.5$

If the initial conditions are not close to NNMs the adequate description of energy exchange between the weakly interacting oscillators is attained in the framework of Limiting Phase Trajectories (LPTs) concept [7], [8] which preserves the particle language. The LPT is the phase trajectory which is maximally distant from the stationary point corresponding to NNM. This concept is equally general as that of NNMs but in contrast to latter the LPT describes not energy conservation but complete energy exchange (CEE) between the oscillators. Using LPT concept we describe two dynamical transitions taking place when nonlinearity (parameter k) grows. First of them is due to bifurcation of normal mode caused by its instability and appearance two additional normal modes (Fig.2c). As this takes place, the complete energy exchange describing by LPT is possible as before. The second dynamic transition occurs when LPT coincides with separatrix (Fig. 2e) and after that the CEE becomes impossible (Fig.2f). Consequently, the transition "CEE – energy localization" on the initially excited oscillator takes place.

This example confirms distinctly the existence of "wave – particle" duality. In this connection the key notions are NNM (for wave –like description) and LPT (for description of "particle" side of duality). Because the history of NNM began more than two centuries ago all aspects of their determination and application are well-known (see, e.g. [5], [6]).

First of all let us note that determination of both NNMs and LPTs turns out to be well defined problems which are greatly simplified if comparing to those for arbitrary solution. NNMs at the phase plane (Fig.2) are nothing other as stationary points which do not depend on time; therefore we have to solve algebraic (transcendental) equations for their determinations instead differential ones. As for LPTs, the drastic simplification consists in the existence of very simple connection between the variables θ and Δ because the value of H for the LPT in integral (9) is equal to zero. Therefore the variables θ and Δ in this case are connected by the equation

$$\cos\Delta = -k\sin 2\theta, \tag{10}$$

so that $\sin\Delta = \pm\sqrt{1-k^2\sin^2 2\theta}$. Then the first of the equations (8) can be written as:

$$\frac{d\theta}{d\tau_2} = \pm\beta\sqrt{1-k^2\sin^2 2\theta}, \tag{11}$$

The solution of Eq. (11) for the plus sign is the elliptic Jacobi's function $\theta = \frac{1}{2}am\,(2\beta\tau_2, k)$. Because $0 \le \theta \le \pi/2$ by definition, one can use the negative sign for $(2n-1)\,\pi < 2\beta\tau_2 < 2n\pi,\ \ n = 1, 2, 3\ldots$

Thus we arrive at the final solution

$$\theta = \frac{1}{2}|am(2\beta\tau_2, k)|, \quad \Delta = \pm\arccos[k\ sn(2\beta\tau_2, k)], \tag{12}$$

with period $K(k)$, i.e., the complete elliptic integral of the first kind for the in-phase oscillations. The solution for the out-of-plane oscillations is

$$\theta = \frac{1}{2}|am(2\beta\tau_2, k)|, \quad \Delta = \pi \pm \arcsin[k\ sn(2\beta\tau_2, k)], \tag{13}$$

The periodic functions (12) are not smooth; $\Delta\,(2\beta\tau_2)$ has breaks at the points $2\beta\tau_2 = (2n-1)\,\pi,\ \ n = 0, 1, \ldots$, and $\theta\,(2\beta\tau_2)$ has discontinuities in the derivative at these points (in terms of distributions theory $d\theta/d\tau_2 = (2\beta/\pi)\Delta$). The value $k = 0.5$ corresponds exactly to the first dynamic transition.

The second dynamic transition occurs when $k = 1$. In this case one can find a simple analytical solution corresponding to the LPT:

$$2\beta\tau_2 = \int_0^{2\theta} \frac{d\,(2\theta)}{\cos 2\theta}, \quad \theta = \frac{1}{2}\arcsin\frac{1-e^{-2\beta\tau_2}}{1+e^{-2\beta\tau_2}} \tag{14}$$

It can be seen from (14) that the LPT actually coincides with a separatrix if $k \to 1 : \theta \to \pi/4$ when $\tau_2 \to \infty$.

It is convenient to introduce further two non-smooth functions $\tau(\tau_2)$, $e(\tau_2)$ (Fig. 3). Similar functions were introduced first in [9] to calculate the smooth oscillatory regimes close to vibro-impact ones. The development of corresponding techniques is also presented in [7].

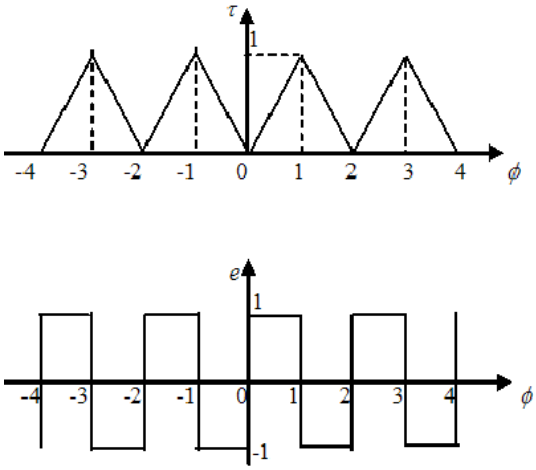


Fig. 3 The non-smooth basic functions $\tau(\tau_2/a)$, $e(\tau_2/a)$, where $2a$ is a halved period (in time τ_2)

The reason for use of non-smooth basic functions becomes clear if to derive the second order equation for θ which is valid for LPTs only:

$$\frac{d^2\theta}{d\tau_2^2} + k^2 \sin 4\theta = 0 \tag{15}$$

We have to keep in mind that the variable θ changes in the limits $0 < \theta < \frac{\pi}{2}$.

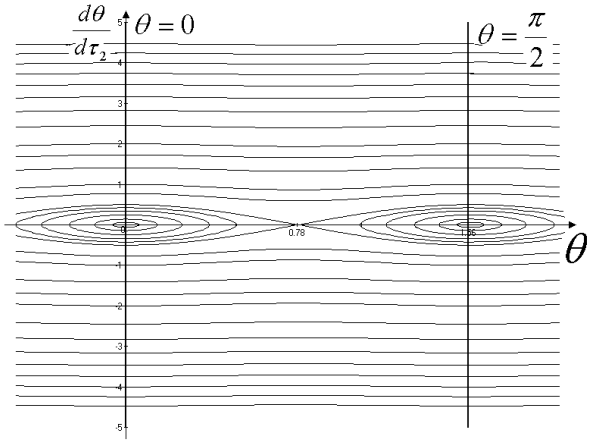


Fig. 4. Phase plane.

The phase plane corresponding to this equation is shown in Fig.4. The LPTs describing the linear beats are piecewise straight lines (and consequently are saw-tooth functions in temporal representation) which become distorted when the nonlinearity appears.

It means that in the case $k = 0$ (the linearized system) the solution (12) can be rewritten in the form $\theta = (\pi/2)\tau$, $\Delta = (\pi/2)e$, $\tau = \tau(\tau_2/a)$, $e = e(\tau_2/a)$ where $a = \pi/2\beta$ (exactly as in a vibro-impact process with velocity $\Delta = \pi/2$). After introducing the basic functions $\tau(\tau_2/a)$, $e(\tau_2/a)$, we can present the solution as

$$\Delta = X_2(\tau) + Y_2(\tau)e\left(\frac{\tau_2}{a}\right) \theta = X_1(\tau) + Y_1(\tau)e\left(\frac{\tau_2}{a}\right), \tag{16}$$

where the smooth functions $X_i(\tau)$, $Y_i(\tau)$ satisfy equations (12):

$$\frac{\partial}{\partial\tau}\left\{\begin{array}{c} X_1 \\ Y_1 \end{array}\right\} = \frac{1}{2}a\beta[\sin(X_2 + Y_2) \mp \sin(X_2 - Y_2)],$$

$$\frac{\partial}{\partial\tau}\left\{\begin{array}{c}X_2\\Y_2\end{array}\right\} = a\beta[ctg2(X_1+Y_1)\cos(X_2+Y_2) \mp ctg2(X_1-Y_1)\cos(X_2-Y_2)] \\ +\tfrac{3a}{2}\alpha N[\cos 2(X_1+Y_1) \mp \cos 2(X_1-Y_1)] \tag{17}$$

This techniques is based on the possibility to express any periodic function in the form (16) that was shown first in [9].

Then, we can search for the solution of equations (17) as follows:

$$X_i = \sum_{l=0}^{\infty} X_{i,l}\tau^l, \quad Y_i = \sum_{l=0}^{\infty} Y_{i,l}\tau^l, \quad j = 1,2 \tag{18}$$

where the generating solution is the linear beat:

$$X_{1,0} = 0, \quad X_{1,1} = \frac{\pi}{2}, \quad Y_{1,0} = 0, \quad X_{2,0} = 0, \quad Y_{2,0} = \frac{\pi}{2}, \tag{19}$$

It can be proved that the presentation (16), taking into account (18), actually recovers the exact solution of the nonlinear problem for the most intensive energy transfer between the oscillators. At that, the expansions (18) restore the exact local representation of the corresponding elliptic function (near $\tau = 0$), but the expressions (16) allow the prediction of the exact global behavior of the system. It is important to note that, even for large enough values of k, the solution appears close to that of linear beats; the only change is the barely seen curvature of the lines that are straight for linear beats, and a change of the period.

One can find corresponding corrections by considering the next order of approximations, namely, $X_{1,0} = 0, \;\; X_{1,1} = \alpha\beta, \;\; Y_{2,0} = \pi/2, \;\; Y_{2,1} = 2\alpha\beta k$, which coincide with those in the expansions of the exact solution.

Summarizing this section one can conclude that dynamics of two weakly coupled nonlinear oscillators demonstrates clearly the "wave-particle" duality compelling to use both descriptions in the same system and pass from one of them to another if the initial conditions change. The manifestation of such duality is closely connected with existence of LPTs which provide a conceptual and specific mathematical tool for description of intensive energy exchange between the oscillators as the particles. This destination of LPTs sheds light on their distinction from NNMs which preserve their initial energy in time.

3 Forced nonlinear oscillator

It was shown recently that the concept of LPT can be extended to various problems, in particular, to the problem of transient oscillations in weakly forced nonlinear oscillator. In this case we deal with energy exchange between the oscillator and the source of energy [10]. If intensive energy exchange is possible both they can be considered as weakly interacting "particles". The stationary states correspond here to steady state modes (SSMs) which are similar to NNMs in the systems with two or more degrees of freedom. In contrast to SSMs, the transient vibrations with intensive energy exchange between the oscillator and the source of energy can be adequately described by LPTs. In such transient oscillations the oscillator may be initially unexcited and then it accepts the maximal amount of energy which depends on the system's parameters and initial conditions. It can be clearly seen if to introduce the appropriate variables (which are in this case the modulus of complex amplitude and the phase shift between oscillator and source of energy) and to use the multiple scale procedure. Then the "wave" description relates to SSM (stationary points in slow time scale) while the "particle" one - to LPT. Here we deal again with two dynamical transitions. The first one is the appearance of new stationary states and separatrix, caused by bifurcation of stationary state, and the second one is the coincidence of LPT and separatrix.

We can consider more complex situation when the frequency of external force is variable in time. In this case two qualitatively new types of energy transition appear. They are both caused by slow frequency change during the vibration and slow passage through resonance. We call the first one as a Landau-Zener (LZ)-type transition by analogy with well-known quantum phenomenon [11], [12]. The second one is autoresonance (AR) [13] which was revealed far long.

The LZ-type process is possible in both linear and nonlinear systems. It leads to irreversible energy transfer to oscillator from energy source till its frequency drift from resonance. On the

contrary, autoresonance exists in nonlinear systems only, and consists in the continuous increase of the oscillator energy in resonance conditions. In both these cases LPT changes continuously during energy transfer and the process at its main stage can be characterized as wandering on LPT family similarly to wandering in weakly coupled oscillatory chains [14]. Irreversible energy exchange is a consequence of such wandering. This happens in the LZ case because the system inevitably leaves the resonance region. In the AR case the energy exchange happens due to continuous synchronization of frequency of external force with oscillator frequency, which in its turn changes because of the nonlinearity. Besides, the transitions from one type of energy transfer to the other caused by variation in system parameters can be observed. In both LZ-type and AR processes one can distinguish two stages at one of which the oscillator is similar to particle while at another stage the wave description dominates.

4 Limiting phase trajectories and the origin of energy localization in nonlinear oscillatory chains

Unexpectedly, the "wave – particle" duality manifests also in periodic nonlinear oscillatory chains modeling, in particular, the oligomer molecules. The analysis of such chains is much more complex than the system of two weakly coupled oscillators and requires extension of the beating notion on the systems consisting of many particles [4].

While use the initial variables, the "weak" links are absent here at all. Therefore the wave representation (in modal variables) can be naturally used in the systems with small number of particles. It corresponds to "strong coupling" between the particles but weak interaction between the normal modes. However, when the number of particles grows, the frequencies of different modes come close that leads to manifestation of intermodal interaction. First of all, it relates to the highest frequency modes. Then the language of particles becomes adequate if initial conditions correspond to excitation of the system playing the role of oscillator in the system with two degrees of freedom.

As a result, all processes in such oscillatory chains turn out to be similar to those in the discussed 2 DoF system (bifurcation due to instability of highest-frequency mode, beating with energy exchange between different parts of the chain), transition to coincidence of LPT and separatrix and so on.

We demonstrate that the spatial energy localization in a finite periodic Fermi-Pasta-Ulam chain results from the inhibition of complete energy exchange between different parts of the chain. The latter process is described by a Limiting Phase Trajectory, which is an alternative to the Nonlinear Normal Modes associated with conservation of energy. The well-defined transition from complete energy exchange to formation of breather-like excitations requires almost twice more energy than the threshold corresponding to the instability of the highest-frequency mode. Analytical results are confirmed by numerical simulations.

We consider the β-FPU system defined by the Hamiltonian

$$H_0 = \sum_{j}^{N} \frac{1}{2} p_j^2 + \frac{1}{2}(q_{j+1} - q_j)^2 + \frac{\beta}{4}(q_{j+1} - q_j)^4 \tag{20}$$

and the periodic boundary conditions ($q_{N+1} = q_1, p_{N+1} = p_1$), where q_j and p_j are the coordinates and the conjugate momenta, respectively, N is the number of particles.

The transformation to normal coordinates is given by the linear canonical transformation

$$q_j = \sum_{k=0}^{N-1} \sigma_{j,k}\xi_k \quad \sigma_{j,k} = \frac{1}{\sqrt{N}}[\sin(\frac{2\pi kj}{N}) + \cos(\frac{2\pi kj}{N})], \quad k = 0, 1, \ldots, N-1. \tag{21}$$

Then the equations of motion can be presented in complex form:

$$i\frac{d\Psi_k}{dt} + \omega_k\Psi_k - \frac{\beta}{8N}\omega_k \sum_{l=1}^{N-1}\sum_{m=1}^{N-1}\sum_{n=1}^{N-1} C_{k,l,m,n}(\Psi_l - \Psi_l^*)(\Psi_m - \Psi_m^*)(\Psi_n - \Psi_n^*) = 0. \tag{22}$$

where

$$\Psi_k = \frac{1}{\sqrt{2}}(\eta_k + i\omega_k\xi_k), \quad \Psi_k^* = \frac{1}{\sqrt{2}}(\eta_k - i\omega_k\xi_k), \tag{23}$$

and ξ_k and η_k are the amplitudes and the momenta of NNMs; the coordinate ξ_0, associated with motion of the center of mass.

Taking into account the dependence of the chain properties from the quantity of the particles, one can consider the value $1/N = \varepsilon$ as a small parameter of the system.

We employ the multiple scale procedure [5] in order to consider the processes on the time intervals greatly exceeding $1/\omega_k$. Following this procedure, we introduce the time scales:

$$\tau_0 = t, \quad \tau_1 = \varepsilon\tau_0 \tag{24}$$

where the "fast" and slow times τ_0, τ_1 correspond to the initial time scale of the system and to the slowly varying envelopes, respectively. The envelope functions φ_k are defined by the relations

$$\Psi_k = \varphi_k e^{i\omega_k t}. \tag{25}$$

We construct an asymptotic representation of φ_k in the form

$$\varphi_k = \sqrt{\varepsilon}(\chi_{k,1} + \varepsilon\chi_{k,2} + \varepsilon^2\chi_{k,3} + \ldots) \tag{26}$$

The two scale expansion based on (24), (26) are used to derive the equations of the leading-order approximation $\chi_{k,1}$:

$$\begin{array}{l} i\frac{d\chi_{N/2}}{d\tau_2} + \frac{3\beta}{4}[|\chi_{N/2}|^2\chi_{N/2} + 2(|\chi_{N/2-1}|^2 + |\chi_{N/2+1}|^2)\chi_{N/2} + (\chi_{N/2-1}^2 + \chi_{N/2+1}^2)\chi_{N/2}^*] = 0 \\ i\frac{d\chi_{N/2-1}}{d\tau_2} - \frac{\pi^2}{2}\chi_{N/2-1} + \frac{3\beta}{8}[(4|\chi_{N/2}|^2 + 3|\chi_{N/2-1}|^2 + 2|\chi_{N/2+1}|^2)\chi_{N/2-1} + \\ \qquad (2\chi_{N/2}^2 + \chi_{N/2+1}^2)\chi_{N/2-1}^*] = 0 \\ i\frac{d\chi_{N/2+1}}{d\tau_2} - \frac{\pi^2}{2}\chi_{N/2+1} + \frac{3\beta}{8}[(4|\chi_{N/2}|^2 + 3|\chi_{N/2+1}|^2 + 2|\chi_{N/2-1}|^2)\chi_{N/2+1} + \\ \qquad (2\chi_{N/2}^2 + \chi_{N/2-1}^2)\chi_{N/2+1}^*] = 0 \end{array} \tag{27}$$

To analyze this system, we turn from the "wave" representation to new "particle" representation. To this end, we introduce the new variables ψ_1, ψ_2, φ by the following formulas

$$\begin{array}{l} \psi_1 = \frac{1}{\sqrt{2}}(\chi_{N/2} - \frac{1}{\sqrt{2}}(\chi_{N/2-1} + \chi_{N/2+1})) \\ \psi_2 = \frac{1}{\sqrt{2}}(\chi_{N/2} + \frac{1}{\sqrt{2}}(\chi_{N/2-1} + \chi_{N/2+1})) \\ \varphi = \frac{1}{\sqrt{2}}(\chi_{N/2-1} - \chi_{N/2+1}) \end{array}, \tag{28}$$

preserving the occupation number in the form $X = |\psi_1|^2 + |\psi_2|^2 + |\varphi|^2$. At first we consider a particular solution corresponding to $\varphi = 0$. Since the occupation number X is the integral of motion, the variables ψ_1 and ψ_2 can be expressed through the "angle variables":

$$\psi_1 = \sqrt{X}\cos\theta\, e^{i\delta_1}; \quad \psi_2 = \sqrt{X}\sin\theta\, e^{i\delta_2}. \tag{29}$$

Then the Hamilton function corresponding to (27) takes the following form in the terms of "angle variables":

$$H(\theta, \Delta) = \frac{X}{64}[27\beta X - 16\pi^2 + 2(8\pi^2 - 3\beta X)\cos\Delta\sin 2\theta - 3\beta X(8 - \cos^2\Delta)\sin^2 2\theta], \tag{30}$$

where $\Delta = \delta_2 - \delta_1$.

The analysis of phase-plane portrait of Hamiltonian (30) shows that there are two stationary points corresponding to the pure π-mode ($\theta = \pi/4, \Delta = 0$) and "pure" mixture of conjugate modes ($\theta = \pi/4, \Delta = \pi$) at a small values of occupation number X (Fig. 5a). While the excitation level grows the π-mode losses its stability that leads to the appearance of two new stationary points with coordinates (Fig. 5b):

$$\begin{array}{ll} (a) & \Delta = 0, \quad \theta = \frac{1}{2}\arcsin(\frac{8\pi^2 - 3\beta X}{21\beta X}) \\ (b) & \Delta = 0, \quad \theta = \frac{\pi}{2} - \frac{1}{2}\arcsin(\frac{8\pi^2 - 3\beta X}{21\beta X}) \end{array} . \tag{31}$$

The threshold of instability of π-mode is equal to $X_c = \pi^2/3\beta$.

Let us consider the phase trajectory describing the transition from the state $\psi_1(\theta = 0)$ to the state $\psi_2(\theta = \pi/2)$. Because it delimits the families of trajectories which encircle the base stationary points (Fig. 5a) we name it as the Limiting Phase Trajectory (LPT) [8],[5]. The passage along this trajectory leads to the complete energy transfer from *one half* of the chain to *another one* and *vice versa*.

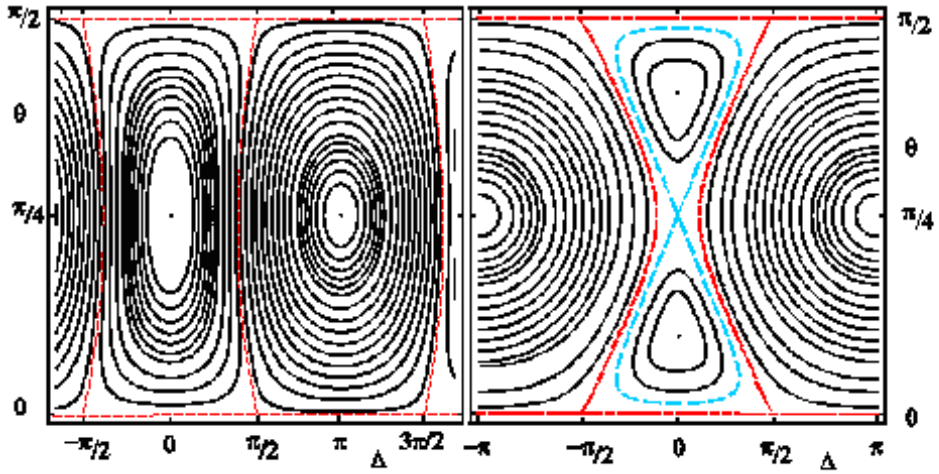


Fig. 5. The truncated phase-plane portrait before (a) and after (b) threshold of instability of the π-mode; the dashed and long-dashed curves correspond to the LPT encircling π-mode and the separatrix, respectively.

While the amplitude X grows, the topology of the phase plane drastically changes (Fig.6). Namely, any energy exchange between the "mixed" states ψ_1 and ψ_2 disappears; after coincidence of LPT and separatrix occurs; this implies that a trajectory starting at a point corresponding to $\theta < \pi/4$ (or $\theta > \pi/4$) and any Δ cannot reach a point corresponding to $\theta > \pi/4/(\theta < \pi/4)$ (excepting all the trajectories surrounding the in-phase stationary points $\Delta = \pm\pi$. Therefore, the energy initially concentrated at the part of the chain remains confined in the excited part (Fig. 7)b.

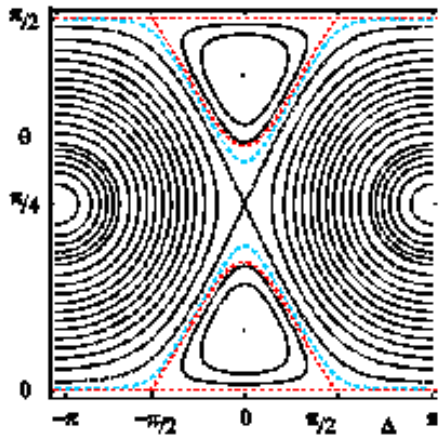


Fig.6. Phase-plane portrait after coincidence of the LPT and the separatrix; long-dashed lines, and short-dashed lines correspond to the separatrix, passing through the unstable stationary

point, and the transient trajectories, respectively; the dotted line depicts the boundaries between the families of transient trajectories and closed ones encircling the stationary points.

An energy threshold associated with the above mentioned localization can be calculated from the condition of equality of the energy corresponding to the LPT and the energy at the unstable p-mode. It is seen in Fig. 5 that the LPT goes through the points $\theta = \pi$ and $\theta = 0$. This means that

$$H(\theta, \Delta)_{|LPT} = \frac{X}{64}(27\beta X - 16\pi^2) \tag{32}$$

Since the energy of the p-mode is equal to zero, it is easy to calculate the respective occupation number $X_{loc} = 16\pi^2/27\beta$ and the energy of the chain $E_{loc} = 16\pi^2/27\beta N$. It now follows that above the excitation level E_{loc} we can observe the localized vibration excitation (a breather).

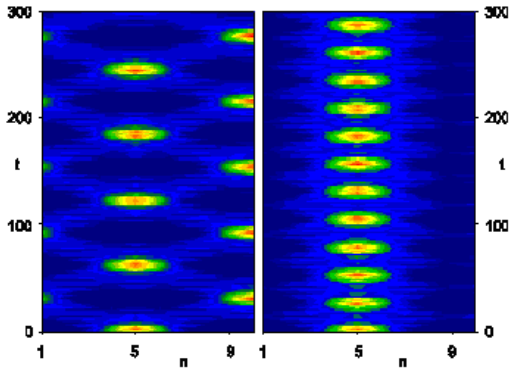


Fig. 7. Transition "beating - localization" in the FPU-chain with 10 particles. The initial conditions correspond to the state ψ_1, and the levels of excitation are $X < X_{loc}$ (a) and $X > X_{loc}$ (b). E and n - the energy (in the relative units) and the number of particles, respectively, t - time (measured in the periods of π-mode - $T_0 = 2\pi\omega_{N/2}$).

Thus we get the solution (31) corresponding to immobile breather. Finally we want to clarify the nature of traveling breathers. We recall that the above results have been obtained under assumption $\varphi = 0$ that corresponds to equal amplitudes of the conjugate modes. Now we assume that the amplitudes of the conjugate modes are slightly different, that is we consider small enough $\varphi \neq 0$. One can show that the equations for functions ψ_1 and ψ_2 include only quadratic terms depending on φ. Therefore, in the framework of the linear approximation, if the value $\varphi \neq 0$ is small enough, there is no qualitatively change in the phase-plane portrait in figures (5, 6). As for behavior of φ in the vicinity of any of stationary points (31), it is described as follows:

$$i\frac{d\varphi}{d\tau_2} - \frac{\pi^2}{2}\varphi + \frac{3}{16}\beta X[2\sin 2\theta\varphi + (3 + \sin 2\theta e^{2i\delta_1})\varphi^*] = 0. \tag{33}$$

The respective eigenvalue

$$\lambda = \pm\frac{\sqrt{891\beta^2X^2 + 120\pi^2\beta X - 384\pi^4}}{56} \tag{34}$$

is imaginary if $X < X_{loc}$, i.e. if the amplitude of excitation is less than the threshold corresponding to coincidence of LPT and separatrix.

The distribution of the vibration amplitude along the chain can be characterized by the mean squared particle displacements $< q_j^2 >$:

$$< q_j^2 >= \frac{\omega_{N/2}}{2\pi}\int_0^{2\pi/\omega_{N/2}} q_j^2(t, \tau_2)dt. \tag{35}$$

If $\varphi = 0$, then there exists a single maximum of vibration amplitude at $j = N/2$. It is easy to demonstrate that small nonzero φ in the equations of motion leads to small oscillations of the breather center when the eigenvalue λ is imaginary. From the other hand, appearance of a real part in the eigenvalue λ at $X > X_{loc}$ leads to the directional motion of the breather.

5 Conclusion

Summarizing, it may be said that an increase of nonlinearity in the periodic FPU chain leads to the transformation of the scenario of the intensive energy exchange between the chain sections. Instead of the complete energy exchange, the formation of stationary or traveling breather-like excitations becomes possible. The transition to the breather-like excitation can be observed even for a chain with a relatively small number of the particles. As the number of particles grows, the localization phenomenon becomes clearly manifested; it resembles a breather in an infinite FPU chain. We would like to underline the fact that in the general case, when all modes are excited, the dynamical transitions are associated nevertheless with the high-frequencies modes. Actually, the transition from the intensive energy exchange between different parts of the oscillatory chain to its spatial localization weakly depends on the "non-resonating modes", and the drastic change in the system behavior can be understood if we take into account only three highest normal modes. So the "wave-particle" duality is clearly seen when we distinguish the spectral ranges which are far or close to frequencies densification region. If in the former range the wave description is completely valid, in the latter one we have to use the "particle" language which allows to study efficiently the intensive energy exchange between different parts (which can be named as the "particles") of the system as well as the transition to energy localization on the excited "particle". Let us note that in the limiting case of infinite chain the localization threshold goes to zero. Therefore the localized excitations which are breathers exist here under arbitrary small levels of excitation. As for long wavelength nonlinear excitations, they are dynamical (for FPU chain) or topological (for Frenkel –Kontorova model) solitons.

The discussed duality manifests also in a wide class of physical problems relating to Solid State Physics (SSP), Nonlinear Optics and Photonics. They are united by common phenomenon denoted by term "Bloch oscillations".

Thus, in SSP it means output from basic paradigm of SSP connecting dynamic processes in crystalline lattice with wave-type excitation of the ground state (phonons magnons, excitons, Cuper pairs in quantum description). In contrast, Bloch oscillations are not excitations of ground state and, similarly complete energy exchange in oscillatory chains are described by LPTs.

Finally, we notice an analogy between arising effectively weak coupling between groups of particles in high-frequency domain of oscillatory chain and necessity of quantum description in the same domain (below Debay temperature) that manifests "wave – particle" duality in both cases.

Acknowledgements

The work was supported by Program of Department of Chemistry and Material Science (Program #2) Russia Academy of Sciences and Russia Basic Research Foundation (grant 08-03-00420a).

References

[1] A. Scott, Nonlinear science: emergence and dynamics of coherent structures. Oxford Univ. Press. 2003

[2] M.J. Ablovitz, H. Segur. Solitons and the inversive scattering transform. Philadelphia: SIAM, 1981

[3] A.I. Manevitch, L.I. Manevitch. The Mechanics of Nonlinear Systems with Internal Resonances. Imperial College Press, London, 2005, 250p

[4] Manevitch L.I., Smirnov V.V. Limiting phase trajectories and origin of localization in Fermi-Pasta-Ulam chains. Submitted to Phys. Rev. E

[5] L.I. Manevitch. The description of localized normal modes in a chain of nonlinear coupled oscillators using complex variables. Nonlinear Dynamics, 25, 95-109, 2001

[6] L.I. Manevitch, Yu.V. Mikhlin, V.N. Pilipchuk. The method of normal vibrations for essentialy nonlinear systems (in Russia. Moscow: Nauka, 1989, 216p.

[7] A.F. Vakakis, L.I. Manevitch, Yu.V. Mikhlin, V.N. Pilipchuk, A.A. Zevin. Normal modes and localization in nonlinear systems. New York: Wiley, 1996, 552p.

[8] L.I. Manevich. New approach to beating phenomenon in coupled nonlinear oscillators chains. 8th Conference on Dynamical Systems-Theory and Applications, Proceedings. Lodz, December 12-15, 2005, Poland, V.1, pp. 119-136; L.I. Manevitch. New approach to beating phenomenon in coupled nonlinear oscillatory chains. Arch. Appl. Mech. v.77 (5), 301-312, 2007

[9] V.N. Pilipchuk. A transformation for vibrating systems based on a non-smooth periodic pair of functions. Doklady AN Ukr. SSR, Ser. A, 4, 37-40, 1988 (in Russia)

[10] L.I. Manevitch, A.I. Musienko. Limiting phase trajectories and energy exchange between anharmonic oscillator and external force. Nonlinear Dynamics, 58, 633-642, 2009

[11] L.D. Landau. Phys. Z. Sowjetunion 2, 46 (1932)

[12] C. Zener, Proc. R. Soc. London, Ser. A 137, 696 (1932)

[13] R. Chacon. Energy-based theory of autoresonance phenomena: application to Duffing-like systems. Europhysics letters, v.70(1), 56-62, 2005

[14] Yu.A. Kosevich, L.I. Manevitch, A.V. Savin. Wandering breathers and self-trapping in weakly coupled nonlinear chains: Classical counterpart of macroscopic tunneling quantum dynamics. Physical Review E 77, 046603(1-20), 2008

119991, 4 Kosygin str., Moscow, Russia

Finite deformations of accreted solids

Alexander V. Manzhirov Sergey A. Lychev
manzh@ipmnet.ru, lychev@ipmnet.ru

Abstract

Basic fundamentals of the mathematical theory of growing solids with finite deformations are under consideration. The classification of various methods of solids accretion is presented. Special attention is paid to the accretion of 3D solids by 2D surfaces. The centrally symmetric problem for an accreted elastic globe is considered. The deformations are supposed to be finite and the material is to be incompressible. The constitutive equations are formulated with respect to complete distortion tensor which may be representing as the composition of initial distortion and compatible deformation gradient. The initial distortion induces the linear connection on the material manifold which becomes a flat space of affine connectivity with nontrivial torsion.

Deformation processes in a solid whose composition, mass, or volume varies in a piecewise continuous manner due to the accretion of new material to the outer surface of a body were studied in many works (see, e.g. [1, 2]). The solid mechanics problems arising in the field of modeling of such processes are completely new and form a separate field of research known as mechanics of accreted solids. Its importance is determined by the fact that the manufacturing of almost all objects of solid mechanics involves accretion: buildings, structures, structural components, machine parts, etc. Specific examples include continuous concrete structure erection, metal solidification, spray deposition of semiconducting films, and crystal growth. One could easily continue this list.

In the framework of the mechanics of growing solids the deformable bodies of changing composition are considered. This means that during the deformation process new pre-stressed parts can join to a solid. Generally speaking parts can either join or separate. So a growing body is a special case of deformable solids in which the deformation process is accompanied by rearrangement of internal cohesion. However this definition covers a much broader class of models than considered in this work.

In the majority of papers which deal with the mechanics of growing solids the theory is constructed as some special replicas of the theory of deformable solids in three-dimensional Euclidean space. Nevertheless the geometric properties of Euclidean space are not enough to describe the stress-strain state of a body which was formed by the continuous joining of pre-stressed parts. It is extremely important that the growing body can be considered as a special class of inhomogeneous body, in which inhomogeneity arises because of nonholonomic distortion, caused by the joining of incompatible stressed parts. From this point of view the mechanics of growing solids have much in common with the theory of defects, in particular with the geometric theory of continuously distributed dislocations. It is noteworthy that the development of this theory strongly influenced by the methods of the Einstein-Cartan geometric theory of gravitation and general theory of relativity. Apparently, the first who applied the methods of Cartan geometry in continuum mechanics was K. Kondo (1955). These ideas have been developed in the works of Bilby et al., E. Kröner, and A. Seeger in which relations between the incompatibility of deformations, the density of defects, and non-trivial geometry of manifolds with non-zero torsion and curvature were established. In this context geometric concepts such as *connection, curvature, torsion, parallelism* are among the basic concepts of the general theory of inhomogeneous solids. This theory was developed by W. Noll [3] and C.C. Wang [4], as well as in the series of papers by M. Epstein and G. Maugin [5]. These fundamental studies form the theoretical basis for the mathematical theory of growing solids.

In this paper we consider the continuous accretion of a solid with the adherence of new material particles to the boundary. We regard the accretion as a union of solids which do not penetrate each other, but have a common parts of boundary.

Note, that continuous joining is a process of continuous adherence of infinitesimal areas to a body, i.e. areas of infinitesimal measure. The infinitesimal areas can be classified. One can consider an infinitely thin layers, threads, and points. Since such infinitesimal field are continuous bodies of various dimensions they can carry the stress–strain state corresponding to their dimension. For example layers can undergo membrane tension, the threads — linear, etc. In this regard, the distribution of stresses in a continuously growing body depends on geometric class of joined infinitesimal areas which implies the construction of different versions of the theory of growing solids. In this paper we consider a body which grows due to continuous adherence of two-dimensional layers considered as material surfaces [6].

The theory of fiber bundles of differentiable manifolds [7] is taken as the geometric foundation of mathematical theory of growing solids. Analytic properties of differentiable manifolds are determined without utilization of prescribed connection. This allow to formulate a boundary value problem in terms of quiet general geometrical properties of reference configuration and determine the particular type of connectivity *a posteriori* taking into account specific kinematic and static characteristics of the accretion process. Above all the geometrical concept of a fiber bundle corresponds to a key features of the growing solid whose growth is modeled as a continuous adhesion of deformed material areas. Such an assembly generates a nontrivial fiber bundle of material manifold. The structure of this bundle is completely determined by the scenario of accretion.

Submission of material manifold as a bundle gives a natural interpretation of the results of accretion which is implemented as a continuous stream of material surfaces deposited to the surface of growth. The annual rings on cross sections of tree trunks may be the appropriate metaphor here. Each layer corresponds to the material surface attached at a fixed moment of time. Hence, base is one-dimensional and each fiber is a two-dimensional manifold.

Note that it can be other types of bundles such as a bundle with two-dimensional fibers and one dimensional base. This type of fibration can be treated as the fibers of the wood. More complex example is illustrated by a bundle wrapped yarn on the ball and so on.

Let us give some remarks regarding the notation in this work. In order to identify the points of the body we introduce a smooth three-dimensional material manifold $\mathfrak{M}$. We assume that $\mathfrak{M}$ is a fibre bundle of a smooth manifold. As we know from differential geometry, a fibre bundle is defined by base $\mathfrak{N}$, structure group G, and projection map π [7]. The material point $\mathfrak{p} \in \mathfrak{M}$ is defined by three coordinates specified in local map U which contains a neighborhood of $\mathfrak{p}$. The set of three coordinates denote gothic symbol $\mathfrak{X}$ that means an ordered triple of numbers $\{\mathfrak{X}^1, \mathfrak{X}^2; \mathfrak{X}^3\}$. The last element of the triple $\mathfrak{X}^3$ is highlighted with a semicolon in notation and determines the coordinates of the base $\mathfrak{N}$. The first two elements $\mathfrak{X}^1, \mathfrak{X}^1$ are the coordinates of the fibre. As each fibre is uniquely determined by the value $\mathfrak{X}^3$ the fibres will be denoted by $\mathfrak{M}_{\mathfrak{X}^3}$. Due to their topological and differential properties the bundles of smooth manifolds endues their regular subsets a sufficiently strong smoothness properties and measurability that allows to define the accreted solid without additional geometric assumptions.

Define a body $\mathfrak{B}$ as an open subset of a material manifold $\mathfrak{M}$ bounded by non-identical fibers. In this case the body $\mathfrak{B}$ can be represented as a union of fibers whose indices are in the open interval (α, β), i.e.

$$\mathfrak{B} = \mathfrak{B}(\alpha, \beta) = \bigcup_{\mathfrak{X}^3 \in (\alpha, \beta)} \mathfrak{M}_{\mathfrak{X}^3}.$$

An accreted solid can be defined as a parametric family of such sets

$$\mathfrak{C} = \left\{ \mathfrak{B}_\gamma = \mathfrak{B}(\alpha, \gamma) \middle| \gamma \in (\alpha, \beta) \right\},$$

where γ is a parameter of the family. While $\alpha \to \beta$ the body degenerates into an infinitely thin ply or a point.

Specify the configuration of a body $\mathfrak{B} \in \mathfrak{M}$ as a set $\varkappa$ of points in Euclidean space $\mathbb{E}^3$, that correspond to the positions of material points, i.e.

$$\varkappa = \left\{ \boldsymbol{X} \in \mathbb{E}^3 \middle| \exists \left\{ \mathfrak{X}^1, \mathfrak{X}^2; \mathfrak{X}^3 \right\} \in \mathfrak{B} \quad \boldsymbol{X} = \boldsymbol{\chi}_\varkappa(\mathfrak{X}^1, \mathfrak{X}^2; \mathfrak{X}^3) \right\},$$

defined by an injective function

$$\boldsymbol{\chi}_\varkappa : \mathfrak{B} \to \mathbb{E}^3.$$

Note that the injectivity property forbids the penetration of solid parts into each other. We also believe that $\boldsymbol{\chi}_{\varkappa}$ is a diffeomorphism.

In an accreted solid like for solid with defects the natural (stress-free) configuration may not exist, moreover, such a configuration exists only in exceptional cases it coherent accretion. Lack of global natural configuration leads to consideration of three configurations. The first one $\varkappa_C$ can be termed as "reference fibers"(like Maugin's "reference crystals"). The set $\varkappa_C$ is not a connected subset of $\mathbb{E}^3$ so is not a configuration in usual sense but with every point $\boldsymbol{x} \in \varkappa_C$ one can associate a linear map

$$\boldsymbol{K}(\mathfrak{X}) : \varkappa_C \to \varkappa_R, \tag{1}$$

where $\varkappa_R$ is the second (reference) configuration that is a connected measurable subset of $\mathbb{E}^3$ with regular boundary. The third configuration $\varkappa$ is actual. One can determine the connection coefficients $\Gamma^{\beta}_{\gamma\alpha}$ on material manifold $\mathfrak{M}$ by tensor field $\boldsymbol{K}$

$$\Gamma^{\beta}_{\gamma\alpha} = \partial_{\alpha} \left(\boldsymbol{K}^{-1}\right)^{\rho}_{\cdot\gamma} K^{\beta}_{\cdot\rho}. \tag{2}$$

The corresponding connection can be nontrivial, i.e. with nonzero torsion. This geometrization of the manifold $\mathfrak{M}$ transforms it into a configuration that is not embedded in three-dimensional Euclidean space.

For simple materials the hyperelastic potential $W_{\varkappa}$ may be represent as follows

$$W_{\varkappa} = W_{\varkappa}\left(\boldsymbol{F}_{\varkappa}, \mathfrak{X}\right),$$

where $\boldsymbol{F}_{\varkappa}$ is a deformation gradient relative to reference configuration $\varkappa$.

In order to obtain particular approximations of $W_{\varkappa}$ one has to proceed the *gauge*. If the deformed solid possesses *natural* (i.e. free of stresses) configuration then the gauge leads to the following conditions:

$$W_{\varkappa}(\mathbf{1}, \mathfrak{X}) = 0, \quad \frac{\partial W_{\varkappa}}{\partial \boldsymbol{F}_{\varkappa}}\Big|_{\boldsymbol{F}_{\varkappa}=\mathbf{1}} = \mathbf{0}.$$

The first condition expresses the fact that a stored elastic energy differs from zero only in a deformed (i.e., a non-natural) state and the second condition shows that stresses in natural state vanish.

If a medium is assumed elastic, then an infinitesimal neighborhood of each of its points has a unique (up to an arbitrary rigid motion) local reference configuration. This implies the existence of a linear mapping $\boldsymbol{K}^{-1}(\boldsymbol{X})$ (1), which transforms an infinitesimal neighborhood of $\boldsymbol{X}$ in a natural (stress-free) state.

Note that material manifold is a bundle and each its fiber $\mathfrak{M}_{\mathfrak{X}^3}$ is associated with a material surface strained before its adhesion to a body. From the mechanical point of view it means that each fiber was deformed from natural state before adhesion. So each individual fiber has a a global two-dimensional natural reference configuration. Of course the whole accreted solid has no global three-dimensional natural reference configuration.

Introduce the distortion tensor field $\boldsymbol{K}(\mathfrak{X}^1, \mathfrak{X}^2; \mathfrak{X}^3)$ as a deformation gradient associated with individual material surface $\mathfrak{M}_{\mathfrak{X}^3}$. It can be quantify with reference to transformation of a surface from natural reference configuration onto configuration that match its position immediately after the adhesion. Thus, at each point of the material manifold tensor field $\boldsymbol{K}(\mathfrak{X})$ is defined. This field is continuously differentiable due to the the continuity of accretion process. Moreover the field $\boldsymbol{K}^{*}\cdot\boldsymbol{K}$ specifies a metric on a surface embedded in three-dimensional Euclidean space on each fiber $\mathfrak{M}_{\mathfrak{X}^3}$.

The deformation of a material surface after adhesion to a solid is determined by the gradient of the deformation $\boldsymbol{F} = \boldsymbol{F}_{\varkappa_R}$. Thus a complete distortion tensor $\boldsymbol{H} = \boldsymbol{F}_{\varkappa_C}$ has the form

$$\boldsymbol{H} = \boldsymbol{K}\cdot\boldsymbol{F},$$

and elastic potential $W_{\varkappa_C}\left(\boldsymbol{H}, \mathfrak{X}\right)$ can be defined on the configuration $\varkappa_C$ only locally since $\varkappa_C$ is not a connected set.

Elastic potential can be determined globally with respect to the configuration $\varkappa_R$. Introduce elastic potential $W_{\varkappa_R}$ that is an elastic energy per unit volume in the reference state $\varkappa_R$ and can be interpreted as a function of three arguments $\boldsymbol{F}$, $\boldsymbol{K}$, $\mathfrak{X}$ (see. [5]), i.e.

$$W_{\varkappa_R}(\boldsymbol{K},\, \boldsymbol{F}, \mathfrak{X}) = J_{\boldsymbol{K}}^{-1} W_{\varkappa_C}(\boldsymbol{H}, \mathfrak{X}) = J_{\boldsymbol{K}}^{-1} W_{\varkappa_C}(\boldsymbol{K}\cdot\boldsymbol{F}, \mathfrak{X}).$$

Note that even if the functional $W_{\varkappa_C}$ is uniform (i.e., it does not depend obviously on material coordinates $\mathfrak{X}$), functional $W_{\varkappa_R}$ is not uniform because $\boldsymbol{K}$ depends on $\mathfrak{X}$. This reflects the difference between the material uniformity and homogeneity [5]

One can express Piola stress tensor $\boldsymbol{T}_{\varkappa}^{\varkappa_R}$ relevant to $\varkappa_R$ by formula

$$\boldsymbol{T}_{\varkappa}^{\varkappa_R} = \frac{\partial W_{\varkappa_R}}{\partial \boldsymbol{F}^*} = J_{\boldsymbol{K}}^{-1} \boldsymbol{K}^* \cdot \frac{\partial W_{\varkappa_C}}{\partial \boldsymbol{H}^*}.$$

The stress tensor $\boldsymbol{T}_{\varkappa}^{\varkappa_C}$ relevant to $\varkappa_C$ can be defined fiber-by-fiber as follows

$$\boldsymbol{T}_{\varkappa}^{\varkappa_C} = \frac{\partial W_{\varkappa_C}}{\partial \boldsymbol{H}^*}.$$

The boundary value problem for an accreted solid is determined by the equations of equilibrium in $V(t)$ with boundary $\Omega(t)$ parametrically dependent on time, i.e.

$$\boldsymbol{\nabla}_{\varkappa} \cdot \left[J_{\boldsymbol{K}}^{-1} \boldsymbol{K}^* \cdot \frac{\partial W_{\varkappa_C}(\boldsymbol{H}, \mathfrak{X})}{\partial \boldsymbol{H}^*}\Big|_{\boldsymbol{H}=\boldsymbol{K}\cdot\boldsymbol{F}} \right] + J_{\varkappa} \boldsymbol{b}_{\varkappa} = \boldsymbol{0},$$

and boundary conditions stated on $\Omega(t)$:

$$\boldsymbol{n} \cdot \left[J_{\boldsymbol{K}}^{-1} \boldsymbol{K}^* \cdot \frac{\partial W_{\varkappa_C}(\boldsymbol{H}, \mathfrak{X})}{\partial \boldsymbol{H}^*}\Big|_{\boldsymbol{H}=\boldsymbol{K}\cdot\boldsymbol{F}} \right] \Bigg|_{\Omega(t)} = \boldsymbol{p}.$$

At the first glance a formal statement of the boundary value problem differs from the classical one only by the fact that the boundary of domain depends parametrically on time. However, there is more profound difference: the elastic potential depends on the tensor field of distortion the determination of which requires additional conditions. Particular form of these conditions depends on the geometrical structure of joined elements, that is in essence on the structure of the bundle of material manifold. If the growth of a body occurs due to continuous influx of prestressed material surfaces to this body then this condition can be written in the form

$$\boldsymbol{P} \cdot \left[J_{\boldsymbol{K}}^{-1} \boldsymbol{K}^* \cdot \frac{\partial W_{\varkappa_C}(\boldsymbol{H}, \mathfrak{X})}{\partial \boldsymbol{H}^*}\Big|_{\boldsymbol{H}=\boldsymbol{K}\cdot\boldsymbol{F}} \right] \cdot \boldsymbol{P} \Bigg|_{\Omega(t)} = \boldsymbol{\mathcal{T}}.$$

Here $\boldsymbol{P} = (\boldsymbol{E} - \boldsymbol{n} \otimes \boldsymbol{n})$ is a projector onto the tangent plane to $\Omega(t)$. This equation expresses the fact that the fibers align with the specified tension determined by the surface tensor $\boldsymbol{\mathcal{T}}$, i.e., two-dimensional tensor of second rank defined in the tangent space of the adhering material surface.

The equation for distortion tensor $\boldsymbol{K}$ provided that the increase is the result of continuous adherence of prestressed surfaces can be obtained from the relations of the theory of material surfaces (theories of solids with a material boundary [6]). Effects of material surface adhering leads to an infinitesimal change of the stress–strain state of an accreted solid but as an elementary act of adhesion occurs during an infinitely small time interval the rate of stress state is finite. This rate can be found from the equations of contact interaction between the spatial body and adhering the material surface. The equation of physical boundary equilibrium (which from the geometrical point of view is a bounding surface of the body in its actual state and from mechanical point of view is a thin film undergoing a membrane state of stress) can be written as follows:

$$\boldsymbol{\nabla}_s \cdot \boldsymbol{\mathcal{T}} + \boldsymbol{b}_s = \boldsymbol{n} \cdot \boldsymbol{T}\Big|_{\Omega(t)},$$

where $\boldsymbol{\nabla}_s$ is the surface nabla operator, $\boldsymbol{b}_s$ is the surface density of external forces acting on $\Omega(t)$. To complete the boundary value problem formulation the condition on the curvilinear boundary

$\partial\Omega(t)$ of the surface $\Omega(t)$ must be specified. This conditions may be of the form $\widetilde{\boldsymbol{n}}\cdot\boldsymbol{T}\Big|_{\partial\Omega(t)} = \widetilde{\boldsymbol{f}}$. Here $\widetilde{\boldsymbol{n}}$ is an external unit normal to the curve $\partial\Omega(t)$ in the tangent plane and $\widetilde{\boldsymbol{f}}$ is a linear density of forces distributed on the curve $\partial\Omega(t)$.

Defined distortion field allows to specify the geometry on the material manifold, determining the connection on it by the formulas (2). The resulting coefficients of affine connection do not possess the symmetry and define a nonzero torsion tensor

$$\mathcal{T}^{\alpha}_{\gamma\beta} = \partial_\gamma \left(\boldsymbol{K}^{-1}\right)^{\rho\cdot}_{\cdot\beta} K^{\alpha\cdot}_{\cdot\rho} - \partial_\beta \left(\boldsymbol{K}^{-1}\right)^{\rho\cdot}_{\cdot\gamma} K^{\alpha\cdot}_{\cdot\rho}.$$

Thus, the material manifold becomes a fiber bungled manifold of affine connections. Each fiber is metrized in a natural state and the stress–strain state of a body can be determined as a result of its deformation from natural reference configuration immersed in the ambient space of higher dimension. This reference configuration represents the region in submanifold with nonzero torsion. Of course the image of such deformation, i.e., actual configuration, immersed in a subspace endowed with Euclidean structure. The non-Euclidean features of reference natural configuration, quantitatively defined by the torsion tensor which characterizes the incompatibility of fibers stress-strain states joined in the process of accretion. It should be noted that such speciality of reference geometry in the framework of infinitesimal strains is manifested as incompatibility of the strain tensor field, which was often mentioned in the literature as a characteristic property of growing bodies.

Let consider the centrally symmetric finite deformation of an accreted elastic globe. In this case material manifold $\mathfrak{M}$ may be represented in $\mathbb{R}^3$ as an open ball with pricked center and radius $\mathfrak{R}$ that admits fibration into concentric spheres $\mathfrak{M}_{\mathfrak{X}^3}$. Each sphere is the fibre and the open interval $\mathfrak{B} = (0, \mathfrak{R})$ is the base of fibration [7]. Last element of material triple $\mathfrak{X}^3 \in \mathfrak{B}$ represents the coordinate on the base and a pair $\mathfrak{X}^1, \mathfrak{X}^2$ are the coordinates of the material point on the fibre. We assume the incompressibility of the material that permit the usage of Rivlin-Ericsen universal solutions for individual spherical fibre [8].

Let $\boldsymbol{e}_r$, $\boldsymbol{e}_\varphi$, $\boldsymbol{e}_\theta$ are the elements of physical basis in spherical coordinates. Let every fiber holds natural configuration that is the sphere immersed in $\mathbb{R}^3$. The union of this fibers is not a configuration because it is not a connected set. But after appropriate individual deformation of each fiber this union can be transformed to the globe. One can obtain the configuration like mentioned but this configuration is not natural (it is stressed). The corresponding distortion can be defined by the following tensor field

$$\boldsymbol{K} = \frac{(r^3-\alpha)^{2/3}}{r^2}\,\boldsymbol{e}_r \otimes \boldsymbol{e}_r + \frac{r}{(r^3-\alpha)^{1/3}}\left(\boldsymbol{e}_\varphi \otimes \boldsymbol{e}_\varphi + \boldsymbol{e}_\theta \otimes \boldsymbol{e}_\theta\right). \tag{3}$$

Here $r = r(\mathfrak{X}^3)$ is the spatial (radial) coordinate, $\alpha = \alpha(\mathfrak{X}^3)$ is the distortion parameter. One can treat the field $\boldsymbol{K}$ as a deformation gradient corresponding to the map $r = \sqrt[3]{r_0^3 + \alpha}$ defined with respect to the individual fiber $\mathfrak{M}_{\mathfrak{X}^3}$, that can be smoothly transformed to natural spherical configuration by $r = r_0$.

Choose one of the possible stressed configurations as a reference configuration and denote it by $\varkappa_R$. The deformation of the reference configuration to the actual one $\varkappa$ is determined by isochoric diffeomorphism $\varkappa_R \to \varkappa$. Under the conditions of central symmetry this map belongs to the assemblage $R = \sqrt[3]{r^3 + A}$, where A is the parameter of the assemblage. The corresponding deformation gradient is

$$\boldsymbol{F} = \frac{r^2}{(r^3+A)^{2/3}}\boldsymbol{e}_r \otimes \boldsymbol{e}_r + \frac{(r^3+A)^{1/3}}{r}\left(\boldsymbol{e}_\varphi \otimes \boldsymbol{e}_\varphi + \boldsymbol{e}_\theta \otimes \boldsymbol{e}_\theta\right).$$

Full deformation gradient $\boldsymbol{H}$ associated with individual fiber may be obtained as a composition of distortion $\boldsymbol{K}$ and deformation gradient $\boldsymbol{F}$ determined in consistency of three dimensional accreted solid, i.e.

$$\boldsymbol{H} = \boldsymbol{K}\cdot\boldsymbol{F} = \frac{(r^3-\alpha)^{2/3}}{(r^3+A)^{2/3}}\boldsymbol{e}_r \otimes \boldsymbol{e}_r + \frac{(r^3+A)^{1/3}}{(r^3-\alpha)^{1/3}}\left(\boldsymbol{e}_\varphi \otimes \boldsymbol{e}_\varphi + \boldsymbol{e}_\theta \otimes \boldsymbol{e}_\theta\right).$$

Corresponding Cauchy–Green strain measure is

$$\boldsymbol{G} = \boldsymbol{H}\cdot\boldsymbol{H}^{*} = \frac{(r^3-\alpha)^{4/3}}{(r^3+A)^{4/3}}\boldsymbol{e}_r\otimes\boldsymbol{e}_r + \frac{(r^3+A)^{2/3}}{(r^3-\alpha)^{2/3}}\left(\boldsymbol{e}_\varphi\otimes\boldsymbol{e}_\varphi + \boldsymbol{e}_\theta\otimes\boldsymbol{e}_\theta\right).$$

One can obtain the invariants of above mentioned measure by the formulas

$$I_1(\boldsymbol{G}) = \frac{(r^3-\alpha)^{4/3}}{(r^3+A)^{4/3}} + 2\frac{(r^3+A)^{2/3}}{(r^3-\alpha)^{2/3}}, \quad I_2(\boldsymbol{G}) = \frac{(r^3+A)^{4/3}}{(r^3-\alpha)^{4/3}} + 2\frac{(r^3-\alpha)^{2/3}}{(r^3+A)^{2/3}}.$$

The inverse measure may be calculated as follows

$$\boldsymbol{G}^{-1} = \frac{(r^3+A)^{4/3}}{(r^3-\alpha)^{4/3}}\boldsymbol{e}_r\otimes\boldsymbol{e}_r + \frac{(r^3-\alpha)^{2/3}}{(r^3+A)^{2/3}}\left(\boldsymbol{e}_\varphi\otimes\boldsymbol{e}_\varphi + \boldsymbol{e}_\theta\otimes\boldsymbol{e}_\theta\right).$$

Consider the equations of equilibrium with the assumption that mass force are absent.

$$\boldsymbol{\nabla}\cdot\boldsymbol{T} = \boldsymbol{0},$$

where $\boldsymbol{T}$ is the Cauchy stress tensor, which may be diadic decomposed as:

$$\boldsymbol{T} = T_{RR}\boldsymbol{e}_R\otimes\boldsymbol{e}_R + T_{\theta\theta}\left(\boldsymbol{e}_\theta\otimes\boldsymbol{e}_\theta + \boldsymbol{e}_\varphi\otimes\boldsymbol{e}_\varphi\right).$$

Suppose that the boundary conditions are formulated in the form:

$$\boldsymbol{n}\cdot\boldsymbol{T}\Big|_{\Gamma_1} = \boldsymbol{B}, \quad \boldsymbol{n}\cdot\boldsymbol{T}\Big|_{\Gamma_2} = \boldsymbol{0}. \tag{4}$$

Here $\boldsymbol{B}$ is the pressure on the inner surface of the globe Γ_1, Γ_2 is the outer surface which is the surface of accretion. Assume that this surface is free of stress. The extra condition determines the tension of accreting fibers f, i.e.

$$\boldsymbol{e}_\theta\cdot\boldsymbol{T}\cdot\boldsymbol{e}_\theta\Big|_{\Gamma_2} = T_{\theta\theta}\Big|_{\Gamma_2} = f. \tag{5}$$

It is important to note that this extra condition is not the boundary condition for the problem stated for the accreted solid. It is the additional condition that permit to determine the distortion $\boldsymbol{K}$ (3) as the parameter $\alpha(R) = \alpha(R(r(\mathfrak{X})))$ of the boundary value problem.

The equilibrium equations and boundary conditions under the assumption of central symmetry in spherical coordinates are

$$\frac{\partial T_{RR}}{\partial R} + \frac{2}{R}\left(T_{RR} - T_{\theta\theta}\right) = 0, \quad T_{RR}\Big|_{r=r_0} = B, \quad T_{RR}\Big|_{r=r_1} = 0,$$

where $r_0 = \sqrt[3]{R_0^3 - A}$, $r_1 = \sqrt[3]{R_1^3 - A}$, R_0 is an inner and R_1 is an outer radius of the globe in actual configuration $\varkappa$.

The Cauchy stress tensor for the incompressible isotropic hyperelastic material may be introduced by relation [8]:

$$\boldsymbol{T} = -p\boldsymbol{E} + 2\frac{\partial W}{\partial I_1}\boldsymbol{G} - 2\frac{\partial W}{\partial I_2}\boldsymbol{G}^{-1},$$

where $p = p(R)$ is the pressure that can be determine from the equilibrium equation and W is the hyperelastic potential (elastic energy). If the configuration $\varkappa_R$ is utilized as reference configuration then the hyperelastic potential should be written as [5]:

$$W = J_{\boldsymbol{K}}^{-1}W_{\varkappa_C}\left(\boldsymbol{H},\mathfrak{X}\right) = J_{\boldsymbol{K}}^{-1}W_{\varkappa_C}\left(\boldsymbol{K}\cdot\boldsymbol{F},\mathfrak{X}\right).$$

Here $W_{\varkappa_C}$ is a potential gauged locally for every individual fiber with respect to natural configuration of this fiber. By virtue of incompressibility of the considered material $J_{\boldsymbol{K}} = 1$. Therefore

$$W = W_{\varkappa_C}\left(\boldsymbol{K}\cdot\boldsymbol{F},\mathfrak{X}\right). \tag{6}$$

The substitution of $\boldsymbol{T}$ from (4_2) into the equilibrium equation gives the equation for pressure p:

$$-\boldsymbol{\nabla}p+2\left(\boldsymbol{G}\cdot\boldsymbol{\nabla}\frac{\partial W}{\partial I_1}-\boldsymbol{G}^{-1}\cdot\boldsymbol{\nabla}\frac{\partial W}{\partial I_2}+\frac{\partial W}{\partial I_1}\boldsymbol{\nabla}\cdot\boldsymbol{G}-\frac{\partial W}{\partial I_2}\boldsymbol{\nabla}\cdot\boldsymbol{G}^{-1}\right)=\boldsymbol{0}.$$

Taking into account that in central symmetrical case $\boldsymbol{\nabla}p=\boldsymbol{e}_R dp/dR$, arrive at the equation for $p(R)$:

$$\begin{aligned}-\frac{dp}{dR}+2\Bigg\{&\frac{(r^3-\alpha)^{4/3}}{(r^3+A)^{4/3}}\frac{d}{dR}\frac{\partial W}{\partial I_1}-\frac{(r^3+A)^{4/3}}{(r^3-\alpha)^{4/3}}\frac{d}{dR}\frac{\partial W}{\partial I_1}+\\&+\frac{\partial W}{\partial I_1}\left[\frac{d}{dR}\frac{(r^3-\alpha)^{4/3}}{(r^3+A)^{4/3}}+\frac{2}{R}\left(\frac{(r^3-\alpha)^{4/3}}{(r^3+A)^{4/3}}-\frac{(r^3+A)^{2/3}}{(r^3-\alpha)^{2/3}}\right)\right]-\\&-\frac{\partial W}{\partial I_2}\left[\frac{d}{dR}\frac{(r^3+A)^{4/3}}{(r^3-\alpha)^{4/3}}+\frac{2}{R}\left(\frac{(r^3+A)^{4/3}}{(r^3-\alpha)^{4/3}}-\frac{(r^3-\alpha)^{2/3}}{(r^3+A)^{2/3}}\right)\right]\Bigg\}=0.\end{aligned}$$

Integral of this equation is obvious

$$\begin{aligned}p(R')=p_0+2&\left[\frac{(r^3-\alpha)^{4/3}}{(r^3+A)^{4/3}}\frac{\partial W}{\partial I_1}-\frac{(r^3+A)^{4/3}}{(r^3-\alpha)^{4/3}}\frac{\partial W}{\partial I_2}\right]-\\-4\int\limits_{R_0}^{R'}&\left\{\frac{\partial W}{\partial I_2}\left(\frac{(r^3+A)^{4/3}}{(r^3-\alpha)^{4/3}}-\frac{(r^3-\alpha)^{2/3}}{(r^3+A)^{2/3}}\right)-\right.\\&\left.-\frac{\partial W}{\partial I_1}\left(\frac{(r^3-\alpha)^{4/3}}{(r^3+A)^{4/3}}-\frac{(r^3+A)^{2/3}}{(r^3-\alpha)^{2/3}}\right)\right\}\frac{dR}{R}.\end{aligned}$$

Here the upper limit of the integration $R'\in(R_0,R_1)$ is the radial coordinate that determines the position of spherical fibre in actual configuration $\varkappa$ and p_0 is the integrating constant corresponding to hydrostatic pressure. By changing variables $R\mapsto r$ the resulting expression can be transform to the form

$$\begin{aligned}p(r')=2&\left[\frac{(r^3-\alpha)^{4/3}}{(r^3+A)^{4/3}}\frac{\partial W}{\partial I_1}-\frac{(r^3+A)^{4/3}}{(r^3-\alpha)^{4/3}}\frac{\partial W}{\partial I_2}\right]-\\&-4\int\limits_{r_0}^{r'}\frac{r^2(A+\alpha)(2r^3+A-\alpha)}{(r^3-\alpha)^{4/3}(r^3+A)^{5/3}}\left(\frac{\partial W}{\partial I_2}+\frac{(r^3-\alpha)^{2/3}}{(r^3+A)^{2/3}}\frac{\partial W}{\partial I_1}\right)dr+p_0.\end{aligned}$$

The upper limit of integration $r'\in(r_0,r_1)$ determines the position of spherical fiber in reference configuration $\varkappa_R$. Thereafter

$$T_{RR}(r')=-p_0+4\int\limits_{r_0}^{r'}\frac{r^2(A+\alpha)(2r^3+A-\alpha)}{(r^3-\alpha)^{4/3}(r^3+A)^{5/3}}\left(\frac{\partial W}{\partial I_2}+\frac{(r^3-\alpha)^{2/3}}{(r^3+A)^{2/3}}\frac{\partial W}{\partial I_1}\right)dr.$$

From the boundary condition $T_{RR}\Big|_{r=r_1}=0$ it follows that

$$T_{RR}(r')=4\int\limits_{r_1}^{r'}\frac{r^2(A+\alpha)(2r^3+A-\alpha)}{(r^3-\alpha)^{4/3}(r^3+A)^{5/3}}\left(\frac{\partial W}{\partial I_2}+\frac{(r^3-\alpha)^{2/3}}{(r^3+A)^{2/3}}\frac{\partial W}{\partial I_1}\right)dr.$$

Circumferential stresses $T_{\theta\theta}$ may be obtained from the equilibrium equation and expressed in terms of T_{RR} as follows

$$T_{\theta\theta}=T_{RR}+\frac{R}{2}\frac{\partial T_{RR}}{\partial R}.$$

This stresses should be equal to prescribed value of tension f (5) in fibre that is on the current boundary, i.e.

$$T_{\theta\theta}\Big|_{\Gamma_2} = T_{\theta\theta}\Big|_{r=r_1} = T_{RR}\Big|_{r=r_1} + \frac{\sqrt[3]{r_1^3+A}}{2}\frac{\partial T_{RR}}{\partial R}\Big|_{r=r_1} = \\ = 2\left[\frac{(A+\alpha)(2r_1^3+A-\alpha)}{(r_1^3-\alpha)^{4/3}(r_1^3+A)^{2/3}}\left(\frac{\partial W}{\partial I_2}+\frac{(r_1^3-\alpha)^{2/3}}{(r_1^3+A)^{2/3}}\frac{\partial W}{\partial I_1}\right)\right]\Bigg|_{r=r_1} = f. \quad (7)$$

This permit to find dependence $\alpha = \alpha(r_1, A, f)$. The value of parameter A may be calculated from the second boundary condition (4).

The relation (7) can be formulated in the terms of stress rate $\dot{T}_{RR}$. Indeed, so far as $T_{RR}\Big|_{r=r_1} = 0$, then

$$\frac{R}{2}\frac{dT_{RR}}{dR}\Big|_{r=r_1} = f.$$

Under the conditions of central symmetry $dR = V dt$, where V is the rate of motion of accretion surface in material manifold (the velocity of accretion surface). Hence

$$\frac{dT_{RR}}{V dt}\Big|_{r=r_1} = \frac{2}{R}f,$$

or introduction of the notion $\boldsymbol{\mathcal{T}}$ for the stress tensor on the material surface [6] which can be represent here as the following dyadic decomposition $\boldsymbol{\mathcal{T}} = f\left(\boldsymbol{e}_\theta \otimes \boldsymbol{e}_\theta + \boldsymbol{e}_\varphi \otimes \boldsymbol{e}_\varphi\right)$ and the notion $\boldsymbol{L}$ for the curvature tensor of mentioned material surface, that is the sphere with radius R, arrive at the equation "in terms of velocities":

$$\dot{T}_{RR}\Big|_{r=r_1} = \frac{2V}{R}f = V\left(\boldsymbol{\mathcal{T}} : \boldsymbol{L}\right).$$

Tensor field of distortion (3) induces the linear connection on material manifold that becomes flat space with affine connectivity with nontrivial torsion [5, 9]. The nonzero components of corresponding torsion tensor are

$$\mathfrak{T}^{\varphi}_{\cdot r\varphi} = \mathfrak{T}^{\theta}_{\cdot r\theta} = \frac{1}{3r^3-3\alpha}\frac{\partial\alpha(r)}{\partial r}, \quad \mathfrak{T}^{\varphi}_{\cdot\varphi r} = \mathfrak{T}^{\theta}_{\cdot\theta r} = -\frac{1}{3r^3-3\alpha}\frac{\partial\alpha(r)}{\partial r}. \quad (8)$$

It should be noted that the torsion tensor (8) is equal to zero in the case $\alpha = \text{Const}$. This situation corresponds to consensual accretion that generates the solid indistinguishable from the instantly created solid. Otherwise if $\alpha = \alpha(\mathfrak{X}^3)$ then the solid obtained in the result of accretion process lacks natural configuration that can be immersed in euclidian three dimensional space $\mathbb{E}^3$. It means that there are no smooth deformations that release the solid from stresses.

Acknowledgements

The research was financially supported by the Russian Foundation for Basic Research (under grants Nos. 08-01-00553-a, 09-08-01194-a, and 10-01-92653-IND-a) and by the Department of Energetics, Mechanical Engineering, Mechanics and Control Processes of the Russian Academy of Sciences (Program No. 13 OE).

References

[1] N. Kh. Aruyunyan and A. V. Manzhirov, Contact Problems in the Theory of Creep [in Russian], NAN RA Publ., Erevan, 1999. 320 p.

[2] N. Kh. Aruyunyan, A. V. Manzhirov, and V. E. Naumov, Contact Problems in Mechanics of Growing Solids [in Russian], Nauka Publ., Moscow, 1991. 175 p.

[3] W. Noll, “Materially uniform simple bodies with inhomogeneities”, Arch. Rat. Mech. Anal., 1967, No. 2, pp. 1–32.

[4] C. C. Wang, On the geometric structure of simple bodies, or mathematical foundations for the theory of continuous distributions of dislocations // Arch. Rat. Mech. Anal., 1967, No. 27, pp. 33–94.

[5] G. A. Maugin, Material Inhomogeneities in Elasticity, Chapman and Hall, London, 1993. 294 p.

[6] M. E. Gurtin and A. I. Murdoch, “A continuum theory of elastic material surfaces”, Arch. Rational Mech. Anal., 1975, Vol. 57, pp. 291–323.

[7] Y. Choquet-Bruhat, C. Dewitt-Morette, and M. Dillard-Bleick, Analysis, Manifolds and Physics. Part 1. Basics, North-Holland, Amsterdam, 1982. 649 p.

[8] A. I. Lurie, Nonlinear Theory of Elasticity, North-Holland, Amsterdam, 1990. 617 p.

[9] C. Wang and C. Truesdell, Introduction to Rational Elasticit, Noordhoff Publ., Amsterdam, 1973. 556 p.

Manzhirov A.V., Lychev S.A. Ishlinsky Institute for Problems in Mechanics of the Russian Academy of Sciences, Vernadsky Ave 101 Bldg 1, Moscow, 119526, Russia

Modulation of gravity in problem of free convection

Anatoly B. Melentyev Eugenie L. Tarunin
a.b.melentyev@mail.ru tarunin@psu.ru

Abstract

Influence of gravity modulations on free convection in a close cavity was investigated in [3, 4, 5]. It was shown that modulation changes critical Grashof number and leads to periodical oscillation regimes. As usual, modulations were symmetrical (asymmetrical modulation was considered only in [5]). In this article we were interested in resonance effects of modulation in case of free convection with heating from below. We used two-field method (stream function and vorticity variables) to solve equations of free convection. At first, resonance effects were considered in symmetrical cases and then we investigated influence of asymmetry. Parameter of asymmetry ξ was induced by periodical movement of a cavity up and down. Dependence of nonlinear solution on parameters of modulation (a - amplitude, ω - frequency, ξ - parameter of asymmetry) was found.

1 Statement of the Problem

The square cavity with a fluid or gas is considered. Temperature is given on the bottom. The temperature is zero on the top and the lateral temeperature is a gradient from the bottom to the top. The modulation of a parameter caused by the movment of the cavity up and down by the periodic sinusoidal law. Asymmetric law of the cavity coordinate $z(t)$ is on the Fig. 1. The geometry of the problem is on Fig. 2. Fig. 1 corresponds the case, when the parameter of

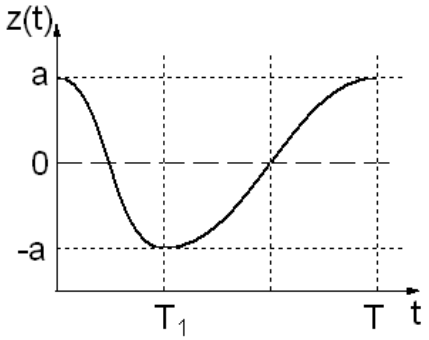


Figure 1: Asymmetric modulation law.

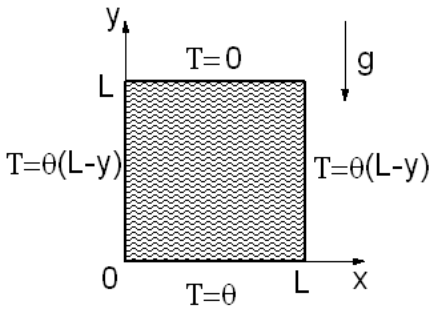


Figure 2: Geometry of the problem.

asymmetry is equal 2:

$$\xi = \frac{T - T_1}{T_1} = 2. \tag{1}$$

If the constant acceleration of gravity is g_0 then the modulated component assumes the form:

$$g(t) = \begin{cases} -a(\frac{\pi}{T_1})^2 \cos\frac{\pi t}{T_1}, 0 \leqslant t < T_1, \\ a(\frac{\pi}{T - T_1})^2 \cos\frac{\pi(t - T_1)}{T - T_1}, T_1 \leqslant t \leqslant T. \end{cases} \tag{2}$$

2 Method of Solving

We use two-field method (stream function and vorticity variables) to solve equations of free convection [1]:

$$\begin{cases} \dfrac{\partial\varphi}{\partial t} + (\dfrac{\partial\psi}{\partial y}\dfrac{\partial\varphi}{\partial x} - \dfrac{\partial\psi}{\partial x}\dfrac{\partial\varphi}{\partial y}) = \Delta\varphi + G\dfrac{\partial T}{\partial x}, \\ \dfrac{\partial T}{\partial t} + (\dfrac{\partial\psi}{\partial y}\dfrac{\partial T}{\partial x} - \dfrac{\partial\psi}{\partial x}\dfrac{\partial T}{\partial y}) = \dfrac{1}{P}\Delta T, \\ \Delta\psi + \varphi = 0, \end{cases} \tag{3}$$

where $G = G_0 + G(t)$ - constant and modulation components of the Grashof number, T - temperature, P - Prandtl number, x,y - spatial coordinates, φ - vorticity of the speed, ψ - stream function.

To solve this system of the equations we use numerical method on the square mesh 40x40. The first and second equation of the system is approximated with the central difference. The third equation calculates with the SOR method. The algorithm of the calculations is in [1]. A choise of the mesh 40x40 given by the fact, that a smaller mesh have the Raynold mesh number more than 2, and so the results are not trusted to due to the countable viscosity [2]. A bigger mesh causes to the longer calculation time.

The reference state for the non-dimensional system is:

$T = 1 - y,$
$\psi = 0,$
$\varphi = 100xy(1-x)(1-y).$

Boundary conditions are:

$T\,|_\Gamma = 1 - y,$
$\psi\,|_\Gamma = 0,$
$\varphi\,|_\Gamma$ defines with Thomas formulas [2].

Values of parameters are:

$P = 1$– Prandtl number, $g_0 = 9.85$ – constant free fall acceleration,
$G_0 = 0 \ldots 200000$ – considered Grashof numbers.

3 Results

3.1 Without Modulations

At first, the case without modulation is considered. The result of numerical solution is the amplitude line of Nusselt number from Grashof number (see Fig. 3). The bold line on the chart after the value 62000 of Grashof number is the average Nusselt number through the period of fluctuation. Dashed lines is maximum and minimum value of Nusselt number through the period of fluctuation. It is remarkable that if we start calculations from reference state then we get one critical Grashof number value (near 62000) where the fluctuation start, but if we start from formed state of bigger Grashof number then we get the second value of critical Grashof number (near 59000), lower than the first one (see Fig. 4). Bold lines on the Fig. 4 correspond the case when calculations started from reference state, and thin lines correspond the case when calculations started from formed state.

3.2 Symmetric and Asymmetric Modulations

The amplitude of modulations of Grashof parameter is 10% of considered Grashof number G_0. And the frequency of the modulations is equal to the frequency of fluctuations corresponding considered

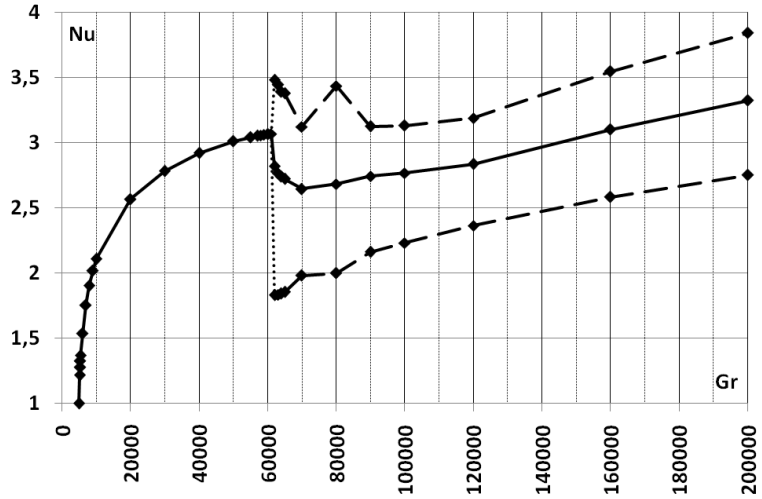


Figure 3: Dependence of Nusselt number from Grashof number (without modulations).

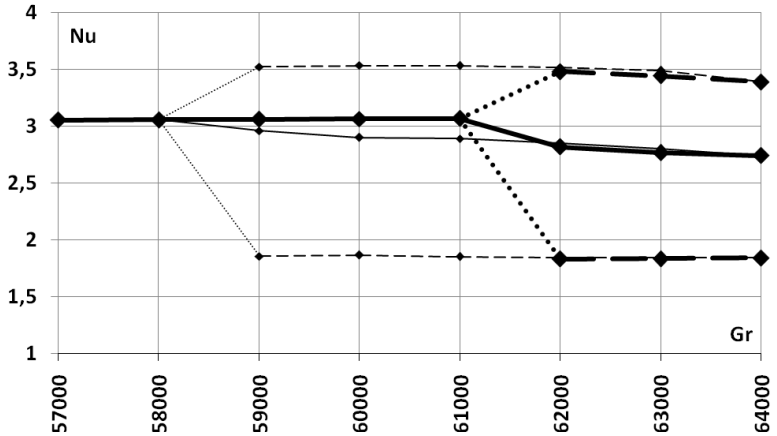


Figure 4: Hysteresis on the amplitude line.

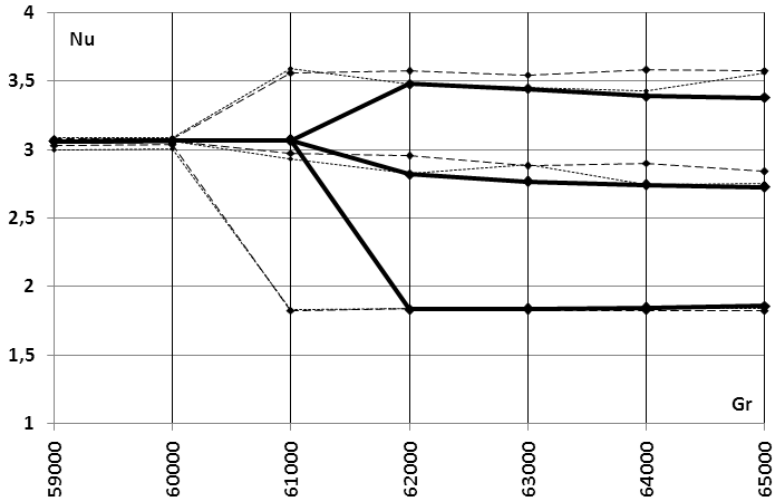


Figure 5: Modulations on the amplitude line chart (calculations from reference state).

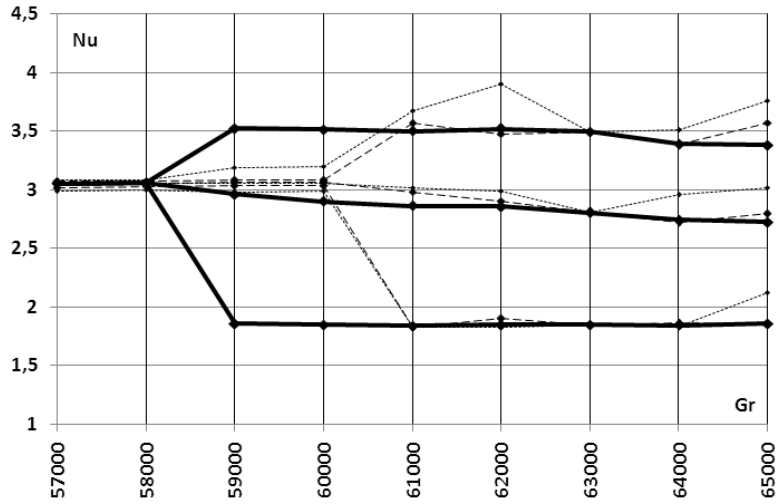


Figure 6: Modulations on the amplitude line chart (calculations from formed state).

Grashof number. Bold lines on the Fig. 5 and Fig. 6 correspond the case without modulations, long dashes correspond the case with symmetrical modulations, small dashes correspond the case with asymmetrical modulations. Critical Grashof number is lower in case with modulations than in case without modulations if calculations started from reference state. But if calculations started from formed state then critical Grashof number is the same in case with modulations as if calculations started from reference state, i.e. critical Grashof number is higher in case with modulations than in case witout modulations.

4 Conclusion

Calculations show that modulation of gravity influences on critical Grashof number value. Difference between symmetrical and asymmetrical modulation effects is not completely researched. It was found that if calculations started from the reference state then we get the critical Grashof number value, which differs from the critical Grashof number, obtained with calculations started from formed state of a higher Grashof number.

References

[1] Gershuni G.Z., Zhukhovickij E.M., Tarunin E.L. Numeric Research of Convection in the Close Cavity. USSR AS Proceedings, MFG, 1966, No 5.

[2] Tarunin E.L. Calculating Experiment in Free Convection Problem. Textbook. Irkutsk: Irkutskiy Universitet, 1990, 228p.

[3] Burde G.I. Numeric Research of Convection in the External Forces Periodical Modulation Case. USSR AS Proceedings, MFG, 1970, No 2.

[4] Gershuni G.Z., Zhukhovickij E.M. Convection Stability of Incompressible Fluid. M: Fizmatgiz, 1972. - 392p.

[5] Kashina L.A., Tarunin E.L. Convective Flows Induced by Periodical but Unharmonic Oscillation of Cavities. Abstract of Joint X European and VI Russian Symposium “Physical Sc. In Microgravity” St. Petersb., 1997, p.15.

Anatoly B. Melentyev, Fontannaya str. 9-178, Perm, Russia, 614002
Eugenie L. Tarunin, Lenina str. 75-5, Perm, Russia, 614068

Multimodel analysis of elasto-plastic problem under complex loading programs

B. E. Melnikov A. S. Semenov
kafedra@ksm.spbstu.ru

Abstract

The basic principles and application examples of the multimodel elastoplastic analysis under complex loading program is considered

1 Introduction

Increasing requires for reliability and durability of structures and their elements with simultaneous material economy have stimulated improvement of constitutive equations for description of elasto-plastic deformation processes. This has led to the development of phenomenological modeling of complex phenomena of irreversible deformation. During the last several decades many works have been devoted to the development of elasto-plastic models, in order to better predict the material behavior under combined variable thermo-mechanical loading.

At the present time a universal theory of inelasticity is absent and even the most accomplished theories can not guarantee adequate description of deformation processes for arbitrary structure under wide range of loading programs. The multilevel numerical stress analysis is one of the most effective approaches for numerical stress analysis of complex structures. Such adaptive constitutive modeling is based on creation of rational (reliable and quite simple) sequence of the elasto-plastic models according to different levels (body, element, point) of structure approximations.

2 General principles of multimodel analysis

At the moment there is no a universal theory of plasticity which is applicable for a wide class of materials and arbitrary paths of loading. In these conditions the multimodel approach [1, 2] for the analysis of inelastic behavior of material and structures under complex loading is probably most rational. The main features of the developed multimodel approach [1] are following:

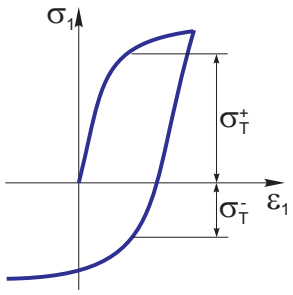
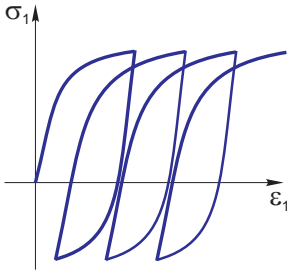
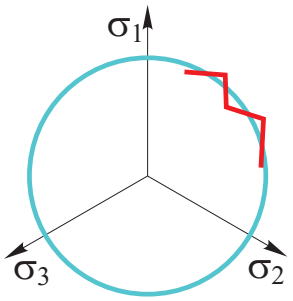
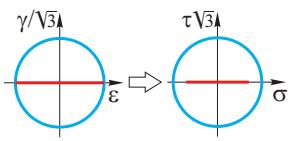
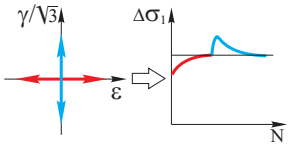
- certification of theories and creation of the elasto-plastic models library;
- determination of the selection criteria system;
- caring out of multivariant sequential clarifying computations to define areas of adequate application.

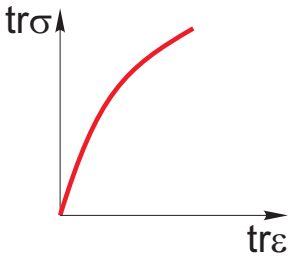
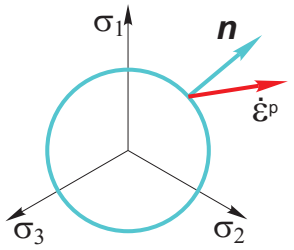
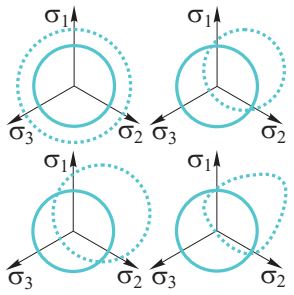
Basic element of automatic selection of material model is using of several developed classifiers (classification of materials, loading conditions, special effects, strain path curvatures and others). The classifiers form preliminary hierarchical sequence of models by way of their complication. The selection of adequate model is performed on the base of iterative FE solutions with models from the generated hierarchical sequence. Control of the iterative procedure is carried out in according to user requirements to the accuracy and computation rate, and also it depends on the availability of obtaining of the additive experimental information.

3 Phenomena of inelastic behavior of metallic materials

Classification of effects (phenomena) of inelastic deformation plays one of main roles in automatic selection of material models. Inelastic behavior of metallic materials under uniaxial and multiaxial loading for the different programs demonstrates existence of large number of phenomena which are not described as a rule by many models. The systematic analysis of these phenomena is considered in [3, 4, 5] for the proportional and non-proportional loadings, rate-dependent and rate-independent behavior, reversible and irreversible deformation. Some important effects under non-proportional loading are given in Table 13.

Table 13: Some typical phenomena of inelastic behavior.

Phenomena	Scheme	Possible mathematical model
Bauschinger's effect *(deformation induced anisotropy)*		$\sqrt{\frac{3}{2}(\mathbf{s}-\boldsymbol{\rho})\cdot\cdot(\mathbf{s}-\boldsymbol{\rho})}-\sigma_Y=0$ $d\boldsymbol{\rho}=cd\boldsymbol{\varepsilon}^p$
Ratchetting effect *(as an illustration - "drop" on the stress- strain curve corresponding to the strain path break)*		$\sqrt{\frac{3}{2}(\mathbf{s}-\boldsymbol{\rho})\cdot\cdot(\mathbf{s}-\boldsymbol{\rho})}-\sigma_Y=0$ $d\boldsymbol{\rho}=cd\boldsymbol{\varepsilon}^p-b\boldsymbol{\rho}d\lambda$
Irreversible deformation under passive loading *(plastic strain accumulation under deformation along the neutral loading surface and nearby it)*		$\dot{\boldsymbol{\varepsilon}}^p=\dot{\lambda}\frac{\partial f_k^{active}}{\partial\boldsymbol{\sigma}}$ $k=1,2,...,n$
Additional hardening effect in nonproportional loading *(cyclic hardening is more strong under the nonproportional loading than that under the proportional loading)*		$\dot{\sigma}_Y=\gamma\left[Q(A)-\sigma_Y\right]\dot{\varepsilon}_i^p$ $A=1-\frac{(\dot{\boldsymbol{\varepsilon}}^p\cdot\cdot\dot{\mathbf{s}})^2}{(\dot{\boldsymbol{\varepsilon}}^p\cdot\cdot\dot{\boldsymbol{\varepsilon}}^p)(\dot{\mathbf{s}}\cdot\cdot\dot{\mathbf{s}})}$
Cross hardening effect *(change of a direction in the proportional cyclic loading leads to the hardening followed by the softening)*		

Hydrostatic pressure effect *(high pressure, porosity)*		$tr\boldsymbol{\varepsilon}^p \neq 0$ $\sqrt{\frac{3}{2}(\mathbf{s}-\boldsymbol{\rho})\cdot\cdot(\mathbf{s}-\boldsymbol{\rho})}-$ $-\sigma_Y(tr\boldsymbol{\sigma})=0$
Non-associate plastic flow *(deviation from normality)*		$\dot{\boldsymbol{\varepsilon}}^p = \dot{\lambda}\frac{\partial g}{\partial \boldsymbol{\sigma}}$ $g \neq f$
Yield surface evolution *(expansion, translation and distortion)*		$\sqrt{(\mathbf{s}-\boldsymbol{\rho})\cdot\cdot{}^4\mathbf{Q}(\lambda)\cdot\cdot(\mathbf{s}-\boldsymbol{\rho})}-$ $-\sigma_Y(\lambda)=0$

The following notations are used in Table 13: σ_Y is the yield limit, $\boldsymbol{\sigma}$ and $\mathbf{s}$ are the stress tensor and deviator, $\boldsymbol{\rho}$ is the micro-stress tensor deviator, $\dot{\boldsymbol{\varepsilon}}^p$ is the tensor of plastic strain rates, $\dot{\varepsilon}_i^p = \sqrt{\frac{2}{3}\dot{\boldsymbol{\varepsilon}}^p\cdot\cdot\dot{\boldsymbol{\varepsilon}}^p}$ is the equivalent plastic deformation rates, λ is the Odquist's parameter (path length in the plastic strain space), in particular for von Mises's criterion: $\lambda = \int\sqrt{\frac{2}{3}\dot{\boldsymbol{\varepsilon}}^p\cdot\cdot\dot{\boldsymbol{\varepsilon}}^p}dt$, g is the plastic potential, f is the yield surface, α_N is Neuber's stress concentration coefficient, K_c is the fracture toughness, denotes a scalar product of tensors, so $\mathbf{A}\cdot\cdot\mathbf{B} = A_{ij}B_{ji}$.

4 Library of elasto-plastic models

The developed library of material models represents generalized data set, including information about limitations on field application, basic experiments for material parameters determination, continuous mathematical model, discrete numerical model, computational algorithm, implementation into finite element program, recommendations about computation strategy. At the present time the developed and implemented into finite element program library of rate-independent (plastic) models includes:

- Plastic flow theories with the various isotropic-kinematic laws of hardening. Relations of these 'classical' models belong to linear tensorial equations convenient for computations.
- Structural (rheologic) models theories. They possess clarity of properties, thermodynamic basis, obvious creation and modification.
- Multisurface theory with one active surface of plastic compliance. The model provides high accuracy of the description for the complex paths of passive loading.

- Endochronic theory of plasticity. The equations can be applied for a wide class of materials from a metal to a soil. This theory does not use the existence of a yield surface and employs the same equations for the loading and unloading processes.

5 Selection criteria system

The determination of the selection criteria system, based on classification of inelastic theories and their domain of advantageous applicability, is one of the main problems in multimodel analysis. Selection criteria system generates necessary conditions for material model on the basis of information concerning loading, available experimental data and discrete model of structure. The choice of rational model, which is the simplest among models satisfied necessary conditions, may be corrected by clarifying sequential computational experiments.

The classical examples of selection criteria are degree of plastic strains development in comparison with elastic strain and curvature (non-proportionality) of loading path. Numerous stress state analysis of elasto-plastic behavior of structures of different degree of complexity allows to formulate a new selection criterion. Suggested criterion is based on consideration of geometrical regulated levels of plastic deformation analysis. Similarly with [1, 2, 6, 8] we have introduced in the following levels:

- Body level **B** considers the body or complex structure as a whole. "Integral" analysis corresponds to initial strength problem. In most cases zones of plasticity are local.
- Element level **E** is introduced for separate part of structure as detailed fragment of structure, area with possible defect, superelement or individual finite element. "Semi-integral" analysis is carried out in this case. In most of cases zones of plasticity can be extensive.
- Point level **P** is the basic level, related to selected points of material continuum or to a model of structure. "Local" analysis is carried out for simplest geometrical object - element of material with homogeneous stress state. The whole object is a zone of plasticity.

Finally, the criterion can be formulated by following manner. Complexity of applying theory of plasticity must correspond to the level of the structure approximation. The levels **E** and **P** with more detail description of the structure geometry and with possibility of extensive zones of plasticity demand more difficult variants of theory adequate to the loading process. Using of simple models is sufficiently at the **B** level of the investigation, when deformation of local zones of plasticity is smoothed by influence of extensive elastic region. Refined computations of first level model can be performed on the basis of obtained information at second and third levels.

6 Results of multimodel computational analysis

The wide range of mentioned above inelastic material models has been implemented into finite element programs PANTOCRATOR [7] (see for details www.pantocrator.narod.ru).

Comparison of the results of numerical finite element analysis and experimental data for series investigated constructions corresponding to the first level **B** (frames, pipelines, vapor producing plant, gas generator, vessel of nuclear reactor) says about relative nearness of different theories predictions. However series of computations corresponding to the second level **E** of the structures considerations (fragment of rolling mill, fastenings of vapor producing plant, various fastening knots, socket, circular ring) have shown that the considerable differences of the prediction of stress-strain state by means of different theories of plasticity were displayed for a developed zone of plasticity and complex history of loading. Set of trials according level **P** carried out on tubular specimens of 1X18H10T steel under a wide range of the combined cyclic loading, including polygonal and circular paths of deformation. In general the results different theories corresponding to the level **P** can be essentially quality differed.

The typical examples of multimodel computations corresponding to the level **P** and comparison with experimental data are shown in Fig. 1, 2. Detailed description of problems is given in [6, 9].

Typical example of multimodel computations corresponding to the level **E** for thin circular ring being the part of more complex structure is shown in Fig. 3.

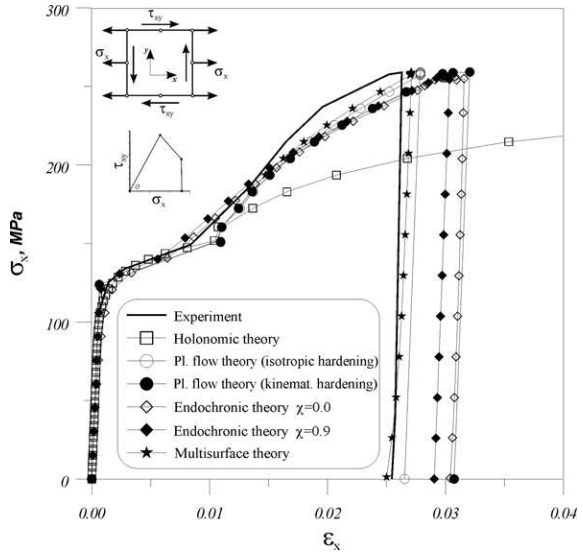


Figure 1: The thin-walled tube under combined axial tension-torsion [6].

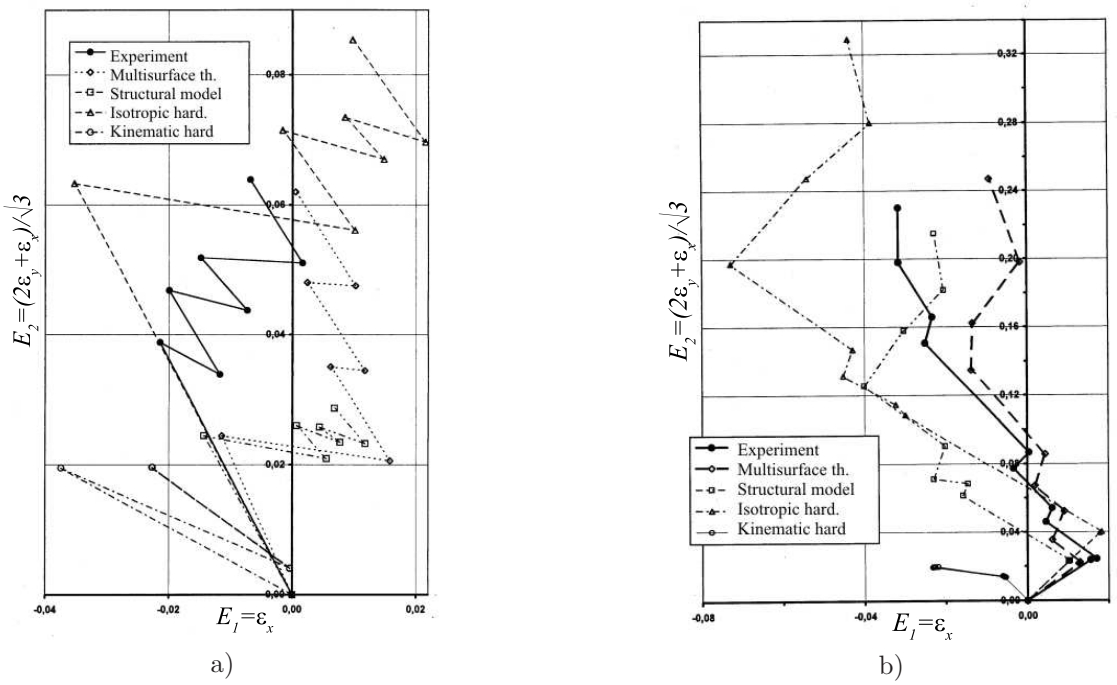


Figure 2: Thin-walled tubes (steel 1X18H10T) under complex cyclic non-proportional loading [9].

The levels **P** and **E** with more detail description of the structure geometry and with possibility of extensive zones of plasticity demand the more difficult variants of theory adequate to the loading process. Using of the simple models is sufficiently at the **B** level of the investigation, when the deformation of local zones of plasticity is smoothed by influence of extensive elastic region.

7 Conclusions

A strategy of automatic choice of a material model has been proposed. Certainly, the method does not claim for a full completeness now. Final purpose is a creation of the automatic system for selection of models meant for the correct computations of the strain-stress state under complex

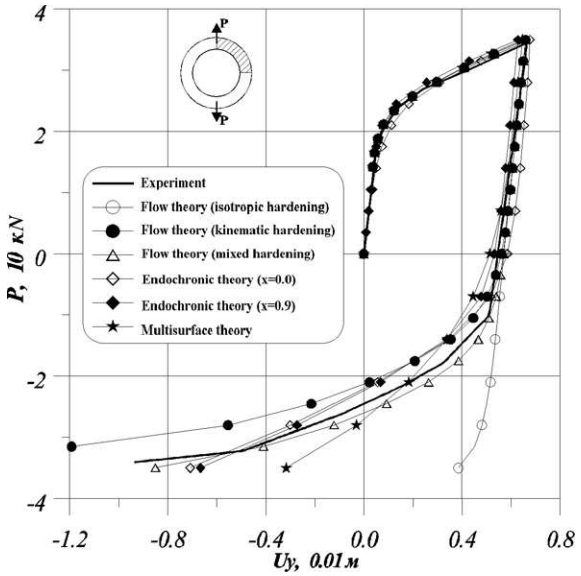


Figure 3: Circular ring under axial tension-compression [6].

loading conditions within the frame of modern finite elements systems. The application of the multimodel method can increase the effectiveness of computations and adequacy of results in the case of structure analysis under complex loading programs. We invite all authors of theories describing inelastic behavior of material to take part in a joint development of the multimodel method and expansion of material library.

Acknowledgements

This work was supported by RFBR grant N 09-01-00506-a.

References

[1] Melnikov, B.E., Semenov, A.S. (1995), 'Strategy of multimodel analysis of elastic-plastic stress-strain state', Proc. Int. Conf. on Comp. in Civil and Build. Eng. Berlin, 1073-1079.

[2] Semenov, A.S., Melnikov B.E. (1998), 'Multimodel analysis of the elasto-plastic and elasto-visco-plastic deformation processes in materials and structures', Proc. Int. Conf. Low Cycle Fatigue and Elasto-Plastic Behavior of Materials, Garmisch-Partenkirchen, 659-664.

[3] Getsov, L.B., Melnikov, B.E., Semenov, A.S. (2002), 'Criteria of choice of thermo-visco-plastic models in stress-strain state analysis of structures', Proc. 1st Conf. of users of programs from CAD-FEM GmbH, Moscow, 340-352.

[4] Benallal A., Cailletaud G., Chaboche J.L., Marquis D., Nouailhas D., Rousset M. (1985), Description and modeling of nonproportional effects in cyclic plasticity. Proc. Second Conf on Biaxial-Multiaxial Fatigue.

[5] Tanaka E., Murakami S., Ooka M. (1985), Effects of strain path shapes on non-proportional cyclic plasticity. J. Mech. Phys. Solids. Vol. 33. P. 559-575.

[6] Semenov A.S. (1996), Improvement of the research methods of thermo-elasto-plastic deformation processes on the base of multimodel analysis and the exact integration of constitutive equations. Ph.D. thesis. St.-Petersburg. 194 p.

[7] Semenov, A.S. (2003), 'PANTOCRATOR finite-element program specialized on the solution of non-linear problems of solid body mechanics', Proc. of 5th Int. Conf. "Sci. and Eng. Problems of Reliability and Service Life of Structures and methods of their decision", St.-Petersburg, 466-480.

[8] Zyczkowski, M. (1981), Combined Loadings in the Theory of Plasticity. Warszawa.

[9] Izotov I.N., Kuznetsov N.P., Melnikov B.E., Mityukov A.G., Musienko A.Y., Semenov A.S. (2001) Modification of the multisurface theory of plasticity with one surface: comparison with experimental data // 4th Int. Workshop on Nondestr. Testing and Comp. Simulat. in Sci. and Eng. Ed. A.I.Melker. Proc. of SPIE. Vol. 4348. P. 390-397.

B.E. Melnikov, 29 Polytechnicheskaya st. St. Petersburg, 195251 Russia
A.S. Semenov, 29 Polytechnicheskaya st. St. Petersburg, 195251 Russia

Influence mechanisms of strains and stresses to diffusion in loaded plate

Mikhail A. Mikolaychuk Anna G. Knyazeva
m.mikolaichuk@gmail.com

Abstract

The model of diffusion saturation of loaded plate by admixture from environment was suggested and investigated. Two possible influence mechanisms of starins and stresses on diffusion were analyzed. First of them related with diffusion activation energy change by lattice deformation. To relate activation energy with stress and strains, which presence in the system, we need introduce some notion, such as activation volume. Activation volume is difference between local volumes of the system in the ground and activated states. Ultima analysi, we can say that the work of stresses, which are presence in the local volume, is explicitly influence to diffusivity. We have used this diffusivity in the our model. Second mechanism consist in a mass transfer of impurity under stresses. It like pressure diffusion mass transfer in a liquids. Interference of first and second mechanisms on the behavior of system relation to physical and geometrical parameters was investigated.

1 Introduction

It is known that stresses and deformations appearing in diffused zone are influenced to diffusion. There are many works dedicated to this phenomena [1, 2, 3].

Diffusion processes dependence of stresses allows to make investigation of different admixture distribution control possibilities. Additional external load is one of this possibilities. Mechanical equilibrium problem in the presence of inner stresses with taking account of feedback between diffusion and mechanical processes must be solved for external load role investigation. In the case of inertia forces are negligibly small (because diffusion in solids is very slow process) it is possible to divide concerned problem to mechanical equilibrium problem and non linear diffusion problem. Investigation of different physical factors effect to diffused zone parameters in quasi-static one axis loading is main goal of this work.

2 Mechanical equilibrium problem

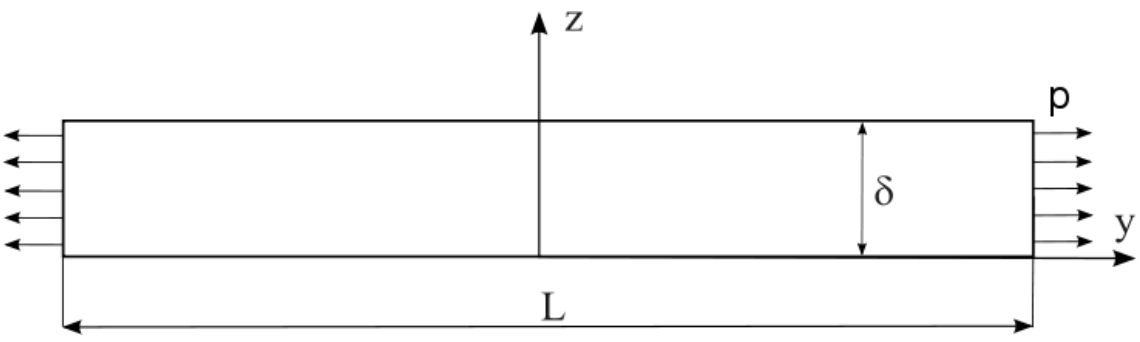


Figure 1: Loaded plate

The plate (Fig: 1) with length L, width h and thickness $\delta(L \gg h \gg \delta)$ in one axis loading was considered. The value of load p is given. Admixture coming through one of the plates planes. Impurity redistribution is result of diffusion processes or mechanical loading.

If there is no diffusion in Oz direction (sample is homogeneous) and external loading is uniform than sample state is plain stress. However, stresses field is three–dimensional in case of admixture coming through plane $z = 0$.

$$\sigma_{ij} = \sigma_{ij}(x, y, z).$$

We can describe stress state of sample with following components of stress tensor: $\sigma_{xx}, \sigma_{yy}, \tau_{xy}$. It is generalized plane stress, and boundary conditions could be written for averages

$$\bar{\sigma}_{xx} = \frac{1}{\delta}\int\limits_0^\delta \sigma_{xx}(x, y, z)\, dz, \;\; \bar{\sigma}_{yy} = \frac{1}{\delta}\int\limits_0^\delta \sigma_{yy}(x, y, z)\, dz, \;\; \bar{\tau}_{xy} = \frac{1}{\delta}\int\limits_0^\delta \tau_{xy}(x, y, z)\, dz.$$

Loading conditions could be written as follows

$$\bar{\sigma}_{yy} = p, \; \bar{\sigma}_{xx} = 0.$$

Because of we are interesting with stresses of diffused zone remote of loaded plates let's assume that $\sigma_{ij} = \sigma_{ij}(z)$, $\varepsilon_{ij} = \varepsilon_{ij}(z)$, than loading conditions could be rewritten

$$p = \frac{1}{\delta}\int\limits_0^\delta \sigma_{yy}(z)\, dz, \; 0 = \frac{1}{\delta}\int\limits_0^\delta \sigma_{xx}(z)\, dz. \tag{1}$$

Using followed conditions shear stresses and deformations can be neglected

$$0 = \frac{1}{\delta}\int\limits_0^\delta \sigma_{yy}(z) z\, dz, \quad 0 = \frac{1}{\delta}\int\limits_0^\delta \sigma_{xx}(z) z\, dz. \tag{2}$$

Using Duhamel — Neumann law of mass – elasticity theory [4] we can found relation between stresses and deformations tensors components

$$\sigma_{ij} = 2\mu\varepsilon_{ij} + \delta_{ij}(\varepsilon_{kk} \cdot \lambda - Kw),$$

where

$$w = 3\left[\sum_{k=i}^{n} \alpha_k(\eta_k - \eta_{k0})\right],$$

λ, μ — Lame constants, K — isothermal compression modulus, η_k — concentration of component k, α_k — concentration expansion coefficients, k — component number, numbers of components equal n, subscript "0" means non deformation state. Required components of stresses and deformations tensors looks like

$$\begin{aligned}
\varepsilon_{zz} &= -\frac{\lambda}{\lambda + 2\mu}(\varepsilon_{xx} + \varepsilon_{yy}) + \frac{K}{\lambda + 2\mu}w, \\
\sigma_{xx} &= -\frac{2\mu}{\lambda + 2\mu}\left[2(\lambda + \mu)\varepsilon_{xx} + \lambda\varepsilon_{yy} - Kw\right], \\
\sigma_{yy} &= -\frac{2\mu}{\lambda + 2\mu}\left[2(\lambda + \mu)\varepsilon_{yy} + \lambda\varepsilon_{xx} - Kw\right].
\end{aligned} \tag{3}$$

Strain compatibility conditions have been used for ε_{yy}, ε_{xx} definition

$$\frac{\partial^2 \varepsilon_{yy}}{\partial^2 z} = 0, \; \frac{\partial^2 \varepsilon_{xx}}{\partial^2 z} = 0,$$

There are two equations because other strain compatibility conditions and equilibrium equations satisfied identically. The solution of strain compatibility conditions

$$\varepsilon_{xx} = Az + B,\ \varepsilon_{yy} = Cz + D. \tag{4}$$

Substitute (4) in (3),

$$\begin{aligned} \sigma_{xx} &= \frac{2\mu}{\lambda + 2\mu}\left[2(\lambda+\mu)(Az+B) + \lambda(Cz+D) - Kw\right], \\ \sigma_{yy} &= \frac{2\mu}{\lambda + 2\mu}\left[2(\lambda+\mu)(Cz+D) + \lambda(Az+B) - Kw\right]. \end{aligned} \tag{5}$$

System of algebraic equations for A, B, C, D integration constants definition have been obtained by (5) in (1), (2) substitution.

$$\begin{aligned} &\alpha A + \beta B + \gamma C + \lambda\delta D - F_1 = 0, \\ &\frac{2\mu}{\lambda + 2\mu}\left[\alpha C + \beta D + \gamma A + \lambda\delta B - F_1\right] = p\delta, \\ &\omega A + \alpha B + \frac{2}{3}\delta\gamma C + \gamma D - F_2 = 0, \\ &\omega C + \alpha D + \frac{2}{3}\delta\gamma A + \gamma B - F_2 = 0, \end{aligned} \tag{6}$$

where

$$\alpha = (\lambda+\mu)\delta^2 = \beta\frac{\delta}{2}, \quad \beta = 2(\lambda+\mu)\delta, \quad \omega = \frac{2}{3}(\lambda+\mu)\delta^3 = \beta\frac{\delta^2}{3}, \quad \gamma = \lambda\frac{\delta^2}{2},$$

$$F_1(t) = K\int_0^\delta w\,dz, \quad F_2(t) = K\int_0^\delta wz\,dz.$$

The systems (6) solution

$$\begin{aligned} A &= \frac{\lambda p}{K\mu\delta} + \frac{4}{\delta^3 K}F_2 - \frac{2}{K}\frac{1}{\delta^2}F_1, \\ B &= -\frac{2}{3}\frac{p}{K\mu}\lambda - \frac{2}{\delta^2 K}F_2 + \frac{4}{3}\frac{1}{K\delta}F_1, \\ C &= -\frac{2}{K\delta}\frac{\lambda+\mu}{\mu}p + \frac{4}{\delta^3 K}F_2 - \frac{2}{\delta^2 K}F_1, \\ D &= \frac{4}{3}\frac{\lambda+\mu}{K\mu}p - \frac{2}{K\delta^2}F_2 + \frac{4}{3\delta K}F_1. \end{aligned} \tag{7}$$

Thus the mechanical equilibrium problem is solved. Obviously all coefficients depends on external load value and impurity distribution type.

3 Diffusion problem

There are two possible types of stresses to diffusion influence. First of them is diffusivity changing related with activation volume variation [5] or with local mechanical work of deformations. This changing given by

$$D^* = D_0' \exp\left[-\frac{k\Pi}{RT}\right],\ k = k_0\frac{m_{ev}}{\rho},\ \Pi = -(\sigma_{xx}\varepsilon_{xx} + \sigma_{yy}\varepsilon_{yy} + \sigma_{zz}\varepsilon_{zz}), \tag{8}$$

where k_0 — deformations work sensitivity of diffusion (sensitivity coefficient), ρ — density of considered system, m_{ev} — average molar mass.

Second type allow take into account mass transfer of admixture under stresses. According to thermodynamic theory [6] flow of matter in the binary mixture given by

$$J = -D_2\frac{\partial \eta}{\partial z} + B_2\eta\frac{\partial}{\partial z}\sigma_{kk}, \tag{9}$$

where subscript "2" means impurity, η — mass concentration of impurity, $\sigma_{kk} = \sigma_{xx} + \sigma_{yy} + \sigma_{zz}$. According to (8)

$$D_2 = D_2^* f(\eta), \quad D_2^* = D_0' \exp(-\frac{k\Pi}{RT})$$

Mass transport coefficient under stresses B_2 for admixture given by

$$B_2 = \alpha_2\frac{D_2^* \cdot m_2}{\rho RT},$$

where α_2 — concentration expansion coefficients, m_2 — molar mass of admixture.

Using second Fick's law

$$\frac{\partial \eta}{\partial t} = -\frac{\partial}{\partial z}J,$$

and equation of flow (9)

$$\frac{\partial \eta}{\partial t} = \frac{\partial}{\partial z}D_2\frac{\partial \eta}{\partial z} - \frac{\partial}{\partial z}B_2\eta\frac{\partial}{\partial z}\sigma_{kk}.$$

Using solve of mechanical equilibrium problem

$$\frac{\partial \eta}{\partial t} = \frac{\partial}{\partial z}\left[\left(D_2 + B_2\eta\frac{12\mu K\Delta\alpha}{\lambda+2\mu}\right)\frac{\partial \eta}{\partial z} - B_2\eta\frac{6\mu K}{\lambda+2\mu}(A+C)\right]. \tag{10}$$

Boundary conditions

$$z = 0 : \eta = \eta_0; \qquad z = \delta : J = 0 \; or \; D_0\frac{\partial \eta}{\partial z} = B_0\eta\frac{\partial \sigma_{kk}}{\partial z}.$$

Initial conditions $\eta = 0$.

4 Dimensionless problem

Parametric investigation would be afficient since main goal of this work is investigation of different physical factors effect to diffused zone parameters. Dimensionless variables

$$\eta, \tau = t\frac{D_2^*}{\delta^2}, \xi = \frac{z}{\delta}, s_{ij} = \frac{\sigma_{ij}}{3K\alpha_2}, e_{ij} = \frac{\varepsilon_{ij}}{3\alpha_2}.$$

Than equation (10) with boundary and initial conditions takes the form

$$\frac{\partial \eta}{\partial \tau} = \frac{\partial}{\partial \xi}\left(\overline{D}_{eff}\frac{\partial \eta}{\partial \xi}\right) - \overline{V}_{eff}\frac{\partial \eta}{\partial \xi}, \tag{11}$$

$$\xi = 0 : \eta = \eta_0; \xi = 1 : J = -\overline{D}_{eff}\frac{\partial \eta}{\partial \xi} - \overline{V}_{eff}\eta = 0, \; \tau = 0 : \eta = 0$$

where

$$\overline{D}_{eff} = \varphi(\varkappa)\cdot\left(f(\eta) + \frac{2h_1}{2h_2+1}\eta\Omega\alpha\right),$$
$$\overline{V}_{eff} = \varphi(\varkappa)\Omega\frac{6}{2h_2+1}\left(-S^e - 2\alpha h_1 I_1 + 4\alpha h_1 I_2\right),$$

$$\varphi(\varkappa) = \exp(\varkappa \cdot \Omega \cdot \frac{3}{3 - h_1} \cdot \overline{\Pi}),$$

$$\overline{\Pi} = s_{11} \cdot e_{11} + s_{22} \cdot e_{22},$$
$$I_1 = \int_0^1 \eta \, d\xi, \quad I_2 = \int_0^1 \eta\xi \, d\xi, \tag{12}$$
$$h_1 = \frac{2\mu}{\lambda + 2\mu}, h_2 = \frac{\lambda}{\lambda + 2\mu} = 1 - h_1, S^e = \frac{p}{3K\alpha_2},$$
$$\Omega = \frac{9\alpha_2^2 m_2 K^2}{RT\rho(\lambda + 2\mu)}, \alpha = \frac{\Delta\alpha}{\alpha_2}, \varkappa = k\frac{\rho}{m_2}.$$

Components of stresses and deformations tensors

$$e_{11} = x_1\xi + y_1, \qquad e_{22} = x_2\xi + y_2,$$
$$e_{33} = -h_2 \cdot (x_1\xi + x_2\xi + y_1 + y_2) + \frac{1 + 2h_2}{3} \cdot \alpha\eta,$$
$$s_{11} = h_1 \cdot \left(\frac{1 + h_2}{1 + 2h_2} \cdot (x_1\xi + y_1) + \frac{3h_2}{1 + 2h_2} \cdot (x_2\xi + y_2) - \alpha\eta \right),$$
$$s_{22} = h_1 \cdot \left(\frac{1 + h_2}{1 + 2h_2} \cdot (x_2\xi + y_2) + \frac{3h_2}{1 + 2h_2} \cdot (x_1\xi + y_1) - \alpha\eta \right),$$

where

$$h_2 = 1 - h_1,$$
$$x_1 = \frac{2h_2}{h_1}S^e + 4\alpha I_2 - 2\alpha I_1, \qquad y_1 = \frac{4h_2}{3h_1}S^e - 2\alpha I_2 + \frac{4}{3}\alpha I_1,$$
$$x_2 = -2\frac{1 + h_2}{h_1}S^e + 4\alpha I_2 - 2\alpha I_1, \qquad y_2 = 4\frac{1 + h_2}{3h_1}S^e - 2\alpha I_2 + \frac{4}{3}\alpha I_1.$$

There are five parameters in the model. Ω, α, $\varkappa$, S^e and h_1. $\overline{D}_{eff}$ – effective diffusivity, $\overline{V}_{eff}$ – effective convection velocity like in the classical mass transfer equation. Relative concentration expansion coefficient α shows difference between matrix and impurities atomic dimension. Ω is a connectivity coefficient. Environment properties described with h_1. $\varkappa$ — is a dimensionless sensitivity coefficient.

The problem was solved numerically. The differential equation 11 included into system was approximated by difference equations; the resultant system of linear algebraic equations was solved by a sweep method.

5 Results

Typical concentration distributions in diffused zone without external loading ($\alpha_c = 0.2$) shown on the figure 2, a. If $\varkappa = 0$ then concentrations distribution looks like diffusion equation solution.

$$\frac{\partial\eta}{\partial t} = \frac{\partial^2\eta}{\partial\xi}$$
$$\xi = 0 : \ \eta = 1; \quad \xi \to \infty : \ \frac{\partial\eta}{\partial\xi},$$
$$\eta = erfc\left(\frac{\xi}{2\sqrt{\tau}}\right).$$

Assuming $\varkappa = 100$ we can see qualitative change of concentration profiles (figure 2, b.). Result of sensitivity coefficient rising shown on the figure 2, c, where greater label correspond to greater

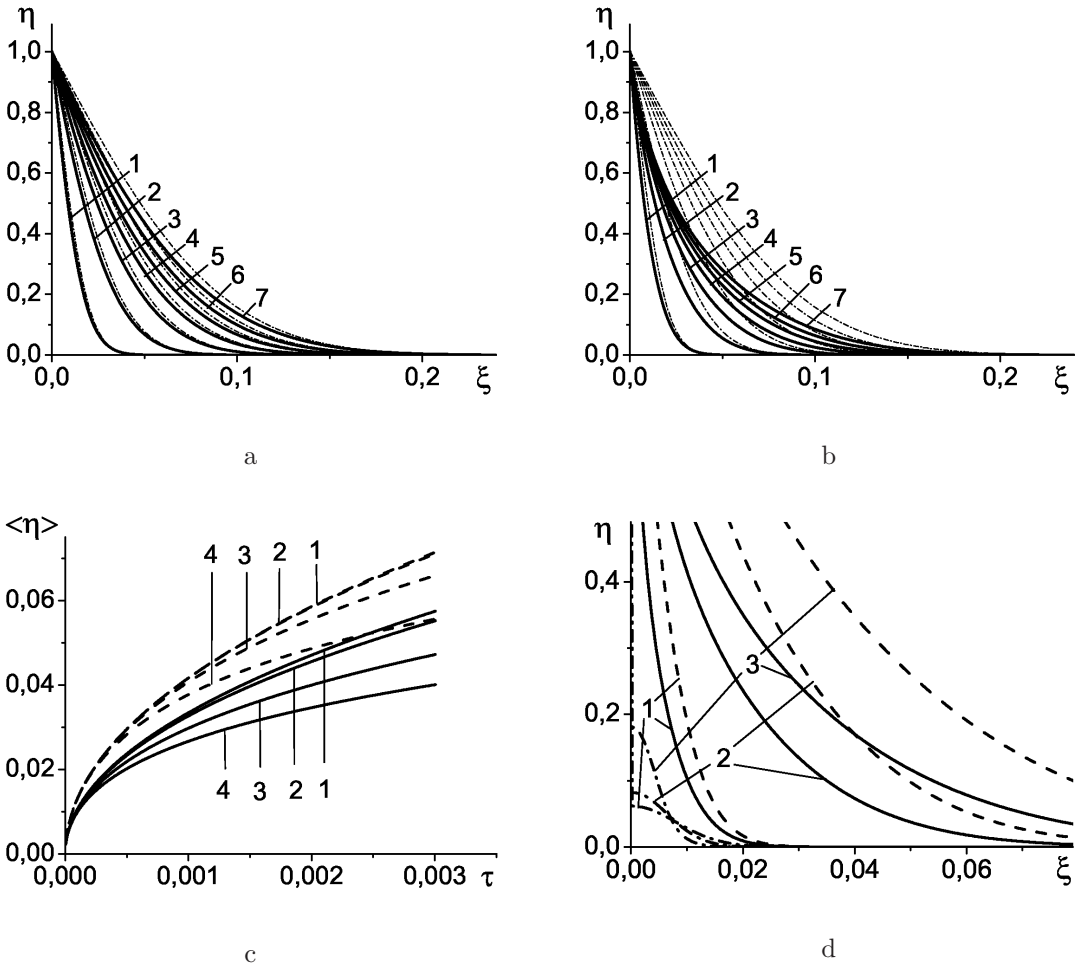


Figure 2: Results of calculation

value of $\varkappa$. Obviously average value of concentration (which shown on this figure) reduce with sensitivity coefficient increase. Changing of concentration distribution with external load shown on figure 2, d. There are $\eta(\xi)$ for two values $\varkappa$ and $S^e = -0.1$ shown on this figure. Obviously external load blocked impurities flow if atomic dimension of impurity more than matrix atomic dimension. Concentrations distribution in case of atomic dimension of impurity less than matrix atomic dimension ($\alpha = -0.2$) indicated by a dotted line.

This work was supported by Russian Foundation for Basic Researches (grant 10-01-00034)

References

[1] Ermeev V.S. Diffusion and stresses. M.:Energoatomizdat,1979. (in Russian)

[2] Stark G.P. Diffusion in solids. M.: Energiya, 1980. (in Russian)

[3] Gurov K.P. Interdiffusion in polyphase metallic systems. M.:Nauka, 1981. (in Russian)

[4] Shermergor T.D. Elasticity theory of microinhomogeneous mediums. M.: Nauka, 1977. (in Russian)

[5] Aziz Michael J. Thermodynamics of diffusion under pressure and stress: Relation to point defect mechanisms //Appl. Phys. Lett., 1997, Vol. 70, no. 21, P. 2810-2812

[6] Knyazeva A.G. Diffusion and rheology in locally equilibrium thermodynamic //Mathematical modelling of systems and processes., 2005, no 13., P. 45–60 (in Russian)

Mikhail A. Mikolaychuk, pr. Akademichesky 2/4, Tomsk, Russia
Anna G. Knyazeva, Akademichesky 2/4, Tomsk, Russia

Investigation of the influence of bleaching on human teeth enamel microstructure

I. A. Morozov A. L. Svistkov O. K. Garishin O. S. Gileva E. S. Erofeeva
ilya.morozov@gmail.com

Abstract

This work focuses on the quantitative analysis of the enamel surface microrelief and the effect of bleaching on the microstructure of enamel surface. The AFM images (15 x 15 micrometers) that exhibited the enamel surface of the unbleached tooth, the tooth bleached once and the tooth bleached thrice were examined. To clarify the general pattern of the enamel microrelief alteration, we applied the so-called cartographic method showing flat areas, cavities and elevations on the surface of a tooth. We present a method for structural analysis of such parameters as density, size, perimeter, area, volume, and fractal dimensions. The obtained results show that the first bleaching removes pellicles (adsorbed salivary protein film) from the surface of teeth enamel, and further bleaching causes enamel wear, especially in the cavity areas of the relief. Elevations and depressions become more round in shape. The structures observed on enamel surface are found to be related by fractal relationships, which is indicative of their self-similarity over the entire range of sizes observed in this study.

1 Introduction

Cosmetic stomatology is the fastest growing segment of the dentistry market. A beautiful smile will always attract attention. The main factors involved in the judgment of human smiles are the optical properties of the tissues of healthy teeth, i.e., enamel color shades, color saturation, lightness, opalescence and brightness. In the past few years, the procedure of teeth bleaching has become increasingly popular, and nearly everyone can afford to have their teeth whitened. However, some researchers note that bleaching agents reduce the mineral content of enamel and have a negative effect on the structure of hard tooth tissues. An extended overview of modern medical research on this subject is available in the paper by N.I. Krikheli and O.O. Yanushevich[1]. By now, many researches have been done to study the influence of different factors on enamel microstructure: age-related changes [2], the use of different beverages [3, 4, 5], dehydration [6], toothpastes [7, 8] and brushes [9], bleaching [1, 10, 11], etc. In the literature, enamel images obtained by scanning microscopy techniques are usually used as accompanying illustrations. A detailed quantitative analysis of microrelief peculiarities will provide further information concerning the state of the enamel structure and its changes caused by external actions. The aim of this study is to develop the analysis techniques for studying the microstructure of teeth enamel using atomic force microscopy (AFM) and to evaluate the effect of bleaching on the microstructure of teeth enamel with the aid of the proposed approach. Our techniques involve: (a) processing of AFM images of enamel surface in general within the framework of the so-called cartographic approach showing plateaus, depressions and elevations on the enamel surface, and (b) structural analysis of separate components of the enamel relief (sizes, shapes, fractal characteristics). Quantitative differences in the microstructure of bleached and unbleached teeth were calculated based on the developed methods.

2 Experiments

Materials for experimental studies were intact human teeth removed for periodontal indications. We performed experiments to obtain data for the enamel surface of the unbleached tooth and

the same tooth bleached once and twice running. For whitening, the 'Opalescent Xtra Boost' gel was used. After each bleaching step, AFM images of the mid-part enamel surface were taken for further comparative analysis. Experiments were performed with a Nano-DST atomic force microscope operating in the semicontact regime. The nominal radius of a probe tip is <10nm. The results presented in this paper are based on averaged data taken from different parts of teeth. The image size is 15x15 micrometer with resolution in the xy plane 1024x1024 points. The results were processed by the algorithms developed by the authors using Matlab.

3 Results and discussion

The microstructure of tooth enamel is a complex relief. At first glance, the AFM images are essentially different and, therefore, difficult to compare (Fig.1). To classify the obtained results, the so-called cartographic method is used. The data are reduced to the average level chosen as follows: performing a small step h from the minimum value of height h to its maximum value, we construct the relationships $\rho = S(h \pm \Delta h)/S$, where $S(h \pm \Delta h)/S$ is the relief area within the interval $h \pm \Delta h$; S is the total area. Figure 1 shows two unprocessed images of enamel and the corresponding curves $\rho(h)$.

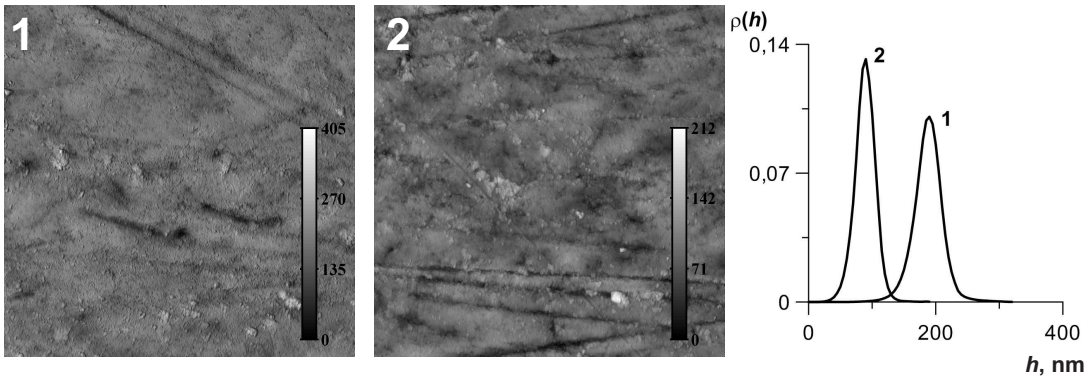


Figure 1: Two unprocessed images of enamel and the relevant relief area curves $\rho(h)$.

All relationships $\rho(h)$ can be plotted quantitatively as shown in Fig.1. As a zero image level, we take the height at which the value $S(h \pm \Delta h)/S$ has its maximum. Further, the relief was separated into 3 components depending on the height relative to the zero level h:

1. $abs(h) < 25nm$ - plateau area;
2. $h \leq -25nm$ - depressions;
3. $h \geq 25nm$ - elevations.

For convenience of visualization, the parts of the enamel relief exceeding in absolute value 100 nm were cut. In the figure, these areas can be observed as black cavities or white mountain-tops. The results of bleaching tests are shown in Fig. 2.

The quantitative results from Figure 2 indicate that the relief of the unbleached tooth, in comparison with the bleached one, is more inhomogeneous; depressions and elevations occupy most of the image. Table 1 gives the values of total roughness R_{rms} (root-mean-square deviation of the height, nm), the percent contributions of flat areas, depressions and elevations to the general pattern of the relief.

The results summarized in Table 1 indicate that the enamel of the tooth bleached once is most inhomogeneous. Based on these data, we can suggest that the first bleaching has fulfilled its function by way of removing the first film (pellicula) and uncovering the intrinsic structure of the enamel. The second bleaching has removed some portion of the upper enamel surface layer - the percentage of both the elevations and the depressions decreases by a factor of 1.5-2. The surface structure obtained using AFM techniques is a complex three-dimensional relief. For performing

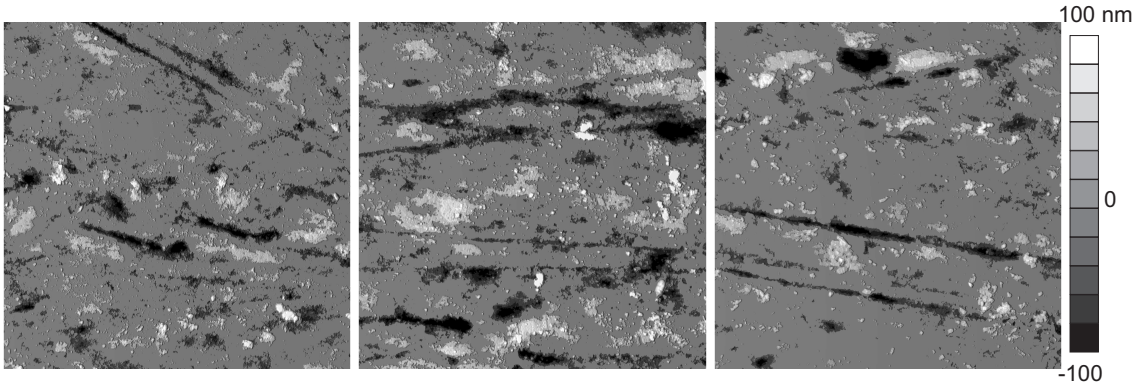


Figure 2: Enamel surface of unbleached (left), bleached (middle) and tooth bleached thrice (right).

Enamel	Roughness	Flat areas, %	Depressions, %	Elevations, %
Unbleached	29	67	19	14
Bleached once	34	59	29	12
Bleached thrice	22	80	12	8

Table 14: Relief characteristics.

the detailed structural analysis of this relief, we apply the procedure analogous to that described in work [12] - as the height h above the zero level increases, the relief is split into separate 'islands'. The structures of elevations ($h > 0$) and depressions ($h < 0$) are analyzed separately. In the latter case, the relief with negative height is inverted and considered further as elevations. Figure 3 shows the cross-sections of the obtained objects for the relief structures shown in Fig.2. The cross-sections of elevations and depressions are shown as bright and dark regions respectively.

Table 2 presents obtained mean values of sizes d, cross-section areas A as well as the volumes

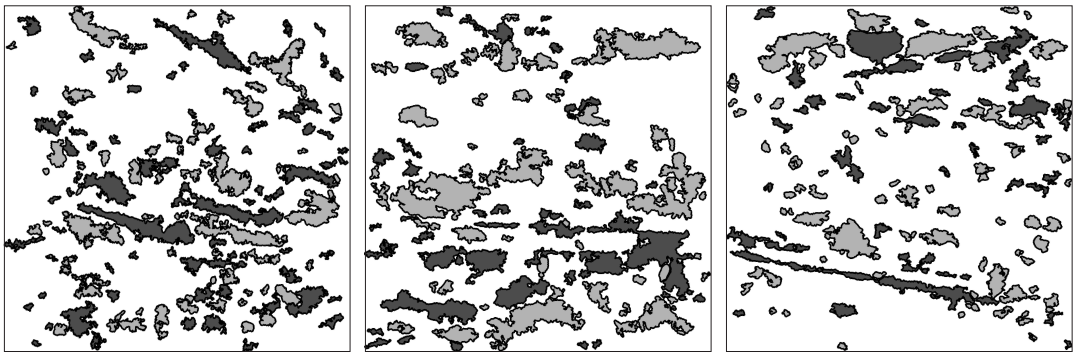


Figure 3: Cross-sections of elevations and depressions.

V of elevations and depressions for unbleached and bleached teeth. The analysis of the geometry of elevations reveals that the first bleaching, as mentioned above, removes some dental plaque from teeth, uncovering thus the enamel surface; the size, area and volume of elevations increase. Further bleaching procedures leads to smoothing the tooth enamel (mean parameters of elevations are reduced). Unlike elevations, the structure of depressions, their sizes, area and volume do not decrease after first bleaching. The average size of depressions increases, i.e., they become more elongated with respect to the horizontal line (Fig.2), while the unchanged volume and the reduced portion of elevations and depressions (Table 1) point to the fact that the negative parts of the relief become deeper. Reduction in the volume of elevations and the constancy (or growth) of the volume of depressions testify that the enamel wear increases in depth faster than the enamel surface is smoothed. Let us perform the fractal analysis of the structure of enamel surface. The relationship between the sectional area of objects and the perimeter can be written as:

Enamel	Elevations			Depressions		
	$d, \mu m$	$A, \mu m^2$	$V, \mu m^3$	$d, \mu m$	$A, \mu m^2$	$V, \mu m^3$
Unbleached	0.38	0.24	0.03	0.43	0.40	0.06
Bleached once	0.47	0.39	0.06	0.59	0.47	0.05
Bleached thrice	0.44	0.27	0.04	0.45	0.32	0.05

Table 15: Mean values of sectional areas and sizes of enamel structures.

$P_k = \mu_1 A_k^{D_p/2}$,

where P_k, A_k are the perimeter and the sectional area of the k-th object; μ_1 is a constant, and D_p is the fractal dimension of the perimeter. Similar relationship exists between the size d_k and the volume V_k of objects:

$V_k = \mu_2 d_k^{D_v}$,
where μ_2 is a constant, and D_v is the fractal dimension of the volume (mass). In double logarithmic coordinates these expressions can be approximated by line using the least square method. Table 3 shows the obtained values of fractal dimensions and the criterion of validity of R-square approximation (the closer its value to unity, the higher the accuracy of approximation). The values of D_v obtained for the unbleached enamel demonstrate the least accuracy of approximation (Table 3). This is probably related to the fact that there are many artificial changes of the tooth surface relief caused by tooth extraction and its first treatment. Thus, we can say with confidence that certain fractal structures are only possible in the case of bleached enamel. The existence of fractal relations between the geometric characteristics of the objects points to the fact that they are self-similar over the entire range of sizes observed in this study.

Enamel	Elevations		Depressions	
	$D_p - R^2$	$D_v - R^2$	$D_p - R^2$	$D_v - R^2$
Unbleached	$1.48 - 0.91$	$2.37 - 0.72$	$1.47 - 0.95$	$2.09 - 0.78$
Bleached once	$1.46 - 0.94$	$2.31 - 0.87$	$1.41 - 0.94$	$2.39 - 0.90$
Bleached thrice	$1.39 - 0.92$	$2.32 - 0.83$	$1.35 - 0.93$	$2.47 - 0.90$

Table 16: Values of fractal dimensions.

To describe the degree of surface roughness, we apply the Hurst index H: $H = 2 - D_p$. Its values for elevations are 0.52, 0.54, 0.61, and for depressions 0.53, 0.59, 0.65. All values $H > 0.5$ and they increase with bleaching. The surface roughness also decreases at the scale under consideration. Elevations and depressions become more round in shape - fractal dimension D_v increases (for the ball $D_v = 3$).

4 Conclusions

We have developed the methods for structural investigation of teeth enamel using atomic force microscopy. In the first stage, the obtained teeth enamel relief was leveled relative to the zero level and considered to be part of the relief, which contributed maximally to the total area of the recorded image. By analogy with the geographical maps, we introduced the notions of flat areas, elevations and depressions on the surface of a tooth. The proposed methods were used to perform the structural analysis of elevations and depressions of the enamel relief and to explore such parameters as compactness, size, perimeter, area, volume and fractal dimensions. The obtained results show that the first bleaching removes pellicle from the surface of enamel, which increases the enamel surface roughness and the mean geometrical characteristics of structures observed on the tooth enamel surface. During further bleaching procedures, the enamel wears down, especially in the lowland regions of the relief. The area and perimeter as well as the volume and size of structural components of the enamel surface are related by fractal relationships, which is indicative of their self-similarity over the entire range of sizes observed. The analysis of the fractal dimension D_p

indicates that the surface roughness decreases at the relevant scale, and elevations and depressions become more round in shape. Based on the obtained results, we can conclude that the single-stage dental bleaching does not affect the intrinsic enamel structure. Repeated bleaching treatment damages enamel structure, especially in the lowland regions of the relief (enamel surface defects increase in depth).

Acknowledgements

This study was supported by the Ministry of industry, innovations and science of Perm Kray (grant No 09-08-99102-r_ofi).

References

[1] N.I. Kriheli, O.O. Janushevich. Vlijanie otbelivajuwih preparatov na pronicaemost' jemali, ee mineral'nyj sostav i strukturu tverdyh tkanej zuba // Rossijskaja stomatologija. 2009. V. 2, N3. P. 20-25.

[2] A.V. Cimbalistov, O.L. Pihur, O.V. Frank-Kameneckaja, V.V. Golubcov, Ju.V. Plotkina. Rezul'taty issledovanija morfologicheskogo stroenija, himicheskogo sostava i parametrov kristallicheskoj reshetki apatitov tverdyh tkanej zubov // Institut stomatologii. 2004. N2(23). P. 60-63.

[3] M. Finke, J.A. Hughes, D.M. Parker, K.D. Jandt. Mechanical properties of in situ demineralised human enamel measured by AFM nanoindentation // Surf. Sci. 2001. V. 491, N3. P. 456-467.

[4] M. Finke, D.M. Parker, K.D. Jandt. Influence of soft drinks on the thickness and morphology of in situ acquired pellicle layer on enamel // J. Colloid Interface Sci. 2002. V. 251, N2. P. 263-270.

[5] C. Machado, W. Lacefield, A Catledge. Human Enamel Nanohardness, Elastic modulus and surface integrity after beverage contact // Braz. Dent. J. 2008. V. 19, N1. P. 68-72.

[6] R. Kubinek, Z. Zapletalova, M. Vujtek, R. Novotny, H. Kolarova, H. Chmelickova. Examination of dentin surface using AFM and SEM // Modern Research and Educational Topics in Microscopy. 2007. V. 2, N3. P. 593-598.

[7] J.J. Ehrhardt. Absolute measurements of the depth of abrasion, a testing method for dentifrices // J. Appl. Sci. Res. 1947. V. A1. P. 87-93.

[8] I.A. Meyers, M.J. McQueen, D. Harbrow, G.J. Seymour. The surface effect of dentifrices // Aust. Dent. J. 2000. V. 45, N2. P. 118-124.

[9] F. Lippert, D.M. Parker, K.D. Jandt. Toothbrush abrasion of surface softened enamel studied with tapping mode AFM and AFM nanoindentation // Caries Research. 2004. V. 38, N5. P. 464-472.

[10] J.E. Dahl, U. Pallesen. Tooth bleaching - a critical review of the biological aspects // Crit. Rev. Oral. Biol. Med. 2003. V. 14, N4. P. 292-304.

[11] M. Ogiwara, Y. Miake, T. Yanagisawa. Changes in dental enamel crystals by bleaching // J. Hard Tissue Biol. 2008. V. 17, N1. P. 11-16.

[12] Morozov I.A. Analiz mikrostruktury napolnennoj reziny pri pomowi atomno-silovoj mikroskopii // Mehanika kompozicionnyh materialov i konstrukcij. 2009. V.15, N1. P. 83-94.

I. Morozov, Institute of continuous media mechanics UB RAS, Perm, Russia

Volume and surface stability of a transversely isotropic material

N. F. Morozov P. E. Tovstik
morozov@nm1016.spb.edu peter.tovstik@mail.ru

Abstract

The modes of stability loss of a compressed transversal isotropic elastic space and half-space are investigated. The modes of stability loss of a compressed plate on an elastic foundation are studied.

1 Introduction

A compressed elastic material loses the volume stability since for the large enough compression the Hadamard condition is not satisfied [1-3]. An elastic half-space loses the surface stability under large enough compression with buckling waves localized near the free plane with amplitude exponentially decreasing as the distance to the free plane is increased [2-4]. A compressed elastic plate lying on an elastic foundation also may lose stability [5-7]. Sketch of the studied problems is shown in Fig. 1.

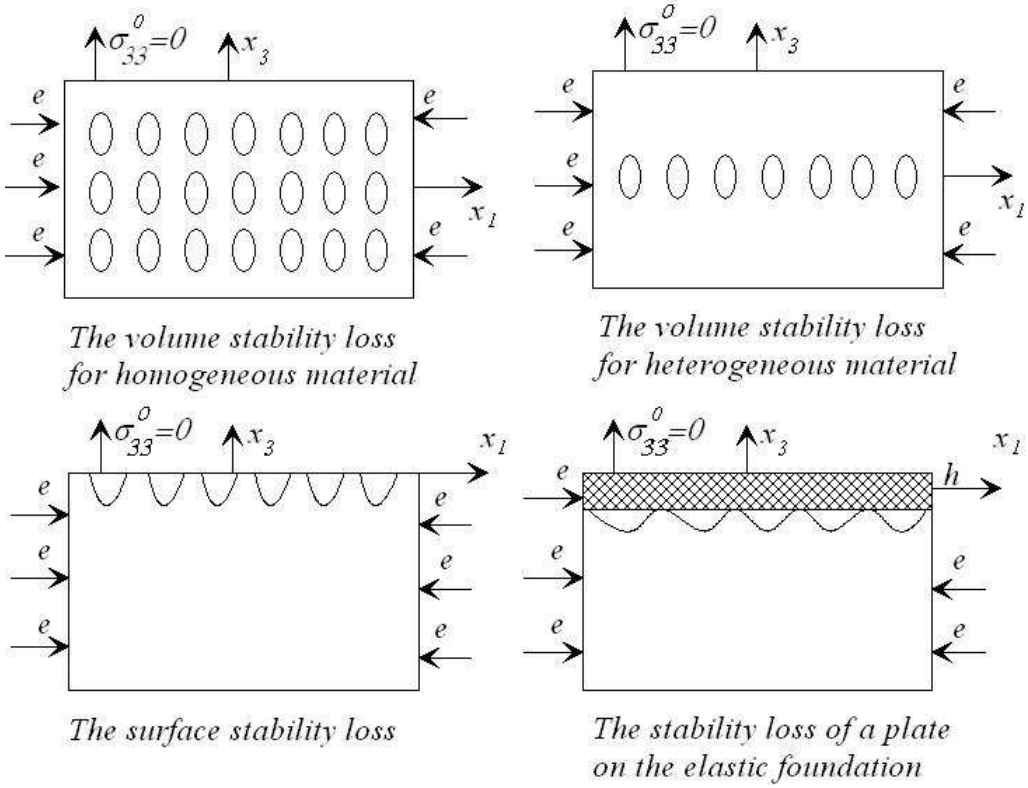


Fig. 1. Sketch of the studied problems.

For these problems the critical compression and the buckling modes for a transversely isotropic linearly elastic material are established. The critical compression is to be found from the equations of bifurcation. The critical compression is definite. But the corresponding buckling modes can not be established with precision.

Let us study a compressed transversely isotropic material in the space $Ox_1x_2x_3$ ($x_3 = z$) in which the horizontal planes z=const are the planes of isotropy. We assume that the constant initial horizontal deformations $\partial u_1^0/\partial x_1 = \partial u_2^0/\partial x_2 = -e$ are given, and the initial vertical stresses are equal to zero ($\sigma_{33}^0 = 0$). These deformations generate the initial horizontal stresses $\sigma_{11}^0 = \sigma_{22}^0 = \sigma_0$ and the initial vertical deformation $\partial u_3^0/\partial z = e_3 > 0$.

We assume that the elastic modules may depend only on the vertical co-ordinate z, and we seek the solution of the bifurcation equations in the form

$$u_k(x_1, x_2, x_3) = u_k(z) \exp\{i(r_1x_1 + r_2x_2)\}, \quad k = 1, 2, 3, \quad i = \sqrt{-1}, \tag{1.1}$$

where u_k are the additional displacements at bifurcation and r_j are unknown wave numbers. It is possible to find only relation between the wave numbers r_j, therefore the wave lengths $L_j = 2\pi/r_j$ remain indefinite. Moreover the bifurcation equations contain only $r = \sqrt{r_1^2 + r_2^2}$ but r_1 and r_2 are not contained in these equations separately.

The bifurcation system of the 6th order may be divided into the an equation of the 2nd order and into a system of the 4th order. Two kinds of buckling modes for volume stability loss are possible. The kind 1 is the rotation mode with the displacements in the plane of isotropy ($u_1, u_2 \neq 0,\ u_3 = 0$), and the critical compression $e^{(1)}$ may be found from the equation of the 2nd order. For the kind 2 the displacements in all the directions are not equal to zero ($u_1, u_2, u_3 \neq 0$), and the critical compression $e^{(2)}$ may be found from the system of the 4th order. Which of the critical values, $e^{(1)}$ or $e^{(2)}$, is smaller (or which of the buckling modes takes place), depends on the elastic modules of the material. If the elastic properties of the material are close to the isotropic ones then the kind 1 is implemented, and, on contrary, if the material is soft in the Oz direction then the kind 2 takes place. If the material is a homogeneous one (the elastic modules are constant) then $u_k(z) = u_k^0\, e^{ir_3z}$, and the buckling mode occupies the entire space. In this case the critical compression does not depend on the wave number r.

If the material is heterogeneous (the elastic modules depend on z) then there is the weakest plane $z = z_*$ near which the buckling mode is localized, and the critical compression depends on the wave number r ($e^{(k)} = f(r)$). If the modules are continuous functions in z then the function $f(r)$ decreases and $f(r) \to f_\infty$ at $r \to \infty$. Here f_∞ is equal to the critical compression of a homogeneous material with the elastic modules coinciding with the values of a heterogeneous material at $z = z_*$. If the modules are piecewise continuous (the space is multi-layered) then sometimes there is the weakest plane, and the minimum of function $f(r)$ is achieved at the finite value $r = r_*$. Therefore the typical wave length $L = 2\pi/r_*$ of the bifurcation mode is found. All these results concer both kinds of buckling modes.

We discuss also surface stability of a compressed transversely isotropic homogeneous half-space $z \leq 0$ with the free plane $z = 0$. The bifurcation system is the same as for the volume stability, but now it is necessary to satisfy the boundary conditions at the free surface $z = 0$, and the decreasing conditions $u_k(z) \to 0$ at $z \to -\infty$. Naturally the critical compression $e^{(s)}$ satisfies the inequality $e^{(s)} < \min\{e^{(1)}, e^{(2)}$. For the surface stability loss only the kind 2 of the buckling mode which is described by the system of the 4th order is possible. As in the case of the volume stability the bifurcation equation contains only $r = \sqrt{r_1^2 + r_2^2}$ but the critical compression $e^(s)$ does not depend on r. The free surface $u_3 = u_3(x_1, x_2, 0)$ after buckling is a double periodic function of x_1 and x_2. But as the wave length $L = 2\pi/r$ so the buckling mode which is described by the relation between r_1 and r_2 remains indefinite. It is interesting to know the free surface mode after buckling in some mechanical, physical and biological problems [8]. In [8] it is indicated that the chessboard-like distribution of strains (namely, with $r_1 = r_2$) is typical for many interfacial problems.

The problem of the interfacial stability is very close to the problem of the surface stability. Let the compressed elastic space consists of two transversely isotropic half-spaces $z > 0$ and $z < 0$ with the various elastic modules. In this case there exists the buckling mode localized near $z = 0$ and the corresponding critical compression $e^{(i)}$. To find them we seek the solution of the bifurcation equations, satisfying the continuity conditions at $z = 0$ and to the decreasing conditions $u_k(z) \to 0$ at $z \to \pm\infty$. The value $e^{(i)}$ satisfies the inequality $e^{(i)} > \min\{e^{(s1)}, e^{(s2)}\}$, where $e^{(s1)}$ and $e^{(s2)}$

are the critical compressions of the free surface stability for each of the studied half-spaces. Here again the wave numbers r_1 and r_2 remain indefinite.

The buckling problem of the infinite compressed plate lying on the soft elastic foundation has a much more definite solution. From the linear equation of bifurcation we find the definite value r and therefore the wave length L. But in a linear approximation the buckling mode which is described by the relation between r_1 and r_2 is still indefinite. In [1,2] the post-buckling behavior of the compressed plate on the elastic foundation is investigated and it is shown that the minimal elastic energy density corresponds to the case with $r_1 = r_2$. Namely we have a chessboard-like buckling mode. It is interesting to verify that in the case of the compressed half-space without a plate in the post-buckling state the energy also be minimized for $r_1 = r_2$.

In all these problems, especially in the cases without a plate, the initial critical strains are large enough. They may be of the order of 0.1–0.3. In [1,5] the influence of the pre-buckling strains on the critical stresses and on the buckling modes is investigated and the non-linear approach is used. It is established that neglect of the preliminary deformations districts essentially the critical stresses as for volume so for surface loss of stability. Only in the case of strong anisotropy with small preliminary deformations the difference between the linear and the non-linear approach is inessential.

2 Pre-buckling state and its bifurcation

Let the elastic potential energy density for an orthotropic material be

$$U = \frac{1}{2}\sum_{i,j=1}^{3} E_{ij}\varepsilon_{ii}\varepsilon_{jj} + \sum_{i\neq j} G_{ij}\varepsilon_{ij}^2, \tag{2.1}$$

where Cauchy–Green deformations ε_{ij} are equal

$$\varepsilon_{ij} = \frac{1}{2}\left(\frac{\partial u_i}{\partial x_j} + \frac{\partial u_j}{\partial x_i} + \sum_{k=1}^{3}\frac{\partial u_k}{\partial x_i}\frac{\partial u_k}{\partial x_j}\right), \tag{2.2}$$

and u_i are the projections of displacements, E_{ij}, G_{ij} are the elastic modules. For a transversely isotropic material the following restrictions are valid

$$E_{11} = E_{22} = E_{12} + 2G_{12}, \quad E_{13} = E_{23}, \quad G_{13} = G_{23}. \tag{2.3}$$

We study the homogeneous plane pre-buckling state in the non-linear approach described by the relations

$$e_i = \frac{\partial u_i^0}{\partial x_i}, \quad \varepsilon_{ii}^0 = e_i + \frac{1}{2}e_i^2, \quad \sigma_i^0 = \sum_{k=1}^{3} E_{ik}\varepsilon_{kk}^0, \quad i = 1,2,3, \tag{2.4}$$

where u_i^0 are the pre-buckling displacements, and assume that

$$\begin{aligned} &e_1 = e_2 = -e, \qquad \sigma_3^0 = 0, \qquad \varepsilon_{11}^0 = \varepsilon_{22}^0 = -e + \frac{e^2}{2}, \qquad \varepsilon_{ij}^0 = 0, \quad i \neq j, \\ &\sigma_1^0 = \sigma_2^0 = \sigma^0 = \left(E_{11} + E_{12} - \frac{2E_{13}^2}{E_{33}}\right)\varepsilon_{11}^0, \qquad e_3 = \sqrt{1 - \frac{4E_{13}}{E_{33}}\varepsilon_{11}^0} - 1. \end{aligned} \tag{2.5}$$

We introduce small perturbations v_i of the pre-buckling state by relations

$$u_i = u_i^0 + l_i v_i, \quad l_i = 1 + e_i. \tag{2.6}$$

Then we get deformations

$$\varepsilon_{ij} = \varepsilon_{ij}^0 + \frac{1}{2}\left(l_i^2\frac{\partial v_i}{\partial x_j} + l_j^2\frac{\partial v_j}{\partial x_i} + \frac{1}{2}\sum_{k=1}^{3} l_k^2\frac{\partial v_k}{\partial x_i}\frac{\partial v_k}{\partial x_j}\right) \tag{2.7}$$

and expand the potential (2.1) by the powers of v_i

$$U = U_0 + U_1 + U_2 + O(v_i^3), \quad U_1 = A_{ik}\frac{\partial v_i}{\partial x_k}, \quad U_2 = A_{ikjn}\frac{\partial v_i}{\partial x_k}\frac{\partial v_j}{\partial x_n}, \tag{2.8}$$

where A_{ik} and A_{ikjn} are the constant coefficients (the summation in the repeated indexes is supposed). The variation of the functional U_2 after integration by parts leads to the equations of equilibrium bifurcation

$$\begin{aligned} M_k(\mathbf{v}) = (E_{kk}l_k^2+\sigma_k^0)\frac{\partial^2 v_k}{\partial x_k^2}+ \\ +\sum_{i\neq k}\left(G_{ki}l_k^2+\sigma_i^0)\frac{\partial^2 v_k}{\partial x_i^2}+(E_{ki}+G_{ki})l_i^2\frac{\partial^2 v_i}{\partial x_k \partial x_i}\right)= 0, \quad k=1,2,3. \end{aligned} \tag{2.9}$$

In the non-linear approach the multipliers l_j take the pre-buckling deformations into account. In the linear approach we put $l_j = 1$ and system (2.9) coincides with the system investigated in [2-4] where the pre-buckling strains and stresses are found in a linear approximation.

Remark 1. System (2.9) may be used also in the case when assumptions (2.5) are not accepted.

The condition of volume instability is that system (2.9) does not have any non-zero bounded solutions.

The condition of the surface instability of the half-space $x_3 \leq 0$ is that system (2.9) does not have any non-zero bounded solutions satisfying boundary conditions $\sigma_{i3} = 0$ on the free surface $x_3 = z = 0$.

Remark 2. Let us study the equations of small waves propagation

$$M_k(\mathbf{v}) - \rho_k\frac{\partial^2 v_k}{\partial t^2} = 0, \quad k = 1,2,3, \tag{2.10}$$

where $M_k(\mathbf{v})$ are the same as in (2.9). Then the condition of volume stability coincides with the condition that system (2.10) is a hyperbolic one. The condition of surface stability coincides with the condition of the Raileigh waves presence on the surface $x_3 = 0$.

We seek solutions of system (2.9) as a double periodic functions of the horizontal co-ordinates x_1, x_2

$$\begin{aligned} &v_1(x_1,x_2,z) = v_1(z)\cos(r_1x_1)\sin(r_2x_2), \\ &v_2(x_1,x_2,z) = v_2(z)\sin(r_1x_1)\cos(r_2x_2), \\ &w(x_1,x_2,z) = w(z)\sin(r_1x_1)\sin(r_2x_2), \qquad w = v_3. \end{aligned} \tag{2.11}$$

As in [5] it is possible to simplify system (2.9). We introduce the auxiliary unknown functions

$$U = (r_1v_1 + r_2v_2)/r, \quad V = (r_2v_1 - r_1v_2)/r, \qquad r^2 = r_1^2 + r_2^2. \tag{2.12}$$

Then system (2.9) divides into two parts

$$\left(G_{13}l^2V'\right)' - r^2(G_{12}l^2+\sigma^0)V = 0, \qquad l = l_1 + l_2, \quad (\,)' = \frac{d(\,)}{dz}; \tag{2.13}$$

$$\begin{aligned} &\left(G_{13}l^2U'\right)' - (E_{11}l^2+\sigma^0)r^2U + (G_{13}l_3rw)' + E_{13}l_3rw' = 0, \\ &-\left(rE_{13}l^2U\right)' - G_{13}l^2U' + \left(E_{33}l_3^2w'\right)' - r^2(G_{13}l_3^2+\sigma^0)w = 0. \end{aligned} \tag{2.14}$$

Equation (2.13) describes the rotation deformations with displacements in the plane of isotropy Ox_1x_2, and system (2.14) describes deformations with displacements in three directions. We refer to the corresponding buckling modes as to the modes of the kind 1 and of the kind 2.

3 Volume stability of a homogeneous material

In this case the elastic modules are constant, and we seek solutions of equations (2.13) and (2.14) in the form

$$\{V, U, w\}(z) = \{V_0, U_0, w_0\}e^{ir_3 z}, \quad i = \sqrt{-1}. \tag{3.1}$$

According to the Hadamard criterion [1] the instability condition is the existence of non-zero solutions of these equations for real r_3.

For equation (2.13) the instability has place at $G_{12}l^2 + \sigma^0 < 0$ or at

$$e > e_n^{(1)} = 1 - \sqrt{1 - \frac{G_{12}E_{33}}{E_{11}E_{33} - E_{13}^2}}, \tag{3.2}$$

and for system (2.14) the instability has place at $G_{13}l_3^2 + \sigma^0 < 0$ or at

$$e > e_n^{(2)} = 1 - \sqrt{1 - \frac{2G_{13}E_{33}}{(E_{11} + E_{12})E_{33} - 2E_{13}(G_{13} + 2E_{13})}}, \tag{3.3}$$

where through $e_n^{(1)}$ and $e_n^{(2)}$ the critical initial compressions are denoted.

It is easy to see that the critical compressions in (3.2) and (3.3) do not depend on the wave numbers r_1, r_2, r_3, which remain indefinite.

For example, as in [5] we choose the elastic modules E_{ij}, G_{ij} for a transversely isotropic material in the following way. We study a multi-layered body with alternating soft and hard elastic isotropic plane layers with parameters

$$E_n,\ \nu_n,\ h_n, \quad n = 1, 2, \tag{3.4}$$

where $E_n,\ \nu_n,\ h_n$ are the Young modules, the Poisson ratios and thicknesses respectively. Averaging the elastic properties in the thickness directions at $h_1,\ h_2 \to 0, \quad h_1/h_2 = const$ leads to the transversely isotropic material. To calculate its modules we use the fact that the strains $\varepsilon_{11},\ \varepsilon_{12},\ \varepsilon_{22}$ and the stresses $\sigma_{13},\ \sigma_{23},\ \sigma_{33}$ at the layers boundaries are continuous. The general case is studied in [5] and here we take a partial case, in which $\nu_1 = \nu_2 = \nu,\ h_1 = h_2$, and the relation $\eta = E_2/E_1$ is the measure of anisotropy. We get

$$\begin{aligned}
&\frac{E_{11}}{E_1} = \frac{(1+\eta^2)(1-2\nu) + 2\eta((1-\nu)^2 + \nu^2)}{2(1+\eta)(1-\nu^2)(1-2\nu)}, \quad \frac{E_{12}}{E_1} = \frac{(1+\eta^2)\nu(1-2\nu) + 2\eta\nu}{2(1+\eta)(1-\nu^2)(1-2\nu)},\\
&\frac{E_{13}}{E_1} = \frac{2\eta\nu}{(1+\eta)(1+\nu)(1-2\nu)}, \quad \frac{E_{33}}{E_1} = \frac{2\eta(1-\nu)}{(1+\eta)(1+\nu)(1-2\nu)},\\
&\frac{G_{12}}{E_1} = \frac{1+\eta}{4(1+\nu)}, \quad \frac{G_{13}}{E_1} = \frac{\eta}{(1+\eta)(1+\nu)}.
\end{aligned} \tag{3.5}$$

For the isotropic material we get $\eta = 1$ and

$$\begin{aligned}
&E_{33} = E_{11} = \frac{E_1(1-\nu)}{(1+\nu)(1-2\nu)}, \quad E_{13} = E_{12} = \frac{E_1\nu}{(1+\nu)(1-2\nu)},\\
&G_{13} = G_{12} = \frac{E_1}{2(1+\nu)}.
\end{aligned} \tag{3.6}$$

For modules (3.5) relations (3.2) and (3.3) can be rewritten respectively

$$e^{(1)} = 1 - \sqrt{\frac{1+\nu}{2}}, \qquad e^{(2)} = 1 - \sqrt{\frac{(1-\eta)^2(1+\nu)}{(1+\eta^2)(1+\nu) + \eta(2-6\nu)}}. \tag{3.7}$$

In Fig. 2 for $\nu = 0.3$ the dependences of the critical compressions $e^{(1)}(\eta)$ and $e^{(2)}(\eta)$ on the measure of anisotropy η are given. The value $e^{(1)}$ does not depend on η and for $\nu = 0.3$ we get $e_l^{(1)} = 0.269$. The curves $e^{(1)}$ and $e^{(2)}(\eta)$ cross at $\eta_* = 0.172$. The boundaries of the stability domain in the plane (η, e) are shown in Fig. 2. Therefore for the isotropic material ($\eta = 1$) and for a comparatively small anisotropy ($1 > \eta > \eta_*$) for the volume loss of stability the buckling mode of the kind 1 has place and for a larger anisotropy with $\eta < \eta_*$ the mode of the kind 2 appears.

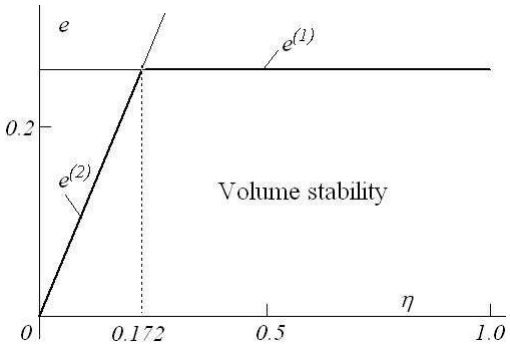


Fig. 2. Dependences $e^{(1)}(\eta)$ and $e^{(2)}(\eta)$, at $\nu = 0.3$.

4 Volume stability of a heterogeneous material

In this case the elastic modules E_{ij} and G_{ij} are functions on z, and therefore $e^{(1)}$ and $e^{(2)}$ are functions on z. Using relations (3.5) we assume that parameters η and ν are functions on z.

Firstly we assume that all these functions on z are continuous and smooth enough and study the volume buckling mode of the kind 1. The critical compression is to be found from the boundary value problem consisting of equation (2.13) and the decreasing conditions

$$\left(G_{13}l^2V'\right)' - r^2(G_{12}l^2 + \sigma^0)V = 0, \qquad V(z) \to 0 \quad \text{at} \quad z \to \pm\infty. \tag{4.1}$$

Let function $e^{(1)}(z)$ defined by (3.2) have a minimum $e^{(1)}_*$ at $z = z_*$ and

$$(e^{(1)})''(z_*) = a_1 > 0. \tag{4.2}$$

Then by using the WBK approximation [9] for $r \gg 1$ we establish that the problem (4.1) has a sequence of solutions localized near the weakest plane $z = z_*$. The solution with the minimal eigenvalue $e^{(1)}$ has asymptotic expansions at $r \to \infty$

$$V(z) = \exp\{-b_1(z - z_*)^2\}\left(1 + O(r^{-1/2})\right), \qquad e^{(1)} = e^{(1)}_* + c_1 r^{-1} + O\left(r^{-2}\right) \tag{4.3}$$

with

$$b_1 = \frac{1}{2}\sqrt{\frac{a_1 f_e}{g_1}}, \qquad c_1 = \frac{1}{2}\sqrt{\frac{a_1 g_1}{f_e}}, \qquad f(e,z) = -\sigma^0 - l^2 G_{12},$$

$$f_e = \frac{\partial f}{\partial e}, \quad g_1 = l^2 G_{13} \quad \text{at} \quad e^{(1)} = e^{(1)}_*,\ z = z_*.$$

Now we study an example and use relations (3.5). The value $e^{(1)}$ (see (3.7)) depends only on ν, and we take

$$\nu(z) = \begin{cases} \nu_1, & |z| > z_1, \\ \nu_1 + (\nu_0 - \nu_1)(1 - (z/z_0)^2), & |z| \le z_1, \end{cases} \qquad \nu_0 > \nu_1, \quad \eta(z) = \eta_0. \tag{4.4}$$

The weakest plane is $z_* = 0$ and the coefficients in relations (4.3) are

$$e^{(1)}_* = 1 - \sqrt{\frac{1+\nu_0}{2}}, \quad a_1 = \frac{\nu_0 - \nu_1}{z_0^2\sqrt{2(1+\nu_0)}}, \quad f_e = \frac{1+\eta_0}{1-\nu_0^2}\sqrt{\frac{1+\nu_0}{8}}. \quad g_1 = \frac{\eta_0}{2(1+\eta_0)}, \tag{4.5}$$

and the critical compression is equal

$$e^{(1)}_{as} = 1 - \sqrt{\frac{1+\nu_0}{2}} + \frac{\sqrt{\eta_0(\nu_0 - \nu_1)(1-\nu_0)}}{2rz_1(1+\eta_0)} + O\left((rz_1)^{-2}\right). \tag{4.6}$$

For numerical illustration we take $\nu_0 = 0.4,\ \nu_1 = 0.2,\ \eta_0 = 0.5$. Then $e^{(1)}_* = 0.16334$. In Table 1 for some values rz_1 the asymptotic values $e^{(1)}_{as}$ are compared to the values $e^{(1)}_{num}$ obtained by the numerical solution of the problem (4.1).

Table 1. Comparison of the asymptotic and numerical values of the critical compression for the kind 1 of the volume loss of stability.

$rz_1 =$	5	10	20	50
$e_{as}^{(1)} =$	0.17968	0.17154	0.16743	0.16498
$e_{num}^{(1)} =$	0.176967	0.17150	0.16742	0.16498

Both values $e_{as}^{(1)}$ and $e_{num}^{(1)}$ go to $e_*^{(1)}$ at $rz_1 \to \infty$.

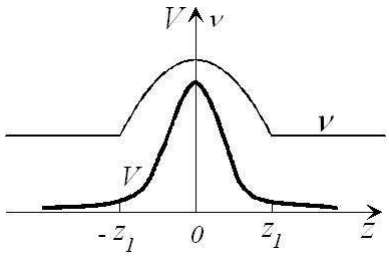


Fig. 3. Dependences $\nu(z)$ and $V(z)$.

The function (4.4) $\nu(z)$ and the localized eigen function $V(z)$ are shown in Fig. 3.

5 Localized buckling modes for the kind 2 of the volume loss of stability

In the similar way as in Section 4 we assume that

$$e_*^{(2)} = \min_z\{e^{(2)}(z)\} = e^{(2)}(z_*), \qquad (e^{(2)})''(z_*) = a_2 > 0. \tag{5.1}$$

The corresponding boundary value problem consists of system (2.14) and of the decreasing conditions

$$\begin{aligned} &\left(G_{13}l^2U'\right)' - (E_{11}l^2 + \sigma^0)r^2U + (G_{13}l_3rw)' + E_{13}l_3rw' = 0,\\ &-\left(rE_{13}l^2U\right)' - G_{13}l^2U' + \left(E_{33}l_3^2w'\right)' - r^2(G_{13}l_3^2 + \sigma^0)w = 0,\\ &U(z), w(z) \to 0 \quad \text{at} \quad z \to \pm\infty. \end{aligned} \tag{5.2}$$

The WBK asymptotic localized solution of this problem at $r \to \infty$ is

$$\begin{aligned} &w(z) = \exp\{-b_2(z - z_*)^2\}\left(1 + O(r^{-1/2})\right),\\ &U(z) = d_2(z - z_*)\exp\{-b_2(z - z_*)^2\}\left(1 + O(r^{-1/2})\right),\\ &e_{as}^{(2)} = e_*^{(2)} + c_2r^{-1} + O\left(r^{-2}\right) \end{aligned} \tag{5.3}$$

with

$$b_2 = \frac{1}{2}\sqrt{\frac{a_2f_e}{g_2}}, \qquad c_2 = \frac{1}{2}\sqrt{\frac{a_2g_2}{f_e}}, \qquad f(e,z) = -\sigma^0 - l_3^2G_{13},$$

$$f_e = \frac{\partial f}{\partial e}, \quad g_2 = l_3^2E_{33} - \frac{(E_{13} + G_{13})^2l^2l_3^2}{E_{11}l^2 + \sigma^0} \quad \text{at} \quad e^{(1)} = e_*^{(1)},\ z = z_*.$$

Let us use relations (3.5). Then the value $e^{(2)}$ (see (3.7)) depends on both parameters η and ν and we take, for example,

$$\eta(z) = \begin{cases} \eta_1, & |z| > z_1,\\ \eta_1 + (\eta_0 - \eta_1)(1 - (z/z_0)^2), & |z| \le z_1, \end{cases} \qquad \eta_0 < \eta_1, \quad \nu(z) = \nu_0. \tag{5.4}$$

For values $\eta_1 = 0.15,\ \eta_0 = 0.1,\ \nu = 0.3$ we get $e_*^{(2)} = 0.1112$.

We intend to fulfill some numerical experiments. For this aim we re-write system (5.2) in the form

$$\sigma' = (E_{11}l^2 + \sigma^0)r^2U - E_{13}l_3^2 rw', \quad \sigma'_{33} = G_{13}l^2 rU' + (G_{13}l_3^2 + \sigma^0)r^2 w,$$
$$U' = \frac{\sigma - G_{13}l_3^2 rw}{G_{13}l^2}, \qquad w' = \frac{\sigma_{33} + E_{13}l^2 rU}{E_{33}l_3^2}. \tag{5.5}$$

The convenience of this form is that it is possible to use this system for a numerical solution in the case of the piecewise elastic modules. All the unknowns $\sigma, \sigma_{33}, U, w$ are to be continuous.

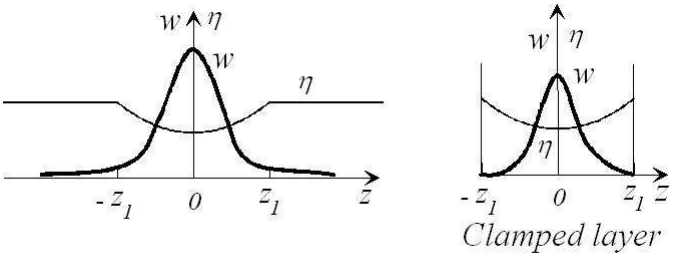


Fig. 4. Function $\eta(z)$ and the eigen function $w(z)$ for the entire space (left) and for the bounded layer.

In the left side of Fig. 4 function (5.4) $\eta(z)$ and the localized solution of system (5.5) are shown. To illustrate the localization we solve numerically the same problem for a bounded layer $|z| \le z_1$ with the boundary conditions

$$U(z) = w(z) = 0 \quad \text{at} \quad z = \pm z_1. \tag{5.6}$$

We denote the critical compression of the last problem as $e_{cl}^{(2)}$.

Table 2. Comparison of the critical compressions for two problems in Fig.4.

$rz_1 =$	5	10	20	30
$e^{(2)} =$	0.1415	0.1271	0.1189	0.1163
$e_{cl}^{(2)} =$	0.1685	0.1291	0.1190	0.1163

In Table 2 comparison of the critical compressions for two problems shown in Fig.4 is presented. It is easy to see that the critical compressions $e^{(2)}$ and $e_{cl}^{(2)}$ become closer for the larger rz_1, and they go to $e_*^{(2)}$ at $rz_1 \to \infty$.

For a homogeneous media the critical compressions $e^{(1)}$ and $e^{(2)}$ do not depend on r (see (3.7)). In contrary to a heterogeneous media they depend on r and decrease with the increase of r (see (4.3) and (5.3)). Therefore we get the smallest critical compression, if the value r is as large as possible or if the wave length $L = 2\pi/r$ is as small as possible. By using the accepted here approach we cannot find the value L. But for the multi-layered media it is possible to estimate the value L.

6 Kind 2 of the buckling modes for a multi-layered heterogeneous media

We study the volume stability loss of the elastic layer $-z_1 \le z \le z_1$. This layer consists of $N = 2n + 1$ layers with identical thicknesses $h = 2z_1/N$ and with various elastic modules (3.5) in which $\nu =$const. For hard layers with numbers $i = 2, 4, \ldots, 2n$ we take $\eta^{(i)} = 1$, and for soft layers with $i = 1, 3, \ldots, N$ we take $\eta^{(i)} = \eta(z^{(i)})$, $z^{(i)} = h(i - 0.5)$ where function $\eta(z)$ is defined by relation (5.4). The dependence $\eta(z)$ is shown in Fig. 5.

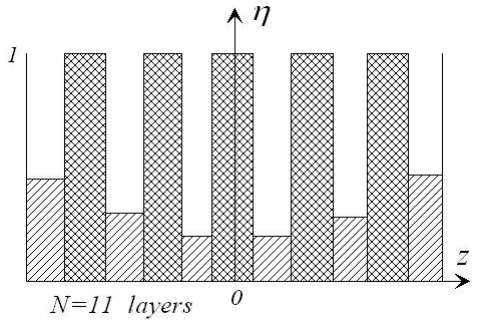


Fig. 5. Dependence $\eta(z)$

We establish that there exists

$$\min_r e^{(2)}(r,N) = e_*^{(2)}(N) \quad \text{at} \quad r = r_*(N). \tag{6.1}$$

Function $e^{(2)}(r,N)$ for fixed N is shown in the left side of Fig. 6. Function $e_*^{(2)}(N)$ decreases and function $r_*(N)$ increases. These functions are shown in the right side of Fig. 6.

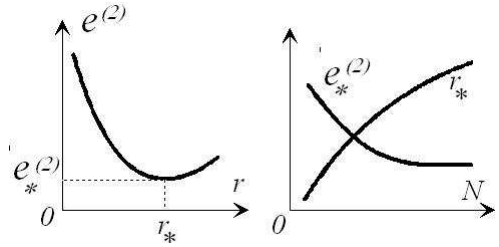


Fig. 5. Functions $e^{(2)}(r,N)$, $e_*^{(2)}(N)$, and $r_*(N)$.

For the numerical example we take in (5.4) $\eta_0 = 0.02$, $\eta_1 = 0.5$ and $\nu = 0.3$. At first we take $N = 11$ and calculate function $e^{(2)}(r,N)$. This function has minimum $e^{(2)}(r,N) = 0.106$ at $r_*(N) = 3.8$. Some values of this function are given in Table 3.

Table 3. Function $e^{(2)}(r,N)$ for $N = 11$.

$rz_1 =$	2	3	3.8	5	7
$e^{(2)}(r,N) =$	0.136	0.109	0.106	0.110	0.124

Values of functions $e_*^{(2)}(N)$ and $r_*(N)$ for various values N are presented in Table 4. These results support the right side of Fig. 6.

Table 4. Functions $e_*^{(2)}(N)$ and $r_*(N)$ for various N.

$N =$	11	21	51	101	201	501	1001
$r_*z_1 =$	3.8	7.6	13.5	20.4	31.3	55	87
$e_*^{(2)} =$	0.106	0.088	0.060	0.046	0.037	0.030	0.027

7 Surface stability

We study the stability of a transversely isotropic homogeneous half-space $x_3 \le 0$ under compression e. The same equations (2.13) and (2.14) may be used. At the free plane $x_3 = z = 0$ the boundary conditions $\sigma_{k3} = 0$ are fulfilled or

$$\frac{\partial V}{\partial z} = 0, \tag{7.1}$$

$$l^2\frac{\partial U}{\partial z}+l_3^2\Delta w=0,\qquad E_{13}l^2U+E_{33}l_3^2\frac{\partial w}{\partial z}=0. \tag{7.2}$$

At $z\to-\infty$ the decreasing conditions are fulfilled $\{V,U,w\}\to 0$.

Equation (2.13) does not have any non-zero bounded solutions satisfying condition (4.1) and decreasing condition at $z\to-\infty$.

We seek solutions of system (2.14) in the form

$$U(z)=U_0e^{r\alpha z},\quad w(z)=w_0e^{r\alpha z},\qquad Re(\alpha)>0. \tag{4.3}$$

Then system (2.14) gives

$$\begin{aligned}&(G_{13}l^2\alpha^2-E_{11}l^2-\sigma^0)U_0-(E_{13}+G_{13})l_3^2\alpha w_0=0,\\&(E_{13}+G_{13})l^2\alpha U_0+(E_{33}l_3^2\alpha^2-G_{13}l_3^2-\sigma^0)w_0=0,\end{aligned} \tag{7.4}$$

and the boundary conditions (7.2) may be re-written in the form

$$l^2\alpha U_0-l_3^2w_0=0,\qquad E_{13}l^2U_0+E_{33}l_3^2\alpha w_0=0. \tag{7.5}$$

The parameter α satisfies equation

$$(G_{13}\alpha^2-E_{11}-\sigma^0l^{-2})(E_{33}\alpha^2-G_{13}-\sigma^0l_3^{-2})+(E_{13}+G_{13})^2\alpha^2=0. \tag{7.6}$$

If $G_{13}l_3^2+\sigma^0>0$ equation (7.6) has two roots α_1 and α_2 with $Re(\alpha_k)>0$ and solution of system (2.14) satisfying the decreasing conditions at $z\to-\infty$ is

$$w=\sum_{k=1,2}C_ke^{r\alpha_kz},\quad U=\sum_{k=1,2}C_kb_ke^{r\alpha_kz},\qquad b_k=\frac{G_{13}l_3^2+\sigma^0-E_{33}l_3^2\alpha_k^2}{(E_{13}+G_{13})l^2\alpha_k}. \tag{7.7}$$

The arbitrary constants C_k may be found from boundary conditions (7.5). As a result we get the equation for critical stress σ^0 or for the initial critical compression $e^{(s)}$

$$\frac{E_{13}l^2b_1+E_{33}l_3^2\alpha_1}{l^2\alpha_1b_1-l_3^2}=\frac{E_{13}l^2b_2+E_{33}l_3^2\alpha_2}{l^2\alpha_2b_2-l_3^2}. \tag{7.8}$$

We can see that equation (7.8) does not contain the wave numbers r_1,r_2 therefore as for the volume stability loss the buckling mode is indefinite.

As an example we use again a material with elastic modules (3.5) and with $\nu=0.3$, and with various η. The critical compressions $e^{(s)}$ for the surface loss of stability as well as for the volume loss of stability $e^{(1)}$ and $e^{(2)}$ (in order to make a comparison) are given in Fig.7.

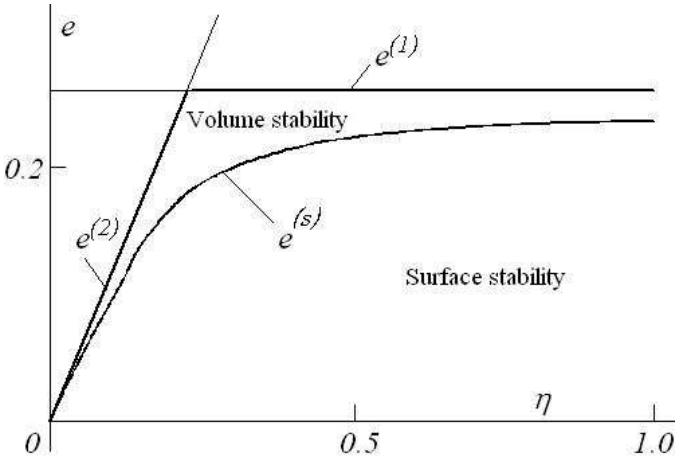


Fig. 7. Comparison of the critical compressions
for the surface ($e^{(s)}$) and for the volume ($e^{(1)}$ and $e^{(2)}$) stability.

According to the general variation principle (in the presence of the additional restrictions the eigen values are larger) the following inequality

$$e^{(s)} < \min\{e^{(1)}, e^{(2)}\} \tag{7.9}$$

is valid.

As it is seen in Fig. 2 and in Fig. 7 the critical compressions are large enough that is why in this paper the nonlinear pre-buckling strains are taken. In [2] the linear approach ($l = l_3 = 1$ in all the relations) is used. In [5] the comparison of a non-linear and of the linear approach is fulfilled and some results are given in Table 5. In columns 2 and 3 the critical compressions for the non-linear approach and in columns 4 and 5 the corresponding values for the linear approach are given.

Table 5. The critical compressions for the surface and for volume stability.

1	2	3	4	5
η	$e^{(s)}$	$\min\{e^{(1)}, e^{(2)}\}$	$e_l^{(s)}$	$\min\{e_l^{(1)}, e_l^{(2)}\}$
1.0	0.230	0.269	0.245	0.194
0.5	0.224	0.269	0.222	0.194
0.2	0.176	0.269	0.144	0.150
0.1	0.105	0.111	0.087	0.089
0.05	0.0539	0.0548	0.0484	0.0488
0.02	0.0216	0.0217	0.0206	0.0207

From Table 5 it follows that for the linear approach the inequality (7.9) is sometimes disturbed. Only for a great level of anisotropy (for $\eta \ll 1$) the difference between the linear and the non-linear approach is small.

8 Interface stability loss

The problem of the stability near the interface between two half-spaces is very close to the problem of the surface stability. We study two compressed homogeneous transversely isotropic elastic half-spaces $z \le 0$ and $z \ge 0$ (see Fig. 8).

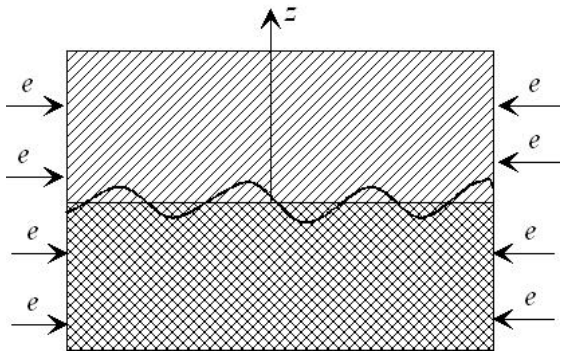


Fig. 8. The interface stability loss.

Let the indexes (d) and (u) correspond to the "down" and "up" half-spaces. According to the variation principle the interface critical compression $e^{(i)}$ lies between the minimal surface critical compression and the minimal volume critical compression, namely it satisfies the inequality

$$\min\{e^{(sd)}, e^{(su)}\} < e^{(i)} < \min\{e_l^{(1d)}, e_l^{(2d)}, e_l^{(1u)}, e_l^{(2u)}\}. \tag{8.1}$$

To find $e^{(i)}$ the same equations (2.13) and (2.14) may be used but only system (2.14) describes

the interface stability loss. Solutions (7.7) for the "down" and "up" half-spaces are

$$\begin{aligned} w^{(d)} &= \sum_{k=1,2} C_k^{(d)} e^{r\alpha_k^{(d)} z}, \quad U^{(d)} = \sum_{k=1,2} C_k^{(d)} b_k^{(d)} e^{r\alpha_k^{(d)} z}, \\ w^{(u)} &= \sum_{k=1,2} C_k^{(u)} e^{r\alpha_k^{(u)} z}, \quad U^{(u)} = \sum_{k=1,2} C_k^{(u)} b_k^{(u)} e^{r\alpha_k^{(d)} z}. \end{aligned} \tag{8.2}$$

Here $\alpha_k^{(d)}$ and $\alpha_k^{(u)}$ satisfy the equation (7.6) in which elastic modules E_{ij}, G_{ij} are changed by $E_{ij}^{(d)}, G_{ij}^{(d)}$ and $E_{ij}^{(d)}, G_{ij}^{(d)}$. The same substitution is made while calculating the values $b_k^{(d)}$ and $b_k^{(u)}$ from relation (7.7). Conditions $\mathrm{Re}(\alpha_k^{(d)}) > 0$ and $\mathrm{Re}(\alpha_k^{(u)}) < 0$ give the decreasing conditions at $z \to \pm\infty$.

We assume that there is a full contact at the plane $z = 0$. The arbitrary constants $C_k^{(d)}$ and $C_k^{(u)}$ are to be found from the conditions that the displacements and the stresses are continuous at $z = 0$

$$\begin{aligned} &U^{(d)} = U^{(u)}, \qquad G_{13}^{(d)} \left(l^2 \left(U^{(d)} \right)' - r l_3^2 w^{(d)} \right) = G_{13}^{(u)} \left(l^2 \left(U^{(u)} \right)' - r l_3^2 w^{(u)} \right), \\ &w^{(d)} = w^{(u)}, \qquad r E_{13}^{(d)} l^2 U^{(d)} + E_{33}^{(d)} l_3^2 \left(w^{(d)} \right)' = r E_{13}^{(u)} l^2 U^{(u)} + E_{33}^{(u)} l_3^2 \left(w^{(u)} \right)'. \end{aligned} \tag{8.3}$$

Equating to zero the determinant of system (8.3) we obtain the equation for the critical interface compression $e^{(i)}$. As in the problems for a homogeneous material the value $e^{(i)}$ does not depend on the wave numbers r_1 and r_2.

9 Stability of a compressed plate on an elastic foundation

The main interest of this problem for us is that on the contrary to the previously discussed problems all the parameters of the buckling modes may be found. Here only an approximate solution is constructed.

We study stability of an infinite compressed plate of thickness h lying on the elastic foundation (see Fig. 1). For simplicity we assume that as the plate so the foundation are made of an isotropic material with the Young modules E, E_0 and the Poisson ratios ν, ν_0 where index 0 is used for the foundation. The homogeneous initial horizontal compression e of a plate is given.

To describe the plate's additional deformations we use the Kirchhof–Love approximation. Then the normal deflection $w(x_1, x_2)$ of the middle plane satisfies to equation [4,6]

$$D\Delta\Delta w - T\Delta w + \sigma_{33}^0 = 0, \qquad \Delta w = \frac{\partial^2 w}{\partial x_1^2} + \frac{\partial^2 w}{\partial x_2^2}. \tag{9.1}$$

Here

$$T = h\sigma_0 = -\frac{Ehe}{1-\nu}, \qquad D = \frac{Eh^3}{12(1-\nu^2)}, \tag{9.2}$$

and σ_{33}^0 is the stress between the plate and the foundation.

We seek the solution of equation (9.1) in the form

$$w(x_1, x_2) = w_0 \cos(r_1 x_1) \cos(r_2 x_2) \tag{9.3}$$

with unknown wave numbers r_1 and r_2. Then it is easy to find the stress σ_{33}^0 in assumption that between the plate and the foundation there is a full contact, and that the foundation has an infinite depth [9,10].

$$\sigma_{33}^0 = c_{33} r w_0, \qquad c_{33} = \frac{E_0(1-\nu_0)}{(1+\nu_0)(3-4\nu_0)}, \quad r = \sqrt{r_1^2 + r_2^2}. \tag{9.4}$$

Then from the equation (9.1) we find

$$e = \frac{(1-\nu)(Dr^3 + c_{33})}{Ehr}, \qquad -\sigma_0 = F_1(r) = \frac{Dr^3 + c_{33}}{hr}. \tag{9.5}$$

By minimizing e in r we find critical values e_* and r_*.

$$(r_*h)^3 = \frac{6(1-\nu^2)(1-\nu_0)}{(1+\nu_0)(3-4\nu_0)}\frac{E_0}{E}, \qquad -e_* = \frac{(1-\nu)(1-\nu_0)}{(1+\nu_0)(3-4\nu_0)}\frac{E_0}{Er_*h}. \tag{9.6}$$

The typical length of buckling waves L is equal to $L = 2\pi/r$ and Kirchhof–Love hypotheses are acceptable only if $h \ll L$ or $rh \ll 1$. To fulfill this inequality it is necessary to suppose that the foundation is soft enough ($E_0 \ll E$).

It is possible to verify exactness of the approximate relations (9.6) comparing them to the exact numerical solution. In the Table 6 some numerical results for $\nu = \nu_0 = 0.3$ are presented. In columns 2 and 3 the exact values r_*^e and e_*^e and in columns 4 and 5 the approximate values r_*^a and e_*^a found by relations (9.6) are presented. The exactness of relations (9.6) grows when the ratio E_0/E decreases.

Table 6. The comparison of the exact and the approximate critical values r_* and e_*.

1	2	3	4	5
E_0/E	$r_*^e h$	e_*^e	$r_*^a h$	e_*^a
0.3	1.449	0.1837	0.990	0.1897
0.1	0.787	0.0963	0.687	0.0912
0.03	0.485	0.0434	0.461	0.0409
0.01	0.327	0.0206	0.319	0.0197

Therefore the length of waves L is found but from the bifurcation equation (9.1) the buckling mode depending on the relation between the wave numbers r_1 and r_2 remains indefinite.

10 Post-critical behavior of a plate on an elastic foundation

To find the relation between r_1 and r_2 we study approximately the initial post-critical behavior of a plate. We calculate the elastic energy density using non-linear expressions for strains in the plate with Kirchhof–Love hypotheses and linear expressions for strains in the foundation.

The elastic energy density of plate U_p is equal to

$$U_p = \frac{E}{2L_1L_2}\int_0^{L_1} dx_1 \int_0^{L_2} dx_2 \int_{-h/2}^{h/2} \left(\varepsilon_{11}^2 + 2\nu\varepsilon_{11}\varepsilon_{22} + \varepsilon_{22}^2 + 21 - \nu\varepsilon_{12}^2\right) dz, \tag{10.1}$$

where

$$\varepsilon_{ij} = \frac{1}{2}\left(\frac{\partial u_i}{\partial x_j} + \frac{\partial u_j}{\partial x_i} - 2z\frac{\partial^2 w}{\partial x_i \partial x_j} + \frac{\partial w}{\partial x_i}\frac{\partial w}{\partial x_j}\right). \tag{10.2}$$

We take $w(x_1, x_2)$ in form (9.3) and choose the horizontal displacements $u_i(x_1, x_2)$ of the plate middle plane so that the energy U_p be minimal. Then we get [4]

$$u_i(x_1, x_2) = \frac{r_i w_0^2}{16}\sin 2r_i x_i\,(1 + \cos 2r_j x_j), \quad i, j = 1, 2, \quad i \neq j. \tag{10.3}$$

The energy density of foundation U_f is equal to

$$U_f = \frac{c_{33} r w_0^2}{8}. \tag{10.4}$$

The total energy density $U = U_p + U_f$ may be written in the form [4]

$$U = \frac{r^2 h w_0^2}{8}(F_1(r) + \sigma_0) + F_2(r_1, r_2)w_0^4, \quad F_2 = \frac{Eh(3r_1^4 + 4\nu r_1^2 r_2^2 + 3r_2^4)}{256(1-\nu^2)}, \tag{10.5}$$

where $F_1(r)$ is the same as in (9.5) and the critical initial compression σ_* is equal to $\sigma_* = -F(r_*)$.

If $|\sigma_0| < |\sigma_*|$ then the energy U is minimal at $w_0 = 0$. If $|\sigma_0| > |\sigma_*|$ then this energy is minimal at

$$w_0^2 = \frac{(\sigma_* - \sigma_0) r_*^2 h}{16 F_2}, \quad r_1 = r_2 = \frac{r_*}{\sqrt{2}}, \quad F_2 = \frac{(3+2\nu) E r_*^4}{64(1-\nu^2)}. \tag{10.6}$$

Therefore in this problem the buckling mode is a chessboard-like one.

In [7] a more complex problem than the one described here is investigated. Between the plate and the foundation there is a thin soft elastic interlayer. A more exact solution that takes into account both the vertical and the horizontal displacements of layers is constructed. The post-critical energy is given again by relation (10.5)

$$U = \frac{r^2 h w_0^2}{8}(F_1(r) + \sigma_0) + F_2(r_1, r_2) w_0^4, \tag{10.7}$$

but the functions $F_1(r)$ and $F_2(r_1, r_2)$ differ from (9.5) and (10.5). The minimum of the function $F_1(r)$ gives the critical value of the initial stress σ_* and the corresponding wave number r_*. At $F_1(r) + \sigma_0 < 0$ the function $F_2(r_1, r_2)$ gives the effect of the non-linear post-critical deformations. As for $r_1^2 + r_2^2 = r_*^2 = const$ this function is minimal at $r_1 = r_2$. Therefore the buckling mode is once again a chessboard-like one.

11 Discussion

In this paper we are limited to the linearly elastic materials and to the compressing initial stresses. The interface problems in a more general statement including extensions, plastic deformations and fractures are investigated in [8,12,13]. In [6] numerous mechanical, physical and biological problems are indicated in which the chessboard-like surface appears. In our paper it is established that the post-critical chessboard-like surface appears in the problems of the compressed plate on the soft foundation. Naturally such surface appears only if the directions Ox_1 and Ox_2 have equal properties, in particular if the initial stresses are equal to each other ($\sigma_{11}^0 = \sigma_{22}^0$). In the opposite case the post-critical surface is $w(x_1, x_2) = w_0 \cos r_1 x_1$ and it may be easily established from the linear bifurcation problem.

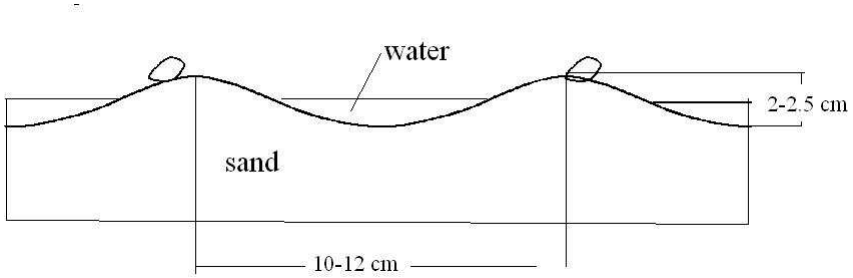


Fig. 9. A chessboard-like surface on a silk bank.

The form of the post-critical surface of the compressed homogeneous elastic half-space is unknown. It seems that this surface is also a chessboard-like one but there is no proof of the fact. To support this intention we report about a natural phenomenon which one of the authors observed on the bank of the Solovetsky island in the White sea. On a rainy day on the plane sandy bank (with clay intrusions) there was a chessboard-like surface (see Fig. 3 in which the vertical section of the surface and its dimensions are shown). A large area of the bank (50-100 meters wide) was covered with such small hills. On the top of each hill there was a small piece of sand which was pressed out of the hill (see Fig. 9). We offer the following explanation to this phenomenon. When the weather is dry the bank is flat. When the weather is rainy sand becomes wet and the horizontal compression appears leading to the loss of stability.

Acknowledgements

The paper is written with the financial support of Russian Foundation of Basic Investigations, grants 09.01.92002 HHC-a, and 10-01.00244-a.

References

[1] Ciarlet P.S. *Mathematical Elasticity.* Amsterdam etc : North-Holland; 1988.

[2] Morozov N.F., and Tovstik P.E. On the modes of the surface stability loss. *Problems of nonlinear mechanics of a deformable rigid body, conf. 2.* 2009. Kazan, pp. 270-273.

[3] Tovstik P.E. The volume and the surface stability of a transversely isotropic material under compression. *Vestnik St.Petersburg Univ. Ser. 1.* 2010. N 1.

[4] Morozov N.F., Paukshto M.V., and Tovstik P.E. Stability of the surface layer under thermal loading. *Izv. Russ. Akad. Nauk. MTT.* 1998. No. 1. pp. 130-139.

[5] Tovstik P.E. Local stability of plates and shallow shells on an elastic foundation. *Izv. Russ. Akad. Nauk. MTT.* 2005. No. 1. pp. 147-160.

[6] Tovstik P.E. Vibrations and stability of a pre-stressed plate on an elastic foundation. *Pricl. Math. Mehh.* Vol.73. No. 1. pp. 106-120; 2009.

[7] Morozov N.F., and Tovstik P.E. On the buckling modes of plate on an elastic foundation. *Izv. Russ. Akad. Nauk. MTT.* 2010 (to be published).

[8] Panin L.E., and Panin V.E. Effect of the "chessboard" and mass transfer in interfacial media of organic and inorganic nature. *Physical Nanomechanics.* 2007. Vol. 10. No. 6. pp. 5-20.

[9] Tovstik P.E., and Smirnov A.L. *Asymptotic Methods in the Buckling Theory of Elastic Shells.* World Scientific. Singpore. New Jersey. London. Hong Kong. 347 p.

[10] Il'gamov M.A., Ivanov V.A., and Gulin B.V. *Strength, Stability and Dynamics of Shells with an Elastic Filler.* Moscow: Nauka; 1977.

[11] Tovstik P.E. The reaction of a pre-stressed orthotropic foundation. *Vestnik St.Petersburg Univ. Ser. 1.* 2006. No 4. Pp. 98-108.

[12] Cherepanov G.P. The theory of thermal stresses in a thin bounding layer. *J. Appl. Phys.* Vol. 78. No. 11; 1995.

[13] Goldstein R.V., Panin V.E., Osipenko N.M., and Derevyagina L.S. Model of the formation of the fracture structure in a layer with hardened near-surface zones. *Physical Nanomechanics..* No. 6. Pp. 23-32; 2005.

Nikita F. Morozov, and Petr E. Tovstik: St.Petersburg State University. Universitetskaya str., 28. Petrodvoretz, St.Petersburg, Russia

Study of the influence of the structure of grain boundaries on their behavior under shear loading.

A. Yu. Nikonov A. I. Dmitriev
nikonov@usgroups.com

Abstract

Molecular dynamics simulation of behavior of grain boundaries in copper bicrystal under shear loading were carried out. The possibility of movement of the grain boundary in a direction perpendicular to the applied load was shown. The influence of grain boundaries structure on such behavior of boundaries was studied. The dependencies of the velocity of grain boundaries on the applied load are analysed. Estimates value of critical stress initiating the movement of the grain boundary was calculated. This behavior of grain boundaries can have a significant influence on the change of microstructure of the material and, as a result of its properties and behaviors under stress.

1 Introduction

Studying of features of behavior of grain boundaries in the loaded polycrystalline materials is the important problem of modern material science. This explains the large number of both experimental and theoretical works [1, 2, 3] devoted to the behavior of the grain boundary under external dynamic influences, including shear. At last time with increasing of computer efficiency, this question is increasingly being studied using computer simulation. Such studies allow to analyze in details various aspects of the investigated problem and to reveal the mechanisms of structural transformation of the crystal lattice in dynamics. So, the behavior of grain boundaries at the high-speed shear loading was investigated in [3]. It was shown that the atoms can move along vortex-like trajectories near the grain boundary. At the same time the motion of the boundaries in the direction perpendicular to the applied loading is observed. Estimation of the grain boundaries motion show abnormally high values (up to 600 m/s) as compared with the velocities of shear loading. At that the changing of the position of grain boundary leads to the growth of one grain due to neighboring one. Thus a redistribution of the configuration of structural defects and changing of the deformation properties of loaded material are taking place. Note that in [3] an ideal symmetrical planar grain boundary of only one type and under certain shear rate was considered. At the same time, the situation in the bulk of a polycrystal can be considerably complicated. Due to the redistribution of stress fields in the polycrystal various loading conditions arbitrarily oriented in respect to the grain boundary can be formed. Besides, the boundaries themselves are different in structure and can manifest different responses to external influence. Thus, the main aim of this paper was to study by the method of computer simulation the behavior of high-angle grain boundaries and grain boundaries with complex structures under conditions of the external shear loading.

2 The object under simulation

Calculations were made within the framework of the method of molecular dynamics based on the program LAMMPS [4] which allows to use efficiently a parallel computing. The copper polycrystal consisting of two grains and containing a planar defect of type high-angle grain boundary in the plane XoZ, as shown in Figure 1,a was selected as an object under simulation. To construct a special type of grain boundaries the algorithm proposed in [5] was used. Figure 1,b shows the

projection on the plane (001) of the bicrystal's structure received as a result of the algorithm described above. This structure corresponds to the grain boundary of type Σ=5(210)[001].

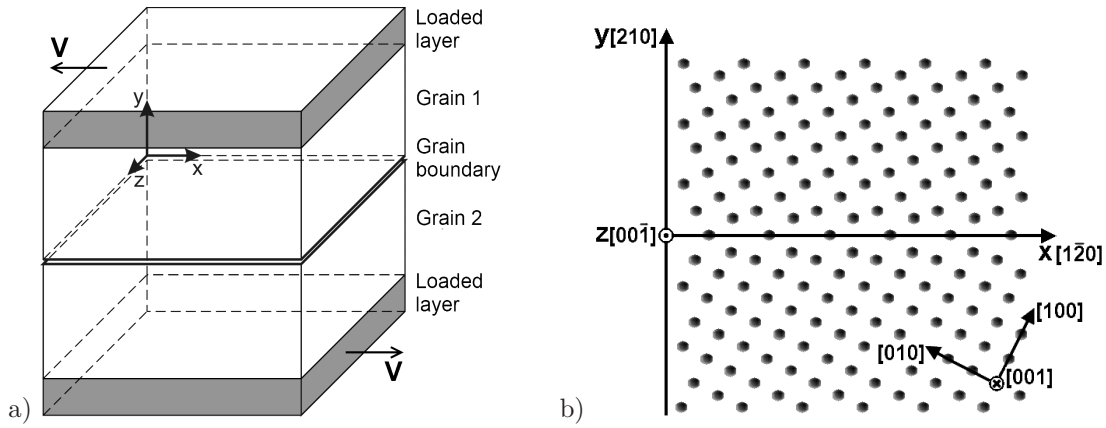


Figure 1: a) Schematic geometry of simulated grain boundary, b) The fragment of the structure of the sample with the boundary of the type Σ=5

The final configuration of the bicrystal with the grain boundary was achieved by finding the minimum energy E ($\overrightarrow{t}$) by shift of one grain relative to another. Initially the shifts in parallel directions to the plane of grain boundary, and then in perpendicular direction were simulated. Then, a standard procedure to achieve the equilibrium configuration of the atomic system by dumping of atom's velocities during the passing of the system through the minimum value of potential energy was used. The specific energy of the grain boundary calculated by this way was 0.952 J/m^2, which is 2 % different from the theoretical value [5]. In order to avoid the effects associated with the symmetry of the ideal lattice, the equilibrium bicrystal was "heated up" up to 100 K.

Loading was applied by set of constant velocities to all atoms of boundary layers, external to the modeled grain boundary. Atoms in loaded layers are moved so that their speed was directed parallel to the axis X. At that, velocities of loaded layers of different grains have been directed in opposite directions, as shown in Fig. 1,a. The thickness of each loaded layers corresponded to two cutoff radius of potential of atomic interaction, which is described in the framework of embedded atom method [6]. This choice was determined by the possibility to describe elastic and surface properties and energy parameters of the defects of the system with sufficiently high degree of accuracy. The equations of motion were integrated with time step Δt=0.001 ps. The total number of atoms was exceeded 200000. Along the plane of the grain boundary periodic boundary conditions were used. The distance between the loaded layers and grain boundary was more than 50 lattice parameters.

3 The behavior of grain boundary Σ=5 with ideal structure

In this paper, we simulated the behavior of grain boundary of a special type for the different velocities of the atoms of the boundary layer. The velocity (V) in different tasks was varied in the range from 5 to 150 m/s. According to the results of simulation the behavior of the grain boundary of a special type Σ=5(210)[001] under the shear loading essentially depends on the direction of the applied influence. So, under shear deformation along the X axis the grain boundary begins to move in a direction perpendicular to the applied loading (in our case along the axis Y), thus leading to a growth of one grain of a polycrystal.

Analysis of time dependence of grain boundary position showed the discrete nature of this motion (Fig. 2a). A detailed analysis of the structure of the boundary at different time steps allowed one to reveal a mechanism of the boundary motion in the direction perpendicular to the applied load. Fig. 2,b, c, d consistently shows the structure of atoms in a time of one such movement. Initially near the boundary the accumulation of stresses caused by shear deformation is taking place. After reaching the critical value atoms marked by dark circles, begin to move in the

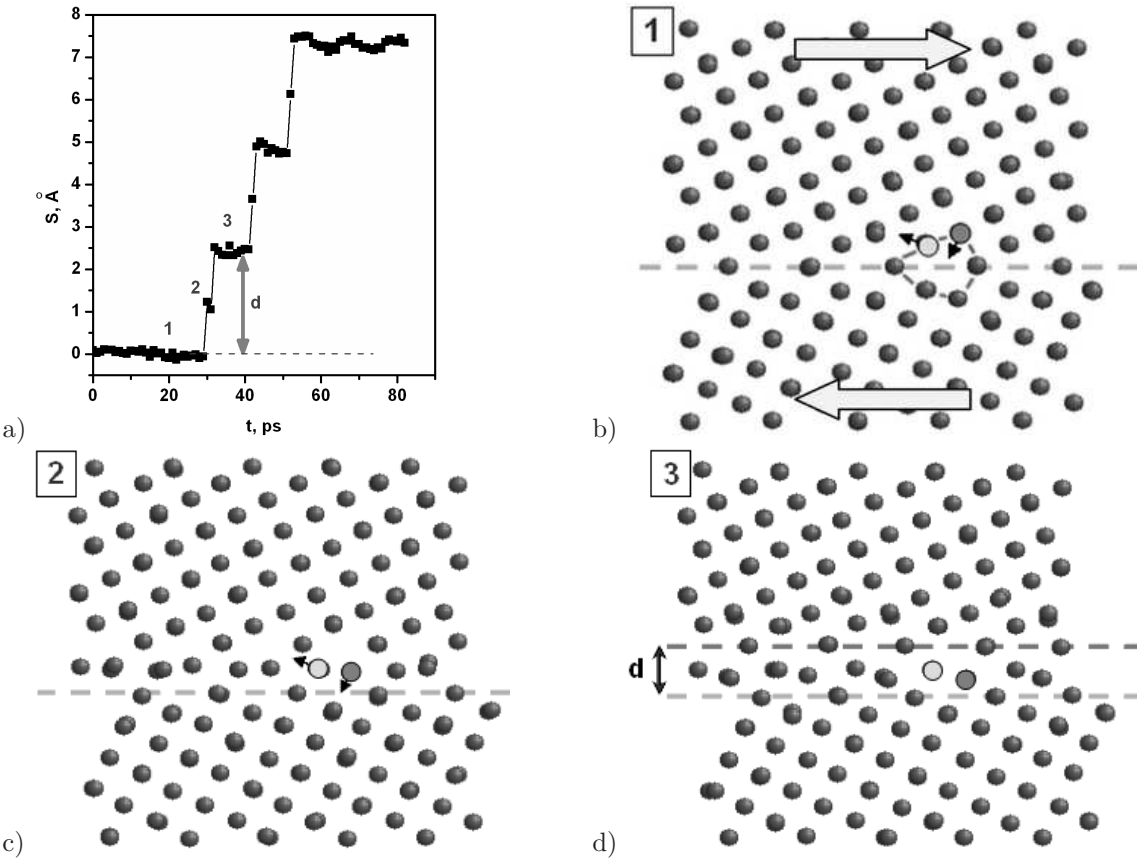


Figure 2: a) Time dependence of Y-coordinates of the grain boundaries. b), c) and d) structure of the central fragment of the simulated bicrystal at the stages of reconfiguration of atomic configuration (see 1, 2 and 3 on the time dependence).

direction of applied shear loading. At the same time they are shifting downward in the interstices of cell grain boundaries (marked by dotted line). The shift is accompanied by "extrusion" of atoms, marked by bright circle in the direction pointed with the arrow. It should be noted that "extrusion" process is facilitated co-directed action of the applied shear stress. Result of such movements is a single act of horizontal relative sliding of grains, which is accompanied by a superstructure of atomic planes of a grain (in our case, bottom). This, in turn, leads to the efficient movement of grain boundary in the perpendicular direction.

Fig. 3 depicts the trajectories of the atoms of the central fragment of the simulated bicrystal in time interval corresponding to a single motion of the boundary. It is evident that the movement takes place simultaneously across the plane of the defect. In this case the atoms in planes adjacent to the plane of the grain boundary are displaced by distances comparable with the lattice parameter, and the atoms in the plane of the defect remained approximately the same position. There is only a slight deviation from their original equilibrium position, which, after a single act of the boundary motion becomes new nodes of atomic lattice of the opposite grain. It is obviously, that the direction of perpendicular motion of grain boundary is defined by lack of symmetry of the boundary in the plane YoZ. Therefore, it is expected that the change of loading direction should lead to a change in the direction of the boundary movement, as was confirmed later by simulation results.

It was found also that at increasing the velocities of the atoms of loaded layers the grain boundary is shifted to a greater distance over the same period of time. This means an increase in the effective speed of the grain boundary movement. Time dependencies of the Y-coordinates of the grain boundary for 4 different loading rates are shown in Fig. 4,a. One can see that when the loading velocity is 10 m/s the displacement of the boundary at t=72 ps is about 2 nm, while at the loading velocity 50 m/s the displacement reaches 10 nm at the same time. Comparative analysis of position of the grain boundary at different times for different strain rates showed that the grain

boundary moves with the alternation of intervals of motion with constant speed and intervals of relative quiescence (Fig. 4,a). It is more visible at small values of shear velocity. Apparently, this alternation of motion is associated with the dynamics of loading and the features of rebuilding the crystal structure of the atomic lattice in the process of moving grain boundary. If to average obtained dependences, i.e. to take the difference of values of grain boundary displacements for the considered loading rates at the same time interval, it is possible to obtain the average values of the velocity of boundary motion as a function of the magnitude of the loading rate. On fig. 4,b such dependence is presented. According to the simulation results, for the boundary of type Σ=5 effective speed of movement of the grain boundary is proportional to the load rate with factor k=4, 59. However, the given dependence is valid only at low loading velocity (less than 100 m/s). At high-speed loading with increasing velocity of loaded layers increasing of velocity of boundary slows down and goes to a limiting value of $\approx$ 500 m/s. To all appearance this limiting value is determined by the maximum velocity of gliding dislocations involved in the formation of the grain boundaries.

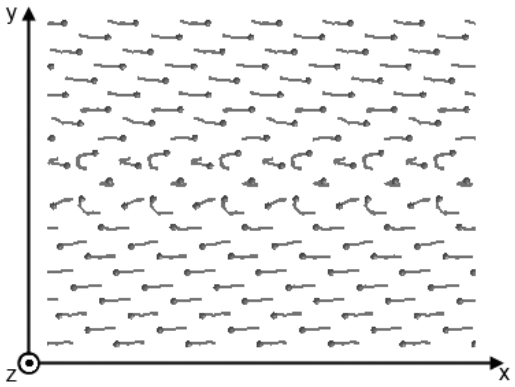
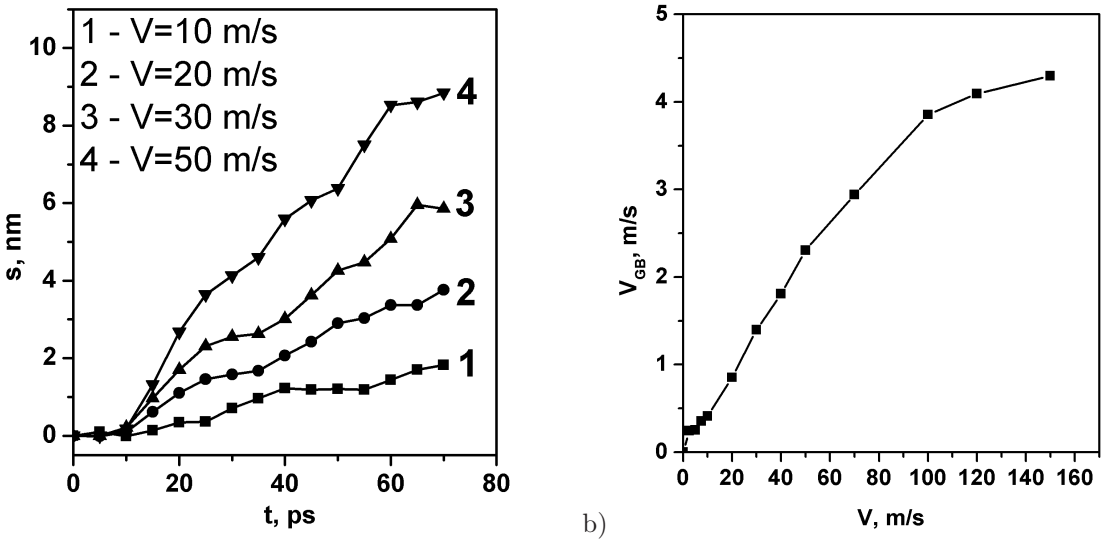


Figure 3: The trajectories of movement of atoms during the time of one transition of a boundary (65 – 72 ps)



a) b)

Figure 4: a) The time dependence of grain boundary displacement for different values of the loading velocity V b) dependence of the velocity of the grain boundary motion in direction perpendicular to the loading on the value of loading.

4 The behavior of grain boundary Σ=5 with structural defect

It is obvious that the considered symmetrical boundary with an ideal structure in real polycrystals practically nonexistent. This is explained by the influence of both the different external influences and the presence of internal defects in the structure of the atomic lattice. In the paper, a study of features of the behavior of grain boundaries of type Σ=5(210)[001], containing a step-like structural defect was carried out. For this aim the considered bicrystal was divided into two parts along a plane YoZ and one part of the sample was shifted relative to the other along the Y axis at a distance equal to |t| and 3|t| (t – translation vector in this direction). A fragment of the central area of the atomic lattice of the bicrystal obtained as a result of the shift on vector |t|, is shown in Fig. 5,a.

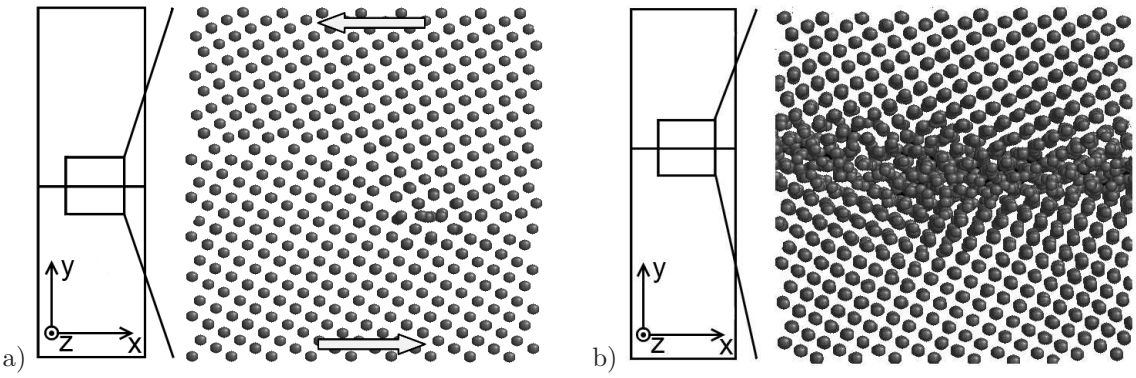


Figure 5: The structure of grain boundary with the step-like defect in height |t|:a) initial, b) after loading.

The grain boundary with the step-like structural defect was subjected to the shear loading with velocity of deformation V=20 m/s. According to the results of simulation, as in the case of a special type of grain boundaries, for the boundary with the step-like structural defect in height |t|, subjected to shear deformation motion of the grain boundary in the direction perpendicular to the applied velocity is observed. However, the presence of a defect in the structure of the boundary leads to decrease of average speed of displacement of the boundary. This is well illustrated in Figure 6, which shows the time dependence of position of the boundary with the step-like structural defect and the boundaries of a special type. According to this dependencies at deformation of 7% (t=60 ps) the difference of displacement of boundary reaches 2.4 nm.

Analysis of the atomic structure in the area near the grain boundary at different time moments showed that during the process of boundary motion its position in atomic planes parallel to XoZ can differ Constructing the projections of all atomic planes of the bicrystal on plane XoZ is manifested in increasing the width of the grain boundaries region which have violation of crystalline order (see Fig. 5,b). Initially, the process of mismatch of atomic configuration occurs at segments of step-like defect oriented perpendicular to the applied shear loading. This is manifested as “smoothing” of the angles of defect of grain boundaries. At further loading the process of mismatch covers also areas of the boundary, oriented parallel to the applied shear loading. Analysis of the structure of atomic lattices in various atomic planes arranged parallel to the plane XoZ, showed that in each plane the violations of atomic order near grain boundary does not occur. It is possible to distinguish quite clearly the structure of each of the grains as well as grain boundary. However, the shape of the boundary is not straight but has a complex shape. Fig. 7 shows the structure of fragments of two atomic planes located parallel to the plane XoZ. The position of the grain boundary in each plane is marked by line. It is seen that the shape of lines in the planes are differ. According to the simulation results, the change of position of boundary within the plane varies in the range of an order of one parameter intergrain cells.

It is obvious, that the complex form leads to an increase in the length of grain boundaries in a separate atomic plane, and the mismatch of the structure of atomic planes mean a general increase of the area of the defect. This in turn means an increase in energy of the defect, so should be a

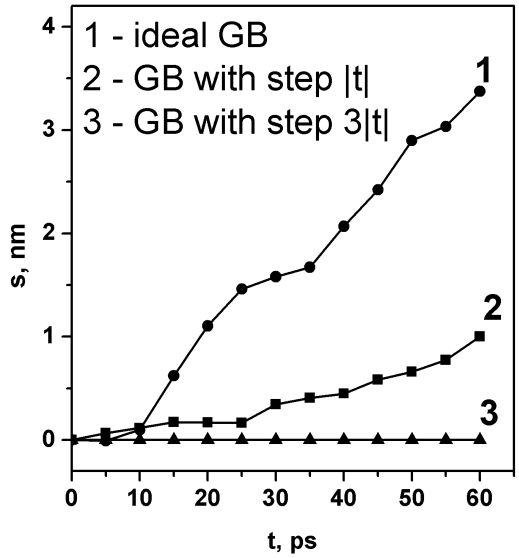


Figure 6: Time dependence of position of grain boundaries with different structure.

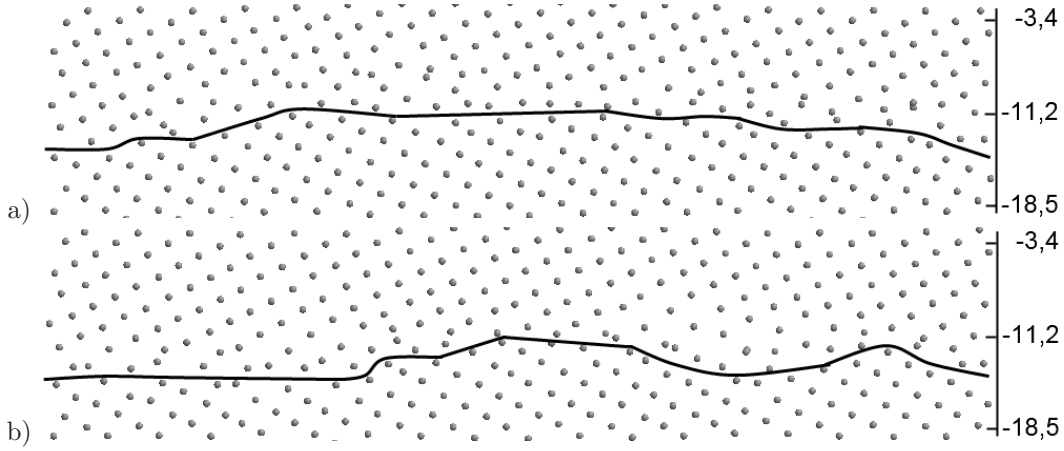


Figure 7: The structure of grain boundaries in various atomic planes parallel to the plane XoZ.

reason of the increased resistance to movement of boundary under external influence. According to this hypothesis, a further increase of energy of the defect by increasing its length should lead to immobility of grain boundary under conditions of the external shear loading. Indeed, at modeling the grain boundary with "step" height 3|t|, subjected to shear deformation, motion of the boundary in the direction perpendicular to the applied load is not observed (see Fig. 7). With increasing of strain a mismatch of segments of step-like defect oriented perpendicular to the applied shear loading is observed only, and further increasing of shear strain leads to a complete restructuring of one of the grains.

5 Conclusions

The mechanism described above of movement of grain boundaries confirms one of the existing hypotheses that the movement of grain boundaries associated with the cooperative movement of group of atoms [7]. According to the results of simulation dynamic properties of the boundary depend on the coordination of the lattice structure near the defect and the length of the border. Low temperature and the symmetry of the boundary significantly increase the mobility of boundary at other things being equal. In conclusion, we note that the observed behavior of grain boundaries can have a significant influence on the change of microstructure of the material and, as a result,

its properties and features of behaviors. The results obtained in this paper can be used for understanding the development of features of plastic deformation in polycrystals under conditions of dynamic loading.

Acknowledgements

Financial support of this research was provided under project of RFBR No 09-08-00311-a.

References

[1] Pozdnyakov V. A., Glezer A. M. Structural mechanisms of fracture of nanocrystalline materials // Physics of the Solid State, 2005, V.47, No.5, P.817–824.

[2] Gutkin M. Yu., Mikaelyan K. N., Ovid'ko I. A. Grain growth and collective migration of grain boundaries during plastic deformation of nanocrystalline materials // Physics of the Solid State, 2008, V.50, No.7, P.1261–1265.

[3] Psakhie S. G., Zolnikov K. P. Anomalously high rate of grain boundary displacement under fast shear loading // Technical Physics Letters, 1997. V.23, No.7, P.555–556.

[4] Plimpton, S.J. Fast Parallel Algorithms for Short-Range Molecular Dynamics // J. Comp. Phys., 1995, V.117, No.1, P.1–19.

[5] Suzuki A., Mishin Y. Atomistic modeling of point defects and diffusion in copper grain boundaries // Interface Sci, 2003, V.11, No.1, P.131–148.

[6] Foiles S.M. Embedded-atom and related methods for modeling metallic systems // MRS Bull, 1996, V.21, No.2, P.24–28.

[7] Gorkaya T., Molodov D.A., Gottstein G. Stress-driven migration of symmetrical ⟨100⟩ tilt grain boundaries in Al bicrystals // Acta Materialia, 2009, V.57, P.5396–5405.

Nikonov A.Yu., Akademichesky 2/4, 634021, Tomsk, Russia
Dmitriev A.I., Akademichesky 2/4, 634021, Tomsk, Russia

Mechanical system simulation via automatic differentiation

Stefan Palis Frank Palis
stefan.palis@ovgu.de

Abstract

This article deals with the application of automatic differentiation to mechanical systems calculation. Here the Hamilton formulation is used because of its structural advantages. The proposed approach permits to simulate a system by using any integration scheme by providing only its Hamiltonian.

1 Introduction

A standard approach of modeling mechanical systems is through Hamilton's Principle leading to the Euler-Lagrange equations of motion or, applying Legendre transformation, to the Hamilton equations of motion. The main structural difference is that Euler-Lagrange equations are, depending on the Lagrangian, implicit differential equations of second order, whereas Hamilton equations are explicit differential equations of first order, depending only on the partial derivatives of the Hamiltonian. These structural advantages of the Hamilton equations of motion can be used in combination with automatic differentiation to derive a numerical integration scheme using only the Hamiltonian of a system. Automatic differentiation is an algorithm calculating derivatives by exploiting the fact that any computation can be decomposed in a sequence of elementary operations, which can be differentiated separately applying the chain rule. For efficiency reason here the reverse mode of automatic differentiation is used. In this paper the combination of automatic differentiation and Hamilton equations of motion is used to simulate the load motion of a crane providing only the system's Hamiltonian, i.e. the system's energy in phase space. Using the presented method laborious and error-prone symbolic derivation of the equations of motion can be avoided.

2 Automatic differentiation

The idea of automatical derivative calculation is quite old [1] but has gained new interest [3] as computer calculation are getting more and more involved. Now there are several tools for many languages [2], [5], [4] with different abilities. Automatic differentiation is based on the application of elementary differentiation rules to elementary functions forming a function $f(x)$. In doing so the intermediate results are immediately evaluated, i.e. the result is not given in form of a symbolic expression but as a real number. Therefore in contrast to symbolic differentiation in automatic differentiation derivatives of a function $f(x)$ are evaluated only in a certain point x. There are basically two modes in automatic differentiation: forward mode and reverse mode.

2.1 Forward mode

The forward mode of automatic differentiation implements the chain rule of differentiation. Here the derivative of each elementary operation is calculated in parallel.

This can be achieved by introducing dual numbers consisting of two components:

$$z = x + \dot{x}d. \tag{1}$$

Here d distinguishes the second component of a dual number with $d^2 = 0$. Therefore elementary arithmetic on dual numbers give the following:

$$z_1 + z_2 = x_1 + x_2 + (\dot{x}_1 + \dot{x}_2)\, d, \tag{2}$$

$$z_1 z_2 = x_1 x_2 + (x_1 \dot{x}_2 + \dot{x}_1 x_2)\, d + \dot{x}_1 \dot{x}_2 d^2 = x_1 x_2 + (x_1 \dot{x}_2 + \dot{x}_1 x_2)\, d, \tag{3}$$

$$\frac{1}{z} = \frac{1}{x + \dot{x}d} \frac{x - \dot{x}d}{x - \dot{x}d} = \frac{x - \dot{x}d}{x^2 - \dot{x}^2 d^2} = \frac{1}{x} - \frac{\dot{x}}{x^2} d. \tag{4}$$

In addition to that elementary functions on dual numbers can be assigned:

$$\sin(z) = \sin(x) + \cos(x)\dot{x}d, \tag{5}$$

$$\cos(z) = \cos(x) - \sin(x)\dot{x}d, \tag{6}$$

$$e^z = e^x + e^x \dot{x}d. \tag{7}$$

In order to calculated now the first derivative of a function $f(x_1, x_2)$ with respect to x_1 one defines the independent variables x_1 and x_2 as dual numbers z_1 and z_2 with $\dot{x}_1 = 1$ and $\dot{x}_2 = 0$ and calculates $f(z_1, z_2)$. Respectively the first derivative of $f(x_1, x_2)$ with respect to x_2 is calculated by setting $\dot{x}_1 = 0$ and $\dot{x}_2 = 1$.

2.1.1 Example

In the following example (8) with the computational graph in figure 1 the step taken by the forward mode of automatic differentiation will be illustrated.

$$z = f(x_1, x_2) = x_1 \sin(x_1 + x_2^2) \tag{8}$$

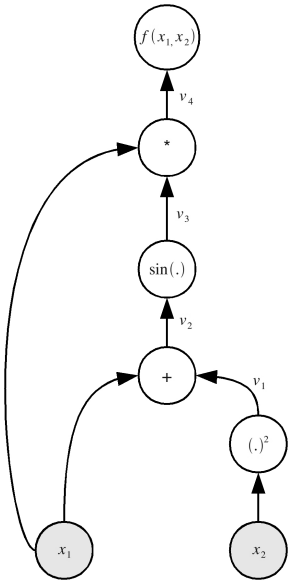


Figure 1: Computational graph of equation (8)

In order to calculate the first partial derivative of f with respect to x_1 $f(z_1, z_2)$ is evaluated for $z_1 = x_1 + 1d$ and $z_2 = x_2$.

$$
\begin{aligned}
v_1 &= z_2^2 = x_2^2 && (9)\\
v_2 &= z_1 + v_1 = \left(x_1 + x_2^2\right) + 1d && (10)\\
v_3 &= \sin(v_2) = \sin\left(x_1 + x_2^2\right) + \cos\left(x_1 + x_2^2\right) d && (11)\\
v_4 &= x_1 v_3 = x_1 \sin\left(x_1 + x_2^2\right) + \underbrace{x_1 \cos\left(x_1 + x_2^2\right)}_{=\frac{\partial f}{\partial x_1}} d = f(z_1, z_2) && (12)
\end{aligned}
$$

In order to calculate the first partial derivative of f with respect to x_2 $f(z_1, z_2)$ is evaluated for $z_1 = x_1$ and $z_2 = x_2 + 1d$.

$$
\begin{aligned}
v_1 &= z_2^2 = x_2^2 + 2x_2 d && (13)\\
v_2 &= z_1 + v_1 = \left(x_1 + x_2^2\right) + 2x_2 d && (14)\\
v_3 &= \sin(v_2) = \sin\left(x_1 + x_2^2\right) + 2x_2 \cos\left(x_1 + x_2^2\right) d && (15)\\
v_4 &= x_1 v_3 = x_1 \sin\left(x_1 + x_2^2\right) + \underbrace{2x_2 x_1 \cos\left(x_1 + x_2^2\right)}_{=\frac{\partial f}{\partial x_2}} d = f(z_1, z_2) && (16)
\end{aligned}
$$

The partial derivatives of f are therefore:

$$
\begin{pmatrix} \frac{\partial f}{\partial x_1} \\ \frac{\partial f}{\partial x_2} \end{pmatrix} = \begin{pmatrix} x_1 \cos\left(x_1 + x_2^2\right) \\ 2x_1 x_2 \cos\left(x_1 + x_2^2\right) \end{pmatrix}. \qquad (17)
$$

2.2 Reverse mode

In contrast to the forward mode the chain rule is implemented starting with the dependent variables. Then the associated numerical value of the derivate of the dependent variable with respect to the corresponding intermediate variable is calculated at each node. As this calculation traces back from the dependent towards the independent variables along the computational graph it performed after function calculation. In contrast to the forward mode the computational graph has to be explicitly constructed and stored, which might result in memory problems. On the other hand the function has to be calculated only ones, whereas in the forward mode the function is calculated for each partial derivate. Therefore the reverse mode should be preferred for problems with more independent variables as dependent.

2.2.1 Example

Applying the reverse mode of automatic differentiation to the example (8) with the computational graph in figure 1 would result in the following operations.

Forward sweep		
1	x_1	$\bar{x}_1 := 0$
2	x_2	$\bar{x}_2 := 0$
3	$v_1 = x_2^2$	$\bar{v}_1 := 0$
4	$v_2 = x_1 + v_1$	$\bar{v}_2 := 0$
5	$v_3 = \sin(v_2)$	$\bar{v}_3 := 0$
6	$v_4 = x_1 v_3$	$\bar{v}_4 := 0$
	$f = v_4$	

Reverse sweep		
	$\frac{\partial f}{\partial v_4} = \bar{f}$	$\bar{f} := 1$
6	$\frac{\partial f}{\partial x_1} = \bar{f}\frac{\partial v_4}{\partial x_1} + \bar{x}_1 = v_3$	$\bar{x}_1 := v_3$
	$\frac{\partial f}{\partial v_3} = \bar{f}\frac{\partial v_4}{\partial v_3} + \bar{v}_3 = x_1$	$\bar{v}_3 := x_1$
5	$\frac{\partial f}{\partial v_2} = \bar{f}\frac{\partial v_3}{\partial v_2} + \bar{v}_2 = x_1 \cos\, v_2$	$\bar{v}_2 := x_1 \cos v_2$
4	$\frac{\partial f}{\partial x_1} = \bar{v}_2\frac{\partial v_2}{\partial x_1} + \bar{x}_1 = x_1 \cos v_2 + v_3$	$\bar{x}_1 := x_1 \cos v_2 + v_3$
	$\frac{\partial f}{\partial v_1} = \bar{v}_2\frac{\partial v_2}{\partial v_1} + \bar{v}_1 = x_1 \cos v_2$	$\bar{v}_1 := x_1 \cos v_2$
3	$\frac{\partial f}{\partial x_2} = \bar{v}_1\frac{\partial v_1}{\partial x_2} + \bar{x}_2 = x_1 \cos v_2 2x_2$	$\bar{x}_2 := 2x_1 x_2 \cos v_2$
2	$\frac{\partial f}{\partial x_2} = \bar{x}_2 = 2x_1 x_2 \cos v_2$	
1	$\frac{\partial f}{\partial x_1} = \bar{x}_1 = x_1 \cos v_2 + v_3$	

2.3 Implementation by operator overloading

In order to implement the forward and reverse mode of automatic differentiation the operator overloading capabilities of Matlab have been used. Here all elementary functions have been redefined for the new data types *dual* and *reverse*, where *dual* represents the dual numbers ($z = x + \dot{x}d$) and *reverse* a node of the computational graph consisting of the value v, the derivative $\bar{v}$, the node index i, the operation identifier and the indices of its arguments.

In the forward mode the independent variables the function have to be defined as *dual*, where only one $\dot{x}_i$ is chosen one ($\dot{x}_i = 1$) all the others are defined zero $\left(\dot{x}_j = 0 \underset{j \neq i}{\forall}\right)$. The result of the function is again of type *dual* containing the partial derivative $\frac{\partial f}{\partial x_i}$ in its dual component.

In the reverse mode a new graph has to be created, then the independent variables are defined as *reverse*. While calculating the function the complete computational graph is constructed in parallel. Using this graph the partial derivatives are calculated in reverse direction.

The following examples show that in order to use automatic differentiation no serious changes in program code are needed.

```
x1 = dual(x1value,1); %define dual variable
x2 = dual(x2value,0); %second argument defines which partial derivative to compute

f = x1*sin(x1 + x2*x2); %compute result and one partial derivative

fvalue = getvalue(f); %get value of f(x1,x2)
dfdx1 = getderiv(f); %get derivative value
```

Figure 2: Example forward mode

```
erzeuge_Graph; %create computational graph
x1 = reverse(x1value); %define reverse variables
x2 = reverse(x2value);

f = x1*sin(x1 + x2*x2); %compute result and computational graph

berechne_Gradient; %reverse sweep for derivative calculation

fvalue = get(f,'value'); %get value of f(x1,x2)
dfdx1 = get(graph{1},'bar'); %get derivative value
dfdx2 = get(graph{2},'bar');
```

Figure 3: Example reverse mode

3 Simulation of Hamilton equations of motions by automatic differentiation

Hamilton's principle states that the dynamics of a physical system are determined by a variational problem of extremizing the following action integral:

$$\int_0^T \mathcal{L}\left(t, q, \dot{q}\right) dt \tag{18}$$

where $\mathcal{L}$ is the system's Lagrangian and q are the generalized coordinates. Applying variational calculus one gets the Euler-Lagrange equations of motion:

$$\frac{d}{dt}\left(\frac{\partial \mathcal{L}}{\partial \dot{q}}\right) - \frac{\partial \mathcal{L}}{\partial q} = 0. \tag{19}$$

Whereas a transformation of the system from generalized coordinates into the phase space $(q, \dot{q}) \rightarrow (q, p)$ by Legendre transformation would result in Hamilton's equations of motion:

$$\begin{pmatrix} \dot{q} \\ \dot{p} \end{pmatrix} = \begin{pmatrix} 0 & 1 \\ -1 & 0 \end{pmatrix} \begin{pmatrix} \frac{\partial H}{\partial q} \\ \frac{\partial H}{\partial p} \end{pmatrix} \tag{20}$$

with the Hamiltonian defined as:

$$H = \dot{q}^T p - \mathcal{L}, \tag{21}$$

where p is the generalized momentum:

$$p = \frac{\partial L}{\partial \dot{q}}. \tag{22}$$

In contrast to the Lagrangian formulation the Hamilton formulation gives an explicit system of differential equations, where only first derivatives of the Hamiltonian H occur. Therefore it is the most appropriate formulation for system's simulation.

Using the Hamilton formulation independent of the integration scheme first partial derivatives of the Hamiltonian have to be evaluated, which very fast results in quite long expressions for more complicated systems. Therefore an automatic differentiation on run-time should be preferred in cases of complex systems as it is less error-prone then a derivation by hand. As the Hamiltonian H is a scalar quantity, which has to be differentiated with respect to the vectors q and p the reverse mode of automatic differentiation should be used for differentiation.

4 Example - gantry crane

In to illustrate the efficiency of the proposed approach we investigated the well known mechanical system of a gantry crane (fig. 4). Here x is the trolley position and φ the sway angle of the load. For the sake simplicity the hoisting gear movement will be neglected resulting in a constant rope length l.

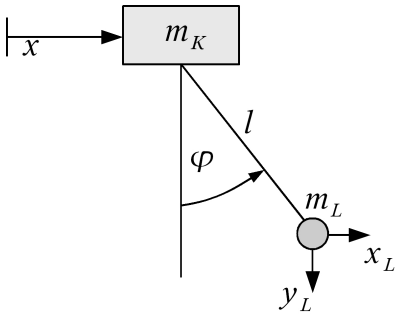


Figure 4: Gantry crane

The Cartesian load coordinates and their velocities are defined as follows.

$$\begin{pmatrix} x_L \\ y_L \end{pmatrix} = \begin{pmatrix} l\sin\varphi + x \\ -l\cos\varphi \end{pmatrix} \tag{23}$$

$$\begin{pmatrix} \dot{x}_L \\ \dot{y}_L \end{pmatrix} = \begin{pmatrix} l\dot{\varphi}\cos\varphi + \dot{x} \\ l\dot{\varphi}\sin\varphi \end{pmatrix} \tag{24}$$

The relevant kinetic and potential energies associated with the load and trolley masses m_K and m_L are defined as follows:

$$T_K = \frac{1}{2}m_K\dot{x}^2, \tag{25}$$

$$T_L = \frac{1}{2}m_L\left(\dot{x}_L^2 + \dot{y}_L^2\right), \tag{26}$$

$$V = m_L g l\left(1-\cos\varphi\right). \tag{27}$$

Therefore one gets the following Lagranian $\mathcal{L}$ in generalized coordinates x, φ.

$$\mathcal{L} = T_K + T_L - V \tag{28}$$

$$= \frac{1}{2}\left(m_K + m_L\right)\dot{x}^2 + \frac{1}{2}m_L\left(l^2\dot{\varphi}^2 + 2l\dot{\varphi}\dot{x}\cos\varphi\right) - m_L g l\left(1-\cos\varphi\right) \tag{29}$$

In order to derive the associated Hamiltonian the generalized momentum is calculated.

$$p = \frac{\partial L}{\partial \dot{q}} = \underbrace{\begin{pmatrix} m_K + m_L & m_L l\cos\varphi \\ m_K l\cos\varphi & m_L l^2 \end{pmatrix}}_{=M} \begin{pmatrix} \dot{x} \\ \dot{\varphi} \end{pmatrix} = M\dot{q} \tag{30}$$

The Hamiltonian of the gantry crane is described by:

$$H = \frac{1}{2}p^T M^{-1} p + V, \tag{31}$$

$$= \frac{1}{2m_K + m_L - m_L\cos(2\varphi)} \begin{pmatrix} p_x & p_\varphi \end{pmatrix} \begin{pmatrix} 1 & \frac{\cos(\varphi)}{l} \\ \frac{\cos(\varphi)}{l} & \frac{m_K+m_L}{l^2 m_L} \end{pmatrix} \begin{pmatrix} p_x \\ p_\varphi \end{pmatrix} + \ldots$$

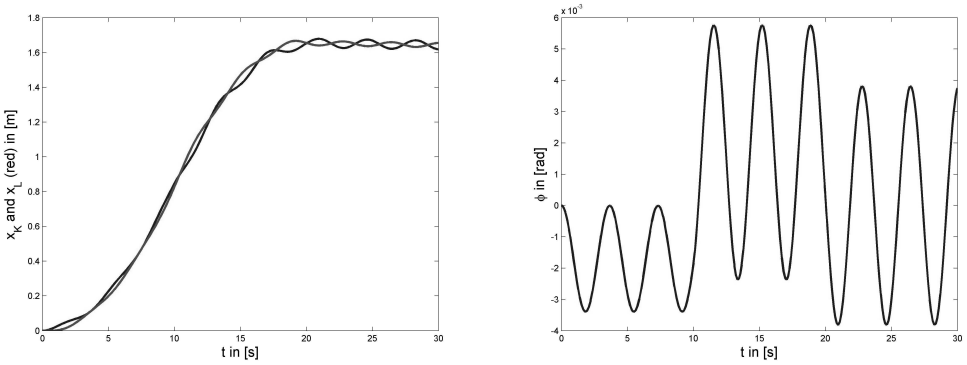


Figure 5: System response

$$\ldots + m_L g l\,(1 - \cos\varphi)\,. \tag{32}$$

In order to simulate the system we use the reverse mode of automatic differentiation initiallizing the computational graph and defining the generalized coordinates (x and φ) and momentums (p_x and p_φ) as reverse variables. Then in the forward sweep the Hamiltonian is calculated and the computational graph constructed. In the reverse sweep the partial derivatives of the Hamiltonian H with respect to the reverse variables are derived.
For time integration the Matlab *ode45* function has been used. Initial states are all zero $(x, \varphi, p_x, p_\varphi)^T = (0, 0, 0, 0)^T$. As a input the following generalized force function $Q_x(t)$ has been chosen:

$$Q_x(t) = 10 * (\sigma(t) - 2\sigma(t - 10) + \sigma(t - 20)). \tag{33}$$

As can be seen in figure 5 one gets feasible results, which are actually the same as the results one would have derived by simulation of the equations of motion using partial derivatives derived by hand.

5 Conclusion and future work

In this paper an approach of facilating mechanical systems simulation has been proposed. It relies on the automatic differentiation of the Hamilton function avoiding long and error-prone calculations by hand. Future work will investigate the application of this approach to much more challenging problems as e.g. the simulation of a rotary crane with non constant rope length [6]. There so far only a reduced model could be used for simulation.

References

[1] R.E. Wengert. A simple automatic derivative evaluation program, 1964.

[2] Andreas Griewank, David Juedes, Jean Utke. Algorithm 755: ADOL-C: A Package for the Automatic Differentiation of Algorithms Written in C/ C++, Article in ACM Transactions on Mathematical Software, 1996.

[3] A. Griewank. Evaluation Derivatives, Principles and Techniques of Algorithmic Differentiation. Frontiers in Appl. Math. 19, Phil., 2000.

[4] Shaun A. Forth. An Efficient Overloaded Implementation of Forward Mode Automatic Differentiation in MATLAB, ACM Transactions on Mathematical Software,2006.

[5] Thomas F. Coleman and Arun Verma. ADMAT: An Automatic Differentiation Toolbox for MATLAB, ACM Transactions on Mathematical Software,2000.

[6] Frank Palis and Stefan Palis. High PerformanceTracking Control of Automated Slewing Cranes. Robotics and Automation in Construction. 2008.

Stefan Palis, University of Magdeburg, Germany
Frank Palis, University of Magdeburg, Germany

The stress-strain state of a cylindrical vault built by using a centering

Dmitry A. Parshin
parshin@ipmnet.ru

Abstract

It is considered a process of gradual building a cylindrical vault on a rigid base. Building is implemented by means of continuous attaching layers of additional material to the being formed vault external surface. The vault internal surface is supported by a rigid circular centering during the whole building process and after its completing. The material used for building manifests properties of creep and aging (in particular, concrete can be considered).

It is stated a linear quasistatic initial-boundary problem of accreted solids mechanics that describes the process of the vault plane deformation under gravity action for the case of small strains. The analytical solution of this non-classical mathematically two-dimensional problem is built in trigonometric series and quadratures.

It is proved a proposition about the structure of technological residual stresses taking place in the completed vault if the centering is removed from it some time after the end of building. This proposition allows to determine efficiently the stresses mentioned. According to it they can be determined as difference between the stresses corresponding to the solved problem of the vault accretion on a centering and stresses corresponding to a certain classical problem of the elasticity theory with zero mass forces.

1 Introduction

Majority of large structures do not appear instantly on the place of their location. They are built there gradually, element by element that is during an accretion process. It is easily seen that the stress-strain state of such structures under gravity action can not be determined only by their final form. Indeed, the weight of every newly added material element exerts additional mechanical influence on the present part of the structure being formed and thus excites its additional strain in compliance with the current stiffness of the structure. That means that the stress-strain state of an accreted structure is formed incrementally. As a result the final state of the completely built structure essentially differs in general case from the state this structure would have if it were exposed to gravity action only on completing. As in the last case the structure would deform as a comprehensive whole.

Thus to determine the stress-strain state of a structure being built under gravity action this action is necessary to take into account during the whole building process. The analysis of accreted bodies deformation, that is of bodies gradually formed due to surface inflow of additional material, lets us make the fundamental conclusion that mentioned accounting can not be correctly implemented in the frameworks of classical solid mechanics, even if we consider the traditional equations and boundary conditions in a time-varying region. It is necessary to use special approaches and methods based on accreted solids mechanics concepts.

Remark that if the structural material used possesses rheological properties than both any actual and the final state of the built structure should considerably depend on the building time mode. During a building process of a structure of such a kind there are two tendencies that are continuously interacting. The first one is the tendency of permanent loading the structure with weight of additional elements and the second one is the stress rearrangement in elements so far added due to strain procrastination under changing structure geometry. The type and the result of

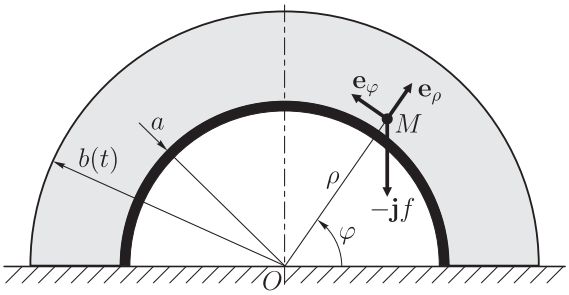


Figure 1:
A vault built by using a centering

this interaction are determined by various particular factors that can be analysed only by solving the corresponding accretion problem.

One can inquire about a few solved problems in accreted solids mechanics in [1, 2, 3, 4, 5, 6, 7, 8]. And the present paper is intended to one problem of gradual raising of a heavy semi-circular vault that manifests properties of creep and aging.

2 Statement of the problem

Let the process of building a cylindrical vault on a horizontal smooth rigid base start at time $t = t_1$. Building is implemented by means of vault erection due to continuous attachment of uniformly thick elementary layers of additional material to its external surface. During the process the internal surface of the vault is supported by a rigid circular centering. The very first layer of the material is directly attached to the centering and adheres to it. The process lasts up to time $t = t_2 > t_1$. During the process and after its completion the vault is attached to the base by a sliding mount that prevents the feet of the vault to be separated from the base but does not prevent their sliding along it.

The material used is homogeneous isotropic aging viscoelastic and originally free of stresses. The process of the building vault deformation is assumed to be quasistatic. We perform our consideration for the case of a plane strain state with small strains.

It is set a task to study the process of forming the stress-strain state of the vault in question under gravity action.

Let a be the internal vault radius (i.e. the external centering radius) and $b(t)$ its external radius at time t, $b(t_1) = a$ (Fig. 1). Let $b(t) \equiv b_{\text{fin}} = b(t_2)$ when $t > t_2$. We consider the continuous, monotone increasing function $b(t)$ to be known. Suppose this function be piecewise continuously differentiable.

We associate with the vault transverse cross-section plane the circular cylindrical coordinate system (ρ, φ, z). Here ρ is the polar radius counted from the arch central axis, φ is the polar angle counted upwards from the base (Fig. 1) and z is the longitudinal coordinate. Let the right orthonormal local frame of this system be $\{\mathbf{e}_\rho, \mathbf{e}_\varphi, \mathbf{k}\}$. If we denote the external unit normal to the base by $\mathbf{j}$, the cubic density of the gravity forces acting on the vault will be equal to $\mathbf{f} = -\mathbf{j}f$, where $f = \text{const}$ is the material specific weight.

We describe the material in the framework of the linear theory of viscoelasticity of homogeneously aging isotropic media[9, 1], i.e. we start from the state equation[5]

$$\mathbf{T}(\mathbf{r},t) = G(t)\big(\mathcal{I} + \mathcal{N}_{\tau_0(\mathbf{r})}\big)\big[2\,\mathbf{E}(\mathbf{r},t) + (\varkappa - 1)\,\mathbf{1}\,\mathrm{tr}\,\mathbf{E}(\mathbf{r},t)\big]. \tag{1}$$

Here $\mathbf{T}$ and $\mathbf{E}$ are stress and small strain tensors, $\mathbf{1}$ is the unit tensor of rank 2; G is elastic shear modulus, $\varkappa = (1-2\nu)^{-1}$, $\nu = \text{const}$ is Poisson's ratio. The viscoelasticity operator $\mathcal{I} + \mathcal{N}_s$ in (1) is determined by the relations: $\mathcal{I} + \mathcal{N}_s = (\mathcal{I} - \mathcal{L}_s)^{-1}$, $\mathcal{L}_s\, f(t) = \int_s^t f(\tau) K(t,\tau)\, d\tau$, $\mathcal{N}_s\, f(t) = \int_s^t f(\tau) R(t,\tau)\, d\tau$, $K(t,\tau) = G(\tau)\,\partial\Delta(t,\tau)/\partial\tau$, $\Delta(t,\tau) = G(\tau)^{-1} + \omega(t,\tau)$ where $\mathcal{I}$ is the identity operator; K and R are creep and relaxation kernels, Δ and ω are specific strain function and creep measure in the case of pure shear. Time t is assumed to be counted from the material fabrication

[5]This equation was suggested by the academician of the Armenian Academy of Sciences N. Kh. Arutyunyan especially for describing creeping processes in concrete and is widely used for this purpose nowadays. Meanwhile, it also well comes to agreement with experimental data for creep of some kinds of polymers, rocks, soil, and ice.

instant; $\tau_0(\mathbf{r})$ is the time at which stresses appear in the point of the body with the position vector $\mathbf{r}$.

In the problem under consideration stresses appear at points of the body at the time of their joining to it. It means that $\tau_0(\mathbf{r}) \equiv \tau_*(\rho)$ where $\tau_*(\rho)$ is the time of attachment of the layer with radius ρ to the vault. It is clear that the equation $\tau_*(\rho) = t$ describes the external surface $\{\rho = b(t)\}$ of the continuously accreted vault, i.e. its instantaneous accretion surface.

Let us introduce the linear integral operator $\mathcal{H}_s = (\mathcal{I} - \mathcal{L}_s)G(t)^{-1}$ with the real parameter s and its reverse operator $\mathcal{H}_s^{-1} = G(t)(\mathcal{I} + \mathcal{N}_s)$. We denote $g^\circ(\mathbf{r}, t) = \mathcal{H}_{\tau_0(\mathbf{r})}\, g(\mathbf{r}, t)$ for an arbitrary tensor function $g(\mathbf{r}, t)$ of point $\mathbf{r}$ of the accreted body and time t. Then the constitutive relation (1) can be written in the form [10]

$$\mathbf{T}^\circ(\mathbf{r}, t) = 2\,\mathbf{E}(\mathbf{r}, t) + (\varkappa - 1)\,\mathbf{1}\,\mathrm{tr}\,\mathbf{E}(\mathbf{r}, t). \tag{2}$$

Note that $g^\circ\big(\mathbf{r}, \tau_0(\mathbf{r})\big) = g\big(\mathbf{r}, \tau_0(\mathbf{r})\big)/G\big(\tau_0(\mathbf{r})\big)$. In our case we have

$$g^\circ\big(\mathbf{r}, \tau_*(\rho)\big) = g\big(\mathbf{r}, \tau_*(\rho)\big)/G\big(\tau_*(\rho)\big). \tag{3}$$

Note also that, by definition, we have the identity $\omega(\tau, \tau) \equiv 0$, $\tau \geqslant 0$. So

$$\mathcal{H}_\tau 1 = \Delta(t, \tau). \tag{4}$$

3 Boundary value problem for the built vault

During a process of accretion elements of additional material are added to the growing solid in the course of its deformation motion in space. It is clear that the entire body formed in such a way cannot in general have an unstressed configuration. It is this fact that is decisive in deformation process of any accreted solid and essentially distinguishes the mechanical behavior of such solids from the behavior of solids of constant composition (i.e. classical bodies in continuum mechanics) and of solids whose boundary is variable because of removal of material. Owing to this characteristic property, it is impossible to define the strain measure of an accreted solid by the method adopted in continuum mechanics; therefore, the Cauchy formulas do not hold for the total strain tensor components, and hence the Saint-Venant conditions of their compatibility are not satisfied.

Note, however, that particles of the material added after their adhesion to the accretion surface continue the motion further in the solid configuration. It means that a sufficiently smooth field of particles velocities is determined in the space region occupied by the entire accreted solid at a given time instant. Therefore, we can expect that the problem on deforming such a solid can be well defined in terms of displacement rates.

Starting from this viewpoint, we write out the analog of the constitutive relation (2) for rates of the mechanical quantities this relation ties together: $\mathbf{S}(\mathbf{r}, t) = 2\,\mathbf{D}(\mathbf{r}, t) + (\varkappa - 1)\,\mathbf{1}\,\mathrm{tr}\,\mathbf{D}(\mathbf{r}, t)$. Here we introduce the tensor $\mathbf{S} = \partial\mathbf{T}^\circ/\partial t$ [10] and the strain rate tensor $\mathbf{D} = (\nabla\mathbf{v}^{\mathrm{T}} + \nabla\mathbf{v})/2$ where $\mathbf{v}(\mathbf{r}, t) = \mathbf{e}_\rho v_\rho + \mathbf{e}_\varphi v_\varphi + \mathbf{k}\, v_z$ is the velocity field describing the motion of accreted body particles. In the considered case of plane strain, we have $\mathbf{k} \cdot \mathbf{v} = 0$, $\partial\mathbf{v}/\partial z = \mathbf{0}$.

The equation for the introduced tensor $\mathbf{S}$ in the region occupied at the current time by the accreted body can be obtained by applying the linear operator $\mathcal{H}_{\tau_0(\mathbf{r})}$ to the equilibrium equation $\nabla \cdot \mathbf{T} + \mathbf{f} = \mathbf{0}$ and by differentiating the result with respect to time t. Due to the fact that the lower limit in the integral operator mentioned depends on a point of the body this integral operator does not commute with the divergence operator. But one can show [10] that in the accretion processes studied in the present paper we can write $(\nabla \cdot \mathbf{T})^\circ = \nabla \cdot \mathbf{T}^\circ$ for the stress tensor. In this case the following analog of the equilibrium equation is satisfied in the entire accreted solid both during and after the process of its accretion: $\nabla \cdot \mathbf{T}^\circ + \mathbf{f}^\circ = \mathbf{0}$. Differentiate it with respect to t: $\nabla \cdot \mathbf{S} + \partial\mathbf{f}^\circ/\partial t = \mathbf{0}$. By calculating with (4) the vector-function $\partial\mathbf{f}^\circ/\partial t = -\mathbf{j}\,h(\rho, t)$, where $h(\rho, t) = f\ \partial\omega\big(t, \tau_*(\rho)\big)/\partial t$, we obtain the equation $\nabla \cdot \mathbf{S} = \mathbf{j}\,h(\rho, t)$. Note that according to properties of creep measure (see, for example, [11]) we have $h(\rho, t) \geqslant 0$ when $t > \tau_*(\rho)$.

Consider now a condition that is to be given on the accretion surface of the body. As we suppose the material to be attached is originally free of stresses the complete stress tensor is required to be equal to zero on the accretion surface:

$$\mathbf{T} = \mathbf{0}, \quad \rho = b(t), \quad t \in [t_1, t_2] \quad \Longleftrightarrow \quad \mathbf{T}\big(\mathbf{r}, \tau_*(\rho)\big) = \mathbf{0}, \quad \rho \in [a, b_{\mathrm{fin}}]. \tag{5}$$

The initial-boundary condition (5) can be transformed to the boundary condition for components of the tensor $\mathbf{S}$ analogous to a classical force condition on a solid surface [10]: $\mathbf{e}_\rho \cdot \mathbf{S} = -\mathbf{j}\, q(t)$, $\rho = b(t)$, $t \in [t_1, t_2]$, where $q(t) = f\, b'(t)/G(t) \geqslant 0$.

After we stop building the vault its external surface remains unloaded. Therefore we are to use an ordinary condition of stress absence for $t > t_2$. An evident analog of this condition for the tensor $\mathbf{S}$ is the boundary condition $\mathbf{e}_\rho \cdot \mathbf{S} = \mathbf{0}$, $\rho = b_{\text{fin}}$. As we suppose that $b(t) \equiv b_{\text{fin}}$ when $t > t_2$, the written above condition for the tensor $\mathbf{S}$ on the accretion surface remains formally valid even after erecting completing and consequently can be used for any $t \geqslant t_1$. However, it is necessary to understand that the nature of this condition during the vault continuous erecting stage and after its completing is different in essence.

On the internal surface $\{\rho = a\}$ of the vault we have to require meeting the kinematic condition of tough adhesion of the material to the centering. To set a problem in velocities it should be the condition $\mathbf{v} = \mathbf{0}$, $\rho = a$.

On the feet $\{\varphi = 0, \pi\}$ of the vault we use the mixed conditions of sliding mount $\mathbf{e}_\varphi \cdot \mathbf{T} \cdot \mathbf{e}_\rho = 0$, $\mathbf{e}_\varphi \cdot \mathbf{v} = 0$. Instead of $\mathbf{T}$ we can obviously put here the tensor $\mathbf{S}$.

Thus we get the following boundary value problem which describes the deforming process of the built vault attached to a centering during and after building:

$$\begin{aligned}
&\nabla \cdot \mathbf{S} = \mathbf{j}\, h(\rho, t), \quad \rho \in \big(a, b(t)\big), \quad \varphi \in (0, \pi), \quad t > t_1;\\
&\mathbf{S} = 2\,\mathbf{D} + (\varkappa - 1)\,\mathbf{1}\,\mathrm{tr}\,\mathbf{D}, \quad \mathbf{D} = \frac{\nabla \mathbf{v}^{\mathrm{T}} + \nabla \mathbf{v}}{2}; \qquad \mathbf{k} \cdot \mathbf{v} = 0, \quad \frac{\partial \mathbf{v}}{\partial z} = \mathbf{0};\\
&\mathbf{v}\big|_{\rho=a} = \mathbf{0}; \qquad \mathbf{e}_\rho \cdot \mathbf{S}\big|_{\rho=b(t)} = -\mathbf{j}\, q(t);\\
&(\mathbf{e}_\varphi \cdot \mathbf{S} \cdot \mathbf{e}_\rho)\big|_{\varphi=0,\pi} = 0, \quad (\mathbf{e}_\varphi \cdot \mathbf{v})\big|_{\varphi=0,\pi} = 0.
\end{aligned} \tag{6}$$

It is seen that this problem has the form of a classical boundary value problem of linear elasticity theory with a parameter t.

4 Solution of the problem. Determining the stresses in the vault

Let us try the radial and circular components v_ρ and v_φ of the velocity vector field $\mathbf{v}$ solving the problem (6) in the form of the trigonometric Fourier expansions. Because of the structure symmetry we have $v_\rho\big|_\varphi = v_\rho\big|_{\pi-\varphi}$, $v_\varphi\big|_\varphi = -v_\varphi\big|_{\pi-\varphi}$. Therefore

$$v_\rho = c_0(\rho, t) + \sum\nolimits_{n=1}^{\infty} c_n(\rho, t) \cos 2n\varphi, \qquad v_\varphi = \sum\nolimits_{n=1}^{\infty} d_n(\rho, t) \sin 2n\varphi. \tag{7}$$

Note that these expansions satisfy the homogenous mixed boundary conditions on the vault feet $\{\varphi = 0, \pi\}$ contained in (6).

After we use (7) in the Lame equations that correspond to (6) we are to solve systems of linear inhomogeneous ordinary differential equations of the second order with respect to ρ with variable coefficients for unknown functions c_0, c_n, d_n. On solving them we get

$$\frac{c_0}{\rho} = \frac{-\beta B_{40} - B_{10}}{2}, \quad \left\{ \begin{matrix} c_n \\ d_n \end{matrix} \right\} \rho^{-1} = \frac{(n \pm \beta) B_{2n} \mp B_{3n}}{4n - 2} \pm \frac{(n \mp \beta) B_{4n} \mp B_{1n}}{4n + 2};$$

$$\mathbf{S} = \mathbf{e}_\rho \mathbf{e}_\rho\, S_\rho + \mathbf{e}_\varphi \mathbf{e}_\varphi\, S_\varphi + \mathbf{k}\,\mathbf{k}\, \nu (S_\rho + S_\varphi) + (\mathbf{e}_\rho \mathbf{e}_\varphi + \mathbf{e}_\varphi \mathbf{e}_\rho)\, S_{\rho\varphi},$$

$$S_{\rho\varphi} = \sum\nolimits_{n=1}^{\infty} \big[B_{1n} - nB_{2n} + B_{3n} - nB_{4n}\big] \sin 2n\varphi, \quad S_{\left\{ \begin{smallmatrix} \rho \\ \varphi \end{smallmatrix} \right\}} = \pm B_{10} - B_{40} + \sum\nolimits_{n=1}^{\infty} \big[\pm B_{1n} \mp (n \pm 1) B_{2n} \mp B_{3n} \pm (n \mp 1) B_{4n}\big] \cos 2n\varphi.$$

Here $\beta = 1 - 2\nu$ if the left side of an equation contains c, and $\beta = 2(1 - \nu)$ if the left side of an equation contains d. We have also introduced the functions

$$B_{1m}(\rho, t) = K_m^+ \Phi_{m+1}(\rho, t) + \big[b(t)/\rho\big]^{2m+2} \alpha_{1m}(t),$$

$$B_{2m}(\rho,t) = \varkappa\,\Phi_m(\rho,t) + \bigl[b(t)/\rho\bigr]^{2m}\alpha_{2m}(t),$$
$$B_{3m}(\rho,t) = K_m^-\Psi_{m-1}(\rho,t) + (\rho/a)^{2m-2}\alpha_{3m}(t),$$
$$B_{4m}(\rho,t) = \varkappa\,\Psi_m(\rho,t) + (\rho/a)^{2m}\alpha_{4m}(t);$$

$$\left\{\begin{matrix}\Phi_m\\ \Psi_m\end{matrix}\right\}(\rho,t) = \frac{\pm k}{2m\mp 1}\int_{\left\{\begin{matrix}a\\ b(t)\end{matrix}\right\}}^{\rho}(\xi/\rho)^{\pm 2m}\,h(\xi,t)\,d\xi.$$

Here $K_m^{\pm} = \bigl[m(2m\pm 3)/(2m\mp 1)\bigr]\varkappa \pm 1$, $k = 2/\bigl[\pi(\varkappa+1)\bigr]$. The functions $\alpha_{jm}(t)$ are to be found from the system of linear algebraic equations that we obtain on satisfying the boundary conditions in (6) on the internal and external vault surfaces. We do not present the expressions for α_{jm} because they are extremely cumbersome.

After the problem (6) is solved, the tensor $\mathbf{T}^\circ$ evolution in every point of the completed vault can be reconstructed from the found rate of this tensor with the initial condition given by (5) and (3): $\mathbf{T}^\circ(\mathbf{r},t) = \int_{\tau_*(\rho)}^{t}\mathbf{S}(\mathbf{r},\tau)\,d\tau$, $t \geqslant \tau_*(\rho)$. According to the definition of the tensor $\mathbf{T}^\circ$, by virtue of the known evolution of this tensor it is possible to determine the evolution of the stress tensor $\mathbf{T}$ by solving the integral Volterra equation of the second kind $\mathbf{g}(\mathbf{r},t) - \int_{\tau_*(\rho)}^{t}\mathbf{g}(\mathbf{r},\tau)K(t,\tau)\,d\tau = \mathbf{T}^\circ(\mathbf{r},t)$ with respect to time t. In this equation the vector $\mathbf{r}$ is a parameter, $\mathbf{g}(\mathbf{r},t) = \mathbf{T}(\mathbf{r},t)/G(t)$ is the required tensor-function.

We can write the solution of the mentioned integral equation in the analytical form: $\mathbf{T}(\mathbf{r},t) = \mathcal{H}^{-1}_{\tau_*(\rho)}\mathbf{T}^\circ(\mathbf{r},t) = G(t)\bigl[\mathbf{T}^\circ(\mathbf{r},t) + \int_{\tau_*(\rho)}^{t}\mathbf{T}^\circ(\mathbf{r},\tau)R(t,\tau)\,d\tau\bigr]$, $t \geqslant \tau_*(\rho)$. However, if the expression for the resolvent R of the creep kernel K is too complicated for calculations using this formula, it is more desirable to solve the equation in question numerically, for example, by a quadrature method [12].

5 Residual stresses in the finished vault after centering removing

Now we know the whole evolution of the built vault stress-strain state under gravity action from the instant of building beginning to an arbitrary far instant after the end of building if the centering is being left attached to the vault on its completing. Let us study the residual stresses taking place in the completed vault after the centering is removed from its internal surface.

Resting upon the linearity of the problem and applying a known correspondence principle in the theory of aging solids viscoelasticity [1] we can prove the following

Proposition

1) Let the stress tensors $\mathbf{T}^\infty(\mathbf{r})$ and $\mathbf{T}_{\rm res}(\mathbf{r})$ define the long-term states of a heavy aging viscoelastic accreted vault under consideration after the process of its building (according to a certain time mode) is completed and the vault is left on the centering or, respectively, the centering is removed. In the first case $\mathbf{t}_a^\infty(\varphi) = -\mathbf{e}_\rho\cdot\mathbf{T}^\infty\big|_{\rho=a}$ is the steady-state centering reaction, and in the second case we have $\mathbf{e}_\rho\cdot\mathbf{T}_{\rm res}\big|_{\rho=a} \equiv \mathbf{0}$.

2) Suppose we have a weightless elastic vault that is built without residual stresses, has the same dimensions as the completed viscoelastic vault in question and the same elastic characteristics as this vault has after a long aging. The elastic vault mentioned is set on a horizontal rigid base and fixed on it with sliding mount, as the erected viscoelastic vault in question, and loaded on the internal surface by the distributed loading $\mathbf{t}_a^\infty$. Let the stress state of such elastic vault be defined by the stress tensor $\mathbf{T}_{\rm el}(\mathbf{r})$ (it can be found from the solution of the corresponding classical problem of the elasticity theory with zero mass forces).

Then $\mathbf{T}_{\rm res} = \mathbf{T}^\infty - \mathbf{T}_{\rm el}$.

Acknowledgements

The work is supported by the Russian Foundation for Basic Research (under grants Nos. 08-01-00553-a, 09-08-01180-a, 09-08-01194-a, and 10-01-92653-IND_a), by the Department of Energetic,

Mechanical Engineering, Mechanics and Control Processes of the Russian Academy of Sciences (Program No. 13 OE), and by the Russian Science Support Foundation.

References

[1] N.Kh. Arutyunyan and A.V. Manzhirov (1999). *Contact Problems in the Theory of Creep*, NAN RA, Erevan [in Russian].

[2] A.V. Manzhirov and V.A. Chernysh (1992). Strengthening of a buried arch by the way of accretion, *Izv. Akad. Nauk. Mekh. Tverd. Tela*, (5), 25–37.

[3] A.V. Manzhirov and D.A. Parshin (2006). Accretion of a viscoelastic ball in a centrally symmetric force field, *Mech. Solids*, **41** (1), 51–64.

[4] A.V. Manzhirov and D.A. Parshin (2006). Modeling the accretion of cylindrical solids on a rotating mandrel with centrifugal forces taken into account, *Mech. Solids*, **41** (6), 121–134.

[5] A.V. Manzhirov and D.A. Parshin (2007). Modeling of the deformation process of accreted conic solids, *Vestn. Samarsk. Gos. Univ. Estestv.-Nauch. Ser.*, **54** (4), 290–303 [in Russian].

[6] A.V. Manzhirov (2007). Mechanics of accreted solids: state-of-the-art, problems, and perspectives, *Topical Problems in Continuum Mechanics* (Proc. Int. Conf., 25–28 Sep. 2007, Tsakhkadzor), Erevan State Univ. Architecture and Civil Eng., Erevan, 243–246 [in Russian].

[7] D.A. Parshin (2007). Strengthening of a conic column by the way of accretion, *Modern Problems in Continuum Mechanics* (Proc. XI Int. Conf., 26–29 Nov. 2007, Rostov-on-Don), TsVVR, Rostov-on-Don, vol. 1, 205–209 [in Russian].

[8] A.V. Manzhirov and D.A. Parshin (2008). New results in the classical problems of Earth and mining sciences, *Modern Problems in Continuum Mechanics* (Proc. XII Int. Conf., 1–5 Dec. 2008, Rostov-on-Don), TsVVR, Rostov-on-Don, vol. 1, 145–149 [in Russian].

[9] N.Kh. Arutyunyan (1966). *Some Problems in the Theory of Creep*, Pergamon Press, Oxford.

[10] A.V. Manzhirov (1995). The general non-inertial initial-boundary value problem for a viscoelastic ageing solid with piecewise-continuous accretion, *J. Appl. Math. Mech.*, **59** (5), 805–816.

[11] N.Kh. Arutyunyan and V.B. Kolmanovskii (1983). *Creep Theory of Inhomogeneous Bodies*, Nauka, Moscow [in Russian].

[12] A.D. Polyanin and A.V. Manzhirov (2008). *Handbook of Integral Equations*, 2nd ed. Chapman and Hall / CRC Press, Boca Raton, London.

Dmitry A. Parshin, Ishlinsky Institute for Problems in Mechanics of the Russian Academy of Sciences, Vernadsky Ave. 101 Bldg 1, Moscow, Russia

Bridged cracks growth criterion

Mikhail Perelmuter
perelm@ipmnet.ru

Abstract

The nonlocal two-parametric fracture criterion of bridged cracks growth is proposed and considered. The necessary condition of the crack tip limit equilibrium is the equality of the energy release rate and the rate of the energy absorbed by the bonds (the first condition of fracture). The second condition of fracture is the condition of the bond limit stretching at the trailing edge of the bridge zone. Based on these two fracture conditions the regimes of the bridged zone and the crack tip equilibrium and growth are considered.

1 Problem formulation

A straight crack of the length 2ℓ at an interface of two dissimilar elastic half-planes is considered. The crack is placed at $|x| \le \ell, y = 0$. Is assumed that the uniform tensile stresses, σ_o, are applied at infinity normal to the interface. Segments of length d (bridged zones) $(\ell - d) \le |x| \le \ell$ adjacent to the tips of the crack where the surfaces of the crack interact with each other are considered. The physical nature of the crack surfaces interaction is generally changed depending on the crack scale and distance from the crack tip. The interatomic and intermolecular forces are limiting mechanisms of the surfaces interaction at the small distances from the crack tips (where the crack opening does not exceed the size of the region of the molecular forces action) while "mechanical" forces prevail at relatively larger distances. These mechanical forces can be caused, e.g., by reinforcing action of fibers in composites or polymer chains connecting the crack surfaces in polymer-polymer joints or polymer joints with other materials (metals, ceramics and etc). To mathematically describe the interaction between the surfaces of the crack, is assumed that there exist bonds between the surfaces of the crack at the bridged zone. The law of deformation of these bonds, which is generally nonlinear, is given.

Under the action of external loads, σ_0, the stresses $Q(x)$ appear in the bonds between the surface of the interface crack at the boundary between different materials. These stresses have the normal $q_y(x)$ and tangential $q_x(x)$ components

$$Q(x) = q_y(x) - iq_x(x),\ i^2 = -1 \tag{1}$$

The surfaces of the crack are acted on by the normal and tangential stresses which are numerically equal to these components.

The opening of the interface crack, $u(x)$ at $|x| \le \ell, y = 0$, can be written as follows

$$u(x) = u_y(x) - iu_x(x) \tag{2}$$

where $u_y(x) = u_y^+(x) - u_y^-(x)$ and $u_x(x) = u_x^+(x) - u_x^-(x)$ are the projections of the crack opening on the coordinate axes, u_x^+, u_y^+ and u_x^-, u_y^- denote the components of the displacements of the upper and lower crack surfaces.

The relation between the crack opening and the bond tractions (the bond deformation law) depends on the physical origin of the bonds and their properties. In the case of spring-like bonds the deformation law can be written as follows [1, 2]

$$u_i(x) = c_0(x,\sigma)q_i(x)\ , c_0(x,\sigma) = \gamma_0(x,\sigma)\frac{H}{E_B} \tag{3}$$

where γ_0 is a dimensionless function, H is a linear scale proportional to the bonding zone thickness, E_B is the effective Young modulus of the bonds and the function c_0 can be considered as the effective bond compliance, $\sigma = \sqrt{q_x^2 + q_y^2}$ is the modulus of the traction vector.

For the bond deformation law similar to (3) (displacements depends on bonds stresses) the bonds stresses and the crack opening along the crack bridged zone can be determined from solution of the singular integral-differential equations system [1, 2].

2 Two parametric fracture criterion

Supposing that the bonds stresses and the crack opening along the crack bridged zone are known, the total potential energy of a body containing a crack with bridged zone (in the absence of body forces) is

$$\Pi = \int\limits_v w(\varepsilon_{ij})dv - \int\limits_{s_e} t_i u_i ds + \int\limits_{s_i} \Phi(u)ds, \tag{4}$$

where $w(\varepsilon_{ij})$ is the density of the deformation energy in the body volume v, ε_{ij} are the components of the strain tensor; t_i, u_i are the tractions and displacements at the body boundary and (or) crack surfaces s_e; $\Phi(u)$ is the density of the strain energy of the bonds in the crack bridged zones, u is the crack opening in the bridged zones of area s_i.

The crack limit equilibrium corresponds to the following condition

$$-\frac{\partial \Pi}{\partial \ell} = -\frac{\partial}{\partial \ell}\left[\int\limits_v w(\varepsilon_{ij})dv - \int\limits_{s_e} t_i u_i ds\right] - \frac{\partial}{\partial \ell}\int\limits_{s_i} \Phi(u)ds = 0 \tag{5}$$

The terms in the brackets represent the strain energy release rate at creation of a new crack surface and the last term is the rate of the energy absorption in the crack bridged zone and is associated with the energy necessary to create a unit of its new surface. Note, that within the framework of the model the rate of the energy absorption depends on the bridged zone size and bond characteristics. The equilibrium bridged zone size is not assumed to be constant. It can be determined from condition (5) while searching for the critical load needs additional conditions of the bond rupture.

The strain energy release rate in the case of an interface crack under the external load σ_0 and the stresses $-Q(x)$ applied to the crack surfaces in the bridged zone can be written as follows [3]

$$G_{tip}(d,\ell) = \left(\frac{k_1+1}{\mu_1} + \frac{k_2+1}{\mu_2}\right)\frac{K_B^2}{16\,\cosh^2(\pi\beta)}\,, \tag{6}$$

where $k_{1,2} = 3 - 4\nu_{1,2}$ or $k_{1,2} = (3-\nu_{1,2})/(1+\nu_{1,2})$ for the plane strain or plane stress states, respectively; $\nu_{1,2}$, $\mu_{1,2}$ are the Poisson ratios and shear moduli of the joint materials $1(y>0)$ and $2(y<0)$, $\alpha = (\mu_2 k_1 + \mu_1)/(\mu_1 k_2 + \mu_2)$, $\beta = \ln\alpha/2\pi$ and $K_B = \sqrt{K_{\rm I}^2 + K_{\rm II}^2}$ is the modulus of the stress intensity factors due to the external loads and the stresses in the crack bridged zone.

The stress intensity factors (SIF) $K_{I,II}$ are determined by [1]

$$\begin{aligned} K_{\rm I} + iK_{\rm II} = \frac{\sigma_0\sqrt{\pi\,\ell}}{(2\ell)^{i\,\beta}}\Bigg[&\left(1 - \frac{2\cosh(\pi\beta)}{\pi}\int\limits_{1-d/\ell}^{1}\frac{p_y(t)}{\sqrt{1-t^2}}dt\right) + \\ &+ i\left(2\beta - \frac{2\cosh(\pi\beta)}{\pi}\int\limits_{1-d/\ell}^{1}\frac{tp_x(t)}{\sqrt{1-t^2}}dt\right)\Bigg] \end{aligned} \tag{7a}$$

$$p_y(x) - ip_x(x) = Q(x)\left(\frac{\ell - x}{\ell + x}\right)^{i\,\beta} \tag{7b}$$

Let us calculate the rate of the energy absorption for the interface crack with bonding. Denote by $U_{bond}(d,\ell)$ the work of the deformation of bonds and by $G_{bond}(d,\ell)$ the rate of the energy absorption per unit thickness of the body. Then

$$U_{bond}(d,\ell) = b\int\limits_{\ell-d}^{\ell}\Phi(u)dx\ , \quad G_{bond}(d,\ell) = \frac{\partial U_{bond}(d,\ell)}{b\,\partial\ell} \tag{8}$$

where b is the body thickness.

The density of the strain energy of the bonds is equal to

$$\Phi(u) = \int\limits_{0}^{u(x)}\sigma(u)du\ , \quad u(x) = \sqrt{u_x^2(x)+u_y^2(x)}, \quad \sigma = \sqrt{q_x^2+q_y^2} \tag{9}$$

After differentiation in formula (8) with respect to the upper and the bottom limits of the integral we can get

$$\frac{\partial U_{bond}(d,\ell)}{b\partial\ell} = \int\limits_{\ell-d}^{\ell}\left(\frac{\partial\,u(x)}{\partial\,\ell}\sigma(u)\right)dx + G_c - G_b, \tag{10}$$

where

$$G_c = \int\limits_{0}^{u(\ell)}\sigma(u)du;\,, \quad G_b = \int\limits_{0}^{u(\ell-d)}\sigma(u)du \tag{11}$$

If we consider the model of the crack with zero opening at the crack tip ($u(\ell)=0$) then $G_c = 0$ and it is necessary to add in the left part of (10) the value of the intrinsic toughness of the matrix material

$$G_c = 2c_m\gamma_m$$

where c_m is the volume fraction of the matrix material and $2\gamma_m$ is the matrix toughness.

Finally, we obtain the following expression for the rate of the energy absorption [4]

$$G_{bond}(d,\ell) = \int\limits_{\ell-d}^{\ell}\left(\frac{\partial\,u_y(x)}{\partial\,\ell}q_y(u) + \frac{\partial\,u_x(x)}{\partial\,\ell}q_x(u)\right)dx - \int\limits_{0}^{u(\ell-d)}\sigma(u)du + G_c \tag{12}$$

where the second term is the density of deformation energy allocated at break of the bond at the trailing edge of the crack bridged zone.

For a homogeneous material or an adhesion layer connecting different materials the following relations are held

$$G_c = G_b = \int\limits_{0}^{u(\ell-d)}\sigma(u)du \tag{13}$$

In this case the expression (12) completely coincides with similar expression from [1, 2].

For a weak matrix material ($G_c \ll G_b$) is supposed $G_c = 0$ in (12). In this case $G_{bond}(d,\ell)\to 0$ if $d/\ell\to 0$ and therefore this approach coincide with Barenblatt's model in this limit [1].

The condition of the crack tip limit equilibrium (5) can be rewritten as follows taking into account formulae (6) and (12)

$$G_{tip}(d,\ell) = G_{bond}(d,\ell) \tag{14a}$$

Condition (14a) is necessary but insufficient for searching for a limit equilibrium state of the crack tip and the bridged zone. This condition enables us to determine the bridged zone size, d_{cr}

, such that the crack tip is in an equilibrium at the given level of the external loads. To search for the limit state of both the crack tip and bridged zone within the framework of the model one should introduce an additional condition, e.g., the condition of bond limit stretching at the trailing edge of the bridged zone $x_0 = \ell - d_{cr}$

$$u(x_0) = ([u_x(x_0)]^2 + [u_y(x_0)]^2)^{1/2} = \delta_{cr} \tag{14b}$$

where δ_{cr} is the bond rupture length.

If

$$G_{tip}(d, \ell) \geq G_{bond}(d, \ell) \tag{15}$$

at a certain bridged zone size, d, and

$$u(\ell - d) < \delta_{cr} \tag{16}$$

then the crack length increases with the bridged zone growth up to the size d_{cr} without bond rupture. This stage of the crack growth can be treated as the system shakedown to the given level of the external loads (subcritical crack growth).

The crack tip advance with simultaneous bond rupture at the trailing edge of the bridged zone occurs if both conditions

$$u(\ell - d) \geq \delta_{cr} \tag{17}$$

and (15) are fulfilled.

The regime of bond rupture at the trailing edge of the bridged zone without the crack tip advance is observed then conditions

$$G_{tip}(d, \ell) < G_{bond}(d, \ell) \tag{18}$$

and (17) are fulfilled. In this case the size of the bridged zone decreases and tends to the limit value d_{cr} at the given load.

The bridged zone size and crack length are reserved within the framework of the model if the inequalities (16) and (18) hold. Thus, the bond rupture characteristics and load level determine the fracture regimes: the crack tip advance with the bridged zone growth; bridged zone shortening without the crack tip advance; the crack tip advance and bond rupture at the trailing edge of the bridged zone.

Solving jointly eqs. (14a-14b) we can determine the critical external loads σ_0, the bridged zone size d_{cr} and the adhesion fracture resistance at the crack limit equilibrium state for given crack length and bond characteristics.

3 Crack with uniform bridged stresses

Analytical consideration of the proposed criterion is performed for the problem of the straight crack in a homogeneous plane with the rectilinear law of the bond stress. In this very simple case the normal bridged stresses in the crack bridged zone are prescribed, uniformly distributed along the bridged zone and independent on the crack opening. The normal displacements of an upper crack surface are given by (plane stress state) [5]

$$\begin{aligned} u_0(x) = \frac{1}{E}\left(2\sigma_0 - \frac{4P_0}{\pi}\arccos\frac{h}{\ell}\right)\sqrt{\ell^2 - x^2} + \\ + \frac{P_0}{\pi E}\left[(x-h)\,F(\ell, x, h) - (x+h)\,F(\ell, x, -h)\right] \end{aligned} \tag{19}$$

where $h = \ell - d$, E is Young modulus of material, σ_0 is an external stress applied normal to the crack plane, P_0 is the normal bridge stress in the crack bridged zone of the size d and $F(\ell, x, h)$ is the source function given by [5]

$$F(\ell, x, \xi) = \ln\frac{\ell^2 - x\xi - \sqrt{(\ell^2 - x^2)(\ell^2 - \xi^2)}}{\ell^2 - x\xi + \sqrt{(\ell^2 - x^2)(\ell^2 - \xi^2)}} \tag{20}$$

Taking into account that in this case $Q(x) = P_0, \beta = 0$ (see (7b)), substituting these values into statement (7) and the crack opening from (19) $u_y(x) = 2u_0(x)$, $u_x(x) = 0$ into statement (12), we get after some tedious calculations the following relationships for the strain energy release rate and for the rate of the energy absorption ($t = d/\ell$)

$$G_{tip}(d,\ell) = G_f\left(1 - Z_0\, A\left(t\right)\right)^2, \quad G_{bond}(d,\ell) = 2G_f\varphi(t) + G_c \tag{21}$$

where

$$Z_0 = \frac{2P_0}{\pi\sigma_0}, \quad G_f = \frac{\sigma_0^2\pi\ell}{E} \tag{22}$$

$$A(t) = \arccos(1-t), \quad B(t) = \sqrt{2t - t^2}, \quad C(t) = (1-t)\ln(1-t) \tag{23}$$

and

$$\varphi(t) = Z_0\left\{A(t) - B(t) - Z_0\left[A(t)\left[A(t) - 2B(t)\right] - 2C(t)\right]\right\} \tag{24}$$

The first fracture condition (14a) can be written using the equations (21-24) as follow

$$2Z_0\left\{\left[2A(t) - B(t)\right] - Z_0\left[1.5A^2(t) - 2A(t)B(t) - 2C(t)\right]\right\} + 2\eta R_0 Z_0^2 - 1 = 0 \tag{25}$$

where

$$\eta = \frac{G_c}{G_b}, \quad G_b = P_0\delta_{cr}, \quad R_0 = \frac{\pi E\delta_{cr}}{8P_0\ell} \tag{26}$$

The second fracture condition (14b) in this case is

$$\frac{B(t)}{Z_0} - \left[A(t)B(t) + C(t)\right] = R_0 \tag{27}$$

The equations (25) and (27) is the nonlinear algebraic system and the solution of this system (if it exists) give us the external critical stress and the size of the crack bridged zone in the crack limit equilibrium state. The nonlinear algebraic system is solved numerically and the main parameters governing the solution of the system are η and R_0. At the fixed value of η the solution of the system exists if $R_0 < R_f$, where R_f is the critical value of R_0 (see section 3.1). If the solution of the system does not exist (under the fixed values of E, P_0, δ_{cr}) then, from mechanical point of view, the size of the crack is less than the crack size of qusiatartic crack growth beginning. In this case the subcritical crack growth is observed (see conditions (15)-(16)).

We shall consider further subcritical growth of a crack with the bridged zone, supposing, that there is initial slit of the size $2\ell_0 \geq 0$ without bonds and the crack bridged zone of the size $2d$ is formed at monotonic increasing of the external loading. Then $t = \ell_0/(\ell_0 + d)$. Let's suppose, that external loading changes in such a manner that at each current size of the crack bridged zone the condition (14a) is satisfied, and the crack opening at the edge of the bridged zone does not exceed the critical value (condition (16)). The dependence of the external loading on the size of the crack bridged zone in this case can be obtained from the equation (25), considering it as the quadratic equation of the parameter Z_0

$$\frac{\sigma_0}{P_0} = \frac{2}{\pi}\left[2A(t) - B(t) + \sqrt{A^2(t) + B^2(t) + 4C(t) + 2\eta R_0}\right] \tag{28}$$

At increase of external loading according to the equation (28) occurs subcritical growth of the crack, the size of the crack bridged zone grows and achieves the critical size if the condition (14b) is fulfilled. For reservation of a quasistatical mode of the crack growth further it is necessary to reduce the external loading so that the equations (14a) and (14b) were carried out together.

Next we shall consider two asymptotic cases for a crack totally filled by bonds (region of a weak material bonds) and a crack with a small bridged zone (the small scale bridging limit).

3.1 Crack totally filled by bonds

Let's consider the crack totally filled by bonds, $t = (d/\ell) = 1$, see eqs. (21-27) under monotonic increasing of an external loading. The condition (27) in this case is reduced to the expression determining the value of critical external loading, at which the break of bonds at the center of a crack begins

$$\frac{\sigma_{cr}}{P_0} = 1 + \frac{2R_0}{\pi} \tag{29}$$

In this problem at monotonic loading the value (12) increases faster than the value (6) and the equality of these functions is achieved at the external loading value σ_m satisfying to the condition (14a). Using the equations (21) we shall receive from the condition (14a) for the crack totally filled by bonds

$$\frac{\sigma_m}{P_0} = 2\left(1 - \frac{1}{\pi}\right) + \sqrt{1 + \frac{4}{\pi^2}\left(1 + 2\eta R_0\right)} \tag{30}$$

The values σ_{cr} and σ_m depend on the values $\eta = const$ and R_0 (this parameter decreases at the crack growth). If $\sigma_{cr} > \sigma_m$ then at the fulfillment of the condition (30) at increase of external loading the crack tip will advance without break of bonds. The fulfillment of the condition (14b) results in the beginning of break of bonds at the center of the crack and formation of the zone free from bonds. Let's determine the critical value of the parameter $R_0 = R_f$, at which $\sigma_{cr} = \sigma_m = \sigma_f$. From the relationships (29-30) is obtained

$$R_f^2 - R_f\left[\pi + 2\left(\eta - 1\right)\right] - \pi = 0$$

and, hence,

$$R_f = \frac{\pi}{2}\left[\left(1 + \frac{2\left(\eta - 1\right)}{\pi}\right) + \sqrt{\left(1 + \frac{2\left(\eta - 1\right)}{\pi}\right)^2 + \frac{4}{\pi}}\right] \tag{31}$$

Note, that in the considered case the crack represents a zone of the weakened bonds in a material and the initial 'ordinary' crack is absent. Thus, the expressions (30) gives an estimation of strength of a material without a crack.

At the fixed parameters of a material and bonds (E, P_0, δ_{cr}) the expressions (26) and (31) allow estimation of the length of an initial crack (ℓ_f), at which quasistatic growth of a crack is started under conditions (14a-14b)

$$\ell_f = \frac{\pi E \delta_{cr}}{8 P_0 R_f} \tag{32}$$

and the numerical calculations show that the solution of the nonlinear algebraic system (the equations (25) and (27)) exists if $R_0 < R_f$. On the other hand, choice of parameters of bond (P_0, δ_{cr}) is possible so that the condition (32) was carried out for a crack of the given size.

3.2 Small size of a crack bridged zone

Let's consider the crack under the small scale bridging condition [6]. In this case $t \to 0$ and the equations (25) and (27) can be written as follow

$$\left(Z_0\xi\right)^2 - 2Z_0\xi - 2\eta R_0 Z_0^2 + 1 = 0, \qquad Z_0(0.5\xi^2 + R_0) - \xi = 0 \tag{33}$$

where $\xi = \sqrt{2d/\ell}$. From eqs.(33) we obtain the critical bridged zone size which is independent on the crack size in a small scale bridging limit

$$d_{cr} = d_\infty = \frac{\pi E \delta_{cr}}{8 P_0}\left(\sqrt{\eta + 1} - \sqrt{\eta}\right)^2 \tag{34}$$

and the critical external stress

$$\sigma_{cr} = \sqrt{(1+\eta)\,\frac{EP_0\delta_{cr}}{\pi\ell}} = \sqrt{\frac{E\,(G_b+G_c)}{\pi\ell}} \tag{35}$$

The size and shape of the crack bridged zone do not change in the case of small scale bridging, therefore, the condition of an autonomy of the bridged zone is satisfied and the energy absorbed to bonds in the bridged zone is equal to the energy released at break of the bond at the edge of the bridged zone. Thus, total flow of the energy to the crack tip is spent for formation of a new surface of the crack. For this reason relationships (34-35) coincide with results which was obtained in [6, 7] using the two-parametric fracture criterion with force first condition of fracture $K_0 - K_b = K_{Ic}$, where K_0 is the SIF due to an external loading, K_b is the SIF due to bonds and K_{Ic} is a matrix toughness.

The expression (28) for subcritical crack growth in the small scale bridging limit is

$$\frac{\sigma_0}{P_0} = \frac{2}{\pi}\left[\sqrt{2t} + \sqrt{2\eta R_0}\,\right], \quad t = \frac{d}{\ell} \tag{36}$$

and this expression coincide with the results in [8] for a material with zero matrix toughness $\eta = 0$.

Acknowledgements

This work was supported by the RFBR, the project number is 08-08-00798-a.

References

[1] Goldstein, RV, Perelmuter, MN. Modelling of bonding at an interface crack, International J. of Fracture, 1999, **99** (1-2), 53-79.

[2] Perelmuter, MN. Polymer interface crack and adhesion resistance, In: Proc. of Workshop 'Mechanical Reliability of Polymeric Materials and Plastic Packages of IC Devices', pp.231-236, Paris, France, 1998

[3] Salganik, RL. Brittle fracture of glued bodies, Appl. Math. Mech. (PMM),1963, **27**, (5), 957-965.

[4] Perelmuter M. A criterion for the growth of cracks with bonds in the end zone, Appl. Math. Mech. (PMM), 2007, **71**, (1), 137-153.

[5] Panasyuk, VV. Limiting Equilibrium of Brittle Solids with Fractures. Michigan Information Service, Detroit, 1971, 284 pp.

[6] Cox, BN, Marshall, DB. Concepts for bridged cracks in fracture and fatigue, Acta metal mater., 1994, **42**, (2), 341-363.

[7] Massabo, R, Cox, BN. Concepts for Bridged Mode II Delamination Cracks, J. Mech. Phys. Solids, 1999, **47**, 1265-1300.

[8] Ungsuwarungsri, T, Knauss, WG. A nonlinear analysis of an equilibrium craze: Part II - Simulation of craze and crack growth, Trans. ASME, J. of Appl. Mech., 1988, **55**, 52-58.

Perelmuter Mikhail
Institute for Problems of Mechanics of RAS,
pr. Vernadkogo, 101-1, 119526, Moscow, Russia

Fatigue assessment of structures in high-cycle segment: technique and problems

S. V. Petinov I. M. Afanasyeva
spetinov@mail.ru

Abstract

Common rules for fatigue assessment of hull structures in formats "Hot–spot – or Notch stress – Fatigue life" are based on implication of elastic behavior of material at critical locations and one may expect a conservative estimation of fatigue resistance. A more physically reliable evaluation of fatigue damage may be provided by applying the "Strain–life" criterion; however, uncertainties imbedded into current procedures, specifically in the high–cycle region, remain and affect the results as shown briefly in an example. The main sources of uncertainties are indicated and the directions of further development of procedures are discussed.

1 Foreword

Fatigue assessment of ship structures is presently a standard component of structural design [5, 9]. The general scheme and principal components of fatigue analysis are established around 40 years ago, and the present methodology is developed with participation of the IACS experts through the recent decades.

The central component of the analysis is the cumulative law of the damage, "harmonizing" the random loading histories and material fatigue resistance data being collected via cyclic loading testing. The latter are given by S–N ("Stress – Life") curves. The loading history is typically assessed in the form of long–term statistical stress distribution and its parameters calculated for a particular structural detail considered prone for fatigue in dependence of the detail location in hull structure, the ship service profile, etc. The local stress raise, stress concentration is typically estimated in the format of "Hot–spot stress", stress at the expected fatigue process site [2, 3, 5, 6]. Also, a deemed more correct procedure of evaluation of local stress, "Notch stress" format is advised alternatively [1, 5]. When a typified hull detail is under the scope, the "Nominal stress" approach can be applied.

The stress analysis has to be carried out using the finite–element method (FEM) via the two–step procedure. First, the finite–element (FE) model of the hull or its representative part (e.g., including 3 cargo compartments) is developed, so–called "global model". Further, the local FE models of selected details are designed in compliance with the applied approach, e.g., "Hot–spot stress". Respectively, the appropriate S–N curve depending on the local stress evaluation procedure has to be chosen from the database.

The common of the above approaches is the assumption of linear elastic behavior of material in the range of service stress and stress concentrations, which is equivalent to application of theoretical stress concentration factors regardless of the stress value. Considering mechanics of fatigue of polycrystalline materials, one would expect uncertainty in assessing the fatigue properties of structural details on the conservative side in the whole stress range. A more physically reliable evaluation of fatigue damage may be provided by applying the "Strain–life" format; however, it concerns mostly the high–stress segment. In the high–cycle range where the plastic strain component becomes unintelligible in mechanical testing and in theoretical interpretations of test results, the "Strain–life" approach barely may be a preferable procedure.

To add, the "Nominal stress" approach is aimed at approximate evaluation of fatigue properties of structural details whereas the "Hot–spot stress" and "Notch stress" schemes have to

provide nearly identical estimations of accumulated fatigue damage or fatigue strength characteristics. However, analysis reveals essential differences in fatigue properties of the same structural details when different approaches are applied. This is shown in examples; the feasible sources of incoherence of results are discussed.

2 Common Procedures of Fatigue Analysis

For illustration a dry–cargo ship "Mormacscan" is selected, which undergone full–scale tests aimed at evaluation of statistical parameters of wave loads [4]. Several of ship particulars are: length, bpp, L = 139 m, beam, B = 20.7 m, midship upper deck section modulus, $W_{min} = 59945m \cdot cm^2$; intended fatigue life defined by the number of "stress cycles" is 10^8; usage factor (sailing time vs. total life) = 0.7.

For simplicity of illustration, the only loading mode was considered, hull bending in vertical plane on assumption that ship was oriented towards the seas. The long–term bending moment distribution is approximated by the two–parameter Weibull formula [6]:

$$Q\left(\Delta M_v > \Delta M_v^*\right) = \exp\left(-\left(\Delta M_v^*/a_M\right)^k\right) \tag{1}$$

where a_M is the scale factor and k is the shape factor of statistical (Weibull) distribution of bending moments; M is the bending moment defined by exceedance $Q = 10^{-8}$ obtained according the rules. If the distribution shape factor is, approximately, $k = 1.05$ (dry cargo ship, with moderate speed), the scale factor can be given by $a_M = \Delta M_v^*/(-\ln(10^{-8}))^{1/k} = 54.77, MNm$. The nominal stress long–term distribution scale factor for the upper deck, midship section, is, respectively, $a_s = a_M/W_{\min} = 9.14, MPa$.

As a representative, an upper deck bracket detail in connection of a longitudinal deck plating stiffener and transverse bulkhead is considered, Fig. 1. The stress raise is expected at the bracket ending weld toe due to localized transfer of stress from the longitudinal flange to the bracket accentuated by blunting of the bracket.

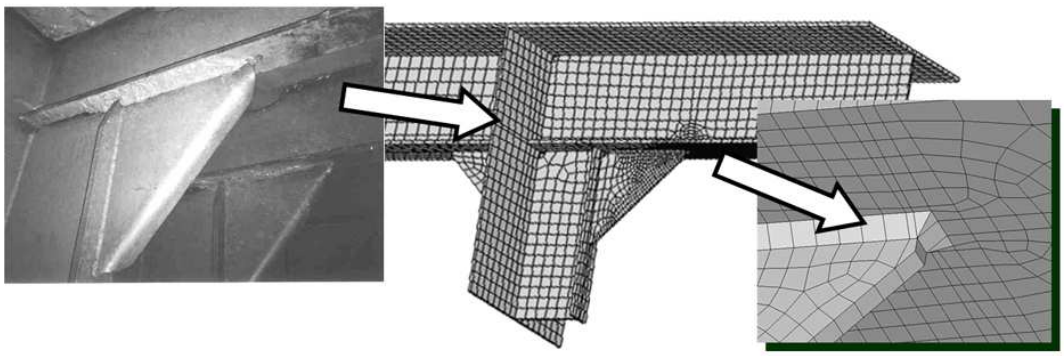


Figure 1: Structural detail and FE model with fragment of FE mesh at the bracket ending

Firstly, the ***hot–spot stress approach*** is used and respectively, FE model of the detail was designed meeting the requirements [5, 8], which needed relatively fine mesh in the area including and surrounding the assumed crack initiation site – the bracket and weld ending, as shown in Fig. 1. The weld profile was assumed with the slope angle 45°, the weld leg equal to 8 mm; the weld toe radius was not considered. Fig. 1 shows also details of geometrical modeling aimed at providing the necessary mesh properties and local stress resolution.

The uniformly distributed tensile stress was applied to the FE model of the detail; calculated stresses in front of the bracket ending and weld were extrapolated to the weld toe and the "hot–spot" stress was found. Respectively, the "hot–spot" stress concentration factor was estimated as $K_{HS} = \sigma_{HS}/\sigma_{nom} = 2.18$. Further, the Weibull "hot–spot" stress distribution scale parameter was obtained: $a_{HS} = 9.14 \cdot 2.18 = 19.92, MPa$.

When the "hot–spot stress" approach is applied the Rules [5] advise the S–N curve of the D–Class (continuous butt–welded joint loaded normally to the weld line) $N(S) = C/S^m$. First, the "single–slope" curve with parameters $C = 1.52 \cdot 10^{12}$ and $m = 3$ is applied, which would result in conservative estimate of damage. The still–water bending moments are not considered; then, according the linear damage summation rule the fatigue damage index is found as:

$$D = (kN_1/Ca_{HS}^k) \int_{S_{\min}}^{S_{\max}} S^{m+k-1} \exp(-(S/a_{HS})^k) dS = 1.68 \tag{2}$$

The Rules [5] do not identify the minimum damaging stress; provisionally, it was taken equal $S_{\min} = 20,\ MPa$, the value in the range of stresses insignificantly influencing the total damage. The damage estimated is essentially greater than might be expected for an ordinary detail without a sharp notch.

Hoping to attain at a more realistic result, the "two–slope" S–N curve (D–class) is applied. The segment characterizes the damage due to stress ranges below conventional fatigue limit stress actuated by the irregular loading successions [2]. This turn the damage becomes $D = (kN_1/C_1a_{HS}^k)(\int_{S_q}^{S_{\max}} S^{m_1+k-1} \exp(-(S/a_{HS})^k) dS + (C_2/C_1) \int_{S_{\min}}^{S_q} S^{m_2+k-1} \exp(-(S/a_{HS})^k) dS) = 1.24$ where $C_1 = 1.52 \cdot 10^{12}$, $m_1 = 3.0$; $S_q = 53.4\ MPa$ is the stress range at the slope transition in the S–N curve at $N = 10^7$ cycles; $C_2 = 2.917 \cdot 10^{16}$ and $m_1 = 5.0$ are the D–class S–N curve parameters at $N \geqslant 10^7$ cycles.

As seen, by taking into account the "post–jog" portion of the S–N curve does not substantially improve the result. It may be explained by the fact that the dominating part of damage is formed due to stress ranges exceeding the "jog" stress range, $S_q = 53.4,\ MPa$ (which corresponds to $N = 10^7$, at nominal stress amplitudes about 12.25 MPa). Again, the damage at rather moderate stress concentration (hot–spot) and moderate loading history ($a_s = 9.14MPa$ [4]) occurs *excessive* for a typical structural detail.

Further, the "Notch stress" approach can be applied to assess the damage. This turn, the FE model with essentially fine mesh at the expected damage area was designed following the IIW instructions [1]: transition from the parent to weld material at the weld toe is radiused, the radius of curvature is taken 1 mm. FE sizes along the arc are equal to 0.2 mm to provide the necessary stress resolution, Fig. 2.

Stress concentration factor ("theoretical") was found equal $K_t = 4.0$, and the scale parameter of the maximum local stress Weibull distribution is $a_{loc} = 9.14 \cdot 4.0 = 36.56,\ MPa$. The respective S–N curve – according the IIW recipes is the FAT225 curve, with parameters of segments:
Segment 1: $N \leqslant 7.59 \cdot 105, S \geqslant 310.7MPa, C1 = 2.20e18, m = 5$;
Segment 2: $7.59 \cdot 105 \leqslant N \leqslant 107, 131.6 \leqslant S \leqslant 310.7, MPa, C2 = 2.278e13, m = 3$;
Segment 3: $N \geqslant 107, S \leqslant 131.6, MPa, C3 = 3.944e17, m = 5$.

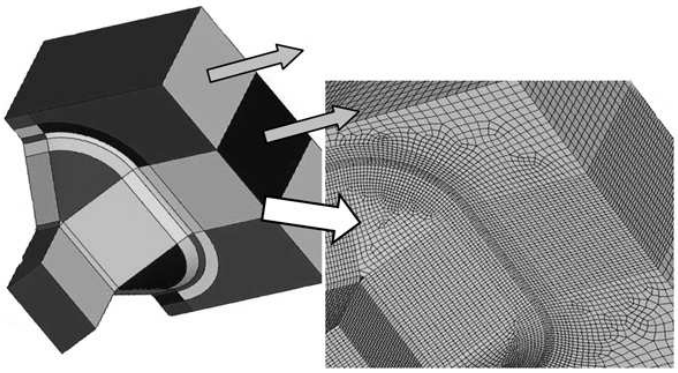


Figure 2: Block geometrical and FE models of the bracket and weld ending, "Notch stress" approach

The accumulated damage in this case occurs equal to: $D = 0.534...0.538$. These values correspond to provisionally assumed minimum damaging stress in the range $S_{min3} = 50...80MPa$. The input of relatively large stress ranges (within Segment 1, $S \geqslant S_{\min 1}$) is found insignificant, around 0.0045.

The total damage might be considered realistic; however the mismatch (almost 3 times, compared to the above results) cannot be regarded acceptable.

Further, deemed a more physically consistent and developed in mechanical engineering "Strain–life" approach may be applied. The approach is based on apprehension of material plasticity directly associated with fatigue damage. It incorporates description of elastic–plastic cyclic properties of material (family of cyclic curves) and material fatigue failure criterion [10]. Several versions of the criterion are developed; in the present analysis a simplified form is selected which provides conservative estimations of the damage. However, the criterion is completed with corrections considering effects of material microplasticity on the damage accumulation in stress concentration area under irregular loading:

$$\Delta\varepsilon = CN^{-\alpha} + 2\beta\sigma_{-1}K_t/EK_f \tag{3}$$

where $C = 0.400, a = 0.654$ [10]; $\sigma_{-1} \approx 110, MPa$, is the fatigue limit stress of the heat–affected zone, rolling skin removed [5]; $\beta = 0.8$, is the correction for the fatigue limit stress decreasing under irregular loading [2]; K_f – fatigue notch factor, $K_f = 1 + (K_t - 1)/(1 + g/r)$, where r is the notch root radius ($r = 1mm$, at the weld toe according the IIW recommendations [1, 3]), g – "material structure parameter", a volume at the notch root dimension approximately corresponding to fatigue crack transition from the shear into the normal opening mode [8]. For hull structural steels (with the yield stress in the range 235 – 390, MPa) this parameter may be defined by relationship: $g = 0.38(350/\sigma_u)^{1.16}$, where σ_u is the ultimate strength, MPa. The cyclic strain at the weld toe may be estimated by applying the empirical formula [10]:

$$\Delta\varepsilon = (K_t\Delta\sigma_n/E)(1 + M_s(r,t)F(\sigma_m)(AK_t\Delta\sigma_n/\sigma_c - 1)^{\beta}) \tag{4}$$

where $\Delta\sigma_n$ is the nominal stress range, $A = 1.25, \beta = 1.20$ are empirical parameters; $M_s\,(r,t)$ is the correction for the scale factor, $M_s\,(r,t) = M_0/\,(1 + (a/t)^s(r/t)^q)$. Here M_0, a, s and q are empirical parameters, obtained from systematic tests of notched specimens [10], $M_0 = 0.155, a = 0.24, s = 0.30$ and $q = 1.50$ for the steel considered; $F\,(\sigma_m)$ is the plastic strain correction for the mean stress effects at the notch root [10], neglected in the present analysis, $F\,(\sigma_m) = 1$. The linear summation procedure (addressed to the "nominal stress" format) results in:

$$D = (N * (\sigma_{-1}/CE)^{1/\alpha}) \int p(\sigma_n)(E\Delta\varepsilon/\sigma_{-1} - 2\beta K_t/K_f)^{1/\alpha} d\sigma_n \tag{5}$$

At the mentioned values of material and loading history parameters the damage index is equal: D = 0.398, assumed acceptable value. However, matching of the damage index with the estimated by the "Notch–stress–Life" approach may be regarded rather casual, insufficient for selection of a preferred method of analysis. To add "more light" into the problem, it may be useful to compare the damage intensity assessed by the above approaches (integrands in (1), (5)). The results are shown in Fig. 3. It is seen, the most essential difference of the damage intensities is concentrated in the range of moderate and small stress amplitudes, related to the high–cycle fatigue.

One more example of fatigue analysis of a typical ship hull structural detail may be appropriate. This is the deck hatch corner structural detail (Fig. 4). In the past it was frequently one of the critical areas of hull structure affected by fatigue. Cracks originated in the deck plating at the opening corner, mostly in welded joints of structural components.

The geometrical model incorporates typical structural components, hatch coaming and longitudinal girder, beams and fragment of the side structure; FE mesh was developed for the most stressed area at the opening rounded corner so that the necessary stress resolution for assessing the stress concentration would be provided, Fig. 4. The stress concentration factor, $K_t = \sigma_{\max}/\sigma_{nom} = 2.54$, was obtained in the case of the hull bending in vertical plane (tensile loading of the detail). The scale factor of local stress long–term distribution for the affected area of the deck detail is: $a_{loc} = 9.14 \cdot 2.54 = 23.2,\ MPa$.

Firstly, the Local (Notch) stress approach was applied (the Hot–spot stress approach in this case is inappropriate since the most stressed area covers in general the base material). The respective Class S–N curve was selected according IACS recommendations (IACS, 2006): it was the C–Class curve with parameters of equation $N(S) = C/S^m$: $C = 4.23 \cdot 10^{13}$ and the slope factor $m = 3.5$ for the S–N curve fragment limited by $N \leqslant 10^7$ cycles. When the single–slope approximation is applied, and minimum damaging stress range provisionally selected (based on analysis of its

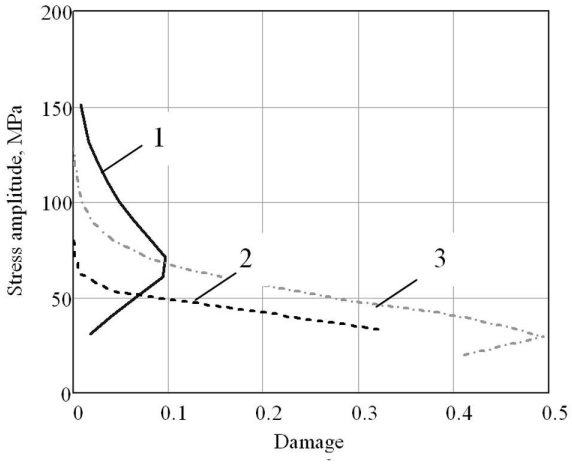


Figure 3: The damage intensity vs. stress amplitude: (1) – "Notch stress" approach; (2) – "Local strain" approach; (3) – "Hot–spot stress" scheme

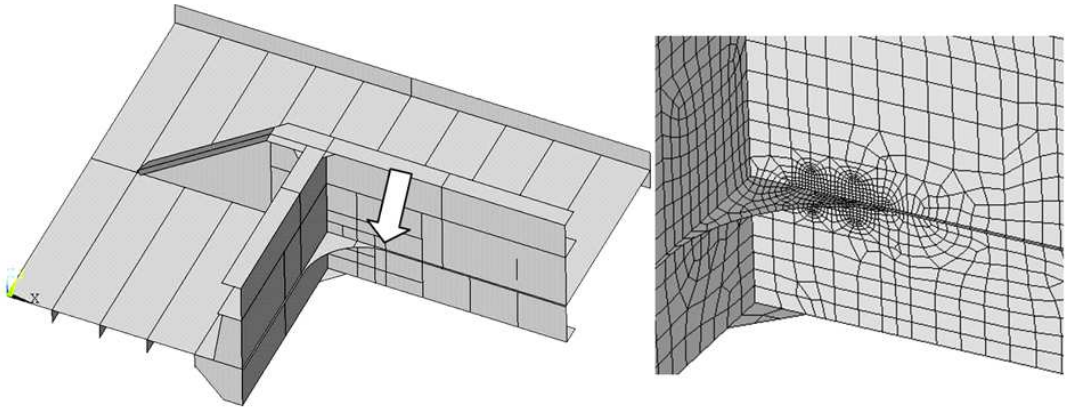


Figure 4: Hatch corner structure: geometrical model, critical area indicated with arrow and respective FE model

influence on the damage index) is $S_{\min} = 30\ MPa$, the accumulated damage results in: $D = (kN_1/Ca_{loc}^k) \int_{S_{\min}}^{S_{\max}} S_{loc}^{m+k-1} \exp(-S_{loc}/a_{loc})^k dS_{loc} = 0.898$

When the two–slope C–Class S–N curve would be applied, the damage calculated occurs somewhat smaller, $D = 0.746$.

It should be immediately noted that these values of the damage index can be considered excessive for the detail design proved by long practice since casualties of 1940–50–ies.

Now, the damage is assessed using the Local strain approach. The Strain–life criterion is accepted in the same form (4), with the same parameters. Fatigue notch factor, K_f, this turn is nearly the same as the theoretical one, i.e., $K_f = 2.53$, because of large radius of curvature of the deck plating. Assuming fatigue limit stress $\sigma_{-1} \approx 110, MPa$ (longitudinal welds in the deck plating–coaming joint), we have the damage index value: $D = 0.024$ offering more than $N = 10^9$ cycles of fatigue life.

Again, the "Notch stress–Life" and "Local strain–Life" approaches result in substantially different values of damage for the same location, the same material and loading history.

3 Conclusions

The above examples cover only two of multiplicity of typical structural details. However, the results of analysis may be indicative of one of the fatigue methodology problems. It is seen that currently advised HSS, Notch stress techniques and Local strain approach did not provide the desired convergence of results of fatigue damage assessment.

The mentioned insufficient confidence may be explained mostly by certain provisions in fatigue models, which concern selection of S–N curves, fairly approximately following the principle of identity of damage in test specimens and in structural detail, design of FE models, selection of the FE type, etc. E.g., the D–Class S–N curve applied in the "Hot–spot stress" approach is attributed to "continuous full penetration butt welds made manually or by an automatic submerged or open arc process ...". The most substantial condition of damage identity [10] in D–Class test specimen and in the detail under the scope with concentrated transfer of stress flow practically is not realized. And moreover, S–N curve FAT225 is defined from FAT160 curve in a sense artificially, as mentioned in [1].

Further, the distinction between the "parent material" and "weld material" is obviously necessary; however, experimental evaluation of fatigue properties of the weld material and material at the weld toe (which is the fusion zone of the joint material) is barely feasible.

And the most important factor is that the S–N methodologies are based on assumption of elastic behavior of material, even in the stress concentration areas. Although the damage accumulated due to the high stress segment of the loading history is overestimated by allowing for elastic deformation, it concerns insignificant part of the total damage.

The most substantial, unnecessary conservative error of the damage assessment develops in the high–cycle region of fatigue where the material microplasticity, ignored in current approaches, reduces effects of stress concentration. This may be considered by applying the notch factor instead of theoretical stress concentration factor, although Peterson's method (and others known in literature) developed for applications in mechanical engineering, needs in adjustment for welded joints.

The Strain–life approach is regarded in ship technology as an optional one. Although it is based on considering effects of cyclic plasticity and may be deemed a more physically rigorous, it reveals the confident assessment of damage mostly in the high–stress region. In the high–cycle segment the plastic strain is being averaged over the volume of gage part of specimen, becomes barely distinctive and cannot be a representative of the damage per load cycle.

Respectively, the structure of the Strain–Life criterion should be re–analyzed and modified; same concerns evaluation of the cyclic stress–strain curves.

Acknowledgements

The work was supported by the Russian Academy of Sciences Grant NP–130E.

References

[1] Fricke, W (2008) Guideline for the Fatigue Assessment by Notch Stress Analysis for Welded Structures, IIW–Doc. XIII–2240r1–08/XV–1289r1–08

[2] Haibach, E (1989) Betriebsfestigkeit. Verfahren und Daten zur Bauteilberechnung. VDI Verlag

[3] Hobbacher, A (2007) Recommendations for Fatigue Design of Welded Joints and Components. IIW Document XIII–2151r1–07 / XV–1254r1–07

[4] Hoffman, D, Lewis, EV (1969) Analysis and Interpretation of Full–scale Data on Midship Bending Stresses of Dry Cargo Ships, Ship Structure Committee Report, SSC–196

[5] IACS (2006) Common Structural Rules for Double Hull Oil Tankers

[6] Korotkin, Ja.I, Rabinovich, ON and Rostovtsev, DM (1987) Wave Loads on Ship Hull. Leningrad, Sudostroenie Publ.

[7] Marshall, PW (1974) Basic Considerations for Tubular Joint Design in Offshore Construction. WRC Bulletin 193. NY

[8] Miller, KJ (1993) Materials Science Perspective of Metal Fatigue Resistance. Materials Science and Technology, Vol .9, pp.453–462

[9] Niemi, E, Fricke, W and Maddox, S (2006): Fatigue Analysis of Welded Joints – Designer's Guide to the Structural Hot–spot Stress Approach. Cambridge, Woodhead Publ.

[10] Petinov, SV (2003) Fatigue Analysis of Ship Structures. Backbone Publishing Co., NJ

Petinov S.V., IPME RAS, 199178, Russia, St. Petersburg, Bolshoi ave. of Vasilievsky Island, 61.
Afanasyeva I.M., "Pratt & Whitney Rus", Russia, St. Petersburg

A high sensitivity device for measuring bio-electrical impedance of human skin

A. Platonov V. Vitkov L. Inieva-Mitusova N. Serbenyuk O. Trifonov
V. Yaroshevskiy
tob@keldysh.ru

Abstract

The results of current R&D of mechanical stimulator for the human foot and sensitive bio-electrical impedance measuring device for bio-mechatronic trainer. The main goal of the joint project of RAS and BAS is to develop new technologies of rehabilitation of spinal patients.

1 Introduction

The Keldysh Institute of Applied Mathematics (Russian Academy of Sciences) in association with the Pavlov Institute of Physiology (Russian Academy of Sciences) and the Institute of Mechanics (Bulgarian Academy of Sciences) are involved in a joint project "Research and development of a system for bio-mechatronic receptor stimulator and functional recovery of spinal patients study". The project aims to develop a new method for spinal patients recovery and creation of new rehabilitation technology based on studies of locomotion control mechanisms of humans and animals, performed by its participants. In contradiction to the common opinion, the carried research showed that a possibility of spinal patient recovery exists. But it demands the development of bio-mechatronic systems for receptor stimulation and research of locomotion recovery in the case of spinal cord injury. Bio-mechatronic system consists of bio-mechanical trainer in conjunction with PC controlled sensors and effector elements, connected to the physician's monitor. A high efficiency of the bio-mechatronic system is reached due to a big variety of sensors and effector elements. The realization of this approach demands the development of new sensor and effector tools and devices. They can be widely used for patient recovery as well as for clinical research and basic physiological studies in animals.

The task of M.V. Keldysh Institute in this project is to develop the algorithms of sensor data processing, control algorithms for electromechanical system elements, algorithms and computer interface of physician with appropriate software tools mechatronic system. The new mechanisms for restoring locomotion functions of spinal patients developed in Pavlov's Institute is based on controlled tactile foot effects of a paralyzed leg. At present a draft human foot stimulator for the treatment of spinal patients and a bio-sensor device for the treatment output are developed by M.V. Keldysh Institute and Institute of Mechanics. In this paper we represent the roadmap of further development of mechatronic stimulator based on mechanical foot stimulator developed by Institute of Mechanics BAS.

2 Objectives and solutions for bio-mechatronic trainer design

It's well known that serious functional changes of human locomotorium happens after a spinal injury or disease. The lost of capability of independent movement happens often. Among the other patients these people has very small chances for health recovery, consumer and social rehabilitation. It is one of the most terrible diseases, that doesn't have treatment yet.

Nowadays the constant grow of the traffic and it's speed results in asignificant increase in traffic injuries . The increment of spinal patients In Russia is about 15,000 every year due to the different accidents. There're nearly 250,000 people in Russia who lost their ability to move because of spinal injuries, according to information from the Internet. U.S. statistics shows that over 4 million citizens have a severe locomotorium dysfunction.

That is why the problem of recovery of spinal patients is very important. In this regard, a number of a number of research centers and special funds were established worldwide aimed at finding effective methods and technical means of rehabilitation of patients with severe motion disabilities.

The systematic studies of control and locomotion activity of the spinal cord in the absence of connection with the higher central nervous system are running in Pavlov Institute of Physiology (RAS) Russia. And significant results were obtained. They proved the need of development of bio-mechatronic trainer, and showed the following results (U.Gerasimenko, O.Nikitin e.t. all 2000-2005ys) [1,2]:

- The existence in humans of the central generator of stepping movements, located in the second waist region of the spinal cord was proved.
- First time in the world an electrical stimulation of the spinal cord were used to start a generator of artificial pacing.
- A crucial importance of information flow from the receptors of the lower extremities in the regulation of activity and the parameters of the generator pacing were showed.

The primary importance of the right timing of haptic stimulation of the spinal patient's foot has been shown in Pavlov's Institute. This stimulation consists of continuous specialized sequential receptor activation. It should start as fast as it possible after injury and last for a very long time period in order to achieve the best results,. This stimulation emulates human walk that is a sequential change of pressure in different areas of the foot. The beneficial effect of these haptic impacts on feet of paralyzed legs allows to restore the metaphorically stepping-reference reflex. It was shown that the magnitude of the pressure on the reference site (foot) is a critical factor for reflex stepping movements recovery.

The first therapy result was achieved in experiments with a spinal cat. A hand massage with an imitation of stepping movements was performed by Dr. O.Nikitin for about a year for this cat. Finally the walking motion of paralyzed hind legs were restored. A prove of functional significance of foots receptors for central walking generator and activity regulation in spinal cord of human was the main breakthrough of this study.

It was a fundamental point for development of a mechatronic treadmill . The device consisted of a racetrack with additional mechanical tools that provided forced steps simulation of the paralyzed hind legs of a cat. A mechatronic control system provided a consistent gravity effect of the stepping legs. It was developed in M.V. Keldysh Intitute and widely used in Pavlov's Institute. For the first time a combination of electrical stimulation of the spinal cord and bio-mechanical stimulation of foot was studied with this treadmill.

The obtained results allow us to formulate the most important requirements for mechatronic bio-trainer: a mandatory load control on the elements of the human foot in the stepping simulation process. An example of desired harmonization of vertical load R on the foot showed at the figure below:

Thus it is possible to make a computer adjustment of the trainer to the patient's weight G and walking speed T. It's important to provide a wide range of the load adjustment, so spinal patient's muscle atrophy could be compensated. Another designation of the developed device is to reduce the total degree of spinal patient's atrophy , that results in loss of muscular weight and dramatic conduction decrease in the lower parts of neural system. The experiments showed a complete decay of the disconnected part of the neural system in 28 days after injury.

3 A problem of foot electro-diagnosing.

A bio-electrical impedance measuring device for human foot supposed to be a diagnostic tool for manual recovery method of spinal patients by Pavlov's Institute. The basis for it was an

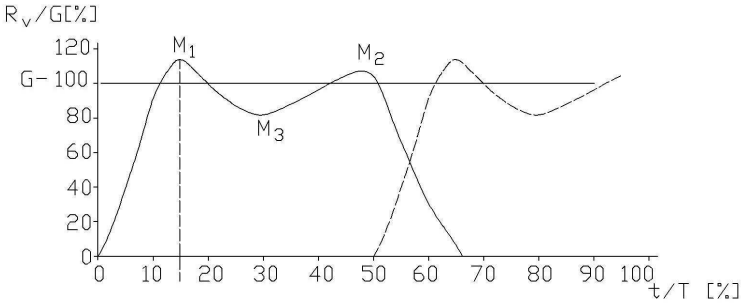


Figure 1: The force to the foot of support legs

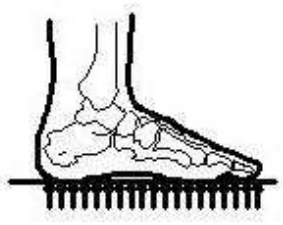


Figure 2: The tactile effector of foot

existence of dermal-visceral arc in human body, that represents the human body's internal organs in different points of the human skin (centrifugal "skin" branch of the arc) . The methods of pressure therapy and electrotherapy of internal organs via skin surface are well known (centripetal "visceral" branch of the arc) . The co-existence of these cutaneous-visceral reflex arcs along with the Pavlov's network of neural circuits is claimed to be proved [3]. For decades they are used in various systems of electro-acupuncture diagnostics, together with manual therapy and experiments on monkeys. The skin-visceral reflex arcs and the reflex arcs existence of the nervous system is explained [3] by general cellular origin and general growth of nerve and skin tissues, together with the blood and lymphatic vessels in the process of embryo-genesis.

Pavlov's Institute showed that a manual therapy of paralyzed feet with damaged neural system can bring a positive result. It looks quite logical to suppose that the main contribution can be brought by remaining dermal-visceral reflex arc. Taking into account that feedback mechanism "reflex ring" based on "reflex arc" by Bernstein [4], one can hope that reactivation and recovery of the feet control via dermal-visceral arc in some way is possible.

This suggestion needs experimental proofs. The device described below is and attempt in Keldysh's institute of developing bio-electrical impedance measuring tool for foot skin by the methods similar to Voll's and Nakatani's.

The skin active areas and biologically active points differ from the rest of the skin by a number of their properties (increased consumption of oxygen, temperature, etc.). The most interesting property of them for the mechatronic systems were discovered in 1946 by Japanese scientist. Any change in the electrical characteristics of these zones depends on external factors and internal conditions of the organism and varies from a value less than 1mm2 to about 1 cm2, and the position drift can be within 2 cm. The most frequently measured electrical parameters are:

- Skin electrical potential. It's 2..3mV higher for the biologically active points then the surrounding area [5] for healthy people. And it can deviate up and down depending on the severity of the disease. There are weak electric currents under the skin also. They are the so-called "own electrical forces" with the magnitude of 3 to 6 mA.

- Bio-electric impedance between two points of the body. Voll-Werner device measures the resistance between the palm and skin active area with the voltage 1,2 - 1,5V and currents from 0 to 20 mA (60 KOhm and more). It scales the response signal within 100 units. The

healthy people are expected to testify in 50-65 units, and the testimony of 70 and above correspond to an inflammatory process reflected by the body, while readings below 50 units signify the decline of the functioning of the organ.

The most interesting skin active aria's meridians of foot for impedance analysis are the ones used in pressed reflexology

One can see that there are plenty of skin active areas on the foot, but only one of them represents a man's feet health condition. It's located near the outside of the heel.

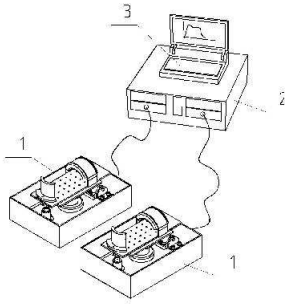


Figure 3: The conception of sensor shoe

And it brings idea of a low informative response in foot electro-diagnosing of spinal patients. It should be testified with primary attention to the mentioned area, that represents condition of foot joints.

4 A model of a high sensitivity device for measuring bio-electrical impedance of human skin.

The requirements applied to the device developed by Keldysh Institute were more demanding then for the devices used in common electro-diagnostic practice. It should have a very hight sensitivity and provide the least influence on the human during measurement cycle.

These requirements are caused by:

- The expectation of a very weak deviations from the normal parameters of the conduction of the patient's insensitive foot.
- The intention to avoid false activation of human organism by the output voltage of the device. In this case it is important to detect the absence of rupture of the dermal-visceral reflex arc with it's organ, but not only indicating the state of the internal organ reflected to the measured point.

The implementation of measurement of human and animal skin impedance is based on constant current approach. Point or surface electrodes applied to the area or point of interest. A program defined constant current is applied to them. The voltage drop between the electrodes is measured. One can notice that the current applied runs through the whole body, not only the skin. That's why a separate study should be taken on this problem, considering unusual diagnostic challenge of paralyzed leg.

The value of measuring current is about 1uA and corresponds to the safety level of the patient. The same approach is implemented in the control algorithms: the smaller impedance the smaller voltage drop at the tested area. The data passed to the PC by USB channel and processed there by software. During the diagnostic process the patient is grounded for safety as well as the device itself. This solution provides the best protection for the patient of the power circuits failures and reduce the electrical and electromagnetic interference on the obtained results.

These are the main requirements considered in device schematics:

- Constant current measurement.

- Operation current range is 1..10uA.
- Impedance should me measured by voltage drop between electrodes.
- The direction of current flow should be software controlled.

There are the main parameters of the developed device:

- PC communication channel USB 1.1.
- Digital power supply is +5V by USB.
- Analog power supply is ±4,5V and provided by 6 AA batteries .
- Maximum consumption current of analog part is 10mA. Life span of the batteries is about 100 hours under these conditions.
- Measuring current from 62 nA to 250uA.
- Measuring voltage ±2.0V
- ADC frequency is 15...240Hz with 12...16bit digitization.

5 The device schematics

The device can be divided in 3 functional modules:

- ADC module.
- Current source module
- DSP module

The ADC module is based on ADS1112 by Texas Instruments and instrumental amplifier AD8224 by Analog Devices.

The AD8224 choice is based on device requirements – the drain currents should be very small, it should have a wide range power supply voltage and built-in ESD protection. This device has the following characteristics:

- Drain current is 25pA.
- Supply voltage is ±18V
- ESD protection is 4kV

The instrumental amplifier AD8224 is connected by differential mode schematic with gain coefficient equal 1. It protects electrodes from external currents and CRM protection of the ADC input. The main interference frequency is 50Hz and comes by air from power supply network. Some times the amplitude of the interference reaches up to 2V at 200kOhm. It was the main reason for maximum extension of input voltage range.

A resistors set with value of 1360KOhm is connected in parallel with output electrodes. It protects ADC module from saturation of the ADC under external interference.

The output of AD8224 is directly connected to the ADS1112. The requirements for the ADC were differential input and at least 12bit quantization. The ADS1112 fits all demands and has some bonuses:

- Variable capture frequency 15..240Hz.
- Variable quantization depth 12..16bit.
- Built-in reference voltage module with accuracy ±1mV

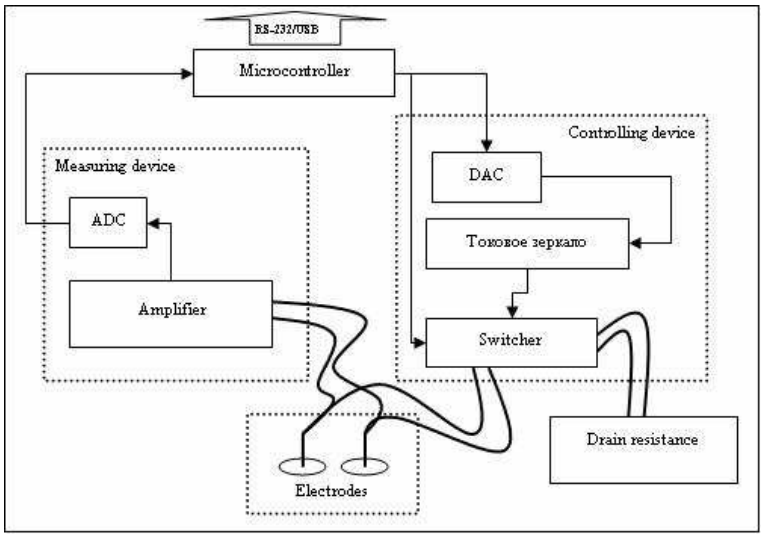


Figure 4: The scheme of device

- Small case.

There's a reference voltage supply REF3220 by Texas Instruments also. It has 4mV accuracy used as a reference source for AD8224.

The current source module consists of digital-to-analog converter and current mirrors set.

The Texas Instrument's DAC2932 was used as a primary current source. It has low voltage (3.3V) power supply and high frequency transfer function – up to 40MHz. It has 12-bit dual channel current output module with scalable range. And it can be adjusted to 500uA full scale current for each channel. But this current can't be passed directly to the electrodes of device because of two reasons. First is the low voltage output – full scale voltage is 3.3V and for small currents it would be much smaller. The second problem is the lack of current direction control. For solving all this problems the set of current mirrors were used.

The current mirror set is assembled from matched transistors by NXP semiconductors PMP4201 and PMP5201 series. There are eight current mirrors, four mirrors for each DAC current channel. They provide the maximum precision transfer function for output circuit and extends output voltage to ± 3.8V with ± 4.5V power supply. Both DAC channel have opposite connection to the electrodes though the current mirrors, as a solution for the current direction switching.

The DSP module is based on MP430F1611 MCU by Texas Instruments. It is a 16-bit RISC CPU with clock frequency up to 16Mhz, ultra low power consumption and wide set of peripherals. The main argument in favor of MSP430 series were low voltage supply 1,8-3.3V and ultra low power consumption 250uA/MIPS. And it has a good tools for software development with C++.

The other parts of DSP module are

- TPS76333 LDV Power convertor from USB to 3.3V
- FT232 RS232-USB converter.
- Indicating LEDs and buttons.

Measurement process can be divided in two parts.

1. ADC reading and regular noise reduction. The ADC reading cycle occurs on the ready-signal, generated by ADC at the end of digitization. After that the data is transferred to the noise clearing software. The maximal, minimal and their timing are detected. The frequency of the noise and phase shift of data are evaluated. The data transferred to the PC upon external request.

2. PC messages and commands processing. In every DSP cycle of ADC reading a check of commands arrival from PC and their execution are performed. This is the list of the commands:

- ADC power up and down.

- Automatic current scaling.
- Manual current set.
- Flash led frequency.
- Current switching mode and it's timing.

The DSP has opened interrupts of timer with 10ms interval and communication port interface for PC connection. The timer works continuously and the communication port only during PC communication.

The current direction switch check and the led flashing control are performed in the timer interrupt. Here's the led flashing algorithm. It changes the state upon the PC request arrival. In the case of absence of the PC requests for 2 seconds led starts flashing with the interval of 2 seconds and the DAC shuts down. During the active data flow from the PC the led frequency is about 10Hz.

At this moment the following function were implemented:

- Adjustment of the device
- Preliminary data analysis for feature detection.

A print screen of it is shown at the

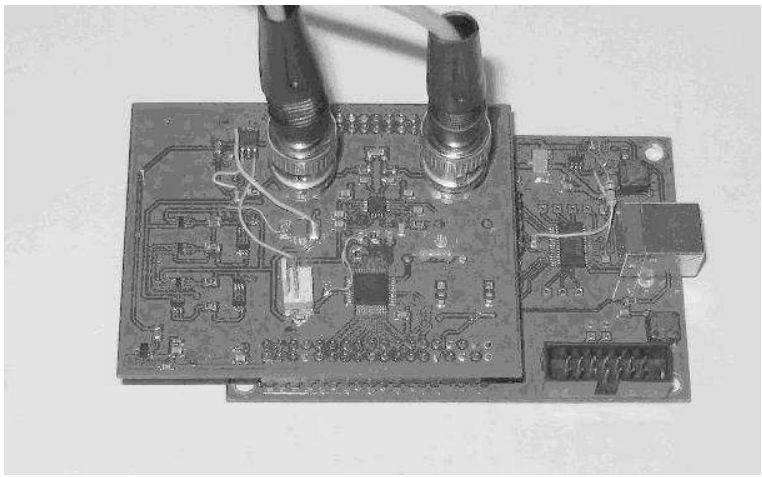


Figure 5: Rhe view on the modet of device (top view)

The picture shows the impedance measurement of fixed resistors. The values doesn't coincide, but the difference doesn't exceed 5

The read line shows the skin resistance at the human finger with one direction 1.22uA current. One should pay attention to the transient process, that depends on human condition and xerosis.

This is an example of switching current with 10sec interval. The impedance was measured between middle and index fingers. The scale in KOhms from 2000 to 4000 is on the left.

The graph shows that transient process is the same after the current direction switch, but the absolute values depends on direction.

The device is ready to be used for experimental studies.

The DSP has opened interrupts of timer with 10ms interval and communication port interface for PC connection. The timer works continuously and the communication port only during PC communication.

The current direction switch check and the led flashing control are performed in the timer interrupt. Here's the led flashing algorithm. It changes the state upon the PC request arrival. In the case of absence of the PC requests for 2 seconds led starts flashing with the interval of 2 seconds and the DAC shuts down. During the active data flow from the PC the led frequency is about 10Hz.

At this moment the following function were implemented:

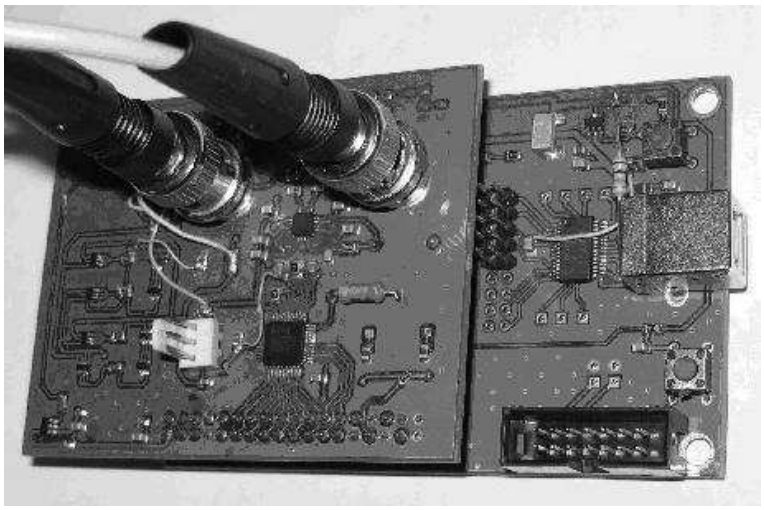


Figure 6: Rhe view on the modet of device (lateral view)

- Adjustment of the device
- Preliminary data analysis for feature detection.

A print screen of it is shown at the figure below.

The picture shows the impedance measurement of fixed resistors. The values doesn't coincide, but the difference doesn't exceed 5

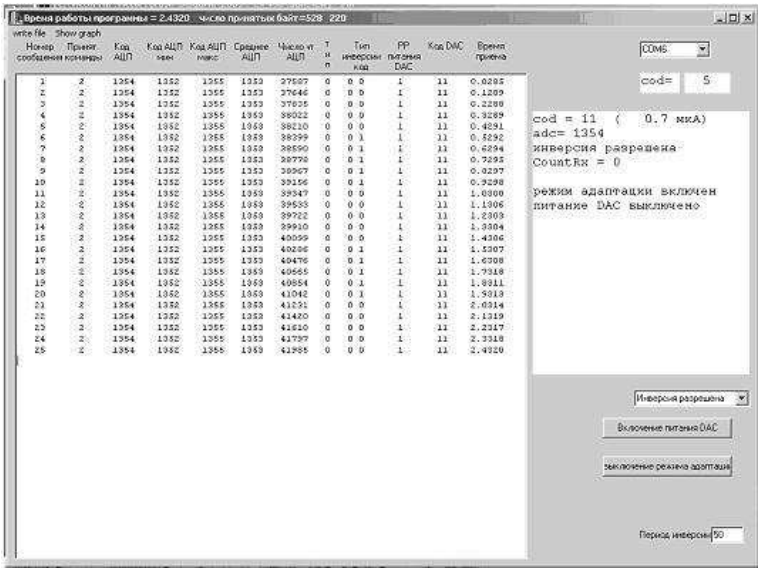


Figure 7: The example of measurements

The read line shows the skin resistance at the human finger with one direction 1.22uA current. One should pay attention to the transient process, that depends on human condition and xerosis.

This is an example of switching current with 10sec interval. The impedance was measured between middle and index fingers. The scale in KOhms from 2000 to 4000 is on the left.

The graph shows that transient process is the same after the current direction switch, but the absolute values depends on direction.

The device is ready to be used for experimental studies.

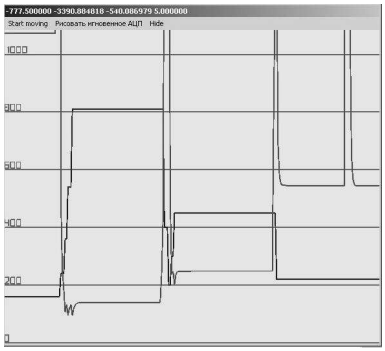


Figure 8: The measurements of fixed resistors

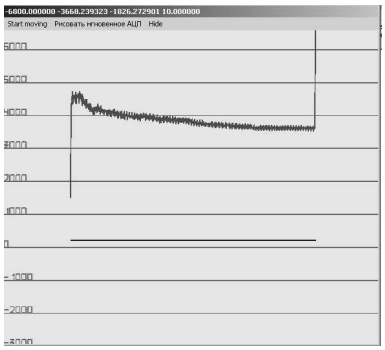


Figure 9: The unidirectional measurement of skin of man

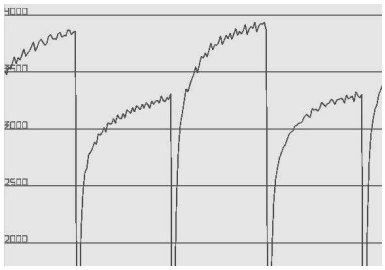


Figure 10: The bipolar measurement of skin of man

6 Conclusion

A problem of spinal patients (humans and animals) rehabilitation is discussed in this paper. A positive results of manual therapy strictly consistent with stepping motion of paralyzed feet obtained in Pavlov's Institute were considered. A treadmill based bio-trainer was developed based on these results. It provided mechatronic gravity force simulation upon the supporting leg during the forced stepping motion.

In this paper we suggest sequential development of mechatronic trainer ("boot", "bed", "treadmill", "exoskeleton"), with the foot tactile stimulation feature, developed in Institute of Mechanics BAS. It's important to mention economic efficiency of such development tactics, it gives feedback at each stage of investment.

Particular attention is paid to the problem of sensory aspect of mechatronic devices for spinal patients rehabilitation, since it is inseparable part from the very first stage. One of the primary tasks of the sensors is to provide an objective diagnosis and monitoring changes of the foot state during treatment. A method of skin impedance measurement with mechanical tools is proposed. It utilize a similar method to the Institute of Mechanics BAS. The proposed variant of "sensored boot" is virtually identical design "mechanical boot", the only difference is the replacement of

the plunger matrix on the matrix of sensors. It will reduce the cost of development and provide unification of similar parts.

The existence of dermal-visceral reflex paths in human body in addition to the reflex paths of the nervous system is sufficiently well proven and studied. The diagnosing tools based on electro-conductivity measuring that use them are well known too. It was suggested that stepping movements recovery of animal's paralyzed legs can be explained by the persistence after an injury or growth of new dermal-visceral reflex paths due to the manual therapy.

A new problem of estimating the state of the paralyzed legs for electropuncture was formulated. Also it includes the problem of determining the points of projection of internal organs to the skin areas and points.

The problems of sensors of bio-trainer and the studies of dermal-visceral processes demands a higher level of the skin impedance measuring devices. The development experience and study of such a device demonstrated the need of algorithms enhancement for higher sensitivity, resolution and noise resistance.

References

[1] Gerasimenko U.P., Makarovskiy A.N., Nikitin O.A.. The comtrol of locomotion activity of the man and animals in conditions in the absence of supraspinal influences. Russian physiology journal by name I.I. Sechenov. 2000, n.86, N.11, p.1502-1511.

[2] D. Okhotsimsky, O. Nikitin, Y. Gerasimenko, N. Serbenjuk, L. Mitutsova, K. Delchev, V. Vitkov, A. Platonov, V. Yaroshevsky. A biomechanical stimulator for scientific-experimental study of the regeneration of spinal cord locomotion capabilities after traumatic break. Proceed. of Inter. Conf. "Advanced Problems in Mechanics 2005", Minisymposium on Biomechanics, June 28-July 5, 2005, St. Petersburg, Russia, 2006, ISBN 5-98883-009-9, pp.394 - 400.

[3] Neborskiy A.G., Neborskiy S.A Electro skin conductivity in validation of the dynamic state man (experimental-theory explanation) / - M.: Medicine, 2007, - 224 p.

[4] Bernstein N.A. About structure of motion. M.: Medgis 1947.-255p.

[5] Chenegin V.I. Galvanic skin reflex, as the method of prediction of functional state of sportsmans. // Estimate and predict. func. State in physiology. - Frunze. 1980. pp. 340-342.

Direct tensor calculus in the problem of mechanical energy dissipation in fluids

M. Podolsky
ttt88@mail.ru

Abstract

In well known educational hydrodynamic literature the problem of mechanical energy dissipation in fluids is considered as a problem for fluids which have shear viscosity μ only. Volume viscosity μ_V is supposed to be equal to zero. Besides, even for the case $\mu_V = 0$ traditional consideration of problem requires awkward and not obvious algebraic transformations.

Direct tensor calculus gives a possibility to receive the solution in a very simple way and to consider the general case when all viscosities (both shear and volume) are taken into account.

In this work compact formulae for power of inner viscous forces are obtained and their physical sense is clarified. Numerical example illustrating the role of volume viscosity is done.

1 Short introduction to tensor algebra and tensor analysis

The main formulae and notations (see [3]), which will be used below, are the following (summation convention is used):

$$\underline{\underline{\alpha}} = \alpha_{ij}\vec{e}_i \otimes \vec{e}_j, \quad \lambda_s(\underline{\underline{\alpha}}) = \alpha_{ij}\vec{e}_i \bullet \vec{e}_j, \quad \lambda_s(\underline{\underline{\alpha}} + \underline{\underline{\beta}}) = \lambda_s(\underline{\underline{\alpha}}) + \lambda_s(\underline{\underline{\beta}}); \tag{1}$$

$$\underline{\underline{E}} = \vec{e}_i \otimes \vec{e}_i, \quad \vec{a} \bullet \underline{\underline{E}} = \underline{\underline{E}} \bullet \vec{a} = \vec{a}, \quad \lambda_s(\underline{\underline{E}}) = 3; \tag{2}$$

$$\underline{\underline{\alpha}} : \underline{\underline{\beta}} = \alpha_{ij}\vec{e}_i \otimes \vec{e}_j : \beta_{mn}\vec{e}_m \otimes \vec{e}_n = \alpha_{ij}\beta_{mn}(\vec{e}_i \bullet \vec{e}_m)(\vec{e}_j \bullet \vec{e}_n) = \alpha_{ij}\beta_{ij}; \tag{3}$$

$$\underline{\underline{\alpha}} : \underline{\underline{\alpha}} = \alpha_{ij}\alpha_{ij} \equiv \sum_{j=1}^{3}\sum_{i=1}^{3}\alpha_{ij}^2 > 0; \tag{4}$$

$$\underline{\underline{\alpha}} : \underline{\underline{E}} = \underline{\underline{E}} : \underline{\underline{\alpha}} = \lambda_s(\underline{\underline{\alpha}}); \tag{5}$$

if one of the tensors $\underline{\underline{\alpha}}$ and $\underline{\underline{\beta}}$ is symmetric and another one is antisymmetric, then

$$\underline{\underline{\alpha}} : \underline{\underline{\beta}} = 0; \tag{6}$$

$$(\underline{\underline{\alpha}} + \underline{\underline{\beta}}) : (\underline{\underline{\varphi}} + \underline{\underline{\psi}}) = \underline{\underline{\alpha}} : \underline{\underline{\varphi}} + \underline{\underline{\beta}} : \underline{\underline{\varphi}} + \underline{\underline{\alpha}} : \underline{\underline{\psi}} + \underline{\underline{\beta}} : \underline{\underline{\psi}}; \tag{7}$$

$$(\vec{a} \bullet \underline{\underline{\alpha}}) \bullet \vec{b} = \vec{a} \bullet (\underline{\underline{\alpha}} \bullet \vec{b}) = \vec{a} \bullet \underline{\underline{\alpha}} \bullet \vec{b}, \quad \vec{a} \bullet \underline{\underline{\alpha}} \bullet \vec{b} = \underline{\underline{\alpha}} : (\vec{a} \otimes \vec{b}); \tag{8}$$

$$\vec{\nabla} \bullet \underline{\underline{\alpha}} \equiv \vec{\nabla} \bullet \underline{\underline{\alpha}}, \quad \vec{\nabla} \bullet (\underline{\underline{\alpha}} \bullet \vec{a}) \equiv \vec{\nabla} \bullet \underbrace{(\underline{\underline{\alpha}} \bullet \vec{a})} = \vec{\nabla} \bullet (\underline{\underline{\alpha}} \bullet \vec{a}) + \vec{\nabla} \bullet (\underline{\underline{\alpha}} \bullet \vec{a}); \tag{9}$$

$$\vec{\nabla} \otimes \vec{a} = \underline{\underline{\varepsilon}}^{(a)} + \underline{\underline{\kappa}}^{(a)}, \tag{10}$$

where $\underline{\underline{\varepsilon}}^{(a)}$ is symmetric tensor, $\underline{\underline{\kappa}}^{(a)}$ is antisymmetric tensor.

Here $\underline{\underline{\alpha}}, \underline{\underline{\beta}}, \underline{\underline{\varphi}}, \underline{\underline{\psi}}$ are tensors (of the second rank); $\lambda_s(\underline{\underline{\alpha}})$ is scalar invariant of tensor $\underline{\underline{\alpha}}$; $\underline{\underline{E}}$ is unit tensor; $\vec{a}, \vec{b}$ are vectors; $\vec{\nabla}$ is Hamilton's operator; $\bullet$, $:$, $\otimes$ are notations of scalar, biscalar of the second type and tensor multiplying operations.

2 Stress tensor, tensor of velocities of deformations, reological equation

Denoting stress by $\vec{p}_n$ and stress tensor by $\underline{\underline{p}}$ one can write

$$\vec{p}_n = \vec{n} \bullet \underline{\underline{p}}, \tag{11}$$

where $\vec{n}$ is unit vector of normal to elementary surface dS.

We have from here ($\vec{v}$ is velocity)

$$\vec{p}_n \bullet \vec{v} = \vec{n} \bullet \underline{\underline{p}} \bullet \vec{v} = \vec{n} \bullet (\underline{\underline{p}} \bullet \vec{v}),$$

and according to Gauss – Ostrogradsky's formula

$$\oint\limits_S \vec{p}_n \bullet \vec{v}\, dS = \int\limits_V \vec{\nabla} \bullet (\underline{\underline{p}} \bullet \vec{v}) dV. \tag{12}$$

Tensor of velocities of deformations is symmetric. It is equal to sum:

$$\underline{\underline{\varepsilon}} = \underline{\underline{\varepsilon}}_V + \underline{\underline{\varepsilon}}_F. \tag{13}$$

Tensor $\underline{\underline{\varepsilon}}_V$ is responsible for volume deformation, tensor $\underline{\underline{\varepsilon}}_F$ – for shape deformation. There are the following formulae for these tensors:

$$\underline{\underline{\varepsilon}}_V = \frac{1}{3}\theta \underline{\underline{E}}, \quad \lambda_s(\underline{\underline{\varepsilon}}_V) = \theta, \qquad \lambda_s(\underline{\underline{\varepsilon}}_F) = 0, \tag{14}$$

where θ is velocity divergence. Reological equation for compressible Newtonian fluid may be written in the following form:

$$\underline{\underline{p}} = \left[-p + \left(\mu_V - \frac{2}{3}\mu \right) \theta \right] \underline{\underline{E}} + 2\mu \underline{\underline{\varepsilon}}. \tag{15}$$

Here p is pressure, μ_V and μ were indicated above. According to (15) $\underline{\underline{p}}$ is symmetric tensor.

3 Energy and motion equations

Let us suppose that there is no energy influx from outside. Then taking (12) into account and using ordinary procedure one can obtain the energy equation in such form

$$\rho \frac{d}{dt} \left(U + \frac{v^2}{2} \right) = \rho \vec{f} \bullet \vec{v} + \vec{\nabla} \bullet (\underline{\underline{p}} \bullet \vec{v}), \tag{16}$$

where U is inner energy (of unit mass of fluid), ρ is density of fluid, $\vec{f}$ is density of mass force. To obtain (16) it is essential to use the formula

$$\frac{d}{dt} \int\limits_V \rho \Phi dV = \int\limits_V \rho \frac{d\Phi}{dt} dV, \tag{17}$$

which is true, if ρ is density of fluid. The equation of fluid motion is

$$\rho \frac{d\vec{v}}{dt} = \rho \vec{f} + \vec{\nabla} \bullet \underline{\underline{p}}. \tag{18}$$

Scalar multiplying both parts of (18) by $\vec{v}$ one can eliminate vector $\vec{f}$ from (16) and (18). Thus we receive the equation

$$\rho \frac{dU}{dt} = \vec{\nabla} \bullet (\underline{\underline{p}} \bullet \vec{v}) - (\vec{\nabla} \bullet \underline{\underline{p}}) \bullet \vec{v}$$

which, because of (9), yields

$$\rho \frac{dU}{dt} = \vec{\nabla} \bullet (\underline{\underline{p}} \bullet \vec{v}). \tag{19}$$

4 Power of inner forces

Let us denote specific (referred to unit volume) power of inner forces by P_{in}. Bearing in mind the formula (16), we can write (see [2])

$$P_{\text{in}} = -\rho\frac{dU}{dt},$$

so that (see (19))

$$P_{\text{in}} = -\vec{\nabla} \bullet (\underline{\underline{p}} \bullet \vec{v}). \tag{20}$$

With assistance of identity (8_2) formula (20) may be rewritten in the form:

$$P_{\text{in}} = -\underline{\underline{p}} : (\vec{\nabla} \otimes \vec{v}),$$

or, according to (7) and (10) (upper index "v" is omitted), in the form

$$P_{\text{in}} = -\underline{\underline{p}} : \underline{\underline{\varepsilon}} - \underline{\underline{p}} : \underline{\underline{\kappa}}.$$

Tensor $\underline{\underline{p}}$ is symmetric, tensor $\underline{\underline{\kappa}}$ is antisymmetric. Hence, according to (6),

$$P_{\text{in}} = -\underline{\underline{p}} : \underline{\underline{\varepsilon}}.$$

Because of (13) and (7) this formula yields

$$P_{\text{in}} = -\underline{\underline{p}} : \underline{\underline{\varepsilon}}_V - \underline{\underline{p}} : \underline{\underline{\varepsilon}}_F.$$

Further we have (see (14), (5), (13), (6), (15), (1_3))

$$\underline{\underline{p}} : \underline{\underline{\varepsilon}}_V = \frac{1}{3}\theta\underline{\underline{p}} : \underline{\underline{E}} = \frac{1}{3}\theta\lambda_s(\underline{\underline{p}}),$$

$$\underline{\underline{\varepsilon}} : \underline{\underline{\varepsilon}}_F = \underline{\underline{\varepsilon}}_V : \underline{\underline{\varepsilon}}_F + \underline{\underline{\varepsilon}}_F : \underline{\underline{\varepsilon}}_F = \underline{\underline{\varepsilon}}_F : \underline{\underline{\varepsilon}}_F,$$

$$\underline{\underline{p}} : \underline{\underline{\varepsilon}}_F = \left[-p + \left(\mu_V - \frac{2}{3}\mu\right)\theta\right] \underline{\underline{E}} : \underline{\underline{\varepsilon}}_F + 2\mu\,\underline{\underline{\varepsilon}} : \underline{\underline{\varepsilon}}_F = 2\mu\,\underline{\underline{\varepsilon}}_F : \underline{\underline{\varepsilon}}_F,$$

$$\lambda_s(\underline{\underline{p}}) = \left[-p + \left(\mu_V - \frac{2}{3}\mu\right)\theta\right] \lambda_s(\underline{\underline{E}}) + 2\mu\lambda_s(\underline{\underline{\varepsilon}}_V + \underline{\underline{\varepsilon}}_F) =$$

$$= 3\left[-p + \left(\mu_V - \frac{2}{3}\mu\right)\theta\right] + 2\mu\theta = -3p + 3\mu_V\theta,$$

so that

$$P_{\text{in}} = \theta p - (\mu_V\theta^2 + 2\mu\,\underline{\underline{\varepsilon}}_F : \underline{\underline{\varepsilon}}_F). \tag{21}$$

5 Power of viscous forces

According to (21) power of viscous forces is equal to

$$P_d = \mu_V\theta^2 + 2\mu\,\underline{\underline{\varepsilon}}_F : \underline{\underline{\varepsilon}}_F. \tag{22}$$

Both terms of this formula are positive. For the second term it follows from (4). Physical sense of formula (22) is obvious. The first component of (22) is responsible for losses caused by volume change (it depends on the divergence θ); the second one depends on the shear deformation and, consequently, it contains tensor $\underline{\underline{\varepsilon}}_F$, which describes the form change. For practical application instead of (22) it appears to be more convenient to use the formula

$$P_d = \mu_V\theta^2 + 2\mu\left(\varepsilon_{ij}\varepsilon_{ij} - \frac{1}{3}\theta^2\right), \tag{23}$$

which follows from equality

$$\underline{\underline{\varepsilon}}_F : \underline{\underline{\varepsilon}}_F = \underline{\underline{\varepsilon}} : \underline{\underline{\varepsilon}} - \frac{1}{3}\theta^2.$$

This equality can be received with assistance of properties of biscalar products and formulae mentioned above. If $\mu_V = 0$ formula (23) gives

$$P_d = 2\mu \left(\varepsilon_{ij}\varepsilon_{ij} - \frac{1}{3}\theta^2 \right). \tag{24}$$

Formulae (24) is generally used but in this case one must prove that the expression in the right part of (24) is positive. Due to application of tensor calculus this fact became obvious. As a conclusion let us consider a simple example. Setting vector $\vec{v}$ equal to

$$\vec{v} = u(t, x_1)\vec{e}_1,$$

we will have

$$\underline{\underline{\varepsilon}} = \varepsilon_{11}\vec{e}_1 \otimes \vec{e}_1, \qquad \theta = \frac{\partial u}{\partial x_1}, \qquad \varepsilon_{11} = \frac{\partial u}{\partial x_1}.$$

All the components ε_{ij} , except ε_{11}, are equal to zero and formula (23) gives (see also [1])

$$P_d = \mu \left(\frac{\mu_V}{\mu} + \frac{4}{3} \right) \left(\frac{\partial u}{\partial x_1} \right)^2.$$

According to [4] ratio $\mu_V/\mu = 2,81$ for water at the temperature $t = 15°C$. It means that the role of volume viscosity may be essential.

References

[1] *Isakovich M.A.* General acoustics. Moscow, 1973. – 495 p.(in Russian).

[2] *Loytsansky L.G.* Mechanics of liquid and gas. Moscow, 2003. – 840 p. (in Russian).

[3] *Podolsky M.E.* Applied tensor algebra. St. Petersburg, 2007. – 247 p. (in Russian).

[4] *Popov D.N.,Panaiotty S.S.,Ryabinin M.V.* Hydromechanics. Moscow, 2002. – 384 p. (in Russian).

Marlen E. Podolsky, 3, Lotsmanskaya Str., Saint Petersburg, 190008, Russia

On the problem of soft toroidal shells designing

Ekaterina Polyakova Vitaly Lutov Victor Chaikin
ekpol@mail.ru

Abstract

In this paper some designing problems of significant practical and theoretical importance concerning the inflatable toroidal shells are considered. An unclosed system for definition of the parameters of the shell produced under given characteristics of the shell in its operating status is obtained. The methods of rational system closure are discussed.

1 Introduction

The complexity of soft shells designing problems is substantially caused by the distinction of the characteristics of the shell geometry and physical condition directly after its manufacturing and in its subsequent operation mode. From mathematical point of view these problems are related to the class of inverse problems, i.e. the problems of definition of such characteristics of the strainless shells which will ensure their transition in the required operation modes under the relevant external actions.

The elementary reasonings allow to result many examples of such forms of soft shells, which can not exist at loadings born up by rigid shells. Therefore, carrying out any project of a soft shell with some desired properties, one should first of all convince himself of the possibility of such shell existence. In the present paper the questions of solvability of problems specified above, as well as the questions of shells designing are considered with reference to a narrow shell class, namely, with reference to a set of inflatable toroidal (topologically equivalent to torus) shells.

The practical importance of this shell class is reasoned by the wide use of inner tubes, vessels; various types of inflatable lift devices and bearing constructions; natatorial facilities and other objects playing the significant role in market economy [1], [2],[3].

2 Definition of the toroidal shell stresses in a given state

The first step in the solution of the problem of existence possibility of the shell, which has the required form in its operation mode under the internal pressure of gas equal to q consists in the proof of the fact, that the existence of such form of the shell does not contradict the equilibrium equations.

Let us assume that the shell in its initial strainless and posterior deformed states is axially symmetric with respect to z-axis.

According to [4] the equilibrium equations in the case of absence of tangential external forces can be written as

$$\begin{aligned} \sigma_{11}\frac{d\theta}{ds} + \sigma_{22}\frac{\cos\theta}{r} &= q, \\ \frac{d}{ds}(\sigma_{11} r) + \sigma_{22}\sin\theta &= 0, \end{aligned} \tag{1}$$

where s is the arc coordinate angular position of the shell's particle M being set up at the corresponding meridian (see Figure 1); $\theta(s)$ is the angle between the tangent unit vector at point M under consideration and z -axis; $r(s)$ is the distance between the particle M and z-axis; $\sigma_{11}(s)$ and

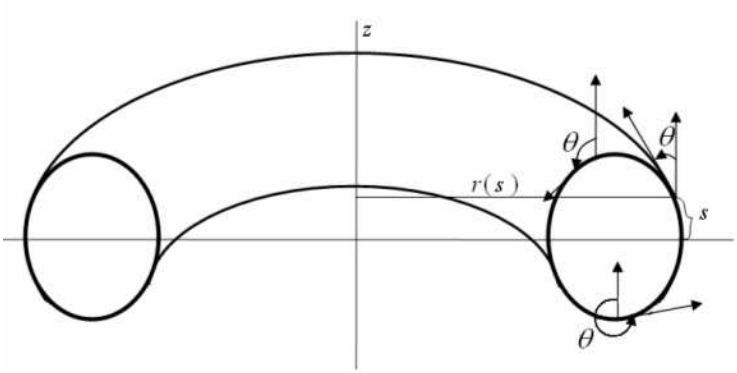


Figure 1: Operation mode under the internal pressure of gas.

$\sigma_{22}(s)$ are stresses in meridional filaments of the shell and in those shell's filaments that form its parallels, respectively.

As far as the shape of the shell is supposed to be given one should consider functions $\theta(s)$ and $r(s)$ as prescribed ones.

The equations (1) form the system determining the unknown functions $\sigma_{11}(s)$ and $\sigma_{22}(s)$. This system is easily reduced to one ordinary differential equation of the first order, which general solution can be obtained in quadrature.

More concretely, having excluded the function $\sigma_{22}(s)$ from the equations (1), we shall get the following equation for definition of $\sigma_{11}(s)$:

$$\frac{d(r\sigma_{11})}{ds} - r\tan\theta\frac{d\theta}{ds}\sigma_{11} = -qr\tan\theta. \tag{2}$$

General solution of the latter equation is given by

$$\sigma_{11} = \frac{D - \int\limits_0^s qr|\cos\theta|\tan\theta ds}{r|\cos\theta|}, \tag{3}$$

where D is an arbitrary constant.

Supposing that arc coordinate s is counted from that point at the meridian, at which $\theta = 0$, we shall have

$$\sigma_{11} = \frac{r(0)\sigma_{11}(0) - \int\limits_0^s qr|\cos\theta|\tan\theta ds}{r|\cos\theta|}. \tag{4}$$

Equalities (1) and (4) yield

$$\sigma_{22} = \frac{qr}{\cos\theta} - \frac{r(0)\sigma_{11}(0) - \int\limits_0^s qr|\cos\theta|\tan\theta ds}{\cos\theta|\cos\theta|}\frac{d\theta}{ds}. \tag{5}$$

In what follows the solution of equilibrium equations (1) having been obtained in this section is applied to definition of stresses of the torus shell.

3 Definition of torus shell stresses

Let us suppose that in operation mode the shell would have the torus shape defined by the equation

$$\vec{r}(\varphi,\psi) = \vec{i}(R+\rho\cos\theta)\cos\psi + \vec{j}(R+\rho\cos\theta)\sin\psi + \vec{k}\rho\sin\theta, \tag{6}$$

where $\vec{r}(\varphi, \psi)$ is radius-vector of the shell's particle corresponding to cylindrical coordinates φ and ψ; $\vec{i}$, $\vec{j}$, $\vec{k}$ are basis vectors of coordinate system $Oxyz$; ρ is radius of meridional circular cross-sections of the torus; R is radius of circle created by the centers of cross-sections mentioned above; θ is the angle counted, as it's shown in Figure 2, from horizontal diameter of the cross-section.

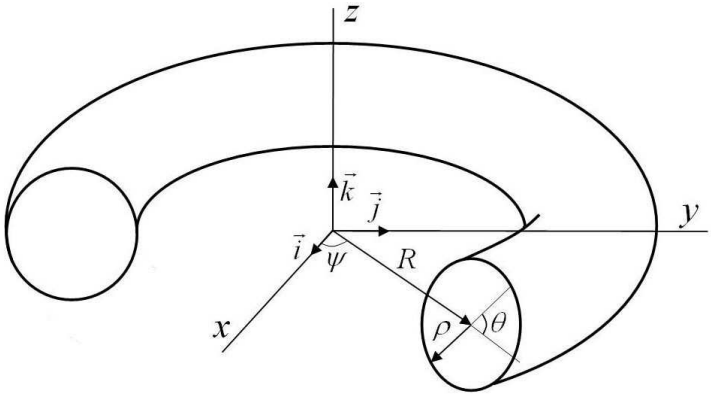


Figure 2: Meridional circular cross-sections of the torus.

In this case

$$r = R + \rho\cos\theta(s), \theta = s/\rho, \tag{7}$$

Therefore, assuming that $q = const$ by dint of equalities (4) and (5) we obtain

$$\sigma_{11} = \frac{r(0)\sigma_{11}(0) - q\rho\int\limits_0^\theta (R + \rho\cos\theta)|\cos\theta|\tan\theta d\theta}{(R + \rho\cos\theta)|\cos\theta|}, \tag{8}$$

$$\sigma_{22} = \frac{q(R + \rho\cos\theta)}{\cos\theta} - \frac{r(0)\sigma_{11}(0) - q\rho\int\limits_0^\theta (R + \rho\cos\theta)|\cos\theta|\tan\theta d\theta}{\rho\cos\theta|\cos\theta|}, \tag{9}$$

For values of θ satisfying the inequality $\cos\theta \geq 0$ formulae (8) and (9) take form of

$$\sigma_{11} = \frac{r(0)\sigma_{11}(0) - q\rho\int\limits_0^\theta (R + \rho\cos\theta)\sin\theta d\theta}{(R + \rho\cos\theta)\cos\theta}, \tag{10}$$

$$\sigma_{22} = \frac{q(R + \rho\cos\theta)}{\cos\theta} - \frac{r(0)\sigma_{11}(0) - q\rho\int\limits_0^\theta (R + \rho\cos\theta)\sin\theta d\theta}{\rho\cos^2\theta}, \tag{11}$$

Integration of (10) and (11) yields

$$\sigma_{11} = \frac{r(0)\sigma_{11}(0) - q\rho R - \frac{1}{2}q\rho^2 + q\rho R\cos\theta + \frac{1}{2}q\rho^2\cos^2\theta}{(R + \rho\cos\theta)\cos\theta}, \tag{12}$$

$$\sigma_{22} = \frac{\frac{1}{2}q\rho^2\cos^2\theta - r(0)\sigma_{11}(0) + q\rho R + \frac{1}{2}q\rho^2}{\rho\cos^2\theta}. \tag{13}$$

It follows from (12) and (13) that at $\theta = \frac{\pi}{2}$ stresses σ_{11} and σ_{22} are bounded only if

$$r(0)\sigma_{11}(0) - q\rho R - \frac{1}{2}q\rho^2 = 0. \tag{14}$$

In this case one obtains

$$\sigma_{11} = q\rho - \frac{1}{2}\frac{q\rho^2\cos\theta}{R + \rho\cos\theta}, \sigma_{22} = \frac{1}{2}q\rho. \tag{15}$$

It can be easily shown that for values of θ satisfying the inequality $\cos\theta \leq 0$ under the condition (14) the expressions (15) are also valid.

4 Designing of a strainless shell transforming to torus in operation mode

Let the desired shell shown in Figure 3 have the shape defined by vector equality

$$\vec{r}^0(\varphi,\psi) = \vec{i}(\tilde{R} + r(\varphi)\cos\varphi)\cos\psi + \vec{j}(\tilde{R} + r(\varphi)\cos\varphi)\sin\psi + \vec{k}r(\varphi)\sin\varphi, \tag{16}$$

where $\vec{r}^0$ is radius-vector of the shell's particle corresponding to Lagrangian coordinates φ and ψ (angle φ is counted from the equatorial plane of the shell); $\tilde{R}$ is radius of some circle located inside the shell (see Figure 3).

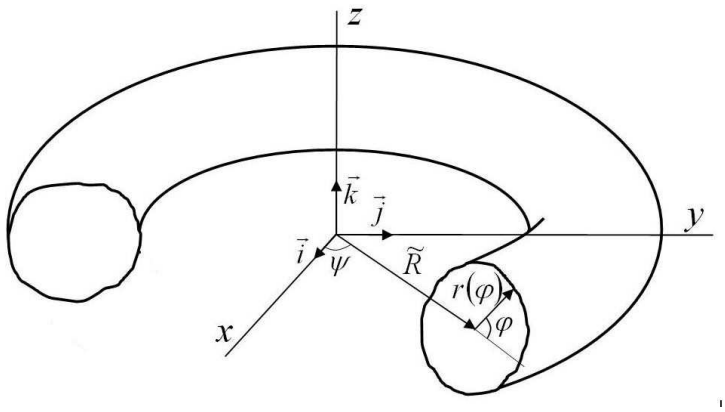


Figure 3: Designing of a strainless shell transforming to torus in operation mode.

The task is to find the value of $\tilde{R}$ and function $r(\varphi)$ that allow the shell under consideration to transform to torus defined by equality

$$\vec{r}(\varphi,\psi) = \vec{i}(R + \rho\cos\theta(\varphi))\cos\psi + \vec{j}(R + \rho\cos\theta(\varphi))\sin\psi + \vec{k}\rho\sin\theta(\varphi), \tag{17}$$

under inner gas pressure equal to p.

We emphasize that angle θ in the latter expression is the desired function of Lagrangian coordinate φ, as well as the function $r(\varphi)$.

Metrical coefficients of the shell in its strainless state are equal to

$$g^0_{11} = r'^2(\varphi) + r^2(\varphi), g^0_{22} = (\tilde{R} + r(\varphi)\cos\varphi)^2, g^0_{12} = g^0_{21} = 0. \tag{18}$$

Metrical coefficients of the shell in its deformed state are equal to

$$g_{11} = \rho^2\theta'^2(\varphi), g_{22} = (R + \rho\cos\theta(\varphi))^2, g_{12} = g_{21} = 0. \tag{19}$$

The extensional strains of meridian and parallel elements of the shell blown up are equal to

$$\varepsilon_1 = \frac{\rho\theta'(\varphi)}{\sqrt{r'^2(\varphi) + r^2(\varphi)}} - 1, \varepsilon_2 = \frac{R - \tilde{R} + \rho\cos\theta(\varphi) - r(\varphi)\cos\varphi}{\tilde{R} + r(\varphi)\cos\varphi}. \tag{20}$$

respectively.

Let us suppose that the following relations take place:

$$\sigma_{11} = k_1(\varphi)\varepsilon_1(\varphi), \sigma_{22} = k_2(\varphi)\varepsilon_2(\varphi), \tag{21}$$

where $k_1(\varphi)$ and $k_2(\varphi)$ are elasticity coefficients of meridional filaments of the shell and of those filaments that form its parallels respectively.

By dint of (15) and (20) we rewrite (21) as

$$\frac{p\rho}{2}\frac{2R + \rho\cos\theta(\varphi)}{R + \rho\cos\theta(\varphi)} = k_1(\varphi)\left(\frac{\rho\theta'(\varphi)}{\sqrt{r'^2(\varphi) + r^2(\varphi)}} - 1\right), \tag{22}$$

$$\frac{p\rho}{2} = k_2(\varphi)\frac{R - \tilde{R} + \rho\cos\theta(\varphi) - r(\varphi)\cos\varphi}{\tilde{R} + r(\varphi)\cos\varphi}. \tag{23}$$

On the base of the latter equations (22) and (23) one can perform the search and quantitative analysis of feasible shells transforming to torus specified by (17) under inner gas pressure equal to p . There are infinitely many variants of such shells since the search is not fully defined by equations (22) and (23).

Acknowledgements

The authors gratefully acknowledge the support for this work provided by Ministry of Education and Science of Russia.

References

[1] Shihirin, V. et al: Elastic mechanisms and constructions, Irkutsk, ISTU, 2006, 286 pp

[2] Obraztsov, I. et al.: Optimal reinforcement of composite shells of rotation, Engineering industry, 1977, 144 pp.

[3] Komkov, M. et al.: Width choice of unidirectional tapes for compact winding of torus shells, Collected papers of MSTU named after N. Bauman, 1986,N 21, pp. 55 63.

[4] Polyakova, E., Chaikin, V.: Applied problems of soft shells and fabrics mechanics, Saint-Petersburg, SPSUTD, 2006, 193 pp.

Ekaterina Polyakova, St-Petersburg State University of Technology and Design, Bolshaya Morskaya St. 18, St.-Petersburg, 191186, Russia

"SMART Hydrogen" and its determination in micro and nanostructures in materials

Anatoly Polyanskiy Vladimir Polyanskiy Elena Chernyaeva
Yury Yakovlev
vapol@electronbeamtech.com

Abstract

The investigation of the micro and nanostructures - hydrogen interaction gives as new information about nano, micro and meso-scale of the material properties. The presentation reports some experimental proof of this interacton on example of high-temperature extraction of hydrogen from aluminum alloys, silicon plates and nanomaterials.

1 Introduction

Hydrogen in small concentrations is containing in all materials.

In the metals, the hydrogen is contained in the traps with various bounding energies. It has been established, cf. [1], that thermo-mechanical loading results in the hydrogen redistribution over the traps. Diffuse hydrogen accumulates mostly in the aluminum alloys while strongly bounded hydrogen accumulates mostly in the titanium alloys.

The hydrogen's influence on materials' properties is of crucial importance. Even for concentrations of about 1 hydrogen atom per 10000 atoms of the matrix one can observe the hydrogen embrittlement.

This influence can not be explained by means of the hypothesis of the uniform distribution of hydrogen in the matter. Only the localization of hydrogen in microdefects, on the grains' boundaries and on the surface of nanostructures in the material can explain the considerable change in mechanical properties.

The difficulties with determination of the small volume hydrogen traps prevents the direct determination such traps in all materials. Only hydrides in titanium and zirconium alloys may be determined as small heterogeneousness during microscopic investigations.

The new highly sensitive hydrogen analyzer AV-1 allows one to observe the hydrogen emission from microcracks and dislocations on the surface of specimen.

2 Experimental Results

The high temperature vacuum-extraction method of the hydrogen content determination enables one to measure addition parameters of the hydrogen content distribution inside the materials.

The highly sensitive hydrogen analyzer AV-1 utilizes the mass-spectrometric principle. The specimen preparation requires a vacuum extractor and an oven. The specimen inside the metal extractor is heated gradually up to an extraction temperature of 400-900^{o}C. The temperature needed for analysis is below the melting temperature of the specimen. The gases released at heating in vacuum are analyzed by means of the mass-spectrometer. The time-dependence of the hydrogen flux $q(t)$ registered by means of the data acquisition system yields the so-called extraction curve.

The hydrogen bound energy levels and diffusion constant may be determined [2]. In extraction curves are well seen small peaks Fig 1.

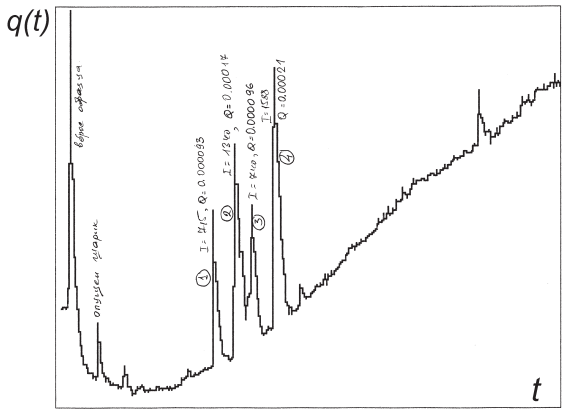


Figure 1: The part of the extraction curve for aluminum alloy D-16 with small peaks

The volume of molecular hydrogen that correspond with this peaks is approximately 10^{-8}-10^{-9} mm^3. The average size of grains in the aluminium alloy D-16 is 0.1 mm. So each small peak may correspond to one micro crack or dislocation on the surface of the the specimen.

This hypothesis has been verified. The experiments on dispersion of the hydrogen diffusion on some specially created defects of the lattice of the silicon monocrystal were carried out. The idea was to create some monocrystal internal defects of the size about 30μm and compare the results of the high-temperature vacuum extraction of hydrogen from the original monocrystal and the monocrystal with the above defects. In order to create the defects we used an infrared pulse laser with the wavelength of 1024 nanometers, the duration of the impulse of 12 nanoseconds and the energy of one impulse 2 mJ. Such a laser is usually used for creating chips in the optical glass. The coherent infrared radiation of an impulse was focused at a certain point in the glass. The size of the focused spot is about 30μm. In the focus the energy density is about $2{\cdot}10^{15}$ W/m^2. Under such energy density the substance can warm up to 1500 ^{o}K depending on the coefficient of radiation absorption. In the warming-up place one observes a visible chip.

We had used plates of monocrystal silicon of the thickness of 0.3 mm.

In order to present the experiment the plates are placed in a parallelepiped made of the optical glass.

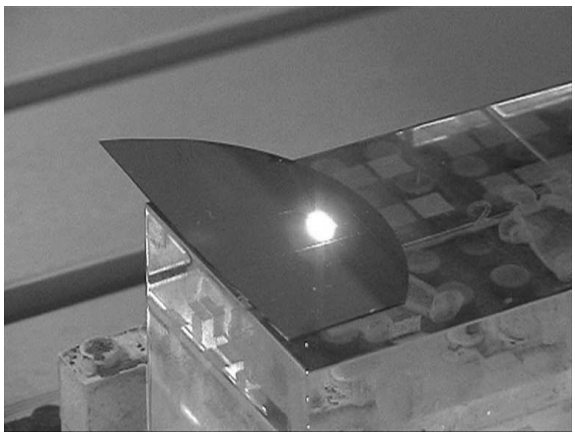


Figure 2: Tests on the silicon plates

The typical curves for the sample with and without defects are shown below. It is easy to observe that after the extraction of the main hydrogen there begins a transfer of the gas accumulated in the defects which in turn results in the noise consisting of a set of peaks. These peaks are due to the emission of hydrogen from silicon. For the regular dimples these peaks become regularised and increase their sizes, that is, the volume of the extracted hydrogen increases as well. Besides, the

temperature, at which these pulsations become considerable for the sample with chips, is 200^{o}C than that for the sample without chips. The observed effect can be interpreted as regularisation under the diffusion caused by a uniform grid of chips on the surfaces of the sample.

Some other plates (not radiated by the laser) and the plate with the chips on the surface were cut on samples of the sizes 8×15 mm^2. After that they were placed in vacuum for carrying out the experiments on the hydrogen diffusion.

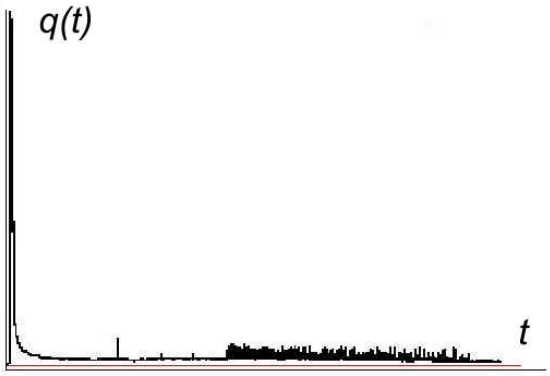


Figure 3: The extraction curve for the non-destructed silicon

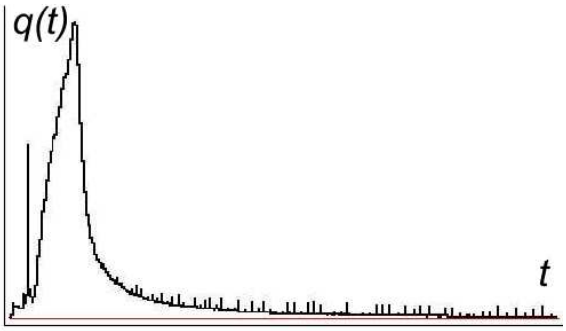


Figure 4: The extraction curve for the destructed silicon

In order to close this part of the present report it is worth mentioning that the most surprising in the results of the performed test is that the number of peaks in Fig. 4 is exactly coincident with the number of dimples in the silicon plates. The understanding of this fact remains to be tackled.

So the verification of the hypothesis gives as ability to determine the micro defects with the hydrogen analyser. We can determine both the number of the surface micro defects and their average volume.

The experiments with steels, including zinc coated steels are described in what follows. The steal plates from St 70 alloy were zincing in galvanic process. The microscopic investigations determined small spherical pores inside thin zinc layer (thickness 10 μm). This plate were cut on samples of the sizes 8×20 mm^2. After that they were analyze in AV-1 parallel with samples without zincing. The fragments of the extraction curves are shown in Fig. 5-6.

One can see that there are many small peaks in the extraction curve of the sample of St 70 with zinc layer. The small pores with diameter 0.1 μm were observed during microscopic investigations. Probably these pores are filled with hydrogen. The spherical form of the pores verifies this hypothesis. The comparison of the analyze results for samples with and without zinc layer gives the hydrogen concentration 1000 ppm in this layer.

Such concentration redistributes inside the steel owing to diffusion under mechanical loading. So the hydrogen brittleness progresses after some cycles of the bending loading.

Internal defects do not cause these small peaks because of hydrogen diffusion. But we can generalize the hypothesis about hydrogen-filled micro defects for the aluminum alloy A8.

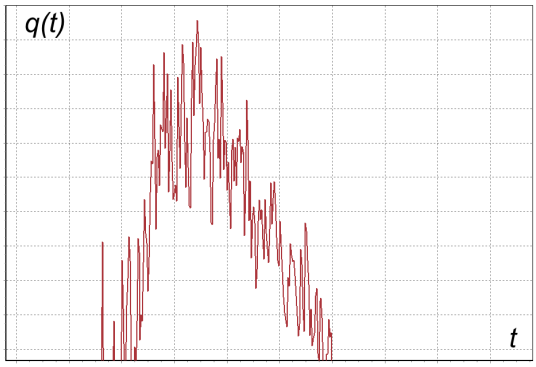


Figure 5: The fragment of the extraction curve - emission of hydrogen from sample of St 70 with zinc layer h=10 μm

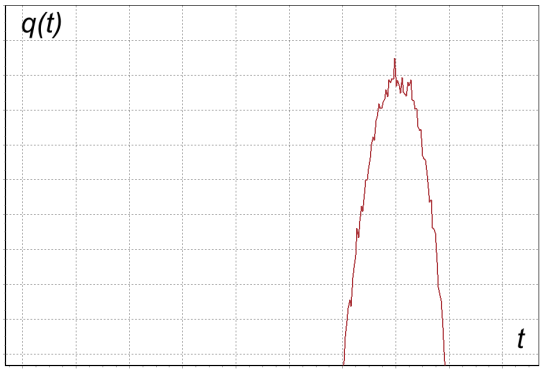


Figure 6: The fragment of the extraction curve - emission of hydrogen from sample of St 70 without zinc layer

Suppose that the structure defect has a form of tubes created the joint of three grains, as shown in Fig.7.

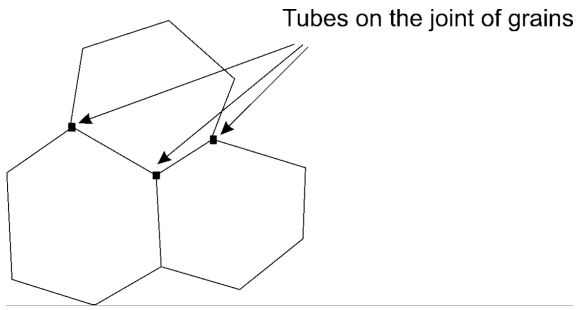


Figure 7: Scheme of the defect position on the joint grains

According to the data available in literature size of grains in technical pure, not annealed aluminum equals d=90μm. Let us take the cavities in the form of tubes. The length of the tube equals the size of the grains. The transverse dimension of the probes not undergoing loading is γ=10% of the length.

To estimate the cavity length, let us suppose that the grain has the form of a cube with length of edge b. Then from the condition of equality of the grain volumes its presentation in the form

sphere and cube one obtains:

$$b^3 = \frac{\pi d^3}{6}$$

In this approximation the volume of one cavity equals $b^3\gamma^2 = 3.8{\cdot}10^{-9}$ cm^3. The amount of hydrogen at each maximum of the extraction curves in Fig.8 is determined by integration of this maximum and equals $Q_1 = 1.18$ n.mm^3, $Q_2 = 0.82$ n.mm^3, $Q_3 = 1.8$ n.mm^3, $Q_4 = 2.7$ n.mm^3. By dividing the total amount of hydrogen by the volume of single cavity and the volume of the analyzed probe one obtains the concentration of defects corresponding to each maximum: $Z_1 = 4.2{\cdot}10^5$ cm^{-3}, $Z_2 = 3.2{\cdot}10^5$ cm^{-3}, $Z_3 = 6.4{\cdot}10^5$ cm^{-3}, $Z_4 = 9.6{\cdot}10^5$ cm^{-3}.

In the above approximation the total number of traps in 1 cm^3 of the probe, calculated from hydrogen amount, is $Z = \sum Z_i = 2.34{\cdot}10^6$ cm^{-3}, and the grain concentration is $2.58{\cdot}10^6$ cm^{-3}. The concentrations coincide within 10%.

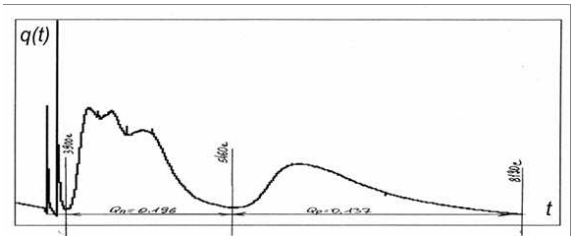


Figure 8: The extraction curve fore pure aluminum A8

Thus one can draw the conclusion that hydrogen at atmospheric pressure fills all cavities along the grain boundaries. Such cavities were discovered during microscopic investigations.

In extraction curves of Fig. 9 we indicate the temperatures of the samples during extraction of the hydrogen. These samples were made from nano-crystalline stainless steel. One can see that one peak corresponds to temperature 450 ^{o}C. This is the temperature of the nanocrystalline stainless steel recrystallization.

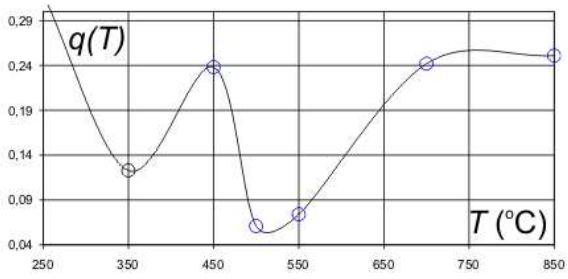


Figure 9: The extraction curve for nanocrystalline stainless steel

When microdefects and nanostructures are present, hydrogen is localized on free surface and decreases the free surface energy. This decrease results in termination of growth of micro- and nanocrystals and, on the other hand, leads to reduction of crack resistance and, in turn, to brittle destruction of the material.

It became clear that for the materials which have no stable chemical link with hydrogen, nearly whole hydrogen is concentrated in microdefects and on the surface of micro- and nanograins. Aluminum alloys, some steels, ceramic and semiconductors eject hydrogen.

Thus, the diagnostics in terms of the amount of extracted hydrogen turns out to be efficient and less effort-consuming than other methods of investigations. For instance, in order to determine an average concentration of microdefects by means of microtomography one needs to conduct measurements of about 12 hours whereas the hydrogen analysis takes 45-60 min.

3 Conclusions

The highly sensitive hydrogen analyzer AV-1 allows one to observe the hydrogen emission from microcracks and dislocations on the surface of specimen. The emission occurs during the specimen heating in vacuum and is fixed in the form of small peaks on the extraction curve.

The results of experimental investigations of aluminum alloys and steels, including zinc coated steels are shown. The size of defects determined by means of optical and probe microscopy is in a good agreement with the volume of hydrogen extracted under the atmospheric pressure. This allows us to assume that the microcracks and defects are filled by hydrogen.

These assumptions were proved on monocrystals of silicon.

Summarising we can say that we suggest a new approach to experimental investigation and diagnostics of microdefects and nanostructure in materials.

Acknowledgements

The financial support of the Sandia Corporation, contract 891092, and the Russian Foundation for Basic Research, grants 08-08-00737 and 08-01-12017, is acknowledged.

References

[1] A.M. Polyanskiy, V.A. Polyanskiy, D.B. Popov-Diumin "Diagnostics of mechanical condition of materials by method of high-temperature hydrogen vacuum-extraction", Proceedings of the Sixth International Congress on Thermal Stresses, vol. 2, Vienna, Austria, (2005) 589-592

[2] A.M. Polyanskiy, V.A. Polyanskiy "Determination of Hydrogen Binding Energy in Various Materials by Means of Absolute Measurements of its Concentration in Solid Probe", Hydrogen Materials Science and Chemistry of Carbon Nanomaterials Editor: T. Nejat Veziroglu, A. Kale Springer science + Business media B.V. (2006) 641-652

Anatoly Polyanskiy, RDC Electron & beam technology Ltd, 195220 p.b. 162 St.-Petersburg, Russia
Vladimir Polyanskiy, St.-Petersburg State Polytechnic University, 195251 Politekhnicheskaya, 29 St.-Petersburg, Russia
Elena Chernyaeva, St.-Petersburg State University, 198504 Petrgof, Universitetskiy 28 St.-Petersburg, Russia
Yury Yakovlev, St.-Petersburg State Polytechnic University, 195251 Politekhnicheskaya, 29 St.-Petersburg, Russia

The Fourier series expansion in the thermal stress problem on rotating work rolls during hot rolling

Sergey Polyanskiy
svpolyanskiy@gmail.com

Abstract

The present report describes the model of rolling mill which has contact patch moving on the surface. With the help of complex variable the problem is reduced to the equations of plain-stress states with a static load. Solution of this problem by Finite Element Methods is difficult because of the high temperature gradient in very thin surface layer of rolling mill.

We suggest a traditional method of the expansion in Fourier series for the numerical solution of thermal problem. This approach makes it possible to sum up the series with high accuracy and take the solution with a minimal number of the harmonics. In other hand we have the analytical solution. Using the temperature fields in closed-form enables obtaining the thermoelastic potential which in turn delivers the thermal stresses. The Airy function allows us to satisfy any boundary conditions on the mill's surface.

1 Introduction

Rolling is the main product in metallurgy. The main problem of hot rolling is the fragile destruction of the surface of mill rolls since it results in decrease of the quality of rolling [1].

The mill rolls made of high strength steel. The rolls are heavy-loaded because of the direct contact interaction with hot rolling. The mill rolls are rotating and the contact patch moves on the surface of mill which leads to a cyclic loading. Evaluation of mechanical stress caused by heating and pressure in the contact patch shows that thermal stresses considerably exceed the pressure. Immediately after the contact with surface of the rolling the mill is subjected to cooling with air-water mixture. Because of the rapid rotation the mill experiences a thermal shock which means that the thermal stresses are localized in a thin surface layer. The temperature gradient in the body of mill is of the order of thousands of degrees Celsius per centimeter.

Simulation of a strain-stress state of the mills is necessary for the development of technology to reduce thermal stress.

The classical method of solution of that problem is constructing of a solution of a differential equation in the form of a Fourier series. The solutions have an analytical representation, but the series are poorly converging. We should take into account dozens of members of the series however the terms of the series are oscillatory in nature and affect the real picture of stress and strain distribution. These problems usually led to applying of the Final Element Method which is a most usable for solution of the thermo-elastic problem.

The particulars of FEA software do not always allow one to obtain the solution. The thermal stresses are localized in a thin surface layer and this leads to poor convergence. Basic functions allow one to solve the problem and the use of computers allows one to take into account hundreds of basic functions.

2 The problem statement

Our problem is to consider the temperature stress in the mill. Cooling and heating of the mill occurs in accordance with the following scheme.

The thermal loading and cooling of the mill is schematically shown in Fig.1. In our case we consider cyclic cooling with water and air but there are also some variant of cooling with water-steam mixture or only with water (air). The sector shows areas of different variants of cooling.

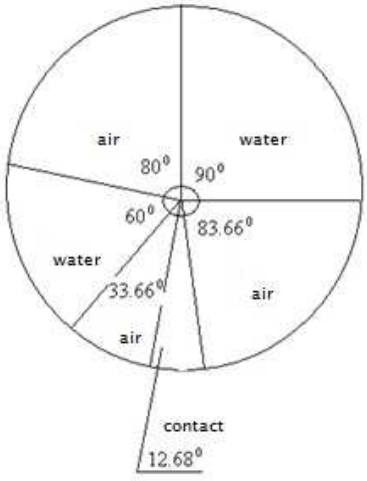


Figure 1: The scheme of cooling of the mill

We suggest that in a narrow zone of the contact we have a certain temperature of surface of the mill (600^{o}C) as an average temperature of the temperature of rolling and the temperature of the mill.

The parameters of cooling medium and the temperature in the contact patch are as follows:

Water: $T_0 = 25^oC, \quad \beta = 41700$ W/m^2 ^{o}K. In this case T_0 is the temperature of the water and β is the thermal conductivity per unit of surface for the cooling with water.

Air: $T_0 = 25^o$C, $\beta = 1700$ W/m^2 ^{o}K. In this case T_0 is the temperature of the air and β is the thermal conductivity per unit of surface for the cooling with air.

Contact: T_0=600^{o}C. Here is the temperature in the contact patch.

Let us state the problem:

$$\lambda \Delta T - \gamma \dot{T} = 0$$

Here: λ =31 W/m ^{o}K is the thermal conductivity of materials of mill; γ =0.673 kJ/kg ^{o}K is the heat capacity of materials of mill; Δ is the two-dimensional Laplace operator; T is the temperature.

Let us calculate the material time-derivative of temperature$\dot{T}$:

$$\dot{T} = \frac{\partial T}{\partial t} + \frac{\partial T}{\partial r}\frac{dr}{dt} + \frac{\partial T}{\partial \varphi}\frac{d\varphi}{dt} = \omega \frac{\partial T}{\partial \varphi} \tag{1}$$

The following problem is the solution of equation of non-stationary conductivity because it is governed by the equation in partial derivatives with three independent variables. For reducing the number of independent variables we use the Eulerian description.

Then $\dot{r}$=0, $\dot{\varphi}$= ω, where ω is the angular velocity of the mill rotation.

As a result we obtain the equation of non-stationary thermal conductivity with two independent variables:

$$\lambda \Delta T - \gamma \omega \frac{\partial T}{\partial \varphi} = 0 \tag{2}$$

Let us solve the problem subjected to the following boundary conditions:

$$0 \le \varphi \le \varphi_0, T = T_0 \tag{3}$$

$$\varphi_0 \le \varphi \le 2\pi, \quad \lambda \frac{\partial T}{\partial r} + \beta \left(T - T_0\right) = 0$$

For example $T_0 = T_0(\varphi)$ in the contact zone ($0 \le \varphi \le \varphi_0$), $T = 600^o$C. Outside this zone the temperature of water-air mixture is T_0 (the temperature of cooling medium):

$$\begin{array}{l} \beta = \beta(\varphi), \\ T_0 = T_0(\varphi) \end{array}$$

The boundary conditions can be rewritten in the form:

$$r = R, \quad \eta \frac{\partial T}{\partial r} + T - T_0 = 0$$

$$\eta = \frac{\lambda}{\beta} = \begin{cases} 0, & 0 \le \varphi \le \varphi_0 \\ \eta(\varphi), & \varphi_0 \le \varphi \le 2\pi \end{cases} \tag{4}$$

3 Solution of the thermal problem

Let us solve this problem by using the approach of mathematical physics.

For the solution of differential equation we use the methods of integral transformation:

$$\frac{1}{2\pi} \int_0^{2\pi} T(r, \varphi) e^{-in\varphi} d\varphi = T_n(r) \tag{5}$$

Then we look for the solution in the form

$$T(r, \varphi) = \sum_{n=-n}^{N} T_n(r) e^{in\varphi} \tag{6}$$

The case of $n = 0$ will be considered separately.

Performing the integral transformation of the equation yields

$$\frac{d^2 T_n}{\partial r^2} + \frac{1}{r} \frac{dT_n}{\partial r} + \left(-\frac{n^2}{r^2} - \frac{in\gamma\omega}{\lambda} \right) T_n = 0 \tag{7}$$

Because

$$\int_0^{2\pi} \frac{\partial T}{\partial \varphi} e^{-in\varphi} d\varphi = \int_0^{2\pi} e^{-in\varphi} dT = T e^{-in\varphi} \Big|_0^{2\pi} + in \int_0^{2\pi} T e^{-in\varphi} d\varphi = in \cdot 2\pi T_n \tag{8}$$

The solution of the equation is expressed in terms of Bessel functions

$$T_n(r) = A_n J_n \left(\sqrt{\frac{-in\omega\gamma}{\lambda}} r \right) + B_n Y_n \left(\sqrt{\frac{-in\omega\gamma}{\lambda}} r \right) \tag{9}$$

whereJ_n, Y_n are the Bessel functions.

As $Y_n(0) = \infty$ and the temperature in the center of mill is limited we have B_n=0. Then

$$T_n = A_n J_n \left(\sqrt{\frac{-in\omega\gamma}{\lambda}} r \right) = A_n J_n \left(-\frac{1-i}{\sqrt{2}} a\xi \right) \tag{10}$$

where

$$\xi = \frac{r}{R}, a = \sqrt{\frac{\omega\gamma\rho}{\lambda}} R \tag{11}$$

and ξ denotes the dimensionless radius, i.e. $0 \le \xi \le 1$.

Let us now proceed to the case $n = 0$.

In this case the equation takes the form:

$$\frac{d^2 T_0}{dr^2} + \frac{1}{r} \frac{dT_0}{\partial r} = \frac{1}{r} \frac{d}{dr} \left(r \frac{dT_0}{\partial r} \right) = 0 \tag{12}$$

Therefore

$$r\frac{dT_0}{dr} = C \tag{13}$$

and

$$T_0 = C\ln r + A_0 \tag{14}$$

As the temperature is bounded at $r = 0$ we have $C = 0$ and $T_0 = const$.

Let us transform the boundary condition. We carry out the integral transformation of the condition (4), to have

$$\frac{1}{2\pi}\int_0^{2\pi}\left[\eta(\varphi)\frac{dT}{\partial r} + T - T_0(\varphi)\right]e^{-in\varphi}d\varphi = 0 \tag{15}$$

We introduce the notations:

$$\frac{1}{2\pi}\int_0^{2\pi} Te^{-in\varphi}d\varphi = T_n(r) \tag{16}$$

$$\frac{1}{2\pi}\int_0^{2\pi} T_0(\varphi)e^{-in\varphi}d\varphi = \tau_n \tag{17}$$

where τ_n is known. We seek $\frac{1}{2\pi}\int_0^{2\pi}\eta(\varphi)\frac{dT}{\partial r}e^{-in\varphi}d\varphi$.

To this end we represent $\eta(\varphi)$ as the Fourier series:

$$\eta(\varphi) = \sum_{k=-k}^{k}\eta_k e^{ik\varphi} \tag{18}$$

where

$$\eta_k = \frac{1}{2\pi}\int_0^{2\pi}\eta(\varphi)e^{-ik\varphi}d\varphi \tag{19}$$

$\eta_k = const$ and depends on the conditions of the contact and cooling.

Let us estimate the integral (19) for $r = R$.

$$\frac{1}{2\pi}\int_0^{2\pi}\eta(\varphi)\frac{dT}{\partial r}e^{-in\varphi}d\varphi = \frac{1}{2\pi}\int_0^{2\pi}\sum_{k=0}^{k}\eta_k e^{ik\varphi}\frac{dT}{\partial r}e^{-in\varphi}d\varphi =$$

$$= \sum_{k=0}^{k}\eta_k\frac{d}{dr}\left(\frac{1}{2\pi}\int_0^{2\pi}Te^{-i(k-n)\varphi}d\varphi\right) = \sum_{k=0}^{k}\eta_k T'_{n-k}$$

As a result we have the boundary conditions for the Bessel functions:

$$\begin{aligned}&\sum_{k=-K}^{K}\tfrac{\eta_k}{r}A_{n-k}J'_{n-k}\left(\tfrac{1-i}{\sqrt{2}}a\sqrt{n}\right) = \\ &= \sum_{k=-K}^{K}\tfrac{\eta_k}{r}A_{n-k}\left[(1-i)a\sqrt{\tfrac{n-k}{2}}J_{n-k-1}\left((1-i)a\sqrt{\tfrac{n-k}{2}}\right) - \right. \\ &\left. - (n-k)J_{n-k}\left((1-i)a\sqrt{\tfrac{n-k}{2}}\right)\right] + A_n J_n\left((1-i)a\sqrt{\tfrac{n-k}{2}}\right) - \tau_n = 0\end{aligned} \tag{20}$$

The result is a system of n equations with n variables. For solution of this system we use the asymptotic representation for Bessel functions because it make the calculation easier and rather accurate.

The form of equations (20) allows using the algorithm with the leading element. The following figure shows the graph of the thermal field

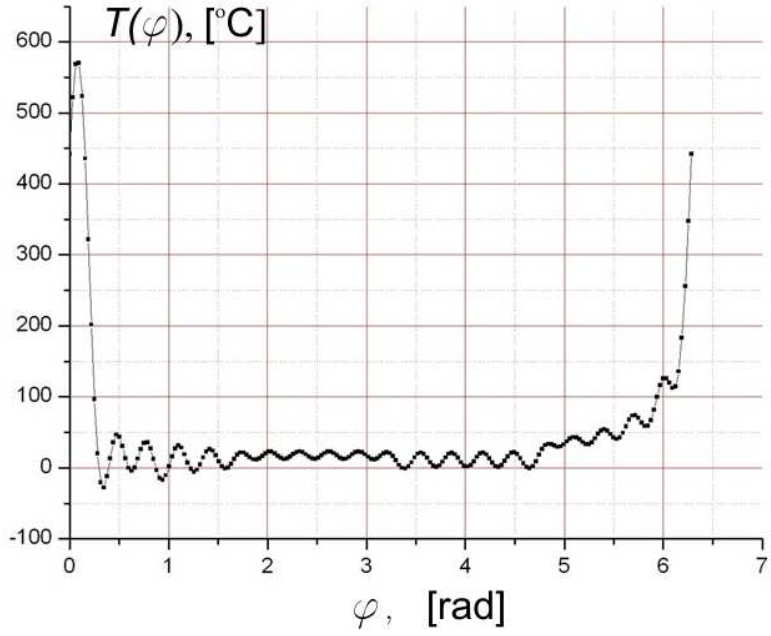


Figure 2: The temperature distribution

4 Calculation of thermal stresses

For determining the thermal stress field we use the thermoelastic potential. In a plane strain formulation the thermoelastic potential satisfies the equation:

$$\Delta\Phi = \frac{1+\nu}{1-\nu}\alpha T \tag{21}$$

$$\underline{u} = \nabla\Phi, \quad \underline{\underline{\varepsilon}} = \nabla\nabla\Phi \tag{22}$$

The stresses are as follows (thermal solution)

$$\sigma_x = -2G\left[\frac{\partial^2\Phi}{\partial y^2} + \frac{\partial^2\Phi}{\partial z^2}\right] = -2G\frac{\partial^2\Phi}{\partial y^2} \tag{23}$$

$$\sigma_y = -2G\frac{\partial^2\Phi}{\partial x^2} \qquad \tau_{xy} = 2G\frac{\partial^2\Phi}{\partial x\partial y} \tag{24}$$

$$\sigma_z = -2G\left[\frac{\partial^2\Phi}{\partial x^2} + \frac{\partial^2\Phi}{\partial y^2}\right] = -2G\Delta\Phi = -2G\frac{1+\nu}{1-\nu}\alpha T = \frac{E}{1-\nu}\alpha T \tag{25}$$

$$\tau_{xz} = 0 = \tau_{yz} \quad \left(\frac{\partial}{\partial z} = 0\right) \tag{26}$$

5 Correction the solution with Airy functions

Now we have the thermal stresses however they do not satisfy the boundary conditions. The Airy function [2] allows us to satisfy any boundary conditions on the mill's surface.

For the correction the solution we use Airy function $U(r,\varphi)$ which satisfies the biharmonic equation:

$$\Delta\Delta U = 0 \tag{27}$$

The solution obtained operates with the thermoelastic potential in terms os the Fourier series $e^{in\varphi}$ Hence the structure of Airy function for the n-th harmonic is:

$$U(r,\varphi) = r^n e^{in\varphi} \tag{28}$$

$$\Delta U(r,\varphi) = \left(\frac{\partial^2}{\partial r^2} + \frac{1}{r}\frac{\partial}{\partial r} + \frac{1}{r^2}\frac{\partial^2}{\partial r^2}\right) r^n e^{in\varphi} = 0 \tag{29}$$

We consider another function:

$$U(r,\varphi) = r^{n+2} e^{in\varphi} \tag{30}$$

$$\Delta U(r,\varphi) = \left(\frac{\partial^2}{\partial r^2} + \frac{1}{r}\frac{\partial}{\partial r} + \frac{1}{r^2}\frac{\partial^2}{\partial r^2}\right) r^{n+2} e^{in\varphi} = 4(n+1) r^n e^{in\varphi} \tag{31}$$

Clearly $\Delta\Delta U = 0$.
So for the correction of solution we use the following systems of functions:

$$U_n = P_n \xi^n e^{in\varphi} + Q_n \xi^{n+2} e^{in\varphi} \tag{32}$$

The stresses are as follows:

$$\sigma_r = \frac{1}{r}\frac{\partial U}{\partial r} + \frac{1}{r^2}\frac{\partial U^2}{\partial \varphi^2}$$

$$\sigma_\varphi = \frac{\partial U^2}{\partial r^2}$$

$$\tau_{r\varphi} = -\frac{\partial}{\partial r}\left(\frac{1}{r}\frac{\partial U}{\partial \varphi}\right)$$

As a result we have solved the problem and satisfy all boundary conditions.

6 Discussion

We use method which enables the regularization with choosing eigenfunctions and limit the number of members of the Fourier series.

The 20-th eigenfunction is of the order of magnitude e^{238}. The discharge grid of computer is full even we use the double precision (16 significant digits).

At the same time the large coefficients in the exponent lead to a very rapid decrease of the eigenfunctions depending on the radius. At a distance of 1-5 mm these coefficients decrease nearly to zero.

Simulations show that the temperature difference on the surface of the mill (of order 500 degrees) is localized in a thin layer of about 2-5 millimeters. This leads to considerable cyclic stresses and then to a fragile destruction of the rolling mill's surface

7 Conclusions

We posed and solved the problem of thermoelasticity for rolls and showed that there are large temperature gradients in a thin surface layer (1-5mm). We obtained the temperature distributions and formulas for the calculating the stresses of the mill using the temperature distributions. Study the conditionality of the solutions, we show that in the thin surface layer, there are large temperature gradients and changes in the eigenfunctions of higher harmonics are about 10^{100}, which defines the ill-conditioned contact problems of the thermoelasticity. The proposed approach to solving such problems is the Tikhonov regularization method.

Acknowledgements

The financial support of the Russian Foundation for Basic Research, grants 08-08-00737 and 08-01-12017, is acknowledged.

References

[1] Hong Li, Youming Wong, Burdest C.F. “Hot deformation behavior and ledeburit refinement mechanism for hypoeutectic lav alloy white cast irons” Materials Scince and Technology- , V. 7, Num. 7.- pp. 660-664. (1991)

[2] S.P. Timoshenko, J.N. Goodier “Theory of Elasticity” , M:“Nauka” (1979)

Sergey Polyanskiy, State Polytechnic University of St. Petersburg, 195251 Politekhnicheskaya, 29 St.-Petersburg, Russia

Solitons and flow in nanotube

I. Yu. Popov O. A. Rodygina S. A. Chivilikhin V. V. Gusarov
popov@mail.ifmo.ru

Abstract

Model of fluid flow in nanotube induced by a soliton in its wall is suggested. Picture of streamlines is obtained. The model is based on the theory of self-adjoint extensions of symmetric operators.

1 Introduction

Flows in nanotubes have many specific features that can't be observed for classical flows. At present there is no theory of nanoflows. In the present paper a variant of nano-hydrodynamical model is suggested. Flow in nanotube depends on many characteristics: chemical composition, structure, wall morphology, etc. Moreover, it is known that there appear some structures in liquid in nanotube due to confinement [1]. In some cases there are dynamical structures induced by flow eddies [2]. It should be stressed that boundary condition, wall structure and profile play crucial role. Namely, it is necessary to take into account vibration and waves in molecular chains forming the nanotube wall. There are experimental evidences of such wall vibration [3]. The most interesting is solitary wave. It is known that there exists stable solution of this type in long molecular chain (so-called "Davidov soliton"). The analogous waves are also in nanotubes [4], [6]. To describe this solution one can consider an exciton of effective mass m interacting with displacement $u(x,t)$ of molecules having masses M from the equilibrium positions at points $x = na$. The corresponding Hamiltonian is [5]:

$$H = \frac{1}{a}\int (\frac{\hbar^2}{2m}\left|\psi_x\right|^2 + \frac{1}{2}Mu_t^2 + MV_0^2U(\rho) - \vartheta\rho\left|\psi\right|^2)dx,$$

where ρ is the relative decreasing of the equilibrium distance a between neighbor molecules, $\rho = -u_x$, V_0 is the longitudinal sound speed in the linear approximation of the chain, θ is the energy which characterizes the interaction of the exciton and the displacement, $U(\rho)$ is the dimensionless potential of intermolecular interaction having minimum at , is the dimensionless potential of intermolecular interaction having minimum at $\rho = 0$, ψ - normalized exciton wave function. The Hamiltonian leads to the following system of equations:

$$i\hbar\psi_t + \frac{\hbar^2}{2m}\psi_{xx} + \vartheta\rho\psi = 0,$$

$$u_{tt} - V_0^2U_{\rho\rho}u_{xx} = \frac{\vartheta}{M}(\left|\psi\right|^2)_x.$$

The system has a stable solution having the form of solitary wave of the profile Φ depending on U . Particularly, for cubic nonlinearity, $U(\rho) = \frac{1}{2}\rho^2 + \frac{\gamma}{3}\rho^3$:

$$\Phi(\xi) = \frac{1}{2}\left(\frac{3\sigma}{4}\right)^{1/3}\left(\frac{\tau}{\gamma}\right)^{1/3} sch^2\left(\frac{1}{2}\left(\frac{\tau\sigma^2}{6\gamma}\right)^{1/3}\xi\right)$$

The speed V of this soliton is as follows:

$$V = V_0\frac{1 + \frac{\tau M}{\gamma m}\left(1 - \frac{3}{5}(\gamma\sigma)^{1/3}(\tau/6)^{2/3}\right)}{1 + \frac{\tau M}{\gamma m}},$$

$$\sigma = \frac{2\vartheta m a^2}{\hbar^2}, \ \ \tau = \frac{\vartheta}{MV_0^2}$$

It should be mentioned that the soliton is stable when $V \ll V$. Geometrically, this solution seems as a local extension of the tube, which moves with the velocity V. This motion causes the motion of the liquid in the neighbourhood of this extension. To describe the flow we use a model in which the local perturbation is replaced by a point-like one [7],[8]. The mathematical background of the model is the theory of self-adjoint extensions of symmetric operators [9]. Consider two-dimensional straight channel (strip). The result for cylindrical channel is absolutely analogous. The Stokes flow for this case is described by the stream function ψ satisfying the biharmonic equation. As for the boundary conditions, it is more convenient to study moving boundary and fixed singularity, i.e. we assume that the normal derivative of the stream function isn't zero (it is equal to the wall velocity). Let us describe briefly the model of point-like perturbation for the Stokes flow. The starting point is the operator Δ_0^2 which is the closure of the restriction of Δ^2 onto the set of smooth functions vanishing in a neighboughood of zero. The domain of the operator is

$$D(\Delta_0^2) = \left\{ u, \ u \in L_2(\Omega), \ \Delta^2 u \in L_2(\Omega), \ u(0) = u'_{x_i}(0) = u''_{x_i x_j}(0) = 0, \ i,j = 1,2 \right\}.$$

Model operator Δ_e^2 is obtained as a self-adjoint extension of symmetric operator Δ_0^2. Due to the correlation $\Delta_0^2 \subset \Delta_e^2 \subset \Delta_0^{2*}$ one can search the extension as a restriction of the adjoint operator. The domain of the operator Δ_0^{2*} consists from the elements of the following form:

$$u(x) = \sum_{i,j=1}^{2} c_{ij}^u g_{x_i x_j}(x) + \sum_{i=1}^{2} c_i^u g_{x_i}(x) + c_0 g(x) +$$
$$\xi(x)(a_0 + \sum_{i=1}^{2} a_i^u x_i + \sum_{i,j=1}^{2} a_{ij}^u \beta_{ij} x_i x_j) + u_0(x).$$

Here $u_0 \in D(\Delta_0)$, $\beta_{ij} = 1$, $i \neq j$, $\beta_{ii} = 2^{-1}$, $\xi(x)-$ smooth cutting function: $\xi(x) = 1$, $|x| \leq 1$, $\xi(x) = 0$, $|x| \geq 2$. To construct the model operator one should establish some correlation between these coefficients in the asymptotic expansion, for example,

$$U_0 = AU_1, \ U_1 = (c_0^u, c_1^u, c_2^u, c_{11}^u, c_{12}^u, c_{22}^u), \ U_0 = (a_0^u, a_1^u, a_2^u, a_{11}^u, a_{12}^u, a_{22}^u), \ A = A*$$

As for detailed description of all classes of extensions, see [10].

The stream function for constructed model operator gives us the model for the Stokes flow with point-like perturbation (rotlet). In our case there are two perturbations in opposite points of the channel walls (soliton position). Let the channel wall be $(x,y): \ x = 0\}$, $\{(x,y): \ x = 2\}$. Due to the linearity of the problem it is possible to consider the equivalent task - moving boundary and point perturbations at fixed positions (instead of moving perturbations and unmoving boundary). The solution has the form of a sum of solutions corresponding to each perturbation (at points $(0,0)$, $(2,0)$:

$$\psi(x,y) = \psi(x,y,0,0) + \psi(x,y,2,0),$$
$$\psi(x,y,0,0) = \Psi(x,y,0,0) + \int_{-\infty}^{\infty} (\Psi(x,y,0,\eta) + \Psi(x,y,2,\eta)) v(\eta) d\eta.$$

Here $\Psi(x,y,0,0)$ is the solution corresponding to the rotlet at the point $(0,0)$. The solution is obtained in explicit form:

$$\psi(x,y,0,0) = \tfrac{x \cdot c}{2} + \mathrm{Re}[\sum_{n=1}^{\infty} (A \cdot [x \cdot \sin(\tfrac{1}{2}\lambda_n \cdot x) - \tan(\tfrac{1}{2}\lambda_n) \cdot \cos(\tfrac{1}{2}\lambda_n \cdot x)] \cdot \exp(-\tfrac{1}{2}\lambda_n \cdot |y|) +$$
$$+ B \cdot [x \cdot \cos(\tfrac{1}{2}\mu_n \cdot x) - \cot(\tfrac{1}{2}\mu_n) \cdot \sin(\tfrac{1}{2}\mu_n \cdot x)] \cdot \exp(-\tfrac{1}{2}\mu_n \cdot |y|) +$$
$$+ \int_{-\infty}^{\infty} \sum_{n=1}^{\infty} (a \cdot [x \cdot \sin(\tfrac{1}{2}\lambda_n \cdot x) - \tan(\tfrac{1}{2}\lambda_n) \cdot \cos(\tfrac{1}{2}\lambda_n \cdot x)] \cdot \exp(-\tfrac{1}{2}\lambda_n \cdot |y - \eta|) +$$
$$+ b \cdot [x \cdot \cos(\tfrac{1}{2}\mu_n \cdot x) - \cot(\tfrac{1}{2}\mu_n) \cdot \sin(\tfrac{1}{2}\mu_n \cdot x)] \cdot \exp(-\tfrac{1}{2}\lambda_n \cdot |y - \eta|)) d\eta \cdot (v - \tfrac{c}{2})].$$

Here λ_n, μ_n are complex roots of equations

$$\sin \lambda_n + \lambda_n = 0,$$

$$\sin\mu_n - \mu_n = 0,$$

A, B, a, b are some constants (model parameters, c, v are flow parameters, namely, c is flux through the cross-section of the channel, v is the rotlet velocity (in our case it is the wall velocity). The pictures of the streamlines are different for different values of the flow parameters. Particularly, for $c = 10, v = 10$ there is a cell occupying the whole cross-section of the channel where one has an eddy. For the flow parameters greater than $c = 50, v = 50$ the cell is divided into two parts by the flow in the centre of the channel.

Acknowledgements

The work is supported by grant 2.1.1/4215 of the program "Development of the potential of high school of Russia 2009-2010".

References

[1] S.A.Chivilikhin, V.V.Gusarov, I.Yu.Popov, A.I.Svitenkov. Model of fluid flow in a nanochannel. Russian J.Math. Phys., Vol. 15, No. 3, 2008, pp. 410-412.

[2] V.V.Gusarov, I.Yu.Popov. Flows in two-dimentional non-autonomous phases in polycrystalline systems. Nuovo Cim. 1996. V. 18D. N 7. P. 799-805.

[3] Z. Insepov, D. Wolf, and A. Hassanein. Nanopumping Using Carbon Nanotubes. Nano Letters. 2006. V.6. N9. pp. 1893-1895.

[4] L.Brizhik, A.Eremko, B.Piette, W.Zakrzewski. Davidov's soliton in zigzag nanotube. Int.J. Quant. Chem. 2010, v. 110, 10-24.

[5] A.S.Davidov. Solitons in Molecular Systems. Dordrecht, Reidel, 1985.

[6] H.Hirori, K.Matsuda, Y.Miyauchi, S.Maruyama, Y.Kanemitsu. Phys Rev Lett 2006, 97, 257401.

[7] I.Yu.Popov. Operator extensions theory and eddies in creeping flow. Physica Scripta. 1993. V. 47. 682-686.

[8] Yu.V.Gugel, I.Yu.Popov, S.L.Popova. Hydrotron: creep and slip. Fluid Dyn. Res. 1996. V. 18 (40), 199-210.

[9] B.S.Pavlov. Extensions theory and solvable models. Uspekhi Mat. Nauk. 1987. N6, 99-131.

[10] I.Yu.Popov. Stokeslet and the operator extension theory. Revista Matematica Univ. Compl. Madrid. 1996. V. 9. N 1. 235-258.

I.Yu.Popov, O.A.Rodygina, S.A.Chivilikhin, St.-Petersburg State University of Information Technologies, Mechanics and Optics, Kronverkskiy, 49, St.-Petersburg, 197101, Russia
St.-Petersburg State Technological Institute (Technical University), Moskovsiy, 26, St.-Petersburg, 190000, Russia

Improvement of the dynamic behaviours of the plant with self synchronizing vibroexciters by means of additional degrees of freedom

Maria A. Potapenko
m.potap@mail.ru

Abstract

The question about possibility of provision of synphase rotation of two unbalanced rotors of vibration plant in selfsynchronizing regime in the first and forth part is discussed. In this case under consideration only the antiphase rotating is "natural stable". The possibility of using for this aim the vibroexciters with additional degree of freedom of rotors or the changing the number of the degrees of freedom of the platform is studied.

In the third part we consider one of arrangements with self-synchronized vibroexciters which can be used in various cases when both horizontal and vertical oscillations of working tool are required. Installations used in foundry manufacture can exemplify this fact.

Forth part is dedicated to the case of the system with self-synchronizing mechanical vibroexciters. It is shown, that so-called "inner pendulum" is obtained when perturb a steady mode of self-synchronization of several inertial vibroexciters.In the case of two activators the equation of semi slow oscillations of "inner pendulum" is obtained.

1 The selfsynchronization of two coaxed unbalanced vibroexciters with inner degree of freedom

1.1 Description Of The Plant

Consider a free solid body fixed by means of springs with certain characteristics and realizing plane oscillations. On the bearer two coaxed unbalanced masses with one rotating degree of freedom are fixed. Within each of debalances a definite additional mass which can oscillate along the debalance's axis is fixed Fig.1.

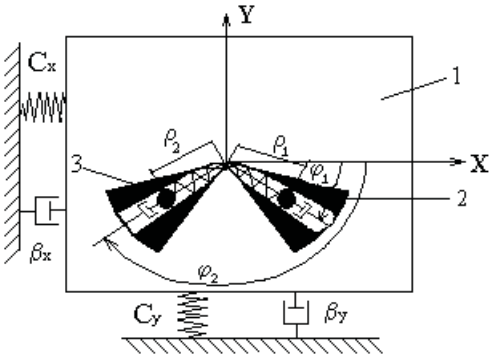


Figure 1: A vibrostand with two debalances having mobile centers of mass

Thereby the vibrostand has two translational degrees of freedom, x and y, each i - debalance having one rotational φ_i and one translational degree of freedom, ρ_i defined by displacement of the additional mass from the axis of rotor.

1.2 The Stationary Regime of Motion of The System

For the stationary synpfase regime of motion of equal vibroexciters, i.e. $\varphi_1 = \varphi_2 = \omega t$; $\rho_1 = \rho_2 = \rho = const$, the system of equations assumed the form [1]

$$\begin{aligned}
&[m_0\varepsilon + m(r+\rho_s)](\ddot{x}\sin\omega t + \ddot{y}\cos\omega t) = K(\omega - \omega_s)\\
&M\ddot{x} = 2[m_0\varepsilon + m(r+\rho)]\omega^2\cos\omega t - \beta_x\dot{x} - C_x x\\
&M\ddot{y} = 2[m_0\varepsilon + m(r+\rho)](-\omega^2\sin\omega t) - \beta_y\dot{y} - C_y y\\
&\omega_\rho^2\rho = (r+\rho)\omega^2 - (\ddot{x}\cos\omega t + \ddot{y}\sin\omega t)
\end{aligned} \tag{1}$$

where $\omega_\rho^2 = \dfrac{C_\rho}{m}$; $M = M^0 + 2m_0 + 2m$, $\beta_\rho = \dfrac{h_\rho}{m}$; $\beta_\sigma = \dfrac{h_\sigma}{m}$.

Here m_o is additional movable mass in the unbalanced mass; m is the mass of the debalance; M is the mass of the whole plant; ε is the eccentricity or the value of displacement of the center of masses of the unbalanced mass from its axis of rotation; r is length of an unstressed spring inside the rotor; ρ is the displacement of the movable mass from the rest or the movable mass radius in the stabilized regime; x is the abscissa of the bearer or the horizontal displacement; y is the ordinate of the bearer or the vertical displacement; ω_ρ is angular velocity of mobile mass ; ω is synchronizable (steady) angular velocity of the rotor; φ is the angle of the rotation of rotor from the rest; β_x, β_y are the coefficients of the damping of oscillations of the bearer along corresponding axes; K is the coefficient of electric damping of the motor; ω_i is the intrinsic (angular) velocity of the unbalanced mass.

After the transformation we can express ρ :

$$\rho = \frac{r\omega^2[(M\omega^2 - C)^2 + \beta^2\omega^2] - 2\omega^4(m_0\varepsilon + mr))(M\omega^2 - C)}{(\omega_\rho^2 - \omega^2)[(M\omega^2 - C)^2 + \beta^2\omega^2] + 2\omega^4 m(M\omega^2 - C)} \tag{2}$$

This equation is an analytical expression for the coordinate ρ of the additional mass in the steady-state regime.

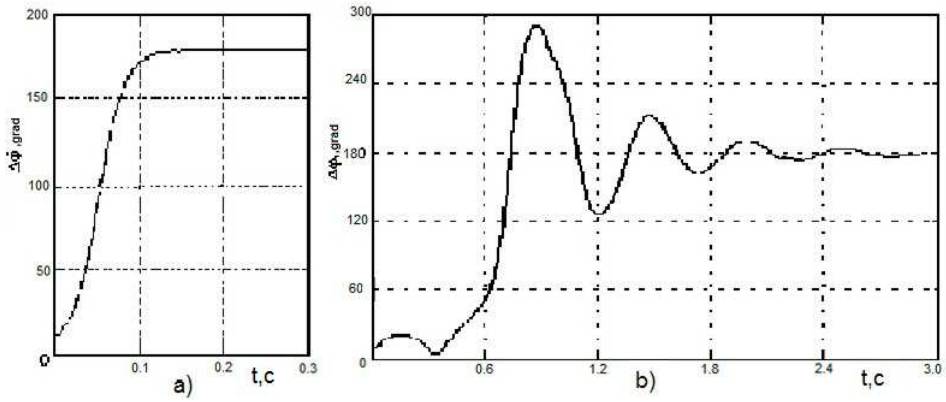


Figure 2: The behaviour of the plant without the movable masses and with inner degrees of freedom in unbalance exciters

On the Fig.2.a) the changing during the time difference of the phases without additional masses in debalances is shown. The curve corresponds to these parameters: $M_0 = 2$ kg,n $m_0 = 1$ kg, $r = 0.01$m, $\varepsilon = 0.035$m, $\beta_x = 84$, $C_x = C_y = 12.6\ \frac{H}{m}$, $\omega_s = 300\ \frac{rad}{c}$.

On the Fig.2.b) the results of the modelling with same initial data as Fig.2.a) with additional movable masses $m = 0.1$kg; $\varepsilon = 0.035$m in the unbalance exciters are presented.

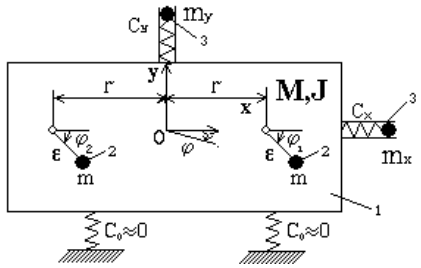


Figure 3: The scheme of system with two movable masses on the bearer

2 Effect of the Additional Degrees of Freedom of the System on Selfsynchronization of Mechanical Vibroexciters

2.1 Problem statement

We will consider a system, consisting of a solid body 1 on which two similar inertial vibroexciters 2 are established symmetrically. Two masses m_x and m_y are fixed to the body by means of elastic elements of the rigidity c . The masses can be displaced in two mutually perpendicular directions (Fig.3). The carrying body can perform flat oscillations perpendicular to the axes of rotation of the rotors. The center of gravity of the body is located half way between the axes of rotation. The body is considered to be softly isolated, i.e. the elastic elements c , connecting it with the fixed base 3, are supposed to have a negligibly small rigidity c. The partial velocities of rotation of the vibroexciters are supposed to be similar and positive [2].

Let us find the stable phasing of the rotation of vibroexciters in the regime of self-synchronization. To this end, we will use the so called integral criterion of stability [2]. In accordance with this criterion we will assume that the rotors are rotating according to the law $\varphi_1 = \varphi_1^o = \sigma_1(\omega t + \alpha_1);\ \varphi_2 = \varphi_1^o = \sigma_2(\omega t + \alpha_2)$.

Here w is an absolute value of the mean angular velocity of the rotation of the rotors; α_i are the initial constant phases of rotation, and each of the values σ_i is equal either to 1 or to -1.

We will take the displacement of the platform x and y from the equilibrium position of the system on the elastic elements, as well as the angles of rotation of the rotors φ_1 and φ_1, counted from the direction of the axis ox clockwise, and the displacements x_1 and y_1 of the masses m_x and m_y from their equilibrium positions to be the generalized coordinates.

Then the expressions for the kinetic and potential energies of the oscillatory part of the system will be written as

$$T = \frac{M}{2}(\dot{x}^2 + \dot{y}^2) + \frac{1}{2}J\dot{\varphi}^2 + \frac{1}{2}m_x\dot{x}_1^2 + \frac{1}{2}m_y\dot{y}_1^2, \quad P = \frac{1}{2}c_x(x_1 - x)^2 + \frac{1}{2}c_y(y_1 - y)^2 \tag{3}$$

Here $M = m + m_x + m_y$ where m is the mass of the carrying body with the rotors and the additional masses, J is the moment of the inertia of the body with the fixed rotors and the additional masses relatively to the axis, passing through its gravity center.

2.2 Equations of motion of the system

The equations of motion of the system under the action of the exciting forces, appearing under the rotation of the rotors of the exciters:

$$\begin{aligned}
&M\ddot{x} - c_x(x_1 - x) = F(\cos(\omega t + \alpha_1) + \cos(\omega t + \alpha_2)) \\
&M\ddot{y} - c_y(y_1 - y) = -F(\sigma_1 \sin(\omega t + \alpha_1) + \sigma_2 \sin(\omega t + \alpha_2)) \\
&J\ddot{\varphi} = Fr(\sigma_1 \sin(\omega t + \alpha_1) - \sigma_2 \sin(\omega t + \alpha_2)) \\
&m_x\ddot{x_1} + c_x(x_1 - x) = 0
\end{aligned} \tag{4}$$

$m_y\ddot{y_1} + c_y(y_1 - x) = 0.$

On the above suppositions the role of the potential function in the system will be played by the expression $D =< T - P >$. Here T and P are the average for the period $\frac{2\pi}{\omega}$ values of the kinetic and potential energies. Having performed the necessary rather cumbersome calculations we obtain

$$D = \frac{F^2}{2M\omega^2} Q \cos\alpha$$

where it is designated $Q = 1 + \sigma_1\sigma_2 - \gamma\sigma_1\sigma_2 + \frac{\eta_x}{z_x^2 - 1} + \sigma_1\sigma_2\frac{\eta_y}{z_y^2 - 1}$. Here $\alpha = \alpha_1 - \alpha_2,\ \gamma = \frac{Mr^2}{J}; \eta_x = \frac{m_x}{M + m_x}; \eta_y = \frac{m_y}{M + m_y};\ z_x^2 = \frac{Mm_xc_x\omega^2}{M + m_x}; z_y^2 = \frac{Mm_yc_y\omega^2}{M + m_y}$.

For the stability of the co-phase rotation it is necessary and sufficient that at $\alpha = 0$ the function D should have a minimum, i.e. so that $Q < 0$.

2.3 Special cases

Let us consider some special cases.

1)The additional masses are absent ($m_x = m_y = 0$), then $Q = 1 + \sigma_1\sigma_2 - \frac{Mr^2}{J}$. This expression coincides with the one, obtained in the book [2].

2) One of the additional masses is absent ($m_x = 0$), then $Q = 1 + \sigma_1\sigma_2 - \frac{Mr^2}{2} + \sigma_1\sigma_2\frac{\eta_y}{z_y^2 - 1}$. The condition of stability of the synchronous motion for the rotation of the rotors in the opposite directions looks as $\frac{Mr^2}{J} > -\frac{\eta_y}{z_y^2 - 1}$. Consideration is given to the possibilities of providing a co-phase synchronous rotation by means of introducing additional degrees of freedom either to the rotors of the exciters or by changing the number of the degrees of freedom of the platform.

The results obtained can be used when producing vibrational machines with self-synchronized vibroexciters, and it is these results that show that by introducing additional masses it is possible to provide the stability of the desired phasing of the rotation of the exciters, which is unstable when these masses are absent.

3 Self-synchronization of Four Mechanical Vibroexciters at Various Variants of Kinematical Connection

3.1 The System Scheme

The system scheme is shown in Fig.4. The rigid platform 1 of mass M is installed on vibroinsulated springs 2 of rather small rigidity C. Two pairs of coaxial mechanical vibroexciters are installed on the end faces of the platform. Eccentricities of the exciter rotors ε and unbalanced masses m in each pair are considered to be identical (ε_h and ε_h, m_h and m_v correspondingly). All vibroexciters are considered possessing identical positive partial angular speeds ω. Intervals of rotors axes from the center of platform masses are denoted by b and h. For the generalized coordinates we'll take horizontal displacement x and vertical displacement y of the platform from the position corresponding to the unstrained elastic elements, rotation angle of the platform φ, read anticlockwise from the line of horizon, and also rotation angles of the rotors φ_s, read according to Fig.4.

3.2 The Task Solution with Using Integral Test of Stability. Potential Energy of System

In the considered case, partial angular speeds of unbalanced vibroexciters are positive and identical or not strongly differ from each other, the platform is softly vibroinsulated, and oscillation part of the system is linear, then the averaged kinetic energy of the platform can be taken for the potential function $D =< T_0 >=< \frac{M}{2}(\dot{x}^2 + \dot{y}^2) + \frac{I}{2}\dot{\varphi}^2) >$

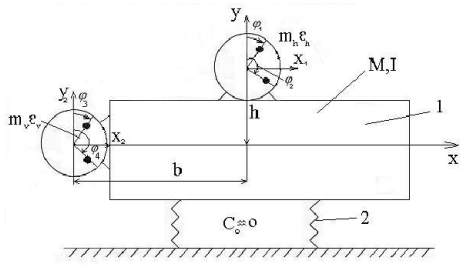


Figure 4: The scheme of system with two pairs of mechanical vibroexciters

Rough minima of function D on phase difference $\alpha_3 - \alpha_4$ corresponds to the steady stationary modes of synchronous rotation of the rotors[4]

The equations of small oscillations of the platform under the specified conditions have the form:

$$\begin{cases} M\ddot{x} = m_h\varepsilon_h\omega^2(\sin\varphi_1 + \sin\varphi_2) + m_v\varepsilon_v\omega^2(\sin\varphi_3 + \sin\varphi_4) \\ M\ddot{y} = m_h\varepsilon_h\omega^2(\cos\varphi_1 + \cos\varphi_2) + m_v\varepsilon_v\omega^2(\cos\varphi_3 + \cos\varphi_4) \\ I\ddot{\varphi} = m_h\varepsilon_h\omega^2 h(\sin\varphi_1 + \sin\varphi_2) + m_v\varepsilon_v\omega^2 b(\cos\varphi_3 + \cos\varphi_4) \end{cases} \tag{5}$$

where $\varphi_s = \sigma_s(\omega t + \alpha_s), s = 1, ..., 4$ and values σ_s assume the directions of rotor rotation: σ_i =1 anticlockwise, σ_i =-1 clockwise.

We obtain:

$$\begin{aligned} D = {} & \sigma_1\sigma_2 m_h^2\varepsilon_h^2\omega^2\cos(\alpha_1 - \alpha_2)\left[\frac{1}{M} + \frac{h^2}{2I}\right] - \sigma_3\sigma_4 m_v^2\varepsilon_v^2\omega^2\cos(\alpha_3 - \alpha_4)\left[\frac{1}{M} + \frac{b^2}{2I}\right] + \\ & + m_h m_v\varepsilon_h\varepsilon_v\omega^2\left(\frac{\sigma_1\sigma_3}{M}\cos(\alpha_1 - \alpha_3) + \frac{\sigma_1\sigma_4}{M}\cos(\alpha_1 - \alpha_4) + \frac{\sigma_2\sigma_3}{M}\cos(\alpha_2 - \alpha_3) + \right. \\ & + \frac{\sigma_2\sigma_4}{M}\cos(\alpha_2 - \alpha_4) - \sigma_1\frac{bh}{2I}\sin(\alpha_3 - \alpha_1) - \sigma_1\frac{bh}{2I}\sin(\alpha_4 - \alpha_1) - \\ & \left. - \sigma_2\frac{bh}{2I}\sin(\alpha_3 - \alpha_2) - \sigma_2\frac{bh}{2I}\sin(\alpha_4 - \alpha_2)\right) + C, \end{aligned} \tag{6}$$

3.3 The Cases of Kinematical Connection of the Rotors in Pairs

1. The upper and side rotors are connected in such a manner that each pair provides rectilinear driving force in vertical and horizontal directions correspondingly. Here: $\sigma_1 = -\sigma_2 = 1$; $\alpha_1 = \alpha_2$; $\sigma_3 = -\sigma_4 = 1$; $\alpha_3 = \alpha_4 + \pi$

2. The upper and side rotors are connected in such a manner that both pairs raise vertical driving force. In this case $\sigma_1 = -\sigma_2 = 1$; $\alpha_1 = \alpha_2$;
$\sigma_3 = -\sigma_4 = 1$; $\alpha_3 = \alpha_4$

It is easy to see, that in both cases functions D do not depend on angles α_s , i.e. the pairs of vibrators are not dynamically connected. Also in the first case for providing the same character of rotors motion there is no need to connect rotors in both pairs kinematically: it is enough to make it only for one pair. The other pair is self-synchronized with the same phases.

4 Slow Oscillations of the Unbalanced Rotors when Perturbing the Self-synchronization Regimes

4.1 The Scheme and the Description of System

The considered system (Fig.5) represents the rigid platform (2), connected with the motionless basis (1) by means of an elastic element with rigidity c and linear dampening element with decrement factor β . Two unbalanced vibroexciters (3), unbalanced rotors, which are set in rotation by asynchronous type electric engines; rotors‘ axes are perpendicular to the oscillation direction of

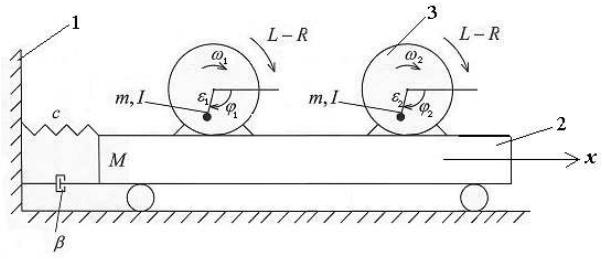


Figure 5: The scheme of system when perturbing the self-synchronization regimes

a platform , are set on the platform. The described system represents the elementary system considered in the theory of self-synchronization of vibroexciters [2].

It is described system of three equations:

$$\begin{aligned} I_s\ddot{\varphi}_s &= L_s(\dot{\varphi}_s) - R(\dot{\varphi}_s) + m_s\varepsilon_s(\ddot{x}sin\varphi_s + gcos\varphi_s) \\ M\ddot{x} + \beta\dot{x} + Cx &= \sum_{j=1}^{2} m_j\varepsilon_j(\ddot{\varphi}_j \sin\varphi_j + \dot{\varphi}_j^2 \cos\varphi_j) \end{aligned} \tag{7}$$

where $s = 1, 2$; m_s,I_s are weight and the inertia moment of a rotor of s-th vibroexciter with respect to axis passing through its centre of gravity; L_s - the rotating moment of the asynchronous electric motor; R_s -the force moment of resistance to the rotation; M - weight of the whole system; ε - eccentricity of a rotor; φ_s - angle of rotation of the rotors,counted from an axis OX on a clockwise direction; x-displacement of a platform from the position corresponding to the unstressed elastic element.

4.2 The Equation of Movement of the Inner Pendulum

As the theoretical researches confirmed by numerous experiments [4] show, system (7) under certain conditions admits stable stationary solutions: $\varphi_s = \ = \omega t + \alpha_s + \psi_s(wt)$ where $\alpha_s = const$; ψ_s, x - 2π - periodic functions with zero averages on this argument. These solutions correspond to the synchronous rotation of activators‘ rotors with average frequency ω.

Near to stationary value $\alpha_s = const$ phase shifts α_s represent slowly changing time functions t, satisfying to the equations:

$$I_s\ddot{\alpha}_s + k_s\dot{\alpha} = \sigma_s L_s(\sigma_s\omega) - R_s^0(\omega) \ + V_s(\alpha_1 - \alpha_k, ..., \alpha_{k-1} - \alpha_k, \omega), \quad s = 1, 2$$

where the vibrating moments $V_s = -\dfrac{m_s\varepsilon_s\omega^2}{2M\Delta}\sum_{j=1}^{k} m_j\varepsilon_j \sin(\alpha_s - \alpha_j - \gamma)$

And each of sizes σ_s can be either 1 or -1. Here: $\Delta = \sqrt{(1-\lambda^2)^2 + 4n^2}$,

$\sin\gamma = -\dfrac{2n}{\Delta}$, $p = \sqrt{\dfrac{c}{M}}$, $n = \dfrac{\beta}{2M\omega}$, $\lambda = \dfrac{p}{\omega}$.

It is also supposed, that $\dot{\alpha}_s << \omega$. For two identical vibrators $L_s - R_s = 0$, and the system is transformed. It is obvious that stationary values of slow variables $\alpha_s = const$ correspond to synchronous motion.

Indicate $\alpha = \alpha_1 - \alpha_2$ and, subtracting the second system equation from the first, we will obtain:

$$I\ddot{\alpha} + k\dot{\alpha} + \frac{(m\varepsilon\omega^2)^2}{M}\frac{p^2 - \omega^2}{((p^2-\omega^2)^2 + 4n^2\omega^2)^2}\sin\alpha = 0$$

Here k - total decrement coefficient. This equation has two stationary solutions $\alpha = \alpha_1 = 0$ and $\alpha = \alpha_2 = \pi$. The first solution $\alpha = \alpha_1 = 0$ is steady in preresonant area $\omega < p$, and the second $\alpha = \alpha_2 = \pi$ - in postresonant area $\omega > p$.

Frequency of relative free rotors‘ oscillations in both cases is determined from the equation:

$$q_2 = \frac{m\varepsilon\omega^2}{\sqrt{MI}} \frac{\sqrt{\mid p^2 - \omega^2 \mid}}{\sqrt{(p^2 - \omega^2)^2 + 4n^2\omega^2}}$$

This frequency is much above the change of angular speed rate of rotors in start-up mode frequency. At the same time, it is much below the speed of rotation.

It is remarkable, that this frequency in $\sqrt{2}$ times more than semi slow rotor oscillation frequencies obtained in work [3].

References

[1] Selected Topics in Vibrational Mechanics./ World Scientific, New Jersey-London/ Edited by I.I. Blekhman, 2004

[2] Blekhman I. Vibrational Mechanics. World Scientific. Singapore-New Jersey-London-Hong Kong,2000

[3] Indeitsev D., Blekhman I. and Fradkov A. Slow motions in systems with inertially excited vibrations.*IFAC ALCOSP 2007*,http://lib.physcon.ru

[4] Blekhman I.I. Self - synchronization of Dynamical Systems, Moscow, Nauka, 1971

Mary A.Potapenko, Saint-Petersburg, Bolshoy pr., 61, Russia

Influence the dispersion in nonequilibrium models for continuous mechanics

Evelina V. Prozorova
prozorova@niimm.spbu.ru

Abstract

We discuss the problems that can be appearing to considerate the angular momentum variation in elementary volume and cross flux through the sides of an elementary volume. The equilibrium conditions of forces are the special case of more common conditions of equilibrium of angular momentum and are followed from these.The aim of this paper is to find the reason for appearing the second viscosity for cross flow at large gradients of the physical values. For normal shock waves angular momentum does not work but the self- diffusion give additional diffusion. The convective flow has the same value as diffusion flow for the Mach number M=1. It will be received in our work. The boundary conditions for rarefied gas near the surface make more accurate than early.

1 Introduction

In the classical Newton mechanics we have four conservation laws: masses, liner moment, energy, angular momentum. In continuous mechanics we use only three first laws. This paper reports on influence the angular momentum variation in an elementary volume and cross flux through the sides of an elementary volume is investigated. The fourth law follows from the hypothesis that the equilibrium conditions of forces are the special case of more common conditions of equilibrium of angular momentum. The relationships between the Boltzmann equation and hydrodynamics are discussed. Some experimental facts tell us about importance of gradients of physical parameters. The modified equations of hydrodynamic follow from the modified Boltzmann equation [1],[2]. The modified Navier-Stokes equations and the law for angular momentum were received. Besides usually convective flows the cross flux performed. The modified laws of conservation were received for the particles without structure. As example for density was take into consideration only the flows of density across the surface an elementary volume. Conclusion of the equation with the more full physical idea as classical was done by Vallander in 1951 year for the cross effects [3]. The self- diffusion, energy and linear momentum were considered for the perfect continuous gas in supposition about internal energy E $E = c_v T$. Here c_v- the coefficient of thermal capacity under constant volume. For great gradients of physical values colliding molecules are belonging to different distribution functions can have different macroparameters (density, temperature, velocity) . The influence variation of the distribution function over times of the mean time τ collisions of particles was suggested B.V.Alexeev [4]. We suggest that the second term in collision integral necessary to take into account. It received after expansion the distribution functions in collision integral over space coordinates near the point x. Differentiating the equilibrium distribution function in the second term of collision integral the structure of formulas by S.V.Vallander can be received. Gas-surface interaction plays an essential role in processes connected with atmosphere re-entry vehicles [5]. It is necessary to know aerodynamic characteristics of the spacecraft for the rarefied gas, transitional rarefied – flow regimes and continuous regimes. It is essential to solve the conjugate problem at any height of the flow, but we have not the theory for all the range of parameter changing. The modified Boltzmann and Navier-Stokes equations are needed boundary conditions The boundary conditions for rarefied gas near the surface make more accurate than early. If we deal with continuous medium, the external boundary for boundary layer condition can be determined

as the value of rotor velocity or as the value of normal velocity. This is valid for the vertical velocity. For the longitudinal velocity it is necessary to include friction. For the rarefied gas the boundary conditions must include the value of gas flow beside the classical boundary conditions. Besides the aim of this paper is to find the reason for appearing the second viscosity for cross flow at large gradients of the physical values. For normal shock waves angular momentum does not work but the self- diffusion give additional diffusion. The convective flow has the same value as diffusion flow for the Mach number M=1. It will be received in our work. Regarding the problem of turbulence we analyze some easy models of numerical simulation and are compared them with value of the third derivative in movement equation.

2 Flows through the sides of an elementary volume

In the classical Boltzmann equation angular momentum does not conserve. In classical mechanics this law was received as equilibrium conditions of forces and than the symmetric pressure is needed for continuous mechanics as from the kinetic theory. For equilibrium conditions we need to take into consideration the equation for angular momentum. The angular momentum M_I does not contain new dimension constants. It is providing exclusive system of equations. The classical laws of conservation were received as the laws of conservation the considered value. Adding the influence of the angular momentum in an elementary volume we do not change this assumption. As example for density one takes into consideration only the flows of density across the surface an elementary volume. It follows from phenomenon conclusion of equation for mass: changing mass in an elementary volume is equal to sum of density flows across the restrictive surface. In general case we have besides convective flow self-diffusion f and self- termodiffusion flows. The fundamental difference between ours and classical equations for the description of continuum mechanics consists in considering the angular momentum variation in an elementary volume, as usually it is disregarded. The elementary volume of an open system exchanges with the surroundings by the components of physical values in all directions. A variation of angular momentum leads to additional diffusion of the particles. For continuous medium some changes of Navier-Stokes equations were proposed in [1],[2]. For gas the laws was obtained from the modified Boltzmann equation. As a result the additional terms with third derivative in equation of movement and with the second derivative in equation for the density are appeared and we have received the modified Navier-Stokes equations in the form

$$\frac{\partial \rho}{\partial t} + \frac{\partial \rho u_i}{\partial x_i} + \frac{\partial}{\partial x_i}\left(x_i \frac{\partial \rho u_i}{\partial x_i} \right) = 0.$$

$$\frac{\partial \rho u_i}{\partial t} + \frac{\partial}{\partial x_i}\left(\rho u_i u_j + P_{ij} + x_i \frac{\partial P_{ij}}{\partial x_i} \right) - \frac{X_i}{m}\rho = 0.$$

$$\frac{\partial}{\partial t}\rho\left(\frac{3}{2}RT + \frac{1}{2}u^2\right) + \frac{\partial}{\partial x_j}\left[\rho u_j\left(\frac{3}{2}RT + \frac{1}{2}u^2\right) + u_k P_{kj} + q_j\right] + \\ + \frac{\partial}{\partial x_i} x_i \frac{\partial}{\partial x_j}\left[\rho u_j\left(\frac{3}{2}RT + \frac{1}{2}u^2\right) + u_k P_{kj} + q_j\right] = 0 \,.$$

Here t is the time, ρ is the density, $x,\ y,\ z$ are the Cartesian coordinates of a particle, u_i are the projections of its velocity, P_{ij} is the stress tensor, X_i are the projections of a volume force, q_j is the heat flow, R is the gas constant, and T is a temperature. From the modified Boltzmann equation besides the usual conservation equations of mass, moment, energy we obtained the equation for angular momentum

$$\frac{\partial \vec{r}}{\partial x} \times \vec{p}_x + \frac{\partial \vec{r}}{\partial y} \times \vec{p}_y + \frac{\partial \vec{r}}{\partial z} \times \vec{p}_z + x_j \frac{\partial}{\partial x_j}\left(\vec{P}_j\right) = M_I$$

Besides angular momentum we need to include the cross process. Let us denote the mass flows

through the faces of elementary cube as

$$Q_x = D_1\frac{d\rho}{dx} + D_2\frac{dT}{dx} \quad , \quad Q_y = D_1\frac{d\rho}{dy} + D_2\frac{dT}{dy}, \quad Q_z = D_1\frac{d\rho}{dz} + D_2\frac{dT}{dz}.$$

Here D_1, D_2 are the coefficients of self-diffusion f and self- termodiffusion respectively.

There $Q_x, Q_y, Q_z$are the flows of mass across the grounds which are perpendicular to axis of coordinates moving with gas at velocity V_i.

$$t_x = k_1\frac{d\rho}{dx} + k_2\frac{dT}{dx}, \quad t_y = k_1\frac{d\rho}{dy} + k_2\frac{dT}{dy}, \quad t_z = k_1\frac{d\rho}{dz} + k_2\frac{dT}{dz}$$

Here t_x, t_x, $t_x$are the flows of energy across the surface.

$$D_1 = \frac{\mu}{\rho}\alpha_1, \quad D_2 = \frac{\mu}{T}\alpha_2, \quad k_1 = \frac{\mu c_v T}{\rho}\beta_1, \quad k_2 = \mu c_v \beta_2$$

Conclusion of the equation with the more full physical idea as classical was done by Vallander in 1951 [3] (without angular momentum). The self- diffusion, energy and linear momentum were considered for the perfect continuous gas in supposition about internal energy E $E = c_v T$. Here c_v- the coefficient of thermal capacity under constant volume. Here ρ- density, D_1, D_2 are coefficient of density, coefficient of thermo-self-diffusion, k_1–coefficient of density thermal conductivity, k_2 – coefficient of temperature thermal conductivity, R – gas constant, μ-viscosity, λ-coefficient of the second viscosity. For perfect gas α_1 , α_2 , β_1 , β_2 , a -the numerical constants are order unit. On account of the above we have new system of equations for continuous mechanics without influence of angular momentum but with cross flows (for general case it is necessary to take into consideration influence angular moment that is turn medium in an elementary volume and cross flow)

$$\tau_{xx} = -R\rho T + \lambda div\mathbf{v} + 2\mu\frac{dv_x}{dx}, \quad \tau_{xy} = \mu\left(\frac{dv_x}{dy} + \frac{dv_y}{dx}\right),$$

$$\frac{\partial\rho}{\partial t} + \rho div\mathbf{v} = \frac{\partial Q_x}{\partial x} + \frac{\partial Q_y}{\partial y} + \frac{\partial Q_z}{\partial z},$$

$$\rho\frac{d\mathbf{v}}{dt} + \mathbf{v}\left(\frac{\partial Q_x}{\partial x} + \frac{\partial Q_y}{\partial y} + \frac{\partial Q_z}{\partial z}\right) = \rho\mathbf{F} + \frac{\partial\bar{\tau}_x}{\partial x} + \frac{\partial\bar{\tau}_y}{\partial y} + \frac{\partial\bar{\tau}_z}{\partial z},$$

$$\rho\frac{dE}{dt} + \left(E - \frac{v^2}{2}\right)\left(\frac{\partial Q_x}{\partial x} + \frac{\partial Q_y}{\partial y} + \frac{\partial Q_z}{\partial z}\right) = \\ = \frac{\partial t_x}{\partial x} + \frac{\partial t_y}{\partial y} + \frac{\partial t_z}{\partial z} + \bar{\tau}_x\frac{\partial\mathbf{v}}{\partial x} + \bar{\tau}_y\frac{\partial\mathbf{v}}{\partial y} + \bar{\tau}_z\frac{\partial\mathbf{v}}{\partial z}.$$

Thus from phenomenological theory these flows can be determined as cross flows without determination of coefficients. The protozoa kinetic theory gives these crossing flows but the general mathematic theory does not contain these effects. Besides, to that effects (flows) can be added the molecule mobility with coefficient which tied together the self-diffusion coefficients $j_F = \rho b\, m_0\mathbf{F}$, $\mathbf{F}$-force, b-molecular mobility, m_0—molecular mass or in case of the variable $\mathbf{F}$=$\mathbf{F}$($\mathbf{x}$,t) besides the force will be worked force moment. The previous equations was received from the Boltzmann equation. Thus besides the term with the angular moment it is need to take into consideration the cross flows. For the kinetic theory it is mean that collision integral can be written as

$$\int(\tilde{f}'f_1' - \tilde{f}\overline{f}_1)d\epsilon d\zeta,$$
$$\tilde{f} = f(t,\chi,\zeta)\ \tilde{f}_1 = f_1(t,\chi,\zeta_1),$$
$$\tilde{f}' = f'(t,\chi,\zeta_1')\ \tilde{f}_1 = f_1' = (t,\chi,\zeta_1')$$

Here f is the one-particle distribution function, $\vec{r}$- radius vector; $\vec{x}$- coordinate of the point and according to definition of f in element of physical volume $d\vec{x}$ near the point $d\vec{-}\xi$ in moment t probable number of molecules with velocity in element $d\vec{\xi}$ near the $\vec{\xi}$ is $f\left(t,\vec{x},\vec{\xi}\right)d\vec{\xi}d\vec{x}$, here I is the collision integral. Solution of the second equation is easier.

$$\tilde{f}'\tilde{f}_1' - \tilde{f}\,\tilde{f}_1 = f'f_1' + \Delta t\left\{\boldsymbol{\xi}'\frac{\partial f'}{\partial x}\left(t,x,\boldsymbol{\xi}'\right)\cdot f_1'\left(t,x,\boldsymbol{\xi}_1'\right) + f_1\left(t,x,\boldsymbol{\xi}'\right)\boldsymbol{\xi}_1'\frac{\partial f_1'}{\partial x}\left(t,x,\boldsymbol{\xi}_1'\right)\right\} -$$
$$-f\,f_1 - \Delta t\left\{\boldsymbol{\xi}\frac{\partial f}{\partial x}\left(t,x,\boldsymbol{\xi}\right)\cdot f_1\left(t,x,\boldsymbol{\xi}_1\right) + \boldsymbol{\xi}_1\frac{\partial f_1}{\partial x}\left(t,x,\boldsymbol{\xi}_1\right)f\left(t,x,\boldsymbol{\xi}\right)\right\} + O\left(\Delta x\right)$$

Here $\Delta\tilde{x}$ is corresponding to $\Delta x_1'$ or Δx_1. Here t is time; ξ are the phase velocity. The general number of collisions of ξ – molecules in element $d\xi$.

$$\left(\tilde{f}'\tilde{f}_1' - \tilde{f}\,\tilde{f}_1\right) \approx \left(f'f_1' - f\,f_1\right) + \Delta t\frac{\partial f}{\partial x}\left(\xi' f_1' + \xi_1' f' - \xi f_1 - \xi_1 f\right)$$

It is essential that n,T, **u** are the function of t**,** **x** but not the function of ξ**.** So solution of the Boltzmann equation by the Chapman-Enskog method as we see is invariant relatively choice of these functions

$$f_0\left(t,x,\boldsymbol{\xi}\right) = n\left(\frac{m}{2\pi kT}\right)^{3/2}\exp\left\{-\frac{m}{2kT}\left(\boldsymbol{\xi}-u\right)^2\right\}$$

$$\frac{\partial f_0}{\partial x} = \frac{1}{n}f_0\frac{\partial n}{\partial x} + \left(-\frac{3}{2}\right)\frac{1}{T}f_0\frac{\partial T}{\partial x} + \frac{mc^2}{2kT^2}f_0\frac{\partial T}{\partial x} + f_0\left(\frac{m}{kT}(\xi-u)\frac{\partial u}{\partial x}\right)$$

$$c = \xi - u$$

Usually we assume that last term for local coordinates equals to zero; probably for our case it is essential (mobility molecules) . For the calculation derivatives this value can be used as all the others are values of more order. The structure of this formula is as formula by Vallander S.V. His formulas can be received for interacting molecules with hard potential. In other case it is necessary to take averaged cross section. In general case (nonstationary) the collision integral can be written in form suggested by B. Aleexeev. Const α ,... are defined by the species of concrete potential. Always in spite of that concrete time for two molecules we will be exploit as average time which is proportional to inverse value of frequency. For numerical solution can be used the average values of collision integrals for concrete velocity. As example is normal shock wave. We discuss this problem as for normal shock wave angular momentum does not work. Than influence of cross flows can be investigated in pure form. The classical structure normal shock waves can be found in [6]

$$\rho u = \rho_0 D = a, \quad p + \rho u^2 + w = p_0 + \rho_0 D^2 = p_{00}, \quad w = -\mu\frac{du}{dx},$$
$$\frac{\gamma}{\gamma-1}\frac{p}{\rho} + \frac{1}{2}u^2 + \frac{1}{\rho_0 D}\left(S + uw\right) = h_0 + \frac{D^2}{2} = h_{00}, \quad S = -k\frac{dT}{dx}, \quad \frac{p}{\rho} = RT$$

All detonations are the same as on the above.

To investigate the weak shock wave for Mach number M = 1 is very difficult. The front of shock wave is not stability for this regime. The cause of instability is not clearly. In my opinion the cause is in the next. Influence of self- diffusion (only of density) leads to

$$\frac{d\rho u}{dx} = \frac{d}{dx}\frac{\mu\alpha_1}{\rho}\frac{d\rho}{dx},$$

$$\rho u\frac{du}{dx} + u\frac{d}{dx}\frac{\mu\alpha_1}{\rho}\frac{d\rho}{dx} + \frac{dp}{dx} - \frac{d}{dx}\,\frac{4}{3}\mu\frac{du}{dx} = 0,$$

$$\rho\frac{d}{dx}c_VT+\left(c_VT-\frac{u^2}{2}\right)\frac{d}{dx}\frac{\mu}{\rho}\alpha\frac{d\rho}{dx}=\frac{4}{3}\mu\left(\frac{du}{dx}\right)^2+\frac{d}{dx}\lambda\frac{dT}{dx}+\frac{d}{dx}\frac{\mu c_VT}{\rho}\frac{d\rho}{dx}$$

So small perturbation can be produced prevalence of convective flux or self-diffusion and shock front can loss stability.

If $\eta=\frac{\rho_0}{\rho}$, we have

$$\frac{d\eta}{dx}-\frac{D\rho_0}{\mu\alpha_1}\eta+\frac{u\rho_0}{\mu\alpha_1}=0$$

From the classical case [6] we resolve

$$\frac{1-\eta}{(\eta-\eta_1)^{\eta_1}}=\frac{1-\sqrt{\eta_1}}{\left(\sqrt{\eta_1}-\eta_1\right)^{\eta_1}}e^{a\frac{\left(M^2-1\right)}{M}\frac{x}{l_0}}=Ae^{a\frac{\left(M^2-1\right)}{M}\frac{x}{l_0}}.$$

Valuing of the self- diffusion flow relativity forward flow we have [7] $\frac{\frac{\mu_0\alpha_1}{\rho_0}\frac{d\eta}{dx}}{\rho_0D_0}\approx 1$ for M = 1.

3 The free mixture flow

As seen from the articles [8],[9] the modified equations have no new constants. So the problem which is similar for classical case has the similar solution too with angular momentum. The order of the new equations (for the density and for the linear moment,energy) is more than in classical case. If we deal with continual medium the external boundary for boundary layer condition can be determined as the value rotor velocity or as value normal velocity. Stationary free mixture layer is appearing in case of movement of two homogeneous liquids flowing in the direction of increase x coordinate. As example the movement with U_1 and U_2velocities which is be in contact with each other at $x=0$, $y=0$, $-\infty<z<\infty$. velocity. Besides the usual classical similar solution [10] it is possible the similar solution by assigning the friction as function of velocity difference U_1-U_2.

$$u\frac{\partial u}{\partial x}+v\frac{\partial u}{\partial y}=\frac{\partial}{\partial y}\left(\mu\frac{\partial u}{\partial y}\right)+\frac{\partial}{\partial y}\left(\nu\frac{\partial^2u}{\partial y^2}\right);$$

$$\frac{\partial u}{\partial x}+\frac{\partial v}{\partial y}=0$$

The boundary conditions for the classical problem

$$u=U_1-U_2,\quad v=0,\quad \mu\frac{\partial u}{\partial y}=\tau_w,\quad y=0;$$
$$u=U_1,\quad y\to\infty,\quad x>0;\quad u=U_\infty,\quad x=0.$$
$$u=U_2,\quad y\to-\infty,\quad x>0.$$

The similar problem of this task

$$-1/2\eta\Phi\frac{d\Phi}{d\eta}+V\frac{d\Phi}{d\eta}=\mu\frac{d^2\Phi}{d\eta^2}+\frac{d}{d\eta}\left(\nu_1\eta\frac{d^2\Phi}{d\eta^2}\right);$$
$$-1/2\eta\frac{d\Phi}{d\eta}+\frac{dV}{d\eta}=0$$

or

$$2\eta\psi''''+2\psi'''+\psi\psi''=0$$

with boundary conditions

$$\psi(0)=0,\qquad \psi'(0)=1-a,\qquad \psi''(0)=\alpha,\qquad \psi'(-\infty)=a.$$

Here 0 conditionally defined contact surface. Account of coordinate y is need to do from contact surface.

4 Influence dispersion near the surface

The problem for moving gas near the surface has some singularities. molecules

The modified Boltmann and Navier-Stokes equations are needed boundary conditions. To solute the Boltzmann equation is more difficult than Navier-Stokes equations. So better to solute Navier-Stokes equations

For the classical case near the surface the Knudsen layer is considered [5]. This layer has the length of order free path. In the previous works the equation for two-particle function was received near the surface in case movement it in gas. Analysis showed that suggested equation can be well for atoms which are moving in normal direction. For general case it is necessary to add the term $X_{22} = \dfrac{\partial f_2}{\partial \xi_2}$. The new term represents interaction surface atoms by them. For the particles without structure the equilibrium become established during one collision. In our case the equation for N-part distribution function was

$$\frac{\partial f_2}{\partial t} + \sum_{i=1}^{2} \left\{ \xi_i \cdot \left[\frac{\partial f_N}{\partial x_i} \right] + \xi_i \cdot \frac{\partial}{\partial x_i} \left[x_j \frac{\partial f_N}{\partial x_j} \right] - \frac{X_i}{m} \frac{\partial f_N}{\partial \xi_i} \right\} + \mathbf{X}_{12} \cdot \frac{\partial f_N}{\partial \xi_1} + \mathbf{X}_{21} \cdot \frac{\partial f_N}{\partial \xi_2} = 0$$

In our case the equation for two-part distribution function was

$$\frac{\partial f_2}{\partial t} + \sum_{i=1}^{2} \left\{ \xi_i \cdot \left[\frac{\partial f_2}{\partial x_i} \right] + \xi_i \cdot \frac{\partial}{\partial x_i} \left[x_j \frac{\partial f_2}{\partial x_j} \right] - \frac{X_i}{m} \frac{\partial f_2}{\partial \xi_i} \right\} + \mathbf{X}_{12} \cdot \frac{\partial f_2}{\partial \xi_1} + \mathbf{X}_{21} \cdot \frac{\partial f_2}{\partial \xi_2} + X_{22} \frac{\partial f_2}{\partial \xi_2} = 0$$

Integrating in ξ we obtain the equation for one-particle distribution function with interaction force gas molecule with surface molecules. Suggested algorithm is easily than classical. For $\xi 2 = 0$ in solid body (without movement of the surface molecules) we have trajectory problem i.e. the usual of DSMC code. The gas state on external boundary layer depends on longitudinal velocity and for velocity with Mach number M=10. The distance is equal to 3E(-8)cm for the time of collision. During this distance the distribution function does not change. Using the condition for invariant of conservation values in the particles without structure and concrete potential of interaction we can received the S.V. Vallander formula.

The next interaction gas molecule with surface molecule will have another velocity as the distribution function has the profile which is close to Maxwell function .These cause different forces on surface and angular momentum. The direction of these angular momentums can be different and the next two molecules as result twist in different direction. It is essential that this effect can be for gas without movement. The probably can be calculation in the future.

5 The influence dispersion on difference approximation

The further aim is investigation influence of high-frequency harmonics registration which are not taking into consideration for discrete presentation on low-frequency. Calculation on detailed network does not permit to answer the question about contribution dissipation of energy at high frequency in general picture of stream. The simple numerical scheme gives wave equation (the approximation is only for space coordinate)

$$\frac{\partial u}{\partial t} + \frac{\partial \frac{u^2}{2}}{\partial x} = \frac{\partial}{\partial x} \left(\mu - \frac{uh}{2} \right) \frac{\partial u}{\partial x}, \quad U = \frac{u_1 + u_2}{2}.$$

$$X = x - Ut$$

$$X = \frac{2}{u_2 - u_1} \left[\left(-\frac{h}{2} u_2 + \mu \right) \ln (u_2 - u) - \left(-\frac{h}{2} u_1 + \mu \right) \ln (u - u_1) \right]$$

(u_1 – the velocity in front of wave, u_2 – the velocity behind the wave).

It is essential that registration of equation in conservative form permits conservation phase, registration of equation in nonconservative form does not keep as amplitude as phase. Employment the second order scheme gives to predominate dispersion for all step of numerical scheme. So to

speak about average value is intricately; difference error which is proportional to the third derivative and value of additional term showing above must coincide with one another. We suggest to choose from this the value of numerical step.

6 Conclusion

Our investigations show that it is necessary to include the low of angular moment conservation in equation of continuous mechanics and the pressure tensor is not symmetric for large gradients of physical values.

References

[1] *E.V.Prozorova* Influence of dispersion in mechanics// Seventh International Workshop on Nondestructive testing and Computer Simulations in Science and Engineering,. Proceedings of SPIE. 2003, Vol.5400, pp.212-219.

[2] *E.V.Prozorova* Influence of the dispersion on the Boltzmann equation for nonhomogeneous case// 25th International symposium on rarefied gas. Proceedings of 25-th International symposium on rarefied gas dynamics, Novosibirsk, 2007. pp1374 –1379

[3] *S. V. Vallander.* The equations for movement viscosity gas. DAN SSSR .1951. V. LXX III, N 1 2. B

[4] *B.V. Alexeev.* Generalized Boltzmann Physical Kinetics. Elsevier, Amsterdam, 2004. 5.

[5] *C. Cercignani.* Mathematical methods in kinetic theory Macmillan. 1969.

[6] *Ya.B. Zeldovich, Yu. P. Rayzer.* The physics shock waves and high temperature hydrodynamics

[7] *V.A.Kononenko, E. V. Prozorova, A.V. Shishkin.* Influence dispersion for gas mechanics with great gradients. 27-th international symposium on Shock waves. St. Peterburg, Repino. pp.406-407

[8] *E.V. Prozorova* Influence dispersion on cross flows for gas mechanics. $http : // sig.balticgrid.org/NDTCS - 2009/news$

[9] *E.V. Prozorova* Prozorova E. Influence of the dispersion on the equations for nonhomogeneous mechanics Rev.Adv.Mater.Sci.19(2009) 14-34 G.K.Batchelor . An introduction to Fluid Dynamics Cambridge. 1970

Evelina V. Prozorova, Mathematics Mechanics Faculty, St. Peterburg State University, University av. 28, Peterhof, 198904, Russia

Influence of porosity percolation on strength and elastic properties of ceramic materials. 3D simulation using movable cellular automata method

Nikita V. Roman Aleksey Yu. Smolin Igor S. Konovalenko
Sergey G. Psakhie
romannv@sibmail.com

Abstract

3D computer simulation of mechanical behavior of a brittle porous material under uniaxial compression is considered. Movable cellular automaton method, which is a representative of particle methods in solid mechanics, is used for computation. In an initial structure the automata are positioned in FCC packing. The pores are set up explicitly by removing single automata from the initial structure. The computational results show that the curve of porosity dependence of strength and elastic properties of the modeled specimens has a break at the porosity about 20 %, i.e. percolation threshold. The obtained results are in good agreement with available experimental data.

Introduction

It is well known that porosity dependence of strength and elastic properties of porous materials is determined by the pore morphology. If porosity is small, each pore is closed and isolated form the others. With porosity increasing the number of pores becomes greater and the distance among pores decreases. When porosity reaches percolation threshold the pores are not closed anymore and consequently form new morphology. Thus, porosity dependence of strength and elastic properties should be changed when percolation threshold is exceeded.

Note, it is very difficult to study the problem experimentally, because of stochastic nature of the pore morphology in real materials. For example, it is impossible to make specimens with various porosity value and the same porous structure. At the same time potentialities of the modern computational mechanics allow to study in detail not only deformation of complex heterogeneous materials but also fracture of such materials.

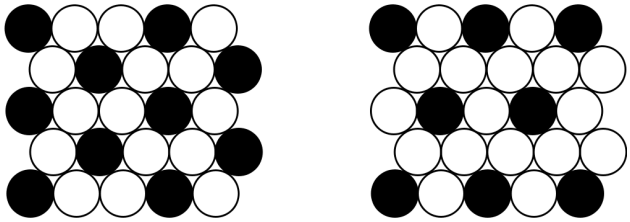
1 Computational model for porous ceramics

For 3D computer simulation of mechanical behavior of a porous material under uniaxial compression we used the movable cellular automaton method (MCA) [1]. MCA is a method in discrete computational mechanics which allows modeling deformation and fracture of heterogeneous material with taking into account the structure of the material explicitly. Modeled material is represented as a set of elements of finite size (automata) interacting with each another according to some pre-determined rules. Mechanical interaction among automata are defined by so called response function, which can be interpreted as a local stress-strain diagram. Equation of translation motion and rotation of the automata are written in many-body approach. This means that interacting force between two automata depends not only on position and state of these automata but also on position and state of their neighboring automata. This allows modeling solid and granular material behavior within the framework of one MCA method.

Response function of automata used in this study corresponded to ZrO_2 ceramics with average size of pores commensurable with the grain size of the material. According to the pore distribution

diagram of this material [2] the automaton size in the computations was 1 μm. All the modeled specimens where bricks with a square base. The loading was applied by assignment of vertical velocity for automata of the top layer of a specimen. At the same time the substrate automata were rigidly fixed. At the initial stage of the loading velocity of the upper automata increased by a sinusoidal law from 0 to 1 cm/s and then was constant.

Pores were generated by removing single automata from the basic structure. The porosity values were varied from 0 to 50 %. Note, that the maximal porosity on the assumption of pore disconnection in closed packing for 2D is $1/2 = 50$ % (Fig. 1,a) while for 3D it is $1/4 = 25$ % (Fig. 1,b). In this case the pores are regularly situated.



(a) (b)

Figure 1: Periodic pores (black) in closed packing

The maximal value of closed porosity for random removing of single automata from FCC packing is 17.6 %. The percolation limit for 3D FCC packing is 19.8 %. Consequently, all the specimens used in this study with porosity greater than 20 % contained clusters of interconnecting pores. For the specimens with porosity greater than 25 % their porosity was interconnected.

In [3] it was shown that porosity structure defined not only elastic, but also strength properties of a material. The clusters of interconnecting pores present a new element of structure in addition to single closed pores. Thus, with porosity increasing the changes of elastic and strength properties of a material are expected after transition of the percolation limit.

2 Determining the representative volume

At the first stage it is required to determine the representative volume of the modeled material. For material without pores the representative volume was determined based on four solid specimens. For this purpose the convergence of effective elastic modulus of the specimen E_{eff} to the automaton elastic modulus E_0 with increasing the specimen size was analyzed.

The convergence was assumed to be satisfied if E_{eff} differed from E_0 not greater then 3 %. The computations showed the representative volume was equal 10 μm of the brick base size. The fracture pattern (cracks) in this specimen is shown in Fig. 2 The cracks are generated from the stress concentrators and propagate along maximum tangential stress direction.

If a material contain pores the cracks may initiate not in the corners but in the region of the highest local porosity. The direction of cracks propagation in such material is defined by the porous topology. Fig. 3 shows the first cracks in porous specimens with various values of porosity. One can see that failure behavior of porous material with large porosity and failure of solid material differs dramatically. In particular, the path of the crack propagation in porous material is rather crinkly.

The fracture pattern of the modeled brittle porous 3D specimens qualitative corresponds to 2D simulation results [3]. The quantitative difference is defined by the fact that porosity in 2D specimen is "interconnected" in the normal direction to the computational plane.

To analyze the dependence of elastic and strength properties of the modeled material on its porosity it is necessary to determine the size of representative specimen (volume). It is obvious that the representative volume for a porous material will be different for different values of porosity. The simulation showed that for porosity value less then 15 % the representative volume was equal 20 μm (Fig. 4). For porosity value from 15 up to 35 % the size of representative volume was found to be 30 μm (Fig. 4,b). For porosity from 35 up to 50 % — 40 μm (Fig. 4,c).



(a) (b)

Figure 2: Fracture pattern of solid ceramic specimen under compression: a) lines connect linked automata, b) lines connect unlinked automata

3 Studying elastic and strength properties of porous ceramics

The loading diagrams of 3D modeled specimens are shown in Fig. 5. They are in good qualitative agreement with 2D simulation results [3, 4]. A quantitative differences is explained by the different influence of porosity on effective porous characteristics in 2D and 3D tasks.

First, it has to be noted that 3D specimens with porosity stochastically distributed in space can demonstrate quasi-viscous regime of fracture like 2D models [4]. To be able to failure in this regime the porosity of 3D specimens has to be greater than 40 % (Fig. 5).

Let us consider dependence of the effective elastic modulus of 3D specimens on its porosity. In Fig. 6,a each square represents the value averaged on five representative specimens with various pore distribution in space. This dependence obviously can be divided into two characteristic parts connected with porous structure: the first corresponds to closed pores (5. . . 20 %), the second corresponds to clusters of interconnected pores (20. . . 50 %). The experimental data taken from [2] are presented in Fig. 6,b for comparison. One can see the computational results are in good qualitative agreement with the experimental data. However, the inclinations of approximating lines showing degree of the influence of porosity on elastic characteristics of a material within the intervals are little bit different for the experimental and computational data. It can be explained by stochastic choice of elements for pore generation in the modeled specimens, and hence by the orientations of clusters of interconnected pores, which leads to reduction of porous structure influence on mechanical properties of a material. Besides, according to [2] percolation transitions in ceramics ZrO_2 cause microstructure change. In particular, internal stresses in ceramics with continuous porous structure restrain grain growth. Thus, simulation of uniaxial compression of brittle porous 3D specimens by the movable cellular automaton method showed that percolation transition from the closed pores to interconnected pores in a porous material leads to change in the dependence of its elastic properties on porosity.

It is necessary to notice that this result could be obtained only in three-dimensional simulation because two-dimensional specimens with interconnected porosity are not topologically connected and do not resist to the mechanical loading. Besides, the porosity value at which formation of interconnected clusters occur in a two-dimensional case (22.4 %) is considerably less than the corresponding percolation limit (69.62 %).

Fig. 7 shows simulated and experimental dependencies of ceramics strength on its porosity. Again it can be divided into two characteristic parts connected with porous structure.

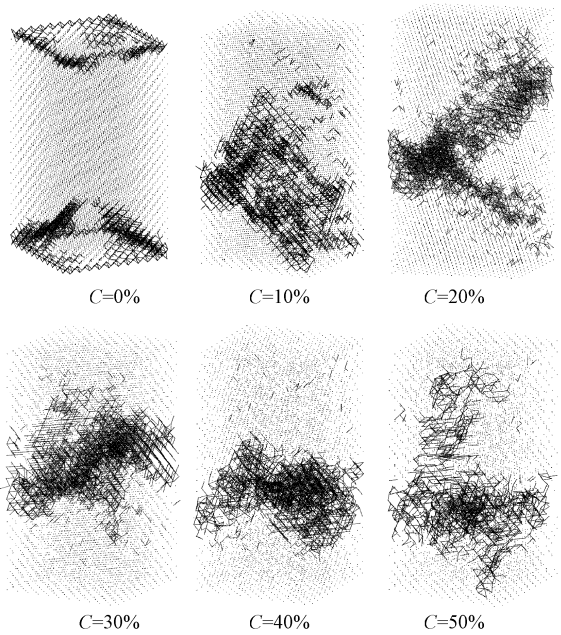


Figure 3: First cracks in specimens with various values of porosity C under compression

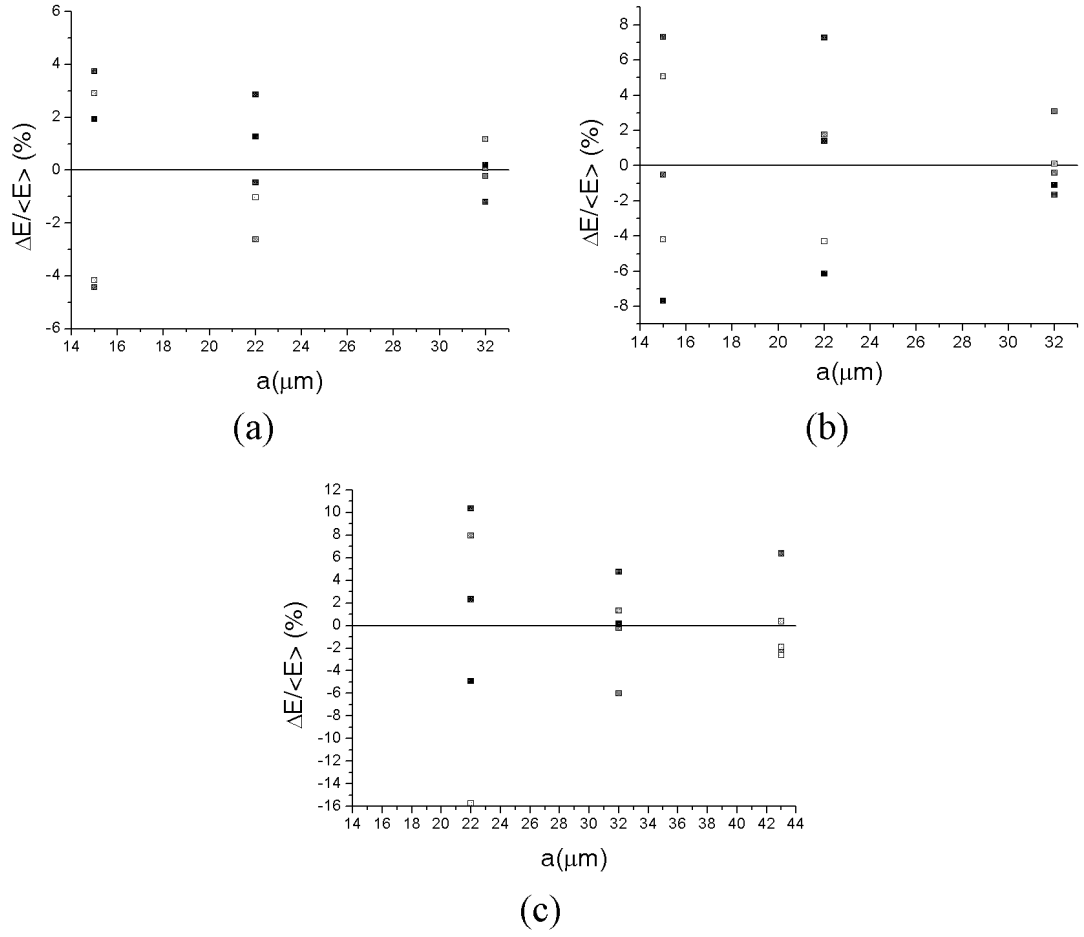


Figure 4: Convergency of effective elastic moduli of the modeled specimens on their basis size for various porosity: a) 10 %, b) 25 %, c) 50 %

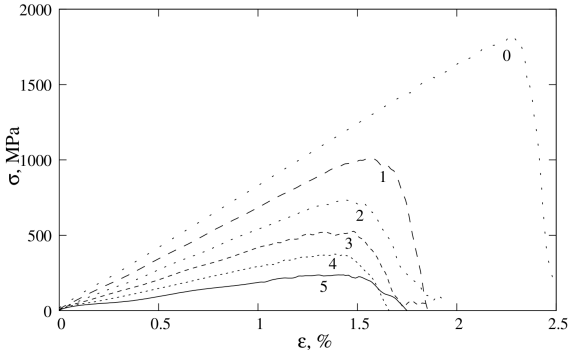
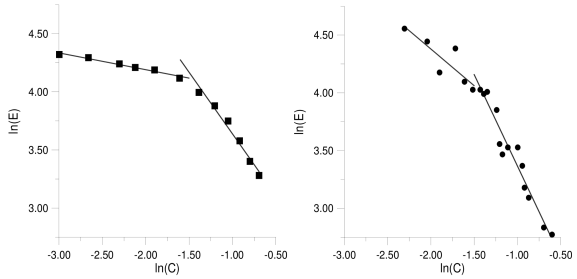
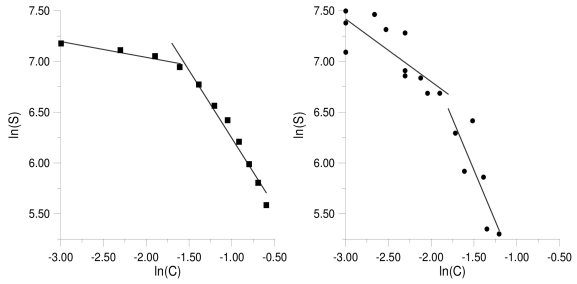


Figure 5: Loading diagrams for ceramics with various porosity $C = n{\cdot}10\,\%$



(a) (b)

Figure 6: Dependences of elastic modulus of ceramics on its porosity in logarithmic coordinates: a) simulation; b) experimental data



(a) (b)

Figure 7: Dependences of ceramics strength on porosity in logarithmic coordinates: a) simulation, b) experimental data

In summary it is necessary to notice that for the purpose of the further application of the proposed 3D MCA model of porous ceramics it is necessary to extend the model with possibility of describing nonlinear properties of materials (degradation of elastic properties, relaxation at high-speed loading, etc.)

Acknowledgements

This study was supported by the Russian Foundation for Basic Research (project 09-07-12016-ofi-m) and by the grant MK-5260.2010.8 of the President of the Russian Federation for supporting young Russian scientists.

References

[1] S. Psakhie, Y. Horie, G. Ostermeyer, et al., Theor. Appl. Fract. Mech. 37, 311 (2001).

[2] S. Kulkov, S. Buyakova, V. Maslovsky, Bulletin of Tomsk State University, 13, 34 (2003).

[3] Ig. Konovalenko, Theoretical research of deformation and destruction of porous materials of medical appointment and biomechanical designs. PhD thesis, Tomsk, 174 (2007).

[4] A. Smolin, Ig. Konovalenko, S. Kul'kov, and S.Psakhie, Tech. Phys. Lett., 32(9), 738 (2006).

Nikita V. Roman, pr. Academicheskii 2/4, Tomsk, 634021 Russia
Aleksey Yu. Smolin, pr. Academicheskii 2/4, Tomsk, 634021 Russia
Igor S. Konovalenko, pr. Academicheskii 2/4, Tomsk, 634021 Russia
Serguey G. Psakhie, pr. Academicheskii 2/4, Tomsk, 634021 Russia

Ever-topical questions regarding the "ever-Hookean" material

E. I. Ryzhak
e_i_ryzhak@mail.ru

Abstract

An old question of whether the Jaumann stress-rate applies for expressing incremental constitutive relations in the case of finite strains and rotations is discussed. Analyzed is the well-known example of the deformation process of monotonic simple shearing of the "ever-Hookean" material. By this is meant a one for which the Jaumann rate of the Cauchy stress is related linearly to strain-rate tensor by virtue of a constant (depending neither on strains, nor on rotations) fourth-order moduli tensor identical to that of Hooke's law.

With regard for known (obtained earlier) dependence of the Cauchy stress on a parameter γ (tangent of the angle of shear) the Hadamard inequality is recorded for the incremental moduli tensor associated with Piola stress; it involves not only moduli, but also current value of the Cauchy stress.

Analysis of the Hadamard inequality shows that it is violated immediately after the value $\gamma = \pi/3$, when the shear stress is still increasing (it begins to decrease after the value $\gamma = \pi/2$). Thus, there will be no oscillation for the shear stress, which is usually "incriminated" to the Jaumann stress-rate: the material will collapse at $\gamma = \pi/3 + 0$, that point pertaining to the rising part of the diagram of shear. The conclusion is drawn that it is the absurd ever-Hookean incremental constitutive relation that causes such a strange behavior of a solid. By no means it is caused by usage of the Jaumann stress-rate, whose adequacy follows directly from the principle of material frame-indifference.

1 The ever-Hookean material

First of all we remind that adequacy of the Jaumann stress-rate for representing the incremental constitutive relation for a material without a natural time [1] is a direct corollary of the principle of material frame-indifference [2], and in this concern any discussions are of no sense.

So, let us introduce and discuss an incremental constitutive relation that can be called the "ever-Hookean" one:

$$\begin{aligned} &\overset{\triangledown}{\boldsymbol{T}} = \boldsymbol{L}^H : \dot{\boldsymbol{\varepsilon}} \\ &\boldsymbol{L}^H = 2G\mathbf{1}^{dev} + K\boldsymbol{I}\otimes\boldsymbol{I} = const, \end{aligned} \tag{1}$$

where $\boldsymbol{T}$ is the Cauchy stress tensor, $\overset{\triangledown}{\boldsymbol{T}}$ is its Jaumann rate, $\dot{\boldsymbol{\varepsilon}}$ is the strain-rate tensor, $\boldsymbol{L}^H$ is the fourth-order moduli tensor of Hooke's law with shear modulus G and bulk modulus K, $\mathbf{1}^{dev}$ is the orthogonal projector onto the space of symmetric second-order deviatoric tensors. The $\boldsymbol{L}^H$ is assumed to depend neither on strains, nor on rotations. At a first sight the relation (1) resembles Hooke's law and seems absolutely natural, but in fact it is awfully unnatural! It can be proved that it has no potential, i.e. it is not hyperelastic; moreover, no initially isotropic elastic materials can ever manifest such an isotropic incremental behavior, since they become incrementally orthotropic in the states corresponding to non-volumetric strains, their moduli tensors $\boldsymbol{L}$ being dependent on strains and rotations of a solid. So, a strange incremental law causes a strange behavior of a solid under deformation, in particular, under simple shearing (to be discussed bellow).

2 Simple shearing of the ever-Hookean material.

Such a process has been analyzed in a number of papers (e.g. [3, 4, 5]) in order to demonstrate inadequacy of the Jaumann stress-rate, which was already commented on above.

Let us discuss the solution obtained there for simple shearing and draw our own conclusions regarding it. Let $(\boldsymbol{e}_1, \boldsymbol{e}_2, \boldsymbol{e}_3)$ be an orthonormal basis, $\boldsymbol{x}$ be a position vector of a material point in the reference configuration, $\boldsymbol{r}(\boldsymbol{x}, \gamma)$ be an actual position vector of the same material point for a certain value of a shear parameter γ:

$$\boldsymbol{r}(\boldsymbol{x}, \gamma) = \boldsymbol{x} \cdot (\boldsymbol{I} + \gamma \boldsymbol{e}_2 \otimes \boldsymbol{e}_1) \tag{2}$$

For the Cauchy stress it was obtained:

$$\boldsymbol{T}(\gamma) = G((\boldsymbol{e}_1 \otimes \boldsymbol{e}_2 + \boldsymbol{e}_2 \otimes \boldsymbol{e}_1)\sin\gamma + (\boldsymbol{e}_1 \otimes \boldsymbol{e}_1 - \boldsymbol{e}_2 \otimes \boldsymbol{e}_2)(1 - \cos\gamma)) \tag{3}$$

$$\boldsymbol{e}_2 \cdot \boldsymbol{T}(\gamma) \cdot \boldsymbol{e}_1 = G\sin\gamma \tag{4}$$

The oscillatory function (4) for shear stress under monotonic shearing was announced to be strange and unrealistic, but one should not forget that the ever-Hookean material is also strange and unrealistic.

Let is show that the oscillatory dependence (4) is not the worst thing here. Consider the Hadamard inequality for the ever-Hookean material with the value $\boldsymbol{T}(\gamma)$ (3) for the Cauchy stress. The sense of the inequality is that it constitutes the universal necessary condition for stability of a solid (under any boundary conditions) and it is also the sufficient condition in some special cases. According to the Basic Hadamard stability theorem [2], the inequality is to be imposed on the moduli tensor $\boldsymbol{C}$ setting the incremental constitutive relation for the Piola stress. Using the notation for isomers of a tensor, the relation between $\boldsymbol{C}, \boldsymbol{L}$ and $\boldsymbol{T}$ can be recorded as follows:

$$\boldsymbol{C} = \boldsymbol{L} + \boldsymbol{T} \otimes \boldsymbol{I} + \frac{1}{2}(\boldsymbol{T} \otimes \boldsymbol{I} - \boldsymbol{I} \otimes \boldsymbol{T})^{(1324)} - \frac{1}{2}(\boldsymbol{T} \otimes \boldsymbol{I} + \boldsymbol{I} \otimes \boldsymbol{T})^{(1342)} \tag{5}$$

$$\begin{aligned} &\boldsymbol{f} \otimes \boldsymbol{g} : \boldsymbol{C} : \boldsymbol{f} \otimes \boldsymbol{g} \mid_{|\boldsymbol{f}|=|\boldsymbol{g}|=1} = \boldsymbol{f} \otimes \boldsymbol{g} : \boldsymbol{L} : \boldsymbol{f} \otimes \boldsymbol{g} + \frac{1}{2}(\boldsymbol{f} \cdot \boldsymbol{T} \cdot \boldsymbol{f} - \boldsymbol{g} \cdot \boldsymbol{T} \cdot \boldsymbol{g}) \geq \\ &\geq min \boldsymbol{f} \otimes \boldsymbol{g} : \boldsymbol{L} : \boldsymbol{f} \otimes \boldsymbol{g} + \frac{1}{2} min(\boldsymbol{f} \cdot \boldsymbol{T} \cdot \boldsymbol{f} - \boldsymbol{g} \cdot \boldsymbol{T} \cdot \boldsymbol{g}) = \\ &= G - \sqrt{\frac{1}{2}\boldsymbol{T} : \boldsymbol{T}} = G - \tau_{max} \geq 0 \end{aligned} \tag{6}$$

It can be proved that in this case

$$\min_{|\boldsymbol{f}|=|\boldsymbol{g}|=1} \boldsymbol{f} \otimes \boldsymbol{g} : \boldsymbol{C} : \boldsymbol{f} \otimes \boldsymbol{g} = G - \sqrt{\frac{1}{2}\boldsymbol{T} : \boldsymbol{T}} = G(1 - \sqrt{2(1 - \cos\gamma)}) \geq 0 \tag{7}$$

The right-hand side of (7) first vanishes at

$$\gamma_* = \frac{\pi}{3} \tag{8}$$

and further deformation becomes impossible since the solid collapses. The value γ_* corresponds to increasing shear stress $\boldsymbol{e}_2 \cdot \boldsymbol{T}(\gamma) \cdot \boldsymbol{e}_1$ (it begins to decrease after $\gamma = \pi/2$). Thus, the oscillations are not able to arise since the collapse of a solid takes place earlier!

To conclude, we remark, that absurdity of the ever-Hookean material is not the exception: in general many quantities and concepts of the classical linear elasticity become absurd when transferred thoughtlessly to a non-linear solid mechanics and to its incremental constitutive relations.

References

[1] Hill R. Some basic principles in the mechanics of solids without a natural time // J. Mech. Phys. Solids. 1959. V.7. P.209-225.

[2] Truesdell C., Noll W. The non-linear field theories of mechanics// Handbuch der Physik. V. III/3. Berlin: Springer, 1965. 602 p.

[3] Dienes J. K. On the analysis of rotation and stress rate in deforming bodies // Acta Mech. 1979. V.32. P.217-232.

[4] Dafalias Y. F. Corotational rates for kinematic hardening at large plastic deformations // J. Appl. Mech. ASME. 1983. V.50. P.561-565

[5] Lee E. H. et al. Stress analysis for anisotropic hardening in finite-deformation plasticity // J. Appl. Mech. ASME. 1983. V.50. P.554-560

Eugene I. Ryzhak, Institute of physics of the Earth, RAS, Moscow.

Kinetic formulation for the Darcy-Stefan problem on phase transitions in a saturated porous ground

Sergey A. Sazhenkov
sazhenkovs@yandex.ru

Abstract

The Cauchy problem for the Darcy–Stefan model, which describes phenomena of freezing and thawing of viscous incompressible fluid filtering through a porous ground, is considered in the presence of nonlinear temperature-depending buoyancy forces. The main result of the paper consists of the theorem on existence of entropy solution to the problem. The proof of the theorem is based on the kinetic formulation which allows to reduce the originally nonlinear problem to a linear form with additional kinetic variable.

1 Introduction

Mathematical modeling of freezing and melting phenomena in porous grounds, with account of convection of the saturating liquid phase is necessary for scientific support of various technologies in industry and agriculture [1]. The main feature of the majority of the relevant problems is that they combine the Stefan problem on phase transitions and the Darcy law of dynamics of viscous continuous media filtering through incompressible porous grounds. In 1999, in [2] there was proposed a multi-dimensional Darcy–Stefan model of rather general form in order to describe effects of freezing of a viscous liquid in a motionless porous soil with allowance for the buoyancy force depending on temperature nonlinearly. The density was supposed to be the same constant for frozen and liquid phases. In [2] the initial-boundary value problem in a bounded domain was considered. The definition of a weak generalized solution was proposed for the formulation in which the unknown functions were the velocity field, the gradient of pressure, and the temperature distribution. The main result of [2] consisted of the theorem on existence of a weak generalized solution to the problem, and the proof was based on the classical methods from the theory of elliptic and parabolic equations.

In the present work, in Section 2, a Cauchy problem for the above described Darcy–Stefan model (Problem D-S) is set such that one of the unknown functions is not temperature but specific internal energy. This clearly brings a new difficulty to the problem since in such setting the heat equation has the degenerate hyperbolic-parabolic type. A definition of entropy solution for Problem D-S is introduced. The main result of the paper consists of Theorem 2 (see in Section 5) on existence of entropy solutions to Problem D-S. To this end, in Section 3, the approximate problem is posed and the corresponding sequence of approximate solutions is constructed. Using the classical methods from the theory of elliptic and parabolic equations the relative compactness of families of approximate values of velocity and pressure is proved. After this, it is necessary to show that the family of approximate values of specific internal energy is relatively compact as well. To this end, in Sections 4 and 5 there is used the version of the method of kinetic equation, which was developed in [3].

2 The problem formulation

Let us consider a thermomechanical system consisting of a motionless heat-conducting porous soil and a continuous medium completely filling the pores. The saturating continuous medium can be in

a liquid or solid state and perform phase transitions between these states. The porous skeleton, i.e., soil, experiences no phase transitions. A standard macroscopic approach (see, e.g., Eqs. (10.7.13)–(10.7.22) in [1]) is used to describe the system. After some additional and simplifying assumptions, the most general model can be reduced to the following formulation of the Darcy–Stefan problem.

Problem D-S. At each time instant $t \in [0,T]$ (T is an arbitrarily defined positive constant), the homogenized continuous medium is assumed to occupy a plane $\mathbb{R}^2$ or a three-dimensional space $\mathbb{R}^3$. Some part of the continuous medium with a temperature $\theta < 0$ occupies a certain domain $Y(t) := \{\mathbf{x} \in \mathbb{R}^d \mid \theta(\mathbf{x},t) < 0\}$ ($d = 2,3$), the remaining part of the continuous medium with a temperature $\theta > 0$ occupies the domain $W(t) := \mathbb{R}^d \setminus \overline{Y(t)} = \{\mathbf{x} \in \mathbb{R}^d \mid \theta(\mathbf{x},t) > 0\}$. The porous medium is in the solid (frozen) state in the domain $Y(t)$ and in the liquid (thawed) state in the domain $W(t)$. The locations of the domains $Y(t)$ and $W(t)$ and the interface $\Gamma(t) = \overline{Y(t)} \cap \overline{W(t)} = \{\mathbf{x} \in \mathbb{R}^d \mid \theta(\mathbf{x},t) = 0\}$ are unknown.

We have to find the distribution of the specific internal energy $e = e(\mathbf{x},t)$, the velocity field $\mathbf{v} = \mathbf{v}(\mathbf{x},t)$, and the distribution of pressures $p_* = p_*(\mathbf{x},t)$, which satisfy the following equations and conditions:
the energy balance equation

$$\partial_t e + \operatorname{div}_x(\vec{v}e) = \Delta_x \theta, \quad \mathbf{x} \in \mathbb{R}^d \setminus \Gamma(t),\ t \in (0,T); \tag{1}$$

the thermodynamic equation of state of the continuous medium

$$\theta = \begin{cases} \theta_s(e) & \text{for } e < 0, \\ 0 & \text{for } e \in [0,l], \\ \theta_l(e) & \text{for } e > l, \end{cases} \tag{2}$$

(the functions θ_s and θ_l are set so that $\theta = \theta(e)$ has a bounded second derivative and is a nonrigorously monotonically increasing function, with $0 < \theta_s'(e), \theta_l'(e) < +\infty\ \forall e \in \mathbb{R} \setminus [0,l]$;
the condition of the absence of motion of the frozen phase

$$\mathbf{v} = 0, \quad \mathbf{x} \in Y(t),\ t \in (0,T); \tag{3}$$

the condition of continuity (condition of incompressibility) and the Darcy filtration law for $\theta \geq 0$

$$\operatorname{div}_x \mathbf{v} = 0, \quad \mathbf{x} \in \overline{W(t)},\ t \in (0,T), \tag{4}$$

$$\mathbf{v} = -\nabla_x p_* + \mathbf{g}(\theta), \quad \mathbf{x} \in \overline{W(t)},\ t \in (0,T); \tag{5}$$

the equations of mass and heat balance on the interface $\Gamma(t)$

$$\mathbf{v} \cdot \mathbf{n} = 0, \quad [\nabla_x \theta]_s^l \cdot \mathbf{n} = l\mathbf{V} \cdot \mathbf{n}, \quad \mathbf{x} \in \Gamma(t), \quad t \in (0,T) \tag{6}$$

(the second condition is also called the Stefan condition);
the bounded periodic initial data for the distribution of the specific internal energy

$$e(\mathbf{x},0) = e_0(\mathbf{x}), \quad (|e_0(\mathbf{x})| \leq c_0 = \text{const}), \quad e_0(\mathbf{x} + \mathbf{k}_i) = e_0(\mathbf{x}), \quad \mathbf{x} \in \mathbb{R}^d; \tag{7}$$

the conditions of spacial periodicity

$$e(\mathbf{x} + \mathbf{k}_i, t) = e(\mathbf{x},t), \quad \mathbf{v}(\mathbf{x} + \mathbf{k}_i, t) = \mathbf{v}(\mathbf{x},t), \quad (\mathbf{x},t) \in \mathbb{R}^d \times [0,T]. \tag{8}$$

In Eqs. (1)–(8) $\mathbf{k}_i$ ($1 \leq i \leq d$) are the orthogonal unit vectors of the standard Cartesian basis in $\mathbb{R}^d$; θ is the temperature of the continuous medium, which is constant for specific internal energy values within the whole nondegenerate interval $[0,l]$, which means the phase transition in the porous component, $\theta = 0$ is the thawing (freezing) temperature, $e = l$ is the latent specific heat of melting, $\mathbf{g} \in C^2(\mathbb{R})$ is the buoyancy, which may be a nonlinear function of temperature in the general case, $\mathbf{n}$ is a unit vector normal to $\Gamma(t)$, which is directed towards $Y(t)$, $\mathbf{V}$ is the velocity of motion of $\Gamma(t)$, $[\nabla_x \theta]_s^l = (\nabla_x \theta)^l - (\nabla_x \theta)_s$ is the jump of the temperature gradient $\nabla_x \theta$ on the boundary $\Gamma(t)$, and $(\nabla_x \theta)^l$ and $(\nabla_x \theta)_s$ are the limiting values of $\nabla_x \theta$ on $\Gamma(t)$ in the domains $W(t)$ and $Y(t)$, respectively.

To formulate the concept of the entropy solution of the Darcy–Stefan problem, we apply the following notation for the linear spaces of periodic functions: $Q = \Omega \times (0,T)$, where Ω is the spatial period $\Omega := [0,1)^d$; Banach spaces $L^p \subset L^p_{loc}(\mathbb{R}^d)$ and $H^{s,p} \subset H^{s,p}_{loc}(\mathbb{R}^d)$ consist of 1-periodic functions and are supplemented with the norms $\|u\|_{L^p} = \|u\|_{L^p(\Omega)}$, $\|u\|_{H^{s,p}} = \|u\|_{H^{s,p}(\Omega)}$; for integer $m \geq 0$, by C^m we denote the closed subspace of 1-periodic functions with respect to $\mathbf{x}$ from $C^m(\mathbb{R}^d)$.

Now we are in a position to introduce a notion of the entropy solution of the Darcy–Stefan problem.

Definition 1. The pair (e, p_*) is called an *entropy solution* of the Darcy–Stefan problem (problem D-S) if it satisfies the conditions of regularity

$$e \in L^\infty(Q), \quad \theta(e), H(e) \in L^2(0,T;H^{1,2}), \quad p_* \in L^2(0,T;H^{2,2}), \tag{9}$$

where $H(e) \stackrel{def}{=} \int^e \sqrt{\theta'(\lambda)}d\lambda$; integral inequality

$$\int_Q \big(\varphi(e)\zeta_t + \varphi^+(e)(-\nabla_x p_* + \mathbf{g}(\theta(e))) \cdot \nabla_x \zeta) + w(e)\Delta_x\zeta - \varphi''(e)|\nabla_x H(e)|^2\zeta\big)d\mathbf{x}dt + \int_\Omega \varphi(e_0)\zeta(\mathbf{x},0)d\mathbf{x} \geq 0, \tag{10}$$

where φ, φ^+, and w are arbitrary functions, such that $\varphi \in C^2_{loc}(\mathbb{R})$, $\varphi''(e) \geq 0$, $\varphi^+(e) = \int^e 1_{\lambda \geq 0}\varphi'(\lambda)d\lambda$, $w(e) = \int^e \varphi'(\lambda)\theta'(\lambda)d\lambda$, $\zeta \in C^2_{loc}(\mathbb{R}^d \times [0,T])$ is an arbitrary non-negative function 1-periodic with respect to $\mathbf{x}$, which vanishes in the neighborhood $\{t = T\}$; and the equation

$$\Delta_x p_* = \mathrm{div}_x\{\mathbf{g}(\theta(e))\} \quad \text{a.e. in } Q. \tag{11}$$

Remark. Once an entropy solution is built, the velocity field can be reconstructed by the formula $\mathbf{v}(\mathbf{x},t) = 1_{e(x,t)\geq 0}\big[-\nabla_x p_*(\mathbf{x},t) + \mathbf{g}(\theta(e(\mathbf{x},t)))\big]$. Also let us notice that, from the physical point of view, values of the pressure p_* make sense only for $\mathbf{x} \in \Omega \setminus Y(t)$, although p_* by the Definition 1 should be defined in the whole domain Ω.

Entropy solution is more restrictive than the standard definition of the weak generalized solution. All possible entropy solutions satisfy the second law of thermodynamics postulating non-negative production of entropy. From the physical viewpoint, this is an advantage of the entropy solution over the standard weak generalized solution.

3 Parabolic approximation of problem D-S

Along with the Darcy–Stefan problem, we consider its parabolic approximation

$$e_t + \mathbf{v} \cdot \nabla_x e^+ = \Delta_x \theta(e) + \varepsilon \Delta_x e, \quad (\mathbf{x},t) \in \mathbb{R}^d \times (0,T); \tag{12}$$

$$\mathbf{v} = -\nabla_x p_* + \mathbf{g}(\theta(e)), \quad \mathrm{div}_x \mathbf{v} = 0, \quad (\mathbf{x},t) \in \mathbb{R}^d \times (0,T); \tag{13}$$

$$e(\mathbf{x}+\mathbf{k}_i,t) = e(\mathbf{x},t), \quad \mathbf{v}(\mathbf{x}+\mathbf{k}_i,t) = \mathbf{v}(\mathbf{x},t), \quad (\mathbf{x},t) \in \mathbb{R}^d \times (0,T) \tag{14}$$

with initial data (7) [in (12), $e^+ = 1_{e\geq 0}e$].

From the well-known facts of the mathematical theory of filtration [5, Chapter 5] it follows that, for any fixed $\varepsilon > 0$, there exists a unique solution $(e_\varepsilon, p_{*\varepsilon}, \mathbf{v}_\varepsilon)$ of the problem (12)–(14); the pressure $p_{*\varepsilon}$ is determined with accuracy to a constant term, which can be fixed by a standard requirement, e.g., $\int_\Omega p_{*\varepsilon}(\mathbf{x},t)d\mathbf{x} = 0$.

The maximum principle and the energy estimate yield that $-c_0 \leq e_\varepsilon \leq c_0$ a.e. in $\mathbb{R}^d \times (0,T)$, $\|\nabla_x\theta(e_\varepsilon)\|_{L^2} + \|\nabla_x H(e_\varepsilon)\|_{L^2} + \varepsilon\|\nabla_x e_\varepsilon\|_{L^2} + \|\nabla_x p_{*\varepsilon}\|_{L^2} \leq c_1$, where the constant c_1 does not depend on ε. These inequalities imply the existence of a sequence of soloutions e_ε, $p_{*\varepsilon}$, $\mathbf{v}_\varepsilon$ of the problem (12)–(14), (7) and five functions e, p_*, $\mathbf{v}$, θ_*, and H_* such that the following limiting relations are valid for $\varepsilon \searrow 0$:

$$e_\varepsilon \to e \qquad \text{weak star in } L^\infty, \tag{15}$$

$$\mathbf{v}_\varepsilon \to \mathbf{v}, \quad \nabla_x p_{*\varepsilon} \to \nabla_x p_* \qquad \text{weakly in } L^2, \tag{16}$$

$$\nabla_x\theta(e_\varepsilon)\to\nabla_x\theta_*,\quad \nabla_x H(e_\varepsilon)\to\nabla_x H_*\qquad \text{weakly in } L^2. \tag{17}$$

Since the Darcy-Stefan problem is nonlinear, to pass to the limit in approximate equations, we have to prove strong convergence of some subsequence of approximate solutions. Firstly, we establish the following partial compactness result:

Proposition 1. *The families* $\{\nabla_x p_{*\varepsilon}\}_{\varepsilon>0}$ *and* $\{\mathbf{v}_\varepsilon\}_{\varepsilon>0}$ *are relatively compact in* $L^2_{loc}(\mathbb{R}^d_x\times(0,T))$.

The proof is based on the use of a standard technique for constructing a priori estimates of solutions of parabolic and elliptic equations.

4 Notion of the kinetic formulation

In the present work, the compactness of subsequences of approximate solutions is justified and the solvability of the Darcy–Stefan problem is proved on the basis of constructing a kinetic equation associated with the problem, which is a tool of the method of the kinetic equation.

The kinetic formulation associated with the Darcy–Stefan problem is constructed similar to [3] and includes the notion of measure-valued mappings corresponding to weakly converging sequences of approximate solutions. In line with this, we introduce some definitions and notations for measure-valued mappings: $Prob(\mathbb{R}^n)$ is the set of probability measures in $\mathbb{R}^n$, i.e., non-negative Radon measures with a unit norm; $\mathbb{M}(\mathbb{R}^n)$ is the space of finite Radon measures above $\mathbb{R}^n$. The norm in $\mathbb{M}(\mathbb{R}^n)$ is introduced in a standard manner [4, Sec. 1.2.8]. The mapping $\mu:\mathbb{R}^d\times(0,T)\mapsto\mathbb{M}(\mathbb{R}^n)$ is called bounded, weak star measurable, and 1-periodic with respect to $\mathbf{x}$, if, for an arbitrary $F\in L^1_{loc}(\mathbb{R}^d_x\times(0,T);C_0(\mathbb{R}^n))$, the function $(\mathbf{x},t)\mapsto\int\limits_{\mathbb{R}^n_p}F(\mathbf{x},t,\mathbf{p})d\mu_{x,t}(\mathbf{p})$ is measurable, and the following equality is valid for $1\le i\le d$: $\int_{\mathbb{R}^n_p}F(\mathbf{x},t,\mathbf{p})d\mu_{x+k_i,t}(\mathbf{p})=\int_{\mathbb{R}^n_p}F(\mathbf{x}-\mathbf{k}_i,t,\mathbf{p})d\mu_{x,t}(\mathbf{p})$. Here $\mu_{x,t}=\mu(\mathbf{x},t)$ is a standard notation, i.e., the measures $\mu_{x,t}$ are parameterized with parameters $\mathbf{x}$ and t. Following definition 2.7 in [4], we denote the linear space consisting of the above-described measure-valued mappings μ by $L^\infty_w(\mathbb{R}^d_x\times(0,T);\mathbb{M}(\mathbb{R}^n))$, and introduce the standard norm in this space.

On the strength of (15) and (17), the Tartar [6] and the Ball [7] theorems imply that we can introduce into considerations the measure-valued functions $\nu\in L^\infty_w(\mathbb{R}^d_x\times(0,T);\,Prob(\mathbb{R}_\lambda))$ and $\sigma\in L^\infty_w(\mathbb{R}^d_x\times(0,T);\,Prob(\mathbb{R}_\lambda\times\mathbb{R}^d_q))$ defined by the formulas

$$\varphi(e_\varepsilon)\underset{\varepsilon\searrow0}{\longrightarrow}\int_{\mathbb{R}_\lambda}\varphi(\lambda)d\nu_{x,t}(\lambda)\text{ weak star in }L^\infty(\mathbb{R}^d_x\times(0,T)) \tag{18}$$

for any $\varphi\in C(\mathbb{R}_\lambda)$, and

$$\psi(e_\varepsilon,\,\nabla_x H(e_\varepsilon))\underset{\varepsilon\searrow0}{\longrightarrow}\int_{\mathbb{R}_\lambda\times\mathbb{R}^d_q}\psi(\lambda,\mathbf{q})d\sigma_{x,t}(\lambda,\mathbf{q})\text{ weak star in }L^\infty(\mathbb{R}^d_x\times(0,T)) \tag{19}$$

for any $\psi\in C(\mathbb{R}_\lambda\times\mathbb{R}^d_q)$, such that $|\psi(\lambda,\mathbf{q})|\le c(1+|\lambda|+|\mathbf{q}|)^r$, $0\le r<2$.

The measures $\nu_{x,t}$ and $\sigma_{x,t}$ are defined for a.e. $(\mathbf{x},t)\in\mathbb{R}^d_x\times(0,T)$ and are called the Young measures associated with the weakly convergent subsequences $\{e_\varepsilon\}$ and $\{e_\varepsilon,\,\nabla_x H(e_\varepsilon)\}$, respectively.

We introduce the distribution function of the measure $\nu_{x,t}$,

$$f(\mathbf{x},t,\lambda)=\int_{\mathbb{R}_s}1_{\lambda\ge s}d\nu_{x,t}(s) \tag{20}$$

and the parameterized Heaviside function

$$f_\varepsilon(\mathbf{x},t,\lambda)=1_{\lambda\ge e_\varepsilon(x,t)}, \tag{21}$$

which is the distribution function of the parameterized measure $\gamma_{e_\varepsilon(x,t)}$ – the Dirac measure on $\mathbb{R}_\lambda$, concentrated at the point $\lambda=e_\varepsilon(\mathbf{x},t)$. By virtue of Eq. (20) and the obvious presentation

$$\varphi(e_\varepsilon(\mathbf{x},t))=-\int_{\mathbb{R}}\varphi'(\lambda)f_\varepsilon(\mathbf{x},t,\lambda)d\lambda\quad\forall\,\varphi\in C^1_0(\mathbb{R})$$

we have the limit relation

$$f_\varepsilon \underset{\varepsilon\searrow 0}{\longrightarrow} f \quad \text{weak star in } L^\infty((0,T)\times\mathbb{R}_\lambda; L^\infty). \tag{22}$$

By virtue of Proposition 1, there exists another subsequence from $\{e_\varepsilon, \mathbf{v}_\varepsilon, p_{*\varepsilon}\}$ such that

$$\mathbf{v}_\varepsilon \underset{\varepsilon\searrow 0}{\longrightarrow} \mathbf{v}, \quad \nabla_x p_{*\varepsilon} \underset{\varepsilon\searrow 0}{\longrightarrow} \nabla_x p_* \quad \text{strongly in } L^2(Q). \tag{23}$$

Then, we denote the parameterized Radon measure on $\mathbb{R}_\lambda$ and the Radon measure on $Q\times\mathbb{R}_\lambda$ defined by the formulas

$$d_\lambda\chi_\varepsilon(\mathbf{x},t,\lambda) = |\nabla_x H(e_\varepsilon)|^2 d\gamma_{e_\varepsilon(x,t)}(\lambda) \quad \text{a. e. on } (\mathbf{x},t)\in\mathbb{R}^d_x\times(0,T), \tag{24}$$

$$dM_\varepsilon(\mathbf{x},t,\lambda) = \varepsilon|\nabla_x e_\varepsilon|^2 d\gamma_{e_\varepsilon(x,t)}(\lambda)d\mathbf{x}dt. \tag{25}$$

by $d_\lambda\chi_\varepsilon(\cdot,\cdot,\lambda)$ and M_ε, respectively.

Using the limiting relations (22), (23), (18), and (19), we can pass to the limit as $\varepsilon\searrow 0$ (by choosing an appropriate subsequence if necessary) in the equations of the approximate problem (12)–(14), (7). Following considerations in the proof of Theorem 5 in [3] we derive the limiting (with respect to $\varepsilon\searrow 0$) formulation (called the kinetic formulation of the Darcy–Stefan problem and, simultaneously, a theorem of solvability for this formulation:

Theorem 1. *Let $(e_\varepsilon, \mathbf{v}_\varepsilon, p_{*\varepsilon})$ be a solution of problem (12)–(14), (7), and the distribution function f_ε and the measures $d_\lambda\chi_\varepsilon$ and M_ε be defined by Eqs. (21), (24), and (25). Then there exists a sequence of small parameters $\varepsilon = \varepsilon_k \underset{k\to\infty}{\longrightarrow} 0$ such that the sequence $\{f_{\varepsilon_k}, \mathbf{v}_{\varepsilon_k}, p_{*\varepsilon_k}, d_\lambda\chi_{\varepsilon_k}, M_{\varepsilon_k}\}_{k=1,2,\ldots}$ converges to the five $(f,\mathbf{u},p_*,d_\lambda\chi,M)$, as $k\to\infty$, and these five functions and measures solve Problem K stated below.*

The convergence $(f_{\varepsilon_k}, \mathbf{u}_{\varepsilon_k}, p_{*\varepsilon_k}, d_\lambda\chi_{\varepsilon_k}, M_{\varepsilon_k}) \underset{k\to\infty}{\longrightarrow} (f,\mathbf{u},p_*,d_\lambda\chi,M)$ is understood in the sense of the limiting relations (22), (23), $d_\lambda\chi_\varepsilon \underset{\varepsilon\searrow 0}{\longrightarrow} d_\lambda\chi$ weak-star in $L^1_w(Q;\mathbb{M}(\mathbb{R}_\lambda))$, and $M_\varepsilon \underset{\varepsilon\searrow 0}{\longrightarrow} M$ weak-star in $\mathbb{M}(Q\times\mathbb{R}_\lambda)$.

Here $L^1_w(Q;\mathbb{M}(\mathbb{R}_\lambda))$ denotes the space of weak-star measurable mappings $\mu\colon Q\mapsto\mathbb{M}(\mathbb{R}_\lambda)$ such that for any $F\in L^\infty(Q;C_0(\mathbb{R}_\lambda))$ the integral $\int_Q\left|\int_{\mathbb{R}_\lambda} F d\nu_{x,t}(\lambda)\right| d\mathbf{x}dt$ is finite.

Problem K (kinetic formulation of the Darcy–Stefan problem). Given initial distribution function $f_0(\mathbf{x},\lambda) = 1_{\lambda\ge e_0(x)}$, where e_0 is defined by condition (7), it is necessary to find a distribution function $f\in L^\infty(\mathbb{R}^d\times(0,T)\times\mathbb{R}_\lambda)$, a velocity field $\mathbf{v}\in L^2(0,T;H^{1,2})$, a pressure distribution $p_*\in L^2(0,T;H^{2,2}))$, a kinetic measure of parabolic dissipation $d_\lambda\chi\in L^1_w(Q;\mathbb{M}(\mathbb{R}_\lambda))$, and a kinetic entropy defect measure $M\in\mathbb{M}(Q\times\mathbb{R}_\lambda)$ satisfying the following requirements.

(a) The function $f(\mathbf{x},t,\lambda)$ is 1-periodic in $\mathbf{x}$, monotonous and right continuous in $\lambda\in\mathbb{R}$. Moreover,

$$f(\mathbf{x},t,\lambda) = 0 \text{ for } \lambda < -c_0 \text{ and } f(\mathbf{x},t,\lambda) = 1 \text{ for } \lambda\ge c_0. \tag{26}$$

In particular, $0\le f\le 1$ a.e. in $Q\times\mathbb{R}_\lambda$. This amounts to the assertion that the Stieltjes measure $\nu_{x,t} = d_\lambda f(\mathbf{x},t,\lambda)$ is a probability measure on $\mathbb{R}_\lambda$, and spt $\nu_{x,t}\subset[-c_0,c_0]$.

(b) The weak-star measurable mapping $(\mathbf{x},t)\mapsto d_\lambda\chi(\mathbf{x},t,\lambda)$ is nonnegative and 1-periodic in $\mathbf{x}$, and the support of the measure $d_\lambda\chi(\cdot,\cdot,\lambda)$ belongs to the strip $[-c_0,c_0]$ a. e. in $\mathbb{R}^d\times(0,T)$.

(c) There exists a weak-star measurable mapping $\sigma\in L^\infty_w(\mathbb{R}^d_x\times(0,T);\, Prob(\mathbb{R}_\lambda\times\mathbb{R}^d_q))$ such that:

– its projection onto the space of the variable λ coincides with $d_\lambda f$, that is $\int_{\mathbb{R}_\lambda}\zeta(\lambda)d_\lambda f(\mathbf{x},t,\lambda) = \int_{\mathbb{R}_\lambda\times\mathbb{R}^d_q}\zeta(\lambda)d\sigma_{x,t}(\lambda,\mathbf{q})$ $\forall\,\zeta\in C(\mathbb{R}_\lambda)$ for a.e. $(\mathbf{x},t)\in\mathbb{R}^d_x\times(0,T)$;

– by means of integral $\chi(\mathbf{x},t,\lambda) := \int_{(-\infty,\lambda]\times\mathbb{R}^d_q}|\mathbf{q}|^2 d\sigma_{x,t}(s,\mathbf{q})$, mapping σ generates the kinetic measure of parabolic dissipation $d_\lambda\chi$;

– mapping σ is related to f by an additional relation $\sqrt{\theta'(\lambda)}\nabla_x f(\mathbf{x},t,\lambda) = -\int_{\mathbb{R}^d_q}\mathbf{q}d\sigma_{x,t}(\lambda,\mathbf{q})$, which is understood in the sense of distributions.

(e) The kinetic entropy defect measure M is non-negative and 1-periodic in $\mathbf{x}$.

(f) The functions and measures f, $\mathbf{v}$, p_*, $d_\lambda\chi$, and M satisfy the equations

$$\partial_t f + 1_{\lambda>0}\,\mathbf{v}\cdot\nabla_x f - \theta'(\lambda)\Delta_x f + \partial_\lambda\left(d_\lambda\chi + M\right) = 0, \quad (\mathbf{x},t,\lambda)\in Q\times\mathbb{R}_\lambda; \tag{27}$$

$$\left[\mathbf{v} + \nabla_x p_* - \mathbf{g}(\theta(\lambda))\right]\partial_\lambda f = 0, \quad (\mathbf{x},t,\lambda)\in Q\times\mathbb{R}_\lambda; \tag{28}$$

$$\mathrm{div}_x\mathbf{v} = 0, \quad (\mathbf{x},t)\in Q, \tag{29}$$

and the initial conditions

$$f(\mathbf{x},0,\lambda) = f_0(\mathbf{x},\lambda), \quad (\mathbf{x},\lambda)\in\Omega\times\mathbb{R}_\lambda. \tag{30}$$

Eq. (27) is called a kinetic equation. The parametrized measures $\nu_{x,t}$ and $\sigma_{x,t}$ in items (a) and (c) of the formulation of problem K arise as $\varepsilon_k\to 0$ from the limiting relations (15) and (17) as the Young measures associated with the sequences $\{e_{\varepsilon_k}\}$ and $\{e_{\varepsilon_k}, \nabla_x H(e_{\varepsilon_k})\}$, respectively.

Eq. (29) is satisfied a.e. in Q. The initial condition (30) is understood in the sense of weak trace. Equations (27) and (28) are understood in the distributions sense.

5 Theorem on Existence of Entropy Solutions

Kinetic equations of the form (27) with involved functions and measures satisfying conditions similar to requirements to the formulation of problem K in items (a)–(e) were studied in detail in [3]. For Eq. (27), considerations in [3] yield the following statement, which leads to the proof of solvability of the Darcy-Stefan problem.

Proposition 2. *The distribution function $f(\mathbf{x},t,\lambda)$ has the structure of the Heaviside function of the variable λ, i.e., there exists a function $e_* = e_*(\mathbf{x},t)$ such that $e_*\in L^\infty(0,T;L^\infty)$, $-c_0\le e_*\le c_0$ a.e. in $\mathbb{R}^d_x\times(0,T)$, and $f(\mathbf{x},t,\lambda) = 1_{\lambda\ge e_*(x,t)}$.*

Substituting representation of f into equations (27) and (28) and using properties of measures M and $d_\lambda\chi$ in the kinetic formulation, after straightforward calculations we justify the following existence theorem, which is the main result of the paper.

Theorem 2. *For any given initial distribution $e_0\in L^\infty$ such that $-c_0\le e_0(\mathbf{x})\le c_0$ a.e. in $\mathbb{R}^d$, there exists at least one entropy solution of the Darcy–Stefan problem.*

Acknowledgements

The work was supported by the Russian Foundation for Basic Research (Grants No. 07-01-00309, 10-01-00447).

References

[1] Bear J. Dynamics of Fluids in Porous Media. Dover Publications, New York, 1988.

[2] Rodrigues J.F. and Urbano J.M. On a Darcy–Stefan problem arising in freezing and thawing of saturated porous media // Contin. Mech. Thermodyn. 1999. V. 11. No. 3. 181–191.

[3] Plotnikov P.I. and Sazhenkov S.A. Kinetic formulation for the Graetz–Nusselt ultra-parabolic equation // J. Math. Anal. Appl. 2005. V. 304. P. 703–724.

[4] Malek J., Nečas J., Rokyta M., and Ružička M. Weak and Measure-valued Solutions to Evolutionary PDEs. London, Chapman and Hall, 1996.

[5] Antontsev S.N., Kazhikhov A.V., and Monakhov V.N. Boundary value problems in mechanics of nonhomogeneous fluids. Amsterdam, North-Holland, 1990.

[6] Tartar L. Compensated compactness method applying to system of conservation laws // In: Systems of Nonlinear PDE, Ball J.M. (ed.). 1983. NATO ASI Series D. Reidel Publ. Comp. 263–285.

[7] Ball J.M. A version of the fundamental theorem for Young measures // In: PDEs and Continuum Models of Phase Transitions. Lecture Notes in Physics. 1989. V. 344. Springer-Verlag. Berlin-Heidelberg-New-York. 241–259.

Sergey A. Sazhenkov, Lavrentyev Institute of Hydrodynamics, Prospekt Lavrentyeva 15, and Novosibirsk State University, Pirogova Street 2, Novosibirsk 630090, Russia

Vibrational lift force acting the cylinder in viscous liquid

Vitaliy D. Schipitsyn Alevtina A. Ivanova
Vital13@bk.ru A.Ivanova@pspu.ru

Abstract

Experimental studies of the lift force acting on a solid in a cavity filled with a viscous liquid and subjected to high-frequency vibration found the force to change no monotonously with the distance to the cavity walls. The horizontal translational vibrations of the cavity generate a repulsive force which is able to keep the heavy body at some distance from the cavity bottom and the light body at some distance from the ceiling. In both situations the body performs oscillations without touching the wall of the cavity. The repulsion vibrational force is significant at a distance comparable with the thickness of viscous boundary layer and decays with increasing of the distance. It case of spherical solids it was found and studied in [1],[2]. At larger distance the repulsion force is changed by vibrational attractive one. The last one quickly decays with the distance.

In overcritical domain when the heavy or light body is suspended near the wall the threshold excitation of the body mean motion along the axis of vibration is found [3],[4]. The body performs a uniform motion along the wall and changes its direction near the end-walls of the cavity. It is found that oscillatory and average dynamics of light and heavy bodies are similar. It is shown that the average motion is caused by the breakdown of the symmetry of the body oscillations.

The present work is devoted to experimental study of dynamics of relatively light cylinder in horizontal rectangular vessel subject to horizontal vibration. The dependence of the lift force (attractive and repulsive ones) on the distance between the solid and the boundary is investigated in the wide range of dimensionless frequency of vibrations. The experimental method consists in a direct measurement of the averaged lift force by its comparison with the body weight. In the presence of intensive vibrations the light cylinder has a stable position near the ceiling of the cavity and it can be held near the bottom by attraction force, too.

1 Experimental data

The Plexiglas cavity is a rectangular parallelepiped with dimensions $120 \times 55 \times 95$ mm^3 (Fig. 1). It is mounted on the plate of the mechanical vibrator which performs horizontal translational oscillation according the harmonic low $X = b \cos \Omega t$.

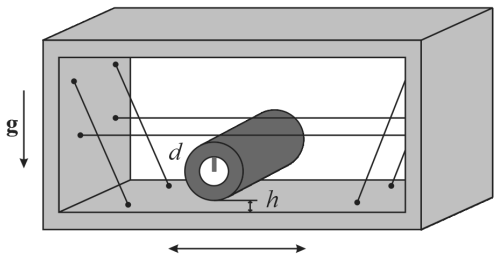


Figure 1: The sketch of the cavity.

The frequency of vibrations varies in the range $f \equiv 2\pi/\Omega = 0 - 25$ Hz, amplitude - $b = 0.1 - 5.5$ cm. The cavity is filled with water-glycerin mixture and contains the light solid. The variation of glycerol concentration allows to change the liquid viscosity in the range $\nu = 0.4 - 2.9$ St. The solid is made of a hollow ebonite cylinder of diameter d (20.2 or 26.0 mm) and length $H = 80.0$ mm. The mean density of all cylinders is $\rho_S = 0.93$ g/cm^3. The end-caps are made by lavsan films which have markers to study angular oscillations of the solid. The experiments are performed in continuous and stroboscope light, the flash is used for photo-registration.

In the experiment the cavity is fastened on the plate of the vibrator as it is shown in Fig. 1 or turned around the horizontal axis. In the latter case the solid touches the cavity ceiling. There are two thin horizontal fibers in the cavity. These fibers hold the cylinder at definite distance from the cavity bottom. The gap width between the solid and the bottom is 5 mm. Another two fibers are stretched at definite angle to the bottom and used to bound the solid drift to the lateral walls and exclude its influence on the solid dynamics.

Let's consider the case when the cylinder has a stable position in the top central part of the cavity and touches the ceiling. At definite amplitude b the increase of the frequency f leads to the threshold repulsion of the solid for the distance h. The decrease of the frequency results in the reduction of the gap width up to zero and the solid touches the ceiling.

The critical frequencies of the transitions "down-up" are measured at different amplitudes of vibrations. It is found out that the solid repulsion and its return happen with hysteresis (Fig. 2).

The dark circles correspond to the repulsion of the cylinder at increase of the frequency of vibration, the empty circles correspond to the return to the ceiling at decrease of the frequency. The threshold frequencies become less at the amplitude increase.

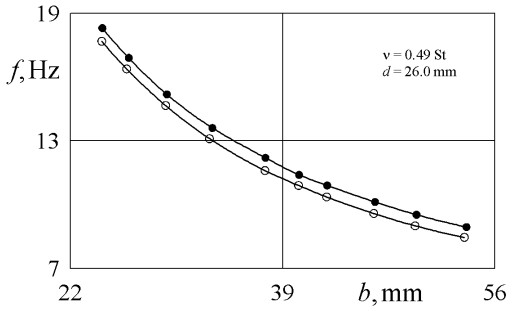


Figure 2: The threshold curves of the solid repulsion (and return) from the ceiling.

In case of intensive vibrations the solid has two stable positions: the examined position near the ceiling and quasi-stationary position near the cavity bottom. The latter state is caused by the action of attractive vibrational force opposite to the gravitational one.

To study this effect the cavity is mounted in the way showed in Fig. 1. The solid keeps the distance from the bottom due to the fibers. At the threshold frequency of vibration the solid goes away from the fibers and hangs at the definite distance h from the bottom.

The position of the cylinder is recorded by the photo camera and the gap width between the bottom (ceiling) and the cylinder is measured. The amplitude of vibrations, the solid size and the liquid viscosity vary in experiments.

Fig. 3, *a* demonstrates the dependence of the gap width h on the frequency of vibrations for different amplitudes b and viscosities ν in case of the repulsion from the ceiling. One can see that with the increase of the frequency the gap width grows and tends to the limit value. In case of decreasing frequency the experimental data coincide to the examined ones and are not shown in Fig. 3, *a*.

Fig. 3, *b* demonstrates the dependence of the distance between the solid and the bottom on the frequency in the conditions of quasi-stationary position of the solid under the influence of attractive vibrational force. The marks correspond to the data in Fig. 3, *a*. The increase of frequency results in the diminishing of the distance between the solid and the cavity bottom but it

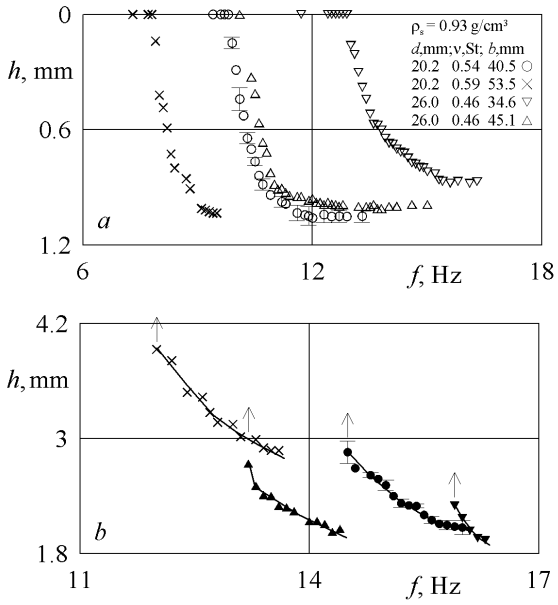


Figure 3: Figure 3: The equilibrium state of the light solid near the ceiling (a) and the bottom (b).

never becomes equal zero. With the decrease of vibration frequency the gap width tends to critical value, the equilibrium is impossible above this value. The arrows demonstrate the critical points of the stability loss: the solid goes away from the bottom and floats to the fibers. The comparison of Fig. 3, a and Fig. 3, b demonstrates that in the equilibrium state the gap width between the solid and the bottom is considerably larger than the width between the solid and the ceiling.

2 Discussion

The averaged dynamics of the oscillating solid in liquid depends on the relative density $\rho \equiv \rho_S/\rho_L$ and is determined by dimensionless frequency of vibrations $\omega = \Omega d^2/\nu$ which characterizes the ratio of the solid size d and thickness of viscous boundary layer $\delta = \sqrt{2\nu/\Omega}$, and by vibrational parameter $W = (b\Omega)^2/(gd)$ [2].

The threshold data for the repulsion of the solid from the ceiling (Fig. 4, curve I) and its return (Fig. 4, curve II) correspond to each other on the plane ω, W; the size of the solid and liquid viscosity vary.

In the limit $\omega > 400$ the threshold values of W (curves I, II) tend to constant value. The hysteresis domain is nonzero in the whole range of dimensionless frequency.

The experiments with different liquids demonstrate that the gap width in the quasi-stationary equilibrium of the solid near the ceiling is comparable with the thickness of the viscous layer $\delta = \sqrt{2\nu/\Omega}$. So, repulsive vibrational force is efficient at the distance of the viscous interaction of the oscillating solid and the cavity boundary and it is appropriate to choose δ as a unit of measure of gap width. Fig. 5 shows the dependence of the dimensionless distance h/δ on the parameter W.

Fig. 5, a demonstrates that all experimental data correspond to each other except the data for the maximum amplitude of vibrations. The quasi-stationary state near the ceiling is realizable only at the distance less than thickness of the viscous Stokes layer (Fig. 5, a). This distance characterizes the domain of repulsive vibrational force action. At the same time the attractive force acts at the distance larger that Stokes layer (Fig. 5, b). Consequently at the distances larger than the radius of viscous interaction the repulsive force changes to the attractive one.

One can see that the curve for repulsion at $b = 53.5$ mm does not agree to the general law

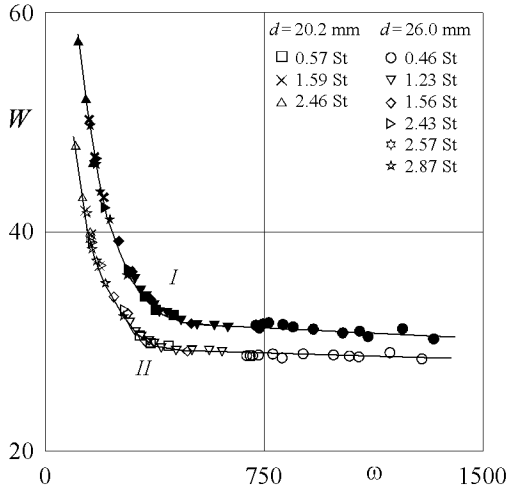


Figure 4: The threshold data for the repulsion of the solid from the ceiling (curve I) and the return of the solid to the boundary (curve II).

on the plane ω, W (Fig. 4). It is well known that increase of the dimensionless amplitude of the solid oscillations leads to the transition from the laminar flow to the detached one. The stability threshold is determined by the dimensionless amplitude of oscillations A/d and in the limit of high frequency $A/d = 1.456\omega^{-1/4}$ [5]. Perhaps the "specific" dynamics of the solid at large amplitude of vibrations (particularly the increase of critical values of W) is caused by the change of the flow regime around the oscillating solid.

When the vibrational lift force equals to the gravitational one the parameter W subject to the coefficient $\pi(1-\rho)/6$ characterizes the inverse value of the dimensionless vibrational lift force with the unit of measure $\rho_L b^2\Omega^2 d$. The interaction between the oscillating solid and immovable wall in the approximation of inviscid flow (at the distance considerably larger than the Stokes layer) is determined by the dimensionless distance h/R, here R - radius of the solid. In this case the solid is under the influence of the attractive force [6]. Fig. 6 demonstrates the dependence of the vibrational parameter W on the distance from the boundary in the equilibrium near the bottom. Different results correspond to various parameters of the experiment (b, d, ν vary).

The extreme right points of different series correspond to the minimum of the interaction curve. At this distance the force is not able to hold the solid near the bottom. The increasing branches of the curves (dotted lines) correspond to the unstable state of the light solid near the bottom when the attractive force decays with the distance (W increases). Line I demonstrates the theoretical attractive force acting on the solid (relative density $\rho \equiv \rho_S/\rho_L = 0.75$) in the limit $h/R \gg 1$ at $\omega \gg 1$. The curve is computed for the case of the interaction of two cylinders at the large distance in the oscillating flow of inviscid liquid [6].

The increase of the dimensionless frequency of vibrations ω leads to the drift of the minimum values of the interaction curves to the lower values of W (Fig. 7).

As the inverse value of W characterizes the attractive force acting on the solid, then the curve in Fig. 7 determines the maximum value of the attractive force. The latter is caused by the distance where the force begins to decay. The increase of the dimensionless frequency results in the decrease of the extremal value of h/R (Fig. 6) and the maximum force increases. The law $W \sim \omega^{-1/2}$ (Fig. 7) is caused by the fact that the distance where the vibrational force changes the direction is of the order of the Stokes layer thickness.

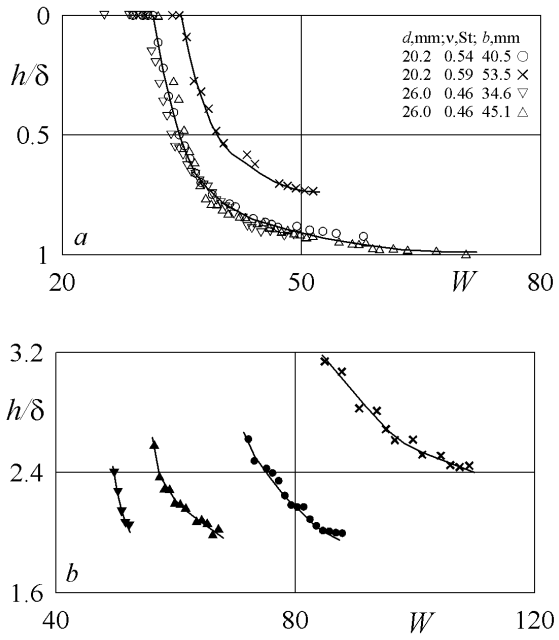


Figure 5: The dependence of the equilibrium state near the ceiling (a) and the bottom (b).

3 Conclusion

The lift force acting on the light solid in the viscous liquid at high-frequency oscillations is experimentally investigated. It is found that the interaction force acting on the oscillating solid is nonmonotonic function of a distance from the wall. In case of potential flow at large distance the oscillating solid is attracted to the wall and the decay of the distance results in the growth of this force. The experiments show that the growth of the attractive force is terminated at some distance. The further decay of the gap width results in the diminishing of the attracting force and appearance of the repulsive one at the distance less than the thickness of the viscous boundary layer.

Acknowledgements

The work is supported by the Russian Foundation for Basic Research (Grant 09-01-00665a) and Academic council of PSPU (grant of 2010).

References

[1] Ivanova A.A., Kozlov V.G., and Kuzaev A.F. Vibrational lift force acting on a body in a fluid near a solid surface // Doklady Physics. 2005. V. 50. No 6. P. 311-314.

[2] Ivanova A.A., Kozlov V.G., and Kuzaev A.F. Vibrational hydrodynamical interaction of sphere with cavity boundary // Fluid Dynamics. 2008. Vol. 43. No 2. P. 194-202.

[3] Ivanova A.A., Kozlov V.G., Schipitsyn V.D. A light body in the cavity filled with liquid at horizontal vibrations // Izv. RAN. Mech. Zhid. i Gaza (submitted).

[4] Schipitsyn V.D. Behaviour of a cylindrical solid in a rectangular cavity with viscous liquid subjected to horizontal vibration // Convective flows... Vol. 4. Perm: PSPU, 2009. P. 169-186.

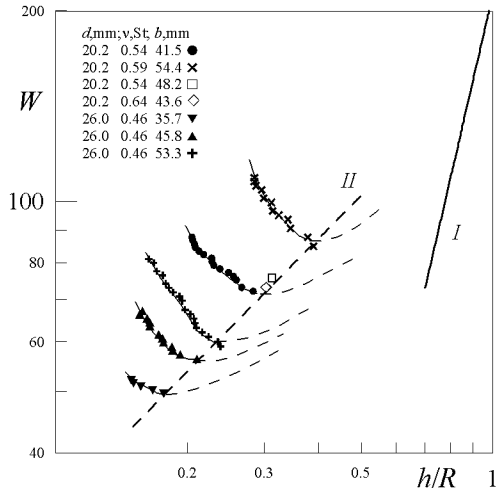


Figure 6: The equilibrium curve for the light solid near the bottom: I - theoretical data in the limit $h/R \gg 1$; experimental curve II corresponds to the law $W = 168(h/R)^{0.7}$.

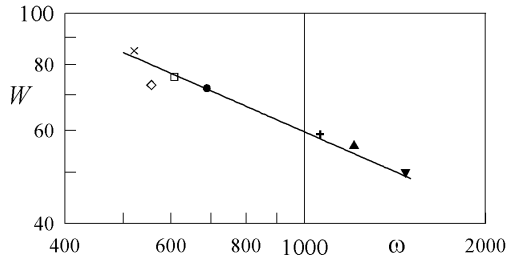


Figure 7: The dependence of the minimum value of W on the dimensionless frequency. The experimental data are approximated by the equation $W = 1880\omega^{-1/2}$. The symbols correspond to Fig. 6.

[5] Sarpkaya T. Force on a circular cylinder in viscous oscillatory flow at low Keulegan - Carpenter numbers // J. Fluid Mech. 1986. V. 165. P. 61-71.

[6] Cherepanov A.A. Influence of vibrations on the hydrodynamical systems: resonances and averaged effects. Doctor of Science thesis. Perm: PSU, 2000. 379 p.

Vitaliy D. Schipitsyn, Perm State Pedagogical University, Russia
Alevtina A. Ivanova, Perm State Pedagogical University, Russia

The force on aerofoil in steady irrotational flow with immobile point vortex

E. V. Semenko
semenko54@mail.ru

Abstract

The problem of plane steady irrotational flow past aerofoil is considered. To stimulate the flow with adjoining to aerofoil cavity we place into fluid domain the immobile point vortex considered as the second streamlined aerofoil with extremely small (vanishing) extent but with non-zero circulation around it.

The set of parameter's values (oncoming flow velocity and circulations around aerofoil and point vortex) when the flow scheme has a form of adjoining to aerofoil cavity is determined. The force on aerofoil is calculated. In particular it turns out that for cavity formation the circulation around point vortex (vortex strength) must be in definite limits depending on vortex position and oncoming flow velocity. At that when the circulation is enough large (close to upper value) the cavity attracts aerofoil, at small (close to lower value) circulations it repels aerofoil.

1 Problem statement, complex velocity

We consider the problem of plane steady irrotational flow past aerofoil L_0. As usual [1] the flow source we place at infinity, let $V_0 = V_x + iV_y$ be oncoming flow velocity, γ_0 be circulation of velocity vector around L_0. To stimulate the flow with adjoining to aerofoil cavity formation we place in flow domain one streamlined aerofoil L_1 yet with non-zero circulation γ_1 around it. Then at some correlation between parameters V_0, γ_0 and γ_1 the streamlines picture (flow scheme) has a form fig. 1 (see [2]), where curves with arrows conditionally depict streamlines, line L is the cavity boundary.

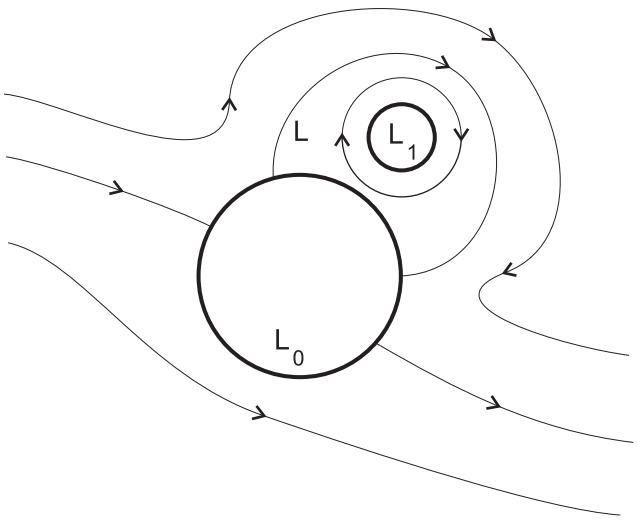


Figure 1: Flow with cavity.

For flow past a pair of aerofoils problem one may find the complex potential or complex velocity [3], [4]. In turn using complex velocity one may determine conditions for parameters when flow scheme has a wanted form of cavity (fig. 1) and by Blasius formula [5] calculate the force on aerofoil. But in such general statement the problem of conditions for parameters determination is very complicated [4] and corresponding formula for force is enough complex too [3] and defies to qualitative theoretical analysis. To simplify the problem we assume that second aerofoil L_1 extent tends to zero, i.e. aerofoil collapses to point forming point vortex. Note to be rigorous the point of vortex position must satisfy Helmholtz law [6], i.e. move with streaming flow. But in our case we consider vortex as just immobile second streamlined aerofoil with vanishing extent. Just in this sense we use the term "immobile point vortex".

Further we consider aerofoil L_0 as circle with center in zero and unit radius. The flow domain $D = \{\, z \mid |z| > 1 \,\}$. Then complex velocity for flow past L_0 has well known form [1], [3]

$$f_0(z) = \overline{V}_0 - \frac{V_0}{z^2} + \frac{\gamma_0}{2\pi i z}\,, \quad z \in D\,.$$

For flow with immobile vortex in point $q \in D$ complex velocity has a form

$$f(z) = \overline{V}_0 - \frac{V_0}{z^2} + \frac{\widetilde{\gamma}}{2\pi i z} + \frac{\gamma_1}{2\pi i}\left(\frac{1}{z-q} - \frac{1}{z-1/\overline{q}}\right), \quad \widetilde{\gamma} = \gamma_0 + \gamma_1\,. \tag{1}$$

The number γ_1 is called vortex strength [6]. One may obtain formula (1) by passage to the limit from complex velocity for flow past pair of aerofoils [3], [4], however this formula is rather evident and well known, see for instance [6].

2 Flow with cavity formation

As it is shown in [2] flow scheme has a form of adjoining to the aerofoil L_0 cavity (fig. 1) if and only if the complex velocity $f(z)$ has four zero on L_0. For simplicity let's admit rather natural assumption that total circulation of velocity vector around infinity is equal to zero ($\widetilde{\gamma} = 0$), then the equation for complex velocity roots has a form

$$ze^{-i\varphi} - \frac{e^{i\varphi}}{z} - i\gamma z\frac{q - 1/\overline{q}}{(z-q)(z-1/\overline{q})} = 0\,,$$

where $\varphi = \arg V_0$ is inclination angle of oncoming flow velocity, $\gamma = \gamma_1/(2\pi|V_0|)$ is reduced vortex strength. Since we are seeking roots on unit circle L_0 then in this equation $z = 1/\overline{z}$ and it is given by

$$ze^{-i\varphi} - \overline{z}e^{i\varphi} - i\frac{\gamma z(q - 1/\overline{q})}{(z-q)(1/\overline{z} - 1/\overline{q})} = 2i\,\mathrm{Im}(ze^{-i\varphi}) + i\frac{\gamma(|q|^2 - 1)}{|z-q|^2} = 0\,.$$

Let $q = re^{ip}$ $(r > 1)$ then we come to equation

$$|z - re^{ip}|^2\mathrm{Im}(ze^{-i\varphi}) + \frac{\gamma(r^2-1)}{2} = |ze^{-ip} - r|^2\mathrm{Im}(ze^{-i\varphi}) + \frac{\gamma(r^2-1)}{2} = 0\,.$$

Let's denote $z = e^{i(t+\varphi)}$ then $\mathrm{Im}(ze^{-i\varphi}) = \sin t$,
$|ze^{-ip} - r|^2 = 1 + r^2 - 2r\cos(t + \varphi - p) = 1 + r^2 - 2r\sin(t + \varphi - p + \pi/2)$
and we obtain the equation

$$\sin(t + \alpha)\sin t - h\sin t = \Gamma\,, \tag{2}$$

$\alpha = \varphi - p + \pi/2$, $h = (1 + r^2)/(2r)$, $\Gamma = \gamma(r^2 - 1)/(4r)$. Note that $h \geqslant 1$ at $r \geqslant 1$.

The equation (2) solvability analysis needs rather laborious and scrupulous work. For short we give the final result without proof.

Theorem 1. *The equation (2) has four different roots $t_j \in [0, 2\pi]$, $j = \overline{1,4}$ if and only if $h \in (1, 2)$ and parameters α and Γ satisfy either condition*
(i) $|\pi - \alpha| < \alpha_0(h)$, $\Gamma \in (\psi_1(h, \pi - \alpha); \psi_2(h, \pi - \alpha))$;

or condition
(ii) $|\alpha| < \alpha_0(h)$, $\Gamma \in (-\psi_2(h,\alpha); -\psi_1(h,\alpha))$;
here $\alpha_0(h)$ *is monotone decreasing function at* $h \in [1,2]$, $\alpha_0(2) = 0$,
$\alpha_0(1) = \alpha_{max} \in (0, \pi/2)$;
$0 < \psi_1(h,\beta) < \psi_2(h,\beta)$, $\psi_1(h,\alpha_0(h)) = \psi_2(h,\alpha_0(h))$.
At that $\psi_1(h,0) = h-1$, $\psi_2(h,0) = h^2/4$.

Coming back to complex velocity we obtain the following statement.

Theorem 2. *The complex velocity* $f(z)$ *in a form (1) in case* $\widetilde{\gamma} = \gamma_0 + \gamma_1 = 0$ *has four zero on* L_0 *if and only if* $r \in (1, 2+\sqrt{3})$ *and inclination angle of oncoming flow velocity* $\varphi = arg V_0$ *and reduced vortex strength* $\gamma = \gamma_1/(2\pi|V_0|)$ *satisfy conditions*

$$|\varphi - p \pm \pi/2| < \beta_0(r)\,, \quad H_1(r,\alpha) < |\gamma| < H_2(r,\alpha)\,,$$

$\gamma > 0$ *at* $|\varphi - p - \pi/2| < \beta_0(r)$ *and* $\gamma < 0$ *at* $|\varphi - p + \pi/2| < \beta_0(r)$.
Here

$$q = re^{ip}\,, \quad \beta_0(r) = \alpha_0\left(\frac{1+r^2}{2r}\right), \alpha = \begin{cases} \pi/2 - \varphi + p, & |\varphi - p - \pi/2| < \beta_0(r), \\ \varphi - p + \pi/2, & |\varphi - p + \pi/2| < \beta_0(r), \end{cases}$$

$$H_{1,2}(r,\alpha) = \frac{4r\psi_{1,2}((1+r^2)/(2r),\alpha)}{r^2-1}\,.$$

Let's turn to obtained statement interpretation. Note that angle p (vector $l_0 = e^{ip}$) specifies the direction from center of circle L_0 to the vortex point q. Angles $p \pm \pi/2$ (vectors $l_1^{\pm} = \pm ie^{ip}$) specify perpendicular to l_0 directions. Angle $\alpha = \varphi - p \pm \pi/2$ is a deviation of oncoming flow velocity V_0 direction from direction l_1^+ or l_1^-. Thus a cavity arises if and only if the distance from vortex point to streamlined aerofoil is not too large ($r - 1 < 1 + \sqrt{3}$) and a deviation of oncoming flow velocity V_0 direction from direction l_1^+ or l_1^- doesn't exceed the magnitude $\beta_0(r) < \pi/2$. The maximum deviation $\beta_0(r)$ monotone decreases with respect to r and tends to zero when r tends to upper value $2 + \sqrt{3}$. In turn at that the reduced vortex strength γ module is bounded above and below by constants depending on r and deviation $\alpha = \varphi - p \pm \pi/2$ and a sign of γ depends on V_0 direction: $\gamma > 0$ when V_0 direction close to l_1^- and $\gamma < 0$ when V_0 direction close to l_1^+.

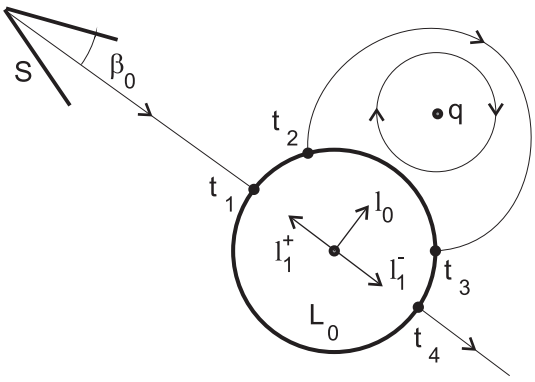


Figure 2: Cavity formation, sector of possible directions.

In fig. 2 it is depicted directions l_0, $l_1^{\pm}$ and for case $\gamma < 0$ conditionally depicted the sector of possible directions V_0 (sector S).

The cavity fails at lower value of reduced vortex strength $|\gamma| = H_1(r,\alpha)$ (when points t_2 and t_3 coalesce and cavity "comes off" the aerofoil L_0) and at upper value $|\gamma| = H_2(r,\alpha)$ (when points t_1 and t_2 or t_3 and t_4 coalesce).

3 The force on aerofoil

The force $F = F_x + iF_y$ on aerofoil L_0 one calculates by Blasius formula [5]

$$\overline{F} = \frac{i\rho}{2} \int\limits_{L_0} f^2(z)\, dz\,,$$

where $\rho = \text{const}$ is a density, $f(z)$ is complex velocity. But due to formula (1)

$$f(z) = \overline{V}_0 - \frac{V_0}{z^2} + \frac{\widetilde{\gamma}}{2\pi i z} + \frac{\gamma_1}{2\pi i(z-q)} - \frac{\gamma_1}{2\pi i(z-1/\overline{q})} = f_1 + f_2 + f_3 + f_4 + f_5\,.$$

As $L_0 = \{\, z \mid |z| = 1 \,\}$, $|q| > 1$ so

$$\int\limits_{L_0} f^2(z)\, dz = 2\pi i(\operatorname{Res} f^2(0) + \operatorname{Res} f^2(1/\overline{q}))\,.$$

But

$$f^2(z) = \sum_{j=1}^{5} f_j^2 + 2 \sum_{\substack{j,k=1 \\ j\neq k}}^{5} f_j f_k\,.$$

It is easy to see that $\operatorname{Res} f_j^2(0) = \operatorname{Res} f_j^2(1/\overline{q}) = 0$, i.e.

$$\int\limits_{L_0} \sum_{j=1}^{5} f_j^2\, dz = 0\,.$$

Absolutely analogously we obtain

$$\int\limits_{L_0} (f_1 f_2 + f_1 f_4 + f_2 f_3)\, dz = 0\,.$$

Further

$$\int\limits_{L_0} f_1 f_3 = 2\pi i \operatorname{Res}(f_1 f_3)\Big|_{z=0} = \widetilde{\gamma}\,\overline{V}_0\,, \quad \int\limits_{L_0} f_1 f_5 = 2\pi i \operatorname{Res}(f_1 f_5)\Big|_{z=1/\overline{q}} = -\gamma_1 \overline{V}_0\,,$$

$$\int\limits_{L_0} f_2 f_4 = 2\pi i \operatorname{Res}(f_2 f_4)\Big|_{z=0} = \frac{\gamma_1 V_0}{q^2}\,, \quad \int\limits_{L_0} f_2 f_5 = -2\pi i \operatorname{Res}(f_2 f_5)\Big|_{z=\infty} = 0\,,$$

$$\int\limits_{L_0} f_3 f_4 = 2\pi i \operatorname{Res}(f_3 f_4)\Big|_{z=0} = -\frac{\widetilde{\gamma}\gamma_1}{2\pi i q}\,, \quad \int\limits_{L_0} f_3 f_5 = -2\pi i \operatorname{Res}(f_3 f_5)\Big|_{z=\infty} = 0\,,$$

$$\int\limits_{L_0} f_4 f_5 = 2\pi i \operatorname{Res}(f_4 f_5)\Big|_{z=1/\overline{q}} = -\frac{\gamma_1^2}{2\pi i(1/\overline{q} - q)} = \frac{\gamma_1^2 \overline{q}}{2\pi i(|q|^2 - 1)}\,.$$

Finally

$$\overline{F} = i\rho \left[\widetilde{\gamma}\overline{V}_0 - \gamma_1 \overline{V}_0 + \frac{V_0 \gamma_1}{q^2} - \frac{\widetilde{\gamma}\gamma_1}{2\pi i q} + \frac{\gamma_1^2 \overline{q}}{2\pi i(|q|^2 - 1)} \right]$$

or

$$F = -i\rho\widetilde{\gamma}V_0 + i\rho\gamma_1 V_0 - i\rho \frac{\overline{V}_0 \gamma_1}{\overline{q}^2} - \frac{\rho\widetilde{\gamma}\gamma_1}{2\pi\overline{q}} + \frac{\rho\gamma_1^2 q}{2\pi(|q|^2 - 1)}\,.$$

The first summand in this expression is a force calculated by Joukowski formula (when $\gamma_1 = 0$), the rest is addition because of vortex presence.

Let's again use rather natural assumption $\widetilde{\gamma} = \gamma_0 + \gamma_1 = 0$ then due to $q = re^{ip}$ we obtain

$$F = i\rho\gamma_1 \left(V_0 - \frac{\overline{V}_0 e^{2ip}}{r^2} \right) + \frac{\rho\gamma_1^2 r e^{ip}}{2\pi(r^2-1)} = F_1 + F_2 \,.$$

Let's analyze the obtained formula. First the summand F_2 doesn't depend on oncoming flow velocity V_0 and coincides with l_0 by direction. The first summand F_1 depends on V_0. Note however that cavity existence conditions impose restrictions on V_0 direction (see section 2) $|\varphi - p \pm \pi/2| = |\alpha| < \beta_0(r)$. Let $\alpha = \varphi - p + \pi/2$, i.e. $\varphi \approx p - \pi/2$ as in fig. 2 (the reduced vortex strength $\gamma < 0$ in this case). Then

$$F_1 = i\rho\gamma_1|V_0| \left(e^{i\varphi} - \frac{e^{-i\varphi}e^{2ip}}{r^2} \right) = i\rho\gamma_1|V_0|e^{ip} \left(e^{i(\varphi-p)} - \frac{e^{-i(\varphi-p)}}{r^2} \right) =$$

$$= i\rho\gamma_1|V_0|e^{ip} \left(e^{i(\alpha-\pi/2)} - \frac{e^{-i(\alpha-\pi/2)}}{r^2} \right) = \rho\gamma_1|V_0|e^{ip} \left(e^{i\alpha} + \frac{e^{-i\alpha}}{r^2} \right) = \rho\gamma_1|V_0|e^{ip}s$$

or due to $\gamma_1 < 0$

$$F_1 = -\rho|\gamma_1||V_0|e^{ip}s\,, \quad s = e^{i\alpha} + \frac{e^{-i\alpha}}{r^2} = \cos\alpha \left(1 + \frac{1}{r^2}\right) + i\sin\alpha \left(1 - \frac{1}{r^2}\right) . \tag{3}$$

It is easy to see the same formula (3) we obtain for F_1 in case $\alpha = \varphi - p - \pi/2$ when $\gamma > 0$.

So

$$F = F_2 + F_1 = \frac{\rho\gamma_1^2 r e^{ip}}{2\pi(r^2-1)} - \rho|\gamma_1||V_0|e^{ip}s = \rho|\gamma_1||V_0|e^{ip} \left(\frac{|\gamma|r}{r^2-1} - s \right)$$

or

$$\begin{aligned} &F = F_R + F_I\,, \\ &F_R = \rho|\gamma_1||V_0|e^{ip} \left(\frac{|\gamma|r}{r^2-1} - \cos\alpha \left(1 + \frac{1}{r^2}\right) \right) , \\ &F_I = -i\rho|\gamma_1||V_0|e^{ip}\sin\alpha \left(1 - \frac{1}{r^2}\right) . \end{aligned} \tag{4}$$

The force F_R directs parallel to vector l_0. Note the expression

$$H = \frac{|\gamma|r}{r^2-1} - \cos\alpha \left(1 + \frac{1}{r^2}\right)$$

may change its sign depending on magnitude of γ. So at $\alpha = 0$ if one take the lower vortex strength $|\gamma| = H_1(r,0) = 4r(h-1)/(r^2-1) = 2(r-1)/(r+1)$ (see theorem 1) then $H = 2r/(r+1)^2 - 1 - 1/r^2 < 0$ at all $r \in (1, 2+\sqrt{3})$. At upper strength $|\gamma| = H_2(r,0) = rh^2/(r^2-1) = (r^2+1)^2/(4r(r^2-1)^2)$ we have $H > 0$ at $r \to 1$. Thus at large vortex strength the force F_R acts in l_0 direction, i.e. the cavity so to speak "attracts" aerofoil, but at small strength cavity to the contrary "repels" aerofoil.

The force F_I is perpendicular to l_0 and coincides with l_1^+ direction at $\sin\alpha < 0$ and with l_1^- direction at $\sin\alpha > 0$.

4 Discussion

So the flow past unit circle L_0 at presence of immobile vortex in point $q = re^{ip}$, $r > 1$ is considered, V_0 is oncoming flow velocity, γ_1 is vortex strength. Thus $l_0 = e^{ip}$ is the unit vector specifying the direction from L_0 center to point of vortex, $l_1^{\pm} = \pm i l_0$ are vectors specifying the perpendicular directions. We assume that total circulation of velocity vector around infinity (the flow source) is equal to zero that automatically means that Joukowski formula gives the zero force. Then if

$r \in (1, 2+\sqrt{3})$, the deviation of V_0 direction from l_1^+ or l_1^- direction doesn't exceed the definite magnitude $\beta_0(r)$ ($|\alpha| = |\arg V_0 - p \pm \pi/2| < \beta_0(r)$) and vortex strength is bounded above and below by given limits $2\pi|V_0|H_1(r,\alpha) < |\gamma_1| < 2\pi|V_0|H_2(r,\alpha)$ then the cavity adjoining to streamlined aerofoil and enclosing point vortex arises (fig. 1, 2). At that the force on aerofoil F is given by formula (4) and generally speaking the force F is not perpendicular to V_0 like in Joukowski formula. However if the velocity V_0 is perpendicular to l_0, i.e. coincides with l_1^+ or l_1^- by direction then the force F acts parallel to l_0 and coincides with l_0 by direction at large vortex strengths (the cavity attracts the aerofoil) but has an opposite direction at small strengths (the cavity repels aerofoil). If the velocity V_0 deviates from $l_1^\pm$ directions then besides the analogously acting along l_0 force there arises perpendicular to l_0 force, its direction depends on to what side the V_0 direction deviates from $l_1^\pm$ directions.

References

[1] Glauert, H. The elements of aerofoil and airscrew theory. Cambridge Science Classics Series, 2nd edn. Cambridge, UK: Cambridge University Press, 1947.

[2] Semenko E.V. Flows on Riemann surface: flows on torus classification (russian). Sibirsky jurnal industrialnoy matematiki, XII, 1(37), 2009, 136-150.

[3] Crowdy, D. Calculating the lift on a finite stack of cylindrical aerofoils. Proc. R. Soc. A 2006 462, 1387-1407.

[4] Semenko E.V. In press. The general form of solution of flows on torus problem (russian). Sibirsky jurnal industrialnoy matematiki.

[5] Acheson, D. Elementary fluid dynamics. Oxford: Oxford University Press, 1990.

[6] Saffman, P. G. Vortex dynamics. Cambridge University Press, 1992.

Semenko E.V., Vybornaya 152-102, Novosibirsk, Russia.

Modeling tribospectroscopy using movable cellular automata

Valeriy V. Sergeev Alexey Yu. Smolin Sergey Yu. Korostelev
Sergey A. Dobrinin
svalera@ispms.tsc.ru

Abstract

Tribospectroscopy is a non-destructive technique for detecting nanoscale pores in surface layer of a material using frequency analysis of the force resisting to sliding of a small counter-body on the material surface. Possibilities of this technique are studied based on 3D modeling by movable cellular automaton method for ceramic coating on steel substrate. Pores position varies in depth and in the direction of counter-body motion. It is shown that a specific frequency at the friction force spectrum corresponds to average distance among the pores.

1 Introduction

The use of nanostructured coatings can significantly improve the operational characteristics of machine elements, mechanisms and structures. In this case the mechanical properties of these coatings strongly depend on the presence of defects and damage of nano-sized scale. In this regard, it is urgent to develop methods for diagnosing such defects. One of the methods of nondestructive testing of coatings, which allows to assess structural defects in thin surface layers of solids, could be based on the approach associated with using friction and measuring parameters of the system response [1], namely tribospectroscopy.

In this paper, the ability of tribospectroscopy method for the analysis of defects in the surface layers of solids are studied by numerical simulation on the example of a metal with high-strength ceramic coating.

2 Description of the model

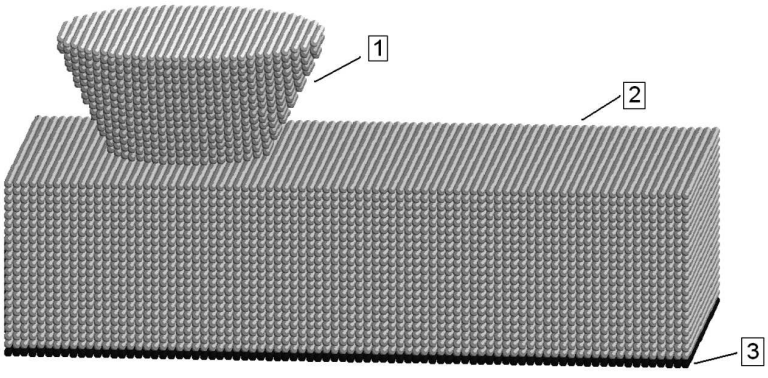


Figure 1: Simulated system: 1 — counterbody, 2 — ceramic coating, 3 — steel substrate

A steel sample coated with ceramic ZrO_2 was simulated (Fig. 1). Thickness of the coating was chosen equal to $H = 60$ nm, the sample length $L = 250$ nm, width $M = 125$ nm, the size of the automaton $d = 3$ nm. Ceramic counterbody had the form of a cone of base diameter 60 nm.

Motion of the counterbody was simulated by setting constant velocity $V = 5$ m/s in the horizontal direction for automata of the upper layer of the counterbody. The lower surface of the sample was fixed, and its lateral surfaces were free. When the counterbody moving the resistance force on the surface, associated with the friction force F, was registered. After simulation, the Fourier transform [2] of the registered friction force $F(t)$ was analysed.

Defects in surface layer was simulated by generating nanosized pores in the coating. The width of the pores was $w = 12$ nm, and height — $h = 3$ nm. The nanopores were alongated perpendicular to the counterbody motion. The nanaopores were periodically arranged with the distance of $P = 30$ nm. In this paper the ability of determining the distance between the defects was analyzed.

3 Analysis of the computational results

Fourier transform of the time dependence of the sliding friction force for defect-free sample is shown in Fig. 2. At this spectrum several frequencies are clearly visible. One frequency corresponds to the periodic parameter of artificial roughness of the sample surface (artificial roughness is associated with discrete structural elements — cellular automata), and is equal to $f_d = V/d = 1{,}6$ GHz. The peaks corresponding to the frequencies nf_d (where n - an integer) are also clearly visible. The amplitude of these peaks decreases with increasing n. Note that the amplitude (~ 0.4 nm) and the period (3 nm) of the artificial roughness in the model are qualitatively consistent with the experimentally measured parameters of surface roughness at the nanoscale level [3].

Let's define the natural frequencies of the simulated system. Transverse sound velocity is defined by the formula $v_S = \sqrt{G/\rho}$, longitudinal sound velocity — $v_P = \sqrt{(K + 4G/3)/\rho}$. The properties values for ZrO_2 ceramics ($G = 30$ GPa, $K = 70$ GPa, $\rho = 5600$ kg/m3) give $v_S = 2315$ m/s and $v_P = 4432$ m/s.

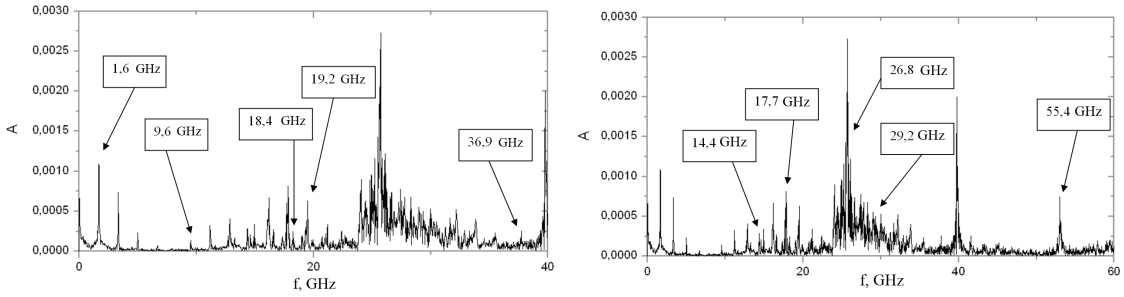


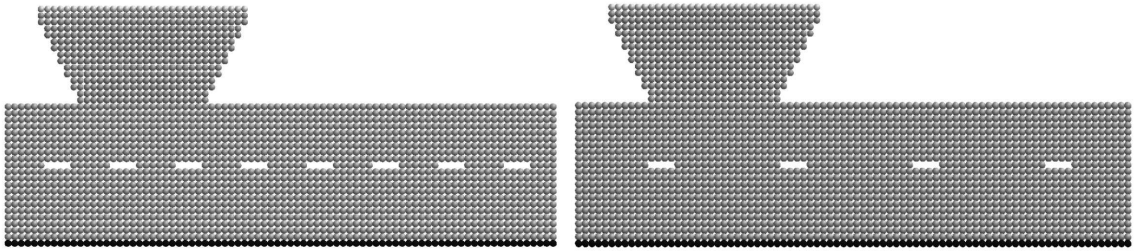
Figure 2: Fourier spectrum of registrations force of friction for the defect-free sample (scale of 1 .. 40 GHz (a) and the scale of 1 .. 60 GHz (b))

Now let's estimate the natural frequencies of the coating. If $l = 60$ nm, in the case of a rod fixed at one end, the first harmonic for the transverse sound is equal to 9.6 GHz, and for the longitudinal sound — 19,2 GHz. In the case of a free rod, the first harmonic of the transverse sound is equal to 18.4 GHz, and for the longitudinal — 36,9 GHz. These frequencies are also visible in Fig. 2a. If $l = 125$ nm (the width of the sample), we obtain for the free rod and for the longitudinal sound velocity the frequency of 17.7 GHz (see Fig. 2b).

Let's estimate the natural frequencies of the indenter. If $l = 40$ nm, in the case of a fixed rod, the first harmonic for the transverse sound is equal to 14.4 GHz, and for the longitudinal sound — 26.8 GHz. In the case of a rod with free ends the first harmonic for the transverse sound is equal to 29.2 GHz and for the longitudinal sound — 55.4 GHz.

All the defined frequencies correspond to peaks of the spectrum in Fig. 2b. Despite the fact that the application of the described approach for evaluating natural frequencies for such a complex system, as shown in Fig. 1 is not obvious, the control calculation of natural frequencies made in the ANSYS program gives the results differing from those found above not greater than 10%.

The presence of periodically arranged nanopores (Fig. 3) leads to pronounced low-frequency peak in the Fourier spectrum of sliding friction resistance force registrations of (Fig. 4). Number 1



a) b)

Figure 3: Nanopores of length of 12 nm located at depth of 30 nm, with a period of 30 nm (a) and 60 nm (b)

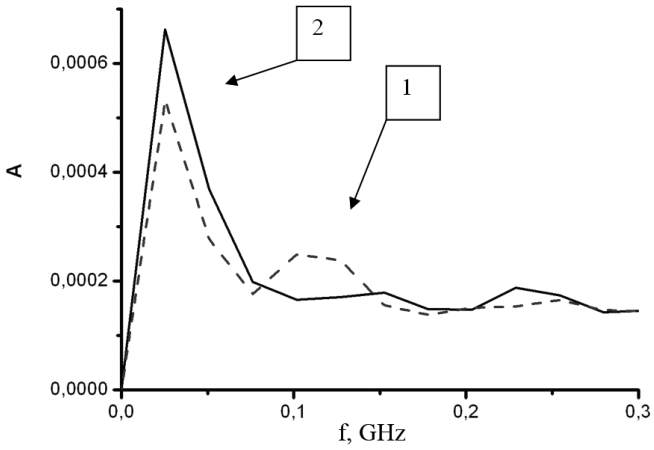


Figure 4: Fourier spectra for defect-free sample (solid line) and the sample with nanopores (dotted line), shown in Fig. 3b

in Fig. 4 denotes a peak corresponding to the typical distance between nanopores, and the number 2 — to the peak corresponding to the path length of the indenter. The frequency of the peak corresponding to the period of nanopores, is given by the formula V/P, where V is velocity of the indenter and P is the period of nanopores. This frequency in our case is equal to 0,15 GHz.

In Fig. 5 the Fourier spectra for samples with various densities of nanopores are shown. Here one can distinguish the frequency corresponding to the size of nanopore ($\sim$ 0.33 GHz), which corresponds to the linear size of $\sim$ 15 nm, and the frequencies corresponding to the distance between the nanopores ($\sim$ 0.1 GHz $\sim$ 0.15 GHz), which correspond to the linear size of $\sim$ 50 nm and $\sim$ 35 nm.

Thus, the results obtained from computer simulation showed that spectral analysis allows to evaluate the average distance among nanopores in the surface layer of a material. In this example, the estimated distance is 35 nm, which with an accuracy of 85% corresponds to a specified value of 30 nm.

4 Conclusions

The revealed effect of nanopore on the of sliding friction resistance force is obviously connected with the surface deflection when the nanoslider passing over a nanopore [1, 4]. In this regard the definition sensitivity must depend on the contact area of the slider with the opposing surface. Diameter of contact with the opposing surface (60 nm) used in these calculations corresponds to the commonly used nanoindenters.

Since three-dimensional calculations are very demanding on computing resources, the path length of the counterbody in the performed calculations was relatively small. Consequently, the

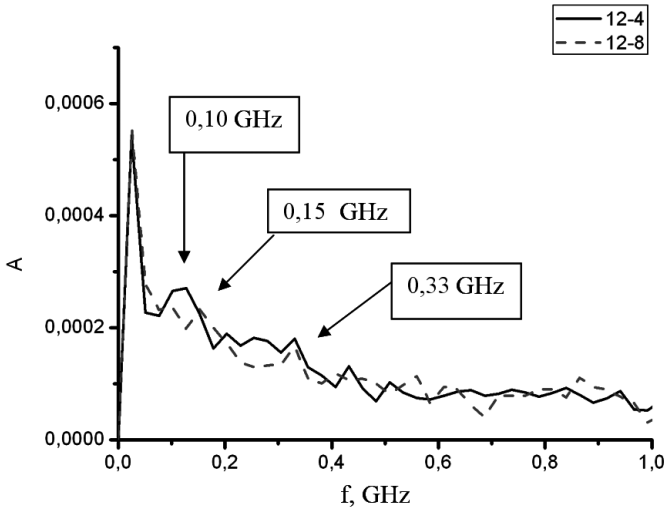


Figure 5: Fourier spectra for the sample with nanopores shown in Fig 3a, (curve 12-8) and Fig. 3b (curve 12-4)

data presented in Figures 4 and 5 have a low frequency resolution. By increasing the path length of the counterbody, the accuracy of the data should grow with increasing the frequency resolution and due to the fact that indenter passing more nanopores.

Thus, the obtained results suggest that nanopores of 12-80 nm can be identified in real experiments by analyzing the spectrum of sliding friction resistance force. The idea of the experimental setup is that the counterbody motion along the surface accompanied with high accuracy measuring of the counterbody movement and of the force acting on it. Consequently, the spectroscopic analysis of the friction force can be seen as a new perspective method for nondestructive testing of a nano-damage in surface layers of solid.

References

[1] S. Psakhie, V. Popov, E. Shilko, A. Smolin, A. Dmitriev, Spectral analysis of the behavior and properties of solid surface layers. Nanotribospectroscopy, Physical Mesomechanics, vol. 12, no. 4, pp. 27-42, 2009.

[2] S. Marple, Jr. Digital Spectral Analysis with Applications. (Prentice-Hall, 1987.)

[3] W. Österle, H. Kloß, I. Urban, A. Dmitriev, Towards a better understanding of brake friction materials, Wear, vol. 263, pp. 1189-1201, 2007.

[4] L. Sedov, Continuum Mechanics [in russian]. (Nauka, 1976.)

Valeriy V. Sergeev, Institute of Strength Physics and Materials Science of the SB RAS, Akademicheskii pr. 2/4, Tomsk, Russia, 634021
Alexey Yu. Smolin, Institute of Strength Physics and Materials Science of the SB RAS, Akademicheskii pr. 2/4, Tomsk, Russia, 634021
Sergey Yu. Korostelev, Institute of Strength Physics and Materials Science of the SB RAS, Akademicheskii pr. 2/4, Tomsk, Russia, 634021
Sergey A. Dobrinin, Institute of Strength Physics and Materials Science of the SB RAS, Akademicheskii pr. 2/4, Tomsk, Russia, 634021

Effect of temperature and filler concentration on the dynamic characteristics of polyethylene-based nanocomposites

Vladimir V. Shadrin Ludmila A. Komar Gennadiy P. Bashin
shadrin@icmm.ru

Abstract

We study experimentally the influence of temperature and filler content on the dynamic moduli of a polyethylene-based nanocomposite. The content of a filler consisting of clay nanoparticles varies from 0% to 15% with a step of 5%. The temperature ranges from −50 to +50 °C. The frequency of cyclic loading is 1 Hz. During the experiments, the dependence of the dynamic modulus of elasticity and the loss modulus on the above parameters has been determined. Apart from the experimental studies, the properties of polyethylene have been investigated in the framework of the structural-phenomenological approach using the Kelvin-Voigt mechanical model. Numerical simulations indicate that the theoretical and experimental results for the dynamic modulus of elasticity agree well, and those for the loss modulus agree satisfactorily. It has been found that at a certain frequency-amplitude vibration regime polyethylene behaves as a viscoelastic material.

Reinforcement of polyethylene with nanoparticles of other materials is a perspective way to improve its mechanical properties and increase its operational life. Addition of a rather small amount of filling particles essentially increases the modulus of elasticity and the strength of the obtained composite and improves its resistance to ignition.

In this study, the influence of a filler consisting of clay nanoparticles on the modulus of elasticity of polyethylene under tension was studied experimentally. The experiments were made using a highly sensitive measuring instrument for dynamic mechanical analysis DMA/SDTA861^e manufactured by Swiss company METTLER TOLEDO.

The dynamic mechanical analysis of the specimens was performed at vibration frequency of 1 Hz and amplitude of 20 μm (0.2% of deformation) at temperatures varying from −50 to +50°C. The objective of the experimental investigation was to determine two components of the complex modulus: its real (dynamic modulus of elasticity or storage modulus E') and imaginary (loss modulus E'') parts [1, 2]. The present investigation is a continuation of the studies described in work [3].

The experiments were made for plane specimens of base length 10.5 mm, width 4 mm and thickness 2 mm. Polyethylene PE-107-2K was used as a matrix. The examined polymer nanocomposite contained a layered clay filler being a mixture of a plenty of thin silica plates 1 nm thick and with transverse dimension varying from 30 nm to several microns.

The obtained results made it possible to determine the character of the temperature dependence of the Young's modulus of the material.

The graphs of the static moduli versus temperature are shown in figures 1. It is seen that the storage modulus of the material increases with increasing filler concentration of the polyethylene. The lower is the ambient temperature the higher is the modulus E'.

Cooling of the molten polyethylene gave rise to the nuclei of crystallization; with a lower rate of cooling, more crystals nucleate. The presence of amorphous and crystalline phases specifies the viscous and elastic components of the complex modulus of polyethylene: with an increase in the amorphous phase, the phase deviation angle φ increases.

The analysis showed an increased hysteresis of the dynamic properties of the polyethylene (both filled and unfilled) subjected to repeated heating-cooling cycles. This can be attributed to the fact that the growth of the crystalline phase of the material during the cooling cycle differs essentially

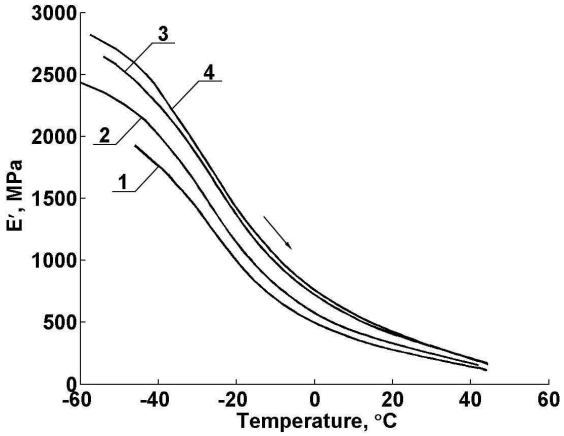


Figure 1: Temperature dependence of the dynamic modulus of elasticity of polyethylene; 1 — filler content of 0%; 2 — filler content of 5%; 3 — filler content of 10%; 4 — filler content of 15%

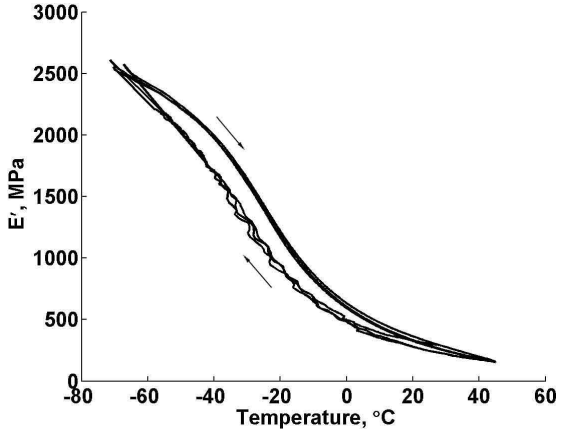


Figure 2: Hysteresis of the storage modulus of the polyethylene subjected cyclic cooling-heating at a rate of 5 degrees per minute

from its reduction during the heating cycle. The processes of crystalline phase growth and disappearance proceed in an asymmetrical manner and require additional power expenditure, leading thus to the occurrence of a hysteresis. The experiments indicated that the value of temperature hysteresis is almost independent of the clay filler content.

Figure 2 shows the graphs of three cooling-heating cycles of the polyethylene specimen with a 10% filler content and a change in its modulus E'.

As one can see, the dynamic modulus of elasticity determined during cooling is markedly smaller than that corresponding to heating.

In the present investigation, an attempt has been made to simulate numerically the behavior of polyethylene under dynamic loading conditions in the framework of the structural-phenomenological scheme (the Kelvin-Voigt mechanical model) (Figure 3).

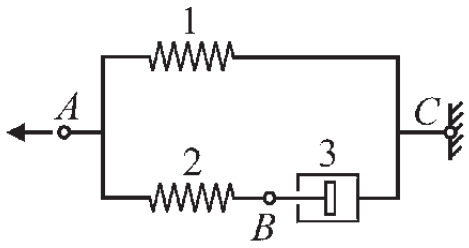


Figure 3: Structural-phenomenological scheme of the viscoelastic behavior of polymeric material

In order that the mathematical model describes adequately the behavior of materials, it is necessary to obey some rules of tensor relations. A complete set of such rules for materials with complex properties is given in work [4]. We adapt these rules to the viscoelastic behavior of polyethylene and obtain the following relations between the stress tensors and the rate-of-strain tensors.

Elements *1* and *2* describe the elastic behavior of the material, and element *3* its viscoelastic behavior. The load that varies with time according to the cyclic law is applied to point A (Figure 3). To each point of the scheme (A, B, C) is assigned the rate-of-strain tensor treated as a tensor parameter required to construct a mathematical model.

To elastic elements *1*,*2* and viscous element *3* of the scheme (Figure 3) are assigned the Cauchy stress tensors and the rate-of-strain tensors of these elements. The rate-of-strain tensor of the left

point A coincides with that of the medium $\mathbf{D}$, and the rate-of-strain tensor of the right point C is equal to zero. The rate-of-strain tensor of the left point A. The rate-of-strain tensors of the elastic and viscous elements are calculated as the difference between the rate-of-strain tensors of the left and right points of these elements. The Cauchy stress tensor of the medium $\mathbf{T}$ is equal to the sum of the Cauchy stress tensors of elastic elements connected to the left point of the scheme. The Cauchy stress tensor of the viscous element, connected on the left to the internal point B of the scheme, is equal to the Cauchy stress tensor of the second elastic element, connected on the right to this point.

The material under study is assumed to be incompressible. The trace of any one of used rate-of-strain tensor of the model is equal to zero.

The model proposed in this research gives an idea of how all tensor characteristics can be combined into a system of constitutive equations describing the properties of the material under finite deformation conditions.

To obtain the Cauchy stress tensors $\mathbf{T}_i$ of elastic elements, we use the mass density of the medium free energy $f = f(\lambda_1^{(i)}, \lambda_2^{(i)}, \lambda_3^{(i)})$ where $\lambda_1^{(i)}$, $\lambda_2^{(i)}$, $\lambda_3^{(i)}$ are the extension ratios of the i-th elastic element.

$$f = \frac{c_1}{\rho}[(\lambda_1^{(1)})^2 + (\lambda_2^{(1)})^2 + (\lambda_3^{(1)})^2 - 3] + \frac{c_2}{\rho}[(\lambda_1^{(2)})^2 + (\lambda_2^{(2)})^2 + (\lambda_3^{(2)})^2 - 3],$$

where c_1 and c_2 are constants. The deviator of the Cauchy stress tensor of the i-th eleastic element is calculated from the formula of the nonlinear theory of elasticity:

$$dev\mathbf{T}_i = dev(\rho \sum_{k=1}^{3} \lambda_k^{(i)} \frac{\partial f}{\partial \lambda_k^{(i)}} \mathbf{e}_k^{(i)} \otimes \mathbf{e}_k^{(i)}),$$

where ρ is the mass density of the medium $\mathbf{e}_1^{(i)}$, $\mathbf{e}_2^{(i)}$, $\mathbf{e}_3^{(i)}$ is the orthonormal triple of eigenvectors of the tensor $\mathbf{V}_i = \lambda_1^{(i)}\mathbf{e}_1^{(i)} \otimes \mathbf{e}_1^{(i)} + \lambda_2^{(i)}\mathbf{e}_2^{(i)} \otimes \mathbf{e}_2^{(i)} + \lambda_3^{(i)}\mathbf{e}_3^{(i)} \otimes \mathbf{e}_3^{(i)}$ of this elastic element. Time variations of the extension ratios of the i-th elastic element are defined by the formula

$$\dot{\lambda}_k^{(i)} = \lambda_k^{(i)}\mathbf{e}_k^{(i)} \otimes \mathbf{e}_k^{(i)} \cdot \mathbf{D}_i, \qquad (k = 1, 2, 3),$$

and the rates of work in this element are determined by the formula

$$\mathbf{T}_i \cdot \mathbf{D}_i = \rho \sum_{k=1}^{3} \frac{\partial f}{\partial \lambda_k^{(i)}} \dot{\lambda}_k^{(i)},$$

where $\mathbf{D}_i$ are the rate-of-strain tensors of elastic elements.

The deviator of the Cauchy stress tensor of the 3d-viscous element is calculated from the formula of the nonlinear theory of elasticity

$$dev\mathbf{T}_3 = 2\eta_3\mathbf{D}_3,$$

where η_3 is the shear viscosity coefficient ($\eta_3 \geq 0$), $\mathbf{D}_3$ is the rate-of-strain tensors of the viscous element. The shear viscosity coefficient η_3 is written as

$$\eta_3 = c_3 \exp(-c_4 \cdot I_D) + c_5,$$

where c_3, c_4 and c_5 are constants; I_D is an invariant of the rate-of-strain tensor of the medium $\mathbf{D}$

$$I_D = \sqrt{3tr(\mathbf{D}^2) - (tr(\mathbf{D}))^2}.$$

Choosing the constants $c_1 = 0.06$, $c_2 = 0.1$, $c_3 = 0.1$, $c_4 = 10.0$ and $c_5 = 0.005$ and using the rates of work of the medium $\mathbf{T} \cdot \mathbf{D}$, we have found the values of the loss tangent $tan\delta$, and the storage modulus E' and the loss modulus E''.

Figure 4 presents the results illustrating the use of the model for calculation of the data for the storage modulus E' and the loss modulus E'' . The dependence of the values of the storage modulus E' (curves *1*, *2*) and the loss modulus E'' (curves *3*, *4*) on the vibration frequency at

3.5 μm (curves *1*, *2*) and 35 μm (curves *3*, *4*) is shown; the solid lines represent calculated values, and the cross and circle symbols — experimental data. As one can see, the model proposed in our research describes fairly well the experimental results for the storage modulus E' (curves *1*) and the loss modulus E'' (curves *3*) at the amplitude of 3.5 μm. It provides an adequate description of the experimental value of the storage modulus E' (curves *2*) at the amplitude of 35 μm. However, it should be noted that the model fails to provide good description of the loss modulus E'' (curves *4*) at the amplitude of 35 μm. To get an adequate description of the experimental results in this case, the model must be complicated by introducing new structural elements in it.

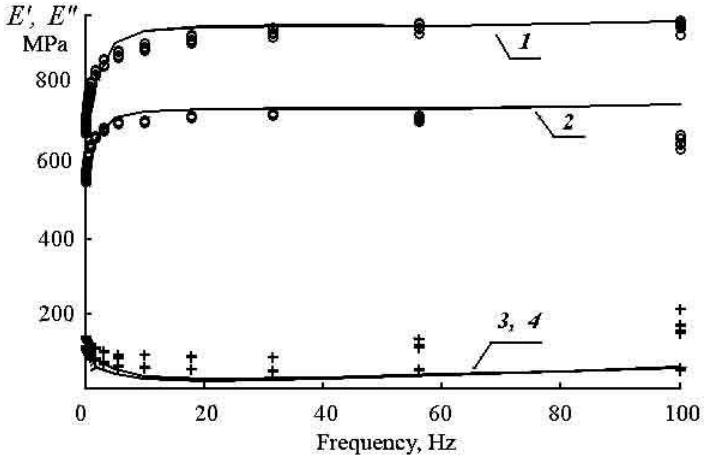


Figure 4: Values of the storage modulus E' (curves *1*, *2*) and the loss modulus E'' (curves *3*, *4*) versus vibration frequency at amplitudes 0.35 μm (curves *1*, *3*) and 3.5 μm (curves *2*, *3*); solid lines — calculated values, cross and symbols — experimental data

The present approach has revealed that polyethylene behaves like a viscoelastic material (the Kelvin-Voigt model). The theoretical curves describe with good accuracy the behavior of polyethylene. In our further research, the model will be complicated to get a more precise description of the experimental data.

The analysis of the obtained results leads us to the following conclusions:

— when the temperature is decreased to -50 °C, the storage modulus E' becomes greater by an order of magnitude compared to the temperature of $+50$ °C;
— the dynamic characteristics of polyethylene depend on the clay nanofiller content, and the higher is the filler content, the greater is the storage modulus of polyethylene;
— there is a pronounced hysteresis in the storage modulus E' during the cyclic cooling/heating process of the polyethylene. Such a hysteresis depends on the rate of temperature change, is the characteristic of the polyethylene matrix, is independent of the content of clay filler and is related to the amorphous-crystalline phase transition of polyethylene caused by temperature changes;
— to obtain the calculation data for the storage modulus E' and the loss modulus E'' , the structural-phenomenological model has been applied. Numerical simulations show good agreement between the theoretical and experimental results for the storage modulus and satisfactory agreement for the loss modulus. The model has been developed to meet the conditions of room temperature, vibration amplitudes of 3.5 μm and 35 μm, and the frequency range 0.1 to 100 Hz. From the analysis of the obtained results, we can conclude that polyethylene behaves as a viscoelastic material.

Acknowledgements

The work is supported by RFBR (grant 09-08-00339-a) and RAS Project 09-C1-1008.

References

[1] Kabanov V.A. et. al. Polymer Encyclopedia — M.: Soviet Encyclopedia, 1977. Vol. 3. — 1152 p. (in russian)

[2] Lykov A.V. Heat/mass transfer: Book of reference. — M.: Energya, 1978. — 480 p. (in russian)

[3] Shadrin V.V., Komar L.A., Bashin G.P. Investigation and mathematical modeling of dynamic properties of polyethylene // Proceedings of the XXXVII Summer School — Conference "Advanced problems in mechanics" — St. Petersburg (Repino), 2009. — P. 581–586. (CD-ROM). (in english)

[4] Svistkov A.L., Lauke B. Structural-phenomenological simulation of the mechanical behavior of rubbers // Polym. Sci., Ser. A, 2008. V. 50, No. 5. — P. 591–599. (in english)

Vladimir V. Shadrin, Institute of Continuous Media Mechanics, Perm, Russia
Ludmila A. Komar, Institute of Continuous Media Mechanics, Perm, Russia
Gennadiy P. Bashin, Perm State University, Perm, Russia

Dynamical systems with various dissipation: background, methods, applications

Maxim V. Shamolin
shamolin@imec.msu.ru

Abstract

This work is devoted to the development of qualitative methods in the theory of nonconservative systems that arise, e.g., in such fields of science as the dynamics a rigid body interacting with a resisting medium, oscillation theory, etc. This material can call the interest of specialists in the qualitative theory of ordinary differential equations, in rigid body dynamics, as well as in fluid and gas dynamics, since the work uses the properties of motion of a rigid body in a medium under the streamline flow conditions. The author obtains the complete integrability cases for nonconservative dynamical systems having nontrivial symmetries.

1 Introduction

In this work, we study the problem on the body motion under the condition that the line of the force applied to the body does not change its orientation with respect to the body and can only displace parallel to itself depending on the angle of attack and, possibly, on other phase variables. Such conditions arise under the plate motion with the so-called "large" angles of attack in a medium under a streamline flow (in this case, the fluid is assumed to be ideal in general, although all this are also true for fluids of a small viscosity, first of all, for the water) or under a separation flow (which is justified by an experiment completely satisfactory). Therefore, the main objects of studying is a family of bodies such that a part of the surface of each of which has a plane part that is flowed by a medium according to the streamline flow laws [1, 2].

From the N. E. Zhukovskii studies, it is known an attempt to model the motion basing on experiments in self-rotations of plates falling in the air [3, 4] (the so-called "Hamburg cardboard"). Here, one needs to take into account such properties of interaction of the medium to the body as the resistance force and the body force. Precisely, the aerodynamic characteristics of a plate are also used for modeling the bird flight [4]. Among the studies of S. A. Chaplygin, we also mention the statement of the problem of heavy body motion in an incompressible fluid [5].

2 Physical assumptions, quasi-stationarity hypothesis, phase variables and linearized equations of motion

Assume that a rigid body of mass m executes a plane-parallel motion in a medium with quadratic resistance law and that a certain part of the exterior body surface is a plane plate being under the medium streamline flow conditions. This means that the action of the medium on the plate reduces to the force $\mathbf{S}$ (applied at the point N) whose line of action is orthogonal to the plate. Let the remained par of the body surface be situated in a volume bounded by the flow surface that goes away from the plate boundary and is not subjected by the medium action.

Let us relate to the body the right coordinate system $Dxyz$ whose axis z moves parallel to itself, and for simplicity, assume that the plane Dzx is the geometric symmetry plane of the body. This ensures the fulfillment of property 2) under the motion satisfying condition 1). To construct the dynamical model, let us introduce the following phase coordinates: the value $v = |\mathbf{v}|$ of the

velocity $\mathbf{v}$ of the point D, the angle α between the vector $\mathbf{v}$ and the axis x, and the algebraic value Ω of the projection of the body absolute angular velocity on the axis z.

Assume that the value of the force $\mathbf{S}$ quadratically depend on v with nonnegative coefficient s_1 ($S = s_1 v^2$). As usual, one represents s_1 in the form $s_1 = \rho P c_x/2$, where c_x is now the dimension-free coefficient of the frontal resistance (ρ is the medium density and P is the plate area). This coefficient depends on the angle of attack, the Struchal number, and other quantities which are usually considered as parameters. In what follows, we also introduce the following additional phase variable of the "Struchal type": $\omega = \Omega D/v$, where D is the characteristic plate transversal size. We restrict ourselves to the dependence of c_x on the pair (α, ω) of variables, i.e., we assume that s_1 (as well as y_N) is a function of the pair (α, ω) of dimension-free variables.

Let us define (purely formally for now) the dependence of s_1 and the ordinate y_N of the point N on the phase coordinates (α, ω). The system of dynamical equations must admit a particular solution of the form $\alpha(t) \equiv 0, \quad \omega(t) \equiv 0$. Therefore, we have the condition $y_N(0,0) = 0$ for the function $y_N(\alpha, \omega)$, and in the linear case, we need to assume that $y_N = D(k\alpha - h\omega)$, where k and h are certain constants. Because the approximation is linear, we can ignore the dependence of s_1 on α and ω.

In what follows, to take into account the action direction of the force $\mathbf{S}$, we introduce the following sigh-alternating auxiliary function $s(\alpha, \omega) = s_1(\alpha, \omega) sign \cos\alpha$.

Therefore, the linearized model of the force medium action contains three parameters s, k, and h, which are determined by the plate form in the plan. As was already mentioned, the first of these parameters, the coefficient s, is dimensional. The parameters k and h are dimension-free because of the method of their introduction [6].

The equations of motion of the center of masses in projections on the axes Dx and Dy of the related coordinate system and the equation of the kinetic moment variation with respect to the König axis have the following form with accuracy up to terms linear in α and Ω (here, σ is the distance DC and I is the central moment of inertia of the body):

$$\dot{v} = -sv^2/m \tag{1}$$

$$v\dot{\alpha} - sv^2\alpha/m + v\Omega - \sigma\dot{\Omega} = 0 \tag{2}$$

$$I\dot{\Omega} = sDv^2(k\alpha - hD\Omega/v) \tag{3}$$

Assuming that $v \neq 0$, introducing the natural parameter σ_1 ($v\,dt = D\,d\sigma_1$), which is usual for such systems, and using the change $\omega = D\Omega/v$ (see above) of the variable Ω and the obvious differentiation formula $D(\dot{}) = vd/d\sigma_1(\,) = v(\,)'$ we arrive at the system

$v' = -\frac{sv}{m}D$

$$I\omega' = \omega(I - mD^2h)\frac{Ds}{m} + sD^3k\alpha \tag{4}$$

$$\alpha' = -\omega\left(1 + \frac{s\sigma D^2}{I}h\right) + sD\left(\frac{1}{m} + \frac{k\sigma D}{I}\right)\alpha \tag{5}$$

in which two latter equations are separated from the first thus forming the independent second-order system 4, 5 and can be studied separately.

Let us transform these equations as follows: exclude α from them introducing the angle of turn ϕ by the formula $\phi' = \omega$; we obtain their linear integral in the form $\alpha - \omega(I/(kmD^2) + \sigma/D) + \phi(1 + \sigma s/m + Is/(km^2D) - hsD/km) = b = \text{const}$. With account for this, the equation for the angle of turn ϕ becomes $I\phi'' + \phi' sD(D^2h - D\sigma k - 2I/m) + \phi sD^3(k + k\sigma s/m + Is/m^2D - hsD/m) = ksD^3b$. It is easy to see that it has the form of the linear pendulum equation; under certain conditions, this pendulum executes oscillations near a certain position ϕ_* determined by the value b of the linear integral.

For $h = 0$, the coefficient of the so-called linear damping is negative, whereas the coefficients of the positional component positive; this allows us to speak about the oscillatory instability of the solution $\phi = \phi_*$. On the contrary, for a sufficiently large h, the solution $\phi = \phi_*$ can be made to be stable, and, moreover, it can loose its oscillatory character, since the coefficient of the positional component becomes negative.

But the main circumstance is that because this linear pendulum is multiparameter, the oscillatory stability of the solution $\phi = \phi_*$ is possible for certain finite values of h, since both mentioned coefficient can be positive in principle.

To describe the results and concrete properties of the body motion, in Institute of Mechanics of M. V. Lomonosov Moscow State University, V. A. Eroshin and V. M. Makarshin carried out experiments in registration of the motion of homogeneous circular cylinders in the water. Owing to the experiment, it becomes possible to find the dimension-free parameters k and h of the medium action on a rigid body.

The experiment allows one to make several important conclusions. The first of them is as follows: the rectilinear stationary free body drag (in the water) is unstable at least with respect to the angle of attack and the angular velocity. The second conclusion obtained from the carried out natural experiment is as follows: in modeling the medium action on the body, it is necessary to take into account the additional parameter characterizing the rotational derivative of the moment with respect to the body angular velocity. This parameter introduces the dissipation into the system. In our linear approximation, the accounting damping moment linearly depends on the body velocity.

3 Beginning of nonlinear analysis

For different bodies, under motion in a medium and under certain conditions, the angles of attack can practically assume any value from the interval $(0, \pi/2)$, and only for the angles close to $\pi/2$, the so-called washing out of the lateral surface is inevitable. Therefore, there arises the necessity of extending the functions y_N and s to finite angles of attack, i.e., the expansion of the domain of the pair of dynamical functions up to the interval $(0, \pi/2)$. But, in fact, it is necessary to extend the dynamical functions to the whole numerical line; this is clear from the following arguments.

In order to pass to a more complete description of the free body motion, let us represent the dynamics equations $mw_c = F,\ I\dot{\Omega} = M$ obtained early in the linear form (see 1-3) as follows:

$$\dot{v}\cos\alpha - \dot{a}v\sin\alpha - \Omega v\sin\alpha + \sigma\Omega^2 = F_x/m \tag{6}$$

$$\dot{v}\sin\alpha + \dot{a}v\cos\alpha + \Omega v\cos\alpha - \sigma\dot{\Omega} = 0 \tag{7}$$

$$I\dot{\Omega} = y_N(\alpha,\omega)F_x, \quad \omega = D\Omega/v \tag{8}$$

As a rule, for various variants of the body motion considered below, the generalized force F_x is quadratic in velocities (v, Ω) and explicitly depends on the auxiliary sign-alternating function $s(\alpha, \omega)$ (for example, $F_x(\alpha, v, \Omega) = -s(\alpha, \omega)v^2$ in the case of the body free drag). Therefore, the class of conceptual bodies and their conceptual motions defines a certain pair of dynamical functions $\big(s(\alpha,\omega),\ y_N(\alpha,\omega)\big)$ belonging to definite function classes.

4 Classes of dynamical functions

The fist stage of the complete nonlinear study of the body motion in a medium under the quasi-stationarity conditions is the study of the corresponding dynamical systems in which the damping is not taken into account (in particular, $h = 0$ in the linear case). The account for the damping is the next labor-consuming stage of studying the problem, which is presented in this work in a sufficient detail. To begin with, we consider the case where the pair of dynamical functions (y_N, s) depends only on the angle of attack. In this case, to qualitatively describe this pair of functions, we use the experimental information about the streamline flow properties.

The classes of dynamical functions to be introduced are sufficiently wide. They consists of smooth, 2π-periodic ($y_N(\alpha)$ is odd and $s(\alpha)$ is even) functions satisfying the following conditions: $y_N(\alpha) > 0$ for $\alpha \in (0, \pi)$, and, moreover, $y_N'(0) > 0$ and $y_N'(\pi) < 0$ (the function class $\{y_N\} = Y$); $s(\alpha) > 0$ for $\alpha \in (0, \pi/2)$, $s(\alpha) < 0$ for $\alpha \in (\pi/2, \pi)$, and, moreover, $s(0) > 0$ and $s'(\pi/2) < 0$ (the function class $\{s\} = \Sigma$). Both y_N and s change the sign under the replacement of α on $\alpha + \pi$. Therefore, $y_N \in Y,\ s \in \Sigma$ In particular, the analytic functions

$$y_N(\alpha) = y_0(\alpha) = A\sin\alpha \in Y \tag{9}$$

$$s(\alpha) = s_0(\alpha) = B\cos\alpha \in \Sigma, \quad A, B > 0 \tag{10}$$

serve as typical representatives of the described classes and correspond to the medium interaction functions obtained by S. A. Chaplygin in studying the plane-parallel flow around of a plane infinite length by a homogeneous medium flow.

In what follows, there rises the product $F(\alpha) = y_N(\alpha)s(\alpha)$ in the dynamical systems considered. It follows from the conditions listed above that F is a sufficiently smooth odd π-periodic functions satisfying the following conditions: $F(\alpha) > 0$ for $\alpha \in (0, \pi/2)$, $F'(0) > 0$, and $F'(\pi/2) < 0$ (the function class $\{F\} = \Phi$). Therefore, $F \in \Phi$ In particular, the analytic function

$$F = F_0(\alpha) = AB \sin\alpha \cos\alpha \in \Phi \tag{11}$$

is also a typical representative of the a function class Φ arisen (and also corresponds to the S. A. Chaplygin case mentioned above).

5 On variable dissipation in system and mechanical and topological analogs

After certain simplifications, the general system 6–8 reduces to second-order pendulum systems in which there is a linear dissipative force with variable coefficient alternating the sign for different angles of attack.

In what follows, it is necessary to note at once an important mechanical analogy arising on the basis of qualitative properties of the free body stationary motion in the medium flow and the pendulum equilibrium. Such an analogy allows us to extend the properties of pendulum nonlinear dynamical systems to the dynamical systems of a free body and obtain some topological analogies. For example, under condition 11, the angle of turn of the pendulum is completely equivalent to the angle of attack in the free body motion. In condition 11 violates (the group of conditions 9 and 10), then the angle of attack of the free body and the angle of turn of the pendulum are trajectorially topologically equivalent.

And so, the results of the presented work are appeared owing to the study of the applied problem on the rigid body motion in a resisting medium [7, 8] where complete lists of transcendental first integrals expressed through a finite combination of elementary functions were obtained. This circumstance allows one to perform a complete analysis of phase trajectories and show those properties of them which exhibit the roughness and preserve for systems of a more general form. Note that similar problems were already appeared in applied aerodynamics in the studies of Central Aero- and Hydrodynamics Institute named after professor N. E. Zhukovskii.

Many results of this work were regularly reported at a number of workshops, including the workshop 'Actual Problems of Geometry and Mechanics' named after professor V. V. Trofimov, which is headed by D. V. Georgievskii and M. V. Shamolin.

Below, we highlight the classes of essentially nonlinear systems of the second and third orders integrable in transcendental (in the sense of theory of functions of one complex variable) elementary functions. For example such systems are five-parametric dynamical systems including the majority of systems that are studied early in the dynamics of a rigid body interacting with a medium:

$$\begin{aligned}
\dot\alpha &= a\sin\alpha + b\omega + \gamma_1\sin^5\alpha + \gamma_2\omega\sin^4\alpha + \\
&\quad + \gamma_3\omega^2\sin^3\alpha + \gamma_4\omega^3\sin^2\alpha + \gamma_5\omega^4\sin\alpha \\
\dot\omega &= c\sin\alpha\cos\alpha + d\omega\cos\alpha + \gamma_1\omega\sin^4\alpha\cos\alpha + \gamma_2\omega^2\sin^3\alpha\cos\alpha + \\
&\quad + \gamma_3\omega^3\sin^2\alpha\cos\alpha + \gamma_4\omega^4\sin\alpha\cos\alpha + \gamma_5\omega^5\cos\alpha
\end{aligned}$$

So, in [7], the author studied and integrated two model variants of the body plane-parallel motion in a resisting medium, which are described by dynamical systems with zero mean variable dissipation.

For example a dynamical system of the form $\dot\alpha = \Omega + \beta\sin\alpha$, $\dot\Omega = -\beta\sin\alpha\cos\alpha$, is relatively structurally stable (relatively rough) and topologically equivalent to the system describing a clamped pendulum placed in the running-out medium flow.

We can find its first integral being a transcendental (in the sense of theory of functions of one complex variable such that it has essentially singular points after continuing it into the complex

domain) functions of phase variables that is expressed through a finite combination of elementary functions.

As is seen, the phase cylinder $\mathbb{R}^2\{\alpha,\Omega\}$ of quasi-velocities of the system considered exhibits an interesting topological structure of partition into trajectories.

On the cylinder, there are two domains (whose closure is just the phase cylinder) filled in by trajectories of perfectly different character. The first domain called oscillatory or finitary (it is simply connected is entirely filled in by trajectories of the following type. Almost every such trajectory starts at the repelling point $(2\pi k,0)$ and ended at the attracting point $\big((2k+1)\pi,0\big)$, $k\in\mathbf{Z}$. An exception is the fixed points $(\pi k,0)$ and separatrices that either emanate from the repelling point $(2\pi k,0)$ and enter the saddles S_{2k} and S_{2k+1} or emanate from the saddles S_{2k+1} and S_{2k+2} and enter the attracting points $\big((2k+1)\pi,0\big)$. Here, $S_k=(-\pi/2+\pi k,(-1)^k\beta)$.

The second domain called rotational (it is two-connected is entirely filled in by rotational motions similar to rotations on the mathematical pendulum plane. These phase trajectories envelope the phase cylinder and are periodic on it.

Although the dynamical system considered is not conservative, in the rotational domain of its phase plane $\mathbb{R}^2\{\alpha,\Omega\}$ it admits the preservation of an invariant measure with variable density. This property characterizes the system considered as a system with zero mean variable dissipation.

As a result of all this, we obtain a family of three-dimensional phase portraits analogous to the plane-parallel dynamics (see [7]).

6 One of the definitions of systems with zero mean variable dissipation

We study the system of ordinary differential equations having a periodic phase coordinate. The systems under study have those symmetries for which in the mean during the period of the periodic coordinate, their phase volume preserves. So, for example, the following pendulum system with smooth right-hand side $\mathbf{V}(\alpha,\omega)$ periodic in α of period T:

$$\dot\alpha=-\omega+f(\alpha),\dot\omega=g(\alpha)$$
$$f(\alpha+T)=f(\alpha),\quad g(\alpha+T)=g(\alpha)$$

preserves its phase area on the phase cylinder during the period T: $\int\limits_0^T \mathrm{div}\mathbf{V}(\alpha,\omega)\,d\alpha =$ $\int\limits_0^T\left(\frac{\partial}{\partial\alpha}\big(-\omega+f(\alpha)\big)+\frac{\partial}{\partial\omega}g(\alpha)\right)d\alpha=\int\limits_0^T f'(\alpha)\,d\alpha=0.$

The system considered is equivalent to the pendulum equation $\ddot\alpha-f'(\alpha)\dot\alpha+g(\alpha)=0$ in which the integral if the coefficient $f'(\alpha)$ standing by the dissipative term $\dot\alpha$ vanishes in the mean during the period.

It is seen that the system considered has those symmetries for which it becomes a system with zero mean variable dissipation in the sense of the following definition.

Definition. Let us consider a smooth autonomous system of the $(n+1)$th order and normal form defined on the cylinder $\mathbb{R}^n\{x\}\times\mathbf{S}^1\{\alpha \bmod 2\pi\}$, where α is a periodic coordinate of period $T>0$. Denote by $\mathrm{div}(x,\alpha)$ the divergence of the right-hand side (which is a function of all phase variables in general and is not identically equal to zero) of this system. Such a system is called a system with zero (nonzero) mean variable dissipation if the function $\int\limits_0^T\mathrm{div}(x,\alpha)\,d\alpha$ is (is not) identically equal to zero. Moreover, in some cases (for example, when at certain points of the circle $\mathbf{S}^1\{\alpha \bmod 2\pi\}$, there arise singularities), this integral is understood in the principal value sense .

Let us consider systems of the form (the dot denotes the derivative in time)

$$\dot\alpha=f_\alpha(\omega,\sin\alpha,\cos\alpha) \tag{12}$$
$$\dot\omega_k=f_k(\omega,\sin\alpha,\cos\alpha),\ k=1,\dots,n, \tag{13}$$

defined on the set $\mathbf{S}^1\{\alpha \bmod 2\pi\}\setminus K\times\mathbb{R}^n\{\omega\}$, $\omega=(\omega_1,\dots,\omega_n)$, where the functions $f_\lambda(u_1,u_2,u_3)$, $\lambda=\alpha,1,\dots,n$, of three variablesu_1, u_2, and u_3 are as follows:

$$f_\lambda(-u_1,-u_2,u_3)=-f_\lambda(u_1,u_2,u_3)$$
$$f_\alpha(u_1,u_2,-u_3)=f_\alpha(u_1,u_2,u_3)$$
$$f_k(u_1,u_2,-u_3)=-f_k(u_1,u_2,u_3)$$

The set K is either empty or consists of finitely many points of the circle $\mathbf{S}^1\{\alpha \bmod 2\pi\}$.

The latter two variables u_2 and u_3 in the functions $f_\lambda(u_1,u_2,u_3)$ depend on one parameter α, but they are distinguished in separate groups for the following reasons. First, not in the whole their domain, they are uniquely expressed from one another, and, second, the first of them is odd, whereas the second is an even function of α, which influences on the symmetry of system 12, 13 differently.

To this system, we put in correspondence the non-autonomous system

$$\frac{d\omega_k}{d\alpha}=\frac{f_k(\omega,\sin\alpha,\cos\alpha)}{f_\alpha(\omega,\sin\alpha,\cos\alpha)}$$

by the substitution $\tau=\sin\alpha$, it reduces to the form $(k=1,\dots,n)$

$$\frac{d\omega_k}{d\tau}=\frac{f_k(\omega,\tau,\varphi_k(\tau))}{f_\alpha(\omega,\tau,\varphi_\alpha(\tau))}$$
$$\varphi_\lambda(-\tau)=\varphi_\lambda(\tau),\lambda=\alpha,1,\dots,n$$

The following assertion immerses the class of systems 12, 13 in the class of dynamical systems with zero mean variable dissipation. The inverse embedding does not hold in general.

Lemma. Systems of the form 12, 13 are dynamical system with zero mean variable dissipation.

This proposition is proved by using the symmetries of system 12, 13 listed above.

In this work, we mainly consider the case where the functions $f_\lambda\big(\omega,\tau,\varphi_k(\tau)\big)$ $(\lambda=\alpha,1,\dots,n)$ are polynomials in ω and τ.

To begin with, let us consider a certain class of autonomous systems on the two-dimensional circular cylinder $\mathbf{S}^1\{\alpha \bmod 2\pi\}\times\mathbb{R}^1\{\omega\}$. For example, to the following pendulum systems (arising in the dynamics of a rigid body interacting with a medium) with parameter $\beta>0$:

$$\dot\alpha=-\omega+\beta\sin\alpha,\quad \dot\omega=\sin\alpha\cos\alpha \tag{14}$$

$$\dot\alpha=-\omega+\beta\sin\alpha\cos^2\alpha+\beta\omega^2\sin\alpha \tag{15}$$
$$\dot\omega=\sin\alpha\cos\alpha-\beta\omega\sin^2\alpha\cos\alpha+\beta\omega^3\cos\alpha \tag{16}$$

in the variables (ω,τ), we put in correspondence the following equations with algebraic right-hand side, respectively:

$$\frac{d\omega}{d\tau}=\frac{\tau}{-\omega+\beta\tau},\quad \frac{d\omega}{d\tau}=\frac{\tau+\beta\omega[\omega^2-\tau^2]}{-\omega+\beta\tau+\beta\tau[\omega^2-\tau^2]}.$$

In this case, systems 14 and 15, 16 are dynamical systems with zero mean variable dissipation, which is easy to verify directly.

For example, system 14 has a first integral of the following form (depending on the value of β, three cases are possible that corresponds to the existence of foci, nodes, or degenerate nodes in the phase portrait of the system):

$$\beta^2-4<0:$$
$$\{\Omega^2+\beta\Omega\sin\alpha+\sin^2\alpha\}\times\exp\left\{\frac{2\beta}{\sqrt{-\beta^2+4}}\arctan\frac{2\Omega+\beta\sin\alpha}{\sqrt{-\beta^2+4}\sin\alpha}\right\}=\text{const}$$

$\beta^2 - 4 > 0$:

$$\left|2\Omega + \left(\beta + \sqrt{\beta^2 - 4}\sin\alpha\right)\right|^{\sqrt{\beta^2-4}-\beta} \times \\ \times \left|2\Omega + \left(\beta - \sqrt{\beta^2 - 4}\sin\alpha\right)\right|^{\sqrt{\beta^2-4}+\beta} = \text{const}$$

$\beta^2 - 4 = 0$:

$$|2\Omega + \beta\sin\alpha| \times \exp\left\{-\frac{\beta\sin\alpha}{2\Omega + \beta\sin\alpha}\right\} = \text{const}$$

The phase portrait of system 15, 16 can be of three different types depending on the values of the parameter β.

In the expression of its first integral, also three cases are possible depending on the value of the constant β and corresponding to the existence of foci, nodes, and degenerate nodes in the phase portrait of the system.

Let us represent the parameter β as the product: $\beta = \sigma^2 n_0^2$; after that, to system 15, 16 we put in correspondence a differential equation of the form

$$\frac{d\omega}{d\tau} = \frac{-n_0^2\tau + \sigma\omega[\omega^2 - n_0^2\tau^2]}{\omega + \sigma n_0^2\tau + \sigma\tau[\omega^2 - n_0^2\tau^2]}, \quad \tau = -\sin\alpha$$

Introduce the following notation: $C_1 = 2 - \sigma n_0$, $C_2 = \sigma n_0$, $C_3 = -2 - \sigma n_0$. Performing a number of changes by the formulas $\omega - n_0\tau = u_1$, $\omega + n_0\tau = v_1$, $u_1 = v_1 t_1$, $v_1^2 = p_1$, where $v_1 \neq 0$, we obtain the Bernoulli-type equation

$$2p_1\left[C_1 t_1 + C_2 + \frac{2\sigma}{n_0}t_1 p_1\right] = \frac{dp_1}{dt_1}[C_3 - C_1 t_1^2]$$

By the known change $p^{-1} = q_1$ for $p_1 \neq 0$, we reduce the latter equation to the form

$$\dot{q_1} = a_1(t_1)q_1 + a_2(t_1)$$

where

$$a_1(t_1) = \frac{2(C_1 t_1 + C_2)}{C_1 t_1^2 - C_3}, \quad a_2(t_1) = \frac{4\sigma t_1}{n_0(C_1 t_1^2 - C_3)}$$

(Here, the dot denotes the derivative in t_1.)

The general solution of the linear homogeneous equation is represented in the form

$$q_{1\,HOM}(t_1) = k(C_1 t_1^2 - C_3)Q(t_1), \quad k = \text{const}$$

where the function Q has the following form depending on the value of the constant C_1:

$$Q(t_1) = e^{t_1}, \quad C_1 = 0$$

$$e^{2\frac{C_2}{\sqrt{-C_1 C_3}}\arctan\sqrt{-\frac{C_1}{C_3}}t_1}, \quad C_1 > 0$$

$$\left(\frac{\sqrt{-C_1}t_1 + \sqrt{-C_3}}{\sqrt{-C_1}t_1 - \sqrt{-C_3}}\right)^{\frac{C_2}{\sqrt{C_1 C_3}}}, \quad C_1 < 0$$

To obtain the solution of the inhomogeneous equation, we assume that the quantity k is a function of t_1; we find it by the quadrature

$$k(t_1) = \frac{4\sigma}{n_0}\int Q^{-1}(t_1)\frac{t_1}{(C_1 t_1^2 - C_3)^2}\,dt_1$$

Therefore, the transcendental first integral of system 15, 16 becomes

$$Q^{-1}(t_1)q_1(C_1 t_1^2 - C_3)^{-1} - \frac{4\sigma}{n_0}\int_{t_0}^{t_1} Q^{-1}(\tau_1)\frac{\tau_1}{(C_1\tau_1^2 - C_3)^2}\,d\tau_1 = C^0$$

where $C^0 = \text{const}$.

As is seen, the final form of the first integral depends on the sign of the constant C_1, and, therefore, three variants are possible. Let us examine each of them.

First variant. $C_1 = 0$. After an elementary calculation, we obtain an additional integral in the form

$$e^{-\frac{u_1}{v_1}}\left(v_1^{-2} + \frac{\sigma^2}{2}(\frac{u_1}{v_1} + 1)\right) = \text{const}$$

Therefore, for $C_1 = 0$, the transcendental first integral of system 15, 16 is expressed through elementary functions.

Second variant. $C_1 > 0$. The integration leads to the function

$$-\frac{\sigma}{4n_0}e^{-2\frac{C_2}{\sqrt{-C_1C_3}}\zeta}\left(\frac{C_2}{\sqrt{-C_1C_3}}\sin 2\zeta + \cos 2\zeta\right)$$

where

$$\zeta = \arctan\sqrt{-\frac{C_1}{C_3}}t_1$$

As is seen, in the case $C_1 > 0$, the additional first integral is expressed through elementary functions.

Third variant. $C_1 < 0$. By equivalent transformations, the integral transforms into

$$\frac{\sigma}{C_1C_2n_0}\left(2\frac{\zeta^{1-\gamma}}{\gamma-1} - 3\frac{\zeta^{-\gamma}}{\gamma} + \frac{\zeta^{-1-\gamma}}{\gamma+1}\right)$$

where

$$\gamma = \frac{C_2}{\sqrt{C_1C_3}} > 1, \quad \zeta = \frac{\sqrt{-C_1}t_1 + \sqrt{-C_3}}{\sqrt{-C_1}t_1 - \sqrt{-C_3}}$$

Therefore, in the case $C_1 < 0$, the additional first integral is also expressed through elementary functions.

And so, we study the connection between the following three properties, which are independent for the first glance, but they are sufficiently harmonically combined on systems from the rigid body dynamics:

1. The distinguished class of systems 12, 13 with the above;
2. The fact that this class of systems consists of systems with zero mean variable dissipation (in the variable α), which allows us to consider them as "almost" conservative systems;
3. In certain (although lower-dimensional) cases, these systems have first integrals, which are transcendental in general.

Let us present one more important example of a higher-order system that has the properties just listed.

To the system

$$c\dot{\alpha} = -z_2 + \beta\sin\alpha \tag{17}$$

$$\dot{z_2} = \sin\alpha\cos\alpha - z_1^2\frac{\cos\alpha}{\sin\alpha} \tag{18}$$

$$\dot{z_1} = z_1z_2\frac{\cos\alpha}{\sin\alpha} \tag{19}$$

which is distinguished considered in the three dimensional domain

$$\mathbf{S}^1\{\alpha \bmod 2\pi\} \setminus \{\alpha = 0,\, \alpha = \pi\} \times \mathbb{R}^2\{z_1, z_2\}$$

(such a system can reduce to an equivalent system on the tangent bundle of the two-dimensional sphere) and describes the spatial motion of a rigid body in a resisting medium [8], we put in correspondence the following system with algebraic right-hand side:

$$\frac{dz_2}{d\tau} = \frac{\tau - z_1^2/\tau}{-z_2 + \beta\tau}, \quad \frac{dz_1}{d\tau} = \frac{z_1 z_2/\tau}{-z_2 + \beta\tau} \tag{20}$$

In this case, it is also seen that system 17–19 is a system with zero mean variable dissipation; in order to obtain a complete correspondence with the definition, it suffices to introduce the new phase variable $z_1^* = \ln|z_1|$.

Moreover, this system has two first integrals (i.e., the full list), which are transcendental functions and are expressed through a finite combination of elementary functions; as was mentioned above, this become possible after establishing its correspondence to the (non-autonomous in general) system of equations 20 with algebraic (polynomial) right-hand side.

Therefore, the systems from the rigid body dynamics presented above not only enter the class of systems 12, 13 and have the mean zero variable dissipation, but they have a full list of transcendental first integrals expressed through a finite combination of elementary functions. In this case, the integration of systems 14 and 15, 16 reduces to the integration of the corresponding equations with algebraic right-hand side.

7 Conclusion

Generally speaking, the dynamics of a rigid body interacting with a medium is just the field where there arise either nonzero mean variable dissipation systems or systems in which the energy loss in the mean during a period can vanish. In the work, we have obtained such a methodology owing to which it becomes possible to finally and analytically study a number of plane and spatial model problems.

In qualitative describing the body interaction with a medium, because of using the experimental information about the properties of the streamline flow around, there arises a definite dispersion in modeling the force-model characteristics. This makes it natural to introduce the definitions of relative roughness (relative structural stability) and to prove such a roughness for the system studied. Moreover, many systems considered are merely (absolutely) Andronov–Pontryagin rough.

All what was said above allows one to estimate the results of the work in to totality as a new direction in qualitative theory of ordinary differential equations and the dynamics of a rigid body interacting with a medium.

Acknowledgements

This work was supported by the Russian Foundation for Basic Research, project no. 08-01-00231-a.

References

[1] M. V. Shamolin, Methods of Analysis of Dynamical Systems with Various Dissipation [in Russian]. Ekzamen, 2007.

[2] M. V. Shamolin, Dynamical Systems with Various Dissipation: Approaches, Methods, and Applications. J. Math. Sci., 2008, **162**, no. 6, pp. 741–908.

[3] N. E. Zhukovskii, On a fall of light oblong bodies rotating around their longitudinal axis, In: A Complete Collection of Works [in Russian], **5**, Fizmatgiz, Moscow, 1937, pp. 72–80, 100–115.

[4] N. E. Zhukovski, On bird soaring, In: A Complete Collection of Works [in Russian], **5**, Fizmatgiz, Moscow, 1937, pp. 49–59.

[5] S. A. Chaplygin, On motion of heavy bodies in an incompressible fluid, In: A Complete Collection of Works [in Russian], **1**, Izd. Akad. Nauk SSSR, Leningrad, 1933, pp. 133–135.

[6] V. A. Eroshin, Experimental study of entrance of an elastic cylinder into water with high speed, Izv. Ross. Akad. Nauk, Mekhanika Zhidkosi Gaza, 1992, **5**, pp. 20–30.

[7] M. V. Shamolin, Some questions of the qualitative theory of ordinary differential equations and dynamics of a rigid body interacting with a medium, J. Math. Sci., 2002, **110**, no. 2, pp. 2526–2555.

[8] M. V. Shamolin, Classes of variable dissipation systems with nonzero mean in the dynamics of a rigid body, J. Math. Sci., 2004, **122**, no. 1, pp. 2841–2915.

Maxim V. Shamolin, Institute of Mechanics, Lomonosov Moscow State University, 1 Michurinskii Ave., 119899 Moscow, Russian Federation

Energy exchange and transition to localization in asymmetric Fermi-Pasta-Ulam oscilliatory chain

D. S. Shepelev V. V. Smirnov L. I. Manevich
deshepelev@gmail.com,vvs@polymer.chph.ras.ru, lmanev@center.chph.ras.ru

Abstract

A finite (periodic) FPU chain has be chosen as a starting point of investigation of physical nature of energy localization phenomenon in nonlinear oscillatory chains. Such approach, realized recently for symmetric FPU chain, has allowed clarifying the conditions of the transition from complete energy exchange between different parts of the oscillatory chain to energy localization on excited group of particles. This result has been obtained on the base of LPT concept developed. The extension of our previous results on the asymmetric FPU chain is the goal of given presentation. We have shown that the account of asymmetry in potential of interaction leads to renormalization of the coefficients of final equations of motion. Therefore the main results obtained for symmetric model remain to be valid qualitatively. As for application to realistic models of molecular systems, the corrections caused by asymmetry of potential of interaction can be significant. Besides, we present the analytical determination of the temporal dependence of the energy distribution in the system.

1 Introduction

Energy localization in nonlinear oscillatory chains has become a problem of great interest since the moment of publication of the FPU original report [1]. A large number of investigations in this field have led to the contemporary theory of solitons [2]. Following this theory, the problem of vibration energy localization for an infinite FPU chain can be asymptotically reduced to finding a localized solution of the nonlinear Schrodinger equation (NLSE) [3], which is a completely integrable system in contrast with a discrete NLSE. Due to the reduction to NLSE, the mathematical origin of the vibration energy localization in an infinite chain can be clearly understood [3, 4]. It was shown recently [5] that intensive energy exchange as well as transition to localization in symmetric Fermi-Pasta-Ulam (FPU) oscillatory chain can be adequately described on the basis of the Limiting Phase Trajectory (LPT) concept. This concept has been introduced at the first time in the papers [6],[7], [8] as an alternative to Nonlinear Normal Mode concept [9], [10]. While the NNM preserves the energy given to it, the LPT corresponds to complete energy exchange between the oscillators. Ceasing of such exchange means a transition to spatial energy localization [5].

The symmetric model of FPU chain is valid for various mechanical problems. However, for application to the problems of Molecular and Polymer Physics it is necessary to consider asymmetric $(\alpha - \beta)$ FPU problem because realistic interatomic potentials of interaction are strongly asymmetric ones. This paper is devoted to extension of the results obtained in [5] at the case of asymmetric FPU-chain. The main motivation for such extension is that realistic potentials of interaction in solid state physics are asymmetric ones.

2 The model and the equations of motion.

We consider the $(\alpha - \beta)$-FPU system defined by the Hamilton function

$$H_0 = \sum_{j=1}^{N} \frac{1}{2}p_j^2 + \frac{1}{2}(q_{j+1} - q_j)^2 + \frac{\alpha}{3}(q_{j+1} - q_j)^3 + \frac{\beta}{4}(q_{j+1} - q_j)^4 \qquad (1)$$

and the periodic boundary conditions ($q_{N+1} = q_1, p_{N+1} = p_1$), where q_j and p_j are the coordinates and the conjugate momenta, respectively, N is the number of particles.

The transformation to normal coordinates is given by the linear canonical transformation

$$q_j = \sum_{k=0}^{N-1} \sigma_{j,k}\xi_k \tag{2}$$

with the coefficients

$$\sigma_{j,k} = \frac{1}{\sqrt{N}}\left(\sin\frac{2\pi kj}{N} + \cos\frac{2\pi kj}{N}\right), \quad k = 0, 1, \ldots, N-1.$$

The transformation (2) allows us to present the quadratic part of Hamilton function as the total energy of the independent oscillators:

$$H_2 = \sum_{k=1}^{N-1} \frac{1}{2}(\eta_k^2 + \omega_k^2\xi_k^2). \tag{3}$$

Here ξ_k and η_k are the amplitudes and the momenta of NNMs; the coordinate ξ_0, associated with motion of the center of mass, is removed from (3). The eigenvalues ω_k have the form

$$\omega_k = \omega_{N/2}\sin\frac{\pi k}{N}, \quad \omega_{N/2} = 2, \quad k = 0, \ldots, N-1. \tag{4}$$

If the number of particles increases, the frequency gap between the highest-frequency mode and nearby modes quickly decreases. In what follows, we consider an even number of particles N. In this case, the frequencies ω_k are bounded by the highest-frequency $\omega_{N/2} = 2$. The zero eigenvalue $\omega_0 = 0$ corresponds to motion of the chain as a rigid body. All eigenvalues in the interval $0 < \omega_k < 2$ are twice degenerate.

The remaining part of the Hamilton function (1) for the periodic $(\alpha - \beta)$-FPU chain has the following form [11]:

$$\begin{aligned} H_{nonlin} =& \frac{\alpha}{3}\sqrt{\frac{2}{N}} \sum_{n,m,k=1}^{N-1} \omega_n\omega_m\omega_k D_{n,m,k}\xi_n\xi_m\xi_k + \\ &+ \frac{\beta}{8N} \sum_{k,l,m,n=1}^{N-1} \omega_k\omega_l\omega_m\omega_n C_{k,l,m,n}\xi_k\xi_l\xi_m\xi_n, \end{aligned} \tag{5}$$

where

$$\begin{aligned} D_{n,m,k} &= -\Delta_{n+m+k} + \Delta_{n+m-k} + \Delta_{n-m+k} + \Delta_{n-m-k}, \\ C_{k,l,m,n} &= -\Delta_{k+l+m+n} + \Delta_{k+l-m-n} + \Delta_{k-l+m-n} + \Delta_{k-l-m+n} \end{aligned}$$

and

$$\begin{cases} (-1)^r, \ if \ r = mN, m \in \mathbb{Z} \\ 0 \qquad\qquad otherwise \end{cases}$$

So the equations of motion can be written as:

$$\begin{aligned} &\frac{d^2\xi_k}{dt^2} + \omega_k^2\xi_k + \frac{\sqrt{2}\alpha\omega_k}{\sqrt{N}} \sum_{n,m=1}^{N-1} \omega_n\omega_m D_{n,m,k}\xi_n\xi_m + \\ &\quad + \frac{\beta\omega_k}{2N} \sum_{l,m,n=1}^{N-1} \omega_l\omega_m\omega_n C_{k,l,m,n}\xi_l\xi_m\xi_n = 0. \end{aligned} \tag{6}$$

To analyze the dynamics of the chain in the context of Eqs (6), we introduce the complex amplitude corresponding to the combination of displacement and velocity in the new basis

$$\Psi_k = \frac{1}{\sqrt{2}}(\eta_k + i\omega_k\xi_k), \quad \Psi_k^* = \frac{1}{\sqrt{2}}(\eta_k - i\omega_k\xi_k).$$

In terms of complex amplitudes, Eqs (6) can be rewritten as

$$i\frac{d\Psi_k}{dt} + \omega_k\Psi_k - \frac{i\alpha\omega_k}{2\sqrt{N}}\sum_{n,m=1}^{N-1} D_{k,n,m}(\Psi_n - \Psi_n^*)(\Psi_m - \Psi_m^*) - \\ - \frac{\beta\omega_k}{8N}\sum_{l,m,n=1}^{N-1} C_{k,l,m,n}(\Psi_l - \Psi_l^*)(\Psi_m - \Psi_m^*)(\Psi_n - \Psi_n^*) = 0. \tag{7}$$

Taking into account the dependence of the chain properties on the number of the particles, one can choose the value $\frac{1}{\sqrt{N}}$ as a small parameter ε.

3 Main asymptotic approximations.

We employ the multiple scale procedure [12] in order to consider the processes in the time intervals greatly exceeding $2\pi/\omega_k$. Following this procedure, we introduce three time scales:

$$\tau_0 = t, \quad \tau_1 = \varepsilon\tau_0, \quad \tau_2 = \varepsilon^2\tau_0 \tag{8}$$

where the "fast" time τ_0 corresponds to the initial time scale of the system, while the slow times τ_1, τ_2, etc. correspond to the slowly varying envelopes. The envelope functions φ_k are defined by the relation

$$\Psi_k = \varphi_k e^{i\omega_k\tau_0}. \tag{9}$$

We construct the asymptotic representation of φ_k in the form

$$\varphi_k = \chi_{k,1} + \varepsilon\chi_{k,2} + \varepsilon^2\chi_{k,3} + \dots \tag{10}$$

On the contrary to the symmetric FPU system, the multiple scale expansion based on the relations (8, 10), when applying to the Hamilton function (5) leads to the functional dependence between the leading-order approximation $\chi_{k,1}$ and the next-order one $\chi_{k,2}$ in the time scale τ_1. The exclusion of the lasts allows to derive the equations for the leading-order approximation $\chi_{k,1}$ in the time scale τ_2.

The particular solutions of Eqs. (7) with indices $(k, N-k)$ correspond to the pairs of the degenerate modes. In what follows, we consider the coupled dynamics of the π-mode ($k = N/2$) and nearby conjugate modes with indices $(N/2+1)$, $(N/2-1)$ and linear frequency $\omega_{N/2-1} = \omega_{N/2+1}$. This choice is inspired by two reasons:

1) A linear combination of the π-mode with conjugate ones leads to a strongly nonuniform (one-hump) distribution of energy.

2) While the number of particles in the chain increases, the frequency gap decreases, and a possibility of resonant energy exchange between the closest modes appears. Actually, the frequency of the π-mode differs from the frequencies of nearby ones by the value of order ε^4:

$$\omega_{N/2\pm1} = 2\sin(\frac{\pi}{N}(\frac{N}{2} \pm 1)) = 2\cos\frac{\pi}{N} \approx \omega_{N/2}\left(1 - \frac{1}{2}\left(\frac{\pi}{N}\right)^2\right). \tag{11}$$

We choose $\omega_{N/2}$ as a basic frequency and take into account its resonant interaction with the frequencies of the nearest conjugate modes. Since the difference between $\omega_{N/2}$ and $\omega_{N/2-1}$ is of order ε^4, the equations for $\chi_{N/2-1,1}$ and $\chi_{N/2+1,1}$ include additional linear terms. Skipping details

of calculations [5], we get the final equations in the form (we omit the second index in the main approximation for amplitudes $\chi_{k,1} = \chi_k$):

$$\begin{cases} i\frac{d\chi_{N/2}}{d\tau_2} + \frac{3\beta_1}{2}\Big(|\chi_{N/2}|^2\chi_{N/2} + 2(|\chi_{N/2-1}|^2 + |\chi_{N/2+1}|^2)\chi_{N/2} + \\ \qquad +(\chi_{N/2-1}^2 + \chi_{N/2+1}^2)\chi_{N/2}^*\Big) = 0 \\ i\frac{d\chi_{N/2-1}}{d\tau_2} - \frac{\pi^2}{2}\chi_{N/2-1} + \frac{3\beta_1}{4}\Big((4|\chi_{N/2}|^2 + 3|\chi_{N/2-1}|^2 + 2|\chi_{N/2+1}|^2)\chi_{N/2-1} + \\ \qquad +(2\chi_{N/2}^2 + \chi_{N/2+1}^2)\chi_{N/2-1}^*\Big) = 0 \\ i\frac{d\chi_{N/2+1}}{d\tau_2} - \frac{\pi^2}{2}\chi_{N/2+1} + \frac{3\beta_1}{4}\Big((4|\chi_{N/2}|^2 + 3|\chi_{N/2+1}|^2 + 2|\chi_{N/2-1}|^2)\chi_{N/2+1} + \\ \qquad +(2\chi_{N/2}^2 + \chi_{N/2-1}^2)\chi_{N/2+1}^*\Big) = 0 \end{cases}, \tag{12}$$

where $\beta_1 = \beta - \frac{16}{3}\alpha^2$. It is remarkable that the equations of motion for asymmetric system have the similar structure as that for the symmetric one, excepting the renormalization of the four-order constant β. So the accounting of asymmetry is reduced to renormalization of constant in the equations and there is no quantitative changes in comparison with equations for the β-FPU chain ($\alpha = 0$). The Hamiltonian corresponding to Eqs. (12) is

$$\begin{aligned} H = -\frac{\pi^2}{2}\Big(|\chi_{N/2+1}|^2 + |\chi_{N/2-1}|^2\Big) + \frac{3\beta_1}{4}\Big(|\chi_{N/2}|^4 + \frac{3}{2}\Big(|\chi_{N/2+1}|^2 + |\chi_{N/2-1}|^2\Big)^2 + \\ +2|\chi_{N/2}|^2(|\chi_{N/2+1}|^2 + |\chi_{N/2-1}|^2) + (\chi_{N/2+1}\chi_{N/2}^* + \chi_{N/2}\chi_{N/2+1}^*)^2 + \\ +(\chi_{N/2-1}\chi_{N/2}^* + \chi_{N/2}\chi_{N/2-1}^*)^2 + \frac{1}{2}(\chi_{N/2+1}\chi_{N/2-1}^* + \chi_{N/2-1}\chi_{N/2+1}^*)^2\Big). \end{aligned} \tag{13}$$

Eqs. (12) possess an additional integral of motion, which is said to be the total "occupation number"

$$X = |\chi_{N/2}|^2 + |\chi_{N/2-1}|^2 + |\chi_{N/2+1}|^2 = const \tag{14}$$

4 From "waves" to "particles"

To analyze the system, we turn from the "wave representation" to the "particle representation". To this end, we introduce the new variables ψ_1, ψ_2, φ by the following formulas

$$\begin{aligned} \psi_1 &= \frac{1}{\sqrt{2}}\Big(\chi_{N/2} - \frac{1}{\sqrt{2}}\Big(\chi_{N/2-1} + \chi_{N/2+1}\Big)\Big), \\ \psi_2 &= \frac{1}{\sqrt{2}}\Big(\chi_{N/2} + \frac{1}{\sqrt{2}}\Big(\chi_{N/2-1} + \chi_{N/2+1}\Big)\Big), \\ \varphi &= \frac{1}{\sqrt{2}}\Big(\chi_{N/2-1} - \chi_{N/2+1}\Big). \end{aligned} \tag{15}$$

preserving the occupation number in the form $X = |\psi_1|^2 + |\psi_2|^2 + |\varphi|^2$. We consider a particular solution corresponding to $\varphi = 0$. Since the occupation number X is the integral of motion, ψ_1 and ψ_2 can be expressed through the "angle variables":

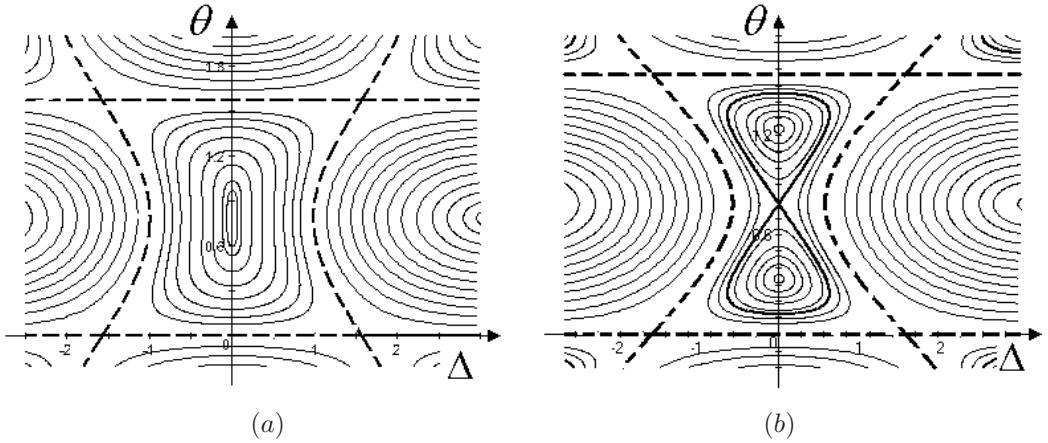
$$\psi_1 = \sqrt{X}\cos\theta e^{i\delta_1}; \quad \psi_2 = \sqrt{X}\sin\theta e^{i\delta_2}. \tag{16}$$

Then Hamiltonian (13) takes the following form:

$$H(\theta, \Delta) = \frac{X}{64}(27\beta_1 X - 16\pi^2 + 2(8\pi^2 - 3\beta_1 X)\cos\Delta\sin 2\theta - 3\beta_1 X(8 - \cos^2\Delta)\sin^2\theta), \tag{17}$$

where $\Delta = \delta_2 - \delta_1$. and Eqs(12) can be rewritten in terms of "angle variables"

$$\frac{\partial\theta}{\partial\tau_2} + \frac{1}{32}(8\pi^2 - 3\beta_1 X + 3\beta_1 X\cos\Delta\sin 2\theta)\sin\Delta = 0$$



(a) (b)

Figure 1: The truncated phase-plane portrait before (a) and after (b) threshold of instability of the π-mode; the long-dashed lines correspond to the LPT.

$$\sin 2\theta \frac{\partial \Delta}{\partial \tau_2} + \frac{1}{16}\cos 2\theta((8\pi^2 - 3\beta_1 X)\cos\Delta - 3\beta_1 X(8 - \cos^2\Delta)\sin 2\theta) = 0 \tag{18}$$

The analysis of phase-plane portrait of Hamiltonian (17) shows that there are two stationary points corresponding to the pure π-mode ($\theta = \pi/4, \Delta = 0$) and "pure" mixture of conjugate modes ($\theta = \pi/4, \Delta = \pi$) (Fig. 1a). When the excitation level reaches $X = \pi^2/3\beta_1$ two new stationary points with coordinates

$$\begin{aligned} &(a) \quad \Delta = 0, \quad \theta = \frac{1}{2}\arcsin\left(\frac{8\pi^2 - 3\beta_1 X}{21\beta_1 X}\right) \\ &(b) \quad \Delta = 0, \quad \theta = \frac{\pi}{2} - \frac{1}{2}\arcsin\left(\frac{8\pi^2 - 3\beta_1 X}{21\beta_1 X}\right) \end{aligned} \tag{19}$$

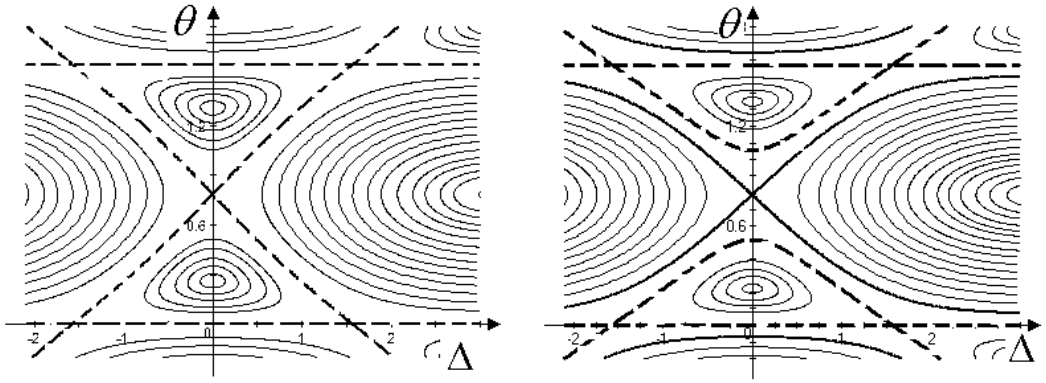
appear. At this instant the π-mode losses its stability that leads to the appearance of separatrix which passes through it (Fig. 1.b). Thus, the threshold of instability of π-mode is equal to $X_c = \pi^2/3\beta_1$, which is in a good accordance with the estimation obtained in the framework of "narrow packet" approximation [13],[14],[15].

Let us consider the phase trajectory describing the transition from the state ψ_1 ($\theta = 0$) to the state ψ_2 ($\theta = \pi/2$) and vice versa. Because it delimits the families of trajectories which encircle the base stationary points (Fig. 1a) we name it the Limiting Phase Trajectory (LPT) [6]. The passage along this trajectory leads to the complete energy transfer from one half of the chain to another one and vice versa. In fact this is an adequate extension of the beating phenomenon, well known in the theory of small degree of freedom systems, on the many-particle ones.

While the amplitude X grows, the separatrix passing through the unstable stationary point enlarges and, finally, its coincidence with LPT occurs (Fig. 2a). After this instant, topology of the phase plane drastically changes (Fig.2b). Namely, any energy exchange between the "mixed" states ψ_1 and ψ_2 disappears; this implies that a trajectory starting at a point corresponding to $\theta < \pi/4$ (or $\theta > \pi/4$) and any Δ cannot reach a point corresponding to $\theta > \pi/4$ ($\theta < \pi/4$) (except all the trajectories surrounding the in-phase stationary points at $\Delta = \pm\pi$ and bounded by the separatrix crossing the unstable point $\theta = \pi/4, \Delta = 0$). Therefore, the energy initially concentrated near the states ψ_1 or ψ_2 remains confined in the excited part of the chain (Fig. 3).

An energy threshold associated with the above mentioned localization can be calculated from the condition of equality of the energy corresponding to the LPT and the energy of the unstable π-mode. The LPT goes through the points $\theta = \pi/2$ and $\theta = 0$. This means that

$$H(\theta, \Delta)|_{LPT} = \frac{X}{64}\left(27\beta_1 - 16\pi^2\right).$$



(a) (b)

Figure 2: Phase-plane portrait: (a) coincidence of the LPT and the separatrix; (b) phase plane after transition to spatial energy localization, long-dashed lines correspond to the LPT.

Since the energy of the π-mode is associated to zero, it is easy to calculate the respective occupation number $X_{loc} = 16\pi^2/27\beta$ and the energy of the chain $E_{loc} = 16\pi^2/27\beta N$. It now follows that above the excitation level E_{loc} we can observe the localized vibration excitation (a breather).

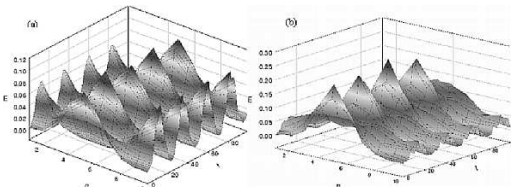


Figure 3: Transition "beating - localization" in the FPU-chain with 10 particles. The initial conditions correspond to the state ψ_1, and the levels of excitation are (a) $X < X_{loc}$ and (b) $X > X_{loc}$. E, n, and t denote the energy, the number of particle, and time, respectively.

If the initial energy is concentrated at the state ψ_1 or ψ_2, the representing point in the phase plane moves along a trajectory encircling the respective stationary point; the temporal evolution of the breather corresponds to the regular variation of its profile (the "breathing" mode of the localized excitation). This effect is depicted in Fig.3 (b).

Contrary to "breathing" breathers corresponding to the passage along the LPT, the stationary points (19) determine new normal modes with invariable non-homogeneous energy distribution, or the breather-like excitations. In spite of these modes existence at any $X > X_c$ the true threshold of localization is equal to X_{loc} because the possibility of the complete energy exchange is preserved for motion along the LPT till $X = X_{loc}$.

Thus we get the solution (19) corresponding to immobile breather. Finally we want to clarify the nature of traveling breathers. We recall that the above results have been obtained under assumption $\varphi = 0$ that corresponds to equal amplitudes of the conjugate modes. Now we assume that the amplitudes of the conjugate modes are slightly different, so we consider small enough $\varphi \neq 0$. One can show that the equations for functions ψ_1 and ψ_2 include only quadratic terms depending on φ. Therefore, in the framework of the linear approximation, if the value $\varphi \neq 0$ is small enough, there is no qualitatively change in the phase-plane portrait in figures (1, 2). As for behavior of φ in the vicinity of any of stationary points (19), it is described as follows:

$$i\frac{d\varphi}{d\tau_2} - \frac{\pi^2}{2}\varphi + \frac{3\beta_1 X}{16}(2\varphi \sin 2\theta + (3 + e^{2i\delta_1} sin2\theta)\varphi^*) = 0.$$

The respective eigenvalue

$$\lambda = \pm\frac{\sqrt{891\beta_1^2X^2 + 120\pi^2\beta_1 X - 384\pi^4}}{56}$$

is imaginary if $X < X_{loc}$, i.e. if the amplitude of excitation is less than the threshold corresponding to coincidence of LPT and separatrix.

Thus, it is clear that small nonzero φ in the equations of motion leads to small oscillations of the breather center as long as the occupation number X is small enough, but the appearance of a real part in the eigenvalue λ at $X > X_{loc}$ leads to the directional motion of the breather (Fig. 4).

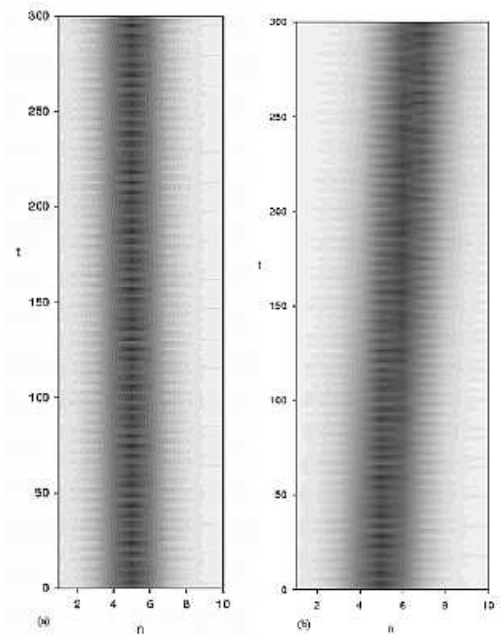


Figure 4: Energy map for (a) static and (b) traveling breathers. The more dark domains correspond to the highest energy level.

5 Analytical solution for LPTs.

Now we analyze the system in angle variables (18) with $X << X_{loc}$. It is seen in Fig.5a that $\theta(\tau_2)$ is close to the straight line, with an almost instant reverse at $\pi/2$. This implies that motion of system (18) is similar to the dynamics of a particle moving with constant velocity between two motion-limiters. In order to describe a solution close to the vibro-impact process, we introduce the new variable $\tau(\phi), \phi = \Omega\tau_2$ ($\Omega = (8\pi^2 - 3\beta_1 X)/16\pi$). The function $\tau(\phi)$ and its derivative $e(\phi) = d\tau/d\phi$ have the form

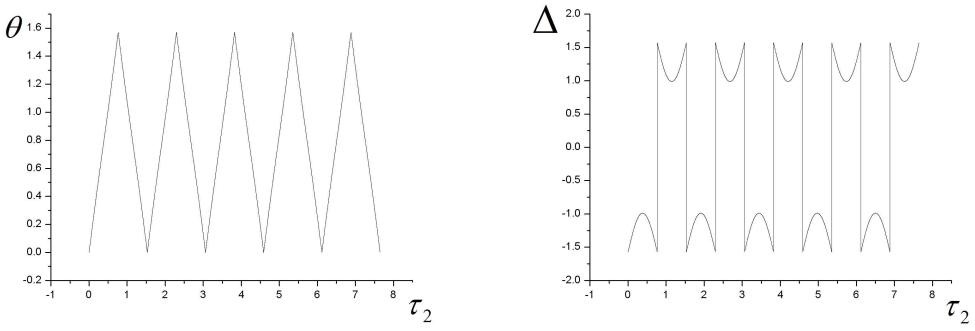
$$\tau(\phi) = \frac{2}{\pi}|\arcsin(\sin\frac{\pi\phi}{2})|, \quad e(\phi) = 1,\ 0 < \phi < 1;\ e(\phi) = -1,\ 1 < \phi < 2. \tag{20}$$

Following [10], we construct an approximate solution as a function of τ; the inverse transformation $\tau_2 = \tau_2(\tau)$ automatically yields a solution $2T$-periodic in τ_2. Taking into account the discontinuity of $\Delta(\tau_2)$, we construct solutions of (18) in the form

$$\theta(\tau_2) = \Theta(\tau), \quad \Delta(\tau_2) = e(\phi)Y(\tau), \quad \frac{d}{d\tau_2} = \Omega e\frac{d}{d\tau} \tag{21}$$

To derive the equations for $\Theta(\tau)$, $Y(\tau)$ we insert (21) into (18). This yields the set of equations

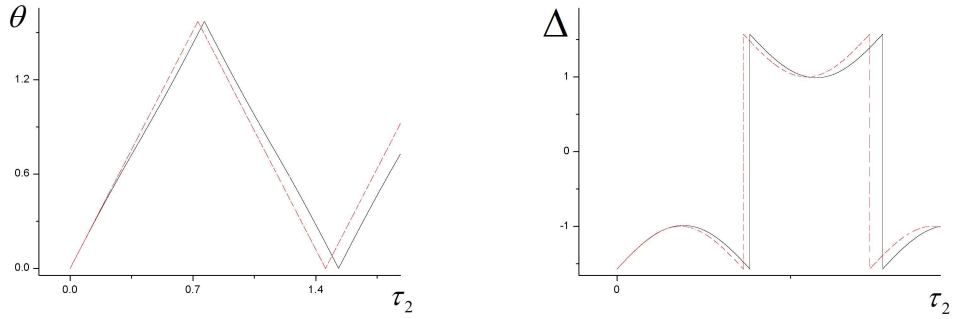
$$\Omega\frac{\partial\Theta}{\partial\tau} + \frac{1}{32}(8\pi^2 - 3\beta_1 X + 3\beta_1 X\cos Y\sin 2\Theta)\sin Y = 0$$



(a) (b)

Figure 5: The numerical solution of angle variable system with $3\beta_1 X = \pi^2$.

$$\Omega\frac{\partial Y}{\partial\tau}\sin 2\Theta + \frac{1}{16}\cos 2\Theta((8\pi^2 - 3\beta_1 X)\cos Y - 3\beta_1 X(8 - \cos^2 Y)\sin 2\Theta) = 0 \tag{22}$$



(a) (b)

Figure 6: Comparing the numerical solution with analytical; solid line is numerical solution, long-dashed – analytical.

It is easy to get the leading-order approximation of system (22) solution:

$$\Theta_0(\tau) = A_0\tau, \quad \Delta_0 + \Delta_1 = -\frac{\pi}{2} + \frac{12\beta_1 X}{8\pi^2 - 3\beta_1 X}\sin A_0\tau, \quad A_0 = \frac{\pi}{2}. \tag{23}$$

Fig. 6 demonstrates that the numerically constructed solution of (18) is in a good agreement with the yielded approximation.

6 Conclusion

This study demonstrates that the energy localization phenomenon in the nonlinear oscillatory chains can be decribed in the framework of unified concept for the systems with both symmetric and asymmetric potentials of interaction. It has been shown that a presence of asymmetric interaction, which is specific for the molecular systems, does not change the features of the energy localization phenomenon observed in the symmetric nonlinear oscillatory chains [5]. In fact, only some renormalization of four-order constant of interaction occurs, that can lead to the effective reducing the influence of nonlinearity in the equations of motion. However, when this renormalized

constant turns out to be too small, the next order terms in the expansion of exact potential energy have to be taken into account. The transition to energy localization seems as the prohibition of the intensive energy exchange between different parts of the system. The latter is the adequate analogy with the beating phenomenon, well studied in the systems of two oscillators. The analytical results for Limiting Phase Trajectories are confirmed with numerical calculations.

Acknowledgements

The work was supported by Program of Department of Chemistry and Material Science (Program #2) Russia Academy of Sciences and Russia Basic Research Foundation (grant 08-03-00420a).

References

[1] E. Fermi, J. Pasta, S. Ulam. Los Alamos Science Laboratory Report No. LA-1940, 1955, unpublished; reprinted in Collected Papers of Enrico Fermi, edited by E. Segre (University of Chicago Press, Chicago, 1965), v.2, p.978

[2] T. Dauxois, M. Peyrard. Physics of Solitons. (Cambridge University Press, 2006)

[3] R.K. Dodd, J.C. Eilbeck, J.D. Gibbon, H.S. Morris. Solitons and Nonlinear Wave Equations. (Academic Press Inc., London, 1982)

[4] A.J. Lichtenberg, R. Livi, M. Pettini, S. Ruffo. The Fermi-Pasta-Ulam problem: A status report, in Lect. Notes Phys. 728, 21, (Springer-Verlag Berlin Heidelberg, 2008)

[5] L.I. Manevitch, V.V. Smirnov. Limiting Phase Trajectories and the origin of energy localization in nonlinear oscillatory chain. Submitted to Phys. Rev. Lett.

[6] L.I. Manevich. New approach to beating phenomenon in coupled nonlinear oscillators chains. 8th Conference on Dynamical Systems-Theory and Applications, Proceedings. Lodz, December 12-15, 2005, Poland, V.1, pp. 119-136

[7] L.I. Manevitch. New approach to beating phenomenon in coupled nonlinear oscillatory chains. Arch. Appl. Mech. v.77 (5), 301-312, 2007

[8] L.I. Manevitch. The description of localized normal modes in a chain of nonlinear coupled oscillators using complex variables. Nonlinear Dynamics, 25, 95-109, 2001

[9] L.I. Manevitch, Yu.V. Mikhlin, V.N. Pilipchuk. The method of normal vibrations for essentialy nonlinear systems (in Russia. Moscow: Nauka, 1989, 216p.

[10] A.F. Vakakis, L.I. Manevitch, Yu.V. Mikhlin, V.N. Pilipchuk, A.A. Zevin. Normal modes and localization in nonlinear systems. New York: Wiley, 1996, 552p.

[11] P.Poggi, S.Ruffo, Exact solutions in the FPU oscillator chain, Physica D 103, 251 (1997)

[12] A.I.Manevich, L.I.Manevich, The mechanics of nonlinear systems with internal resonances, (Imperial College Press, London, 2005)

[13] T.Dauxois, R.Khomeriki, F.Piazza, S.Ruffo, The Anti-FPU Problem, Chaos 15, 015110, (2005)

[14] G.P.Berman, F.M.Izrailev, The Fermi-Pasta-Ulam problem: 50 years of progress, Chaos, 15, 15104 (2005)

[15] G.P.Berman, A.R.Kolovsky, Zh. Eksp. Theor.Fiz. 87, 1938 (1984); Sov.Phys.JETP 60, 1116 (1984)

119991, 4 Kosygin str., Moscow, Russia

Study of features of deformation response of interfacial zones in block-structured medium to low-amplitude dynamic mechanical actions

Evgeny V. Shilko Sergey V. Astafurov Alexander S. Grigoriev
Sergey G. Psakhie
shilko@ispms.tsc.ru

Abstract

Theoretical analysis of some general features of deformation response of interfacial zones in block-structured media (including geological medium) to low-amplitude dynamic mechanical actions is carried out. Influence of type of dynamic action and stress conditions is analyzed. Investigation results make an important contribution to development of an approach to estimation of proximity of stress state of plane discontinuities (faults and large cracks) in rock massifs to critical (threshold) value wherein seismogenerating unsteady slip can take place.

1 Introduction

An important direction in deformable solid physics and mechanics is investigation of features of mechanical response of so-called block-structured materials and media. This term combines materials, which mechanical behavior is defined significantly by processes of strain localization at block boundaries (interfacial regions between structural elements). Typical representative of this class of materials is hierarchically organized geological medium [1].

An important feature of block-structured geomedium is that its fragments are in complex stressed state. Relation of internal stresses to strength characteristics of interfacial regions appreciably defines deformation and relaxation capacity of the mechanism concerned with relative block displacement. As the shear stress at an active block boundary reaches limiting (threshold) value, its local deformation mode can change qualitatively from slow deformation (creeping) to dynamic deformation (referred to as unstable sliding). Note that according to modern notion, acts of dynamic block sliding are seismogenerating events those magnitude can reach 6-7 [2]. Thus, an urgent task in geomechanics is to develop methods of estimating the local stress state at active interfaces of fragments of rock massifs or the earth's crust.

Theoretical studies as well as experiments on prestressed rock samples and fragments of plane discontinuities in rock massifs revealed an important effect consisting in deformation response of prestressed interfacially structured materials to dynamic perturbations of stress state in form of irreversible relative displacement of blocks [2, 3, 4]. This allowed different authors to formulate the idea about the possibility of estimation of shear stress level in the fragments of active fault zones by measuring deformation response on testing dynamic actions. Nevertheless to transform this idea into practical approach it is necessary to have information about the character of connection between shear stress level in interfacial zone and deformation response to dynamic perturbation of local stress state. This information could be obtained in particular on the base of computer-aided simulation of fragments of block interfaces being under complex stress condition. In the present paper this study was done with use of the movable cellular automaton method [5]. This method is a representative of discrete element approach [6]. Over last decade it is successfully employed for studying the peculiarities of deformation and fracture of indurated, unconsolidated and loose media [5, 7, 8].

2 Problem statement

In previously carried out investigation the authors revealed qualitative effect of sharp change of deformation response of shear zones under change of character of stress-strain state [4]. These results allowed authors to propose the way to development of an approach to diagnostics of shear stress level at sections of active interfaces of structural blocks in rock massif. The approach could be based on long-time monitoring of dynamics of natural and man-caused displacements in studied part of active block boundary. Formulation of the approach needs detail study of features and peculiarities of deformation response of active block boundaries to dynamic actions of different kinds.

Presented theoretical study is accented on analysis of difference of deformation response of block boundary being under complex stress condition to dynamic perturbation of stress state by elastic P- and S-waves. For solving the problem posed, a two-dimensional structural model of the interface between elements of a block medium was considered (Fig. 1). The model includes the interface itself and contiguous block fragments (hereinafter referred to as blocks). The model blocks were assumed to be monolithic, brittle and of high strength (curve 1 in Fig. 1b). The mechanical response of interfacial region featured irreversible strain accumulation and simulated the mechanical properties of a cataclasites (curve 2 in Fig. 1b). For mathematical description of elastoplastic response of the interface and of the blocks in the framework of the movable cellular automaton method, the model described in [9] was used. Analogy of plane stress approximation was applied.

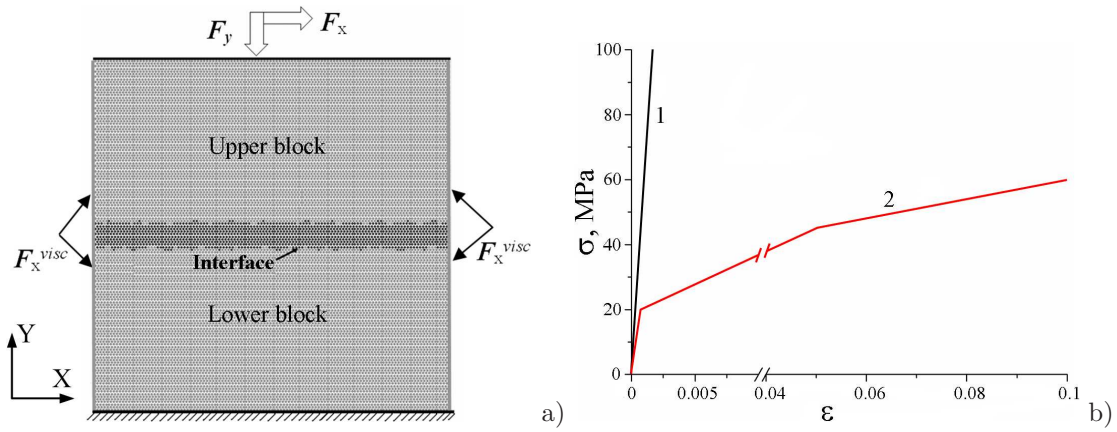


Figure 1: Structure and loading pattern of the model interface (a) and response functions (b) of the automata of the blocks (1) and interfacial region (2). Automaton response function is an analogue of unified hardening curve in deformable solid mechanics [5, 9]. Viscous force F_x^{visc} models dissipative and "inertial" influence of surroundings of simulated fragment of interface. It is calculated with the formula: F_x^{visc}=-$\alpha \cdot V_x^{visc}$, where V_x^{visc} is horizontal component of velocity of corresponding automaton of the specimen lateral surface.

The lower surface of the specimen was rigidly fixed while external load was applied to the upper surface (Fig. 1a). Dissipative and "inertial" influence of surroundings of simulated fragment of interface was modeled by "applying" an additional viscous force to the automata of the lateral surfaces. The initial stress state of the system was specified by applying an external force with normal (F_y) and tangential (F_x) components to the upper surface of the model specimen (Fig. 1a) with subsequent relaxation of the system. In the calculations, we used different values of normal force F_y, whose specific value (hereinafter referred to as σ_y) varied in the range from 20% to 40% of the yield stress of interface material. On completion of the relaxation stage, response of model interface to dynamic pulse testing loading by P- and S-waves was studied.

In the work, we considered different shear stress levels at the interface for which f_x=F_x/F_x^{max}, where F_x^{max} is the limiting (maximum) shear resistance force at considered value of F_y. Note that shear resistance curve has a profile typical of interfaces in rock massif fragments and is characterized by three main stages: a quasielastic stage (Fig. 2, stage I), a quasiplastic stage (stage II) and a

stage beyond the ultimate strength (stage III).

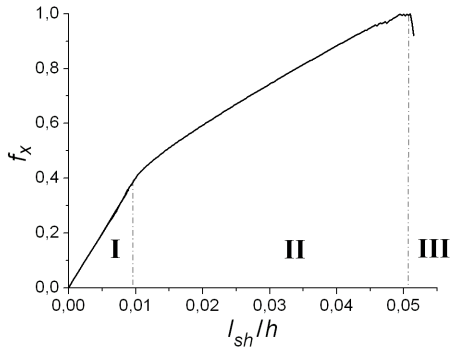


Figure 2: Dependence of force f_x of resistance to the shear displacement of active (upper) block of the model interface on the value of displacement l_{sh}. In the diagram shown, shear displacement is normalized to the interface layer thickness h. Normal stress (σ_y) value is 20% of the yield stress of interface material.

Testing pulse dynamic action on the sample being under loading with forces F_x and F_y was carried out by "instantaneous" (for T=3·10-5 s) assigning a sinusoidally changing velocity V_y=-V_A·sin($2\pi t/T$) in Y-direction (compressive P-wave) or V_x= V_A·sin($2\pi t/T$) in X-direction (S-wave) to the cellular automata of the upper surface (V_A=0.001 m/s in both cases). On completion of the P-wave pulse loading, the normal force F_y was again applied to the upper surface (applied shear force F_x remains unchanged all the time). In a similar manner, on completion of the S-wave pulse loading, the shear force F_x was again applied to the upper surface (applied normal force F_y remains unchanged all the time).

3 Discussion of simulation results

It is common knowledge that even small dynamic exposure gives rise to irreversible relative block displacements if shear stress level (f_x) at the interface exceeds some threshold value. This threshold, as a rule, is below the point of "formal" transition from quasielastic to quasiplastic response stage. Its value is defined to a large degree by the value of applied normal load (F_y). The observed effect is connected with inhomogeneous distribution of stresses in interface region that is a consequence of inhomogeneous distribution of mechanical properties. Stress state of some areas of the interface can be beyond the yield point, even though integral value of applied shear stress is relatively small. This leads to accumulation of irreversible deformation in these areas during elastic wave propagation.

Simulation results showed that reveal that the path length l_x of the upper block along the X-direction varies over order of magnitude with the shear stress level f_x, and this variation has a clearly defined nonlinear character (hereinafter the value of initiated displacement l_x will be presented in dimensionless form γ_x=l_x/h obtained by normalization of l_x to interface thickness h). Fig. 3a shows the curve $\gamma_x(f_x)$ for the case of pulse loading by P-wave. This curve has three main regions. In the first region, which is far from the point of formal transition to quasiplastic response of the interface (stage I in Fig. 2), value of dynamically initiated displacements is nearly constant. In the second region (near the formal point separating stages I and II in Fig. 2) γ_x increases greatly, and its derivative γ_x'=$d\gamma_x/df_x$ reaches the maximum close to transition point (Fig. 3b). In the third stage (in the range of quasiplastic response of the interface) the value of initiated displacements becomes "stable", and rate of increase of initiated shear displacements (γ_x') rapidly decreases close to zero. Thus, as the shear stress level approaches the formal boundary of quasielastic-to-quasiplastic response transition, qualitative variations occur in deformation response of the interface to dynamic loading. Revealed effect is important for formulation of the approach to diagnostics of stress state of block interfaces in block-structured geomedium.

Presented result correlates with results of previous investigation [4]. Nevertheless detail study shows that character of interface deformation response depends to a great extent not only by

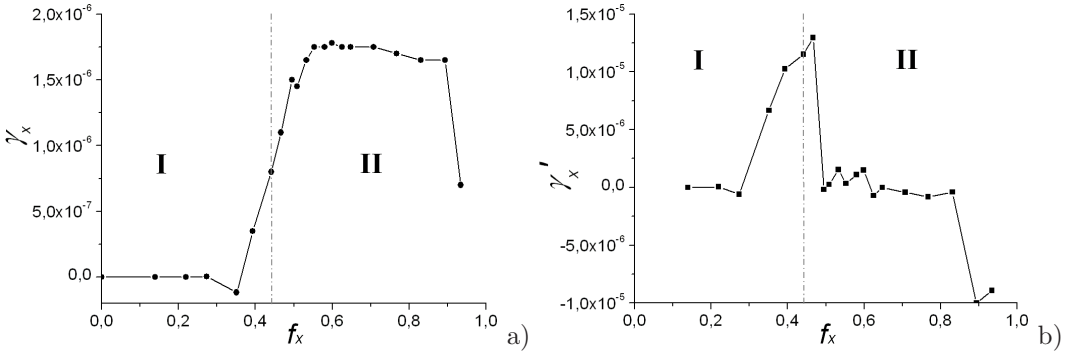


Figure 3: Reduced pulse-initiated shear displacement γ_x of the upper block (a) and its derivative $\gamma_x^{'}$ (b) versus the shear stress level f_x (compressive P-wave loading). Value of normal stress σ_y amounts to 20% of the yield stress of interface material. Hereinafter points show results of numerical simulation at corresponding values of f_x. Vertical dashed line symbolically separates stages of quasielastic (I) and quasiplastic response of studied interface.

shear stress level f_x, but by applied normal load F_y and by type of incident wave as well. Fig. 4 shows diagrams of interface deformation response to pulse loading by P-wave at normal stress σ_y corresponding to 40% of the yield stress of interface material. It is seen that under large normal load the region of great increase of initiated shear displacement extends far in the stage of quasiplastic interface response. Effective slope of this region therewith decreases nearly proportional to increase of σ_y. (see Fig. 3a and 4a). At the same time, sample shear resistance curves $f_x(l_{sh})$ at different σ_y (within considered range of normal stress values) vary weakly. Hence character of change of block boundary deformation response to testing pulse actions by compressive P-waves with shear stress level is appreciably defined by normal stress value. Note that similar conclusion is true for pulse actions by "tensile" P-waves ($V_y = V_A \cdot \sin(2\pi t/T)$ in Y-direction).

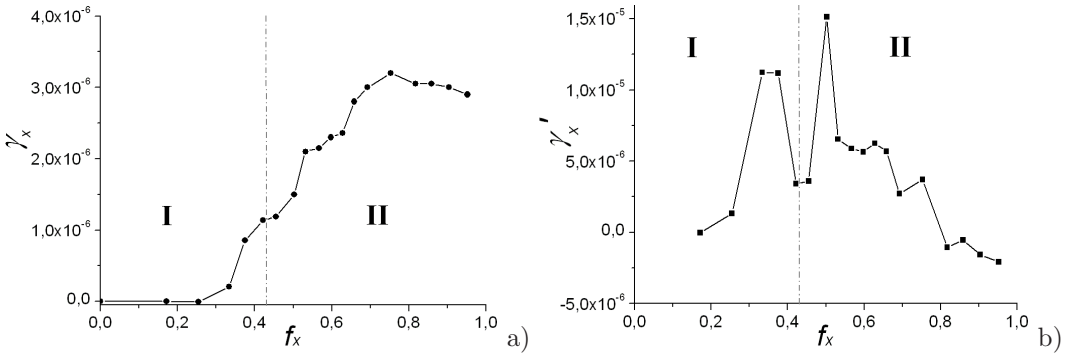


Figure 4: Reduced pulse-initiated shear displacement γ_x of the upper block (a) and its derivative $\gamma_x^{'}$ (b) versus the shear stress level f_x (compressive P-wave loading). Value of normal stress σ_y amounts to 40% of the yield stress of interface material.

At the same time, pulse testing actions with use of elastic S-waves looks more promising. Fig. 5 shows curves of deformation response of the model block boundary to dynamic exposure to S-waves at two values of applied normal stress σ_y. It is seen that dependencies $\gamma_x(f_x)$ at different σ_y as well as $\gamma_x^{'}(f_x)$ at different σ_y are close to each other. The region of great increase of γ_x is strongly pronounced in all cases, and its completion is associated with the point of "formal" transition from quasielastic (I) to quasiplastic (II) response stage. Hence characteristics of interface shear deformation response to dynamic exposure to S-waves insignificantly depend on value of normal stress σ_y (at least within the range of "moderate" values of σ_y).

As shown in the paper [10], an important characteristic of stress-strain state of shear zone is the value of its dilation (widening). Therefore irreversible change of width (thickness) of considered interface (l_y) under pulse testing actions was analyzed within the framework of the study. Simu-

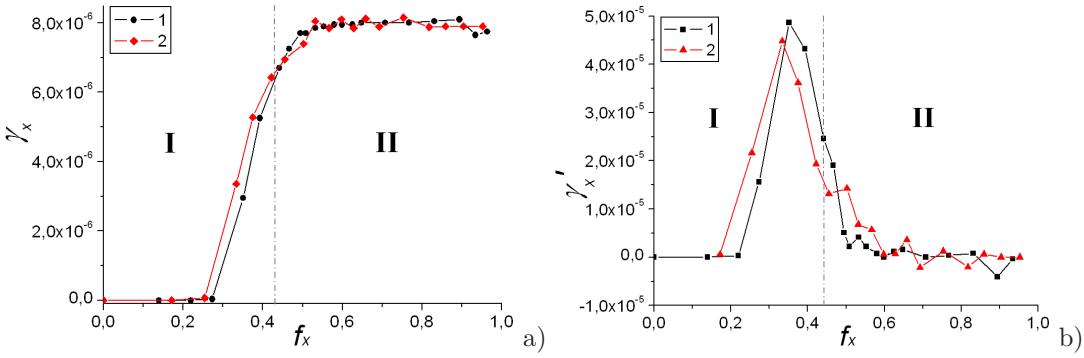


Figure 5: Reduced pulse-initiated shear displacement γ_x of the upper block (a) and its derivative $\gamma_x^{'}$ (b) versus the shear stress level f_x (S-wave loading). Curves 1 and 2 show interface deformation response at σ_y amounting respectively to 20% and 40% of the yield stress.

lation results showed that shear stress dependency of interface widening is also characterized by "jump" of the value of initiated displacement $\gamma_y{=}l_y/h$ in the region of transition from quasielastic to quasiplastic response stage (Fig. 6 and 7). In both cases (actions by P- and S-waves) the maximum of γ_y increases nearly linearly with normal stress σ_y (Fig. 6a and 7a).

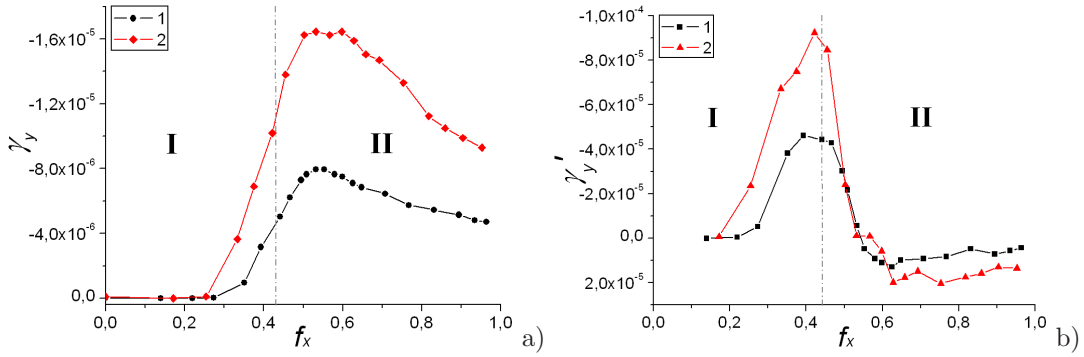


Figure 6: Reduced pulse-initiated normal displacement γ_y of the upper block (a) and its derivative $\gamma_y^{'}$ (b) versus the shear stress level f_x (compressive P-wave loading). Curves 1 and 2 show interface deformation response at σ_y amounting respectively to 20% and 40% of the yield stress.

At the same time, in case of S-waves absolute change of maximum value of derivative $\gamma_y^{'}{=}d\gamma_y/df_x$ with σ_y is much smaller than in case of P-waves. In particular, maximum value of $\gamma_y^{'}$ increases less than 20% under exposure to S-waves (Fig. 7b) and about 100% under exposure to P-waves (Fig. 6b) as σ_y increases twice. Thus, characteristics of "dilational" deformation response to exposure to elastic S-waves also demonstrate relatively small dependence on the value of normal stress σ_y (at least within the range of "moderate" values of σ_y).

Simulation results lead to an important conclusion that both theoretical and experimental study of deformation response of real fragments of fault zones to testing pulse dynamic exposure could be carried out with use of local sources of pulse perturbations of stress state, which generate mainly S-waves. In that case obtained data about interface deformation response could be interpreted the most unambiguously and will reliably characterize the shear stress level, i.e. the proximity of shear stress at the interface to the current value of stress corresponding to beginning of the stage of "macroscopic" irreversible deformation.

4 Future trends

In the general case fragments of geomedium (including fault zones) are under the condition of nonequaxial compression. Such stress state is characterized both by normal stress (σ_y) and by

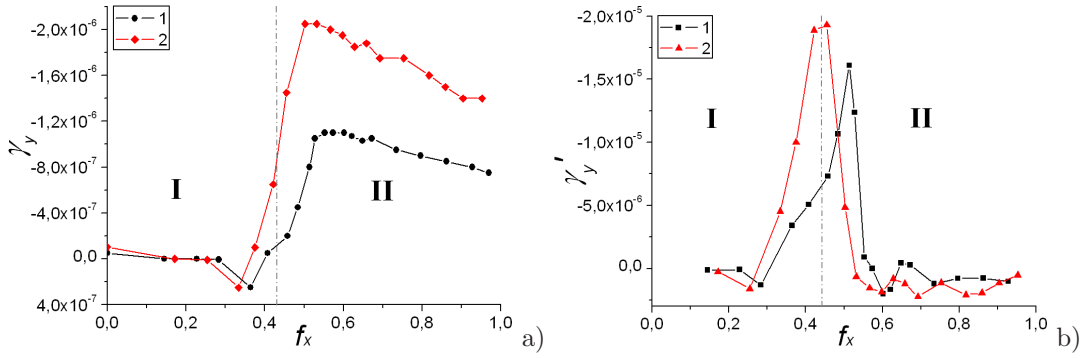


Figure 7: Reduced pulse-initiated normal displacement γ_y of the upper block (a) and its derivative $\gamma_y^{'}$ (b) versus the shear stress level f_x (S-wave loading). Curves 1 and 2 show interface deformation response at σ_y amounting respectively to 20% and 40% of the yield stress.

side compressive stress (σ_x). Results of previous study show that value of (σ_x) and ratio (σ_x)/(σ_y) (referred to as degree of the degree of nonequiaxiality of compression) have strong influence on dilatational effects during shear deformation of block-structured medium [10]. It is evident that these parameters of stress state should have an influence on features and the value of deformation response of structural block boundaries to testing dynamic actions. Such investigations are carried out at present time.

Other direction of planned study is analysis of change of interface deformation response to low-amplitude dynamic perturbations of stress state with depth of occurrence of considered medium layer. Such investigations are of fundamental importance since they gives an important information about character of behavior of block-structured geophysical medium under the conditions of complex and nonstationary stress field.

Acknowledgements

The investigation has been carried out at partial financial support of the RFBR Grant No. 09-05-00968-a, RAS Presidium Project No.11.2, Grant of the President of Russian Federation (MK-130.2010.5) and Russian Science Support Foundation.

References

[1] Sadovskiy M.A. // Transact. USSR Acad. Sci. Earth Sci. Ser. 1983. V.269. N 1. P.8-11.

[2] Kocharyan G.G. etc. // Doklady Earth Sciences. 2008. V.418. P.132-135.

[3] Ruzhich V.V. etc. // Russ. Geol. Geophys. 1999. V.40. P.356-368.

[4] Shilko E.V. // Phys. Mesomech. 2010. V.13. N 1-2. P.25-31.

[5] Psakhie S.G. etc. // Theor. Appl. Fract. Mech. 2001. V.37. P.311-334.

[6] Potyondy D.O. etc. // Int. J. Rock Mech. Min. Sci. 2004. V.41. P.1329-1364.

[7] Goldin S.V. etc. // Phys. Mesomech. 2001. V.4. N 3. P.91-97.

[8] Psakhie S.G. etc. // Tribol. Int. 2007. V.40. P.995-1003.

[9] Shilko E.V. etc. // Proc. of APM 2009. 2009. P.587-594.

[10] Astafurov S.V. etc. // Phys. Mesomech. 2009. V.12. N 6. P.23-32 (Rus.).

Evgeny V. Shilko, ISPMS SB RAS, pr. Akademicheskii 2/4, Tomsk, Russia, 634021
Sergey V. Astafurov, ISPMS SB RAS, pr. Akademicheskii 2/4, Tomsk, Russia, 634021
Alexander Yu. Grigoriev, Tomsk State University, pr. Lenina 36, Tomsk, Russia, 634050
Sergey G. Psakhie, ISPMS SB RAS, pr. Akademicheskii 2/4, Tomsk, Russia, 634021

Water droplet non-equilibrium interaction with flame zone

N. N. Smirnov V. F. Nikitin V. A. Nerchenko P. Andreini G. Manzini
ebifsun1@mech.math.msu.su giovanni.manzini@polimi.it

Abstract

The paper describes the results of investigation for non-equilibrium effects in fluid droplet flame interaction resulting in rapid droplet evaporation. The obtained solutions made it possible to compare the results with that provided by the existing equilibrium models and to determine the applicability limits for the existing equilibrium models.

The dimensionless criterion was developed characterizing the deviation of small liquid droplet evaporation process from the equilibrium, which permits to determine applicability limits for equilibrium models.

Investigating the behavior of individual droplets in a heated air flow allowed distinguishing two scenarios for droplet heating and evaporation. Small droplets undergo successively heating, then cooling due to heat losses for evaporation, and then rapid heating till the end of their life time. Larger droplets could directly be heated up to a critical temperature and then evaporate rapidly. Atomization of droplets interferes the heating and evaporation scenario.

1 Introduction

The goals of this study are the elaborations of heat, momentum and mass transfer models of fuel and water spray liquid droplets (fuel spray and water mist fire scenarios) and of fuel pool liquid (pool fire scenarios). Mainly the paper is focused on the heat transfer and the liquid - vapour phase transition. Such focus is needed to clarify the free burning and the fire suppression phenomena, particularly related to water mist systems effectiveness in the control, suppression and extinction of different type of fire. The problem of droplet interaction with the streaming gas flow was investigated taking into account mechanical drag, atomization of droplets, non-equilibrium heat and mass transfer. In modeling droplets breakup in a gas flow the inertia of the process should be taken into account. Fragmentation does not take place instantaneously: it needs time for small droplets to separate from the initial one, i. e. it needs a definite time for the liquid bridges between the droplets to be established, elongated and broken.

Mathematical models for individual droplets evaporation incorporated in polydispersed mixtures modeling, are usually based on the assumptions of the equilibrium character of phase transitions. [5] Adequate modeling of evaporation, which is extremely important for small droplets and sprays [1-4]. Comparison of theoretical and experimental data shows that this assumption being undoubtedly valid for large droplets and flat surfaces, brings to essential errors for small droplets [4, 10, 11].

The aim of the present study is to develop a mathematical model for the non-equilibrium evaporation of droplets and to determine the applicability limits for the existing quasi-equilibrium models.

2 Mathematical model

We regard an axis-symmetrical problem in the coordinate system with the center coinciding with the center of a droplet, the zone $x > x_W$ occupied by a gas mixture, the zone $0 < x < x_W$ – by liquid, $x = x_W$ being the phase interface.

The system of equations for the gas mixture above the interface ($x > x_W$) has the form:

$$\frac{\partial \rho}{\partial t} + \frac{1}{x^k}\frac{\partial \rho v x^k}{\partial x} = 0, \tag{1}$$

$$\frac{\partial \rho Y_i}{\partial t} + \frac{1}{x^k}\frac{\partial \rho Y_i v x^k}{\partial x} = \frac{1}{x^k}\frac{\partial}{\partial x}(x^k \rho D_i \frac{\partial Y_i}{\partial x}), \tag{2}$$

$$\frac{\partial \rho h}{\partial t} + \frac{1}{x^k}\frac{\partial \rho h v x^k}{\partial x} = \frac{1}{x^k}\frac{\partial}{\partial x}(x^k \lambda \frac{\partial T}{\partial x}) + \frac{1}{x^k}\frac{\partial}{\partial x}(x^k \rho T \sum_{i=1}^{N} D_i c_{pi} \frac{\partial Y_i}{\partial x}), \tag{3}$$

$$p = \rho \frac{R}{m} T = \rho R T \sum_{i=1}^{N} \frac{Y_i}{m_1} = \text{const}, \tag{4}$$

where ρ is density of the mixture; v – velocity; Y_i – mass concentration of the i-th component; m_i – its molar mass; D_i – diffusion coefficient; λ – heat conductivity; T – temperature; $h = c_p T = \sum_{i=1}^{N} c_{pi} Y_i T$ – specific enthalpy of the mixture; c_{pi} – specific heat capacity of the component at constant pressure; $k = 0, 1, 2$ correspond to the cases of plane, cylindrical and spherical symmetry respectively. Fluid $0 < x < x_W$ is assumed to be single component and uniformly heated.

The boundary conditions at phase interface $x = x_W$ are:

$$(\rho v)_g = (\rho v)_l = \dot{m}, \tag{5}$$

$$(\rho v Y_i)_g - (\rho D_i \frac{\partial Y_i}{\partial x})_g = (\rho v Y_i)_l - (\rho D_i \frac{\partial Y_i}{\partial x})_l = \dot{m}_i, \tag{6}$$

$$\sum_{i=1}^{N} h_{Li} \dot{m}_i = (\lambda \frac{\partial T}{\partial x})_g + (\lambda \frac{\partial T}{\partial x})_l + \dot{m} L \Delta h_x, \tag{7}$$

where subscripts g, l denote the values of parameters in gas and liquid phases respectively; h_{Li} is the specific enthalpy of phase transition. The modified Hertz-Knudsen equation for non-equilibrium evaporation will serve as an additional boundary condition:

$$p_i = p_e X_i = p_i^*(T_W) - \frac{1}{\delta_i}\sqrt{\frac{2\pi R T}{m_i}} \dot{m}_i, \tag{8}$$

where X_i is the molar concentration of the i-th component; p_i is the partial pressure of the i-th component above the interface; δ_i is the accommodation coefficient; $p_i^*(T_W)$ is the equilibrium vapor pressure for the i-th component at a temperature T_W , which could be determined from the Clausius-Clapeyron equation or its simplified solutions:

$$\frac{p_0}{p_i^*} = \exp \frac{h_{Li} m_i}{R} (\frac{1}{T_W} - \frac{1}{T_0}). \tag{9}$$

The boundary conditions at infinity ($x \to \infty$) are the following:

$$T = T_e, \quad Y_i = Y_{ie}, \quad i = 1, ..., N. \tag{10}$$

The boundary conditions in the center ($x \to 0$) are:

$$\frac{\partial T}{\partial x} = 0, \quad \frac{\partial Y_i}{\partial x} = 0, \quad i = 1, ..., N. \tag{11}$$

To solve the system (1)-(5) along with the boundary conditions (7)-(11) one needs to pose initial distributions for temperature and concentrations, which would not contradict the boundary conditions.

The sensitivity of results on non-equilibrium evaporation to variation of droplets radii and other parameters [11] brought us to the necessity to search for a universal dimensionless parameter, which could characterize the deviation of the evaporation process from an equilibrium one. To obtain an analytical solution we regard the simplified problem of a steady-state evaporation of a single droplet under non-equilibrium conditions.

3 Steady-state solution for non-equilibrium evaporation

Regard the steady-state problem of non-equilibrium evaporation of uni-component uniformly heated liquid droplet of a constant radius. The governing system of equations takes the form:

$x > x_W$:

$$\frac{d}{dx}(\rho v x^2) = 0, \tag{12}$$

$$\frac{d}{dx}(\rho Y_i v x^2) = \frac{d}{dx}(x^2 \rho D_i \frac{dY_i}{dx}), \quad i = 1, ..., N, \tag{13}$$

$$\frac{d}{dx}(\rho h v x^2) = \frac{d}{dx}(x^2 \lambda \frac{\partial y}{\partial x}) + \frac{d}{dx}(x^2 \rho T \sum_{i=1}^{N} D_i c_{pi} \frac{dY_i}{dx}), \tag{14}$$

$$p = \rho \frac{R}{m} T = \rho R T \sum_{i=1}^{N} \frac{Y_i}{m_1} = \text{const}; \tag{15}$$

$0 < x < x_W$:

$$Y_{Nl} = 1, \quad Y_{il} = 0, \quad 1 = 1, .., N-1, \quad T = T_W; \tag{16}$$

$x = x_W$:

$$(\rho v)_g = (\rho v)_l = \dot{m}, \tag{17}$$

$$\dot{m} Y_{ig} = (\rho D_i \frac{dY_i}{dx})_g, \tag{18}$$

$$\dot{m}(Y_{Ng} - 1) = (\rho D_N \frac{dY_N}{dx})_g, \tag{19}$$

$$h_L \dot{m} = (\lambda \frac{dT}{dx})_g, \tag{20}$$

$$p_e X_i = p_i^*(T_W) - \Delta p_i, \tag{21}$$

where $\Delta p_i = \frac{1}{\delta_i} \sqrt{\frac{2\pi RT}{m_i}} \dot{m}_i$ for the non-equilibrium model of phase transitions, and $\Delta p_i = 0$ – for an equilibrium one. The boundary conditions at infinity ($x \to \infty$) take the form:

$$T = T_e, \quad Y_i = Y_{ie}, \quad i = 1, ..., N. \tag{22}$$

As it follows from the equation (12) and the boundary condition (17) the following integral is valid within the gas phase:

$$\rho v = \dot{m} \frac{x_W^2}{x}. \tag{23}$$

The equation (14) could be converted into the following form:

$$\frac{d}{dx}(\rho v h x^2) = \frac{d}{dx}(x^2 \frac{\lambda}{c_p} \frac{\partial T}{\partial x}) + \frac{d}{dx}(x^2 \lambda T \sum_{i=1}^{N} (Le_i - 1) \frac{dY_i}{dx}), \tag{24}$$

which shows that for gases ($Le_i = \frac{\rho D_i c_{pi}}{\lambda} \approx 1$) the last term in the right hand side of the equation could be neglected.

On introducing the following dimensionless variables

$$z = \frac{x}{x_W}, \quad \chi_h = \frac{h}{h_e}, \quad \chi_l = \frac{h_l}{h_e}, \quad \chi_i = Y_i, \quad Pe = \frac{\dot{m} x_W}{\rho D}$$

the system of equations (13), (14) takes the form:

$$\frac{d\chi_i}{dz} = \frac{d}{dz}(\frac{z^2}{Pe} \frac{d\chi_i}{dz}), \quad i = 1, ..., N, h. \tag{25}$$

The boundary conditions for $z = 1$ are

$$\chi_{iW} = \frac{1}{Pe}(\frac{d\chi_{ig}}{dz})_W, \quad \chi_{NW} - 1 = \frac{1}{Pe}(\frac{d\chi_{Ng}}{dz})_W, \tag{26}$$

$$\chi_L = (\frac{1}{Pe}\frac{d\chi_h}{dz})_W, \tag{27}$$

$$X_N = X_N^* - \varsigma_N, \tag{28}$$

where $\varsigma_N = \frac{\Delta p_N}{p_e} = PeI_N\sqrt{\frac{c_{pe}m_e}{c_{pN}m_N}\chi_{hW}}$,

$$I_N = \frac{D_{eN}}{\delta_N x_W}\sqrt{\frac{2\pi}{R_e T_e}}. \tag{29}$$

Due to our derivations the deviation of the process from the equilibrium one could be characterized by a dimensionless parameter I_N.

The boundary conditions at infinity ($z \to \infty$) are:

$$\chi_h = 1, \quad \chi_i = Y_{ie}, \quad i = 1, ..., N. \tag{30}$$

Introducing a new variable

$$\xi(z) = \int_z^\infty \frac{Pe}{z^2}dz \Rightarrow \frac{d}{dz} = -\frac{Pe}{z^2}\frac{d}{d\xi}, \tag{31}$$

one could transform the equation (25) as follows

$$\frac{d\chi_j}{d\xi} = -\frac{d^2\chi_j}{d\xi^2}. \tag{32}$$

The solution of (32) is the following:

$$\chi_j = A_j + B_i e^{-\xi}, \quad j = 1, ..., N, h, \tag{33}$$

where A_j, B_j can be determined from the boundary conditions:

$$Y_{jW} = Y_{je}e^{-\xi_W}, \quad j = 1, ..., N-1;$$
$$Y_{NW} = 1 - (1 - Y_{Ne})e^{-\xi_W},$$
$$\chi_{hW} = 1 + \chi_L(1 - e^{\xi_W}). \tag{34}$$

Substituting (34) into the boundary condition (28) one obtains the equation determining the dimensionless evaporation rate ξ_W or the Peclet number Pe:

$$Y_{NW}\frac{m_W}{m_N} = X_N^*(\chi_{hW}) - PeI_N\sqrt{\Gamma_{eW}\frac{m_W}{m_N}\chi_{hW}}, \quad m_W = (\sum_{i=1}^N \frac{Y_{iW}}{m_i})^{-1},$$
$$\Gamma_{eW} = \frac{\gamma_e(\gamma_W - 1)}{\gamma_W(\gamma_e - 1)}, \quad \gamma = \frac{c_p}{c_v},$$
$$X_N^* = \frac{p_0}{p_e}\exp(\chi_L\frac{m_W}{m_N}\frac{\gamma_W}{(\gamma_W - 1)}(\frac{1}{\chi_{h0}} - \frac{1}{\chi_{hW}})). \tag{35}$$

The last expression for the phase equilibrium function could be also substituted by the data from the tables on the thermophysical properties of substances [13].

The solutions (33) providing flow parameters distribution around evaporating droplet were analyzed in [20].

The set of equations (34), (35) allows to determine the unknown Peclet number in non-equilibrium phase transitions as a function of the following parameters:

$$\frac{m_i}{m_N}, \quad \chi_L, \quad \frac{p_0}{p_e}, \quad Y_{ie}, \quad \Gamma_{eW}, \quad X_N^*(\chi_{hW}), \quad I_N.$$

The first six of them characterize the media and the boundary conditions. The seventh parameter I_N characterizes the deviation of the system from the equilibrium state. The value I_N is zero for the case of equilibrium, and it grows remaining positive($I_N > 0$) with the increase of the deviation from the equilibrium.

4 The role of non-equilibrium effects

To investigate the influence of non-equilibrium effects in phase transitions Peclet numbers for droplets evaporation were determined for different values of I_N parameter (Figure 1). The values of the other governing parameters were assumed to be the following

$$\frac{m_i}{m_N} = 4.75, \chi_L = 0.54, \frac{p_0}{p_e} = 1, Y_{Ne} = 0.1, \Gamma_{eW} = 1, \chi_{h0} = 0.9.$$

The Figure 1 gives the plots of Peclet numbers, obtained within the frames of non-equilibrium (Pe_{ne}) and quasi-equilibrium (Pe_{eq}) models. The value of $|\delta Pe|$ is also plotted in Figure 2 to characterize the relative deviation of Peclet number from its equilibrium value ($\delta Pe = \frac{Pe_{ne} - Pe_{eq}}{Pe_{eq}}$). The Peclet number for non-equilibrium evaporation could be determined by the formula

$$\frac{Pe}{Pe_{eq}} = \Psi_s(I_N, \frac{m_i}{m_N}, \chi_L, \frac{p_0}{p_e}, Y_{ie}, \Gamma_{eW}, X_N^*(\chi_{hW})), \tag{36}$$

where in the value of the Ψ_s – factor as a function of I_N parameter for the chosen values of other governing parameters is shown in Figure 2. The equilibrium Peclet number as obtained from the quasi-steady solution has the following form:

$$Pe_{eq} = \ln(1 + \frac{c_{pe}T_e - c_{pW}T_W}{h_L}). \tag{37}$$

The results of comparison of non-equilibrium and quasi-equilibrium Peclet numbers for droplet evaporation show that the rate of evaporation strongly depends on the value of the parameter I_N . On increasing I_N Peclet number decreases rapidly as compared with the equilibrium evaporation; the deviations of the evaporation rates from those predicted by the equilibrium model turn to be larger and larger. For $I_N < 1$ the divergence of equilibrium and non-equilibrium solutions $|\delta Pe|$ does not exceed 4 percent, for $I_N = 10$ the deviations increases up to 25 percent, for $I_N > 100$ the deviation surpasses an order of magnitude. Thus in order to have adequate estimates for small droplets evaporation rate one needs to use the non-equilibrium model for $I_N > 1$.

To have adequate data for small droplets ($I_N > 1$) evaporation rates it is necessary to use the non-equilibrium model.

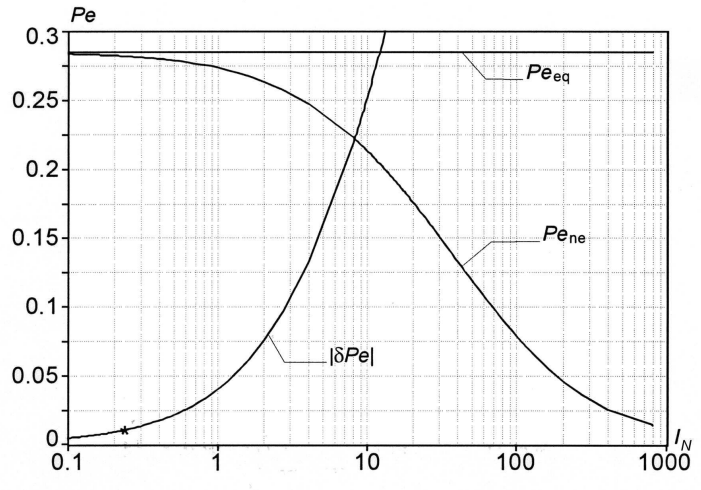


Figure 1: Peclet number variation versus I_N parameter for equilibrium and non-equilibrium evaporation.

An analytical formula was obtained in [20] for dimensionless evaporation rate ξ_W assuming it to be a small value $\xi_0 \ll 1$, which meant that $Pe \ll 1$.

The results of theoretical and numerical analysis show that in order to have adequate data for evaporation rates of small droplets ($I_N > 1$) it is necessary to use the non-equilibrium model.

5 Quasi-steady solution for a single droplet evaporation

Investigations of unsteady-state droplet evaporation show that for small droplets flow parameters in gas phase reach their quasi-steady values very quickly. Thus the quasi-steady approximation regarding droplet evaporation could be used, which means that its radius decreases in time much slower than gas flow parameters come to a steady state. Thus it is assumed, that the rate of droplet evaporation for each time moment could be determined based on the obtained steady non-equilibrium solution. Then the decrease of the droplet radius can be determined by the following formula:

$$\frac{dx_W}{dt} = -\frac{\dot{m}}{\rho_{Nl}}. \tag{38}$$

On introducing dimensionless variables

$$r = \frac{x_W}{x_{W0}}, \quad \tau = \frac{t}{t_0}, \quad t_0 = \frac{\rho_{Nl} x_{W0}^2}{2\rho_e D_e Pe_{eq}} \tag{39}$$

equation (40) takes the form

$$\frac{dr}{d\tau} = -\frac{\dot{m} t_0}{\rho_{Nl} x_{W0}} = -\frac{Pe}{r}\frac{\rho_e D_e t_0}{\rho_{Nl} x_{W0}^2} = -\frac{1}{2r}\frac{Pe}{Pe_{eq}}, \tag{40}$$

where x_{W0} is the initial radius, t_0 is the characteristic time for droplet evaporation under equilibrium conditions.

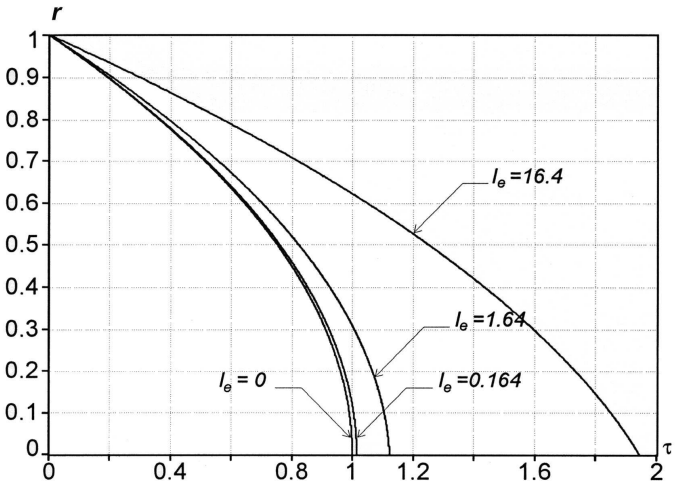


Figure 2: Droplet dimensionless radius variation versus time for different initial values of I_{Ne} parameter characterizing deviation of the system from the equilibrium.

Figure 2 presents the comparison of $r(\tau)$ functions (trajectories) obtained for different initial values of I parameter ($I_e = \frac{D_e}{\delta_N x_{W0}}\sqrt{\frac{2\pi}{R_e T_e}}$) characterizing initial deviation of the system from an equilibrium state [11]. Increasing the initial deviation from the equilibrium brings to a decrease of the slope of the curve and increases the actual time for droplet evaporation.

The results present in Figure 2 could serve as an estimate for the effect of non-equilibrium evaporation on droplet life time. On decreasing droplet radius parameter I_e itself increases thus bringing to a more strong deviation from equilibrium. Approximations present in [20] make it possible to provide analytical formula for Peclet number dependence on I_e parameter for small ξ_W :

$$Pe = \frac{Pe_{eq}}{1 + K \cdot I_e} = \frac{Pe_{eq}}{1 + \frac{x_{We}}{x_W}\frac{K_1}{\delta}}, \tag{41}$$

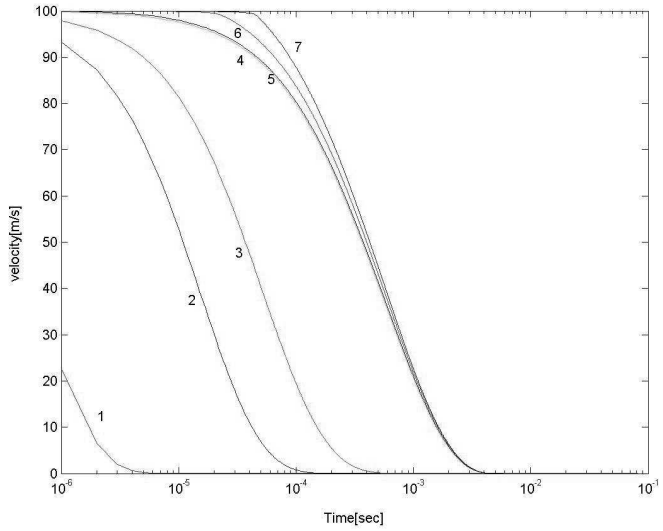


Figure 3: Velocity relaxation versus time for droplets of different diameters. $V_0 = 100m/s$, taking into account atomization.

where δ is accommodation coefficient. Substituting (43) in (42) and solving the differential equation one obtains

$$r = -\frac{K_1}{\delta} + \sqrt{(\frac{K_1}{\delta} + 1)^2 - \tau}.$$

Thus characteristic time for droplet evaporation is always greater than unity and increases on decreasing accommodation coefficient:

$$\tau = 1 + 2\frac{K_1}{\delta}.$$

6 Droplet evaporation in a streaming flow

Droplets in quiescent gas could be observed only in microgravity and investigation of their evaporation is performed to obtain material and kinetic data. Under normal gravity condition on evaporating in a heated atmosphere droplet generates a cooler environment due to energy consumption for evaporation. Thus thermo-convective induced flows are possible. Another case is streaming flows, which are characterized by presence of velocity difference between gas and droplet. The mathematical model for droplet evaporation moving in a heated gas was present in [19, 21].

The problem of droplet interaction with the streaming gas flow was investigated taking into account mechanical drag, atomization of droplets, non-equilibrium heat and mass transfer. A series of model problems was regarded, in which gas flow and droplet initially had different relative velocities and temperatures, and then relaxation took place. Those model problems are similar to that encountered in shock wave initiation of detonation in combustible dispersed fuel-air mixtures. The two-phase flow becomes strongly non-equilibrium behind the shock wave, because due to mechanical inertia droplets keep their speed practically constant and gas accelerates on passing the shock wave. Besides, due to thermal inertia, temperature inside droplets practically does not change, while gas temperature increases instantaneously behind the shock wave. Due to that reason gas temperature in all the numerical experiments was assumed to be higher than the boiling temperature for liquid droplets.

The thermophysical properties for gas and droplets were assumed similar for all numerical experiments: ambient pressure $p = 1.013$ bar, temperature $T = 1000$ K, gaseous phase – air, liquid – n-decane ($C_{10}H_{22}$). Initial droplet temperature was assumed to be $T = 300$ K.

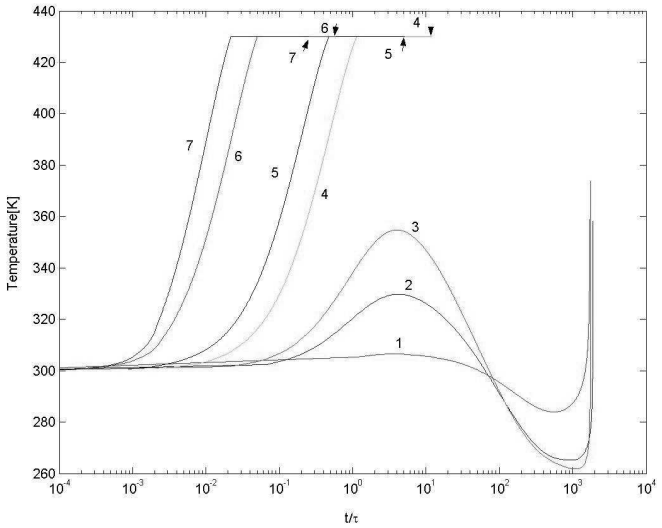


Figure 4: Mean droplet temperature variation versus time for droplets of different diameters. $V_0 = 100m/s$, taking into account atomization.

The relaxation processes for droplets of different diameters were regarded. Numbered lines on the successive figures correspond to the following initial diameters of droplets (curves 1(1 μm), 2(5 μm), 3(10 μm), 4(50 μm), 5(100 μm), 6(500 μm), 7(1000 μm)). Figures 3-6 illustrate parameters of droplets variation in the process of mechanical and thermal relaxation for the set of numerical experiments assuming initial velocity difference to be equal to 100 m/s. One could distinguish the characteristic time for each droplet being the function of its initial diameter and relative gas velocity.

$$\tau = \frac{v_0}{a_0}, \text{where } a_0 = \frac{f_d(t=0)}{m_0}.$$

Figure 3 illustrates velocity relaxation. It is seen that on decreasing initial droplet radius the relaxation process turns to be faster. The decrease of the relaxation time is monotonous. Some curves begin lower than 50 m/s because the relaxation process is too fast for small droplets, and the time scale on the x-axis is logarithmic beginning from a definite small value.

Figure 4 illustrates droplet temperature variation versus time for droplets of different initial diameters.

The dynamics of droplet heating is the following. For small droplets (curves 1(1 μm), 2(5 μm), 3(10 μm)) in the very beginning the temperature increases due to external heating. On rapid decrease of droplet relative velocity evaporation in the stream of gas brings to a decrease of temperature. Then on decreasing droplet radius heat fluxes growth brings to an increase of temperature until the droplet disappears. The first increase of temperature is higher for larger droplets, which relative velocity decreases much slower than for small droplets (curves 4(50 μm), 5(100 μm), 6(500 μm), 7(1000 μm)). Large droplets follow different scenario: the first increase of their temperature goes as high as up to the critical value. Then evaporation takes place at a critical temperature very rapidly. Arrows with numbers in Figures 4 and 6 indicate the end of droplet life time. That is the reason for a larger droplet (curves 5, 6, 7 in Figure 4) to have a shorter life time. As it is seen from the figure all maxima and minima of temperature correspond to nearly the same normalized time moments independently on initial droplet radius. The difference between the two scenarios for droplet behavior in the stream of heated air could be clearly distinguished from this figure.

Figure 5 illustrates droplet diameter variation due to evaporation. It is seen from the figure that evaporation time increases with the increase of initial droplet diameter, but the increase does not take place monotonously: the increase of life time (curves 1, 2, 3) changes for a decrease

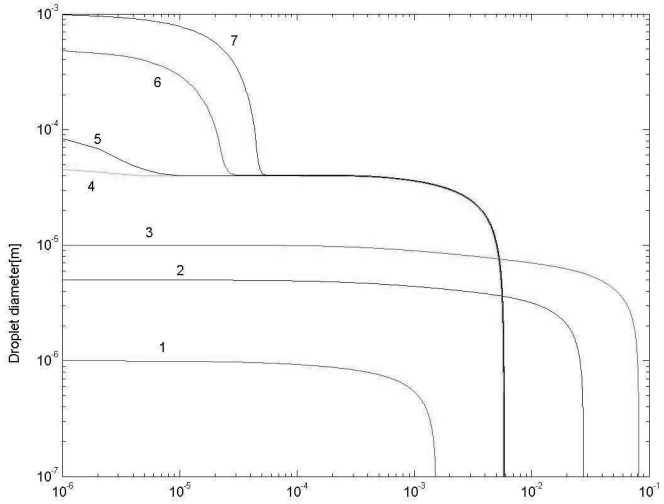


Figure 5: Droplet diameter variation versus time for droplets of different diameters. $V_0 = 100m/s$, taking into account atomization.

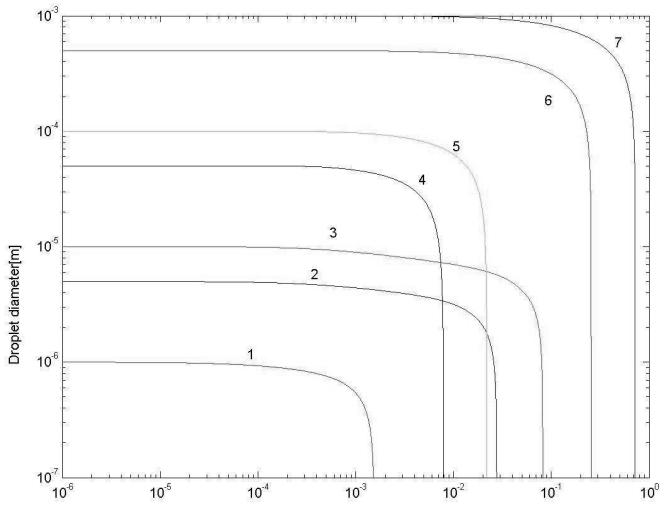


Figure 6: Droplet diameter variation versus time for droplets of different diameters. $V_0 = 100m/s$, atomization not taken into account.

(curves 4, 5, 6). That testifies the effect of manifestation of different mechanisms depending on the characteristic size of droplets. The first rapid decrease of droplet radius (curves 5, 6, 7 in Figure 5) is due to atomization of large droplets. The breakup of large droplets (Figure 5) brings to the conditions that behavior of droplets of initial diameter 100 μm, 500 microns and 1000 microns looks absolutely similar after some time necessary for atomization to proceed.

Atomization of droplets changes droplet lifetime and evaporation scenario for large droplets. Figure 6 illustrates droplet diameter variation for droplets of different initial size in interaction with streaming flow not accounting for atomization. Comparison with Figure 5 representing results with account of atomization clearly demonstrates the effect.

7 Droplet cloud injection into heated atmosphere of high pressure chamber

To investigate the cloud slowing down, heating of particles and surrounding atmosphere, atomization of droplets and shock wave formation due to the transformation of the kinetic energy of the cloud into thermal and kinetic energy of the surrounding gas it is necessary to apply the models for multiphase media accounting for the two-way coupling effects for fragments and gas, thermochemical and mechanical destruction of fragments.

Mathematical models for the non-equilibrium polydispersed mixture flows and breakup of pressurized vessels in non-uniform internal loading are described in details in the papers [19, 20, 21].

The cloud of small droplets injected into the chamber slows down very rapidly due to the drag forces. The deceleration for fragments is proportional to $\frac{1}{r_0}$ and grows up with the decrease of a characteristic size r_0. The velocity variation versus distance could be estimated by formula:

$$v_{rel} = v_{rel}^0 \exp(-\frac{3}{8} C_d \frac{\rho}{\rho_c} \frac{x}{\rho_0}). \tag{42}$$

It is seen from (44) that on decreasing droplet size the slowing down distance also decreases. Since droplet cloud incorporates a variety of droplets having different size and speed its evolution could bring to a peculiar non-uniform pattern of droplets distribution within the combustion chamber.

On slowing down the cloud its kinetic energy is converted into the internal energy of the surrounding gas. Droplets are being heated and evaporate. Thus mixture formation takes place.

Numerical modeling of jet injection into a gas-filled cylindrical containment from the wall along the axis was performed based on the developed mathematical models [16, 19]. A cylindrical containment of 0.1 m radius and 0.2 m height was regarded. A cloud of small droplets, characterized by the average diameter 0.3 mm and stochastic deviations 0.05 mm was injected from left bottom along the axis. The fragments initial temperature was 400 K with stochastic deviations 10 K; maximal velocity in the axial direction was assumed to be 20 m/s, average velocity 15 m/s with stochastic deviations 5 m/s both in axial and radial directions. The average density of liquid was assumed as $\rho_c = 1000 kg/m^3$, viscosity and surface tension in the liquid 10^{-3} Ns and 10^{-2} N/m respectively. The gas pressure inside the containment was varied from 0.01 MPa up to 1.5 MPa, initial temperature $T_0 = 700$ K, molar mass 0.028 kg/mol.

Figures 7 and 8 show the model particles location for the two successive times. The initial pressure of gas inside the containment was rather low: $p_0 = 0.01$ MPa (0.1 atm). The size of circles showing model particles is much larger than their real size, but directly proportional to it. The intensity of color reflects particles temperature.

Figures 9, 10 and 11 illustrate the model particles locations for the case of a relatively high gas pressure inside the containment ($p_0 = 1$ MPa (10 atm)). The aerodynamic drag is much more essential for the present case. On entering the containment fragmentation of liquid droplets due to their interaction with the atmosphere brings to a formation of very fine droplets in the front part of the cloud (Figure 9). The droplets, representing smaller fragments, are illustrated by dots in Figure 9. Nevertheless, the major mass of the cloud is represented by those dots, and only a smaller number of low velocity particles keep its initial size.

The small droplets slow down very rapidly and loose their kinetic energy much faster then the large ones. thus the large fragments, that had initially much lower velocity, come to overtake the small ones (Figures 10, 11).

8 Conclusions

The dimensionless criterion was developed characterizing the deviation of small liquid droplet evaporation process from the equilibrium, which permits to determine applicability limits for equilibrium models.

It was demonstrated that non-equilibrium models more adequately describe final stages of droplet evaporation. Those models are free from the common drawbacks of all quasi-equilibrium

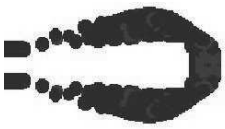


Figure 7: Model particles location for droplet cloud injection into the chamber with low gas pressure $p_0 = 0.01$ MPa (0.1 atm).

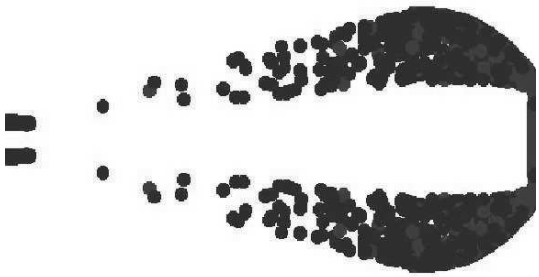


Figure 8: Successive stage for droplet cloud injection into the chamber with low gas pressure $p_0 = 0.01$ MPa (0.1 atm).



Figure 9: Model particles location for droplet cloud injection into the chamber with high gas pressure $p_0 = 1$ MPa (10 atm).

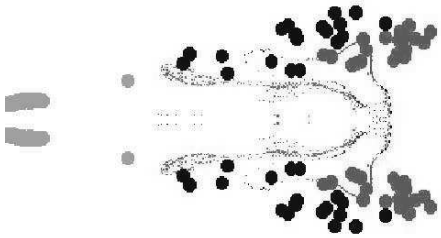


Figure 10: Successive stage for droplet cloud injection into the chamber with high gas pressure $p_0 = 1$ MPa (10 atm).

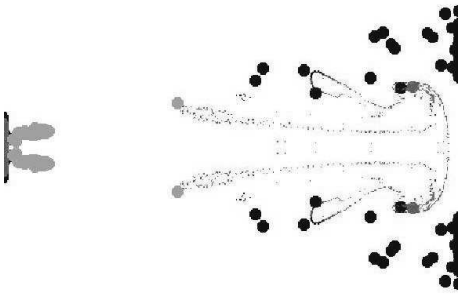


Figure 11: Final stage for droplet cloud injection into the chamber with high gas pressure $p_0 = 1$ MPa (10 atm).

models, because non-equilibrium approach allows to avoid non-physical growth of the evaporation rate on decreasing droplet radius.

Accounting for non-equilibrium effects produces an influence on the integral characteristics of droplet evaporation process. The lifetime for single evaporating droplet could be several times

longer under non-equilibrium conditions as compared with equilibrium ones.

Investigating the behavior of individual droplets in a heated air flow allowed distinguish two scenarios for droplet heating and evaporation. Small droplets undergo successively heating, then cooling due to heat losses for evaporation, and then rapid heating till the end of their life time. Larger droplets could directly be heated up to a critical temperature and then evaporate rapidly. Atomization affects droplet life time.

Investigation of poly-dispersed multi-velocity droplet cloud injection into the heated atmosphere of a combustion chamber showed that flow scenario essentially depends on gas state (pressure and temperature) inside the chamber. The fastest droplets undergo fragmentation and slow down rapidly, while the slowest droplets remain big and overtake small ones. This droplet size separation effect manifests stronger for the case of higher gas density inside the chamber.

Acknowledgements

The present research was supported by the Russian Foundation for Basic Research and EINSTEIN Consortium, Italy (Project Code 09-03-92421).

References

[1] Fuchs N.A. Evaporation and droplet growth in gaseous media. Pergamon Press, London, 1959.

[2] Kampher G.M. On the limits of equilibrium regime for droplet evaporation. Proc MADI, Moscow, 1974, Issue 71, pp. 43-52.

[3] Ivchenko I.N. On heat and mass transfer in evaporation and condensation growth of small spherical droplets. Thermophysics of High Temperatures, 1985, vol. 23, No 4, pp. 787-791.

[4] Miller R.S., Harstad K., Bellan J. Evaluation of equilibrium and non-equilibrium models for many-droplet gas-liquid flow simulations. International Journal of Multiphase Flow, 1998, vol. 24, No 6, pp. 1025-1055.

[5] Smirnov N.N., Zverev I.N. Heterogeneous Combustion. Moscow, Moscow Univ. Publ., 1992.

[6] Smirnov N.N. Heat and Mass Transfer in Unsteady-State Diffusion Combustion of a Condensed Fuel Surface. International Journal of Heat and Mass Transfer, 1986, vol. 29, No 5, pp.673-679.

[7] Smirnov N.N., Nikitin V.F., Baskakov V.V. Unsteady-State Combustion of Fuel Droplets in Weightlessness. Physical Sciences in Microgravity. Proc. X-th Europ., VI-th Russ. Symp. Moscow, 1997, vol. 1, pp. 409-416.

[8] Smirnov N.N., Nikitin V.F., Baskakov V.V. Droplets and Polydispersed Sprays Combustion Under Microgravity. Advanced Combustion Research Proc. ESA Workshop, C.N.R.S., Orleans, 1997, 15 p.

[9] Tanabe M., Konig J., Moriue O., Eigenbrod Ch., Sato J., Kono M., Rath H.J. Autoignition Behaviour of Single Hydrocarbon Fuel Droplets. Proc. Drop Tower Days in Bremen, Bremen, 1996, pp. 310-312.

[10] Smirnov N.N., Kulchitskiy A.V. Non-equilibrium Effects in Liquid Fuel Droplets Combustion. Proc. 51-st IAF Congress, Rio de Janeiro, 2000, IAF-00-J.4.09, 9 p.

[11] Kulchitskiy A.V., Smirnov N.N., Accounting for Non-equilibrium Effects in Evaporation of solution droplet. Journal of Engineering Thermophysics, 2000, vol. 10, No 4, 293-314.

[12] Picker G., Straub J. Evaporation Coefficient Determined from Vapor Bubbles Growing under Microgravity Conditions. Heat Transfer 1998, Proc. 11th IHTC,Kyongju, 1988, vol. 2.

[13] Vargaftic N.B. Handbook on Thermophysical Properties for Fluids and Gases. Moscow, Science Publ., 1963.

[14] Chernyi G.G. Gas Dynamics. Moscow, Science Publ., 1990.

[15] Smirnov N.N., Pushkin V.N., Dushin V.R., Kulchitskiy A.V. Microgravity investigation of laminar flame propagation in monodisperse gas-droplet mixtures. Acta Astronautica, 2007, vol. 61, 626-636.

[16] Smirnov N.N. Nikitin V.F. Khadem J. Aliari Shourekhdeli Sh. Onset of Detonation in Polydispersed Fuel-Air Mixtures. Proceedings of the Combustion Institute. 2006, vol. 31, pp. 832-841.

[17] Azzopardi B.J., Hewitt G.F., Multiphase Sci.Tech., 9, (1997), 109-204.

[18] Smirnov N.N., Int.J.Heat Mass Transfer, 1988, vol. 31, No 4, pp. 779–793.

[19] Smirnov N.N. (Ed.) Space Debris Hazard Evaluation and Mitigation. Taylor and Francis, London-New York, 2002.

[20] V.R. Dushin, A.V. Kulchitskiy, V.A. Nerchenko, V.F. Nikitin, E.S. Osadchaya, Yu.G. Phylippov, N.N. Smirnov. Mathematical simulation for non-equilibrium droplet evaporation. Acta Astronautica, 2008, vol. 63, pp 1360-1371.

[21] Nikitin V.F., Betelin V.B., Dushin V.R. , Kulchitskiy A.V., Kushnirenko A.G., Osadchaya E.S., Smirnov N.N. Non-equilibrium effects on gas - fluid interfaces in droplet jet injection into combustion chamber computer simulation. Proc. 60-th Internat. Astronautical Congress, Daegeon, 2009, IAC-09-A2.2.05, 11 p.

N. N. Smirnov, V. F. Nikitin, V. A. Nerchenko, Moscow M.V. Lomonosov State University, Moscow, Russia
Pierangelo Andreini, Giovanni Manzini, Politecnico di Milano, Milan, Italy

Wave formation on free surface on interaction with a body moving under free surface

M. N. Smirnova K. A. Kondrat'ev A. V. Zvyaguin
wonrims@inbox.ru

Abstract

The two-dimensional problem of surface waves formation and interaction under the conditions of thin body motion in compressible fluid near free surface was regarded. The fluid is assumed occupying infinite semi-space, gravity is neglected as compared with fluid inertia. The solution was obtained for a problem of infinite and finite span plate motion in compressible fluid at a definite depth, constant velocity and inclination angle. The solution allows determining free surface shape, drag and lift forces. In the limiting cases of relatively small and relatively big depth the obtained solution permitted analytical approximation. For relatively thin fluid layer above the moving body the resistance force depends on body thickness, inclination and Mach number, while for relatively thick fluid layer the force depends on body length, inclination angle and Mach number as well. The solution was obtained numerically for all the range of variation of governing parameters. Approximation formulas for numerical solution were developed, which coincide with analytical formulas for the limiting cases.

1 Introduction

The problem is relevant to underwater high velocity gliding of thin wing, which is often used to reduce resistance of the glider. During the motion in water the wing having a definite angle of attack produces a lift force, which leads to suspending of a boat thus reducing the overall resistance to the resistance of the wing. The goal of the overall solution was in developing analytical and semi-analytical formulas for evaluating the lift and drag forces. Another important application is determining resistance force being the function of the depth in underwater motion of a bullet or shell. The problem of gliding over the free surface of water of infinite and finite depth was regarded within the frames of linear [1–4] and non-linear [5, 6] statements, and found its generalized classical solution in [7]. High speed streaming flows accounting for fluid compressibility were investigated in [8–10].

2 Mathematical statement of the problem

The two-dimensional problem of fluid streaming thin body motion of infinite (Fig. 1, 2) and finite (Fig. 3) span with velocity parallel to free surface is regarded under the assumption of flow separation from the upper or lower surface of the body. In case of cavity formation it is closed at some distance from the body. Pressure on free surface is assumed equal to vapor ambient pressure. Pressure in the cavity is assumed equal to the value depended on the constant of cavitation. Fluid is assumed to be ideal, depth – infinite, mass forces – negligibly small, flow field – plane. Velocity field in fluid is assumed to be potential

$$\overrightarrow{V} = \overrightarrow{V_0} + grad\varphi, \tag{1}$$

fluid will be regarded as linear compressible

$$P = P_0 + a^2(\rho - \rho_0), a^2 = (\frac{dP}{d\rho})_{\rho_0}, \tag{2}$$

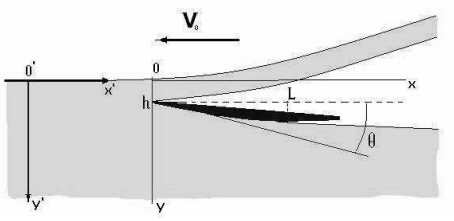


Figure 1: Thin body streaming by a compressible fluid at a depth h , constant velocity V_0 parallel to free surface and inclination angle θ. Flow separation from the upper surface.

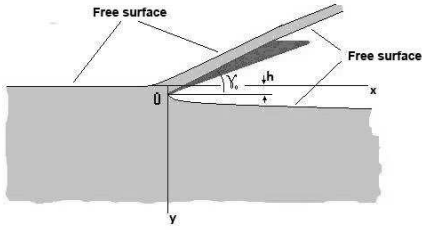


Figure 2: Thin body streaming by a compressible fluid at a depth h , constant velocity V_0 parallel to free surface and inclination angle θ. Flow separation from the bottom surface.

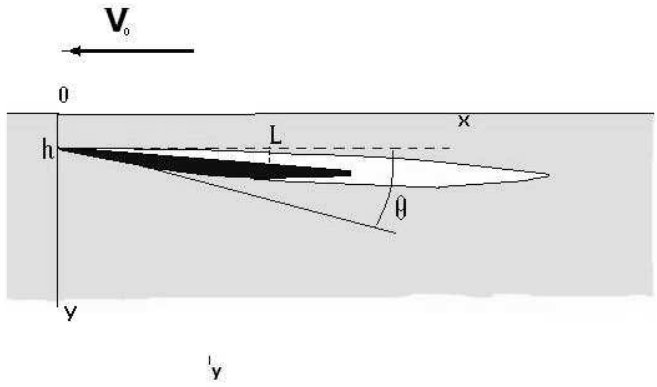


Figure 3: Thin body streaming by a compressible fluid at a depth h , constant velocity V_0 parallel to free surface and inclination angle θ. Flow separation from the upper surface. Closed cavity.

where $\varphi(x, y, t)$ – disturbance velocity potential, P, ρ – fluid pressure and density, P_0, ρ_0 – pressure and density in quiescent fluid, a – sonic velocity.

Fluid flow satisfies continuity equation

$$\frac{d\rho}{dt} + \rho \mathrm{div}\overrightarrow{V} = 0, \tag{3}$$

pressure is determined by Cauchy-Lagrange integral

$$\frac{\partial\varphi}{\partial t} + \frac{(grad\varphi)^2}{2} + \int \frac{dP}{\rho} = \mathrm{c(t)}. \tag{4}$$

Flow induced variations of density and velocity are considered small values.

$$\frac{\rho'}{\rho} = \frac{\rho - \rho_0}{\rho} \ll 1, \frac{V_x}{V_0} \ll 1, \frac{V_y}{V_0} \ll 1,$$

where V_x, V_y – disturbance velocity components.

Then it follows from continuity equation (3), integral (4) and relationships (1), (2) neglecting small values of the orders higher than one, flow potential under the condition of steady-state flow satisfies the equation

$$V_0^2 \frac{\partial^2\varphi}{\partial x} = a^2(\frac{\partial^2\varphi}{\partial x} + \frac{\partial^2\varphi}{\partial y}), \tag{5}$$

and fluid pressure is determined

$$P - P_0 = \rho_0 V_0 \frac{\partial \varphi}{\partial x}. \tag{6}$$

Boundary conditions should be satisfied on the free surfaces, on the body surface contacting fluid and in the cavity. On the free surface and in the cavity constant pressure is assumed, on the fluid-body contact streaming condition of the equality of normal velocity component. The obstacle being thin and inclination angle being small all disturbances could be considered small, and boundary conditions take the form

$$\begin{aligned}
&y = 0 \quad P - P_0 = 0;\\
&y = h^+, 0 < x < L \quad V_y = \frac{\partial \varphi}{\partial y} = V_0 \sin\theta;\\
&1.\quad y = h^-, 0 < x; \quad y = h^+, L < x \quad P - P_0 = 0;\\
&2.\quad y = h^-, L < x; \quad y = h^+, 0 < x \quad P - P_0 = 0;\\
&3.\quad y = h^-, 0 < x < S; \quad y = h^+, L < x < S\\
&P - P_0 = -\Delta P, \Delta P = C_{cav.min} \frac{\rho_0 V_0^2}{2};\\
&y = h^{\pm}, L < x \quad V_x = \frac{\partial \varphi}{\partial x} = 0.
\end{aligned} \tag{7}$$

Substituting in (7) dynamical equation (6) boundary conditions look as follows

$$\begin{aligned}
&y = 0 \quad \frac{\partial \varphi}{\partial x} = 0;\\
&y = h^+, 0 < x < L \quad \frac{\partial \varphi}{\partial y} = V_0 \sin\theta;\\
&1.\quad y = h^-, 0 < x; \quad y = h^+, L < x \quad \frac{\partial \varphi}{\partial x} = 0;\\
&2.\quad y = h^-, L < x; \quad y = h^+, 0 < x \quad \frac{\partial \varphi}{\partial x} = 0;\\
&3.\quad y = h^-, 0 < x < S; \quad y = h^+, L < x < S\\
&\frac{\partial \varphi}{\partial x} = -\frac{\Delta P}{\rho_0 V_0};\\
&y = h^{\pm}, L < x \quad \frac{\partial \varphi}{\partial x} = 0.
\end{aligned} \tag{8}$$

Thus equation (5) with boundary conditions (8) present a closed form statement of the problem.

3 Problem solution

We assume the flow to be subsonic. Then on introducing dimensionless parameter $\alpha = \sqrt{1 - M^2}$, where $M = \frac{V_0}{a}$ – Mach number and dimensionless functions and variables

$$\varphi^* = \frac{\pi \varphi}{ah}, \quad p^* = \frac{P - P_0}{\rho_0 a^2}, \quad l = \frac{\pi L}{\alpha h}, \quad s = \frac{\pi S}{\alpha h}, \quad x^* = \frac{\pi x}{\alpha h}, \quad y^* = \frac{\pi y}{h}, \tag{9}$$

equations and boundary conditions take the form

$$\begin{aligned}
&\frac{\partial^2\varphi^*}{\partial x^{*2}}+\frac{\partial^2\varphi^*}{\partial y^{*2}}=0,\quad p^*=\frac{M}{\alpha}\frac{\partial\varphi^*}{\partial x^*};\\
&y^*=0\quad \frac{\partial\varphi^*}{\partial x^*}=0;\\
&y^*=\pi^+, 0<x^*<l\quad \frac{\partial\varphi^*}{\partial y^*}=\frac{M\gamma(x^*)}{\alpha};\\
&1.\quad y^*=\pi^-, 0<x^*;\quad y^*=\pi^+, l<x^*\quad \frac{\partial\varphi^*}{\partial x^*}=0;\\
&2.\quad y^*=\pi^-, l<x^*;\quad y^*=\pi^+, 0<x^*\quad \frac{\partial\varphi^*}{\partial x^*}=0;\\
&3.\quad y^*=\pi^-, 0<x^*<s;\quad y^*=\pi^+, l<x^*<s\\
&\frac{\partial\varphi^*}{\partial x^*}=-\frac{\Delta P\alpha}{\rho_0 V_0 a};\\
&y^*=\pi^\pm, l<x^*\quad \frac{\partial\varphi^*}{\partial x^*}=0.
\end{aligned}\tag{10}$$

$$\sin\theta\approx\tan\theta=\frac{dy}{dx}=\frac{1}{\alpha}\frac{dy^*}{dx^*}=\frac{\gamma(x^*)}{\alpha}.$$

In successive derivations star in dimensionless value symbols will be omitted. The problem is reduced to developing analytical function in the domain $y>0$ with a cut $y=\pi, x>0$, satisfying boundary conditions (10). The solution will be developed in the form of a real part for the analytical function of a complex variable $\varphi(x,y)=Re\Phi(z), z=x+iy$. Thus development of the analytical function is reduced to Riemann-Hilbert problem. The latter for a special function type is reduced to Dirichlet problem. The solution for the Dirichlet problem is given by Schwarz integral. In case inclination angle is constant this integral can be taken in elementary functions. The projections of forces are given by the following formulas:

$$X=\frac{\rho_0 a^2 h M^2\gamma_0^2(\sqrt{u_0^+}-1)^2}{2\alpha^2},\qquad Y=-\frac{\rho_0 a^2 h M^2\gamma_0(\sqrt{u_0^+}-1)^2}{2\alpha}$$

– flow separation from the upper surface of the body, singularity at the front edge of the plate.

$$X=\frac{\rho_0 a^2 h M^2\gamma_0^2(2\sqrt{u_0^+}-3u_0^++u_0^{+2})}{\alpha^2 u_0^+},\qquad Y=-\frac{\rho_0 a^2 h M^2\gamma_0(2\sqrt{u_0^+}-3u_0^++u_0^{+2})}{\alpha u_0^+}$$

– flow separation from the upper surface of the body, singularity at the rear edge of the plate.

$$X=\frac{\rho_0 a^2 h M^2\gamma_0^2(\sqrt{u_0^-}-1)^2}{2\alpha^2},\qquad Y=\frac{\rho_0 a^2 h M^2\gamma_0(\sqrt{u_0^-}-1)^2}{2\alpha}$$

– flow separation from the lower surface of the body, singularity at the front edge of the plate.

$$X=\frac{\rho_0 a^2 h M^2\gamma_0^2(-2\sqrt{u_0^-}+3u_0^--u_0^{-2})}{\alpha^2 u_0^-},\qquad Y=\frac{\rho_0 a^2 h M^2\gamma_0(-2\sqrt{u_0^-}+3u_0^--u_0^{-2})}{\alpha u_0^-}$$

–flow separation from the lower surface of the body, singularity at the rear edge of the plate.

$$\begin{aligned}
X=&\frac{\rho_0 a^2 h M^2\gamma_0^2(2\sqrt{u_0^+}-3u_0^++u_0^{+2})}{\alpha^2 u_0^+}+\\
&+\frac{ahM\gamma_0\Delta P(u_0^++1)}{2\pi V_0}\ln\Big|\frac{(1+\sqrt{\frac{s_0^+-u_0^+}{s_0^+-1}})(1-\sqrt{\frac{s_0^--u_0^+}{s_0^--1}})}{(1-\sqrt{\frac{s_0^+-u_0^+}{s_0^+-1}})(1+\sqrt{\frac{s_0^--u_0^+}{s_0^--1}})}\Big|\frac{(2\sqrt{u_0^+}-3u_0^++u_0^{+2})}{(u_0^+-1)^3}+\\
&+\frac{M^2\gamma_0^2\Delta P h}{\pi\alpha^2}(u_0^+-\ln u_0^+-1),
\end{aligned}$$

$$Y = -\frac{\rho_0 a^2 h M^2 \gamma_0 (2\sqrt{u_0^+} - 3u_0^+ + u_0^{+2})}{\alpha u_0^+} -$$
$$- \frac{ahM\alpha\Delta P(u_0^+ + 1)}{2\pi V_0} \ln \left| \frac{(1 + \sqrt{\frac{s_0^+ - u_0^+}{s_0^+ - 1}})(1 - \sqrt{\frac{s_0^- - u_0^+}{s_0^- - 1}})}{(1 - \sqrt{\frac{s_0^+ - u_0^+}{s_0^+ - 1}})(1 + \sqrt{\frac{s_0^- - u_0^+}{s_0^- - 1}})} \right| \frac{(2\sqrt{u_0^+} - 3u_0^+ + u_0^{+2})}{(u_0^+ - 1)^3} -$$
$$- \frac{M^2 \gamma_0 \Delta P h}{\pi\alpha} (u_0^+ - \ln u_0^+ - 1)$$

– flow separation from the upper surface of the body, singularity at the front edge of the plate, closed cavity.

The projection X represents the drag force, and projection Y – lift force, where $u_0^{\pm}$ are the roots of algebraic equation

$$l = u_0^+ - \ln |u_0^+| - 1.$$

The length of the cavity is determined from the condition of equality of the sum of upper and lower borders of the cavity vertical movements to vertical size of the cavity. In case of relatively small depth the following relation between the lengths of the body and cavity was obtained:

$$\frac{L}{S} = \frac{2e^{-\frac{2\pi L}{\alpha h}}}{1 + e^{-\frac{2\pi L}{\alpha h}} \frac{(\frac{2}{\alpha} - 1)\rho_0 V_0^2 \gamma_0 \pi}{\Delta P \alpha} \sqrt{\frac{\pi L}{\alpha h}}}. \tag{11}$$

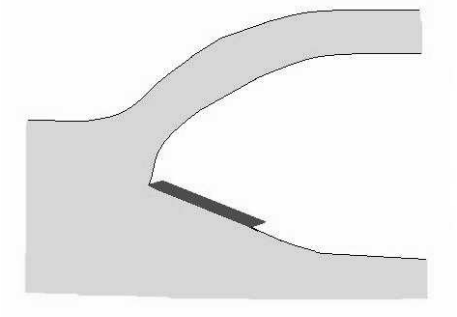


Figure 4: Free surface shape for the case of flow separation from the upper surface, singularity located at the front edge.

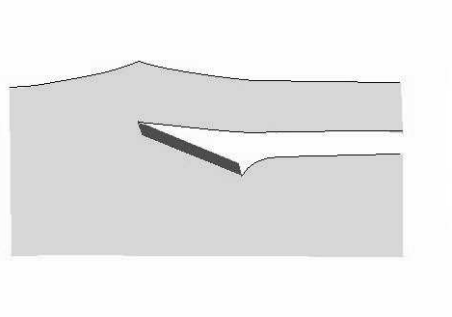


Figure 5: Free surface shape for the case of flow separation from the upper surface, singularity located at the rear edge.

4 Results and discussion

Analysis of obtained results shows the asymptotic behavior of the forces depending on the ratio of body length, fluid layer thickness and pressure in the cavity.

In case fluid separation takes place from the upper side of the body two flow scenarios are possible having singularity on the front edge (Fig. 4) and on the rear edge (Fig. 5). The front edge separation case has the following asymptotic solutions:

1) $\frac{h}{L} \to 0: \quad X = \frac{\rho_0 a^2 h M^2 \gamma_0^2}{2\alpha^2} (\sqrt{\frac{\pi L}{\alpha h}} - 1)^2, \quad Y = -\frac{\rho_0 a^2 h M^2 \gamma_0}{2\alpha} (\sqrt{\frac{\pi L}{\alpha h}} - 1)^2;$

2) $\frac{h}{L} \to \infty: \quad X = \frac{\rho_0 a^2 M^2 \gamma_0^2 \pi L}{2\alpha^3}, \quad Y = -\frac{\rho_0 a^2 M^2 \gamma_0 \pi L}{2\alpha^2}.$

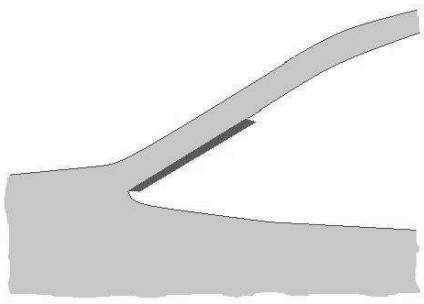


Figure 6: Free surface shape for the case of flow separation from the bottom surface, singularity located at front edge.

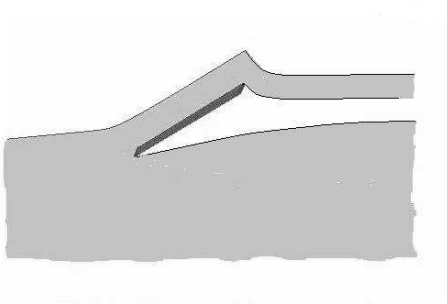


Figure 7: Free surface shape for the case of flow separation from the bottom surface, singularity located at rear edge.

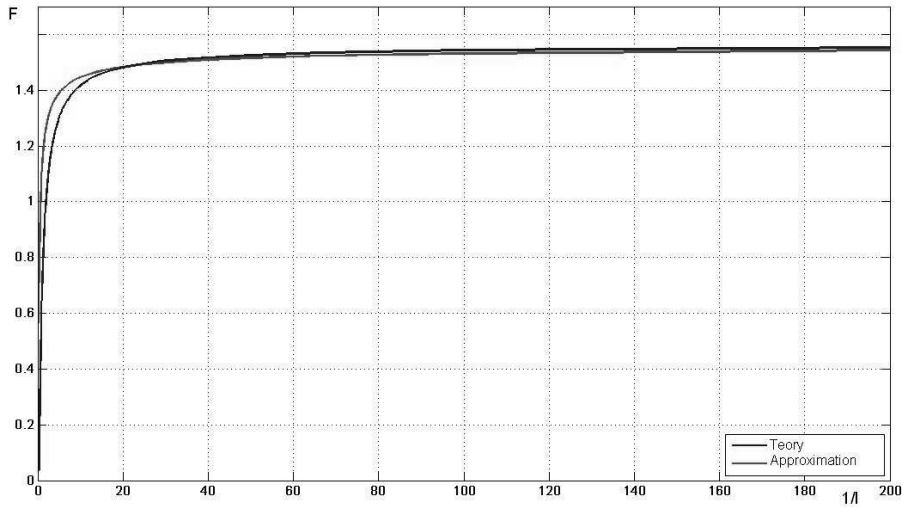


Figure 8: Relation between the force F_X and dimensionless parameter $\frac{1}{l}$ obtained numerically and using approximation formula in case flow separation from the bottom of the body having singularity on the front edge.

Approximation formulas for dimensionless forces depending from parameter $l = \frac{\pi L}{\alpha h}$ were developed:

$$F_X = \frac{X\alpha^3}{\frac{1}{2}\rho_0 V_0^2 \gamma_0^2 L} = \pi - \frac{\pi}{2} e^{-0.7l}, \quad F_Y = \frac{Y\alpha^2}{\frac{1}{2}\rho_0 V_0^2 \gamma_0 L} = -\pi + \frac{\pi}{2} e^{-0.7l}.$$

The rear edge separation case has the following asymptotic solutions:

$$1) \quad \frac{h}{L} \to 0: \quad X = \frac{\rho_0 a^2 h M^2 \gamma_0^2}{\alpha^2}\left(2\sqrt{\frac{\alpha h}{\pi L}} - 3 + \frac{\pi L}{\alpha h}\right), \quad Y = -\frac{\rho_0 a^2 h M^2 \gamma_0}{\alpha}\left(2\sqrt{\frac{\alpha h}{\pi L}} - 3 + \frac{\pi L}{\alpha h}\right);$$

$$2) \quad \frac{h}{L} \to \infty: \quad X = 3\frac{\rho_0 a^2 M^2 \gamma_0^2 \pi L}{\alpha^3}, \quad Y = -3\frac{\rho_0 a^2 M^2 \gamma_0 \pi L}{\alpha^2}.$$

Approximation formulas for dimensionless forces depending from parameter $l = \frac{\pi L}{\alpha h}$ were developed:

$$F_X = \frac{X\alpha^3}{\frac{1}{2}\rho_0 V_0^2 \gamma_0^2 L} = 2\pi + \pi(1 - 0.4l^{0.4})e^{-0.8l}, \quad F_Y = \frac{Y\alpha^2}{\frac{1}{2}\rho_0 V_0^2 \gamma_0 L} = -2\pi - \pi(1 - 0.4l^{0.4})e^{-0.8l}.$$

Diagrams of relation between the force F_X and dimensionless parameter $\frac{1}{l}$ obtained numerically and using approximation formula are shown on picture Fig. 9.

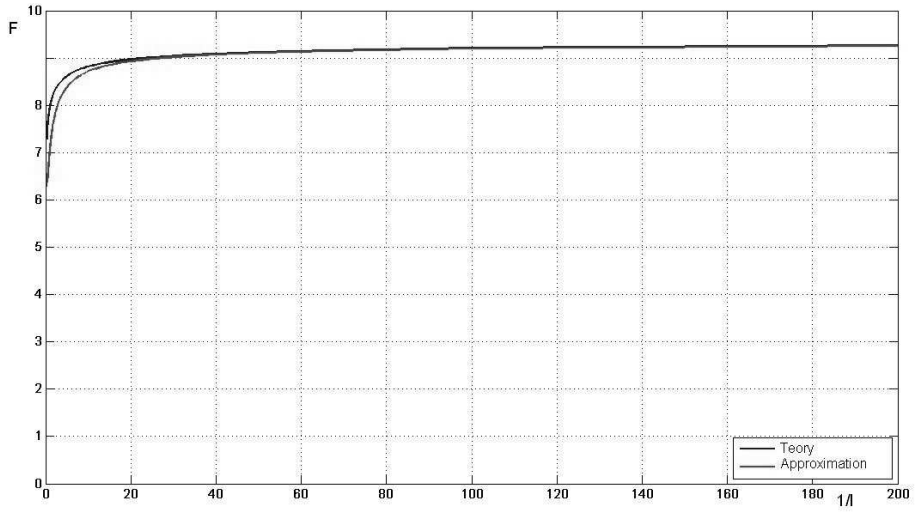


Figure 9: Relation between the force F_X and dimensionless parameter $\frac{1}{l}$ obtained numerically and using approximation formula in case flow separation from the upper side of the body having singularity on the rear edge.

In case fluid separation takes place from the bottom of the body two flow scenarios are possible having singularity on the front edge (Fig. 6) and on the rear edge (Fig. 7). The front edge separation case has the following asymptotic solutions:

$$1) \quad \frac{h}{L} \to 0: \quad X = \frac{\rho_0 a^2 h M^2 \gamma_0^2}{2\alpha^2}, \quad Y = \frac{\rho_0 a^2 h M^2 \gamma_0}{2\alpha};$$

$$2) \quad \frac{h}{L} \to \infty: \quad X = \frac{\rho_0 a^2 M^2 \gamma_0^2 \pi L}{4\alpha^3}, \quad Y = \frac{\rho_0 a^2 M^2 \gamma_0 \pi L}{4\alpha^2}.$$

Approximation formulas for dimensionless forces depending from parameter $l = \frac{\pi L}{\alpha h}$ were developed:

$$F_X = \frac{X\alpha^3}{\frac{1}{2}\rho_0 V_0^2 \gamma_0^2 L} = \frac{\pi}{2}(1 - 0.1l^{0.5})e^{-0.7l}, \quad F_Y = \frac{Y\alpha^2}{\frac{1}{2}\rho_0 V_0^2 \gamma_0 L} = \frac{\pi}{2}(1 - 0.1l^{0.5})e^{-0.7l}.$$

Diagrams of relation between the force F_X and dimensionless parameter $\frac{1}{l}$ obtained numerically and using approximation formula are shown on picture Fig. 8. The rear edge separation case has the following asymptotic solutions:

$$1) \quad \frac{h}{L} \to 0: \quad X = -\frac{2\rho_0 a^2 h M^2 \gamma_0^2}{\alpha^2} e^{\frac{\pi L}{2\alpha h}}, \quad Y = -\frac{2\rho_0 a^2 h M^2 \gamma_0}{\alpha} e^{\frac{\pi L}{2\alpha h}};$$

$$2) \quad \frac{h}{L} \to \infty: \quad X = \frac{3}{2}\frac{\rho_0 a^2 M^2 \gamma_0^2 \pi L}{\alpha^3}, \quad Y = \frac{3}{2}\frac{\rho_0 a^2 M^2 \gamma_0 \pi L}{\alpha^2}.$$

Approximation formulas for dimensionless forces depending from parameter $l = \frac{\pi L}{\alpha h}$ were developed:

$$F_X = \frac{X\alpha^3}{\frac{1}{2}\rho_0 V_0^2 \gamma_0^2 L} = 2\pi + \pi(1 - 0.4l^{0.4})e^{-0.8l}, \quad F_Y = \frac{Y\alpha^2}{\frac{1}{2}\rho_0 V_0^2 \gamma_0 L} = 2\pi + \pi(1 - 0.4l^{0.4})e^{-0.8l}.$$

Using the relation (11) the drag and lift forces in case of cavity formation may be estimated for relatively small depth:

$$X = \frac{\rho_0 a^2 M^2 \gamma_0^2 \pi L}{\alpha^3} + \frac{\gamma_0 \Delta P \pi L^2}{2h\alpha^2}\left(\frac{2\pi L}{\alpha h} + \ln\left(1 + e^{-\frac{2\pi L}{\alpha h}}\frac{(\frac{2}{\alpha} - 1)\rho_0 V_0^2 \gamma_0 \pi}{\Delta P \alpha}\sqrt{\frac{\pi L}{\alpha h}}\right)\right) + \frac{M^2 \gamma_0^2 \Delta P L}{\alpha^3},$$

$$Y = -\frac{\rho_0 a^2 M^2 \gamma_0 \pi L}{\alpha^2} - \frac{\Delta P \pi L^2}{2h\alpha}\left(\frac{2\pi L}{\alpha h} + \ln\left(1 + e^{-\frac{2\pi L}{\alpha h}}\frac{(\frac{2}{\alpha} - 1)\rho_0 V_0^2 \gamma_0 \pi}{\Delta P \alpha}\sqrt{\frac{\pi L}{\alpha h}}\right)\right) - \frac{M^2 \gamma_0 \Delta P L}{\alpha^2}.$$

5 Conclusions

The solution was obtained for a problem of body motion in compressible fluid at a depth, constant velocity and inclination angle. Both cases of positive and negative inclination were regarded, which means flow separation from the upper side and bottom side of the wing. Both cases of infinite cavity behind the body and final length cavity were regarded. For the case of final length cavity vapor pressure in it is less then the pressure on free surface. The solution allows determining drag and lift forces in the limiting cases, the relation between the body length and the cavity length in the case of small depth. It was shown that on Mach number tending to unity both forces infinitely increase, for relatively thick fluid layer above the moving wing forces do not depend on layer thickness, and for relatively thin fluid layer forces depend on layer thickness. The forces increase when the pressure in the cavity decreases. When the pressure in the cavity tends to pressure on the free surface the length of the cavity decreases and the forces tend to appropriate values for infinite span wing.

Acknowledgements

The research was performed within the frame of RFFI project 09-08-92002.

References

[1] Gurevich M.I., Yanpolskii A.R. On motion of a gliding plate. Techniques of the aviation fleet, 1933, 10.

[2] Haskind M.D. Plane problem on gliding over the surface of heavy fluid. Proc. Acad. Sci. USSR, Tech.Sci. Ser., 1943, 1-2.

[3] Gurevich M.I. Gliding of a circle segment over the surface of heavy fluid. TsAGI Tech. Papers, 1937, 153, 1 - 6.

[4] Chaplyguin Yu.S. Gliding on the surface of fluid of final depth. Journ. Applied Math. and Mech., 1941, 5, 2.

[5] Chaplyguin Yu.S. Gliding of a flat plate of infinite span over the surface of heavy fluid. TsAGI Tech. Papers, 1942, 508.

[6] Green A. E. The gliding of a plate on a stream of finite depth. Proc. Cambridge Phil. Soc., 1935, 31, 4.

[7] Sedov L.I. Plane problems of hydrodynamics and aerodynamics. Moscow: Science Publ., 1980.

[8] Smirnova M.N. , A.V. Zvyaguin. Motion of a rigid body in compressible fluid with a free surface. Proc. 6-th IASME/WSEAS Conference, Rhodes, 2008, 1, 61-66.

[9] Zvyaguin A.V., Smirnova M.N. Motion of a slender body near the free surface of compressible fluid. Moscow University Mechanics Bulletin, 2009, 64, 2, 5-15.

[10] Smirnova M.N., Zvyaguin A.V. Fluid flow interaction with an obstacle near free surface. Acta Astronautica 64 (2009) 288-294.

M. N. Smirnova, Faculty of Mechanics and Mathematics, Moscow M.V. Lomonosov State University, Moscow 119992, Leninskie Gory 1, Russia

Time-frequencies analysis of acoustic vibration in friction: comparison of experiment and simulation

Aleksey Yu. Smolin Andrey I. Dmitriev Sergey A. Dobrynin
Eugenii A. Kolubaev
asmolin@ispms.tsc.ru

Abstract

Acoustic vibrations in friction obtained from both experiment and simulation are analyzed using wavelet transform. The experiments have been made on steel under sliding friction. The simulations have been performed using movable cellular automaton method. Similarity of acoustic spectra for the experimental and simulation results is revealed also as their correspondence with wear particle size.

Introduction

A special attention has been paid to study of processes related to the elastic vibrations generated in sliding friction in recent years [1–3]. It is known that the spectrum of acoustic vibrations generated in a friction pair is extremely varied and difficult to analyze. First it is a "set" of natural frequencies of different parts of the system and the friction unit in a whole. It also contains the frequency of random and periodic nature, sound and ultrasonic range, which depend on the regime of sliding and loading conditions. One should take into account the superposition of elastic waves emitted by a great number of separate spots of real contact, caused by the movement of conjugated surfaces. Besides, these waves can be accompanied by modulation and interference. That is why use of time-frequency signal analysis, in particular window Fourier transform and wavelet transform, may be considered as an effective approach in dealing with the study of acoustic oscillations in the tribological systems. Thus, using modeling of friction at the contact spot it was shown in [4] that Fourier analysis of elastic waves allows to investigate features of formation of friction layer in a model system. It was also further noted that acoustic vibrations in friction can be amplitude-and frequency-modulated, and therefore to study them it is advised to apply time-frequency analysis.

The purpose of this study was to determine the frequency-time structure of the acoustic signal in friction of Hadfield steel, as well as to compare the experimental data with the modeling results.

1 Tribotechnical tests

Tribotechnical tests of shaft-bush type were conducted on a friction machine 2168 UMT-1 (Fig. 1,a). These tests used bush samples with inner diameter of 31.1 mm, outer diameter of 39 mm and width of 10 mm. The bushes were made of Hadfield steel. This steel (0.9–1.4% C; 13.0% Mn; 0.8–1.0% Cr) has unique properties: high plasticity, the ability to intense strain hardening, as well as low wear rate in sliding friction. To avoid turning the bush a recess was made in the holder and fixation executed by the screw. The shafts with a diameter of 30.0 mm made by steel 42HM4F thermally treated to reach a hardness of 56 HRC. The speed of rotation of the shaft was about $40\,\mathrm{min}^{-1}$, which corresponded to the linear velocity of 0.067 m/s. The loading was carried out with pneumomechanism via the bush to create a pressure of about 1–3 MPa in the contact zone of the shaft and bush. Tests were conducted under conditions of dry friction.

To register the friction sound a microphone Behringer XM8500 was used, which had the unevenness of amplitude-frequency response characteristics ±5 dB in the frequency range from 100 to

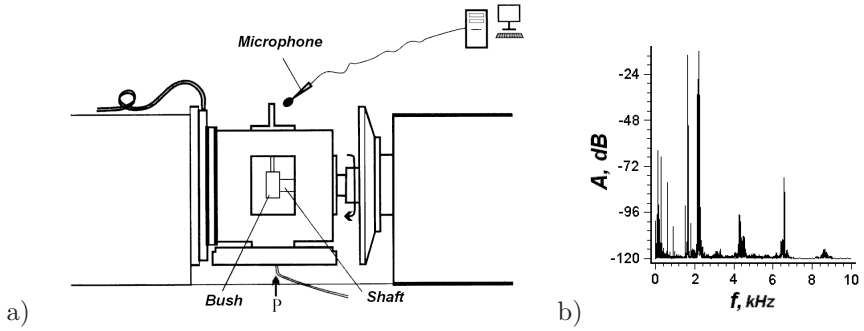


Figure 1: Scheme of tribotechnical tests with recording the friction sound (a) and spectrum of the sound (b).

15000 Hz. The microphone was mounted at a distance of 30 cm from the friction unit. The sound signal and its parameters were recorded on a personal computer.

Fig. 1,b shows the Fourier transform of a sound signal received at the above-described setup [5]. Note that in our experiments the microphone records the sound waves in air, which are actually vibrations of pressure (longitudinal waves). It is natural to expect that the spectrum of the signal contain the natural frequencies of the elements of the experimental setup. However, the spectrum itself does not allow to answer the question, what is the reason of excitation of various frequencies of the system and at what times during the experiment this excitation occurs.

To answer this question let's use the means of time-frequency analysis and consider a typical sound signal (Fig. 2,a). It can be seen quasi-periodic bursts of vibration intensity, which correlate with the period of rotation of the shaft. In [6] it was showed that the wear of Hadfield steel was mainly occured due to oxidation and destruction of the surface layer. It was also noted that in friction on the specimen surface a nanostructured layer of thickness $\sim 5\,\mu$m was formed, where strain was localized and accumulated. With the accumulation of a critical strain the nanostructured layer disrupted and wear particles were formed. It seems these disruptions cause a sharp increase of the acoustic signal intensity.

Fig. 2,b presents the wavelet transform [7] of the recorded signal. It shows that the bursts of acoustic oscillation intensity occur on the background of a constant signal which has a homogeneous structure. Frequencies of the background signal lie in the range of 10 to 900 Hz, and the oscillations are amplitude-modulated by some non-periodic signal. Given that the natural frequencies p of simple homogeneous bodies (rod, plate) are related to their characteristic size l and sound velocity v as $p \sim v/l$ [8], we can conclude that the background vibrations correspond to natural frequencies of the building elements (walls, beam, floor), as well as the massive parts of the setup. It should be noted that vibrations of this range are observed in setup operation also without the friction unit, therefore they are not analyzed later.

Window Fourier transform of the recorded signal is presented in Fig. 2,c. Due to the linear scale of frequencies it is easier to analyze high-frequency part of the signal. However, the limitation of the package "LastWave" [9] used for signal analysis makes it impossible to see here the detailed temporal features of the background signal at low frequencies, which can be clearly seen from the wavelet image in Fig. 2,b.

The acoustic oscillations intensity bursts have a higher frequency and their spectrum does not overlap with the spectrum of the background (Fig. 2). Typical frequency of these bursts is 1.7 kHz for the first one and 2.2, 4.4, 6.6, 8.6 kHz for the second one. For different leading pressure these frequencies vary only slightly (within 5 %). We should also note the correlation of the bursts frequency with natural frequencies of such parts of the experimental setup as holder of the bush and the shaft with the counterbody.

As noted above, a sharp increase in the intensity of the acoustic signal may be associated with the destruction of the nanostructured surface layer. Fig. 3 shows SEM images of wear particles obtained for Hadfield steel. It is seen that the characteristic size of the particles can be divided into two groups: small particles of iron oxide with an average size $d = 1$–$3\,\mu$m, and coarse particles sometimes coated by oxide with an average size $d = 30$–$40\ \mu$m. When the contact surfaces with

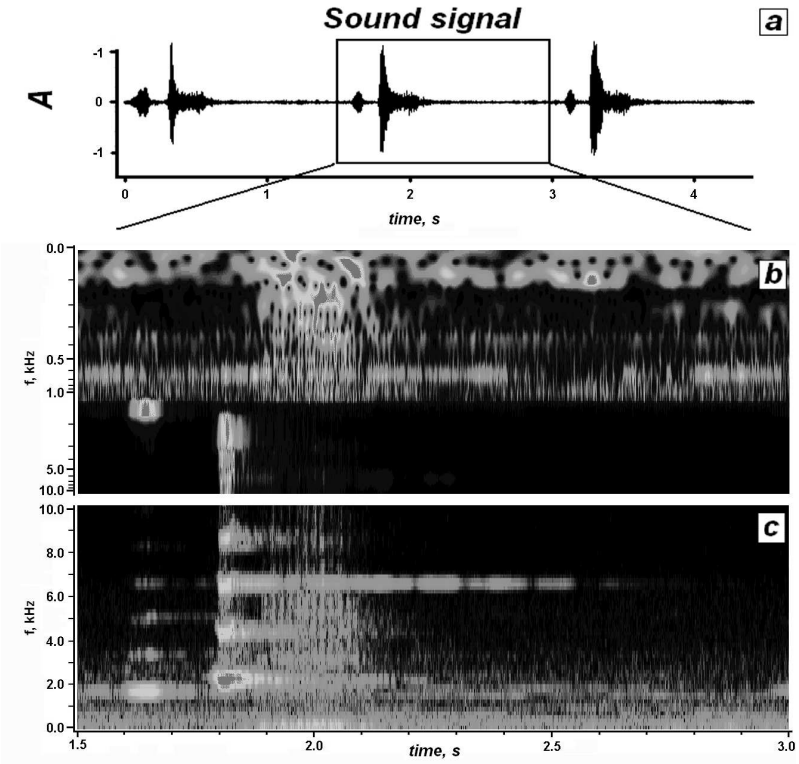


Figure 2: Sound signal (a), its wavelet (b) and window Fourier transform (c)

characteristic size of roughness corresponding to the large wear particles move with relative velocity V, multiple collisions occur and cause generation of elastic waves with a frequency $p = V/d$. Taking into account the relative velocity $V = 0.067\,\mathrm{m/s}$, the frequency of elastic vibration is $\sim$1.7 and $\sim$2.2 kHz correspondingly, which corresponds to the main frequency of the first and second bursts of intensity of the acoustic signal. Others frequencies observed can be interpreted as harmonics of the higher order.

Note, that the experimental acoustic signals in friction, are sufficiently complex to analyze and contain much information even in the sound range. In this regard, the computer simulation should be used for better understanding of the spectrum structure of such signals, where one can study in detail the processes occurring in the contact points, and analyze the influence of individual factors on the acoustic spectrum of the generated elastic waves.

2 Numerical model of friction

Simulation of sliding friction was carried out by the scheme proposed in [4]. Fig. 4,a shows a scheme of friction zone. Areas of real contact, which account several percent of the nominal contact area of the interacting bodies, circled by dotted lines. Within the framework of the coupled discrete-continual approach a part of the actual contact zone, located between the vertical lines shown in Fig. 4,a was simulated. Taking into account the characteristic scale of the surface layers where mechanisms underlying friction and wear were developed, the simulated size of the assembly was chosen, the diameter of movable cellular automata corresponded to 2.5 nm. Size of the computational region was 450 nm horizontally and 500 nm vertically, grid cell size was 10 nm. The detailed procedure of coupling the methods of continuum mechanics with discrete method of movable cellular automata is presented in [10].

Fragment of the structure of the computational region is shown in Fig. 4,b. Here the region I was simulated by discrete method of movable cellular automata, and in the region II dynamic equations of solid mechanics were solved by finite difference method. Only part of the grid is shown to reduce the vertical size of the picture. Registration of elastic waves was carried out by the

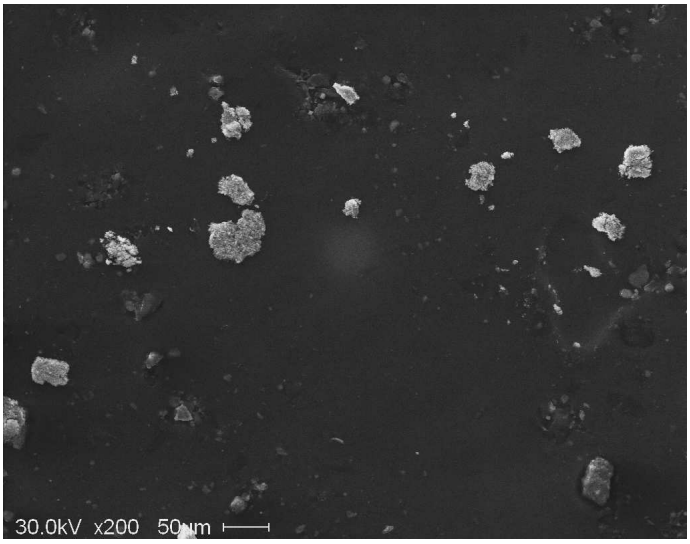
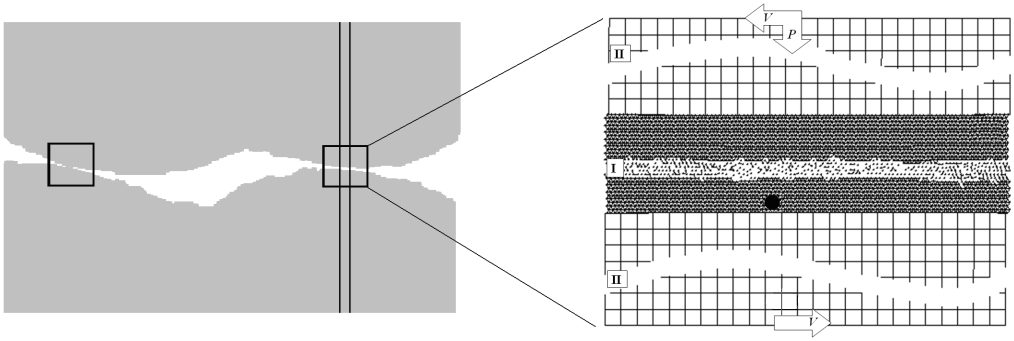


Figure 3: Wear particles for Hadfield steel friction



(a) (b)

Figure 4: Scheme of friction zone (a) and the modelled region (b)

"gauge" pointed by black dot in Fig. 4,b. It recorded such parameters as velocity components (V_X and V_Y), stress intensity (I) and pressure (P). For the outer surfaces of the blocks (respectively, top for the upper one and bottom for the lower one) the horizontal velocity V steadily increased from 0 to $V_m = 10\,\mathrm{m/sec}$ was set. At the same time the loading pressure P on the upper surface increased with time to the maximum value $P_m = 127.5\,\mathrm{MPa}$. The bottom surface was fixed on the axis Y. Periodic boundary conditions were set in the horizontal direction. Parameters of the model material corresponded to steel (density $\rho = 7800\,\mathrm{kg/m^3}$, Young's modulus $E = 206\,\mathrm{GPa}$, Poisson ratio $\nu = 0.3$, yield stress $\sigma_Y = 510\,\mathrm{MPa}$, strength $\sigma_S = 920$ MPa, ultimate strain $\varepsilon_S = 0.112$).

3 Comparison of the experiment and simulation

Fig. 5 shows the Fourier transform of elastic waves recorded by the "gauge" (Fig. 4,b) in the computer simulation described in detail in [4]. It was noted in [4] that on the Fourier transforms of registrations of velocity components along X and Y axis the peaks corresponding to the first and subsequent harmonics of the natural frequencies of the system are clearly observed. In the Fourier transforms of registrations of the stress intensity and pressure the peaks corresponding to the width of the sample and the characteristic size of the micro-roughness in the contact zone were observed.

Comparison of the data presented in Fig. 5 and 1,b shows that the experimental spectrum

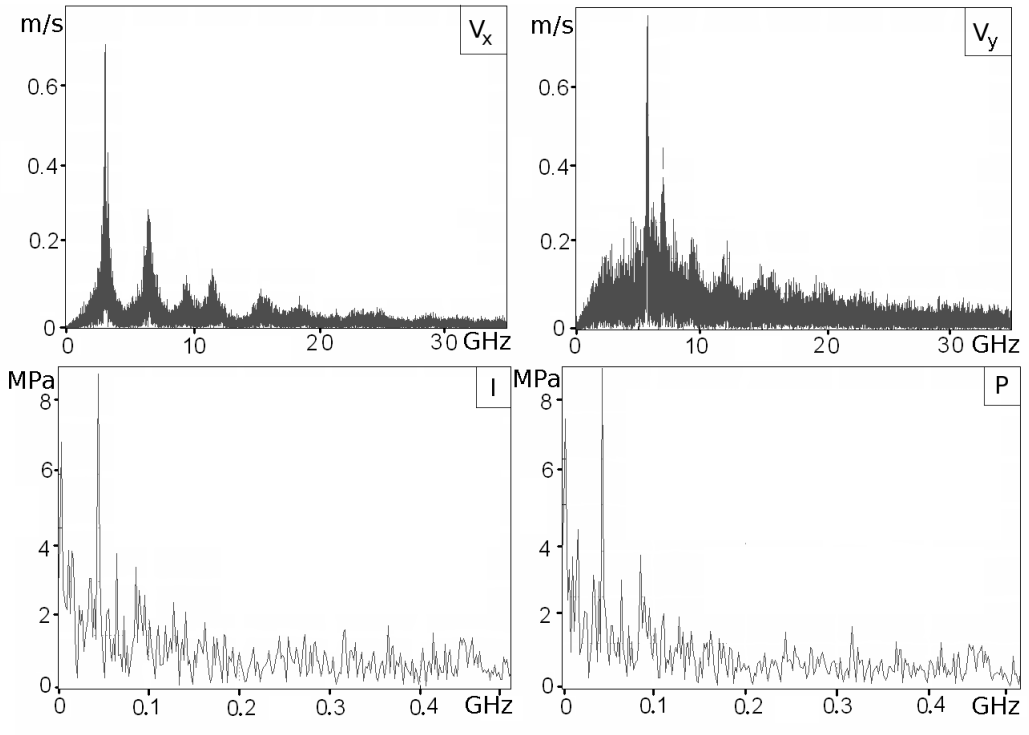


Figure 5: Fourier transform of simulated data

of the signal qualitatively corresponds to the spectrum of the pressure obtained from the model calculations. Note that in the experiments microphone records sound waves in air which are actually variations of pressure (longitudinal waves). Quantitative estimates show that the observed spectra correspond to different frequency ranges. If the experimental data range is up to 20 kHz, the data of computer simulation show the range of frequencies up to 500 kHz. The difference in the ranges can be explained by the deifferent dimensions in simulated sample and the experimental one. Note that there are technical difficulties of modeling the sample of real size. However, the observed qualitative agreement in the results suggests a possible similarity of the processes taking place at different scales, responsible for the generation of elastic waves.

Acknowledgements

This study was supported by the Russian Foundation for Basic Research (projects 09-07-12016-ofi-m, 09-03-12039-ofi-m), by the Department of Energy, Machine Building, Mechanics, and Control Processes of the Russian Academy of Sciences (project 13.13.3) and by Integration project 117 of the Siberian Division of the Russian Academy of Sciences with other institutions.

References

[1] Baranov V.M., et al. Acoustic emission in friction (Enorgoatomizdat, 1998, in Russian)

[2] Krishtal M.M. et al. // Tyazholoe mashinostroenie. 2007. No 12. PP. 14-18. (in Russian)

[3] Kuksenko V.S., et al // Tech. Phys. Lett., 2007, V. 33, N 1, PP. 62-64.

[4] Smolin A. Yu., et al. // Tech. Phys. Lett., 2007, V. 33, N 7, PP. 600-603.

[5] Kolubaev A.V., et al. // Tech. Phys., 2008, V. 53, N 2, PP. 204-210.

[6] Ivanov Yu.F., et al. // Phys. Mesomech., 2006, V. 9, N 6, PP. 83-90.

[7] Malat S. A Wavelet Tour of Signal Processing (Academic Press, 1998)

[8] Biderman V.L. Theory of mechanical oscillations (Vysshaya shkola, 1980, in Russian)

[9] http://www.cmap.polytechnique.fr/ lastwave/

[10] Psakhie S.G., et al. // Phys. Mesomech., 2003, V. 6, N 6, PP. 11-21.

Aleksey Yu. Smolin, pr. Academicheskii 2/4, Tomsk, 634021 Rissia
Andrey I. Dmitriev, pr. Academicheskii 2/4, Tomsk, 634021 Rissia
Sergey A. Dobrynin, pr. Academicheskii 2/4, Tomsk, 634021 Rissia
Eugenii A. Kolubaev, pr. Academicheskii 2/4, Tomsk, 634021 Rissia

Motion of an elastic body in fluid under vibration

V. S. Sorokin I. I. Blekhman V. B. Vasilkov
slavos87@mail.ru

Abstract

The effect of gas bubbles sinking in fluid under vibration was observed and described in papers [1,2]. In paper [2] the necessary condition for the arising of the effect was the presence of the standing wave in fluid, which for relatively low frequencies is possible only in gas saturated fluid.

In paper [3] it was supposed that the effect of gas bubble sinking in oscillating fluid can occur in the absence of the standing wave, i.e. in fluid without other bubbles. In this case gas bubble sinking takes place due to the deformability of the bubble under the action of fast varying pressure, which occurs by oscillations and is proportional to the mass of the liquid column placed above. In the present paper this supposition is confirmed by theoretical and experimental research.

Thereby, there are two different mechanisms, two explanations of the effect of gas bubble sinking in vertically oscillating fluid - "wave" and "nonwave", "vibrational". For the first explanation the gradient of the wave amplitude is the key factor, while for the second – the compressibility of the bubble.

To verify the analytical results the series of natural experiments was conducted in the Joint Laboratory of Vibrational Mechanics IPME RAS.

1 Model system

Motion of a bubble in a fluid, which is situated in harmonically oscillating with amplitude A and frequency ω volume, is analyzed (Fig.1.). The fluid is considered to be incompressible and uniformly oscillating with the volume. The height of the fluid column in the volume is designated as H_0.

In our analysis we take into account bubble volume pulsations caused by the influence of the varying pressure, which is exerted on the bubble due to the fluid oscillations.

The pulsations are considered to be isothermal and quasistatic, i.e. the following condition is held

$$P_t V_b = P_e V_{b0} = const \tag{1}$$

Where V_b - current volume of the bubble, V_{b0} - volume of the bubble near the free surface of the fluid, P_e - external pressure, which can be considered to be equal to the atmospheric pressure P_0 in the most simple case,

$$P_t = P_e + \rho x(g + A\omega^2 \sin \omega t) \tag{2}$$

– current value of the fluid pressure exerted on the bubble, x - coordinate of the center of the bubble, calculated from the free surface, ρ - density of the fluid, g - gravity acceleration. For the fulfilment of the assumption, that motion of the bubble is quasistatic, it is necessary for the frequency ω to be smaller sufficiently then the frequency λ of its free oscillations. This assumption fulfills for bubbles with radius $R < 2$ sm and frequencies $\omega < 280$ 1/s [4] (see section 5).

From equalities (1) and (2) we obtain

$$V_b = \frac{P_e V_{b0}}{P_e + \rho x(g + A\omega^2 \sin \omega t)} \tag{3}$$

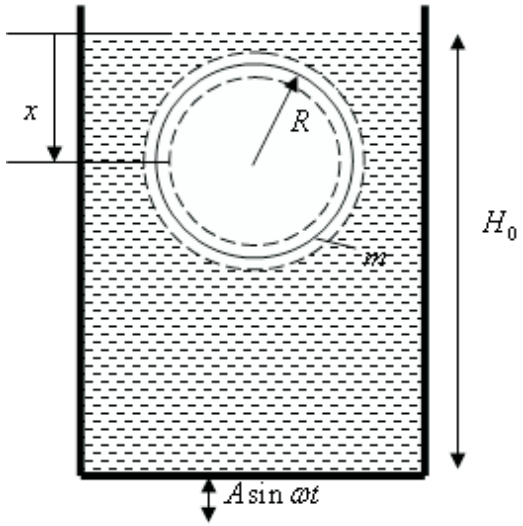


Figure 1: Model of a bubble in a fluid

We assume that the following inequality fulfils

$$\left(\frac{\rho H_0(g+A\omega^2)}{P_e}\right)^2 \ll 1 \tag{4}$$

i.e. in the bottom of the volume $x = H_0$ value of the external pressure is much greater then the sum of the hydrostatic pressure and the pressure caused by inertial forces. For example when $P_e = P_0 = 10$ m of water column and $A\omega^2 = 14g$, $H_0 = 0.2$ m we obtain $\rho H_0(g+A\omega^2) = 0.2 \cdot 15 = 3$ m of water column, and $\left(\rho H_0(g+A\omega^2)/P_e\right)^2 = 0.09$. We note that assumption (4) is not necessary, though it simplifies the analytical study significantly; in numerical experiments it can be omitted.

Then, the expression (3) can be written in the form

$$V_b = \frac{V_{b0}}{1+\frac{\rho x}{P_e}(g+A\omega^2\sin\omega t)} \approx V_{b0}\left[1-\frac{\rho x g}{P_e}(1+\frac{A\omega^2}{g}\sin\omega t)\right] \tag{5}$$

Introducing non-dimensional small parameter

$$\gamma = \frac{\rho H_0 g}{P_e} \ll 1 \tag{6}$$

and load coefficient

$$w = \frac{A\omega^2}{g} \tag{7}$$

we transform the expression (5) for the current volume of the bubble to the form

$$V_b = V_{b0}(1-\gamma\frac{x}{H_0}-\gamma\frac{x}{H_0}w\sin\omega t) \tag{8}$$

In the present paper we analyze the motion of the bubble in the presence of high intensity vibration $w >> 1$.

Due to the employed assumption (4) fluid pressure at the bottom of the volume is always positive

$$P_d = P_e + \rho H_0(g + A\omega^2\sin\omega t) > 0 \tag{9}$$

i.e. the fluid is never detached from the bottom of the volume.

2 Governing equation

Equation of motion of the bubble have the form

$$(m+m_0)\ddot{x} = -F(\dot{x}) + (m-\rho V_b)(A\omega^2 \sin\omega t + g) \tag{10}$$

Here m is the mass of the bubble (particles attached to the bubble), which is usually much smaller then the mass of the fluid in it's volume. The fulfillment of this condition lead to the fact that the Archimedes force is much greater then the weight of the bubble (particles attached to the bubble), i.e. it rises when vibration is absent. m_0 - is the added mass of the fluid, defined by the formula $m_0 = \chi V_b \rho$, with χ being an added mass coefficient, with the magnitude of $\chi = 1/2$.

$F(\dot{x})$ is the resistance force to gas bubble motion. In the general case this force is defined by the following expression [5,6,7]

$$F(\dot{x}) = 4\rho R^2 \Psi(\mathrm{Re})\dot{x}^2 \mathrm{sgn}\dot{x} \tag{11}$$

Where, as above, ρ is the density of the fluid, R is the radius of the bubble, and $\Psi(\mathrm{Re})$ is the coefficient of resistance, whose dependence on Reynolds number

$$\mathrm{Re} = 2\rho R V/\mu \tag{12}$$

is given by the classical Rayleigh diagram [6,7,8]. In formula (12) μ is the dynamic viscosity of the fluid, V is velocity of bubble's motion. Formulas (11) and (12), strictly speaking, are valid in the case of motion with constant velocity. However in the problems, similar to the analyzed, velocity $\dot{x}$ is varying significantly during one period of oscillations. So, for these problems question about the applicability of the formula (11), and question about the magnitude of the velocity, which should be used for determination of the Reynolds number, are stated (see for example [9,10,11]). Formula (11) can be employed in the case of variable velocity $\dot{x}$ (so-called stationarity hypothesis), sometimes (in the case of large Reynolds number Re) with the linear term being added [10]. There are no clear rules about the value of the velocity V in the equation (12). In the present paper the average velocity of the motion of the bubble is meant by the velocity V. The corresponding Reynolds number is considered to be "large" ($\mathrm{Re} > 1000$), but less then the Reynolds number corresponding to the flow crisis $\mathrm{Re} \approx 2 \cdot 10^5$. Under this assumption, according to the Rayleigh diagram, the resistance coefficient can be considered to be approximately constant:

$$\Psi(\mathrm{Re}) \approx 0.2 \equiv \Psi_\infty$$

3 Solution by the method of direct separation of motions

3.1 Equations of "fast" and "slow" motions

For the solution of the problem we use the concept of vibrational mechanics and the method of direct separation of motions [12]. We search solutions to (10) in the form

$$x = X(t) + \psi(t,\tau)$$

here X - "slow", and ψ - "fast", 2π - periodic in dimensionless ("fast") time $\tau = \omega t$ variable, with average zero:

$$\langle \psi(t,\tau) \rangle = 0$$

where for any $h = h(t,\tau)$, T - periodic in τ, we define $\langle h(t,\tau)\rangle = \frac{1}{T}\int\limits_0^T h d\tau$.

The following equations for the new variables X and ψ are obtained

$$\begin{aligned}&(m+m_{01})\ddot{X} - \gamma \cdot m_{01}(\tfrac{X}{H_0}\ddot{X} + \tfrac{\langle\psi\ddot{\psi}\rangle}{H_0} + w(\tfrac{X}{H_0}\left\langle\ddot{\psi}\sin\omega t\right\rangle + \tfrac{\langle\psi\sin\omega t\rangle}{H_0}\ddot{X} + \\ &+\tfrac{\langle\ddot{\psi}\psi\sin\omega t\rangle}{H_0})) = -\left\langle F(\dot{X}+\dot{\psi})\right\rangle + (m-\rho V_{b0})g + \gamma\cdot\rho V_{b0}(\tfrac{X}{H_0}g + \\ &+\tfrac{A\omega^2}{H_0}\langle\psi\sin\omega t\rangle + w(\tfrac{X}{H_0}\tfrac{A\omega^2}{2} + \tfrac{\langle\psi\sin^2\omega t\rangle}{H_0}A\omega^2 + \tfrac{\langle\psi\sin\omega t\rangle}{H_0}g))\end{aligned} \tag{13}$$

$$
\begin{aligned}
&(m+m_{01})\ddot{\psi}-\gamma\cdot m_{01}(\tfrac{X}{H_0}\ddot{\psi}+\tfrac{\psi}{H_0}\ddot{X}+\tfrac{\psi\ddot{\psi}-\langle\psi\ddot{\psi}\rangle}{H_0}+w(\tfrac{X}{H_0}((\ddot{X}+\ddot{\psi})\sin\omega t-\\
&-\left\langle\ddot{\psi}\sin\omega t\right\rangle)+\ddot{X}(\tfrac{\psi\sin\omega t}{H_0}-\tfrac{\langle\psi\sin\omega t\rangle}{H_0})+\tfrac{\psi\ddot{\psi}\sin\omega t}{H_0}-\tfrac{\langle\psi\ddot{\psi}\sin\omega t\rangle}{H_0})=\\
&=-F(\dot{X}+\dot{\psi})+\left\langle F(\dot{X}+\dot{\psi})\right\rangle+(m-\rho V_{b0})A\omega^2\sin\omega t+\\
&\gamma\cdot\rho V_{b0}(\tfrac{X}{H_0}A\omega^2\sin\omega t+\tfrac{\psi}{H_0}g+\tfrac{A\omega^2}{H_0}(\psi\sin\omega t-\langle\psi\sin\omega t\rangle)+\\
&+w(\tfrac{X+\psi}{H_0}\sin\omega t(A\omega^2\sin\omega t+g)-\tfrac{X}{H_0}\tfrac{A\omega^2}{2}-\tfrac{\langle\psi\sin^2\omega t\rangle}{H_0}A\omega^2-\tfrac{\langle\psi\sin\omega t\rangle}{H_0}g))
\end{aligned}
\tag{14}
$$

where $m_{01}=\chi\rho V_{b0}$ - is the added mass of the fluid near the free surface in the absence of vibration.

The equation of "slow" motion (13) is simplified using correlation (6) and inequalities $w>>1$, $\frac{A}{H_0}<<1$, $\frac{\psi}{H_0}<<1$. So this equation can be written in the form

$$
\begin{aligned}
&(m+m_{01})\ddot{X}-\gamma\cdot m_{01}w\tfrac{X}{H_0}\left\langle\ddot{\psi}\sin\omega t\right\rangle=-\left\langle F(\dot{X}+\dot{\psi})\right\rangle+(m-\rho V_{b0})g+\\
&+\gamma\cdot\rho V_{b0}w\tfrac{X}{H_0}\tfrac{A\omega^2}{2}
\end{aligned}
\tag{15}
$$

The essential advantage of the method of direct separation of motions is a possibility to solve the equations of "fast" motions in an approximate manner, if, as is typical, the equation of "slow" motion is the one of primary interest. In this case we neglect all terms with the small parameter γ. As a result, the equation of "fast" motion (14) can be written in the form

$$
(m+m_{01})\ddot{\psi}=-F(\dot{X}+\dot{\psi})+\left\langle F(\dot{X}+\dot{\psi})\right\rangle+(m-\rho V_{b0})A\omega^2\sin\omega t \tag{16}
$$

As it was noted above, in the present paper we consider the case of high intensity vibration, when $w>>1$. Hence we assume that the following condition is held $\left|\dot{\psi}\right|>>\left|\dot{X}\right|$, i.e. "fast" component of the velocity is much larger then the "slow" component (Verification of this assumption is provided in section 5). So the expression $-F(\dot{X}+\dot{\psi})+\left\langle F(\dot{X}+\dot{\psi})\right\rangle$ is transformed to form:

$$
-F(\dot{X}+\dot{\psi})+\left\langle F(\dot{X}+\dot{\psi})\right\rangle=-4\rho R_0^2\Psi_\infty\dot{\psi}^2\mathrm{sgn}\dot{\psi} \tag{17}
$$

where $R_0=\sqrt[3]{\frac{3}{4\pi}V_{b0}}$ - bubble's radius near the free surface of the fluid in the absence of vibration.

As a result, we obtain the equation of "fast" motions in the form

$$
(m+m_{01})\ddot{\psi}=-4\rho R_0^2\Psi_\infty\dot{\psi}^2\mathrm{sgn}\dot{\psi}+(m-\rho V_{b0})A\omega^2\sin\omega t \tag{18}
$$

3.2 The solution of the equation of "fast" motions

Approximate solution of the equation of "fast" motions (18) is sought in the form

$$
\psi=B\sin(\omega t+\phi) \tag{19}
$$

Multiplying the equation (18) by $\sin(\omega t+\phi)$ and integrating on the period $T=\frac{2\pi}{\omega}$, we obtain

$$
-\frac{(m+m_{01})B}{2}=(m-\rho V_{b0})A\frac{\cos\phi}{2} \tag{20}
$$

Multiplying the equation (18) by $\cos(\omega t+\phi)$ and integrating on the period T:

$$
0=-\frac{16}{3\pi}\rho R_0^2\Psi_\infty B^2-(m-\rho V_{b0})A\frac{\sin\phi}{2} \tag{21}
$$

The amplitude B of bubble's "fast" oscillations is determined from the equation

$$
(\frac{16}{3\pi})^2\rho^2R_0^4\Psi_\infty^2B^4+\frac{(m+m_{01})^2}{4}B^2-\frac{(m-\rho V_{b0})^2}{4}A^2=0 \tag{22}
$$

the positive solution of which has the form

$$B^2 = \frac{2(m-\rho V_{b0})^2 A^2}{(m+m_{01})^2 + \sqrt{(m+m_{01})^4 + \frac{16^3}{9\pi^2}(m-\rho V_{b0})^2 \rho^2 R_0^4 \Psi_\infty^2 A^2}} \tag{23}$$

Using the condition $m << \rho V_{b0}$, we transform the expression (23) to the form:

$$B^2 = \frac{2A^2}{\chi^2 + \sqrt{\chi^4 + \frac{16^2}{\pi^4}\Psi_\infty^2 \frac{A^2}{R_0^2}}} \tag{24}$$

To obtain the equation of "slow" motion from (15) it is sufficient to determine the function $\left\langle \ddot{\psi} \sin \omega t \right\rangle$. But $\left\langle \ddot{\psi} \sin \omega t \right\rangle = -\omega^2 B \frac{\cos\phi}{2}$, and $\frac{\cos\phi}{2} = -\frac{(m+m_{01})B}{2(m-\rho V_{b0})A}$. So we obtain

$$\left\langle \ddot{\psi} \sin \omega t \right\rangle = -\frac{\omega^2 A}{\frac{k+\chi}{1-k} + \sqrt{(\frac{k+\chi}{1-k})^2 + \frac{16^2}{\pi^4}\frac{\Psi_\infty^2}{(k+\chi)^2}(\frac{A}{R_0})^2}} \tag{25}$$

where k - is the ratio of the mass of the bubble m to the mass of the fluid in its volume ρV_{b0}. Taking into account the condition $k << 1$ we transform the formula (25) to the form

$$\left\langle \ddot{\psi} \sin \omega t \right\rangle = -\frac{\omega^2 A}{\chi + \sqrt{\chi^2 + \frac{16^2}{\pi^4}\frac{1}{\chi^2}\frac{A^2}{R_0^2}\Psi_\infty^2}} \tag{26}$$

4 The effect of gas bubble sinking in fluid

4.1 The condition of gas bubble sinking

The equation of "slow" motions (15) can be written in the form

$$(m+m_{01})\ddot{X} + \left\langle F(\dot{X}+\dot{\psi}) \right\rangle = \gamma \cdot \rho V_{b0} w \frac{X}{H_0}(\frac{A\omega^2}{2} + \chi \left\langle \ddot{\psi} \sin \omega t \right\rangle) - (\rho V_{b0} - m)g \tag{27}$$

The condition of gas bubble sinking can be determined from the form of the equation (27). Indeed, if the expression written in the right side of the equation is positive, then the bubble will sink after certain period of time, which depends on the initial velocity, if it is negative, then the bubble will rise. So the condition of gas bubble sinking can be written in the form

$$\gamma \cdot \rho V_{b0} w \frac{X}{H_0}(\frac{A\omega^2}{2} + \chi \left\langle \ddot{\psi} \sin \omega t \right\rangle) > (\rho V_{b0} - m)g \tag{28}$$

Using the expression (26) and taking into account that $m << \rho V_{b0}$, we transform the condition (28) to the form

$$\gamma \cdot w^2 \frac{X}{H_0}(\frac{1}{2} - \frac{1}{1+\sqrt{1+\theta\frac{A^2}{R_0^2}}}) > 1 \tag{29}$$

where the coefficient $\theta = \frac{16^2}{\pi^4}\frac{\Psi_\infty^2}{\chi^4} \equiv 1.68$.

The "slow" variable X exists in the left side of the inequality (29), so the fulfillment of the condition of gas bubble sinking in fluid depends on its current position in the fluid. In other words, if the bubble is situated in the position with coordinate $X > X_0$, then it will sink, if in the position $X < X_0$, then it will rise, i.e. gas bubble sinking in fluid occurs only from some certain depth X_0. Value X_0 is determined from the expression

$$X_0 = \frac{2H_0}{\gamma \cdot w^2} \cdot \frac{1+\sqrt{1+\theta\frac{A^2}{R_0^2}}}{\sqrt{1+\theta\frac{A^2}{R_0^2}} - 1} \tag{30}$$

For any magnitudes of parameters X_0 is positive. If $X_0 > H_0$, then gas bubble rises in the whole volume. The case when $X_0 < H_0$ seems to be the most interesting - bubbles situated lower then some level will sink, situated higher - will rise.

For example, when the external pressure P_e is equal to the atmospheric pressure $P_e = P_0 = 10m$ of water column and the height of the fluid column in the volume is equal to $H_0 = 0.16$ m the small parameter γ is equal to $\gamma = 0.016$. The volume of the bubble is considered to be equal to $V_{b0} = 0.1 \cdot 10^{-6} m^3$ (radius $R_0 = 2.9$ mm). The amplitude of the external force is equal to $A = 6.5$ mm and the frequency $\omega = 170$ 1/s. Then the load coefficient is equal to $w = 19$. Using formula (30) for the X_0 we obtain $X_0 = 0.7H_0$, i.e. bubbles situated in the positions with coordinates $H_0 > X > 0.7H_0$ will sink in the fluid. We note that in this case the condition (4) fulfills, because $(\rho H_0(g + A\omega^2)/P_e)^2 = 0.1$. For the frequency of the external force $\omega = 195$ 1/s and the same values of the rest parameters using formula (30) we obtain $X_0 = 0.4H_0$ (in this case $(\rho H_0(g + A\omega^2)/P_e)^2 = 0.17$).

4.2 Physical explanation of the effect of gas bubble sinking in fluid

The reason for gas bubble sinking in an oscillating fluid is the influence of the "dynamic" Archimedes force on it: $-\rho V_b(g + A\omega^2 \sin \omega t)$. Therefore for better understanding of this effect we, for a start, give the physical interpretation of the Archimedes force in stationary fluid.

The only volume force, effective in stationary fluid, is the gravity force g. Therefore the fluid pressure at some distance x from its free surface is equal to $P = P_e + \rho x g$, where $\rho x g$ is the hydrostatic and P_e is external pressures. Now consider a gas bubble in this fluid. The pressure integral taken through the upper half of its surface is less, than taken through the lower. Because the greater x the greater P. The upward Archimedes force exerted on the bubble is the result of the difference between these two integrals.

Now consider oscillating fluid. Volume forces, effective in it, are the gravity force g and the force of inertia $A\omega^2 \sin \omega t$ (A - amplitude, and ω - frequency of vibration). Hence the fluid pressure at some distance x from its free surface is equal to $P = P_e + \rho x(g + A\omega^2 \sin \omega t)$. Now we consider a gas bubble in this fluid and describe the influence of the "dynamic" Archimedes force on it. While $g + A\omega^2 \sin \omega t > 0$ the pressure integral taken through the upper half of bubble surface is less, than taken through the lower, because the greater x the greater P. An upward force exerted on the bubble while $g + A\omega^2 \sin \omega t > 0$ is the result of the difference between these two integrals. While $g + A\omega^2 \sin \omega t < 0$ the pressure integral taken through the upper half of bubble's surface is greater, than taken through the lower half. Hence there is a force exerting while $g + A\omega^2 \sin \omega t < 0$ and absorbing the bubble deep into the fluid. The influence of the "dynamic" Archimedes force on the bubble is boiled down to these two forces, pushing out for one period of time and absorbing for another.

So, for the period of time while $g + A\omega^2 \sin \omega t > 0$ the upward force is exerting on the bubble, and for the period of time while $g + A\omega^2 \sin \omega t < 0$ - the downward force, and both of them depend on its volume. However the fluid pressure on the bubble is greater for the first period of time, than for the second. But the more the pressure the less the volume of the bubble. So, while $g + A\omega^2 \sin \omega t > 0$ the volume of the bubble is less than while $g + A\omega^2 \sin \omega t < 0$.

As a result, for the high intensity of vibration $\frac{A\omega^2}{g} >> 1$, when the periods of time $g + A\omega^2 \sin \omega t > 0$ and $g + A\omega^2 \sin \omega t < 0$ are approximately equal, the period of upward force exerting on the bubble is a little greater than the period of downward force exerting on it. But the "average" volume of the bubble for the period of time while $g + A\omega^2 \sin \omega t < 0$ in this case is significantly greater, than for the period of time while $g + A\omega^2 \sin \omega t > 0$. So the total value of the downward force effective while $g + A\omega^2 \sin \omega t < 0$ can become greater than the total value of the upward force effective while $g + A\omega^2 \sin \omega t > 0$. As a result, the total force exerted on the bubble for the whole period of time (while $g + A\omega^2 \sin \omega t <> 0$) will be absorbing, and the bubble will sink in the fluid.

4.3 The solution of the equation of "slow" motion

In this section we find solutions of the equation of "slow" motion (27). For this purpose the average value of the resistance force $\left\langle F(\dot{X} + \dot{\psi}) \right\rangle$ have to be determined. In the case of high

intensity vibration the amplitude of the velocity of fast bubble oscillations $B\omega$ can be considered to be much lager then the absolute value of the "slow" velocity $\left|\dot{X}\right|$ (see section 5). To determine the average value of the resistance force we use expression [12]:

$$\left\langle F(\dot{X}+\dot{\psi})\right\rangle = \frac{16}{\pi}\rho\Psi_\infty R_0^2\dot{X}B\omega \tag{31}$$

So, equation (27) transforms to the form:

$$m_{01}\ddot{X} + \frac{16}{\pi}\rho\Psi_\infty R_0^2\dot{X}B\omega = \gamma\cdot\rho V_{b0}w\frac{X}{H_0}A\omega^2(\frac{1}{2} - \frac{1}{1+\sqrt{1+\theta\frac{A^2}{R_0^2}}}) - \rho V_{b0}g \tag{32}$$

(the mass m of the bubble is neglected). The "slow" acceleration of the bubble $\ddot{X}$ can be considered to be small, so the equation (32) can be written if the form:

$$\frac{12}{\pi^2}\Psi_\infty\dot{X}\frac{B}{R_0}\omega = g(\gamma\cdot w^2(\frac{1}{2} - \frac{1}{1+\sqrt{1+\theta\frac{A^2}{R_0^2}}})\frac{X}{H_0} - 1) \tag{33}$$

which can be rewritten:

$$\dot{X} = q(\frac{X}{X_0} - 1) \tag{34}$$

where $q = \frac{\pi^2}{12\cdot\Psi_\infty}\frac{R_0}{B}\frac{g}{\omega}$, X_0 is determined by the expression (30), and the amplitude B by the formula (24). Actually q is the absolute value of the "slow" levitation velocity of a rigid bubble. I.e. if we had not taken into account pulsations of bubble's volume, then we would obtain the value q for the "'slow" velocity of it's levitation.

As is seen from the equation (34), the velocity of gas bubble falling or rising in fluid is depending on the coordinate X. For $X = X_0$ this velocity is equal to zero. For the frequency of the external force $\omega = 195$ 1/s and the same values of the rest parameters as in section 4.1., we obtain $B = 9.1$ mm, and $q = 6.7$ sm/s.

5 Verification of the assumptions used in the analysis

Here we discuss the main assumptions used in our analysis.

The assumption, that motion of the bubble is quasistatic, fulfills because even for the bubbles with diameter 4 sm the value of the natural frequency of radial oscillations exceeds 850 1/s [4]. The considered frequencies of vibration are less then 250 1/s, and gas bubbles diameters are less then 3 sm.

Composing the equation of "fast" motions (18) and solving the equation (27) of "slow" motion we have assumed that $\left|\dot{X}\right|$ is small as compared with the amplitude of "fast" oscillations $B\omega$. Here we verify this assumption. The "slow" velocity of bubble's motion is determined from the formula (34). So the ratio of the amplitude $B\omega$ to the absolute value of the "slow" velocity is equal to

$$\xi = \frac{X_0 B\omega}{q\left|X - X_0\right|} \tag{35}$$

but $\frac{B\omega}{q} >> 1$, so $\xi >> 1$ for the all magnitudes of X, i.e. the considered assumption really fulfills. For example, for frequency $\omega = 195$ 1/s and the same magnitudes of the rest parameters as in section 4.1. we obtain $\frac{B\omega}{q} = 26.7$.

6 Comparison with the results of natural experiment

Series of experiments was conducted on special devices installed on the universal vibrating stand of "Mekhanobr" institute (Fig. 2) to verify the obtained theoretical results.

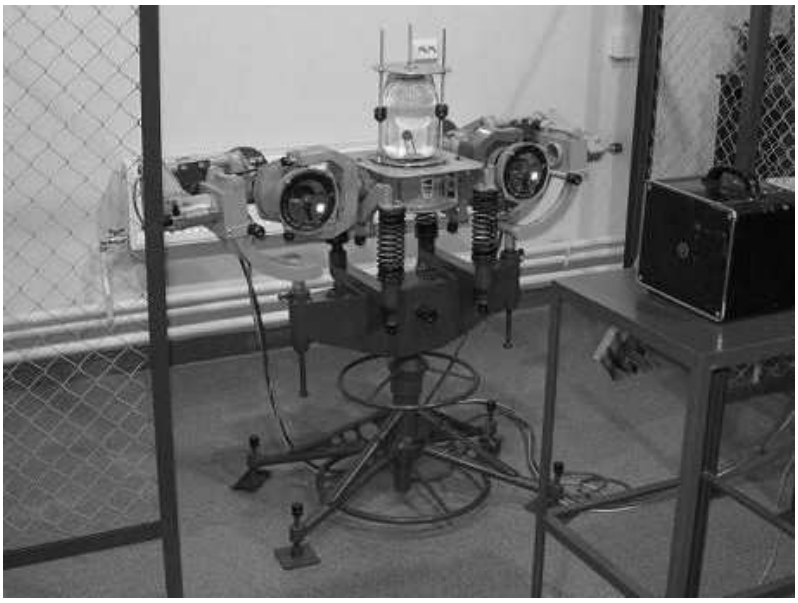


Figure 2: Universal vibrating stand

Vessel, which was almost full to the brim with the water (the height of the air column is 1-2 mm) and closed by the plastic cover, fastened at the stand. The external pressure on the free surface of the water was equal to the atmospheric pressure, and generation of the large quantity of bubbles due to the emergence of the turbulent coating surface [13] was prevented by the small amount of air in the vessel. A deformable rubber ball, filled with air, was attached to the bottom of the vessel by the thread (Fig.3a). The mass of the rubber was negligibly small as compared with the mass of the water in bubble's volume; the influence of the rubber's tensile force on the pressure inside the ball can be also neglected. So this ball can be considered as the simplest gas bubble model.

The height of the water column in the vessel was equal to 214 mm. The experiment was conducted for balls with different diameters (from 12 mm to 30 mm) and for different lengths of the thread, i.e. initial distances from the bottom of the vessel (from 33 mm to 170 mm). The amplitude of the external force was fixed and equal to 4,3 mm. The frequency of the external force was increasing from 0 to 200 rad/s. In every test it was obtained, that the ball slumped to the bottom of the vessel when the certain magnitude of the frequency of the external force was achieved (Fig.3b). Further increasing of the frequency did not influence the ball's position – it was still in the bottom of the vessel. The decreasing of the frequency led to the ball's rising, i.e. it returned to the initial position. Thereby theoretical conclusion that the effect of gas bubble sinking can occur in uniformly oscillating fluid was entirely confirmed by the experiment.

It was obtained that the decreasing of the initial distance from the bottom of the vessel to the ball (the length of the thread) as well as the decreasing of the size of the ball lead to the decreasing of the frequency ω_*. These results are in good agreement with the theoretical results. The magnitudes of the overloads necessary for the occurring of the effect of rubber balls sinking in the water were slightly smaller then the magnitudes of the overloads necessary for the occurring of the effect of gas bubbles sinking in gas saturated fluid [1,2]. This can be explained by the following facts: rubber balls had some mass (from 30 mg to 80 mg), their form was not ideally round, the thread had some influence on the balls "fast" oscillations.

To verify the assumption, that the effect of gas bubble sinking is associated with the variations of its volume due to vibration, the experiment with nondeformable rigid ball, whose density was much smaller then the density of the water, was conducted. The effect of sinking was not registered in this case.

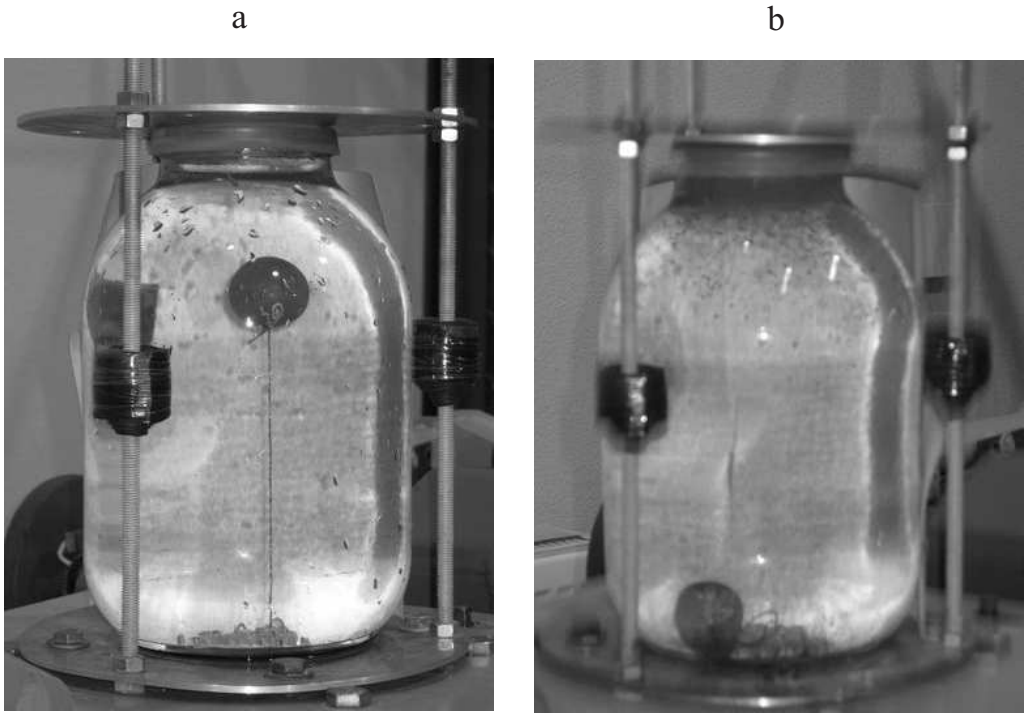


Figure 3: Sinking of the gas bubble model (deformable rubber ball) in vibrating vessel with the water: a - the ball in the motionless vessel, b - the ball in vibrating vessel after the achievement of the frequency ω_*

7 Conclusion

In the present paper the effect of gas bubble sinking in uniformly oscillating incompressible fluid was theoretically established and experimentally confirmed. Conditions necessary for the presence of the effect are obtained. Expression for the average velocity of gas bubble sinking or rising, which considerably depends on the depth of it's submergence and vibration parameters, is determined. These results can be used to control corresponding technological processes.

Thereby, the results of the paper supplement the multitude of the previous studies devoted to the "wave" mechanism of gas bubble sinking. As opposed to this mechanism, the mechanism, analyzed in the present paper, can be called vibrational.

Acknowledgements

Work is carried out with financial support from the Russian Foundation of Fundamental Research, grants 10-08-00201 and 08-08-00090.

References

[1] Buchanan R. H., Jameson G.J. Cycling migration of bubbles in vertically vibrating liquid columns. Ind. Eng. Chem. Fundamen., 1962, 1(2), 82-86.

[2] Blekhman I.I., Vaisberg L.A., Blekhman L.I., Vasilkov V.B., Yakimova K.S. "Anomalous" Phenomena in Fluid under Action of Vibration. Doklady Physics, 2008, v. 53, No 10, pp. 520-524

[3] Sorokin V.S., Blekhman I.I. Motion of a body with variable volume (a gas bubble) in an oscillating fluid, Proceeding of the APM 2009, 2009, 633-642

[4] Batchelor G.K. Compression waves in suspension of gas bubbles in liquid (In Russian), Mechanics, 3, 1968, pp. 65-84.

[5] Bogdanovich A.M. Theoretical background and methods of efficient separation in gravitational enrichment of raw materials (in Russian) Doctoral Degree Thesis. ZAO Mekhanobr engineering, Saint Petersburg, 2002

[6] Kisevalter B.V. Theory of gravitational enrichment processes (in Russian). Nedra, Moscow, 1979

[7] Bogdanov O.S. Handbook on enrichment of raw materials (in Russian) 2nd Edition extended and corrected. Nedra, Moscow, 1982

[8] Houghton G. The behaviour of particles in a sinusoidal velocity field, Proceedings of the Royal society of London, series A, Vol. 272., 3, 1962, 33-43.

[9] Granat N.L. Motion of a rigid body in pulsating flow of viscous fluid (In Russian), Pr. Of USSR AS, Mechanics and engineering, 1, 1960

[10] Granat N.L. Sizeable oscillations of a ball in viscous fluid (In Russian), Pr. Of the Institute of hydraulic engineering, Vol. 76, 1964

[11] Loytsyanskiy L.G. Free and forced oscillations with the presence of quadratic and intermediate between linear and quadratic resistance laws (In Russian), Engineering book, Vol. 18, 1954, pp. 139-148

[12] Blekhman I.I. Vibrational Mechanics, World Scientific, Singapore, 2000

[13] Tatevosian R.A. Analysis of the regularities of water-air system vibroturbulisation (in Russian), Theoretical fundamentals of chemistry technology, Vol. 11, 1, 1977, pp. 153-155

Sorokin V.S., V.O., 22 linya, 3, Saint-Petersburg, 199106, Russia

Comment

Jet force, which existence is conditioned by the fact that deformable bubble is so-called system with variable composition – certain fluid mass is regularly joining and detaching from it, was not taken into account in the present study. In addition, the pulsations of gas bubble volume were not taken into account then determining the effective resistance force to its motion. These two factors do not qualitatively affect drawn in the paper conclusion about the presence of the effect of gas bubble falling in uniformly oscillating fluid, but their accounting lead to some quantitative changes in the obtained formulas (i.e. expression (30) for X_0 is substituted by $X_0 = \dfrac{2H_0}{\gamma \cdot w^2} \cdot \dfrac{2\left(1+\sqrt{1+\theta\dfrac{A^2}{R_0^2}}\right)+\theta\dfrac{A^2}{R_0^2}}{2\left(1+\sqrt{1+\theta\dfrac{A^2}{R_0^2}}\right)+\dfrac{\theta}{3}\dfrac{A^2}{R_0^2}}$. The reference list should be supplemented with the reference on the following paper: Bleich H.H.: Effect of Vibrations on the Motion of Small Gas Bubbles in a Liquid. *Jet Propulsion. Journal of the American Rocket Society*, vol. 26, 11, pp. 958 – 964, 978, 1956, which is relevant to the considered problem.

The mathematical modeling of conversion regimes in the gas-less systems with regard to mechanical process

Svetlana N. Sorokova Anna G. Knyazeva
s_sorokova@mail.ru

Abstract

In this work the conversion regimes in the gas-less systems are analyzed taking into account the coupling of heat transfer and deformation processes. We formulate and investigate the mathematical model of chemical conversions accompanied by volume change and are connected with various physical phenomena - melting, heat transfer, appearance of stress and deformation as a result of high temperature gradient and change material properties. We assume the relation between the components of stress and strain tensors satisfy to the generalized Maxwell model of viscoelastic medium, that allows to use this model for description of conversion regimes in wide region of temperature variation.

1 Introduction

The systems are called gas-less when chemical conversions in them go without gas phase contribution [1]. Full absence of gasification (both evaporations and formation of gaseous reaction products) is typically for gas-less combustion. Firstly, the possibility of gas-less conversion had been shown when termite combustion has been studied. Further wide class of gas-less systems had been found during the development of self-sustaining high-temperature synthesis method for refractory compounds. That stimulated the further development of gas-less combustion. One of primary features of such systems consists in the independence of combustion rate on pressure [1]. The gas-less systems are the simplest condensed systems and hence can be considered as convenient model for investigations. In addition these systems have important practical applications connected with the new substances synthesis in combustion regime.

This work is devoted to the analysis of conversion regimes in gas-less systems taking into account the interrelation between the heat transfer and deformations processes. In the papers [2, 3], it had been shown, that the interaction of the thermal and mechanical processes leads to appearance of different conversion regimes: quick and slow. Stresses and strains were considered elastic and satisfying to generalize Djuamelya-Neyman relations. In the work [3] the mathematical model had been suggested based on the Maxvell model for viscoelastic body to describe the gas-less conversions. In the work [4], it had been shown, that the model of such type is applicable to the description of mechanical behaviors of the materials possessing the properties of liquid or solid body in different temperature intervals. Separate examples presented in this work had shown, that the features of connected model, typical for elastic stresses [2, 3], are maintained in viscoelastic model.

The object of this work consists in detailed investigation of the chemical conversions regimes, determination of existence conditions for stationary regimes and investigation of their stability to small perturbations.

2 General equations

In the general case, non-stationary equation system, which is required for simulation of conversion front propagation in the gas-less systems in deformable medium, includes the heat conduction

equation

$$c\rho\frac{\partial T}{\partial t} = \nabla\cdot(a_T\nabla T) - 3K\alpha_T T\frac{\partial \varepsilon_{kk}}{\partial t} + Q_r\sum_{l=1}^{n}\frac{\partial y_l}{\partial t}, \tag{1}$$

the motion equation

$$\rho\frac{d\mathbf{v}}{dt} = \nabla\cdot\hat{\sigma} \tag{2}$$

and the elements balance equations

$$\frac{\partial y_l}{\partial t} = \phi_l, \tag{3}$$

where T is the temperature ; c, ρ are the heat capacity and density respectively; a_T is the coefficient of heat conductivity; Q_r is the heat release due to chemical reactions; y_l is the mole concentrations of reactants and reaction products; $\mathbf{v}$ is the velocity vector; ε_{ij} are the components of Koshi strain tensor; ε_{kk} are the first invariant of strain tensor; K is the bulk modulus, λ, μ are the Lamer coefficients; $\hat{\sigma}$ is the stress tensor with σ_{ij} components.

For small deformations we suppose that $\rho \sim const$.

To describe the deformable system in wide region of temperature change we shall take advantage of the Maxvell model of the viscoelastic medium [3, 5]. This model permits the limiting cases of viscous liquid and elastic body. The relations between the stress and strain tensors components take the form [5, 6]

$$\frac{\partial \sigma_{ij}}{\partial t} + \frac{\mu}{\kappa}\sigma_{ij} = 2\mu\frac{\partial \varepsilon_{ij}}{\partial t} + \delta_{ij}\Big[\frac{\partial}{\partial t}(\lambda\varepsilon_{kk} - K\omega) + \frac{\mu}{\kappa}K(\varepsilon_{kk} - \omega)\Big], \tag{4}$$

in generalization of this model, where δ_{ij} - Kronecker delta,

$$\delta_{ij} = \begin{cases} 1, & i = j \\ 0, & i \neq j \end{cases};$$

κ is the coefficient of shear viscosity. In the limiting case $\kappa \to \infty$ we obtain typical relations of Djuamelya-Neyman from equation (4); in the case $\kappa \to 0$ we obtain the relations between σ_{ij} and ε_{ij} components typical for ideal viscous liquid with the spherical stresses tensor.

Here ω - relative change of local volume owing to change of temperature and concentration of the components participating in reactions

$$\omega = 3\Big[\alpha_T(T - T_0) + \sum_{l=1}^{n}\alpha_l(C_l - C_{l,0})\Big]$$

where α_T is the linear heat expansion coefficient; C_l are the mass concentrations of reactants and reaction products; α_l is the concentration expansion coefficients [7]; the index zero relates to the initial condition.

Boundary and initial conditions allow concretize the problem, and same additional conditions allow to simplify it.

3 Example of particular problem

3.1 Problem formulation

As an example of the joint solution of the system of heat conduction equation, kinetics equations and equations describing the mechanical behavior, let's consider the process of sintering of pressing powders the Ti–$TiAl_3$ in the form of the parallelepiped with the sizes l_1, l_2, l_3 in the vacuum furnace at regulated heating [7].

In the simplest approximation, we can neglect in the equation (1) the work of mechanical stresses, and inertia powers in the equation (2). For temperatures far from melting temperature,

we can restrict the model by the case thermo-elastic stresses ($\kappa \to \infty$), then usual Djuamelya-Neyman relations follow from equation (4)

$$\sigma_{ij} = 2\mu\varepsilon_{ij} + \delta_{ij}[\lambda\varepsilon_{kk} - K\omega]$$

and

$$\varepsilon_{kk} = \frac{\sigma_{kk}}{3K} + \omega. \tag{5}$$

Let's assume, that heating of the sample is carried out by radiation at regulated change of temperature of the vacuum furnace walls, and the sample is free from external loadings. Then the boundary conditions take the form

$$x_1 = 0, x_1 = l_1, x_2 = 0, x_2 = l_2, x_3 = 0, x_3 = l_3 : -a_T\frac{\partial T}{\partial x} = -\varepsilon_T\sigma_T(T^4 - T_e^4), \tag{6}$$

where σ_T is the Stefan-Boltzmann constant; ε_T is the emissivity. The temperature of walls of the vacuum chamber (T_e) changes according to law

$$T_e = \begin{cases} v_1 t + T_0, & T \le T_{c1} \\ v_1 t + T_0, & T_{c1} < T \le T_{c2} \\ T_{c2}, & T_{c2} < T \end{cases}$$

where v_1, v_2 — heating speeds known from experiment; t_* is the time of heating; T_0 is the initial temperature; T_{c1}, T_{c2} — known sintering temperatures.

According to state diagram of the system Ti–Al [8], we can write the six chemical reactions

$$TiAl_3 \to TiAl + 2Al; \quad Ti + Al \to TiAl; \quad 2Ti + TiAl_3 \to 3TiAl;$$

$$2Ti + TiAl \to Ti_3Al; \quad 3Ti + Al \to Ti_3Al; \quad Ti_3Al \to 2Ti + TiAl.$$

in the area of atomic concentration which interesting from the practical point of view. We determine the mass concentrations of reactants and reaction products as:

$$y_1 = [TiAl_3], \quad y_2 = [Ti], \quad y_3 = [Al], \quad y_4 = [TiAl], \quad y_5 = [Ti_3Al].$$

Then, according [9] and on base of mass action law, we shall obtain

$$\begin{aligned}
\frac{dy_1}{dt} &= -y_1\varphi_1 - y_1y_2^2\varphi_3, \\
\frac{dy_2}{dt} &= -y_2y_3\varphi_2 - 2y_1y_2^2\varphi_3 - 2y_4y_2^2\varphi_4 - 3y_3y_2^3\varphi_5 + 2y_5\varphi_6, \\
\frac{dy_3}{dt} &= 2y_1\varphi_1 - y_2y_3\varphi_2 - y_3y_2^2\varphi_5, \\
\frac{dy_4}{dt} &= y_1\varphi_1 + y_2y_3\varphi_2 + 3y_1y_2^2\varphi_3 - y_2^2y_4\varphi_4 + y_5\varphi_6, \\
\frac{dy_5}{dt} &= y_4y_2^2\varphi_4 + y_3y_2^3\varphi_5 - y_5\varphi_6,
\end{aligned} \tag{7}$$

where we take into account that all chemical reactions are inhibited by the layer of the product $y = y_4 + y_5$ [1]:

$$\varphi_i = k_i exp\left(-\frac{E_{ai}}{RT}\right) exp(-m_i y) y^{-n_i}, \quad i = 1, \ldots, 6$$

n, m are the stagnation parameters; k_i, E_{ai} are the pre-exponential factor and activation energy.

Considering, that the sample has the small sizes in the comparison with thickness of heating layer, which can form during the specific reaction time, we can neglect the distribution of temperature in the sample. Then we shall integrate the heat conductivity equation (1) along specimen

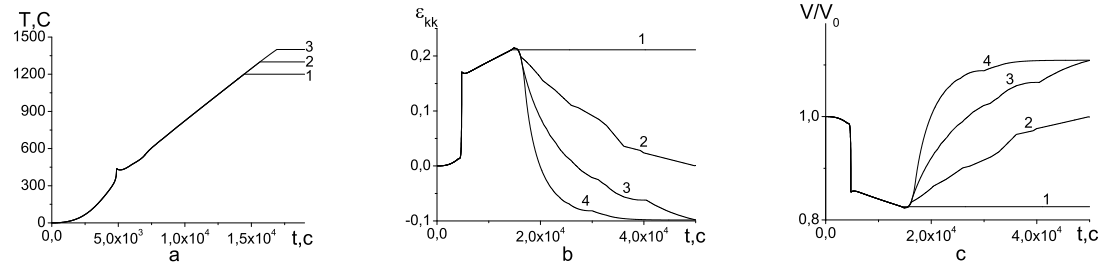


Figure 1: Change of temperature of the sample (a), volumetric strains (b) and relative change of volume (c) during heating and sintering at the variation of the sintering temperature: $1. - T_{c2,1} = 1200^0C$; $2. - T_{c2,2} = 1300^0C$; $3. T_{c2,3} = 1350^0C$; $4. - T_{c2,4} = 1400^0C$

volume taking into consideration the boundary conditions (6). As an result, we obtain the heat balance equation

$$Vc\rho\frac{dT}{dt} = -\varepsilon_T\sigma_T\big(T^4 - T_e^4\big)S_n + \sum_{i=1}^{6} q_i, \tag{8}$$

where S_n is the total surface area of sample, V is its volume, q_i are the heat release functions of chemical reactions [7].

As the sample is free from action of external forces we have $\sigma_{kk} = 0$. Therefore, the simple equation for determining bulk deformations is obtained from equation (5):

$$\varepsilon_{kk} = \omega. \tag{9}$$

Then we can evaluate the volumetric change of the sample. Let's present ε_{kk} as

$$\varepsilon_{kk} = \frac{\rho^{-1} - \rho_0^{-1}}{\rho_0^{-1}} = \frac{\gamma^{-1} - \gamma_0^{-1}}{\gamma_0^{-1}}$$

or

$$\frac{\gamma}{\gamma_0} = \frac{1}{1 + \varepsilon_{kk}} \tag{10}$$

Initial conditions take the form

$$t = 0: \quad T = T_0, \quad y_1 = y_{10}, \quad y_2 = y_{20}, \quad y_3 = 0, \quad y_4 = 0, \quad y_5 = 0. \tag{11}$$

3.2 Numerical investigation

The problem (7)-(11) was solved numerically with use of Runge-Qutta method for a thermal part of the problem and implicit Euler's method for the kinetic part of the problem. Parameters of the model were determined by special methods [7]. The phase and element structure of sample; dependences of elements and phases concentrations on time at various parameters of the model (typical for technological conditions) are Results of numerical research.

In fig. 1, dependences on time of temperature of the sample (a), volumetric deformations (b) and relative change of volume (c) are presented. Calculations were carried out for following initial conditions: $y_1[TiAl_3] = 0.4$ mol/cm^3, $y_2[Ti] = 0.6$ mol/cm^3, $T_{c1} = 400^0C$. The analysis of the results has shown, that first five reactions are initiated during heating pressing that leads to the peak appearance on temperature curves (fig.1,a). In turn, it leads to the origin of compression strains and to the reduction of sample volume approximately to twenty percent (fig.1 b, c, 1 curve). With sintering temperature increasing (that corresponds to plateau on temperature curves, fig.1, a) the reverse reaction of Ti_3Al decomposition initiates. It leads also to the change of final phase structure of the sample (Fig. 2, 1 and 2 curves) and to the reduction of volumetric strains,

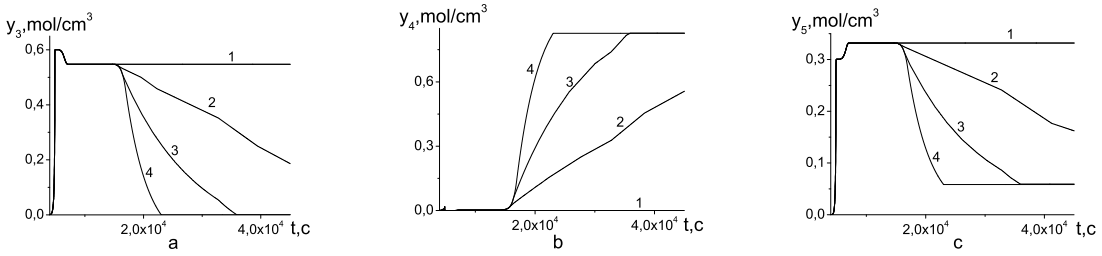


Figure 2: Change of concentration of phases Al (a), $TiAl$ (b) and Ti_3Al (c) at change of temperature of sintering: $1. - T_{c2,1} = 1200^0C$; $2. - T_{c2,2} = 1300^0C$; $3. T_{c2,3} = 1350^0C$; $4. - T_{c2,4} = 1400^0C$

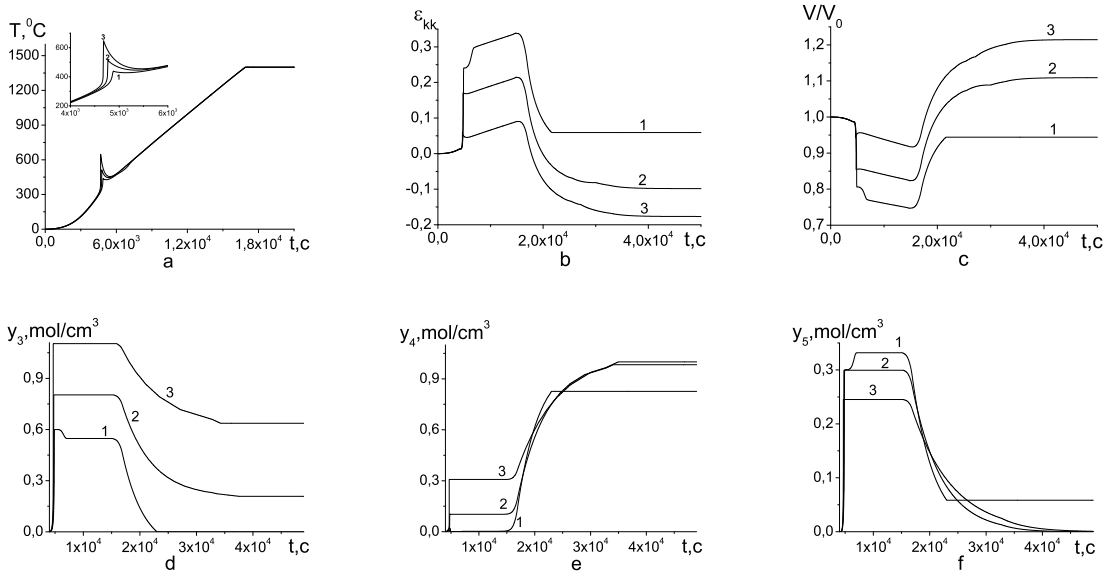


Figure 3: Change of temperature of the sample (a), volumetric strains (b), relative change of volume (c) and molal concentrations of phases of $Al, TiAl$ and Ti_3Al (d)-(f) versus time at the vary of initial molal concentrations of $TiAl_3, Ti$: $1. - y_1[TiAl_3] = 0.3\ mol/cm^3$; $y_2[Ti] = 0.7\ mol/cm^3$; $2. - y_1[TiAl_3] = 0.4\ mol/cm^3$; $y_2[Ti] = 0.6\ mol/cm^3$; $3. - y_1[TiAl_3] = 0.5\ mol/cm^3$; $y_2[Ti] = 0.5\ mol/cm^3$

that is the sample volume increases to ten percent from an initial condition (fig. 1, a, b, 1 and 4 curves). The further temperature increasing leads to the reduction the time necessary for reactions completion in the system (fig. 2, (a) - (c), 2 and 4 curves).

Let's notice, that discovered local maximum on the temperature curve connected with the heat release in the $TiAl_3$ decomposition reaction is observed no under all heating conditions of the sample and is small, therefore there the difficulties to identify it experimentally.

The change of temperature (a), volumetric deformations (b), relative change of volume (c) and concentrations of phases of Al, $TiAl$ and Ti_3Al (d)—(f) versus time in during heating and sintering are demonstrated in fig. 3 at various of initial molal concentrations of $TiAl_3$, Ti. During the heating, the increase of local peak on temperature curves is observed with reduction of initial concentration due to the heat release from first chemical reaction. The concentration of phases Al and $TiAl$ increase, bat concentration Ti_3Al decrease. Hence, the "pure" Al phase is keeped and completely Ti_3Al phase is spended for $TiAl$ phase generation because the speed of reverse reaction reduces.

It is shown from pictures, the volume change of the sample is different during initial and end final stages of the process. During the heating the volume decreases due to reduction of initial

concentration Ti But the specimen volume increases to the sintering process completion. It follows from the analysis of pictures (1,c) and (3,c), that it is possible to choose such initial concentration of $TiAl_3$, Ti and sintering temperature of T_{c2}, that the volume of pressing will not change during the sintering.

As a whole, results do not conflict with experimentally observed regularities [10].

4 Other examples of the problem

Within the mathematical model (1)-(4), the regimes of exothermic mix conversion on base during the heaving of the scanning electronic beam had been investigated. The estimations of the thermal and concentration stresses accompanying the synthesis process were given. It was shown, that the interrelation between thermal and mechanical processes results to new quantitative and to qualitative results.

The analytical and numerical research of possible solutions of type the traveling wave of the problem on front propagation in viscoelastic medium was carried out on the basis of the given mathematical statement (1)-(4) [11]. It was revealed, that the different regimes of front propagation of reaction exist (including slow combustion and solid-phase detonation), analogously to the coupling models of solid-phase combustion for thermoelastic body. The viscous stresses bring the additional features.

The analysis of the stability of self-similar solutions was carried out. It was found that time of a relaxation of viscous stresses effects essential on the limits of steady-state combustion) [12]. From the mathematical point of view, the account of interaction of the different phenomena leads to the appearance in model of nonlinear terms, which lead to change of types of the equations and systems when the parameters vary [13]. It leads to the necessity to develop the special numerical algorithms.

References

[1] Merzhanov A.G. Preprint.Chernogolovka, 1973.

[2] Timokhin A.M., Knyazeva A.G.//Russian Journal of Physical Chemistry B. 1996. V. 15, No 10. P. 1497 - 1514.

[3] Knyazeva A.G.//Journal of Applied Mechanics and Technical Physics, 2003, V. 44, No 2. P.14-26.

[4] Knyazeva A.G., Dyukarev E.A.//Journal “Combustion, Explosion and Shock Waves”. 2000. V. 36, No 4. P. 41-51.

[5] Boley B., Weiner J. Theory of thermal stresses. 1964.

[6] Eremeev V.C. Diffusion and stresses. 1984.

[7] Sorokova S.N., Knyazeva A.G.// Book of reports of the XIII International scientifically-practical conference of students, postgraduate students and young scientists “Modern thecnics and technologies”, V. 2. P. 212-214

[8] Mishin Y., Herzig Chr.//Acta mater. 48 (2000). P. 589-623.

[9] Aldushin A.P., Merzhanov A.G., Khaikin B.I.//Doklady Physical Chemistry. 5(1972). P. 1139-1142.

[10] Pribytkov G.A., Andreeva I.A., Korjova V.V.//Russia journal “The fundamental problems of modern materials science”. 2007. V.4. No 2. P. 128-133.

[11] Knyazeva A.G., Sorokova S.N.//Journal “Combustion, Explosion and Shock Waves”. 2006. V. 42. No 5. P.63-73.

[12] Knyazeva A.G., Sorokova S.N.//Journal "Combustion, Explosion and Shock Waves". 2006. V. 42. No 4. P.50-60.

[13] Sorokova S.N., Knyazeva A.G. //The materials of 3 All-Russian conferences of young scientist "Fundamental problems of new technologies in third thousand years". P. 397-400.

Svetlana N. Sorokova, Tomsk, Russia
Anna G. Knyazeva, Tomsk, Russia

Bounds for compact invariant sets of nonlinear systems possessing first integrals with applications to two hamiltonian systems

Konstantin E. Starkov
konst@citedi.mx

Abstract

In this work we consider two Hamiltonian systems and describe how to derive localization bounds for the domain containing all compact invariant sets.One of these system is the Hamiltonian system appeared in studies of dynamics of hydrogenic atoms. Another one is a class of systems with cubic potential and two degrees of freedom.

1 Introduction

Computing a domain which contains all compact invariant sets of a nonlinear multidimensional continuous-time system is a problem studied intensively during the last years, see e.g. [4],[5],[7]. Finding such domain means its description with help of equations and inequalities depending on parameters of a system and is important for analysis of its long-time dynamics. Localization methods elaborated in these papers are formulated in terms of extrema of some differentiable functions called localizing. The goal of this work is to suggest an approach to a solution of the localization problem for a nonlinear system possessing a first integral. This approach is a generalization of considerations containing in [7] for a localization of compact invariant sets of natural polynomial Hamiltonian systems. Its use allows us not only to extend a class of nonlinear systems for which this method works but find a class of localizing functions which may refine the localization domain as well. Two examples of systems to be considered in this paper are related to Hamiltonian systems. The paper is organized as follows. Useful assertions are given in Section 2. In Section 3 we describe how to localize compact invariant sets of the system possessing a first integral. In Section 4 we examine the Hamiltonian system appeared in studies of dynamics of hydrogenic atoms, see e.g. [1],[2],[3] . In Section 5 we solve the localization problem of all compact invariant sets for one class of systems with cubic potential and two degrees of freedom, see in [6]

2 Some preliminaries and necessary notations

Let us introduce some objects and recall helpful assertions, see e.g. [4],[5]. We consider a $C^\infty-$ differentiable system

$$\dot{x} = F(x), \tag{1}$$

with $x \in \mathbf{R}^n$, $F(x) = (F_1(x), \ldots, F_n(x))^T$ and $F_i(x) \in C^\infty(\mathbf{R}^n)$, $i = 1, \ldots, n$.

Let $h(x) \in C^\infty(\mathbf{R}^n)$ be a function such that h is not the first integral of the system (1). The function h is used in the solution of the localization problem of compact invariant sets and is called a localizing function. Suppose that we are interested in the localization of all compact invariant sets located in some set $N \subset \mathbf{R}^n$ where N is an invariant set for the system (1) or a domain. By $S(h)$ we denote the set $\{x \in \mathbf{R}^n : L_F h(x) = 0\}$, where $L_F h(x)$ is a Lie derivative with respect to F. Further, we define $h_{\inf}(N) := \inf\{h(x) \mid x \in N \cap S(h)\}$, $h_{\sup}(N) := \sup\{h(x) \mid x \in N \cap S(h)\}$.

Proposition 1 *If $N \cap S(h) = \emptyset$ then the system (1) has no compact invariant sets located in N.*

Theorem 2 *For any $h(x) \in C^\infty(\mathbf{R}^n)$ all compact invariant sets of the system (1) located in N are contained in the set defined by the formula*

$$K(N) = \{x \in N : h_{\inf}(N) \le h(x) \le h_{\sup}(N)\}$$

as well.

Any of sets $K(N)$ is called a localization set. Now we remind another result called the iteration theorem, [4].

Theorem 3 *Let $h_m(x), m = 1, 2, \dots$ be a sequence of functions from $C^\infty(\mathbf{R}^n)$. Sets*

$$K_1 = K_{h_1}, \quad K_m = K_{m-1} \cap K_{m-1,m}, \quad m > 1,$$

with

$$K_{m-1,m} = \{x : h_{m,\inf} \le h_m(x) \le h_{m,\sup}\},$$
$$h_{m,.\,\sup} = \sup_{S_{h_m} \cap K_{m-1}} h_m(x),$$
$$h_{m,\inf} = \inf_{S_{h_m} \cap K_{m-1}} h_m(x),$$

contain all compact invariant sets of of the system (1) and $K_1 \supseteq K_2 \supseteq \cdots \supseteq K_m \supseteq \dots$.

Below by F we denote the vector field which corresponds the system under investigation.

3 Localization bounds for systems with first integrals

Suppose that the system (1) possesses a polynomial first integral H of degree $k := \deg H$. Further, assume that there are a localizing function h and real parameter μ_* such that the set M defined by the equation $H(x) + \mu_* L_F h(x) = l$ is compact for some real l. Then we have that

$$K(H^{-1}(l)) = \{\inf_M h \le h \mid_{H^{-1}(l)} \le \sup_M h\} \tag{2}$$

is a localization set for all compact invariant sets contained inside the level set $H^{-1}(l)$. We notice that in this case each of sets $H^{-1}(l)$ and $S(h)$ may be noncompact.

4 Localization bounds for compact invariant sets for equations of dynamics for hydrogenic atoms in external fields

In this section we examine the system defined by the Hamiltonian

$$\begin{aligned} H(x_1, x_2, y_1, y_2) &= \frac{1}{2}(y_1^2 + y_2^2) + \frac{\varepsilon}{2}(x_1^2 + x_2^2) + \frac{m^2}{2}(\frac{1}{x_1^2} + \frac{1}{x_2^2}) + \\ &\quad A(x_1^6 + x_2^6) + B(x_1^4 x_2^2 + x_1^2 x_2^4) + C(x_2^4 - x_1^4). \end{aligned} \tag{3}$$

This system was treated in works [3] devoted to studies of dynamics of hydrogenic atoms in external fields. In the formula (3) parameters are chosen as follows: $A; C; m > 0; \varepsilon < 0; B = \gamma - A$; see [1].

Taking the function h_1 we consider for any real μ the equality

$$\begin{aligned} l &= H - \mu L_F h_1 = A(1+6\mu)(x_1^6 + x_2^6) + B(1+6\mu)(x_1^4 x_2^2 + x_1^2 x_2^4) - \\ &\quad C(1+4\mu)x_1^4 + C(1+4\mu)x_2^4 + \frac{\varepsilon(1+2\mu)}{2}(x_1^2 + x_2^2) + \frac{m^2(1-2\mu)}{2}(\frac{1}{x_1^2} + \frac{1}{x_2^2}) + \\ &\quad \frac{(1-2\mu)}{2}(y_1^2 + y_2^2). \end{aligned} \tag{4}$$

In what follows, we impose the condition

$$-\frac{1}{6} < \mu < \frac{1}{2}. \tag{5}$$

Firstly, we have

Lemma 4 *The sextic in (4) is positive definite if and only if* $A > -B$.

Let us consider Case 1: $B > 0$. In this version of the work we describe briefly omitting details how to derive conditions of the existence of polytopic bounds for the set M.

In order to do this we introduce functions

$$G_i(x) = (x^3 + a_{1i}x + a_2\frac{1}{x})^2 + a_0(x + a_3\frac{1}{x})^2, i = 1, 2.$$

It can be demonstrated that one may assign values $\mu_*; \varepsilon_*, a_{j*}, j = 0, 2, 3; a_{0*} > 0; a_{1i*}, i = 1, 2$ for parameters $\mu; \varepsilon, a_j, j = 0, 2, 3; a_0 > 0; a_{1i}, i = 1, 2$, correspondingly and

$$e_* = 4a_{0*}a_{3*}$$

in a such way that

$$\begin{aligned} \frac{1}{A(1+6\mu_*)}(H - \mu_* L_F h_1) &= \frac{(1-2\mu_*)}{2A(1+6\mu_*)}(y_1^2 + y_2^2) + \\ \frac{B}{A}(x_1^4x_2^2 + x_1^2x_2^4) + G_1(x_1) + G_2(x_2) + e_* &\geq \frac{(1-2\mu_*)}{2A(1+6\mu_*)}(y_1^2 + y_2^2) + \\ & \quad G_1(x_1) + G_2(x_2) + e_*. \end{aligned} \tag{6}$$

Here $\mu_* \neq 0$ is contained in some neighborhood of 0 satisfying the condition (5). We show that if $l > e_*$ then the equation (4), with $\mu = \mu_*$, defines the compact set M.

Now let us derive localization bounds provided

$$l > A(1 + 6\mu_*)e_*. \tag{7}$$

With this goal we shall compute parameters of a polytope P containing M.

Firstly, we have bounds

$$\mid y_i \mid \leq \frac{2(l - A(1 + 6\mu_*)e_*)}{1 - 2\mu_*}. \tag{8}$$

In order to avoid cumbersome formulae we provide bounds for other variables in terms of coefficients of polynomials G_1 and G_2 only. Now we introduce the notation

$$\eta_1 := \frac{l - A(1 + 6\mu_*)e_*}{A(1 + 6\mu_*)a_{0*}}.$$

Assume that, in addition to (7), l satisfies

$$\frac{1}{4}\eta_1 - a_{3*} > 0 \tag{9}$$

as well. This yields the estimate

$$\mid x_j \mid \leq \eta_2 := \sqrt{\frac{\eta_1 - 2a_{3*} + \sqrt{\eta_1^2 - 4a_{3*}\eta_1}}{2}}, j = 1, 2. \tag{10}$$

One may improve bounds (10) by examination the first square expression in G_i. Indeed, let us define

$$\eta_3 := \sqrt{a_{0*}\eta_1}; \eta_4 := \frac{(a_{1i*} - a_*)^2}{4} - a_{2*} + \frac{\eta_3^2}{4a},$$

where a is such positive parameter that $a \geq a_{1i*}$ and $\eta_4 > 0$. We get from (6) that $\mid x_i^4 + a_{1i*}x_i^2 + a_{2*} \mid \leq \eta_3 \mid x_i \mid$ for $i = 1; 2$. This inequality implies

$$(x_i^2 + \frac{a_{1i*} - a}{2})^2 + a(\mid x_i \mid - \frac{\eta_3}{2a})^2 \leq \eta_4.$$

So we obtain

$$\mid x_i \mid \leq \eta_5 := \min\{\sqrt{\frac{a - a_{1i*}}{2} + \sqrt{\eta_4}}; \frac{\eta_3}{2a} + \sqrt{\frac{\eta_4}{a}}\}. \tag{11}$$

So we get from (10)- (11) that

$$\mid x_i \mid \leq \eta_6 := \min\{\eta_2; \eta_5\}. \tag{12}$$

Now we define

$$h_1^* = \frac{4(l - A(1 + 6\mu_*)e_*)\eta_6}{1 - 2\mu_*}; h_{1*} = -h_1^*. \tag{13}$$

By construction, the polytope P defined by (8) and (12) contains M. Further,

$$h_{1\,\sup}(H^{-1}(l)) \leq \max_{P \cap H^{-1}(l)} h_1 \leq h_{1*}; h_1^* \leq \min_{P \cap H^{-1}(l)} h_1 \leq h_{1\,\inf}(H^{-1}(l))$$

and we come to the following result:

Theorem 5 *Assume that parameters of the system defined by the Hamiltonian (3) are such that the corresponding set M is compact . If $l > e_*$ and satisfies inequalities (7)- (9) then all compact invariant sets located in $H^{-1}(l)$ are contained in the set $K_1 = \{h_{1*} \leq h_1(x, y) \leq h_1^*\}$ as well, with bounds h_{1*} and h_1^* defined by formulae (13).*

Finally, we show that the Case 2: $A > -B$ may be reduced to the first one by using lemma.

5 Localization bounds for compact invariant sets of the generalized Hénon-Heiles Hamiltonian system

Below we obtain the polytopic localization bound for all compact invariant sets of a Hamiltonian system with a cubic potential and two degrees of freedom provided one quadratic inequality imposed on parameters of this system is imposed. Namely, we consider the following generalization of the Hénon-Heiles Hamiltonian system:

$$\begin{aligned} \dot{p}_1 &= -aq_1 - 2cq_1q_2 - eq_2^2 \\ \dot{p}_2 &= -bq_2 - cq_1^2 - dq_2^2 - 2eq_1q_2 \\ \dot{q}_1 &= p_1 \\ \dot{q}_2 &= p_2 \end{aligned} \tag{14}$$

which is defined by the Hamiltonian $H(p_1, p_2, q_1, q_2) = \frac{1}{2}(p_1^2 + p_2^2 + aq_1^2 + bq_2^2) + cq_1^2q_2 + \frac{1}{3}dq_2^3 + eq_1q_2^2$. Parameters a and b are supposed to be positive. We show that if $cd > e^2$ then this system possesses a polytope containing all compact invariant sets of (14) and provide explicit formulae for it.

Step 1. Localization bounds for $p_2 + \lambda q_2$.

By using the localizing function $h_2 = p_2 + \lambda q_2$, with λ be a real nonzero parameter we derive

Proposition 6 *Let*

$$cd > e^2. \tag{15}$$

Then all compact invariant sets are contained in the one-parameter family of localization sets

$$\begin{aligned} K(h_2; \lambda) &= \{p_2 + \lambda q_2 \geq r_2(\lambda) := -\frac{(\lambda^2 + b)^2 c}{4\lambda(cd - e^2)}, \lambda > 0\}; \\ K(h_2; \lambda) &= \{p_2 + \lambda q_2 \leq r_2(\lambda), \lambda < 0\}. \end{aligned}$$

Below we assume everywhere that the condition (15) holds.
Step 2. Localization bounds for p_2.
By applying the function $h_3 = p_2$ and results of the 1st step we come to

Theorem 7 *All compact invariant sets are located in the frustum*

$$K(h_3) = \{-r_3 \le p_2 \le r_3\},$$

where

$$r_3 := \frac{6bc + c + b^2c}{cd - e^2}.$$

Step 3. Localization bounds for p_1

Let us apply a localizing function $h_4 = \lambda p_1 + p_2$. Here $\lambda \in (\lambda_-, \lambda_+)$, with

$$\lambda_\pm = \frac{-e \pm \sqrt{4cd - 3e^2}}{2c}.$$

Next, we have introduce notations

$$\eta_1(\lambda) = \frac{(bc - \lambda^2 ac - \lambda ae)^2}{4c(cd - \lambda^2 c^2 - \lambda ce - e^2)^2} + \frac{\lambda^2 a^2}{4c}$$

and

$$\begin{aligned} \eta_2 &= \sqrt{\frac{c\eta_1}{cd - \lambda^2 c^2 - \lambda ce - e^2}} + \frac{bc - \lambda^2 ac - \lambda ae}{2(cd - \lambda^2 c^2 - \lambda ce - e^2)}; \\ \eta_3 &= \sqrt{\frac{\eta_1}{c}} + \frac{\lambda a}{c} + \frac{\lambda c + e}{c}\eta_2. \end{aligned}$$

Using these notations we show that the polytope P_3 :

$$\begin{aligned} -\eta_2 &\le q_2 \le \eta_2; \\ -\eta_3 &\le q_1 \le \eta_3 \end{aligned}$$

in the $(q_1, q_2)-$ linear space contains $S(h_4)$. Now we derive from the formula $H(p, q) = l$ that the inequality

$$p_1^2 \le 2l + 2c\eta_2\eta_3^2 + \frac{2d}{3}\eta_2^3 + 2e\eta_2^2\eta_3 + r_3 + a\eta_3^2 + b\eta_2^2 \tag{16}$$

holds on $K(h_3) \cap H^{-1}(l) \cap P_3$. By r_4^2 we denote the right side of (16), $r_4 > 0$. Then we get the localization set

$$K(h_4) := K(H^{-1}(l); h_4) = \{-r_4 \le p_1 \le r_4\}.$$

Step 4. Localization bounds for q_1 and q_2. We have from the main theorem in [7]:

Proposition 8 *Take any real $l > 0$. Then*

$$K(H^{-1}(l); h_u) = \{-\frac{6\sqrt{5}l}{5}(\frac{\sqrt{a}}{a} + \frac{\sqrt{b}}{b}) \le p_1q_1 + p_2q_2 \le \frac{6\sqrt{5}l}{5}(\frac{\sqrt{a}}{a} + \frac{\sqrt{b}}{b})\}.$$

Now we introduce notations

$$\begin{aligned} r_5 &= \frac{6\sqrt{5}l}{5}(\frac{\sqrt{a}}{a} + \frac{\sqrt{b}}{b}) + \frac{b^2c}{8(cd - e^2)}, \\ r_6 &= \sqrt{\frac{2cr_5}{cd - e^2}} + \frac{bc}{2(cd - e^2)}, \\ r_7 &= \sqrt{\frac{2r_5}{c}} + \frac{r_5}{c}. \end{aligned}$$

In these notations by applying the iteration theorem and the last assertion we can get

Theorem 9 *If the condition (15) holds then all compact invariant sets contained in the level set* $H^{-1}(l)$, *with* $l > 0$, *are contained in the polytope*

$$\begin{array}{rcl} -r_4 & \leq & p_1 \leq r_4; \\ -r_3 & \leq & p_2 \leq r_3; \\ -\sqrt{r_6^2 + r_7^2 + 2r_3} & \leq & q_i \leq \sqrt{r_6^2 + r_7^2 + 2r_3}, i = 1, 2, \end{array} \tag{17}$$

Similarly, in case $l = 0$ we introduce notations

$$\begin{array}{rcl} r_8 & : & = \dfrac{bc}{cd - e^2}, \\ r_9 & : & = \dfrac{b}{2\sqrt{cd - e^2}} + \dfrac{be}{cd - e^2}. \end{array}$$

Then we establish

Theorem 10 *If the condition (15) holds then all compact invariant sets contained in the level set* $H^{-1}(0)$ *are contained in the polytope defined by the first two inequalities in (17) and inequality* $-\sqrt{r_9^2 + r_8^2 + 2r_3} \leq q_i \leq \sqrt{r_9^2 + r_8^2 + 2r_3}, i = 1, 2.$

6 Acknowledgment

This work was supported by the Conacyt project "Análisis de localización de conjuntos compactos invariantes de sistemas no lineales con dinámica compleja y sus aplicaciones", N. 000000000078890, Mexico.

References

[1] Beims, M.W. & Gallas, J.A.C. "Integrals of motion and quantum operators for hydrogenic atoms in external fields", Physical Review A 62, 043410, 2000.

[2] Ganesan, K. & Lakshmanan, M. "Quantum chaos of the hydrogenic atom in a generalized van der Waals potential", Physical Review A 48, 964, 1993.

[3] Kharbach, J., Dekkaki, S., Ouazzani, A. T.-H. & Ouazzani-Jamil, M. "Bifurcations of the common level sets of atomic hydrogen in van der Waals potential", International Journal of Bifurcations and Chaos 13, 107-114, 2003.

[4] Krishchenko, A.P. & Starkov, K.E. "Localization of compact invariant sets of the Lorenz system", Physics Letters A 353, 383-388, 2006.

[5] Krishchenko, A.P. & Starkov, K.E. "Estimation of the domain containing all compact invariant sets of a system modelling the amplitude of a plasma instability", Physics Letters A, 367, 65-72, 2007.

[6] Maciejewski, A., Radzki, W. & Rybicki, S. "Periodic trajectories near degenerate equilibria in the Henon-Heiles and Yang-Mills Hamiltonian systems", Journal of Dynamics and Differential Equations, 17, 475-488, 2005.

[7] Starkov, K.E."Universal localizing bounds for compact invariant sets of natural polynomial Hamiltonian systems", Physics Letters A 372, 6269-6272, 2008

Konstantin E. Starkov, CITEDI-IPN, Av. del Parque 1310, Mesa de Otay, Tijuana, Baja California

Hybrid algorithms in computational model updating procedures for hydromechanical systems

V. D. Sulimov P. M. Shkapov
spm@bmstu.ru

Abstract

Reliable computer modelling in hydromechanical system dynamics is very important for studies related to the safety of aerospace structures and equipment components in the nuclear power industry. Computational dynamic model updating is a powerful means to produce these accurate and reliable models. The method uses an initial computational model and measured spectral data of the system to modify physical parameters of the initial model. Problems of computational model validation are formulated as inverse spectral problems. Incompleteness of registered spectral data and presence of multiple frequencies result in the error function being non-convex and non-differentiable. As the function has numerous local minima, it is necessary to use global optimization methods. Two novel global optimization algorithms combining a Metropolis-based stochastic algorithm and deterministic gradient techniques or a space-filling curve method are introduced. Implementations of the hybrid algorithms are discussed. Results of successful computational experiments are presented to illustrate the efficiency of the approach.

1 Introduction

Up-to-date development and operational processes for aerospace and nuclear power structures impose heavy demands on the accuracy and computational reliability of mathematical models. A number of recent papers are devoted to modelling and simulation problems in connection with satellite dynamics for control purposes, construction of aircraft structural components, finite element model updating for in-core components of reactors, construction of a simulation framework for technical systems life cycle cost analysis, analytical evaluation of design and operating two-phase circulation flow characteristics under external reactor vessel cooling [1–5]. Evidently structural design and analysis requires a computational model representing the physical behaviour of the structure. In actual practice in the field of structural dynamics, numerical estimates generally do not sufficiently match the measured data obtained from vibration experiments [6]. The modern methodology to reduce the above discrepancies is to update the assumptions made for physical idealizations and parameters of the computational model until the agreement between numerical predictions and experimental results satisfy practical requirements. In particular, appreciable effort has been made in the development of special-purpose procedures for updating parameters of computational models using data extracted from vibration tests. The much used approach to computational model updating is the inverse sensitivity technique where residuals between numerical and measured eigenvalues and/or mode shapes are minimized in order to improve user-selected parameters. The finite element model updating method [7] has been proved to be a reliable approach for structural dynamics problems.

In the gradient-based inverse sensitivity methods of the model updating is critically important to define an appropriate error function between the computed and measured modal data. The estimated parameters can be obtained by minimizing the error function, which is generally a nonlinear function of the updating parameters. Moreover, in defining the error function the correct pairing of computed modal data with the measured modal data is essential. The reason is that the pairing of computed and experimental modal data based on the sequential order of mode numbers may not be correct at all times. With the aim of establishing the correct modal correspondence

the modal assurance criterion is generally used. One further important stage in model updating is the selection of the parameters to be updated. In particular, the computed natural frequencies and corresponding mode shapes of the computational model should be sensitive to the selected updating parameters. Quite often only the measured eigenvalues are used for model updating. This is because firstly the measured mode shapes contain more noise than the natural frequencies and secondly the mode shapes are not very sensitive to parameter changes. Nevertheless, the mode shapes are necessary to ensure that the modes under consideration are paired correctly. The objective function in the minimization problem is the weighted sum of squares of the error in the eigenvalues. The problem is non-linear and requires an appropriate iterative solution, and in turn this requires the formulation and computation of the sensitivity matrix of the function to be minimized with respect to the updating parameters. The eigenvalue derivatives with respect to the updating parameters can be evaluated by the differentiation of the characteristic structural dynamic equation. Possible availability of repeated or very close eigenvalues one should take into account. As the minimization problem is usually ill-conditioned, then various regularization techniques should be applied [8, 9].

The inverse problems under study are solved for perfect but incomplete spectral data. The results of corresponding direct problem solutions have been confirmed by using the finite-element code ANSYS. Incompleteness of the experimental spectral data and presence of repeated eigenvalues result in the error function being non-convex and non-differentiable. Since the error function has numerous local minima, it is necessary to use global optimization methods. Properties of deterministic global optimization algorithms are well-studied. Thus a modified tunnelling algorithm had been used for the diagnostic problem of the nuclear reactor primary circuit [10]. It is common knowledge that the performance of deterministic algorithms essentially depends on the problem dimension. Implementation of two novel hybrid algorithms is discussed. Both of them combine the recent stochastic algorithm PCA [11] with the deterministic gradient technique and also with the space-filling curve method [12].

The plan of the remainder of this paper is as follows. The section following contains statement of the computational model updating problem. Section 3 provides brief description of hybrid global optimization algorithms. In section 4 successful computational experiments for two model updating problems are presented to illustrate peculiarities of the proposed approach. Section 5 gives conclusions and discussion on further work.

2 Formulation of the problem

It is supposed that a set of performance index values associated with a computational model to be updated is defined by a set of controlling variables. Experimental spectral data registered by permanent instrumentation may be incomplete. So the goal is to determine vectors of controlling variables using only measured data on natural frequencies of the object. The standard approach is to set the inverse spectral problem and then to solve the corresponding least squares problem

$$\min_{x \in X \subset R^n} f(x), \tag{1}$$

where $f(x) = \sum_{i=1}^{N} w_i \left(\zeta_i(x) - \zeta_i^*\right)^2$; $x, X-$the vector of controlling variables and its feasible domain of the error function $f(x)$ respectively; the w_i stand for weighting factors that reflect the confidence level in the measurements; N is the number of eigenvalues under consideration; $\zeta_i(x)$ and ζ_i^* denote the eigenvalues that correspond to computed (solutions of the direct problem) and to measured natural frequencies respectively;

$$X = \left\{ x_i \;\middle|\; x_i^L \le x_i \le x_i^U;\ i = \overline{1,n} \right\}; \tag{2}$$

here $x_i^L, x_i^U-$the lower and upper bounds on the ith controlling variable.

As practical observations show, the error function in the considered problem is often multiextremal. Therefore, it is necessary to turn to methods of global optimization. It is clear that if the measured spectral data exactly match to the computational model then the solution of the minimization problem will cause error function to take its global minimum value of zero. Let us

suppose that there is a unique solution of the ill-posed inverse spectral problem and that this corresponds to the global minimum of the error function. However, the fact is that the theoretical question of the uniqueness of solutions of the problem may not be relevant to practical applications in which there is the additional complication of accuracy of experimental measurements. Furthermore, some complications may arise due to incompleteness of measured spectral data, influence of the two-phase interference on the flow dynamics, the presence of noise, etc. Within the scope of this work we take it as a convenient and reasonable assumption that global minimization of the error function in the above inverse problem will yield correct model updating for objects under consideration.

3 Hybrid global optimization algorithms

3.1 The hybrid algorithm NMPCA with a Nelder-Mead Simplex

The modern Particle Collision Algorithm [11] has some essential advantages in relation to well known stochastic global optimization algorithms such as the Genetic Algorithms, Simulated Annealing, Fast Simulated Annealing, etc. Specifically, the PCA does not require any additional parameters other than the number of iterations; the algorithm is extremely easy to implement and can be applied to both continuous and discrete optimization problems. The original PCA works as follows. First an initial configuration is chosen, then a modification of the old configuration into a new one is implemented. The qualities of the two configurations are compared. A decision then is made on whether the new configuration is acceptable. If it is, the current configuration acts as the old configuration for the next step. If it is not acceptable, the algorithm proceeds with a new change of the old configuration. It is pertinent to note that acceptance of current trial solution with certain probability may avoid the convergence to local optima.

However, the PCA is in its early stages. In spite of its advantages over Genetic Algorithm and Simulated Annealing in solving test problems, practical application of the PCA is restricted because of solutions remain too expensive. As possible development, the local search procedure in the algorithm could be improved. It seems promising to use gradient methods for local minimization of the error function. But in so doing the problem of non-differentiability of the function should be taken into account.

A hybridization of the PCA and the deterministic Nelder-Mead Simplex algorithm was introduced in [13]. The NMPCA algorithm was applied to a nuclear reactor core design optimization problem. During processing two procedures are performing: a wide search in the solution space using the stochastic PCA and a local search in the promising areas with the deterministic simplex algorithm. The local search procedure is performed iteratively until a certain number of fitness function evaluations being reached. It is pertinent to note that the convergence theory for Nelder-Mead simplex method is far from completion; so the method can fail to converge or converge to non-stationary points [14]. By this is meant that the question of reliability of the algorithm as a whole is still an open question.

3.2 The hybrid algorithm PCAHS with a gradient local search

As an alternative to the NMPCA a novel hybrid algorithm was introduced in [15]. In this new version of the global optimization algorithm the local search mechanism is a standard deterministic linearization method. Inverse problems are considered to be substantially difficult because of the kinks connected with presence of the repeated or very close frequencies in registered spectra for the computational model under updating. The difficulty motivated the development of algorithms for the solution of the minimization problem via some smooth approximation, which could be minimized by using any of the efficient classical approaches for smooth optimization. Several approximations to smooth out the kinks may be introduced. One of them results in a continuously differentiable approximate fitness function, whereas another one leads to a twice continuously differentiable approximate function. These approximations replace the original function in some neighborhoods of directional differentiability points. Moreover, this approach preserves such important property of the original function as its convexity. It is clear that the approach makes it possible to implement efficient gradient techniques in the solution process. In general case the error

function is not differentiable everywhere, so the implementation of the smoothing technique may be quite pertinent. Computational experiments show the principal applicability of the proposed hybrid algorithm PCAHS for solving the inverse spectral problems.

3.3 The hybrid algorithm PCASFC

Some powerful algorithms for multi-extremal non-convex optimization problem are based on reducing the initial multi-dimensional problem to the equivalent problem of one dimension. This reduction can be executed by applying Peano-type space-filling curves mapping a unit interval on the real axis onto a multi-dimensional hypercube [16]. The Peano curve development maps the segment $[0,\ 1]$ of the real axis R^1 into the hypercube $X \subset R^n$ that has been determined in (2). Actually, this is the case of continuous single-valued mapping that offers finding point $x(z) = (x_1(z),\ \ldots\ , x_n(z))^T \in X$ for each point $z \in [0,\ 1]$:

$$\min_{x \in X} f(x_1, ..., x_n) = \min_{0 \le z \le 1} \phi(z).$$

So, the initial multi-dimensional minimization problem (1) is equivalent to the above one-dimensional problem of finding the global minima of the discontinuous multi-extremal function $\phi(z)$. The Hilbert technique is used here for building the development of the Peano space-filling curve depending on a parameter m that stands for the number of subdivision levels.

The approach needs not any derivatives of the function to be minimized with updating parameters. Some disadvantage of this approach is in the fact that one-dimensional problem obtained by the above reduction leaks some information on the closeness of iteration points in the initial multi-dimensional space.

Algorithm SFC: reduction of the problem dimension using the space-filling curve method.

0. Set formally the point x^* of local minimum. Let two small numbers $\gamma_1 > 0, \quad \gamma_2 > 0$, and the vector of constraints $\beta \in R^n$ be given. Let $k = 0,\ m = 1$.

1. The local minimization phase: find new point x^* (after l sub-iterations); set $k = k + l$. If $f\left(x^k\right) = 0$ then go to step 2. If $f\left(x^k\right) < \gamma_1$ and $x_i^k > \beta_i$ for some $i \in I^x, \quad I^x = \{1,\ 2,\ \ldots\ , n\}$, then build the effective sub-vector x_{eff}^k, reduce the multi-dimensional problem to the one-dimensional form and go to step 2. Else, go to step of stochastic scanning.

2. Set $m = m + 1$. If $m \le m_{\max}$ then go to step 3. Else, go to step 4.

3. Define the current value z_* using the development of the Peano curve and calculate the current approximation of $\phi(z_*)$. If $\phi(z_*) \ge \gamma_2$ then go to step 2.

4. Reconstruct x^* and $f(x^*)$ using z_* and $\phi(z_*)$.

5. Define the point of local minimum $x^{LM} = x^*$, stop.

The pseudo code brief description of the hybrid PCASFC algorithm that combines the PCA and the deterministic space-filling curve method is as follows.

0. Generate an initial solution *Old_Config*
1. For $n = 0$ to # iterations
Generate a stochastic perturbation of the solution
If Fitness *(New_Config)* > Fitness *(Old_Config)*
Old_Config := *New_Config*
Local search ( )
Else
Scattering ( )
End If
End For
2. Local search ( )
Apply procedure of local search
using the Space-Filling Curve Algorithm
Return
3. Scattering ( )
p_{scatt} = 1−(Fitness (New_Config)) / (*Best Fitness*)
If p_{scatt} > random(0, 1)
Old_Config := random solution

Else
Exploration ( )
End If
Return

4 Computational results

In this section two numerical examples of hybrid algorithms PCAHS and PCASFC applications to inverse spectral problems for VVER-1000 nuclear reactor equipment are presented. In the first example the updating of the computational model of the coolant two-phase flow dynamics in the primary circuit is carried out. The second example is devoted to the steam pipe finite element model updating.

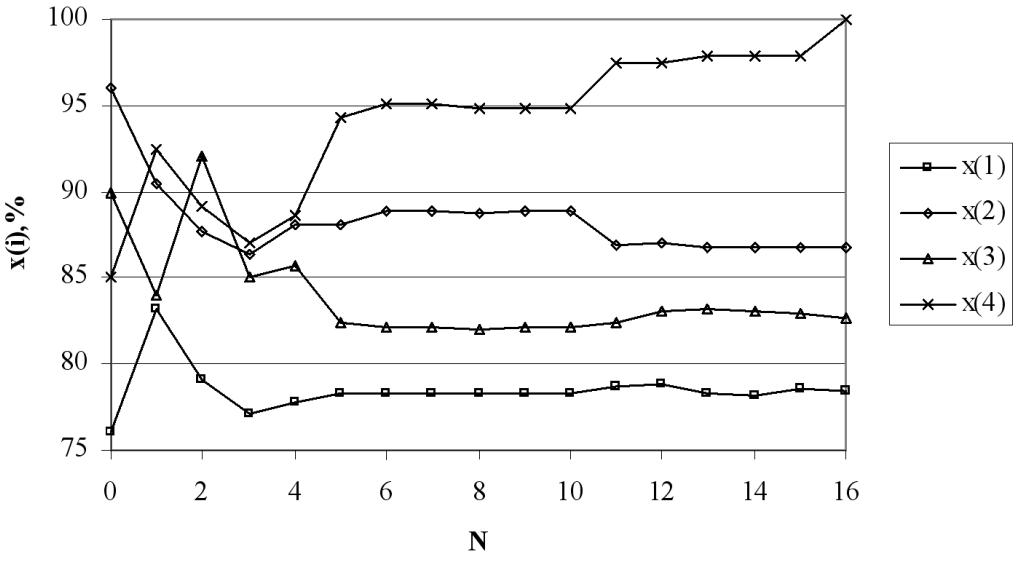


Figure 1: Number of final iterations of the PCAHS vs. relative velocities (Example 1).

Example 1. The computations were performed in connection with the problem of identification of the coolant phase constitution in the VVER-1000 primary circuit. Appearance of the second phase is possible: in a coolant heating zone (pressure tank of the pressurizer), in an exit volume of the reactor pressure vessel (RPV), in a core barrel of the RPV, in exit volumes of main circulating pumps. In order to formulate the inverse problems two vectors of relative acoustic velocities in a coolant flowing throw the specified zones are introduced. Let now the anomalous coolant state constitution be characterized by the vector of controlling variables: $x_1^* = 78.5\%$; $x_2^* = 87.5\%$; $x_3^* = 82.0\%$; $x_4^* = 100\%$. The error function is determined using ten lower spectral components. Table 1 displays the known spectral data for the considered model upating problem. Here we have: $i-$mode number; ω_i-natural ith frequency of the coolant oscillation under normal conditions (without appearance of the second phase in the coolant); ω_i^*- natural ith frequency of the coolant oscillation with the availability of anomalies in coolant phase constitution.

Table 17: Given spectral data for Example 1

i	1	2	3	4	5	6	7	8	9	10
ω_i, Hz	0.89	6.77	9.82	15.44	15.96	18.94	24.57	26.69	27.07	30.52
ω_i^*, Hz	0.82	6.77	9.34	15.33	15.96	18.86	21.36	26.67	26.93	29.37

The approximate solution reached by using the PCAHS algorithm is: $x_1^* \approx 78.43\%$; $x_2^* \approx 86.74\%$; $x_3^* \approx 82.71\%$; $x_4^* = 100\%$. Fig. 1 and Fig. 2 illustrate the solution history (final iterations

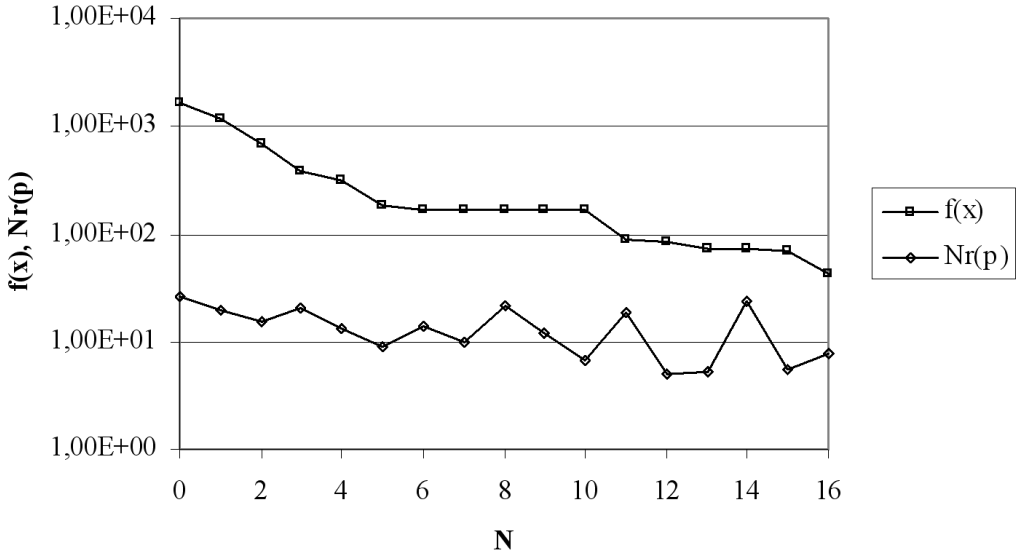


Figure 2: Number of final iterations of the PCAHS vs. error function and search gradient norm (Example 1).

of the hybrid algorithm). The inaccuracy of the relative acoustical velocity computing is about 1%. As follows from the results obtained in this example the coolant phase constitution anomalies are conditioned by boiling process in the coolant heating zone, in the exit volume of the reactor pressure vessel and in the core barrel of the RPV.

Example 2. The object under consideration is a steam pipe from the connection with the second circulating loop steam collector to the support on the wall of the airtight zone. Spacing supporting units bound the vertical displacements of the pipe only. The stiffness of each spacing unit is $c = 40.0$ MN/m. Anomalous state of the object is characterized by decrease of the stiffness characteristics. The spectra corresponding to normal state and anomalous one of the object are given. It is convenient to introduce the following controlling variables: $x_i = (c_i/c) \cdot 100\%$, where $c_i \leq c$ is the current stiffness of the ith supporting unit. First we consider the problem for known spectral data presented in Table 2. Here we have: $i-$mode number; ω_i-natural ith frequency of the object oscillation under normal conditions; ω_i^*- natural ith frequency of the object oscillation with abnormal state of the supporting units.

Table 18: Given spectral data for Example 2

i	1	2	3	4	5	6	7	8
ω_i, Hz	13.35	23.46	26.14	27.67	35.96	44.81	51.15	56.90
ω_i^*, Hz	9.19	16.98	20.93	26.31	34.04	43.60	51.10	56.90

Let the anomalous state of the supporting units be characterized by the following vector of controlling variables: $x_1^* = 38\%$, $x_2^* = 63\%$, $x_3^* = 2\%$, $x_4^* = 85\%$. The error function in this example is determined using eight lower spectral components. Controlling parameters dependence on the number of subdivision levels m of the hybrid algorithm PCASFC is shown in Fig. 3; the corresponding dependence for the error function $f(x)$ is presented here too.

The approximate solution of the model updating problem reached by using the PCASFC algorithm is: $x_1^* \approx 38.09\%$; $x_2^* \approx 62.47\%$; $x_3^* \approx 1.22\%$; $x_4^* = 85.21\%$. The inaccuracy in computation of the controlling variables is less than 2%. Maximal relative error in defining the eigenfrequencies is about 3%.

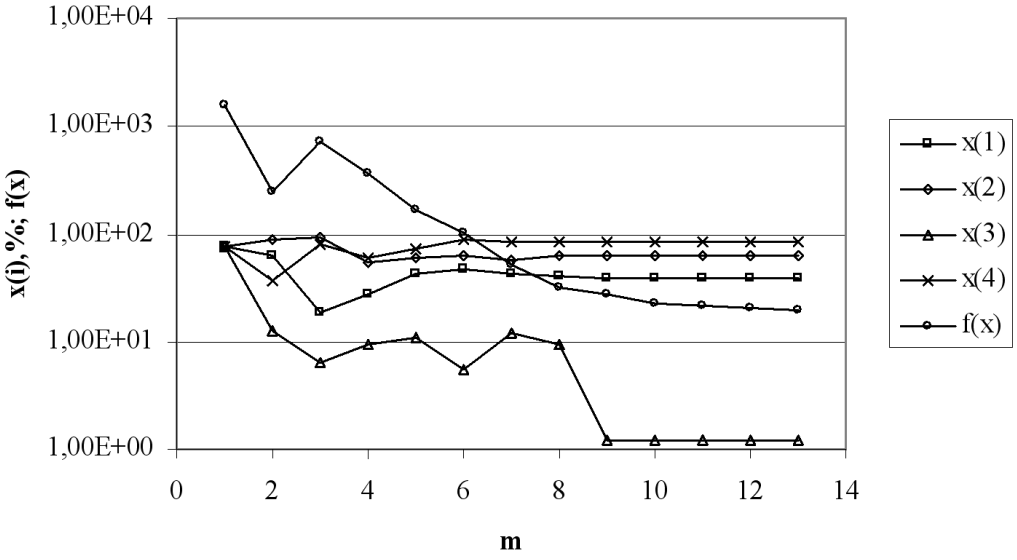


Figure 3: Number of subdivision levels of the PCAHS vs. error function and controlling variables (Example 2).

5 Conclusions

Two novel global optimization algorithms combining a Metropolis-based algorithm and deterministic gradient technique or space-filling curve method for local search are presented. Smoothing approximations are introduced during the local search that makes it possible to expand the PCAHS algorithm on the class of non-differentiable problems. The PCASFC algorithm being introduced here does not require any gradient information. Both the algorithms were used for solving inverse spectral problems in connection with computational model updating for the two-phase coolant flow in the nuclear reactor primary circuit and for the steam pipe supporting units. Numerical experiments show the principal applicability of the proposed hybrid algorithms for solving the above model updating problems. The future work will be devoted to increasing the computational efficiency of tools for solution the model updating problems with regard to noisy data.

Acknowledgements

This research is partially supported by the program "Leading Scientific Schools" of Russian Federation (the grant NSh-5271.2010.8).

References

[1] T. Pulecchi, F. Casella, M. Lovera. Object-oriented modeling for spacecraft dynamics: Tools and applications. Simulation Modelling Practice and Theory 18, 63–86, 2010.

[2] F.A.C. Viana, V. Steffen Jr., S. Butkewitsch, M. de Fritas Leal. Optimization of aircraft structural components by using nature-inspired algorithms and multi-fidelity approximations. Journal of Global Optimization 45, 427–449, 2009.

[3] J.K. Sinha, A. Rama Rao, R.K. Sinha. Realistic seismic qualification using the updating finite element model for in-core components of reactors. Nuclear Engineering and Design 236, 232–237, 2006.

[4] D.G. Cople, E. S. Brick. A simulation framework for technical systems life cycle cost analysis. Simulation Modelling Practice and Theory 18, 9–34, 2010.

[5] J.W. Park. Analytical evaluation of two-phase natural circulation flow characteristics under external reactor vessel cooling. Annals of Nuclear Energy 36, 1668–1675, 2009.

[6] D. Göge, M. Link. Assessment of computational model updating procedures with regard to model validation. Aerospace Science and Technology 7, 47–61, 2003.

[7] M.I. Friswell, J.E. Mottershead. Finite Element Model Updating in Structural Dynamics. Kluwer Academic Publishers, Dordrecht, 1995.

[8] H. Ahmadian, J.E. Mottershead, M.I. Friswell. Regularization methods for finite element model updating. Mechanical Systems and Signal Processing 12, 47–64, 1998.

[9] S. Kindermann, A. Neubauer. On the convergence of the quasioptimality criterion for (iterated) Tikhonov regularization. Inverse Problems and Imaging 2, 291–299, 2008.

[10] V.G. Kinelev, P.M. Shkapov, V.D. Sulimov. Application of global optimization to VVER-1000 reactor diagnostics. Progress in Nuclear Energy 43, 51–56, 2003.

[11] W.F. Sacco, C.R.E. de Oliveira, C.M.N.A. Pereira. Two stochastic algorithms applied to nuclear reactor core design. Progress in Nuclear Energy 48, 525–539, 2006.

[12] H. Sagan. Space-Filling Curves. Kluwer Academic Publishers, Dordrecht, 1994.

[13] W.F. Sacco, H.A. Filho, N. Henderson, C.R.E. de Oliveira. A Metropolis algorithm with Nelder-Mead Simplex applied to nuclear reactor core design. Annals of Nuclear Energy 35, 861–867, 2008.

[14] K.I.M. McKinnon. Convergence of the Nelder-Mead simplex method to a non-stationary point. SIAM J. Optimization 9, 148–158, 1998.

[15] V.D. Sulimov, P.M. Shkapov. Hybrid algorithms applied to inverse spectral problems for hydromechanical systems // Proceedings of the XXXVII International Summer School-Conference "Advanced Problems in Mechanics" APM 2009. St. Petersburg (Repino), June 30 – July 5, 2009. – http://apm-conf.spb.ru – St. Petersburg, 2009. – P. 658-668.

[16] R.G. Strongin, Y.D. Sergeev. Global optimization: fractal approach and non-redundant parallelism. Journal of Global Optimization 27, 25–50, 2003.

V. D. Sulimov, Baumanskaya 2nd str. 5, Moscow, 105005, Russia.
P. M. Shkapov, Baumanskaya 2nd str. 5, Moscow, 105005, Russia.

Structural-phenomenological model of the mechanical behavior of elastomeric nanocomposites based on styrene butadiene rubber

A. L. Svistkov A. G. Pelevin A. A. Adamov B. Lauke K. W. Stöckelhuber
G. Heinrich
pelevin@icmm.ru

Abstract

We present a theoretical study of the mechanical behavior of elastomeric nanocomposites based on butadiene-styrene polymer and some other fillers of varying volume fraction. To construct constitutive equations, we use the scheme consisting of points connected by elastic, viscous, plastic and transmission elements. The properties of each element are described by equations of the nonlinear theory of elasticity, the theory of nonlinear viscous fluids and the the-ory of plastic flow under finite deformation conditions. A step-by-step algorithm is used to derive the model constants. It is shown that the constants for constitutive equations determined at earlier steps remain unchanged at further steps. Experiments (cyclic loading tests, including relaxation and creep) carried out have provided much information concerning the viscoelastic properties of rubber.

Model of the mechanical behavior of rubber

The mechanical behavior of rubber is described by the model schematically represented in Fig. 1, where each point corresponds to a particular set of constitutive equations. The scheme shows how the tensor nonlinear equations are combined into the system of equations used to calculate the complex viscoelastic behavior of the medium deformed in an arbitrary way. The algorithm for constructing constitutive equations consisting of separate groups of equations (elastic, viscous, plastic, transmission) is described in detail in work [1]. The model uses the approach that is based on additive decomposition of the deformation-rate tensor of the medium into the deformation-rate tensors of the scheme elements [2]. The internal scheme points are required to meet the condition of correlation of the Cauchy stress tensors [1]. The scheme for the mechanical behavior of the material involves transmission, elastic, viscous and plastic elements that correspond to the following equations:

The material is assumed to be incompressible. The deviator of the Cauchy stress tensor of the elastic element is calculated from the equations of the theory of elasticity

$$\operatorname{dev}\mathbf{T}_i = \operatorname{dev}\left(\rho\sum_{k=1}^{3}\lambda_k^{(i)}\frac{\partial f}{\partial\lambda_k^{(i)}}\,\mathbf{n}_k^{(i)}\otimes\mathbf{n}_k^{(i)}\right),$$

in which the mass density of the medium free energy f depends on the extension ratios of elastic elements.

$$f = f(\lambda_1^{(2)},\lambda_2^{(2)},\lambda_3^{(2)},\lambda_1^{(5)},\lambda_2^{(5)},\lambda_3^{(5)},\lambda_1^{(7)},\lambda_2^{(7)},\lambda_3^{(7)}),$$

where $\lambda_1^{(i)}$, $\lambda_2^{(i)}$, $\lambda_3^{(i)}$ and $\mathbf{n}_1^{(i)}$, $\mathbf{n}_2^{(i)}$, $\mathbf{n}_3^{(i)}$ — are the extension ratios and eigenvectors of the stretch tensor $\mathbf{V}_i$ of the i-th elastic element . Time variations in the tensor $\mathbf{V}_i$ are calculated by the evolution equation.

$$\frac{2}{\nu_i}\,\mathbf{Y}_i{}^{0.5}\,\mathbf{D}_i\mathbf{Y}_i{}^{0.5} = \dot{\mathbf{Y}}_i - \mathbf{Y}_i\,\mathbf{W}_{\mathbf{R}}^{\mathrm{T}} - \mathbf{W}_{\mathbf{R}}\,\mathbf{Y}_i, \qquad \mathbf{W}_{\mathbf{R}} = \dot{\mathbf{R}}\,\mathbf{R}^{\mathrm{T}}.$$

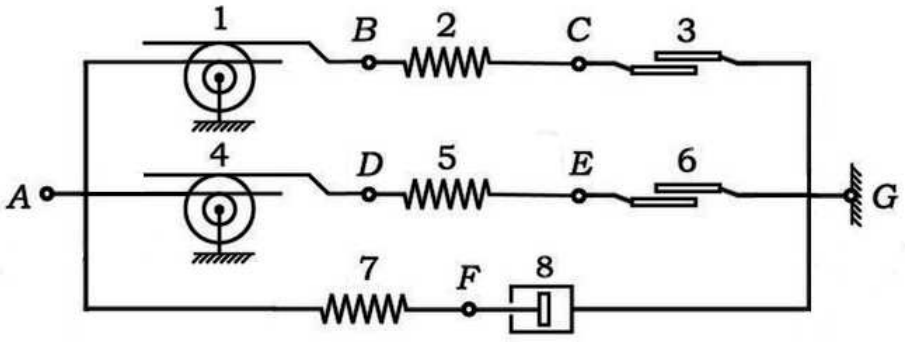


Figure 1: Schematic of the model of the mechanical behavior of rubber

The formula uses the following notations:

$$\mathbf{Y}_i = \mathbf{V}_i{}^{\frac{2}{\nu_m}}, \qquad \nu_m > 0,$$

where $\mathbf{R}$ — is the rotation tensor in the polar decomposition $\mathbf{F} = \mathbf{VR}$ of the strain gradient of the medium $\mathbf{F}$ into the left stretch tensor $\mathbf{V}$ and the rotation $\mathbf{R}$; ν_m is the ratio of the m-th transmission element, which is connected on the left to the elastic element under consideration. The rate of work done in the i-th elastic element is determined by the formula

$$\mathbf{T}_i \cdot \mathbf{D}_i = \rho \sum_{k=1}^{3} \frac{\partial f}{\partial \lambda_k^{(i)}} \dot{\lambda}_k^{(i)} - \frac{\rho\, \dot{\nu}_m}{\nu_m} \sum_{k=1}^{3} \frac{\partial f}{\partial \lambda_k^{(i)}} \lambda_k^{(i)} \ln(\lambda_k^{(i)}).$$

The structural deformation of the elastomeric binder fraction and the macroscopic deformation of the rubber differ significantly. This difference is taken into account by the transmission elements. Application of these elements increases the strain rate tensor at the right point of the transmission element by a factor of ν_m in comparison with the corresponding tensor at the left point and simultaneously decreases the Cauchy stress tensor.

$$\mathbf{D}_m^{\text{left}} = \frac{1}{\nu_m} \mathbf{D}_m^{\text{right}}, \qquad \mathbf{T}_m^{\text{left}} = \nu_k\, \mathbf{T}_m^{\text{right}}.$$

The deviator of the Cauchy stress tensor $\mathbf{T}_j$ of the viscous element is calculated from the equations of the theory of nonlinear viscous fluid using the appropriate strain rate tensor $\mathbf{D}_j$:

$$\operatorname{dev} \mathbf{T}_j = 2\, \eta_j\, \mathbf{D}_j,$$

For the n-th plastic element, the Cauchy stress tensor deviator is determined by the equations of the theory of plastic flow

$$\mathbf{D}_n = \sqrt{\frac{\mathbf{D}_n \cdot \mathbf{D}_n}{\operatorname{dev}\mathbf{T}_n \cdot \operatorname{dev}\mathbf{T}_n}}\, \operatorname{dev}\mathbf{T}_n,$$

To complete the system of equations, the proportional relation between the strain rate tensors of the plastic element $\mathbf{D}_n$ and that of the material is used $\mathbf{D}$.

$$\sqrt{\mathbf{D}_n \cdot \mathbf{D}_n} = \kappa_n \sqrt{\mathbf{D} \cdot \mathbf{D}},$$

where the term κ_n is the non-negative function obtained from the relation

$$\kappa_n = \begin{cases} 0, & \text{when } \Phi_n(\mathbf{T}, ...) < g_n, \\ \zeta_n(g_n), & \text{when } \Phi_n(\mathbf{T}, ...) = g_n. \end{cases}$$

The flow function Φ_n that is used to formulate the criterion for the development of plastic deformations in the medium is the function of the Cauchy stress tensor $\mathbf{T}$ of the medium. The plastic deformation of the medium takes place only in the case when the flow function Φ_n reaches its maximum value over the entire history of the medium development.

$$g_n = \max \Phi_n.$$

Experiment

In our earlier works, we carried out a series of experiments specially designed to provide complex cyclic loading of rubber [3]. Each cycle consisted of stretching with constant velocity, stress relaxation at fixed extension, unloading at constant strain rate and creep. Suggested experiments provided a great deal of information concerning the mechanical properties of the material. Testing of one specimen during one experiment gave the results for material softening after the first stretching (Mallinz effect), viscoelastic properties, relaxation and creep. Determination of the constants of the model can be realized in a step-by-step manner, using the data acquired at the previous steps. In the present study, to get more precise information for the material, the experiments have

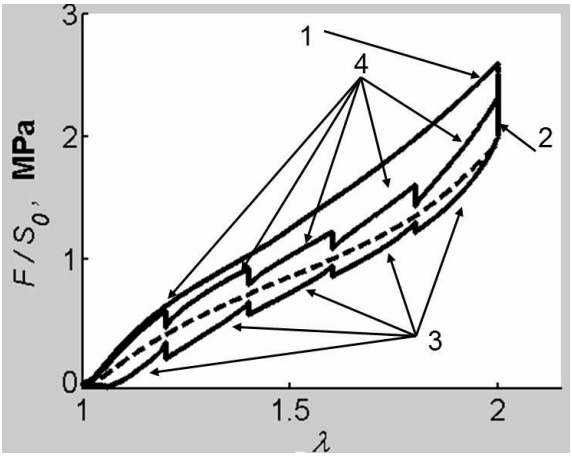


Figure 2: Experimental results obtained during the cycle. Solid line: 1 - first loading; 2 - 20-mintute relaxation; 3 - unloading with stops for 5-minute stress relaxation; 4 - stretching with stops for 5-minute stress relaxation. Dotted line: the curve illustrating the elastic properties of the material goes through the equilibrium points of relaxation from top and bottom.

been complicated (Fig. 2). Three cycles with maximum extension, $\lambda = 1.5$, $\lambda = 2.0$, $\lambda = 2.5$ were included in the experiment. During each cycle, the material was stretched to reach the prescribed value ($\lambda = 1.5$, or $\lambda = 2.0$, or $\lambda = 2.5$), and then the stress relaxation process was observed during 20 minutes. Next, the material was unloaded with repeated stops (in all, four stops) for short relaxation during 5 minutes. When zero stress was reached, the creep of the material was observed during 20 minutes. The stops were realized at the same values of stretching as in the case of unloading with repeated stops.

Thus, the analysis of the results obtained during one deformation cycle has revealed the softening effect after the first loading (Mallinz effect) and made it possible to study the viscoe-lastic properties of the material during the loading stage and the process of stress relaxation. The curve illustrating the elastic properties of the material was plotted by the equilibrium points of relaxation from top and bottom acquired at the stages of stretching and unloading with repeated stops for different extension. The material was stretched and unloaded with constant velocity $|\dot{\lambda}| = 1/60\ s^{-1}$.

Tested materials

During the experiments, 14 elastomeric nanocomposites based on butadiene-styrene rubber and 7 types of a filler of different modification of its surface, including carbon black, were tested (Tab. 19). The filler volume fraction was 20 and 40 phr.

Table 19: Nanocomposite formulation

Nano-composite code name	Polymer S-SBR Buna VSL 5025	filers					
		fumed Silica		precip. Silica		Carbon Black N330	Silane TESPT SI69
		Aerosil R974	Aerosil 200	Ultrasil VN3	Coupsil 8113		
SX00	100						
SX01	100	20					
SX02	100	40					
SX03	100		20				
SX04	100		40				
SX05	100		20				1.6
SX06	100		40				3.2
SX07	100			20			1.6
SX08	100			40			3.2
SX09	100					20	
SX10	100					40	
SX11	100				20		
SX12	100				40		
SX13	100			20			
SX14	100			40			

Results

At the first stage, the elastic properties of pure polymer SX00 described by the first and second elements of the scheme (Fig. 1) have been modeled. For pure polymer, the ratio of the first transmission element is equal to unity, and no fibers are formed in the deformed materials. Therefore, the elastic properties can be described by the second element of the scheme (Fig. 1), and the potential of the medium takes the form:

$$w = w_2 = c_1^{(2)}\left(\sum_{i=1}^{3}(\lambda_i^{(2)})^2 - 3\right) + c_2^{(2)}\left(\sum_{i=1}^{3}(\frac{1}{\lambda_i^{(2)}})^2 - 3\right).$$

Simulations show that $c_1^{(2)} = 0.1854$, $c_2^{(2)} = 0$. Then we have modeled the elastic properties of composites. The addition of fillers produces a significant change in the elastic properties of composites, and therefore we have used a transmission element to take into account these changes. We assumed for composites that the elastic constants are $c_1^{(2)} = 0.1076$, $c_2^{(2)} = 0.778$, and their sum is equal to the elastic constant of pure polymer,$c_1^{(2)} + c_2^{(2)} = 0.1854$. The obtained constants $c_1^{(2)}$, $c_2^{(2)}$ and the values of the ratio ν_1 of the first element are summarized in Tab. 20.

Finally, we have modeled the elastic properties of fibers described by the fourth and fifth elements of the scheme (Fig. 1). Figure 3 presents the results of simulations for the specimen SX10 (technical carbon). We assumed that the elastic properties of the deformed material change due to the failure of aggregates. This process is taken into account by changing the ratio of the first element. The elastic properties remain unchanged.

The potential of the fifth elastic element is expressed as:

$$w_5 = \begin{cases} 0, & \text{where } \xi_5 < 0, \\ c_1^{(5)}\xi_5, & \text{where } \xi_5 \geq 0. \end{cases}$$

and

$$\xi_5 = (\lambda_1^{(5)} - 1)(\lambda_2^{(5)} - 1)(\lambda_3^{(5)} - 1).$$

Then, the potential of free energy of the medium can be written as a sum $w = w_2 + w_5$. The constant $c^{(5)}$ has been derived for both the even and odd specimens. The calculated constants $c^{(5)}$ and the values of the ratio of the fifth element are summarized in Tab. 21.

Table 20: Values of constants $c_1^{(2)}$, $c_2^{(2)}$ and ν_1

Nanocomposite code name	$c_1^{(2)}$	$c_2^{(2)}$	ν_1 ($\lambda = 1.5$)	ν_1 ($\lambda = 2.0$)	ν_1 ($\lambda = 2.5$)
SX00	0.1854	0	1.0000	1.0000	1.0000
SX01	0.1076	0.0778	1.2725	1.2134	1.1792
SX02	0.1076	0.0778	1.5152	1.3852	1.3358
SX03	0.1076	0.0778	1.2633	1.2152	1.1916
SX04	0.1076	0.0778	1.8063	1.6440	1.5556
SX05	0.1076	0.0778	1.4396	1.3821	1.3440
SX06	0.1076	0.0778	1.8152	1.6719	1.6158
SX07	0.1076	0.0778	1.4069	1.3674	1.3380
SX08	0.1076	0.0778	1.7234	1.6271	1.5677
SX09	0.1076	0.0778	1.3567	1.3361	1.3086
SX10	0.1076	0.0778	1.6672	1.5868	1.5226
SX11	0.1076	0.0778	1.3940	1.3614	1.3328
SX12	0.1076	0.0778	1.7018	1.6069	1.5467
SX13	0.1076	0.0778	1.2881	1.2390	1.2095
SX14	0.1076	0.0778	1.6983	1.5422	1.4603

Table 21: Values of constants $c^{(5)}$ and ν_5

Nanocomposite code name	$c^{(5)}$	ν_5
SX01	0.0012	4.3756
SX02	0.0923	3.6227
SX03	0.0012	4.4669
SX04	0.0923	3.6882
SX05	0.0012	4.3956
SX06	0.0923	3.6882
SX07	0.0012	4.4613
SX08	0.0923	3.9824
SX09	0.0012	4.1491
SX10	0.0923	4.1604
SX11	0.0012	3.8328
SX12	0.0923	3.9310
SX13	0.0012	3.5441
SX14	0.0923	3.5795

Conclusion

We have carried out a series of experiments to study the mechanical behavior of materials. The experimental results collected in these tests gave a great deal of information concerning the mechanical behavior of the examined material. It has been found that the proposed model (Fig. 1) can describe adequately the elastic properties of the material. Based on the results for constants summarized in Tab. 20 and 21, we conclude that an increase in the filler fraction is reflected in our model as an increase in the ratio ν_1 and an increase in the constant $c^{(5)}$ of fibers. The difference between the elastic constants $c_1^{(2)}$,$c_2^{(2)}$ for pure polymer (SX00) and composites (SX01-SX14) suggests that filler incorporation causes the structural rearrangement of the material (Tab. 20). The model developed can also be used to describe the viscoelastic properties of materials [3]. Calculations carried out in the framework of the present study aid in the determination of the mechanisms responsible for the viscoelastic properties of materials, which will be the subject of

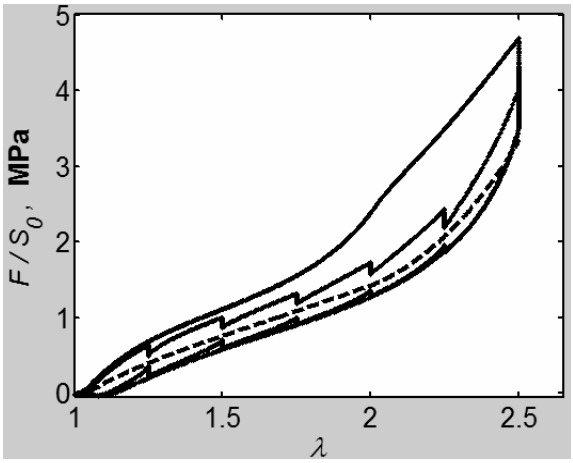


Figure 3: Solid line - experimental results for the specimen SX10 (cycle $\lambda = 2.5$); dotted line - theoretical calculations of the elastic properties of the material and fibers (elements 1,2,4,5 of the scheme).

our further research.

Acknowledgements

This work was supported basic research program (RAS Program 09-T-1-1006) and the state contract No 02.740.11.0442.

References

[1] Svistkov A.L., Lauke B., Heinrich G. Modeling of viscoelastic properties and softening of rubber materials // Proceedings of 5th European conference "Constitutive models for rubbers" Paris, 2007. P. 113-118.

[2] Palmov V.A. Comparison of different approaches in viscoelastoplasticity for large strain // ZAMM. 2000. V. 80. P. 801-806.

[3] Pelevin A.G., Lauke B., Heinrich G., Svistkov A.L., Adamov A.A. Algorithm of constant definition for a visco-elastic rubber model based on cyclic experiments, stress relaxation and creep data // Proceedings of the sixth European conference on Constitutive models for rubber - Dresden, Germany, 2009 - P. 79-84.

Svistkov A.L., Pelevin A.G., Adamov A.A., Institute of continuous media mechanics UB RAS, Perm, Russia
Lauke B., K.W. Stöckelhuber, Heinrich G.,Leibniz-Institut für Polymerforschung Dresden e.V., Dresden, Germany

Experimental research of a run-up process of a vibrating machine with an unbalance excitation

A. V. Sylyvonyuk N. P. Yaroshevich
Andriy.Sylyvonyuk@gmail.com, m_yaroshevich@mail.ru

Abstract

There given the experimental research results of the process of the acceleration of vibration machine with an unbalance exciter, which is rotated from the asynchronous motor.

During the research there has been found the vibrorecords of angle speed of exciter rotor rotation, vibrorecords of moving body mass centre of the machine in the vertical and horizontal directions, conducted a vibration acceleration spectral analysis; fixed trajectory fields of machine mass centre. Experimental data was recorded of electric motors of different capacities, of different rigidities of spring suspension, of different summary inertia moments as well as exciter rotor statistic moments, of different distances between the exciter rotor axis and the moving body mass centre.

1 Introduction

Promising direction intensification of technological processes in many different industries is using a vibration technology. Application of vibrating machines and devices is widely used and has a strong tendency to rise further.

Inertial (unbalanced) drive is widely practiced in vibrational machines and devices owing to its simplicity and possibility of obtaining considerable motive forces at small overall dimensions and relatively small mass. Machines with inertial vibroexciters are mostly postresonance ones. Their operation is stable enough in stationary regime. However in start and run-out periods a problem of passing through resonance frequencies zone arises. In particular, sticking of rotor rotating frequency close by one of its own frequencies may occur at starting, that is Zommerfield's effect may develop. Passing through resonance zone in these cases involves considerable oscillations in the system and, correspondingly, dynamic loads on the construction elements. Besides, uprated engine power is needed.

Zommerfield's effect was studied by different methods in many researches, the review of which can be found in references [1-7]. However, those were mainly theoretical papers. In the present research there shown the experimental research results of the acceleration process of vibration machine with lifting body plane motion.

2 Description of experimental vibration machine

For the experimental research was designed and built an experimental vibrating machine (Fig. 1). Machine consists of welded frame carrier (support for the body) which is based soft cylindrical spiral springs for supporting a massive frame. By spring-hung frame rigidly mounted bearing support one-shaft unbalanced vibroexciter, which in turn consists of a shaft, still enshrined in it two and two moving unbalances regulation. Amplitude settings can be changed by turning the adjusting unbalances relatively fixed. To realize high-modes, provides for the establishment of one to four additional removable unbalances. Furthermore, by the pair (opposite each other) a removable unbalances can increase the total moment of inertia of the rotor of the fungus. To the same end of rotor shaft placement agent provided a steel disk with a large moment of inertia.

Vibroexciter driven three-phase asynchronous motor type, with which it is connected with petal compensating coupling. Unbalance axle shaft and is placed horizontally in a vertical plane passing through the center of gravity system. Installing between the frame and bearing shaft vibroexciter special pads ($18mm$ thick) can change the position of the shaft axis relative center of gravity system.

With the installation of one to three additional steel plates at different heights above support the body ($20mm$, $65mm$, $105mm$) may change the mass, center of mass position in the vertical plane and moment of inertia spring-hung support the body. To change the elastic stiffness coefficients support the suspension of the body was made three sets of springs with different characteristics. Note that to reduce the stiffness of suspension springs can reduce the number from six to four.

Under the influence of disturbing efforts unbalanced vibroexciter arising in its rotation, the body provides support for small plane-parallel vibrations in the vertical plane.

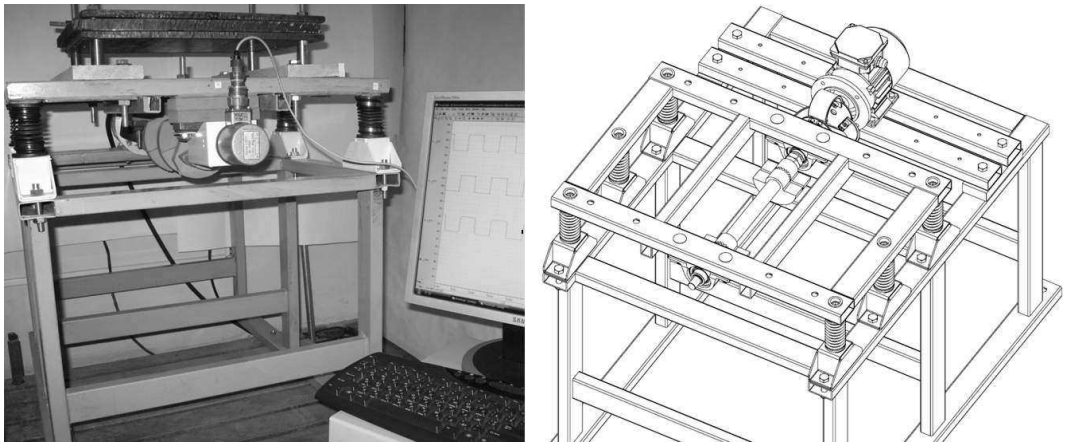


Figure 1: Experimental vibrationa lmachine and its solid model.

Parameters of (basic variant) the machine: $M = 51,5kg$; $m = 8,5kg$; $\varepsilon = 0,0053m$; $J = 1,95kg \cdot m^2$; $I = 0,0089kg \cdot m^2$; $l = 0,275m$; $b = 0,06m$ – parameters which define the fastening place for upper spring ends relative to the moving body mass centre; $h = 0,129m$ – distance from moving body mass centre to the exciter rotor axis. The inertia moment of additional steel disc is $I = 0,0022kg \cdot m^2$. Spring parameters: set No1: $d = 4,0mm$, $D = 45mm$, $H = 110mm$, $n = 7$; set No2: $d = 3,5mm$, $D = 41mm$, $H = 88mm$, $n = 5$, set No3: $d = 4,0mm$, $D = 44,3mm$, $H = 100mm$, $n = 6$. There were used asynchronous three-phase electric motors 4A56V4U3 (GOST R 51689-2000) powered $P = 0,18kW$ with nominal rotation frequency $n = 1350rpm$, (basic variant) and $P = 0,12kW$, $P = 0,09kW$.

3 Determination of parametres of the vibration machine and methods of experimental investigations

Parameters of the vibratory system were determined experimentally, calculated by formula estimation taken from courses on theoretical mechanics and strengths of materials and also with the help of SolidWorks software, where trimeric solid model of the vibratory system has been created (fig.1) SolidWorks programme allows defining moments of inertia of a moving body and vibroexciter rotor with a coupling, static moments of vibroexciter rotor as well as the position of a mass centre of a sprung moving body very accurately.

Total hardness coefficient of an extension, compression and shift of six springs of an elastic suspension has been experimentally found by the ratio of the gravitation of the load attached to the frame or hung over the block to the measured static shift of the moving body caused by this force. The measurement was made in the vertical and horizontal directions and was calculated by a computational procedure for checking [8]. The frequency of a rotor rotation of the vibroexciter was found with the help of a clock-type tachometre TCh-10P (admissible error of data when measuring

rotation frequency is $\pm 1\%$) and an electronic stroboscope MT 565 (an error $\pm 0,01\%$ of a rotation frequency).

To determine time dependences of the angular velocity of the vibroexciter rotor on time, a photoelectric transducer of angular displacements (encoder) of BE178A5 model (used in automatic machine control systems, for data communication between machine actuating mechanisms and a numeric program control device) was used. The signal of the transducer is sent to the microcontroller ATMEGA8, which is connected to the computer by a sound card. The microcontroller functions here as a frequency divider so the sound card of the computer is meant for the maximum sample frequency 96 kHz and the angular displacement transmitter sends the signal with the frequency of 25,6 kHz. In so doing the condition Shannon is being performed but for achievement of better results, a frequency divider with the coefficient of 2 is used so the frequency at the output of the microcontroller ATMEGA8 is 12,8kHz what is straight proportional to the frequency of the vibroexciter rotor rotation.

The calculation of the coefficient of the viscous resistance by the vibratory coordinates was made by means of the record of free damped vibrations of the moving body. After the electric motor was switched off, during the process of deceleration, the vibration acceleration of the moving body mass centre in the vertical and horizontal directions was being recorded. The required coefficient can be easily calculated with a logarithmic decrement of the vibrations by means of measuring of the ratio of two (to be more accurate - i) successive maximum deviations on the acceleration vibrorecord (fig. 2). For this purpose a three-axis accelerometer MMA 7260 QT ($\pm 1,5g - 6g$) was used. Equivalent analog signals of acceleration coordinates projection on axes X and Y are read by an analog-digital transducer (computer sound card), where they were processed and displayed as data array and graphs.

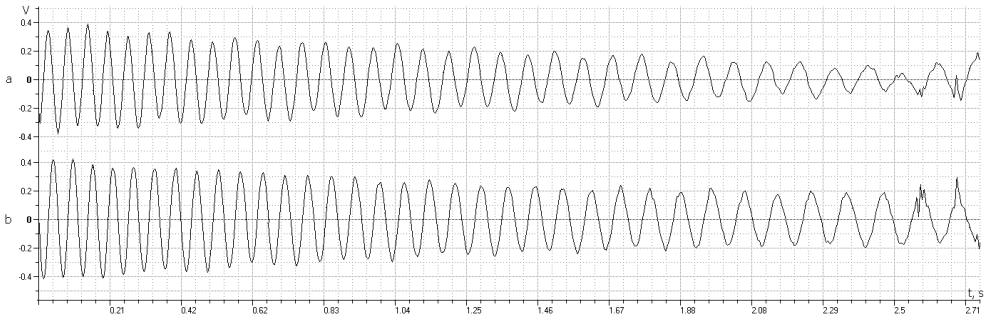


Figure 2: Vibrorecord of moving body mass centre acceleration during deceleration: *a)* in the vertical direction; *b)* in the horizontal direction.

To calculate a coefficient of the strength of vibrations the formula $\beta = \frac{2\Lambda M}{T}$ is used, where $\Lambda = \frac{1}{i} ln \frac{y_n}{y_{n+i}}$ – a logarithmic decrement of damped vibrations; y_n, y_{n+i} – maximum displacements remoted in the direction of the time rise by periods of vibrations; T – average value of damped period of vibrations. For vibrorecords shown in the fig. 2 the parameters of the system are as follows:$\beta_y = 38,5\frac{kg}{s}$; $\Lambda = 0,0265$; $i = 40$; $T = 0,071s$; $\beta_x = 37,5\frac{kg}{s}$; $\Lambda = 0,0238$; $i = 39$; $T = 0,065s$.

It should be noted that the relation of successive errors of a vibrational value in the zone of deceleration is approximately the same along the whole interval of vibrorecords (this confirms the proportionality of the resistance force to the first degree of speed), except the narrow resonance range; the increase of vibration amplitudes (by $1 - 3mm$) and the position of the moving body mass centre (to $45mm$) insignificantly influences on logarithmic decrement of vibration damping. To calculate the decrement of damping in the zone of the resonance with the acceptable accuracy is very difficult, that is why the value of the coefficient of strength in this zone was taken equal to the coefficient of the preresonance zone grew proportionally to the increase of the amplitude.

Maximum vibration amplitudes of the spring-hung moving body were fixed on the plane of trajectories scratched on the smoked glass rigidly fastened in the mass centre by the steel point. The image on the glass was scanned, enlarged (zoomed) by several times and then was printed out. Having measured the image the values of maximum amplitudes of moving body mass centre

vibrations of the machine in the vertical and horizontal directions were found.

4 Results of the experiments and their analysis

In the fig. 3 shown vibrorecords of horizontal and vertical moving body mass centre acceleration during deceleration, established regime of the movement and deceleration in real time with the sampling frequency $96kHz$, in the fig. 4 – there shown a spectral analysis of arrays recorded above.

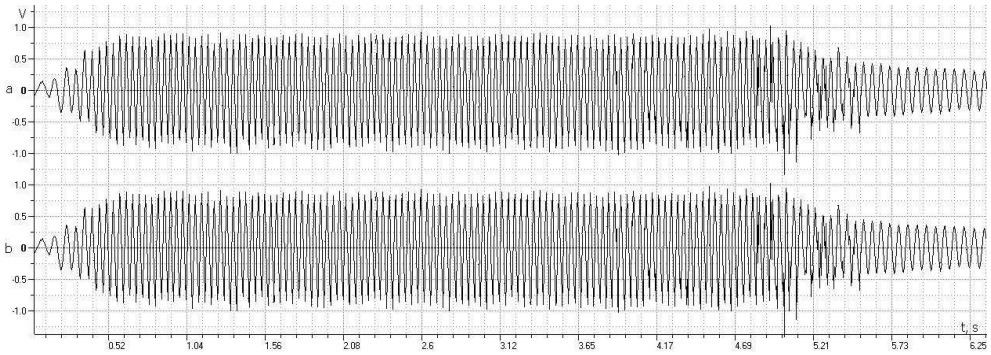


Figure 3: Vibrorecord of moving body mass centre acceleration during deceleration: *a)* in the vertical direction; *b)* in the horizontal direction.

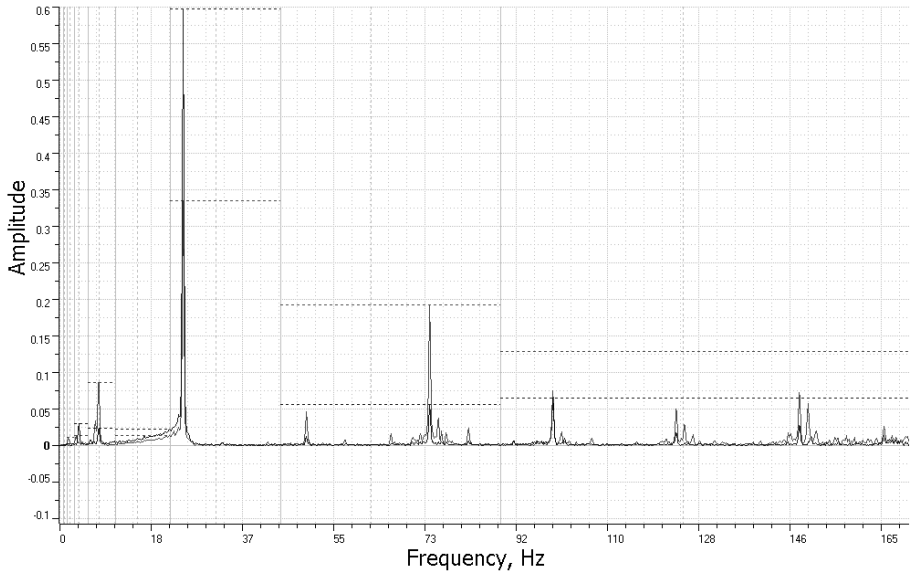


Figure 4: Spectral analysis of vibration acceleration of moving body mass centre in the horizontal and vertical directions.

From fig. 3 follows that at the moment of acceleration the growth of the moving body vibration acceleration is relatively not high and its value is greatly lower than in the established regime of movements; during deceleration gradual decrease of acceleration with a marked splash in the zone of resonance is observed but the value of splashes does not exceed the value of acceleration in the established regime. The average value of vibration acceleration of the moving body mass centre in the horizontal and vertical directions in the established regime consequently makes $19,6m/s^2$ and $16,5m/s^2$ what is close to values found when modeling the process of acceleration with the same parameters of the system ($19,4m/s^2$ and $18,2m/s^2$).

The results of the spectral analysis prove that the splashes of the vibration acceleration amplitude occur both during the acceleration as well as during the deceleration on the same frequencies close to resonance ones ($3,5Hz$; $7,8Hz$ – in case of horizontal vibrations; $3,8Hz$ - in case of vertical vibrations), on the frequency of established forced vibration ($24,7Hz$), and also on the frequencies multiple of them. It should be mentioned that the spectral analysis of the signal has been carried out in the demo version of the PowerGRAPH software.

In fig. 5-8 there shown vibrorecords of angular velocity of vibroexciter rotor during the acceleration of the vibration machine. Analyzing the graphs one can state that the experiment definitely proves the theory. On the graphs which meet highly-loaded regimes of acceleration there can be clearly observed preresonance areas with relatively rapid increase of angular velocity, initial resonance areas in which the increase of velocity considerably slows down (decelerates), final resonance areas where velocity quickly grows again and postresonance areas where velocity growth gradually decelerates as it approaches to the fixed stationary value. The higher static moments of vibroexciters (fig. 6 a, b) or the higher the rigidity of the suspension (fig. 5 b, 6 b, 7 a) the more apparent become the mentioned peculiarities in changes of rotor angle velocity; therewith the "hang-up" of the velocity (approximate values of the velocity to the horizontal areas of the curve) is carried out on the lower frequencies of the rotor rotation. Hence, with such values $c_y = 2,95 \cdot 10^4 N/m$, $c_x = 1,7 \cdot 10^4 N/m$ the marked "hang-up" is observed on the frequencies of $57,8s^{-1}$ and $82,9s^{-1}$; with $c_y = 3,9 \cdot 10^4 N/m$, $c_x = 1,7 \cdot 10^4 N/m$ on the frequencies of $81,6s^{-1}$ and $117,4s^{-1}$.

As it must be according to the results of modeling, the increase of the distance between the exciter axis and the moving body mass centre distinctly makes the duration of electric motor rotor acceleration grow (from $0,73s$ to $0,90s$, fig.7). time of acceleration also considerably grows when the motor is less powerful) fig. 7 a, 8 a) or in case of higher total inertia moment of vibroexciter rotor (fig. 8). Of course, when the acceleration lasts longer, resonance vibration amplitudes of vibration machine are higher.

In the fig.9 there outlined the fields of the machine mass centre trajectories during acceleration for different total inertia moments of vibroexciter rotor: of electric motor power and rigidity of the moving body spring suspension as well as for the movement periods when the 'hang-up' of the exciter velocity occurs and for the established regime. In accordance with the received data it follows:

- change of the value in the moment of exciter rotor inertia can lead to the considerable difference in maximum resonance amplitudes of moving body vibrations. Hence, on the increase of inertia moment by 25 % in case of regimes with low electric motor power reserve, maximum amplitudes grow more than twofold (fig. 9 a, b) while in case of regimes with enough power reserve on the same change of the inertia moments the difference between maximum amplitudes is not considerable – 5-8 % (fig. 9 c, d);

- the decrease of the suspension rigidity causes the deceleration of maximum resonance amplitudes, herewith the effect of decrease depends on the regime used. So, in case of the regime with a double growth of the maximum amplitude (with the overrated inertia moment of the vibroexciter) during which the start accompanied with the bangs of the spring coil, the change of the springs used e.i set 3 for ($c_y = 3,9 \cdot 10^4 N/m$, $c_x = 1,7 \cdot 10^4 N/m$)for the set 1 $c_y = 2,95 \cdot 10^4 N/m$, $c_x = 1,7 \cdot 10^4 N/m$ allows normal acceleration. In doing so in case 1(fig. 9 b) maximum resonance amplitudes are higher that the amplitudes of the established movements by 4–4,5 times, while in case 2 (fig. 9 f) by 2–2,2 times.

- the increase of the motor power causes the decrease of maximum resonance amplitudes. For instance, on changing the motor of power P=120 W for the power of $P = 180W$ there reduction of the of maximum amplitudes by 7-10% is observed (fig. 9 c, e).

It should be noted that on exciter velocity 'hang-up', maximum amplitudes during the acceleration are several times higher than the established ones (fig. 9 h, i); the amplitudes of the established regime are approximately the same for all tested regimes.

As it follows from the given results the vibrations of the machine moving body mass centre have very complicated nature. However, found fields of trajectories give pretty an interesting vision of the behavior of the vibration system during the start.

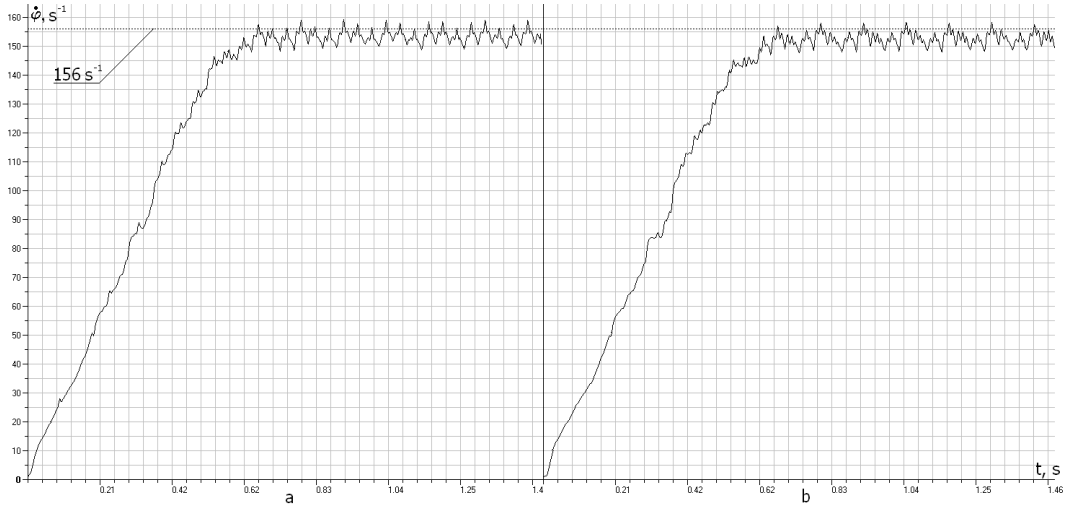


Figure 5: Vibrorecords of angular velocity of exciter rotor during the acceleration, spring 2: a) $m\varepsilon = 0,066kg \cdot m$; b) $m\varepsilon = 0,089kg \cdot m$.

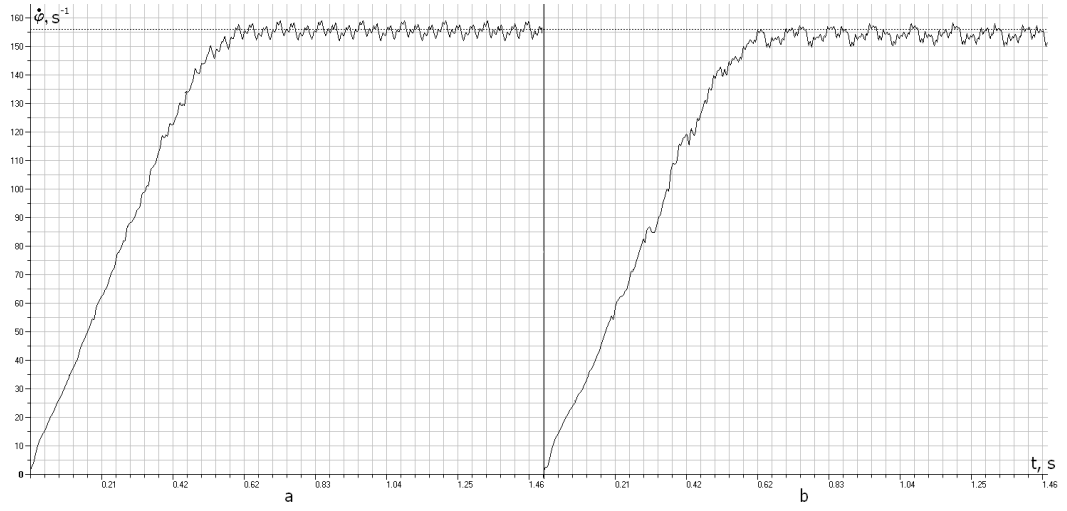


Figure 6: Vibrorecords of angular velocity of exciter rotor during the acceleration, spring 3: a) $m\varepsilon = 0,045kg \cdot m$; b) $m\varepsilon = 0,089kg \cdot m$.

In fig. 10 there given vibrorecords of exciter rotor angular velocity during its 'hang-up' in the resonance zone while the acceleration with insufficient for machine chosen parameters motor power. In the graph one can observe the exciter rotor braking before the first ($p_x = 17,9s^{-1}$) and the second ($p_y = 17,9s^{-1}$) natural frequencies and a 'hang-up' before the third frequency ($p_\varphi = 52,9s^{-1}$); half-slow and quick vibrations of the exciter frequency are markedly seen. It should be mentioned that to implement an angular velocity 'hang-up' of the exciter rotor with its further vibrations in the resonance zone (without reaching the established postresonance regime) was very problematically as with such a regime very intensive resonance vibrations occur (fig. 9 h) which are accompanied with spring coil bangs and even with the 'spring off' of springs from fastening plugs. The decrease of the total moment of the exciter rotor (by means of removing additional steel disc with $I = 0,0022kg \cdot m^2$) with the same vibration machine parameters allows to accelerate motor rotor to the nominal speed.

It should be noted that the specific of change in exciter rotation frequency during passage resonance system in the reverse direction with the electric motor switched off (i.e. during deceleration) – availability in the initial resonance zone areas with a rapid decrease of angular velocity and further its short-time 'hang-ups' after passage of the zone fig. 11 a). It should be also observed that

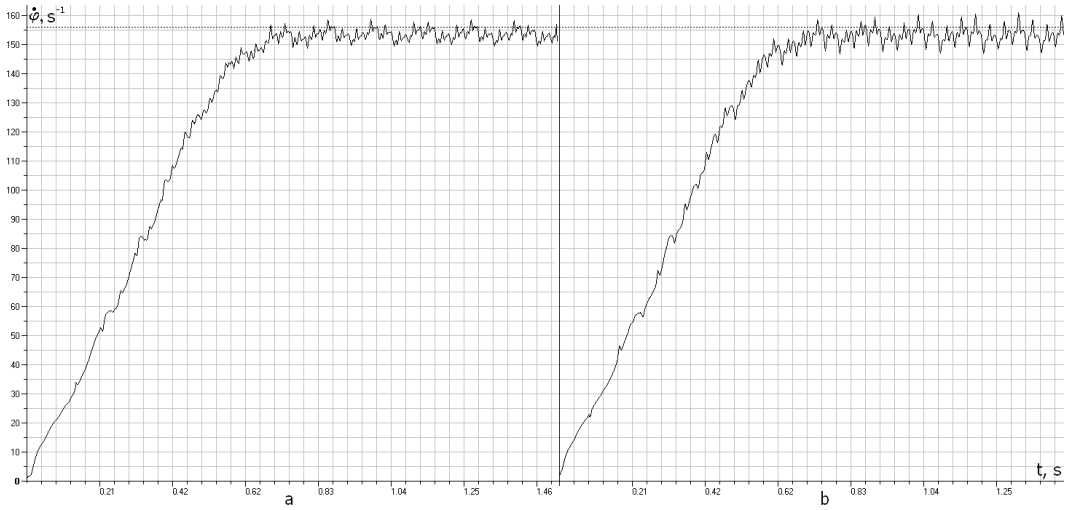


Figure 7: Vibrorecords of exciter rotor angular velocity during the acceleration for different distances between its axis and mass the moving body mass centre. (spring 1, $m\varepsilon = 0,089kg \cdot m$): a) $129mm$; b) $169mm$.

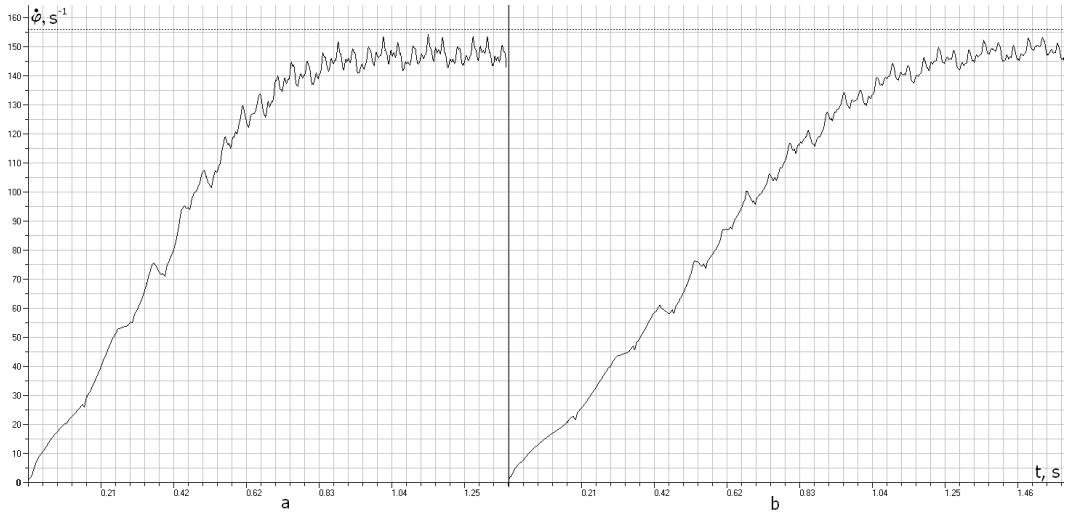


Figure 8: Vibrorecords of exciter rotor angular velocity during the acceleration with a motor to power $P = 0,12kW$, of the spring No 1: a)$I = 0,0089kg \cdot m^2$; b)$I = 0,0111kg \cdot m^2$.

on the graph showing deceleration after termination of exciter rotor rotation ($t = 9,7s$), velocity curve does not show the changes of the exciter vibration direction.

In the fig. 11 b it is shown the passage of the system the resonance zone during deceleration when using a frequency transducer AFC-120 ("TWERD", Poland) of 0,37 kW – braking is caused by constant current supply. As it is seen from vibrorecords duration of transitional processes has been considerably reduced. So using modern electronic industrial devices the problem of deceleration can be solved relatively easy. Possibilities to control which are programmed into the scalar transducer for improving dynamic of vibrating machine acceleration are not sufficient.

In fig. 12 there given time dependences of exciter velocity found during numeric modeling of vibrating machine acceleration with vibrating machine parameters. According to fig. 5 a, b and fig. 12 a, b one can state sufficient quantitative research results coincidence. In both cases there is a small divergency in the acceleration duration: during numerical modeling – 0,72 s and 0,92 s, during experiment – 0,63 s and 0,74 s; with an established regime found similar values of exciter rotation average angular velocity (modeling – $155,1s^{-1}$ and $154,7s^{-1}$, research – $154,4s^{-1}$ and $153,9s^{-1}$). As it is observed that the increase of static moments of the exciter, average velocity

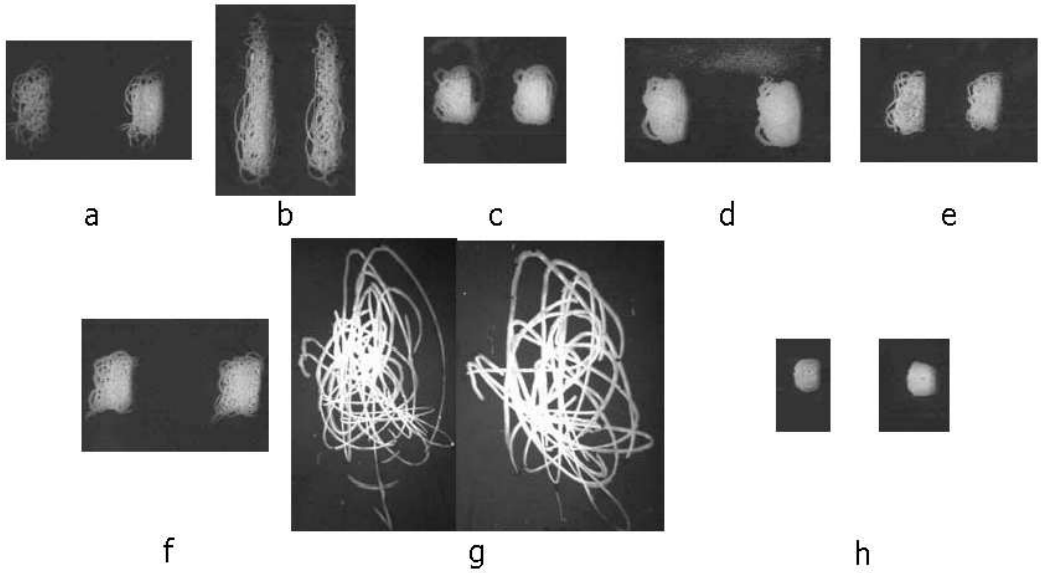


Figure 9: Fields of the trajectories of the machine mass centre during acceleration: a) $I = 0,0089kg \cdot m^2$, $P = 120W$, springs 3; b) $I = 0,011kg \cdot m^2$, $P = 120W$, springs 3; c) $I = 0,0089kg \cdot m^2$, $P = 180W$, Spring 1; d) $I = 0,011kg \cdot m^2$, $P = 180W$, spring 1; e) $I = 0,0089kg \cdot m^2$, $P = 120W$, springs 1; f) $I = 0,011kg \cdot m^2$, $P = 120W$, spring 1; g) "hang-up"; h) established regimes.

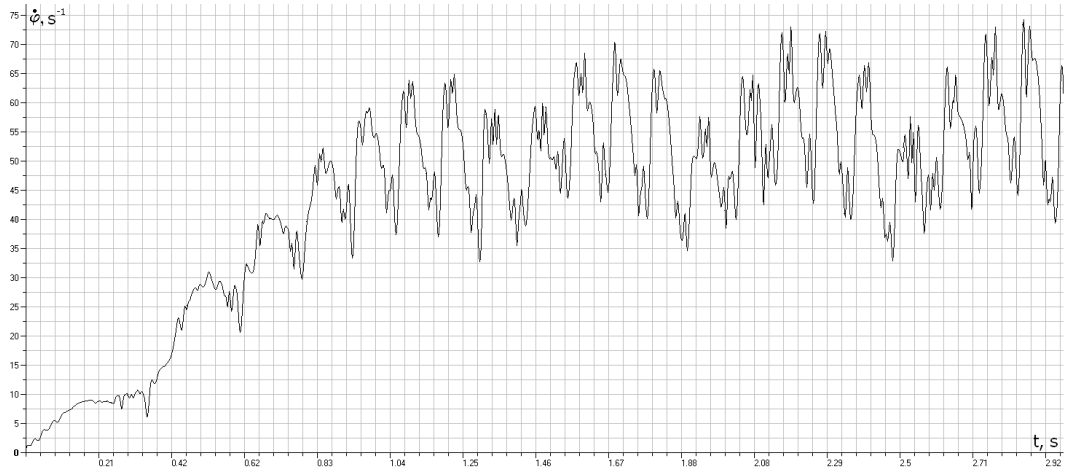


Figure 10: Vibrorecords of exciter rotor angular velocity in case of its 'hang-up' in the resonance zone during acceleration.

value are slightly decreased. Exciter rotor angular velocity 'hang-up' (fig. 12 b and fig. 6 b) is noticed on the similar frequencies when modeling – $51,5s^{-1}$, $70,8s^{-1}$, $96,8s^{-1}$, when doing a research – $56,5s^{-1}$, $81,6s^{-1}$, $117,4s^{-1}$.

It should be also mentioned that for light-loaded regimes a significant area of a curve's vibrospeed during acceleration shows equally -accelerated movement with stable acceleration $\varepsilon_1 = 282s^{-1}$, the quantity of which is approximate to the value measured by $\varepsilon_1 \approx L_n/I = 300s^{-1}$ (fig. 6, a).

As you can see on the graph exciter rotor acceleration (fig. 11) in case of vibration system with such natural frequencies $p_\varphi = 46,2s^{-1}$, $p_y = 23,9s^{-1}$, $p_x = 17,9s^{-1}$, swift decrease of exciter rotation angular velocity is observed with frequency value of $44,0s^{-1}$ and on the frequency of $29,5s^{-1}$ its 'hang-up' occurs; in case of system with natural frequencies $p_\varphi = 52,9s^{-1}$, $p_y = 27,5s^{-1}$, $p_x = 18,1s^{-1}$ the decrease of velocity is observed with frequency $52s^{-1}$, and on the

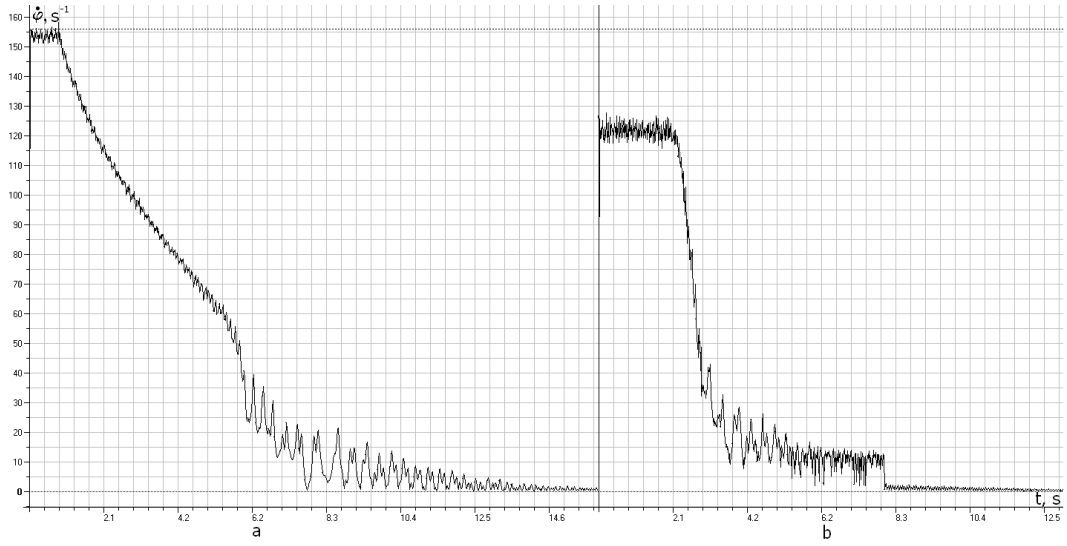


Figure 11: Vibrograms of exciter rotor angular velocity $m\varepsilon = 0,089kg \cdot m$): a) spring 1; b) braking by means of using constant current with frequency transducer: $P = 120W$.

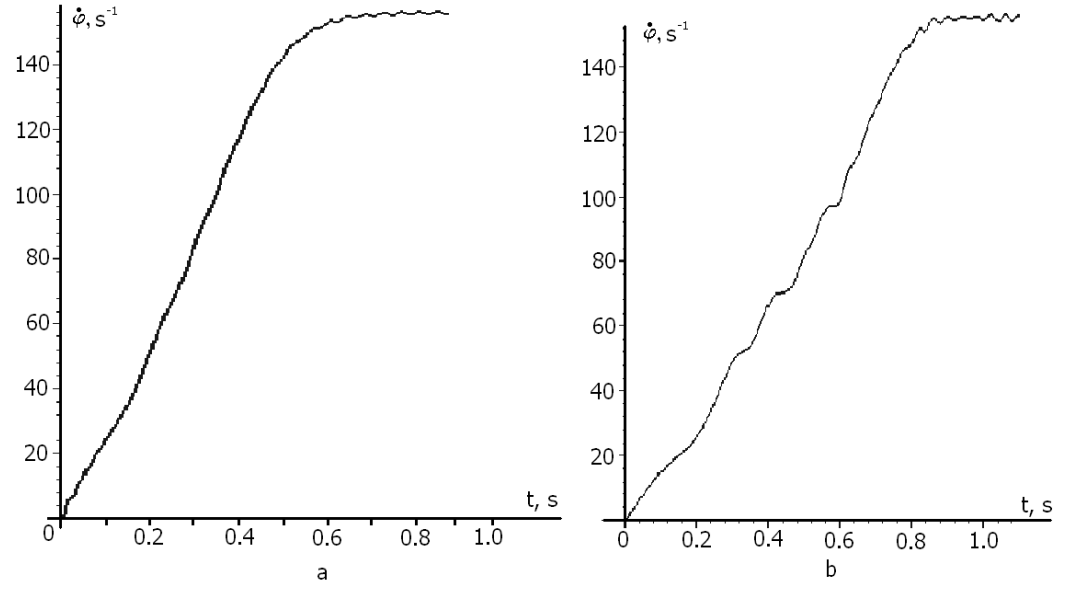


Figure 12: Time dependencies of exciter angular velocity in case of numerical acceleration modeling, spring 3: a) $m\varepsilon = 0,045kg \cdot m$; b) $m\varepsilon = 0,089kg \cdot m$.

frequency of $37,7s^{-1}$ it 'hangs up'.

It should be said that work of experimental vibration machine was characterized by sufficiently high stability herewith relation of forced vibration frequency to the frequency of natural vertical vibrations was in the interval of 5.5 to 6.3 (depending on the set of springs), what meets upper values of recommended ranges and the relation of transverse rigidity of springs to the axis one was approximate to 1:2.

5 Conclusion

Thereby conducted experimental researches correspond to classical concepts [4], confirm key theoretical research findings [9] as well as numeric modeling results [10, 11].

References

[1] Blekhman I.I. Synchronization in Nature and Technology. Moscow: Nauka, 1981. – 351 p. (in Russian).

[2] 2. Oscillations of nonlinear mechanical systems. Vibration in technology: Handbook in 6 vol., 2 (Mashinostrojenie, Moskow, 1978). – 551 p. (in Russian).

[3] F.F. Alifov, K.V. Frolov. Interaction of nonlinear oscillatory systems with sources of power. Moscow: Nauka, 1985. – 328 p.(in Russian).

[4] Blekhman I.I.Vibrational mechanics, Fizmatlit, Moscow – 400 (in Russian). English translation : Vibrational mechanics. Singapore, world Scientific, 2000. – 509 p. (in Russian).

[5] Fildin A. Nonlinear Oscillations in Mechanical Engineering. Berlin, Heidelberg. Springer-Verlag. 2006. – 358 p.

[6] Krasnopolskaya T.Z., Shvets A. Yu. Regular and random dynamics of the system with limited excitation. Moscow - Izhevsk, 2008. – 280 p. (in Russian).

[7] Blekhman I.I., Indieytshev D.A., Fradkov A.I. Slow motions in systems with inertial excitation of oscillations // Problems of machine building and reliability of machines, Ni1 2008. 25-31. (in Russian).

[8] Iorish Y.I. Vibrometry/ Y.I. Iorish - M.: State Scientific and Technical Publishing House of Machine-building Lterature. – 1963. – 771 p.

[9] Blekhman I.I., Yaroshevich N.P. Transient regimes in inertially excited postresonance vibrational devices with several degrees of freedom of the carrying system //Proceeding of the XXXVII Summer School "Advanced Problems in Mechanics". APM 2009. – St.Peterburg. – 2009. – P. 195-202.

[10] Yaroshevich T.S., Sylyvonyuk A.V. Investigation of dynamic processes in vibration machine with unbalanced vibro-exciters and asynchronous electric motor //Proceeding of the XXXVI Summer School "Advanced Problems in Mechanics". APM 2008. – St.Peterburg. – 2008. – P. 724-730.

[11] Yaroshevych T.S. Investigation of vibration machine with unbalanced drive run-up/ Yaroshevich T.S. // Visnyk NU 'Lvivska Politehnika', 2007. – No. 557. – P.94-102.

A.V. Sylyvonyuk, 75 Lvivska Str., Lutsk, 43018, Ukraine
N.P. Yaroshevich, 75 Lvivska Str., Lutsk, 43018, Ukraine

Sear rupture mechanism of super-brittleness of hard rocks

Boris G. Tarasov
tarasov@civil.uwa.edu.au

Abstract

The paper discusses the variation of rock brittleness with confining pressure σ_3 for rocks of different hardness, failed under triaxial compression with $\sigma_1 > \sigma_2 = \sigma_3$ typical for great depth. Shear is the only form of large scale rupture of rock mass at depth and for laboratory specimens within a certain range of confining pressure σ_3. A decrease in rock brittleness with rising confining pressure σ_3 has been widely reported and is perhaps the most comprehensively studied aspect of rock behaviour. The paper draws attention to a less studied hard rock property - embrittlement with increase in σ_3. The brittleness variation in this case follows a typical pattern of initially increasing, reaching a maximum at some level of σ_3 and than ultimately decreasing since all rocks become ductile at very high σ_3. The harder the rock the greater is the effect of embrittlement. Experimental results presented in the paper show that most hard rocks under the effect of confining pressure increase their brittleness dramatically and become hundreds of times more brittle compared with uniaxial compression approaching absolute brittleness at confined conditions corresponding to maximum earthquake activity. The rupture energy at these conditions becomes vanishingly small.

A special shear rupture mechanism is proposed to explain this phenomenon. In accordance with this mechanism the embrittlement results from reduction of friction within the rupture head. The efficiency of this mechanism is a function of rock hardness and confining pressure. In most hard rocks failed within a certain range of confining pressure this mechanism can create transient negative shear resistance - referred to as 'negative friction' - which makes rocks superbrittle and failure inevitably uncontrollable and violent. The new concept advances our knowledge about hard rock properties at great depths and earthquake mechanisms.

1 Introduction

The paper discusses rock brittleness variation under the effect of confining pressure σ_3 for rocks of different hardness tested to failure under triaxial compression $\sigma_1 > \sigma_2 = \sigma_3$. The analysis concerns rocks that exhibit failure in a form of shear rupture under confined conditions. Acoustic emission studies suggest that shear rupture development is associated mainly with the post-peak stage of deformation [1– 4]. Comprehensive experimental studies of shear rupture development have been conducted on relatively soft rocks due to the possibility of rupture control in the post-peak region [5, 6]. The decrease in rock brittleness with rising confining pressure σ_3 established in such studies is in agreement with common frictional shear rupture models [3, 7– 12].

The paper draws attention to a less studied hard rock property - increasing brittleness with increase in σ_3 [13, 14]. Hard rocks are mainly magmatic and metamorphic rocks with homogeneous and low porosity fine-grained structure: e.g. granite, basalt, dolerite, diabase, gabbro, quartzite, etc. The paucity of data on post-peak properties of hard rocks and corresponding shear rupture mechanisms results from the impossibility of rupture control within a certain (embrittlement) range of confining pressure σ_3. Analysis of new experimental results and available experimental data conducted in the paper shows that the brittleness variation for hard rocks follows a typical pattern of initially increasing as σ_3 increases, reaching a maximum at some level of σ_3 and than ultimately decreasing since all rocks become ductile at very high σ_3. The harder the rock the greater is the effect of embrittlement. Some rocks show tremendous embrittlement approaching absolute brittleness.

In this paper we propose further development of a new shear rupture mechanism [15– 19] that is believed to operate in hard rocks within the embrittlement pressure range. The new concept advances our knowledge about hard rock properties at high confining pressure and great depths.

2 Brittleness variation of hard rocks with confining pressure

2.1 Brittleness index for rocks tested at triaxial compression

There are many different criteria for characterisation of rock brittleness for different practical and scientific aims [20– 22]. To characterise rock brittleness variation under the effect of confining pressure σ_3 under triaxial compression $\sigma_1 > \sigma_2 = \sigma_3$ we use a brittleness index, the meaning of which is illustrated in Figure 1.

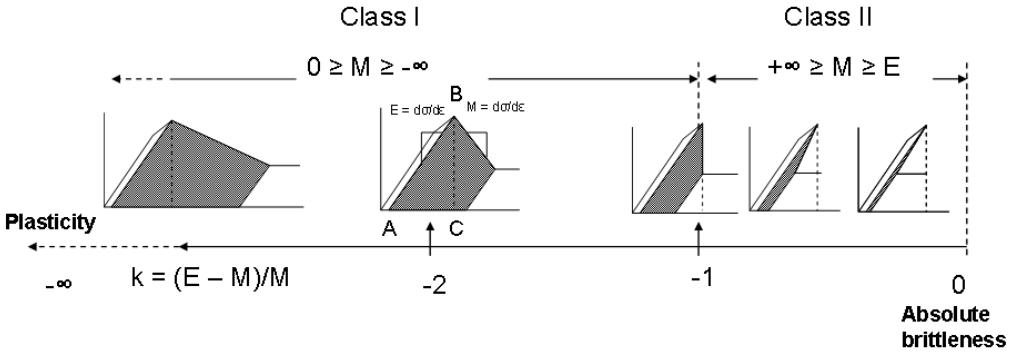


Figure 1: Scale of brittleness index $k = \dfrac{E - M}{M}$ with characteristic shapes of complete stress-strain curves.

The scale of brittleness index k in Figure 1 is accompanied by complete stress-strain curves with characteristic shapes of the post-peak parts. The complete stress-strain curves (differential stress $\sigma = (\sigma_1 - \sigma_3)$ vs. axial strain ε) shown schematically in Figure 1 have the same pre-peak profiles but differ in the post-peak region. The curves characterised by negative post-peak modulus $M = \dfrac{d\sigma}{d\varepsilon} < 0$ represent rocks of Class I [23]. The curves with positive modulus $M > 0$ represent rocks of Class II [23]. After failure, strength of rocks of both classes becomes constant and equal to a residual strength determined by friction in the rupture zone (horizontal part of the post-peak curves).

The shaded areas on the graphs correspond to energy consumption of the rupture process (rupture energy) in the post-peak region. For rocks of both classes the elastic energy accumulated within the specimen body during loading (area ABC) is the source of the rupture process. The difference in the rupture processes between rocks of Class I and II is as follows. In Class I the amount of elastic energy stored in the specimen body is less than the rupture energy (shaded area), hence, additional work must be done to cause complete failure beyond the peak stress. For Class II the amount of available elastic energy exceeds the rupture energy. Class II rocks exhibit spontaneous failure even for a hypothetically perfectly stiff testing machine. To control rupture development for rocks of Class II the excess elastic energy must be extracted from the specimen by reverse strain.

The elastic energy dW_e withdrawn from the specimen at the rupture development in the post-peak region can be absorbed by the rupture process (rupture energy) and transmitted into a dynamic process (released energy). The withdrawn energy can be estimated by equation (1):

$$dW_e = \frac{d\sigma_2}{2E} \tag{1}$$

Here $E = \dfrac{d\sigma}{d\varepsilon}$ is the unloading elastic modulus. The rupture energy dW_r can be estimated as

$$dW_r = \frac{d\sigma^2(E-M)}{2EM} \tag{2}$$

The brittleness index, k, may be defined, representing the ratio between the rupture energy dW_r and the corresponding elastic energy dW_e withdrawn from the specimen during this rupture process, with k expressed as:

$$k = \frac{dW_r}{dW_e} = \frac{E-M}{M} \tag{3}$$

Hence, the brittleness index $k = \dfrac{E-M}{M}$ characterises the capability of the rock for self-sustaining failure due to the elastic energy dW_e available from the material. The index k is negative because the elastic energy is treated as positive, while the rupture energy is negative, and its range is $-\infty < k < 0$. The value of $k = 0$ corresponds to absolute material brittleness when the rupture energy is equal to zero. At ductile or plastic behaviour $M \to 0$ and $k = -\infty$. When $k = -1$ the post-peak part of the complete stress-strain diagram is vertical ($M = \infty$). This situation represents a boundary between Class I and Class II rocks. For $k < -1$ the rupture development should be not self-sustaining because the rupture energy exceeds the elastic energy available from the material body. For $k > -1$ the rupture development should be self-sustaining. The greater k is, the more violent the rupture becomes.

2.2 Rock brittleness variation due to confining pressure

To determine the effect of confining pressure on brittleness index $k = \dfrac{E-M}{M}$, it is necessary to have a set of complete stress-strain curves obtained experimentally at different levels of confining pressure. A new super stiff testing apparatus [14] was used by the author to control the rupture process in hard rocks which allowed obtaining the following paradoxical results. Figure 2 shows

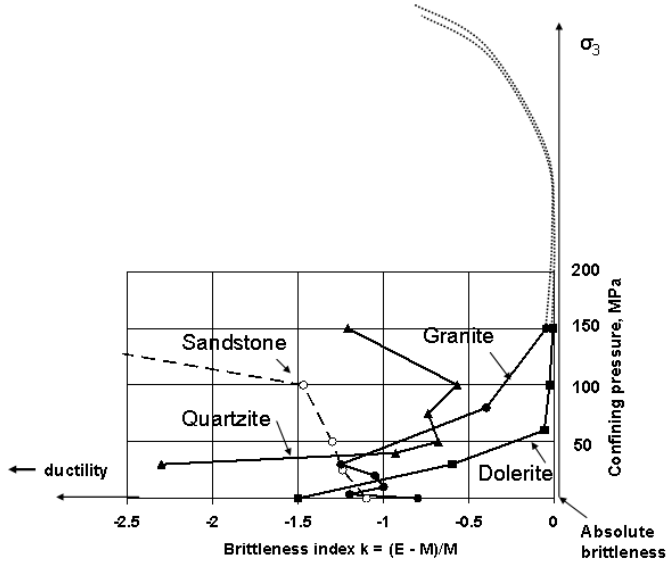


Figure 2: Variation of brittleness index $k = \dfrac{E-M}{M}$ versus confining pressure σ_3 for rocks of different hardness.

the variation of brittleness index k with confining pressure σ_3 for sandstone, quartzite, Westerly granite [24] and dolerite, with brittleness increasing from left to right. Confining pressure range in the experiments is from $\sigma_3 = 0$ up to $\sigma_3 = 150MPa$. Rock hardness increases from sandstone

to dolerite. The graph for sandstone shows that increase in σ_3 makes the rock less brittle. This behaviour is typical for relatively soft rocks and is in agreement with common understanding of rock brittleness variation with rising confining pressure. For the quartzite, increase in σ_3 within the range of $0 - 100MPa$ makes it more brittle. At greater σ_3 the brittleness decreases. The graph for granite shows that, at very low σ_3, the rock brittleness can decrease with rising σ_3 exhibiting features of soft rocks; however, with further increase of σ_3 the granite becomes more and more brittle. Results obtained for the dolerite specimens demonstrate increase in brittleness with rising σ_3. At $\sigma_3 = 75MPa$ the dolerite became 250 times more brittle compared with uniaxial compression ($k_0 = -1.5$; $k_{75} = 0.006$). At $\sigma_3 = 100$ and $150MPa$ the brittleness increased significantly further and the rupture control became impossible. The dashed lines indicate the expected brittleness variation for granite and dolerite at greater σ_3: the brittleness continues to increase until it reaches a maximum at some level of σ_3 and than decreases since all rocks become ductile at very high σ_3. For less hard rock (such as the quartzite) the mode of brittleness variation is similar but the maximum brittleness is lower and the range of confining pressure where embrittlement takes place is smaller. The softer the rock, the less embrittlement occurs.

3 Shear rupture mechanism responsible for rock embrittlement

In general, increasing brittleness of hard rock with increasing σ_3 is a well known effect. Mechanisms of embrittlement associated with rock material compaction or pore collapse at high confining pressure have been explored by others [25– 27]. Another form of embrittlement was observed in studies of stick-slip phenomena on existing faults, associated with the transition from stable sliding to stick-slip behaviour [28]. However, the mechanism responsible for the brittleness variation of intact hard rocks of low porosity and fine-grained structure, illustrated in Figure 2, has not been explored and is of a very different nature. Below we discuss this mechanism. It is known that

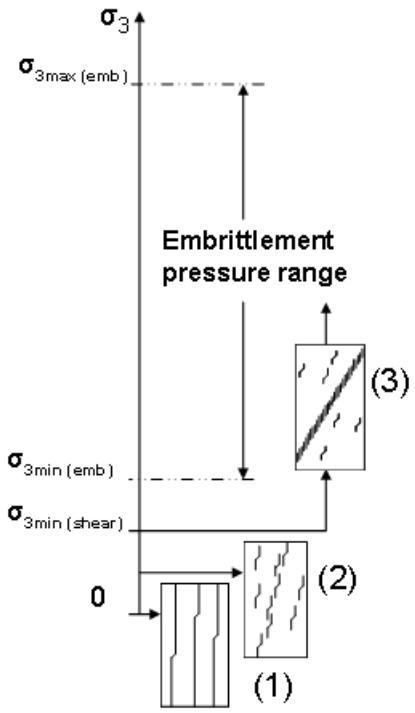


Figure 3: Typical variation in failure pattern with increase in confining pressure σ_3.

the confining pressure σ_3 influences the fracture patterns [27, 29] as illustrated in Figure 3. Three types of fracture patterns are normally distinguished:

1. *Splitting by long tensile cracks.* Experiments show that under uniaxial compression artificial inclined planes inserted in brittle materials cannot propagate in their own plane. They extend in a form of long tensile cracks (wings) oriented in the direction of the major stress σ_1 [30, 31]. Brittle rocks tested under uniaxial conditions and at low confining stresses also fail in this mode [23, 13]. In both cases the tensile cracks are caused by tensile stress concentration acting at the edges of artificial or natural micro planes (defects) in the material structure [9, 30, 31].

2. *Distributed micro-cracking.* Increasing the confining pressure suppresses the development of long tensile cracks, reducing their length and leading to the formation of local 'shear-crack' defects comprising shear and crack elements. The number of these local defects increases during loading until finally they combine to form a general rupture normally with very rough surfaces [13, 9, 32, 33].

3. *Shear rupture.* Starting from a certain level of $\sigma_3 = \sigma_{3min(shear)}$ (different for different rocks) the character of failure changes: rocks fail due to formation of a plane macroscopic shear rupture capable of propagating in its own plane. Studies [3, 12] show that the macroscopic shear rupture can start from a microscopic shear plane (defect) and propagate due to creation of an echelon of short tensile cracks in front of the propagating rupture.

Despite the fact that in all three cases both shear and crack elements are involved in the failure process the rupture mechanism activated for $\sigma_3 \geq \sigma_{3min(shear)}$ differs fundamentally from those at lower σ_3. For $\sigma_3 < \sigma_{3min(shear)}$ the formation of relatively long tensile cracks changes the stress field in the surrounding area, prohibiting the formation of new neighbour tensile cracks generated on the basis of the existing 'shear-crack' defects. These represent self-isolating features. For $\sigma_3 \geq \sigma_{3min(shear)}$ the tensile cracks become short enough to contribute to the shear rupture but without significantly affecting the stress conditions at the shear rupture tips necessary for the creation of further tensile cracks. This mechanism creates the universal structure of shear ruptures represented by an echelon of blocks (or slabs) separated by tensile cracks [3, 7, 8, 10–12]. Such structure is referred to in the literature as a 'domino' or 'book shelf' structure.

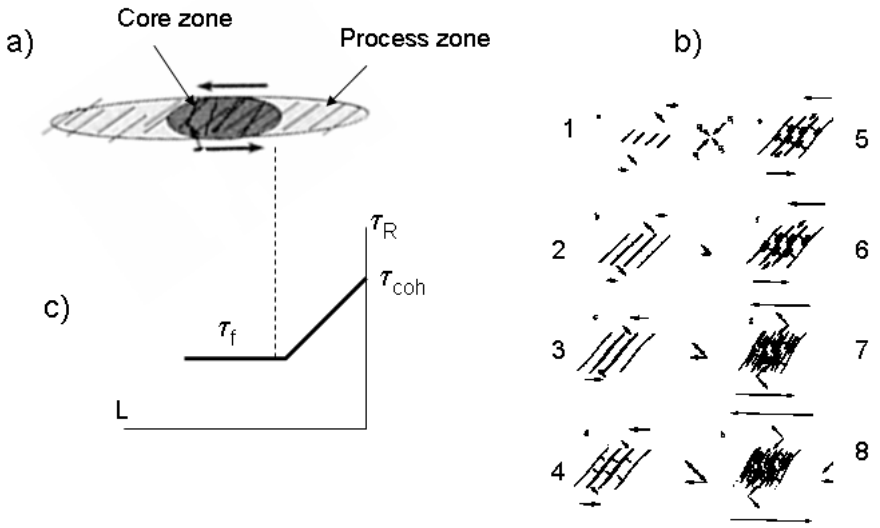


Figure 4: Common shear rupture models suggesting friction mobilization within the rupture zone due to collapse of rotating blocks (slabs) at shear displacement: a) Reches and Lockner [3], b) King and Sammis [8]. c) The graph illustrates variation of shear resistance within the process zone from cohesive τ_{coh} to frictional τ_f values.

Figure 4 illustrates modern understanding of this shear rupture mechanism. Figure 4a shows a shear rupture model proposed by Reches and Lockner [3]. The shear rupture involves two specific zones: process and core zones. Within the process zone the formation of tensile cracks takes place.

The structure of this zone is represented by blocks (slabs) separated by the tensile cracks. During shear displacement of the rupture faces, these blocks are subjected to rotation and collapse. Figure 4b shows a model by King and Sammis [8] illustrating the collapse process at the block rotation. Within the process zone the shear resistance decreases from the cohesive strength τ_{coh} at the rupture tip to a minimum value determined by friction τ_f due to complete crushing of the blocks (see graph in Figure 4). The crushed rock material (gouge) represents the structure of the core zone, the shear resistance of which is determined by friction.

All existing shear rupture models consider rupture development as a frictional process similar to that discussed above [3, 7, 8, 10 – 12]. In accordance with these models increase in confining pressure should be accompanied by increase in friction within the rupture zone which makes the rupture process less brittle. Variation of the brittleness index k for sandstone in Figure 2 is in accordance with these models. The question is: what is the rupture mechanism that causes tremendous embrittlement of hard rocks with rising σ_3.

Since the fault structure with an echelon of blocks separated by tensile cracks (domino structure) represents a fundamental feature of shear ruptures, it must play a very important role in rupture behaviour. At confining pressures $\sigma_3 < \sigma_{3min(shear)}$ (see Figure 3) the fracture patterns stays the same. However, increase in σ_3 causes further reduction in the length of the tensile cracks (and, consequently, the blocks) reducing the width of the shear rupture. We can suppose that within a certain (embrittlement) pressure range $\sigma_{3min(emb)} \leq \sigma_3 \leq \sigma_{3max(emb)}$ the blocks become short enough to withstand rotation without failure [15 – 19]. In this case the blocks can operate as hinges, eliminating friction. This can happen in hard rocks only because very strong material is required to achieve this. The very high strength of the rotating blocks for these conditions is explained also by the scale effect: the smaller the rock fragment the stronger it is. The thickness of shear ruptures developed in laboratory specimens at the embrittlement pressure condition is a fraction of a millimeter (about $1/10\,mm$ [16]). This means that the block length is of similar magnitude.

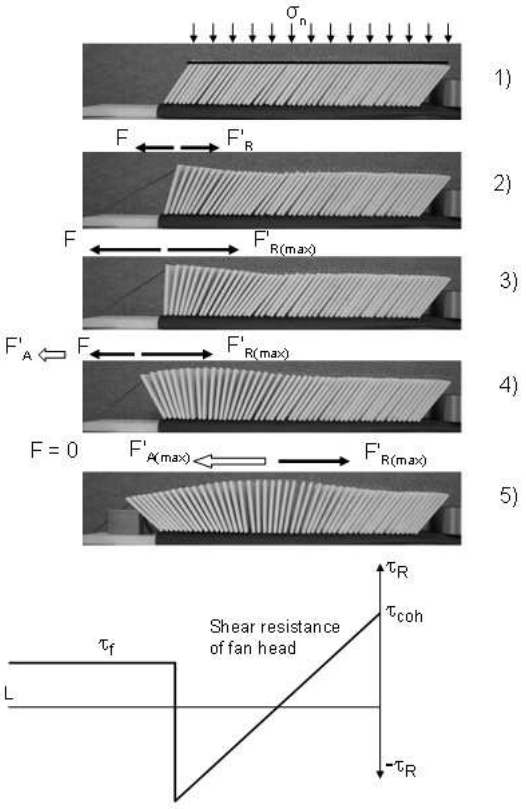


Figure 5: A physical model of the fan head formation.

It is observed in experiments that shear rupture can start very close to the specimen surface and then propagate across the specimen body [1, 4]. A physical model in Figure 5 illustrates

features of shear rupture development associated with the block rotation. All blocks of the model are confined by two elastic belts (on top and bottom) representing material of the rupture faces. Normal stress σ_n is applied to the structure and the rupture propagates from left to right. This model introduces a key role of elasticity of the face material in the fault structure development. Due to elasticity of the face material the rotating blocks are separated by splitting and rotated sequentially, forming eventually a fan-shaped structure. The picture illustrates different stages of the rupture propagation. The forces shown indicate schematically the variation in shear resistance of the growing rupture head (here, F is the applied force; F'_R and F'_A are reactive and active forces). The forces F'_R and F'_A are functions of normal stress σ_n, modulus E of the face material and geometrical characteristics of the rotating blocks (e.g. block length and initial angle of block inclination to the rupture axis). Initially, even though the resistance to shear for each individual block decreases with its rotation the total rupture resistance increases due to involving new blocks in the structure. The shear resistance reaches maximum, F'_{Rmax}, at the moment when the first half of the fan structure is formed.

A remarkable feature of the rotating blocks located in the second half of the fan structure is the creation of an active force F'_A under the effect of the normal stress σ_n. This force assists block rotation and, consequently, fracture propagation. At completion of the fan-structure formation the value of the active force becomes equal to the reactive force $F'_{Amax} = F'_{Rmax}$. Thus the fan-structure represents a self-equilibrating mechanism and can move as a wave without shear resistance. Elastic energy accumulated within the face material in the first half of the fan head releases in the second half. Due to the fact that all existing fault models consider the fault resistance as frictional we refer to the negative resistance symbolically as 'negative friction'. In the idealised model the resistance to rupture propagation is determined only by the tensile strength of the material associated with consecutive separation of blocks in front of the propagating rupture. This resistance can be extremely small due to low tensile strength and very small length of rotating blocks. The fan-head mechanism minimises both (a) the rupture energy due to splitting of rotating blocks sequentially (one by one) and (b) the shear resistance due to the self-equilibrating structure. This mechanism makes the failure process inevitably spontaneous and abnormally violent.

The graph in Figure 5 shows schematically variation of shear resistance τ_R along the fan-head rupture. At the tip of the fan head the resistance is characterised by cohesive strength τ_{coh} and decreases to a negative value the maximum of which is at the end of the head. Within the core zone the resistance is determined by friction τ_f. Compare this graph with the graph reflecting variation of shear resistance along the process zone for the frictional model in Figure 4. It is important that the fan head can propagate independently of the core zone, which can remain immobile due to high frictional resistance. The fan-head mechanism makes the rupture head very manoeuvrable and capable of creating very curvilinear shear ruptures. The fan-head mechanism is characterised by very small rupture energy.

Experiments conducted on the physical model presented in Figure 5 showed that the length L_{fh} of the fan head is a function of the normal stress (σ_n), the elastic modulus (E) of the rupture face material, the length (r) and width (s) of the blocks, and angle (α) of the initial block orientation relative to the rupture plane. Increase in σ_n reduces the fan head length L_{fh} while increasing E increases L_{fh}. It should be emphasised that the length L_{fh} represents actually a critical rupture length at which spontaneous rupture development becomes inevitable, with no chance to control further rupture propagation due to the vanishingly small rupture energy. The proposed mechanism shows that the critical rupture length is a function of geometrical features of the rupture structure, in contrast with existing shear rupture models that determine the critical length on the basis of Griffith's energy approach [34].

4 Mechanism of brittleness variation with confining pressure

4.1 Model of brittleness variation

Now we can discuss the reason for the specific rock brittleness variation with confining pressure shown in Figure 2. The variation of rock brittleness with rising σ_3 is commonly divided into three

categories: brittle, semi-brittle (or transitional) and ductile (or plastic) [27, 34]. The degree of brittleness within the brittle zone is not normally differentiated. Let us consider first the variation in brittleness versus confining pressure σ_3 on the basis of experimental results presented in Figure 2 for Westerly granite and dolerite.

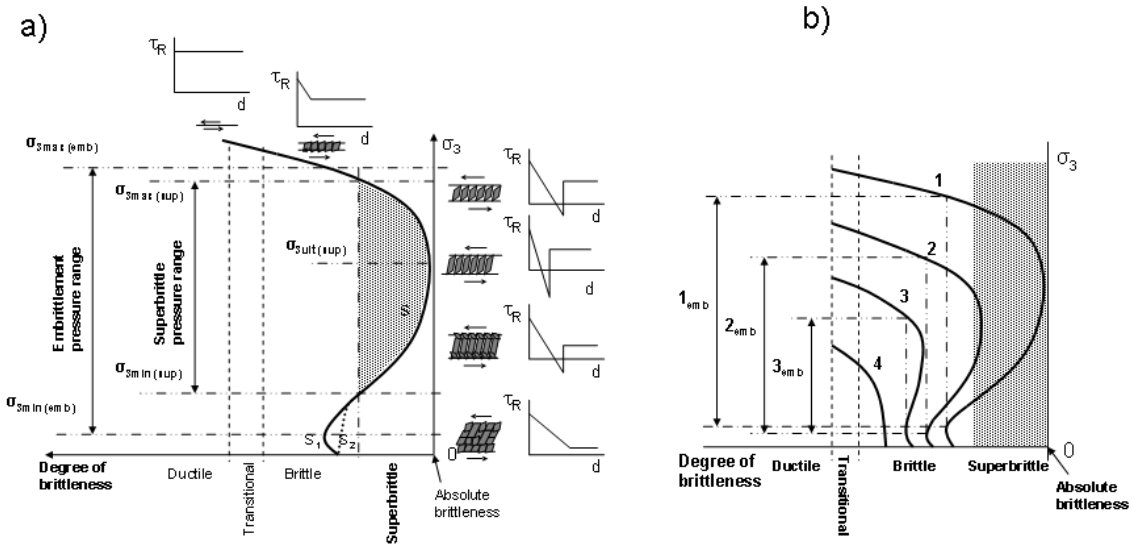


Figure 6: a) Mechanism responsible for brittleness variation versus confining pressure σ_3; b) Theoretical curves illustrating brittleness variation for four rocks of different hardness and different capability to embrittlement.

Figure 6a illustrates this variation schematically. The horizontal axis here represents the degree of brittleness and involves the traditional categories (brittle, transitional, ductile) as well as a new one - superbrittle. Figure 6a explains the essence of the rock brittleness variation with σ_3 showing fragments of shear ruptures with characteristic features of the fault structure. Within the range of confining pressure $0 - \sigma_{3min(emb)}$ the brittleness variation can accord with the commonly accepted frictional model due to collapsing of the long rotating blocks (curve S_1 observed for Westerly granite). Within the embrittlement pressure range, $\sigma_{3min(emb)} - \sigma_{3max(emb)}$, due to shortening of the rotating blocks, the frictionless mechanism is activated, increasing the rock brittleness compared with the frictional rupture mechanism. The efficiency of the frictionless mechanism is determined by how perfect and uniform the fault structure is. At the low end of the embrittlement pressure range, when the relative length (length/thickness) of the block is still large, the blocks are subjected to partial destruction (buckling) as they rotate. At higher σ_3, with shorter blocks, this imperfection decreases, rendering the frictionless mechanism more efficient. The optimal efficiency takes place at $\sigma_{3ult(emb)}$ when the blocks rotate with minimum destruction making the material ultimately brittle. At greater σ_3 the efficiency reduces because shorter blocks gradually lose any potential for creating negative resistance from rotation. Finally very short blocks lose this capability completely and the rock behaviour returns to the commonly accepted frictional mode. Idealised stress-displacement curves on the right illustrate evolution of the rupture resistance with displacement for different conditions of the rotating blocks, showing the negative shear resistance occurring over a certain σ_3 range.

In accordance with this model of rock embrittlement, two specific zones of confining pressure ?3 can be distinguished. 1) *Embrittlement pressure range* $(\sigma_{3min(emb)} - \sigma_{3max(emb)})$ – a zone where the frictionless mechanism is activated decreasing the frictional rupture resistance. 2) *Superbrittle pressure range* $(\sigma_{3min(sup)} - \sigma_{3max(sup)})$ - a zone where the frictionless mechanism is capable of creating 'negative friction'. This zone is shown by the shaded area. Figure 6b shows theoretical curves illustrating brittleness variation for four rocks of different hardness and different capability of embrittlement. The embrittlement pressure range for rocks 1, 2, and 3 are indicated in the picture. The softer the rock the less embrittlement occurs. Soft rocks (4) with normal frictional rupture mechanism do not exhibit embrittlement at all. Compare these theoretical curves with

experimental results presented in Figure 2.

4.2 Low and high pressure boundaries of the frictionless mechanism operation

Using experimental data we can estimate stress boundaries for embrittlement ($\sigma_{3min(emb)}$, $\sigma_{3max(emb)}$) and superbrittle behaviour ($\sigma_{3min(sup)}$, $\sigma_{3max(sup)}$) for certain rocks. The lower limit for embrittlement $\sigma_{3min(emb)}$ corresponds to the confining pressure from which rock brittleness starts to increase. This may be estimated approximately for Westerly granite, dolerite and quartzite as $30MPa$. The lower limit for superbrittle behaviour $\sigma_{3min(sup)}$ corresponds approximately to the confining stress at which rupture control becomes impossible (when the effect of 'negative friction' comes into play). Special comprehensive experimental studies are needed to determine the exact level for these rocks. Here we estimate roughly that $\sigma_{3min(sup)} \approx 100 - 150MPa$ for Westerly granite and $\sigma_{3min(sup)} \approx 50 - 60MPa$ for dolerite, while the defected quartzite did not show superbrittle behaviour.

What is the upper level, $\sigma_{3max(emb)}$, at which the frictionless mechanism should be suppressed and the rupture mechanism return to the commonly assumed frictional response? We can estimate this on the basis of the following experimental results. An important change in the fracture mechanism was observed experimentally by Shimada [27] at the level of confining pressure when the cohesive strength equals the frictional strength. Two types of brittle fracture, 'low-pressure' and 'high-pressure' types, were distinguished:

1. The low-pressure type fracture occurs when the cohesive strength is higher than the frictional strength, the main features being: a) numerous microcracks and crushed zones associated with the main fault, which is oriented at 15^o - 40^o to the major stress σ_1 direction; b) rapid increase in acoustic emission (AE) as a final explosive-like fracture is approached.

2. The high-pressure type fracture occurs when the cohesive strength is lower than the frictional strength, with characteristic features being: (a) there are fewer microcracks in total and they are not concentrated close to the main fault but are homogeneously distributed throughout the specimen, suggesting that cataclastic ductile flow could occur; (b) AE activity remains constant followed by a sudden final fracture; (c) the main fault is sharp and oriented at approximately 45^o to the compressive stress σ_1 direction.

It is known that AE events in a brittle rock mainly correspond to the generation of microcracks. The frictionless mechanism discussed above is associated with intensive microcracking in the fan head before and during instability. At high $\sigma_3 > \sigma_{3max(emb)}$ the frictionless mechanism is substituted by a frictional shear rupture mechanism that cannot generate such AE activity. On the basis of the above experiments we can suppose that the frictionless ruptures described here correspond to a form of low-pressure rupture. It is established [27] that at room temperature the confining pressure boundary between low- and high-pressure ruptures corresponds to $800MPa$ for Mannari granite and gabbro, $1000MPa$ for dunite, and $2000MPa$ for eclogite. These pressure levels can be considered as the high pressure boundary ($\sigma_3 = \sigma_{3max(emb)}$) for the frictionless mechanism in these rocks at room temperature. The high pressure boundary for superbrittle rock behaviour ($\sigma_3 = \sigma_{3max(sup)}$) should be lower. Special experimental studies are needed to determine the exact level for these rocks. Here we estimate roughly the high pressure boundary for superbrittle behaviour for Mannari granite as $\sigma_{3max(sup)} \approx 600MPa$. Westerly granite has similar mechanical properties to Mannari granite [27]. Hence, we can suppose that for Westerly granite boundary levels of confining pressure are: $\sigma_{3min(emb)} \approx 30MPa$, $\sigma_{3max(emb)} \approx 800MPa$, $\sigma_{3min(sup)} \approx 100 - 150MPa$ and $\sigma_{3max(sup)} \approx 600MPa$.

Figure 7 shows variation of brittleness index k versus confining pressure for Westerly granite in accordance with the above estimations. The estimated pressure range of superbrittle granite behaviour corresponds to depth range between ~ 4 and $\sim 20km$. If account is taken of the influence of increasing temperature with depth on the quality of the frictionless mechanism, the pressure limits $\sigma_{3max(emb)}$ and $\sigma_{3max(sup)}$ should be reduced. The range of superbrittleness is roughly corresponds to the seismogenic zone with maximum earthquake activity at about $5 - 10km$. We can presume that the thickness of the seismogenic layer, as well as positions of the upper and lower cut-off in seismicity, are determined by superbrittle rock conditions.

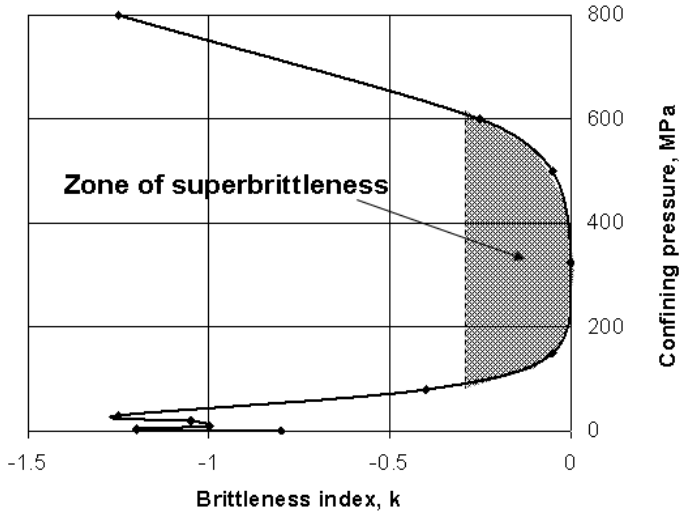


Figure 7: Variation of brittleness index k versus confining pressure for Westerly granite estimated on the basis of experimental data.

5 Conclusions

The most important conclusions are summarized below:

1. Experimental results presented in the paper show that increase in confining pressure σ_3 causes embrittlement of hard rocks. The brittleness variation in this case typically follows a pattern of increasing with increasing σ_3, reaching a maximum at some level of σ_3 and than ultimately decreasing since all rocks become ductile at very high σ_3. The rock brittleness is a function of σ_3 and rock hardness. The harder the rock the greater is the effect of embrittlement. Most hard rocks at highly confined conditions can become hundreds of times more brittle compared with uniaxial compression approaching absolute brittleness. The rupture energy at these conditions becomes vanishingly small.

2. A special shear rupture mechanism is proposed that is believed to operate in hard rocks within the embrittlement pressure range. In accordance with this mechanism the embrittlement results from reduction of friction within the rupture zone. The essence of the mechanism is the point that rotating blocks, representing the typical domino-like structure of shear ruptures, can rotate at the rupture displacement without collapse, essentially operating as hinges.

3. Previously unexplored properties of hard rocks - increase in brittleness with rising confining pressure with superbrittle behaviour for conditions corresponding to the depths of maximum earthquake activity - give ground to suppose that earthquake depth activity is a function of rock brittleness variation.

Acknowledgements

This work was supported over a number of years by the Centre for Offshore Foundation Systems at the University of Western Australia, which was established under the Australian Research Council's Special Research Centre scheme and is now supported by the State Government of Western Australia through the Centre of Excellence in Science and Innovation program. This support is gratefully acknowledged.

References

[1] Lockner, D.A., Byerlee, J.D., Kuksenko, V., Ponomarev, A. and Sidorin, A. Quasi-static fault growth and shear fracture energy in granite. Nature, 1991; 350: 39 42.

[2] Moore D.E., Summers R., and Byerlee J.D. Faults, fractures and other deformation features produced during loading of granite in triaxial equipment. U.S. Gelo. Surv. Open File Rep., 1990. 90-349.

[3] Reches, Z. and Lockner, D., A. Nucleation and growth of faults in brittle rocks. J. Geophys. Res. Vol. 99, No. B9, 1994; 18159-18173.

[4] Lei, X., Kusunose K, Rao M.V.M.S., Nishizawa O. and Satoh T. Quasi-static fault growth and cracking in homogeneous brittle rock under triaxial compression using acoustic emission monitoring. J. Geophys. Res. 2000; Vol. 105. No. B3, pp. 6127-6139.

[5] Rummel F., and Fairhurst C. Determination of the post-failure behaviour of brittle rock using a servo-controlled testing machine. Rock Mech. 1970; 2, 189-204.

[6] Crouch S.L. The post-failure behaviour of norite in triaxial compression. Eng. Geol. 1972; 6. 19-30.

[7] Peng, S. and Johnson, A.M. Crack growth and faulting in cylindrical specimens of Chelmsford granite. Int. J. Rock Mech. Min. Sci. 1972; 9, 37-86.

[8] King, G.C.P. and Sammis, C.G. The mechanisms of finite brittle strain. PAGEOPH, 1992; 138, 4, 611-640.

[9] Horii, H., and Nemat-Nasser, S. Compression-induced microcrack growth in brittle solids: Axial splitting and shear failure, J. Geophys. Res., 1985; 90, 3105-3125.

[10] Mandel, G. Faulting in brittle rocks, Springer-Verlag Berlin Heidelberg. 2000.

[11] Cox, S.J.D. and Scholz, C.H. On the formation and growth of faults: an experimental study. J. Struct. Geol., 1988; 10, pp. 413-430.

[12] Renshaw C.E and Shulson E.M. Universal behaviour in compressive failure of brittle materials. Nature, 2001; Vol 412, 897-900.

[13] Stavrogin A.N. and Tarasov B.G. Experimental physics and rock mechanics. Balkema, 2001.

[14] Tarasov B.G. and Dyskin A.V. The phenomenon of anomalous rock embrittlement. Proc. Sixth Int. Symp. on Rockburst and Seismicity in Mines, 2005; p. 311-317.

[15] Tarasov B.G., and Randolph, M.F. Frictionless shear at great depth and other paradoxes of hard rocks. Int. J. Rock Mech. Min. Sci. 2008; 45; 316-328 .

[16] Tarasov, B.G. and Randolph, M.F. Paradoxical features of primary shear fractures and general faults. Proc. 4th International Seminar on Deep and High Stress Mining, Perth, Australia, 2007; p. 165-182.

[17] Tarasov B.G. and Ortlepp W.D. Shock loading-unloading mechanism in rockburst shear fractures in quartzite causing genesis of polyhedral sub-particle in the fault gouge. Proc. 4th International Seminar on Deep and High Stress Mining, Perth, Australia, 2007; p. 183-192.

[18] Tarasov B.G. Intersonic shear rupture mechanism. Int. J. Rock Mech. Min. Sci. 2008; 45: 914-928.

[19] Tarasov B.G. New insight into the nature of shear rupture propagation in pristine rocks and pre-existing faults. Keynote address. Proc. 1st Southern Hemisphere Int. Rock Mechanics Symp., Australia, 2008; p. 37-68.

[20] Andreev G.E. Brittle failure of rock materials: test results and constitutive models. A.A. Balkema, Rotterdam, 1995, p. 287.

[21] Okubo C.H.S and Nishimatsu Y. A study of the Class II behaviour of rock. Rock Mechanics and Rick Engineering 1990; 23, 261-273.

[22] Hajiabkolmajid V., Kaiser P. and Martin C.D. Mobilised strength components in brittle failure of rock. Geotechnique, 2003; 53, No. 3, 327-336.

[23] Wawersik W.R. and Fairhurst C. A study of brittle rock fracture in laboratory compression experiments. Int. J. Rock Mech. Min. Sci. 1970; 7, 561-575.

[24] Wawersik W.R. and Brace W.F. Post-failure behavior of a granite and diabase. Rock Mechanics 1971; 3, 61-85.

[25] Zhang J. Wong T.F. and davis D.M. High pressure embrittlement and shear-enhanced compaction of Berea sandstone: acoustic emission measurement and microstructural observation. In Rock Mechanics Contributions nd Challengers (eds Hustrulid W.A. and Johson G.A.) Balkema, 1990; 653-660.

[26] Wong T.F., Szeto H. and Zhang J. Effect of loading path and porosity on the failure mode of porous rocks Appl. Mech. Rev. 1992; 45: 281-293.

[27] Shimada M. Mechanical behaviour of rocks under high pressure conditions. Balkema, 2000.

[28] Byerlee J.D and Brace W.F. High-pressure mechanical instability in rocks. Science 1969; 164: 713-715.

[29] Kirby S.H. and McCormick J.W. Inelastic properties of rocks and minerals: strength and rheology. In CRC Handbook of Physical Properties of Rocks (ed. Carmichael R.S.) 1984; Vol. 3: 139-280. Boca Raton, Florida: CRC Press.

[30] Adams M. and Sines. G. Crack extension from flaws in a brittle material subjected to compression. Tectonophysics, 1978; 49: 97-118.

[31] Germanovich L.N., Salganik R.L., Dyskin A.V. lee K.K. Mechanisms of brittle failure of rock with pre-existing cracks in compression. Pure Appl. Geophys. 1994; 143: 117-149.

[32] Brace W.F and Bombolakis E.G. A note on brittle crack growth in compression, J. Geophys. Res. 1963; 68, 3709-37-13.

[33] Ashby M.F and Hallam S.D. The failure of brittle solids containing small cracks under compressive stress states. Acta Metall. 1986; 34, 497-510.

[34] Scholz, C. H. The mechanics of earthquakes and faulting. Cambridge University Press. 2002.

Boris G. Tarasov, The University of Western Australia, Perth, Australia

Tensor approach for mathematical modeling of geomagnetic field

Alexey A. Tikhonov, Kirill A. Antipov
aatikhonov@rambler.ru

Abstract

To develop a mathematical model of rotational motion of an artificial Earth's satellite about its center of mass under the action of various forces (magnetic, Lorentz, etc.) caused by the geomagnetic field, it is necessary to know the induction of the Earth's magnetic field (EMF) as a function of the radius vector of a given point in the near-Earth space. Because the EMF possesses a complex structure and the above-mentioned functional dependence is unavailable in explicit analytic form, a set of approximate models of the EMF should be used. The simplest and well known such model - a right dipole (aligned with the axis of rotation) allowed to solve a lot of problems, but it does not enable one to reveal in detail the influence of diurnal EMF rotation on the rotation motion of a satellite. The next and more realistic EMF approximation - an inclined magnetic dipole - does not suffer from the above-mentioned drawback. However, it is shown in [1] that not all corrections to the magnetic induction of the EMF of the same order of magnitude are taken into account in the course of transformation from the model of aligned dipole to the model of inclined dipole. So, to develop the EMF model accurately accounting for the absence of axial symmetry of the EMF with respect to the axis of diurnal rotation of the Earth, in general, the effect of the quadrupole component of the geomagnetic potential on the EMF induction (and, probably, even the components of higher orders) must be taken into consideration.

The mathematical ground for the construction of the EMF induction in quadrupole approximation was suggested in [2]. The development of this mathematical ground given in [3], allowed to construct first, second and third multipole components of the EMF induction. The question on the probability of construction the multipole tensors of the 5-th and higher ranks was stated.

In this paper the answer on this question is given. The multipole tensor $\mathrm{M}^{(n)}$ of rank n is introduced and studied. The algorithm for analytical construction of the $\mathrm{M}^{(n)}$ components is elaborated. In particular, earlier unknown tensors $\mathrm{M}^{(5)}$, $\mathrm{M}^{(6)}$, $\mathrm{M}^{(7)}$ are constructed. The EMF induction was written in convenient and concise multipole form. Thus, the solution of the problem, started in [2] and continued in [3], was led to its logical completion.

1 Coordinate systems and angles

Let us introduce the necessary coordinate systems. The system O_EXYZ (with unit vectors $\vec{\tau}_1, \vec{\tau}_2, \vec{\tau}_3$) is rigidly connected with the Earth (Fig 1), where the O_EX axis is directed to the point of intersection between the zero meridian and the equator, and the O_EZ axis corresponds to the positive direction of the axis of diurnal rotation of the Earth. As all the other coordinate systems used in the present work, this is a right-handed Cartesian rectangular coordinate system. The spherical coordinates r, θ^*, λ^* are also shown in Fig 1.

Fig 2 shows the auxiliary coordinate system $O_EX^0Y^0Z^0$ (unit vectors $\vec{\tau}_1^0, \vec{\tau}_2^0, \vec{\tau}_3^0$), whose O_EX^0 axis is directed to the ascending node of the satellite orbit Ω, and the O_EZ^0 axis is perpendicular to the orbital plane of the satellite. The angles u, Ω_π and ν are the argument of latitude, perigee argument (perigee is shown by π point in Fig 2), and true anomaly, respectively. The orbital coordinate system $C\xi\eta\zeta$ with the origin in the satellite's center of mass is shown in Fig 2 also. Its $C\eta$ axis is perpendicular to the orbital plane of the satellite, and the $C\zeta$ axis is parallel to the

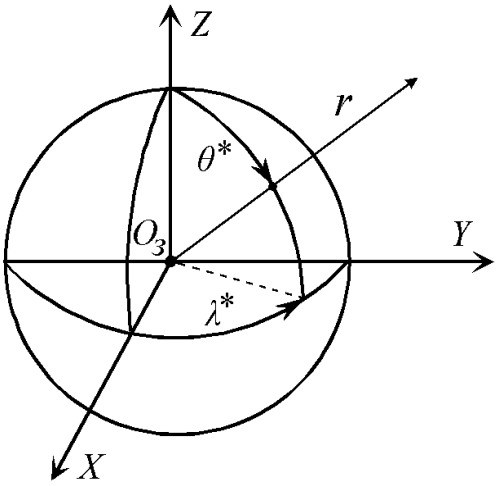


Figure 1:

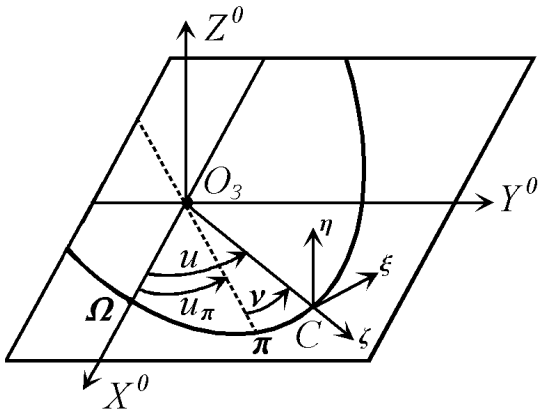


Figure 2:

radius vector of the center of mass of the satellite with respect to the center of mass of the Earth O_E.

It is convenient to calculate the EMF induction with the use of spherical coordinates r, θ, λ, which are shown in Fig 4. The unit vectors $\vec{\xi}_0, \vec{\eta}_0, \vec{\zeta}_0$ of the orbital coordinate system coincide with the unit vectors $\vec{e}_\lambda, \vec{e}_\theta, \vec{e}_r$ of the moving basis of spherical coordinates r, θ and λ in the center of mass of the satellite, while the center of mass by itself has the spherical coordinates $r = r_C$, $\theta = 0$ and $\lambda = u$.

The mutual orientation of the coordinate systems $O_E XYZ$ and $O_E X^0 Y^0 Z^0$ is shown in Fig 3, where i is the inclination of the satellite's orbit and ϕ is the hour angle of the ascending node of the orbit.

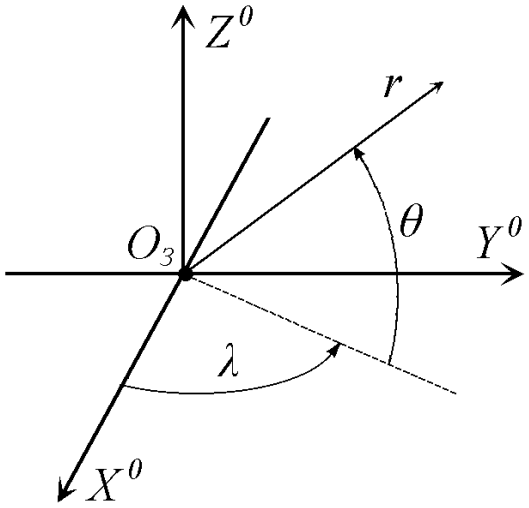


Figure 3:

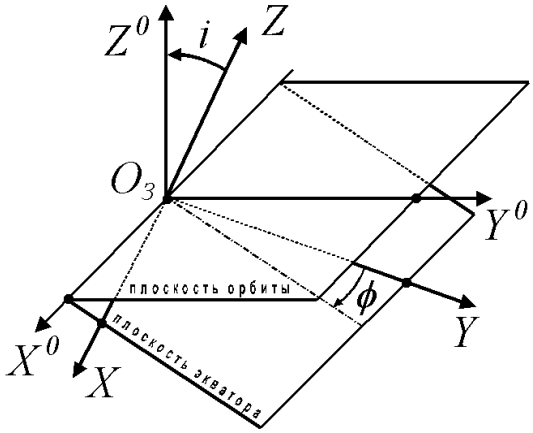


Figure 4:

The components of the direction cosine matrix $\mathbf{\Gamma} = (\gamma_{ij})$ $(i = \overline{1,3},\ j = \overline{1,3})$, which determine the mutual orientation of the coordinate systems $O_E XYZ$ and $O_E X^0 Y^0 Z^0$ in accordance with the equations $\vec{\tau}_i^0 = \sum\limits_{j=1}^{3} \gamma_{ij}\, \vec{\tau}_j,\ i = \overline{1,3}$, are expressed in terms of the angles i and ϕ as

$$\gamma_{11} = \cos\phi, \qquad \gamma_{12} = -\sin\phi, \qquad \gamma_{13} = 0,$$
$$\gamma_{21} = \cos i \sin\phi, \qquad \gamma_{22} = \cos i \cos\phi, \qquad \gamma_{23} = \sin i,$$

$$\gamma_{31} = -\sin i \sin\phi, \qquad \gamma_{32} = -\sin i \cos\phi, \qquad \gamma_{33} = \cos i.$$

Considering the transformation of the coordinates of radius-vector

$$\vec{r} = (X^0, Y^0, Z^0)^\top = r(\cos\theta\cos\lambda,\ \cos\theta\sin\lambda,\ \sin\theta)^\top$$

in transition from the coordinate system $O_E X^0 Y^0 Z^0$ to the system $O_E XYZ$, in which

$$\vec{r} = (X, Y, Z)^\top = r(\sin\theta^*\cos\lambda^*,\ \sin\theta^*\sin\lambda^*,\ \cos\theta^*)^\top, \tag{1}$$

one can obtain that the angles θ^* and λ^* are connected with the angles θ and λ by the relations

$$\mathbf{S}^*(\theta^*, \lambda^*) = \mathbf{\Gamma}^\top \mathbf{S}(\lambda, \theta),$$

where $\mathbf{S}^*(\theta^*, \lambda^*) = \begin{pmatrix} \sin\theta^*\cos\lambda^* \\ \sin\theta^*\sin\lambda^* \\ \cos\theta^* \end{pmatrix}$, $\mathbf{S}(\lambda, \theta) = \begin{pmatrix} \cos\theta\cos\lambda \\ \cos\theta\sin\lambda \\ \sin\theta \end{pmatrix}$.

2 The potential of the Earth's magnetic field

Following the results presented in [4], we assume that the external EMF, produced by the plasma envelope of the Earth, is negligible as compared with the proper EMF, whose origin is in the interiors of the Earth's globe. The proper EMF is the potential vector field, whose potential is commonly presented as a function of the spherical coordinates r, θ^*, λ^* in the form of the Legendre expansion:

$$U^* = \sum_{n=1}^{\infty} U_n^* = \sum_{n=1}^{\infty} \frac{{R_E}^{n+2}}{r^{n+1}} \sum_{m=0}^{n} P_n^m(\cos\theta^*)(g_n^m \cos m\lambda^* + h_n^m \sin m\lambda^*). \tag{2}$$

Here R_E is the average Earth's radius, $P_n^0(x) = \dfrac{1}{2^n n!}\dfrac{d^n}{dx^n}(x^2-1)^{(n)}$ are the Legendre polynomials, and $P_n^m(x) = k_n^m(1-x^2)^{m/2}\dfrac{d^m}{dx^m}P_n^0(x)$ are the associated Legendre functions quasi-orthonormalized according to Schmidt and $k_n^m = \sqrt{\varepsilon_m \dfrac{(n-m)!}{(n+m)!}}$ are the normalization factors, in which $\varepsilon_0 = 1$ and $\varepsilon_m = 2$ at $m \geqslant 1$. The values of geomagnetic coefficients g_n^m and h_n^m, according to the model of International Geomagnetic Reference Field IGRF-2005 can be taken from [5].

In the applied investigations the approximation of the expansion (2) with N terms is used:

$$U^* = \sum_{n=1}^{N} U_n^*\,. \tag{3}$$

Here U_1^* is the potential of the dipole component of the EMF, while the others U_n^* are the potentials of multipole components of the n-th order:

$$U_n^* = \frac{{R_E}^{n+2}}{r^{n+1}} \sum_{m=0}^{n} P_n^m(\cos\theta^*)(g_n^m \cos m\lambda^* + h_n^m \sin m\lambda^*). \tag{4}$$

In the Cartesian coordinates XYZ

$$U_1^* = \frac{R_E^3}{r^3}\left(g_1^1 X + h_1^1 Y + g_1^0 Z\right) = \frac{{R_E}^3\, \mathbb{M}^{(1)} \cdot \vec{r}}{r^3},$$

where $R_E^3\ \mathbb{M}^{(1)} = R_E^3\ (g_1^1,\ h_1^1,\ g_1^0)^\top$ is the magnetic moment of the dipole component of EMF (named in consequence briefly by dipole magnetic moment).

Earlier it was shown in [3] that the potential (4) may be approximated by the sum of the four terms, and U_n^* $(n \le 4)$ may be written in the form

$$U_n^* = \frac{R_E^{n+2}}{r^{2n+1}} \mathbb{M}^{(n)} \underbrace{\cdots}_{n} (\otimes^n \vec{r}). \tag{5}$$

Here $\mathbb{M}^{(n)}$ is the multipole tensor of rank n depending on geomagnetic coefficients only, $R_E^{n+2}\mathbb{M}^{(n)}$ is the magnetic moment of n-th order, tensor $\otimes^n \vec{r}$ of rank n is defined by induction in the following way:

$$\otimes^1 \vec{r} = \vec{r}, \quad \otimes^{n+1} \vec{r} = \otimes^n \vec{r} \otimes \vec{r}.$$

The operation $\underbrace{\cdots}_{n}$ is defined for the pair of tensors A and B of rank n as

$$A \underbrace{\cdots}_{n} B = \sum_{i_1} \sum_{i_2} \dots \sum_{i_n} A_{i_m, i_{m-1}, \dots, i_n, i_{n-1}, \dots, i_2, i_1} \times B_{i_1, i_2, \dots, i_{n-1}, i_n, \dots, i_{p-1}, i_p}.$$

Let us turn to the desired representation of potential U_n^* in the form (3), (5) with an arbitrary number N and unknown tensors $\mathbb{M}^{(n)}$.

From one side each of the terms U_n^* in the sum (3) has the form (4). From the other side U_n^* depends on vector $\vec{r}$, which in its turn may be expressed in the spherical coordinates r, θ^*, λ^* with unknown coefficients $M_{i_1,\, i_2,\, \dots\, ,\, i_n}$. By equating the corresponding coefficients at the same combinations of trigonometric functions, we obtain the algebraic system, in which however the number of unknowns is larger that the number of equations. In order to close the system one should use the additional relations following from the consideration of the multipole tensors $\mathbb{M}^{(n)}$ properties. It was revealed in [3] that for arbitrary n the multipole tensor possesses the following properties:

1. Tensor $\mathbb{M}^{(n)}$ is symmetric with respect to any pair of indices (i.e., invariant with respect to transposition),

2. Any contraction of the tensor $\mathbb{M}^{(n)}$ is equal to zero (for example, the contraction over the first pair of indices is equal to zero: $\sum\limits_{k=1}^{3} M_{k,\, k,\, i_3,\, \dots\, ,\, i_n} = 0$).

The involving of these properties and corresponding relations result in algebraic system, which allows to obtain a unique expressions of the unknown multipole tensors components in terms of the geomagnetic coefficients. The algorithm for analytical construction of the multipole tensor components for an arbitrary rank n is elaborated. This algorithm is based on the symbolic computation methods and was adopted for *Maple*.

As a result the following components of the first six multipole tensors were obtained:

$$M_{11} = \frac{1}{2}\left(\sqrt{3} g_2^2 - g_2^0\right), \qquad M_{12} = \frac{\sqrt{3}}{2} h_2^2, \qquad M_{13} = \frac{\sqrt{3}}{2} g_2^1,$$

$$M_{22} = -\frac{1}{2}\left(g_2^0 + \sqrt{3}\, g_2^2\right), \qquad M_{23} = \frac{\sqrt{3}}{2} h_2^1, \qquad M_{33} = g_2^0,$$

$$M_{111} = \frac{\sqrt{6}}{12}\left(\sqrt{15}\, g_3^3 - 3\, g_3^1\right), \qquad M_{112} = \frac{\sqrt{6}}{12}\left(\sqrt{15}\, h_3^3 - h_3^1\right),$$

$$M_{113} = \frac{1}{6}\left(\sqrt{15}\, g_3^2 - 3\, g_3^0\right), \qquad M_{122} = -\frac{\sqrt{6}}{12}\left(\sqrt{15}\, g_3^3 + g_3^1\right),$$

$$M_{123} = \frac{\sqrt{15}}{6} h_3^2, \qquad M_{133} = \frac{\sqrt{6}}{3} g_3^1$$

$$M_{222} = -\frac{\sqrt{6}}{12}\left(\sqrt{15}\, h_3^3 + 3\, h_3^1\right), \qquad M_{223} = -\frac{1}{6}\left(\sqrt{15}\, g_3^2 + 3\, g_3^0\right),$$

$$M_{233} = \frac{\sqrt{6}}{3} h_3^1, \qquad M_{333} = g_3^0,$$

$$M_{1111} = \frac{1}{8}\left(\sqrt{35}\,g_4^4 - 2\sqrt{5}\,g_4^2 + 3\,g_4^0\right), \qquad M_{1112} = \frac{\sqrt{5}}{8}\left(\sqrt{7}\,h_4^4 - h_4^2\right),$$
$$M_{1113} = \frac{\sqrt{10}}{16}\left(\sqrt{7}\,g_4^3 - 3\,g_4^1\right), \qquad M_{1122} = \frac{1}{8}\left(g_4^0 - \sqrt{35}\,g_4^4\right),$$
$$M_{1123} = \frac{\sqrt{10}}{16}\left(\sqrt{7}\,h_4^3 - h_4^1\right), \qquad M_{1133} = \frac{1}{4}\left(\sqrt{5}\,g_4^2 - 2\,g_4^0\right),$$
$$M_{1222} = -\frac{\sqrt{5}}{8}\left(\sqrt{7}\,h_4^4 + h_4^2\right), \qquad M_{1223} = -\frac{\sqrt{10}}{16}\left(g_4^1 + \sqrt{7}\,g_4^3\right),$$
$$M_{1233} = \frac{\sqrt{5}}{4}\,h_4^2, \qquad M_{1333} = \frac{\sqrt{10}}{4}\,g_4^1,$$
$$M_{2222} = \frac{1}{8}\left(3\,g_4^0 + \sqrt{35}\,g_4^4 + 2\sqrt{5}\,g_4^2\right), \qquad M_{2223} = -\frac{\sqrt{10}}{16}\left(\sqrt{7}\,h_4^3 + 3\,h_4^1\right),$$
$$M_{2233} = -\frac{1}{4}\left(2\,g_4^0 + \sqrt{5}\,g_4^2\right), \qquad M_{2333} = \frac{\sqrt{10}}{4}\,h_4^1,$$
$$M_{3333} = g_4^0,$$

$$M_{11111} = \frac{1}{16}\left(3\sqrt{14}\,g_5^5 - \sqrt{70}\,g_5^3 + 2\sqrt{15}\,g_5^1\right),$$
$$M_{11112} = \frac{1}{80}\left(15\sqrt{14}\,h_5^5 - 3\sqrt{70}\,h_5^3 + 2\sqrt{15}\,h_5^1\right),$$
$$M_{11113} = \frac{1}{40}\left(3\sqrt{35}\,g_5^4 + 15\,g_5^0 - 2\sqrt{105}\,g_5^2\right),$$
$$M_{11122} = \frac{1}{80}\left(-15\sqrt{14}\,g_5^5 + \sqrt{70}\,g_5^3 + 2\sqrt{15}\,g_5^1\right),$$
$$M_{11123} = \frac{\sqrt{35}}{40}\left(3\,h_5^4 - \sqrt{3}\,h_5^2\right), \quad M_{11133} = \frac{\sqrt{5}}{20}\left(\sqrt{14}\,g_5^3 - 3\sqrt{3}\,g_5^1\right),$$
$$M_{11222} = \frac{1}{80}\left(-15\sqrt{14}\,h_5^5 - \sqrt{70}\,h_5^3 + 2\sqrt{15}\,h_5^1\right),$$
$$M_{11223} = \frac{1}{40}\left(-3\sqrt{35}\,g_5^4 + 5\,g_5^0\right), \quad M_{11233} = \frac{\sqrt{5}}{20}\left(\sqrt{14}\,h_5^3 - \sqrt{3}\,h_5^1\right),$$
$$M_{11333} = \frac{1}{20}\left(\sqrt{105}\,g_5^2 - 10\,g_5^0\right),$$
$$M_{12222} = \frac{1}{80}\left(3\sqrt{70}\,g_5^3 + 15\sqrt{14}\,g_5^5 + 2\sqrt{15}\,g_5^1\right),$$
$$M_{12223} = -\frac{\sqrt{35}}{40}\left(\sqrt{3}\,h_5^2 + 3\,h_5^4\right), \quad M_{12233} = -\frac{\sqrt{5}}{20}\left(\sqrt{14}\,g_5^3 + \sqrt{3}\,g_5^1\right),$$
$$M_{12333} = \frac{\sqrt{105}}{20}\,h_5^2, \quad M_{13333} = \frac{\sqrt{15}}{5}\,g_5^1,$$
$$M_{22222} = \frac{1}{16}\left(\sqrt{70}\,h_5^3 + 3\sqrt{14}\,h_5^5 + 2\sqrt{15}\,h_5^1\right),$$
$$M_{22223} = \frac{1}{40}\left(2\sqrt{105}\,g_5^2 + 15\,g_5^0 + 3\sqrt{35}\,g_5^4\right),$$
$$M_{22233} = -\frac{\sqrt{5}}{20}\left(\sqrt{14}\,h_5^3 + 3\sqrt{3}\,h_5^1\right), \quad M_{22333} = -\frac{1}{20}\left(\sqrt{105}\,g_5^2 + 10\,g_5^0\right),$$
$$M_{23333} = \frac{\sqrt{15}}{5}\,h_5^1, \quad M_{33333} = g_5^0,$$

$$M_{111111} = \frac{1}{32}\left(-6\sqrt{7}\,g_6^4 + \sqrt{210}\,g_6^2 + \sqrt{462}\,g_6^6 - 10\,g_6^0,\right)$$
$$M_{111112} = \frac{\sqrt{7}}{96}\left(3\sqrt{66}\,h_6^6 + \sqrt{30}\,h_6^2 - 12\,h_6^4\right),$$
$$M_{111113} = \frac{\sqrt{7}}{96}\left(3\sqrt{22}\,g_6^5 - 3\sqrt{30}\,g_6^3 + 10\sqrt{3}\,g_6^1\right),$$

$$M_{111122} = \frac{1}{480}\left(30\sqrt{7}\,g_6^4 + \sqrt{210}\,g_6^2 - 15\sqrt{462}\,g_6^6 - 30\,g_6^0\right),$$
$$M_{111123} = \frac{\sqrt{7}}{480}\left(-9\sqrt{30}\,h_6^3 + 15\sqrt{22}\,h_6^5 + 10\sqrt{3}\,h_6^1\right),$$
$$M_{111133} = \frac{1}{120}\left(15\sqrt{7}\,g_6^4 - 4\sqrt{210}\,g_6^2 + 45\,g_6^0\right),$$
$$M_{111222} = \frac{\sqrt{21}}{160}\left(-5\sqrt{22}\,h_6^6 + \sqrt{10}\,h_6^2\right),$$
$$M_{111223} = \frac{\sqrt{7}}{480}\left(-15\sqrt{22}\,g_6^5 + 3\sqrt{30}\,g_6^3 + 10\sqrt{3}\,g_6^1\right),$$
$$M_{111233} = \frac{\sqrt{7}}{120}\left(15\,h_6^4 - 2\sqrt{30}\,h_6^2\right), \quad M_{111333} = \frac{\sqrt{21}}{40}\left(\sqrt{10}\,g_6^3 - 5\,g_6^1\right),$$
$$M_{112222} = \frac{1}{480}\left(-\sqrt{210}\,g_6^2 + 30\sqrt{7}\,g_6^4 + 15\sqrt{462}\,g_6^6 - 30\,g_6^0\right),$$
$$M_{112223} = \frac{\sqrt{7}}{480}\left(-3\sqrt{30}\,h_6^3 - 15\sqrt{22}\,h_6^5 + 10\sqrt{3}\,h_6^1\right),$$
$$M_{112233} = \frac{1}{8}\left(g_6^0 - \sqrt{7}\,g_6^4\right), \quad M_{112333} = \frac{\sqrt{21}}{120}\left(3\sqrt{10}\,h_6^3 - 5\,h_6^1\right),$$
$$M_{113333} = \frac{1}{30}\left(-15\,g_6^0 + \sqrt{210}\,g_6^2\right),$$
$$M_{122222} = \frac{\sqrt{7}}{96}\left(\sqrt{30}\,h_6^2 + 12\,h_6^4 + 3\sqrt{66}\,h_6^6\right),$$
$$M_{122223} = \frac{\sqrt{7}}{480}\left(15\sqrt{22}\,g_6^5 + 3\sqrt{30}\,g_6^3 + 10\sqrt{3}\,g_6^1\right),$$
$$M_{122233} = -\frac{\sqrt{7}}{120}\left(2\sqrt{30}\,h_6^2 + 15\,h_6^4\right), \quad M_{122333} = -\frac{\sqrt{7}}{120}\left(3\sqrt{30}\,g_6^3 + 5\sqrt{3}\,g_6^1\right),$$
$$M_{123333} = \frac{\sqrt{210}}{30}\,h_6^2, \quad M_{133333} = \frac{\sqrt{21}}{6}\,g_6^1,$$
$$M_{222222} = -\frac{1}{32}\left(10\,g_6^0 + \sqrt{462}\,g_6^6 + \sqrt{210}\,g_6^2 + 6\sqrt{7}\,g_6^4\right),$$
$$M_{222223} = \frac{\sqrt{7}}{96}\left(3\sqrt{30}\,h_6^3 + 3\sqrt{22}\,h_6^5 + 10\sqrt{3}\,h_6^1\right),$$
$$M_{222233} = \frac{1}{120}\left(45\,g_6^0 + 4\sqrt{210}\,g_6^2 + 15\sqrt{7}\,g_6^4,\right)$$
$$M_{222333} = -\frac{\sqrt{7}}{40}\left(\sqrt{30}\,h_6^3 + 5\sqrt{3}\,h_6^1\right), \quad M_{223333} = -\frac{1}{30}\left(15\,g_6^0 + \sqrt{210}\,g_6^2\right),$$
$$M_{233333} = \frac{\sqrt{21}}{6}\,h_6^1, \quad M_{333333} = g_6^0.$$

Thus, the possibility of the EMF potential representation in the form (3) with an arbitrary number of terms N was justified.

3 The induction of the Earth's magnetic field

Having the EMF potential represented in the form (3), (5), let us pass to the finding out the induction of the EMF, defined by the equation

$$\vec{B} = -\operatorname{grad} U^*. \tag{6}$$

We obtain:

$$\vec{B} = -\sum_{n=1}^{N} \operatorname{grad} U_n^* = \sum_{n=1}^{N} \vec{B}^{(n)}. \tag{7}$$

As it was shown in [2], it is convenient to express the potential (3) as a function of the spherical coordinates $r,\ \theta,\ \lambda$. In this case we shall write the potential without *, and the projections of the EMF induction on the axes of the orbital frame may be written the form

$$\left(B_\xi,\ B_\eta,\ B_\zeta\right)^T = -\left(\frac{1}{R}\frac{\partial U}{\partial \lambda},\ \frac{1}{R}\frac{\partial U}{\partial \theta},\ \frac{\partial U}{\partial r}\right)^T_{\substack{\lambda=u\\ \theta=0\\ r=R}}. \tag{8}$$

In order to represent the potential (3) as a function of the spherical coordinates $r,\ \theta,\ \lambda$, let us express it in the form of a function of Cartesian coordinates X, Y, Z. Next, by performing an orthogonal transformation of coordinates with the matrix $\mathbf{\Gamma}$, this expression will be presented as a function of Cartesian coordinates X^0, Y^0, Z^0. Finally, expressing the latter in terms of the spherical coordinates $r,\ \theta,\ \lambda$, we get the required expression for potential (3), (5).

In accordance with the stated plan first we obtain the potential (3) as a function of Cartesian coordinates X^0, Y^0, Z^0 by the coordinates transformation with matrix $\mathbf{\Gamma}$:

$$U^* = \frac{R_E^3}{r^2}\mathrm{M}_0^{(1)} \cdot \vec{r}^{\,0} + \frac{R_E^4}{r^3}\mathrm{M}_0^{(2)} \cdot\cdot (\otimes^2 \vec{r}^{\,0}) + \cdots + \frac{R_E^{N+2}}{r^{N+1}}\mathrm{M}_0^{(N)} \underbrace{\cdots}_{N} (\otimes^N \vec{r}^{\,0}). \tag{9}$$

Here $\vec{r}^{\,0}$ is the unit vector $\vec{r}/r$ in projections on the coordinate axes $X^0\,Y^0\,Z^0$, and $\mathrm{M}_0^{(n)}$ is the multipole tensor of rank n, transformed to the axes of the coordinate system $O_E\,X^0\,Y^0\,Z^0$ according to the formula

$$\left(\mathrm{M}_0^{(n)}\right)_{i_1,i_2,\ldots,i_n} = \sum_{j_1,j_2,\ldots,j_n=1}^{3} \gamma_{i_1,j_1}\gamma_{i_2,j_2}\cdots\gamma_{i_n,j_n}\mathrm{M}^{(n)}_{j_1,j_2,\ldots,j_n}.$$

Next, substituting in (9) the projections of the vector $\vec{r}^{\,0}$ on the axes of the coordinate system $O_E\,X^0\,Y^0\,Z^0$, expressed in terms of the spherical coordinates r, θ and λ

$$r_1^0 = \cos\theta\cos\lambda, \quad r_2^0 = \cos\theta\sin\lambda, \quad r_3^0 = \sin\theta,$$

we obtain the potential (9) as a function of the spherical coordinates r, θ and λ:

$$U = \sum_{n=1}^{N} \frac{R_E^{n+2}}{r^{n+1}}\mathrm{M}_0^{(n)} \underbrace{\cdots}_{n} (\otimes^n \vec{r}^{\,0}). \tag{10}$$

For finding the EMF induction in the satellite's center of mass in projections on the axes of the orbital frame, we substitute (10) into (8), taking into account that $(\otimes^n \vec{r}^{\,0})$ depends only on λ and θ, while $r = R$:

$$\begin{pmatrix} B_\xi \\ B_\eta \\ B_\zeta \end{pmatrix} = -\begin{pmatrix} \sum\limits_{n=1}^{N}\left(\frac{R_E}{R}\right)^{n+2}\mathrm{M}_0^{(n)}\underbrace{\cdots}_{n}\frac{\partial}{\partial\lambda}(\otimes^n\vec{r}^{\,0}) \\ \sum\limits_{n=1}^{N}\left(\frac{R_E}{R}\right)^{n+2}\mathrm{M}_0^{(n)}\underbrace{\cdots}_{n}\frac{\partial}{\partial\theta}(\otimes^n\vec{r}^{\,0}) \\ -\sum\limits_{n=1}^{N}(n+1)\left(\frac{R_E}{R}\right)^{n+2}\mathrm{M}_0^{(n)}\underbrace{\cdots}_{n}(\otimes^n\vec{r}^{\,0}) \end{pmatrix}_{\substack{\lambda=u\\ \theta=0}}. \tag{11}$$

Let us calculate the partial derivatives in (11). Consider $\dfrac{\partial}{\partial\lambda}(\otimes^n\vec{r}^{\,0})$ and find the $(j_1, j_2, \ldots, j_n)$-th element of this tensor for any $j_m = \overline{1,3},\ m = \overline{1,n}$:

$$\left(\frac{\partial(\otimes^n\vec{r}^{\,0})}{\partial\lambda}\right)_{j_1,j_2,\ldots,j_n} = \sum_{k=1}^{n} r^0_{j_1}r^0_{j_2}\cdots\ r^0_{j_{k-1}}\frac{\partial\, r^0_{j_k}}{\partial\,\lambda}\,r^0_{j_{k+1}}\cdots\ r^0_{j_{n-1}}r^0_{j_n}. \tag{12}$$

Therefore

$$\mathrm{M}_0^{(n)} \underbrace{\cdots}_{n} \frac{\partial\,(\otimes^n \vec{r}^{\,0})}{\partial\lambda} = \\ = \sum_{j_1=1}^{3}\sum_{j_2=1}^{3}\cdots\sum_{j_n=1}^{3}\sum_{k=1}^{n}\left(\mathrm{M}_0^{(n)}\right)_{j_n, j_{n-1}, \ldots, j_1} r^0_{j_1} r^0_{j_2} \cdots \frac{\partial\, r^0_{j_k}}{\partial\,\lambda} \cdots r^0_{j_{n-1}} r^0_{j_n}. \quad (13)$$

Since

$$\sum_{j_1=1}^{3}\sum_{j_2=1}^{3}\cdots\sum_{j_n=1}^{3}\sum_{k=1}^{n} r^0_{j_1} r^0_{j_2} \cdots \frac{\partial\, r^0_{j_k}}{\partial\,\lambda} \cdots r^0_{j_{n-1}} r^0_{j_n} = \\ = n\sum_{j_1=1}^{3}\sum_{j_2=1}^{3}\cdots\sum_{j_n=1}^{3}\frac{\partial\, r^0_{j_1}}{\partial\,\lambda}\, r^0_{j_2} r^0_{j_3} \cdots r^0_{j_{n-1}} r^0_{j_n}, \quad (14)$$

then collecting similar terms in expression (13) and taking into account the symmetry of tensors $\mathrm{M}_0^{(n)}$ with respect to any pair of indicies, we obtain

$$\mathrm{M}_0^{(n)} \underbrace{\cdots}_{n} \frac{\partial\,(\otimes^n \vec{r}^{\,0})}{\partial\lambda} = \\ = n\sum_{j_1=1}^{3}\sum_{j_2=1}^{3}\cdots\sum_{j_n=1}^{3}\left(\mathrm{M}_0^{(n)}\right)_{j_n, j_{n-1}, \ldots, j_1}\frac{\partial\, r^0_{j_1}}{\partial\,\lambda}\, r^0_{j_2} r^0_{j_3} \cdots r^0_{j_{n-1}} r^0_{j_n}. \quad (15)$$

Hence

$$\mathrm{M}_0^{(n)} \underbrace{\cdots}_{n} \left.\frac{\partial\,(\otimes^n \vec{r}^{\,0})}{\partial\lambda}\right|_{\substack{\lambda=u\\ \theta=0\\ r=R}} = n\mathrm{M}_0^{(n)} \underbrace{\cdots}_{n} T_\lambda^{(n)}, \quad (16)$$

where

$$T_\lambda^{(n)} = T_\lambda \otimes^{n-1} T_r, \qquad T_\lambda = \left.\frac{\partial \vec{r}^{\,0}}{\partial\lambda}\right|_{\substack{\lambda=u\\ \theta=0}} = (-\sin u,\, \cos u,\, 0)^\top,$$
$$T_r = \vec{r}^{\,0}\big|_{\substack{\lambda=u\\ \theta=0}} = (\cos u,\, \sin u,\, 0)^\top.$$

Performing the operations analogous to (12) – (15) for variable θ, we obtain

$$\mathrm{M}_0^{(n)} \underbrace{\cdots}_{n} \left.\frac{\partial\,(\otimes^n \vec{r}^{\,0})}{\partial\theta}\right|_{\substack{\lambda=u\\ \theta=0\\ r=R}} = n\mathrm{M}_0^{(n)} \underbrace{\cdots}_{n} T_\theta^{(n)}, \quad (17)$$

where

$$T_\theta^{(n)} = T_\theta \otimes^{n-1} T_r, \qquad T_\theta = \left.\frac{\partial \vec{r}^{\,0}}{\partial\theta}\right|_{\substack{\lambda=u\\ \theta=0}} = (0,\, 0,\, 1)^\top,$$
$$T_r = \vec{r}^{\,0}\big|_{\substack{\lambda=u\\ \theta=0}} = (\cos u,\, \sin u,\, 0)^\top.$$

Substituting in (11) the results of computation of partial derivatives (16) and (17) and taking into account the formula (7), we obtain the EMF induction in projections on the axes of the orbital frame as

$$\vec{B} = \sum_{n=1}^{N} \vec{B}^{(n)},$$

where

$$\begin{pmatrix} B_\xi^{(n)} \\ B_\eta^{(n)} \\ B_\zeta^{(n)} \end{pmatrix} = -\left(\frac{R_E}{R}\right)^{n+2} \begin{pmatrix} n\,\mathrm{M}_0^{(n)} \underbrace{\cdots}_{n} \mathrm{T}_\lambda^{(n)} \\ n\,\mathrm{M}_0^{(n)} \underbrace{\cdots}_{n} \mathrm{T}_\theta^{(n)} \\ -(n+1)\,\mathrm{M}_0^{(n)} \underbrace{\cdots}_{n} \mathrm{T}_r^{(n)} \end{pmatrix}. \tag{18}$$

So, the multipole structure of the EMF is proved and the algorithm for the multipole representation of the EMF induction with an arbitrary degree of precision is elaborated. It should be emphasized that the expression of the EMF potential in terms of its multipole tensors get a convenient and concise form of presentation of the EMF induction projections on the axes of the orbital frame. Otherwise, if the potential of the EMF is used in the form (2) with an arbitrary number of terms, these projections (quite cumbersome trigonometric expressions) have to be written in explicit form rather than in the contracted format as in (18). This advantage of tensor notation turns out to be fruitful in analytical studies, in the studies, based on the methods of symbolic computations (just due to the methods of symbolic computations it succeeded to overcome the large difficulties, appeared at the construction of high-ordered multipole EMF models), and in numerical experiments.

References

[1] A.A. Tikhonov Refinement of the Oblique Dipole Model in the Evolution of Rotary Motion of a Charged Body in the Geomagnetic Field // Cosmic Research 2002, vol. 40 (N 2), pp. 171-177.

[2] K.G. Petrov, A.A. Tikhonov The moment of Lorentz forces acting on a charged satellite in the Earth's magnetic field. Part 1: The Earth's magnetic field strength in the orbital coordinate system //Vestnik of St.-Petersburg State University 1999, vol. 1 (N 1), pp. 92-100.

[3] A.A. Tikhonov, K.G. Petrov Multipole Models of the Earth's Magnetic Field // Cosmic Research 2002, vol. 40(N 3), pp. 219-229.

[4] V.A. Sarychev, M.Yu. Ovchinnikov Magnetic systems of attitude control for Earth's artificial satellites, Itogi Nauki Tekh., Ser: Issled Kosm Prostr., vol. 23, Moscow: VINITI, 1985.

[5] S. Macmillan and S. Maus International Geomagnetic Reference Field – the tenth generation // Earth Planets Space, Vol. 57, (N 12), pp. 1135-1140, 2005.

Alexey A. Tikhonov, Saint-Petersburg, Russia
Kirill A. Antipov, Saint-Petersburg, Russia

Two-dimensional models of plates made of an anisotropic material

P. E. Tovstik T. P. Tovstik
peter.tovstik@mail.ru, tovstik_t@mail.ru

Abstract

Two-dimensional model of plate made of an anisotropic material described by 21 elastic modules is investigated. For this aim the generalized Timoshenko–Reissner hypothesis is proposed. As static problems so free vibrations are studied.

1 Introduction

Numerous investigations including monographs [1–4] are devoted to derivation of two-dimensional (2D) models of plates and shells from the three-dimensional (3D) equations of the theory of elasticity. The presence of anisotropy of a material introduces additional difficulties. The 2D models for isotropic and transversely isotropic materials [2–6] have been investigated well. The general anisotropy described by 21 elastic modules have been investigated much less. The plane stressed state (i.e., the problem on an anisotropic beam) in the case of the general anisotropy is considered in [7], and the volume stressed state is studied in [8]. It is shown that, in general case (in contrary to isotropic or orthotropic materials), both the Kirchhoff–Love and Timoshenko–Reissner hypothesis result in 2D models, which are erroneous in the major terms with respect to the small thickness parameter equal to the ratio between the plate thickness and the wavelength. In [7,8] for deriving the 2D model it is used the generalized Timoshenko–Reissner hypothesis according to which the plane element normal before the strain does not remain rectilinear. Comparing the 2D models with the results of the asymptotic solution of the 3D problem, we assume that the external load and the solution together with it are harmonic functions of tangential coordinates. It is shown that, in the case of the dominantly flexural strain, the constructed 2D model is asymptotically exact in the major terms with respect to the small thickness parameter.

But the accepted in [7,8] hypothesis should be define more precisely because some boundary conditions at the face planes of plate are not satisfied. As a result it leads to a not great error in the case when the elastic modules in the transversal directions are comparatively small. In [9] for a beam the more precise hypothesis, free from this defect, is introduced and here this hypothesis is used for a plate. The analysis is bounded with the internal stress state and the boundary layer is not studied.

2 Equations of equilibrium. Elasticity relations

We consider the problem on the strain (or free vibrations) of a plate $-\infty < x_1, x_2 < \infty,\ -h/2 \le x_3 \le h/2$ from an anisotropic material in the case of the general anisotropy. We consider the face planes as free and ignore the boundary conditions at the edges. Equations of equilibrium after the separation of the time-dependent multiplier $e^{i\omega t}$ (ω is the vibration frequency) have the form

$$\frac{\partial \sigma_{i1}}{\partial x_1} + \frac{\partial \sigma_{i2}}{\partial x_2} + \frac{\partial \sigma_{i3}}{\partial x_3} + \rho\omega^2 u_i + f_i(x_1, x_2, x_3) = 0, \quad i = 1, 2, 3. \tag{2.1}$$

where f_i are the densities of the external load.

Writing the relations between the stresses σ_{ij} and the strains ε_{ij} we divide them into the groups of tangential $\sigma_t,\ \varepsilon_t$ and the non-tangential $\sigma_n,\ \varepsilon_n$ stresses and strains

$$\begin{aligned} &\sigma_t = (\sigma_{11},\, \sigma_{12},\, \sigma_{22})^T, \quad \sigma_n = (\sigma_{13},\, \sigma_{23},\, \sigma_{33})^T, \\ &\varepsilon_t = (\varepsilon_{11},\, \varepsilon_{12},\, \varepsilon_{22})^T, \quad \varepsilon_n = (\varepsilon_{13},\, \varepsilon_{23},\, \varepsilon_{33})^T; \end{aligned} \tag{2.2}$$

the superscript ^{T} designates the transposition. Then the relation between stresses and strains is written in the matrix form

$$\sigma_t = \mathbf{A}\cdot\varepsilon_t + \mathbf{B}\cdot\varepsilon_n, \quad \sigma_n = \mathbf{B}^T\cdot\varepsilon_t + \mathbf{C}\cdot\varepsilon_n, \tag{2.3}$$

where $\mathbf{A} = \{A_{ij}\},\ \mathbf{B} = \{B_{ij}\},\ \mathbf{C} = \{C_{ij}\}$ are the elastic-modules matrices, the matrices $\mathbf{A}$ and $\mathbf{C}$ being symmetric. Relations (2.3) contain 21 elastic modules. It is assumed that the matrix

$$\begin{pmatrix} \mathbf{A} & \mathbf{B} \\ \mathbf{B}^T & \mathbf{C} \end{pmatrix} \tag{2.4}$$

of the sixth order is positively determined.

The strains ε_{ij} are determined from the formulas

$$\varepsilon_{ii} = \frac{\partial u_i}{\partial x_i}, \qquad \varepsilon_{ij} = \frac{\partial u_i}{\partial x_j} + \frac{\partial u_j}{\partial x_i}, \quad i,j = 1,2,3. \tag{2.5}$$

The following elastic-energy density corresponds to relations (2.2)

$$2\Pi = \varepsilon_t^T\cdot\mathbf{A}\cdot\varepsilon_t + 2\,\varepsilon_t^T\cdot\mathbf{B}\cdot\varepsilon_n + \varepsilon_n^T\cdot\mathbf{C}\cdot\varepsilon_n. \tag{2.6}$$

The boundary conditions at the face planes are

$$\sigma_{i3} = 0, \quad i = 1,2,3 \quad \text{at} \quad z = \pm h/2. \tag{2.7}$$

If, for example, $\sigma_{i3} = \sigma_{i3}^0 \neq 0$ at $z = h/2$ we again use homogeneous conditions (2.7) and the surface load σ_{i3}^0 include in the volume loads as $f_i = f_i^0 + \sigma_{i3}^0\delta(z - h/2)$, where $\delta(z)$ is the Dirac delta-function.

As in the Kirchhoff–Love and Timoshenko–Reissner models we accept that the normal stresses can be neglected $\sigma_{33} = 0$. Using the relation $\sigma_{33} = 0$ we exclude the strain ε_{33} from the relations (2.3). Then they become

$$\sigma_t = \mathbf{A}^*\cdot\varepsilon_t + \mathbf{B}^*\cdot\varepsilon_n^*, \quad \sigma_n^* = \mathbf{B}^{*T}\cdot\varepsilon_t + \mathbf{C}^*\cdot\varepsilon_n^*, \tag{2.8}$$

where in contrary to (2.2) $\sigma_n^* = (\sigma_{13},\, \sigma_{23})^T,\ \varepsilon_n^* = (\varepsilon_{13},\, \varepsilon_{23})^T$. The elements of matrixes $\mathbf{A}^*(3\times3)$, $\mathbf{B}^*(3\times2)$, $\mathbf{C}^*(2\times2)$ are as follows

$$A_{ij}^* = A_{ij} - \frac{B_{i3}B_{j3}}{C_{33}}, \quad B_{ij}^* = B_{ij} - \frac{B_{i3}C_{j3}}{C_{33}}, \quad C_{ij}^* = C_{ij} - \frac{C_{i3}C_{j3}}{C_{33}}. \tag{2.9}$$

We study the long-waved approximation and introduce the small thickness parameter μ by the relation

$$\mu = \frac{h}{L}, \tag{2.10}$$

where L is the wave length. We will neglect the terms of the order of μ^2 compared with unit. At first we assume that all elastic modules in (2.4) are of the identity asymptotic orders.

3 The more precise Timoshenko–Reissner model

The 2D models differ by the assumptions of the distributions of the transversal shear deformations $\varepsilon_{i3},\ i = 1,2$ in the normal direction.

According to the Kirchhoff–Love model the relations $\varepsilon_{i3} = 0$ are accepted.

According to the Timoshenko–Reissner model the relations $\varepsilon_{i3} = \gamma_i$ or the relations $\varepsilon_{i3} = \gamma_i(1-4z^2/h^2)$ is accepted. In the case of the last relations for the orthotropic plates the boundary conditions (2.7) are satisfied.

Both the Kirchhoff–Love and the Timoshenko–Reissner hypotheses in the case of the general anisotropy do not lead in the major terms with respect to the small thickness parameter μ to the correct 2D model. Which is why in [7,8] the relations

$$\varepsilon_{i3} = \gamma_i + \delta_i z, \quad i = 1, 2. \tag{3.1}$$

were accepted. These relations for the orthotropic plates give the model which have the same exactness as the Kirchhoff–Love model. But in this model the boundary conditions (2.7) are not fulfilled. As a result the shear stiffness of the plate in the transversal direction is not exact. For the orthotropic plates the Timoshenko–Reissner model gives equivalent transversal shear modulus kG_{i3} with the correcting multiplier $k = 5/6$. But the model (3.1) gives the value $k = 1$ and describes the shear deformations incorrectly. Therefore as in [9] we accept

$$\varepsilon_{i3} = \gamma_i + \delta_i z + \beta_i \left(\frac{z^2}{h^2} - \frac{1}{12}\right), \quad i = 1, 2. \tag{3.2}$$

where γ_i are the average shear angles. The parameters δ_i and β_i are to be find from (2.7).

It follows from (2.5) that the tangential displacements and strains are equal to

$$\begin{aligned}
&u_i(z) = v_i + \varphi_i z + \delta_i \left(\frac{z^2}{2} - \frac{h^2}{24}\right) + \beta_i \left(\frac{z^3}{3h^2} - \frac{z}{12}\right), \quad \varphi_i = \gamma_i - \frac{\partial w}{\partial x_i},\\
&\varepsilon_{ii} = \frac{\partial v_i}{\partial x_i} + z\frac{\partial \varphi_i}{\partial x_i} + \frac{\partial \delta_i}{\partial x_i}\left(\frac{z^2}{2} - \frac{h^2}{24}\right) + \frac{\partial \beta_i}{\partial x_i}\left(\frac{z^3}{3h^2} - \frac{z}{12}\right), \quad i = 1, 2,\\
&\varepsilon_{12} = \frac{\partial v_1}{\partial x_2} + \frac{\partial v_2}{\partial x_1} + z\left(\frac{\partial \varphi_1}{\partial x_2} + \frac{\partial \varphi_2}{\partial x_1}\right) + \left(\frac{\partial \delta_1}{\partial x_2} + \frac{\partial \delta_2}{\partial x_1}\right)\left(\frac{z^2}{2} - \frac{h^2}{24}\right) +\\
&\quad + \left(\frac{\partial \beta_1}{\partial x_2} + \frac{\partial \beta_2}{\partial x_1}\right)\left(\frac{z^3}{3h^2} - \frac{z}{12}\right),
\end{aligned} \tag{3.3}$$

where v_i are the average displacements and φ_i are the average angles of the normal fibers rotation.

Conditions (2.7) gives

$$\mathbf{B}^{*T} \cdot \mathbf{K}(\varphi) + \mathbf{C}^* \cdot \delta = 0, \qquad \mathbf{B}^{*T} \cdot \big(\mathbf{K}(v) + h^2\mathbf{K}(\delta)/12\big) + \mathbf{C}^* \cdot (\gamma + \beta/6) = 0, \tag{3.4}$$

where $\varphi = (\varphi_1, \varphi_2)^T$, $v = (v_1, v_2)^T$, $\delta = (\delta_1, \delta_2)^T$, $\gamma = (\gamma_1, \gamma_2)^T$, $\beta = (\beta_1, \beta_2)^T$, and the operator $\mathbf{K}(y)$ is defined by the relation

$$\mathbf{K}(y) \equiv \left(\frac{\partial y_1}{\partial x_1},\ \frac{\partial y_1}{\partial x_2} + \frac{\partial y_2}{\partial x_1},\ \frac{\partial y_2}{\partial x_2}\right)^T, \qquad y = \{\varphi, v, \delta\}. \tag{3.5}$$

Relations (3.4) may be rewritten in the form

$$\delta = -\mathbf{C}^{*-1} \cdot \mathbf{B}^{*T} \cdot \mathbf{K}(\varphi), \qquad \gamma + \beta/6 = -\mathbf{C}^{*-1} \cdot \mathbf{B}^{*T} \cdot (\mathbf{K}(v) + h^2\mathbf{K}(\delta)/12). \tag{3.6}$$

4 The 2D equilibrium equations

The system (2.1) averaging leads to the 2D equilibrium equations. The integration of these equations over the thickness and the integration of the first two ($i = 1, 2$) equations over the thickness after multiplying by z gives the set of equations

$$\begin{aligned}
&\frac{\partial T_{i1}}{\partial x_1} + \frac{\partial T_{i2}}{\partial x_2} + \rho h\omega^2 v_i + F_i = 0, \quad \frac{\partial Q_1}{\partial x_1} + \frac{\partial Q_2}{\partial x_2} + \rho h\omega^2 w + F_3 = 0,\\
&\frac{\partial M_{i1}}{\partial x_1} + \frac{\partial M_{i2}}{\partial x_2} - Q_i + \rho J\omega^2\left(\varphi_i - \frac{\beta_i}{30}\right) + m_i = 0, \qquad J = \frac{h^3}{12}, \quad i = 1, 2,
\end{aligned} \tag{4.1}$$

where

$$\{T_{ij}, Q_i, F_i\} = \int\limits_{-h/2}^{h/2} \{\sigma_{ij}, \sigma_{3i}, f_i\}\, dz, \quad \{M_{ij}, m_i\} = \int\limits_{-h/2}^{h/2} \{\sigma_{ij}, f_i\}\, z dz, \quad i,j = 1,2. \tag{4.2}$$

The system (4.1) is acceptable as for isotropic so for anisotropic plates. We substitute into it the expressions for stresses from relations (3.4) and (3.2). The formulas for stress-resultants and for stress-couples are

$$\begin{aligned} &\mathbf{T} = h\left(\mathbf{A}^* \cdot \mathbf{K}(v) + \mathbf{B}^* \cdot \gamma\right), && \mathbf{T} = (T_{11}, T_{12}, T_{22})^T, \\ &\mathbf{Q} = h\left(\mathbf{B}^{*T} \cdot \mathbf{K}(v) + \mathbf{C}^* \cdot \gamma\right), && \mathbf{Q} = (Q_1, Q_2)^T, \\ &\mathbf{M} = J\left(\mathbf{A}^* \cdot (\mathbf{K}(\varphi) - \mathbf{K}(\beta)/30) + \mathbf{B}^* \cdot \delta\right), && \mathbf{M} = (M_{11}, M_{12}, M_{22})^T, \end{aligned} \tag{4.3}$$

where the designation (3.5) is used.

Set (4.1) is the set of 10th order equations with respect to the unknown functions $v_1, v_2, w, \varphi_1, \varphi_2$. The functions $\gamma_i, \delta_i, \beta_i,\ i = 1,2$, in this system may be excluded with the help of relations (3.3) and (3.6). Contrary to the isotropic or orthotropic plates, this set is not divided into two sets describing the longitudinal and the flexural strains (if $\mathbf{B}^* = 0$, the indicated division takes place).

5 Asymptotic analysis and simplification

This analysis concerns only the internal stressed state and ignores the boundary layer near the plate edges (as to the letter statement, see, for example [4]). We first consider the case when all elastic modules in relations (2.3) have the same asymptotic order E. Let L be the characteristic strain wavelength in the tangential directions ($L \gg h$), let F be the general order of the distributed loads F_i, and let the effect of small distributed moments m_i be neglected.

We consider the static problem ($\omega = 0$) for $F_3 \neq 0$. The orders of the basic unknowns prove to be the same as for an isotropic plate

$$v_i \sim \frac{FL}{E\mu}, \quad w \sim \frac{FL}{E\mu^3}, \quad \varphi_i \sim \frac{F}{E\mu^3}, \quad \gamma_i, \beta_i \sim \frac{F}{E\mu}, \quad \delta_i \sim \frac{F}{EL\mu^3}. \tag{5.1}$$

We exclude the shear stress-resultants from the set (4.1)

$$\frac{\partial^2 M_{11}}{\partial x_1^2} + 2\frac{\partial^2 M_{12}}{\partial x_1 \partial x_2} + \frac{\partial^2 M_{22}}{\partial x_2^2} + F_3 = 0. \tag{5.2}$$

With the error of the order of μ^2, due to (3.6) instead of the relation (4.3) we get

$$\mathbf{M} = J\mathbf{A}^{**} \cdot \mathbf{K}(\varphi), \tag{5.3}$$

where

$$\mathbf{A}^{**} = \mathbf{A}^* - \mathbf{B}^* \cdot \mathbf{C}^{*-1} \cdot \mathbf{B}^{*T} = \mathbf{A} - \mathbf{B} \cdot \mathbf{C}^{-1} \cdot \mathbf{B}^T, \tag{5.4}$$

Due to the inequality $|\gamma_i| \ll |\varphi_i|$, it is possible to put approximately that $\varphi_i = -\partial w/\partial x_i$. Then equation (5.2) becomes

$$-J \sum_{i,j,k,l=1,2} A^{**}_{k+i-1,j+l-1} \frac{\partial^4 w}{\partial x_i \partial x_j \partial x_k \partial x_l} + F_3 = 0, \tag{5.5}$$

For the isotropic plate equation (5.5) transforms into the well known equation $-D\boldsymbol{\Delta}\boldsymbol{\Delta}w + F_3 = 0$, where $\boldsymbol{\Delta}$ is the Laplace operator, $D = Eh^3/(12(1-\nu^2))$ is the cylindrical stiffness.

If the deflection w is found, from relations (4.3) we obtain

$$\begin{aligned} &\gamma = \mathbf{C}^{*-1} \cdot \left(Q/h - \mathbf{B}^{*T} \cdot \mathbf{K}(v)\right), \qquad Q_i = \frac{\partial M_{i1}}{\partial x_1} + \frac{\partial M_{i2}}{\partial x_2}, \\ &\mathbf{T} = h\,\mathbf{A}^{**} \cdot \mathbf{K}(v) + \mathbf{B}^* \cdot \mathbf{C}^{*-1} \cdot Q. \end{aligned} \tag{5.6}$$

Now the first equation (4.1) contains only the unknowns v_i.

We turn to the problem of free vibrations and consider the dispersion equation with the assumption that the form of vibrations is described by the doubly periodic functions of variables x_1 and x_2

$$\{u_k, w, \varphi_k\}(x_1, x_2) = \{u_k^0, w^0, \varphi_k^0\} e^{i(r_1 x_1 + r_2 x_2)}. \tag{5.7}$$

Equating the determinant of set (4.1) to zero, we obtain the dispersion equation in the form

$$D(\lambda, q_1, q_2, \mu_1) = 0, \qquad \lambda = \frac{\rho h^2 \omega^2}{E}, \quad r_k h = \mu_1 q_k, \ k = 1, 2, \quad \mu_1 = \frac{2\pi h}{L} = 2\pi\mu. \tag{5.8}$$

Here λ is the frequency parameter, and q_k are the dimensionless wave numbers. Relative to λ equation (5.8) is the algebraic equation of the fifth degree. Its lowest root is

$$\lambda_1 = \frac{\mu_1^4}{12} \sum_{i,j,k,l=1,2} A^{**}_{k+i-1,j+l-1} q_i q_j q_k q_l + O(\mu_1^5) \tag{5.9}$$

or

$$\lambda_1 = \frac{\mu_1^4}{12} \left(A^{**}_{11} q_1^4 + 4A^{**}_{12} q_1^3 q_2 + (4A^{**}_{22} + 2A^{**}_{13}) q_1^2 q_2^2 + 4A^{**}_{23} q_1 q_2^3 + A^{**}_{33} q_2^4 \right) + O(\mu_1^5), \tag{5.10}$$

where the modules A^{**}_{ij} are related to E. The rest four roots of equation (5.8) have the higher $\lambda_k = O(\mu_1^2),\ k = 2, 3, 4, 5$, and they correspond to the longitudinal and to shear vibrations.

In [6-9] the asymptotic solution of the 3D equations (2.1) is fulfilled. Equation (5.5) and relation (5.9) coincide with the major approximation with respect μ of the 3D asymptotic solution. The both hypotheses (3.1) and (3.2) give the same result at the relations (5.1), (5.6), and (5.9) delivering. At the same time both the Kirchhoff–Love hypotheses and Timoshenko–Reissner hypotheses at $\delta = 0$ do not lead to the correct 2D models.

As it is shown in [5] for the orthotropic plate, the influence of the summand with $\beta \neq 0$ in (3.2) is essential only for the small shear stiffness in the transversal direction. For the anisotropic plate this case is studied below.

6 Equations for a small transversal stiffness

As it shown in [5], the influences of bending and of shear on the orthotropic plate deflection are of the same order if $C_{11}/A_{11} = O(\mu^2)$. Which is why we assume here that

$$A_{ij} \sim E, \qquad B_{ij},\ C_{ij} \sim E\mu^2. \tag{6.1}$$

Then with the error of the μ^2 the following estimations are valid

$$A^*_{ij} = A^{**}_{ij} = A_{ij} \sim E, \quad B^*_{ij},\ C^*_{ij} \sim E\mu^2. \tag{6.2}$$

For the static problem ($\omega = 0$) under the assumptions (6.1) and $F_3 \neq 0$ the orders of unknowns are

$$w \sim \frac{FL}{E\mu^3}, \quad \varphi_i, \gamma_i \sim \frac{F}{E\mu^3}, \quad v_i \sim \frac{FL}{E\mu}, \quad \delta_i \sim \frac{F}{EL\mu^3}, \quad M_{ij} \sim FL^2, \quad T_i, Q_i \sim FL. \tag{6.3}$$

Due to estimations (6.3) the second relations (3.6) with the error of the order μ^2 accept the form $\beta_i = -6\gamma_i$, and the relations (3.2) turn to

$$\varepsilon_{i3} = \frac{3}{2}\gamma_i \left(1 - \frac{4z^2}{h^2}\right) + \delta_i z. \tag{6.4}$$

In these assumptions we rewrite relations (4.3)

$$\begin{aligned} &\mathbf{Q} = h\,\mathbf{C}^* \cdot \gamma, \qquad \mathbf{T} = h\,\mathbf{A} \cdot \mathbf{K}(v) + h\,\mathbf{B}^* \cdot \gamma, \\ &\mathbf{M} = J\,\mathbf{A} \cdot ((6/5)\mathbf{K}(\gamma) - \mathbf{K}(\nabla \cdot w)), \qquad \nabla = \left(\frac{\partial}{\partial x_1}, \frac{\partial}{\partial x_2}\right). \end{aligned} \tag{6.5}$$

Set (4.1) accepts the form

$$\nabla \cdot \hat{\mathbf{T}} + \hat{\mathbf{F}} = 0, \qquad \nabla \cdot \mathbf{Q} + F_3 = 0, \qquad \nabla \cdot \hat{\mathbf{M}} - \mathbf{Q}^{\mathbf{T}} = 0, \tag{6.6}$$

with

$$\hat{\mathbf{T}} = \begin{pmatrix} T_{11} & T_{12} \\ T_{12} & T_{22} \end{pmatrix}, \qquad \hat{\mathbf{M}} = \begin{pmatrix} M_{11} & M_{12} \\ M_{12} & M_{22} \end{pmatrix}, \qquad \hat{\mathbf{F}} = (F_1, F_2). \tag{6.7}$$

Due to relations (6.5) the second and the third equations (6.6) give the system for the unknowns w, γ_1, γ_2. When these functions are found, the unknowns v_1, v_2 may be found from the first equation (6.6).

7 Partial solution for the harmonic external load

In general case (in contrary to Section 5) it is impossible to find the equation containing only the deflection w. We put

$$F_j = F_j^0 e^{i(r_1 x_1 + r_2 x_2)}, \quad j = 1, 2, 3, \tag{7.1}$$

and seek the partial solution of system (6.6) in the form

$$\{v_j, w, \gamma_j\}(x_1, x_2) = \{v_j^0, w^0, \gamma_j^0\} e^{i(r_1 x_1 + r_2 x_2)}, \quad q_j = h r_j, \qquad j = 1, 2. \tag{7.2}$$

The third equation (6.6) gives equations from which the values γ_1^0 and γ_2^0 may be expressed through w^0

$$f_{11}\gamma_1^0 + f_{12}\gamma_2^0 = i a_1 w^0/h, \qquad f_{12}\gamma_1^0 + f_{22}\gamma_2^0 = i a_2 w^0/h, \tag{7.3}$$

where

$$\begin{aligned} f_{11} &= C_{11}^* + (1/10)e_{11}, \quad e_{11} = A_{11}q_1^2 + 2A_{12}q_1q_2 + A_{22}q_2^2, \\ f_{12} &= C_{12}^* + (1/10)e_{12}, \quad e_{12} = A_{12}q_1^2 + (A_{13} + A_{22})q_1q_2 + A_{23}q_2^2, \\ f_{22} &= C_{22}^* + (1/10)e_{22}, \quad e_{22} = A_{22}q_1^2 + 2A_{23}q_1q_2 + A_{33}q_2^2, \end{aligned} \tag{7.4}$$

$$\begin{aligned} a_1 &= (1/12)(A_{12}q_1^3 + 3A_{12}q_1^2q_2 + (2A_{22} + A_{13})q_1q_2^2 + A_{23}q_2^2), \\ a_2 &= (1/12)(A_{11}q_1^3 + (2A_{22} + A_{13})q_1^2q_2 + 3A_{23}q_1q_2^2 + A_{33}q_2^2). \end{aligned} \tag{7.5}$$

From equations (7.3) we find

$$\gamma_j^0 = \frac{i b_j}{h} w^0, \quad j = 1, 2, \qquad b_1 = \frac{a_1 f_{22} - a_2 f_{12}}{f_{11}f_{22} - f_{12}^2}, \quad b_2 = \frac{a_2 f_{12} - a_1 f_{11}}{f_{11}f_{22} - f_{12}^2}. \tag{7.6}$$

The second equation (6.6) gives

$$w^0 = \frac{h F_3^0}{c}, \quad c(q_1, q_2) = q_1(C_{11}^* b_1 + C_{12}^* b_2) + q_2(C_{12}^* b_1 + C_{22}^* b_2). \tag{7.7}$$

Finally from the first equation (6.6) we find the equations for the unknowns v_1^0 and v_2^0

$$e_{11}v_1^0 + e_{12}v_2^0 = h(F_1^0 - d_1 F_3^0), \qquad e_{12}v_1^0 + e_{22}v_2^0 = h(F_2^0 - d_2 F_3^0), \tag{7.8}$$

where

$$\begin{aligned} d_1 &= \left((B_{11}^* b_1 + B_{12}^* b_2)q_1 + (B_{21}^* b_1 + B_{22}^* b_2)q_2\right)/c, \\ d_2 &= \left((B_{21}^* b_1 + B_{22}^* b_2)q_1 + (B_{31}^* b_1 + B_{32}^* b_2)q_2\right)/c. \end{aligned} \tag{7.9}$$

We assume that the wave numbers q_j are of the order of μ and that the estimations (6.2) are fulfilled. Then we find the orders of the introduced values

$$f_{ij}, e_{ij} \sim E\mu^2, \quad a_j \sim E\mu^3, \quad b_j \sim \mu, \quad c \sim E\mu^4, \quad d_j \sim 1. \tag{7.10}$$

With these estimations it is easy to verify that the estimations (6.3) are fulfilled. From relations (7.4) it follows that the effects of the orders of the bending and the shear deformations on the plate deflection w^0 are identical. The longitudinal external loads F_1 and F_2 in the zero approximation

do not effect on the deflection w^0. The effects of the longitudinal (F_1, F_2) and of the transversal (F_3) loads of the longitudinal displacements are of the identical orders.

In the assumptions (6.2) we consider the free vibrations problem. As in Section 5, the dispersion equation for system (4.1) has 5 roots. Its lowest root corresponding to the flexural vibrations is equal to

$$\lambda_1 = \rho h^2 \omega^2 = c(q_1, q_2) = O(E\mu^4), \tag{7.11}$$

where the function $c(q_1, q_2)$ is defined by relation (7.7).

8 Material with the general anisotropy

As in [7], we study the plate of the anisotropic material obtained by the averaging of the isotropic material reinforced by the system of the small extensible fibers. The fibers are disposed in the planes $x_1 z$ and are inclined by the angle α to the axis x_1. The potential energy density Π for this anisotropic material is equal to

$$\begin{aligned}\Pi = \frac{1}{2}\frac{E(1-\beta)}{1-\nu^2}[\varepsilon_{11}^2+\varepsilon_{22}^2+\varepsilon_{33}^2 + 2\nu(\varepsilon_{11}\varepsilon_{22}+\varepsilon_{11}\varepsilon_{33}+\varepsilon_{22}\varepsilon_{33})+ \\ +\frac{1}{2}(1-\nu)(\varepsilon_{12}^2+\varepsilon_{13}^2+\varepsilon_{23}^2)] + \frac{1}{2}\beta E_n(\varepsilon_{11}\cos^2\alpha + \varepsilon_{13}\sin\alpha\cos\alpha + \varepsilon_{33}\sin^2\alpha)^2,\end{aligned} \tag{8.1}$$

where E and ν are the Young modulus and the Poisson ratio of the matrix, E_n is the Young modulus for fibers, and β is the part of volume occupied by fibers.

We accept the stresses σ_{ij} from the relation

$$\sigma_{ij} = \frac{\partial \Pi}{\partial \varepsilon_{ij}}. \tag{8.2}$$

After the comparison relations (8.2) and (2.3) we obtain the elastic modules of this anisotropic material

$$\begin{aligned}&A_{11} = E_1 + \beta E_n \cos^4\alpha, \quad A_{13} = E_1\nu, \quad A_{33} = B_{33} = E_1, \quad A_{22} = C_{22} = E_2, \\ &B_{11} = \beta E_n \sin\alpha\cos^3\alpha, \quad B_{13} = E_1\nu + \beta E_n \sin^2\alpha\cos^2\alpha, \\ &C_{11} = E_2 + \beta E_n \sin^2\alpha\cos^2\alpha, \quad C_{13} = \beta E_n \sin^3\alpha\cos\alpha, \quad C_{33} = E_1 + \beta E_n \sin^4\alpha, \\ &E_1 = \frac{E(1-\beta)}{1-\nu^2}, \quad E_2 = \frac{E(1-\beta)}{2(1+\nu)}.\end{aligned} \tag{8.4}$$

In this example the rest elastic modules are equal to zero. We remind that the matrixes of elastic modules $\mathbf{A}$ and $\mathbf{C}$ are symmetric, and matrix $\mathbf{B}$ is not symmetric.

9 Conclusions

By using the cinematic hypothesis (3.2) about the shear deformations distribution, for the material with the general anisotropy the 2D equations, describing the deformation and the free vibrations of a plate, are delivered. These equations are of the same exactness as the Timoshenko–Reissner equations for the orthotropic material.

Acknowledgements

The paper is written with the financial support of Russian Foundation of Basic Investigations, grants 09.01.92002 HHC-a, and 10-01.00244-a.

References

[1] L.H.Donnell Beams, Plates and Shells. 1976. McGraw-Hill, Inc.

[2] S.A.Ambartsumjan General theory of anisotropic shells. Moscow. Nauka. 1974. 446 p. (in Russian).

[3] V.A.Rodionova, B.F.Titaev, and K.F.Chernykh Applied theory of anisotropic plates and shells. St.Petersburg Univ. 1996. 280 p. (in Russian).

[4] L.A.Agalovjan Asymptotic theory of anisotropic plates and shells. Moscow. Nauka. 1997. 414 p. (in Russian).

[5] P.E.Tovstik On the asymptotic character of approximate models of beams, plates and shells // Vestnik St.Petersburg Univ. Ser. 1. 2007. N 3. Pp. 49–54 (in Russian).

[6] P.E.Tovstik, and T.P.Tovstik On the 2D models of plates and shells including the shear // ZAMM. 2007. **87**. No 2. 160–171.

[7] P.E.Tovstik, and T.P.Tovstik Two-dimensional models of plates made of an anisotropic material // In "Computer methods in mechanics of continuous media". Issue 3. St. Petersburg Univ. 2008. Pp. 4–16 (in Russian).

[8] P.E.Tovstik Two-dimensional models of plates made of an anisotropic material // Doklady Russian Academy Sci. V. 425. 4, Pp. 489-491.= Doklady Physics. 2009. Vol. 54. No 4, pp. 205-209.

[9] P.E.Tovstik, and T.P.Tovstik One-dimensional models of beam made of an anisotropic material with the inclined anisotropy // Izv. RAS. Mekhanika Tverdoto Tela (to be published, in Russian).

Petr E. Tovstik, St.Petersburg State University. Universitetsky str., 28. St.Petersburg, Russia
Tatiana P. Tovstik, Institute of Problems of Mechanical Engineering Russian Academy of Sciences, Bolshoi Prospect 61, RUS-199178, St.Petersburg, Russia

Modeling mechanochemistry of the diffusion controlled chemical reaction front propagation in elastic solids

Elena N. Vilchevskaya Alexander B.Freidin
vilchevska@gmail.com

Abstract

Based on the general consideration of a chemical reaction front propagation in an elastic solid developed in [1] we focus on the statement and solution of a simplest 3D-boundary value problem. We study an oxidation of a ball under external loading. For simplicity sake we use a linearized chemical affinity tensor in a small strain approach. We emphasize the role of internal stresses induced by oxide formation. We demonstrate that, depending on boundary conditions and material and chemical reaction parameters, the reaction may be blocked by the oxide growth because of internal stresses.

1 Statement of the problem: chemical affinity and the reaction front kinetics in a spherically-symmetric problem

Let us consider a linear-elastic ball of the radius R under pressure p. Suppose that a chemical reaction of the oxidizing type

$$\nu_- A_- + \nu_* A_* \to \nu_+ A_+ \tag{1}$$

starts from the ball surface. Hear A_-, A_* and A_+ are chemical formulae of reacting constituents, ν_-, ν_* and ν_+ are stoichiometric coefficients. We assume that A_- (initial material) and A_+ ("oxide") are solids constituents, and A_* ("oxidant") is a gas. An example of the reaction (1) is the oxidation of silicon

$$\mathrm{Si} + \mathrm{O_2} \to \mathrm{SiO_2} \quad (\nu_- = \nu_* = \nu_+ = 1) \tag{2}$$

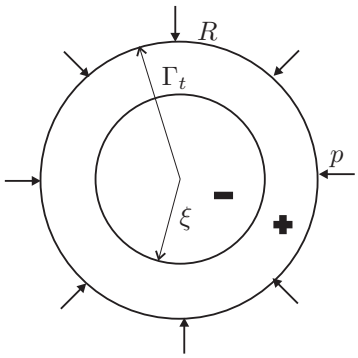


Figure 1: Chemical reactions in a spherically-symmetric problem

We suppose that the chemical reaction is localized at the chemical reaction front Γ_t between v_- and v_+, and the reaction is sustained by the diffusion of A_* to Γ_t through v_+ (Fig. 1). We assume that the diffusion of A_* occurs only in v_+ until the chemical reaction front is reached by molecules of A_*. For simplicity sake we assume that diffusion of A_* does not affect strains of the solid skeleton in v_+.

It is accepted that the chemical reaction front velocity $V_N^\Gamma \equiv V^*$ is determined by the convolution of the chemical affinity tensor $\mathbf{A}$ with a normal $\mathbf{N}$ to the front and it was shown [1] that the chemical affinity tensor has a form:

$$\mathbf{A} = \nu_+ M_+ \widetilde{\mathbf{M}}_+ - \nu_- M_- \widetilde{\mathbf{M}}_- - \nu_* M_* \widetilde{\mathbf{M}}_*, \tag{3}$$

$$\widetilde{\mathbf{M}}_+ = f_+\,\mathbf{E} - \frac{1}{\rho_g}(\mathbf{S}_+^g)^T\cdot\mathbf{F}_+^e, \quad \widetilde{\mathbf{M}}_- = f_-\,\mathbf{E} - \frac{1}{\rho_0}\mathbf{S}_-^T\cdot\mathbf{F}_-^e, \quad \widetilde{\mathbf{M}}_* = \mu_*\,\mathbf{E} \tag{4}$$

where M_-, M_+ and M_* are the molar masses of A_-, A_+ and A_*, ρ_0 and ρ_g are mass densities of stress-free constituents A_- and A_+, $f_- = f_-(\mathbf{F}_-^e)$ and $f_+ = f_+(\mathbf{F}_+^e)$ are free energies of A_- and A_+ per unit mass, $\mathbf{S}_-$ and $\mathbf{S}_+^g$ are the Piola-Kirhgoff stress tensors referred to initial configuration of A_- and stress-free configuration of oxide A_+, $\mathbf{F}_-^e$ and $\mathbf{F}_+^e$ are elastic deformation gradients in A_- and A_+, μ_* is a chemical potential of the gas constituent, $\mathbf{E}$ is the unit tensor.

In a linear thermodynamic approach

$$V^* = -\kappa A_N, \quad \kappa > 0, \quad A_N = \mathbf{N}\cdot\mathbf{A}\cdot\mathbf{N} \tag{5}$$

If the chemical transformation tensor $\mathbf{G}$ is isotropic, i.e. $\mathbf{G} = g\mathbf{E}$, then the total deformation gradient $\mathbf{F}_+$

$$\mathbf{F}_+ = g\mathbf{F}_+^e, \quad g = \left(\frac{\nu_+ M_+}{\nu_- M_-}\frac{\rho_0}{\rho_g}\right)^{1/3} \tag{6}$$

where g is a chemical transformation parameter.

The traction continuity condition across the reaction front takes the form

$$\mathbf{S}_-\cdot\mathbf{N} = g^2\mathbf{S}_+^g\cdot\mathbf{N} \tag{7}$$

From (3), (4), (6) and (7) it follows that

$$A_N = \frac{\nu_- M_-}{\rho_-}\left((g^3\rho_g f_+ - \rho_0 f_-) - \mathbf{N}\cdot\mathbf{S}_-\cdot(\mathbf{F}_+ - \mathbf{F}_-)\cdot\mathbf{N}\right) - \nu_* M_*\mu_* \tag{8}$$

The representation of A_N in the form (8) is convenient for further linearization in a case of small strains, when $\mathbf{F} = \mathbf{E} + \nabla\mathbf{u}$, $|\nabla\mathbf{u}| \ll 1$

$$g \equiv 1 + \varepsilon^{ch}, \quad |\varepsilon^{ch}| \ll 1$$

and $|\nabla\mathbf{u}|$ and $|\varepsilon^{ch}|$ are the values of the same order. In this case we obtain the same expression for A_N as we would have in the case of the coherent interface:

$$hA_N = [f] - \boldsymbol{\sigma} : [\boldsymbol{\varepsilon}] - h\nu_* M_*\mu_*, \qquad h = \frac{\rho_0}{\nu_- M_-} \tag{9}$$

From now f is a free energy density per unit volume in initial stress-free state. $\boldsymbol{\sigma}$ is Cauchy stress tensor, a jump $[\varphi] = \varphi_+ - \varphi_-$.

Free energy densities of solid constituents is represented by quadratic dependencies

$$f_\pm = f_\pm^0(T) + \frac{1}{2}\left(\boldsymbol{\varepsilon} - \boldsymbol{\varepsilon}_\pm^{ch}\right) : \mathbf{C}_\pm : \left(\boldsymbol{\varepsilon} - \boldsymbol{\varepsilon}_\pm^{ch}\right) \tag{10}$$

where T is the temperature, $\boldsymbol{\varepsilon}_-^{ch} = 0$, $\boldsymbol{\varepsilon}_+^{ch} = \varepsilon^{ch}\mathbf{E}$. Then the constitutive equations take the form

$$\boldsymbol{\sigma}_\pm = \mathbf{C}_\pm : (\boldsymbol{\varepsilon}_\pm - \boldsymbol{\varepsilon}_\pm^{ch}) \tag{11}$$

We assume that solid constituents are isotropic. Then

$$\mathbf{C}_\pm = K_\pm\mathbf{E}\mathbf{E} + 2\mu_\pm\left(\mathbf{I} - \frac{1}{3}\mathbf{E}\mathbf{E}\right) \tag{12}$$

where $K_\pm$ are bulk moduli, $\mu_\pm$ are shear moduli.

We take the chemical potential of the gas constituent A_* in a form

$$M_*\mu_* = \eta(T) + RT\ln(c)$$

where c is partial volume fraction of A_*.

We suppose that oxide form a spherical layer V_+, then initial material forms the spherical kernel V_-. In a case of spherical symmetry we use spherical coordinates r, φ, θ. Radial displacements in initial material and oxide are given by Lame formula,

$$u_\pm = B_\pm r + D_\pm / r^2 \tag{13}$$

where $B_\pm$, $D_\pm$ are found from boundary conditions, displacement and traction continuity conditions on the reaction front and condition of singularity absence in the center.

Stress and strain tensors are spherical in V_-:

$$\varepsilon_r^- = \varepsilon_\varphi^- = \varepsilon_\theta^- = B_-, \quad \sigma_r^- = \sigma_\varphi^- = \sigma_\theta^- = 3K_- B_- \tag{14}$$

By (11) and (13) strains and stresses in the oxide domain V_+

$$\begin{aligned} &\varepsilon_r^+ = B_+ - 2D_+/r^3, \qquad \varepsilon_\varphi^+ = \varepsilon_\theta^+ = B_+ + D_+/r^3 \\ &\sigma_r^+ = K_+(3B_+ - \vartheta) - 4\mu_+ D_+/r^3, \\ &\sigma_\varphi^+ = \sigma_\theta^+ = K_+(3B_+ - \vartheta) - 4\mu_+ D_+/r^3 \end{aligned} \tag{15}$$

Then

$$\begin{aligned} &hA_N = \gamma_* + \frac{1}{2}(9K_1 B_+ B_- - 3K_+(B_+ - B_-)\vartheta + K_+\vartheta^2) - hRT\ln(c), \\ &K_1 = K_+ - K_-, \qquad \gamma_* = f_+^0(T) - f_-^0(T) - h\eta(T), \quad \vartheta = 3\varepsilon^{ch} \end{aligned} \tag{16}$$

The linear thermodynamic relationship (5) is used not far from the chemical equilibrium. In case of chemical equilibrium the rates of direct and reverse chemical reactions are equal and in this case [3] $A_N = 0$

Given stresses at the reaction front, the condition $A_N = 0$ determines so-called equilibrium concentration c_{eq} of the oxidant by the equation

$$A_N(c_{eq}) = 0 \tag{17}$$

Then the velocity of the chemical reaction front is determined by the formula [2]

$$V_* = \frac{k_* \nu_- M_-}{\rho_- M_*}\,(c(\xi) - c_{eq}) \tag{18}$$

where k_* is the parameter of the reaction, $c(\xi)$ is the concentration of the oxidant A_* at the chemical reaction front, ξ is the position (the radius) of the front , c_{eq} is the concentration of the oxidant A_* that would be equilibrium at the stress acting at the front.

Thus, to describe the chemical reaction front kinetic we have to solve the equation (17) taking into account the dependencies of the stresses on the chemical reaction front position ξ, and to find $c(\xi)$ from the solution of the diffusion problem.

2 Oxidant equilibrium concentration

By (16), the condition (17) takes the form

$$2\gamma_* + 9K_1 B_+ B_- - 3K_+(B_+ - B_-)\vartheta + K_+\vartheta^2 - 2hRT\ln(c_{eq}) = 0,$$

where

$$\begin{aligned} &B_- = \frac{d_+ p + 4\mu_+ K_+(1-\rho^3)\vartheta}{3\left(4\mu_+ K_1 \rho^3 - K_+ d_-\right)}, \qquad B_+ = \frac{d_- p - 4K_+(4\mu_+(\rho^3 - 1) - 3K_-)\vartheta}{3\left(4\mu_+ K_1 \rho^3 - K_+ d_-\right)}, \\ &p = -\sigma_r|_{r=R}, \quad \rho = \xi/R, \quad d_\pm = 3K_\pm + 4\mu_+ \end{aligned} \tag{19}$$

Substituting (19) into (2) yields

$$\frac{d_- d_+(K_1 p + 2K_+ K_- \vartheta)p - 4K_- K_+ \mu_+(4\mu_+ K_1 \rho^6 + K_+ d_-(1 - 2\rho^3))\vartheta^2}{2\left(4\mu_+ K_1 \rho^3 - K_+ d_-\right)^2} + \tag{20}$$

$$\gamma_* - hRT\ln(c_{eq}) = 0$$

The equation (20) determines the dependence of equilibrium concentration c_{eq} on applied external pressure p and relative radius ρ of the chemical reaction front.

Let c^0_{eq} is the equilibrium concentration at the beginning of oxidation, when $\rho = 1$. From (20) it follows that

$$\ln(c^0_{eq}) = \frac{1}{RTh}\left(\gamma_* - \frac{d_-(K_1 p + 2K_-K_+\vartheta)p + 4K_-K_+\mu_+\vartheta^2}{2d_+K_-^2}\right) \tag{21}$$

The dependencies of the initial equilibrium concentration are shown in Fig. 2 for two cases, $K_+ > K_-$ and $K_+ < K_-$.

The dependence $c^0_{eq}(p)$ is not monotonic. If $K_+ > K_-$ then the dependence contains a minimal point (p_*, c^*_{eq}), where

$$p_* = -\frac{K_-K_+\vartheta}{K_1} \tag{22}$$

and the minimal value c^*_{eq} is given by formula

$$\ln(c^*_{eq}) = \frac{1}{hRT}\left(\gamma_* - \frac{K_-K_+\vartheta^2}{2K_1}\right) \tag{23}$$

If $K_+ < K_-$ then relationships (23) and (22) determine the maximal point.

The oxidation reaction cannot start if the concentration c_0 at the internal surface of the ball is less then c^0_{eq}.

If $K_+ > K_-$ and $c_0 < c^*_{eq}$ then from the linear kinetics model it can follow that the reaction cannot start whatever pressure is. If $K_+ < K_-$ and $c_0 > c^*_{eq}$ then the reaction starts at any pressure.

Note that there is pressure

$$p_0 = -\frac{2K_-K_+\vartheta}{K_1} \tag{24}$$

such that $c_{eq}(p_0) = c_{eq}(p = 0)$.

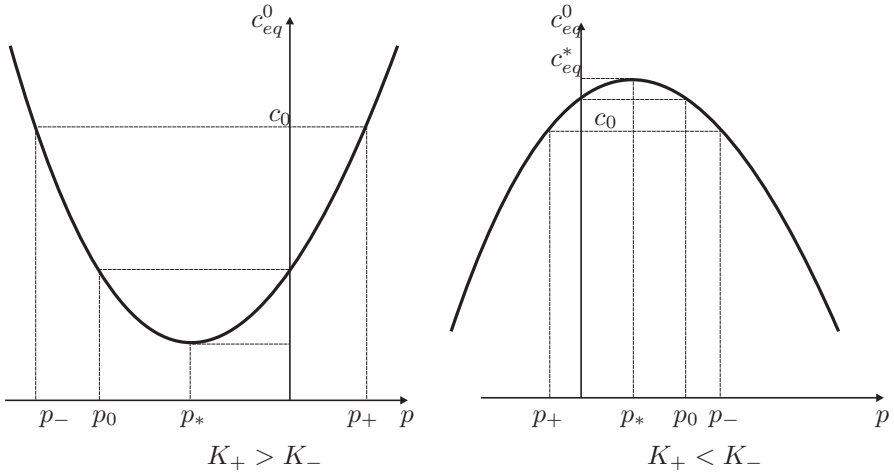


Figure 2: Dependence of initial equilibrium concentration on pressure $p = -\sigma_r|_R$

Given oxidant concentration c_0 at the ball surface, the reaction can start only if the following conditions are satisfied:

$$\begin{aligned} &K_1 > 0, \qquad p < p_- \quad \text{or } p > p_+ \\ &K_1 < 0, \qquad p_- \le p \le p_+, \end{aligned} \tag{25}$$

where the limit values of pressure

$$p_{\pm} = \frac{K_-}{K_1}\left(-K_+\vartheta \pm \sqrt{\frac{d_+(K_-K_+\vartheta^2 - 2K_1(\gamma_* - hRT\ln(c_0))}{d_-}}\right) \tag{26}$$

If the reaction front moves then stresses at the front change and, thus, the equilibrium concentration changes. The dependencies of equilibrium concentration on the oxide thickness $\zeta = R - \xi_*$ are shown in Fig. 3 at different values of pressure for two cases: $\vartheta > 0$ and, for completeness sake, $\vartheta < 0$. The equilibrium concentration decreases as the thickness grows.

The character of pressure influence depends on the sign of the chemical reaction deformation ϑ. If $\vartheta > 0$ then c_{eq} increases if p increases. If $\vartheta < 0$ then c_{eq} decreases if p increases.

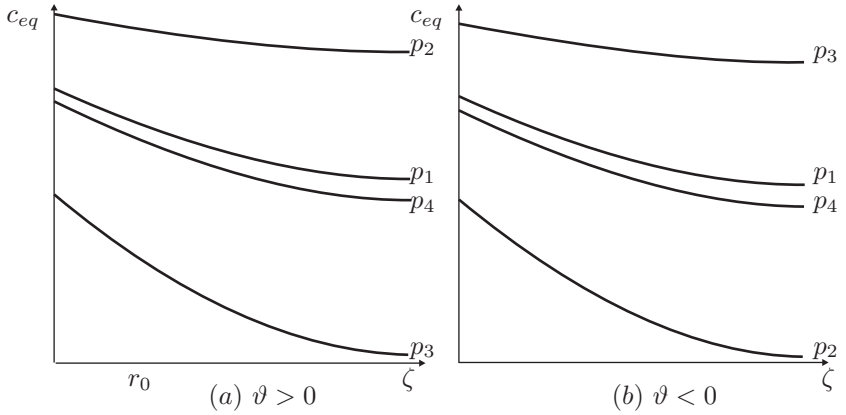


Figure 3: Dependence of equilibrium concentration on the oxide zone thickness, $K_1 < 0$, $p_1 = 0$, $p_2 > 0$, $p_3 < 0$, (a) $p_4 > p_0 > 0$, (b) $p_4 < p_0 < 0$

2.1 Diffusion problem

The concentration of the gas constituent determined by the diffusion equation

$$\frac{\partial c}{\partial t} = -\nabla \cdot \mathbf{J}, \qquad \mathbf{J} = -D\nabla\mu_* \tag{27}$$

where $\mathbf{J}$ is the gas flux, D is the diffusion coefficient.

Assuming that the temperature is constant and the gas concentration depends only on r we can write the flux in spherical coordinates:

$$\mathbf{J} = -D\nabla c = -D\frac{\partial c}{\partial r}\mathbf{e}_r \tag{28}$$

As the result in the steady-state approximation

$$\frac{\partial^2 c}{\partial r^2} + \frac{2}{r}\frac{\partial c}{\partial r} = 0, \qquad r \in [r_0,\, R] \tag{29}$$

$$c = c_0 \quad \text{at } r = R, \tag{30}$$

$$D\frac{\partial c}{\partial r} + k_*\nu_*(c - c_{eq}) = 0 \quad \text{at } r = \xi. \tag{31}$$

The condition (31) is mass balance at the reaction front between mass flux due to the diffusion and the mass sink due to chemical reaction. It is assumed that the chemical reaction rate is proportional to the deviation of the concentration from the equilibrium value.

It is easy to show that the oxidant concentration at the reaction front

$$c(\xi_*) = \frac{(c_0 - c_{eq})D}{k_*\nu_*R\rho(1-\rho_) + D} \tag{32}$$

The gas constituent distribution inside the oxide zone is shown in Fig. 4 for various positions of the reaction front. Fig. 5 represents the dependence of the reaction front velocity on the reaction front position and the size of the oxide zone for various pressure. It is seen that for $p \simeq p_+$ the velocity of oxide zone growth does not change, since in this case the concentration of the gas on the boundary is almost equal to the initial equilibrium concentration. Fig. 5 is constructed for $\xi \simeq R/3$ as further oxide growth does not influence on the velocity. The situation depends on the sign of ϑ. If $\vartheta < 0$ then pressure accelerates the chemical reaction front propagation. Fig. 6 demonstrates how the diffusion coefficient D affects chemical reaction front propagation.

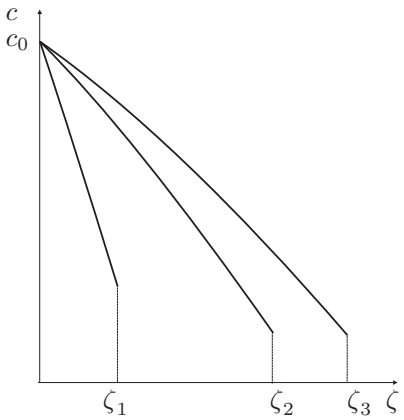


Figure 4: Gas distribution inside the oxide zone

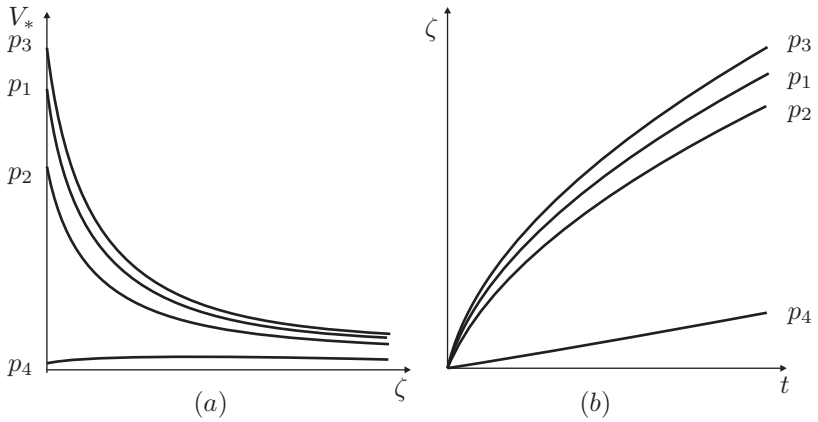


Figure 5: (a) Dependence of the reaction front velocity on the reaction front position (b) Oxide zone growth. $K_+ > K_-$, $\vartheta > 0$ $p_1 = 0$, $p_2 > 0$, $p_0 < p_3 < 0$, $p_4 \simeq p_+$

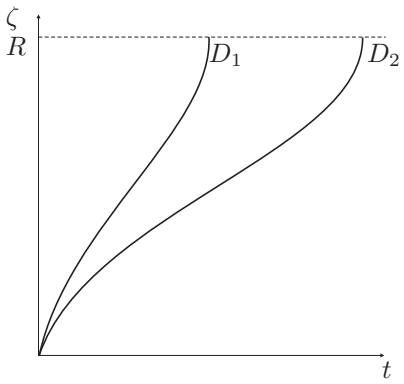


Figure 6: Oxide zone growth $D_1 > D_2$

3 Boundary conditions effects

The external pressure was prescribed at the ball boundary in above considerations. Now consider a case of a given radial displacement u_0. Then $\vartheta^0 = 3u_0/R$ is average volume strains.

Constants $B_\pm$ are determined as

$$B_- = \frac{d_+\vartheta^0 - 3K_+(1-\rho^3)\vartheta}{3\left(3K_1\rho^3 + d_-\right)}, \qquad B_+ = \frac{d_-\vartheta^0 + 3K_+\rho^3\vartheta}{3\left(3K_1\rho^3 + d_-\right)} \tag{33}$$

The equation for equilibrium concentration takes the form:

$$\frac{d_-d_+(K_1\vartheta^0 - 2K_+\vartheta)\vartheta^0 + K_+(9K_-K_1\rho^6 + 6K_-d_-\rho^3 - d_-(d_- + 3K_+))\vartheta^2}{2\left(3K_1\rho^3 + d_-\right)^2} + \tag{34}$$

$$\gamma_* - hRT\ln(c_{eq}) = 0$$

The equilibrium concentration at which the oxidation process starts is determined by the relationship

$$\ln(c^0_{eq}) = \frac{1}{RTh}\left(\gamma_* + \frac{d_-(K_1\vartheta^0 - 2K_+\vartheta)\vartheta^0 + K_+\mu_+\vartheta^2}{2d_+}\right) \tag{35}$$

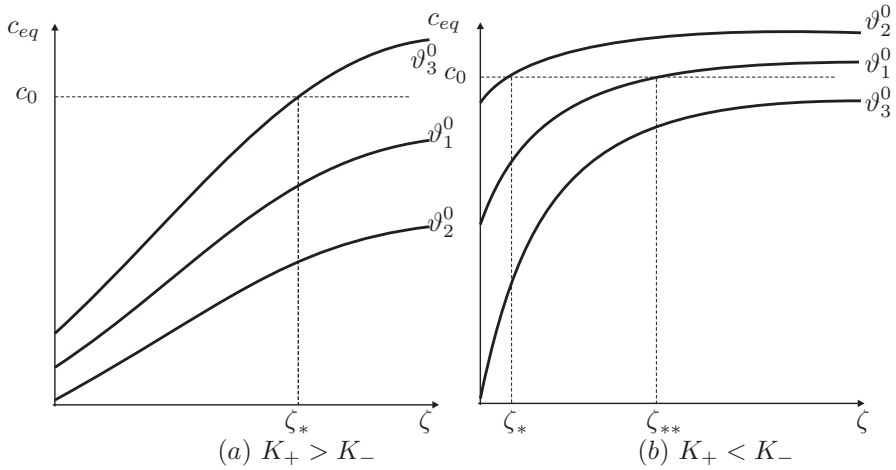


Figure 7: Dependence of the equilibrium concentration at the reaction front on the oxide zone thickness, $\vartheta > 0$, $\vartheta_0^0 = 0$, $\vartheta_2^0 > 0$, $\vartheta_3^0 < 0$

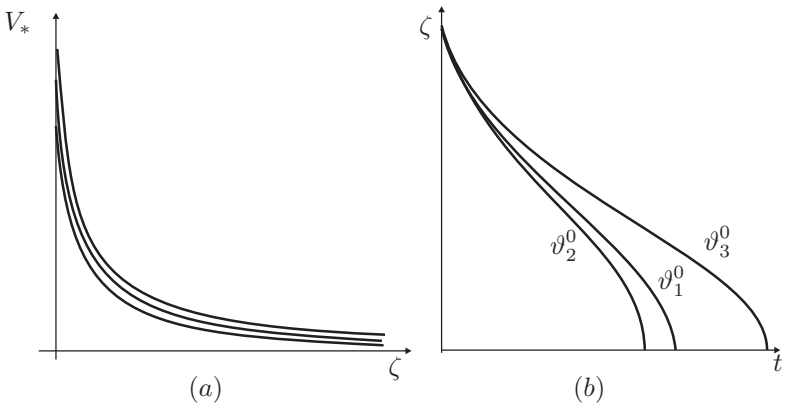


Figure 8: (a) Dependence of the equilibrium concentration at the reaction front on the oxide zone thickness, (b) Oxide zone growth. $K_+ > K_-$, $\vartheta > 0$ $\vartheta_0^0 = 0$, $\vartheta_2^0 > 0$, $\vartheta_3^0 < 0$

Fig. 7 demonstrates the dependence of c_{eq} on the size of the oxide zone. In contrast to the case when the pressure is given as boundary condition there exists a threshold thickness of the oxide

such that the oxidation is blocked if $\zeta > \zeta_*$. Fig. 8 shows the oxide zone growth at given external displacements. From the graph it follows that if $u_0 > 0$ then external loading accelerates the chemical reaction front. On the contrary, if $u_0 < 0$ then external loading decelerate the chemical reaction front.

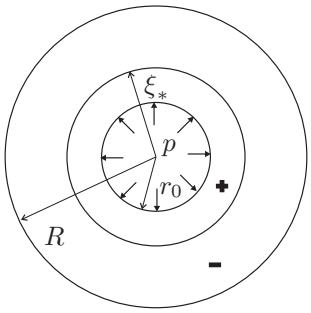
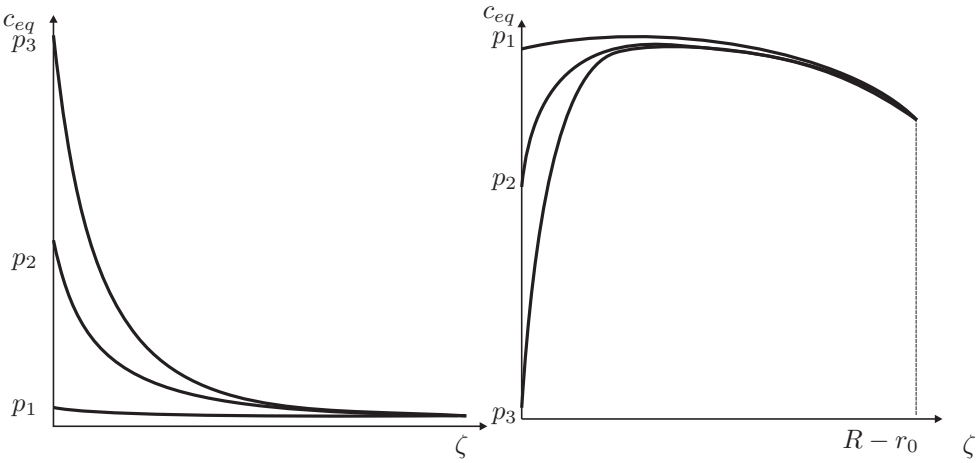


Figure 9: A spherical container under internal pressure.

Consider now a spherical thickwalled container, $r \in [R_0, R]$ (Fig. 9). Assume that the pressure p is prescribed inside the internal spherical hole, and the concentration of the oxidant c_0 is given inside the hole. The reaction starts at the hole surface.

The dependencies of the equilibrium concentration on the oxide zone thickness $\zeta = \xi - r_0$ is shown in Fig. 10. In absence of internal pressure the equilibrium concentration is almost unchanged during the front propagation. If $p \neq 0$ then the equilibrium concentration strictly depends on the front position. The front velocity dependencies are shown in Fig. 12.

Figures 10 – 12 demonstrate variety of behaviors, depending on the relationship between bulk moduli, pressure, radius of the internal hole. Obviously, this variety can be related with internal stresses induced by the chemical reaction.



(a) $K_+ > K_-$ (b) $K_+ < K_-$

Figure 10: Dependence of the equilibrium concentration on the oxide zone thickness, $\vartheta > 0$, $r_0 = 0.1R$, $p_1 = 0$, $p_2 > 0$, $p_3 < 0$

4 Conclusions

A problem of oxidation of a ball in small strain approach and linear thermodynamic approach is formulated. If we neglect the interconnections between the diffusion of a gas component and deformations of a solid component, then stresses affect the diffusion and chemical reaction front kinetics through the equilibrium concentration of the gas component. Variety of behaviors is demonstrated. The role of internal stresses induced by the chemical reaction is emphasized. Threshold effects are detected. It is shown that the oxide zone growth may block the oxidation process.

Acknowledgements

This work was supported by Sandia National Laboratories and RFBR grant 10-01-00670-a

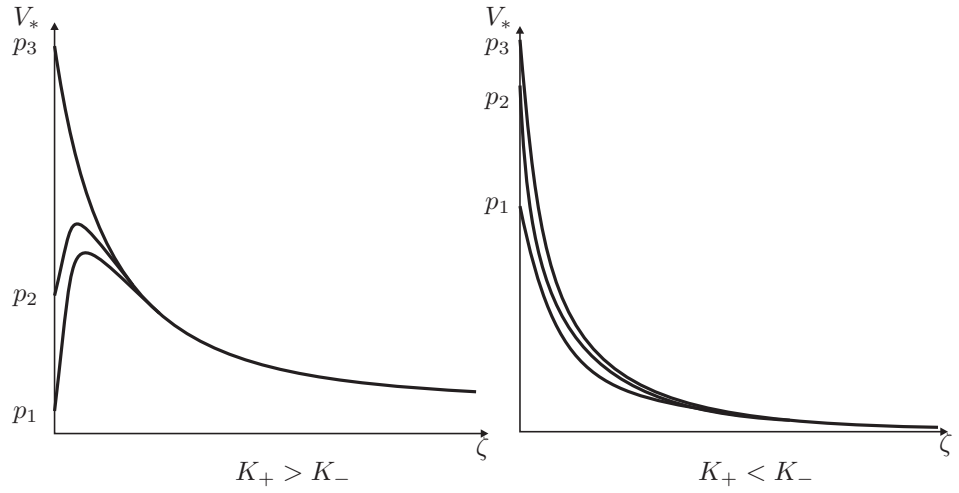
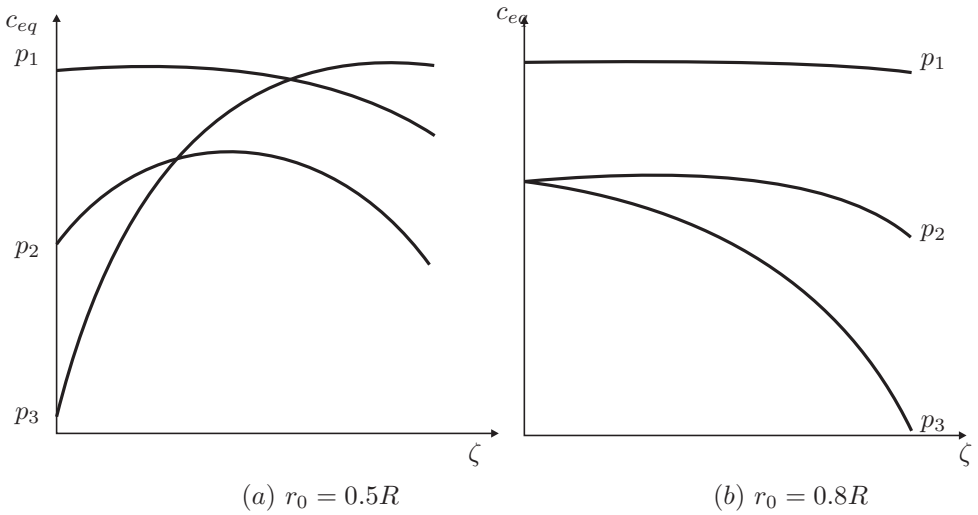


Figure 11: Dependence of the reaction front velocity on the oxide zone thickness, $\vartheta > 0$ $p_1 = 0$, $p_2 > 0$, $p_3 < 0$



(a) $r_0 = 0.5R$ (b) $r_0 = 0.8R$

Figure 12: Dependence of the equilibrium concentration on the oxide zone thickness, $\vartheta > 0$, $r_0 = 0.1R$, $p_1 = 0$, $p_2 > 0$ $p_3 < 0$

References

[1] A.B.Freidin. On chemical reaction fronts in nonlinear elastic solids. Proceedings of XXXVI International Summer School-Conference APM' 2009. Eds: D. A. Indeitsev, A. M. Krivtsov. St.Petersburg. Institute for problems in mechanical Engineering. 2009. P.231-237.

[2] E.N. Vilchevskaya, A.B. Freidin. Modelling a chemical reaction front propagation in elastic solids: 1D case. Proceedings of XXXVI International Summer School-Conference APM' 2009. Eds: D. A. Indeitsev, A. M. Krivtsov. St.Petersburg. Institute for problems in mechanical Engineering. 2009. P.681-691.

[3] P. Glansdorff, I. Prigogine, Thermodynamic theory of structure, stability and fluctuations, Wiley-Interscience, London, NY, Sydney, Toronto.

Elena N. Vilchevskaya, Alexander B. Freidin, IPME, Bolshoi 61, V.O., St.Petersburg, Russia

Heat transfer and overcritical convection in rotating horizontal annulus

Alexey A. Vjatkin Victor G. Kozlov Rustam R. Sabirov
vjatkin_aa@pspu.ru kozlov@pspu.ru sabirov@pspu.ru

Abstract

The thermal convection in a horizontal cylindrical layer of liquid rotating around its axis is experimentally investigated. The heat transfer and the structure of convective flows depending on rotation rate and temperature difference of the layer boundaries are studied. The focus is on the case of the higher temperature of the interior boundary. Different regimes of convection are found out. At rather fast rotation the spatially periodic system of thermovibrational convective rolls parallel to the axis of rotation is excited, it is described in [1]. At lower rotation (in overcritical domain) the system of the rolls oriented perpendicularly to the axis of rotation appears, it is accompanied with the critical change of heat transfer, as well. The size of these transversal rolls is comparable with the annulus thickness and is small compared to the longwise rolls size. The quasi-stationary gravitational convection exists together with the vibrational one. At very slow rotation the system of crescent rolls elongated in a vertical plane appears. These rolls are similar to the gravitational convective structures in the immovable horizontal annulus. The temperature oscillations of the external boundary recorded by the temperature sensor are studied. The dimensionless parameter controlling the period of temperature oscillations in the annulus is determined.

1 Introduction

In [1] it is revealed that the thermal convection in a rotating horizontal annulus arises independently on the positive or negative temperature difference between the layer boundaries. If the external boundary has higher temperature the convection arises due to centrifugal force and it is determined by centrifugal Rayleigh number. At higher temperature of the internal boundary the centrifugal force plays a stabilizing role but thermal convection excites nevertheless. It is caused by thermovibrational mechanism [2] [3]; the convection is generated due to the oscillation of nonisothermal liquid in the cavity frame caused by the gravity. The averaged thermal convection in the cavity rotating around its axis is determined by both centrifugal Rayleigh number $Ra = \Omega^2 R\beta\Theta h^3/\nu\chi$ and modified vibrational parameter $R_v = (g\beta\Theta h)^2/2\nu\chi\Omega^2$, here β, ν and χ - coefficients of volume expansion, kinematic viscosity and thermal conductivity of liquid, h - the layer thickness, R - mean radius of the layer, Θ - temperature difference between the boundaries, $\Omega \equiv 2\pi n$ - angular velocity of rotation (n - velocity of rotation). The important parameter is the dimensionless frequency of rotation $\omega \equiv \Omega h^2/\nu$ which determines both the structure of convective flows and the efficiency of vibroconvective mechanism. This parameter characterizes both Coriolis force action and the ratio of the cavity size and the thickness of Stokes boundary layer.

2 Experimental setup and technique

The annulus layer of thickness $h = 7$ mm and length $l = 230$ mm is formed by coaxial cylinders *1* and *2* (Fig. 1). The internal aluminum cylinder has a diameter $d = 60$ mm, the external is made of Plexiglas pipe with wall thickness 3 mm. The heating of internal boundary and cooling of the external one is produced by pumping water from the jet thermostats through the metal cylinder *1* (T_1) and a jacket between thin-walled coaxial Plexiglas pipes *2* and *3* (T_3). The temperature T_1

of the internal layer boundary and temperature T_3 of the liquid in the jacket *5* are measured by thermo resistors with resistance about 100 Ohm made of a copper wire with diameter 0.05 mm. The temperature T_2 of external boundary of the liquid layer is measured by the integral thermo resistor. It consists of several loops of a copper wire with diameter 0.02 mm extended along the axis of a layer and glued to the boundary by transparent film of thickness 0.1 mm and width 10 mm. The resistance of the sensor is 90 Ohm. For the temperature measurement the device "Thermodat" with an accuracy of 0.1 K is used. The data from the "Thermodat" are registered on the computer. The rotation of the installation around the horizontal axis is produced by means of the step-by-step engine, it provides the uniform rotation in all the range of rotation speed n (instability of speed does not exceed 0.001 rps). The rotation frequency varies in an interval n =0.1-0.5 rps and is controlled by means of a digital tachometer. The more detailed description of experimental installation is available in [1].

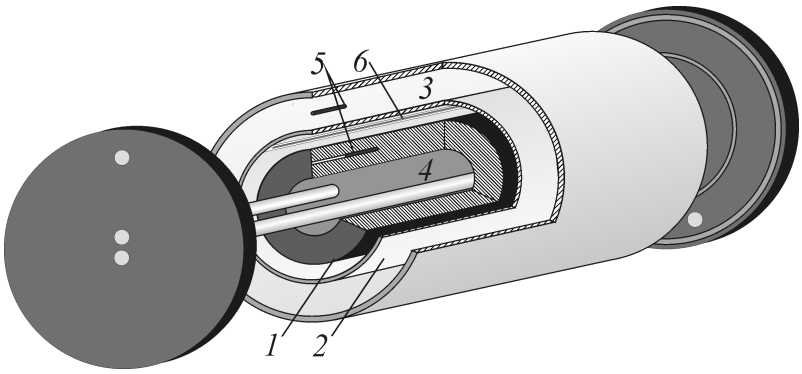


Figure 1: The sketch of the cavity.

The distilled water serves as a working liquid. The technique of experiments is the following. With the help of the thermostats the temperatures of internal border of the layer T_1 and of the liquid in the water shirt T_3 are defined, the cavity is subject to rotation with the definite high enough frequency. The temperature of external border of the layer T_2 is measured on each step after the coming to the stationary regime of convection. The difference of temperatures of the liquid layer boundaries $\Theta = T_2 - T_1$ and the temperature drop on the wall of the Plexiglas pipe $\Delta T = T_3 - T_2$ characterizing a thermal flux through the annulus are calculated. The value $\Theta + \Delta T$ remains constant with variation of velocity of cavity rotation in each experience. The experiments are repeated at various values of temperature T_1 and T_3. The aluminum powder with a small amount of surface active surfactants is added in a working liquid for visualization of convective structures (accordingly 0.03 and 0.2 proc. from fluid mass, correspondingly).

3 Results of experiment

At fast rotation the convection is absent and the heat transfer equals to the molecular one. The decrease of the rotation rate results in the threshold excitation of the spatially periodic system of rolls stretched along the axis of rotation. The wavelength of these structures of vibroconvective nature [1] is very large: the perimeter equals to three pairs of rotating rolls. The appearance of vibrational convection is followed by the increase of the heat transfer. The dependence of the external liquid boundary temperature T_2 on the rotation velocity n at $\Theta + \Delta T$ =25.6 K is presented in Fig. 2,*a*. The heat transfer is characterized by Nusselt number Nu which is the ratio of the mean heat flux in the presence and in the absence of convection at definite temperature difference Θ. The domain *1* (Fig. 2,*a* and *b*) corresponds to the absence of convection, $Nu = 1$ is a result of stabilizing action of the centrifugal force. The total heat flux is nearly molecular. The total heat flux is nearly molecular. The decrease of the rotation rate is followed by the threshold excitation of convection (dashed line between domains *1* and *2*).

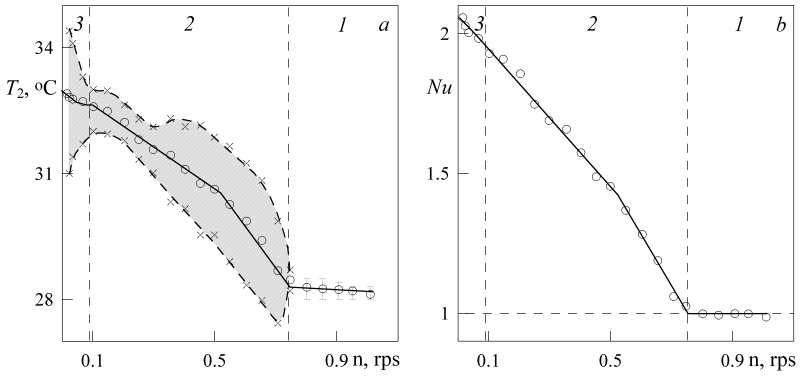


Figure 2: The experimental data at $\Theta + \Delta T$ =25.6 K.

The temperature sensor at the external boundary of annulus registers the temperature oscillations (the shaded domain in Fig. 2,*a*). The observations demonstrate these oscillations to be determined by slow azimuth drift of vibroconvective rolls in the cavity frame. The drift is co-directional to the rotation of the gravity field in the cavity frame which is opposite to the direction of the cavity rotation in the laboratory frame. Fig. 3 presents the time evolution of the external boundary temperature variation with time at n=0.69 (*a*), 0.58 (*b*) and 0.34 rps (*c*). The decrease of the rotation rate results in the reduction of the period of oscillations which is caused by drift velocity enhancement. The amplitude of oscillations crucially increases in the course of convection evolution and reaches the maximum value. The increase of the temperature difference between the boundaries of the layer leads to the raise of the maximum amplitude of oscillations. The spectral analysis of the data (Fourier analysis is used) allows to determine the averaged value of T_2 and the period of oscillations.

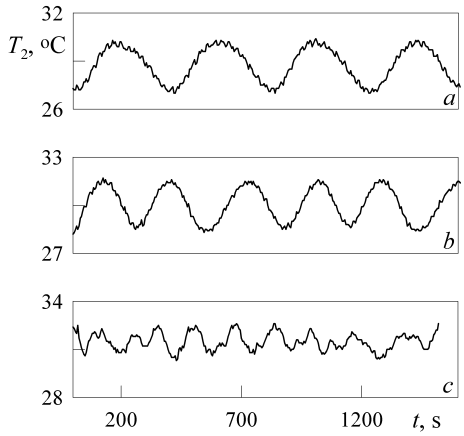


Figure 3: The temperature oscillations recorded by the temperature sensor mounted on the external boundary of the layer.

The further decrease of n results in the appearance of the spatially periodic system of convective rolls oriented perpendicularly to the axis of rotation, it is also followed by change of heat transfer (Fig. 2,*b*). The size of these transversal rolls is comparable with the annulus thickness and small in comparison with the longwise rolls size. The recorded temperature oscillations become less regular in the presence of transversal rolls (Fig. 3,*c*). The amplitude of oscillations decreases but Fourier analysis demonstrates that the low-frequency oscillations (caused by the drift of vibroconvective

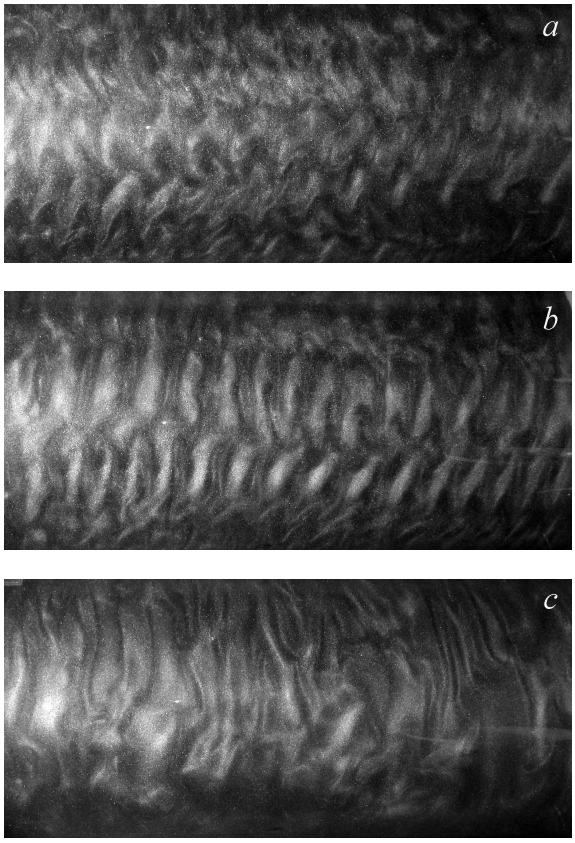


Figure 4: The photos of convective flows.

rolls) exist as before. One could expect that the transversal short-wave rolls are caused by the excitation of the gravitational convective instability in the upper part of the layer where the unstable liquid stratification in gravity field appears [4]. It is worth noting that under conditions of gravitational convection (when rotation is absent) in the limit of the thin layer the convective rolls normally are parallel to the annulus axis [5]. The transversal orientation of convective rolls could be caused by the cavity rotation. So, the long-wave longwise rolls and short-wave transversal rolls coexist in the definite range of the rotation rate. The decrease of the rotation velocity leads to the intensification of gravitational rolls and decay of the vibroconvective ones. It can be seen on the photos of the convective structures (Fig. 4, side view) at velocity n=0.29 (a), 0.19 (b) and 0.09 rps (c).

The vibroconvective vortices disappear at critical value of n (Fig. 2, dashed line between domains *2* and *3*). The experiments demonstrate that the laminar convective flow has a shape of two symmetric crescent vortices. These vortices consist of ascending currents near the hot internal boundary and descending currents near the cold external ones. In the absence of rotation the centers of the vortices are shifted to the upper part of the cavity. At slow rotation the vortices are shifted in the direction of the cavity rotation and keep the same shape. The origin of the temperature oscillations in the domains *3* differs from the oscillations in the domain *2*. (caused by the drift of vibroconvective rolles). At low rotation the maximum of the temperature of external boundary is detected when the sensor is at the top part of the layer and the temperature minimum - at the lower part. Thus the period of temperature oscillations in the layer equals to the period of the cavity rotation.

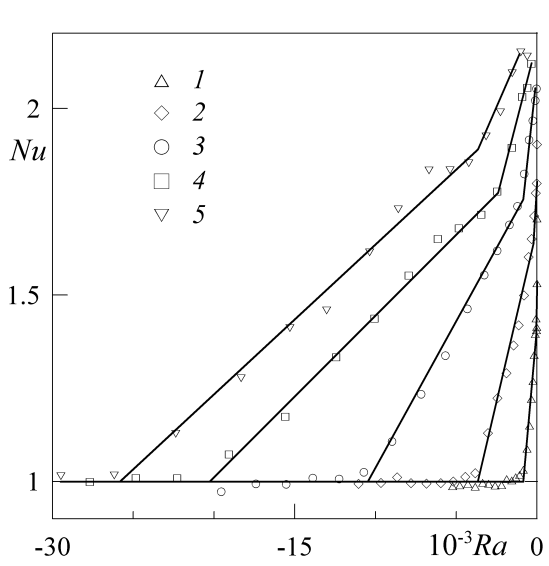


Figure 5: The dependence of Nusselt number on Rayleigh number at different values $\Theta + \Delta T$.

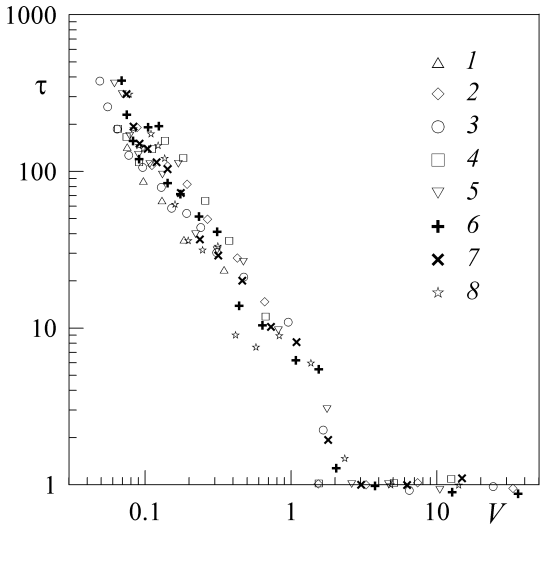


Figure 6: The dependence of the dimensionless period of temperature oscillations on the parameter V.

4 Discussion of results

Fig. 5 demonstrates the dependence of Nusselt number Nu on the centrifugal Rayleigh number at $\Theta + \Delta T$ =12.9 (*1*), 19.0 (*2*), 26.2 (*3*), 32.9 (*4*) and 36.5 K (*5*). At large values of Ra (fast rotation) convection is absent (Nu =1). The gentle slope of the curves corresponds to vibrational convection and joint existence of gravitational convection and thermovibrational one. The greatest growth of the heat transfer with the decreasing of Ra is at pure gravitational convection.

Fig. 6 summarizes the results of temperature oscillations at $\Theta+\Delta T$ =9.4 (*1*), 12.9 (*2*), 15.3 (*3*), 19.0 (*4*), 22.2 (*5*), 28.2 (*6*), 32.9 (*7*) and 36.5 K (*8*) on the plane of dimensionless parameters τ and V, here period $\tau \equiv T\Omega/2\pi$ and $V \equiv \Omega^2 R/g\beta\Theta$ (T - the period of the temperature oscillations, R - mean radius of the layer). All the results are in agreement with each other. The parameter V characterizes the mean velocity of the azimuth drift of the liquid layer generated by the oscillations of nonisothermal liquid in the cavity frame caused by gravity (in the limit of relatively fast rotation).

5 Conclusion

The thermal convection in a horizontal cylindrical layer of liquid rotating around its own axis is experimentally investigated. The heat transfer and the structure of convective flows depending on rotation rate and temperature difference of the layer boundaries are studied. Different regimes of convection are found out. At rather fast rotation the spatially periodic system of thermovibrational convective rolls parallel to the axis of rotation is excited. At lower rotation the system of the rolls oriented perpendicularly to the axis of rotation appears, it is followed by the critical change of heat transfer, as well. The spatial period of these transversal rolls is comparable with the annulus thickness and is small compared to the longwise rolls size. It is found that these rolls are of quasistationary gravitational nature. At very slow rotation the system of crescent rolls elongated in a vertical plane appears. These rolls are similar to the gravitational convective structures in the immovable horizontal annulus. The temperature oscillations of the external boundary recorded by the temperature sensors are studied. It is shown that the dimensionless period of the oscillations $\tau = T\Omega/2\pi$ is determined by parameter $V = \Omega^2 R/g\beta\Theta$.

Acknowledgements

This work is supported by Rosobrazonanie (Templan N 0120.0600475) and the Academic council of PSPU (grant of 2010).

References

[1] Vjatkin A.A., Ivanova A.A., Kozlov V.G. Convective stability of a nonisothermal fluid in a rotating horizontal coaxial gap // Fluid Dynamics. 2010. V. 45. N 1. P. 10-18.

[2] Ivanova A.A., Kozlov V.G., Rylova V.V. Thermal convection in a plane layer rotating about a horizontal axis // Fluid Dynamics. 2003. V. 38. N 1. P. 9-17.

[3] Kozlov V.G. Thermal vibrational convection in rotating cavities // Fluid Dynamics. 2004. V. 39. N 1. P. 3-11.

[4] Rao Y.-F., Miki Y., Fukuda K., et al. Flow patterns of natural convection in horizontal cylindrical annuli // Int. J. Heat Mass Transfer. 1985. No. 28. P. 705-714.

[5] Powe R.E., Carley C.T., Bishop E.H. Free convective flow patterns in cylindrical annuli // J. Heat Transfer. 1969. V. 91. No. 3. P. 310-314.

Victor G. Kozlov, Perm State Pedagogical University, Russia
Alexey A. Vjatkin, Perm State Pedagogical University, Russia
Rustam R. Sabirov, Perm State Pedagogical University, Russia

The hydrogen material interaction during cyclic mechanical loading

Yuriy Yakovlev Vladimir Polyanskiy
info@electronbeamtech.com

Abstract

The two-continuum model of solid allows one to describe the influence of small concentration of hydrogen on the mechanical properties of materials in terms of changing the bonding energy of the second continuum, the latter being responsible for the hydrogen concentration. The experimental technique and experimental results are described in the report. We discuss and model the hydrogen redistribution during fatigue loading.

1 Introduction

Hydrogen is contained in all structural materials. It is known that under mechanical loads the hydrogen inside the metal is concentrated in the areas of tensile mechanical stresses (the Gorsky effect [1]).

On the other hand, elevated hydrogen concentrations are often one of the causes of destruction. Saturation with hydrogen from the outside ultimately leads to hydrogen brittleness.

Accumulation of hydrogen in the destruction zone occurs both by ingress from outside and by redistribution of natural hydrogen inside the material.

For practically all the structural materials, natural hydrogen concentrations are as low as decimal ppm fractions to ppm units, and there have been very few studies of their effect on the mechanical properties.

It is known that the hydrogen inside the materials, is located in traps with different binding energies. In steels the total hydrogen content is 0.1-6 n.sm^3/100g, while it is only hydrogen with a low binding energy that affects the strength, i.e. diffusively mobile hydrogen. In aluminum alloys the entire hydrogen diluted in the metal has a low binding energy - about 0.2-0.8 eV. The concentrations that are critical for the mechanical strength of weakly bound hydrogen in steels and aluminum alloys are similar - they are decimal ppm fractions. In aluminum alloys it includes the entire diluted hydrogen, while in steels it is up to 5-10% of the total amount of diluted hydrogen.

Measuring such low hydrogen concentrations for the sample mass of 1-3 g presents a scientific and engineering problem. Therefore, as a rule all the information on the connection between hydrogen concentrations and the mechanical state of the metals was obtained after preliminary saturation of the samples with hydrogen. Saturation from the outside results in a disturbance of the natural picture of hydrogen distribution in accordance with binding energies, and thus the laws established experimentally do not always work in case of usual mechanical loading.

We have developed a precision analyzer (AV-1) that allows accurate measuring of the natural concentrations. The sensitivity of the analyzer is such that it is possible to measure the amount of hydrogen in the traps whose volume is several thousand times lower than the total amount of hydrogen extracted from the sample.

The method of high-temperature vacuum extraction using analyzer AV-1 was applied for investigating the defective structure of materials subjected to fatigue failure and to destruction at uniaxial tension. When this method is applied, the sample does not heat up to a melting temperature; consequently “natural” hydrogen must carry the information on the status of the crystal lattice of the metal after its manufacture and operation.

The method developed for analysis of the dynamic curves of vacuum extraction enables us to determine the binding energy and the volumes of traps of various nature, and the constants of hydrogen diffusion in the sample under examination.

2 Experimental equipment

The precision hydrogen analyzer AV-1 was developed for determination of hydrogen content in metals and alloys under plant laboratory conditions and used for output control of castings from different alloys.

The analyzer operates on the mass-spectrometric principle. The sample preparation includes the application of a vacuum extractor and an oven. In the process of analysis the metal sample inside the metal extractor gradually heats up to an extraction temperature of 400-800 ^{o}C. The temperature of the analysis is below the melting temperature of the sample. The gases released at heating in vacuum are analyzed by the mass-spectrometer. The time dependence of the hydrogen flow $q(t)$ is registered by the digital registration system in the form of an extraction curve. We have developed a highly measurement complex for absolute measurement of hydrogen content in a solid sample of practically any composition.

3 Assessment of the hydrogen binding energy in metal and of diffusion constants

The high sensitivity of AV-1 and representative statistical data (about 30,000 points per curve) make it possible to see a number of maxima on the extraction curve. By the position of the maximum and by its shape, one can determine the binding energy, the diffusion constants and the cumulative volume of the flux which each peak corresponds to [2].

The highly sensitive hydrogen analyzer AV-1 utilizes the mass-spectrometric principle. The specimen preparation requires a vacuum extractor and an oven. The specimen inside the metal extractor is heated gradually up to an extraction temperature of 400-900^{o}C. The temperature needed for analysis is below the melting temperature of the specimen. The gases released at heating in vacuum are analyzed by means of the mass-spectrometer. The time-dependence of the hydrogen flux $q(t)$ registered by means of the data acquisition system yields the so-called extraction curve.

Fig. 1 shows the experimental curve for titanium alloy PT-7M. Near the peaks one can see the hydrogen binding energies that correspond to them.

Fig. 2 shows the experimental extraction curve for monocrystal silicon indicating the hydrogen binding energies that correspond to each peak.

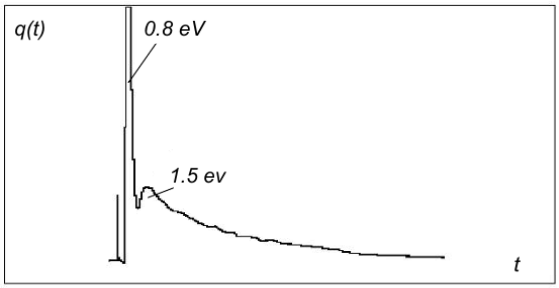


Figure 1: Extraction curve for titanium alloy PT-7M indicating the binding energies that correspond to separate peaks of the curve

As a result of numerous tests it was possible to establish that the hydrogen in metals and semiconductor materials occupies discrete energy levels. E.g., for aluminum alloys, 2-4 levels can be observed within the 0.2 to 0.8 eV range.

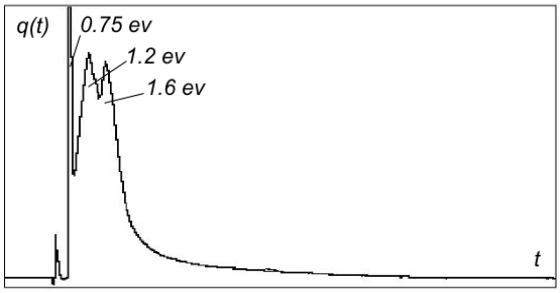


Figure 2: Extraction curve for for monocrystal silicon indicating the binding energies that correspond to separate peaks of the curve

4 Accumulation and redistribution of hydrogen in the process of operation of structural materials

Our equipment enables separating various binding energies, even those of weakly bound diffusely hydrogen, and register redistribution of hydrogen in the traps under destruction. Thus in the case of fatigue destruction the distribution of hydrogen over the binding energies in the destruction zone changes radically. The total amount of the diluted hydrogen also increases, but not so significantly.

Investigations of the hydrogen distribution were carried out on the specimens made of aluminum alloys. These specimens were subjected to cyclic uniaxial tension with the number of cycles up to 10 million. After the mechanical (fatigue) testing has been performed, small specimens from the broken and non-broken large specimens are shown in Figs.3 and 4.



Figure 3: Scheme of cutting small specimens for hydrogen testing from a large specimen broken under fatigue test

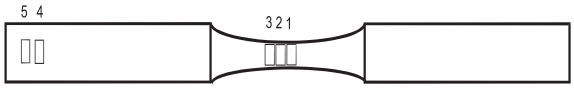


Figure 4: Scheme of cutting specimens for hydrogen testing from a large specimen non-broken under fatigue test

The growth in the hydrogen concentration with increase in the number of cycles is revealed. The hydrogen distribution over binding energy for broken end non-broken specimens is principally different. Figures 5 and 6 display the typical extraction curves for the neck of the broken and non-broken specimens.

The analysis of the experimental data shows that full concentration of hydrogen is approximately equal everywhere. In the destruction zone, practically all the hydrogen is in the diffusively mobile state and, on the contrary, it is in the strongly bound state in the zone without plastic flow

5 A two continuum model

Basic principles of the above mentioned hypothesis can be illustrated on example of analysis of the one-dimensional chain consisting of identical particles which are the point mass m_0 (the atom mass in the crystal lattice of a material). They are connected to each other by the identical nonlinear springs of the length a , cf. Figure 7.

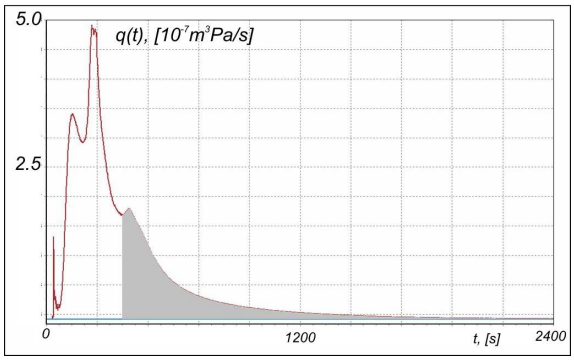


Figure 5: Extraction curve for specimen number 1 cut from broken neck

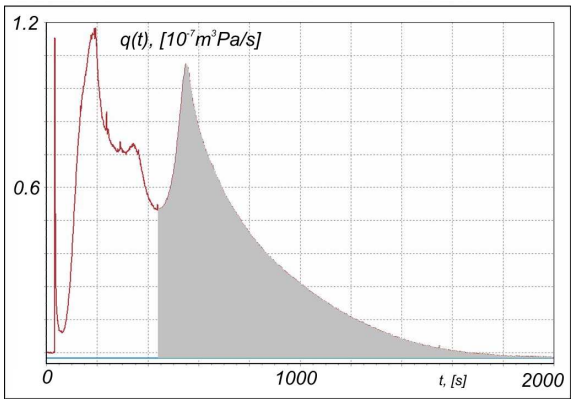


Figure 6: Extraction curve for specimen number 1 cut from non-broken neck



Figure 7: The schematics of the material model

The basic equation of the motion in the long-wave approximation is given by, cf. [3]

$$m_0\ddot{u} = -a[f(a(1+u'))]' \tag{1}$$

where a dot denotes the time derivative. As for small deformations $\varepsilon = \partial u/\partial x$ we arrive at the following equation

$$\ddot{u} - \vartheta_0^2 u'' = 0, \qquad \vartheta_0 = a\sqrt{C/m_0}$$

since $f[a(1+\varepsilon)] \approx -Ca\varepsilon = -Ca\partial u/\partial x$.

The weakening of the internuclear bonds caused by "landing" of the hydrogen particles (or other mobile internal elements of structure) can produce the chain formations of new internuclear bonds, see Figure 8, as the consecutive connections of elastic bonds of the basic lattice and the introduced elastic bonds of new elements (e.g. hydrogen particles). Obviously, such chain is possible under the assumption that the mass of particles of a mobile structure is small, i.e.$m_0 >> m_H$.

Equivalent rigidity of the new bond can be obtained from the equation

$$\frac{N_\Sigma}{C_\Sigma} = \frac{N_0}{C_0} + \frac{N_H^+}{C_H} \qquad N_\Sigma = N_0 + N_H^+$$

The constitutive equation for this medium is as follows

$$\sigma^{(1)} = E_\Sigma \varepsilon, \qquad E_\Sigma = \frac{E_0 E_H}{n_0 E_H + n^+ E_0}, \qquad n_0 = \frac{N_0}{N_\Sigma}, \qquad n^+ = \frac{N_H^+}{N_\Sigma}, \qquad n_0 + n^+ = 1.$$

Here N_Σ denotes the total number of the particles in the elementary volume, is the number of the particles connected by the weaken bonds, N_H^+ is the number of hydrogen particles attached to the lattice with the bonds of rigidity C_H. Finally, n_0, n^+ are the concentrations of the corresponding particles.

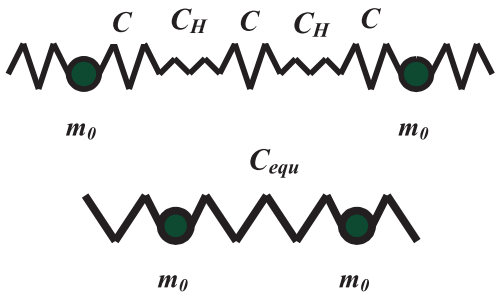


Figure 8: The model of the material with hydrogen particles

For small deformations the nonlinear force $f = f(a(1 + u'))$ in Eq. (1) can be introduced as

$$f = -C_\Sigma a \varepsilon = -E_\Sigma \varepsilon$$

The equivalent modulus of the lattice E_Σ, can be decreased essentially, since $E_H \ll E_0$ ($C_H \ll C_0$), and has a strong dependence on the concentration of the attached particles n^+.

The number of the lattice settled by the hydrogen particles depends on the stress state of the lattice at every point and, in general, on time. The unknown functional dependence of E_Σ on $n^+(\varepsilon, x, t)$ should be determined with the help of the model of two-component continuum.

The details of the theory of two-component continuum can be found in [3]; therefore we are presenting here only the final results with some necessary explanation of the processes.

From the state equation we have $\sigma = \sigma(\varepsilon, n^+(\varepsilon, x, t))$, thus,

$$\sigma = E_0 \varepsilon \left[1 - \frac{n_H^+}{n^+ + n_0 E_H E_0} \right], \tag{2}$$

and the essential dependence of the stress state on concentration of the bonded hydrogen becomes evident.

The hydrogen concentration is described by the equation for n^+

$$\frac{\partial^2 n^+}{\partial t^2} + (\alpha + \beta) \frac{\partial n^+}{\partial t} + A \cdot D(\varepsilon_{st}) \left[\beta \frac{\partial^2 n^+}{\partial x^2} + \frac{\partial^3 n^+}{\partial t \partial x^2} \right] = 0. \tag{3}$$

Here $A = C_H^2 kj$, α and β are some constants, and $D(\varepsilon_{st})$ denotes the hydrogen diffusion constant.

Equations (2) and (3) form a system for modeling the hydrogen influence on the dependence $\sigma(\varepsilon)$ for the material.

Equation (3) is of the hyperbolic type with moving front of the bound hydrogen concentration. The Fourier method assumes the substitution $n^+(t, x) = T_{n^+}(t) \cdot X_{n^+}(x)$ that yields:

$$\frac{\ddot{T}_{n^+}(t) + (\alpha + \beta)\dot{T}_{n^+}(t)}{\frac{C_H^2}{k} D(\varepsilon_{st})(\beta T_{n^+}(t) + \dot{T}_{n^+}(t))} = \frac{X''_{n^+}(x)}{X_{n^+}(x)}.$$

Equation for function$X_{n^+}(x)$ is :

$$X''_{n^+}(x) + \gamma_x^2 X_{n^+}(x) = 0.$$

Equation for function $T_{n^+}(t)$is:

$$\ddot{T}_{n^+}(t) + (\alpha + \beta + \gamma_x^2 \frac{C_H^2}{k} D(\varepsilon_{st}))\dot{T}_{n^+}(t) + \gamma_x^2 \frac{C_H^2}{k} D(\varepsilon_{st})\beta T_{n^+}(t) = 0.$$

Substituting $G(\varepsilon_{st}) = \frac{C_H^2}{k} D(\varepsilon_{st})\gamma_x^2$ we obtain:

$$\ddot{T}_{n^+}(t) + (\alpha + \beta + G(\varepsilon_{st}))\dot{T}_{n^+}(t) + G(\varepsilon_{st})\beta T_{n^+}(t) = 0.$$

This is the linear equation with floating factor$G(\varepsilon_{st}(t))$. The term $D(\varepsilon_{st})$ has the physical interpretation as powerful hydrogen diffusion channel. During the cyclic loading by harmonic force we have a harmonic deformation: $\varepsilon_{st} = \varepsilon_1 \cos(\omega t)$. As a first approximation we can take $D(\varepsilon_{st}) = D_0 + D_1 \cos(\omega t)$ and obtain the equation with cyclic coefficients

$$\ddot{T}_{n^+}(t) + (\alpha + \beta + (G_0 + G_1 \cos(\omega t)))\dot{T}_{n^+}(t) + (G_0 + G_1 \cos(\omega t))\beta T_{n^+}(t) = 0,$$

Here $\omega_0 = \sqrt{G_0 \beta} = C_H \gamma_x \sqrt{\frac{D_0 \beta}{k}}$ is the intrinsic frequency of the hydrogen redistribution. The frequency depends of total hydrogen concentration, the parameter of the volume distribution (γ_x) end energy redistribution coefficient (β). The time-dependent increasing of hydrogen concentration lead to increasing the intrinsic frequency. Hence during the fatigue loading we have $\omega_0 = 2\omega$, or

$$C_H = \frac{2\omega}{\gamma_x} \sqrt{\frac{k}{D_0 \beta}}.$$

This hydrogen concentration is critical for the parametric resonance. And we will have parametric instability that may be interpreted as dynamic hydrogen embrittlement during cyclic loading.

6 Discussion of the results

The capability of gases for dilution in metals is known [4]. In many cases the gases that do not form stable chemical compounds with alloy components are accumulated along the grain boundaries in traps of various nature.

There is a known method of examining the dislocation structure of solids by low-temperature saturation of metals with inert gases (helium, argon etc.). Upon subsequent heating of the samples up to various temperatures, the dynamics of the gas release was studied. The dislocations and the rate of dislocation density change are determined by using the dynamic curves of gas release and the extraction curves. It was experimentally discovered that adsorption of gas molecules with a very high binding energy is possible in micro-defects on the free surface of the crystal. E.g., the binding energy for chemically inert helium is about 1 eV, which is close to the chemical bond energy [5].

In many cases it is impossible to explain elevated concentrations by hydrogen diffusion from the environment as the normal hydrogen concentration in the air is 0.5 ppmv. The literature provides descriptions of two mechanisms of hydrogen accumulation – transfer by micro-defects inside the material and release of hydrogen from water at corrosion.

In our experiments we managed to study the fine structure of hydrogen bonds in metal. We studied natural concentrations and discovered that the fatigue phenomenon at uniaxial tension are accompanied by accumulation of weakly bound hydrogen. The accumulation itself can be explained by the processes of hydrogen transfer at formation of new structural micro-defects in the destruction zone. It is most probable that, at application of strains, hydrogen is bound with free surfaces thus causing weakening of the material due to a reduction of the free energy and fixation of the defects. After rupture, the tensile stresses disappear and the hydrogen is squeezed out into a weakly bound state.

We are of the opinion that the hydrogen has the discreet character of the energy levels in the solid body. Therefore each peak of the extraction curves corresponds to a different character of the hydrogen bond with the crystal lattice of the material.

If our hypotheses are true, the prevention of hydrogen diffusion inside the material serves to substantial increase its fatigue strength and the maximum deformations. The same effect can be

obtained by decreasing the gas permeability of the material surface, e.g. by designing parts with an increased surface tension or by using special coatings. The absence of hydrogen inflow from the outside will increase the service life of the part.

This fact makes it possible to use the measurement results for hydrogen concentration distribution according to binding energies not only for analysis of the causes of destruction and material quality control, but also for the development of new materials with enhanced mechanical characteristics.

Application of the methods developed to non-metallic material opens yet another application area of hydrogen diagnostics.

The two continuum model provides us with the ability to determine the critical hydrogen concentration from one of the hydrogen embrittlement sets in [3]. We apply this model to fatigue test and also obtain the critical concentration for dynamic hydrogen embrittlement. The linear approximation makes impossible to model of the hydrogen content with increasing trend, because the eigenfunctions are orthogonal. But we can determine the beginning of the destruction process - the point of instability.

We need for nonlinear approximation for the modeling of the hydrogen accumulation during fatigue test.

It is very important that the intrinsic frequency $\omega_0 = C_H \gamma_x \sqrt{\frac{D_0 \beta}{k}}$ is small, because $C_H << 1$. But fatigue loading frequency is also small (often $\omega << 1$). Thus the frequencies coincidence during real fatigue loading is very probable.

7 Conclusions

We have developed the equipment that makes it possible to obtain information on the structure of hydrogen bonds within the material according to the hydrogen extraction curve at heating a sample in vacuum. The accuracy of determination of the extraction curve makes it possible to obtain information on both the hydrogen binding energy in the metal and on the concentration of mechanical flaws.

The experiments we conducted have confirmed that the fatigue phenomena and destruction of structural materials are accompanied by increased concentration of lightly bound hydrogen in the destruction zone.

It was first detected that mechanical loads result in a substantial redistribution of hydrogen according to the binding energies inside metals.

The suggested calculation methods enable us to make approximation of the experimental extraction curves and determine the diffusion constant and the activation energy for every peak of the curve.

This approach to investigation of the properties of materials does not require preliminary saturation of the samples under study with hydrogen. Natural hydrogen within the metal carries the information on the past history of the material, which, once the methods are further developed, will make it possible to obtain more detailed information from the measured extraction curves.

The application of the two continuum model to fatigue task give the hydrogen concentration that are critical for material destruction. Such fatigue destruction has a nature of parametric instability during the cyclic redistribution of the hydrogen under the cyclic loading.

Acknowledgements

The financial support of the Sandia Corporation, contract 891092, and the Russian Foundation for Basic Research, grants 08-08-00737 and 08-01-12017, is acknowledged.

References

[1] W.S. Gorsky “Theorie des elastichen Nachwirkung in ungeordneten Mischkristallen (elastische Narchwirkung zweiter Art)”, Physikalische Zeitschrift der Sowjetunion, 8, (1935) 457-471

[2] A.M. Polyanskiy, V.A. Polyanskiy, D.B. Popov-Diumin, "Diagnostics of mechanical condition of materials by method of high-temperature hydrogen vacuum-extraction", Proceedings of the Sixth International Congress on Thermal Stresses, vol. 2, Vienna, Austria, (2005) 589-592

[3] D.A. Indeitsev, B.N. Semenov "About a model of structural-phase transformations under hydrogen influence" Acta Mechanica Vol.195, (2008) 295-304

[4] B.A. Kolachev, Hydrogen brittleness of metals, Metallurgy, Moscow, 1985.

[5] O.V. Klyavin "Dislocation dynamic diffusion in crystal bodies", FTT, v. 35, No 3, (1993) 513-541.

Vladimir Polyanskiy, St.-Petersburg State Polytechnic University, 195251 Politekhnicheskaya, 29 St.-Petersburg, Russia
Yury Yakovlev, St.-Petersburg State Polytechnic University, 195251 Politekhnicheskaya, 29 St.-Petersburg, Russia

Symbiotic cellular automata method and its application to simulation of the mechanical response of lignite

S. Zavsek A. V. Dimaki E. V. Shilko A. I. Dmitriev J. Pezdic S. G. Psakhie
dav@ispms.tsc.ru

Abstract

The method of symbiotic cellular automata, which combines two approaches to describe the simulated media - the method of classical cellular automata and method of movable cellular automata, has been developed for modeling and study of heterogeneous materials. The paper describes the developed method and the results of its verification and application to simulation of the mechanical response of coal specimens, containing the adsorbed gas, under uniaxial loading in a gas atmosphere. It is shown that the presence of adsorbed gas and the external gas atmosphere can have a significant impact on the nature of the mechanical response of lignite.

1 Introduction

Modern methods of computer-aided simulation, such as FEM, FDM, classical and movable cellular automata (MCA) [1, 2], allow the adequate description of the mechanical behavior of media in different states of aggregation. For example, to describe the mechanical behavior of solid medium there is a wide range of methods, of which the most popular is the finite element method, as well as various types of particle method. Simulation of flow of gas and liquid in various porous media and media containing the channels and cracks is carried out by means of such modern methods as LBM [3] and methods based on solving the Navier-Stokes equations on the finite-difference mesh.

However, attempts of description of the multiphase medium containing interacting solid, liquid and gaseous phases within a unified approach, met with a number of difficulties arising, in the first place, because of necessity to provide the interconnection between decisions of equations, which are simulating the behavior of each phase. Authors propose an approach to solve this problem, called the method of symbiotic cellular automata (SCA). This method is based on simple phenomenological assumptions about the character of sorption processes and the influence of contained gases on the mechanical response of coal in a seam [4]. SCA method was verified within the simulation of sorption processes in lignite [5]. There are introduced results of application of SCA method for modeling the mechanical response of samples of lignite, containing the adsorbed gas, under uniaxial loading.

2 Description of symbiotic cellular automata method

Symbiotic cellular automata method is a combination of classical cellular automata [6] and MCA [1, 2] approaches. In the framework of this method the investigated medium is considered as a superposition of two interrelated media. One of them is described by a set of movable cellular automata and another - by a mesh of classical cellular automata (Fig. 1a). In the framework of SCA method the step of calculation consists of two main substeps. First of them is the step of the MCA model. It is called “mechanical step”. At this substep motion equations of movable automata are being solved, energy dissipation due to internal friction and plastic deformation is calculated. Thus, the process of mass transfer due to mechanical loading is considered at the first substep. In the framework of the MCA method, we consider the simulated media as an ensemble of interacting finite size elements (automata).

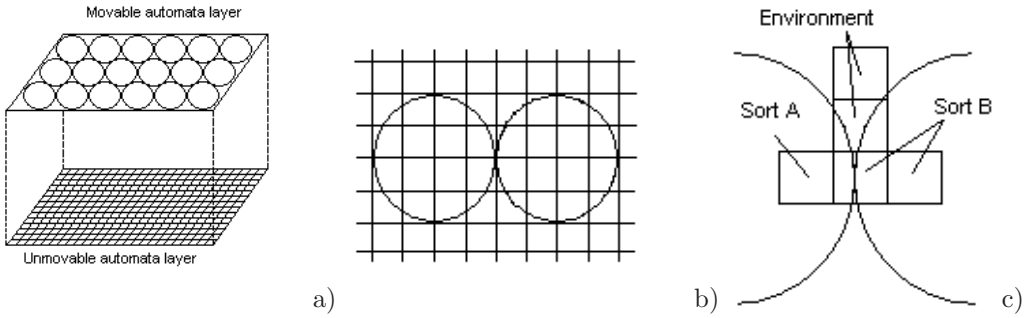


Figure 1: a) Layers of movable and classical cellular automata; b) Projection of pair of movable cellular automata to unmovable (classical) net; c) Definition of unmovable automata sort.

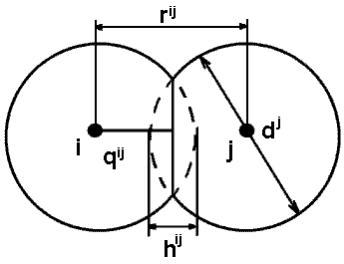


Figure 2: The overlapping parameter definition for a pair of movable automata

The concept of the MCA method is based on conventional concept of cellular automata developed by means of incorporating of some basic postulates and relations of approach of particle-based methods [7]. The movable cellular automaton is an object of finite size, possessing translational and rotational degrees of freedom. Interaction between automata is defined by normal (acting along the line connecting the mass centers) and tangential forces, each of which is the sum of the corresponding potential and the dissipative component.

Within the MCA approach a many-body interaction is used. Furthermore, a new type of states, viz., the state of a pair of automata, in comparison to conventional cellular automata method is introduced. The new type of state leads to a new parameter to define the criteria for switching of the inter-automata relationships – the automata overlapping parameters: $h_{ij}=r_{ij}-r_{oij}$ (see Fig. 2).

Here r_{ij} is the initial distance between the centers of the neighboring elements, and r_{oij} is defined as $r_{oij} = (d_i + d_j)/2$, where $d_{i(j)}$ is the automaton size. In the simplest case there are two states of the pair: linked ($h_{ij} < h_{ij}^{max}$) and unlinked ($h_{ij} > h_{ij}^{max}$). h_{ij}^{max} means some critical value defined by the solved problem. The linked state is indicative of chemical bonds between elements (one piece of material) and the unlinked state indicates that there is no chemical bond between automata (independent parts of materials).

In the simplest case the linear approximation of real complex stress-strain curve can be used to reproduce the automaton response function. Depending on the theory and simulated material properties the inter-automata interaction can be represented by response functions of different types. For example, the elastic properties of brittle materials can be described as simple linear response. In this case the loading and unloading will follow the same curve. To take into account the damage generation at a scale level lower than automaton size, the degradation response function should be used [1, 2].

Next for the mechanical – "net" substep is performed on a mesh of classical cellular automata. At this substep the process of mass transfer of gas in the pores and channels is considered, as well as the values of the forces acting on the movable cellular automata from gas phase are calculated. The configuration of pores and channels through which gas propagates, is projected to the mesh of classical cellular automata from the MCA layer (fig. 1b). This symbiotic approach combines solutions for mechanical and gas dynamic problems and allows description of multiphase heterogeneous

media.

It is necessary to note that accuracy of hybrid method depends on the relation between the size of classical automaton and movable automaton diameter (fig. 1b). With decreasing this ratio the accuracy of simulation will increase.

During simulation of response and fracture of porous solids with gases inside pores it is necessary to estimate volumes of pores and macro-cracks in the specimen. Also, it is necessary to consider the amount of gas, which is dissolved in the bulk of material. For this aim the special parameter of concentration of absorbed gases in the volume of automaton was introduced into the model.

In the present model, the Mendeleev-Klapeyron equation is applied to describe the state of gaseous phase:

$$PV = N_\mu RT, \tag{1}$$

where P is the pressure of gas, N_μ is the number of moles of gas in the volume V, T is current temperature of gas.

There are two types of sorption processes on the boundaries between solid material and closed free volumes and surroundings filled with gases: adsorption of gas on the surface of solid phase and desorption of gas into the volume of pore, crack or surroundings. These two processes are the manifestations of one complex sorption process on the inter-phase boundary.

In a very wide range of gas concentrations in solids and in the surrounding atmosphere it is possible to consider adsorption and desorption processes as independent. In the simplest case these processes are described by the following linear equations:

$$I_{ads} = \alpha_{ads}(\mu_{solid}^{\max} - \mu_{solid})\mu_{env} \tag{2}$$

– intensity of adsorption process ($[I_{ads}] = \frac{mole}{s*m^2}$),

$$I_{des} = K_{des}(\mu_{solid} - \mu_{solid}^{\min}) \tag{3}$$

– intensity of desorption process ($[I_{des}] = \frac{mole}{s*m^2}$). Here α_{ads} – is the adsorption intensity coefficient; $K_{ads(des)}$ – is the desorption coefficient, μ_{env} – is the concentration of the gas in the atmosphere; mu_{solid} – is the concentration of the gas in solid (material of the specimen); $\mu_{solid}^{\min}$ and $\mu_{solid}^{\max}$ – are the minimal and maximal possible concentrations of gas in solid, consequently.

Note that both sorption coefficients are not the constants but the functions of material and gas physical-chemical properties. It means that α_{ads} and $K_{ads(des)}$ depend on chemical affinity of molecules of gas and solid. One of the manifestations of this dependence is so-called saturated concentration of gas in the material of the specimen $\mu_{solid}^{\max}$. Coefficients $K_{ads(des)}$ are also the functions of morphology of the surface of solid. It means that intensity of sorption process strongly depends on microstructure of the surface. The third very important factor of adsorption and desorption processes is temperature T of the system.

The change of quantity of gas in the closed free volume is calculated as follows:

$$\Delta N_i^{sorp} = S\Delta t \sum_{k=1}^{N_{bound}} \left(I_k^{des} - I_k^{ads}\right), \tag{4}$$

where k – is the number of boundary cells in the volume, $\Delta\, t$ – is the time step, N_{bound} – is the number of cells at the boundary with solid. The values of sorption coefficients were obtained from the experimental data, proposed in the paper [4].

The presence of gas in the surrounding of solid-state components (or in macropores), as well as in the bulk material (discontinuities in the structure, taken into the accounted implicitly), leads to appearance of additional forces acting on the solid surface and causing the growth of internal stresses in the bulk of material. There is the following method of calculating the influence of gas pressure in the "macropores" on the response of movable cellular automata. In the simplest approximation it is believed, as that the pressure of surrounding gas to the surface (or part of the surface) of movable automaton is applied normally to it, as this pressure leads only to translation motion of movable automaton. In this case the equation, describing the translational dynamics of movable cellular automata, can be written as:

$$\frac{d^2\vec{R}_k}{dt^2} = \frac{1}{m_k}\left[\sum_l \left(\vec{F}_{norm}^{kl} + \vec{F}_{\tan g}^{kl}\right) + \vec{F}_k^{gas}\right], \tag{5}$$

Here the indices k and l enumerate the movable automata, and $\vec{F}_k^{gas}$ – is the total force, acting from the surrounding gas, applied to the center of mass of movable automaton:

$$\vec{F}_k^{gas} = S \sum_{a=1}^{N_k^{surf}} \sum_{b=1}^{N_a^{gas}} P_b \vec{n}_{ba}, \tag{6}$$

where the index a enumerates the "surface" classical cellular automata, which "are belonging" to k-th movable automaton (N_k^{surf} is – the number of such CCA), the index b enumerates the CCA, which are bordering with "surface" a-th MCA, and are parts of macropores (N_a^{gas} – number of such CCA; in case of a square packing $N_a^{gas} \leq 3$), P_b – gas pressure in the volume of the CCA b; $\vec{n}_{ba}$ – a unit vector directed perpendicular to the square, separating the automata b and a, in the direction of the automaton a (inside the movable cellular automaton), S – "contact square" of CCA.

In addition, the external (from the macropores) and internal (from the micropores) gas pressure leads to a change in stress state of movable cellular automata. In the framework of the formalism of calculation of the potential interaction of movable cellular automata such effects can be considered by means of modifying the expression for the medium stress in the pair of k-th and l-th movable automata:

$$\begin{cases} \sigma_y^{kl} = \sigma_{kl} \\ \sigma_x^{kl} = \frac{\sum_{m \neq l} \sigma_{km} |\cos(\alpha_{kl,km})|}{T_x} - \frac{S \sum_{a=1}^{N_k^{surf}} \sum_{b=1}^{N_a^{gas}} P_b \vec{n}_{ba} \left|\cos\left(\beta_{kl,\vec{n}_{ba}}\right)\right|}{T_x S_0^{kl}} \\ \sigma_{mean}^{kl} = \frac{\sigma_x^{kl} + \sigma_y^{kl}}{3} + P_{gas}^k \end{cases} . \tag{7}$$

Here the second term on the right side of the expression for σ_x^{kl} – is the contribution of pressure from the macropores, ($\beta_{kl,\vec{n}_{ba}}$ – angle between the direction of the unit vector $\vec{n}_{ba}$ and the X-axis of local coordinate system in a k-l-th pair of MCA with the origin at the center of mass of the k-th MCA), and the term P_{gas}^k the expression for σ_{mean}^{kl} is the contribution of the gas pressure in internal porosity in the volume of k-th MCA. In the simplest case, when the porosity of the solid material is small, and the characteristic pore sizes are much smaller than the average distance between them, the linear approximation of value P_{gas}^k can be defined as:

$$P_{gas}^k = P_{pores}^k \nu_k, \tag{8}$$

where P_{pores}^k – is pore pressure in the volume of a k-th MCA, νk – porosity of the material.

3 Simulation of fracture of detritus in the atmosphere of carbon dioxide

To demonstrate the possibilities of SCA method and its applicability for describing the "porous solid – gas" media, a series of calculations were made. In these calculations the effect of the gas phase (CO_2) on the mechanical response and the failure of the samples of fine detritus was studied. Mechanical properties of fine detritus and xylite inclusions were used as given in [4].

The response and failure of fine detritus under uniaxial compression of CO_2 in the atmosphere and in vacuum were simulated. Size of specimens was 5x10 cm, loading rate was $V = 0.02$ m/sec. Volume concentration of CO_2 in fine detritus and xylite was set equal to the characteristic values in coal seams under the lateral pressure 42 bar [8].

Fig. 3 presents the results of simulation, reflecting the evolution of the structure of inter-automata links for the both considered cases. Typically, the behavior of the simulated samples at initial stage of loading is identical. Place of birth of fractures is an area of the interface between the xylite inclusions and fine detritus matrix.

According to fig. 3, failures occur at approximately the same values of strain $\sim 1.20\%$. With the occurrence of the first damages in the structure of the samples, differences in the further evolution are being observed. In the lower left corner of the specimen the crack is formed. However, if in the absence of gaseous atmosphere, this happens when the strain is 1.23%, then in the presence

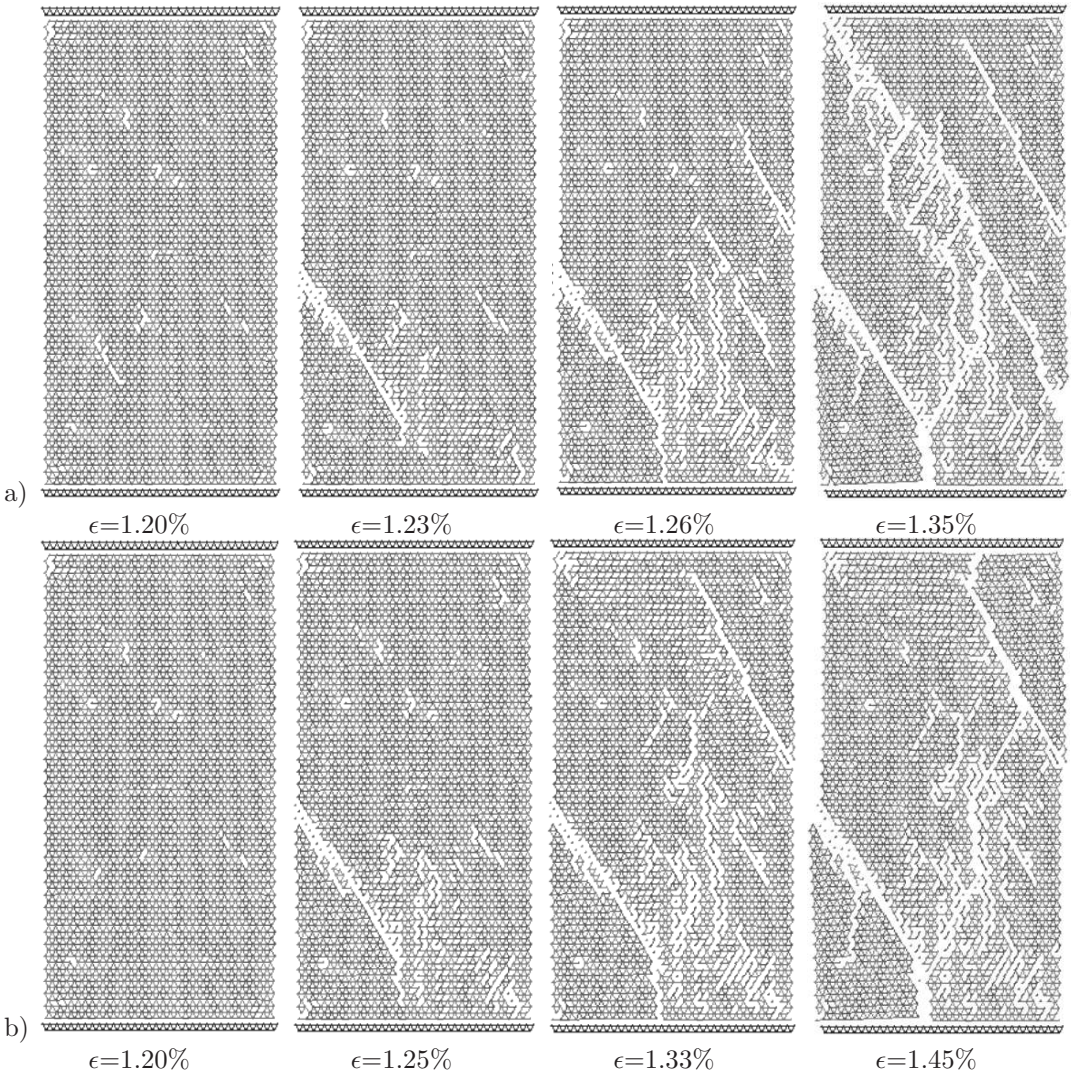


Figure 3: Stages of the fracture of model specimen of fine detritus in the atmosphere of CO_2 at different pressures P_{gas}: a) $P_{gas} = 0$ bar; b) $P_{gas} = P_{atm} = 1$ bar .

of the gas atmosphere the crack is formed within the deformation of 1.25%. Furthermore, this difference only increases. Approximately identical pictures with cracks can be identified with the deformations of 1.26% in the absence of gas atmosphere and of 1.33% in the presence of an atmosphere of CO_2.

Complete destruction of the sample in vacuum occurs by means of the formation of a cross-cutting diagonal macrocrack. This corresponds to a deformation of $\sim 1.35\%$. The destruction of the sample in Fig. 3b occurs by the formation of vertical cracks, which occur at the deformation of 1.45%. Also, many inter-automata links are broken in the upper part of the sample.

Thus, little increasing of surrounding atmosphere pressure from 0 to 1 bar resulted in an increase of strength and ultimate strain of specimens at 2–5% without a noticeable change in Young's modulus. Also, the fracture pattern of specimens has undergone some changes. The results suggest that even relatively low atmospheric pressure is able to exert some influence on the response and the fracture of materials having relatively low strength.

4 Discussion and conclusions

The approach, describing the behavior of two-phase medium under external influence, is proposed. This approach, called as SCA method, represents the combination of methods of classical and movable cellular automata.

Verification of this approach was carried out by means of comparison of the results of modeling of the samples of fine detritus in the CO_2 atmosphere with the results of experimental studies performed by researchers of Velenje coal mine (Geological Faculty, University of Slovenia) [8]. These results demonstrate a qualitative agreement between model and experimental data. It is proposed to use the SCA method to describe the mechanical response of coals with direct taking into the account the influence of high-pressure gas atmosphere, as well as sorption processes.

It is clear that the proposed approach does not cover the entire spectrum of processes in such a complex system like a multiphase heterogeneous medium. In particular, the proposed model does not take into account the filtration processes, the phase transitions etc. In addition, since the simulated physical processes have different (several orders of magnitude) characteristic times, within the framework of the proposed approach it is possible to simulate only the first few seconds. Furthermore, we use a 2D approximation of the simulated object. Of course, this restriction greatly influences the outcome of the investigated problem.

Nevertheless, proper selection of model parameters allows obtaining good agreement with the results of natural experiments. This demonstrates the correct formulation of the problem and qualitatively correct description of the basic processes occurring in the system.

Further directions of development of the method are the introduction to the model the state equation for non-ideal gas, which is important for realistic CO_2 simulation, as well as the possibility of modeling filtration processes in porous solid body.

References

[1] Psakhie, S.G. etc. // Phys. mesomech, 1998, 1 (2), 89-94.

[2] Psakhie, S.G. etc. // Theor. Appl. Fract. Mech., 2001, 37, 311-334.

[3] Sukop, M.C. and Daniel T.T.J. Lattice Boltzmann Modeling: An Introduction for Geoscientists and Engineers. Springer, 2007. - 172 P.

[4] Zavsek, S. etc. // Proc. Int. Conf. on New Challenges in Mesomech., 2002., pp. 19-25.

[5] Zavsek, S. etc. // 11th Int. Conf. on Fracture, 2005, March 20-25, 4502/1-4502/6.

[6] Wolfram, S. Theory and applications of cellular automata. - New Jersey: World Scientific, 1986. - 560 p.

[7] Psakhe, S.G. etc. // Pisma v zhurnal tekhnicheskoi fiziki, 1995, 21 (20), 72-76.

[8] Pezdic, J. etc // RMZ - Materials and Geoenvironment, 1999, 46 (3) - PP. 555-568.

Simon Zavsek, Velenje Coal Mine, Partizanska 78, 3320 Velenje, Slovenia
Andrey V. Dimaki, ISPMS SB RAS, Akademicheskii av. 2/4, Tomsk, Russia, 634021
Evgeny V. Shilko, ISPMS SB RAS, Akademicheskii av. 2/4, Tomsk, Russia, 634021
Andrey I. Dmitriev, ISPMS SB RAS, Akademicheskii av. 2/4, Tomsk, Russia, 634021
Joze Pezdic, Velenje Coal Mine, Partizanska 78, 3320 Velenje, Slovenia
Sergey G. Psakhie, ISPMS SB RAS, Akademicheskii av. 2/4, Tomsk, Russia, 634021

The theory of continuous medium with free rotation without coupled stresses.

E. Zdanchuk V. Lalin
zelizaveta@yandex.ru

Abstract

New continuous medium classification has been suggested in the paper "On continuous medium classification. New models in structural mechanics" by Lalin V.V. As a result, new class of continuous medium models was found out. We called it "medium without coupled stresses with free rotation". Basic equations for linear free rotation medium without coupled stresses are presented. New effect in infinite linear elastic space has been found out: the existence of angles of rotation harmonic oscillations.

Continuous mediums classification was suggested in the paper [1]. It is based on two criteria, there are kinematic and force criterions.

By force criterion all continuous mediums are divided into two classes: with- or without coupled stresses. Coupled stress tensor $\underline{\underline{M}}$ may be differ from zero in mediums with coupled stresses ($\underline{\underline{M}} \neq 0$). There is no coupled stress tensor in mediums without coupled stresses ($\underline{\underline{M}} = 0$).

By kinematic criterion all continuous mediums are divided into two classes: with or without free rotation.

Equality $\underline{\omega} = \frac{1}{2} rot \underline{\nu}$ is satisfied in a medium without free rotation, where $\underline{\nu}$ is a linear velocity, $\underline{\omega}$ - angular velocity. In this medium particles have three degrees of freedom and no rotary inertia.

Linear and angle velocity are independent in medium with free rotation. There is inequality $\underline{\omega} \neq \frac{1}{2} rot \underline{\nu}$ in this type of mediums.In this medium particles have six degrees of freedom. It is needed to take account of rotary inertia in dynamic problems in this mediums.

Note, that equality $\underline{\nu} = \dot{\underline{u}}$, $\underline{\omega} = \dot{\underline{\varphi}}$ is satisfied in geometrically linear problems, where $\underline{u}$ is a displacement vector, $\underline{\varphi}$ is a vector of infinitesimal rotation (the point marks derivative with respect to time). That's why $\underline{\varphi} = \frac{1}{2} rot \underline{u}$ can be kinematic criterion in medium without free rotation in geometrically linear problems.

The combination of criteria gives us 4 classes of all continuous mediums. (tab 1).

Table 1

	without free rotation	with free rotation
without coupled stresses	I $\underline{\underline{M}} = 0$ $\underline{\omega} = \frac{1}{2} rot \underline{\nu}$	II $\underline{\underline{M}} = 0$ $\underline{\omega} \neq \frac{1}{2} rot \underline{\nu}$
with coupled stresses	III $\underline{\underline{M}} \neq 0$ $\underline{\omega} = \frac{1}{2} rot \underline{\nu}$	IV $\underline{\underline{M}} \neq 0$ $\underline{\omega} \neq \frac{1}{2} rot \underline{\nu}$

For example we consider these classes for one- and three-dimensional elastic mediums.

The class IV is an ordinary coupled theory of elasticity [2]. The class III ia a coupled theory of elasticity without free rotation, sometimes it's called a Kossera's pseudocontinuum [2]. The class I is a classic theory of elasticity[3].

The class II is a new class of continuous mediums. It is with free rotation and without coupled stresses. In these mediums coupled stresses are equal to zero, displacements and rotations are independent.It is needed to take account of rotary inertia in dynamic problems of this mediums. As it will be seen from later on static problem for these mediums is equal to static problem for a classic theory of elasticity from class I, if volumetric distributed moment loads are equal to zero. That's why researchers took no notice of existence of this class II.

For one-dimensional mediums class IV is the Timoshenko's beam.[4] (this model takes into account transverse shear deformations). The class III is a classic Bernoulli-Euler's beam [4]. The class I is a classic thread[5]. The class II is a new model of a thread.There are no bending moments, but cross forces are unequal to zero[1]; if volumetric distributed moment loads are equal to zero, static problem for the class II is equal to static problem for a classic thread.

Linear problems aren't researched in class II, because it is a new class. In this paper we present basic equations for linear medium from class II. Also wave motions in isotropic space are researched.

Let us define that ρ is a volume density, $\underline{\underline{J}}$ is a volume density of inertia tensor, $\underline{r}$ is a radius-vector, V is a volume, S is a surface limiting volume V, $\underline{f}$ is a volumetric load, $\underline{n}$ is a vector of unit outer normal to surface S, $\underline{\underline{I}}$ is a unit tensor, $\underline{\underline{\tau}}$ is a nonsymmetric stress tensor,

$$\underline{\underline{\tau}} = \underline{\underline{\sigma}} + \underline{T} \times \underline{\underline{I}}, \tag{1}$$

$\underline{\underline{\sigma}}$ is a symmetric part of the tensor $\underline{\underline{\tau}}$, $\underline{T}$ is a vector determining antisymmetric part of the tensor $\underline{\underline{\tau}}$, $\underline{\underline{\tau}}_x$-is a vector invariant of the tensor $\underline{\underline{\tau}}$

$$\underline{\underline{\tau}}_x = -2\underline{T} \tag{2}$$

— follows from (1), ∇ is a Hamilton operator [3], $\nabla \underline{u}$ is a displacement vector's gradient,

$$\nabla \underline{u} = \underline{\underline{\varepsilon}} - \underline{\Omega} \times \underline{\underline{I}}, \tag{3}$$

$\underline{\underline{\varepsilon}} = \frac{1}{2}(\nabla \underline{u} + \nabla \underline{u}^T)$ is a symmetric strain tensor, $\underline{\Omega} = \frac{1}{2} rot \underline{u}$ is a vector determining antisymmetric part of the tensor $\nabla \underline{u}$, $\underline{\gamma} = 2(\underline{\varphi} - \underline{\Omega}) = 2\varphi - rot\underline{u}$ is a deformation vector fits vector $\underline{\mathrm{T}}$.

From the momentum balancing equation

$$\frac{d}{dt}\int_V \rho \dot{\underline{u}} dV = \int_V \underline{f} dV + \int_S \underline{n} \cdot \cdot \underline{\underline{\tau}} dS$$

we derive first motion equation:

$$\nabla \cdot \underline{\underline{\tau}} + \underline{f} = \rho \ddot{\underline{u}}. \tag{4}$$

From the kinetic moment balancing equation (we think that volumetric and surface distributed moment loads are equal to zero)

$$\frac{d}{dt}\int_V (\underline{r} \times \rho \dot{\underline{u}} + \underline{\underline{J}} \cdot \dot{\underline{\varphi}}) dV = \int_V \underline{r} \times \underline{f} dV + \int_S \underline{r} \times \underline{n} \cdot \underline{\underline{\tau}} dS$$

using (4) we can get second motion equation:

$$\underline{\underline{\tau}}_x = \underline{\underline{J}} \cdot \ddot{\underline{\varphi}}. \tag{5}$$

We can write motion equation, with the help of (1) :

$$\nabla \cdot \underline{\underline{\sigma}} + \nabla \times \underline{T} + \underline{f} = \rho \ddot{\underline{u}} \tag{6}$$

$$-2\underline{T} = \underline{\underline{J}} \cdot \ddot{\underline{\varphi}}.$$

From the energy balancing equation:

$$\frac{d}{dt}\int_V (\frac{1}{2}\rho \dot{\underline{u}}^2 + \frac{1}{2}\dot{\underline{\varphi}} \cdot \underline{\underline{J}} \cdot \dot{\underline{\varphi}} + \Pi) dV = \int_V \underline{f} \cdot \dot{\underline{u}} dV + \int_S \underline{n} \cdot \underline{\underline{\tau}} \cdot \dot{\underline{u}} dS$$

where Π is a strain energy volume density,using motion equation we can get:

$$\dot{\Pi} = \underline{\underline{\tau}}^T \cdot \cdot \nabla \dot{\underline{u}} - \underline{\underline{\tau}}_x \cdot \dot{\underline{\varphi}}. \tag{7}$$

By putting (3) in (7), we get

$$\dot{\Pi} = \underline{\underline{\sigma}} \cdot \cdot \dot{\underline{\underline{\varepsilon}}} + \underline{T} \cdot \dot{\underline{\gamma}}, \tag{8}$$

where

$$\dot{\underline{\underline{\varepsilon}}} = \frac{1}{2}(\nabla\dot{\underline{u}} + \nabla\dot{\underline{u}}^T) \tag{9}$$

$$\dot{\underline{\gamma}} = 2(\dot{\underline{\varphi}} - \dot{\Omega}).$$

In linear problems deformation's expressions follow from (9):

$$\underline{\underline{\varepsilon}} = \frac{1}{2}(\nabla\underline{u} + \nabla\underline{u}^T) \tag{10}$$

$$\underline{\gamma} = 2(\underline{\varphi} - \underline{\Omega})$$

A strain energy depends only from deformations in elastic solid: $\Pi = \Pi(\varepsilon, \gamma)$, then

$$\dot{\Pi} = \frac{\partial\Pi}{\partial\underline{\underline{\varepsilon}}} \cdot\cdot\, \dot{\underline{\underline{\varepsilon}}} + \frac{\partial\Pi}{\partial\underline{\gamma}} \cdot \dot{\underline{\gamma}} \tag{11}$$

We substitute (11) in (8) and get equations:

$$\underline{\underline{\sigma}} = \frac{\partial\Pi}{\partial\underline{\underline{\varepsilon}}}; \tag{12}$$

$$\underline{T} = \frac{\partial\Pi}{\partial\underline{\gamma}}.$$

For isotropic body Hooke law is derived from (12) for symmetric stress tensor $\underline{\underline{\sigma}}$

$$\underline{\underline{\sigma}} = 2\mu\underline{\underline{\varepsilon}} + \lambda\underline{\underline{I}}tr\underline{\underline{\varepsilon}} \tag{13}$$

For vector $\underline{T}$:

$$\underline{T} = \alpha\underline{\gamma} \tag{14}$$

where λ, μ are Lame constants, α is an additional elastic constant.

Thereby, total system of equations of our medium is:

$$\nabla \cdot \underline{\underline{\sigma}} + \nabla \times \underline{T} + \underline{f} = \rho\underline{\ddot{u}} \tag{15}$$

$$-2\underline{T} = \underline{\underline{J}} \cdot \underline{\ddot{\varphi}}$$

$$\underline{\underline{\varepsilon}} = \frac{1}{2}(\nabla\underline{u} + \nabla\underline{u}^T)$$

$$\underline{\gamma} = 2(\underline{\varphi} - \underline{\Omega})$$

$$\underline{\underline{\sigma}} = 2\mu\underline{\underline{\varepsilon}} + \lambda\underline{\underline{I}}tr\underline{\underline{\varepsilon}}$$

$$\underline{T} = \alpha\underline{\gamma}$$

In static problems $\ddot{u} = 0; \ddot{\varphi} = 0$, so $\underline{T} = 0$, so $\underline{\gamma} = 0$ and system of equations (15) puts on

$$\nabla \cdot \underline{\underline{\sigma}} + \underline{f} = 0$$

$$\underline{\underline{\varepsilon}} = \frac{1}{2}(\nabla\underline{u} + \nabla\underline{u}^T)$$

$$\underline{\underline{\sigma}} = 2\mu\underline{\underline{\varepsilon}} + \lambda\underline{\underline{I}}tr\underline{\underline{\varepsilon}},$$

that is the system of equations of classic elasticity theory.

Lets prove a uniqueness of the theorem of problem (15): Only one function $u(x,t)$ and $\varphi(x,t)$ can exist in volume V and $t \geq 0$ that satisfied equations (15) and initial and boundary conditions:

$$\underline{u} = u_0 \text{ on the } S_1 \tag{16}$$

$$n\underline{\underline{T}} = p \text{ on the } S_2$$

$$\underline{u}|_{t=0} = u^*(x,y,z)$$

$$\frac{\partial \underline{u}}{\partial t}|_{t=0} = \upsilon^*(x,y,z)$$

Let there exist two solutions of this problem:

$$u_1(x,t), \varphi_1(x,t)$$

$$u_2(x,t), \varphi_2(x,t)$$

Consider $u(x,t) = u_1(x,t) - u_2(x,t), \varphi(x,t) = \varphi_1(x,t) - \varphi_2(x,t)$. Clearly functions u, φ satisfy the homogeneous equations (15) and homogeneous conditions (16). We'll prove that $\underline{u} \equiv 0; \underline{\varphi} \equiv 0$.

Consider $E(t) = \frac{1}{2}\int_V (\underline{\underline{\sigma}} \cdot \cdot \underline{\underline{\varepsilon}} + \underline{T} \cdot \underline{\gamma} + \rho \underline{\dot{U}^2} + J\dot{\underline{\varphi}})dV$, we will show that it isn't depend on t. Physical meaning of the $E(t)$ is total medium's energy. We calculate $\frac{dE}{dt}$ and obtain by integrating by parts:

$$\frac{dE}{dt} = \int_V -(\nabla \cdot \underline{\underline{\sigma}}) \cdot \underline{\dot{U}} dV + \int_S \underline{n} \cdot \underline{\underline{\sigma}} \cdot \underline{\dot{u}} dS + \int_V \underline{T} \cdot 2\underline{\dot{\varphi}} dV$$
$$- \int_V (\nabla \times \underline{T})\underline{\dot{u}} dV - \int_S \underline{n} \cdot \underline{\underline{\sigma}} \cdot \underline{\dot{u}} dS + \int_V \rho \underline{\dot{u}\ddot{u}} dV + \int_V J\underline{\dot{\varphi}\ddot{\varphi}} dV$$

Using homogeneous boundary conditions and equations (15) we get $\dot{E} = 0$. Using homogeneous initial conditions we get $E = 0$.

$$\nabla \underline{u} = 0, \quad \underline{\dot{u}} = 0, \quad \nabla \underline{\varphi} = 0, \quad \underline{\dot{\varphi}} = 0,$$

because E depend on $\nabla \underline{u}, \nabla \underline{\varphi}, \underline{\dot{u}}, \underline{\dot{\varphi}}$ quadratically.

So $\underline{u} = const; \underline{\varphi} = const$. Using homogeneous initial conditions we get $\underline{u} \equiv 0; \underline{\varphi} \equiv 0$, q.e.d.

From system (15) we get motion equations expressed in $\underline{u}, \underline{\varphi}$.

$$\mu \triangle \underline{u} + (\lambda + \mu)\nabla\nabla \cdot \underline{u} - \alpha\ rotrot\underline{u} + 2\alpha\ rot\underline{\varphi} = \rho\underline{\ddot{u}} \tag{17}$$

$$2\alpha(rot\underline{u} - 2\underline{\varphi}) = J\underline{\ddot{\varphi}},$$

where the inertia tensor is the spherical tensor: $\underline{\underline{J}} = J\underline{\underline{I}}$, $\triangle = \nabla \cdot \nabla$ is the Laplace operator.

Using divergence operator to the first equation from (16) we get

$$(\lambda + 2\mu)\triangle\theta = \rho\ddot{\theta}, \tag{18}$$

where $\theta = \nabla \cdot \underline{u} = tr\underline{\underline{\varepsilon}}$ is a volume strain.

The equation (17) is equal to the wave equation for a volume strain in classic elasticity theory [2]. So velocity of expansion and compression waves in our theory is equal to velocity in classic elasticity theory.

Using divergence operator to the second equation from (15) we get

$$-4\alpha\Phi = J\ddot{\Phi}, \tag{19}$$

where $\Phi = \nabla \cdot \underline{\varphi}$.

Expression (19) isn't the wave equation, it's the harmonic oscillations equation.

So there is a new effect in continuous medium with free rotation without coupled stresses.That is internal harmonic oscillations of Φ with frequency $\omega = \sqrt{\frac{J}{4\alpha}}$, and medium's points displacements can be equal to zero.

References

[1] Lalin V.V..On continuous medium classification. New models in structural mechanics. VII international conference “Problems of solid strength and transport constructions”, PGUPS, Saint Petersburg, 2008.

[2] Nowacki W..Theory of Asymmetric Elasticity.Oxford.New-York.Toronto et al.:Pergamon Press,1986.

[3] Lurie A.I..Theory of Elasticity.Berlin,Springer 2005

[4] Jilin P.A..Applied mechanics.Theory of thin elastic bars.Polytechnical University.Saint Petersburg,2007

[5] Merkin D.R..Mechanics of thread.“Nauka”.Moskow,1981

Elizaveta Zdanchuk, Polytechnicheskaya str. 29, Saint Petersburg. Russia
Vladimir Lalin, Polytechnicheskaya str. 29, Saint Petersburg. Russia

Dynamics of snap-through of bi-stable composite plates

A. F. Arrieta† S. A. Neild* D. J. Wagg* P. Hagedorn†
andres.arrieta@dyn.tu-darmstadt.de

Abstract

Multi-stable composites are a new type of composites considered for adaptive structures applications due to its ability to attain two statically stable configurations. Most of the research carried out on this composite material has focused on studying and modelling the static properties of bi-stable composites using low order models and finite element techniques. However, the operational conditions for real applications incorporating bi-stable, or in general multi-stable, composites would include dynamic loads. Yet, few studies have addressed the dynamic response of bi-stable composites.

In this paper a low order model to capture the main dynamic features of the snap-through instability triggered by dynamic loads for a bi-stable composite plate with unrestricted boundaries is presented. Experiments are conducted revealing complex oscillations when constant snap-through between stable states occurs. Numerical simulations are compared to experimental results showing good agreement. In particular, the model captures complex oscillations exhibiting similar evidence of a chaotic response for high levels of forcing.

1 Introduction

Adaptive structures are novel engineering structures capable of adjusting their properties to enhance performance. In particular, structures capable of adaptive their shape to operate optimally in different environments, known as morphing structures, have received much attention in the past two decades. Curved composite laminates exhibiting multiple statically stable shapes are a promising advance of this type of technologies [1, 2]. In the context of multi-stable composites, bi-stable laminates have been the main subject of the research for morphing structures due to their manufacturing ease. The bi-stability results from asymmetric residual thermal stresses induced during the curing process due to an unsymmetric stacking sequence [3]. The transition between the stable states is achieved by a snap-through mechanism which is strongly nonlinear in nature [4]. Most studies on bi-stable composites have focused on achieving configuration change, i.e. snap-through, under static loadings [5]. However, these structures will inevitably be exposed to high levels of dynamic excitation. Thus the dynamic response needs to be addressed, particularly excitations that could trigger snap-through. Yet, very little work on the dynamics of bi-stable composites has been carried out. The nonlinear dynamics around a single stable shape of a bi-stable composite plate were extensively studied in [6]. A simple model capturing the complex nonlinear dynamics associated to subharmonic resonances was developed. However, cross-well oscillations and snap-through dynamics were not on the scope of this work. Simple single degree-of-freedom models describing the dynamics of a square bi-stable plate have been presented [7, 8]. Qualitative agreement was achieved and evidence of complex dynamics for oscillations involving snap-through were shown. However, dynamic oscillations triggering snap-through were not studied in detail.

The purpose of this paper is to study the dynamics of snap-through for a bi-stable plate. A simple model including piece-wise defined restoring forces in the nonlinear modal equations developed in Ref. [6] is presented to account for oscillations including snap-through. A square bi-stable carbon-fiber epoxy $[0_4 - 90_4]_T$ plate is used as experimental specimen. Experiments are performed investigating the features of dynamically induce snap-through. A condition defining the onset of the snap-through instability is introduced. Strong nonlinear oscillations showing characteristics of chaotic behaviour are observed for steady state constant snap-through between stable states. Numerical simulations for dynamically triggered snap-through are obtained and

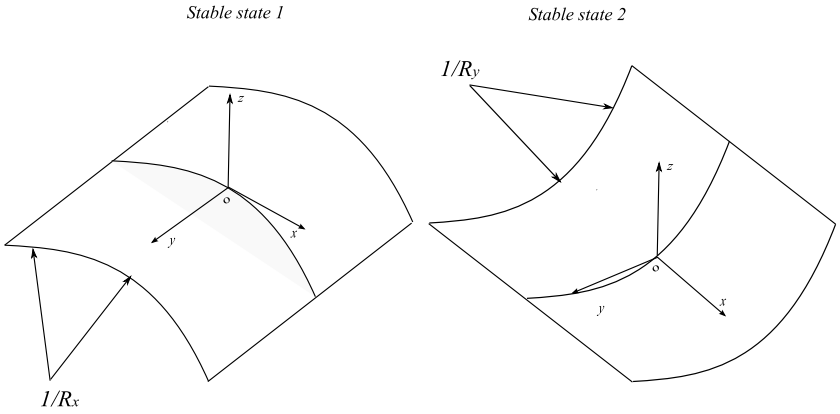


Figure 1: Statically stable figures of a bi-stable composite.

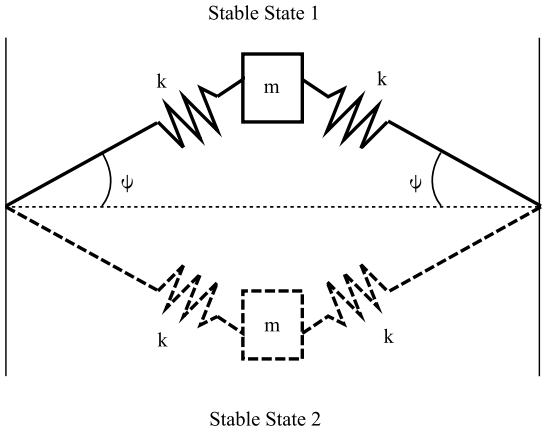


Figure 2: Double-hinge mechanism to model snap-through.

compared to experimental results showing good agreement. In particular, the model captured the experimentally observed features indicating chaotic behavior for constant snap-through.

2 Bi-stable composites and snap-through

Bi-stable composites are a class of curved composites capable of attaining two statically stable shapes. A schematic diagram of the stable configurations of a bi-stable composite plate is shown in Fig. 1. Ideally a bi-stable square plate will exhibit equal curvatures in each of its stable states, this means that each stable configuration would exhibit equal radii of curvature. The curvature direction for each state is orthogonal to the other as can be seen in Fig. 1. This property is defined as a perfect orthogonal symmetry between the stable configurations of the plate.

The change between stable states is achieved as by jump phenomenon known as snap-through. The snap-through mechanism is a sudden event where the structure undergoes large amplitude displacements. This mechanism is been conceptually studied using the model schematically presented in Fig. 2. The basic idea of this model is that the dynamic response of a system that can undergo a snap-through is only affected by it when a *critical displacement* is reached triggering the instability. Based on this, we assume that the oscillations confined to one stable state are unaffected by the presence of the second stable configuration. Only when a critical displacement is reached, the snap-through mechanism plays a part in the dynamic response. This deflection threshold is fairly straight forward to define for a lumped mass system such as the one shown in Fig. 2. This is not the case for a continuum such as the bi-stable composites we are dealing with, as each point on the plate undergoes a different displacement when a snap-through is triggered. However, it is assumed that the deflection shape of the bi-stable plate may be modelled with linear mode shapes,

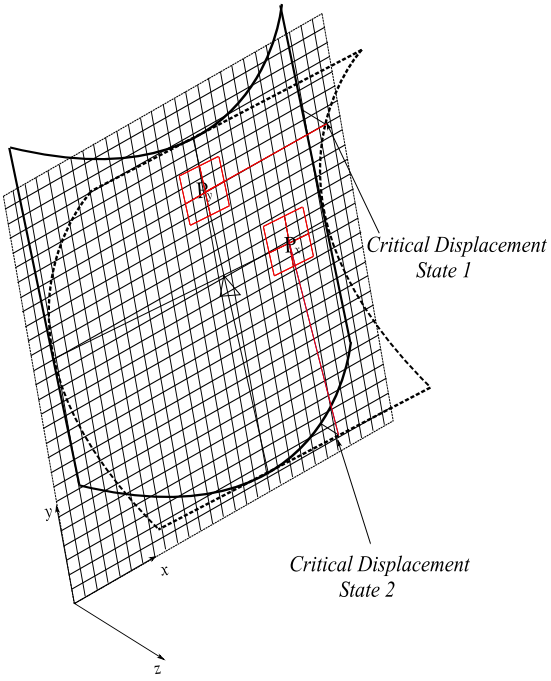


Figure 3: Critical displacement for a bi-stable composite. The critical displacement for point P_x is 5 mm, P_y this value is 1.5 mm.

therefore the relative deflection at any instant of the forcing period between points on the plate remains proportional. As a result, once a point reaches its critical displacement a snap-through is triggered as all the points in the plate must have also reached their particular threshold due to the proportionality relation. This provides a simple condition to define the forcing level required to trigger the instability. In view of this, we assume that the critical displacement for a point on the plate is given by the static deflection required to reach the flat unstable configuration as illustrated in Fig. 3.

In the ideal case, this is for bi-stable plates with perfect orthogonal symmetry, the values for the critical displacement would be equal. However, any real specimen will not respond in a perfect orthogonal symmetrical manner as the manufacturing process has limited accuracy. Thus, the static curvature of each state show different values for any real specimen. Therefore, each stable configuration has different critical displacement values. At this point we define stable state 2 as the configuration exhibiting a smaller curvature, and stable state 1 with the larger. We define the x-direction to coincide with the curved direction of stable state 1, hence the curved direction of stable state 2 coincides with the y-direction, as can be seen in Fig. 3. For the realistic case where asymmetric curvatures occur, the critical displacement for each stable state would be associated to the static deflection of a point laying on a line perpendicular to the flat direction of the relevant configuration. For simplicity this are defined using the reference points P_x and P_y shown in Fig. 3, where the associated critical displacements values for each stable state are presented.

As a result of the differences in the static curvature of any real bi-stable plate an asymmetric potential double well results, as schematically shown in Fig. 4. It can be seen that the energy to pass the maximum (hilltop) depends on which state the system is initially oscillating.

3 Model for dynamics of oscillations including snap-through

A model for the dynamics of a bi-stable plate confined to a stable configuration was developed in Ref. [6]. The nonlinear modal equations of motion were written as [6]

$$\ddot{W_{10}} + 2\zeta_{w_1}\omega_{w_1}\dot{W_{10}} + \omega_{w_1}^2 W_{10} + \alpha_{11}W_{10}^2 + \alpha_{13}W_{10}W_{11} = \mathcal{Q}_{10}\sin(\Omega t), \tag{1}$$

$$\ddot{W_{01}} + 2\zeta_{w_2}\omega_{w_2}\dot{W_{01}} + \omega_{w_2}^2 W_{01} + \alpha_{22}{W_{01}}^2 + \alpha_{23}W_{01}W_{11} = \mathcal{Q}_{01}\sin(\Omega t), \tag{2}$$

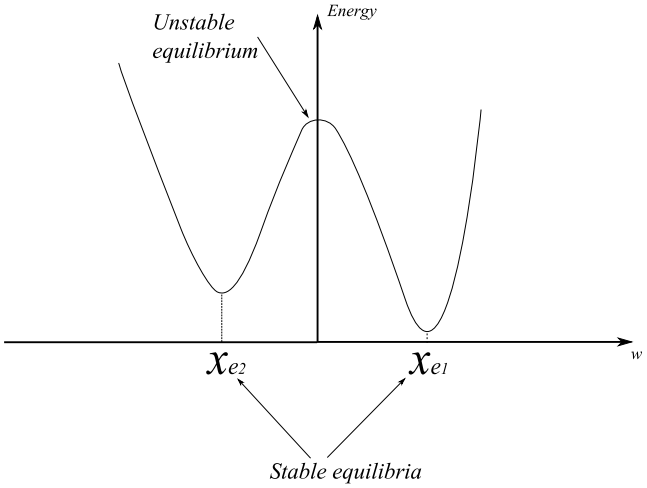


Figure 4: Potential well schematic diagram for a bi-stable plate.

$$\ddot{W_{11}} + 2\zeta_{w_3}\omega_{w_3}\dot{W_{11}} + \omega_{w_3}^2 W_{11} = \mathcal{Q}_{11}\sin(\Omega t), \tag{3}$$

where W_{10} is the time response coefficient of the transverse displacement for mode w_1 at 17.6 Hz, W_{01} is the time response coefficient of the transverse displacement for mode w_2 at 19.4 Hz, W_{11} is the time response coefficient of the transverse displacement for mode w_3 at 45.4 Hz, Ω is the forcing frequency, $\mathcal{Q}_{ij}$ is the modal participation factor for the time response W_{ij}, α_{ij} is the coefficient for the nonlinear quadratic term for an interaction between modes (w_i, w_j). The total transverse displacement for an arbitrary point on the plate is given by adding the contribution of each mode to the deflection as

$$x = \Theta_{w_1}(x,y)_{P_i} W_{10} + \Theta_{w_2}(x,y)_{P_i} W_{01} + \Theta_{w_3}(x,y)_{P_i} W_{11}, \tag{4}$$

where $\Theta_{x_1}(x,y)_{P_i}$, $\Theta_{w_2}(x,y)_{P_i}$ and $\Theta_{w_3}(x,y)_{P_i}$ are the values of the mode shapes associated with modes w_1, w_2 and w_1 evaluated at the arbitrary point P_i.

In order for the presented model to account for the oscillations involving the two stable configurations the results shown in section 2 are employed. As discussed then, only after reaching a critical deflection threshold the snap-through instability would be triggered. Thus, using the *critical displacement* condition to mark the onset of snap-through, we introduce a piece-wise defined restoring force into equations (1)-(3) to obtain,

$$\ddot{W_{10}} + 2\zeta_{w_1^{si}}\omega_{w_1^{si}}\dot{W_{10}} + F_1(w) = \mathcal{Q}_{10}\sin(\Omega t), \tag{5}$$

$$\ddot{W_{01}} + 2\zeta_{w_2^{si}}\omega_{w_2^{si}}\dot{W_{01}} + F_2(w) = \mathcal{Q}_{01}\sin(\Omega t), \tag{6}$$

$$\ddot{W_{11}} + 2\zeta_{w_3^{si}}\omega_{w_3^{si}}\dot{W_{11}} + F_3(w) = \mathcal{Q}_{11}\sin(\Omega t), \tag{7}$$

where the restoring force for each mode is given by

$$F_1(w) = \begin{cases} \omega_{w_1^{s2}}^2(W_{10} + w_e^{s2}) + \alpha_{11}(W_{10} + w_e^{s2})^2 \\ +\alpha_{13}(W_{10} + w_e^{s2})(W_{11} + w_e^{s2}), & for\ w(x,y,t) < 0 \\ 0, & for\ w(x,y,t) = 0 \\ \omega_{w_1^{s2}}^2(W_{10} - w_e^{s1}) + \alpha_{11}(W_{10} - w_e^{s1})^2 \\ +\alpha_{13}(W_{10} - w_e^{s1})(W_{11} - w_e^{s1}), & for\ w(x,y,t) > 0 \end{cases}, \tag{8}$$

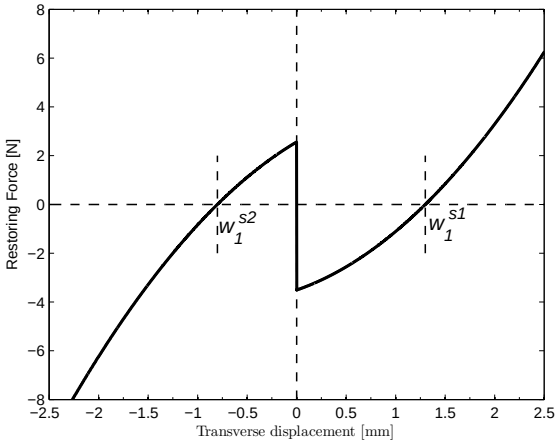


Figure 5: Quadratic restoring force including snap-through nonlinearity for mode w_1.

$$F_2(w) = \begin{cases} \omega^2_{w_2^{s2}}(W_{01} + w_e^{s2}) + \alpha_{11}(W_{10} + w_e^{s2})^2 \\ +\alpha_{13}(W_{10} + w_e^{s2})(W_{11} + w_e^{s2}), & for\ w(x,y,t) < 0 \\ 0, & for\ w(x,y,t) = 0 \\ \omega^2_{w_2^{s1}}(W_{01} - w_e^{s1}) + \alpha_{22}(W_{10} - w_e^{s1})^2 \\ +\alpha_{23}(W_{01} - w_e^{s1})(W_{11} - w_e^{s1}), & for\ w(x,y,t) > 0 \end{cases}, \tag{9}$$

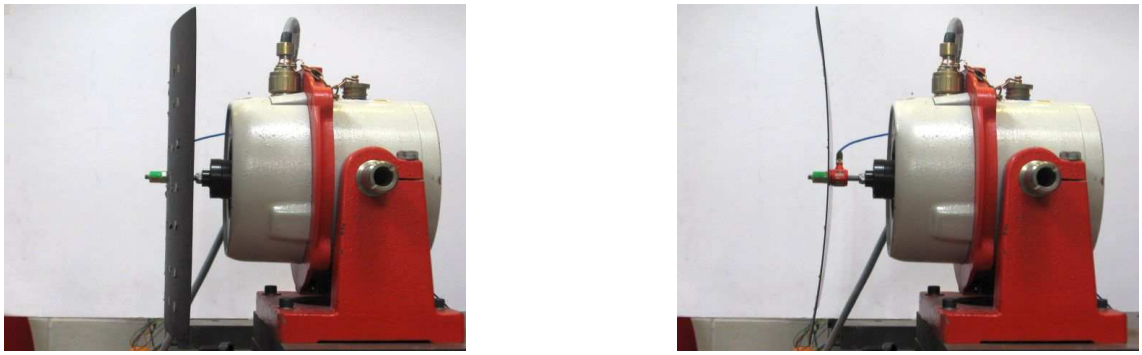
$$F_3(w) = \begin{cases} \omega^2_{w_3^{s2}}(W_{11} + w_e^{s2}(\Omega)), & for\ w(x,y,t) < 0 \\ 0, & for\ w(x,y,t) = 0 \\ \omega^2_{w_3^{s1}}(W_{11} - w_e^{s1}(\Omega)), & for\ w(x,y,t) > 0 \end{cases}, \tag{10}$$

where $\omega_{w_i^{sj}}$ is the natural frequency of the i mode in the j state, for example $\omega_{w_3^{s1}}$ is the natural frequency of mode w_3 for stable state 1, and the time response and nonlinear coupling coefficients, W_{ij} and α_{ij} were defined above. The equilibrium positions for state 1 and state 2 w_e^{s1} and w_e^{s2} are assumed to be equal to the static critical displacements. The above definition gives a piece-wise quadratic restoring force for modes w_1 and w_2, and a piece-wise linear restoring force for mode w_3. For illustration, the restoring force for mode w_1 is schematically shown in Fig. 5.

4 Experimental dynamic response

An unsymmetrically laminated $[0_4 - 90_4]_T$ bi-stable plate with dimensions 300x300 mm is used as the specimen for this study. The two stable configurations of the specimen are shown in Figs. 6(a) and 6(b). The experimental assembly used to perform the experiments is shown in Fig. 7. The experimental specimen was attached to a Ling shaker (electromechanical shaker) in order to induce vibration to the system. The external forcing was applied at the centre of the bi-stable composite plate in order to simulate free edge boundary conditions. A load cell was located between the shaker and the plate to measure the external force acting on the specimen. The experimental specimen was mounted on a steel table of large mass in order to ensure no interaction between the plate and its surroundings as seen in Fig. 7. A differential laser vibrometer measured relative displacement between the centre of the specimen and a given point on the laminate obtaining time series for the displacement response.

The main objective of the experimental tests was to investigate the main features of dynamically induced snap-through. To illustrate this the displacement and force response for a forcing frequency of 35 Hz for snap-through from state 2 to state 1 are shown in Fig. 8. Inspecting Fig. 8(a) at around



(a) State 1 (b) State 2

Figure 6: Bi-stable plate mounted on Ling shaker. (a) Stable state 1. (b) Stable state 2.

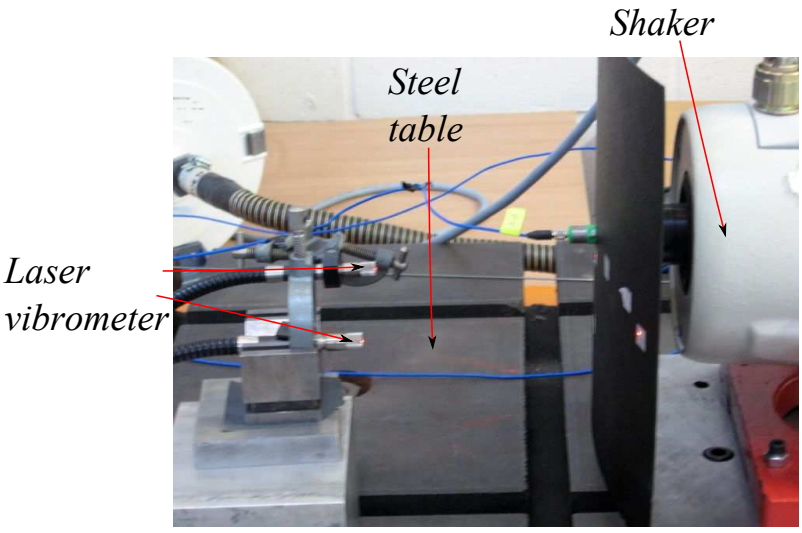
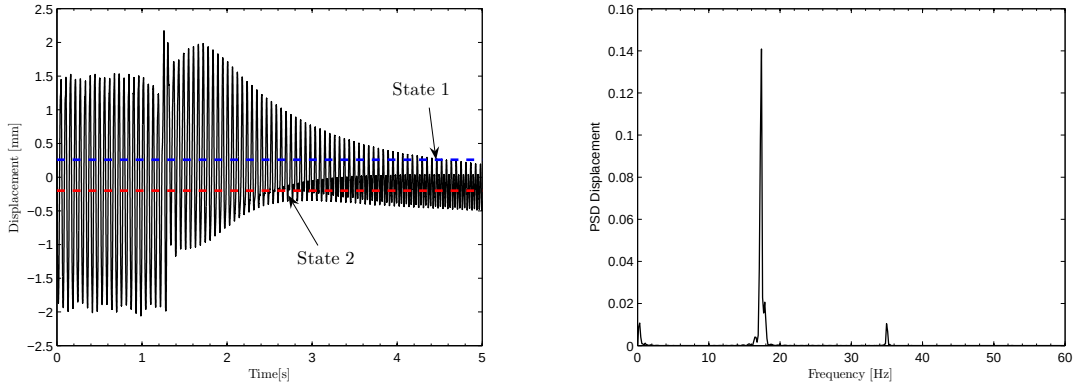
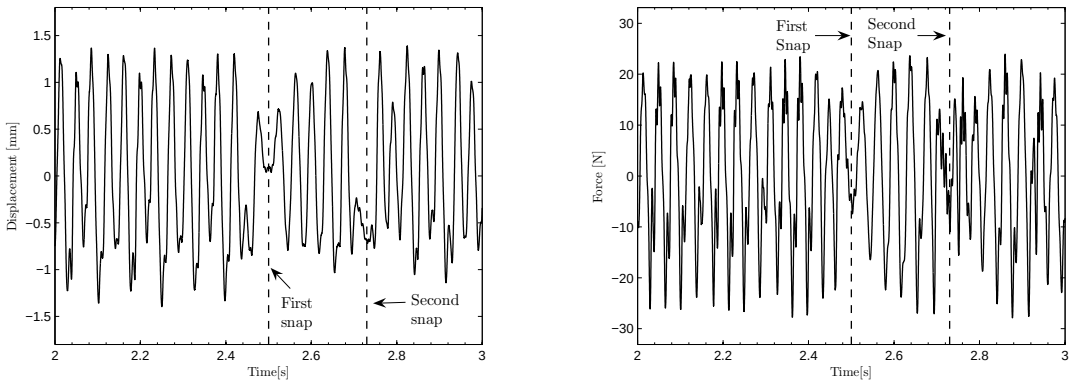


Figure 7: Experimental Assembly. Ling shaker V405, vibrometer OFV-552



(a) (b)

Figure 8: Experimental response for a dynamically induced snap-through from state 2 to state 1. Forcing frequency Ω=35.0 Hz.(a) Displacement time response. (b) Displacement power spectrum.



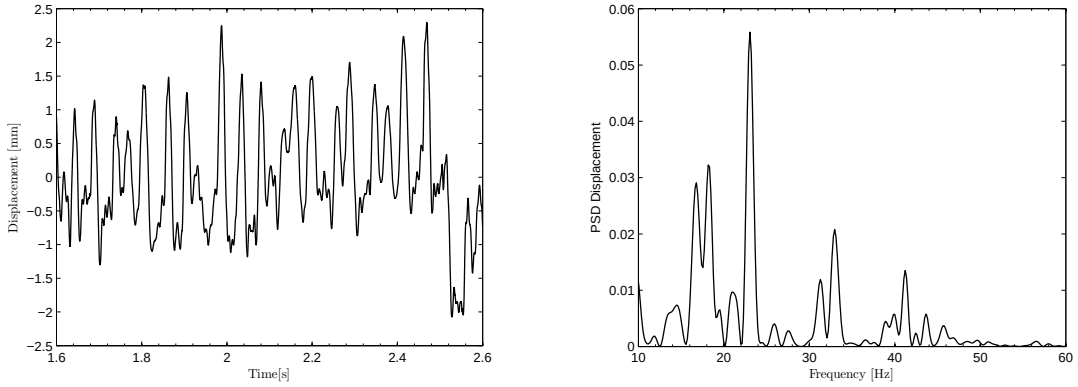
(a) (b)

Figure 9: Experimental response for a dynamically induced snap-through from state 1 to constant snap-through. Forcing frequency Ω=27.0 Hz.(a) Displacement time response. (b) Force time response.

1.2 s a very noticeable spike appears in both the displacement and force time series, this marks the instant where the snap-through is dynamically triggered. An interesting observation is the difference between the centre value of the displacement response before an after the snap-through. This corresponds to the displacement underwent by the structure to snap from stable state 2 to stable state 1. The time series then settles down to a similar centre value due to the measuring nature of laser vibrometers (constant displacements cannot be measured with a laser as the velocity would be zero).

As the forcing amplitude is further increased a dynamic snap-through from state 1 to state 2 is induced. As described in Fig. 4 due to manufacturing asymmetries the difference between the energy required to overcome the unstable equilibrium separating stable equilibria is different. As a result, when a snap-through is induced from an initial condition laying in the potential well of stable state 1, the energy given to the plate is sufficient to trigger a snap-through back from stable state 2 to state 1 as shown in Fig. 9. The first snap-through is induced at around 2.44 s, where a marked change in both the displacement and force time responses is seen. After this event the plate returns to oscillate around stable state 1 for a brief time followed by a second snap-through at 2.6 s.

If enough energy is given to the system a state of constant snap-through between states is observed as presented in Fig. 10(a). In this case the energy put into the system is large enough for it



(a) (b)

Figure 10: Experimental response for a constant snap-through between stable states. Forcing frequency Ω=23.0 Hz.(a) Displacement time response. (b) Displacement power spectrum.

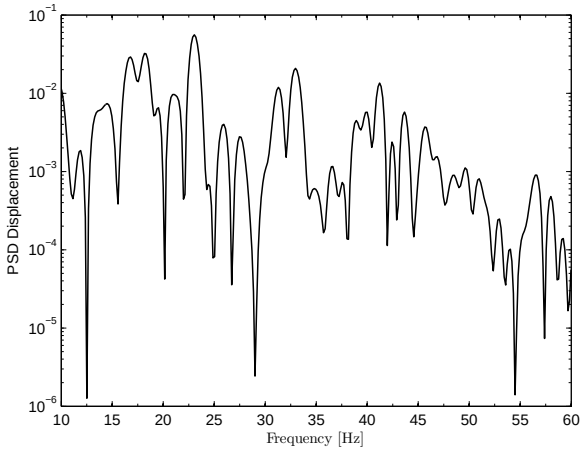
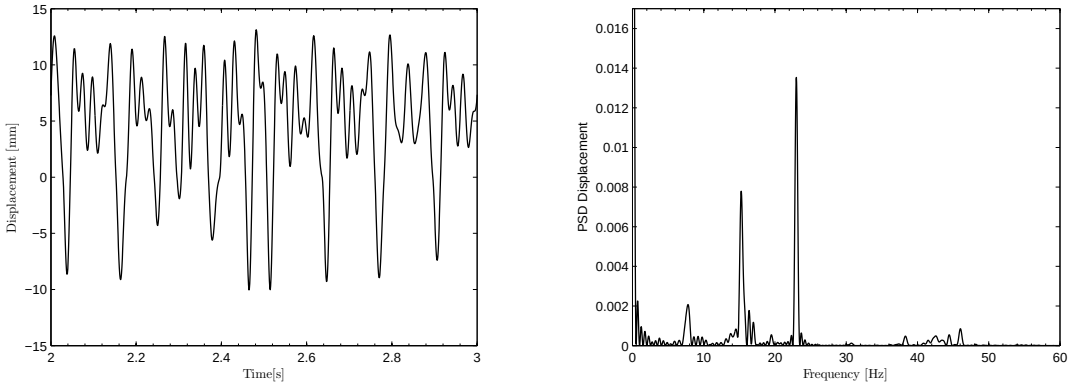


Figure 11: Experimental displacement power spectrum showing broadband peaks for a forcing frequency of Ω=23.0 Hz.

to immediately jump back to stable state 1, thus a continuous steady state snapping between stable states is observed. These are, in energy terms, continuous cross-well oscillations. This response shows a very erratic non repeating behaviour in the time response. Inspecting the spectrum with a logarithmic scale for the PDS of the displacement in Fig. 11, broadband peaks are observed in the response for this forcing amplitude. The non-repeating character of the displacement response and the broadband spectrum showing not only peaks at modal frequencies and its integer multiples, but also peaks at incommensurate frequencies of the modes is an indication of a chaotic response [9].

5 Simulation results and model validation

To validate the proposed model, numerical simulations are obtained and compare to the experimental results for the complete dynamics of the plate. A simulated time series showing oscillations involving constant snap-through between stable states is given in Fig. 12(a) for a forcing frequency of 23 Hz. The time response shows a non-repeating behaviour where oscillations between the minimum and maximum values appear to occur near a dominant frequency. However periods of oscillations around only one state followed for oscillations around both stable states are a clear sign of the non-periodic nature of the response. The power spectrum of the time series shows



(a) (b)

Figure 12: Simulated response for a dynamically induced snap-through from state 1 to constant snap-through. Forcing frequency Ω=23.0 Hz. (a) Displacement time response. (b) Displacement power spectrum. Compare with experimental data in Figs. 10(a) and 10(b).

more than three peaks at incommensurate frequencies, around 7, 13, 41 and 43 Hz in Fig. 12(b). Additionally, broadband peaks are observed for this response regime in Fig. 13. The obtained results are in good agreement with the observed experimental features of oscillations including snap-through, in particular the same indications pointing to a chaotic behaviour for this response regime are captured by the model.

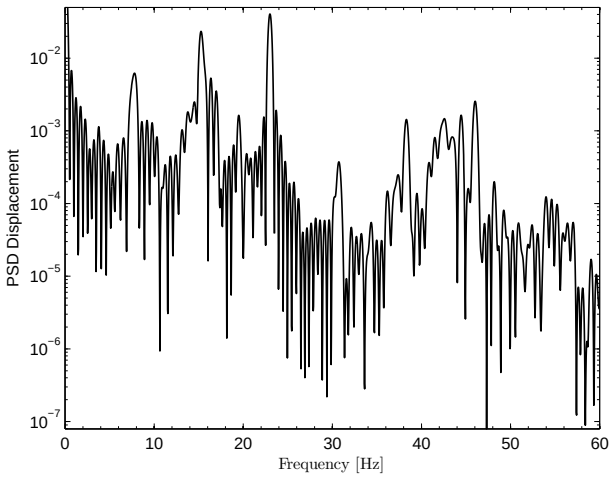


Figure 13: Simulated power spectrum for the displacement response of a dynamically induced snap-through from state 1 to constant snap-through showing a broadband peaks. Forcing frequency Ω=23.0 Hz. Compare with experimental data in Fig. 11.

6 Summary and conclusions

The dynamic features of snap-through for a bi-stable plate were experimentally investigated and modelled using a simple low order model. A condition marking the onset of snap-through governed by a displacement threshold was defined as *critical displacement*. Experimental results showed complex nonlinear behaviour related to the snap-through instability for steady state jumps between stable states of the bi-stable plate. Furthermore, evidence was observed indicating this behaviour

exhibits characteristics of chaotic oscillations. A good qualitative match was obtained for the dynamics of snap-through with the developed model. In particular, the model captured complex nonlinear oscillations occurring for continuous snap-through from one state to the other, matching the experimentally observed features indication a chaotic response. The insight gained on the dynamics of snap-through could be potentially exploited to develop actuation strategies to achieve morphing between stable states, i.e. desired snap-through, for applications incorporating bi-stable composites.

Acknowledgements

The authors would like to acknowledge the support of the European Commission; Andres F. Arrieta is supported by a Marie Curie RTN Research Fellowship.

References

[1] M.-L. Dano and M.W. Hyer: Thermally-induced deformation behavior of unsymmetric laminates. Int. J. Solids Struct. 35, 2101-2120 (1998)

[2] C. G. Diaconu, P. M. Weaver, F. Mattioni, Concepts for morphing airfoil sections using bi-stable laminated composite structures, *Thin-Walled Structures*, 46, (2008) 689-701.

[3] M. Schlecht, K. Schulte, Advanced calculation of the room-temperature shapes of unsymmetric laminates, *Journal of Composite Materials*, 33. (1999) 1472-1490.

[4] S.V. Sokorin and A.V. Terentiev: On Modal Interaction, Stability and Nonlinear Dynamics of a Model Two D.O.F. Mechanical System Performing Snap-Through Motion. Nonlinear Dyn. 16, 239-257 (1998)

[5] M.-L. Dano and M.W. Hyer: Snap-through of unsymmetric fiber-reinforced composite laminates. Int. J. Solids Struct. 39, 175-198 (2002)

[6] A.F. Arrieta, S.A. Neild and D.J. Wagg: Nonlinear dynamic response and modelling of a bi-stable composite plate for applications to adaptive structures. Nonlinear Dyn., 58, 259-272 (2009)

[7] A.F. Arrieta, F. Mattioni, S.A. Neild, P.M. Weaver, D.J. Wagg, and K. Potter: Nonlinear dynamics of a bi-stable composite laminate plate with applications to adaptive structures. In: 2nd European Conference for Aero-Space Sciences(EUCASS2007), Brussels, July (2007)

[8] A. Carrella,F. Mattioni, A.F. Arrieta, M.I. Friswell, D.J. Wagg, P.M. Weaver: Static And Dynamic Analysis Of A Bistable Plate For Application In Morphing Structures. In: 7th European conference on structural dynamics, Southampton, UK, July 7-9 (2008)

[9] J.M.T. Thompson and H.B. Stewart: Nonlinear Dynamics and Chaos. Wiley, (2002)

† *A.F. Arrieta and P. Hagedorn, System Reliability and Machine Acoustics, Dynamics and Vibrations Group Technische Universität Darmstadt, LOEWE-Zentrum AdRIA, Darmstadt, 64289 Germany*

* *D.J Wagg and S.A. Neild, Department of Mechanical Engineering, University of Bristol, University Walk, Bristol,U.K. BS8 1TR*